

Fikret Necati Catbas · Shamim Pakzad · Vitomir Racic
Aleksandar Pavic · Paul Reynolds *Editors*

Topics in Dynamics of Civil Structures, Volume 4

Proceedings of the 31st IMAC, A Conference
on Structural Dynamics, 2013



Conference Proceedings of the Society for Experimental Mechanics Series

Series Editor

Tom Proulx

Society for Experimental Mechanics, Inc.,

Bethel, CT, USA

For further volumes:

<http://www.springer.com/series/8922>

Fikret Necati Catbas • Shamim Pakzad • Vitomir Racic • Aleksandar Pavic
Paul Reynolds
Editors

Topics in Dynamics of Civil Structures, Volume 4

Proceedings of the 31st IMAC, A Conference on Structural
Dynamics, 2013

 Springer

المنارة للاستشارات

www.manaraa.com

Editors

Fikret Necati Catbas
Engineering Department
University of Central Florida
Orlando, FL, USA

Shamim Pakzad
Department of Civil and Environmental Engineering
Lehigh University
Bethlehem, PA, USA

Vitomir Racic
Department of Civil and Structural Engineering
University of Sheffield
Sheffield, UK

Aleksandar Pavic
Department of Civil and Structural Engineering
University of Sheffield
Sheffield, UK

Paul Reynolds
Department of Civil and Structural Engineering
University of Sheffield
Sheffield, UK

ISSN 2191-5644 ISSN 2191-5652 (electronic)
ISBN 978-1-4614-6554-6 ISBN 978-1-4614-6555-3 (eBook)
DOI 10.1007/978-1-4614-6555-3
Springer New York Heidelberg Dordrecht London

Library of Congress Control Number: 2013940064

© The Society for Experimental Mechanics, Inc. 2013

This work is subject to copyright. All rights are reserved by the Publisher, whether the whole or part of the material is concerned, specifically the rights of translation, reprinting, reuse of illustrations, recitation, broadcasting, reproduction on microfilms or in any other physical way, and transmission or information storage and retrieval, electronic adaptation, computer software, or by similar or dissimilar methodology now known or hereafter developed. Exempted from this legal reservation are brief excerpts in connection with reviews or scholarly analysis or material supplied specifically for the purpose of being entered and executed on a computer system, for exclusive use by the purchaser of the work. Duplication of this publication or parts thereof is permitted only under the provisions of the Copyright Law of the Publisher's location, in its current version, and permission for use must always be obtained from Springer. Permissions for use may be obtained through RightsLink at the Copyright Clearance Center. Violations are liable to prosecution under the respective Copyright Law.

The use of general descriptive names, registered names, trademarks, service marks, etc. in this publication does not imply, even in the absence of a specific statement, that such names are exempt from the relevant protective laws and regulations and therefore free for general use.

While the advice and information in this book are believed to be true and accurate at the date of publication, neither the authors nor the editors nor the publisher can accept any legal responsibility for any errors or omissions that may be made. The publisher makes no warranty, express or implied, with respect to the material contained herein.

Printed on acid-free paper

Springer is part of Springer Science+Business Media (www.springer.com)

Preface

Topics in Dynamics of Civil Structures, Volume 4: Proceedings of the 31st IMAC, A Conference on Structural Dynamics, 2013 represents one of the seven volumes of technical papers presented at the 31st IMAC, a conference and exposition on structural dynamics, 2013, organized by the Society for Experimental Mechanics, held in Garden Grove, California, from February 11 to 14, 2013. The full proceedings also include volumes on nonlinear dynamics; experimental dynamics substructuring; dynamics of bridges; model validation and uncertainty quantification; special topics in structural dynamics; and modal analysis.

Each collection presents early findings from experimental and computational investigations on an important area within structural dynamics. The dynamics of civil structures is one of these areas.

Understanding the dynamic response of large civil structures improves design and safety, extends life, and reduces maintenance. IMAC has become a principal technical venue for dissemination of the latest techniques devoted to field testing of civil structural systems and components, processing of response data and identification of dynamic structural properties, calibration and validation of numerical structural models, and assessment of structural condition based on dynamic properties.

The organizers would like to thank the authors, presenters, session organizers, and session chairs for their participation in this track.

Orlando, FL, USA
Bethlehem, PA, USA
Sheffield, UK
Sheffield, UK
Sheffield, UK

Fikret Necati Catbas
Shamim Pakzad
Vitomir Racic
Aleksandar Pavic
Paul Reynolds

Contents

1	Accurate Damping Estimation by Automated OMA Procedures	1
	C. Rainieri and G. Fabbrocino	
2	Real-Time Structural Health Monitoring and Damage Detection	11
	Yavuz Kaya and Erdal Safak	
3	Improved Substructure Identification Through Use of an Active Control Device	21
	Charles DeVore, Erik A. Johnson, and Richard E. Christenson	
4	Hybrid MPC: An Application to Semiactive Control of Structures	27
	Wael M. Elhaddad and Erik A. Johnson	
5	Findings with AVC Design for Mitigation of Human Induced Vibrations in Office Floors	37
	Donald Nyawako, Paul Reynolds, and Malcolm Hudson	
6	Power Requirements for Active Control of Floor Vibrations	45
	M.J. Hudson, P. Reynolds, and D.S. Nyawako	
7	Tuning TMDs to “Fix” Floors in MDOF Shear Buildings	55
	Jennifer Rinker	
8	Precise Stiffness Control with MR Dampers	61
	Marcin Maślanka and Felix Weber	
9	Employing Hybrid Tuned Mass Damper to Solve Off-Tuning Problems for Controlling Human Induced Vibration in Stadia	71
	Nima Noormohammadi and Paul Reynolds	
10	Semi-Active TMD Concept for Volgograd Bridge	79
	Felix Weber, Johann Distl, and Marcin Maślanka	
11	A New Shape Memory Alloy-Based Damping Device Dedicated to Civil Engineering Cables	89
	G. Helbert, L. Dieng, T. Lecompte, S. Arbab-Chirani, S. Calloch, and P. Pilvin	
12	Using Pall Friction Dampers for Seismic Retrofit of a 4-Story Steel Building in Iran	101
	Seyed Mehdi Zahraei, Alireza Moradi, and Mohammadreza Moradi	
13	Modal Identification of a 5-Story RC Building Tested on the NEES-UCSD Shake Table	109
	Rodrigo Astroza, Hamed Ebrahimiyan, Joel P. Conte, Jose I. Restrepo, and Tara C. Hutchinson	
14	Modal Testing of a Repaired Building After 2010 Chile Earthquake	119
	Manuel Archila, Ruben Boroschek, Carlos E. Ventura, and Sheri Molnar	
15	System Identification and Displacement Profiles of Multi-Span Skewed Bridges with Seat Type Abutments	127
	Seku Catacoli, Carlos E. Ventura, and Steve McDonald	

16	Robustness of Modal Parameter Estimation Methods Applied to Lightweight Structures	137
	Kristoffer A. Dickow, Poul Henning Kirkegaard, and Lars V. Andersen	
17	A Comparative Study of System Identification Techniques Under Ambient Vibration	145
	Muhammad S. Rahman and David T. Lau	
18	Some Implications of Human-Structure Interaction	155
	Lars Pedersen	
19	Evolution of Dynamic Properties of a 5-Story RC Building During Construction	163
	Rodrigo Astroza, Hamed Ebrahimián, Joel P. Conte, Tara C. Hutchinson, and Jose I. Restrepo	
20	Structural Dynamic Parameter Identification and the Effect of Test Techniques	175
	A. Devin, P.J. Fanning, C.J. Middleton, and A. Pavić	
21	Comparison of Damping Models for Space Flight Cables	183
	Kaitlin Spak, Gregory Agnes, and Daniel Inman	
22	Forced 3D Nonlinear Dynamics of a Hanging Cable Under Multiple Resonance Conditions	195
	R. Alaggio, F. Benedettini, G. Rega, and D. Zulli	
23	Computationally Efficient Design of Semiactive Structural Control in the Presence of Measurement Noise	203
	Mahmoud Kamalzare, Erik A. Johnson, and Steven F. Wojtkiewicz	
24	Optimal Nonlinear Control Using a Non-quadratic Cost Function for Scalar Systems	211
	Elham Hemmat-Abiri and Erik A. Johnson	
25	Optimal Sensor Placement with a Statistical Criterion for Subspace-Based Damage Detection	219
	Michael Döhler, Kenny Kwan, and Dionisio Bernal	
26	Application of Efficient Model Correction for Damage Assessment Using Limited Measurements	231
	Yi-Cheng Wu and Chin-Hsiung Loh	
27	Theory Based Sensitivity Analysis and Damage Detection of Steel Roof Sheeting for Hailstone Impact	243
	P. Sharafi, Lip H. Teh, and Muhammad N.S. Hadi	
28	Long-Term Dynamic Monitoring of an Offshore Wind Turbine	253
	Christof Devriendt, Filipe Magalhães, Mahmoud El Kafafy, Gert De Sitter, Álvaro Cunha, and Patrick Guillaume	
29	Nondestructive Evaluation of Surface Crack Depth in Concrete	269
	Ninel Alver and Masayasu Ohtsu	
30	An Improved Methodology for Anomaly Detection Based on Time Series Modeling	277
	Qipei Mei and Mustafa Gul	
31	Response Surface Model Updating for Nonlinear Structures	283
	Golnaz Shahidi and Shamim N. Pakzad	
32	Application of Multivariate Statistically Based Algorithms for Civil Structures Anomaly Detection	289
	Masoud Malekzadeh, Mustafa Gul, and F. Necati Catbas	
33	System Identification of a Three-Story Precast Concrete Parking Structure	299
	Andrea Belleri, Babak Moaveni, and Jose I. Restrepo	
34	Structural Damage Localization Using Sensor Cluster Based Regression Schemes	307
	Ruigen Yao and Shamim N. Pakzad	
35	Operational Modal Analysis Based on Multivariable Transmissibility Functions: Revisited	317
	Wout Weijtjens, Gert de Sitter, Christof Devriendt, and Patrick Guillaume	
36	Diagnosis of Building Vibration Sources via Time-Frequency Analysis	327
	Linda M. Hanagan and Martin W. Trethewey	

37	Medial-Lateral Gait Patterns in Healthy Adult Walkers	337
	Daniel Claff, M.S. Williams, A. Blakeborough, and J. Stebbins	
38	Quantifying Differences Between Walking Locomotion on Rigid and Flexible Pavements	349
	M.V. Istrate, S. Zivanovic, A. Lorenzana, N. Ibán, and H.V. Dang	
39	Using MSD Model to Simulate Human-Structure Interaction During Walking	357
	E. Shahabpoor, A. Pavic, and V. Racic	
40	Effect of Sensory Stimuli on Dynamic Loading Induced by People Bouncing	365
	Vitomir Racic, James M.W. Brownjohn, Shu Wang, Mark T. Elliot, and Alan Wing	
41	Design and Construction of a Very Lively Bridge	371
	S. Živanović, R.P. Johnson, H.V. Dang, and J. Dobrić	
42	Experimental Results from a Laboratory Test Program to Examine Human-Structure Interaction	381
	Kelly A. Salyards and Nicholas C. Noss	
43	Alleviation of Wind-induced Vibrations of Railings in a Building	391
	C.M. Hou and W.D. Zhu	
44	Operational Modal Analysis of a Slender Footbridge to Serviceability Purposes	403
	Anna Cappellini, Stefano Manzoni, Marcello Vanali, and Elena Mola	
45	Optimal Sensor Placement for Structural Health Monitoring of Power Transmission Tower-Line Systems	415
	José Antonio Vergara, Rafael Castro-Triguero, David Bullejos, Rafael Gallego, and Diego Zamora	
46	Evaluation of Economical Dynamic Exciters for Vibration Testing of Bridges	423
	E.V. Fernstrom, J.L. Carreiro, and K.A. Grimmelman	
47	Assessment of Floor Vibrations for Building Re-use: A Case Study	435
	Brad Pridham	
48	Experimental Validation on a Continuous Modulated Wave-Form Command Shaping Applied on Damped Systems	445
	Khaled A. Alhazza	
49	Quantification of Damping Effect of Humans on Lightly Damped Staircases	453
	Anna Cappellini, Stefano Manzoni, and Marcello Vanali	
50	Robust Design Optimization of Steel Moment Resisting Frame Under Ground Motion Uncertainty	461
	Zhifeng Liu, Sez Atamturktur, and Hsein Juang	
51	Structural Assessment of Fort Sumter Masonry Coastal Fortification Subject to Foundation Settlements .	471
	Sez Atamturktur, Saurabh Prabhu, and Rick Dorrance	
52	Condition Assessment of a Coal Mine Shiploader	485
	Carlos E. Ventura, Freddy Pina, Steve Yee, and Christopher Prychon	
53	Experimental Assessment of Structure Borne Noise Generated by a Braking Resistor	495
	F. Braghin, F. Cheli, and G. Galli	
54	Pre-Test Nonlinear FE Modeling and Simulation of a Full-Scale Five-Story Reinforced Concrete Building	503
	Hamed Ebrahimián, Rodrigo Astroza, Joel P. Conte, Jose I. Restrepo, and Tara C. Hutchinson	
55	The Dynamic Stiffening Effects of Non-Structural Partitions in Building Floors	513
	C.J. Middleton and A. Pavic	
56	Experimental Characterization and Predictive Modeling of a Residential-Scale Wind Turbine	521
	Jordan B. Chipka, Andrew R. Lisicki, Chuong T. Nguyen, Stuart G. Taylor, Gyuhae Park, Curtt N. Ammerman, and Charles R. Farrar	

57 Sizing Optimization of Trapezoidal Corrugated Roof Sheeting, Supporting Solar Panels, Under Wind Loading	535
P. Sharafi, Lip H. Teh, and Muhammad N.S. Hadi	
58 Establishment of Optimized Digging Trajectory for Hydraulic Excavator	543
Tatsuya Yoshida, Takayuki Koizumi, Nobutaka Tsujiuchi, Kan Chen, and Yozo Nakamoto	
59 Modeling, Simulation, and Optimization of California High-Speed Rail Bridge Under Earthquakes	555
Yong Li and Joel P. Conte	

Chapter 1

Accurate Damping Estimation by Automated OMA Procedures

C. Rainieri and G. Fabbrocino

Abstract Systems and techniques for fast damage detection based on vibration analysis are becoming very attractive in different engineering fields. Modal-based damage detection algorithms are well-known techniques for structural health assessment. However, the lack of automated modal identification and tracking procedures has been for long a relevant limit to their extensive use. The development of several automated output-only modal identification procedures in the last few years has led to a renewed interest in modal-based damage detection. However, robustness of automated modal identification algorithms, computational efforts and reliability of modal parameter estimates (in particular, damping) still represent open issues. In this paper, a novel algorithm for automated output-only modal parameter estimation is adopted to obtain reliable and very accurate modal parameter estimates. An extensive validation of the algorithm for continuous monitoring application is carried out based on simulated data. The obtained results point out that the algorithm provides fairly robust, accurate and precise estimates of the modal parameters, including damping ratios. This may potentially lead to a standardized, extensive characterization of modal damping ratios in structures, which is useful to gain knowledge about damping mechanisms in structures and to develop predictive models.

Keywords Vibration based structural health monitoring • Automated operational modal analysis • Damping • Second order blind identification • Stochastic subspace identification

1.1 Introduction

Vibration based Structural Health Monitoring (SHM) techniques are again gaining in popularity nowadays thanks to the recent development of several algorithms for automated identification [1] and tracking [2] of modal parameters based on Operational Modal Analysis (OMA) methods. Damage detection techniques based on changes of the modal parameters of the monitored structure over time are well-established methods for structural health assessment [3], in spite of some limitations in terms of damage localization and, above all, quantification, as well as drawbacks related to sensitivity to measurement quality and environmental and operational factors [4]. Nevertheless, the continuous monitoring of modal parameters has a large potential in performance and health assessment of civil engineering structures [5]. Applications range from prompt detection of damage and degradation phenomena [6] to post-earthquake health assessment and emergency management [7, 8]. An automated, accurate estimation of modal parameters plays also a primary role in the assessment of the dynamic behavior of complex structural systems such as geotechnical [9, 10] and historical structures [11, 12]. Even if several solutions for automated output-only modal identification are currently available, they show different performance in terms of robustness and accuracy of estimates. This can be addressed also to the drawbacks [1] typically encountered in the algorithms:

- threshold based peak and physical pole detection;
- need of a preliminary calibration phase at each new application;

C. Rainieri (✉) • G. Fabbrocino
Structural and Geotechnical Dynamics Laboratory StreGa, Dipartimento di Bioscienze e Territorio, University of Molise,
Via Duca degli Abruzzi, 86039 Termoli, Italy
e-mail: carlo.rainieri@unimol.it, giovanni.fabbrocino@unimol.it

- static settings of thresholds and parameters which may be unsuitable to track the natural changes in modal properties of structures due to damage or environmental effects;
- sensitivity to noise, problems of false or missed identification.

Moreover, a number of algorithms do not provide damping estimates; whenever they are able to estimate modal damping, the resulting values are usually very scattered. The fairly large scatter associated to damping estimates, in comparison with that of natural frequency and mode shape estimates, is well documented in the literature. Even if the scatter can be partially addressed to inherent limitations of the estimators and the adoption of an equivalent viscous damping model [13], appropriate data processing procedures have to be adopted in order to minimize the estimation error and enhance robustness and accuracy of automated modal identification algorithms also with respect to the problem of modal damping estimation.

A thorough performance assessment of automated modal identification algorithms is rarely reported in the literature. However, the evaluation of the quality of modal estimates automatically extracted from measurements of the dynamic response of structures under operational conditions is a fundamental step in view of proper post-processing of modal parameters for damage detection and performance evaluation purposes.

In the present paper, a procedure for fully automated output-only modal identification, based on the combination of different OMA techniques, is described. The idea behind the novel approach is the simplification of the analysis and interpretation of the stabilization diagram for the separation of physical from spurious poles taking advantage of the Blind Source Separation (BSS) [14] operated by the Second Order Blind Identification (SOBI) [15, 16] procedure. The main objective of the novel strategy is a robust and accurate identification of modal parameters in operational conditions, including modal damping ratios even if in the limits of the adopted estimator. Its key feature is the absence of any analysis parameters to be tuned at each new monitoring application. In the development of the algorithm, specific attention has been devoted to the control of response time and computational efforts [17], also through a reduction of the length of the analyzed records, without affecting the quality of the estimates. This is relevant, in particular, for SHM applications in seismically prone areas [2].

A thorough performance assessment of the algorithm is attempted based on automated processing of a large number of simulated datasets. The herein illustrated results show that the algorithm is characterized by a high success rate. The performance assessment based on simulated data is still in progress. However, the preliminary results seem to confirm the robustness and accuracy of the algorithm, which therefore has a potential in the continuous vibration based monitoring of civil structures.

1.2 Theoretical Background of the Automated Modal Identification Algorithm

The core of the novel automated modal identification algorithm is the Stochastic Subspace Identification (SSI) [18] method for OMA. However, it is not directly applied to the multivariate time series of the structural response but, after a pre-processing step, to the single sources obtained from the Joint Approximate Diagonalization (JAD) [19] of a number of time shifted covariance matrices.

SSI is classified as a time domain, parametric modal identification method. When parametric system identification techniques are used for the estimation of the modal parameters of structures, the definition of the model order, equal to twice the number of eigenfrequencies, represents the key issue. The control theory provides several techniques to automatically set the model order in a way able to maximize the prediction capacity of the identified model [20]. However, when SSI is applied in the context of experimental modal analysis, the attention is not focused on the prediction capability of the model as such, but on the possibility to get accurate and reliable estimates of the modal parameters. In order to find the modal properties of the system it is worth plotting a stabilization diagram. The order of the system is over-specified and the search for vertical alignments of stable poles allows for the discrimination of physical from spurious modes. Even if the stabilization diagram plays a primary role in experimental modal analysis, the selection of physical modes in the alignments of stable poles is often not straightforward, since the quality of the stabilization diagram depends on a number of parameters (number of block rows, maximum model order) and thresholds (allowable scatter between the modal properties evaluated at consecutive model orders) [18, 21] resulting in a relevant role of the analyst's judgement.

The stabilization diagram represents a useful tool for bias errors identification [22], such as the bias of the model, related to spurious modes, and the bias of the modes. Spurious modes can be classified as noise modes, which arise due to physical reasons—measurement noise, characteristics of excitation -, and mathematical modes, due to over-estimation of the system order. The stabilization diagram allows for the discrimination of most spurious modes, since they often do not fulfil stabilization criteria like in the case of physical poles. Other spurious poles can be identified and removed according to physical criteria, for instance, the expected damping ratio range. The bias of the modes can be associated, on the other

hand, to the under-estimation of the system order, so that a single identified mode is actually the combination of different modes (either physical or noisy). If the stabilization diagram is plotted until appropriately high values of the model order, the splitting of one column in the stabilization chart into two separate columns, starting from a given model order, is a commonly observed phenomenon. Thus, the mode estimate is biased below this model order since it is the result of the combination of different poles. A bias of the modes may occur also if, for a given maximum model order, the number of block rows is over-specified. In [23] it is shown how, for a given maximum model order, the quality of stabilization first improves and then gets worse for increasing values of the number of block rows. Thus, it is possible to carry out a sensitivity analysis for different values of the number of block rows in order to set it in a way able to minimize the variance of the modal parameter estimates at different model orders.

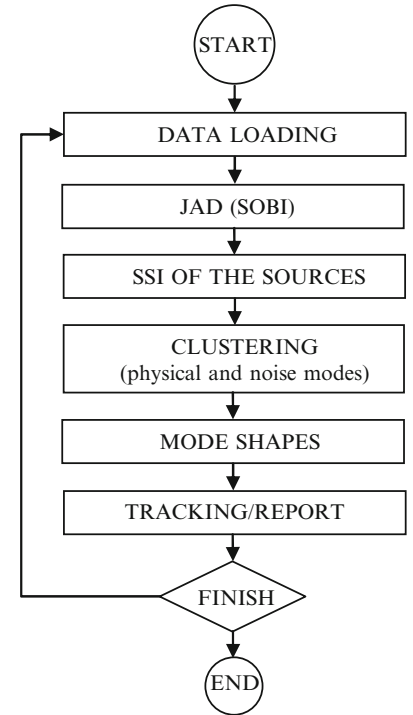
Evaluation and control of the accuracy of modal parameter estimates are critical in view of modal based damage detection. This basically relies on the comparison between the modal parameters or the modal model of a structure in a damaged state and those in a reference (undamaged) state. Shifts of natural frequencies, increases in damping, changes in mode shapes and other similar damage sensitive features are key parameters to assess the health state of the monitored structure [3]. A comprehensive review of these methods and the issues concerning the removal of environmental effects that also lead to changes in the modal parameters are out of the scope of the present paper. A number of methods for removal of environmental effects can be found in the literature [24, 25]. However, inaccurate identifications of modal parameters may still occur, thus negatively affecting the performance of damage detection algorithms [26], eventually leading to false alarms or missed identifications.

A number of simulation studies have pointed out how the modal parameter estimates provided by parametric methods such as SSI are by far more accurate than those provided by non-parametric procedures [27, 28]. However, the automated interpretation of stabilization diagrams is a very complex activity and a lot of research efforts have been spent on this task [28]. In the present paper a novel approach to the automated output-only modal parameter identification is proposed and it is extensively tested in order to assess the robustness, accuracy and precision of estimates in view of continuous monitoring applications. The method is based on SSI and the selection of physical poles in the stabilization diagram by clustering techniques, but it takes advantage of the BSS operated by SOBI at a preliminary stage in order to simplify the interpretation of the stabilization diagram. In fact, as a result of the BSS phase, the raw data associated to the measured structural response are transformed into sources [15] which can be well-separated (they show the contribution of a single mode to the structural response), not well-separated (noise or minor contributions from other modes could be superimposed to the contribution of the main mode) or just noise sources [17]. The sources are obtained through JAD of p time-shifted covariance matrices until the sum of the off-diagonal terms is under a user-defined threshold ϵ [19]. The idea under the proposed approach for automated output-only modal identification is to take advantage of the BSS to simplify the analysis of the data and the interpretation of the stabilization diagram by extracting the modal information from the single sources and not the multivariate time series of raw data. The sources are analyzed one-by-one according to the SSI method and the physical poles are separated from the spurious one by means of clustering techniques and mode validation criteria. The interpretation of the stabilization diagram, therefore, becomes easier since it basically reports information about only one mode at the time.

The flowchart of the proposed algorithm is shown in Fig. 1.1. The JAD phase leads to a preliminary discrimination between modal contributions and noise. The sources, including both modal and noise sources, are then passed, one-by-one, to the SSI-based step for the estimation of natural frequencies and damping ratios and identification of noise sources. This step of the algorithm takes advantage of advanced clustering techniques [29] to identify the physical poles. For each source, the poles provided by the SSI are grouped into clusters according to the hierarchical clustering method. The cluster characterized by the largest number of elements is selected as representative of the mode. At the end of this phase a further selection and validation of the poles in each cluster is carried out. Clusters that do not fulfil the validation checks are removed from the dataset. In particular, the average damping ratio in each cluster has to be in the range $0 \div 5\%$ and the corresponding coefficient of variation not larger than 10%. The first limitation is based on an empirical observation about the behaviour of civil structures in operational conditions, which are usually weakly damped. The second limitation comes from the observation that physical modes are characterized by small standard deviations, while spurious modes show much larger values of this parameter [28]. Checks about the physical significance of the estimates are also carried out (for instance, checks of the sign of damping). As a final stage, the natural frequency and damping ratio estimates in each cluster are normalized in the range $[0, 1]$ and a k-means clustering algorithm with $k = 2$ cluster is applied, allowing the presence of empty clusters. This last step eventually removes still present spurious poles and slightly improves the accuracy of estimates. It is worth pointing out that the validation criteria have to be applied after the hierarchical clustering stage, since they might remove all the spurious poles and a number of physical poles could be separated and lost as a result of the clustering stage.

The final values of the natural frequency and damping ratio for the identified modes are obtained by a sensitivity analysis with respect to the number of block rows in SSI, for a fixed value of the maximum model order in the stabilization diagram. The cluster characterized by the minimum variance of the estimates when i ranges in a certain interval with a certain step Δi

Fig. 1.1 Flowchart of the automated modal identification algorithm



is finally selected as the one providing the best estimate of the modal parameters for a given structural mode. Mode shape estimates are finally obtained, in the current stage of implementation, from Singular Value Decomposition (SVD) of the output Power Spectral Density (PSD) matrix at the previously estimated frequency of the mode [30].

The previous considerations about the automated identification algorithm highlight how the source separation at the first step makes the discrimination of physical and noise modes easier and more reliable. The sensitivity analysis with respect to the number of block rows and the grouping of the poles in clusters leads to a robust identification of modal parameters and to a quantification of the precision of the estimates.

1.3 Performance Assessment of the Algorithm Against Simulated Data

The performance of the proposed algorithm in terms of accuracy and reliability of estimates has been investigated through a statistical analysis of the results obtained from simulated data continuously generated through the application of a Gaussian white noise to a 4-DOF system. The mass and stiffness matrices of the system are given by Eqs. (1.1) and (1.2):

$$[m] = \begin{bmatrix} 5 & 0 & 0 & 0 \\ 0 & 5 & 0 & 0 \\ 0 & 0 & 5 & 0 \\ 0 & 0 & 0 & 10 \end{bmatrix} kg \quad (1.1)$$

$$[k] = \begin{bmatrix} 400 & -200 & 0 & 0 \\ -200 & 400 & -200 & 0 \\ 0 & -200 & 400 & -200 \\ 0 & 0 & -200 & 600 \end{bmatrix} \frac{N}{m} \quad (1.2)$$

$$[c] = a_0 [m] + a_1 [k] \quad (1.3)$$

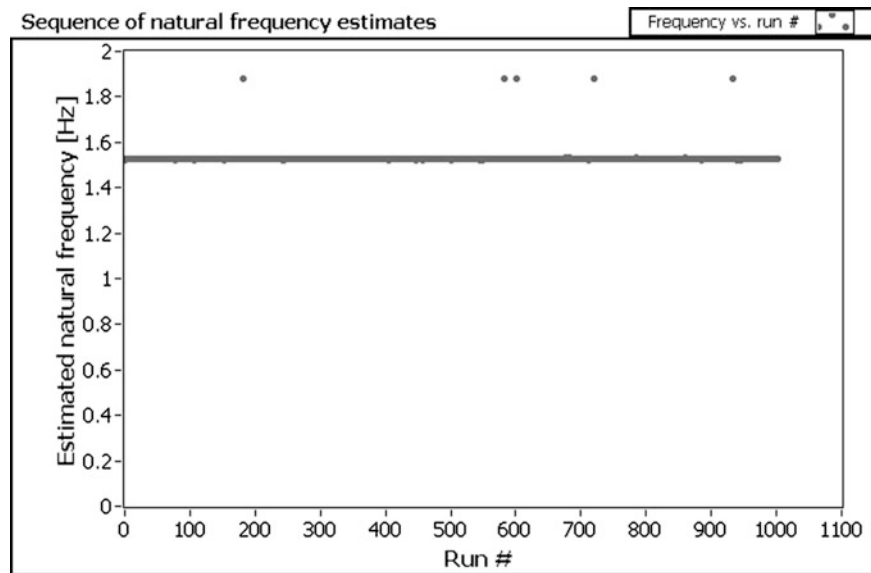
while Rayleigh damping is used to model structural damping. Thus, the damping matrix has been obtained as per Eq. (1.3). The a_0 and a_1 coefficients in Eq. (1.3) have been computed by setting a value of 1% of the modal damping ratio for the first and last mode of the system. Thus, the simulated 4-DOF system is characterized by the following modal properties (Table 1.1):

Table 1.1 Modal properties of the simulated 4-DOF system

Mode #	Natural frequency (Hz)	Damping ratio (%)
I	0.668	1.00
II	1.137	0.88
III	1.526	0.92
IV	1.879	1.00

Table 1.2 Success rate of automated modal identification over 1000 runs

Mode #	Success rate (%)
I	99.7
II	99.6
III	99.5
IV	99.8

Fig. 1.2 Sample sequence of values of estimated natural frequencies in 1000 runs

The system matrices and, therefore, the associated modal parameters have been kept constant in all runs in order to focus the attention only on the uncertainties associated to inherent limitations of the estimator. The performance of the method when uncertain system matrices are adopted, so that the modal parameters can slightly change at each run as an effect of the deviation of the system matrices from their nominal values, is out of the scope of the present paper and it will be discussed elsewhere.

The system response to Gaussian white noise $N(0,1)$ has been simulated 1000 times. The input has been applied at DOF #1. Each simulated dataset consisted of four measurement channels; the total record length was 3600 s and the sampling frequency was 10 Hz. Gaussian white noise has been added to the system response in order to simulate the effect of measurement noise. The obtained datasets, characterized by a SNR equal to 5 dB, have been then processed by the proposed algorithm in order to automatically extract the modal parameters of the system. The analysis of the simulated datasets has been carried out considering a number of block rows i ranging between 20 and 80 with $\Delta i = 2$ and considering a maximum model order of 16 in the construction of the stabilization diagram for each analyzed source.

The analysis of the obtained results has pointed out that the algorithm carries out automated output-only modal identification in a very robust way. In fact, a success rate [31] larger than 99% has been obtained for all modes (Table 1.2). Just in a few runs the modal parameters have not been properly identified (Fig. 1.2). However, such wrong estimates can be easily removed through the analysis of the extreme values in order to identify modal parameter estimates, which are outside the 3σ range.

In Tables 1.3 and 1.4 the results obtained from application of the proposed algorithm to the simulated data after removal of extreme values (associated to wrong modal parameter estimates) are summarized. They point out how the estimates are very close to the nominal values in at least the 50% of the cases. In fact, the median values are very close to the nominal ones and the interquartile range is very narrow and in the order of 0.001 Hz for natural frequency estimates and 0.1% for damping ratios.

Larger errors are associated to damping estimates, as expected. However, the analysis of the scatter of the natural frequency and damping estimates with respect to the nominal values point out that, with the exception of the previously

Table 1.3 Summary of automated modal identification results (after removal of extreme values): natural frequencies

Mode #	f_{nominal} (Hz)	μ_f (Hz)	σ_f (Hz)	f_{min} (Hz)	25 th centile	50 th centile	75 th centile	95 th centile	f_{max} (Hz)
I	0.668	0.668	0.000745	0.666	0.667	0.668	0.668	0.669	0.670
II	1.137	1.137	0.000901	1.135	1.137	1.137	1.138	1.139	1.141
III	1.526	1.526	0.001164	1.520	1.525	1.526	1.527	1.528	1.531
IV	1.879	1.879	0.001467	1.873	1.878	1.879	1.880	1.881	1.884

Table 1.4 Summary of automated modal identification results (after removal of extreme values): damping ratios

Mode #	ξ_{nominal} (%)	μ_ξ (%)	σ_ξ (%)	ξ_{min} (%)	25 th centile	50 th centile	75 th centile	95 th centile	ξ_{max} (%)
I	1.00	1.02	0.11	0.70	0.94	1.02	1.10	1.21	1.36
II	0.88	0.89	0.08	0.67	0.84	0.89	0.94	1.02	1.13
III	0.92	0.93	0.07	0.73	0.88	0.93	0.98	1.05	1.15
IV	1.00	1.01	0.08	0.79	0.96	1.01	1.06	1.14	1.23

Table 1.5 Summary of automated modal identification results (after extreme values removal): frequency scatter

Mode #	Δf_{min} (%)	25 th centile	50 th centile	75 th centile	95 th centile	Δf_{max} (%)
I	0.000025	0.04	0.07	0.13	0.23	0.36
II	0.000010	0.02	0.05	0.09	0.16	0.29
III	0.000036	0.02	0.05	0.08	0.15	0.38
IV	0.000006	0.02	0.05	0.09	0.15	0.30

Table 1.6 Summary of automated modal identification results (after removal of extreme values): damping scatter

Mode #	$\Delta \xi_{\text{min}}$ (%)	25 th centile	50 th centile	75 th centile	95 th centile	$\Delta \xi_{\text{max}}$ (%)
I	0.02	3.7	7.4	12.8	22.5	36.1
II	0.01	2.8	5.9	10.3	17.6	28.0
III	0.01	2.6	5.5	9.0	15.5	24.3
IV	0.01	2.4	5.1	8.7	15.4	22.7

Table 1.7 Analysis of coefficient of variation of identified natural frequencies (after removal of extreme values)

Mode #	$\gamma_{f,\text{min}}$ (%)	25 th centile	50 th centile	75 th centile	95 th centile	$\gamma_{f,\text{max}}$ (%)
I	0.0003	0.002	0.004	0.01	0.03	0.18
II	0.0002	0.002	0.006	0.01	0.03	0.09
III	0.0002	0.003	0.006	0.01	0.03	0.07
IV	0.0005	0.004	0.008	0.01	0.04	0.51

Table 1.8 Analysis of coefficient of variation of identified damping ratios (after removal of extreme values)

Mode #	$\gamma_{\xi,\text{min}}$ (%)	25 th centile	50 th centile	75 th centile	95 th centile	$\gamma_{\xi,\text{max}}$ (%)
I	0.03	4.24	4.81	5.75	6.92	9.66
II	1.21	1.82	2.29	3.05	4.19	6.99
III	0.18	0.91	1.19	1.63	2.57	5.51
IV	0.15	1.18	1.52	1.99	3.28	9.14

mentioned extreme values which affect less than 1% of the estimates, in the 95% of the runs the error is lower than 0.25% for frequencies (Table 1.5) and 23% for damping ratios (Table 1.6). Moreover, the typical scatter of damping ratio is in the range [2%, 10%] (50% of the values of scatter associated to damping estimates are in this range).

The natural frequency and damping ratio estimates provided by the proposed algorithm are average values of the poles grouped in a cluster representative of the identified mode. The analysis of their coefficient of variation shows that the modal estimates provided by the algorithm are not only fairly robust and accurate, but also precise. In fact, the coefficient of variation is typically well under 0.1% for natural frequencies (Table 1.7) and 10% (the rejection limit set in the algorithm) for damping ratios (Table 1.8).

The distributions of the identified damping ratios after 1000 runs for the four modes are depicted in Fig. 1.3. The associated means, modes and medians are reported in Table 1.9. They are very close each other and to the nominal values of modal damping ratios. Taking into account the uncertainty associated to damping estimates, the mode of damping values is given with one decimal place only.

The statistical analysis of the results can be eventually further refined by removing also outliers. However, the results after outlier removal are very consistent with the previous ones (to this aim compare Tables 1.3, 1.4, 1.10 and 1.11). The marginal refinements associated to outlier removal confirm the robustness and accuracy of the algorithm.

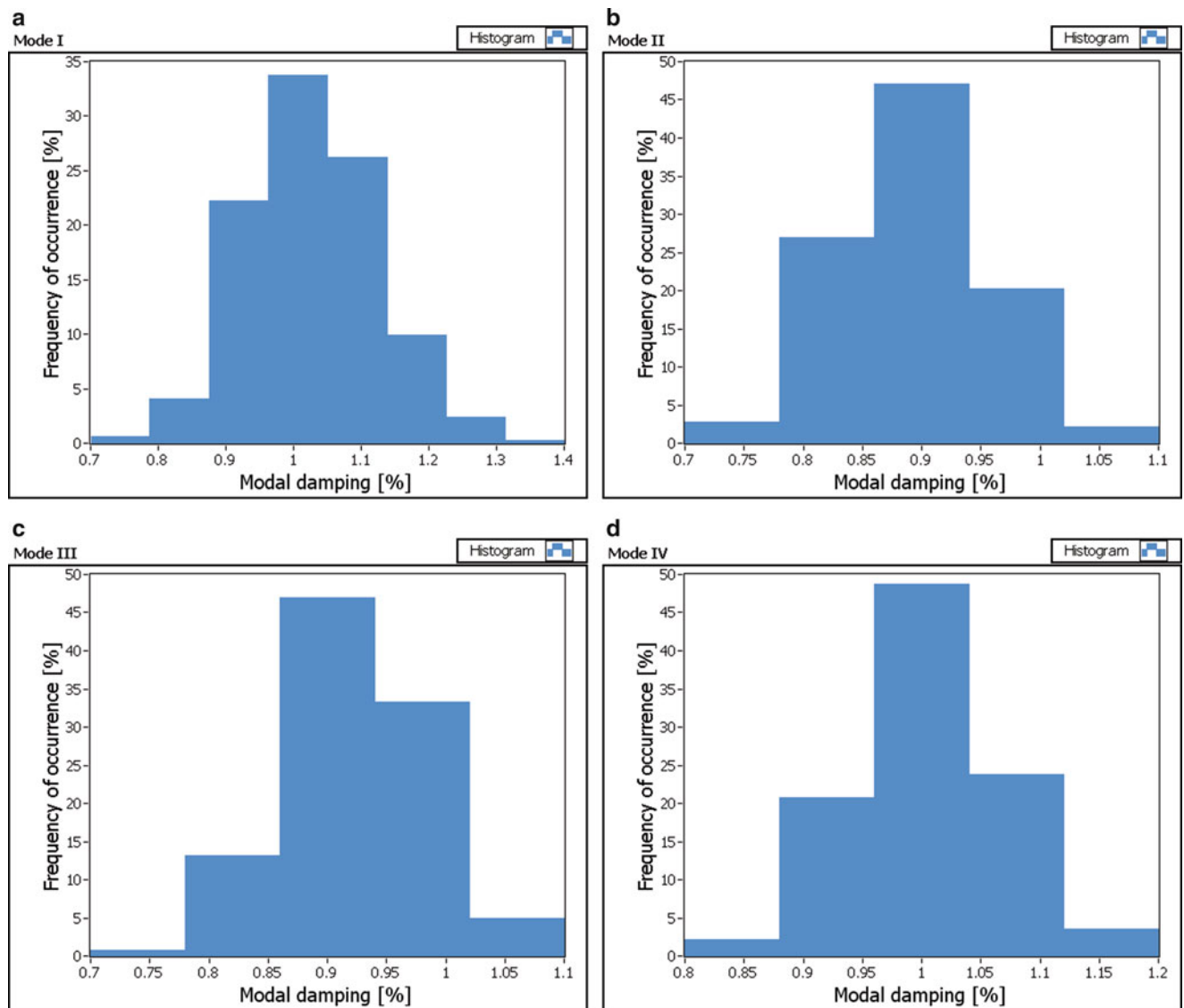


Fig. 1.3 Histograms of modal damping ratio estimates (after removal of extreme values): mode I (a), II (b), III (c), IV (d)

Table 1.9 Comparison of mean, mode and median of identified damping ratios with the corresponding nominal values (after removal of extreme values)

Mode #	ξ_{nominal} (%)	μ_{ξ} (%)	ξ_{median} (%)	ξ_{mode} (%)
I	1.00	1.02	1.02	1.0
II	0.88	0.89	0.89	0.9
III	0.92	0.93	0.93	0.9
IV	1.00	1.01	1.01	1.0

Table 1.10 Summary of automated modal identification results (after outlier removal): natural frequencies

Mode #	f_{nominal} (Hz)	μ_f (Hz)	σ_f (Hz)	f_{min} (Hz)	25 th centile	50 th centile	75 th centile	95 th centile	f_{max} (Hz)
I	0.668	0.668	0.000723	0.666	0.667	0.668	0.668	0.669	0.670
II	1.137	1.137	0.000863	1.135	1.137	1.137	1.138	1.139	1.140
III	1.526	1.526	0.001045	1.523	1.525	1.526	1.527	1.528	1.529
IV	1.879	1.879	0.001339	1.875	1.878	1.879	1.880	1.881	1.883

Table 1.11 Summary of automated modal identification results (after outlier removal): damping ratios

Mode #	ξ_{nominal} (%)	μ_{ξ} (%)	σ_{ξ} (%)	ξ_{min} (%)	25 th centile	50 th centile	75 th centile	95 th centile	ξ_{max} (%)
I	1.00	1.02	0.11	0.74	0.94	1.02	1.10	1.21	1.33
II	0.88	0.89	0.08	0.69	0.84	0.89	0.94	1.02	1.09
III	0.92	0.93	0.07	0.73	0.88	0.93	0.98	1.05	1.12
IV	1.00	1.01	0.07	0.82	0.96	1.01	1.06	1.13	1.20

1.4 Conclusions

A novel, hybrid approach to automated output-only modal identification for SHM applications has been described in the present paper. It is based on the combination of selected OMA techniques and clustering strategies for the discrimination between structural and noise modes and the selection of the dynamic properties of physical modes. Its performance has been assessed against simulated data generated by a 4-DOF system excited by a Gaussian white noise. The results obtained from 1000 runs have been analyzed in order to assess the performance of the algorithm in terms of robustness, accuracy and precision. Encouraging results have been obtained, in particular as the possibility to estimate damping ratios in an accurate and fully automated way is concerned. Further investigations are in progress to assess the performance of the algorithm in the case of uncertain system matrices, when the modal parameters slightly change at each run as an effect of the deviation of the system matrices from their nominal values. All these tests will provide an extensive characterization of the performance of the algorithm in view of continuous, long term vibration based SHM applications.

Acknowledgements The present work is carried out within the activities of AT2 – LR 2 – Task 3 of the ReLuis-DPC Executive Project 2010-2013, rep. 823. Support of ReLuis Consortium is therefore gratefully acknowledged.

References

- Rainieri C, Fabbrocino G (2010) Automated output-only dynamic identification of civil engineering structures. *Mech Syst Signal Process* 24(3):678–695
- Rainieri C, Fabbrocino G, Cosenza E (2011) Near real-time tracking of dynamic properties for standalone structural health monitoring systems. *Mech Syst Signal Process* 25(8):3010–3026
- Doebling SW, Farrar CR, Prime MB, Shevitz DW (1996) Damage identification and health monitoring of structural and mechanical systems from changes in their vibration characteristics: a literature review, Technical Report LA-13070-MS, UC-900, Los Alamos National Laboratory, New Mexico 87545
- Peeters B, De Roeck G (2001) One-year monitoring of the Z24-Bridge: environmental effects versus damage events. *Earthquake Eng Struct Dyn* 30:149–171
- Rainieri C, Fabbrocino G, Cosenza E (2008) Integrated systems for Structural Health Monitoring: worldwide applications and perspectives. In: Proceedings of the fourth European workshop on structural health monitoring, Cracow
- Magalhaes F, Cunha A, Caetano E (2012) Vibration based structural health monitoring of an arch bridge: from automated OMA to damage detection. *Mech Syst Signal Process* 28:212–228
- Rainieri C, Fabbrocino G, Manfredi G, Dolce M (2012) Robust output-only modal identification and monitoring of buildings in the presence of dynamic interactions for rapid post-earthquake emergency management. *Eng Struct* 34:436–446
- Rainieri C, Fabbrocino G, Cosenza E (2010) Integrated seismic early warning and structural health monitoring of critical civil infrastructures in seismically prone areas. *Struct Health Monit-Int J* 10(3):291–308
- Fabbrocino G, Laorenza C, Rainieri C, Santucci De Magistris F (2009) Seismic monitoring of structural and geotechnical integrated systems. *Mater Forum* 33:404–419
- Rainieri C, Fabbrocino G, Santucci de Magistris F (2012) An integrated seismic monitoring system for a full-scale embedded retaining wall. *Geotechnical Test J* 36. doi:10.1520/GTJ20120067
- Rainieri C, Fabbrocino G (2011) Operational modal analysis for the characterization of heritage structures. *GEOFIZIKA* 28:127–143
- Conte C, Rainieri C, Aiello MA, Fabbrocino G (2011) On-site assessment of masonry vaults: dynamic tests and numerical analysis. *GEOFIZIKA* 28:109–126
- Rainieri C, Fabbrocino G, Cosenza E (2010) Some remarks on experimental estimation of damping for seismic design of civil constructions. *Shock Vib* 17(4–5):383–395
- Ans B, Héroult J, Jutten C (1985) Adaptive neural architectures: detection of primitives. In: Proceedings of COGNITIVA'85, Paris, France, pp 593–597
- Poncelet F, Kerschen G, Golinvall JC, Verhelst D (2007) Output-only modal analysis using blind source separation techniques. *Mech Syst Signal Process* 21:2335–2358
- Belouchrani A, Abed-Meraim K, Cardoso JF, Moulines E (1997) A blind source separation technique using second-order statistics. *IEEE Trans Signal Process* 45:434–444

17. Rainieri C, Fabbrocino G (2012) A hybrid automated modal identification algorithm for Structural Health Monitoring: a comparative assessment. In: Proceedings of the international conference on noise and vibration engineering ISMA2012, Leuven
18. Van Overschee P, De Moor B (1996) Subspace identification for linear systems: theory—implementation—applications. Kluwer Academic Publishers, Dordrecht
19. Cardoso JF, Souloumiac A (1996) Jacobi angles for simultaneous diagonalization. *SIAM J Matrix Anal Appl* 17:161–164
20. Ljung L (1999) System identification: theory for the user, 2nd edn. Prentice Hall, Upper Saddle River
21. Peeters B (2000) System identification and damage detection in civil engineering. Ph.D. Thesis, Katholieke Universiteit Leuven, Leuven
22. Reynders E, Pintelon R, De Roeck G (2008) Uncertainty bounds on modal parameters obtained from stochastic subspace identification. *Mech Syst Signal Process* 22:948–969
23. Rainieri C, Fabbrocino G, Cosenza E (2010) On damping experimental estimation. In: Proceedings of the tenth international conference on computational structures technology, Valencia
24. Deraemaeker A, Reynders E, De Roeck G, Kullaa J (2008) Vibration-based structural health monitoring using output-only measurements under changing environment. *Mech Syst Signal Process* 22:34–56
25. Lämsä V, Kullaa J (2008) Data normalization with partially measured environmental or operational variables. In: Proceedings of the fourth European workshop on structural health monitoring, Cracow
26. Magalhães F, Cunha A, Caetano E (2010) Continuous dynamic monitoring of an arch bridge: strategy to eliminate the environmental and operational effects and detect damages. In: Proceedings of the international conference on noise and vibration engineering ISMA2010, Leuven
27. Peeters B, De Roeck G (2001) Stochastic system identification for operational modal analysis: a review. *ASME J Dyn Syst Meas Contr* 123(4):659–667
28. Reynders E, Houbrechts J, De Roeck G (2012) Fully automated (operational) modal analysis. *Mech Syst Signal Process* 29:228–250
29. Tan P-N, Steinbach M, Kumar V (2006) Introduction to data mining. Pearson Addison-Wesley, Reading
30. Brincker R, Zhang L, Andersen P (2000) Modal identification from ambient responses using frequency domain decomposition. In: Proceedings of the 18th SEM international modal analysis conference, San Antonio
31. Magalhaes F, Cunha A, Caetano E (2012) Online automatic identification of the modal parameters of a long span arch bridge. *Mech Syst Signal Process* 23:316–329

Chapter 2

Real-Time Structural Health Monitoring and Damage Detection

Yavuz Kaya and Erdal Safak

Abstract Structural health monitoring (SHM) contains continuous structural vibration monitoring, extraction of damage sensitive features of structure from measurements, and statistical analysis of those features to detect and locate the damage in structures. In other words, SHM involves data collection, continuous monitoring and analyzing them in real-time. Changes in modal properties of structures during their service life are strongly related to damage in structures, which makes accurate estimation of modal properties an essential step in SHM. Therefore, both monitoring and accurate identification of real-time modal properties (modal frequency, damping ratio, and mode shape) are of crucial importance in order to have a good estimate in SHM. In this paper, a real-time modal identification techniques along with a damage detection algorithm based on inter-story drift calculation has been developed for SHM. The modal identification technique is based on the modification of standard spectral analysis tools for real-time data, and utilizes running time windows to keep track of time variations of structures' modal properties. On the other hand, the damage detection algorithm makes use of inter-story drifts, which is calculated by narrow-band filtering the recorded data around modal frequency and very sensitive to structural damage, by estimating the contribution of each identified mode of structure. A software package called *REC_MIDS* is developed for real-time modal identification. The software includes various user-selectable algorithms to identify modal properties, as well as options to plot their time variations and animations. The software has been tested with the ambient vibration data recorded from the Hagia Sophia Museum, a 1500 year-old historical structure in Istanbul, Turkey. Modal properties of the structure have been identified accurately in real-time. Results of the Hagia Sophia test have been compared with the previous studies conducted by different researchers. Comparison shows that the results of the *REC_MIDS* are in good agreement with that of the previous studies.

Keywords Real-time data processing • Modal identification • Damage detection • Structural health monitoring • Inter-story drift

2.1 Introduction

The term SHM involves continuous monitoring of the dynamic characteristics of a structure by digital instruments (e.g., acceleration sensors). The main objective in SHM is to keep track of the changes in the dynamic characteristics of the structural system in order both to detect and locate the damage, and to make a decision automatically whether the damage is in dangerous level for the structure or not. Damage detection typically involves data processing to explore changes both in the dynamic properties of structures (e.g., modal frequency, damping ratio, and mode shape), and inter-story drifts. Since the damage in structures causes loss in their stiffness's, and the dynamic properties of structure are directly related to the stiffness, it is logical to use the changes in natural frequencies as a damage indicator [1]. However, analyses of recorded data from structures clearly show that changes in natural frequency are not always a reliable indicator of damage as the response of the

Y. Kaya (✉)
The University of British Columbia, Vancouver, BC, Canada
e-mail: kayaya@mail.ubc.ca

E. Safak
Bogazici University, Istanbul, Turkey
e-mail: erdal.safak@boun.edu.tr

damaged structure is nonlinear, and in most case hysteretic. Moreover, various environmental factors (e.g., temperature) can change natural frequency of structures without any damage in the structure. Likewise, the inter-story drifts, if not calculated by integrating the band-pass filtered acceleration data, is not a reliable damage indicator as the errors generated by the noise in the records are exponentially amplified during such integration.

In this research paper, an attempt is made both to keep track of changes in modal properties of structures, and to calculate inter-story drifts accurately by utilizing the ambient vibration records, which are characterized by very low amplitudes and signal-to-noise-ratio (SNR). Ambient vibration data are always available in the structure and their length can be made infinitely long. These facts allow ambient records to be considered as stationary data (i.e., their frequency and temporal characteristics do not change with time). Moreover, since the ambient vibration records contain large number of excitation sources, it is quite reasonable to assume that the both the noise and the excitation are wide-band random processes, which make it possible for advanced stochastic techniques (e.g., statistical signal processing) to be utilized.

In buildings inter-story drift refers to the relative displacement between adjacent floors. The accuracy of inter-story drifts is extremely increased by narrow-band filtering the recorded data around modal frequencies before calculating the inter-story drifts. As long as the ambient vibration data contains large amplitudes (e.g., data taken from high-rise building), the developed algorithm to calculate inter-story drifts will yield accurate result. It should still be kept in mind that higher mode contributions to inter-story drift calculation cannot be accounted for due to low SNR in higher frequencies.

A software package, *REC_MIDS*, is developed for both real-time modal identification and inter-story drift calculation. The software includes various user-selectable algorithms to identify modal properties, as well as options to plot their time variations and animations. The software has been tested with the ambient vibration data recorded from the Hagia Sophia Museum, a 1500 year-old historical structure in Istanbul, Turkey. Modal properties of the structure have been identified accurately in real-time. Results are compared with the previous studies carried out by different researchers. Comparison shows that the results of the *REC_MIDS* are in good agreement with that of the previous studies.

2.2 Real-Time Data Processing and Modal Identification

A smart algorithm is developed to process the real-time data instantaneously. The developed algorithm works in the following way. The real-time data are segmented using two separate windows: *truncated window*, and *running window*, one within the other as show in Fig. 2.1. The real-time data in the *truncated window* is processed by means of successive *running windows*. The data in each *running window* is analyzed separately, and sequential analysis results are averaged in order to form the overall output for the *truncated window*, which is almost identical to the output that would have been obtained if the *truncated data*, free of noise, had been processed at a time. Once the analysis of the *truncated window* is finished, it is shifted in time, as shown in Fig. 2.1, by predefined overlap ratio, and the above procedure is repeated.

The *running window* moves within the *truncated window* with predefined overlap ratio as indicated in Fig. 2.1. Increasing the overlap ratio increases the number of successive running windows. The bigger the number of running windows the less the effect of noise in the overall analysis result. In other words increasing the number of *running windows* increases the accuracy in the overall output. However, increasing the overlap ratio also increases the elapsed time (i.e. total calculation time) to estimate the overall output for the *truncated window* due to increase in the number of *running windows*. Time delay in real-time operation occurs when elapsed time falls behind the real-time data streaming speed.

The length of *running window* is structure specific. It depends on the modal characteristics of the structure, especially on the smallest modal frequency of the structure. It must be at least two times bigger than the maximum modal period of the structure. Length of the *truncated window*, on the other hand, depends on the signal-to-noise ratio (SNR), also know as noise level, of the real-time streaming data. If real-time data contains too much noise, then the length of the *truncated window* should be such long that the affect of noise in the analysis result is minimized by means of increasing the number of *running windows*, and averaging. Too long *truncated window* may not provide sufficient accuracy in case of sudden change in environmental loads, whereas too short *truncation window* may not provide sufficient noise reduction due to decrease in the number of averaging. Apparently there is no unique solution to determine the optimum length for the *truncated window*. In order to define the optimum window lengths, it is strongly recommended to collect a set of experimental data (i.e. ambient vibration data) from structure under consideration, and then analyze them with varying window lengths and other parameters. Calculating the optimum window lengths is an ad hoc operation, which should be done separately for each structure by an engineer.

Common practice to calculate the displacements using acceleration data is to take double integration of the recorded acceleration data. Simple integration of acceleration signals produce significant amount of errors depending on the sampling resolution [2], moreover, shows that the integration and subtraction exponentially amplify the errors generated by the noise

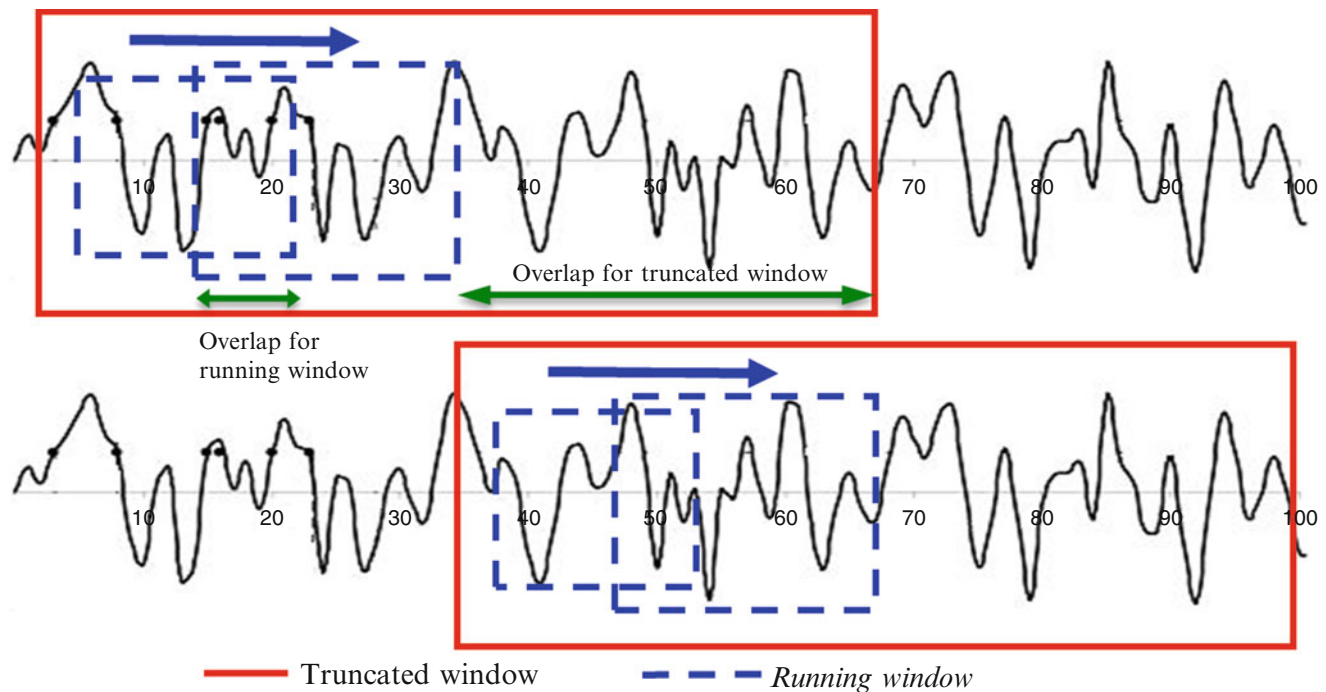


Fig. 2.1 Running window moves within the truncated window by a predefined overlap ratio. The data in each running window is analysed separately, and sequential analysis results are averaged to form the overall output for the truncated window

in records, particularly for high frequencies. This is due to so-called Brownian motion where the variance of an integrated noisy-signal (i.e. signal dominated by noise) increases by a factor of t (time), which obviously causes the integration to go to infinite. Thus this clearly demonstrates the fact that the integration will go to infinite because of existence of the noise in the entire frequency band of the signal. One-way of overcoming this problem is to band-pass filter the real-time data around each modal frequency (utilizing the frequency-band selections) to eliminate the frequency components that is dominated by noise. Even though the noise is still present in the pass band of the filter, the SNR of the filtered data will be higher than that of unfiltered one due to structural resonance effect within the pass band of the filter. This way one can make sure that the integration of narrowband filtered data will not go to infinite but yields to the modal displacement of structure.

In multi-story buildings, the term inter-story drift denotes the relative displacement between two adjacent floors whereas in this study the term refers to the relative displacements between any two sensors in a specified direction. Eventually inter-story drift controls structural damage based on the lateral displacements in multi-story buildings. The inter-story drifts that are calculated by taking the difference of double integrated acceleration data are usually inaccurate if the SNR of ambient records are low. However, for large amplitude vibration data (i.e. ambient vibration data of a high-rise structure), such inter-story drift values can be accurately calculated by narrow-band filtering the data around each modal frequency of the structure. Such filtering provide high SNR ratio. Therefore, one can calculate the inter-story drifts for each modal response of the structure by band-pass filtering though some of the higher mode contributions to inter-story drift cannot be calculated such accurately. This is because of the fact that even though the data is band-pass filtered around each modal frequency, the SNR of signal decreases at higher frequencies because the amplitude of modal response become such small that they are still buried by noise at higher frequencies. Therefore one has to decide how many modal responses of the structure can be calculated accurately and then the inter-story drifts are calculated simply summing up the contribution of all calculated modal responses. An automatic algorithm developed to calculate the contribution of each modal response to inter-story drifts

The developed algorithm calculates the inter-story drifts based on the estimated modal displacements of the structure. Raw data in *running window* is band-passed filtered separately around each modal frequency to calculate each modal response of the structure. The resulting filtered data is then double integrated to calculate the modal displacements. The total displacement of the structure is calculated by summing up the contribution of all of the calculated modal displacement. The calculated inter-story drifts are compared with different threshold values that correspond to different damage levels (i.e. performance levels) of the structure. The procedure is repeated for all inter-story drifts in the structure. Any inter-story drift exceeding specified threshold values indicates damage in structure. More detail about real-time data processing can be found in [3, 4].

2.3 Description of REC_MIDS

The capabilities of *REC_MIDS* include real-time data processing and analysis by using a large number of techniques, varying from standard Fourier analysis to stochastic-adaptive filters; real-time identification of structure's modal properties (modal frequencies, damping, and mode shapes); displacements and inter-story drifts; and 3D animations of total and modal responses. The software has the options to automatically give warnings when a response quantity exceeds specified threshold levels, to save any of the measured or calculated output parameters, and to generate and send automatic warning email to specified addresses.

A typical screen-shot of the *REC_MIDS* is shown in Fig. 2.2. The graphical display of the *REC_MIDS* is designed to allow the user to monitor the recorded structural response characteristics in real time, along with the estimated modal properties and the animations of vibrations in a single window.

Left-up window displays calculated displacements at user-selected sensor locations, whereas right-up window shows the smoothed Fourier Amplitude Spectra of the user-selected signals over an adjustable frequency range. Two left-bottom windows display the real-time calculated modal frequency and modal damping ratio of the structure. Right-bottom window animates user-selected structural mode estimated in real-time. All these windows are continuously updated in real-time to reveal the latest modal properties of the structure.

In *REC_MIDS*, the term inter-story drift refers to the relative displacement between any two sensors in a specified direction. The inter-story drift calculated between these two sensors is linearly distributed to the stories between these sensors. In ambient vibration conditions, noise can cause erroneous drift values, especially in higher modes, if the drifts are calculated from the original signals. Therefore, the inter-story drift calculations are not done on the original waveforms, but on modal waveforms in order to minimize the effects of noise in the signal. The band-pass filters are used to obtain modal waveforms. Drift waveforms can be monitored in the main window of *REC_MIDS* (Fig. 2.3). In theory, one can define in *REC_MIDS* as many inter-story drifts as the CPU of the computer can handle. However, the calculation of inter-story drifts involves large number of computations, and therefore defining too many inter-story drifts may cause delays in keeping up with the real-time data stream.

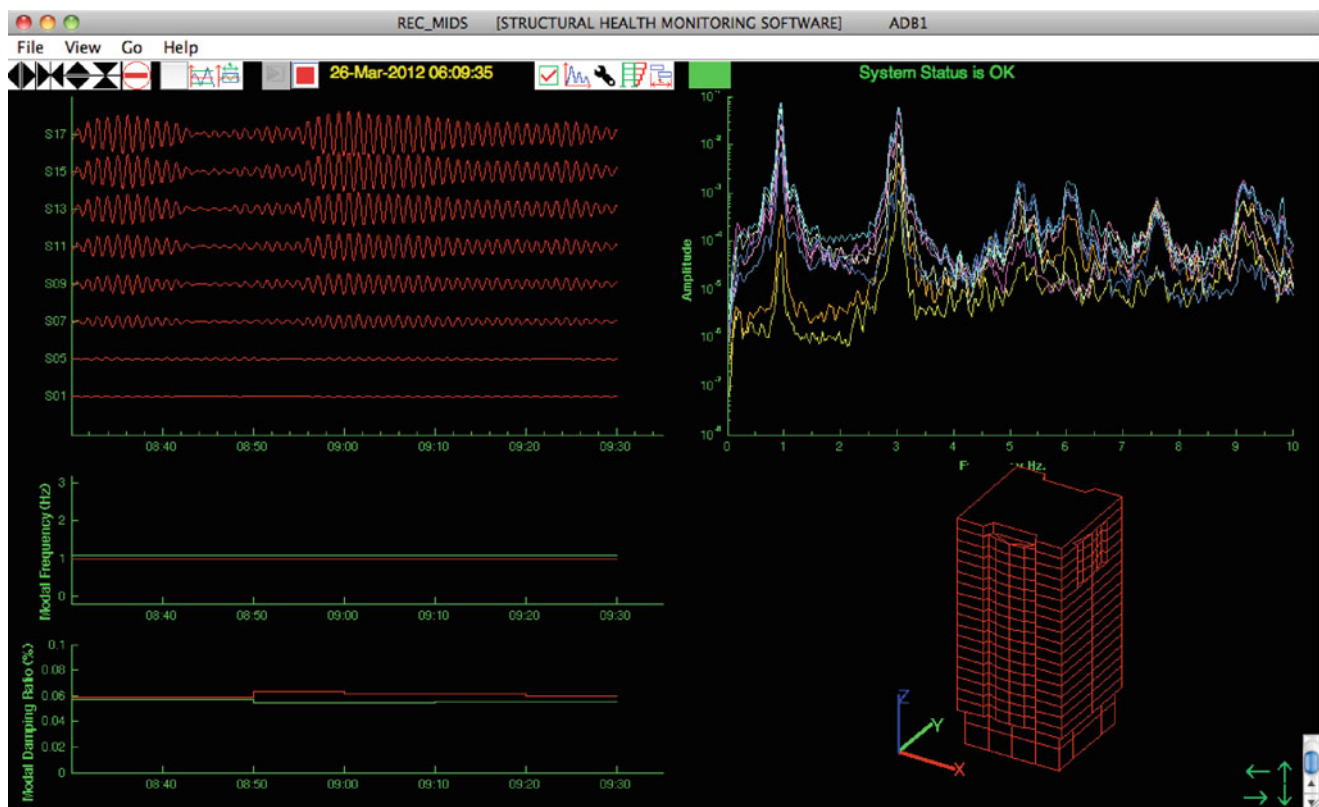


Fig. 2.2 A typical screen-shot of *REC_MIDS* that contains different windows to monitor the latest modal properties of the structure

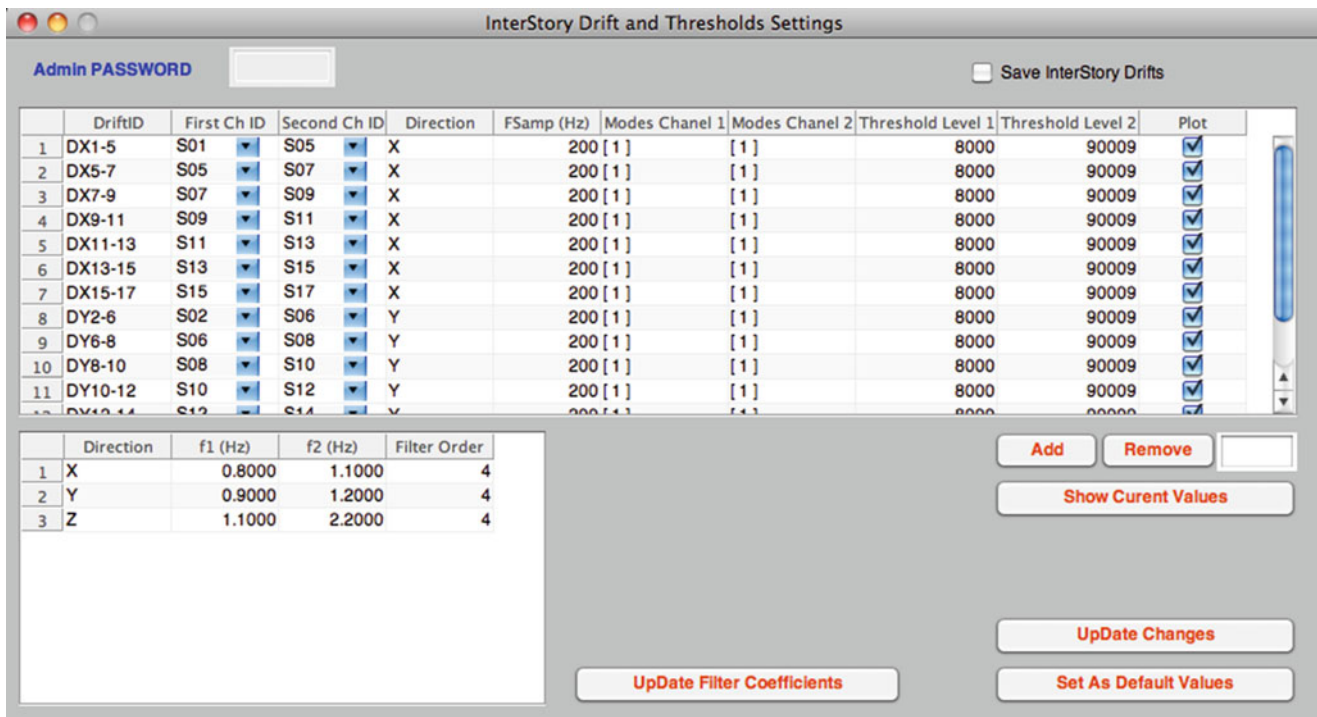


Fig. 2.3 The inter-story drift and threshold settings window. The user can define as many inter-story drifts as the CPU of the computer can handle

The *Event Detection Settings* window, shown in Fig. 2.4, is used to set up the channels and the threshold values that will be used to detect possible damage, and to issue warnings and alerts in case of an event that pushes the response of the structure to critical levels.

By default, the event detection algorithm embedded in *REC_MIDS* runs every 1 s using the past 4 s of data. These values are user adjustable. A smart algorithm embedded in *REC_MIDS* determines how many inter-story drifts and acceleration values exceeded the specified threshold values, as well as the top-floor displacement threshold value and wind speed threshold value. Based on the different combinations of the threshold value exceedance, and an automatic notification message/email are issued to user specified recipients. More detail about the event detection algorithm can be found in user manual [4], which can be downloaded from www.koeri.boun.edu.tr.

2.4 Application of REC_MIDS at Hagia Sophia Museum

Hagia Sophia (in Turkish Ayasofya) as seen in Fig. 2.5 is one of the most magnificent buildings in Istanbul, Turkey. Hagia Sophia museum suffered from several earthquakes and as a result partially destroyed. The eastern part of the dome collapsed along with the arch and semidome on the side of the church on May 7th, 1558. It is rebuilt with new design of the dome (less shallow so as to reduce the lateral stresses). An earthquake damaged the western side of the building on February 9th 1869, which is repaired in 1879. A violent earthquake resulted in collapse of the western apse and caused partial damage to the dome on October 25th, 1968. The church interior suffered very much in the Latin sack of Constantinople in 1204, when it was stripped of all its sacred relics and other precious objects. During the Latin occupation, Hagia Sophia served as the Roman Catholic cathedral of the city. Following the recapture of Constantinople by the Byzantines in 1261, Hagia Sophia was re-consecrated as a Greek Orthodox sanctuary. In 1348, the eastern half of the dome collapsed, and was afterwards repaired.

The imperial gate leads to the central nave of Hagia Sophia. The dome is approximately 55 m high and 32 m wide. Due to repairs and earthquakes over the centuries, the dome lost its original shape and not completely circular anymore. The ceiling is completely covered with mosaics. The dome rests on four large arches, which are supported by four pillars. Weight of the dome is transmitted to semi-domes in the north and south, and to the lower sections. The interior contains 107 columns, 40

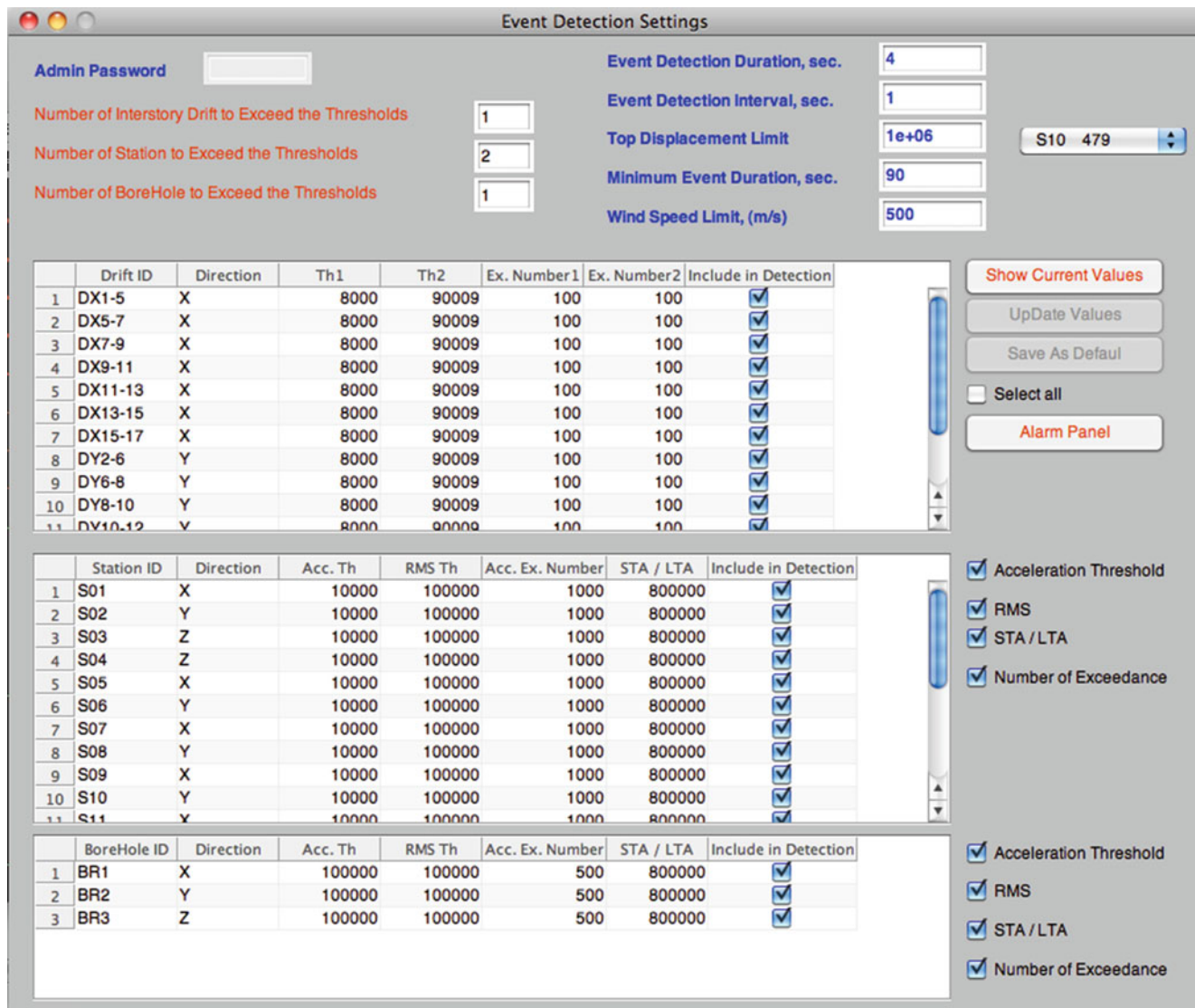


Fig. 2.4 Event Detection settings window. The user can set up the channels and threshold values that is used to detect possible damage, and to send automatic warning and alert emails in case of an event

of these are found on the ground floor and the rest are up in the gallery. Over the years, buttresses have been built outside, against almost every wall, to lessen the stress of the building and to counteract the damage caused by earthquakes.

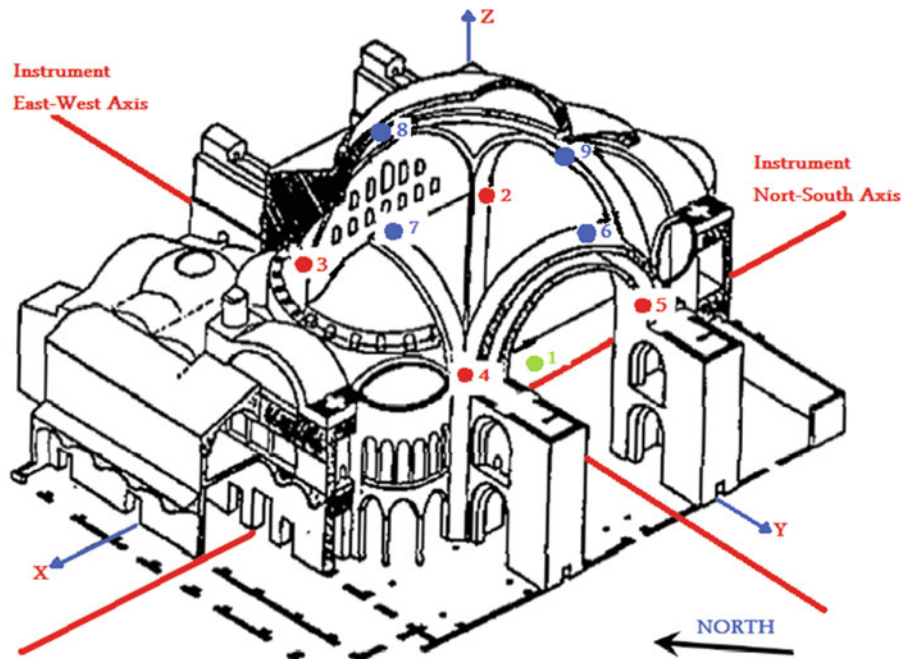
2.5 Instrumentation of the Structure

The first strong motion network that has been installed in the structure was in August 1991 though many changes have been made since then. The latest instrument setup that is present at the museum can be seen in Fig. 2.2. The instruments basically cover the three different levels of the structure. One instrument is at the ground level while four of them are located at cornice level next to the springing points of the four main arches. The last four instruments are located at dome base level on the crowns of the main arch. All instruments are Guralp system CMG-5 accelerometers that are compact triaxial, force-feedback instruments, and suitable for rapid deployment.

Fig. 2.5 General view of Hagia Sophia



Fig. 2.6 Strong motion instrumentation in Hagia Sophia covers three different levels of the structure: ground level, cornice level, and dome base level



2.6 Data Collection and Results

Value of certain parameters of *REC_MIDS* has to be set up before analyzing the ambient vibration data of Hagia Sophia Museum. The necessary parameters are the decimation order, the filter corner frequencies and filter order, smoothing window length, frequency band limits, and modal property calculation methods. The sampling interval of the records is 200 Hz. All records from structure are decimated by 2, and standard 4th order of band-pass Butterworth filter with corner frequencies of 0.2 and 20 Hz is applied to the decimated data.

The running window length is selected as 1 min. The truncated data is further divided into equal size of running windows each have a length of 30 s. Each running window is overlapped with 90% and Hamming type of smoothing window is used to smooth the calculated FAS. The optimum smoothing window length is estimated as seven.

Twenty three hour length of real-time ambient vibration data was collected from Hagia Sophia Museum and was analyzed using *REC_MIDS*. The starting time of the real-time vibration data is 08:00 am, 17th of March, 2009 and the end time is 06:00 am, 18th of March, 2009. One-hour duration of real-time raw data is depicted in Fig. 2.7 for all stations installed in Hagia Sophia Museum. It is observed that the maximum mean acceleration amplitudes at the top of main arches are amplified

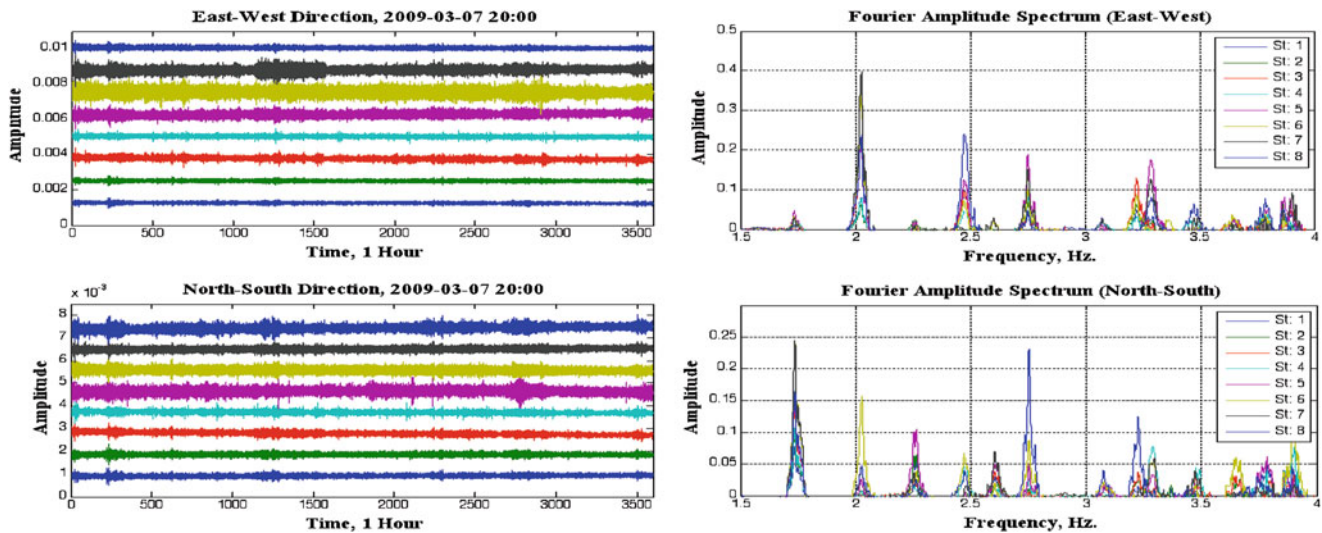


Fig. 2.7 Ambient vibration data of Hagia Sofia for 23 h and for all channels

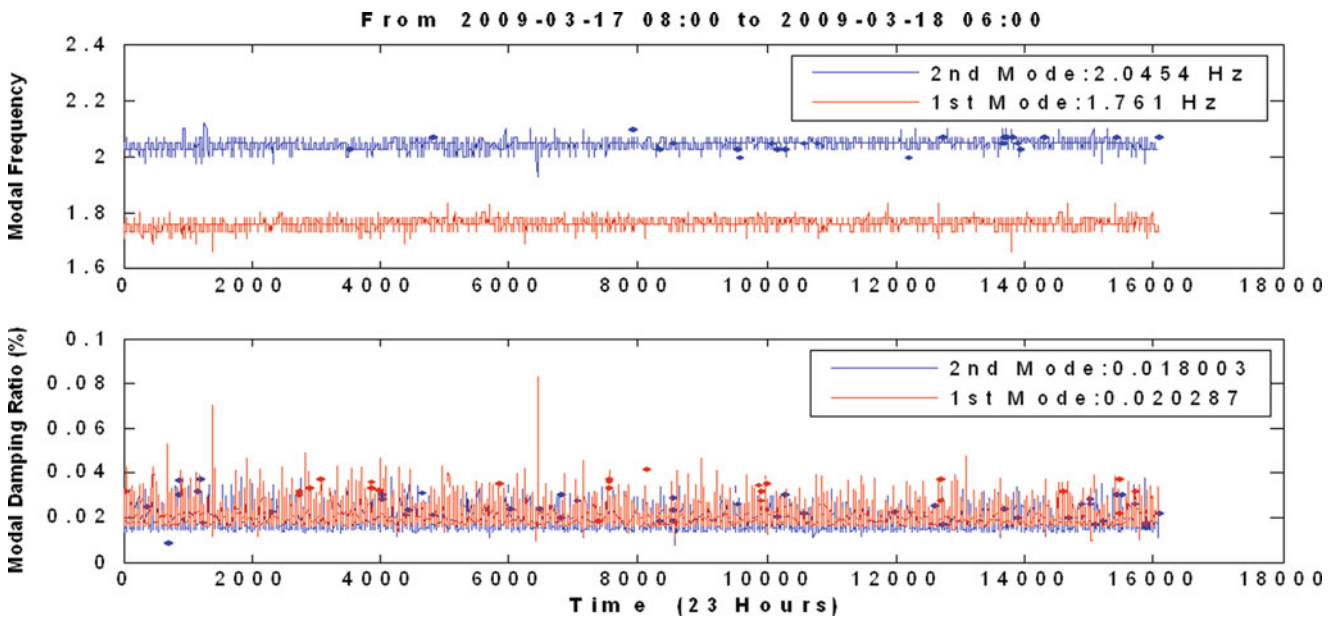


Fig. 2.8 Result of 23-h processing shows the variation of predominant modal frequencies and damping ratios of the structure with respect to time (23 h)

by a factor of at least two in both East-west and in North-south directions when compared to that of the amplitudes at the top of main columns. Modal frequencies can be clearly seen from the FAS of the recorded ambient data. Some of the modal frequencies of the structure are estimated as 1.7, 2.26, and 2.75 Hz in North-south direction whereas 2.02 and 2.47 Hz in East-west direction, respectively.

The result of the modal identification shows that the mean value of the first two predominant modal frequencies, as shown in Fig. 2.8, for measurement location 1 during 23 h duration are 1.761 and 2.045 Hz in East-west and North-south directions, respectively. Time variations of the first two predominant modal frequencies do not show any significant variations for the measurement location number 1 as seen in Fig. 2.8. Nevertheless, these results could not be correlated with respect to temperature and wind velocity because those data were not measured during the ambient vibration. The modal damping ratios of the first two modes are very small. It is well known that the damping in structure is proportional to the amplitude of the vibration. Since the amplitudes of the vibrations (real-time acceleration data) during the ambient vibration are not large enough, the damping in the structure is not considerably large.

2.7 Conclusion

For structural safety, it is important to detect and locate damage in structures as soon as they occur. SHM provides the best tools for this. Accurate estimation of dynamic properties of structures is the critical component of SHM. Since the SHM data flow in real time, the data analysis should also be done in real time. This study presents some tools and techniques for real-time data analysis. It includes on-line data processing methods and real-time modal identification tools. A MATLAB-based software is developed for this purpose. The developed software, *REC_MIDS*, has been tested using the data from the SHM system at the Hagia Sophia Museum in Istanbul, Turkey. It has been proven that the model identification can be done with significant accuracy by *REC_MIDS*. More detail about the software can be found in [4] on www.koeri.boun.edu.tr.

References

1. Safak E (2006) Real-time structural monitoring and damage detection by acceleration and GPS sensors. In: 8th US National Conference on earthquake engineering San Francisco, 18–22 April 2006
2. Safak E (2005): Analysis of ambient ground and structural vibration data. Abstracts, Annual meeting of the seismological society of America, Incline Village/Lake Tahoe, 27–29 April 2005
3. Kaya Y (2009) Tools and techniques for modal identification. Ph.D. Dissertation, Bogazici University
4. Kaya Y (2012) REC_MIDS user manual. www.koeri.boun.edu.tr. Accessed 10 Jan 2010

Chapter 3

Improved Substructure Identification Through Use of an Active Control Device

Charles DeVore, Erik A. Johnson, and Richard E. Christenson

Abstract Increasingly, researchers turn to substructure identification for civil structural health monitoring for a variety of reasons. First, substructure identification provides inherent damage localization. Second, substructure identification provides greater numerical conditioning than full structure identification because only a small subset of the degrees of freedom are considered in each analysis. Third, substructure identification is perfectly suited for a decentralized implementation within a network of wireless sensors. This implementation can realize cost savings in installation and operation.

While the benefits of substructure identification are many-fold, current research shows that certain structure-substructure combinations admit poor performance. Research demonstrates that single story substructures in a shear building are poorly identified (if at all) when interstory acceleration response is low in a specific frequency range. This result shows that portions of the structure are unable to be identified properly with substructure identification.

To overcome these results, this paper temporarily re-purposes a structural control device to change the global dynamics of the structure to improve substructure identification at a particular story. A control law for an active mass damper is developed to increase the interstory response at a particular story, which, when implemented, will improve substructure identification of that story. The control law is developed in simulation and will later be tested experimentally on a four story, 12 ft. steel building excited by base motion.

Keywords Structural Health Monitoring • Structural Control • Structural Dynamics • Damage Detection • Experimental Methods

3.1 Introduction

Following a major earthquake, it is imperative to check buildings for damage. Current practice requires visual inspection to determine if a building is safe, damaged, or unsafe [1]. This practice suffers from three deficiencies. First, visual inspection is costly, requiring teams of trained inspectors. Second, visual inspection is time-intensive because it often takes weeks or months to inspect damaged buildings in an area. Third, visual inspection is inherently subjective and cannot detect damage that is hidden behind partitions and other obstructions.

To overcome the limitations of visual inspections, many researchers have turned their attention to structural health monitoring (SHM). SHM includes automated and data-driven techniques that use measurements of the building response to determine if damage has occurred. Within the class of SHM techniques, several researchers have turned to substructure identification as a way to detect common forms of structural damage. Substructure identification works by identifying a reduced order model of a portion of the structure and detecting damage through stiffness changes. This approach is uniquely beneficial because it reduces the complexity of the analysis model which often makes identification more sensitive to

C. DeVore (✉) • E.A. Johnson
Sonny Astani Department of Civil and Environmental Engineering, University of Southern California,
3620 S Vermont Ave, Los Angeles, CA 90089, USA
e-mail: cdevore@usc.edu; JohnsonE@usc.edu

R.E. Christenson
Department of Civil and Environmental Engineering, University of Connecticut, 261 Glenbrook Rd., Storrs, CT 06269, USA
e-mail: rchrste@engr.uconn.edu

structural damage when compared to global modal methods. In the past two decades, researchers advanced substructure identification through a variety of techniques including an extended Kalman filter (EKF) [2], an auto-regressive moving average with exogenous input (ARMAX) model [3], substructure isolation methods [4], and others.

This study focuses on substructure identification of a shear building in the frequency domain. Zhang and Johnson [5, 6] proposed a method to identify a single story of a shear building by treating it as a single degree of freedom (SDOF) system and using measured accelerations. Within this study, the authors observed that different stories within a uniform shear building exhibit different identification performance. In a follow-up study, Zhang and Johnson [7, 8] proposed using a structural control device to temporarily change the closed-loop dynamics of the structure in a specific way to improve the identification of a particular story.

This paper uses the results of DeVore *et al* [9] to design a feedback controller to improve identification of the second story of an experimental structure. In DeVore *et al* [9], the authors use substructure identification to detect damage in a four story, shear, laboratory-scale experimental building, showing that substructure identification was unable to identify the second story stiffness. Therefore, this paper details the design of a feedback controller to improve substructure identification of the second story.

3.2 Substructure Identification

This section describes the derivation of the substructure identification estimator. First, the reduced order model is described. Second, the estimator is formulated using Newton's second law. Third, the derived estimator is implemented using estimated frequency response functions and least squares estimation. Finally, an approximate error prediction is discussed.

3.2.1 Reduced Order Model

The reduced order model (ROM) used in this study is a shear building model. This model assumes that each floor level can be treated as an independent degree of freedom (DOF) that moves laterally with no rotation. Furthermore, the restoring force provided by the columns is linear in displacement and velocity of the adjacent floor levels. This model is appropriate for civil buildings that have a high beam to column stiffness ratio.

Within the context of substructure identification, the shear building ROM suggests using a single story as the substructure model. Thus, the model function is a SDOF oscillator with transfer function given by

$$H_{\text{MOD}}(s) = \frac{1}{1 + \frac{c_i}{m_i s} + \frac{k_i}{m_i s^2}} \quad (3.1)$$

This model function will be used to estimate the story stiffness and damping parameters (k_i and c_i) of the i^{th} story.

3.2.2 Estimator Formulation

To generate an estimator suitable for the ROM and the selected model function, start with the equation of motion (EOM) for the i^{th} story.

$$m_i \ddot{x}_i + c_i (\dot{x}_i - \dot{x}_{i-1}) + k_i (x_i - x_{i-1}) + c_{i+1} (\dot{x}_i - \dot{x}_{i+1}) + k_{i+1} (x_i - x_{i+1}) = 0 \quad (3.2)$$

Next apply the Laplace transform and various identities to realize $H_{\text{MOD}}(s)$.

$$\frac{1}{1 + \frac{c_i}{m_i s} + \frac{k_i}{m_i s^2}} = \frac{H_{\ddot{x}_i, \ddot{u}_g}(s) - H_{\ddot{x}_{i-1}, \ddot{u}_g}(s)}{-H_{\ddot{x}_{i-1}, \ddot{u}_g}(s) + [H_{\ddot{x}_{i+1}, \ddot{u}_g}(s) - H_{\ddot{x}_i, \ddot{u}_g}(s)] \left(\frac{c_{i+1}}{m_i s} + \frac{k_{i+1}}{m_i s^2} \right)} \quad (3.3)$$

Herein, the right side of (3.3) is referred to as the function of estimated quantities, $H_{\text{EST}}(s)$. This function relates the acceleration response of the i^{th} and adjacent stories to the model function. As such, $H_{\text{EST}}(s)$ will be used to transform

measured acceleration to the model function. It is noted that $H_{\text{EST}}(s)$ requires *a priori* knowledge of the parameters k_{i+1} and c_{i+1} of the story above, which can be provided by a top-down identification where the top story is identified by exploiting free surface boundary conditions. Then, the identified stiffness value is used for identification of the story below and repeated down the height of the structure.

3.2.3 Estimator Implementation

To implement the substructure identification estimator derived in the previous section, an identification functional is created that evaluates the distance between $H_{\text{ROM}}(s)$ and $H_{\text{EST}}(s)$. Thus, for a given value of k_i and c_i , the identification functional is,

$$J = \int |H_{\text{MOD}}(j\omega) - H_{\text{EST}}(j\omega)|^2 d\omega \quad (3.4)$$

Here the integral is evaluated along the imaginary axis as $s = j\omega$. This allows for frequency response functions (FRFs) to be used that are more easily estimated from acceleration records.

In a realistic SHM scenario, the excitation is not measured, which precludes the estimation of input-output FRFs. Instead, $H_{\text{EST}}(j\omega)$ can be formulated to use the interstory FRF, $H_{\ddot{x}_m, \ddot{x}_n}$, with acceleration at the n^{th} floor taken as input and acceleration at the m^{th} floor taken as output. Moreover, by using the acceleration from the identified and adjacent floors (\ddot{x}_{i-1} , \ddot{x}_i , and \ddot{x}_{i+1}), the estimation of $H_{\text{EST}}(j\omega)$ can be decentralized and written three ways. For example,

$$H_{\text{EST}}^{(\ddot{x}_{i-1})}(H_{\ddot{x}_i, \ddot{x}_{i-1}}, H_{\ddot{x}_{i+1}, \ddot{x}_{i-1}}, j\omega) = \frac{1 - H_{\ddot{x}_i, \ddot{x}_{i-1}}}{1 + (H_{\ddot{x}_{i+1}, \ddot{x}_{i-1}} - H_{\ddot{x}_i, \ddot{x}_{i-1}}) \left(\frac{jc_{i+1}}{m_i\omega} + \frac{k_{i+1}}{m_i\omega^2} \right)} \quad (3.5)$$

where $H_{\text{EST}}^{(\ddot{x}_{i-1})}$ is H_{EST} with the floor below, the $(i-1)^{\text{th}}$ floor, chosen as the input signal. By formulating the FRF substructure estimator in three separate ways, the estimator can be designed to use, at each frequency, the most accurate of the three formulas. This is implemented by using as the input, the signal that has the highest power at a particular frequency, which corresponds to a higher signal to noise ratio (SNR).

Finally, with $H_{\text{EST}}(j\omega)$ estimated, k_i and c_i can be estimated using nonlinear least squares estimation. The least squares estimate (LSE) is found by minimizing the sum of the squares error between $H_{\text{MOD}}(j\omega_n)$ and H_{EST} . The sum of the squares error is

$$S(\boldsymbol{\theta}) = \sum_{n=1}^N |H_{\text{MOD}}(j\omega_n, \boldsymbol{\theta}) - H_{\text{EST}}(j\omega_n)|^2 \quad (3.6)$$

where $\boldsymbol{\theta} = [k_i, c_i]^T$ is the vector of identified quantities.

3.2.4 Error Prediction

There are certain structure–substructure combinations that lead to poor identification performance as predicted [5] and observed [9]. This study argues that poor identification performance is predicted when there is low magnitude of the interstory acceleration response in the frequency range near interstory natural frequency $\omega_{i,0} = \sqrt{k_i/m_i}$. For the test bed structure (Fig. 3.1a), a pole–zero cancellation is observed at the interstory natural frequency, which, combined with low damping, makes identification of the second story stiffness impossible with substructure identification. This behavior is observed in the frequency response graph in Fig. 3.1b.

3.3 Methods

This section describes the methods used in this study. First, the experimental apparatus is introduced, including the structure, excitation source, and sensors. Next, the the control design procedure is detailed and a feedback controller is designed.

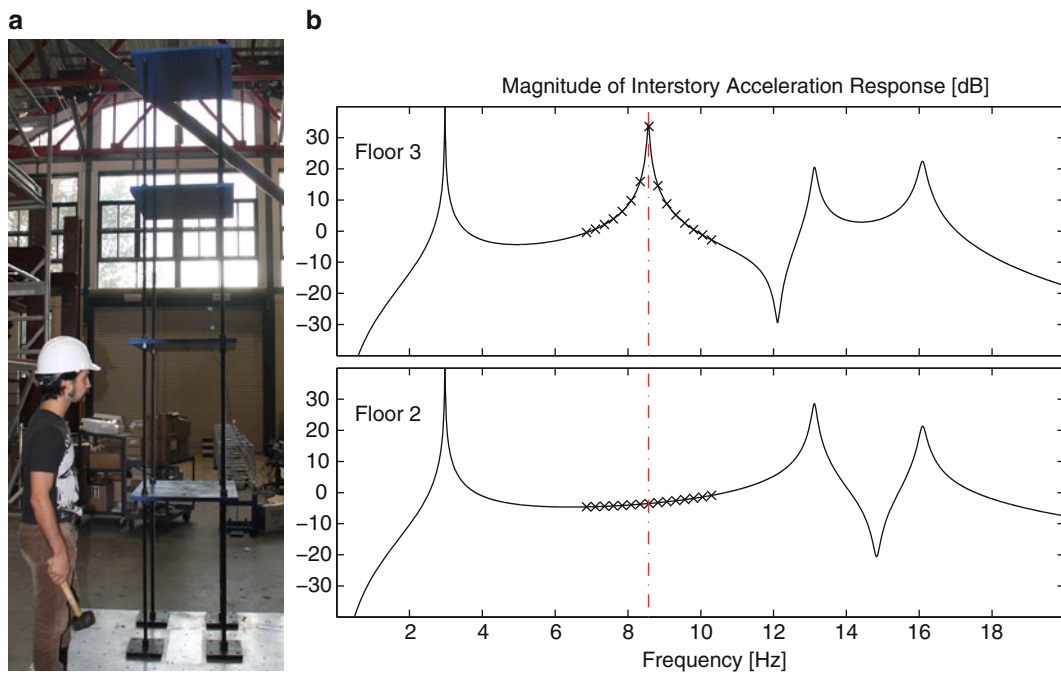


Fig. 3.1 (a) Experimental structure and (b) plot of interstory acceleration FRF for each story in the structure. *Markers* indicate frequency values that are used in nonlinear regression and the *red dashed line* indicates the maximum response of $H_{MOD}(j\omega)$. Nominal parameters are used

Table 3.1 Nominal story parameters for four story structure

k_i	126.3 kN/m
c_i	65.3 N/(m/s)
m_i	84.3 kg

3.3.1 Experimental Apparatus

The experimental apparatus is based on a previous experimental study performed at the University of Connecticut [9]. The structure is a four-story, uniform shear building that is symmetric in both plan directions. The building is formed by supporting steel floor plates by four threaded rod columns at the corners. The columns are secured with nuts and lock washers installed above and below each floor plate to ensure the columns behave as fixed-fixed at each story. The nominal parameters for each story level are computed and summarized in Table 3.1.

The excitation source is base motion provided by a 3 ton, uniaxial, 2 m \times 2 m shake table. It is run in displacement control and provides a band-limited white noise base excitation. The command signal is pre-filtered such that the shake table achieves a nominally flat acceleration response. The average power of the excitation is characterized by the standard deviation of the table acceleration which is 0.1 m/s².

The response of the structure is measured by PCB capacitive accelerometers installed on each floor along the plan centerline in the direction of excitation. The accelerometers are sampled at 256 Hz for 512 seconds for each trial. A noise analysis is performed and the accelerometers are found to have SNR of 30 dB.

3.3.2 Control Design

To improve the identification performance of the second story stiffness parameter, a feedback controller for an active mass driver (AMD) is designed consistent with the error analysis described in Section 3.2.4 and [7]. The AMD is installed on the top floor of the structure and it is assumed that the AMD is able to apply a perfect force command. This assumption is unrealistic but control design can be later extended to use an experimentally-derived transfer function from AMD command

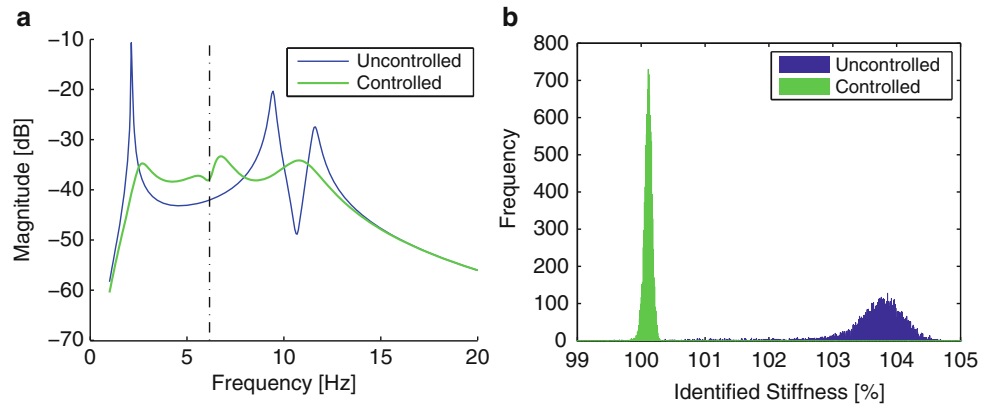


Fig. 3.2 (a) Second story interstory acceleration frequency response with and without control. The interstory natural frequency is marked by a dashed line. (b) Histogram of identified second story stiffness values expressed as a percentage of the nominal stiffness. The total number of samples is 10,000 with 876 outliers for the uncontrolled system and 78 outliers with controlled system. Outliers are defined as identification results outside the range of (99%, 105%)

to AMD force or, more generally, structural response. A shear building model is used with the nominal parameters found in the previous section, which was found to have good agreement with experimental values [9]. In this study, it is assumed that perfect state estimation is available and, therefore, closed-loop poles \mathbf{p} are used as the search space for control design. This innovation allows specifying the closed-loop poles and finding a feedback gain $\mathbf{K}(\mathbf{p})$ using pole placement. As such, the controller is found by minimizing the functional

$$\arg \max_{\mathbf{p}} \int_{0.8\omega_0}^{1.2\omega_0} \left| W(j\omega) H_{\ddot{x}_i - \ddot{x}_{i-1}, \ddot{u}_g}^{\mathbf{K}(\mathbf{p})}(j\omega) \right|^2 d\omega \quad (3.7)$$

where $H_{\ddot{x}_i - \ddot{x}_{i-1}, \ddot{u}_g}^{\mathbf{K}(\mathbf{p})}$ is the closed-loop interstory acceleration frequency response function for the i^{th} story given closed-loop poles \mathbf{p} and $W(j\omega)$ is a weighting function that assumes the shape of a SDOF oscillator. The minimization is subject to the constraints that the real component of the closed loop poles are less than the largest real component of the uncontrolled poles and that the damping of the closed loop system be larger than 10% in each mode (*i.e.*, $\text{Re } p_i < -0.1|p_i|$). An additional constraint that the force applied be less than 100 N is used but is found to be an inactive constraint as the force levels were significantly smaller. Numerical optimization is provided by the MATLAB[®] command `fmincon` using an interior-point algorithm.

The damping constraint was found to have a significant effect on the controller design by limiting the maximum response below -30 dB. Likewise, the control functional had the effect of placing two poles near the interstory natural frequency (6.16 Hz). The effect of the controller on the second story interstory acceleration response is shown in Fig. 3.2a.

3.4 Results

To verify the improved identification performance of controlled substructure identification, Monte Carlo simulation is used. Acceleration time histories are generated and then analyzed using the substructure identification methods described in Section 3.2.3 to find the second story stiffness parameter. The stiffness parameter is recorded and the process is repeated 10,000 times for both the uncontrolled and controlled systems.

The results of Monte Carlo simulation are summarized by the statistics in Table 3.2 and the histogram in Fig. 3.2b. Gaussian sample statistics (mean and standard deviation) are reported with robust statistics (median and inter-quartile range (IQR)) because, while the identified stiffness parameter converges to a Gaussian distribution, there are significant outliers. By direct comparison of the statistics and visual inspection of the histogram, it is evident that the controlled system exhibits increased accuracy and decreased variance, whereas the uncontrolled identification has significant bias as well as large deviations.

Table 3.2 Identification statistics for second story stiffness with and without control expressed as a percentage of the nominal value

	Mean	St. dev.	Median	IQR
Uncontrolled	107.12	13.43	103.79	0.53
Controlled	99.72	4.41	100.11	0.08

3.5 Conclusions

The results indicate that the identification accuracy and precision of the second story stiffness is much greater using the designed feedback controller. Further, there are fewer trials for which identification fails, evidenced by a decreased number of outliers (876 decreased to 78). While the controller enables superior identification performance, it relies on full state estimation which will not be available in a laboratory setting. Prior to implementation in experiment, it is necessary to design and simulate the effects of a state observer on identification performance. Experimental verification is planned using the developed feedback controller.

References

1. ATC (1989) ATC-20: procedures for postearthquake safety evaluation of buildings, Tech. Rep. Applied Technology Council, Redwood City
2. Koh CG, See LM, Balendra T (1991) Estimation of structural parameters in time domain: a substructure approach. *Earthquake Eng Struct Dynam* 20(8):787–801
3. Xing Z, Mita A (2012) A substructure approach to local damage detection of shear structure. *Struct Contr Health Monit* 19(2):309–318
4. Hou J, Jankowski Ł, Ou J (2011) A substructure isolation method for local structural health monitoring. *Struct Contr Health Monit* 18(6): 601–618
5. Zhang D, Johnson EA (2013) Substructure identification for shear structures I: substructure identification method. *Struct Contr Health Monit* 20(5):804–820
6. Zhang D, Johnson EA (2006) Substructure parameter identification method for shear type structures. In: *Proceedings of 4th world conference on structural control and monitoring*, San Diego, CA, 2006
7. Zhang D, Johnson EA (2013) Substructure identification for shear structures II: controlled substructure identification. *Struct Contr Health Monit* 20(5):821–834
8. Zhang D, Johnson EA (2006) Controlled substructure identification method for shear type structure. In: *Proceedings of 4th world conference on structural control and monitoring 2*, San Diego, CA, 2006
9. DeVore C, Jiang Z, Johnson EA, Christenson RE, Stromquist-Levoir G (2012) Experimental verification of substructure identification for damage detection. In: *Proceedings of the 2012 engineering mechanics institute conference*, South Bend, IN, 2012

Chapter 4

Hybrid MPC: An Application to Semiactive Control of Structures

Wael M. Elhaddad and Erik A. Johnson

Abstract In clipped LQR, a common strategy for semiactive structural control, a primary feedback controller is designed using LQR and a secondary controller clips forces that the semiactive control device cannot realize. However, when the primary controller commands highly non-dissipative forces, the frequent clipping may render a controller far from being optimal. A hybrid system model is better suited for semiactive control as it accurately models the passivity constraints by introducing auxiliary variables into the system model. In this paper, a hybrid model predictive control (MPC) scheme, which uses a system model with both continuous and discrete variables, is used for semiactive control of structures. Optimizing this control results in a mixed integer quadratic programming problem, which can be solved numerically to find the optimal control input. It is shown that hybrid MPC produces nonlinear state feedback control laws that achieve significantly better performance for some control objectives (e.g., the reduction of absolute acceleration). Responses of a typical structure to historical earthquakes, and response statistics from a Monte Carlo simulation with stochastic excitation, are computed. Compared to clipped LQR, hybrid MPC is found to be more consistent in the reduction of the objective functions, although it is more computationally expensive.

Keywords Structural control • Semiactive dampers • Hybrid systems • Model predictive control • Clipped LQR

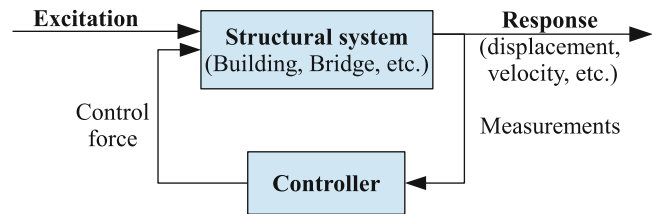
4.1 Introduction

In the past few decades, extensive research was conducted to study structural control and its application in natural hazards mitigation [1], with the main focus of protecting buildings and bridges against strong earthquakes and extreme winds. Significant efforts were devoted in realizing structural control systems for real-life applications, to protect structural systems, and consequently, human lives; such an application is of great social and economic importance. Today, many buildings and bridges around the world employ structural control systems for vibration reduction [2]. Researchers have investigated the application of different control strategies in structures, such as passive, active, hybrid and semiactive control. Although, passive control strategies [3] are the best established and most well-accepted for structural vibration reduction, they are not the most efficient control technique as they cannot adapt to different loading events and structural conditions. On the other hand, active control strategies are more adaptive and efficient in vibration reduction, though they suffer from reliability issues [1] since they can render a structure unstable and can demand power that might not be available during an extreme loading event such as an earthquake or severe wind exposure.

Recently, semiactive strategies based on controllable passive devices have emerged as an alternative for vibration reduction in structures. Controllable passive devices are ones that exert forces through purely passive means, such as a controllable damper or controllable stiffener, but have controllable properties that affect those forces. Some examples of controllable passive devices are variable orifice dampers, variable friction devices, variable stiffness devices and controllable fluid dampers (e.g., magnetorheological (MR) and electrorheological (ER) fluid dampers) [1, 2, 4–6].

W.M. Elhaddad (✉) • E.A. Johnson
Sonny Astani Department of Civil and Environmental Engineering, University of Southern California,
3620 S Vermont Ave, Los Angeles, CA 90089, USA
e-mail: welhadda@usc.edu; JohnsonE@usc.edu

Fig. 4.1 Feedback control for structural systems



Thus, the main benefits of using semiactive control are its inherent stability, as it does not introduce energy into the controlled structure, its ability to focus on multiple (and possibly changing) objectives, exerting a force that can depend on non-local information, as well as the low power requirement that is critical in the case of natural hazards like earthquakes [7]. In addition, it has been shown that semiactive control is capable, in some cases, of achieving performances comparable to that of a fully active system [7]. It is, thus, beneficial to advance the understanding of the behavior of structural systems controlled with such devices, to be able to take full advantage of their capabilities.

Since both active and semiactive control systems have the ability to adapt to different operating conditions, they rely on control algorithms to achieve this adaptability. Both strategies make use of measurements and observations of current structure state, as shown in Fig. 4.1. The measurements are then provided as a feedback to the controllers that are responsible for making a decision about how the device should adapt to the current state of the system in order to efficiently reduce its future vibrations.

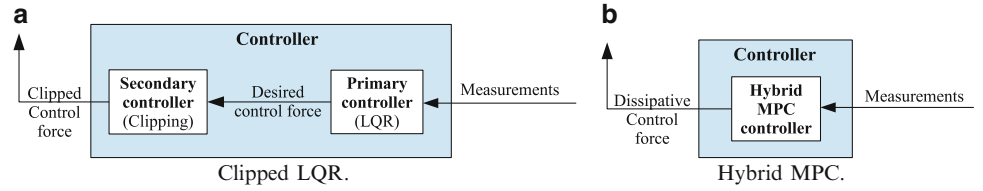
4.2 Motivation

The design process of semiactive control for vibration reduction of structures is crucial in order to obtain an effective use of the control device. Different feedback control strategies can be used to minimize vibrations in structures controlled with semiactive devices [8]. Some examples of these control laws are neural/fuzzy control strategies [9], Lyapunov control [8, 10, 11], pseudo-negative stiffness control [12], performance-guarantee approaches [13, 14] and LMI control [15]. Many other applications of semiactive control are based on the clipped-optimal control technique [7], where the desired control input is determined by initially assuming an unconstrained device force model. Then, any non-dissipative force is clipped from the desired control, as shown in Fig. 4.2a, to ensure that the resulting input is dissipative and realizable by the semiactive device. However, when the desired control is highly non-dissipative, the frequent clipping may render the clipped control strategy far from being optimal, as the design methodology does not, and cannot, consider the semiactive control device's inherent passivity constraints — *i.e.*, that it can only exert dissipative forces regardless of the command it is given. For that reason, the design of control with such a method is inconsistent in the minimization of the objective functions. The result of such inconsistency is the use of heuristic approaches that usually involve large scale parametric studies [16, 17] and is not guaranteed optimality.

Model predictive control (MPC) has been employed for control design in different applications. MPC has been widely adopted in industrial engineering in the past three decades [18]. The method is an iterative scheme that seeks to control the future outputs of a dynamical system by using a model to predict those outputs throughout a finite horizon in the future. The MPC scheme attempts to optimize the future outputs of the dynamical system by manipulating the future inputs, given the current state of the system. When the optimal sequence of future inputs is determined, only the first input is implemented and the whole process is repeated again to determine the next optimized input. Today, the MPC method lends itself to different control applications, including applications in automotive, aerospace and process industries.

The main idea of MPC is minimizing a quadratic cost function written in terms of the predicted states and control input in the future time steps, which is why the method is sometimes called in the literature the *receding horizon method*. The number of steps used to predict system states in the future is called the *prediction horizon*, whereas the number of steps over which a control input is considered is called the *control horizon*. The control and prediction horizons for this study are assumed to be equal, which is the case in many applications of MPC. The resulting optimization problem is a quadratic programming problem in terms of the control inputs at each time step of the control horizon. This optimization process is repeated at each time step, which requires that the system analysis be performed fast enough so that the result can be obtained during the sampling time and the control input can be implemented in real time. Although, this can readily be implemented for simple models with a few degrees-of-freedom (DOFs), it can be computationally expensive for higher order or nonlinear systems. Standard MPC has been successfully applied for active control of civil structures, but cannot be easily and directly applied to semiactive strategies because of the nonlinear inequality constraint that arises from the passivity requirements of controllable passive devices.

Fig. 4.2 Semiactive control strategies



The application of MPC in structural control has been investigated previously by Mei et al. [19]. In their study, the potential of MPC in structural control was demonstrated on building models with active tendon systems with full state feedback, later extended [20] to use acceleration feedback. Those implementations are, however, not suitable for structures controlled with semiactive devices as they fail to handle the nonlinear passivity constraints that characterize the behavior of such devices.

Hybrid systems are time evolving systems that exhibit mixed dynamics due to interacting physical laws, logical conditions and/or different operating modes [21]. Hybrid systems can be represented in different forms, such as piecewise affine functions [22], discrete hybrid automata [23] and mixed logical dynamical (MLD) system models [24] — all mathematically equivalent [25]. In this paper, MLD systems are used to model structures controlled with a semiactive device as a hybrid system.

A *hybrid system model* is well suited for the design of semiactive control as it can accurately reflect the nonlinear constraints of a semiactive device by introducing *auxiliary variables* into the system model. Hybrid MPC is an MPC scheme that finds optimal control strategies for a hybrid system model. Optimization of this control results in a mixed integer quadratic programming (MIQP) problem, which can be solved numerically to find the optimal control input. The resulting control force satisfies the passivity constraint and no longer needs clipping as shown in Fig. 4.2b. The on-line implementation of hybrid MPC must solve the optimization problem during the sampling time of the system, which is a computationally challenging problem with a complex system model and/or anything but the shortest time horizons. On the other hand, an off-line implementation will carry out most of the computations *a priori*, resulting in less demanding computation, such as a table look-up, to be carried out in real time during the sampling time.

As shown subsequently in the numerical example, hybrid MPC is readily applied to structural systems with a few degrees-of-freedom. In contrast with control laws derived from unconstrained system models (*e.g.*, clipped LQR), hybrid MPC produces nonlinear state feedback control laws that can achieve significantly better performance for some control objectives (*e.g.*, the reduction of absolute accelerations). Despite the nonlinear nature of the control laws, it is found that they satisfy the homogeneity property (*i.e.*, they scale linearly when the state vector is scaled). This property can be exploited to reduce the dimension of table look-ups. The resulting off-line implementation of hybrid MPC is orders of magnitude faster than the on-line implementation, which enables rapid computation of response statistics from a Monte Carlo simulation with stochastic excitation. Compared to clipped LQR, hybrid MPC is found to be more consistent in the reduction of the objective functions, which can help avoid using heuristic approaches and parametric studies in the structural control design. However, it is computationally expensive to design for large structural systems with the current implementations and optimization tools; further research is required to facilitate application to more complex structures.

4.3 Formulation

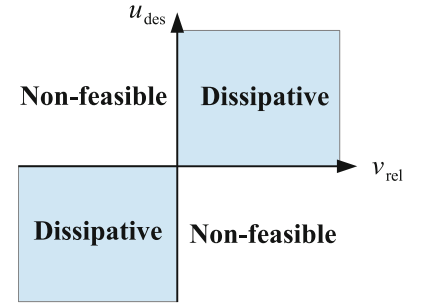
Consider a structure with n degrees of freedom that is subjected to an external excitation and is controlled by some devices to reduce its response. The equations of motion for such a structure can be written in matrix form as:

$$\mathbf{M}\ddot{\mathbf{x}}(t) + \mathbf{C}\dot{\mathbf{x}}(t) + \mathbf{K}\mathbf{x}(t) = \bar{\mathbf{B}}_{\mathbf{w}}\mathbf{w}(t) + \bar{\mathbf{B}}_{\mathbf{u}}\mathbf{u}(t) \quad (4.1)$$

where \mathbf{M} , \mathbf{C} and \mathbf{K} are the mass, damping and stiffness matrices of the structural system, respectively; \mathbf{x} is the displacement vector of the structure relative to the ground; \mathbf{w} is the external excitation (*e.g.*, ground acceleration or wind forces) with influence matrix $\bar{\mathbf{B}}_{\mathbf{w}}$; \mathbf{u} is the damping force exerted by the control device with influence matrix $\bar{\mathbf{B}}_{\mathbf{u}}$. The same set of equations can also be written in continuous-time state space form as follows:

$$\dot{\mathbf{z}}(t) = \mathbf{A}\mathbf{z}(t) + \mathbf{B}_{\mathbf{w}}\mathbf{w}(t) + \mathbf{B}_{\mathbf{u}}\mathbf{u}(t) \quad (4.2)$$

Fig. 4.3 Idealized model of the passivity constraint for controllable damping devices



in which

$$\mathbf{z} = \begin{bmatrix} \mathbf{x} \\ \dot{\mathbf{x}} \end{bmatrix}, \quad \mathbf{A} = \begin{bmatrix} \mathbf{0} & \mathbf{I} \\ \mathbf{M}^{-1}\mathbf{K} & \mathbf{M}^{-1}\mathbf{C} \end{bmatrix}, \quad \mathbf{B}_w = \begin{bmatrix} \mathbf{0} \\ \mathbf{M}^{-1}\bar{\mathbf{B}}_w \end{bmatrix} \quad \text{and} \quad \mathbf{B}_u = \begin{bmatrix} \mathbf{0} \\ \mathbf{M}^{-1}\bar{\mathbf{B}}_u \end{bmatrix}$$

where \mathbf{z} is the state vector, \mathbf{A} is the state matrix, \mathbf{B}_w is the influence matrix of the excitation and \mathbf{B}_u is the influence matrix of the control force.

4.3.1 Clipped-Optimal Control

Generally, the optimal control design for a linear unconstrained system can be obtained using LQR, where the objective is to minimize an infinite-horizon quadratic performance index of the form:

$$J = \int_0^{\infty} [\mathbf{z}^T \mathbf{Q} \mathbf{z} + 2\mathbf{z}^T \mathbf{N} \mathbf{u} + \mathbf{u}^T \mathbf{R} \mathbf{u}] dt \quad (4.3)$$

in which \mathbf{Q} , \mathbf{R} and \mathbf{N} are weighting matrices for the different objective terms. If the external excitation is assumed to be white noise with zero mean, the certainty equivalence property [26, 27] of stochastic control theory will apply, and the stochastic optimal control is equivalent to the optimal control obtained from deterministic analysis that assumes an initial condition and ignores the excitation. The LQR control design is a quadratic programming problem, whose optimal solution is a linear state feedback controller [28] with feedback gain \mathbf{K}_{LQR} :

$$\mathbf{u}_{\text{des}}(t) = -\mathbf{K}_{\text{LQR}} \mathbf{z}(t) = -[\mathbf{R}^{-1}(\mathbf{B}^T \mathbf{P} + \mathbf{N}^T)] \mathbf{z}(t) \quad (4.4)$$

where \mathbf{P} is the positive definite solution of the algebraic Riccati equation given by:

$$(\mathbf{A} - \mathbf{B}\mathbf{R}^{-1}\mathbf{N}^T)^T \mathbf{P} + \mathbf{P}(\mathbf{A} - \mathbf{B}\mathbf{R}^{-1}\mathbf{N}^T) - \mathbf{P}\mathbf{B}\mathbf{R}^{-1}\mathbf{B}^T \mathbf{P} + \mathbf{Q} - \mathbf{N}\mathbf{R}^{-1}\mathbf{N}^T = 0 \quad (4.5)$$

Assuming the states of the structural system (*i.e.*, displacements and velocities) can be measured or estimated, then (4.4) can be used to determine the required control input, and the device can be commanded with the desired damping force. However, semiactive devices can only exert dissipative forces; any non-dissipative forces commanded will not be realized. For that reason, the previous design does not generally result in optimal control forces for controllable passive devices unless, of course, the desired control forces are purely dissipative. This technique is called the *clipped-optimal control* algorithm [8] because a primary controller is obtained assuming unconstrained damping forces (*i.e.*, the passivity constraints of semiactive device is ignored in this stage), and the device will only exert the desired forces that are dissipative. This behavior can be modeled in simulations as if a secondary controller exists that clips the nondissipative control forces.

Different semiactive devices have different constraints on the achievable damping forces; however, they all share the passivity constraint. For the sake of generality, an idealized model is adopted for modeling the passivity constraint, as illustrated graphically in Fig. 4.3. It is assumed that all dissipative forces are realizable by the device and all nondissipative forces are infeasible. The passivity constraint is a nonlinear constraint that can be written as:

$$u_{\text{des}} \cdot v_{\text{rel}} \geq 0 \quad (4.6)$$

where u_{des} is the desired control force and v_{rel} is the relative velocity across the semiactive device (chosen with sign convention such that a positive dissipative force resists motion in the positive velocity direction). The resulting control force, that the semiactive device will realize, can be calculated as follows:

$$u_{\text{sa}} = u_{\text{des}} \cdot H[u_{\text{des}} \cdot v_{\text{rel}}] = \begin{cases} u_{\text{des}}, & u_{\text{des}} \cdot v_{\text{rel}} \geq 0 \\ 0, & u_{\text{des}} \cdot v_{\text{rel}} < 0 \end{cases} \quad (4.7)$$

where $H[\cdot]$ is the Heaviside step function.

4.3.2 Hybrid MPC for the Design of Semiactive Structural Control

Generally, a discrete time form of a mixed logical dynamical system can be written as [21]:

$$\mathbf{z}_{k+1} = \tilde{\mathbf{A}}\mathbf{z}_k + \tilde{\mathbf{B}}_u\mathbf{u}_k + \tilde{\mathbf{B}}_\delta\delta_k + \tilde{\mathbf{B}}_v\mathbf{v}_k \quad (4.8a)$$

$$\mathbf{E}_\delta\delta_k + \mathbf{E}_v\mathbf{v}_k \leq \mathbf{E}_u\mathbf{u}_k + \mathbf{E}_z\mathbf{z}_k + \mathbf{E}_0 \quad (4.8b)$$

where \mathbf{z}_k is the state vector at time $k\Delta t$; and Δt is the sampling time of the system. δ_k and \mathbf{v}_k are auxiliary vectors that are binary indicator (*i.e.*, 0 or 1) and real vector functions, respectively, of the states and inputs, and are governed by the inequality in (4.8b). It will be shown later in the numerical example that the nonlinear passivity constraint described in (4.6) can be transformed to linear inequalities as in (4.8b). Note that the certainty equivalence is assumed, similar to the previous section, where the optimal stochastic control can be obtained from deterministic analysis that assumes an initial condition and ignores the excitation.

An MPC scheme based on hybrid model (4.8), can be used to determine the optimal input for semiactive control devices [29]. Such a method is denoted, herein, a *hybrid MPC*. The main idea is to minimize a quadratic cost function similar to the one used in (4.3) for LQR design; however, this scheme should consider the hybrid system model in order to account for the passivity constraint. Since the hybrid system used here is in discrete form, hence the cost function must be written as a summation for p steps, instead of an integral, such as:

$$J(\boldsymbol{\xi}, \mathbf{z}_0) \triangleq \mathbf{z}_p^T \mathbf{Q}_p \mathbf{z}_p + \sum_{k=1}^{p-1} [\mathbf{z}_k^T \mathbf{Q} \mathbf{z}_k + 2\mathbf{z}_k^T \mathbf{N} \mathbf{u}_k + \mathbf{u}_k^T \mathbf{R} \mathbf{u}_k] \quad (4.9)$$

where $\boldsymbol{\xi} = [\mathbf{u}_0^T, \delta_0^T, \mathbf{v}_0^T, \dots, \mathbf{u}_{p-1}^T, \delta_{p-1}^T, \mathbf{v}_{p-1}^T]^T$ is a vector that concatenates the optimization parameters together, including both the control inputs and the auxiliary variables at all time steps within the horizon [29]; and \mathbf{z}_0 is the current state vector of the system. The first term in (4.9) is the terminal cost term, which is added to emulate an infinite horizon cost function, where \mathbf{Q}_p is the solution of the Riccati equation associated with the discrete LQR problem that minimizes an infinite horizon quadratic cost as in:

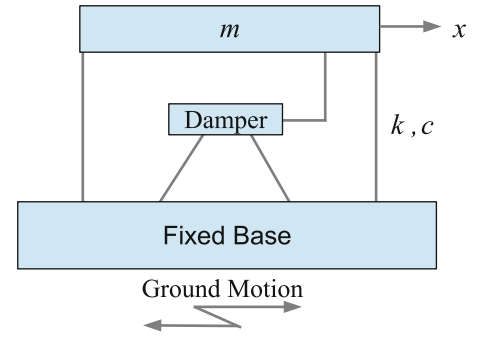
$$\min_{\mathbf{K}_{\text{LQR}}} \sum_{k=1}^{\infty} [\mathbf{z}_k^T \mathbf{Q} \mathbf{z}_k + 2\mathbf{z}_k^T \mathbf{N} \mathbf{u}_k + \mathbf{u}_k^T \mathbf{R} \mathbf{u}_k] \quad (4.10)$$

Note that a horizon of $p = 1$ step results, then, in a control identical to clipped LQR. Cost function (4.9), which is quadratic, must be minimized subject to the linear equality in state equation (4.8a) and to inequality constraints (4.8b), written in terms of both binary and real variables. The resulting optimization problem is a MIQP problem that, when solved, will provide the optimal control input [21].

4.4 Numerical Example

In this section, a numerical application to a single degree of freedom (SDOF) structural model is presented to demonstrate the potential of hybrid MPC in optimization of semiactive control design. Control designs were performed using both clipped

Fig. 4.4 SDOF structure



LQR and hybrid MPC; their respective control performances are compared for various ground motion records and for a Gaussian white noise excitation. The SDOF structural model considered here is shown in Fig. 4.4 with equation of motion:

$$m\ddot{x} + c\dot{x} + kx = -m\ddot{x}_g - u \quad (4.11)$$

where \ddot{x}_g is the ground acceleration.

The model parameters used for this structure are $m = 100 \text{ Mg}$, $k = 3.948 \text{ MN/m}$ and $c = 62.833 \text{ kN}\cdot\text{s/m}$, which results in natural frequency $\omega = 2\pi \text{ rad/s}$ and damping ratio $\zeta = 0.05$.

First, semiactive control is designed using the clipped LQR strategy discussed previously in section 4.3.1. The objective of the control design is the minimization of the absolute acceleration of the structure; this is accomplished by using the weighting matrices:

$$\mathbf{Q} = \begin{bmatrix} \omega^4 & 2\zeta\omega^3 \\ 2\zeta\omega^3 & 4\zeta^2\omega^2 \end{bmatrix}, \quad \mathbf{N} = \begin{bmatrix} \omega^2/m \\ 2\zeta\omega/m \end{bmatrix} \quad \text{and} \quad \mathbf{R} = m^{-2}$$

The dissipativity constraint of the semiactive device can be incorporated into the hybrid MPC formulation (which is not possible for the design of the primary LQR controller for clipped-optimal control). Additionally, without loss of generality, the optimization converges faster with limits on the responses and the control force. Together, these result in three pairs of inequality constraints. **(1)** The nonlinear passivity constraint in this case is $u\dot{x} \geq 0$. Using auxiliary binary variables $\delta_{\dot{x}_k} \equiv \delta_{\dot{x}_k} = H[\dot{x}_k]$ and $\delta_{u_k} = H[u_k]$, the passivity constraint can be expressed as a single equality constraint $\delta_{\dot{x}_k} = \delta_{u_k}$ or, to be consistent with the inequality constraints in (4.8b), as the pair of inequalities $\delta_{\dot{x}_k} \leq \delta_{u_k}$ and $\delta_{\dot{x}_k} \geq \delta_{u_k}$. **(2)** A constraint on the velocity can be expressed as a single nonlinear inequality $|\dot{x}_k| \leq v_{\max}$ or, amenable for use in (4.8b), a pair of linear inequalities $\dot{x}_k \leq v_{\max}\delta_{\dot{x}_k}$ (constraining \dot{x}_k when it is positive) and $\dot{x}_k \geq -v_{\max}(1 - \delta_{\dot{x}_k})$ (when \dot{x}_k is negative) using the auxiliary binary variables. **(3)** A constraint on the control force can be expressed similar to the velocity: nonlinear $|u_k| \leq u_{\max}$ or the linear pair $u_k \leq u_{\max}\delta_{u_k}$ and $u_k \geq -u_{\max}(1 - \delta_{u_k})$. In this example, $v_{\max} = 10 \text{ m/s}$ and $u_{\max}/m = 100 \text{ m/s}^2$. The resulting MLD system, similar to (4.8), is then:

$$\mathbf{z}_{k+1} = \tilde{\mathbf{A}}\mathbf{z}_k + \tilde{\mathbf{B}}_u u_k \quad (4.12a)$$

$$\mathbf{E}_\delta \delta_k \leq \mathbf{E}_u u_k + \mathbf{E}_z \mathbf{z}_k + \mathbf{E}_0 \quad (4.12b)$$

where

$$\delta_k = \begin{bmatrix} \delta_{\dot{x}_k} \\ \delta_{u_k} \end{bmatrix} \in \{0, 1\}^2, \quad \mathbf{E}_\delta = \begin{bmatrix} -v_{\max} & 0 \\ v_{\max} & 0 \\ 0 & -u_{\max} \\ 0 & u_{\max} \\ 1 & -1 \\ -1 & 1 \end{bmatrix}, \quad \mathbf{E}_u = \begin{bmatrix} 0 \\ 0 \\ -1 \\ 1 \\ 0 \\ 0 \end{bmatrix}, \quad \mathbf{E}_z = \begin{bmatrix} 0 & -1 \\ 0 & -1 \\ 0 & 0 \\ 0 & 0 \\ 0 & 0 \\ 0 & 0 \end{bmatrix} \quad \text{and} \quad \mathbf{E}_0 = \begin{bmatrix} 0 \\ v_{\max} \\ 0 \\ u_{\max} \\ 0 \\ 0 \end{bmatrix}.$$

In order to design the control using hybrid MPC, an optimization problem as in (4.9) must be solved subject to equality constraint (4.12a) and inequality constraint (4.12b). The control for this structural model was designed using both clipped LQR and hybrid MPC; the resulting control forces as functions of the state vector are shown in Fig. 4.5. The hybrid system model of the SDOF structure was generated in MATLAB[®] using a toolbox called YALMIP [30], which can be used for fast

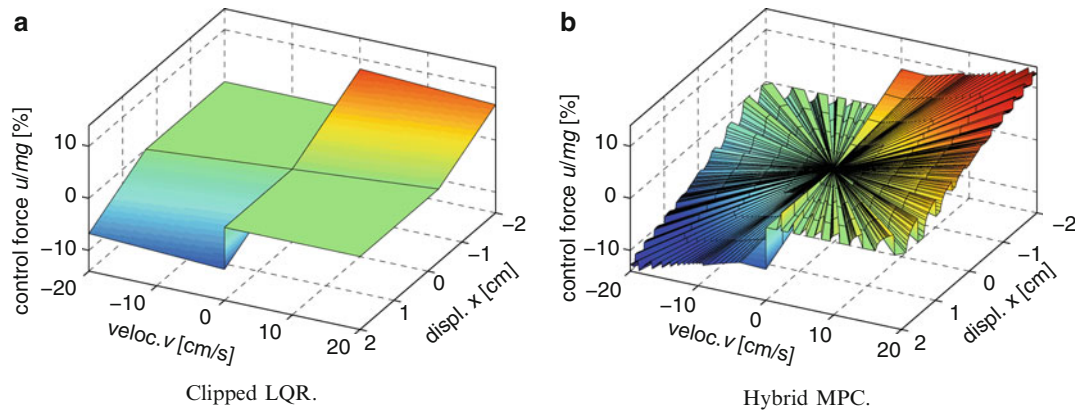


Fig. 4.5 Comparison of control input for SDOF system

Table 4.1 Minimum cost for various hybrid MPC prediction horizons

p	Cost
1	41.49 ^a
5	44.19
10	40.55
15	33.17
20	31.49
25	31.22
30	31.01
40	30.93
50	30.84

^a =CLQR

prototyping of optimization problems, and is used here to solve the resulting MIQP problems. This toolbox relies on one of several supported external solvers to perform the optimization. In this study, two different solvers were used: IBM CPLEX [31] and Gurobi Optimizer [32]. As a verification of the numerical optimization, both solvers were found to give the same solution for the MIQP problems involved in the presented examples.

For hybrid MPC, a suitable prediction horizon needs to be selected. A parametric study was performed, using the Northridge 1994 (Rinaldi) earthquake record as the excitation, to study the effectiveness of the control obtained from hybrid MPC for different prediction horizons. For a time step of 0.02 secs, the parametric study is shown in Table 4.1. Based on the parametric study, the prediction horizon selected in this study is 30 steps, 0.02 secs each, which provides a good compromise between accuracy and computational expense.

The two control inputs obtained from clipped LQR and hybrid MPC show drastic differences. The control law obtained from LQR is a linear function of the states as in (4.4), and a significant part of it gets clipped when the linear control law commands non-dissipative forces as shown in Fig. 4.5a. On the other hand, the control obtained from hybrid MPC scheme is nonlinear and is generally more dissipative. The differences suggests that the hybrid MPC strategy is using the damping device more efficiently; however, in order to quantitatively compare both strategies, the controlled structure must be simulated under the effect of excitation.

Simulations were performed for the SDOF structure subjected to several historical earthquakes, including the 1940 El Centro and 1995 Kobe records. Simulation results are compared in Table 4.2, including peak responses, control force and values of the objective function. The results show that the hybrid MPC strategy results, consistently, in lower peak responses and cost values. Although, the control was designed to minimize the absolute acceleration, the results show that hybrid MPC can achieve significant reduction, compared to clipped LQR, in the displacements and velocities as well, which suggests that the clipped LQR strategy is not using the damping device effectively.

The previous simulations illustrate the efficacy of the proposed hybrid MPC for control design of structures subjected to earthquakes. It is also beneficial to examine the efficacy of the resulting control when the structure is subjected to wind loading. The loads induced on structures by winds are random and often assumed to be a wide-band stochastic process. Without loss of generality, the wind is approximated here as a Gaussian white noise. In order to quantify the control strategies' efficacy for wind response mitigation, a Monte Carlo simulation is carried out where the controlled SDOF model was subjected to 8 second samples of zero-mean Gaussian white noise excitation, which was a sufficient time for the system

Table 4.2 Comparison of peak responses, control force and cost values using historical earthquakes

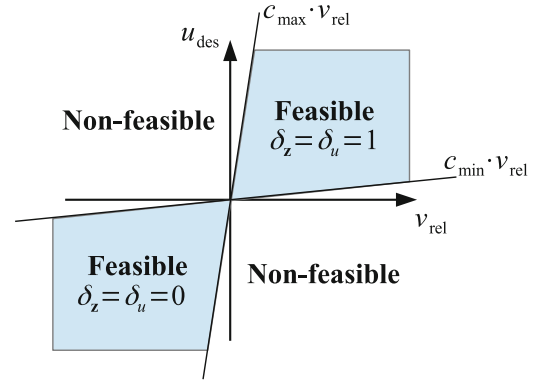
	El Centro 1940			Kobe 1995		
	CLQR	HMPC	Δ [%]	CLQR	HMPC	Δ [%]
x_{\max} [cm]	5.58	4.29	-23	6.77	4.73	-30
\dot{x}_{\max} [cm/s]	39.82	32.80	-18	34.08	24.12	-29
$\ddot{x}_{\max}^{\text{abs}}$ [cm/s ²]	221.3	189.5	-15	268.5	202.7	-24
u_{\max}/mg [%]	22.13	17.21	-22	27.25	18.99	-30
cost [m ² /s ³]	4.761	4.117	-14	3.761	2.804	-25

Note: Δ is the percent change from Clipped LQR to Hybrid MPC; negative numbers are improvements

Table 4.3 Root-mean-square response using Monte Carlo simulation with 1 million realizations

(a) Idealized model I				(b) Idealized model II				
Response	CLQR	HMPC	Δ [%]	Response	Passive-on	CLQR	HMPC	Δ [%]
\ddot{x}_{abs} [cm/s ²]	36.88	32.68	-11	\ddot{x}_{abs} [cm/s ²]	37.79	38.95	33.56	-14
u/mg [%]	4.078	3.472	-15	u/mg [%]	3.109	2.302	2.325	+1
x [cm]	1.374	1.041	-24	x [cm]	0.488	1.215	0.849	-30

Fig. 4.6 More realistic model for passivity constraint



to reach a stationary response. Responses were obtained for 1 million randomly generated samples and output statistics were computed and compared. Root mean square (RMS) statistics for the stationary response are presented in Table 4.3.

In addition to the idealized model for the semiactive device, described in Fig. 4.3, another idealized model shown in Fig. 4.6 is also considered in the Monte Carlo simulations. This model considers a minimum and maximum energy dissipation in the damping device, which is considered a more realistic representation of a smart damper (*e.g.*, MR damper), and is helpful in this study to illustrate the inconsistency in the clipped LQR design of semiactive control. In this section, the model in Fig. 4.3 is denoted “idealized model I” and the model in Fig. 4.6 is denoted “idealized model II.” For idealized model II, it is assumed the maximum and minimum damping coefficients are $c_{\max} = 10^4$ kN·s/m and $c_{\min} = 1$ kN·s/m which represents a real MR damper.

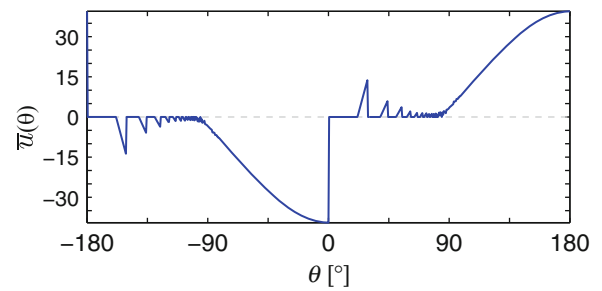
Despite the fact that hybrid MPC can be implemented in real-time for the SDOF model, the on-line implementation is not computationally practical for carrying out a Monte Carlo simulation with 1 million realizations. In order to make Monte Carlo simulation computationally less demanding, an off-line implementation of hybrid MPC is employed, which speeds up the computation by two orders of magnitude. The implementation suggested here uses table look-up and linear interpolation and exploits the property that the nonlinear control input in Fig. 4.5b is a homogeneous function of order 1 (*i.e.*, it scales linearly when the state vector scales) and, hence, can be written using radial coordinates in the form:

$$u_{\text{HMPC}}(x, \dot{x}) = u(r, \theta) = r \cdot \bar{u}(\theta), \quad \text{where } x = r \cos \theta \text{ and } \dot{x} = r \sin \theta \quad (4.13)$$

The nonlinear function $\bar{u}(\theta)$, shown in Fig. 4.7, can be determined *a priori* (before hybrid MPC is implemented), so that most of the computational effort is done off-line and only limited computations are performed during the simulations. The off-line implementation used here is based on a one-dimensional table lookup for the function $\bar{u}(\theta)$.

The results from Monte Carlo simulation for idealized model I (Table 4.3a) shows that hybrid MPC achieves 11% reduction in the stationary RMS absolute acceleration compared to clipped LQR. In addition, hybrid MPC reduces RMS displacement by 24%, compared to clipped LQR. Not only does the hybrid MPC strategy reduce the structural response,

Fig. 4.7 Hybrid MPC control input for unit magnitude state vector



but it does so with a RMS device force that is smaller by 15%, which suggests that hybrid MPC is, in fact, making a more efficient use of the damping device. Results from idealized model II (Table 4.3b) show a similar pattern in the achievable reduction of response. Compared to clipped LQR, hybrid MPC reduces RMS displacements and absolute accelerations by 30% and 14%, respectively. The required damping force, on the other hand, has increased very modestly by 1%. Table 4.3b also shows the results for a passive-on case, for which it was assumed the damping device is a viscous damper with a damping constant c_{\max} ; this represents a semiactive device being operated at its maximum dissipative power. Although the passive-on case is more efficient in reducing displacement compared to the two semiactive control strategies, it must be noted that the main objective used in the control design in this example is the reduction of absolute accelerations. One of the most important observations in Table 4.3b is the fact that the passive-on case performs better than the clipped LQR strategy in reducing the absolute acceleration. In fact, this is the main reason why the design of semiactive control using clipped optimal strategy is performed using heuristic approaches involving large parametric studies, because the clipped optimal method is not consistent in minimizing the cost functions and the control optimality is not guaranteed.

4.5 Conclusions

In this paper, the design of semiactive structural control using hybrid MPC method was investigated. The performance of this control design was compared to clipped-optimal control design for a SDOF structural model. The following conclusions can be drawn from the results:

1. Clipped-optimal control strategies are based on unconstrained force models, which might not provide an optimal control performance for semiactive structural control.
2. The nonlinear passivity constraints that characterize semiactive dampers can be taken into account by using a hybrid system model, resulting in a set of linear constraints that makes optimization more tractable, which can be employed by MPC for control design.
3. The optimal control laws for semiactive structural control are generally nonlinear and can achieve higher performance compared to clipped-optimal control strategies for some control objectives.
4. Although better semiactive control designs can be achieved using hybrid MPC, the method is computationally intensive if an on-line implementation is used because MIQP problems have to be solved during the sampling time of the system. Off-line implementations can be more practical for large structural systems, where most of the computations can be carried out *a priori*, resulting in less demanding computations to be carried out during the sampling time.

Acknowledgements The authors gratefully acknowledge the partial support of this work by the National Science Foundation, through awards CMMI 08-26634 and 11-00528, and by a USC Viterbi Doctoral Fellowship. Any opinions, findings, and conclusions or recommendations expressed in this material are those of the authors and do not necessarily reflect the views of the National Science Foundation or of the University of Southern California.

References

1. Spencer BF Jr, Nagarajaiah S (2003) State of the art of structural control. *J Struct Eng* 129(7):845–856
2. Spencer BF Jr, Sain MK (1997) Controlling buildings: a new frontier in feedback. *Contr. Syst. IEEE* 17(6):19–35
3. Soong TT, Dargush GF (1997) *Passive energy dissipation systems in structural engineering*. Wiley, Chichester
4. Housner GW, Bergman LA, Caughey TK, Chassiakos AG, Claus RO, Masri SF, Skelton RE, Soong TT, Spencer BF Jr, Yao JTP (1997) *Structural control: past, present, and future*. *J Eng Mech* 123(9):897–971

5. Symans MD, Constantinou MC (1999) Semi-active control systems for seismic protection of structures: a state-of-the-art review. *Eng Struct* 21(6):469–487
6. Soong TT, Spencer BF Jr (2002) Supplemental energy dissipation: state-of-the-art and state-of-the-practice. *Eng Struct* 24(3):243–259
7. Dyke SJ, Spencer BF, Sain MK, Carlson JD (1996) Modeling and control of magnetorheological dampers for seismic response reduction. *Smart Mater Struct* 5(5):565–575
8. Jansen LM, Dyke SJ (2000) Semiactive control strategies for MR dampers: comparative study. *J Eng Mech* 126(8):795–803
9. Sun L, Goto Y (1994) Application of fuzzy theory to variable dampers for bridge vibration control. In: *Proceedings of the 1st world conference on structural control*, pp WP1:31–40, Los Angeles, CA, August 1994
10. Gavin H (2001) Control of seismically excited vibration using electrorheological materials and Lyapunov methods. *IEEE Trans Contr Syst Tech* 9(1):27–36
11. Wang X, Gordaninejad F (2002) Lyapunov-based control of a bridge using magneto-rheological fluid dampers. *J Intell Mater Syst Struct* 13(7–8):415–419
12. Iemura H, Pradono MH (2009) Advances in the development of pseudo-negative-stiffness dampers for seismic response control. *Struct Contr Health Monit* 16(7–8):784–799
13. Scruggs JT, Taflanidis AA, Iwan WD (2007) Non-linear stochastic controllers for semiactive and regenerative systems with guaranteed quadratic performance bounds Part 1: state feedback control. *Struct Contr Health Monit* 14(8):1101–1120
14. Scruggs JT, Taflanidis AA, Iwan WD (2007) Non-linear stochastic controllers for semiactive and regenerative systems with guaranteed quadratic performance bounds Part 2: output feedback control. *Struct Contr Health Monit* 14(8):1121–1137
15. Johnson EA, Erkus B (2007) Dissipativity and performance analysis of smart dampers via LMI synthesis. *Struct Contr Health Monit* 14(3): 471–496
16. Johnson EA, Baker GA, Spencer BF Jr, Fujino Y (2007) Semiactive damping of stay cables. *J Eng Mech* 133(1):1–11
17. Ramallo JC, Johnson EA, Spencer BF Jr (2002) “Smart” base isolation systems. *J Eng Mech* 128(10):1088–1099
18. Qin SJ, Badgwell TA (2003) A survey of industrial model predictive control technology. *Contr Eng Pract* 11(7):733–764
19. Mei G, Kareem A, Kantor JC (2001) Real-time model predictive control of structures under earthquakes. *Earthquake Eng Struct Dynam* 30(7):995–1019
20. Mei G, Kareem A, Kantor JC (2002) Model predictive control of structures under earthquakes using acceleration feedback. *J Eng Mech* 128(5):574–585
21. Bemporad A, Morari M (1999) Control of systems integrating logic, dynamics, and constraints. *Automatica* 35(3):407–427
22. Sontag E (1981) Nonlinear regulation: the piecewise linear approach. *IEEE Trans Automat Contr* 26(2):346–358
23. Alur R, Courcoubetis C, Henzinger T, Ho P (1993) Hybrid automata: an algorithmic approach to the specification and verification of hybrid systems. In: Grossman R, Nerode A, Ravn A, Rischel H (eds) *Hybrid systems. Lecture notes in computer science*, vol 736. Springer, Berlin, pp 209–229
24. Bemporad A (2002) An efficient technique for translating mixed logical dynamical systems into piecewise affine systems. In: *Proceedings of the 41st IEEE conference on decision and control, 2002*, vol 2, pp 1970–1975, 2002
25. Heemels WPMH, De Schutter B, Bemporad A (2001) On the equivalence of classes of hybrid dynamical models. In: *Proceedings of the 40th IEEE conference on decision and control, 2001*, vol 1, pp 364–369, 2001
26. Van de Water H, Willems J (1981) The certainty equivalence property in stochastic control theory. *IEEE Trans Automat Contr* 26(5):1080–1087
27. Chow GP (1976) *Analysis and control of dynamic economic systems*. Wiley, New York
28. Hespanha JP (2009) *Linear systems theory*. Princeton Press, Princeton
29. Giorgetti N, Bemporad A, Tseng HE, Hrovat D (2005) Hybrid model predictive control application towards optimal semi-active suspension. In: *Proceedings of the IEEE international symposium on industrial electronics, 2005. ISIE 2005*, vol 1, pp 391–398, 2005
30. Löfberg J (2004) YALMIP: a toolbox for modeling and optimization in MATLAB. In: *2004 IEEE international symposium on computer aided control systems design*, pp 284–289, 2004
31. IBM (2012) IBM ILOG CPLEX Optimizer. <http://www.ibm.com/software/integration/optimization/cplex-optimizer/>. Accessed 9 Sept 2012
32. Gurobi (2012) Gurobi Optimizer Reference Manual. <http://www.gurobi.com>. Accessed 9 Sept 2012

Chapter 5

Findings with AVC Design for Mitigation of Human Induced Vibrations in Office Floors

Donald Nyawako, Paul Reynolds, and Malcolm Hudson

Abstract In recent years, there have been extensive active vibration control (AVC) studies for the mitigation of human induced vibrations in a series of office floors, in which such vibrations are deemed to be ‘problematic’ and have been found to affect only certain sections of the floors. These floors are predominantly open-plan in layout and comprise of different structural configurations for their respective bays and this influences their dynamic characteristics. Most of the AVC studies have comprised extensive analytical predictions and experimental implementations of different controller schemes. The primary measures of vibration mitigation performance have been by frequency response function (FRF) measurements, responses to controlled walking tests, and in-service monitoring, all tests with and without AVC.

This paper looks at AVC studies in three different office floor case studies in past field trials. Some of the estimated modal properties for each of these floors from experimental modal analysis (EMA) tests are shown as well as some selected mode shapes of fundamental modes of vibration. These reflect the variability in their dynamic characteristics by virtue of their different designs and thus the potential for their ‘liveliness’ under human induced excitation. An overview of some of the controller schemes pursued in the various field trials are mentioned as well as a brief insight being provided into some challenges encountered in their designs and the physical siting of the collocated sensor and actuator pairs used in the field trials. The measure for the vibration mitigation performances in this work is in the form of uncontrolled and controlled point acceleration FRFs which show attenuations in the target modes of vibration between 13 and 18 dB. These tests also show the variability in vibration mitigation performances between the various controllers.

Keywords Active vibration control • Vibration mitigation • Frequency response function • Experimental modal analysis

5.1 Introduction

The liveliness in many contemporary floor structures under human induced loading is often the result of advancements in materials, design and construction technologies that lead to progressively longer, structurally more efficient and slender floors. They also tend to be more open plan and with fewer internal partitions [1, 2], which in turn contributes to their low internal damping characteristics as well as low and closely spaced natural frequencies, sometimes falling within the range of frequencies produced by human activities.

Active vibration control (AVC) technologies are emerging as an attractive means of controlling human-induced vibrations in floors based on recent field trials. When compared with alternatives such as tuned mass dampers, AVC technologies make use of much smaller units, provide quicker and more efficient control, have the ability to adapt to changes in the structural dynamic properties and can tackle multiple modes simultaneously [3, 4]. However, at present they suffer from initial high installation costs and the need for regular maintenance and a constant power supply.

Primary requirements for an AVC system for mitigation of human-induced vibrations in floors is that it should be simple, reliable and low-cost, which actually are typical requirements for AVC systems that are demanded for any application. Additional challenges imposed by modelling errors, control and observation spillover influences, time delay issues, changes

D. Nyawako (✉) • P. Reynolds • M. Hudson
Vibration Engineering Section, Department of Civil and Structural Engineering, University of Sheffield,
Sir Frederick Mappin Building, Mappin Street, Sheffield, S1 3JD UK
e-mail: d.nyawako@sheffield.ac.uk; p.reynolds@sheffield.ac.uk; m.j.hudson@sheffield.ac.uk

in structural properties over time as well as control design errors must be addressed in order to achieve AVC systems that offer robustness with respect to the vibration mitigation performance and stability [4, 5].

AVC studies for mitigation of human induced vibrations in floors have focused mainly on direct output feedback (DOFB) approaches in collocated sensor and actuator pairs and more recently the tendency is towards trials with model-based controllers. Typical controller schemes that have been investigated in both laboratory and field trials include direct velocity feedback (DVF), compensated acceleration feedback (CAF), response dependent velocity feedback (RDVF), on-off velocity and acceleration feedback schemes, integral resonant control, and pole-placement type schemes [3, 6–12].

To date, there has been a fairly good understanding of the requirements for AVC systems needed for mitigation of human-induced vibrations in floors. The sensors used in past and on-going studies are piezoelectric accelerometers with integral signal conditioning, while the actuators are commercially available APS Dynamics models 113 and 400 electrodynamic shakers. This paper examines some selected past AVC field trials in a number of office floor structures which suffer from vibration serviceability problems under human induced dynamic loading. An overview of the office floor configurations in past field trials is provided as well as some results from experimental modal analysis (EMA) tests, being point acceleration frequency response function (FRF) measurements and some selected mode shapes from modal parameter estimates. Additionally, the controller schemes used in the field trials are outlined and uncontrolled and controlled FRF measurements from the field trials are presented. Finally, some conclusions are set out.

5.2 Floor Configurations Tested

Three different floor configurations, for which AVC studies have been undertaken in past field trials are briefly described here. All these floors have sections or bays which are susceptible to human-induced vibrations or transmission problems from human-induced activities in upper floors. All these floors are fully fitted out with office furniture, partitions, suspended ceilings and false flooring. Floor 1, shown in Fig. 5.1a, is a composite steel-concrete floor in a steel framed office building. The primary beams span approximately 12 m between the column lines, the secondary beams span between the primary beams and the composite slab spans between the secondary beams. Columns are located along the two sides of the building as well as along the centreline. The point numbers, TP1 to TP46 are the locations that were selected for EMA tests. Four excitation points were used (TPs 04, 07, 31 and 36) and responses were measured at all TPs, resulting in 4 columns of the FRF matrix. Figure 5.2a shows the point acceleration FRFs.

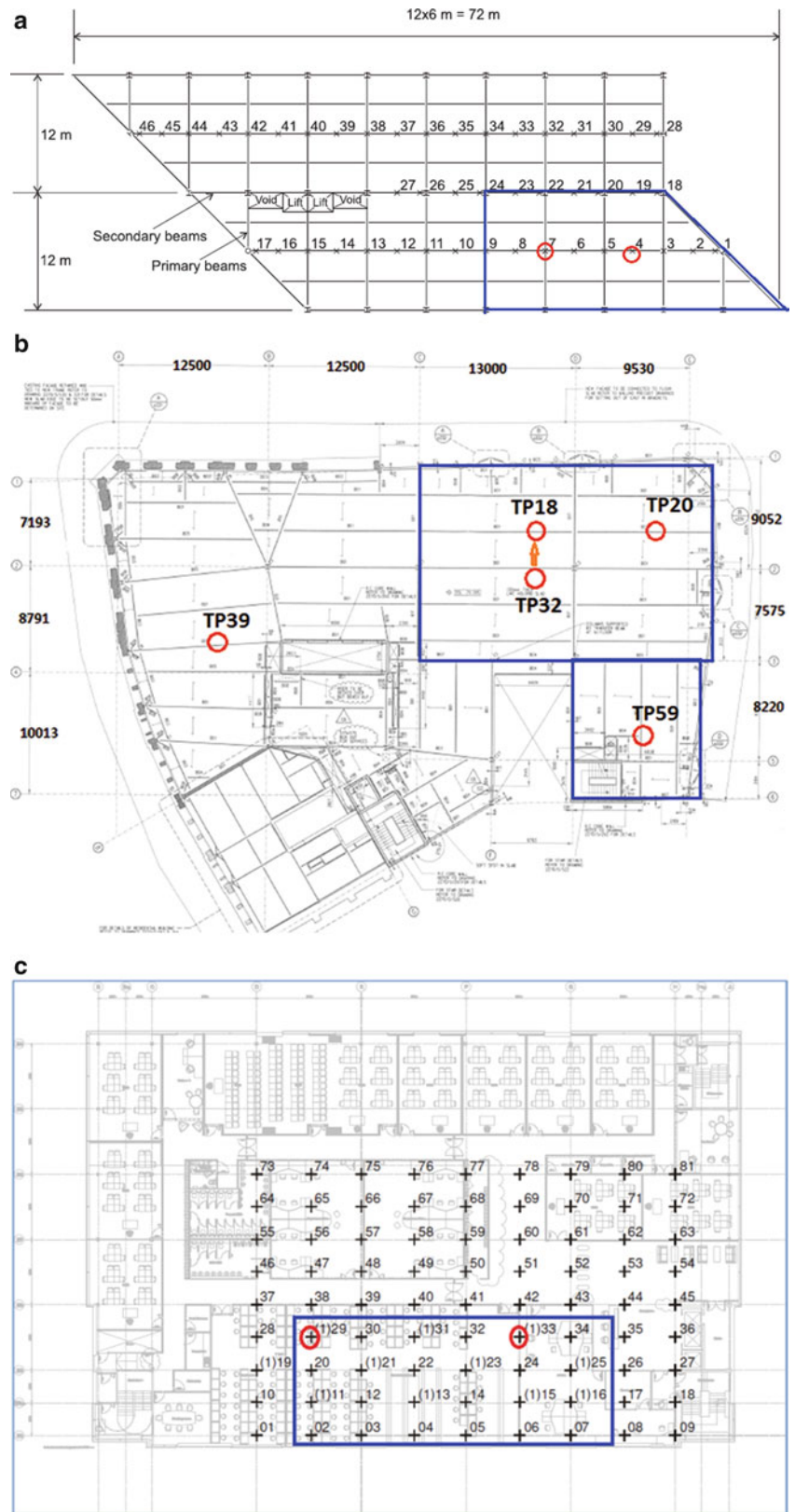
Floor 2 is also a composite steel-concrete floor in a steel framed office building. This structure is highly irregular by design with the primary beams varying from 7.193 to 10.013 m in length and spanning between the column lines as shown in Fig. 5.1b. The secondary beams also vary in length between 9.53 and 13.0 m whilst spanning across the primary beams, and the composite slabs span one-way between these secondary beams. Columns are again located along the two sides of the building as well as along the centreline. The point numbers, TP1 to TP69 are the locations that were selected for the EMA tests. Four excitation points were used (TPs 20, 32, 39 and 59) and responses were measured at all TPs, again resulting in 4 columns of the FRF matrix. Figure 5.2b shows the point acceleration FRFs from the EMA.

The structure on which floor 3 is built on is a fairly regular steel-framed building that has been constructed on top of a reinforced concrete building. Figure 5.1c shows a plan view of this floor and with the numbered locations being the test points for the EMA tests. Within the steel-framed building, the primary floor beams, 6.0 m in length, span between the column lines. The secondary beams, 9.8 m in length, span between the primary beams and the composite slab spans between the secondary beams. The point numbers, TP1 to TP81 on the college floor are the locations that were selected for the EMA tests. TPs shown using the parenthesis indicate points both on the college floor and gym floor above. Four excitation points were used (TPs 29, 33, 49 and 53) and responses were measured at all TPs, also resulting in 4 columns of the FRF matrix. Figure 5.2 shows the point acceleration FRFs from EMA.

In the EMA tests, four APS Dynamics electrodynamic shakers were used ($2 \times$ model 400 and $2 \times$ model 133) to excite the floors. They were driven with statistically uncorrelated random signals so that FRFs corresponding with individual shakers could be evaluated. The shaker forces were measured using Endevco 7754A-1000 accelerometers that were attached to the inertial masses. Responses were measured using arrays of 20–24 Honeywell QA750 servo accelerometers that were mounted on levelled Perspex base plates, and these were ‘roved’ over the entire floor areas. Data acquisition was carried out using a Data Physics Mobilyzer II digital spectrum analyser with 24 24-bit input channels and 4 output channels to supply drive signals to the shakers.

For all floors, the locations marked in blue were deemed to be the liveliest sections and for which the AVC studies were focused. Floors 1 and 2 are susceptible to human-induced vibrations from people walking within the office, whilst floor 3 suffers from transmission of vibrations from human activities in a gymnasium floor above. In all these floors, the EMA tests

Fig. 5.1 Floor plans for each of the floor configurations. (a) Floor 1; (b) Floor 2; (c) Floor 3



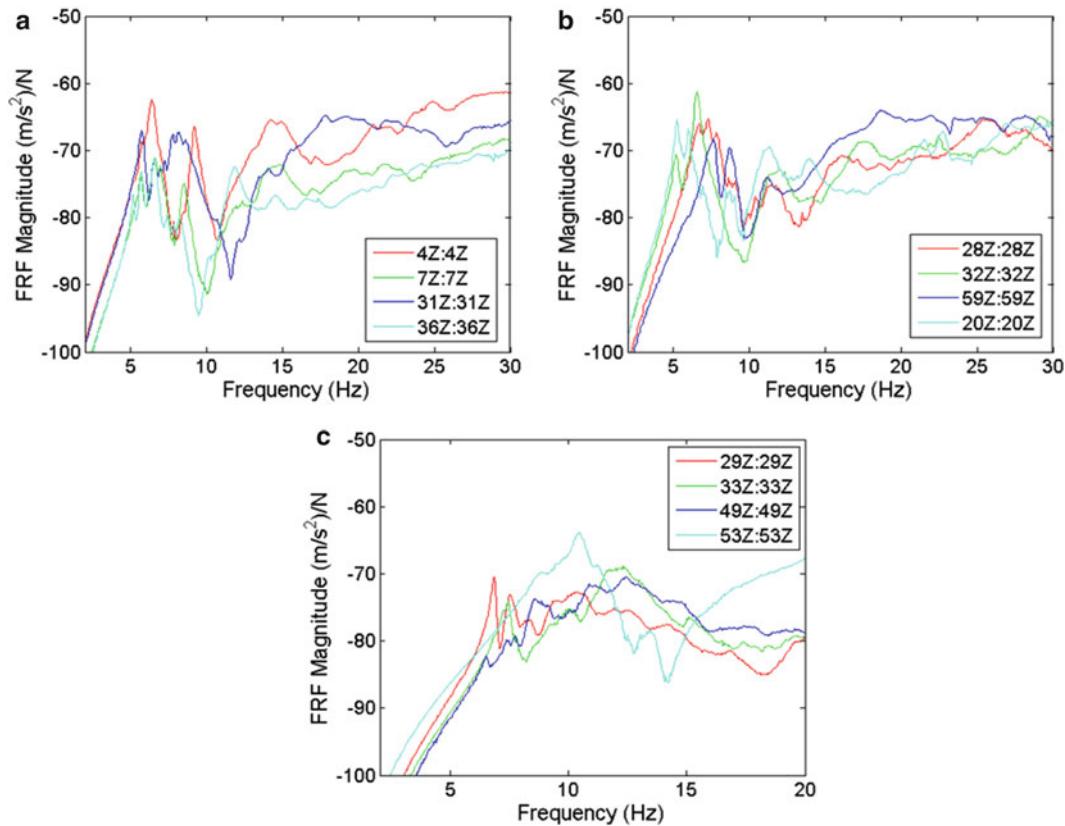


Fig. 5.2 Point acceleration FRFs for each of the three floors. (a) Floor 1; (b) Floor 2; (c) Floor 3

undertaken enabled their modal properties to be estimated, i.e. the natural frequencies, modal damping ratios, mode shapes and modal masses of the modes of interest. Figure 5.3 shows some selected mode shapes, identified from EMA tests, of some low modes of vibration in each of the floors. These are mode shapes from global modes identified from shakers at TPs 4 and 7 in floor 1, TPs 20 and 32 in floor 2, and TPs 29 and 33 in floor 3. Table 5.1 shows the fundamental modes estimates from ME'scope software for each of the floors.

5.3 Active Vibration Control Designs and Feasibility

AVC controllers for each of the three floors are described comprised of collocated sensor and actuator pairs at pre-selected locations deemed to be most lively under human-induced loading as highlighted in Fig. 5.1. These are TPs 4 and 7 on floor 1, TPs 18 and 20 on floor 2, and TPs 29 and 33 on floor 3. Typical installations of the actuator and sensor pairs in each of these floors are shown in Fig. 5.4a–c. Note that TP 18 was selected in floor 2 as it was inconvenient to site the collocated actuator-sensor pair for in-service monitoring at TP32 due to obstruction from 'services' and desks. The global mode at TP32 was also observable and controllable at TP18 as can be seen in Fig. 5.3. The actuators used in the AVC tests were two APS Dynamics model 400 electrodynamic shakers with four Endevco 7754A-100 accelerometers, where two accelerometers were used for providing the response/feedback signals and the other two being used to monitor the control forces. There is a limitation in this work on the number of actuators that can be deployed, which is a maximum of 2. All of the control schemes in the experimental study are implemented in dSPACE hardware (an Advanced Control Education Kit, ACE1103, consisting of a DS1103 PowerPC GX/1 GHz controller board and CLP1103 LED panel) and National Instruments Kits (2 NI cRIO-9081 chassis with 2 sets of NI9215 and NI9263 input and output modules).

Amongst the controller schemes investigated in these studies to mitigate human-induced vibrations have comprised of DOFB approaches, for example, DVF without and with compensation, RDVF, PI (proportional-integral, similar in principle to CAF), Integral Resonant controllers and model-based controllers, for example, pole-placement, LQG, IMSC types.

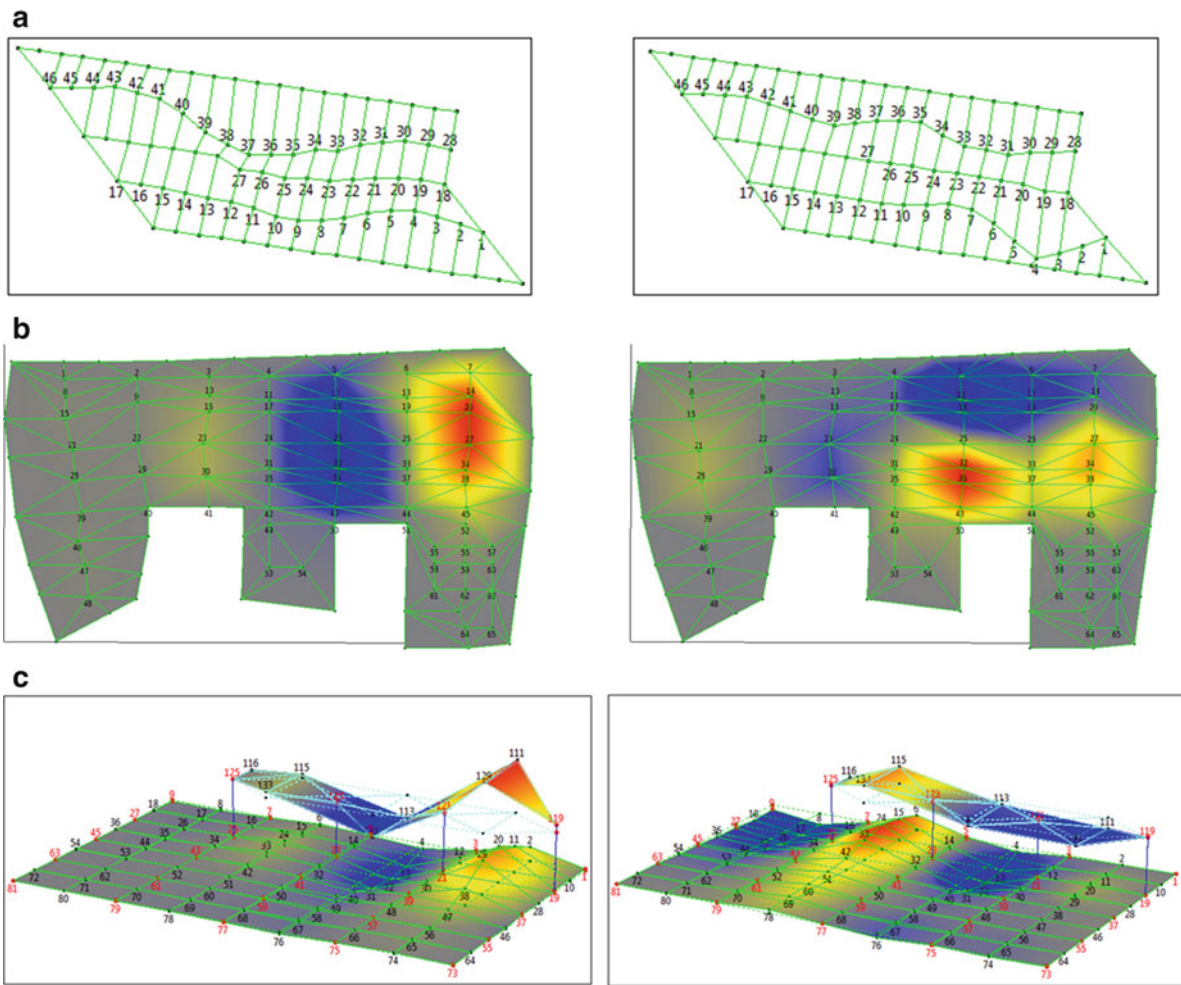


Fig. 5.3 Typical mode shapes of vibration for selected modes. (a) Floor 1 (Shaker at TP7, TP7) Mode 1 (5.20 Hz, $\zeta = 1.74\%$), Mode 5 (6.36 Hz, $\zeta = 2.93\%$); (b) Floor 2 (Shaker at TP20, TP32) Mode 1 (5.24 Hz, $\zeta = 4.15\%$), Mode 3 (6.53 Hz, $\zeta = 2.27\%$); (c) Floor 3 (Shaker at TP29, TP33) Mode 2 (6.87 Hz, $\zeta = 1.50\%$), Mode 3 (7.58 Hz, $\zeta = 1.70\%$)

Table 5.1 Summary of estimated modal properties for first five modes for floors 1, 2 and 3

Mode	Floor 1		Floor 2		Floor 3	
	Natural frequency (Hz)	Damping ratio (%)	Natural frequency (Hz)	Damping ratio (%)	Natural frequency (Hz)	Damping ratio (%)
1	4.86	1.7	5.24	4.2	6.56	1.2
2	5.20	4.2	6.00	1.8	6.87	1.5
3	5.34	1.4	6.53	2.3	7.58	1.7
4	5.76	2.3	7.70	2.0	8.54	1.3
5	6.36	2.9	8.63	2.9	8.97	1.1

Full details of these past controllers and associated designs can be seen in [7–12]. All the controllers used were designed with adequate stability margins and a typical DVF scheme with inner loop actuator compensation as is shown in Fig. 5.5. Amongst the key challenges encountered in these designs included:

- Limits being placed on the design feedback gains, particularly with DOFB approaches to prevent actuator stroke saturation instability as well as prevent high frequency instabilities, for example, with DVF.
- Determination of suitable reduced order models (ROM) for reduced-order controller designs from EMA tests. EMA tests with the present actuators and for different floor structures are often limited to a narrow frequency bandwidth and good judgment of obtaining ROM is necessary for robust controller designs and predictions of closed-loop performances.



Fig. 5.4 Typical collocated sensor and actuator pairs at TPs 4, 18 and 29 in floors 1, 2 and 3 (a–c), respectively (note that the additional shaker here is used for uncontrolled and controlled FRF tests only)

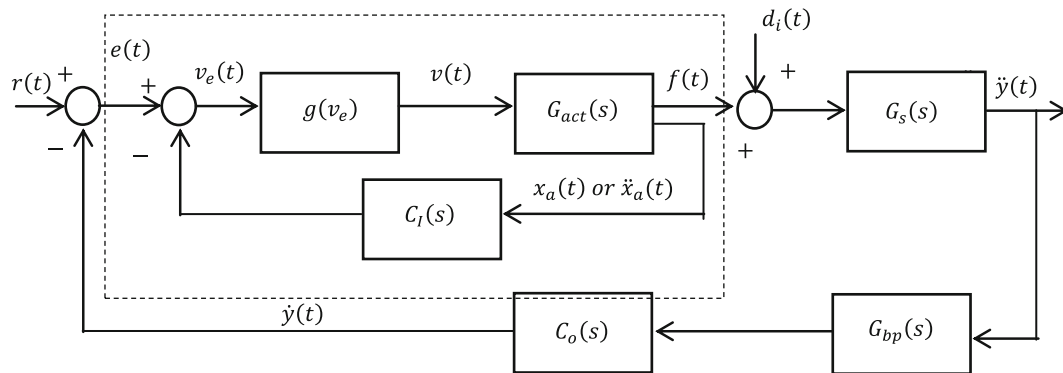


Fig. 5.5 Direct velocity feedback with an inner loop actuator compensator, where: $G_s(s)$, Floor model; $G_{act}(s)$, Actuator model; $G_{bp}(s)$, Band pass filter (2nd order Butterworth); $C_o(s)$, Transfer function of outer loop; $C_i(s)$, Transfer function of inner loop; $x_a(t)$, Displacement of actuator moving mass; $\ddot{x}_a(t)$, Acceleration of actuator moving mass; $r(t)$; Reference signal; $\ddot{y}(t)$, Structural acceleration response; $\dot{y}(t)$, Structural velocity response; $f(t)$, Actuator force; $v(t)$, Final control voltage signal; $v_e(t)$, Initial control voltage signal; $d_i(t)$, Input disturbance; $e(t)$, Error signal; $g(v_e)$; Saturation nonlinearity

All field trials comprised of FRF tests, monitoring of responses to controlled walking tests and in-service monitoring studies with and without AVC. A variety of controller schemes were also investigated in each of the floors. This paper only shows findings from the point acceleration FRF tests at the pre-selected locations on each of the floor structures. Figure 5.6 shows the uncontrolled and controlled FRFs measured experimentally, which were found to be identical to the analytically predicted ones for the controller schemes selected in each floor scenario.

In each of the FRF tests in Fig. 5.6, there is considerable enhancement in damping characteristics for each of the floors with the AVC system in operation. Attenuations of between 13 and 18 dB in target vibration modes were realised. The noisy nature of the FRF measurements in Fig. 5.6c for TPs 29 and 33 associated with floor 3 were as a result of the on-going activities in the upper gymnasium floor when these tests were being undertaken.

A quick observation of some of the selected mode shapes in Fig. 5.3 reflects their different characteristics. Some modes of vibration are quite localised whilst others engage several bays. These features influence their controllability and observability properties during AVC design, and as a result would dictate the feasible number of actuators and sensors needed to effectively control a given floor area. For example, considering Fig. 5.3c based on floor 3, a single actuator sited at TP29 would not be effective in controlling the dominant mode at TP33 and vice versa as the vibration modes are quite localised. Effective control of this floor would entail use of multiple combinations of actuator and sensor pairs. Considering Fig. 5.3b based on floor 2, some global vibration modes can be controlled either at TP20 or TP32 as they are observable in both locations. This floor can be controlled adequately to some extent using the two actuator-sensor pairs available. This is often an additional challenge with designing AVC systems for floor structures.

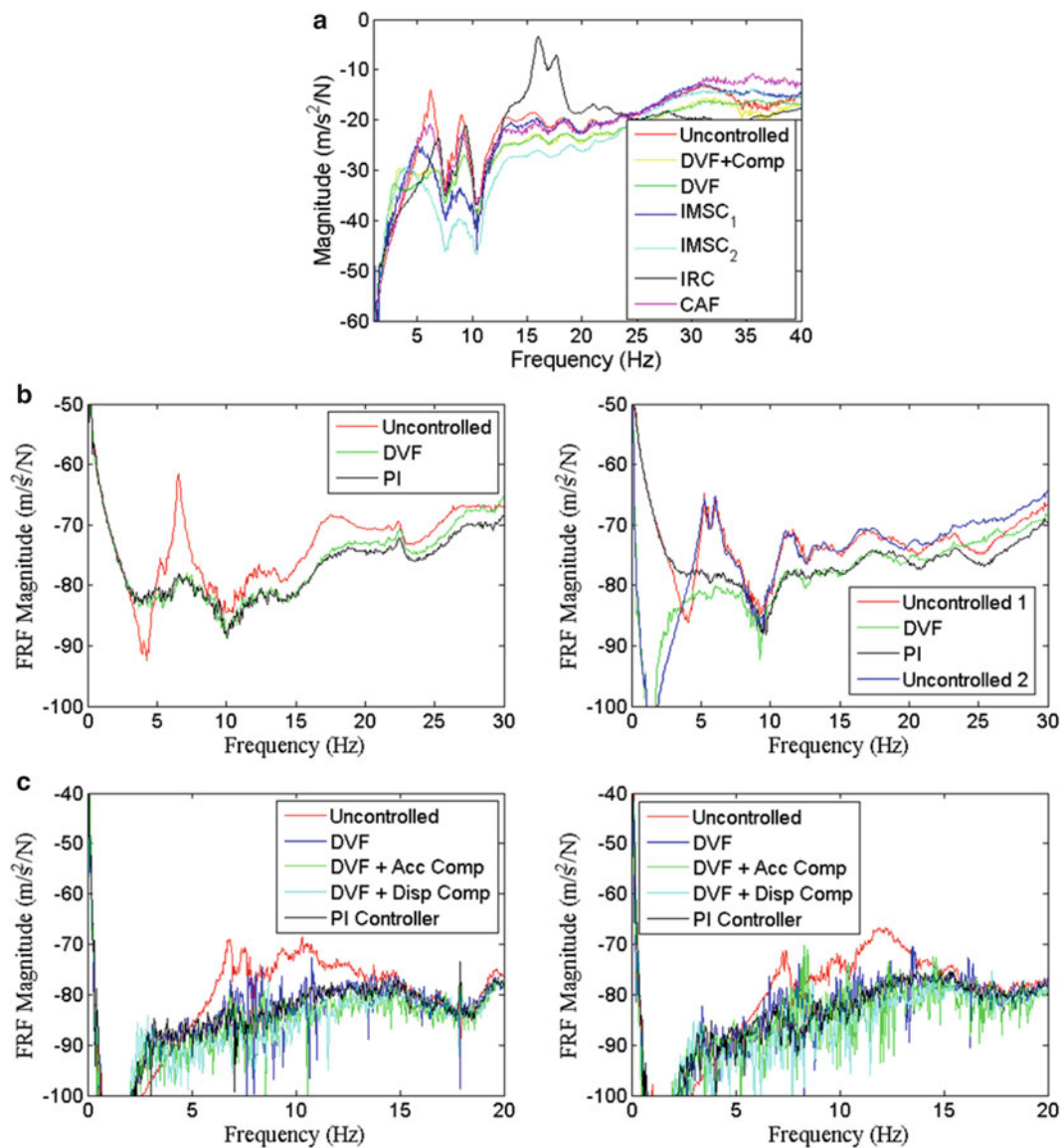


Fig. 5.6 Uncontrolled and controlled FRFs measured in field trials (DVF + Comp – Direct velocity feedback with compensation, DVF + Acc Comp – Direct velocity feedback with acceleration compensator, DVF + Disp Comp – Direct velocity feedback with displacement compensator). (a) Floor 1 (TP4); (b) Floor 2 (TP18, TP20); (c) Floor 3 (TP29, TP33)

5.4 Conclusions

These field trials reveal AVC as a viable and potential technology for mitigation of human-induced vibrations in problem floors as can be seen in Fig. 5.6. There are challenges, however, that must be overcome before it can be fully realised, stemming from higher installation and maintenance costs. Additional challenges imposed by modelling errors, control and observation spillover influences, time delay issues, changes in structural properties over time as well as control design errors must be addressed in order to achieve AVC systems that offer robustness with respect to the vibration mitigation performance and stability. Compromises also have to be made with respect to location of services and hence inability to locate actuators at desired locations.

A further pertinent issue as pertains to the realisation of AVC schemes mainly arises from controllability and observability conditions which mainly arise from floor configuration, which is in turn influenced by its design. This governs how many actuators and sensors are feasible to control a given problem floor. As seen in this work, in some floors, e.g. floor 3, where the global vibration mode extends over several bays, it is possible to use a local point for control. In other floors, e.g. floor 2

where vibration modes are pretty much localised, there would be a need for multiple actuators to control all problematic modes. A judicious decision must therefore be made on the combinations of actuators and sensors needed to effectively control human-induced vibrations in a floor considered as being ‘problematic’ under human-induced vibrations.

Acknowledgements The authors would like to acknowledge the financial assistance provided by the UK Engineering and Physical Sciences Research Council (EPSRC) through a responsive mode grant entitled “Active Control of Human-Induced Vibration” (Ref: EP/H009825/1), Leadership Fellowship grant entitled “Advanced Technologies for Mitigation of Human-Induced Vibration” (Ref: EP/J004081/1) and Platform Grant entitled “Dynamic Performance of Large Civil Engineering Structures: An Integrated Approach to Management, Design and Assessment” (Ref: EP/G061130/1).

References

1. Setareh M, Hanson RD (1992) Tuned mass dampers to control floor vibration from humans. *J Struct Eng* 118(3):741–762
2. Murray TM (1998) Floor vibration and the electronic office. *Mod Steel Constr* August 1998:24–28
3. Hanagan LM, Murray TM (1997) Active control approach for reducing floor vibrations. *J Struct Eng* 123(11):1497–1505
4. Housner GW, Bergman LA, Caughey TK, Chassiakos AG, Claus RO, Masri SF, Skelton RE, Soong TT, Spencer BF, Yao JTP (1997) Structural control: past, present, and future. *J Eng Mech* 123(9):897–971
5. Yang JN, Soong TT (1988) Review paper: recent advances in active control of civil engineering structures. *Probabilistic Eng Mech* 3(4): 179–188
6. Hanagan LM, Murray TM, Premaratne K (2003) Controlling floor vibration with active and passive devices. *Shock Vib Dig* 35(5):347–365
7. Diaz IM, Reynolds P (2009) Robust saturated control of human-induced floor vibrations via a proof-mass actuator. *Smart Mater Struct* 18:1–10
8. Diaz IM, Reynolds P (2010) Acceleration feedback control of human-induced floor vibrations. *Eng Struct* 32:163–173
9. Diaz IM, Reynolds P (2010) On-off nonlinear active control of floor vibrations. *Mech Syst Signal Process* 24:1711–1726
10. Diaz IM, Pereira E, Reynolds P (2010) Integral resonant control scheme for cancelling human-induced vibrations in light-weight pedestrian structures. *Struct Control Health Monit*. doi:0.1002/stc.423
11. Nyawako D, Reynolds P (2009) Response-dependent velocity feedback control for mitigation of human-induced floor vibrations. *Smart Mater Struct* 18:1–14
12. Diaz IM, Pereira E, Hudson MJ, Reynolds P (2012) Enhancing active vibration control of pedestrian structures using inertial actuators with local feedback control. *Eng Struct* 41:157–166

Chapter 6

Power Requirements for Active Control of Floor Vibrations

M.J. Hudson, P. Reynolds, and D.S. Nyawako

Abstract Recent research has made significant developments towards improved Active Vibration Control (AVC) technology for the mitigation of annoying vibrations in floor structures. However, there are very few examples of permanent AVC installations in floor structures; this is in part due to the requirement of a continuous power supply and the ensuing electricity costs. This paper investigates potential improvements to AVC from the perspective of the choice of control algorithm. Firstly, the use of model-based controllers as opposed to the direct output feedback controllers that have been used in most prior research effort is considered. For a model-based (MB) controller, because the controller can be designed to target modes within a specific frequency band of interest, it is possible that control effort is used more effectively for a given reduction in response. Secondly, the potential benefits of using a switching-off rule to reduce the actuator effort during periods of low structural response is investigated. Future actuators and amplifiers could incorporate a switching-off rule similar to this in order to minimise the overhead costs associated with running the amplifier. The changes in potential electricity consumption for the previously declared control laws are experimentally determined through direct measurement of the power drawn by the actuator. The results from these analyses are compared and conclusions drawn.

Keywords Active vibration control power experimental

6.1 Introduction

There have been numerous papers in recent years examining the use of Active Vibration Control (AVC) for the mitigation of annoying vibrations in floor structures [1–4]. These have been shown to be very effective at reducing the vibration responses of the floors. However, when real floor structures are observed to require vibration mitigation, it is generally only passive technologies such as Tuned Mass Dampers (TMDs) that are utilised; very rarely is AVC considered as it is still at a relatively new stage for this application.

Whilst AVC is a fairly well developed technology in other fields, e.g. aeronautics, space and marine, its use for the mitigation of floor vibrations is still emerging. This is one of the reasons why the hardware associated with it is typically expensive. In addition to this, AVC has on-going costs associated with running the active devices. Over the life of a building this could amount to substantial electricity costs. The research in this paper investigates the issue of on-going electricity costs from the perspective of controller design.

Much research into AVC for floors has focussed on the use of direct output feedback controllers. For example, Direct Velocity Feedback (DVF) has been the basis of much research [1, 5, 6]. Here, the structural acceleration from the accelerometers is integrated and a constant gain applied to the resulting velocity. In the absence of actuator dynamics this results in a predominant augmentation of the structural damping. However, actuator dynamics have a destabilising effect for high feedback gains. Developments from DVF have included: Response Dependent Velocity Feedback (RDVF) [7]; Compensated

M.J. Hudson (✉) • D.S. Nyawako
Department of Civil and Structural Engineering, University of Sheffield, UK
e-mail: m.j.hudson@sheffield.ac.uk; d.s.nyawko@sheffield.ac.uk

P. Reynolds
Full Scale Dynamics Limited, Sheffield, UK
e-mail: p.reynolds@sheffield.ac.uk

Acceleration Feedback (CAF) [3]; DVF with a feedthrough term [4] and On-Off nonlinear control [8]. These developments all utilise the key benefit of DVF, namely that the structural damping is effectively enhanced, but offer some improvement. For example, RDVF effectively employs an automatic gain selection for DVF, whilst CAF and DVF with a feedthrough term deal with some of the instability issues brought about through the dynamics of the actuators. The On-Off nonlinear control aims to eliminate stability issues that can arise through non-optimal feedback gain choice when using DVF.

Alongside these developments, model-based controllers are being investigated for this application; research in this field for the application of floor vibrations is on-going however presently available literature is much less common. For example, an LQR controller was examined by Nyawako [2] which used the threshold of human perception of vibrations and output constrained control for the optimisation procedure. Further to this, Independent Modal Space Control (IMSC) and Pole-Placement technologies have been investigated by [9] to isolate individual problematic modes in an attempt to reduce spillover instability and improve robust performance.

There are two aspects from the currently developed control laws that have potential to facilitate savings in power requirements for AVC of floor vibrations. Firstly, there is the possibility of using a model-based controller that utilises known structural dynamics in order to control specific modes of vibration. For example, IMSC provides a framework through which one can control low frequency modes that are more likely to be problematic whilst leaving higher frequency modes uncontrolled. In theory, this could allow the controller to reduce the energy used for control purposes whilst still achieving vibration mitigation performance for critical structural modes of vibration. Secondly, the use of a switching-off rule as used in the on-off control could be utilised. This would allow the actuator to become inactive during periods of low structural response and only be active when the response exceeded a particular threshold. This paper investigates these two ideas through experimental research performed on a laboratory slab structure. A specially developed power meter is used to measure the RMS real power drawn at the mains socket while the actuator is operating. Measuring at this point accounts for all losses within the amplifier and actuator circuit and is indicative of the amount of electricity the user would be charged.

The structural system and walking force applied to the structure are described in Section 6.2. The development of the control algorithms is discussed in Section 6.3. Following from this, the results from the experimental tests are provided in Section 6.4. Finally, conclusions are drawn in Section 6.5.

6.2 System Description

6.2.1 Modal Properties (EMA)

The structure used for this testing is a laboratory slab strip at the University of Sheffield. This is a $11.2\text{m} \times 2.0\text{m} \times 0.275\text{m}$ reinforced concrete slab spanning 10.8m between knife edge supports. The modal properties of this structure were determined through a forced vibration test using one APS dynamics model 400 shaker located 2.7m from the support and 0.2m from the long edge of the slab, and 21 Honeywell QA accelerometers located on 3×7 grid throughout the structure. The data were processed in ME'Scope and modal parameters identified using global curve fitting with the Ortho Polynomial method. The resulting mode shapes are shown in Fig. 6.1 and modal parameters in Table 6.1.

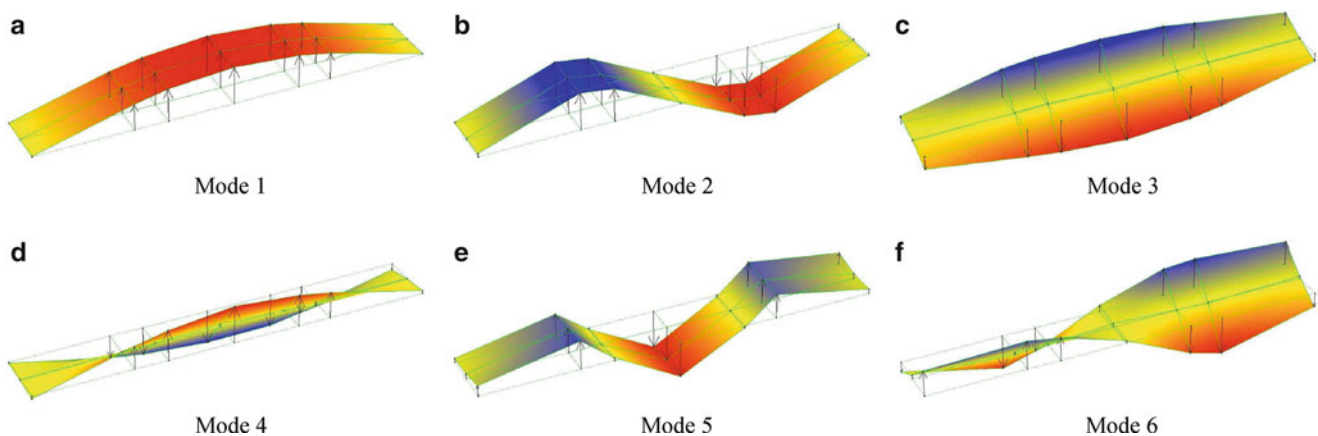
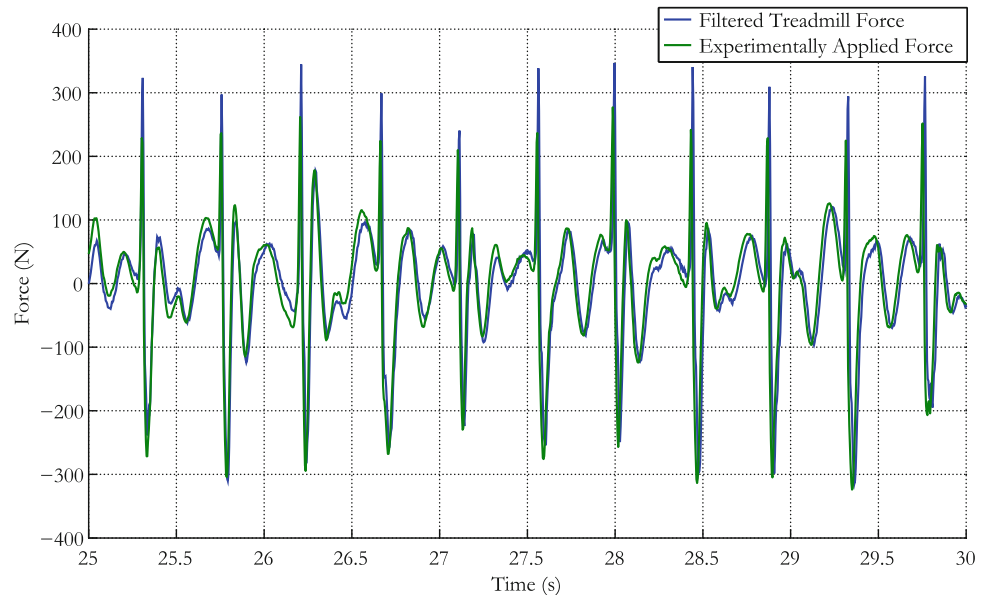


Fig. 6.1 First six modes of vibration of slab strip

Table 6.1 Modal properties for first six modes of vibration of slab strip

Mode number	Natural frequency/Hz	Damping ratio/%	Modal mass/kg
1	4.6	2.2	6010
2	16.8	0.5	6010
3	26.1	1.2	3540
4	28.7	1.1	21250
5	37.7	1.2	7310
6	51.4	2.3	2600

Fig. 6.2 Measured and theoretical walking time history

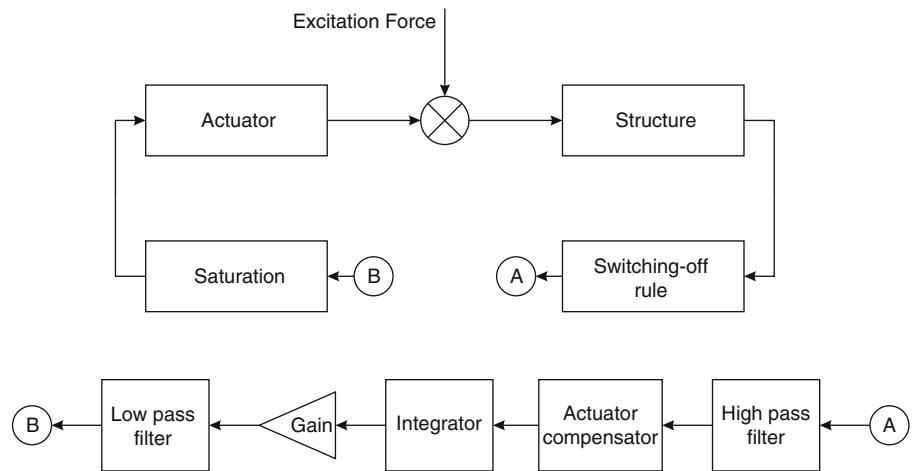
6.2.2 Walking Force

The aim of this paper is to determine and compare the typical power demand from the active control system due to walking excitation. However, in order that comparisons may be accurately made, the excitation must be repeatable which human walking is not: there is both intra- and inter-person variability with walking excitation [10]. Therefore, it was decided that the excitation would be provided by another inertial mass actuator generating a force representative of walking. This is done by converting a walking force time history into a command voltage such that when this is used to drive the actuator a force representative of walking is generated.

The force time history for a pedestrian walking at around 2.2Hz to 2.3Hz was measured using an instrumented treadmill [11]. This frequency of walking has a second harmonic that will excite the first structural mode of vibration. However, it is very difficult to generate the 2.3Hz component of this walking because of the stroke limits of the inertial mass actuator. As this frequency component is not actually exciting the structure in any way, it was deemed justifiable to remove this component from the time history through the use of an 8th order high-pass Butterworth filter at 3Hz. It is worth noting that a high order filter, such as this, significantly modifies the phase of the signal. However, it has been shown that the phases between walking harmonics are random [10] so this additional phase contribution is not a problem.

The inverse of the actuator dynamics were modified with the use of a 2nd order high-pass Butterworth filter at 0.5Hz to avoid magnification of low frequency components. The result of this filtering is shown in Fig. 6.2. Here, the measured force time history after filtering at 3Hz is shown along with the force measured from the actuator when simulating this force time history. A close correlation is observed between the experimental force and the filtered treadmill data, with the exception that the amplitude of the sharp peaks are slightly reduced for the experimental force. This is not a problem as these peaks correspond with excitation at 2.25Hz, i.e. the component that we have tried to filter out because they do not contribute to excitation of the structure. Therefore this difference does not preclude the actuators from generating an effective walking force.

Fig. 6.3 Control architecture for the DVF controller



6.3 Active Controllers

6.3.1 DOFB

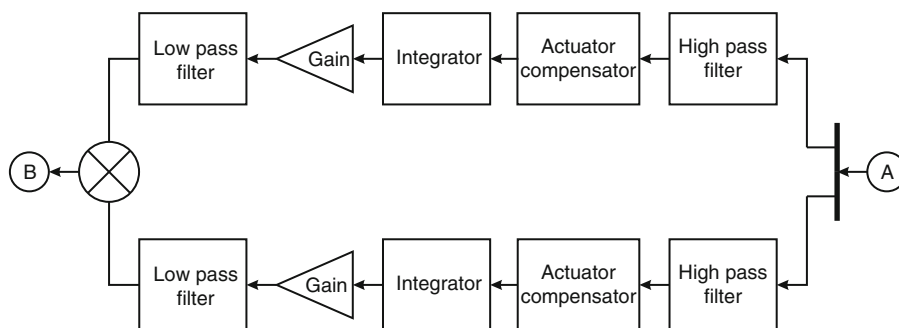
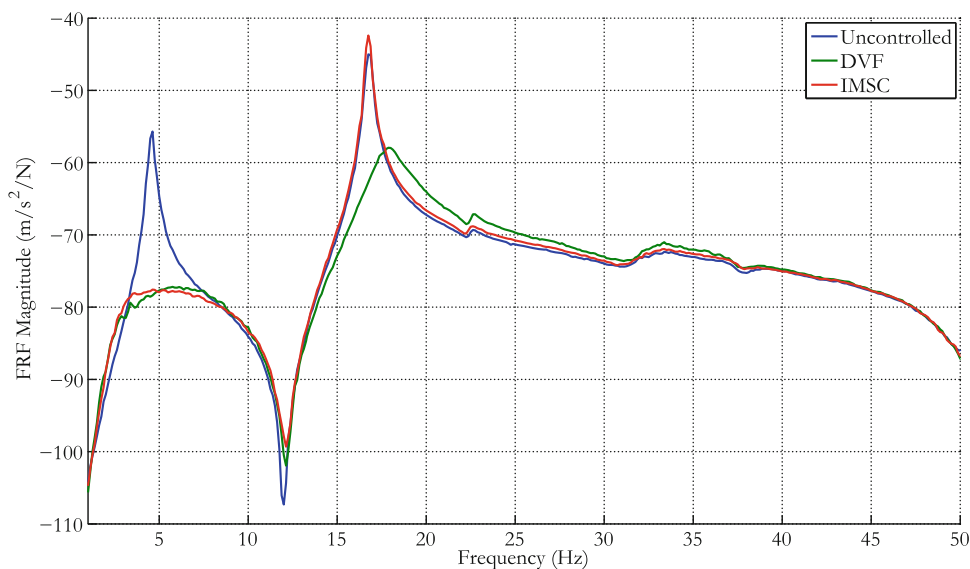
The direct output feedback controller used in this study is a modified form of Direct Velocity Feedback (DVF). Here, the acceleration signal from the accelerometer is passed through a 2nd order high-pass filter at 1Hz to remove low frequency components before being integrated to yield a velocity signal. A 1st order low-pass filter is also included at 50Hz to avoid the actuator attempting to control very high frequency modes and noise. Finally, an actuator compensator is included to artificially reduce the natural frequency and increase the damping ratio of the actuator. The feedback gain is chosen such that a gain margin of 2 and a phase margin of 30° are achieved. A saturation non-linearity at 2V is included in the command signal in order to reduce the chance of stroke saturation occurring at low frequencies and to avoid force saturation. In addition to this, for some of the tests a switching-off rule has been incorporated to deactivate the actuator when the RMS of a previous block of data is below a threshold value. The schematic for this controller is shown in Fig. 6.3.

6.3.2 MB

The model based controller used in this study is an Independent Modal Space Control (IMSC) design, as described by Nyawako et al. [9]. The active control configuration is very similar to that described in this study. It was demonstrated that one actuator and two accelerometers can control the first mode of vibration whilst leaving the second mode un-attenuated. Here, the simple dynamics of the structure are utilised to simplify the design process. The structural mode shapes' orthogonality condition is utilised, resulting in the actuator being located at one third span and the two accelerometers at third and two-third spans respectively. In this way, the accelerometers and actuators are located at nodal points for modes 3–6, as shown in Fig. 6.1 and the phase of the second mode differs by exactly 180° between the two accelerometers. This means that the acceleration signal from each accelerometer can be combined and the resultant signal will only feedback to control the first mode of vibration. The controller schematic is shown in Fig. 6.4.

6.4 Experimental Results

The power demand of the actuator and amplifier was measured through the use of a custom built power meter. This device samples the mains voltage and current supply at 2.8kHz to calculate the average power over 5 mains cycles (0.1 seconds). The power meter was used to monitor the APS Electroynamics model 124 EP extended power amplifier when this was used to drive the APS Electroynamics model 400 shakers with attached reaction masses. Monitoring the power at this point accounts for all losses within the amplifier and actuator circuit and therefore is indicative of the amount of electricity the device is drawing from the grid.

Fig. 6.4 Controller design for IMSC**Fig. 6.5** FRFs for DVF and IMSC controllers

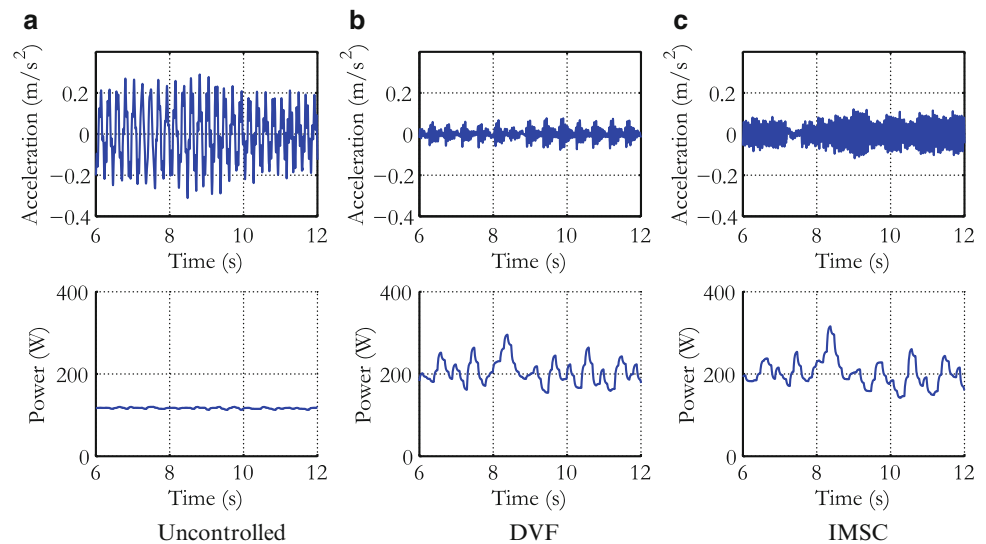
Both controller types were configured on the laboratory slab structure as described in Section 6.3, and FRF measurements were taken to validate the controllers were performing as expected. The results of this are shown in Fig. 6.5. Here it is observed that DVF successfully reduces the magnitude of response for both modes, whilst IMSC reduces the response for mode 1, but does not reduce the response of mode 2. In fact, a slight increase in the response is noted for mode 2. It is believed that this is due to the assumption that the shape function at the location of both accelerometers is exactly equal and opposite for mode 2. However, slight differences could be expected in reality which may result in the slight deterioration in response at this frequency.

As previously discussed, the aim of this paper is to investigate the power demand of AVC for human-induced floor vibrations. Therefore, two different walking time histories were synthesised using the actuator: one at around 2.25Hz in order to achieve resonance with the first mode of vibration through the second harmonic of the walking force, and one at 2.5Hz in order to impart as much energy into the system at higher frequencies as is realistic. The idea behind this second time history is that the impulses due to each footfall will significantly excite the second mode of vibration and so the difference between DVF and the IMSC controller (which controls the first mode but does not control the second mode) should become apparent. In addition to these forces, real walking was conducted on the slab strip for comparative purposes. This set of walking types was applied to the structure with 1) no control, 2) control using DVF controller, and 3) control using IMSC controller. Note that the gain for both DVF and IMSC had to be reduced to 80% of the original value for the case of the real walking excitation in order to avoid stroke saturation from the quasi-static structural response to the 2.25Hz component of the force.

Typical time histories for the acceleration response and the power demand are shown in Fig. 6.6, whilst the maximum response measured and average power for each of the experiments is shown in Fig. 6.7. The maximum response is characterised by the R factor which is the maximum of the running one second RMS of the W_b frequency weighted acceleration signal, normalised by $0.005m/s^2$ which is taken as the perceived limit of human perception of vibrations.

These results show that both controllers reduce the maximum R factor recorded for all walking excitation types, as should be expected. However, it is particularly interesting to note the results for the 2.25Hz excitation which aimed to target the first

Fig. 6.6 Acceleration and average power measured for 2.25Hz synthesised walking excitation



mode of vibration. Here, IMSC does not reduce the response of the structure as much as DVF despite the FRFs in Fig. 6.5 showing the magnitude of response for the first mode to be approximately equal for these two controllers. This is because this excitation also has significant higher frequency components that excited the second mode of vibration. Considering the power demand, it is important to note that the amplifiers were left running but had no command voltage applied to them for the uncontrolled case. This is the reason why all uncontrolled cases reported an average power of 114W - these are the overhead required for the amplifier to run itself. A marginal improvement in the power demand for IMSC over DVF was observed for all three excitation types. However, the response of the structure is significantly higher with IMSC.

6.4.1 Variations in DVF Feedback Gain

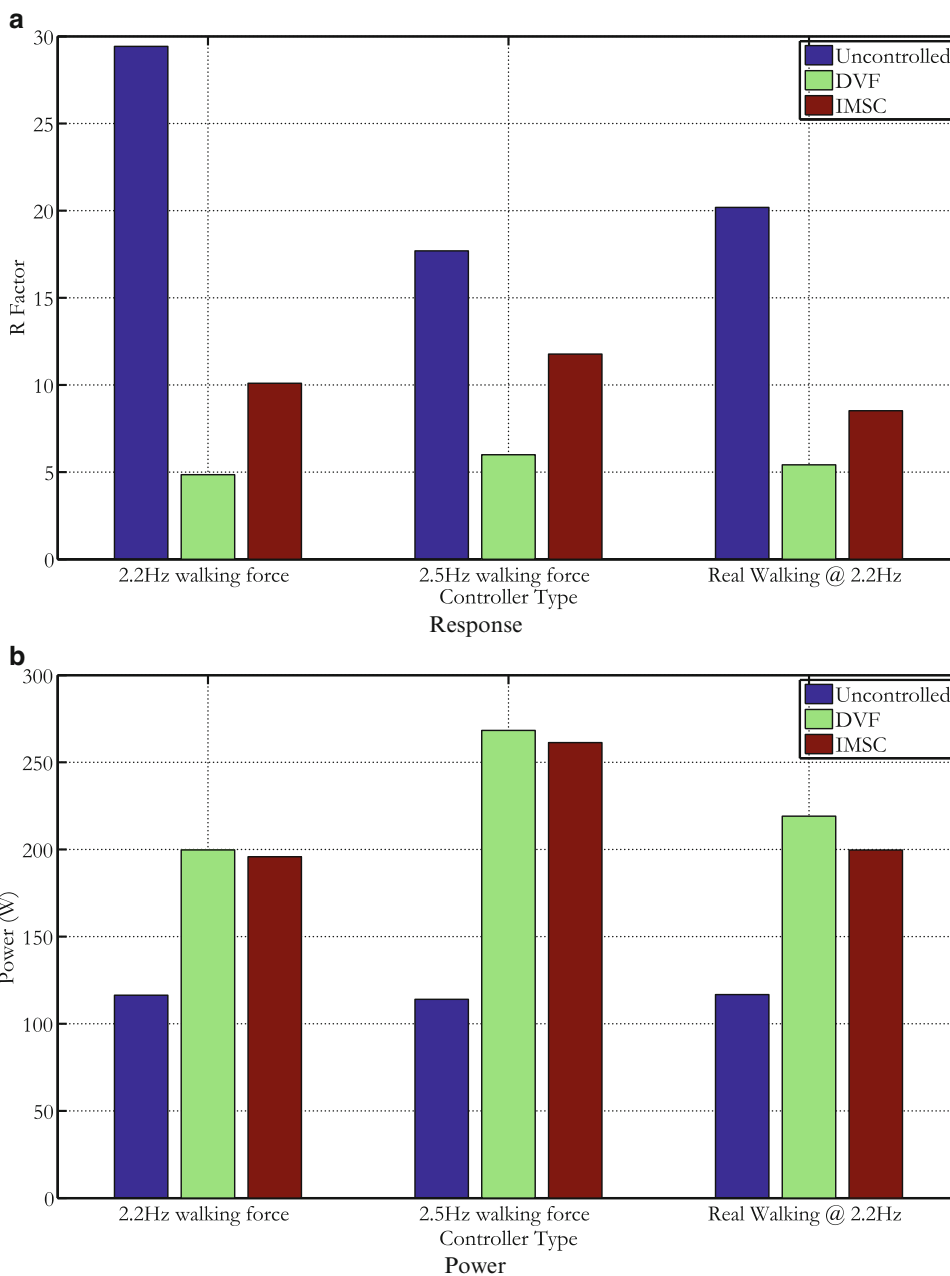
In order to explore this area further, the feedback gain of the DVF controller was systematically decreased and the experiment repeated. The resulting changes to the controlled structure's FRF are presented in Fig. 6.8, and the results for these controllers subject to the walking excitation are shown in Fig. 6.9

It is apparent that by varying the feedback gain for DVF we have arrived at a set of controllers that all lie closer to the utopian goal of zero response for zero power demand than the IMSC controller. This means that for this structure the DVF controller is the preferred choice and this is due to the significant contribution to the structural acceleration from the second mode of vibration. It is crucial to note that this does not mean that DVF is "better" than IMSC or other model-based controllers; it means that there is no benefit in designing a model-based controller to intentionally not control higher frequency modes (within a range excitable by human walking) with the idea of reducing power consumption because little power saving is made and the structural response can be significantly higher.

6.4.2 Use of a Switching Off Rule

The effect of using a switching-off rule is considered next. The idea here is to prevent the actuator from working when the response of the structure is below a threshold, such that power savings can be made whilst keeping the large responses low. The nature of the excitation/structural system in this study is such that high response levels are achieved and maintained for the entire test duration. This means that the switching-off rule must be set relatively high so that its effect can be seen. A range of different thresholds were chosen, namely from $R = 4$ to $R = 8$ (with frequency weights applied assuming the response is dominated by the first mode of vibration). In addition to this, a range of time periods used to calculate the RMS response were considered - 1s, 0.5s and 0.25s. A 2nd order low pass filter at 1Hz was used to remove low frequency components of the measured acceleration before the RMS block was calculated. The differences in both vibration response and average power are very small for the controllers tested. This means that the results are more strongly influenced by both

Fig. 6.7 Maximum response factor and average power measured for various types of excitation



external excitation and variance in the amplifier overhead. Therefore, in order to improve reliability of the experiments, each test was repeated several times and averages of the results were taken. These averaged results from all the tests with the switching-off rule for DVF are shown in Fig. 6.10 where they are compared with the results for varying the gain in DVF.

Here it is seen that by using a high threshold, i.e. a higher level of response is permitted before the actuator turns on, the maximum response is increased and the average power is decreased. This effect is observed for all RMS block sizes. However, when compared with a simple linear decrease in the gain for DVF it is seen that reducing the gain is a more effective solution for this situation; the average power required for a certain level of response is high when using a switching off rule. The reason for this can be found by examining the time history of the power demand and structural response, as shown in Fig. 6.11.

The threshold for the switching-off rule in the controller shown in Fig. 6.11 is at an RMS acceleration of $0.042m/s^2$ which approximately equates to an R factor of 8. The power demand for the switching-off controller rises rapidly to a high level as soon as the threshold is exceeded. As the response reduces below the threshold the controller switches off. However the continuous excitation will cause an increase in the response. This means that at the instant in time when the response

Fig. 6.8 FRFs for uncontrolled structure and DVF with gains varying from 5% to 100% of optimal

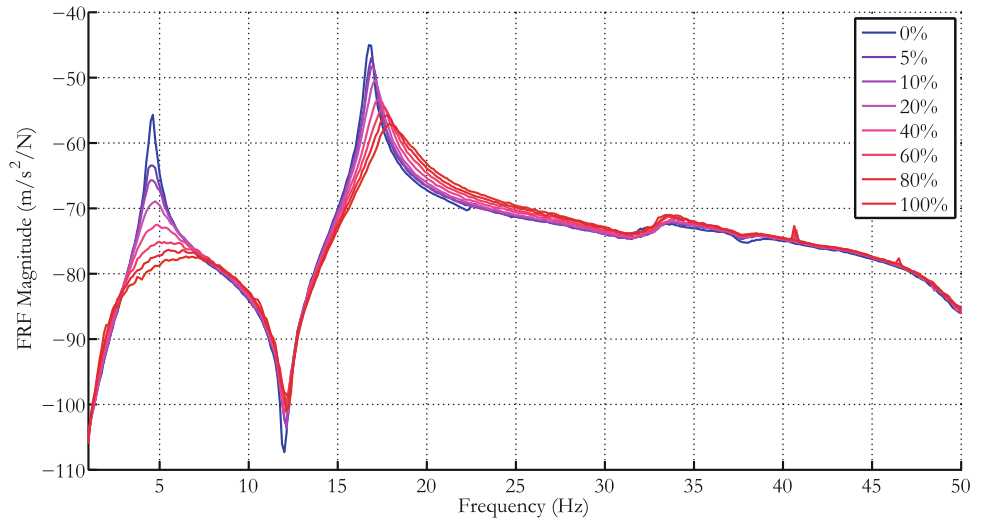
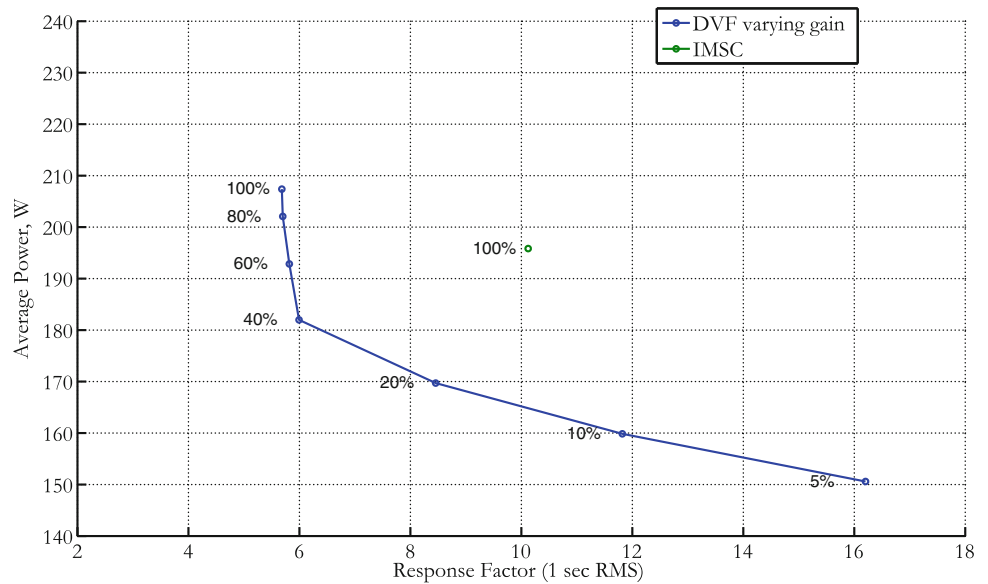


Fig. 6.9 Average power and maximum R factor for various feedback gains (as indicated by % of optimal) of DVF and IMSC



increases above the threshold again, the controller will have to work harder to reduce the response than if it had been working all the time. In addition to this, the delay introduced by having to wait one second to determine the RMS of the acceleration means that the response could actually be higher than the threshold. Evidence of this is seen in Fig. 6.11 where the same threshold values are used for each block size, but the response factor measured is lower for the smaller blocks. The continuous nature of the excitation used in these tests meant that the response alternated between being under and over the switching-off threshold relatively rapidly. This increases the proportion of power spikes relative to the total duration. As Fig. 6.11 shows, the power demand is low when the response is below threshold, high immediately after the response exceeds the threshold, and approximately the same as the controller without a switching-off rule once the response has exceeded the threshold for a short duration. Therefore, the effectiveness of using a switching-off controller is dependent on the ratio of low to high levels of response.

Finally, a relatively simple deadzone was considered. This is effectively a special case of the switching off rule where the block size for calculating the RMS of the acceleration is one sample. Thresholds varying from $R = 1$ to $R = 8$ were considered (with the same assumption of frequency weighting being for the first mode of vibration as in previous tests). The results of this are shown in Fig. 6.12.

Here, again the compromise between increase in response and reduction in power is observed as the deadzone threshold changes. However, all the solutions lie further from the utopian goal compared with simply changing the DVF gain.

Fig. 6.10 Comparing effect on response and power of varying DVF gain with varying switching-off parameters

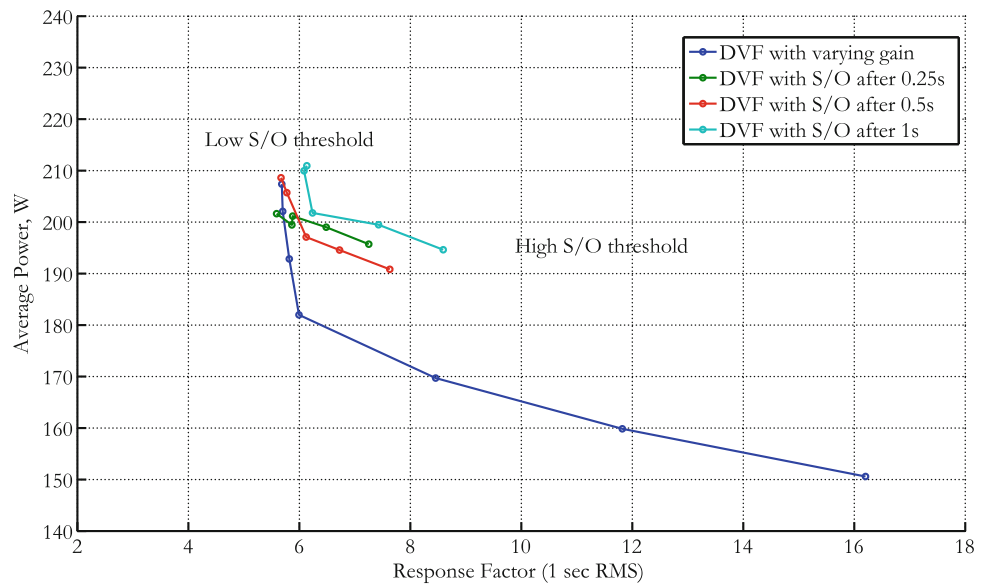
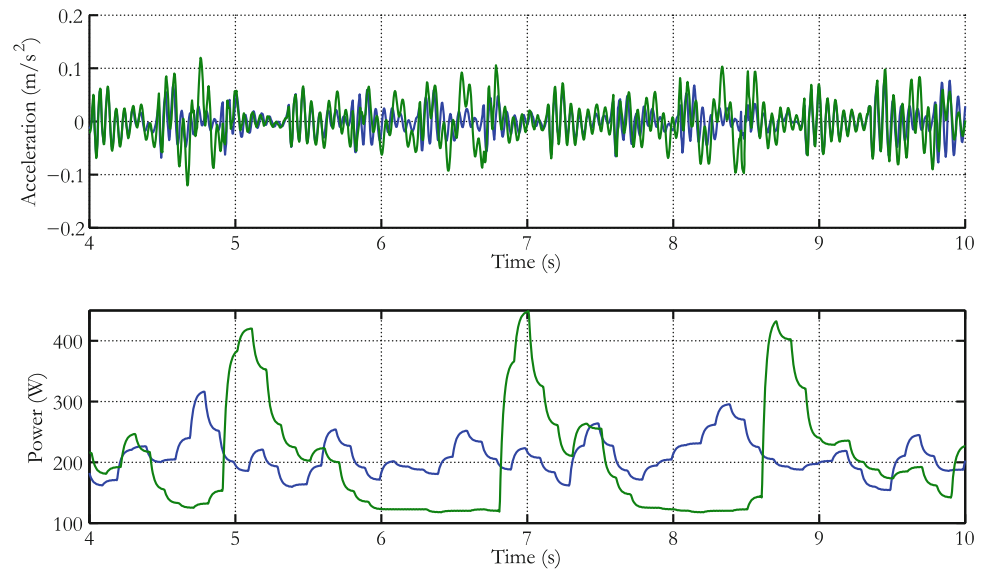


Fig. 6.11 Time history for AVC power demand and structural response without a switching-off rule and with



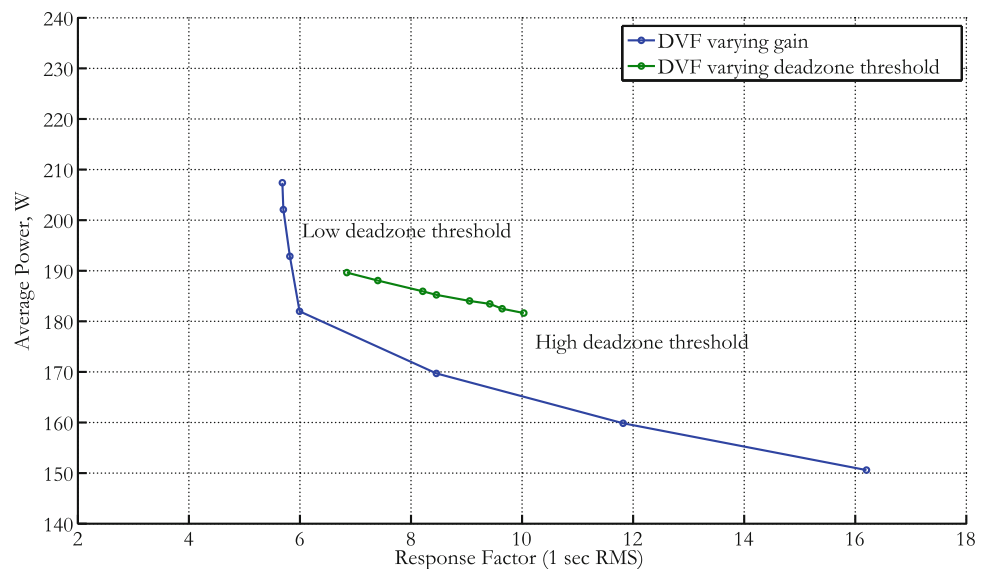
6.5 Conclusions

The power requirements of various active control configurations have been investigated. A repeatable walking force has been generated by inertial actuators and this facilitates direct comparisons between controller types for the same excitation input.

It immediately becomes apparent that there is a high power demand from these actuators when the force output from the actuator is zero. These overheads contribute a significant portion of the total average power demand from the shakers: the largest average power recorded was about 270W indicating that, for these tests, at best the overheads accounted for 40% of the total. Future work should certainly investigate the use of improved amplifiers that have much lower overheads. If it is possible to reduce, or even remove this overhead completely, possibly through the use of Class-D amplifiers, then very significant power savings can be realised.

With regards to specific controllers tested, it was observed that no significant power savings were made by using IMSC to intentionally not control the second vertical mode of vibration, when compared with a simple DVF controller. Indeed, the marginal power savings made are far outweighed by the increase in response despite the relatively high frequency of this mode.

Fig. 6.12 Comparing effect on response and power of varying DVF gain with varying deadzone threshold



For this excitation type the most effective way to reduce the power requirements of the controller are to use a simple DVF controller with a reduced feedback gain. Although the use of a switching off rule did achieve power savings, the structural response was higher than DVF for any given average power requirement. However, other excitation types may not result in the same conclusion: the effectiveness of the switching off rule is dependent on the proportion of time the controller switches from inactive to active resulting in large transient increases in power demand. The use of a deadzone (i.e. a switching off rule with block size of one) was similarly not as effective as a simple reduction in feedback gain for DVF.

Future work should consider working towards predicting the power requirements of an AVC system based on the command signal without the need for a power monitor device. This would then allow predictions for typical power requirements of AVC due to in-service loading in real structures and thus enable predictions for how much electricity would be required for AVC during the building's operational life. In addition to this, there is the potential to achieve material savings through the design of AVC into new floors whose design is governed by vibration serviceability. The overall cost savings due to fewer materials being used in construction, both financial and environmental, should be calculated for these structures and compared with the ongoing costs associated with AVC to determine the cost effectiveness of this strategy.

Acknowledgements The authors would like to acknowledge the financial support given by the UK Engineering and Physical Sciences Research Council via Industrial CASE Award with WSP Buildings (Voucher Number 08002020), the Responsive Mode Grant (Ref. EP/H009825/1), Platform Grant (Ref. EP/G061130/1) and Leadership Fellowship Grant (Ref. EP/J004081/1).

References

- Hanagan LM (1994) Active control of floor vibrations. Phd thesis, Polytechnic Institute and State University, Virginia
- Nyawako D (2009) An active control approach for mitigation of human-induced vibrations in floors. Phd thesis, The University of Sheffield, Sheffield, UK
- Díaz IM, Reynolds P (2010) Eng Struct 32(1):163–173
- Díaz IM, Reynolds P (2009) Smart materials and structures, vol 18, p 125024, Porto, IOP Publishing, Bristol, UK
- Hanagan LM, Murray TM (1998) AISC Eng J 35(4):123–127
- Hanagan LM (2005) J Architect Eng 11(1):14–18
- Nyawako D, Reynolds P (2009) Smart Mater Struct 18. doi: [10.1088/0964-1726/18/7/075002](https://doi.org/10.1088/0964-1726/18/7/075002)
- Díaz IM, Reynolds P (2010) Mech Syst Signal Process 24:1711–1726
- Nyawako D, Reynolds P, Hudson M (2012) Proc SPIE 2012
- Zivanović S, Pavić A, Reynolds P (2007) Eng Struct 29(6):942–954
- Racic V (2009) Experimental measurement and mathematical modelling of near-periodic human-induced dynamic force signals. Phd thesis, University of Sheffield

Chapter 7

Tuning TMDs to “Fix” Floors in MDOF Shear Buildings

Jennifer Rinker

Abstract Many researchers have examined the optimal design of tuned mass dampers (TMDs) for vibration reduction in single-degree-of-freedom (SDOF) and multiple-degree-of-freedom (MDOF) systems. This work focuses on the design of damped TMDs to “fix” selected floors of a harmonically base-excited building in shear such that the vibrational amplitudes of the selected floors are zero. This method does not require the fixed floors, referred to as “fixed nodes,” to coincide with the floors to which the TMDs are attached. This paper presents the proposed tuning method and addresses the feasible arrangements of the fixed and TMD floors. The proposed tuning method is demonstrated with a simulation of a 3-DOF shear building, along with a discussion on the effects of mistuning on the TMD performance.

Keywords tuned-mass dampers • shear buildings • tuning procedure • base excitation • enforcing nodes

7.1 Introduction

Tuned mass dampers (TMDs) are spring-mass-damper systems that are attached to a primary system to divert energy and lessen the vibration of the primary system. Ideally, the primary system is being excited harmonically and the excitation frequency is known exactly. The selection of the TMD parameters, referred to as the “tuning” of the TMDs, can be done in a variety of ways. The most classical tuning method was introduced by Den Hartog [1], who tuned the TMDs to keep the amplitude of the primary mass small. Many other researchers have also used a variety of optimization techniques to determine the optimal TMD parameters for a selected cost function [2–4].

A different method for tuning TMDs selects the TMD parameters so that locations of zero vibrational amplitude, referred to as “fixed nodes,” are enforced at desired locations in the system. This method has been investigated by Cha for elastic systems [5], systems with multiple excitation frequencies [6], and damped Euler-Bernoulli beams [7]. The fixed nodes and TMDs need not be collocated, and any number of fixed nodes may be enforced in a continuous system with the same number of attachments. Cha’s tuning procedure first determines the steady-state forces the attachments must apply to the system in order to enforce the fixed nodes at the desired locations. Once these required attachment forces are known, it is trivial to determine the steady-state deflection of the system subjected to the attachment forces, check that the required attachment forces are passive, and then solve for the TMD parameters.

The research presented in this paper focuses on modifying this tuning procedure to be used in a discrete system. This modified tuning procedure is derived and presented in Section 7.2, simulation results for an example 3-DOF shear building are presented in Section 7.3, and the work is summarized in Section 7.4.

J. Rinker (✉)
Duke University, 121 Hudson Hall, Box 90287, Durham, NC 27708, USA
e-mail: jennifer.rinker@duke.edu

7.2 Theory

Consider a discrete primary system with N degrees of freedom that is excited harmonically at N_f locations with a single frequency. It is desired to enforce N_a fixed nodes in the system, which requires tuning N_a attachments. After replacing the attachments with their unknown restoring forces, the equation of motion in generalized coordinates \mathbf{x} is

$$[M]\ddot{\mathbf{x}} + [C]\dot{\mathbf{x}} + [K]\mathbf{x} = \mathbf{F} \quad (7.1)$$

where \mathbf{F} contains contributions from the external forcing and from the attachments.

Assume that the external forcing is harmonic with frequency ω and that the system is in steady-state, in which case

$$\mathbf{F} = \bar{\mathbf{F}} e^{j\omega t}, \quad (7.2)$$

$$\mathbf{x} = \bar{\mathbf{x}} e^{j\omega t}, \quad (7.3)$$

where $\bar{\cdot}$ indicates phasor notation, and $j = \sqrt{-1}$. Substituting these equations into Eq. (7.1) and simplifying yields

$$(-\omega^2[M] + j\omega[C] + [K])\bar{\mathbf{x}} = \bar{\mathbf{F}}. \quad (7.4)$$

Separating the forcing vector into the external and attachment forces yields

$$\bar{\mathbf{F}} = \bar{\mathbf{F}}_e + \bar{\mathbf{F}}_a \quad (7.5)$$

where $\bar{\mathbf{F}}_e$ has N_f nonzero entries and $\bar{\mathbf{F}}_a$ has N_a nonzero entries that correspond to the N_a attachments to be tuned and/or the N_a fixed nodes to be enforced. Defining the impedance matrix as $[Z] = -\omega^2[M] + j\omega[C] + [K]$ and combining Eqs. (7.4) and (7.5) yields

$$\bar{\mathbf{x}} = [Z]^{-1} (\bar{\mathbf{F}}_e + \bar{\mathbf{F}}_a). \quad (7.6)$$

Note that $\bar{\mathbf{F}}_e$ and $[Z]^{-1}$ are known, $\bar{\mathbf{F}}_a$ is to be determined, and the fixed node enforcement will set the corresponding entries of $\bar{\mathbf{x}}$ to zero.

Define two “selection matrices” $[S_n]$ and $[S_a]$ of ones and zeros such that:

$$\bar{\mathbf{F}}_a = [S_a]\bar{\mathbf{f}}_a, \quad \mathbf{0} = [S_n]\bar{\mathbf{x}}, \quad (7.7)$$

where $\bar{\mathbf{f}}_a$ is a vector of the N_a attachment phasors that are required to enforce the desired fixed nodes. Note that $[S_n] \in \mathbb{R}^{N_a \times N}$ and the i th row contains a one at the i th fixed node location; $[S_a] \in \mathbb{R}^{N \times N_a}$ and the j th column contains a one at the j th attachment location.

Combining Eqs. (7.6) and (7.7) yields the following expression for the required attachment forces:

$$\bar{\mathbf{f}}_a = -([S_n][Z]^{-1}[S_a])^{-1} [S_n][Z]^{-1} \bar{\mathbf{F}}_e. \quad (7.8)$$

Once the attachment forces have been found they may be substituted into Eq. (7.6) to determine the steady-state deflection of the system $\bar{\mathbf{x}}$.

At this point it is necessary to verify that the required attachment forces can be delivered by a passive system. In particular, the phase of the required restoring force at a particular location must lag behind the steady-state deflection at that point by no more than 180° . In other words, once $\bar{\mathbf{f}}_a$ has been found, one must verify that

$$0 \leq \angle \bar{x}_i - \angle \bar{f}_{a,i} < \pi \quad (7.9)$$

for all attachment locations i . Note that this matches the result in Cha and Rinker [7].

Because the complex relationship between \bar{x}_i and $\bar{f}_{a,i}$ is known but there are three unknown TMD parameters, the designer must choose one parameter and subsequently solve for the other two. This paper follows the method laid out in Cha and Rinker [7], prescribing the absolute displacement of the TMD $|\bar{x}_i + \bar{d}_i|$, where \bar{d}_i is the relative displacement of the i th TMD. However, one could easily choose any of the TMD parameters (e.g. the stiffness k_i or damper value c_i) and solve for the other TMD parameters. From the referenced paper,

$$m_i = \frac{|\bar{f}_a^i|}{\omega^2 |\bar{x}_i + \bar{d}_i|}, \quad (7.10)$$

$$k_i = \frac{(a_i^2 + b_i^2 - a_i m_i \omega^2) m_i \omega^2}{b_i^2 + (a_i - m_i \omega^2)^2}, \quad (7.11)$$

$$c_i = \frac{-b_i m_i^2 \omega^3}{b_i^2 + (a_i - m_i \omega^2)^2}, \quad (7.12)$$

where $a_i = \Re(\bar{f}_a^i / \bar{x}_i)$ and $b_i = \Im(\bar{f}_a^i / \bar{x}_i)$. Once the TMD parameters have been chosen, the matrix governing equation for the system with the tuned attachments can be assembled and the fixed node enforcement verified.

The tuning procedure may then be summarized as follows:

1. Select a fixed node and attachment arrangement.
2. Use Eq. (7.8) to solve for the required attachment forces.
3. Determine the steady-state deflections with Eq. (7.6) and verify passivity with Eq. (7.9).
4. Choose an amplitude for the TMD.
5. Solve for m_i , k_i , and c_i using Eqs. (7.10)–(7.12).

7.3 Example

Consider a 3-DOF shear building with the parameters shown in Table 7.1. The building is subjected to a harmonic base excitation $x(t) = \bar{x}_b e^{j\omega t}$, where $\bar{x}_b = 0.1$ m and $\omega = 20$ rad/s. Then,

$$[M] = \begin{bmatrix} m_1 & 0 & 0 \\ 0 & m_2 & 0 \\ 0 & 0 & m_3 \end{bmatrix} = \begin{bmatrix} 1001 & 0 & 0 \\ 0 & 999 & 0 \\ 0 & 0 & 1000 \end{bmatrix} \text{ kg}, \quad (7.13)$$

$$[K] = \begin{bmatrix} k_1 + k_2 & -k_2 & 0 \\ -k_2 & k_2 + k_3 & -k_3 \\ 0 & -k_3 & k_3 \end{bmatrix} = \begin{bmatrix} 891 & -441 & 0 \\ -441 & 908 & -467 \\ 0 & -467 & 467 \end{bmatrix} \text{ kN/m}, \quad (7.14)$$

$$[C] = \begin{bmatrix} c_1 + c_2 & -c_2 & 0 \\ -c_2 & c_2 + c_3 & -c_3 \\ 0 & -c_3 & c_3 \end{bmatrix} = \begin{bmatrix} 117 & -63 & 0 \\ -63 & 142 & -79 \\ 0 & -79 & 79 \end{bmatrix} \text{ kN/m}, \quad (7.15)$$

$$\bar{F}_e = \begin{bmatrix} \bar{x}_b (k_1 + j\omega c_1) \\ 0 \\ 0 \end{bmatrix} = \begin{bmatrix} 45 + 0.108j \\ 0 \\ 0 \end{bmatrix} \text{ kN}. \quad (7.16)$$

Consider the case where a single TMD is attached to the first floor and it is desired to enforce a fixed node at the second floor to remove its vibration. Using the procedure laid out in Section 7.2 with $|d_i| = 0.3$ m, the resulting TMD parameters are $m_a = 375.0$ kg, $k_a = 150.0$ kN/m, $c_a = 0$ kg/s, and the deflected shapes of the building with and without the TMD are shown in Fig. 7.1.

There are two items of note in this example. The first is that the TMD is now undamped, despite the fact that this is a damped system, and the second is that this arrangement of the TMD and desired fixed node leads to vibration suppression in *all three* floors of the building, not just the second. These two facts are not unrelated, and explaining the latter observation will produce an explanation for the former.

Table 7.1 Parameters for 3-DOF shear building example

Parameter	Floor 1	Floor 2	Floor 3
m_i (kg)	1001	999	1000
k_i (kN/m)	450	441	467
c_i (kg/s)	54	63	79

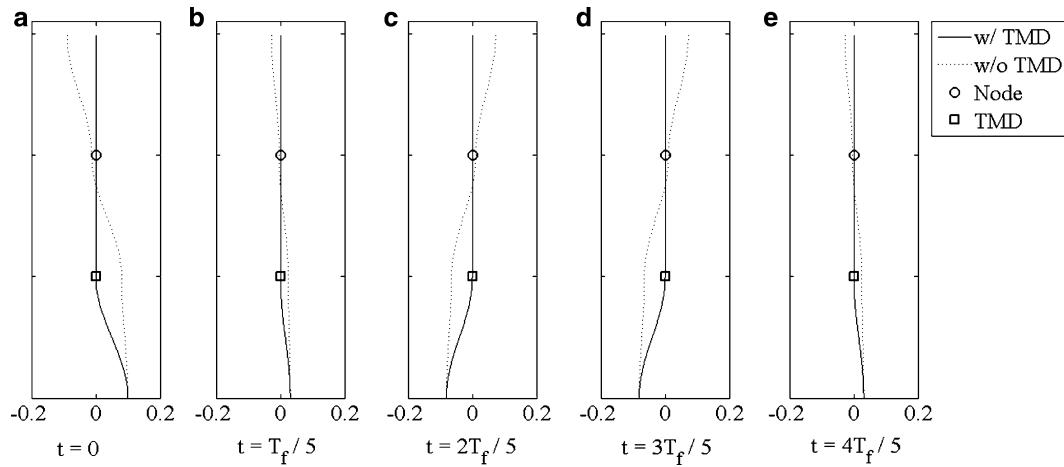


Fig. 7.1 Snapshots of displacement (m) of system with and without TMD

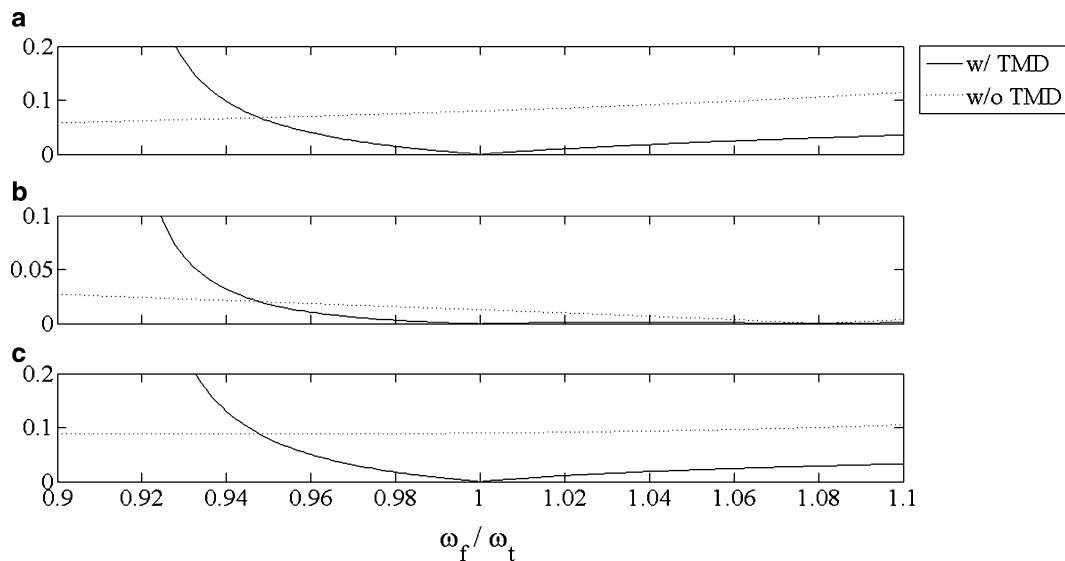


Fig. 7.2 Plots of the amplitude (m) of vibration for (a) Floor 1, (b) Floor 2, and (c) Floor 3 as ω_f varies

This fixed node and TMD arrangement is not the only arrangement that produces these same values for the TMD parameters and the same vibration suppression in all three floors; in fact, any arrangement that places the TMD on the first floor of the building yields these parameters and the vibration suppression in all floors. This is logically intuitive. If the TMD enforces a fixed node at the first floor, then no vibration can be transmitted to the higher floors. Thus, enforcing fixed nodes at the second or third floors is equivalent to enforcing a fixed node at the first floor. In that case, this particular example reduces to the system where the TMD and desired fixed node are collocated on the first floor, in which case the solution features no damper [7]. Note that, by extension, this is true for all cases where the desired fixed node is located on the same floor or above the floor where the TMD is attached.

On the other hand, if the desired fixed node is located below the attachment location, then the required attachment force violates passivity and the TMD/fixed-floor arrangement is infeasible. However, while this was true for all possible arrangements in this particular system, it is not necessarily true for other shear building systems. For example, if $\bar{F}_e = [10 \ 60 \ 70]^T$ N, it is possible to place the TMD on the second floor but enforce a fixed node on the first floor. However, this results in an amplification of the third-floor oscillation, so care should always be taken to examine the global system behavior.

Lastly, it is useful to examine what consequences could result from mistuning (i.e., if the actual forcing frequency differs from the tuning frequency). Let ω_f be the true forcing frequency of the system and ω_t be the frequency used in Eqs. (7.4), (7.11) and (7.12). A plot of the amplitudes of vibration of the floors for varying values of ω_f/ω_t is shown in Fig. 7.2. Note that if $\omega_f/\omega_t = 1$ then the system is perfectly tuned and all floors have zero vibration, which matches the

earlier result. It is interesting to see that, even with mistuning, if the variation in ω_f is approximately less than 5% of the tuning frequency, the system with the TMD features less vibration than that without the TMD. However, if the variation in ω_f is less than this bound, the system with the TMD has much larger vibration on all three floors.

7.4 Conclusions

This paper develops a procedure to choose the parameters of TMDs in harmonically forced discrete systems to enforce locations of zero amplitude in the system. A 3-DOF shear building with harmonic base excitation and a single TMD is presented as an example. It is shown that fixing floors at or above the TMD location results in zero vibration for all floors at and above the TMD location, whereas placing the TMD above the fixed node is an infeasible arrangement. The paper also includes an examination of the effects of mistuning upon the system with the TMD and shows that if the error in frequencies is less than 5%, then the system with the TMD features less vibration than the system with no TMD, though the floors are no longer perfectly fixed.

References

1. Den Hartog JP (1934) Mechanical vibrations. McGraw-Hill Book Company, New York
2. Jacquot RG (1978) Optimal dynamic vibration absorbers for general beam system. *J Sound Vib* 60(4):535–542
3. Zuo L, Nayfeh SA (2004) Minimax optimization of multi-degree-of-freedom tuned-mass dampers. *J Sound Vib* 272(3–5):893–908
4. Luft RW (1979) Optimal tuned mass dampers for buildings. *J Struct Div-ASCE* 105(12):2766–2772
5. Cha PD (2005) Enforcing nodes at required locations in a harmonically excited structure using simple oscillators. *J Sound Vib* 279(3–5):799–781
6. Cha PD, Ren G (2006) Inverse problem of imposing nodes to suppress vibration for a structure subjected to multiple harmonic excitations. *J Sound Vib* 290(1–2):425–447
7. Cha PD, Rinker JM Enforcing nodes to suppress vibration along a harmonically forced damped Euler-Bernoulli beam. *J Vib Acoust* 134:5

Chapter 8

Precise Stiffness Control with MR Dampers

Marcin Maślanka and Felix Weber

Abstract Magnetorheological (MR) dampers can be used not only as controllable damping devices but also to emulate a controllable positive or negative stiffness in combination with the dissipative force. However, the dissipative nature of MR dampers constrains the stiffness control. This work formulates the problem of combined stiffness and damping control with MR dampers if the damper is subjected to pure harmonic motion. A new method is presented that ends up in precise stiffness emulation with MR dampers, also when the sum of the stiffness and dissipative forces is constrained by the semi-active nature and residual force of MR dampers. The new control concept is applied to a semi-active tuned mass damper with an MR damper (MR-STMD). The numerical and experimental results demonstrate that the MR-STMD outperforms the passive TMD significantly.

Keywords MR damper • Stiffness • Control • Semi-active • TMD

8.1 Introduction

Magnetorheological (MR) dampers are controllable damping devices with MR fluid that continuously and reversibly changes from a free-flowing state to a semi-solid state under the application of a magnetic field. If constant current is applied to a coil that creates a magnetic field in the MR damper, the actual MR damper force under harmonic excitation can be roughly modeled with the Bingham model as the sum of a Coulomb friction force and a viscous damping force [1]. However, by controlling the current in the MR damper coil, and thus forcing the MR fluid to change its properties over time, it might be possible to obtain any desired damping force characteristics with MR dampers. In order to track the desired control force with MR dampers, the usual method is to use a feed-forward force tracking control. In this approach an inverse model of an MR damper is used to calculate, in real time, the current that should be applied to the MR damper coil to get the actual MR damper force as desired [2]. In this way, the real-time controlled MR damper may accurately track the force of e.g. a viscous damper [3], or any other desired control force calculated by different control algorithms, provided that the desired control force is fully dissipative and within the controllable force range of the MR damper. In particular, recent research has shown that MR dampers can be used to emulate a controllable positive or negative dynamic stiffness. Negative stiffness control with MR dampers has received especially great interest due to its role in increasing the damping efficiency [4]. However, the dissipative nature of MR dampers significantly constrains the stiffness control. If the desired control force is active during some parts of a vibration cycle, it cannot be tracked with MR dampers and the usual method is to clip active desired forces to zero. The clipping operation represents a significant constraint in stiffness control with MR dampers. The stiffness control with MR dampers is further constrained by the MR damper and current driver dynamics and by the MR damper residual

M. Maślanka (✉)

Faculty of Mechanical Engineering and Robotics, Department of Process Control, AGH University of Science and Technology,
al. A. Mickiewicza 30, 30-059 Krakow, Poland
e-mail: marcin.maslanka@agh.edu.pl

F. Weber

Empa, Swiss Federal Laboratories for Materials Science and Technology, Structural Engineering Research Laboratory,
Ueberlandstrasse 129, CH-8600 Duebendorf, Switzerland

force, i.e. the force at zero current. This paper aims to show how to compensate for the constraints due to clipping and residual force in stiffness control with MR dampers under harmonic excitation.

The next section formulates the problem of combined stiffness and damping control with MR dampers. Later, a new method is presented which guarantees precise stiffness emulation with MR dampers, even in cases when the desired control force is constrained by the clipping and the residual MR damper force. The method is validated both by simulations and experiments in a semi-active tuned mass damper with an MR damper (MR-STMD). The paper is closed with conclusions.

8.2 Combined Stiffness and Damping Control with MR Dampers Under Harmonic Excitation

The goal of the combined stiffness and damping control with an MR damper is to generate the desired positive or negative dynamic stiffness and, at the same time, to dissipate the desired amount of energy to realize the damping. In other words, the goal is to emulate, with an MR damper, the dynamic behavior of the parallel configuration of a spring, with positive or negative stiffness, and a passive damper. Assuming harmonic excitation, this goal can be achieved by different approaches.

The desired control force to be tracked with the real-time controlled MR damper can be defined directly as the sum of a positive or negative stiffness force and a viscous damping force, which then necessitates the clipping of active desired forces to fulfill semi-active requirements (Fig. 8.1a). This approach of semi-active stiffness and damping control was first studied in [5] where the semi-active hydraulic damper was used to generate negative stiffness and the approach was denoted as pseudo

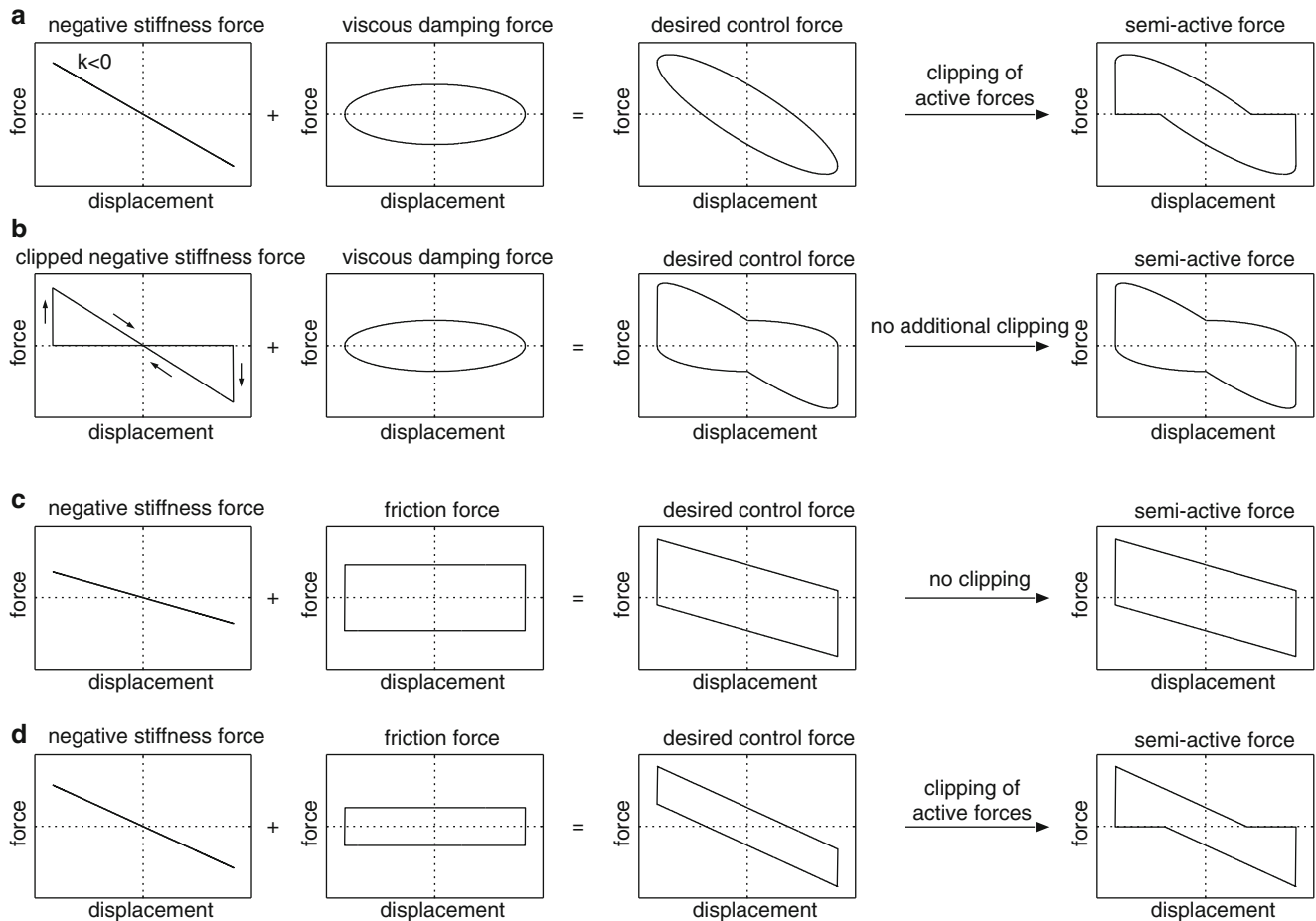


Fig. 8.1 Negative stiffness and damping control for MR dampers under harmonic excitation: clipped stiffness-viscous damping force (a), clipped stiffness force plus viscous damping force (b), stiffness-friction force (c), clipped stiffness-friction force (d)

negative stiffness control. The term ‘pseudo’ indicates a different mechanism of semi-actively realized dynamic stiffness. It is underlined in [6] that semi-active dampers cannot actively ‘push’ the structure in the same direction as the structural displacement, and therefore cannot realize ‘true’, but only ‘pseudo’ negative stiffness. Nevertheless, the negative stiffness is generated and, as a result, the high damping performance of this approach was reported e.g. in [7]. The desired control force can also be defined as the sum of an already clipped stiffness force and a viscous damping force (Fig. 8.1b). However, these two approaches are always constrained by clipping and give lower stiffness and higher energy dissipation than desired. The increase in energy dissipation due to the clipping of active forces is graphically illustrated by an area constrained by the force displacement loop, which is larger after clipping than before clipping (Fig. 8.1a).

Alternatively, the desired control force can be composed of a stiffness force and a Coulomb friction force. In this approach the desired control force does not necessitate clipping and can be fully tracked with MR dampers if the Coulomb friction force is larger or equal to the maximum stiffness force (Fig. 8.1c). This method was investigated e.g. in [8]. The method guarantees precise stiffness emulation with MR dampers but it requires large friction forces that might result in excessively large energy dissipation. However, if the friction force is lower than the maximum stiffness force, it also ends up in clipping (Fig. 8.1d), and the resulting stiffness is lower and damping (energy dissipation) higher than desired. Since the stiffness and damping that result from the semi-active force in Fig. 8.1a–d are coupled quantities, the independent control of one of them, which does not affect the other, is not possible.

This paper shows that by necessary modification of the approach presented in Fig. 8.1d the equivalent stiffness resulting from the semi-active force might be equal to the desired stiffness despite clipping and residual force constraints.

8.3 Precise Stiffness Control with MR Dampers when Desired Control Force is Composed of Stiffness and Friction Forces

8.3.1 Desired Control Force and Resulting Semi-active Force

The desired control force f_{des} that is to be tracked by the real-time controlled MR damper is the sum of a desired stiffness force and a desired Coulomb friction damping force

$$f_{des} = k_{des} x_d + F_{des}^f \operatorname{sgn}(\dot{x}_d) \quad (8.1)$$

where x_d is the MR damper relative displacement which is assumed to be harmonic, \dot{x}_d is the corresponding velocity, k_{des} is the desired positive or negative stiffness, and F_{des}^f is the desired friction force. For harmonic motion, the desired friction force is calculated such that it is energy equivalent to the desired viscous damping coefficient c_{des}

$$F_{des}^f = \frac{\pi}{4} c_{des} \omega_d X_d \quad (8.2)$$

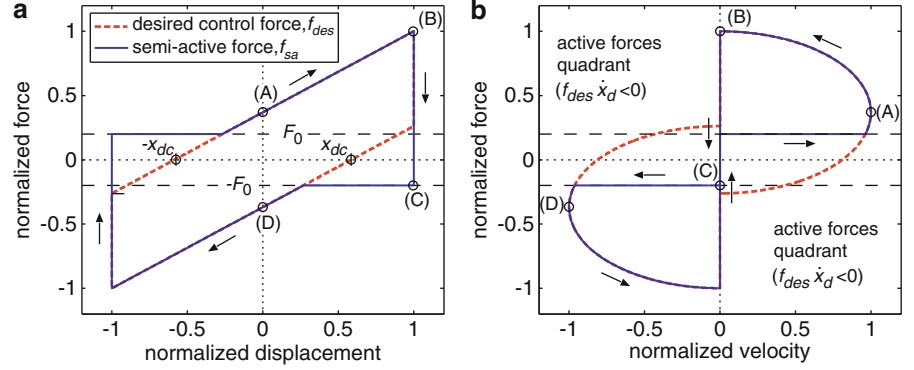
where ω_d is the circular frequency and X_d is the amplitude of the MR damper displacement x_d .

As indicated in Sect. 8.2, if the magnitude of the desired stiffness force $|k_{des}| X_d$ is larger than F_{des}^f , the desired control force (8.1) becomes partially active during a vibration cycle and the active forces are clipped to zero (Fig. 8.1d). Besides the clipping, f_{des} is also constrained by the residual force of MR dampers, which is typically considered as pure friction force F_0 . Both constraints result in the semi-active force f_{sa}

$$f_{sa} = \begin{cases} F_0 & : f_{des} < F_0, \dot{x}_d > 0 \\ -F_0 & : f_{des} > -F_0, \dot{x}_d < 0. \\ f_{des} & : otherwise \end{cases} \quad (8.3)$$

If f_{sa} is not constrained, i.e. if $F_{des}^f \geq |k_{des}| X_d + F_0$, the equivalent stiffness k_{eq} and the equivalent viscous damping coefficient c_{eq} , which might be derived from f_{sa} , are equal to their desired counterparts k_{des} and c_{des} . This situation is depicted in Fig. 8.1c for zero residual force.

Fig. 8.2 Desired control force and semi-active force versus displacement x_d (a) and velocity \dot{x}_d (b)



8.3.2 Equivalent Stiffness and Equivalent Viscous Damping

Figure 8.1d shows the semi-active force for $F_{des}^f < |k_{des}| X_d$. This situation is illustrated in detail in Fig. 8.2 for the case when the residual force F_0 is higher than zero. It can be noted that the clipping of the active forces, which would result in zero force for $|x_d| > |x_{dc}|$ and $f_{des} \dot{x}_d < 0$, does not constrain the desired force as strongly as the residual force F_0 .

Assuming harmonic motion, the equivalent stiffness resulting from the semi-active force in Fig. 8.2 can be derived from the potential energy that is stored and released by the device during half a cycle. This is one of the methods used in the linearization of nonlinear springs. The potential energy V_1 stored at maximum displacement is equal to the work done from point (A) to point (B) (Fig. 8.2a). For the positive desired stiffness $k_{des} > 0$, V_1 is

$$V_1 = \int_0^{x_d} f_{sa} dx_d = F_{des}^f X_d + 0.5 X_d^2 k_{des}. \quad (8.4)$$

The potential energy release V_2 from point (B) to point (D), also for $k_{des} > 0$, is

$$V_2 = \int_{x_d}^0 f_{sa} dx_d = -F_0 X_d - \frac{(F_{des}^f - F_0)^2}{2k_{des}} \quad (8.5)$$

The sought equivalent stiffness is $k_{eq} = (V_1 + V_2)/X_d^2$ which yields

$$k_{eq} = \frac{1}{2} k_{des} + \text{sgn}(k_{des}) \frac{F_{des}^f - F_0}{X_d} - \text{sgn}(F_{des}^f - F_0) \frac{(F_{des}^f - F_0)^2}{2 k_{des} X_d^2} \quad (8.6)$$

where the signum functions are added such that (8.6) is valid for positive and negative desired stiffness as well, and also for the case when the desired friction force F_{des}^f is smaller than F_0 , but larger or equal to $-|k_{des}| X_d + F_0$.

Finally, the general expression for the equivalent stiffness resulting from the semi-active force (8.3) can be written in the form

$$k_{eq} = \begin{cases} k_{des} & : F_{des}^f \geq |k_{des}| X_d + F_0 \\ \frac{1}{2} k_{des} + \text{sgn}(k_{des}) \frac{F_{des}^f - F_0}{X_d} - \text{sgn}(F_{des}^f - F_0) \frac{(F_{des}^f - F_0)^2}{2 k_{des} X_d^2} & : -|k_{des}| X_d + F_0 \leq F_{des}^f < |k_{des}| X_d + F_0 \\ 0 & : F_{des}^f < -|k_{des}| X_d + F_0 \end{cases} \quad (8.7)$$

The equivalent stiffness k_{eq} (8.7) is equal to the desired stiffness k_{des} if the force (8.1) is not constrained by clipping and/or the residual force. Otherwise, if $F_{des}^f < |k_{des}| X_d + F_0$, the equivalent stiffness k_{eq} is always lower in absolute value

than the desired stiffness. If the residual force is larger than the maximum value of the desired force (8.1), the stiffness control is not possible, and therefore the equivalent stiffness becomes zero.

Since stiffness and damping cannot be controlled independently with MR dampers, the precise stiffness control (PSC) approach is presented, which leads to $k_{eq} = k_{des}$ with an additional increase in energy dissipation.

8.3.3 Formulation of Precise Stiffness Control (PSC)

The basic idea is to replace k_{des} in (8.1) by the corrected stiffness k^* which yields the corrected desired force f_{des}^* as follows

$$f_{des}^* = k^* x_d + F_{des}^f \operatorname{sgn}(\dot{x}_d). \quad (8.8)$$

f_{des}^* generates the corrected semi-active force f_{sa}^* that is constrained by the clipping of active forces and the residual force F_0 , similarly to f_{sa} (8.3). The corrected stiffness k^* should be calculated such that the equivalent stiffness resulting from f_{sa}^* is equal to the desired stiffness, thus $k_{eq}^* := k_{des}$.

The equivalent stiffness of the corrected semi-active force f_{sa}^* becomes

$$k_{eq}^* = \frac{1}{2} k^* + \operatorname{sgn}(k^*) \frac{F_{des}^f - F_0}{X_d} - \operatorname{sgn}(F_{des}^f - F_0) \frac{(F_{des}^f - F_0)^2}{2 k^* X_d^2}. \quad (8.9)$$

The sought k^* can be obtained by substituting k_{des} for k_{eq}^* in (8.9) and solving the quadratic equation which finally yields the feasible solution $k^* = \operatorname{sgn}(k_{des}) \left(-b + \sqrt{b^2 - 4ac} \right) / 2a$ with $a = X_d^2$, $b = 2X_d \left(F_{des}^f - F_0 - X_d |k_{des}| \right)$ and $c = -\operatorname{sgn}(F_{des}^f - F_0) \left(F_{des}^f - F_0 \right)^2$. Since stiffness correction is only needed when f_{sa}^* is constrained, i.e. if $F_{des}^f < |k_{des}| X_d + F_0$, the general formulation of the corrected stiffness becomes

$$k^* = \begin{cases} k_{des} & : |k_{des}| \leq \frac{F_{des}^f - F_0}{X_d} \\ \frac{\operatorname{sgn}(k_{des})}{X_d} \left\{ - \left(F_{des}^f - F_0 - X_d |k_{des}| \right) + \sqrt{\left(F_{des}^f - F_0 - X_d |k_{des}| \right)^2 + \operatorname{sgn}(F_{des}^f - F_0) \left(F_{des}^f - F_0 \right)^2} \right\} & : |k_{des}| > \frac{F_{des}^f - F_0}{X_d} \end{cases} \quad (8.10)$$

The proposed approach guarantees that the resulting equivalent stiffness equals its desired value. This method yields correct resulting stiffness and increases resulting energy dissipation.

8.4 Precise Stiffness Control in Application to a Semi-active TMD

8.4.1 A Semi-active TMD with an MR Damper (MR-STMD)

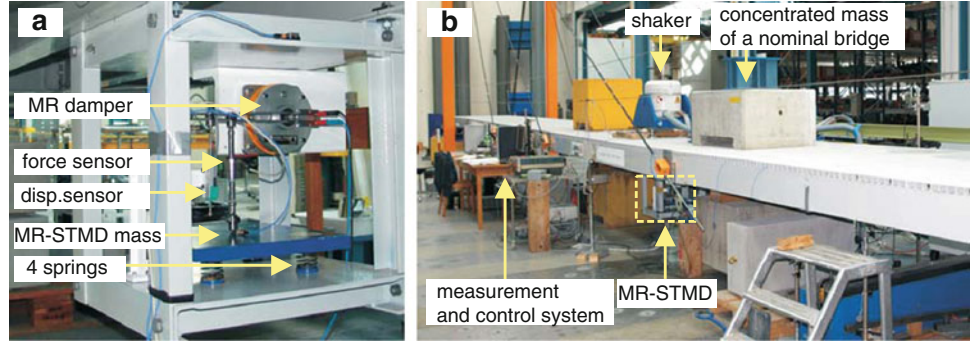
We consider a semi-active TMD with an MR damper (MR-STMD) proposed in [9]. The MR-STMD is composed of its mass m_2 , a spring k_2 , and the real-time controlled MR damper which operates in parallel with the spring. The mass and the passive spring of the MR-STMD are tuned to the target mode of the main structure according to Den Hartog's classic formulae as follows [10]

$$m_2 = \mu m_1 \quad (8.11)$$

$$k_2 = k_1 \frac{\mu}{(\mu + 1)^2} \quad (8.12)$$

where μ is a chosen mass ratio, m_1 is a modal mass and k_1 is a modal stiffness of the main structure.

Fig. 8.3 Prototype MR-STMD (a) and Empa bridge with an attached MR-STMD (b)



The MR damper in the MR-STMD is used to adjust the natural frequency and damping of the MR-STMD according to Den Hartog's formulae to the actual frequency of the main structure. The desired MR damper force is the sum of the stiffness force and the Coulomb friction force (8.1), where the desired stiffness and the desired friction force are calculated for the actual frequency of vibration ω_w and actual MR damper displacement amplitude X_d as [9]

$$k_{des} = k_1 \frac{\tilde{\mu}}{(\tilde{\mu} + 1)^2} - k_2 \quad (8.13)$$

$$c_{des} = \alpha \left(2 \tilde{\zeta}_2 m_2 \omega_w \right) \quad (8.14)$$

$$F_{des}^f = \frac{\pi}{4} c_{des} \omega_w X_d \quad (8.15)$$

where $\alpha < 1$ enables damping reduction (note that in [9] α is fixed to 1), and the parameters $\tilde{\mu}$ and $\tilde{\zeta}_2$ are given by

$$\tilde{\mu} = \mu \left(\frac{\omega_w}{\omega_1} \right)^2 \quad (8.16)$$

$$\tilde{\zeta}_2 = \sqrt{\frac{3 \tilde{\mu}}{8 (\tilde{\mu} + 1)^3}} \quad (8.17)$$

The original concept of the MR-STMD proposed in [9] is used to validate the PSC approach by simulations and experiments. Both in the original MR-STMD and the MR-STMD with PSC, the desired stiffness and damping are calculated from (8.13) and (8.14). The desired control force for the MR-STMD is calculated from (8.1) and for the MR-STMD with PSC from (8.8) and (8.10).

8.4.2 Simulation Model and Experimental Setup

In simulations, a lightly damped mass–spring–damper model subjected to harmonic force excitation is considered, with a mass $m_1 = 1,681$ kg, a stiffness $k_1 = 656.48$ kN/m, a natural frequency $f_1 = 3.145$ Hz and a damping ratio $\zeta_1 = 0.4$ %. The system is fitted with an MR-STMD of a mass $m_2 = 26.325$ kg, a passive spring with a stiffness $k_2 = 9.966$ kN/m and an MR damper modeled as ideal semi-active damper with a residual force $F_0 = 2$ N. The force excitation amplitude is $F_w = 105$ N and the frequency of excitation ranges from 2.3 to 3.8 Hz. For each simulated frequency a dynamic amplification factor $X_1/X_{1-static}$ [10] is calculated from the steady state amplitude X_1 of the primary structure as $X_1 k_1/F_w$. The simulations were run in MATLAB®/Simulink with an ode5 solver and a fixed step size of 1 ms.

In experiments, the same setup and testing procedure were used as in [9]. The setup consists of a prototype MR-STMD (Fig. 8.3a) installed on a rack at the anti-node of the first bending mode of the laboratory bridge at Empa with a main span of 15.6 m (Fig. 8.3b). The prototype MR-STMD consists of its mass, four compression springs and a rotational MR damper connected with the MR-STMD mass by a cantilever beam and a force sensor that measures the actual MR damper force. The displacement sensor measures the relative displacement of the MR-STMD mass. The bridge is excited by the

Fig. 8.4 Simulated (a) and measured (b) dynamic amplification for a nominal bridge

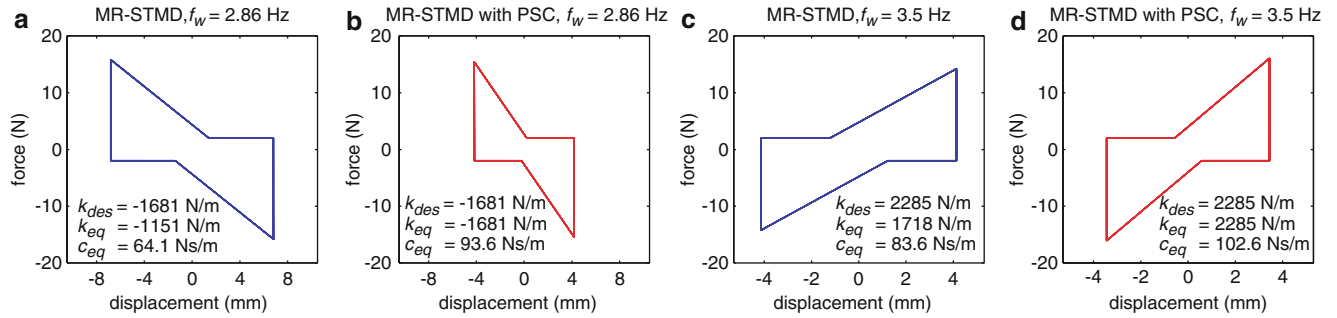
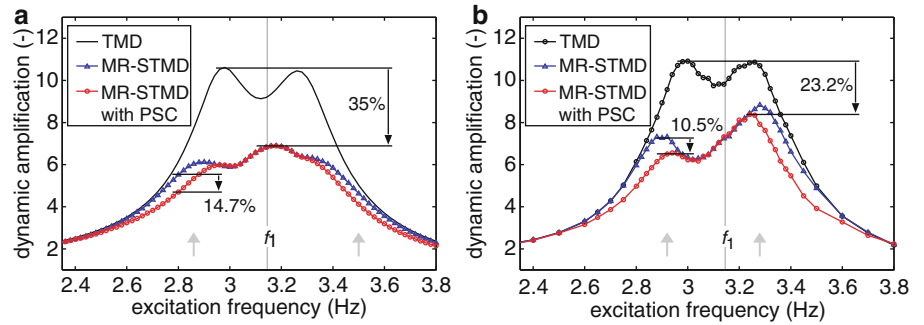


Fig. 8.5 Simulated MR damper force versus displacement for MR-STMD and MR-STMD with PSC at two selected excitation frequencies

electrodynamic shaker placed on the bridge deck, also at the anti-node position. To evaluate the MR-STMD performance, the measured dynamic amplification factor is derived in the same way as in simulations from the steady state amplitude of the measured anti-node bridge displacement X_1 and the amplitude of excitation force which is calculated as the product of the inertial shaker mass and its acceleration. The identified modal parameters of the bridge in its nominal configuration, and the parameters of the MR-STMD are as those used in simulations. The MR damper force is controlled as in [9], using a model-based feed-forward approach with an additional force feedback and the superior decision-based negative current control. The real-time control environment comprises the dSPACE® controller board and MATLAB®/Simulink Real-Time Workshop. The MR damper current is controlled by the KEPCO® current driver operating in the voltage-input current-output mode.

8.4.3 Simulated and Measured Vibration Attenuation Performance of the MR-STMD for a Nominal Bridge

The bridge, with its nominal mass and known modal parameters that were used in the design of passive elements of the MR-STMD based on (8.11) and (8.12), is denoted as nominal. For this configuration, Fig. 8.4 presents the simulated and measured responses of an optimally tuned Den Hartog’s TMD [10], in comparison to the responses of the MR-STMD without and with PSC obtained for $\alpha = 0.7$ (8.14). Figure 8.4 shows that the peak response for the MR-STMD is, both in simulations and experiments, visibly lower than for TMD. The observed improvement is related to the damping reduction in the MR-STMD and can be even larger for lower α [11]. It is also evident from Fig. 8.4 that the MR-STMD with PSC performs better than the MR-STMD without PSC and the measured improvement reaches 10.5 %.

In order to explain the differences observed between the simulated and measured responses in Fig. 8.4, the MR damper force at selected frequencies is presented in Figs. 8.5 and 8.6 and discussed. The frequencies chosen for the analysis are depicted in Fig. 8.4 with gray arrows.

Figure 8.5 presents the simulated MR damper force which precisely follows a semi-active force given by (8.3). For frequencies smaller than $f_1 = 3.145$ Hz (Fig. 8.5a, b), the MR damper emulates negative stiffness, around f_1 the MR damper exerts pure friction force, and for frequencies larger than f_1 positive stiffness is emulated (Fig. 8.5c, d). The numbers given in the plots in Fig. 8.5 indicate that, for the MR-STMD with PSC, the equivalent stiffness k_{eq} calculated from the simulated MR damper force is always equal to the desired stiffness, but the equivalent viscous damping coefficient c_{eq} is larger than for

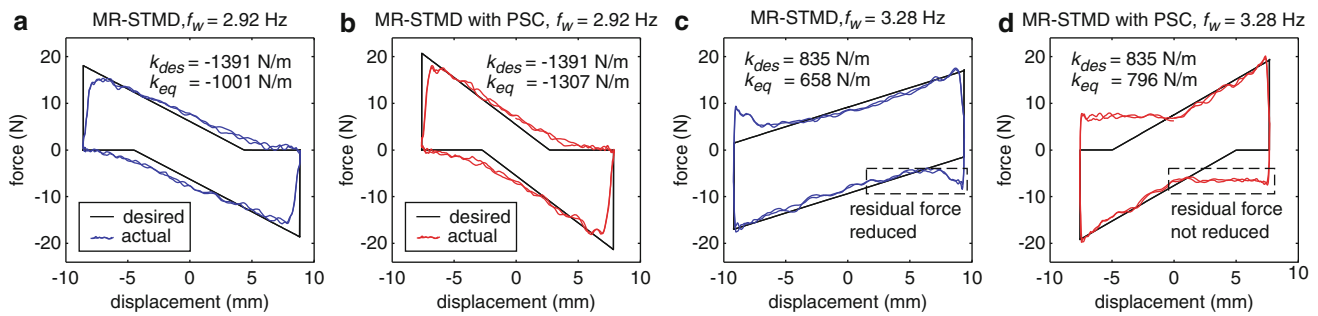
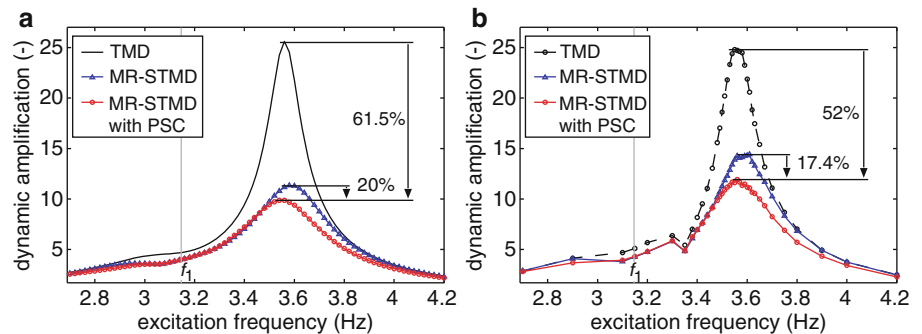


Fig. 8.6 Measured clipped desired control force and actual MR damper force versus displacement for MR-STMD and MR-STMD with PSC at two selected excitation frequencies

Fig. 8.7 Simulated (a) and measured (b) dynamic amplification for a lighter bridge



the MR-STMD without PSC. The increase in energy dissipation due to PSC limits the performance of the MR-STMD with PSC which would be better if the energy dissipation in the MR damper was smaller. Further discussion on this topic is given in [11], and especially in [12], where the semi-active vibration absorber with as low as possible damping is realized.

Figure 8.6 shows how the measured actual MR damper force differs from the ideal semi-active force. For instance, in negative stiffness control (Fig. 8.6a, b), the most difficult part is to track the sharp edges in the desired control force at maximum displacements since the fast increase in the MR damper force is limited by the MR damper and current driver dynamics. In positive stiffness control (Fig. 8.6c, d), the most difficult part is to quickly decrease the MR damper force from its absolute maximum value to zero. The actual MR damper force cannot be step decreased to zero due to the remanent magnetization effect in the MR damper, which results in nonzero residual force. The residual force in Fig. 8.6d is higher than 2 N assumed in the simulations. These force tracking errors explain why the measured responses in Fig. 8.4 differ from the simulated ones.

8.4.4 Simulated and Measured Vibration Attenuation Performance of the MR-STMD for a Lighter Bridge

Despite the deteriorating effects due to force tracking errors, the performance of the MR-STMD with PSC is better than without PSC, especially for large desired stiffness. This is illustrated both by simulations and experiments in Fig. 8.7, where the responses due to TMD and the MR-STMD with and without PSC are compared for a lighter bridge, i.e. the bridge with its mass decreased such that the natural frequency of its first bending mode is shifted by +10.87%. It should be noted that the concentrated mass of the bridge (Fig. 8.3) was changed without any changes in the MR-STMD or its control algorithm. In this configuration the TMD is detuned and the responses of the MR-STMD with and without PSC are much better than for TMD. Figure 8.7 indicates that the peak response of the MR-STMD with PSC is 61.5% better in simulations than for TMD, and 52% better in experiments. In addition, the peak response of MR-STMD with PSC is lower than for the MR-STMD without PSC by 20% in simulations, and by 17.4% in experiments. These results are obtained for $\alpha = 0.7$.

8.5 Conclusions

The proposed precise stiffness control (PSC) method is valid for harmonic excitation and can be used in stiffness control with MR dampers when the desired stiffness and the desired viscous damping are known. The method results in the equivalent stiffness which is equal to the desired stiffness even if the desired control force is constrained by the clipping of active forces and the MR damper residual force. The dynamic stiffness generated with the MR damper due to PSC is nonlinear and the equivalent stiffness is calculated from the potential energy balance during half a cycle of harmonic vibrations. The PSC method increases the energy dissipation in the MR damper which is recognized as a drawback.

The method is validated in application to a semi-active TMD with an MR damper (MR-STMD) attached to the laboratory bridge. Both the simulated and the measured results confirm that the MR-STMD with PSC performs better than without PSC. The measured improvement due to PSC is of about 10 % in the nominal bridge and 17 % in the lighter bridge with the natural frequency increased by 10.87 %. It is expected that further improvement would be achieved if the PSC method was accompanied with as low as possible energy dissipation in the MR damper [12].

Acknowledgements This research was supported by AGH University of Science and Technology, Department of Process Control, Krakow, Poland (statutory research funds No. 11.11.130.560) and Empa, Swiss Federal Laboratories for Materials Science and Technology, Dübendorf, Switzerland. The authors gratefully acknowledge the technical support of the industrial partner Maurer Söhne GmbH & Co. KG, Munich, Germany.

References

1. Wang DH, Liao WH (2011) Magnetorheological fluid dampers: a review of parametric modelling. *Smart Mater Struct* 20(2):023001
2. Xia PQ (2003) An inverse model of MR damper using optimal neural network and system identification. *J Sound Vib* 266(5):1009–1023
3. Maślanka M, Sapiński B, Snamina J (2007) Experimental study of vibration control of a cable with an attached MR damper. *J Theor Appl Mech* 45(4):893–917
4. Høgsberg J (2011) The role of negative stiffness in semi-active control of magneto-rheological dampers. *Struct Control Health Monitor* 18(3):289–304
5. Iemura H, Igarashi A, Nakata N (2001) Semi-active control of full-scale structures using variable joint damper system. In: *Proceedings of the 14th KKNN symposium civil engineering, Kyoto, Japan, 5–7 November 2001*, pp. 41–46
6. Nagarajaiah S (2010) Adaptive stiffness systems: recent developments in structural control using semiactive/smart variable stiffness and adaptive passive stiffness. In: *Proceedings of the 5th world conference on structural control and monitoring, Tokyo, Japan, 12–14 July 2010*, paper No. 007, available at: <http://www.bridge.t.u-tokyo.ac.jp/WCSCM5/>
7. Weber F, Boston C (2011) Clipped viscous damping with negative stiffness for semi-active cable damping. *Smart Mater Struct* 20(4):045007
8. Weber F, Boston C, Maślanka M (2011) An adaptive tuned mass damper based on the emulation of positive and negative stiffness with an MR damper. *Smart Mater Struct* 20:015012
9. Weber F, Maślanka M (2012) Frequency and damping adaptation of a TMD with controlled MR damper. *Smart Mater Struct* 21(5):055011
10. Den Hartog JP (1934) *Mechanical vibrations*. McGraw-Hill, New York
11. Maślanka M, Weber F (2012) Precise stiffness control with MR dampers and its application to semi-active tuned mass dampers. *J Intell Mater Syst Struct*, Submitted
12. Weber F (2012) Semi-active vibration absorber based on real-time controlled MR damper. *Smart Mater Struct*, Submitted

Chapter 9

Employing Hybrid Tuned Mass Damper to Solve Off-Tuning Problems for Controlling Human Induced Vibration in Stadia

Nima Noormohammadi and Paul Reynolds

Abstract A key objective in the design of any sports stadium is to include maximum number of spectators with minimum obstruction in the visual cone. This functional requirement often results in employing one or more cantilevered tiers, which in turn culminates in more slender grandstands often with relatively low natural frequencies and modal damping ratios. These natural frequencies may sometimes fall in the range of frequencies of human movement which can possibly excite the structure in resonance resulting in vibration serviceability issues. One of the available techniques to reduce excessive responses is to use passive vibration control techniques such as Tuned Mass Dampers (TMD). However, the off-tuning problem is a substantial drawback of this technique, whereby changes in natural frequencies caused by crowd-structure interaction may detune the TMDs. This paper presents a study into the possibility of using hybrid (combination of active and passive control) technology to augment the vibration serviceability of sports stadia. It shows a comparative analysis of vibration mitigation performances that are likely to be attained by utilising a passive TMD and the proposed HTMD. An appropriate control scheme is utilised with the proposed HTMD to deal with the off-tuning issues in TMDs caused by crowd loading, and is shown to be effective.

Keywords Human induced vibration • Hybrid control • Active/passive control • Hybrid tuned mass damper • HTMD

9.1 Introduction

It is well known that there is a possibility for concert arenas and grandstands to be vulnerable to human activities such as jumping and bobbing. This is evident mainly in relatively slender structures as a result of expansion in material technologies and structural design skills, rising and increasing utilisation of sport stadia for live music performances and also more energetic and active audiences who have more synchronised movements [1–5].

In order to deal with this problem and satisfy vibration serviceability criteria, various kinds of control methods have been proposed and executed including passive, active, semi-active and hybrid vibration control.

Passive vibration control is an established method to improve the performance of a structure by dissipating vibration energy by applying additional dissipating materials or equipment to the structure and, as a result, the damping and occasionally stiffness of the structure increase. They have relatively simple design and there is no requisite for external power sources [6]. However, they might not be completely engaged especially at low levels of vibrations [7, 8]. In addition, they also have the possible drawback of off-tuning [9–11], which is mostly due to the change of natural frequency of the structure in the presence of human occupants [12, 13].

Hybrid control contains an integration of passive and active control systems. It is created by the combination of active and passive segments (also known as composite active-passive controllers) to reduce structural response mostly by energy dissipation through the passive part, whereas the active part is included to improve its performance. In hybrid control systems the active part is smaller and less power is required than for a fully active system [8, 14].

N. Noormohammadi (✉) • P. Reynolds
Vibration Engineering Section, Department of Civil and Structural Engineering, University of Sheffield,
Sir Frederick Mappin Building, Mappin Street, Sheffield, S1 3JD UK
e-mail: nima.noor@sheffield.ac.uk; p.reynolds@sheffield.ac.uk

The work presented here demonstrates the effect of employing a passive control method (Tuned Mass Damper (TMD)) and a proposed hybrid control strategy (TMD with active element), which aims to improve the vibration performance of a typical stadium structure. A suitable control algorithm is developed with the proposed HTMD to deal with off-tuning issues in TMDs produced particularly by crowd loading. The dynamic properties of the employed stadium here are obtained from past stadia modal testing [12]. Also, in order to have more accurate outcome from both active and passive spectators in stadium, the suggested model in [13] was occupied.

9.2 Model of Grandstand

The structure considered in this study is a 7 m cantilevered upper seating tier situated in the corner of a football stadium located in United Kingdom (Fig. 9.1) [12]. In-service monitoring during a lively music performance confirmed that the highlighted area was quite lively and had a maximum acceleration higher than the guidance recommended at the time.

The first vertical natural frequency of the structure is 4.34 Hz derived from both ambient test and updated finite element (FE) model (Table 9.1) [12, 13]. However, due to the measured human-structure interaction phenomenon and also from the model of the stadium in the presence of both active and passive spectators, the frequency of the structure dropped from 4.34 to 3.2 Hz [13, 15]. This placed the structure in the second harmonic of the music's frequency which has the frequency of 1.6 Hz. It should be noticed that in [12, 13] the frequency of the full structure is 3.80 Hz. This difference is due to the assumption of choosing the number of occupied people in this paper, which are only the first seven rows of the tier (i.e. only the cantilever part).

A state space approach is employed [15] in order to use the three-degree-of-freedom (3DOF) model (Fig. 9.2) that was proposed in [13]. The states of the system (Eq. 9.1) are [15]:

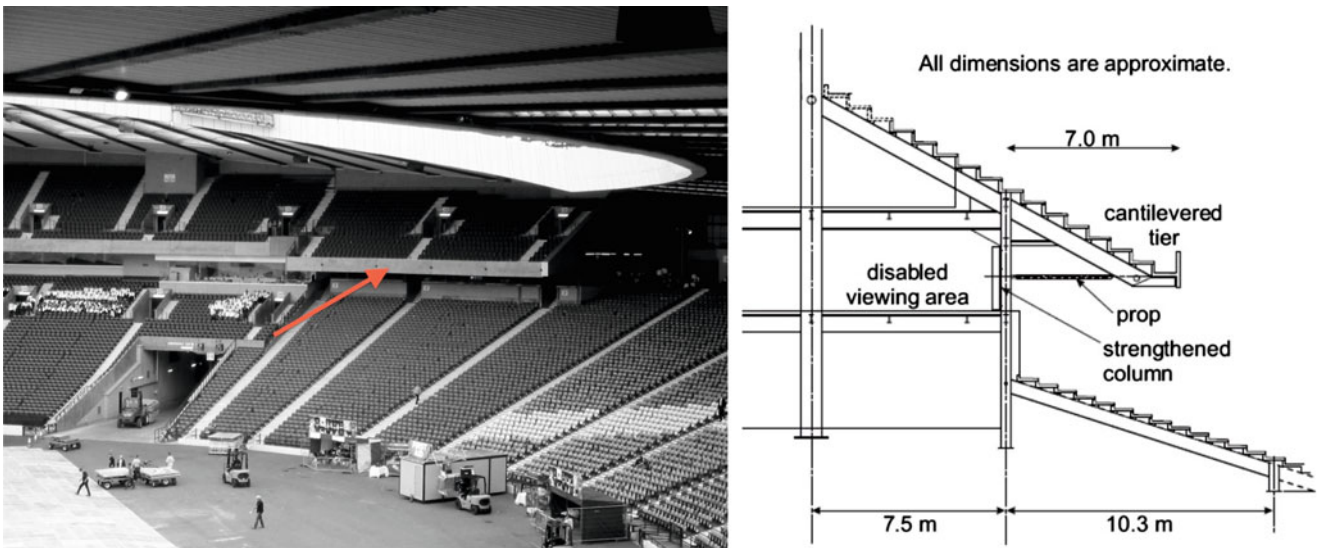
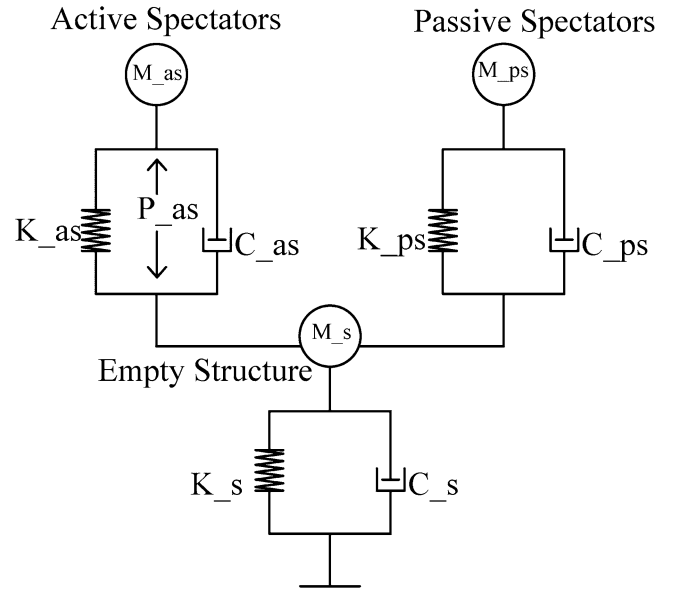


Fig. 9.1 View of the modeled seating deck (left) and cross section of the tier (right) [12]

Table 9.1 Dynamic properties of the stadium

Structure	Frequency (Hz)	Damping ratio (%)	Modal mass (kg)	Modal damping (Ns/m)	Modal stiffness (N/m)
Empty	4.34	3.70	82,811	167,105	61,578,233
Full	3.20	11.00	108,019	567,396	61,578,233

Fig. 9.2 3DOF model of the structure [15]



$$\begin{cases} X_1 = x_s \\ X_2 = \dot{x}_s \\ X_5 = x_{as} \\ X_6 = \dot{x}_{as} \\ X_7 = x_{ps} \\ X_8 = \dot{x}_{ps} \end{cases} \therefore \begin{cases} \dot{X}_1 = X_2 \\ \dot{X}_5 = X_6 \\ \dot{X}_7 = X_8 \end{cases} \quad (9.1)$$

In Fig. 9.2, m_s is the mass of the empty structure, m_{as} is the total mass of active spectators and m_{ps} is the total mass of passive spectators. Also c_s, c_{as}, c_{ps} and k_s, k_{as}, k_{ps} are the respective damping coefficients and stiffnesses of the empty structure, active and passive spectators. P_{as} is the motion induced force produced within the body unit [3]. $\ddot{x}_s, \ddot{x}_{as}, \ddot{x}_{ps}$ are the accelerations associated with the masses of the structure, active and passive spectators, respectively. Further, $\dot{x}_s, \dot{x}_{as}, \dot{x}_{ps}$ and x_s, x_{as}, x_{ps} are velocity and displacement of the structure, active and passive spectators, respectively.

The state space representation of Fig. 9.2 is given in Eq. (9.2) where Y_1, Y_2 and Y_3 are the displacement, velocity and acceleration of the main structure, respectively.

$$\begin{cases} \dot{X}_1 \\ \dot{X}_2 \\ \dot{X}_5 \\ \dot{X}_6 \\ \dot{X}_7 \\ \dot{X}_8 \end{cases} = \begin{bmatrix} 0 & 1 & 0 & 0 & 0 & 0 \\ -\frac{(k_s+k_{as}+k_{ps})}{m_s} & -\frac{(c_s+c_{as}+c_{ps})}{m_s} & \frac{k_{as}}{m_s} & \frac{c_{as}}{m_s} & \frac{k_{ps}}{m_s} & \frac{c_{ps}}{m_s} \\ 0 & 0 & 0 & 1 & 0 & 0 \\ \frac{k_{as}}{m_{as}} & \frac{c_{as}}{m_{as}} & -\frac{k_{as}}{m_{as}} & -\frac{c_{as}}{m_{as}} & 0 & 0 \\ 0 & 0 & 0 & 0 & 0 & 1 \\ \frac{k_{ps}}{m_{ps}} & \frac{c_{ps}}{m_{ps}} & 0 & 0 & -\frac{k_{ps}}{m_{ps}} & -\frac{c_{ps}}{m_{ps}} \end{bmatrix} * \begin{cases} X_1 \\ X_2 \\ X_5 \\ X_6 \\ X_7 \\ X_8 \end{cases} + \begin{bmatrix} 0 \\ \frac{1}{m_s} \\ 0 \\ -\frac{1}{m_{as}} \\ 0 \\ 0 \end{bmatrix} * \{P_{as}\}$$

$$\begin{cases} Y_1 \\ Y_2 \\ Y_3 \end{cases} = \begin{bmatrix} 1 & 0 & 0 & 0 & 0 & 0 \\ 0 & 1 & 0 & 0 & 0 & 0 \\ -\frac{(k_s+k_{as}+k_{ps})}{m_s} & -\frac{(c_s+c_{as}+c_{ps})}{m_s} & \frac{k_{as}}{m_s} & \frac{c_{as}}{m_s} & \frac{k_{ps}}{m_s} & \frac{c_{ps}}{m_s} \end{bmatrix} * \begin{cases} X_1 \\ X_2 \\ X_5 \\ X_6 \\ X_7 \\ X_8 \end{cases} + \begin{bmatrix} 0 \\ 0 \\ \frac{1}{m_s} \end{bmatrix} * \{P_{as}\}. \quad (9.2)$$

9.3 Hybrid Tuned Mass Damper (HTMD)

Figure 9.3 illustrates the model of a HTMD attached to the stadium structure with both active and passive parts. This HTMD (Fig. 9.4) consists of a passive TMD integrated with an active element (i.e. actuator). The vibration energy dissipation is achieved by the passive part whereas the active part helps the system to improve its performance by dealing with the off-tuning problem and low-level vibration issues.

Using the equations of motion derived by the authors in [15], the state space approach of the HTMD system is shown in Eq. (9.3). It should be noticed that as shown in [15], the DOF of the active part of the HTMD can be replaced by the inertia force of the actuator (i.e. $F_{I,a}$) in the equations of motion of the system. This force is derived using a transfer function between the actuator's input voltage (V_{in}) and its inertia force ($F_{I,a}$) [15]. This transfer function is included in the state space matrix in Eq. (9.3).

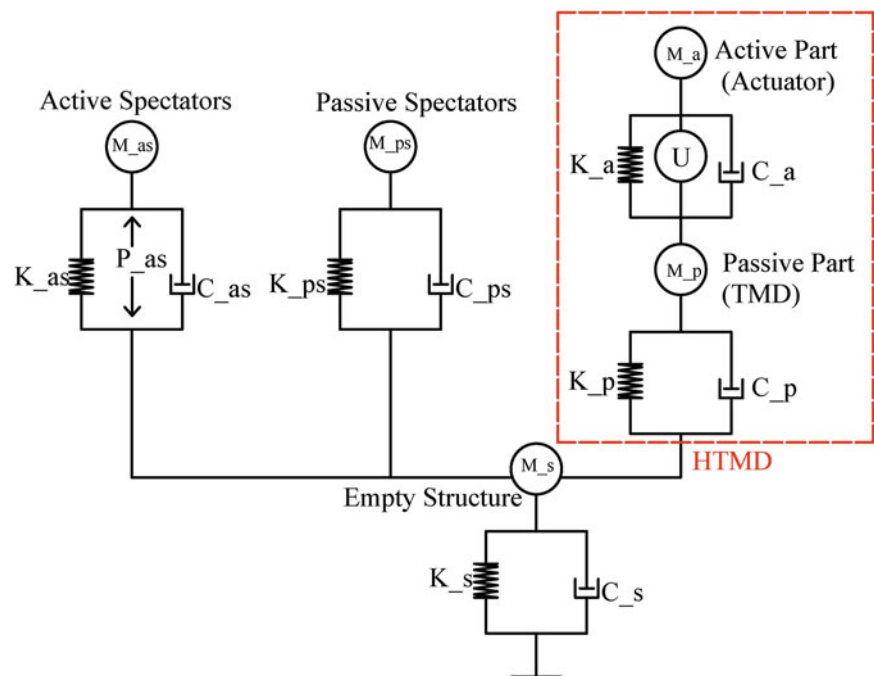


Fig. 9.3 HTMD attached to the stadium cantilever

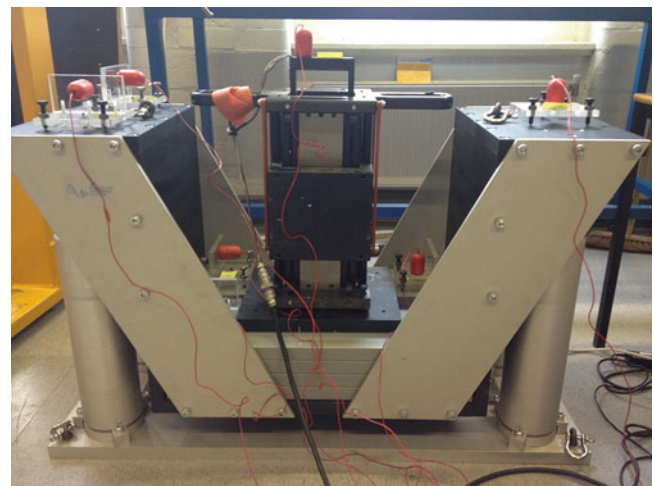


Fig. 9.4 Laboratory HTMD

$$\begin{aligned}
\begin{pmatrix} \dot{X}_1 \\ \dot{X}_2 \\ \dot{X}_3 \\ \dot{X}_4 \\ \dot{X}_5 \\ \dot{X}_6 \\ \dot{X}_7 \\ \dot{X}_8 \\ \dot{X}_9 \\ \dot{X}_{10} \\ \dot{X}_{11} \end{pmatrix} &= \begin{bmatrix} 0 & 1 & 0 & 0 & 0 & 0 & 0 & 0 & 0 & 0 & 0 & 0 \\ -\frac{(k_s+k_p+k_{as}+k_{ps})}{m_s} & -\frac{(c_s+c_p+c_{as}+c_{ps})}{m_s} & \frac{k_p}{m_s} & \frac{c_p}{m_s} & \frac{k_{as}}{m_s} & \frac{c_{as}}{m_s} & \frac{k_{ps}}{m_s} & \frac{c_{ps}}{m_s} & 0 & 0 & 0 & 0 \\ 0 & 0 & 0 & 1 & 0 & 0 & 0 & 0 & 0 & 0 & 0 & 0 \\ \frac{k_p}{m_p} & \frac{c_p}{m_p} & -\frac{k_p}{m_p} & -\frac{c_p}{m_p} & 0 & 0 & 0 & 0 & 0 & 0 & 0 & 0 \\ 0 & 0 & 0 & 0 & 0 & 1 & 0 & 0 & 0 & 0 & 0 & 0 \\ \frac{k_{as}}{m_{as}} & \frac{c_{as}}{m_{as}} & 0 & 0 & -\frac{k_{as}}{m_{as}} & -\frac{c_{as}}{m_{as}} & 0 & 0 & 0 & 0 & 0 & 0 \\ 0 & 0 & 0 & 0 & 0 & 0 & 0 & 1 & 0 & 0 & 0 & 0 \\ \frac{k_{ps}}{m_{ps}} & \frac{c_{ps}}{m_{ps}} & 0 & 0 & 0 & 0 & -\frac{k_{ps}}{m_{ps}} & -\frac{c_{ps}}{m_{ps}} & 0 & 0 & 0 & 0 \\ 0 & 0 & 0 & 0 & 0 & 0 & 0 & 0 & 0 & 1 & 0 & 0 \\ 0 & 0 & 0 & 0 & 0 & 0 & 0 & 0 & 0 & 0 & 1 & 0 \\ 0 & 0 & 0 & 0 & 0 & 0 & 0 & 0 & 0 & 0 & 0 & 1 \end{bmatrix} \\
\begin{pmatrix} X_1 \\ X_2 \\ X_3 \\ X_4 \\ X_5 \\ X_6 \\ X_7 \\ X_8 \\ X_9 \\ X_{10} \\ X_{11} \end{pmatrix} &+ \begin{bmatrix} 0 & 0 & 0 \\ \frac{1}{m_s} & 0 & 0 \\ 0 & 0 & 0 \\ 0 & \frac{1}{m_p} & 0 \\ 0 & 0 & 0 \\ -\frac{1}{m_{as}} & 0 & 0 \\ 0 & 0 & 0 \\ 0 & 0 & 0 \\ 0 & 0 & 0 \\ 0 & 0 & 0 \\ 0 & 0 & w_a \end{bmatrix} \begin{pmatrix} P_{as} \\ F_{I,a} \\ V_{in} \end{pmatrix} \\
\begin{pmatrix} Y_1 \\ Y_2 \\ Y_3 \\ Y_4 \\ Y_5 \\ Y_6 \\ Y_{13} \\ Y_{14} \\ Y_{15} \end{pmatrix} &= \begin{bmatrix} 1 & 0 & 0 & 0 & 0 & 0 & 0 & 0 & 0 & 0 & 0 & 0 \\ 0 & 1 & 0 & 0 & 0 & 0 & 0 & 0 & 0 & 0 & 0 & 0 \\ -\frac{(k_s+k_p+k_{as}+k_{ps})}{m_s} & -\frac{(c_s+c_p+c_{as}+c_{ps})}{m_s} & \frac{k_p}{m_s} & \frac{c_p}{m_s} & \frac{k_{as}}{m_s} & \frac{c_{as}}{m_s} & \frac{k_{ps}}{m_s} & \frac{c_{ps}}{m_s} & 0 & 0 & 0 & 0 \\ 0 & 0 & 1 & 0 & 0 & 0 & 0 & 0 & 0 & 0 & 0 & 0 \\ 0 & 0 & 0 & 1 & 0 & 0 & 0 & 0 & 0 & 0 & 0 & 0 \\ \frac{k_p}{m_p} & \frac{c_p}{m_p} & -\frac{k_p}{m_p} & -\frac{c_p}{m_p} & 0 & 0 & 0 & 0 & 0 & 0 & 0 & 0 \\ 0 & 0 & 0 & 0 & 0 & 0 & 0 & 0 & 1 & 0 & 0 & 0 \\ 0 & 0 & 0 & 0 & 0 & 0 & 0 & 0 & 0 & 1 & 0 & 0 \\ 0 & 0 & 0 & 0 & 0 & 0 & 0 & 0 & 0 & 0 & m_a & 0 \end{bmatrix} \begin{pmatrix} X_1 \\ X_2 \\ X_3 \\ X_4 \\ X_5 \\ X_6 \\ X_7 \\ X_8 \\ X_9 \\ X_{10} \\ X_{11} \end{pmatrix} \\
&+ \begin{bmatrix} 0 & 0 & 0 \\ 0 & 0 & 0 \\ 0 & 0 & 0 \\ 0 & 0 & 0 \\ 0 & 0 & 0 \\ 0 & 0 & 0 \\ 0 & 0 & 0 \\ 0 & 0 & 0 \\ 0 & 0 & 0 \end{bmatrix} \begin{pmatrix} P_{as} \\ F_{I,a} \\ v_{in} \end{pmatrix}
\end{aligned} \tag{9.3}$$

where m_p, c_p, k_p and m_a, c_a, k_a are mass, stiffness and damping of the passive and active part of the HTMD respectively. ε and w_a are respective actuator's low pass filter element and force-voltage characteristic. Y_4, Y_5, Y_6 are displacement, velocity and acceleration of the passive part of HTMD respectively. In addition, Y_{13}, Y_{14}, Y_{15} are associated with displacement, velocity and inertia force of the active part of HTMD.

As was discussed in [15], for the proposed HTMD, two feedback gains including G_1 and G_2 are employed. The role of these are to produce a “Driving Force” which enhances the TMD’s inertia force and also provides an “Active Damping Force” which regulates the damping force of the HTMD respectively. Herein, in addition to these previous two gains, another two extra additional feedback gains are introduced (G_3 and G_4), which are displacement and acceleration feedback of the passive part of the TMD respectively. The role of these two is to change the dynamic properties of the TMD which leads to tune it to the new frequency. In another words, these two gains deal with off-tuning of the HTMD.

$$\begin{cases} \text{Driving Force} = G_1 * \ddot{x}_s \\ \text{Active Damping} = G_2 * \dot{x}_p \\ \text{Tuning Force} = G_3 * x_p \\ \text{Tuning Force} = G_4 * \ddot{x}_p \end{cases} \quad (9.4)$$

9.4 Analytical Study

In order to compare the performance of the HTMD with passive TMD under the off-tuning problem, an analytical simulation was implemented in the MATLAB/Simulink software. The same random white noise signal was applied as an external excitation to the uncontrolled structure, the structure with a passive TMD and finally to the structure with an HTMD. As an evaluation method, frequency response function (FRF) plots were produced. The occupied TMD and HTMD’s properties (i.e. mass, stiffness and damping ratios) are in Table 9.2. The passive TMD in [15] was tuned to the situation where the ratio of active/passive people in the stadium was 40:60. Also, the frequency of the structure in this case was 3.20 Hz. Figure 9.5 shows the FRF of the system when the passive TMD is tuned to 3.20 Hz. As was shown in [15], the HTMD performs better compared to an equivalent passive TMD, even when it is properly tuned to the structural frequency.

To investigate the effect of off-tuning due the changes in the frequency of the structure, the percentage of the active spectators in stadium was changed to various ratios from 1% to 99%, as indicated in Table 9.3. This resulted in a change of the total mass of the DOF of active spectators (i.e. m_{as}), which leads to a variation in the frequency of the main structure. As is shown in Table 9.3, the frequency of the structure varies from 2.68 to 5.18 Hz whilst the passive TMD is tuned to 3.20 Hz.

As the result of the changing frequency of the main structure, the TMD becomes detuned and its effectiveness is reduced. However, the proposed HTMD can deal with this off-tuning by employing the introduced feedback gains. In order to select the appropriate gain, firstly root locus analyses were performed for individual gains separately to achieve the range of the

Table 9.2 Dynamic properties of the HTMD and TMD

	Mass ratio (%)	Frequency ratio (%)	Frequency (Hz)	Damping ratio (%)	Mass (kg)	Damping (Ns/m)	Stiffness (N/m)
TMD	2.6	98.40	3.15	5.1	2,174	4,412	850,786
HTMD	2.6	98.40	3.15	5.1	2,174	4,412	850,786

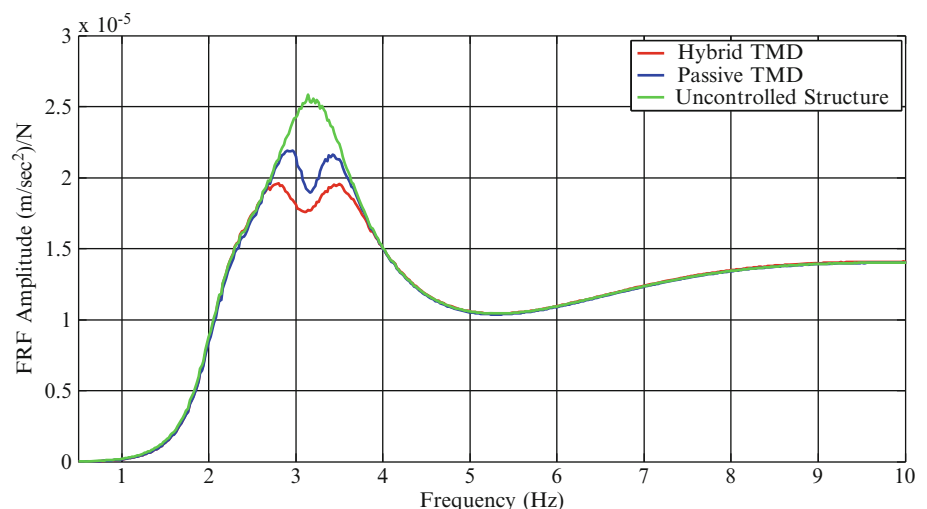


Fig. 9.5 FRF of the structure with natural frequency of 3.20 Hz

Table 9.3 Properties of the structure with different ratios of active people

Scenario	Active people (%)	Mass of active people m_{as} (kg)	Mass of passive people m_{ps} (kg)	Frequency of the structure (Hz)	Changing of the frequency of the main structure (%)
1	1	970	96005	2.68	-15
2	5	4849	92126	2.68	-15
3	10	9698	87278	2.78	-12
4	20	19395	77580	2.86	-9
5	30	29093	67883	3.04	-3
6	40	38790	58185	3.20	0
7	60	58185	38790	3.52	+12
8	80	77580	19395	4.14	+31
9	99	96005	970	5.18	+64

Table 9.4 Comparison of the TMD and HTMD performance in off-tuning

Scenario	G_1	G_3	G_2	G_4	TMD peak reduction (%)	HTMD peak reduction (%)	TMD reduction at resonance (%)	HTMD reduction at resonance (%)
1	0	0	-44	-2	4	40	4	44
2	0	0	-41	-2	1	33	1	36
3	0	0	-36	-2	5	28	9	34
4	0	0	-28	-1	7	22	9	27
5	0	0	-17	-1	10	19	22	22
6	-40	-4125	-61	-11	15	24	26	31
7	-40	-1375	-22	-2	7	24	8	36
8	-10	-4400	-8	-2	3	10	3	17
9	-5	-8250	-55	-1	1	8	1	11

gains to guarantee stability of the system. Following this, a manual sensitivity approach (considering the effect of changing the gains on the response) was applied by combining the gains and achieving the minimum peaks in the calculated FRFs.

Table 9.4 shows the selected HTMD gains and the percentage of the response reduction compared with the uncontrolled structure and the structure with passive TMD. For the comparison between TMD and HTMD, both peaks of the FRF and also the response of FRF at the structural resonant frequency have been considered. As is noted in Table 9.4, below the frequency of the tuning, since the differences in the frequency (e.g. 15%) are not high compared to those above 3.20 Hz, it is sufficient to just employ one of the tuning gains, G_4 (i.e. acceleration of the TMD), in addition to HTMD damping force gain, G_2 , to deal with off-tuning and to reduce the response over the frequency band encompassing the structural mode. However, above the tuning frequency (3.20 Hz), due to larger differences in the frequencies (up to 64%), in addition to off-tuning, the HTMD needs to expend more effort to enhance its performance which is the reduction in the response. Hence, another off-tuning gain G_3 in addition to driving force gain (i.e. G_1) is applied to the HTMD to drive the HTMD more compare to the less sever scenario (less than 3.20 Hz).

In addition to this, Fig. 9.6 shows plots of the FRF amplitudes for different scenarios. It demonstrates that the performance of TMD is reduced when the structural frequency changes, whereas the HTMD is able to compensate for the detuning.

9.5 Conclusions

Dealing with off-tuning stadium structures is an important concern for vibration control of stadia. This might occur due to changing number of spectators and even by changes in the number of active and passive people during a single event. Passive tuned mass dampers as a conventional method for vibration control have reduced effectiveness in the presence of off-tuning, since a change in the frequency of the primary structure leads to a detuned TMD.

Employing an HTMD in a grandstand has been investigated here by altering the percentage of the active and passive people which leads to modification of the resonant frequency of the primary structure. It has been shown that the proposed HTMD has the capability to deal with off-tuning when the frequency of the primary structure changes.

Acknowledgements The authors would like to acknowledge the financial assistance provided by the UK Engineering and Physical Sciences Research Council (EPSRC) through Leadership Fellowship grant "Advanced Technologies for Mitigation of Human-Induced Vibration" (Ref. EP/J004081/1) and platform grant "Dynamic Performance of Large Civil Engineering Structures: An Integrated Approach to Management, Design and Assessment" (Ref. EP/G061130/1).

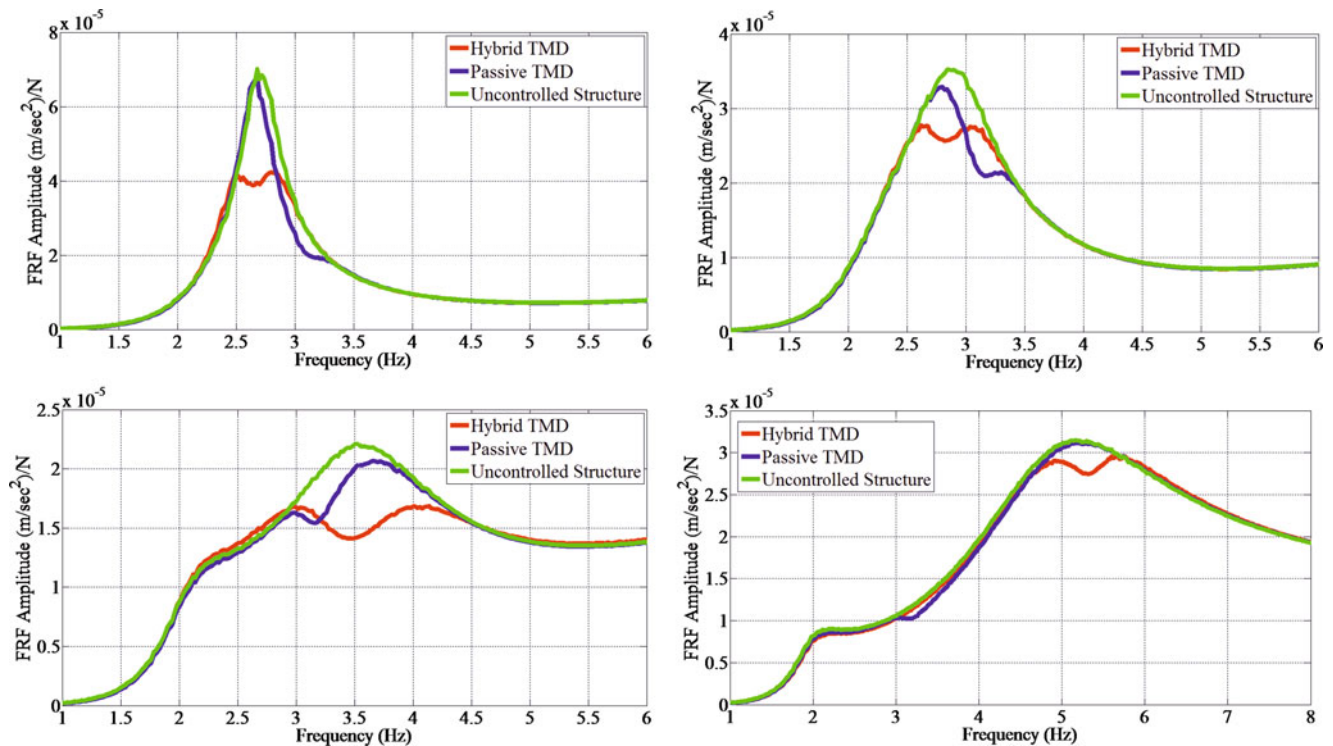


Fig. 9.6 FRF scenario 1 (top-left), scenario 4 (top-right), scenario 7 (bottom-left), scenario 9 (bottom-right)

References

1. I. of S. Engineers (2001) Dynamic performance requirements for permanent grandstands subject to crowd action: interim guidance on assessment and design. The Institution of Structural Engineers, London, pp 1–22
2. Kasperski M, Niemann HJ (1993) Man induced vibrations of a stand structure. In: Proceedings of the EUROLYN, pp 977–983
3. Institution of Structural Engineers, IStructE, and I. of S. Engineers (2008) Dynamic performance requirements for permanent grandstands subject to crowd action: recommendations for management, design and assessment. vol. SD/03/26, November. The Institution of Structural Engineers, The Department for Communities and Local Government, The Department for Culture Media and Sport, London, pp 1–22
4. Parkhouse JG, Ewins DJ (2006) Crowd-induced rhythmic loading. Struct Build 159(SB5):247–259
5. Ellis B, Ji T, Littler J (2000) The response of grandstands to dynamic crowd loads. Proc Inst Civil Eng Struct Build 140(4):355–365
6. Housner GW, Bergman LA, Caughey TK, Chassiakos AG, Claus RO, Masri SF, Skelton RE, Soong TT, Spencer BF, Yao JTP (1997) Structural control: past, present, and future. J Eng Mech 123(9):897–971
7. Nyawako DS, Reynolds P (2007) Technologies for mitigation of human-induced vibrations in civil engineering structures. Shock Vib Digest 39(6):465–493
8. Soong T, Spencer JBF (2002) Supplemental energy dissipation: state-of-the-art and state-of-the-practice. Eng Struct 24(3):243–259
9. Sims ND (2007) Vibration absorbers for chatter suppression: a new analytical tuning methodology. J Sound Vib 301(3–5):592–607
10. Bae J-S, Hwang J-H, Roh J-H, Kim J-H, Yi M-S, Lim JH (2012) Vibration suppression of a cantilever beam using magnetically tuned-mass-damper. J Sound Vib 331(26):5669–5684
11. Aguirre G, Gorostiaga M, Porchez T, Muñoz J (2012) Self-tuning semi-active tuned-mass damper for machine tool chatter suppression. In: ISMA2012-USD2012, pp 109–124
12. Reynolds P, Pavic A (2005) The dynamic performance of sports stadia under crowd dynamic loading at concert events. In: Sixth European conference on dynamics EUROLYN, pp 473–479
13. Pavic A, Reynolds P (2008) Experimental verification of novel 3DOF model for grandstand crowd-structure interaction. In: 26th international modal analysis conference (IMAC XXVI)
14. Wang CM, Yan N, Balendra T (1999) Control on dynamic structural response using active-passive composite-tuned mass dampers. J Vib Control 5(3):475–489
15. Noormohammadi N, Reynolds P (2012) Control of human induced vibrations in stadia using a hybrid tuned mass damper. In: Noise and vibration engineering, ISMA2012, pp 1119–1132

Chapter 10

Semi-Active TMD Concept for Volgograd Bridge

Felix Weber, Johann Distl, and Marcin Maślanka

Abstract The Volgograd Bridge in Russia is known not only for its record length but also for the large amplitude vibrations induced by wind in May 2010. This paper describes the development of a new semi-active TMD with a magnetorheological damper (MR-STMD) that was installed on the Volgograd Bridge in fall 2011. The main feature of the MR-STMD concept is that the real-time controlled MR damper emulates a controllable stiffness force and a controllable friction force. The controllable stiffness force augments or diminishes the stiffness of the passive springs and thereby tunes the MR-STMD frequency to the actual frequency of the bridge. The controllable friction force generates frequency dependent energy dissipation. The small-scale prototype was experimentally tested on the 19.2 m long Empa bridge for various modal masses and disturbing frequencies. After that, the full-scale MR dampers were tested at Empa by hybrid testing for the expected frequencies and amplitudes of the bridge. Finally, the frequency controllability of one full-scale MR-STMD was verified at the University of the German Armed Forces, Munich. All tests confirm that the new technology can compensate for the frequency sensitivity of passive TMDs and works at high efficiency.

Keywords Bridge • Vibrations • Control • Semi-active • TMD

10.1 Introduction

Volgograd Bridge in Russia with its total length of 7.1 km and maximum span of 155 m is one of the longest road bridges in Europe (Fig. 10.1a). The bridge was opened for traffic in October 2009. In May 2010, intensive wind-induced vibrations of the bridge occurred with a maximum amplitude of 400 mm (Fig. 10.1b). Later analysis showed that the first three vertical bending modes of the bridge with their nominal frequencies of 0.45, 0.57 and 0.68 Hz have to be damped with multiple mass dampers. The tuned mass dampers (TMDs), consisting of a mass, a spring and a viscous damper, are passive devices that are successfully installed in many bridges. However, the TMD has to be precisely tuned to one targeted mode of the bridge and, if the natural frequency of this mode varies with time, the TMD loses its efficiency, and may no longer provide sufficient protection from vibrations. Since Volgograd Bridge is designed in a very slender way and is made of steel, the uncertainty of its bending modes natural frequencies due to the influence of ambient temperature has to be taken into account. With natural frequency uncertainty of several percent, passive TMDs do not represent the best solution. Therefore, in late fall 2011, Volgograd Bridge was fitted with the world's first installation of adaptive semi-active tuned mass dampers with MR dampers (MR-STMDs). This paper describes the research work carried out on the MR-STMD development.

F. Weber (✉)

Empa, Swiss Federal Laboratories for Materials Science and Technology, Structural Engineering Research Laboratory,
Ueberlandstrasse 129, CH-8600 Dübendorf, Switzerland
e-mail: felix.weber@empa.ch

J. Distl

Maurer Söhne GmbH and Co. KG, Frankfurter Ring 193, 80807 Munich, Germany
e-mail: distl@maurer-soehne.de

M. Maślanka

Faculty of Mechanical Engineering and Robotics, Department of Process Control, AGH University of Science and Technology,
al. A.Mickiewicza 30, 30-059 Krakow, Poland
e-mail: marcin.maslanka@agh.edu.pl



Fig. 10.1 Volgograd Bridge (photo: J. Distl) (a) and its vibrations in May, 2010 (source: RT news channel at youtube.com) (b)

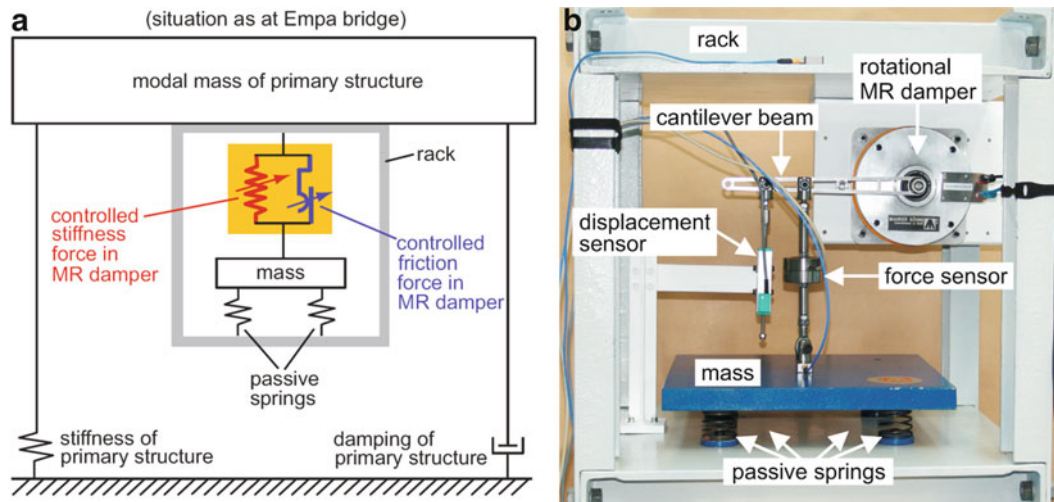


Fig. 10.2 A conceptual sketch (a) and a photograph (b) of the MR-STMD prototype [1]

The next section presents the main features of the MR-STMD concept which was first presented in [1]. Later, the results of experiments on a small-scale MR-STMD prototype are briefly discussed. After that, the full-scale MR dampers and full-scale MR-STMDs for Volgograd Bridge are described together with the results of their experimental tests. The paper is closed with conclusions.

10.2 The Concept of MR-STMD

10.2.1 General Description

The basic idea of the MR-STMD is to replace the passive oil damper in the TMD by a real-time controlled MR damper which is used to adjust both the natural frequency and the damping of the MR-STMD to the actual frequency of the main structure. A characteristic feature of the MR-STMD is that the MR damper is used not only to control the damping but also, or primarily, to control the stiffness of the MR-STMD. For this goal, the MR damper force is controlled in real time to track the force which is the sum of the stiffness force and the friction force. A conceptual sketch of the MR-STMD attached to the primary structure is shown in Fig. 10.2a. The controlled stiffness force in the MR damper augments or diminishes the stiffness of the passive springs and thereby tunes the natural frequency of the MR-STMD to the actual frequency of the primary structure. The controlled friction force in the MR damper generates frequency dependent energy dissipation.

10.2.2 Small-scale MR-STMD Prototype for Laboratory Testing

Figure 10.2b presents the MR-STMD prototype. It consists of a mass supported by four compression springs and the rotational MR damper with maximum torque of 45 nm. The springs and the housing of the MR damper are fixed to the steel rack, which is designed to easily attach the MR-STMD to the primary structure. The rotational MR damper is connected to the mass by a 150 mm cantilever beam and a vertical rod with a force sensor which measures the actual MR damper force applied to the mass. The displacement sensor measures the relative displacement of the mass. The mass m_2 and the passive springs stiffness k_2 of the MR-STMD are tuned as described in the following section.

10.2.3 Mass and Springs Stiffness of the MR-STMD

The mass m_2 and the passive springs stiffness k_2 of the MR-STMD are tuned to the target mode of the primary structure according to Den Hartog's tuning law [2] as

$$m_2 = \mu m_1 \quad (10.1)$$

$$k_2 = k_1 \frac{\mu}{(\mu + 1)^2} \quad (10.2)$$

where m_1 and k_1 are the modal mass and modal stiffness of the primary structure target mode and μ is the predefined mass ratio. The mass ratio is the main design parameter that determines the peak efficiency for both TMD and MR-STMD. A typical mass ratio for TMDs installed in civil engineering structures is of about 1–2%.

10.2.4 Desired Force for the Real-time Controlled MR Damper

The desired force f_{des} which is to be tracked by the real-time controlled MR damper is the sum of the stiffness force and the Coulomb friction force

$$f_{des} = k_{des} x_d + F_{des}^f \operatorname{sgn}(\dot{x}_d) \quad (10.3)$$

where k_{des} is the desired stiffness, F_{des}^f is the desired friction force, x_d is the relative displacement of the MR-STMD mass and \dot{x}_d is the relative velocity, of which only the sign is needed.

The desired positive or negative stiffness in (10.3) is calculated as

$$k_{des} = k_1 \frac{\tilde{\mu}}{(\tilde{\mu} + 1)^2} - k_2 \quad (10.4)$$

where the parameter $\tilde{\mu}$ depends on the *actual frequency* of vibrations $\omega_w = 2\pi f_w$ and the nominal natural frequency of the primary structure target mode $\omega_1 = \sqrt{k_1/m_1}$ as follows

$$\tilde{\mu} = \mu (\omega_w / \omega_1)^2. \quad (10.5)$$

Assuming harmonic excitation, the desired friction in (10.3) is calculated such that the MR damper dissipates the same energy during one cycle of vibrations as a viscous damper with the desired viscous damping coefficient c_{des} , thus

$$F_{des}^f = \frac{\pi}{4} c_{des} \omega_w X_d \quad (10.6)$$

where X_d is an amplitude of x_d and the desired viscous damping coefficient c_{des} is calculated based on Den Hartog's tuning law [2] which is slightly modified to make it dependent on the actual frequency of vibrations ω_w

$$c_{des} = 2 \tilde{\zeta}_2 m_2 \omega_w \quad (10.7)$$

$$\tilde{\zeta}_2 = \sqrt{\frac{3 \tilde{\mu}}{8 (\tilde{\mu} + 1)^3}}. \quad (10.8)$$

It should be noted that (10.4) and (10.6) represent the conservative tuning approach for the MR-STMD. For example, if the actual frequency of vibrations ω_w is equal to ω_1 , the desired stiffness k_{des} (10.4) is zero, and the MR-STMD operates as a passive Den Hartog's TMD where the MR damper is used to track the pure friction force which is energy equivalent to the optimal Den Hartog's viscous damper (10.7). In this case, better performance of the MR-STMD could be achieved with reduced friction force (10.6).

10.2.5 Semi-active Control Force that Takes into Account the MR Damper Constraints

The desired force (10.3) can be fully tracked with the MR damper only if it is fully dissipative and if it is larger than the residual MR damper force, i.e. the force at zero current applied to the MR damper. The desired force (10.3) is fully dissipative if the magnitude of the desired stiffness force $|k_{des}| \dot{X}_d$ is equal or smaller than F_{des}^f , i.e. if $|k_{des}| \leq (\pi/4) c_{des} \omega_w$. Otherwise, if the desired force becomes active during some parts of a vibration cycle, the active desired forces should be clipped to zero to fulfill the semi-active requirements of the MR damper. The clipped semi-active force is further constrained by the MR damper residual force which is often modeled as a friction force F_0 . Hence, the semi-active control force f_{sa} that takes into account both the clipping and the residual force of the MR damper, and can therefore be tracked by the real-time controlled MR damper, is expressed as

$$f_{sa} = \begin{cases} F_0 & : f_{des} < F_0, \dot{x}_d > 0 \\ -F_0 & : f_{des} > -F_0, \dot{x}_d < 0 \\ f_{des} & : otherwise \end{cases} \quad (10.9)$$

The clipping and the MR damper residual force make the MR-STMD performance lower since the equivalent stiffness and the equivalent damping that result from the clipped semi-active forces are no longer equal to their desired counterparts as further discussed in [3, 4].

10.2.6 MR-STMD in the Event of Power Breakdown

As underlined in [5], semi-active or active damping systems must be able to provide protection of the primary structure even if their control systems fail. The MR-STMD was designed to fulfill this requirement. Since the mass, and especially the passive springs of the MR-STMD, are tuned as for Den Hartog's TMD (10.2), the efficiency of the MR-STMD in the event of power breakdown is similar to the efficiency of the TMD with a small viscous damping coefficient. Without a control signal, the residual MR damper force depends on the MR fluid properties and the MR damper structure design [6] and can be shaped in the MR-STMD design process by both of these. However, from the control point of view the residual force should be as small as possible, so that there is a trade-off between the fail-safe large and the control-motivated low residual force.

10.3 Experimental Validation of the MR-STMD Prototype

10.3.1 Experimental Setup

The MR-STMD prototype was validated on a 19.2 m long laboratory bridge at Empa (Fig. 10.3a). The MR-STMD was attached at the anti-node position of the first vertical bending mode of the bridge. The mass $m_2 = 26.325$ kg and passive springs stiffness $k_2 = 9.966$ kN/m of the MR-STMD were tuned to the identified natural frequency $f_1 = 3.145$ Hz and modal

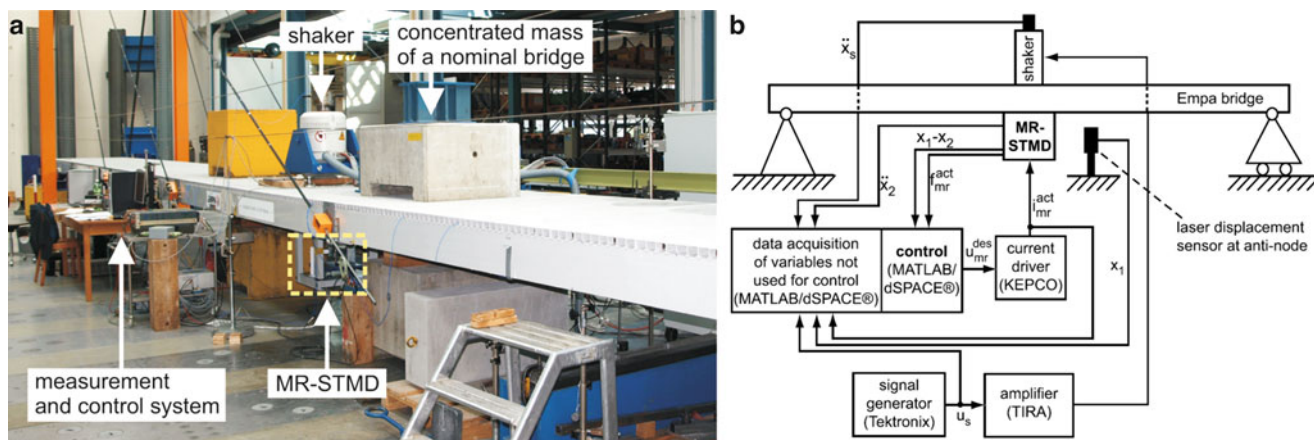


Fig. 10.3 A photograph (a) and a sketch (b) of the experimental setup [1]

mass $m_1 = 1681$ kg of the first vertical bending mode. The electrodynamic shaker with an inertial mass of 32.5 kg was also placed on the bridge at the anti-node position to realize harmonic force excitation with its amplitude and frequency commanded manually with a signal generator.

The setup, together with its measurement and control system, is schematically depicted in Fig. 10.3b. The control algorithm for the MR damper was implemented and run in MATLAB[®]/dSPACE[®]. The desired force (10.3) was calculated in real time based on the measured relative displacement x_d , which was also used to estimate the actual frequency of vibrations ω_w needed in (10.5) and (10.6). The MR damper force tracking control was realized by using an inverse model of the MR damper and a proportional force feedback to ensure good agreement between the desired and the actual MR damper force.

10.3.2 Testing Procedure

The goal was to validate the damping performance of the MR-STMD for the case when its mass and passive springs stiffness are tuned to the target mode of the bridge as well as for the case when they become de-tuned due to changes in the natural frequency of the target mode. The changes in the natural frequency were realized by adding or removing masses from the bridge deck without any changes in the MR-STMD configuration or its control algorithm. For each tested bridge configuration, the measured performance of the MR-STMD was then compared with the performance of a Den Hartog's TMD tuned to the target mode. In order to make this comparison fair, the TMD was realized with exactly the same mass and passive springs as in the MR-STMD and the optimal Den Hartog's viscous damping force was precisely emulated with the MR damper. At each excitation frequency ranging from 2.3 to 3.8 Hz, a dynamic amplification $X_1/X_{1-static} = X_1 k_1 / F_w$ was calculated from the steady-state displacement amplitude X_1 measured at the anti-node of the target mode and from the force excitation amplitude F_w calculated with the measured acceleration of the inertial mass of the shaker.

10.3.3 The Performance of MR-STMD and TMD for a Bridge with Natural Frequency Uncertainty

Figure 10.4 presents the collection of the measurement results obtained for the bridge with different masses and therefore different natural frequencies of its first vertical bending mode under consideration. Both the MR-STMD and the TMD are tuned to the nominal frequency $f_1 = 3.145$ Hz and therefore, when f_1 does not change, the dynamic amplification around f_1 is approximately the same for the MR-STMD and TMD. The important features of the MR-STMD are demonstrated when the natural frequency of the target mode is subjected to uncertainties. Due to the natural frequency shift ranging from -12.2% to $+10.9\%$ of f_1 , the passive TMD becomes detuned and consequently a significant deterioration of its damping performance is observed in Fig. 10.4a. For the same natural frequency shifts, the damping performance of the MR-STMD is visibly better (Fig. 10.4b). The measured reduction of the peak response due to the MR-STMD is of 56% for the natural frequency shift of -12.2% , and 63% for the shift of $+10.9\%$. These results confirm the high damping potential of the MR-STMD concept

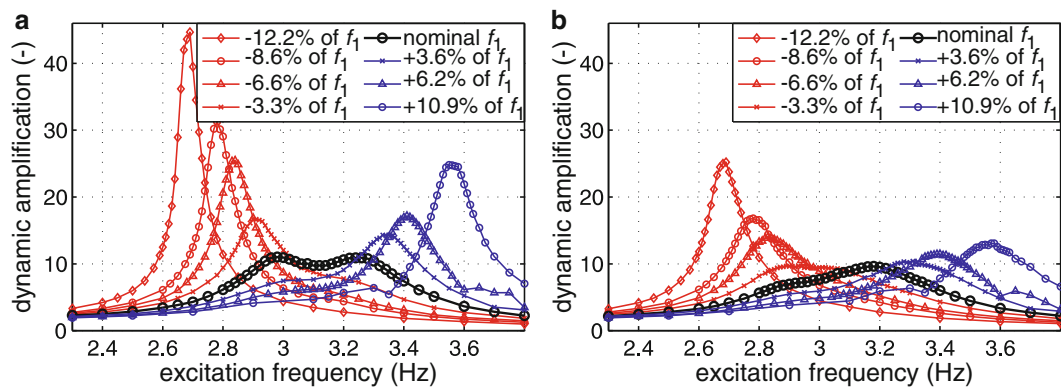


Fig. 10.4 Measured dynamic amplification for TMD (a) and MR-STMD (b) for a bridge with natural frequency uncertainty

when compared with the passive TMD. Further improvement of the MR-STMD performance is notified in [3] where the so-called precise stiffness control approach is applied and the controlled friction force in the MR damper is reduced.

Although in all the experimental tests the natural frequency shift was realized by adding or removing masses to or from the bridge deck, it is expected that similar results would be achieved if the natural frequency shift was due to changes in the bridge stiffness.

10.4 Semi-active Damping System for Volgograd Bridge

The MR-STMD was chosen by the customer for the mitigation of the Volgograd Bridge because of the promising results shown in [1] and since several resonance frequencies can be targeted due to the real-time tuning of the MR-STMD to the actual frequency of vibration. This feature allows reducing the mass of the MR-STMD compared to the mass of the passive TMD.

The solution for Volgograd Bridge comprises twelve fully controlled MR-STMDs installed on the bridge girder at three locations. At each location, there are four MR-STMDs, which are pre-tuned to one of three targeted vertical bending modes of the bridge. The three locations were chosen such that the MR-STMDs always act at the anti-node of the targeted mode. Each MR-STMD consists of a mass of 5,200 kg, springs, and a rotational MR damper. The mass ratios of four MR-STMDs together targeting one of the three modes with nominal frequencies of 0.45, 0.57 and 0.68 Hz are 0.84%, 0.97% and 1.14%, respectively. The focus of the next sections is on the full-scale MR dampers and MR-STMDs installed on the bridge.

10.5 Hybrid Testing of Full-scale MR Dampers

10.5.1 Full-scale MR Damper, Experimental Setup and Tests Performed

Figure 10.5a presents one rotational MR damper with gearing that is used in the MR-STMD for Volgograd Bridge. The MR damper comprises a cylindrical disk surrounded by the MR fluid with properties dependent on the applied magnetic field. The restoring torque of the MR damper is controlled with the current in the MR damper coil that creates the magnetic field. The gearing transmits the controllable restoring torque of the MR damper into the controllable force acting on the MR-STMD mass. The maximum MR damper force measured in this configuration is of 6 kN.

Before installation on Volgograd Bridge, the MR dampers with their sensors and control hardware were tested at Empa laboratories in a setup presented in Fig. 10.5b. The housing of the MR damper was attached to a strong floor and the hydraulic cylinder was used to impose a controlled displacement. The MR dampers were first tested at constant currents to determine their inverse models from the measured steady-state force displacement characteristics. Later, the force tracking control with MR dampers was developed and optimized. Finally, each of the real-time controlled MR dampers was subjected to series of hybrid simulation tests to validate its operation under 12 various motion scenarios that can occur in the bridge. The tests

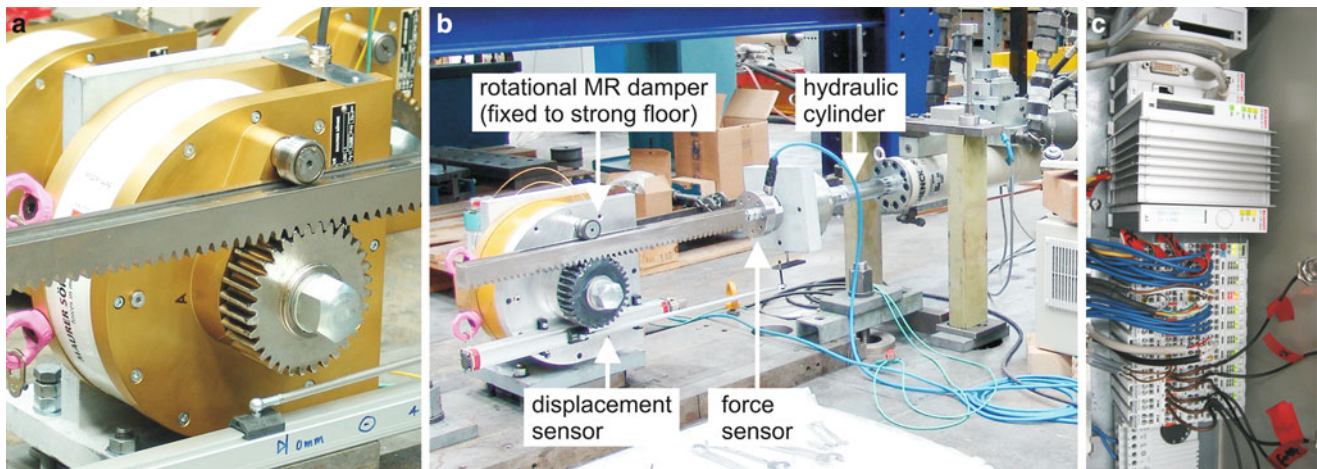


Fig. 10.5 Full-scale rotational MR damper (a), experimental setup at Empa (b) and the MR damper control hardware (c)

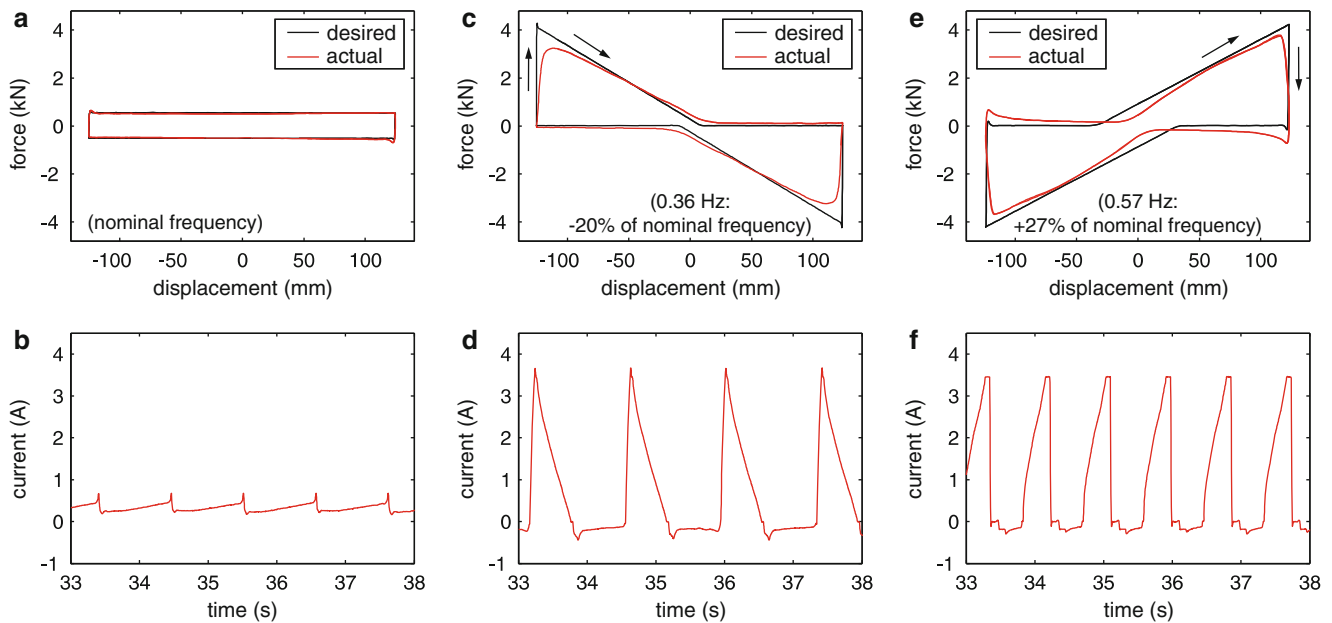


Fig. 10.6 Clipped desired force and actual MR damper force versus displacement, and current versus time, for three frequencies: force (a) and current (b) at nominal frequency, force (c) and current (d) at frequency decreased by 20%, force (e) and current (f) at frequency increased by 27%

were carried out with exactly the same autonomous control system configuration as later installed on the bridge and with a complete control algorithm developed at Empa and running on a programmable real-time controller (Fig. 10.5c).

10.5.2 Clipped Desired Force and Actual Force of Real-time Controlled MR Damper

Figure 10.6 presents the selected results of tests of the MR damper for MR-STMD targeting mode 1 with a nominal frequency of 0.45 Hz. The tests aimed to verify the adequacy of the MR damper force tracking control at various frequencies and amplitudes of motion. In Fig. 10.6a, b the desired force (10.3) and the actual MR damper force together with the corresponding current are presented under harmonic displacement with an amplitude of 125 mm and a nominal frequency that results in zero desired stiffness (10.4). The desired pure friction force in Fig. 10.6a is precisely emulated with the MR damper.

If the frequency of excitation is lower than f_1 , the desired stiffness (10.4) is negative. In this case, tracking of the clipped desired force with the MR damper requires a fast increase in the MR damper force at maximum displacements (Fig. 10.6c), which is a challenging task. Satisfactory agreement between the clipped desired force and the actual force in Fig. 10.6c was achieved using a high quality current driver that enabled a fast increase of the MR damper current (Fig. 10.6d). Furthermore, the very low residual force in Fig. 10.6c was achieved due to the application of negative current which helps to compensate for the remanent magnetization effects in the MR damper.

If the frequency of excitation is higher than f_1 , the desired stiffness (10.4) is positive. In this case, the clipped desired force quickly changes from its maximum value to zero, which is easier to achieve with the MR damper even if the desired stiffness is large as in Fig. 10.6e. The presented results confirm the satisfactory quality of the developed force tracking control scheme.

10.6 Experimental Validation of Full-scale MR-STMDs

10.6.1 A Full-scale MR-STMD

One MR-STMD for Volgograd Bridge, consisting of a mass of 5200 kg, a set of 12 springs, and a rotational MR damper installed in the middle of the mass, is shown in Fig. 10.7a. The MR-STMD is equipped with two sensors: a displacement sensor, which measures the relative displacement of the mass (Fig. 10.7b), and the MR damper force sensor (Fig. 10.7c).

The MR-STMD in Fig. 10.7 is one of four MR-STMDs which target mode 2 of the nominal frequency 0.57 Hz. The MR-STMDs for mode 1 and mode 3 have different springs but the same mass with its maximum displacement of ± 300 mm.

10.6.2 Forced Vibration Tests that Validate the Adaptive Features of the Full-scale MR-STMD

The forced vibration tests of the full-scale MR-STMD for Volgograd Bridge were performed at the University of the German Armed Forces, Munich, Germany. The hydraulic cylinder with controlled displacement was connected in the middle of the MR-STMD mass, as shown in Fig. 10.7c. The MR-STMD targeting mode 2 was tested at different frequencies around the nominal frequency 0.57 Hz. The goal of the tests was to verify if the controlled MR-STMD is able to adapt its resonant frequency within the desirable range. For the purpose of these tests, the control code was slightly modified. The desired stiffness was calculated not for the actual frequency ω_w as in (10.4), but for the manually prescribed resonant frequency of the MR-STMD such that the total MR-STMD stiffness, which is the sum of the passive springs stiffness and the stiffness controlled in the MR damper, gives the resonant frequency of the MR-STMD as prescribed. All the remaining parts of the control algorithm were not changed. At each tested excitation frequency the magnitude of frequency response of the



Fig. 10.7 Single full-scale MR-STMD: general view (a), displacement sensor (b), MR damper installation and force sensor (c)

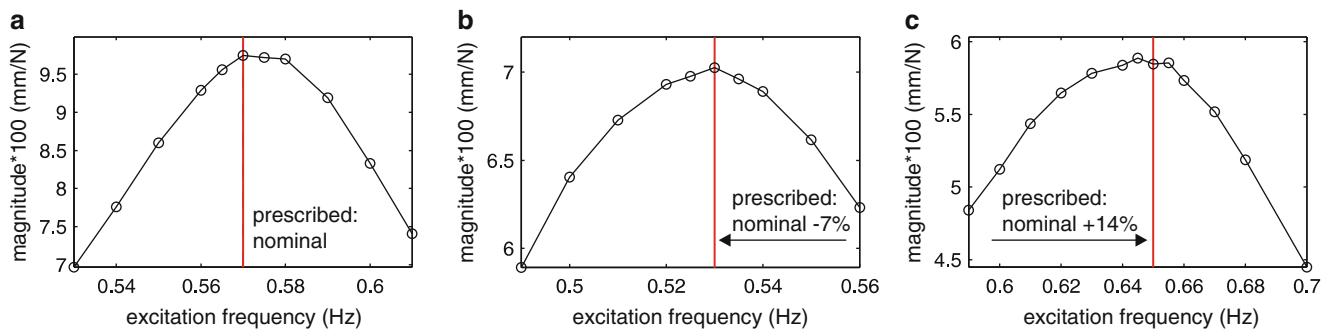


Fig. 10.8 Frequency response of the MR-STMD targeting mode 2 for the prescribed frequency equal to the nominal frequency of mode 2 (a) and for the prescribed frequency 7% smaller (b), or 14% larger (c), than the nominal frequency of mode 2

Fig. 10.9 Installation of MR-STMDs on Volgograd Bridge (photo: J. Distl)



MR-STMD was evaluated as $rms(x_2)/rms(f_{exc})$, where x_2 is the measured steady-state displacement of the MR-STMD mass and f_{exc} is the measured excitation force. The test was fulfilled if the frequency response showed the peak value at the prescribed frequency. Figure 10.8 presents the obtained frequency responses for the three selected out of the total of 11 prescribed resonance frequencies that were tested. The presented results confirm that the full-scale MR-STMD has the ability to adaptively change its resonant frequency by controlling the MR damper force. The tests demonstrated that the natural frequency of the MR-STMD for mode 2 of Volgograd Bridge could be lowered to 0.47 Hz, which corresponds to the frequency shift of -18% , and increased to 0.68 Hz, which corresponds to the frequency shift of $+20\%$.

10.7 Conclusions

This paper describes the concept of a semi-active tuned mass damper with real-time controlled MR damper (MR-STMD) that was installed in the Volgograd Bridge, Russia (Fig. 10.9), by the industrial partner of the project in fall 2011 to protect the bridge from vibrations that occurred for the first time in May 2010. The system consists of 12 MR-STMDs. The mass spring systems of always four devices are designed to the nominal frequency of one targeted mode, i.e., 0.45, 0.57 and 0.68 Hz. However, all 12 devices are controlled in real-time to the actual frequency of vibration, hence all 12 MR-STMDs mitigate the actual mode of vibration. As a direct result, the MR-STMD concept generates approximately the same vibration reduction in the bridge as if passive TMDs with approximately twice as much mass were installed.

In order to guarantee robustness of the MR-STMD system, the control code of the MR-STMDs in the Volgograd Bridge is extended by self-diagnostic procedures and actions to be undertaken in case of fault detection. The control hardware is accessible via Internet that allows controlling variables remotely and re-programming code if necessary. The power supply includes a backup system for a maximum of 48 h.

The experimental validation of the MR-STMD concept at the University of the German Armed Forces, Munich, demonstrated that the MR-STMD concept allows for frequency tuning within a frequency band of roughly $\pm 18\%$ of the nominal target frequency. The tests at the Empa bridge, Switzerland, showed that the MR-STMD concept is able to compensate for the frequency sensitivity of the passive TMD and the maximum improvement between the MR-STMD and the passive TMD is on the order of 50% for frequency shifts of approximately $\pm 10\%$.

Acknowledgements This work was supported by Empa, Swiss Federal Laboratories for Materials Science and Technology, Dübendorf, Switzerland, by the industrial partner Maurer Söhne GmbH & Co. KG, Munich, Germany and by AGH University of Science and Technology, Department of Process Control, Krakow, Poland (statutory research funds No. 11.11.130.560).

References

1. Weber F, Maślanka M (2012) Frequency and damping adaptation of a TMD with controlled MR damper. *Smart Mater Struct* 21(5):055011
2. Den Hartog JP (1934) *Mechanical vibrations*. McGraw-Hill, New York
3. Maślanka M, Weber F (2012) Precise stiffness control with MR dampers and its application to semi-active tuned mass dampers. *J Intell Mat Syst Struct*, Submitted
4. Weber F (2012) Semi-active vibration absorber based on real-time controlled MR damper. *Smart Mater Struct*, Submitted
5. Casciati F, Rodellar J, Yildirim U (2012) Active and semi-active control of structures – theory and applications: a review of recent advances. *J Intell Mat Syst Struct* 23(11):1181–1195
6. Zhu X, Jing X, Cheng L (2012) Magnetorheological fluid dampers: a review on structure design and analysis. *J Intell Mat Syst Struct* 23(8): 839–873

Chapter 11

A New Shape Memory Alloy-Based Damping Device Dedicated to Civil Engineering Cables

G. Helbert, L. Dieng, T. Lecompte, S. Arbab-Chirani, S. Calloch, and P. Pilvin

Abstract Most of civil engineering cable structures are subjected to potential damages mainly due to dynamic oscillations induced by wind, rain or traffic. If vibration amplitudes of bridge cables for example are too high, it may cause a fatigue phenomenon. Recently, researches had been conducted dealing with the use of damping devices in order to reduce vibration amplitudes of cables. Thin shape memory alloy (SMA) NiTi (Nickel-Titanium) wires were used as a simplified damping device on a realistic full scale 50 m long cable specimen in Ifsttar (Nantes - France) laboratory facility, and its efficiency was shown. It has been done using finite element simulations, as well as experimental test methods. The aim of this work is to link the wire material behavior with the local damping induced along the cable qualitatively. Indeed, thermomechanical energy dissipation of the NiTi-based wires enables their damping power. The hysteretic behavior in NiTi-based alloys demonstrates a consequent dissipation because of an exothermic martensitic transformation and then an endothermic reverse transformation.

Keywords Civil engineering cable • Shape Memory Alloys • Dampers • Vibration • Modal analysis

11.1 Introduction

Cables of civil engineering structures are subjected to two kinds of damage mechanisms : fatigue and corrosion. Furthermore, when cables are subjected to high amplitude vibrations, there is friction between steel wires or between wires and the anchorages [1–6]. This phenomenon is called fretting-fatigue [7, 8].

To avoid fatigue and fretting-fatigue phenomena, one needs to reduce cable oscillation amplitudes by increasing the cable damping ratio. Indeed, stay cables have quite a low intrinsic damping capacity (less than 0.01%). The most conventional way of limiting or eliminating high amplitudes cable-stay vibration consists in increasing their structural damping capacity by fitting special devices. Currently, different sorts of passive damping devices have been set up on bridges on duty [9, 10].

However, the damping systems described in [10] are not appropriate for too high amplitudes and frequencies. To expand the damping range and to get a better efficiency, a Ni-Ti-based Shape Memory Alloys damping device (SMA) was used as a damping device in the same way as the external dampers kind presented in [11, 12] and [13].

SMA are part of the smart material class, because they accommodate their response (mechanical and thermomechanical behaviors) according to the stimulations (natural or induced). In particular, NiTi SMA owns interesting properties because of the solid-solid martensitic transformation : the superelastic behavior (significant reversible strains at fixed temperature, Fig. 11.1) and a strong damping capacity, especially during the martensite transformation. The first one offers a structural fatigue resistance, whereas the second one enables the material to reach faster the threshold stress of the vibrating

G. Helbert • L. Dieng (✉)

SOA - IFSTTAR Centre de Nantes - Route de Bouaye - BP: 4129, 44341 Bouguenais, France
e-mail: lamine.dieng@ifsttar.fr

T. Lecompte • P. Pilvin

LIMATB - Université de Bretagne SUD - Rue de Saint-Maudé, BP 92116 - 56321 Lorient Cedex, France

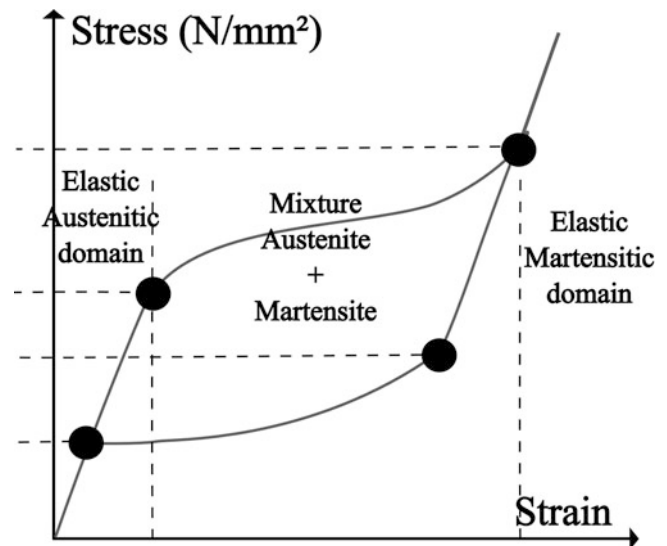
S. Arbab-Chirani

LBMS - École Nationale d'Ingénieurs de Brest, Technopôle Brest-Iroise, CS 73862, 29238 Brest Cedex 3, France

S. Calloch

LBMS - École Nationale Supérieure des Ingénieurs des Études et Techniques d'Armement, 2 rue François Verny, 29806 Brest Cedex 9, France

Fig. 11.1 Superelastic behavior of NiTi at fixed temperature $T > T_{AusteniteFinish}$



components. Some studies have been dealt with damping power of NiTi-based structures. A study led by Piedboeuf and Gauvin in [14] deals with the strain amplitude, the frequency and the temperature effects on the damping behavior of a NiTi alloy and a recent paper of Branco [15] deals with the NiTi applications in civil engineering, in particular with the cycling behavior of NiTi wires. A paper of Zbiciak was about the dynamic analysis of a pseudoelastic NiTi beam [16]. Recently, the efficiency of the SMA damper in controlling the cable displacement was assessed and compared with the tuned mass damper (TMD) device, using numerical models. The numerical results presented by Ben Mekki in [17] show the efficiency of the SMA damper to mitigate the high free vibrations and the harmonic vibrations on short cables (less than 5 m) better than an optimal Tuned Mass Damper (TMD).

The first aim of this paper, consists of the numerical approach of the dynamic response of a pre-stressed horizontal civil engineering steel-made cable, after the release of a transverse force induced in the middle of the cable.

The second aim is to model the NiTi-based damper device effect set up perpendicular to the cable. The device is located at the same level as the induced force. The emphasis is layed on the wire energy dissipation effect on the dynamic behavior of the system, thanks to the finite element simulation. In particular, the SMA superelastic behavior is modelled in a different way than the Auricchio's model used in [17]. The model developed by Bouvet et al. in [18] is adapted to a NiTi-based alloy and is implemented in a Finite Element code MSC Marc & Mentat, thanks to a user subroutine.

11.2 Finite Element Analysis

The Finite Element simulations are modelled on experimental tests realized in Ifsttar Laboratory facilities (Fig. 11.2a, b).

11.2.1 Numerical Modelling of a Civil Engineering Cable

In the experimental set up, two laser sensors were used in order to get the vertical displacement of the cable. The first one was located near the damper location and the second one near the force location. Hence, the interest of the finite element simulations is to get information at each element node. In order to validate the simulation, the attention is focused on the transverse displacement of the cable, on the modal frequency values and on the damping ratio along the cable.

The finite element model was computed using Marc & Mentat finite element code. The cable is modelled using beam elements. This beam element is a straight, Euler-Bernoulli beam in space, which allows linear elastic and nonlinear elastic and inelastic material response. Indeed, two nodes element is the most common element used in the model of high pre-stressed cables according to Thai and Kim [19]. Large curvature changes are neglected in the large displacement formulation.

Fig. 11.2 (a) Experimental set up (b) Bench test (Ifsttar facilities)

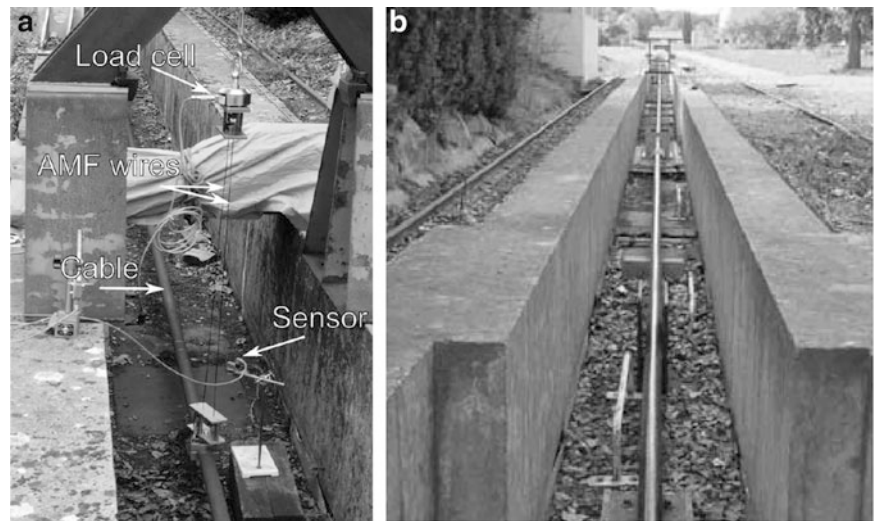
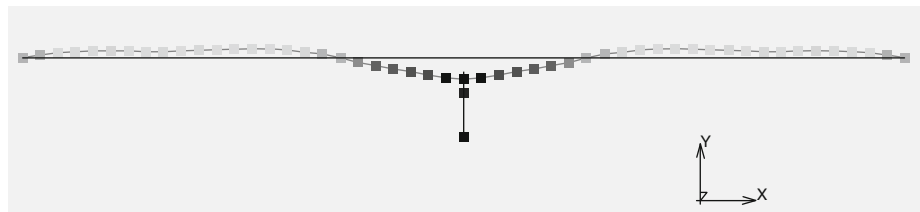


Table 11.1 Physical and geometrical characteristics of the “experimental cable” specimen and the “numerical cable”

Characteristics	Length L	Diameter D	Mass density
Real cable	50m	55mm	16.1kg/m
Numerical beam	50m	50.19mm	8136.9kg.m ⁻³

Fig. 11.3 Numerical set up



Linear interpolation is used along the axis of the beam (constant axial force) with cubic displacement normal to the beam axis (linear variation in curvature). For this type of element, three parameters need to be defined: the section area A , the moment of inertia of section about local x-axis (I_{xx}) and the moment of inertia of section about local y-axis (I_{yy}). Input model parameters are calculated in agreement with the experimental cable values. Thus, Young’s modulus E is lower than steel modulus ($E=190$ GPa) cause of the slip between the wires, which affects the stiffness of the cable, and Poisson’s ratio ν is the 0.3 steel value [20]. The bending stiffnesses of the section are calculated as $E I_{xx}$ and $E I_{yy}$. The torsional stiffness of the section is calculated as $\frac{E}{2(1+\nu)}(I_{xx} + I_{yy})$. The effective cross-section A^* must take in account the empty space between the wires. The bending stiffness is assumed to be 33% lower than in steel case, according to experimental tests [20].

$$(EI)^* = \left(\frac{2}{3}\right) \cdot EI \quad (11.1)$$

So the effective cross-section of the beam and the corresponding diameter have to be reevaluated. Table 11.1 reports the parameters used on the numerical model compared to real cable characteristics.

The 50m-long numerical cable is meshed into fifty 1m-long beam elements. The mechanical behavior of these elements is supposed to be elastic and linear. Initially, a vertical force is applied around the middle point of a horizontal cable. To put the “numerical cable” on vibration, the force is suddenly released in 0.05 s, according to the experimental tests. The force took several values during the experimental tests (2kN, 3kN, 4kN and 5kN). The “numerical cable” is assumed to be fixed-end : the end nodes have no degrees of freedom. An initial stress affected to the whole elements corresponds to an axial tension T of 900kN, in accordance with the experimental value. The sag-effect in the cable is neglected unlike in the Ben Mekki’s work.

Figure 11.3 show a figure of the vibrating numerical set up.

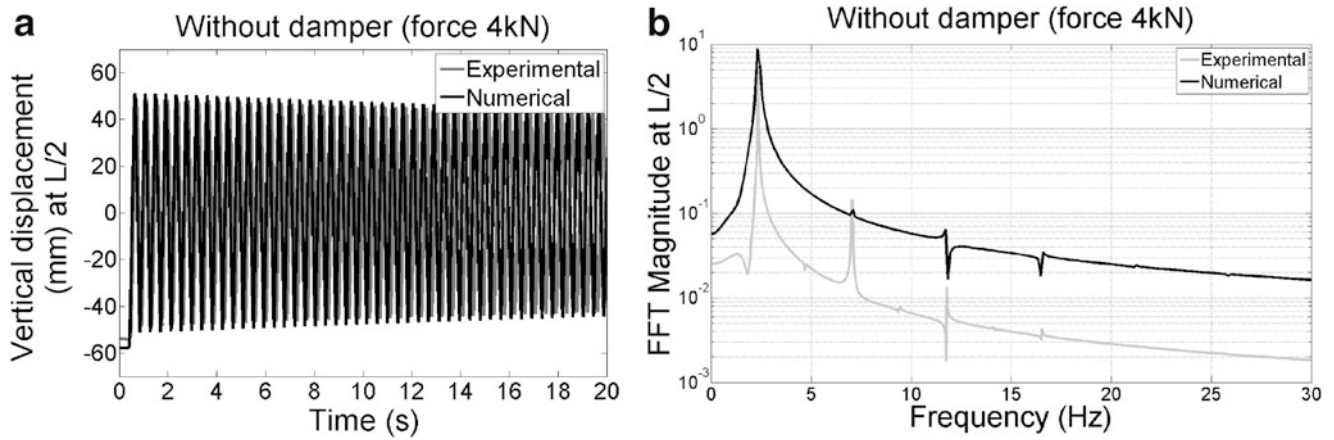


Fig. 11.4 (a) Displacement at the middle of the cable (b) Fourier frequency spectrum at the middle of the cable

Anatically, the following differential equilibrium equation of a chord, governs the mechanical behavior of the cable.

$$EI \frac{\partial^4 y(x,t)}{\partial x^4} - T \frac{\partial^2 y(x,t)}{\partial t^2} + \frac{\mu}{L} \frac{\partial^2 y(x,t)}{\partial x^2} = 0 \quad (11.2)$$

where EI is the bending stiffness.

When the dimensionless parameter $\zeta = \frac{1}{L} \sqrt{\frac{EI}{T}}$, obtained from the previous equation (11.2), is well below 1, the bending stiffness can be neglected. Thus, the cable can be considered as a chord on the dynamic behavior aspect. Thanks to this assumption, the modal frequencies values can be determined from the equation (11.3).

$$f_n = \frac{n}{2L} \sqrt{\frac{T}{\mu}} \quad (11.3)$$

where n is the mode rank, T is the tension in the cable, L is the cable length and μ is the mass per unit length of the cable. Anatically, the value of 2.34 Hz is found for the 1st mode of the “cable system” from equation (11.3).

Two preliminary analysis were conducted with different dynamic methods (such as modal and transient analysis) in order to validate the cable modeling. Modal analysis and transient dynamic analysis give approximatively the same first mode frequency values : 2.43 Hz (modal) and 2.39 Hz (transient dynamics), against 2.34 Hz experimentally, according to the Fast Fourier Transform (FFT) spectrum (Fig. 11.4-b)).

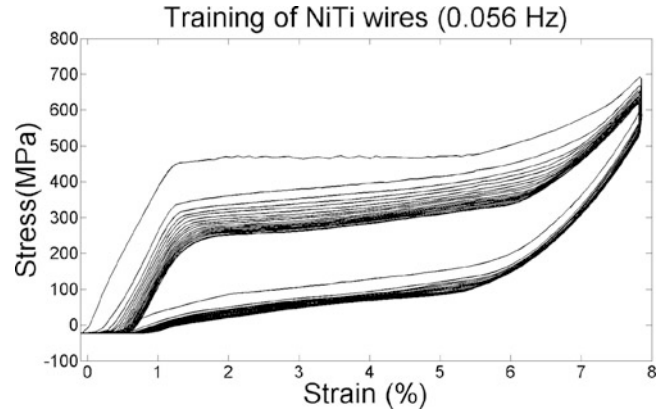
Furthermore, a second study plots the vertical displacement of each node on the cable thanks to a transient dynamic analysis, based on the Newmark-Beta dynamic operator [21]. It reveals an intrinsic damping ratio of 10^{-6} which will be neglected compared to the cable intrinsic damping ratio. This integration scheme is less dissipative than that of Houbolt [22] and therefore better suited to the solve of the linear and non-linear problems of mechanical vibration [23]. Furthermore, Newmark-Beta is a very stable method.

Initially, a Rayleigh viscous damping, corresponding to the first mode damping ratio of the free cable experimental configuration, is assigned on the whole cable elements to represent the intrinsic damping of a cable, due to the friction between the strand wires [24]. Indeed, the damping ratio (corresponding to the 1st mode) evaluated from the experimental curves does not depend on the location along the cable. The Rayleigh viscous damping is presented in relation (11.4).

$$[C] = \alpha [M] + \beta [K] = 2\xi\omega \quad (11.4)$$

With C the Rayleigh damping matrix, M the mass matrix and K the stiffness matrix of the system “cable”, ξ the modal damping ratio and ω the natural pulsation. The mass coefficient α and the stiffness coefficient β are determined respectively by $\alpha = \xi \frac{2\omega_i \omega_j}{\omega_i + \omega_j}$ and $\beta = \xi \frac{2}{\omega_i + \omega_j}$ with $\omega_{k=i,j}$ the natural angular frequency of the k^{th} mode of vibration. Here, $\alpha = 7.5210^{-3}$ and $\beta = 1.4310^{-5}$, for $\omega_1 = 15.016 \text{ rad.s}^{-1}$ and $\omega_2 = 30.032 \text{ rad.s}^{-1}$, and $\xi = 0.00033$.

Fig. 11.5 Training of the NiTi wire realized in IFSTTAR



The evaluation of the experimental and the numerical transient analysis damping ratios ξ consisted of plotting the logarithmic decrement δ from the Hilbert envelop of the displacement signal.

$$\xi = \frac{\delta}{2\pi f_k T} \quad (11.5)$$

With f_k the natural frequency of the n^{th} considered vibration mode.

Figure 11.4a, b show the comparison between experimental and numerical curves of the vertical displacement at the middle of the cable and the associated Fast Fourier Transform spectrum. The finite element model adequately approaches the experimental signal in terms of amplitude and damping ratio (Fig. 11.4a). The error, which is reflected in the amplitude, is resulting from the difficulty of representing the distribution of the force along the cable, which is not well-extracted from the experimental tests. The numerical Fourier spectrum is coherent with experimental results and gives closed modal frequency values (Fig. 11.4b). Even-number ranking modes are not visible in the numerical spectrum because the signal was taken and the force was exerted at $L/2$ (common nodes of all even-number ranking nodes), which is not exactly right in the experimental case for practical reasons : the displacement sensor and the force could not be exactly located in the cable midpoint. The first mode is the main mode (or the most energetic according to the FFT spectrum) because the signal is taken at its antinode, exactly where the force was located.

11.2.2 Action of the NiTi-Based Damping Device

11.2.2.1 Presentation of the Damping Device Model

The final aim of this study is to evaluate the consequences of the set up of a damping device on the cable damping behavior. The damping device consists of two NiTi-based alloy wires, fixed at the ground on one hand and at a specific location on the cable on the other hand. The wire is 1.20m long and its cross-section area is $5.3 \cdot 10^{-6} m^2$.

The material used for all the experimental tests is a NiTi polycrystalline SMA (Ni : 56.3 % at., C : 40ppm, N+O : 0.0210 % at., Co \leq 0.005 % at., Cu \leq 0.005 % at., Cr \leq 0.005 % at., Nb \leq 0.005 % at., H \leq 0.001 % at., Ti : balance) provided by Memry (Bethel, Connecticut). Wires are in austenite state at room temperature and above. The real mass density is affected to the “numerical wire”. Before its use, the NiTi wire specimen was trained in the Ifsttar Laboratory in order to stabilize the hysteretic stress-strain curve (Fig. 11.5).

The wire is modelled by a single truss element. A truss element is defined as a deformable, two-nodes element with a linear interpolation along the length that is subjected to loads in the axial direction. The loads can be tensile or compressive. The element has three degrees of freedom per node. There is a single integration point at the centroid of the element. The mass matrix uses two-points integration. The element is 1.20m long and its cross-section-area is equal to the cross-section area of the two experimental wires ($10.6 \cdot 10^{-6} m^2$) to simplify the model.

Fig. 11.6 Description of model parameters

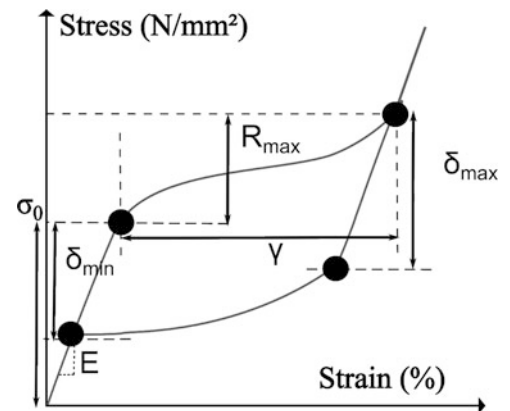


Table 11.2 Parameters of the material modeled

Parameters	σ^0 (MPa)	γ	E (GPa)	δ^{min} (MPa)	δ^{max} (MPa)	R^{min} (MPa)	R^{max} (MPa)
Physical description	Yield stress	Maximal transformation strain-modulus	Young	–	–	–	–
Value	140	6.9%	35	12	10	0	237

11.2.2.2 Superelastic Model General Description

The superelastic behavior available at a fixed temperature is implemented in the Marc & Mentat code via a user's subroutine. Superelasticity means the possibility for a material to be significantly stretched without any remaining strain after loading. In NiTi, this behavior is possible thanks to a crystal rearranging. The phenomenological model was developed by Bouvet et al. [18] from the generalized plasticity frameworks with two yield surfaces corresponding respectively to the martensitic and austenitic elastic domains. The intersection of the two surfaces is associated to the elastic domain for the mixture of both phases.

The hardening functions corresponding to the direct and reverse martensitic transformations are determined from the 100th cycle (not visible in the Fig. 11.5). The hardening direct g_{dir} and the hardening reverse g_{rev} of the model are governed respectively by a polynomial function and a hyperbolic sinus-based function.

We have to note that dynamic behavior change of NiTi alloy, induced by strain rate and temperature effects, are not taken in account in the model, and this aspect will be the topic of future works.

In the following parts, the parameters adopted, as shown in the Fig. 11.6, are given in Table 11.2.

11.2.3 Numerical Model of a Civil Engineering Cable Equipped with a “Damping Device”

One node of the “numerical” wire is linked to the middle point node of the cable constitutive elements. Displacement and force are totally transmitted between the two linked nodes. The other node of the wire truss element has no degree of freedom because it is assumed to be clamped in the ground.

The truss which follows the superelastic behavior is initially pre-stressed by a force of 1kN, in order to stretch it and to increase the mean value of displacements subjected by the wire, in the same way as the experimental tests. It enables the shape memory alloy to undergo the martensitic transformation faster.

Because of a low diameter, the wire has to avoid any compression load because of the buckling phenomena which could be disastrous for its mechanical resistance. Indeed, a special device was established to impose that the device works only in tension during experimental tests. The outline of the real damper was presented in a previous study [12]. Thus, the model does not allow any compressive behavior : if the stress is a compression stress, the code removes the stress. This point involves an assymetric oscillation of the damping device, as shown in the section 11.3.

11.3 Numerical Results

The aim of this section is to compare the numerical with the experimental results in the case where the applied force (of 4kN) and the damper is located at the cable midpoint.

11.3.1 Qualitative Comparison Between Experimental and Numerical Results

Experimental and numerical displacements of the cable midpoint, with and without the damping device, are represented in the time domain in Fig. 11.7a, b and in the frequency domain in Figs. 11.8a, b and 11.9a, b. The Fig. 11.8a, b represent the Fast Fourier Transform spectrum for the ten first seconds, whereas the Fig. 11.9a, b represent the five following seconds. Indeed, two phases of vibration are considered because of the shape of the decrement logarithmic where two damping phases (two straight lines) can be observed, as shown in Fig. 11.10.

The SMA damper allows a very fast reduction of the amplitude of the displacement after less than 10 seconds of vibration. In the “without damper” case, the cable is still vibrating after 120 seconds, according to numerical and experimental approaches. One can note that the logarithmic decrement is higher (Fig. 11.10a, b), and amplitudes of vibration are hardly limited from the beginning of oscillations (Fig. 11.7a, b), with the introduction of the damper. Furthermore, the symmetry does not exist any more because of the set up of the one-way damping device, even if the phenomenon is more obvious on the experimental curve.

The frequency spectrum response obtained by FFT shows the value of the first mode frequency (2.34 Hz), when the device is not introduced. The signal spectrum “With damper” contains only one main frequency at about 3Hz and noise (Fig. 11.8). The random presence of other peaks seems to predict an evolution of the first mode frequency indirectly related to time.

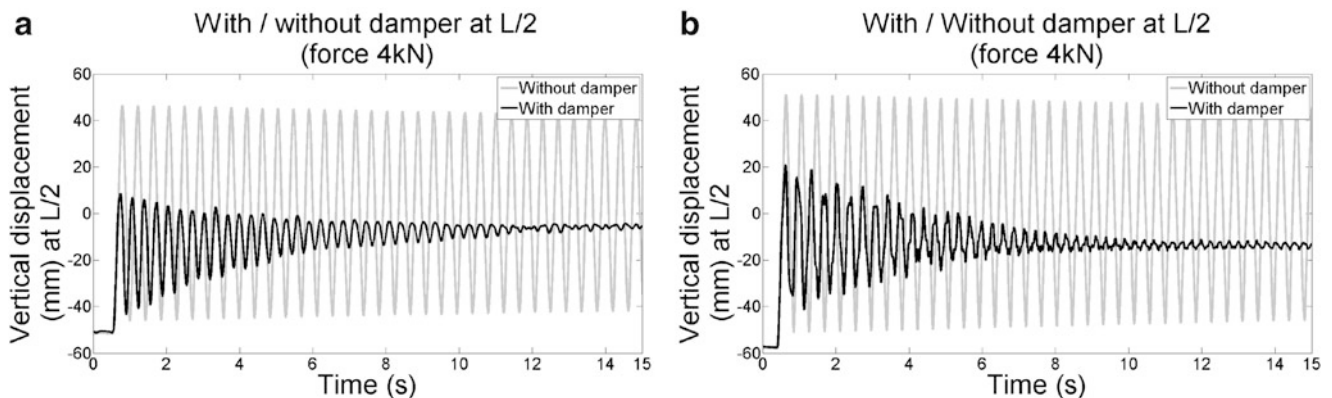


Fig. 11.7 (a) Experimental signal (b) Numerical signal

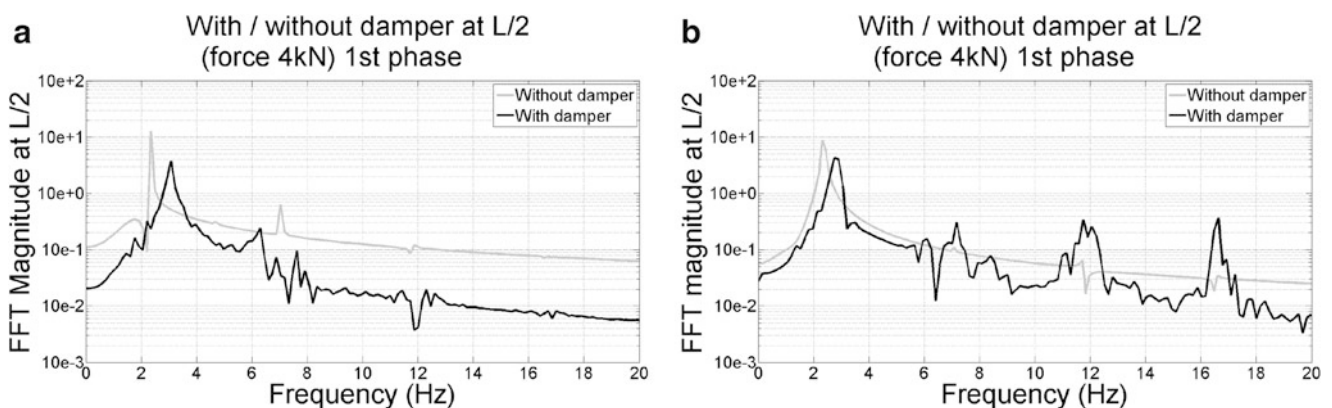


Fig. 11.8 (a) Experimental signal (b) Numerical signal

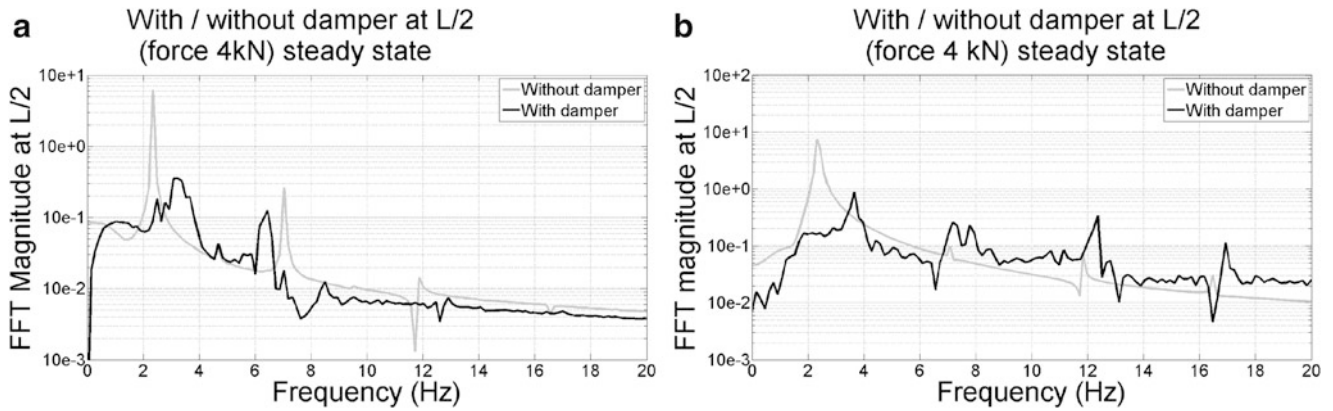


Fig. 11.9 (a) Experimental signal (b) Numerical signal

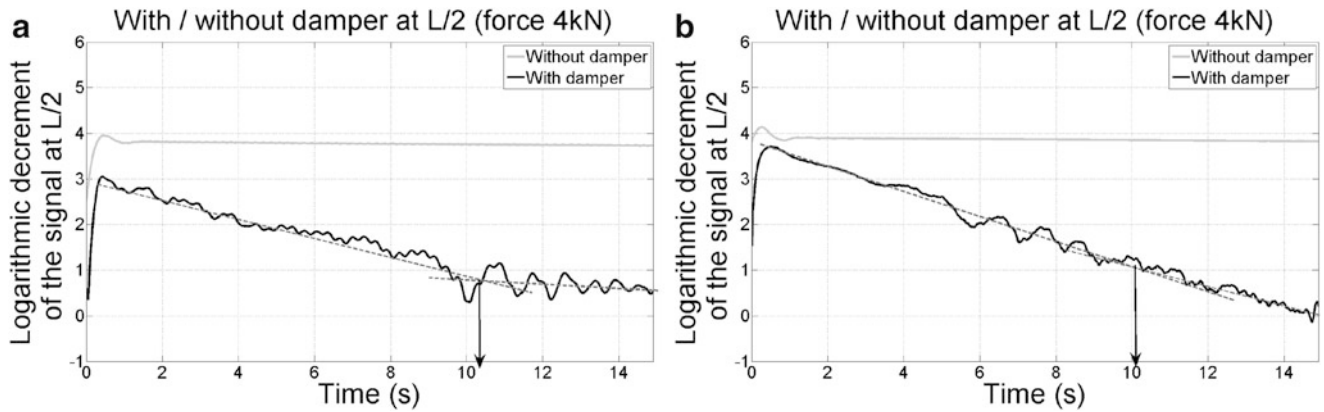


Fig. 11.10 (a) Experimental signal (b) Numerical signal

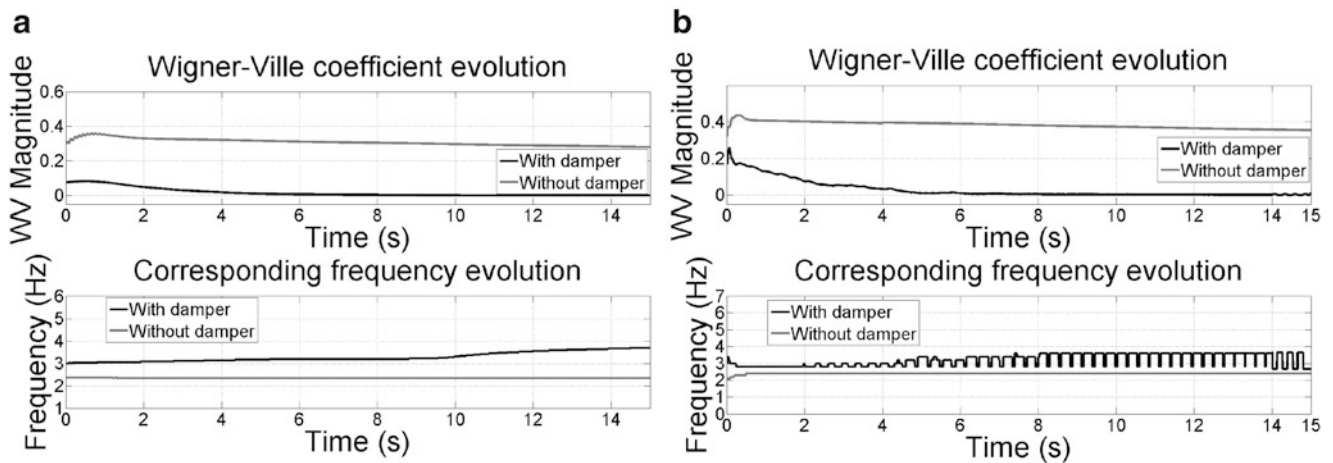


Fig. 11.11 (a) Experimental signal (b) Numerical signal

Wigner-Ville Transform (Fig. 11.11a, b) is used to study the frequency evolution : it shows an increase of the first modal value during damping effect. In Fig. 11.11, the maximum of Wigner-Ville Transform value at each given increment time and the corresponding frequency was extracted from the Wigner-Ville spectrogram. The Fig. 11.11a, b show the decrease of the Wigner-Ville Transform values, corresponding to an energy dissipation. The signal spectrum of the second phase corresponds to the end of the frequency evolution (Fig. 11.8a, b), and the first mode peak has clearly decreased.

Table 11.3 Modal parameters

	Configuration	f_1	F_1	ξ_1
Experimental tests	Without SMA	2.34 Hz	11	0.00033
	With SMA (1 st stage [0, ≈ 10s])	3 Hz	3	0.0116
	With SMA (2 nd stage [≈ 10, 15s])	3.5 Hz	2	0.003
Numerical tests	Without SMA	2.4 Hz	10	0.00036
	With SMA (1 st stage [0, ≈ 10s])	3 Hz	6	0.023
	With SMA (2 nd stage [≈ 10, 15 s])	3.6 Hz	1	0.004

For the cable with SMA damper, f_1 increases from about 2.7 to 3.5 Hz, during the fifteen seconds after releasing of the cable. An interesting observation can be done about the time evolution of the numerical first modal frequency according to the Wigner-Ville Transform : the average frequency increases in the same way than in the experimental case but the frequency takes the “without damper” value of 2.4Hz at each oscillation, during the period when the damper is disabled (stress removed by the code).

On the qualitative point of view, numerical model is in good accordance with experimental observations. One can observe a small difference between the two initial amplitudes which can be explained by an imprecise spatial and time load distribution on the cable at $t=0$, in the numerical model. Once the cable is released by the force, the cable takes a coherent chord-like shape and the two signals become similar.

11.3.2 Modal Parameters Extraction

The relation (11.6) is one solution of the differential equilibrium equation of a chord given in equation (11.2) [10].

$$y(t) = \sum_{n=1}^N A_n \sin\left(\frac{n\pi x}{L}\right) \exp(-2\xi_n \pi f_n t) \sin\left(2\pi f_n \sqrt{1 - \xi_n^2} t + \phi_n\right) \quad (11.6)$$

The parameters of the analytical equation (11.6) providing the displacement of each cable point according to time are : the modal frequencies f_n , the modal damping ratios ξ_n and the amplitudes A_n , associated to each node rank n . One can add the magnitudes of the Fourier frequency spectrum F_n . These parameters are chosen to compare experimental and numerical results. ϕ_n is the modal phase. Only modal parameters values of the first mode ($n = 1$) are presented in the Table 11.3, while its contribution in terms of amplitude is more important in this damper configuration.

Qualitatively, the same phenomenon can be observed, between numerical and experimental results, which shows a coherence between the two approaches of the study. In both approaches for the case “with damper”, the first frequency increases, damping ratio is high and decreases during the signal. The damping phenomenon can be illustrated by the FFT magnitude values.

Quantitatively, numerical results are in good accordance with experimental results, which enables to certify the finite element model. One can observe that the damping ratio is higher for the numerical approach despite low precision offered by the logarithmic decrement method. This comparison can be illustrated by a stronger Wigner-Ville Transform decrease in the previous Fig. 11.11b than in Fig. 11.11a. Furthermore, the NiTi superelastic model whose the parameters are determined on average, overestimates the damping ratio at the beginning of the signal because the strain rate is high and its effects on the hysteresis area are not taken in account. Indeed, the more the strain rate (beyond about 30%/min that is the case here), the less the strain dissipated energy density [15, 25]. The last part of the paper is dealing with the link between damping power and hysteresis loop area, thanks to the Finite Element simulation.

11.3.3 Effect of Energy Dissipation on the Damping Power for the Numerical Approach

The additional damping ratio of the numerical modeling “cable + damper” compared to the numerical cable only can be directly linked to the mechanical energy dissipation of the NiTi wire. The energy dissipation can be quantified by measuring the hysteresis area of the different loops that one can see on the stress-strain curve of the wire in Fig. 11.12. Thus, Piedboeuf

Fig. 11.12 Mechanical behavior of NiTi wire during damping (finite elements)

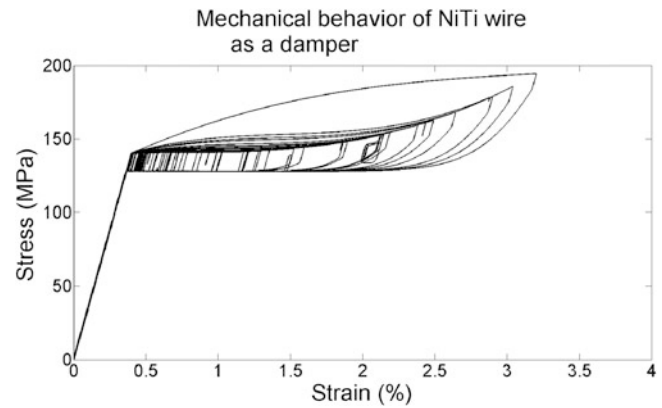
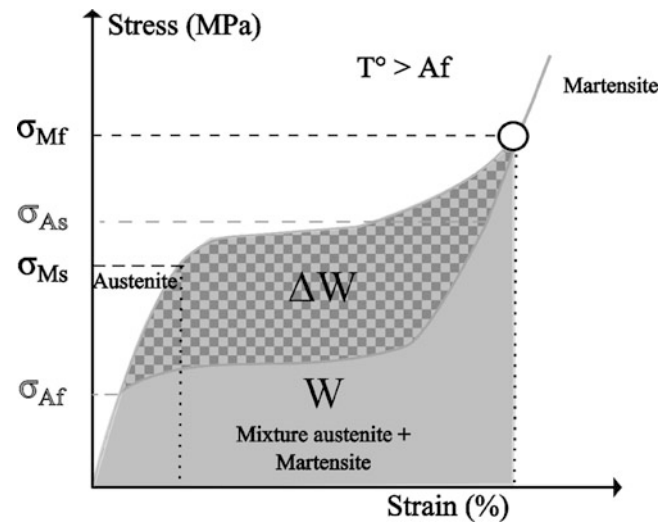


Fig. 11.13 Physical description of energy dissipation



et Gauvin defined, according to the defined variables, presented in Fig. 11.13, the loss factor for a non-linear material by the equation (11.7).

$$\eta = \frac{1}{2\pi} \frac{2\Delta W}{W - \frac{1}{2}\Delta W} \quad (11.7)$$

The approximation of the damping ratio ξ is:

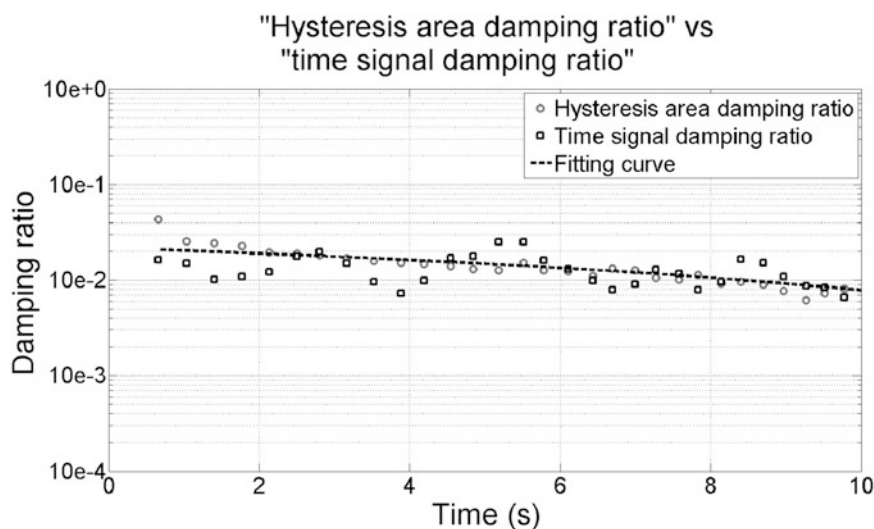
$$\eta = 2\xi \quad (11.8)$$

For the loops in Fig. 11.12, ξ evolution is given in Fig. 11.14.

Damping ratio calculated for each loop hysteresis area slightly decreases, according to the relation (11.7), but not directly with the loop area evolution. This shows that the damping ratio is not directly proportional to the hysteresis loops area but also depends on their “height” on the $\sigma - \epsilon$ plane. The damping ratio evolution can be related with the frequency evolution as considered by Schmidt and Lammering in [26]. Furthermore, the approximated damping ratio purposed by Piedboeuf and Gauvin agrees with the classical damping power calculation of a NiTi-based damping device, given in the previous section, as shown in Fig. 11.14.

One can draw a parallele between the damping ratio phases identified in Fig. 11.10a, b and the two domains undergone. During the first phase, when the damper is established, one can observe the martensitic transformation and a strong damping ratio. During the second phase, only the elastic austenitic domain is undergone and the slope of the decrement logarithmic is equivalent to for the “without damper” configuration (Fig. 11.10). In the second phase, the cable can be considered as totally damped. Here, the border between the two phases is exactly the exit of the last loop, i.e. the end of the last oscillation when the wire stress has reached the yield stress. The second phase can not be plotted in Fig. 11.14 by “hysteresis area damping ratio” method because there is no hysteresis loop left.

Fig. 11.14 Comparison of damping ratio according to time by two means



Better results could be obtained, knowing perfectly the mechanical behavior of the NiTi wires at the start of the experimental tests, which is not the case here for instrumentation practical reasons.

11.4 Conclusion

In this paper, a NiTi-based damping device dedicated to civil engineering cables is presented. A brief description of an application of a simplified SMA damper to mitigate oscillations artificially induced in realistic cables, as well as the corresponding finite element model are detailed. The cable consists of an assembly of beams, while NiTi wire is a single truss element whose a SMA superelastic model is attached. The efficiency of the system is shown and the corresponding finite element transient analysis is validated, as regards modal analysis. The emphasis is layed on the wire mechanical behavior effect on the device damping power, and on its dissipation energy in particular. The points to pay attention to and the future leads to optimize the damper set up on civil engineering cables are mentionned. The improvement of the SMA model could be the key of future works, in order to take in account NiTi strain rate and self-heating phenomena. set up of simplified damping devices could be done on bridges in use.

Acknowledgements Thanks to Daniel Bruhat, Richard Michel, Christophe Mingam and Grégoire Laurence for their participation in the experimental set up and the measurements.

References

1. Matsumoto M, Shiraishi N, Kitazawa M, Knisely C, Shirato H, Kim Y, Tsujii M (1990) Aerodynamic behavior of inclined circular cylinders-cable aerodynamics. *J Wind Eng Ind Aerod* 33(12):63–72
2. Matsumoto M, Shiraishi N, Shirato H (1992) Rain-wind induced vibration of cables of cable-stayed bridges. *J Wind Eng Ind Aerod* 43(1): 2011–2022
3. Matsumoto M, Saitoh T, Kitazawa M, Shirato H, Nishizaki T, Response characteristics of rain-wind induced vibration of stay-cables of cable-stayed bridges. *J Wind Eng Ind Aerod* 57(23):323–333
4. Matsumoto M, Daito Y, Kanamura T, Shigemura Y, Sakuma S, Ishizaki H (1998) Wind-induced vibration of cables of cable-stayed bridges. *J Wind Eng Ind Aerod* 74:1015–1027
5. Matsumoto M, Yagi T, Shigemura Y, Tsushima D (2001) Vortex-induced cable vibration of cable-stayed bridges at high reduced wind velocity. *J Wind Eng Ind Aerod* 89(78):633–647
6. Zuo D, Jones NP (2010) Interpretation of field observations of wind - and rain-wind-induced stay cable vibrations. *J Wind Eng Ind Aerod* 98:73–87
7. Perier V, Dieng L, Gaillet L, Tessier C, Fouvry S (2009) Fretting-fatigue behaviour of bridge engineering cables in a solution of sodium chloride. *Wear* 267(1–4):308–314
8. Perier V, Dieng L, Gaillet L, Tessier C, Fouvry S (2011) Influence of an aqueous environment on the fretting behaviour of steel wires used in civil engineering cables. *Wear* 271:1585–1593

9. Jensen CN (2002) Optimal damping of stays in cable-stayed bridges for in-plane vibrations. *J Sound Vib* 256(1):499–513
10. Chaussin R, Bourmand Y, Chabert A, Demilecamps L, Demonte A, Jartoux P, Labouret P, Le Gall D, Lecinq B, Lefaucheur D, Neant C (2001) Cip recommendations on cable stays. Report, SETRA, Nov 2001
11. Torra V, Isalgue A, Martorell F, Terriault P, Lovey FC (2007) Built in dampers for family homes via sma: An ansys computation scheme based on mesoscopic and microscopic experimental analyses. *Eng Struct* 29:1889–1902
12. Torra V, Isalgue A, Auguet C, Carreras G, Lovey FC, Terriault P, Dieng L (2011) Sma in mitigation of extreme loads in civil engineering: damping actions in stayed cables. *Appl Mech Mater* 82(539):539–544
13. Torra V, Isalgue A, Carreras G, Lovey FC, Soul H, Terriault P, Dieng L (2010) Experimental study of damping in civil engineering structures using smart materials (niti sma): application to stayed cables for bridges. In: 1st international conference on mechanical engineering (ICOME), p 6, Virtual forum, 7–21 May 2010, Zurich, Switzerland
14. Piedboeuf MC, Gauvin R, Thomas M (1998) Damping behaviour of shape memory alloys: strain amplitude, frequency and temperature effects. *J Sound Vib* 214(5):895–901
15. Branco M, Guerreiro L, Mahesh KK, Braz Fernandes FM (2012) Effect of load cycling on the phase transformations in niti wires for civil engineering applications. *Construct Build Mater* 36:508–519
16. Zbiciak A (2010) Dynamic analysis of pseudoelastic sma beam. *Int J Mech Sci* 52:56–64
17. Ben Mekki O, Auricchio F (2011) Performance evaluation of shape-memory-alloy superelastic behavior to control a stay cable in cable-stayed bridges. *Int J Non Lin Mech* 46(1):470–477
18. Bouvet C, Calloch S, LExcellent C (2004) A phenomenological model for pseudoelasticity of shape memory alloys under multiaxial proportional and nonproportional loadings. *Eur J Mech A/Solids* 23:37–61
19. Thai HT, Kim S (2011) Nonlinear static and dynamic analysis of cable structures. *Finite Elem Anal Des* 47:237–246
20. Brignon and Gourmelon (1989) *Les ponts suspendus en france*
21. Newmark NM (1959) A method for computation of structural dynamics. *J Eng Mech (ASCE)* 85(1):67–94
22. Gmur T (1997) *Dynamique des structures 'Structural Dynamics'*. Presses Polytechniques et Universitaires Romandes
23. Marc (2008) Volume A: theory and user information. MSC Software, USA
24. Yu A-T (1952) Vibration damping of stranded cable. *Proc Soc Exp Stress Anal* 9:141–158
25. Dayananda G, Subba Rao M (2008) Effect of strain rate on properties of superelastic niti thin wire. *Mater Sci Eng A* 486:96–103
26. Schmidt I, Lammering R (2004) The damping behaviour of superelastic niti components. *Mater Sci Eng A* 378:70–75

Chapter 12

Using Pall Friction Dampers for Seismic Retrofit of a 4-Story Steel Building in Iran

Seyed Mehdi Zahraei, Alireza Moradi, and Mohammadreza Moradi

Abstract Past earthquakes in Iran have caused severe damage to existing steel buildings without adequate resistance and ductility against earthquakes. Competent methods for seismic retrofitting are required in order to prevent damage and casualty. Among effective seismic retrofit methods, passive control reduces seismic vulnerability by mitigating seismic demand and increasing ductility. One of the most suitable methods in passive control system is to use pall friction damper in the braced steel structures. Main advantage of this friction damper is its almost rectangular force-deformation hysteretic loops with high-energy dissipations, without any need to specific technology. In this paper, while introducing the performance of pall friction dampers and their design, seismic retrofit of an existing 4-story steel simple frame in Iran is investigated by using such dampers.

Keywords Seismic design and retrofit • Pall friction damper • Passive control • Ductility • Steel frame

12.1 Introduction

All the damages and losses during recent severe earthquakes have caused the concern of finding an appropriate solution to stand against this natural disaster. Nowadays, applying new methods in structural seismic design, and improving the quality of the structural materials, are among the common approaches to accomplish this objective. Recent methods, which are based on distributing energy in structures, have been developed to control seismic vibrations and reduce the effect of the earthquake force. The large amount of energy is exerted into the structures during an earthquake, including potential and kinetic energy, which somehow needs to be damped in the structure. If there is no damping system, the structure vibrates continuously. But, in practice there is a damping system caused by structural properties, which creates some reactions against structural vibration. Moreover, performance of the building can be improved by installing an energy absorber (damper). In this method, dampers absorb and dissipate part of the earthquake energy.

In this study, first, seismic vibration control of structures is presented and then, by considering friction dampers as one of the seismic vibration control methods, analytical evaluation of the effects of Pall friction dampers on the seismic response of the steel frame during earthquake is discussed.

S.M. Zahraei • A. Moradi
Department of Civil Engineering, Islamic Azad University, Central Tehran Branch, Tehran, Iran

M. Moradi (✉)
College of Natural and Applied Sciences, University of Guam, Mangilao 96923, Guam
e-mail: mremoradi@gmail.com

12.2 Seismic Vibration Control of Structures

Structural vibration control is actually an attempt to reduce structural displacement or acceleration, which are the main sources of structural damage during earthquake. There are several classifications to facilitate investigations about different control systems. These classifications are based on either dynamic properties of structures or location and distribution of the control system in the structures. Based on the latter classification, there are four control systems: Passive, Active, Semi-Active and Hybrid.

12.2.1 *Passive Control Systems*

A passive control system operates without requiring an external power source. This system consists of one or more devices designed to modify the structural properties such as ductility and stiffness and dissipate energy, leading to reduction in structural vibrations. Friction damper is a type of passive Control system [1].

12.2.2 *Active Control Systems*

Unlike passive control system, active control systems require an external power source for operation and controlling structural vibrations. In these systems, special devices generate and apply forces to the structure. These forces act opposite direction of the destructive forces and work as a damper. These systems need special equipments such as hydraulic actuator (as the external stimulator) and accurate control systems (sensitive receptor and hardware and software equipment) [1].

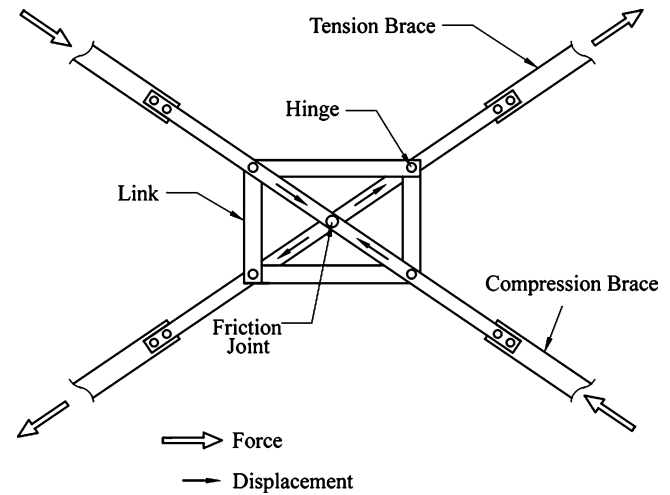
12.2.3 *Semi-Active Control Systems*

Comparing the performance of the active and passive control systems leads to development of semi-active control systems. In this system, the control force is developed through appropriate adjustment of the mechanical properties of the semi-active control system devices without applying external forces. These devices can be defined as the passive control dampers. Since these devices are able to actively control the vibration without requiring high-level external power force, they have been used a lot recently. Some of these semi-active systems have the ability to operate just by using battery, which is a remarkable property, since it is probable that the main power source becomes disconnected during earthquake [1].

12.2.4 *Hybrid Control Systems*

Using the combinations of active and passive control is called hybrid control system. The objective of developing such a system is to enhance the efficiency of the passive control system and to reduce the required external power in active control system. These systems work similar to active control systems during low amplitude excitation (weak and medium earthquake). Actually in low amplitude excitation, external excitation is not large enough for appropriate performance of the passive control systems and active control system operates just by low level of external force. The hybrid control systems work similar to passive control systems during high amplitude excitation (strong earthquake). During high amplitude excitation, active control systems do not perform properly because of the saturation limits on generating external power while the passive control system operates efficiently. Although, hybrid control system are more expensive, they are more efficient and have a better performance than the passive and active control system [1].

Fig. 12.1 Details of the Pall friction damper



12.3 Pall Friction Dampers

The most effective, reliable and economical method to dissipate energy and extract kinetic energy from a moving body is the friction brake. In 1979, the principle of friction brake inspired Pall and his colleagues and they started to develop the friction dampers for structures. Actually, friction dampers use the mechanism of solid frictions to dissipate energy. Similar to automobiles, the motion of vibrating building can be reduced by dissipating energy in friction. These studies led to the development of the Pall friction damper in 1982 [2, 3].

The Pall friction damper is made of a set of special steel plates, which can create the convenient frictional performance. These plates are bolted together with a high strength screws and they are designed not to slip during wind. These dampers slide over each other at the determined optimum slip load prior to yielding of structural members and dissipate the big portion of the earthquake energy. This makes the structure remain in the elastic range or delay the yielding of the structural member during major earthquake [4]. Figure 12.1 shows the details of the pall friction damper.

Figure 12.2 shows five stages of behavior of the pall friction dampers during a typical load cycle including deformed shape of the frame in each stage. Response of the frame member in each stage is described below [5]:

First stage: Both braces are active and behave elastically in tension and compression.

Second stage: The compression brace buckles while the tension brace continues to behave elastically in tension.

Third stage: Before yielding is started in the tension brace, the device is designed to slip. When slippage occurs, the four links are activated and deform into a rhomboid shape; this deformation pattern eliminate the buckled shape of the compression brace. Therefore, after the slippage, the compression brace is still straight and the axial force in compression brace equals to buckling load.

Fourth stage: The straightened brace can immediately absorb energy in tension when the load is reversed.

Fifth stage: Load in brace 1 becomes more than the buckling load and the second stage is repeated. This is followed by the third stage and cycle is completed.

It should be noted that the Pall friction dampers works properly if the device slips before the structural members and tensional brace yields or compressive brace deforms significantly. Moreover, to be more efficient, slip load should be set such that the friction mechanism does not work during weak and medium earthquakes [5].

12.4 Using Pall Friction Dampers to Retrofit a 4-Story Steel Frame

In this study, one of the internal frames of a 4-story steel frame is chosen for retrofitting. Since the old buildings in Iran do not have bracing as the lateral resistance system, a simple frame with hollow-tile as the floor system is considered. It should be mentioned that the existing infill panel is considered as a support for lateral resistance system. The building is hospital in a region with high risk of earthquake and the soil is type 3. Since the building is old, it was just designed for gravity load and not the lateral load. Dead load for the floors and roof are 650 and 600 kg/m² respectively and live load for the floors

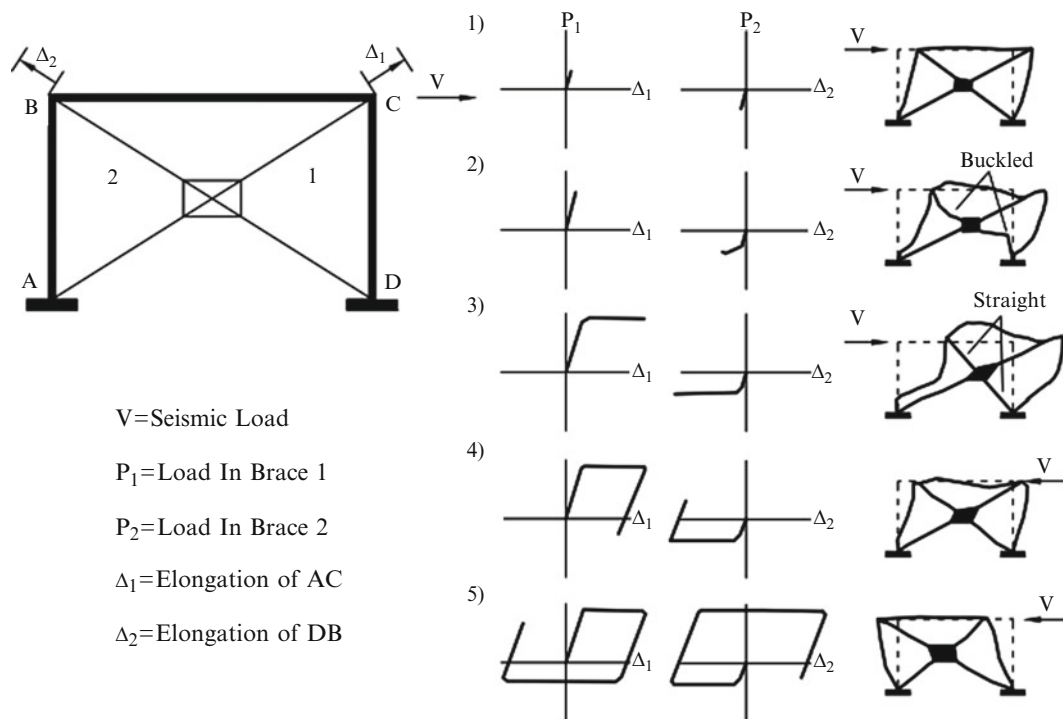


Fig. 12.2 Idealized hysteretic behavior of a simple one-storey friction damped frame [5]

and roof are 300 and 150 kg/m^2 respectively. These values are defined based on the Iranian National building regulation part 6: Loading. Figure 12.3 shows location of pall friction dampers in the frame and floor plan. All the spans are 5 m and each storey has 3 m height in the steel frame. Frame was designed using ETABS-9.1.4 based on AISC-ASD89 specification. Table 12.1 shows the information of the structural members.

12.5 Design of the Pall Friction Damper

The crucial part of the design of friction dampers is to determine the optimum slip load. The movement of the damper in an elastic brace constitutes nonlinearity. Moreover, the amount of energy dissipation is proportional to the displacement. Therefore, nonlinear time history dynamic analysis, which is used in this study, is an accurate procedure to find the value of the optimum slip load. In this method, structural response can be evaluated during and after earthquake [3, 6].

Hysteresis loop of the damper is similar to the rectangular loop of the material with elastic perfectly plastic behavior. Therefore, sliding load is considered as virtual yielding force in bracing. PERFORM-3D [7] is used for nonlinear time history dynamic analysis of the frame with the dampers. The analyses are based on the Iranian Standard Seismic Code No. 2800 third edition [8]. Three accelerographs, as presented in Table 12.2, are used in these analyses. H1 components are used for the analysis of this study.

In the analyses, yielding stress of the brace in tension is assigned equal to the stress in braces during sliding. The maximum displacements of the stories are considered as the frame response in nonlinear dynamic analysis. This procedure is performed for different values of yielding stress in tension. The sliding design load, which corresponds to the minimum structural response, is considered as the optimum sliding load.

Figure 12.4 shows the maximum story drift in terms of sliding load. It can be seen that displacement is reduced by increasing the sliding load and after passing the sliding load of 25 ton , displacement increases. Therefore, optimum sliding load is equal to 25 ton in all the stories.

Fig. 12.3 Location of the Pall friction damper in the frame and floor plan

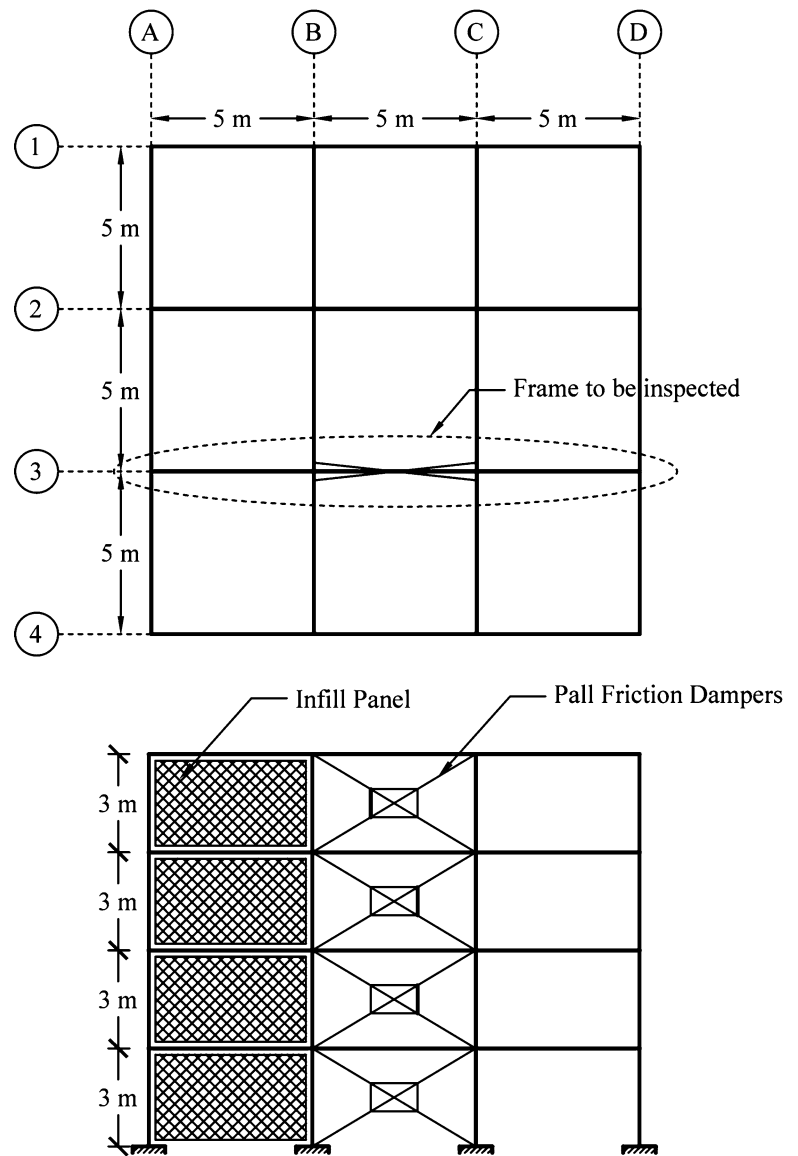


Table 12.1 Specification of the frame members

Floor	Beams	Interior columns	Exterior columns
4	IPE330 + PL120 × 5	BOX 100 × 5	BOX 100 × 5
3	IPE330 + PL130 × 10	BOX 150 × 10	BOX 120 × 8
2	IPE330 + PL130 × 10	BOX 150 × 10	BOX 120 × 10
1	IPE330 + PL130 × 10	BOX 200 × 10	BOX 150 × 10

Table 12.2 Specification of the earthquake records

Earthquake	Year	Station	Direction	PGA (g)	Soil type	Duration (s)
Tabas	1978	9101	H1	0.836	III	32.84
			H2	0.852		
Imperial Valley	1979	Bonds Corner	H1	0.588	III	37.61
			H2	0.775		
Cape Mendocino	1992	89156 Petrolia	H1	0.590	III	36
			H2	0.662		

Fig. 12.4 The maximum story drift in terms of slip force under the Tabas earthquake

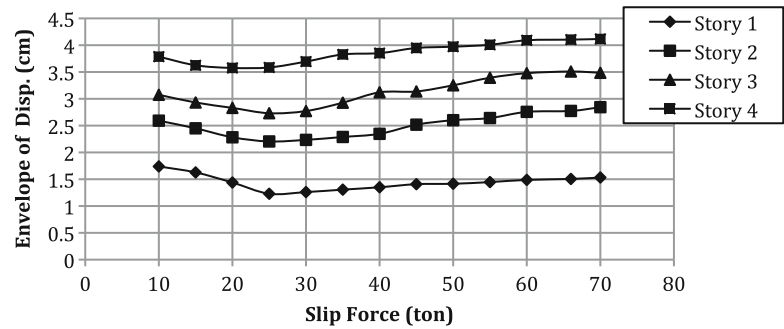
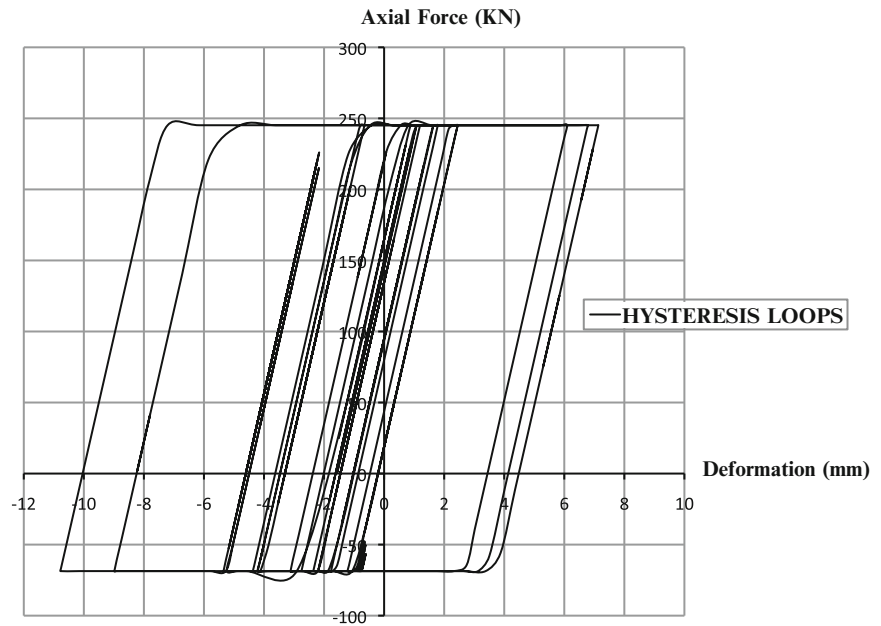


Fig. 12.5 Hysteresis loop of the Pall friction damper under Tabas earthquake



12.6 The Effect of the Pall Friction Damper on the Roof Lateral Displacement

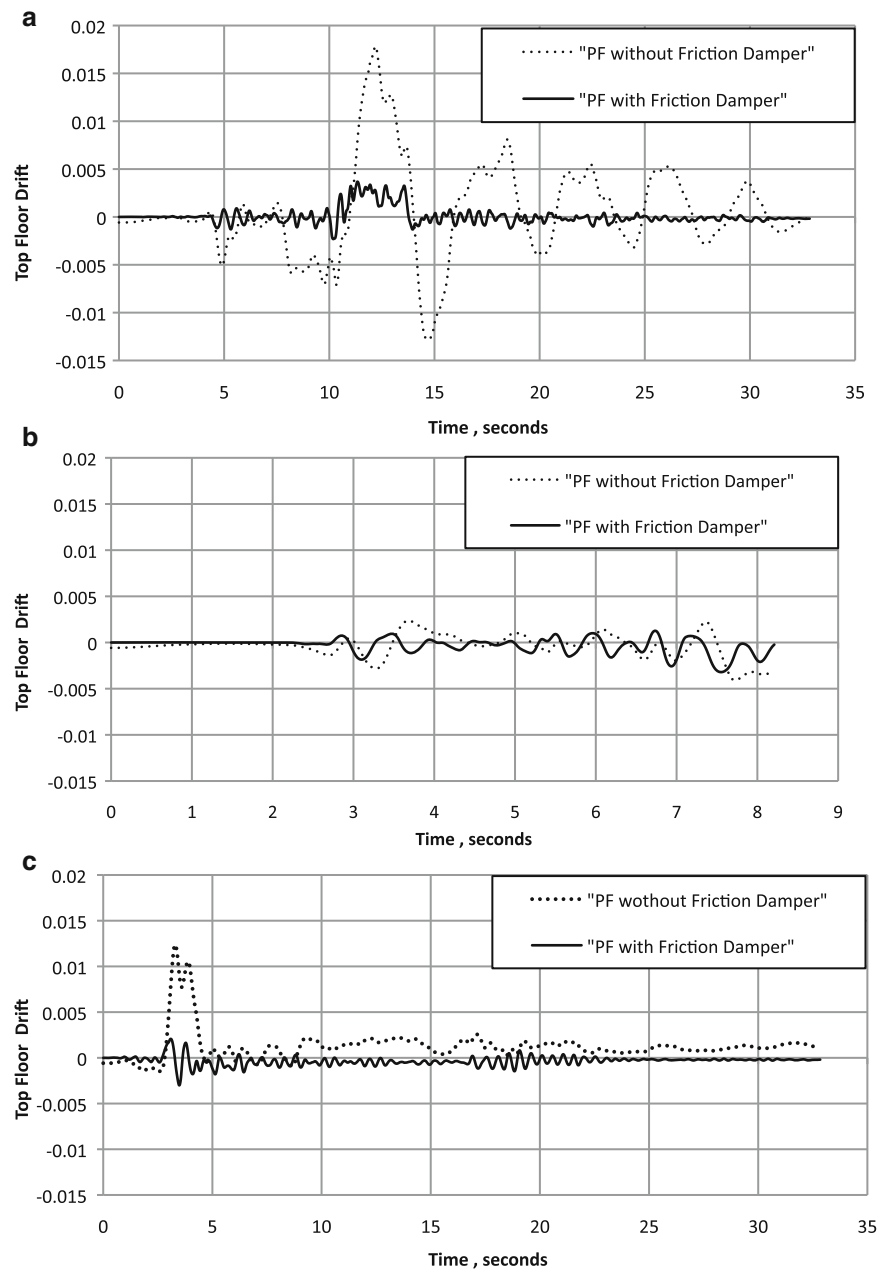
Figure 12.5 shows the hysteresis loop of the Pall friction damper under Tabas earthquake. The area under this hysteresis graph represents the amount of the energy, which is absorbed by the friction damper. Figure 12.6 shows top floor drift for the frame with and without Pall friction damper under the Tabas, Imperial Valley and Cape Mendocino earthquake. As a case in point, it can be seen that installing Pall friction damper in the frame reduces the maximum displacement 80% for Tabas earthquake. This reduction is the result of the frame ductility caused by Pall friction damper absorbing in fact most portion of the earthquake energy that means the beams and columns absorb less energy and remain in elastic range. This leads to reduction of floor drift in the frame with Pall friction damper compared to the simple frame without Pall friction dampers.

12.7 Conclusion

Since Pall friction dampers are cheap and have simple mechanism, they are considered as one of the decent methods in structural vibration control. In this paper, a simple 4-story steel frame, which had a weak performance against earthquake, was retrofitted by adding pall friction damper. Nonlinear time history dynamic analysis was performed on the frame by applying the Tabas, Imperial Valley and Cape Mendocino earthquake based on the 2800 Iranian seismic code. Here is the result:

- Optimum sliding load equal to 25 ton is achieved by performing time history dynamic analysis
- Top floor drift is reduced in the frame with Pall friction damper compared to the frame without damper. This is the reason of dissipation of large portion of the earthquake energy by Pall friction damper.

Fig. 12.6 Top floor drift for the frame with and without Pall friction damper under the (a) Tabas (b) Imperial Valley (c) Cape Mendocino earthquake



References

1. Dole M (1995) Passive control of structure. In: Duma G (ed) Proceeding of 10th European conference on earthquake engineering, Rotterdam, pp 1903–1912
2. Soong TT, Dargush GF (1997) Passive energy dissipation systems in structural engineering, 1st edn. Wiley, Chichester
3. Pasquin PT (2002) Friction damper for seismic rehabilitation of Eaton building Montreal. In: 4th structural specialty conference of Canadian society for civil engineering, 2002, Montreal, Canada
4. Friedrichs B (1997) Dampers do the job at Davis. ASCE J Struct 67(9):2A–5A
5. Cherry S, Filiatrault A (1993) Seismic response control of building using friction dampers. EERI Earthquake Spectra 9(3):447–466
6. Pall RT, Pall A, Leboeuf N, Pasquin C (2004) Friction damper for seismic rehabilitation of Eaton building, Montreal. In: Thirteenth world conference on earthquake engineering, Vancouver, Paper No.1949, 2004
7. Powell G (2006) RAM PERFROM-3D Version 4.0.1 user guide, Ram International, 2006
8. Building and Housing Research Center (2005) Manual for design building in Iran against earthquake, 3rd edn. Standard No. 2800

Chapter 13

Modal Identification of a 5-Story RC Building Tested on the NEES-UCSD Shake Table

Rodrigo Astroza, Hamed Ebrahimian, Joel P. Conte, Jose I. Restrepo, and Tara C. Hutchinson

Abstract A full scale five-story reinforced concrete building was built and tested on the NEES-UCSD shake table. The purpose of this experimental program was to study the response of the structure and nonstructural systems and components (NCSSs) and their dynamic interaction during seismic excitation of different intensities. The building specimen was tested under base-isolated and fixed-based conditions. In the fixed-based configuration the building was subjected to a sequence of earthquake motion tests designed to progressively damage the structure. Before and after each seismic test, ambient vibration data were recorded and additionally, low amplitude white noise base excitation tests were conducted at key stages during the test protocol. A quasi-linear response of the building can be assumed due to the low intensity of the excitation and consequently modal parameters might change due to the structural and nonstructural damage. Using the vibration data recorded by 72 accelerometers, three system identification methods, including two output-only (SSI-DATA and NExT-ERA) and one input-output (DSI), are used to estimate the modal properties of the fixed-base structure at different levels of structural and nonstructural damage. Results allow comparison of the identified modal parameters obtained by different methods as well as the performance of these methods and studying the effect of the structural and nonstructural damage on the dynamic parameters. The results show that the modal properties obtained by different methods are in good agreement and that the effect of structural/nonstructural damage is clearly evidenced via the changes induced on the estimated modal parameters of the building.

Keywords System identification • Full-scale specimen • Shake table test • Structural damage • Non-structural components

13.1 Introduction

Vibration-based damage detection has attracted attention in the field of earthquake engineering over the past 30 years because it potentially allows to identify and locate the damage by means of studying the variation of the dynamic characteristics of a structure from an initial state to a state after the structure has been excited by natural or human-made loads, or simply because the structure has suffered aging or cumulative deterioration in some components. Experimental and operational modal analyses are the main techniques to estimate the modal parameters (natural frequencies, damping ratios and mode shapes) from recorded structural vibration data. The identification results can be further used to apply vibration-based damage detection techniques, comparing the modal properties at different damage states of a structure. A comprehensive and detailed literature review on vibration-based damage detection can be found in [1, 2].

R. Astroza (✉)

University of California, 9500 Gilman Drive, San Diego, CA, 92093 USA

Universidad de Los Andes, Av. San Carlos de Apoquindo 2200, LAs Condes, Santiago, Chile

e-mail: rastroza@ucsd.edu

H. Ebrahimian • J.P. Conte • J.I. Restrepo • T.C. Hutchinson

University of California, 9500 Gilman Drive, San Diego, CA, 92093 USA

e-mail: hebrahim@ucsd.edu; jpconte@ucsd.edu; jrestrepo@ucsd.edu; tahutchinson@ucsd.edu

In the case of buildings structures, because of the high risk and difficulty to perform progressive damage tests as well as the scarcity of heavily damaged and densely instrumented buildings, shaking table tests have produced important, high quality and unique data to assess the dynamic properties of buildings at different states of damage [3–6].

In this study the measured vibration response of a full-scale five-story reinforced concrete (RC) frame building outfitted with a wide range of nonstructural components and systems (NCSs), built and tested on the Network for Earthquake Engineering Simulation at the University of California San Diego (NEES-UCSD) shake table, is analyzed. The modal properties of the test specimen are identified using output-only and input-output methods with ambient vibration and low amplitude white noise base excitation data at different damage states, which were induced by seismic base excitations of increasing amplitude.

13.2 Description of the Specimen

The test building is a full-scale 5-story cast-in place reinforced concrete frame building (special moment resisting frame). It has two bays in the longitudinal direction (direction of shaking) and one bay in the transversal direction, with plan dimensions of 6.6 by 11.0 [m]. The building has a floor-to-floor height of 4.27 m, a total height, measured from the top of the foundation to the top of the roof slab, of 21.34 [m] and an estimated total weight of 4420 [kN], including the structure and all nonstructural components but excluding the foundation (which has a weight of 1870 [kN] approximately). A pair of identical moment resisting frames in the North and South bays provides the seismic resisting system. Different structural detailing is adopted for the beams located at the different floors, however, their strengths are consistent at each floor. The specimen has six 66×46 [cm] columns reinforced with 6#6 and 4#9 longitudinal bars and a prefabricated transverse reinforcement grid (baugrid). The floor system consists of a 20.3 [cm] thick conventionally reinforced concrete slab at all levels. There are two main openings on each slab to accommodate a steel stair assembly and a functioning elevator, each of which run the full height of the building. Two transverse concrete walls 15.2 [cm] thick provide the support for the elevator guiderails. Detailed information about the structural system, nonstructural components and their design considerations can be found in [7]. Figure 13.1 shows the test specimen and schematic plan and elevation views.

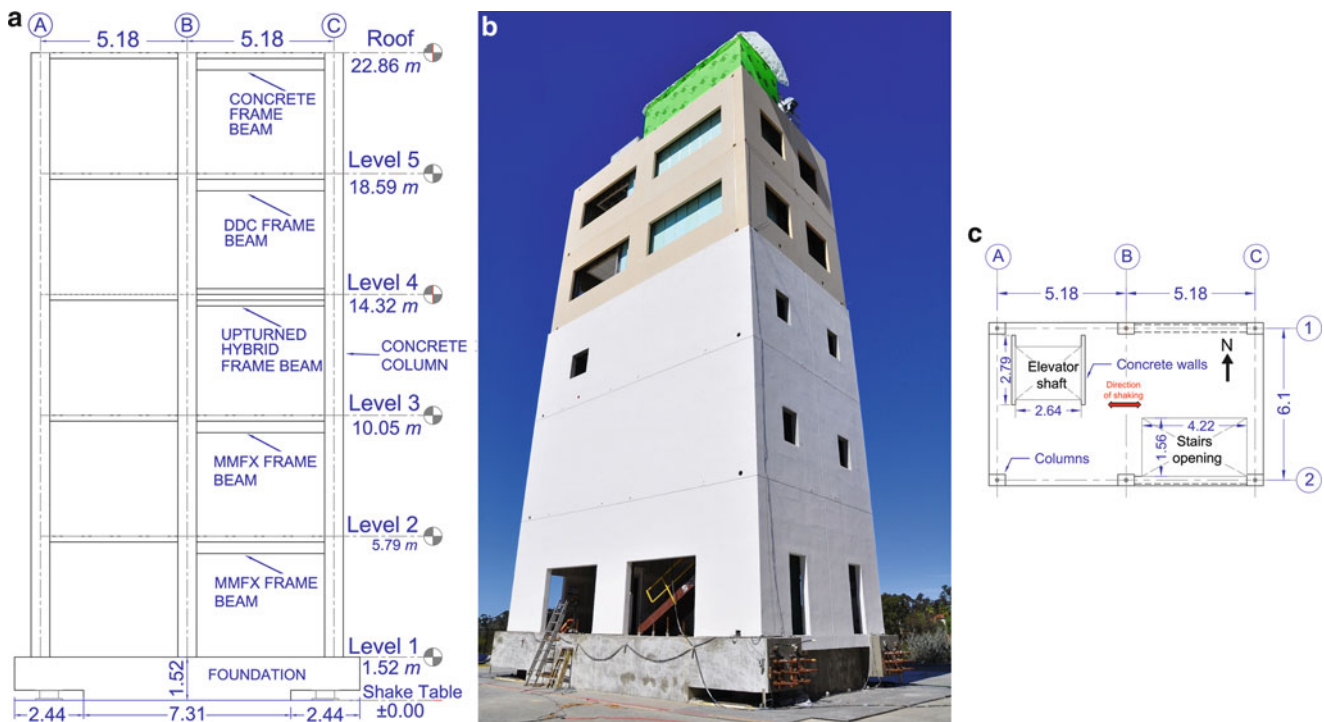


Fig. 13.1 Test specimen (a) schematic South elevation view, (a) completed structure, (c) schematic plan view

13.3 Instrumentation Plan and Dynamic Tests

13.3.1 Instrumentation Plan

A dense accelerometer array is deployed in the building, consisting of four triaxial accelerometers per floor (one at each corner). In addition, two triaxial accelerometers are installed on the platen of the shake table and one at the bottom of the foundation block of the shake table. In this study, the acceleration response of the building measured by the 72 accelerometers is used to identify the dynamic properties of the test specimen. The data are sampled at 200 Hz and the acceleration time series are detrended and filtered using a band-pass order 4 IIR Butterworth filter with cut-off frequencies at 0.15 and 25 Hz, frequency range which covers all the modes participating significantly in the response of the system.

13.3.2 Dynamic Tests

A sequence of dynamic tests is applied to the building during the period of seismic testing of the fixed-base structure (May 2012), including ambient vibration and forced vibration tests (low amplitude white noise and seismic base excitations) using the NEES-UCSD shake table. The seismic input motions correspond to spectrally matched motions, except the ICA motion, which were defined using different seed records. The input motions are defined based on global and local performance criteria with selection and order of application targeted towards progressively damaging the building-nonstructural system. Ten minutes of ambient vibration data are collected before and after each seismic test. In addition, white noise base excitation is imposed on the structure at key states of damage. Table 13.1 summarizes the seismic test protocol and the recorded data used in this study.

13.4 System Identification Methods

In order to estimate the modal properties of the building specimen at different damage states, two state-of-the-art output-only system identification methods, both assuming broad-band excitation, are used for the ambient data: Data-Driven Stochastic Subspace Identification (SSI-DATA) and Natural Excitation Technique combined with Eigensystem Realization Algorithm (NExT-ERA). For the low amplitude white noise base excitation data, in addition to the two abovementioned output-only methods, one input-output method is considered: Combined Deterministic-Stochastic Subspace Identification (DSI).

Table 13.1 Dynamic data used in this study

Date	Description	Name	Damage state
May 7, 2012	Ambient vibration 1	AMB1	DS0
	6 min WN (1.5%g RMS)	WN1A	DS0
	<i>Canoga Park (1994 Northridge earthq.)</i>	<i>FB:1-CNP100</i>	
May 9, 2012	Ambient vibration 2	AMB2	DS1
	<i>LA City Terrace (1994 Northridge earthq.)</i>	<i>FB:2-LAC100</i>	
	Ambient vibration 3	AMB3	DS2
May 11, 2012	<i>ICA 50% (2007 Pisco earthq.)</i>	<i>FB:3-ICA50</i>	
	Ambient vibration 4	AMB4	DS3
	<i>ICA 100% (2007 Pisco earthq.)</i>	<i>FB:4-ICA100</i>	
May 15, 2012	6 min WN (1.5%g RMS)	WN2A	DS4
	Ambient vibration 5	AMB5	DS4
	<i>TAPS Pump Station 67% (2002 Denali earthq.)</i>	<i>FB:5-DEN67</i>	
May 15, 2012	6 min WN (1.5%g RMS)	WN3A	DS5
	Ambient vibration 6	AMB6	DS5
	<i>TAPS Pump Station 100% (2002 Denali earthq.)</i>	<i>FB:6-DEN100</i>	
	Ambient vibration 7	AMB7	DS6

The three methods used in this paper work with the state-space formulation of the equation of dynamic equilibrium (state equation), which, in conjunction with the measurement equation, define the state-space model:

$$x_{k+1} = A_d \times x_k + B_d \times u_k + w_k \quad (13.1)$$

$$y_k = C_d \times x_k + D_d \times u_k + v_k \quad (13.2)$$

Where x_k : state vector at time k

y_k : output vector at time k

w_k : process noise vector at time k

B_d : discrete input matrix

D_d : discrete direct feed-through matrix

u_k : input vector at time k

v_k : measurement noise vector at time k

A_d : discrete state matrix (dynamical system matrix)

C_d : discrete output matrix

From the relationship between the discrete and continuous state matrices ($A_d = e^{A_c \times \Delta t}$, where Δt is the sampling time) it can be proven that their eigenvectors (Ψ) are identical, while the continuous and discrete eigenvalues (λ_i and μ_i respectively) satisfy the condition:

$$\lambda_i = \frac{\ln(\mu_i)}{\Delta t} \quad (13.3)$$

Then, from the eigenvalues and eigenvectors of the discrete state matrix (A_d) and the discrete output matrix (C_d), the modal frequencies, modal damping ratios and mode shapes of the system can be obtained by using respectively:

$$\omega_i = |\lambda_i| \quad \xi_i = -\frac{\text{Re}(\lambda_i)}{|\lambda_i|} \quad \Phi = C_d \times \Psi \quad (13.4)$$

SSI-DATA and NEXT-ERA correspond to output-only system identification methods ($u_k = 0$ in Eq. 13.1) while DSI is an input-output method. The three methods assume that v_k and w_k are zero-mean white vectors. The order of the model is defined by using stabilization diagram, with criteria of $\Delta f \leq 1\%$, $\Delta \xi \leq 5\%$ and $(1-\text{MAC}) \leq 2\%$. Exhaustive explanations for SSI-DATA, DSI and NEXT-ERA can be found in [8] and [9].

13.5 System Identification Results

13.5.1 System Identification Based on Ambient Vibrations

Figures 13.2 and 13.3 show the natural frequencies and damping ratios obtained for the ambient vibration data recorded at different damage states using SSI-DATA and NEXT-ERA. It can be seen that the natural frequencies estimated by SSI and NEXT-ERA are in very good agreement for all the damage states. Also, the natural frequencies decrease as the damage increases in the system. The higher modes seem to be less sensitive to low levels of damage than lower modes, which begin to decrease from the initial states of damage.

The damping ratios have a good agreement, being better at lower modes than higher modes, however their variability is larger than those of the natural frequencies. The estimated damping ratios do not show a clear trend as the damage progresses, but they are in the range 0–5%, which is in agreement with previous studies in similar structures.

It is important to note that in the undamaged state (DS0), the lowest frequency corresponds to the mode 1–T+To. Because the seismic motions excite the building along its longitudinal direction, from DS1 onwards, mode 1–L has the lowest associated natural frequency (see Fig. 13.2). This is because most of the structural and nonstructural damage is produced in the direction of seismic excitation; therefore the lateral stiffness in this direction degrades faster than the transversal direction. A similar observation can be observed for the higher modes (2–T+To, 2–L and 2–L+To).

Since the mode shapes identified with the methods used in this work are complex-valued, the realized modes are computed using the method proposed by [10]. The polar plot of the mode shapes are shown in Fig. 13.4, while the realized modes are

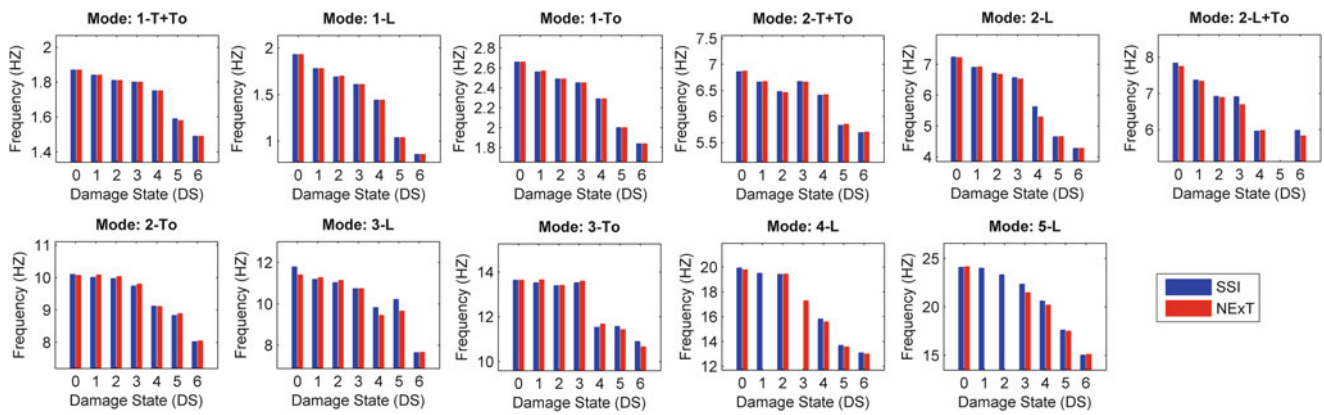


Fig. 13.2 Natural frequencies identified using ambient vibration data at different damage states

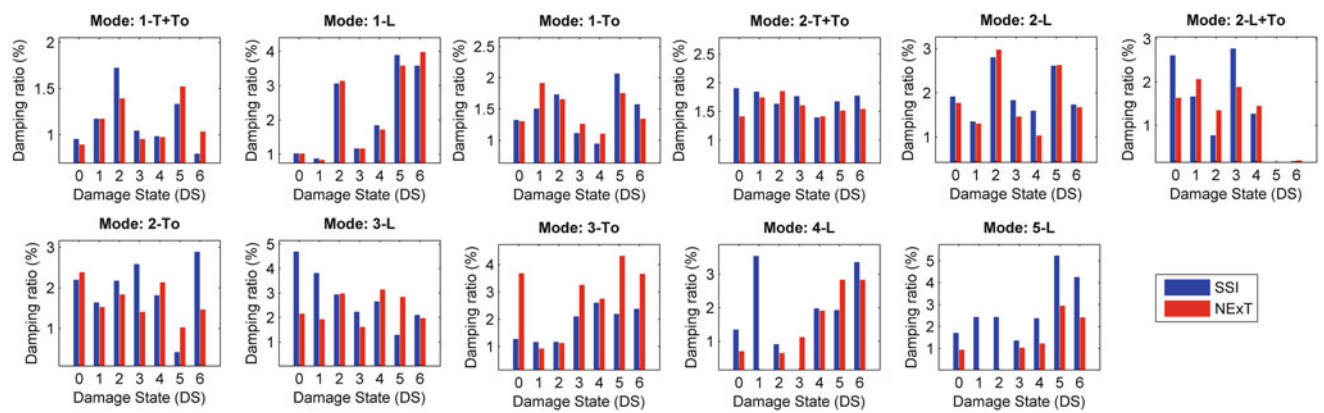
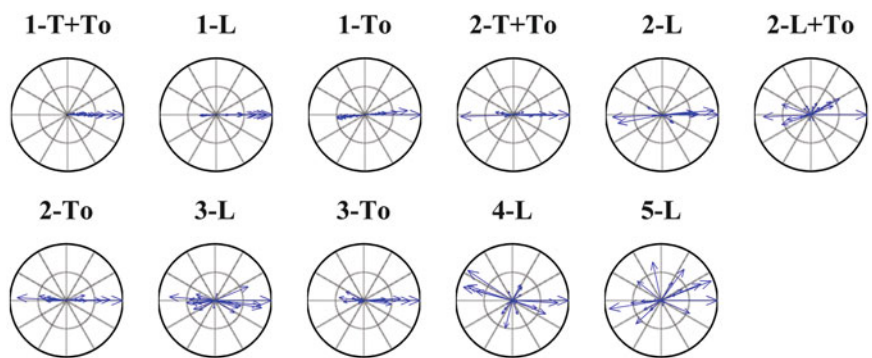


Fig. 13.3 Damping ratios identified using ambient vibration data at different damage states

Fig. 13.4 Polar plot for AMB1 (undamaged structure DS0) using SSI-DATA



presented in Fig. 13.5. It is observed that the first five longitudinal, the first three torsional and two coupled translational-torsional modes can be identified using the ambient vibration data, and most of these mode shapes are identified as almost perfectly classically-damped.

The MAC coefficient proposed by [11] is used to compare the modes shapes estimated by SSI and NExT-ERA for the test AMB1 (Fig. 13.6). Most of the values in the diagonal (corresponding modes) reach values close to one, therefore it can be concluded that the mode shapes between both methods are consistent. A similar pattern is repeated for all the states of damage. In the same way to the damping ratios, the agreement between mode shapes is better for the lower modes than for the higher modes. This is due to the fact that the participation of the higher modes is less compare to the lower modes and consequently the signal-to-noise-ratio (SNR) is lower for the higher modes.

Fig. 13.5 Mode shapes identified for AMB1 (undamaged state DS0) using SSI-DATA

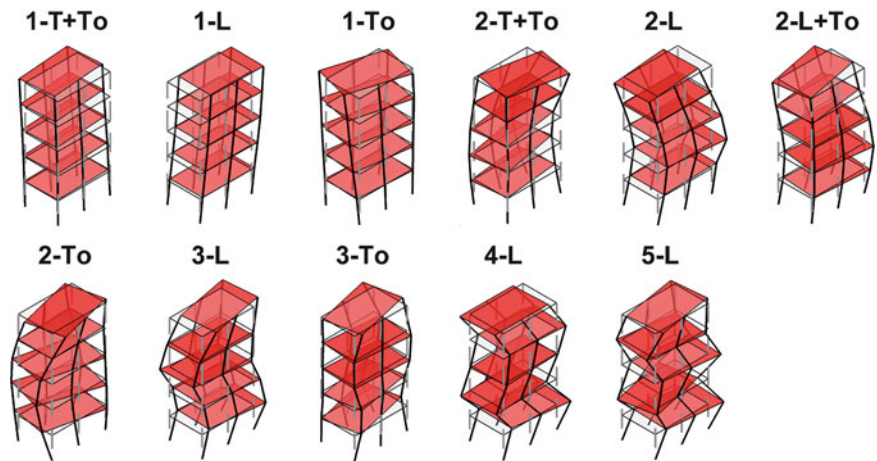
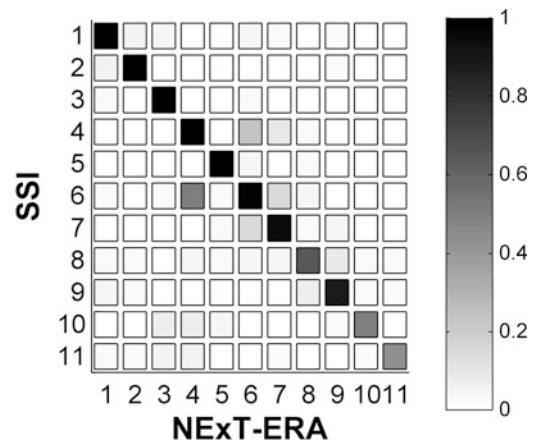


Fig. 13.6 MAC values for AMB1 (undamaged state DS0)



13.5.2 System Identification Based on White Noise RMS = 1.5 %g

At damage states DS0, DS4 and DS5, 6 min of white noise base excitation with a RMS acceleration of 1.5 %g was applied to the test specimen. Figures 13.7 and 13.8 show the natural frequencies and damping ratios obtained for the white noise data recorded at the three damage states using SSI-DATA, NExT-ERA and DSI. Similar to the case of ambient vibrations, the natural frequencies estimated by the different methods are in very good agreement and they decrease as the damage progresses in the system, however frequencies associated with the longitudinal modes have greater reductions than the other modes. This is because, as explained before, most of the structural and nonstructural damage is produced in the direction of the excitation. It is noticed that for all the white noise tests, the mode with the lowest natural frequency corresponds to the first longitudinal mode (1-L). Comparing the natural frequencies obtained by ambient vibration and white noise data at the same damage states, it is seen that they decrease in a similar percentage if they are normalized with the respective undamaged state DS0.

The damping ratios are higher than the corresponding values obtained using ambient vibrations, but the discrepancies between the methods are also larger, especially between the output-only and input-output methods. The estimated damping ratios do not show a clear trend as the damage progresses and they are in the range of 0–10%. The longitudinal modes present higher values of damping ratio.

The polar plot of the mode shapes are shown in Fig. 13.9, while the realized modes are presented in Fig. 13.10. Most of the mode shapes, especially the lower modes, are practically classically damped and by comparing the mode shapes obtained from ambient vibration and white noise data it can be seen that they are in good agreement. Because the excitation of the white noise is only in the longitudinal direction of the building, the identification process of the modes having components in the transversal direction (including torsional modes) is more difficult than the identification of the longitudinal modes.

The MAC coefficient is used to compare the modes shapes identified by the three different methods (Fig. 13.11). Most of the values in the diagonal (corresponding modes) reach values close to one, therefore it can be concluded that the mode

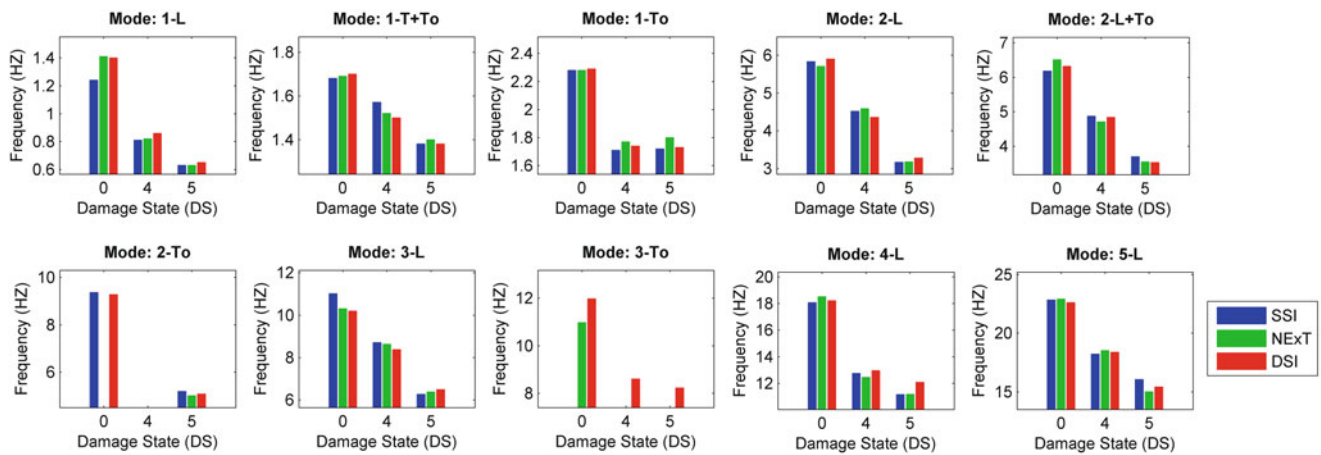


Fig. 13.7 Natural frequencies identified using ambient WN data ($RMS = 1.5\%g$) at different damage states

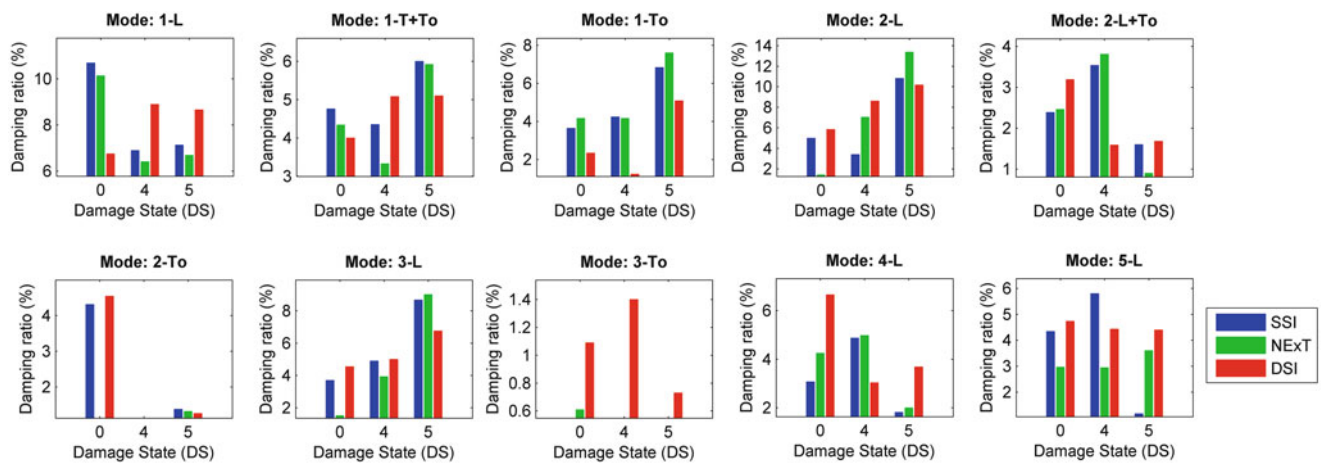
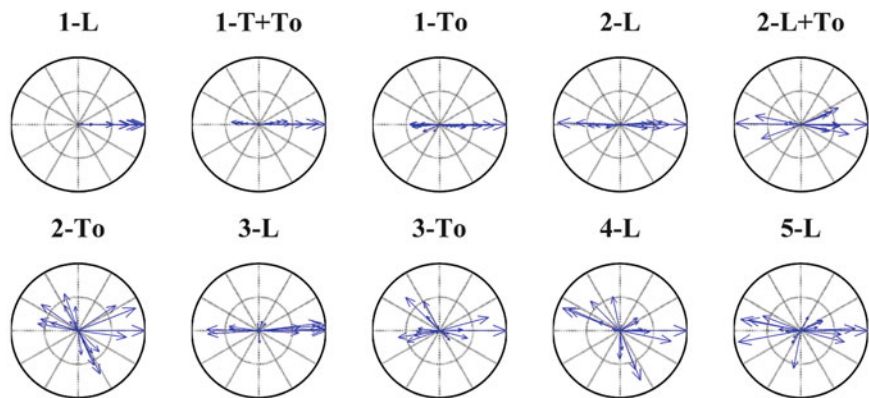


Fig. 13.8 Damping ratio identified using ambient WN data ($RMS = 1.5\%g$) at different damage states

Fig. 13.9 Polar plot of mode shapes identified using WN1A (undamaged state DS0) using DSI



shapes between the methods are consistent. A similar pattern is valid for all the states of damage. Similarly to the damping ratios, the agreement between mode shapes is better for lower modes than for higher modes. As explained previously, this is due to the fact that the participation of the higher modes is less compared to the lower modes and consequently the signal-to-noise-ratio (SNR) is lower for higher modes.

Fig. 13.10 Mode shapes identified for WN1A (undamaged state DS0) using DSI

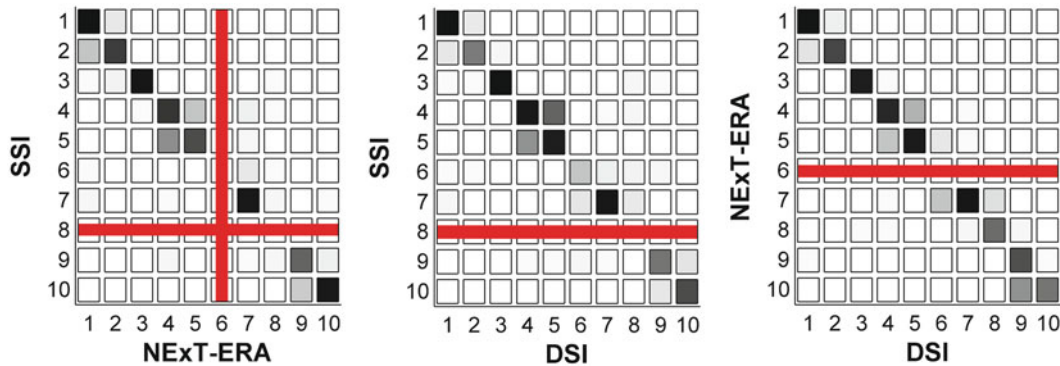
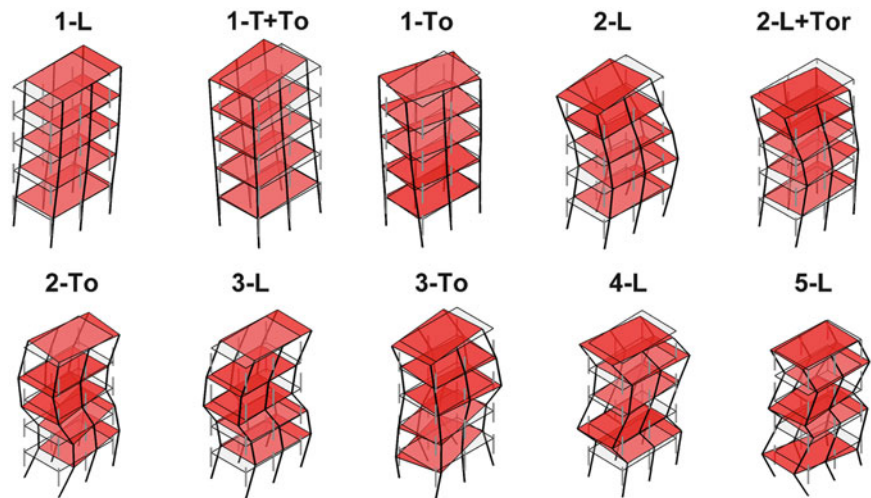


Fig. 13.11 MAC values for WN1A

13.6 Conclusions

A full-scale five-story RC frame building outfitted with a wide range of NCSs was built and tested on the NEES-UCSD shake table. While it was rigidly fixed to the shake table, the building was subjected to a sequence of earthquake motion tests designed to progressively damage the structure and NCSs. By using the ambient vibration data recorded before and after each seismic test and low amplitude white noise base excitation data conducted at key states of damage, the modal properties of the test specimen are identified using output-only (SSI-DATA) and (NEXT-ERA) and input-output (DSI) methods. Because of the low intensity of the excitations, a quasi-linear response is assumed and consequently the identified modal parameters basically change due to the structural and nonstructural damage induced by the seismic motions.

The results show that the natural frequencies decrease as more damage is induced in the nonstructural and structural components. The magnitude of reduction, which is due to the degradation of the stiffness of the system, is greater in the longitudinal modes, which correspond to the direction of the excitation. The damping ratios do not show a clear trend as a function of the damage, but longitudinal modes reach higher values compared to coupled translational-torsional and torsional modes.

Finally, the correlation between the mode shapes obtained by different methods is studied using the MAC coefficient. The results show a good agreement between different methods for each state of damage.

Acknowledgements This project was a collaboration between four academic institutions: The University of California at San Diego, San Diego State University, Howard University, and Worcester Polytechnic Institute, four major funding sources: The National Science Foundation, Englekirk Advisory Board, Charles Pankow Foundation and the California Seismic Safety Commission, and over 40 industry partners. Additional details may be found at bncs.ucsd.edu. Through the NSF-NEESR program, a portion of funding was provided by grant number CMMI-0936505 with Dr. Joy Pauschke as program manager. The above support is gratefully acknowledged. Support of graduate students Consuelo Aranda, Michelle Chen, Elias Espino, Steve Mintz, Elide Pantoli and Xiang Wang, the NEES@UCSD and NEES@UCLA staff, and consulting contributions of Robert

Bachman, Chair of the project's Engineering Regulatory Committee, are greatly appreciated. Design of the test building was led by Englekirk Structural Engineers, and the efforts of Dr. Robert Englekirk and Mahmoud Faghihi are greatly appreciated in this regard. Opinions and findings in this study are those of the authors and do not necessarily reflect the views of the sponsors.

References

1. Doebling SW, Farrar CR, Prime MB, Shevit DW (1996) Damage identification and health monitoring of structural and mechanical systems from changes in their vibration characteristics: a literature review, Los Alamos National Laboratory Report LA-13070-MS, 1996
2. Fan W, Qiao PZ (2011) Vibration-based damage identification methods: a review and comparative study. *Struct Health Monit* 10(5):83–111
3. Moaveni B, He X, Conte JP, Restrepo JI, Panagiotou M (2011) System identification study of a seven-story full-scale building slice tested on the UCSD-NEES shake table. *ASCE J Struct Eng* 137(6):705–717
4. Moaveni B, Stavridis A, Shing PB (2010) System identification of a three-story infilled RC frame tested on the UCSD-NEES shake table. In: *Proceedings of 28th international modal analysis conference (IMAC-XXVIII)*, Jacksonville, 2010
5. Ji X, Fenves G, Kajiwara K, Nakashima M (2011) Seismic damage detection of a full-scale shaking table test structure. *ASCE J Struct Eng* 137(1):14–21
6. Hien H, Mita A (2011) Damage identification of full scale four-story steel building using multi-input multi-output models. In: *Proceedings of SPIE 7981, sensors and smart structures technologies for civil, mechanical, and aerospace systems*, San Diego, California, 7–10 March.
7. Chen M et al (2012) Design and construction of a full-scale 5-story base isolated building outfitted with nonstructural components for earthquake testing at the UCSD-NEES Facility. *ASCE 43th Structures Congress*, 2012
8. Van Overschee P, De Moor B (1996) *Subspace identification for linear systems: theory, implementation, applications*. Kluwer Academic Publishers, Dordrecht, The Netherlands
9. James GH, Carne TG, Lauffer JP (1993) The natural excitation technique (NExT) for modal parameter extraction from operating wind turbines, SAND92-1666, UC-261. Sandia National Laboratories, Sandia
10. Imregun M, Ewins DJ (1993) Realization of complex mode shapes. In: *XI international modal analysis conference (IMAC)*, Florida, 1993
11. Allemang RJ, Brown DJ (1982) A correlation coefficient for modal vector analysis. In: *I international modal analysis conference (IMAC)*, Orlando, US, pp 110–116

Chapter 14

Modal Testing of a Repaired Building After 2010 Chile Earthquake

Manuel Archila, Ruben Boroschek, Carlos E. Ventura, and Sheri Molnar

Abstract A 24 storey reinforced concrete residential building in the city of Concepcion, Chile, was severely damaged during the 2010 M_W 8.8 Maule earthquake. After the earthquake structural elements at the base of the building were repaired in an attempt to restore the structure to its original state. A modal test using ambient vibrations was conducted on this repaired building to determine its dynamic properties. Additional studies using ambient vibrations at near free field locations confirm that ground conditions may have contributed to seismic amplification of the ground shaking at frequencies that were dominant in the seismic response of this high-rise building. This amplification of ground shaking can be considered an important contributing factor to the damage suffered by this building.

Keywords Ambient vibration • Microtremor • Modal testing • Site period • Earthquake damage

14.1 Introduction

On February 27, 2010 at 3:34 am local time a M_W 8.8 megathrust earthquake struck off the coast of Chile causing strong shaking and triggering a tsunami that affected cities along the Pacific Coast of Chile. The city of Concepcion, located at an epicentral distance of 100 km was severely impacted by this earthquake. The aftermath of this earthquake left many high-rise buildings with severe seismic damage, including the collapse of a residential 15 storey building shown in Fig. 14.1. Many studies are still underway to determine the causes of the structural damage of buildings throughout Chile.

Field investigations have led engineers to suggest that walls in high rise Chilean buildings subjected to large axial compressive forces and bending action during the 2010 M_W 8.8 earthquake induced high stresses on the concrete and steel rebars, such that the concrete crushed and rebar buckled under these demands [1]. There is concern that building code provisions in Chile for design and detailing of reinforced concrete walls need to be improved to prevent this type of widespread damage.

After the earthquake, many damaged buildings were repaired to make them safe and allow for re-occupancy. The first and fourth authors visited the city of Concepcion in January 2012 to perform ambient vibration tests on the ground surface and in repaired structures. These ambient vibration tests were conducted to estimate the natural frequency of the subsoil, i.e. site period, and the modal properties of a repaired residential building. This paper presents and discusses selected results of our ambient vibration testing campaign in Concepcion.

M. Archila (✉) • C.E. Ventura • S. Molnar

Department of Civil Engineering, The University of British Columbia, 6250 Applied Science Lane, Vancouver, BC, Canada V6T-1Z4
e-mail: marchila@interchange.ubc.ca

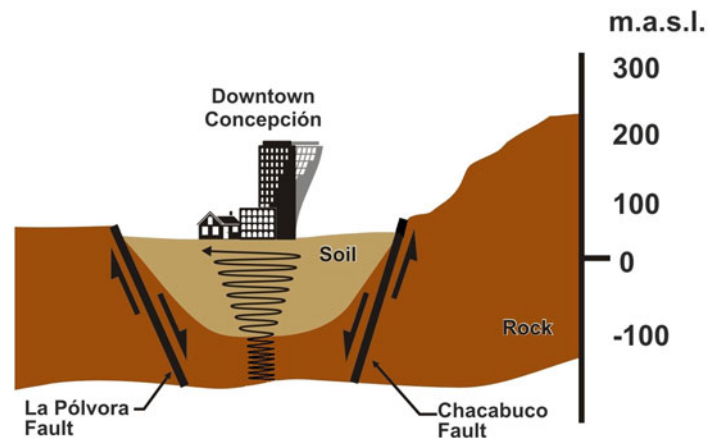
R. Boroschek

Department of Civil Engineering, University of Chile, Av. Blanco Encalada 2002, Santiago, Chile

Fig. 14.1 Photo of a 15 storey reinforced concrete building in Concepcion city that collapsed during 2010 Chile earthquake (Photo courtesy of Perry Adebar)



Fig. 14.2 Geologic profile across city of Concepcion and cartoon of seismic amplification in basin deposits (Adapted from [7])



14.2 Ground Conditions at Concepcion City

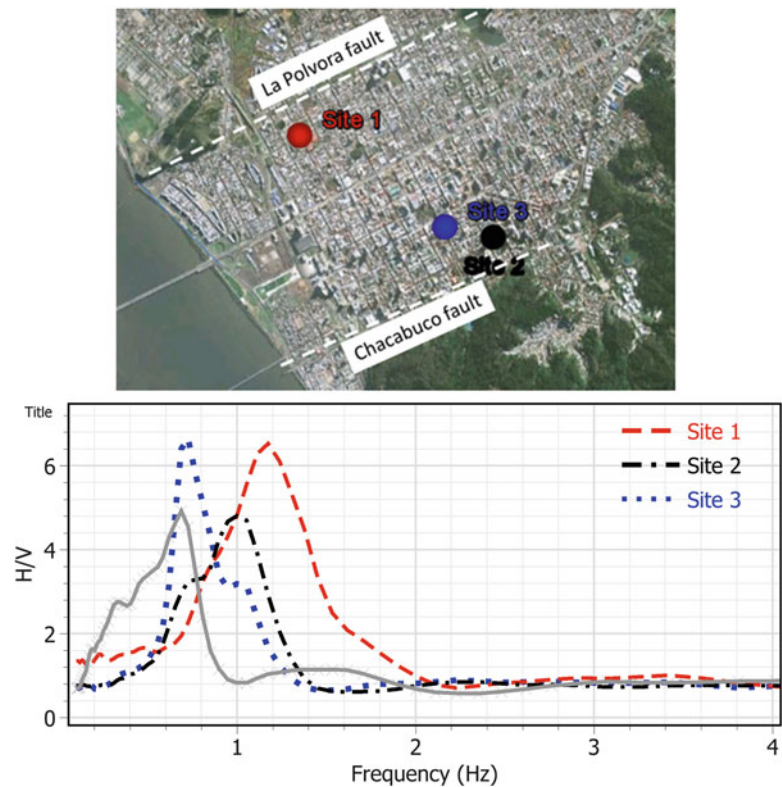
The city of Concepcion is surrounded by the Bio Bio River to the South, and rock formations elsewhere. A large part of the city of Concepcion is founded on a valley of alluvium sediments. These sediments have settled within a graben (basin) structure. Figure 14.2 shows the La Polvora and Chacabuco Faults, which delineate the graben boundary. This deep deposit of soil under the city has given rise to seismic amplification of earthquake shaking in past earthquakes.

The depth of this deposit varies across the city, decreasing towards the rocky edges of Concepcion and deepening towards downtown Concepcion as shown in Fig. 14.2. This varying profile of soil deposit depth results in different levels of subsoil dynamic amplification and natural frequency of vibration across the region. The subsoil fundamental frequency decreases from the edge of the city towards downtown Concepcion as determined from a campaign of free-field ambient vibration measurements [2].

14.3 Site Fundamental Frequency

The fundamental frequency of the soil deposit at different locations across the city of Concepcion was retrieved from microtremor measurements using the H/V ratio analysis technique developed by Nakamura [3]. This processing technique makes use of vertical and horizontal components; this is a cost-effective method to determine the fundamental frequency

Fig. 14.3 *Top panel:* locations of three free-field ambient-vibration test sites denoted by *coloured circles*. *Bottom panel:* H/V spectral ratios from average ambient vibration and 2010 M_w 8.8 earthquake (*solid line*) recordings



of a soil deposit. The frequency of the peak H/V spectrum ratio is a proxy of the fundamental frequency of the ground.

The microtremor measurements were conducted with a single triaxial seismometer (TROMINO[®]), which was temporarily installed on the ground to record ambient vibrations for 20 min at a sampling rate of 128 Hz. The spectral ratio of average horizontal to vertical motion was calculated with the Geopsy program [4]. The spectral ratio analyses were performed using 60-s time windows that were 5%-cosine tapered and fast Fourier transformed to 10% proportionally smoothed spectra.

The results from free-field microtremor measurements at three sites are presented in this paper. Figure 14.3 shows site 1 is located south of the La Polvora fault, site 2 is located immediately north of the Chacabuco fault and site 3 is located closest to the centre of downtown Concepcion. Figure 14.3 also shows the average ambient-vibration H/V ratio results for these three sites; site 3 exhibits the lowest peak frequency (0.70 Hz) related to thick basin deposits, whereas sites 1 and 2 exhibit higher peak frequencies (1.16 and 0.97 Hz, respectively) towards the basin edges.

The 2010 M_w 8.8 earthquake was recorded by the strong-motion instrument at site 3. The highest recorded peak acceleration here was 0.40 g, which corresponds to a very strong shaking. The H/V ratios from the ambient vibration measurement (solid line) and the strong motion earthquake record (dashed line) are compared in Fig. 14.3. The average ambient-vibration peak frequency is 0.72 Hz and the strong motion peak frequency is 0.70 Hz. Significant differences are observed in the shape of the H/V ratio curve.

14.4 Buildings Description and 2010 Chile Earthquake Damage

14.4.1 Building 1

A modern 12 storey reinforced concrete which exhibited severe damage in structural and non-structural components is shown in Fig. 14.4. The construction of this building was finalized in 2006. This building was located within a distance of 80 m from measurement site 1 described above. The building has an L-shape and comprises two separate building towers, one



Fig. 14.4 Damage observed in 12-storey reinforced concrete building



Fig. 14.5 Elevation of 24 Storey Building and ambient vibration measurements

tower has approximate plan dimensions of 28 m long by 12 m wide and the other is 35 m by 12 m. The structural system provided to withstand earthquakes was shear walls.

The pictures in Fig. 14.4 show that the windows of the panoramic elevator suffered extensive damage. Partial collapse of the roof structure above the elevator was observed. The base of the walls above ground showed extensive cracking in horizontal and diagonal patterns. This building was considered inhabitable after the earthquake and has been slated for demolition. No access was allowed to this building; however the fundamental frequency of a shear wall building can be estimated using a rule of thumb described in equation 1.

$$f_n = \frac{1}{(T_n)} = \frac{1}{(0.075N)} = \frac{1}{(0.075 * 12)} = 1.11 \text{ Hz} \quad (14.1)$$

where N is equal to the number of storey above ground level. Comparing the fundamental frequency of site 1 of 1.16 Hz and the estimated fundamental frequency of this building, it is clear that seismic amplification of motion could take place due to resonance. This correlation confirms that ground conditions played an important role on the seismic damage caused by the earthquake which rendered the building inhabitable.

14.4.2 Building 2

A 24 storey repaired reinforced concrete building for residential occupancy was subject to modal testing. The building has 23 stories above ground level and one basement storey. The approximate plan layout dimensions are 40 m by 15 m. The structural system to withstand earthquake and gravity loading is comprised of slender reinforced concrete walls. Figure 14.5 shows pictures from the building and the ambient vibration tests performed on the ground (site 2) and the building.

The building had been opened only for a month before the Chile earthquake of February 27, 2010. Residents evacuated the building as the shaking was very strong. No apparent damage was observable on this building from the outside, however

Table 14.1 Summary of modal properties

Mode	Frequency (Hz)	Damping ratio (%)
Mode 1	0.61	1.901
Mode 2	0.66	1.783
Mode 3	0.85	1.893
Mode 4	2.79	1.551
Mode 5	3.10	2.004
Mode 6	3.46	1.694

posterior inspection of the structure showed that the walls at the base of the building were severely damaged. The structure was subsequently repaired.

14.5 Description of the Modal Test on Building 2

14.5.1 Testing Technique

Output-Only Modal analysis (OMA) techniques were used in this study [5]. The modal properties sought were natural frequencies, mode shapes and damping ratios. Input excitations were not recorded and ambient vibrations were recorded only. The Enhanced Frequency Domain Decomposition (EFDD) method available in the program ARTeMIS v. 4.1 [6] was used to process the data.

14.5.2 Test Setup

The test was conducted using a set of 3 triaxial high-resolution accelerometers (TROMINO[®]), the same sensors as used for the free-field microtremor measurements. The internal clocks of the sensors were synchronized to a common reference time through a Global Positioning System (GPS). A reference sensor was located at the roof of the building and two roving sensors were placed at each one of the following floors: 1, 5, 9, 13, 17, 20 and 23. Because there was no satellite visibility from inside the building, the accelerometers were synchronized at the roof level with satellite visibility readily available. After synchronization, the accelerometers were placed inside of the building to perform the corresponding measurement at different floor levels. Recordings of ambient vibrations were taken for periods of 20 min at each floor using a sampling rate of 512 Hz. An illustration of the different test setups is shown in Fig. 14.6.

14.6 Modal Model

The model was developed using the seven different setups depicted in Fig. 14.6. The peak picking method was used to select frequencies from the singular value decomposition plot shown in Fig. 14.7. Six modal frequencies were identified. The summary of the modal properties obtained are listed in Table 14.1. The fundamental frequencies of the translational modes are 0.61 and 0.85 Hz in the transverse and longitudinal directions, respectively. The damping ratios range between 1.5% and 2.0% which is expected at the ambient vibration level. The corresponding modal shapes are presented in Fig. 14.8, only floors where measurements were taken are shown for clarity.

The fundamental frequency of the soil profile at site 2 where the building is located was determined to be 0.97 Hz (Fig. 14.2), and the dominant frequencies of vibration of the repaired building range between 0.61 Hz to 0.85 Hz. The frequencies are comparable and confirm that ground conditions also played an important role on seismic amplification of demands on the building that led to the severe earthquake damage observed.

There is no information available regarding the condition of the building before the 2010 M_w 8.8 earthquake. The building blueprints are not publicly available, and this prevents creation of any computer model to estimate the dynamic properties of the original building. Notwithstanding it is clear that the ambient vibrations measurements show that torsion is present in the dominant modes which might be a consequence of the earthquake damage.

Fig. 14.6 Location of sensors over building height

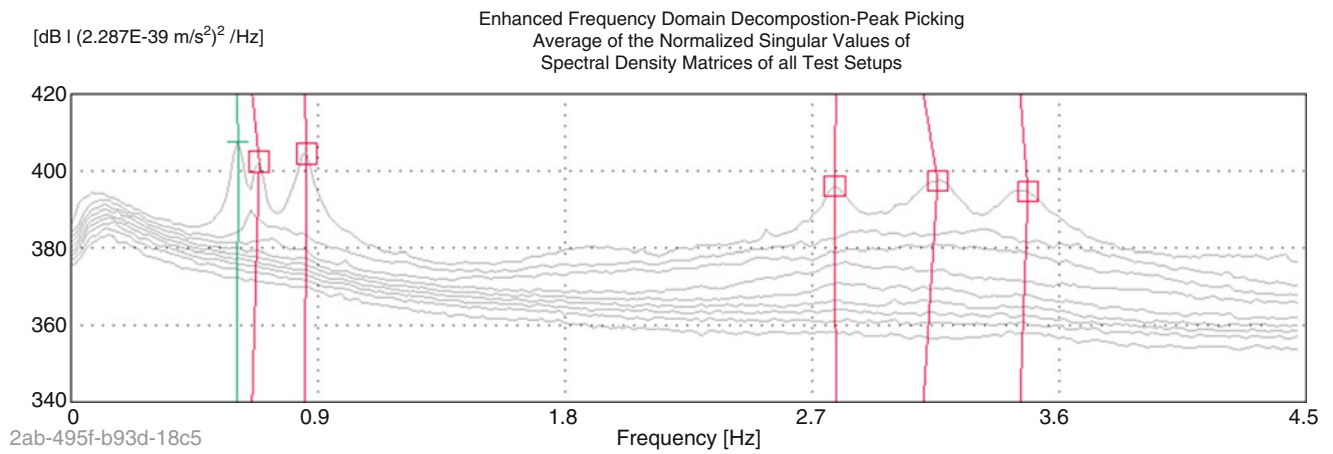
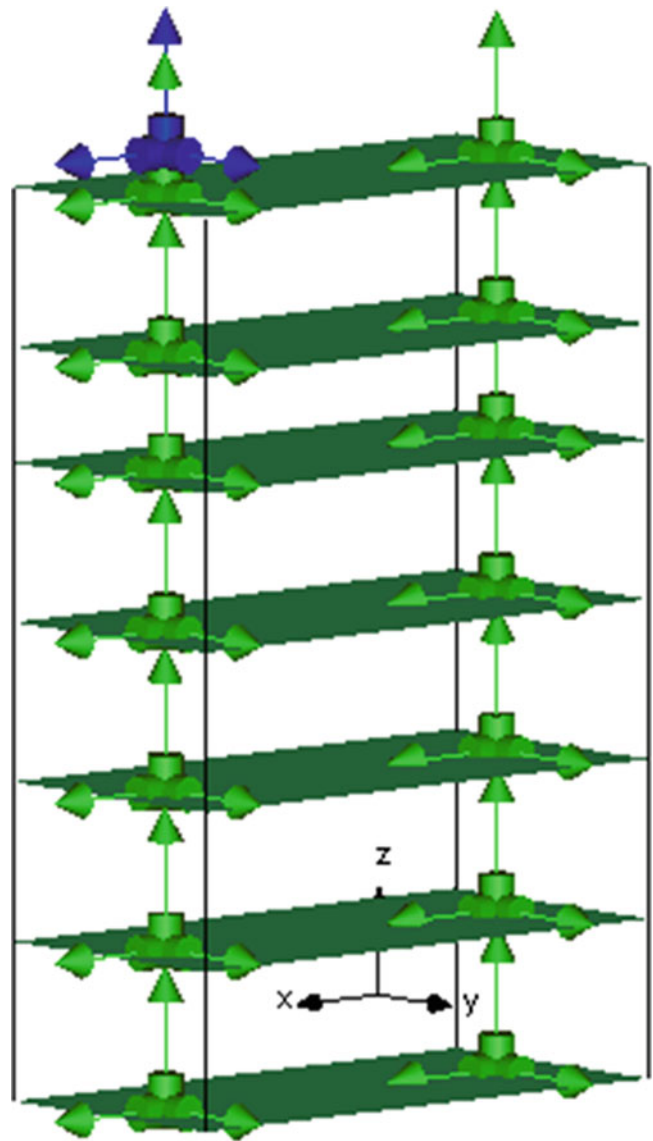


Fig. 14.7 Plot of Singular Value Decomposition of the average of all measurements

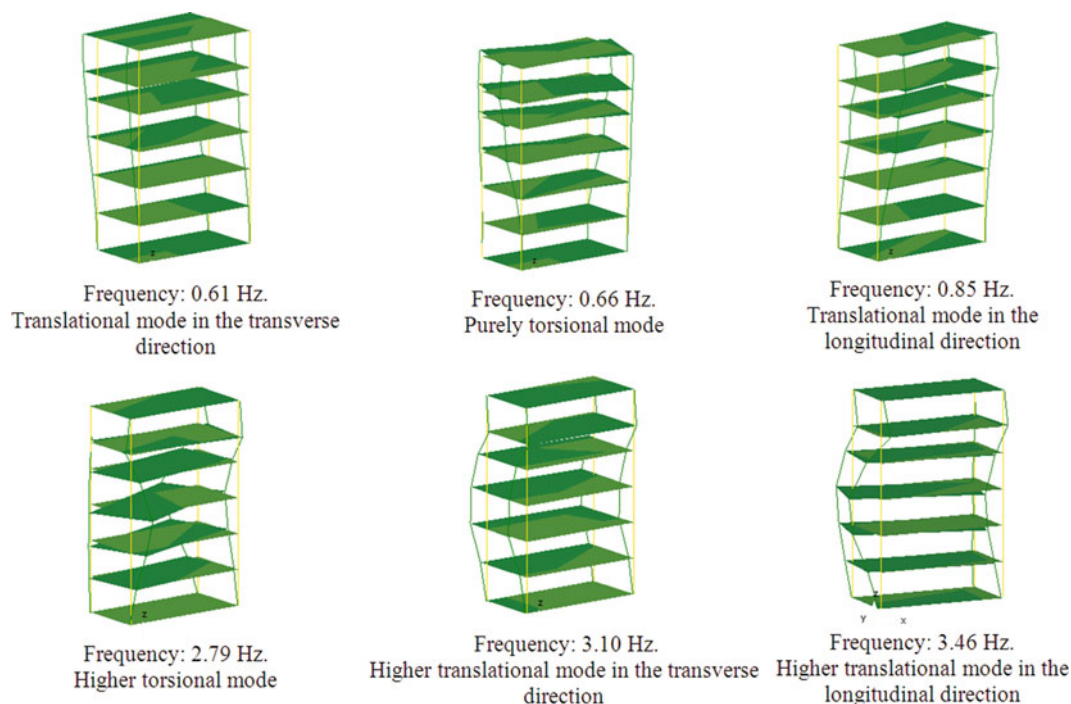


Fig. 14.8 Modal shapes of repaired high-rise building

14.7 Remarks

The estimates of the fundamental frequency of the ground at different locations across the city of Concepcion correlated well with the dominant frequencies of vibration of surrounding buildings which experienced severe damage during the 2010 M_w 8.8 earthquake. This close relation confirms that ground conditions had an important role in amplifying the seismic demands that were exerted upon high rise buildings.

The mode shapes retrieved from the ambient vibration measurements of the 24 storey repaired building were strongly influenced by torsional vibration. There is no evidence available to confirm if this condition of torsional response corresponded to the original state of the building or was inflicted by the earthquake damage. As an engineering practice in active seismic regions ambient vibrations should be performed on structures to monitor mode shapes throughout their different states, undamaged, damaged and repaired, to assess severity of damage and confirm the effectiveness of repairs in restoring the structure to its original condition.

Acknowledgements The financial support to conduct these studies was provided by the Civil Engineering Department at University of Chile and the Earthquake Engineering Research Facility of the Civil Engineering Department at The University of British Columbia, in Canada.

References

1. Ghosh S, Cleland N (2010) Observations from the February 27, 2010 earthquake in Chile. PCI Reconnaissance Team Report. 2010
2. Ramirez P, Vivallo J (2009) Microzonificación sísmica de la ciudad de Concepción—Chile. In: XII Chilean Geological Conference, Congreso Geológico Chileno, Santiago, 2009
3. Nakamura Y (1989) A method for dynamic characteristics estimation of subsurface using microtremor on the ground surface. Q Rep RTRI 30(1):25–33
4. Geopsy Software (2008) Network of Research Infrastructures for European Seismology, Institut de Recherche pour le Développement—Laboratoire de Géophysique Interne et Tectonophysique. France
5. Brincker R, Zhang L, Andersen P (2000) Modal identification from ambient responses using frequency domain decomposition. In: Proceedings of 18th international modal analysis conference—IMAC, San Antonio, pp 625–630, 2000
6. Structural Vibration Solutions A/S (2006) Artemis Extractor Pro 2008. Version 4.1. Structural Vibration Solutions A/S, Denmark
7. Bray JD, Frost D (2010) Geo-Engineering Reconnaissance of the February 27, 2010 Maule, Chile Earthquake. Geoenvironmental Extreme Events Reconnaissance (GEER). 2010

Chapter 15

System Identification and Displacement Profiles of Multi-Span Skewed Bridges with Seat Type Abutments

Seku Catacoli, Carlos E. Ventura, and Steve McDonald

Abstract Skewed bridges are classified as irregular structures due to the geometry of the deck and bents. The evaluation of their dynamic response is challenging as it requires a combination of several modes of vibration. In this study, the results of ambient vibration tests performed on four bridges in British Columbia, Canada are used to identify the dynamic properties and the displacement profiles of multi-span skewed bridges with seat type abutments. The frequencies of vibration, the modes of vibrations and the modal dampings are identified using frequency and time domain techniques. In addition, the directionality in the transverse and longitudinal response for skewed bridges with different levels of lateral restraint and deck flexibility is discussed. This paper improves the understanding of the dynamic response of skewed bridges, in particular their lateral response to seismic loads. This understanding contributes to having a better assessment of the seismic demands that skewed structures will undergo and to the development of displacement based design methods for these structures.

Keywords Skewed bridges • Ambient vibration tests • Displacement profiles • Seat type abutments

15.1 Introduction

Skewed bridges are irregular structures due to the geometry of the deck and bents (Fig. 15.1). A good understanding of the dynamic properties and the lateral displacement demands is needed in the current displacement-based design procedures for skewed bridges [1], in which the displacement demand is directly compared with the provided displacement capacity to ensure the desirable seismic performance. This is particularly important in skewed bridges with seat type abutments, in which, given their support details, pounding between the deck and its abutments is more likely to happen in many cases leading to the unseating of the superstructure.

Skewed bridges have different stiffnesses and strengths depending upon the orientation of the axes along which these properties are determined. An accurate estimation of the transverse and longitudinal demands is connected to a proper identification of the so called “preferred response directions”. The preferred response directions are the directions in which the critical transverse and longitudinal demands respectively occur [2, 3]. These directions are given by the predominant directions of the transverse and longitudinal modes of vibration. A number of authors have conducted experimental and analytical studies to identify the dynamic parameters of skewed bridges with integral abutments [4–7]. However, a better understanding of the dynamic properties and the displacement profiles of skewed bridges with seat type abutments is required, and will improve the evaluation of the maximum displacement demands for these structures.

The University of British Columbia (UBC) and the Ministry of Transportation (MoT) have undertaken a study to evaluate the seismic response and the effects of Soil-Structure-Interaction (SSI) on skewed bridges. In this study, the whole soil-foundation-structure and embankment-abutment-structure systems are simulated using 3D finite element and simplified numerical models. The results are complemented with ambient vibration tests conducted at typical skewed bridges. This paper discusses the results for four multi-span skewed bridges with seat type abutments.

S. Catacoli (✉) • C.E. Ventura • S. McDonald
Civil Engineering Department, University of British Columbia, Vancouver, BC, Canada
e-mail: sesamory@interchange.ubc.ca; ventura@civil.ubc.ca; smcivil@interchange.ubc.ca



Fig. 15.1 Typical multi-span skewed bridge



Fig. 15.2 Highway 99 and 24th avenue underpass (HWY 24th)

15.2 Description of Bridges

15.2.1 Highway 99 and 24th Avenue Underpass (HWY 24th)

The structure was built in 2006 and is located along Highway 99 in Surrey, British Columbia, Canada (Fig. 15.2). The bridge is 48 m long, 19 m wide, and has two continuous spans with seat-type abutments. The superstructure consists of a concrete deck slab supported on 0.8 m deep precast concrete box stringers. The substructure consists of 0.8 m diameter, 3.3 m high multi-column frames with concrete cap beams. The abutment and pier foundations consist of strip footings.



Fig. 15.3 Annacis highway and Highway 10 underpass (HWY 10th)



Fig. 15.4 Highway 1 and Lougheed highway underpass (LHH-EB underpass)

15.2.2 Highway 10 Underpass (HWY 10)

The structure was built in 1985 and is located along Annacis Highway in Surrey, British Columbia, Canada (Fig. 15.3). The bridge is 71 m long, 22.1 m wide, and has two spans with seat-type abutments. The superstructure consists of a concrete deck slab supported on nine 1.9 m deep, concrete I-girders. The superstructure is discontinuous and fixed-connected to the cap beam at midspan. The substructure consists of a multicolumn frame with a set of five concrete columns which are 1 m in diameter. The foundations consist of steel pipe piles filled with concrete.

15.2.3 Highway 1 and Lougheed Highway Underpass (LHH-EB Underpass)

The underpass was built in 2012. It is located in Burnaby, B.C. at Highway 1 and Lougheed Highway. The three-span bridge is approximately 135 m long and 26 m wide. Its construction consists of a concrete deck slab supported on 2.2 m deep steel girders, which are supported by multicolumn frames with a set of eight columns which are 1.22 m diameter. Both ends rest on bent abutments, and are connected by approach slabs. There are also expansion joints on all four spans. The foundation consists of 1.22 m diameter steel pipe piles (Fig. 15.4).



Fig. 15.5 Douglas road underpass (Douglas Rd)

Table 15.1 Summary of bridge characteristics

Structure	Length (m)	Spans		Width (m)	Clearance (m)	Skew angle (degrees)	Substructure		
		No.	Lengths (m)				Type	Abutments	Superstructure type
HWY 24th	48	2	23-23	19	4.9	37	Multi-column-frames ($\phi = 0.8$ m)	Seat type	Continuous—concrete box girders
HWY 10th	71	2	36-36	22.1	9.1	31	Multi-column-frames ($\phi = 1.0$ m)	Seat-type	Discontinuous—reinforced concrete I-girders
LHH-EB Underpass	135	3	37-58-37	26	5.0	54–57	Multi-column-frames ($\phi = 1.22$ m)	Bent seat-type	Continuous—concrete steel girders
Douglas Rd	83	4	12-22-21-21	17	4.6	28	Multi-column-frames ($\phi = 0.6$ m)	Seat-type	Discontinuous—concrete box girders

15.2.4 Douglas Road Underpass (Douglas Rd)

The underpass, built in 1962, is located at Highway 1 and Douglas Road. It is four spans with a total length of 83 m and a width of 17 m (Fig. 15.5). The superstructure consists of a concrete slab deck with precast post-tensioned box girders. The substructure has multicolumn frames with four columns, which are 0.6 m in diameter. Pad footings are used for the piers. The abutments are seat-type; and the slab is discontinuous at midspan, whereas the girders are discontinuous at all supports. At the internal piers, expansion bearings exist; but at the abutments there are fixed bearings.

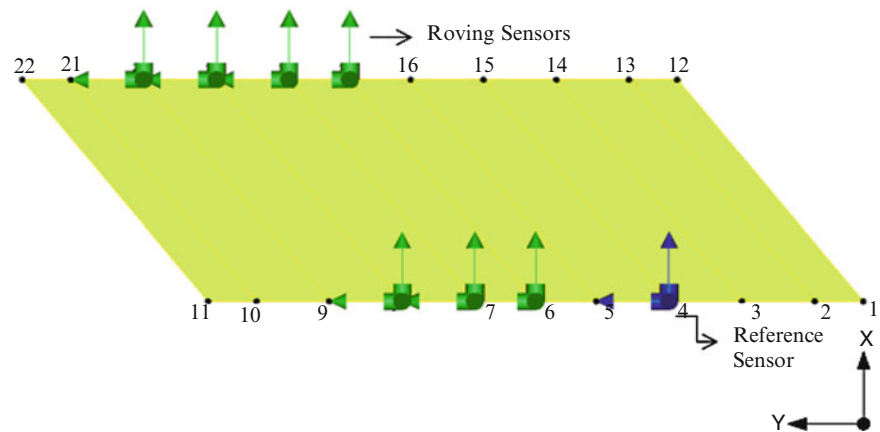
The following table summarizes the characteristics of the structures tested (Table 15.1).

15.3 Field Testing

Ambient Vibration Testing involves measuring a structure's response to typical forces that it is subjected to every day. These ambient forces can be wind, traffic, human activities, etc. This method of testing provides a cheap, non-invasive, and non-destructive method for obtaining modal parameters of large structures. With Ambient Vibration Testing you avoid having to physically excite the structure with heavy equipment, which results in the disruption of the structure's typical operation. The response that you obtain from these tests is characteristic of the true operating conditions of the structure. To obtain the modal parameters of the structure, Modal Operational Analysis algorithms are used to process the data [4, 9].

Ambient vibration testing is typically carried out by using sensitive accelerometers or other types of sensors, along with a multi-channel data acquisition system. Some inconveniences in using the sensors involve cable handling, sensor balancing, signal clipping, and power supply issues. The Earthquake Engineering Research Facility (EERF) at the University of British Columbia (UBC) carries out ambient vibration tests with its nine wireless Tromino sensors. These instruments were set to

Fig. 15.6 Typical test setup for HWY 24th



record high gain velocities, low gain velocities and accelerations at 128 samples per second. The Trominos are equipped with GPS and radio antennas for time synchronization.

In 2012, members of the EERF-UBC team carried out ambient vibration tests on the HWY 24th, HWY 10th, LHH-EB Underpass and Douglas Rd bridges. During the tests, one unit stayed at the same location and is called a reference sensor, while the others are moved along the bridge to cover different testing locations and are called roving sensors. Figure 15.6 shows a typical test setup for HWY 24th. All the bridges were open to traffic. There were 20 testing locations along the sidewalks of HWY 24th, 32 along HWY 10th, 59 along LHH-EB Underpass and 38 along Douglas Rd. In addition to this, there were two testing locations at each approach and at least one free field measurement for all the bridges. All measurements were taken for 30 min in each setup.

It is important to point out that LHH-EB underpass was partially open to traffic, and did not have sidewalks. As a result, the test could only be conducted on the two southbound lanes that were closed to traffic.

15.4 Data Analysis and Results

The natural frequencies, mode shapes and dampings of the bridges were identified using the ARTeMIS Extractor [8].

For convenience, the presentation of results is divided into the identification of the dynamic properties in the vertical direction and the identification of the in-plane dynamic properties.

15.4.1 System Identification in the Vertical Direction

The Enhanced Frequency Domain Decomposition (EFDD) technique was used to undertake the modal identification analysis. For the Highway 99 and 24th Avenue Underpass seven modes of vibration in the vertical direction were clearly identified. For this two span continuous structure, Fig. 15.7 displays well-defined vertical antisymmetric, vertical symmetric and torsional modes. The system identification in the vertical direction undertaken for all the bridges is summarized in Table 15.2.

15.4.2 In-plane System Identification and Lateral Displacement Profiles

As traffic was the main excitation on the bridges, mainly the vertical modes are excited during the test and the identification of the in-plane motions (transverse, longitudinal and rotation) becomes more challenging. In order to identify the in-plane modes of vibrations, which are fundamental for seismic assessment, the Stochastic Subspace Identification (SSI) technique [9] was used, in addition to the Enhanced Frequency Domain Decomposition (EFDD) technique.

The frequencies and modes of vibration obtained using both techniques are similar (Tables 15.3 and 15.4). The frequencies are consistent with the boundary conditions of the bridges in each direction. For instance, HWY 24th has strong shear keys at abutments in the transverse direction and is seated on expansion bearing in the longitudinal direction. Consistently, the

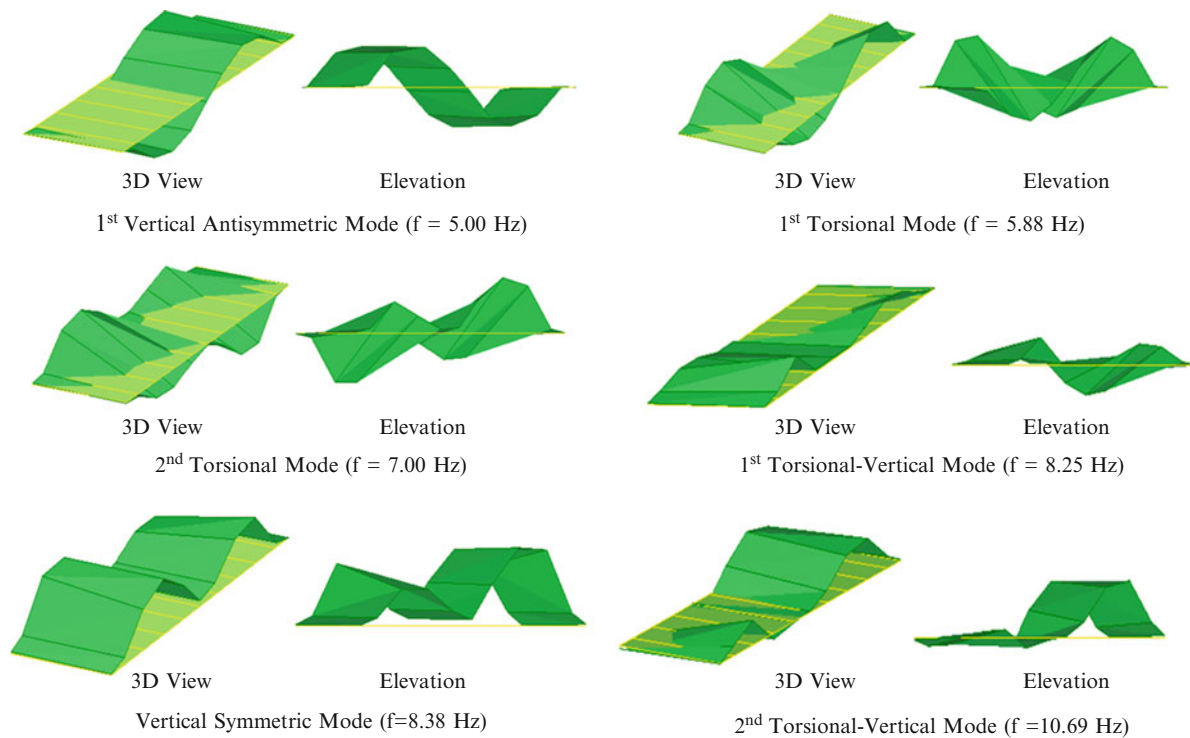


Fig. 15.7 Vertical and Torsional modes of vibration for HWY 24th

transverse frequency of vibration is 10.66 Hz, and the longitudinal 0.97 Hz. Similarly, HWY 10th, which is also a two span bridge seated on expansion joints but with weaker shear keys, has a transverse frequency of 4.76 Hz, and a longitudinal frequency of 1.09 Hz. The consistency observed between the frequency of vibration and the level of lateral restraint in each direction, also suggests that the modal response of skewed bridges could be uncoupled in each direction.

The frequency of vibration for in-plane rotation could only be identified for the HWY 24th (Table 15.3). The value obtained (11.72 Hz) is considered high, and is close to the transverse frequency identified (10.66 Hz). The damping ratios of the bridges tested are also similar in both techniques, EFDD and SSI. The estimated modal dampings vary from 0.24 % to 3.63 % (Tables 15.3 and 15.4). These in-plane damping ratios are similar to the values reported for straight bridges using ambient vibration tests [10].

The transverse and longitudinal modes of vibration are used to study the lateral displacement profiles of skewed bridges for different configurations and boundary conditions. As presented in Table 15.2, the transverse and longitudinal displacement profiles of a two span skewed bridge with seat type abutments and continuous deck as HWY 24th, is in agreement with a rigid deck assumption. In the same way, the transverse displacement profile of a three span skewed bridge with bent type abutments, expansion bearings, and continuous deck as LHH-EB Underpass, is consistent with a rigid deck profile.

In contrast, the transverse displacement profiles of a two span skewed bridge with discontinuous deck as HWY 10th, has a parabolic shape more in agreement to what is expected for a flexible deck. A similar flexible transverse profile is observed for Douglas Rd which is a four spans skewed bridge with discontinuous deck.

The transverse and longitudinal modes of vibration are also used to study the directionality in the lateral response of skewed bridges. The predominant direction of the mode is defined as the azimuth in which the mode tends to move. The predominant direction for each mode was estimated by comparing at abutments and at mid-span, the nodal coordinates of the undeformed geometry with respect to the nodal coordinates of the mode of vibration. The evaluation of the predominant direction of response for the bridges tested illustrates that the predominant direction of the transverse response occurs in the azimuth of the skew bents, whereas the predominant direction of the longitudinal response is perpendicular to the azimuth of the skew bents (Tables 15.3, 15.4 and 15.5).

Table 15.2 Summary of system identification in the vertical direction

Order	Freq. (Hz)	Mode characteristic
<i>HWY 24</i>		
1	5	1st Vertical Antisymmetric
2	5.88	1st Torsional
3	7	2nd Torsional
4	8.25	3rd Torsional
5	8.34	2nd Vertical Symmetric
6	10.69	4th Torsional
<i>HWY 10</i>		
1	5.406	1st Vertical Antisymmetric
2	5.688	2nd Vertical Symmetric
3	7.406	1st Torsional
4	7.781	2nd Torsional
5	10.41	1st Torsional-Vertical
6	10.78	2nd Torsional-Vertical
7	13.97	Torsional-Longitudinal
<i>LHH-EB Underpass</i>		
1	2.31	1st Vertical
2	2.77	1st Torsional
3	4.05	2nd Torsional
4	4.20	Torsional
5	5.06	Vertical
6	6.34	Vertical-Torsional
7	6.84	Vertical-Torsional
8	8.69	Torsional
9	9.59	Torsional
10	10.44	Vertical
11	11.63	Vertical
12	12.52	Vertical
<i>Douglas Rd</i>		
1	1.938	1st Torsional (Third Span)
2	2.625	1st Vertical
3	3.625	Longitudinal-Vertical
4	4.625	Longitudinal-Vertical
5	4.875	2nd Vertical Symmetric
6	5.313	3rd Vertical
7	6.688	Torsional
8	8.0	Vertical-Transverse
9	8.813	Vertical Antisymmetric-Transverse
10	9.063	Vertical Symmetric-Transverse
11	9.375	3rd Vertical
12	9.813	Vertical-2nd Transverse

15.5 Conclusions

The traditional approach for the assessment of the lateral demand of multi-span skewed bridges with seat type abutments considers that the transverse and longitudinal responses are coupled. In contrast, the result of the ambient vibration tests conducted in this research for bridges with different level of transverse restraint indicate that the lateral response can be uncoupled by using the transverse and longitudinal modes of vibration and their predominant directionalities. The results illustrate that the predominant direction of the transverse mode occurs in the azimuth of the skew bents; whereas the predominant direction of the longitudinal mode is perpendicular to the azimuth of the skew. These results were validated using analysis with the EFDD and the SSI methods.

In addition, the lateral displacement profile of the skewed bridges with continuous deck studied is in good agreement with the profile described by a rigid deck motion. On the other hand, the lateral displacement profile of the bridges with discontinuous deck seems to be more in agreement to the profiles described by flexible decks. Finally, in the vertical direction, the ambient vibration study captured the frequencies and modes of vibration below 13 Hz for all the bridges tested.

Table 15.3 Summary of in-plane system identification using the EFDD technique


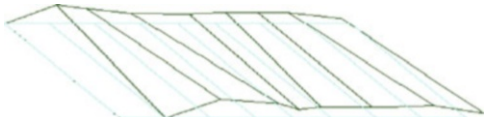
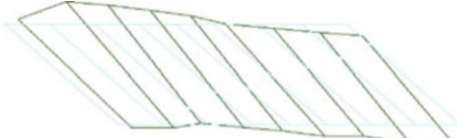

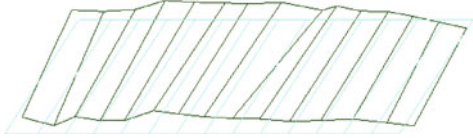
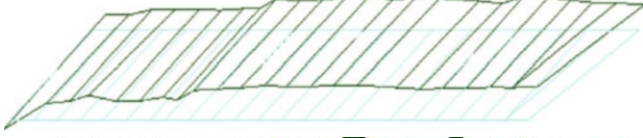
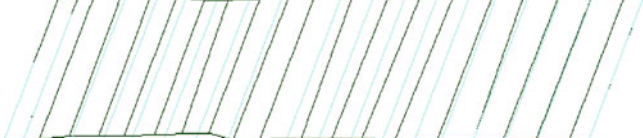
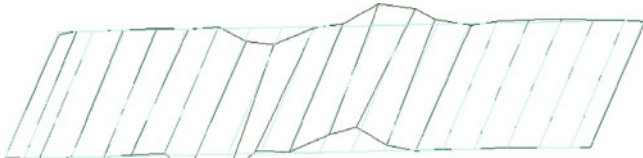
	Mode of vibration	Freq. (Hz)	ξ (%)	Description (plan view)
HWY 24th	1st Longitudinal	0.97	1.96	
	1st Transverse	10.66	1.53	
	In-plane Rotation	11.72	0.51	
HWY 10th	1st Longitudinal	1.09	0.57	
	1st Transverse	4.67	1.71	
LHH-EB Underpass	1st Transverse	1.72	3.05	
Douglas Rd	1st Longitudinal	2.31	2.36	
	1st Transverse	0.42	0.90	

Table 15.4 Summary of in-plane system identification using the SSI technique

	Mode of vibration	Freq. (Hz)	ξ (%)
HWY 24th	1st Longitudinal	—	—
	1st Transverse	10.52	2.15
	In-plane Rotation	12.44	3.63
HWY 10th	1st Transverse	4.69	1.96
LHH-EB Underpass	1st Transverse	1.96	1.90
Douglas Rd	1st Transverse	0.42	0.75
	1st Longitudinal	2.32	0.24

Table 15.5 Predominant direction of transverse response

	Azimuth of transverse mode (degrees)	Skew angle, ϕ (degrees)
HWY 24th	39 to 42	37
HWY 10th	32 to 34	31
LHH-EB Underpass	54 to 56	54–57

Acknowledgements This study was conducted with financial support from the Ministry of Transportation of British Columbia, Canada and the Natural Sciences and Engineering Research Council of Canada. Support provided by Professor Albert Ortiz from University of Medellin and the field testing team from the University of British Columbia is acknowledged with thanks.

References

1. American Association of State Highway and Transportation Officials (AASHTO) (2009) Guide specifications for LRFD seismic bridge design. AASHTO
2. Stewart JP et al (2011) Representation of bidirectional ground motions for design spectra in building codes. *Earthquake Spectra* 27(3):927–937
3. Catacoli S, Ventura C, McDonald S (2012) Directionality in the transverse response of skewed multi-span bridges with integral abutments. In: Proceedings of the 30th IMAC, a conference on structural dynamics, doi: [10.1007/978-1-4614-2413-0](https://doi.org/10.1007/978-1-4614-2413-0). Topics on the Dynamics of Civil Structures, Volume 1 Conference Proceedings of the Society for Experimental Mechanics Series 2012, pp 139–143
4. Carvajal JC, Ventura CE, Huffman S (2009) Ambient vibration testing of multi-span bridges with integral deck-abutments. In: Proceedings of the IMAC-XXVII. February 9–12, 2009, Orlando
5. Maleki S (2001) Free vibration of skew bridges. *J Vib Control* 7:935–52
6. Srinivasan RS, Munaswamy K (1978) Dynamic response of skew bridge decks. *Earthquake Eng Struct Dyn* 6:139–56
7. Ghobarah AA (1974) Seismic analysis of skewed highway bridges with intermediate supports. *Earthquake Eng Struct Dyn* 2(3):235–40
8. Artemis Extractor Software (1999–2011) Structural vibrations solutions, vol 5.3. Artemis Extractor Software, Denmark
9. TurekM, Ventura C (2005) Vibration testing of the Deltaport way bridge. In: Proceedings of the IMAC-XXIII, Orlando, January 31–February 3, 2005

Chapter 16

Robustness of Modal Parameter Estimation Methods Applied to Lightweight Structures

Kristoffer A. Dickow, Poul Henning Kirkegaard, and Lars V. Andersen

Abstract On-going research is concerned with the losses that occur at junctions in lightweight building structures. Recently the authors have investigated the underlying uncertainties related to both measurement, material and craftsmanship of timber junctions by means of repeated modal testing on a number of nominally identical test subjects. However, the literature on modal testing of timber structures is rather limited and the applicability and robustness of different curve fitting methods for modal analysis of such structures is not described in detail. The aim of this paper is to investigate the robustness of two parameter estimation methods built into the commercial modal testing software B&K Pulse Reflex Advanced Modal Analysis. The investigations are done by means of frequency response functions generated from a finite-element model and subjected to artificial noise before being analyzed with Pulse Reflex. The ability to handle closely spaced modes and broad frequency ranges is investigated for a numerical model of a lightweight junction under different signal-to-noise ratios. The selection of both excitation points and response points are discussed. It is found that both the Rational Fraction Polynomial-Z method and the Polyreference Time method are fairly robust and well suited for the structure being analyzed.

Keywords Lightweight structure • modal analysis • parameter estimation • robustness • finite element

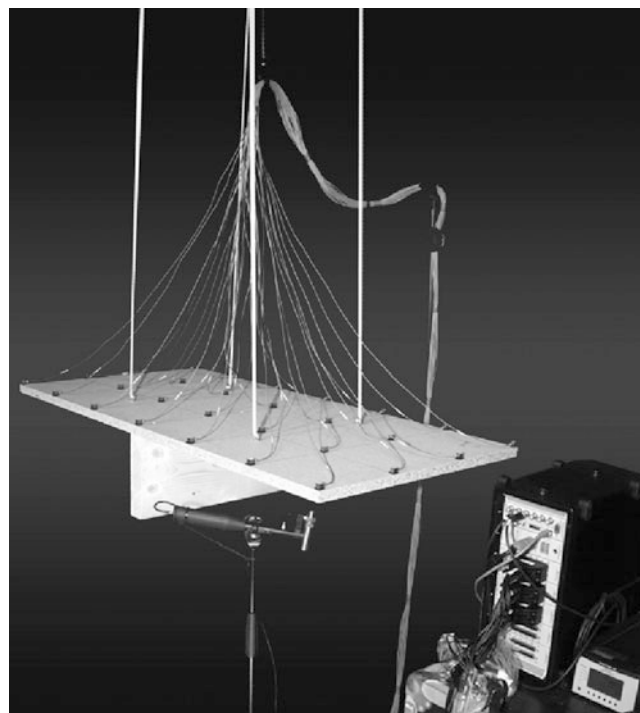
16.1 Introduction

Currently, lightweight building techniques are advancing due to an increasing awareness regarding the use of environmentally friendly materials combined with low production costs, quick installation and easy transportation. However, lightweight building structures suffer serious drawbacks in terms of poor low frequency sound insulation, due to the low mass of the constructions. As the trend is going towards increasing demands to the acoustic performance of building elements, inaccurate prediction methods and poor performance calls for over-dimensioning of the elements. This increases both weight and cost, which contradicts the idea of using lightweight elements in a building. Modern production techniques with prefabricated lightweight modules are rapidly evolving, and encourage re-thinking the design of building elements. On-going research is concerned with the losses that occur at junctions in lightweight structures. Recently the authors have investigated the underlying uncertainties related to both measurement, material and craftsmanship of timber junctions by means of repeated modal testing on a number of nominally identical test subjects [1]. However, the literature on modal testing of timber structures is rather limited and the applicability and robustness of different curve fitters for modal analysis of such structures is not described in detail. Lightweight structures often have non-linear properties, and since conventional modal analysis is based on linear theory, the applicability of modal analysis of such structures depends on how well the principle of superposition of modes fits the dynamic behavior of the structure. Furthermore, closely spaced modes and broad frequency ranges of interest needs to be dealt with in the process of modal parameter estimation.

The present paper compares two different curve fitting methods implemented in the commercial software Pulse Reflex Advanced Modal Analysis from Brüel & Kjær. One is the *Rational Fraction Polynomial-Z* method, and the other is the *Polyreference Time* method. Both are global higher order curve fitting methods, generally well suited for a wide range of analyses.

K.A. Dickow (✉) • P.H. Kirkegaard • L.V. Andersen
Aalborg University, Department of Civil Engineering, Sohngaardsholmsvej 57, 9000 Aalborg, Denmark
e-mail: kad@civil.aau.dk; phk@civil.aau.dk; la@civil.aau.dk

Fig. 16.1 Experimental setup used for measurements in [1]



The robustness of each of the two methods is investigated by applying increasing amounts of noise to the frequency response functions (FRFs), which are being analyzed in Pulse Reflex. The ability of each method to correctly capture all the modes—when influenced by noise—is used to judge the robustness of the methods. The frequency response functions are obtained from a non-linear numerical model made with the finite element (FE) code Abaqus [2]. The structure being modeled is a T-junction between a particleboard plate and a spruce beam (as subjected to measurements in [1], see Fig. 16.1). The only non-linearities included in the FE model are the contact properties of the junction itself. The materials are assumed to have linear elastic properties. A comparison of modes found by modal analysis of the non-linear model, to modes found by the (computationally) much simpler Lanczos Eigenvalue solver—which is built in to Abaqus—is included, to demonstrate why linear perturbation analysis does not work for this type of structure.

The use of a numerical model—rather than actual measurements—has been chosen to ensure a controlled environment, such that the initial FRFs are unbiased by measurement error and noise. However, there is a tradeoff, since the numerical model may introduce numerical error, and/or may not mimic the behavior of actual real life wooden junctions in sufficient detail. By using a dynamic implicit time domain solver in Abaqus, the model accounts for non-linear contact properties in the coupling.

In Section 16.2 the methodology is described in detail. Sections 16.3 and 16.4 present and discuss the results, while ideas for future work are proposed in Section 16.5. Finally, findings are summarized and conclusions drawn in Section 16.6.

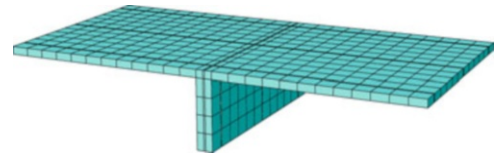
16.2 Methodology

The analyses presented here consist of three main stages:

1. A series of measurements for modal analysis is simulated by a numerical FE-model in Abaqus. Impact testing using three excitation points and 32 response points is simulated by utilizing an implicit dynamic solver.
2. The response time signals for each degree-of-freedom (DOF) at each impact are exported from Abaqus as acceleration signals. These are then imported into Matlab, where Gaussian white noise is added before applying an exponential window and calculating the FRFs by means of the fast Fourier transform (FFT).
3. The resulting FRFs are imported in Pulse Reflex Advanced Modal Analysis where they are analyzed using each of the two curve fitting methods being investigated in the present paper.

The following sections describe each step of the analysis in detail.

Fig. 16.2 FE mesh model in Abaqus



16.2.1 Computational Model in Abaqus

The T-junction is modeled in the commercial FEM package Abaqus. The model consists of just two parts; the plate and the beam. The two parts are supposed to be connected to each other by three screws, which for simplicity are modeled as full surface ties at three 5 mm by 5 mm square interfaces. The contact between the remaining parts of the surfaces is assumed to have a tangential friction coefficient of 0.5, while the normal behavior is modeled using linear pressure-overclosure with contact stiffness 50 GN/m.

All parts are modeled using solid continuum finite elements. 20-node brick elements with quadratic spatial interpolation of the displacement are adopted. The mesh size is put to 50 mm to ensure a sufficiently high resolution of the model in the investigated frequency range. The mesh is designed such that the nodes constituting the plate mesh align with the nodes on the frame structure. The mesh is shown in Fig. 16.2. As three-dimensional solid continuum elements have no rotational degrees of freedom, only displacements are considered. Free-free boundary conditions are assumed. Isotropic and homogeneous materials are assumed if not directly stated otherwise.

The material properties are the same as used in [1]. The properties of the beam are: Young's modulus $E = 8.5$ GPa, Poisson ratio $\nu = 0.3$, density $\rho = 480$ kg/m³. Damping is set to 5% of the stiffness. The damping is applied as structural damping, i.e. the damping forces are assumed proportional to the forces caused by stressing of the structure. This simulates the effects of friction in the timber. Generally a spruce beam would not be expected to have isotropic material properties, but since it (in terms of stiffness) mainly contributes in one direction in the present experiment, it is assumed to be isotropic. Regarding the material properties of the particleboard plates, experiments have shown that they behave in an orthotropic manner, which may be related to the way such plates are manufactured. As a crude estimate, a quick fit has been made by adjusting the Young's Moduli and shear moduli until a decent fit between measurement and model (in terms of natural frequencies and modeshapes) was obtained. The resulting values are: Young's moduli $E_1 = 3.45$ GPa, $E_2 = 3.00$ GPa and $E_3 = 4.00$ GPa, Poisson ratio $\nu_{12} = \nu_{13} = \nu_{23} = 0.2$, shear moduli $G_{12} = 1.35$ GPa and $G_{13} = G_{23} = 1.20$ GPa, density $\rho = 645$ kg/m³. Damping is set to 2% of the stiffness.

Each impact has been modeled as a concentrated force in a single node located at the bottom of the plate, while the responses are taken at nodes on the top of the plate. The responses are extracted as acceleration in nodes corresponding to where accelerometers had been placed in [1]. Likewise, the impact nodes correspond to positions of excitation used in [1]. The (transient) impact signal is a narrow Gauss shaped signal:

$$y = a \cdot e^{-\frac{(t-t_0)^2}{2 \cdot b^2}}, \quad (16.1)$$

where $a = 100$ N, $t_0 = 0.01$ s, and $b = 7 \cdot 10^{-5}$ s. By utilizing dynamic implicit time integration in Abaqus/Standard and requesting output a time points with a sample rate of 10 kHz for a time period of two seconds after each impact, acceleration time signals are obtained for each DOF for each of the three impacts. From these time signals, the FRFs can be calculated and subjected to modal analysis, which will be described in the following sections.

16.2.2 Post Processing in Matlab

The time signals from Abaqus are imported to Matlab, where the transformation from time domain to frequency domain is carried out by means of the fast Fourier transform. Before applying the FFT, noise is added to the signals by means of the Matlab function `awgn()` – Add White Gaussian Noise. After adding noise, an exponential window is applied before performing the FFT. Finally, frequency response functions are obtained as the frequency domain ratio of response (acceleration) to excitation (force). SNRs from 50 to 0 dB are considered in 5 dB steps.

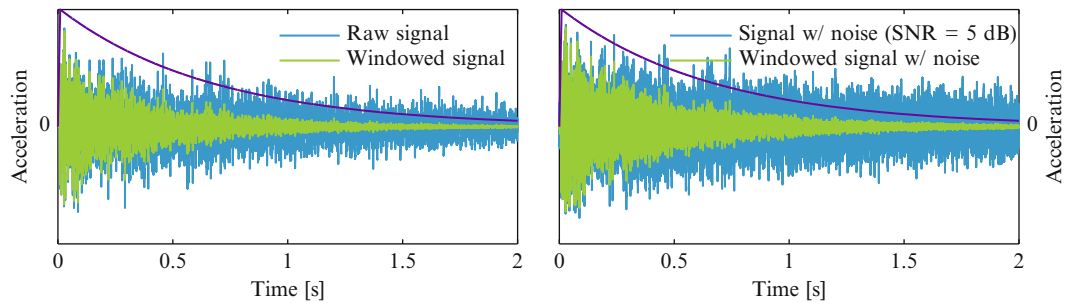


Fig. 16.3 Driving point acceleration response signal before and after applying an exponential window. *Left:* Without additional noise. *Right:* Gaussian white noise added with signal-to-noise ratio 5 dB

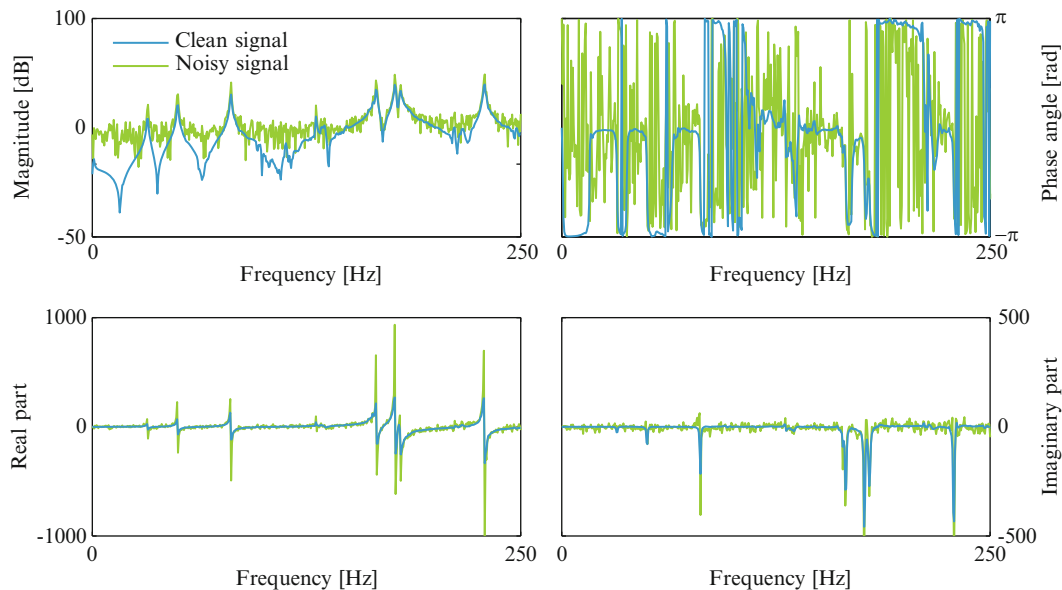


Fig. 16.4 Driving point frequency response function with and without added Gaussian white noise (SNR 5 dB)

Figure 16.3 shows an example of a time signal obtained from Abaqus before and after applying noise and windowing. The signal depicted in the figure is a driving point response, and the amount of noise added is such that the signal-to-noise ratio is 5 dB. The corresponding FRFs are shown in Fig. 16.4

16.2.3 Modal Analysis in Pulse Reflex

The FRFs are imported to B&K Pulse Reflex Advanced Modal Analysis, where they are subjected to modal parameter estimation by two different methods: The Rational Fraction Polynomial-Z method and the Polyreference Time method. The frequency range of analysis is 20-250 Hz. Both methods are global higher order methods and all settings have been left at their default values.

Figure 16.5 shows the geometry as seen in Pulse Reflex with 32 response DOFs and three impact DOFs. Analyses have been carried out using all three impacts at once as well as for each impact alone.

Once a stability diagram is generated, the built-in automatic mode select function is used to obtain an unbiased selection of modes. An example of such a stability diagram is given in Fig. 16.6, which shows a screen dump from Pulse Reflex. After the mode table have been generated by the automatic procedure, the modes are examined one by one in order to reject falsely selected modes.

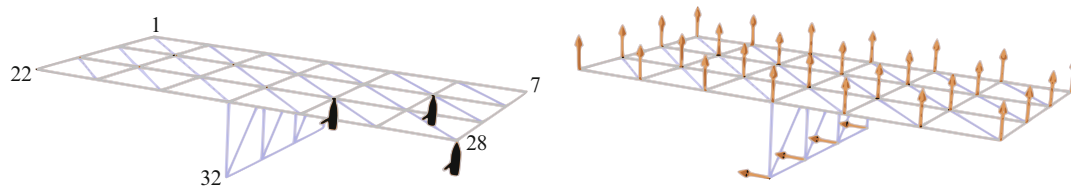
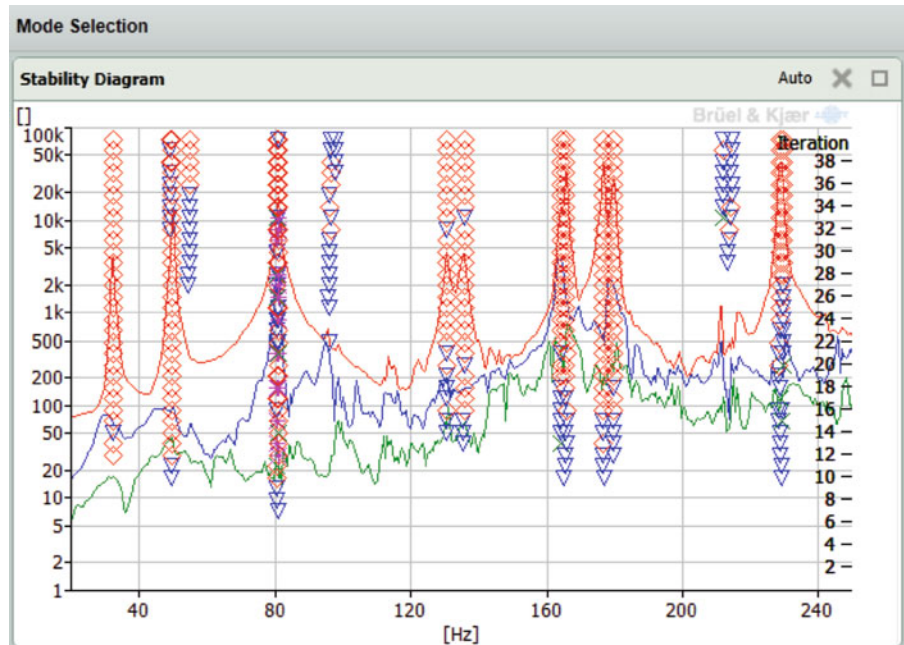


Fig. 16.5 Left: Impact DOFs. Right: Response DOFs

Fig. 16.6 Stability diagram in B&K Pulse Reflex



16.3 Results

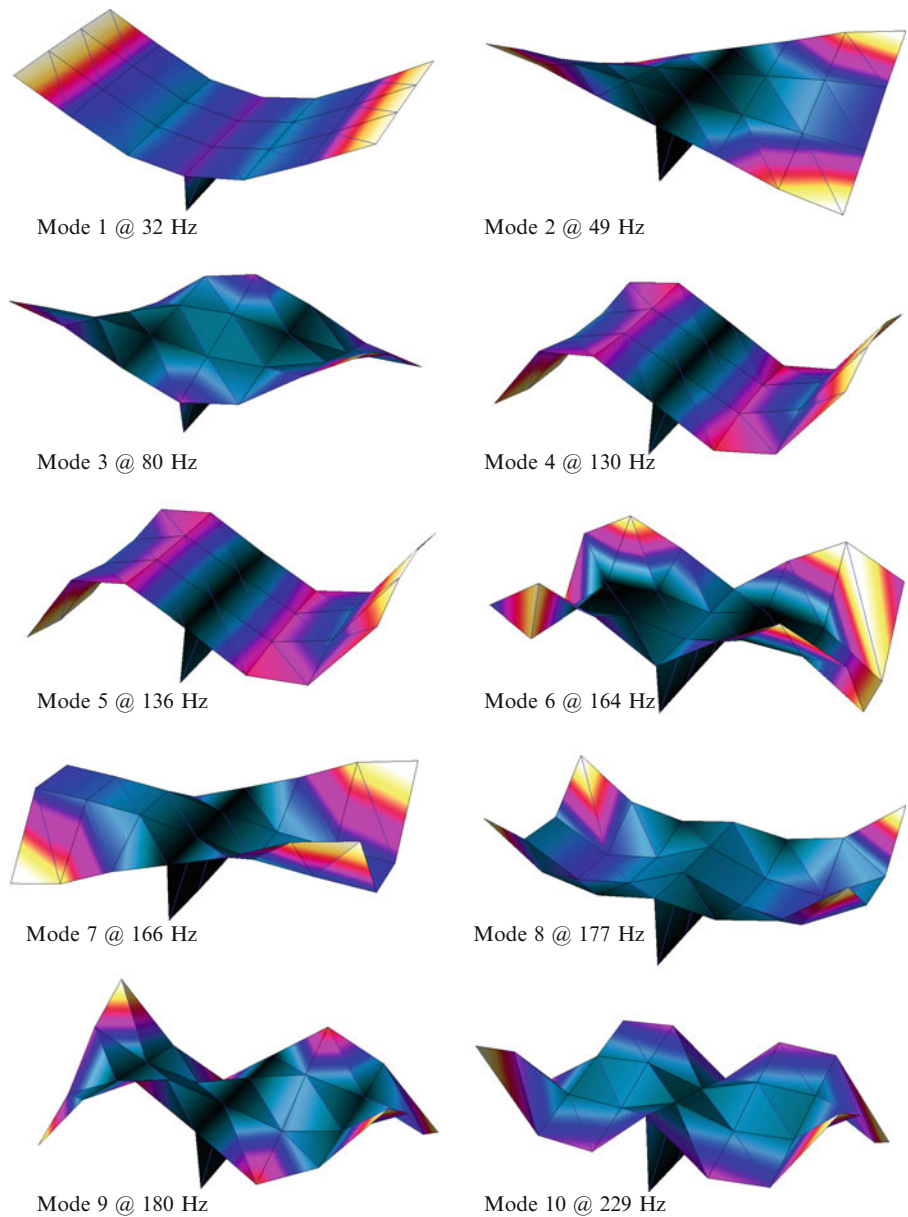
Figure 16.7 shows the modeshapes of the structure within the frequency range of interest. Notice how two of the shapes are nearly identical – this behavior has been observed in measurements [1] of a number of nominally identical structures in previous investigations. It is believed that this behavior is caused by the first torsional mode of the beam exciting the second bending mode of the plate, and vice versa.

Each of the two curve fitting methods has been tested with various amounts of noise added to the signal before analysis. In Pulse Reflex the ‘auto’ mode select feature has been utilized to ensure objective results without user interference. The auto-generated mode table has been compared to the reference case (i.e. the noise free case) and based on either low MAC value (see [3]) or extreme complexity, some of the modes have been rejected. The results are depicted in Fig. 16.8, where the numbers of ‘correctly found’ modes are plotted against the signal-to-noise ratios for each of the two methods. The results are shown for four cases; 1) All three impact DOFs are used, 2), 3) and 4) only one impact DOF is used for the analysis.

Figure 16.9 shows a comparison of modal parameters found by the two curve fitters being investigated. The data are for the case of using all three impacts for analysis and the plots show mean value and standard deviation for signal-to-noise ratios ranging from 50 dB to 0 dB in 5 dB steps.

Finally, Table 16.1 shows a comparison of natural frequencies for modes found by modal analysis of the non-linear model to those found by using a linear perturbation in Abaqus (Lanczos solver). Since contact properties cannot change during a linear perturbation, only the ‘screw’ interfaces are tied, while the remaining parts of the plate and beam are free to move, regardless of whether it is physically possible or not.

Fig. 16.7 Modeshapes from Pulse Reflex



16.4 Discussion

From Fig. 16.8 it is seen, that no single impact point sufficiently covers the all of the modes, while in the case of using all three impact positions, both the Rational Fraction Polynomial-Z and the Polyreference Time method are fairly robust in regards to capturing all the modes even when the ‘measurements’ are contaminated with noise at relatively high levels. At relative noise levels up to SNR 5 dB, all modes are found by both methods (except at SNR 35 dB, where the polyreference time method misses one mode). The Rational Fraction Polynomial-Z method, however, selects more ‘false’ modes than the Polyreference Time method does.

Looking at the modal parameters shown in Fig. 16.9, it is seen that the two methods are in good agreement with each other at both natural frequencies and damping values. The results are similar and the standard deviations are low. For the complexity it is seen that the Rational Fraction Polynomial-Z method is better at capturing the sixth mode, while the Polyreference Time method is slightly better at the third mode. However, at the third mode both methods have significantly higher standard deviation than at the other modes.

Regarding the damping values, it should be emphasized that the exponential window adds significant amounts of damping, especially at the lower frequencies.

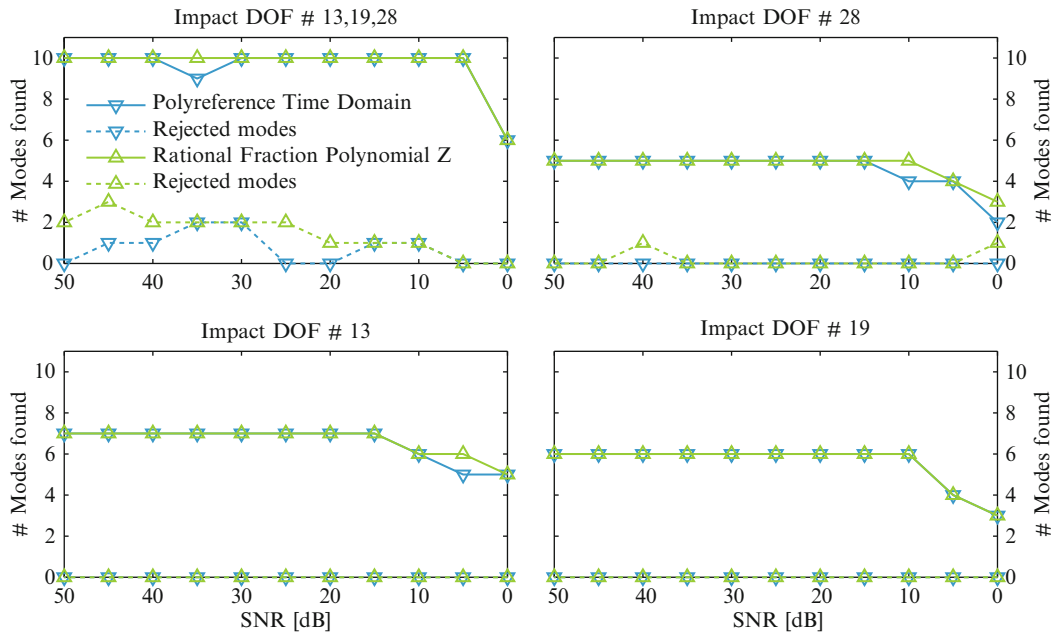


Fig. 16.8 Number of modes found by the ‘auto’ select feature in the modal analysis software. The modes are compared to a reference set by means of MAC value and frequency. ‘False’ modes have been rejected. *Top left:* Analysis using three driving points. *Top right and bottom:* Only one of the three driving points has been used for the analysis

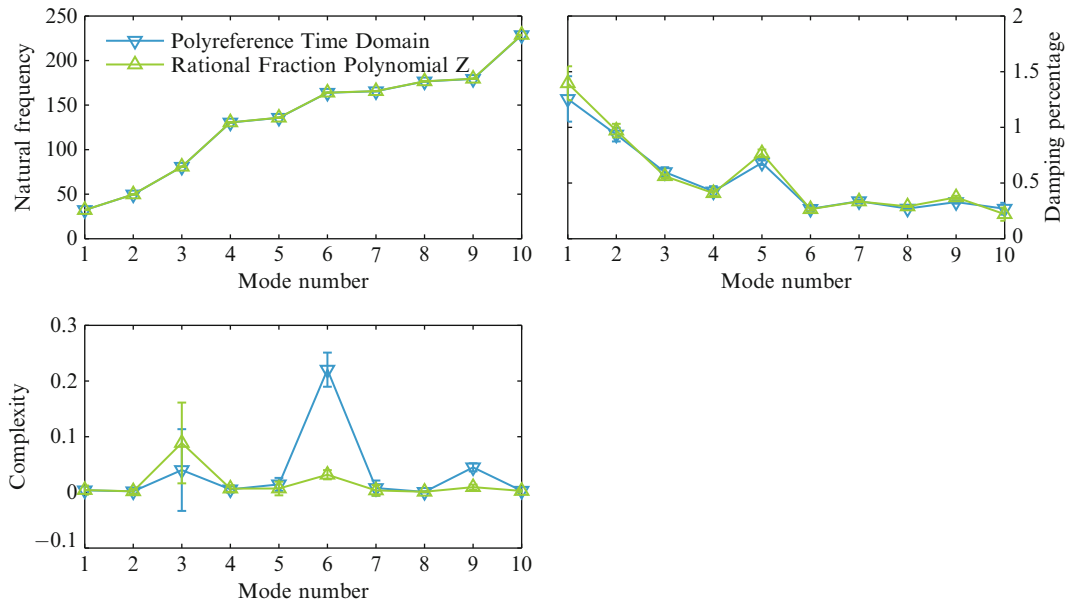


Fig. 16.9 Modal parameters for each mode, depicted with standard deviation (*error bars*) across SNRs ranging from 50 dB to 0 dB in 5 dB steps. *Top left:* Natural frequency. *Top right:* Damping percentage. *Bottom left:* Complexity

Finally, from Table 16.1 it is demonstrated how a linear perturbation analysis is not directly applicable for this type of junction, unless action is taken to account for the interaction between the two parts of structure, e.g. by assuming a linear elastic relation, which may or may not work depending on the type of junction considered. Notice how the structure is much stiffer at two modes with the strongest coupling between torsion of the beam and bending of the plate (mode numbers four and five), compared to what is predicted by the linear perturbation analysis. In the linear perturbation, the first torsion mode of the beam is only lightly coupled to the plate (at 43 Hz), while the actual mode (when including non-linear contact properties) is to be found at 130/136 Hz.

Table 16.1 Natural frequency of the first ten modes found by Pulse Reflex (non-linear contact properties) and linear perturbation in Abaqus, respectively

Mode no.	1	2	3	4	5	6	7	8	9	10
Reflex [Hz]	32	49	80	130	136	164	166	177	180	229
Lanczos [Hz]	32	45	81	43	103	164	165	175	171	227

16.5 Future Work

Modeling the true behavior of screw connections in wooden junctions is not an easy task, since effects like friction, elasticity, damping and deformation may be important factors subject to great variation between nominally identical junctions. An extension of the work presented here would be to include bolt loads instead of surface tie constraints for the screw connections in the Abaqus model. By using bolt loads, the behavior of screw connections may possibly be closer to how real connections behave. However, plastic deformation of the wood will probably have to be taken into account as well. Preferably, a decent linear approximation should be found (if possible), since this would simplify the computations significantly.

Furthermore, it still seems that measured signals are significantly more damped than the simulated responses from the present analysis. The effect of added damping from the surrounding air needs to be investigated.

16.6 Conclusion

The robustness of two parameter estimation methods built into the commercial modal testing software B&K Pulse Reflex Advanced Modal Analysis has been investigated in the present paper. The investigations were based on simulated impact tests inspired by actual measurements done by the authors in a previous paper [1]. The structure being modeled was a T-junction between a particleboard plate and a spruce beam, connected to each other by screws. The simulations were utilizing an FE model made with the commercial FE code Abaqus. The FE model included non-linear contact properties, and the effect of those were discussed.

Two different parameter estimation methods were compared: The Rational Fraction Polynomial-Z method and the Polyreference Time method. The robustness of each of the two methods was investigated by applying increasing amounts of noise to the frequency response functions, before they were analyzed in Pulse Reflex. The ability of each method to correctly capture all the modes—when influenced by noise—was used to judge the robustness of the methods. To ensure unbiased mode selection, the built-in automatic mode selection feature of Pulse Reflex was used.

It has been found that both the Rational Fraction Polynomial-Z method and the Polyreference Time method are fairly robust and well suited for the structure being analyzed. Overall, the Rational Fraction Polynomial-Z method seems to perform slightly better than the Polyreference Time method, but at the cost of including more ‘false’ modes in the auto selected mode table.

The investigations showed that no single impact position was sufficient in capturing all of the modes within the observed frequency range.

It should be noted, that the robustness of the underlying Abaqus time domain solver has not been thoroughly investigated.

Acknowledgements The present research is part of the Interreg project “Silent Spaces”, funded by the European Union. The authors highly appreciate the financial support.

References

1. Dickow KA, Andersen LV, Kirkegaard PH (2012) An evaluation of test and physical uncertainty of measuring vibration in wooden junctions. In: Proceedings of ISMA2012/USD2012, Leuven, Belgium, September 2012
2. ABAQUS Analysis (2010) User’s manual version 6.10. Dassault Systmes Simulia Corp., Providence
3. Allemang RJ (2003) The modal assurance criterion – twenty years of use and abuse. *Sound Vib* 37:14–23

Chapter 17

A Comparative Study of System Identification Techniques Under Ambient Vibration

Muhammad S. Rahman and David T. Lau

Abstract This paper presents the dynamic properties of the Confederation Bridge extracted by four output-only system identification algorithms applied to vibration monitoring data. The purpose of this study is to evaluate the efficiency and accuracy of different modal identification methods, particularly in the presence of high level of uncertainty and noise related to field measurement data. The modal estimates obtained using these alternative approaches are compared and verified against the modal properties from the finite element model.

Keywords Ambient vibration • Operational modal analysis • Structural health monitoring • System identification • Continuous monitoring

17.1 Introduction

Accurate and timely assessment of maintenance and repair requirements of bridges is important for ensuring public safety and for efficient allocation of limited resources by bridge engineers and transportation authorities. Recently the topic of vibration based structural health monitoring (VBSHM) has attracted considerable interest, which offers the possibility of obtaining more accurate and objective information with respect to the deterioration and damage condition of instrumented structures. The comprehensive monitoring project of the Confederation Bridge in eastern Canada represents a unique opportunity to advance the development of VBSHM techniques for performance assessment because of the availability of long-term continuous monitoring information covering not only the dynamic responses of the structure but also other important variables such as concrete temperatures, material properties, weather data, etc. The comprehensive datasets help to better understand and characterize short and long-term structural behaviour of the bridge. Furthermore, due to its particular location, the bridge is exposed to harsh environmental condition including high wind and moving ice floes as well as wide range of seasonal environmental fluctuations which make it an ideal setting for studying the practical applicability of VBSHM due to high level of uncertainties present in the environmental and loading conditions. Previously, Stochastic Subspace Identification (SSI) method was employed to extract the modal information and verify the expected dynamic behaviour of the bridge under different loading scenarios [1].

The latest development of promising output-only modal identification technique, PolyMAX allows new capabilities in automatic data processing for the estimation of modal parameters due to its ability in providing a clear stabilization diagram of the system poles of the monitored structure.

In this context, this present work is focused on the analysis of the ambient vibration data of the Confederation Bridge with the purpose of obtaining insights on the accuracy and efficiency of four different identification methods: the Frequency Domain Decomposition (FDD) [2], Eigensystem Realization Algorithm [3], SSI [4] and PolyMAX [5] methods. FDD, ERA and PolyMAX methods have been added to the existing Confederation Bridge monitoring software platform, Signal Processing Platform for Analysis of Structural Health (SPPLASH) [6] and the results obtained by these four identification algorithms are compared with finite element model of the bridge.

M.S. Rahman (✉) • D.T. Lau

Department of Civil and Environmental Engineering, Ottawa-Carleton Bridge Research Institute, Carleton University,
1125 Colonel By Drive, Ottawa, ON, K1S 5B6 Canada
e-mail: mrahma12@connect.carleton.ca; dtl@connect.carleton.ca

17.2 The Confederation Bridge

The Confederation Bridge is a prestressed concrete box girder structure, spanning the Northumberland Strait, linking Borden, Prince Edward Island, and Cape Tormentine, New Brunswick in Eastern Canada. To cover the 12.9 km long shore-to-shore distance the bridge is divided into 21 approach spans, two transition spans of 165 m each and 43 main spans of 250 m each at a typical height of 40 m above the mean sea level. The main-span portion of the bridge is comprised of 22 repetitive structural frame modules of 500 m length each. Each module is composed of a 440 m portal frame, made up of a 250 m centre span and two 95 m overhangs, one on each side of the centre span, plus a 60 m simply supported drop-in expansion span (Fig. 17.1). The portal frame is constructed of four types of prefabricated component units, pier base, pier shaft, main girder and fixed drop-in span girder. A continuous frame structure is constructed by post-tensioning of the individual structural pieces together. The bridge girders are single cell trapezoidal box girders with section depth varying from 14 m above the piers to 4.5 m at mid-span of the drop-in girder, and a cross-section width varying from 5.0 m at the bottom to 7.0 m at the top, with 2.5 m deck overhangs.

17.3 Continuous Monitoring System

A comprehensive long-term monitoring system on the Confederation Bridge has been in operation since the bridge opening in 1997 in order to collect data and information about its behaviour and performance. The monitoring system measures and records both environmental and bridge response data related to ice forces, short and long-term deflections, thermal effects, corrosion and dynamic responses. The sensors of the monitoring system are installed on two adjacent spans of the bridge, a drop-in span and a rigid frame. The dynamic responses of the structure, due to the effects of wind, traffic, ice floe, and earthquake loadings are captured by 62 accelerometers distributed over the instrumented section of the bridge. In this study, the recorded signals from 50 of these accelerometers are used, which are shown in Fig. 17.2. The sensors and data loggers operate in continuous buffered data collection mode, which upon triggering by detection of specific dynamic

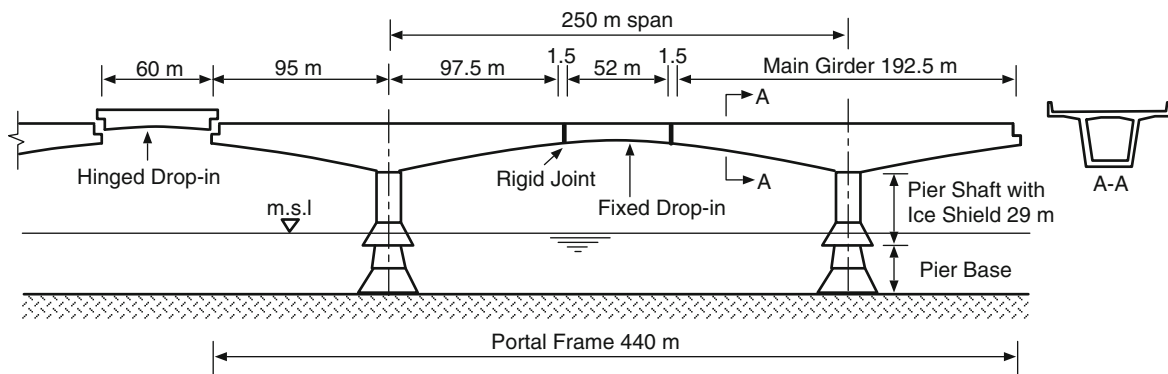


Fig. 17.1 Typical frame layout of the Confederation Bridge

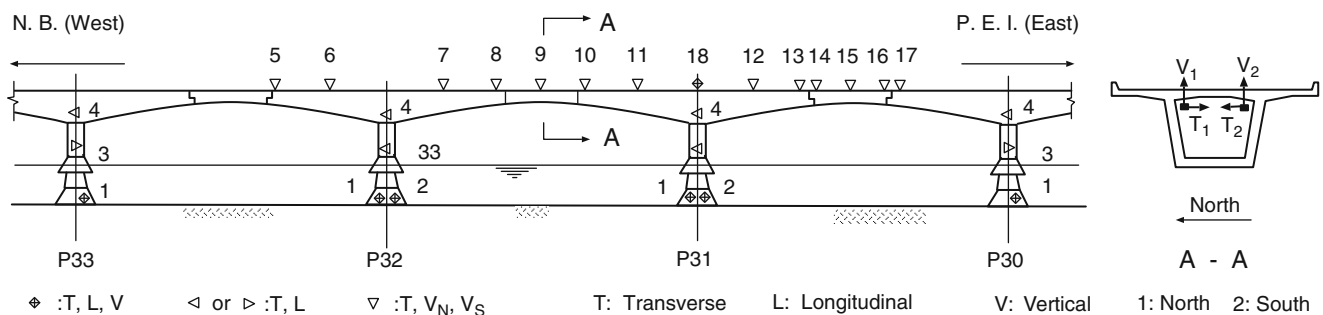


Fig. 17.2 Location of accelerometers in the Confederation Bridge monitoring system

events, such as heavy traffic or high winds, or simply upon user request, store the acceleration time history response data at the sampling rate of 125 Hz. Otherwise, only statistic information determined from the time history data, such as mean, maximum, minimum and standard deviation, are stored. A detailed description of the continuous monitoring system has been presented in [7].

17.4 Monitoring Datasets

A total of 14 data sets, sampled at 125 Hz, have been selected from the Confederation Bridge monitoring database for the present study. The first twelve datasets are recorded within a short period of time (2 days) during which the environmental conditions and loading scenarios can be considered constant. Figure 17.3 shows that the average temperature of the concrete at the instrumented section of the bridge and the wind speed at the bridge site at the time of the 14 datasets. It shows that average temperature and wind speed are relatively consistent during the time of the 12 datasets. The range of average concrete temperature is -2.7°C to -1.4°C , while the average wind speed range is 7.2 m/s to 14.8 m/s. The ranges of these values, 1.3°C and 7.6 m/s are reasonable when compared to the yearly variations of 45°C and 30 m/s for the typical annual average environmental conditions at the bridge site. The remaining 2 events are characterized by high wind scenario. The average wind speed was 35 m/s and the bridge was closed for traffic during these wind events.

17.5 System Identification

The following processing tasks on the data as well as the system identification are carried out using SPPLASH:

- Baseline adjustment of the acceleration time histories by removing any voltage drift from the accelerometer signals.
- Low pass filtering with a cut off frequency of 9 Hz using a Chebyshev type II filter of order 12. This eliminates the high frequency noise and signal components, enhancing response signal in the band of interest (0-5.5 Hz). The filtering is performed in the forward and reverse directions to eliminate nonlinear phase distortion. The low-pass filtering also serves as an anti-aliasing filter for the subsequent down-sampling of the data.
- Down-sampling of the data to 1/3rd of the original sampling rate of 125Hz corresponding to a sampling time of 24 ms. To enhance the frequency resolution of the Frequency Domain Decomposition (FDD) method data are down sampled 5 times resulting in a sampling interval of 40 ms.

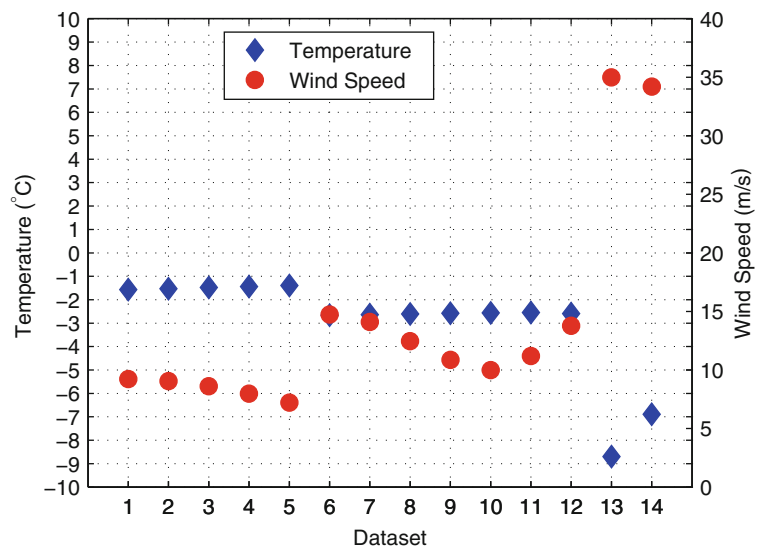


Fig. 17.3 Average concrete temperature and average wind speed of 14 datasets

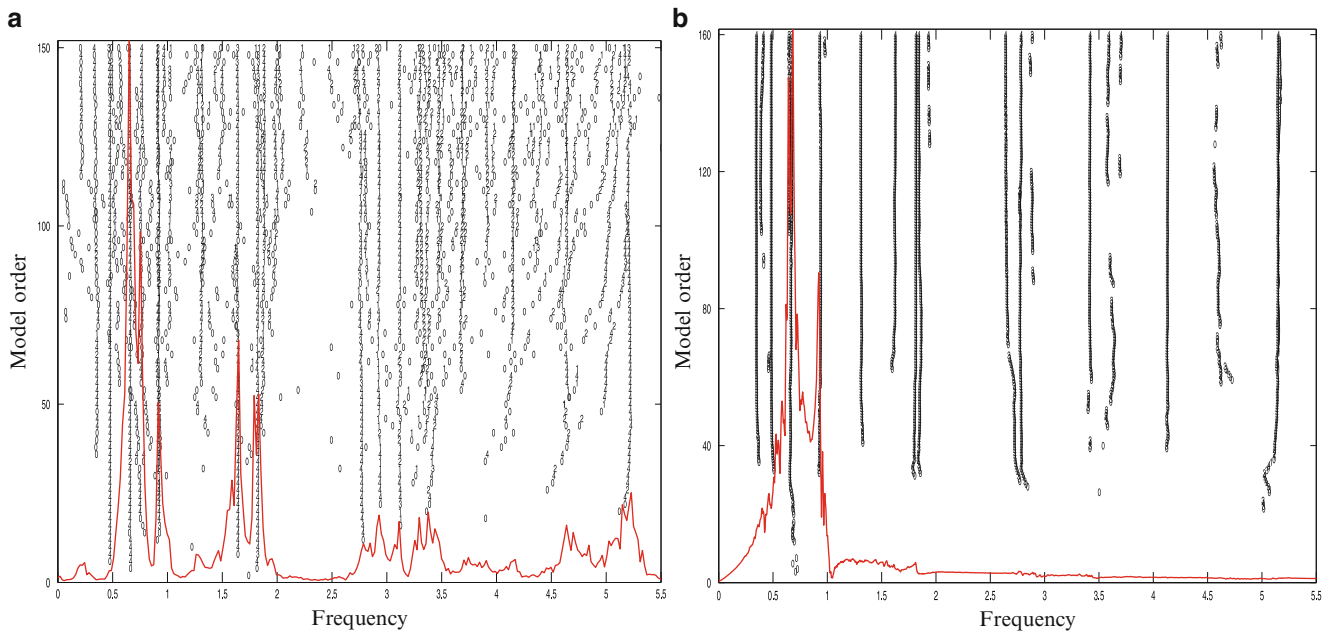


Fig. 17.4 Stabilization diagram. (a) SSI method; (b) PolyMAX method

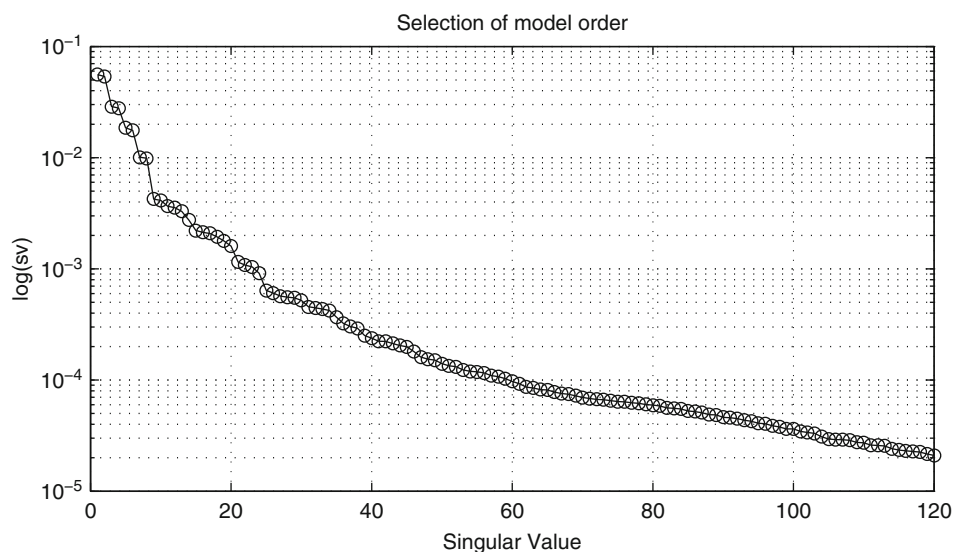
17.5.1 Stochastic Subspace Identification (SSI)

Four vertical and two lateral sensors at monitoring locations 7 and 9 are used as reference sensors for cross-correlation computation. These sensors are suitable references because of their relatively high response amplitudes and because their locations do not simultaneously coincide with modal nodes of any of the important vibration modes of the bridge. In the present study, proper models are identified by the SSI method with a model order of 150 i.e. models containing 75 modes. Even though the actual model order of the data analyzed here is typically around 40, a relatively high maximum model is used in the construction of the stabilization diagrams to allow for a clear visualization of stabilized trends. The number of block rows used in the construction of the Hankel matrix which forms the basis of the system identification, is taken as 250 for all datasets analyzed. In the assessment of the stabilized modal parameters, a stabilization limit of 0.5% is chosen for frequency identification, whereas for mode shape and damping the limits are 1% and 15% respectively. Figure 17.4a shows the stabilization diagram for dataset 1 obtained by SSI method.

17.5.2 PolyMAX Method

Here, the primary identification data, positive power spectrum is estimated via the correlogram approach with 2048 correlation lag time. The same 6 sensors (4 vertical and 2 lateral) at monitoring locations 7 and 9, selected in the SSI method are used as reference sensors here. To reduce the error due to leakage, a 1% exponential window is applied prior to correlogram spectrum estimation. To generate the stabilization diagram by the PolyMAX method, the model order between 150 and 200 is selected and the same stabilization criteria as in the SSI method for frequency, mode shape and damping are employed. Figure 17.4b shows a typical stabilization diagram for one of the dataset obtained by the PolyMAX method. The stable poles can be easily picked from clear stabilization diagram. Interesting to note that there are gaps in some of the vertical line indicating these frequencies are not being identified within a specific band of model order. Furthermore, PolyMAX needs higher model order to stabilize poles.

Fig. 17.5 Singular value of block Hankel matrix



17.5.3 Eigensystem Realization Algorithm (ERA)

For the ERA method, the correlations calculated with respect to the same 6 sensors at monitoring locations 7 and 9 (4 vertical and 2 lateral sensors) are used as identification data. A Hankel matrix of the dimension 8750×600 corresponding to 9.3 s of “free response” data is evaluated. As can be seen in Fig. 17.5 there is no “gap” in the singular value i.e. it is very difficult to determine the number of modes being excited by just examining the singular value plot. In most of the datasets, the truncation of block Hankel matrix is carried out with the model order of 50 to 60 so that approximately 25-30 modes are identified. As the frequency range of interest is 0-5.5 Hz, only the frequencies below 5.5 Hz are considered in the system identification analysis. Modes with high damping ratio are discarded. A threshold of 5% damping ratio is established for the present study. Repeated modes are eliminated based on the lowest energy content given by the singular values. Frequencies within 20% of each other and MAC value of 0.8 are used to identify such modes.

17.5.4 Frequency Domain Decomposition (FDD)

The spectra are estimated via Welch periodogram method using 2048 points FFT with a Hamming window of 50% segment overlap. This results in a frequency resolution of 0.0122 Hz for singular value plot. For each dataset, two spectral matrices were calculated, one for vertical and another one for lateral accelerations. Then, a singular value decomposition of the spectral matrices was performed to evaluate the corresponding non-zero singular values. Figure 17.6 shows the average singular values of all datasets for both directions. Damping estimate is performed in time domain assuming a SDOF around a peak via enhanced FDD.

17.6 Analysis Results from Monitoring Data

Modal vibration frequencies, mode shapes and damping ratios obtained by four system identification methods of the fourteen monitoring datasets described earlier are presented here. The results are also compared to the theoretical values based on the calculated finite element model [8] to examine the correlation between extracted and analytical modal properties.

17.6.1 Modal Frequencies

Table 17.1 presents a summary of the modal frequencies extracted from the monitoring data and the corresponding values from the shell finite element models. Both SSI and PolyMAX algorithms are able to identify 21 modes below 5.5 Hz.

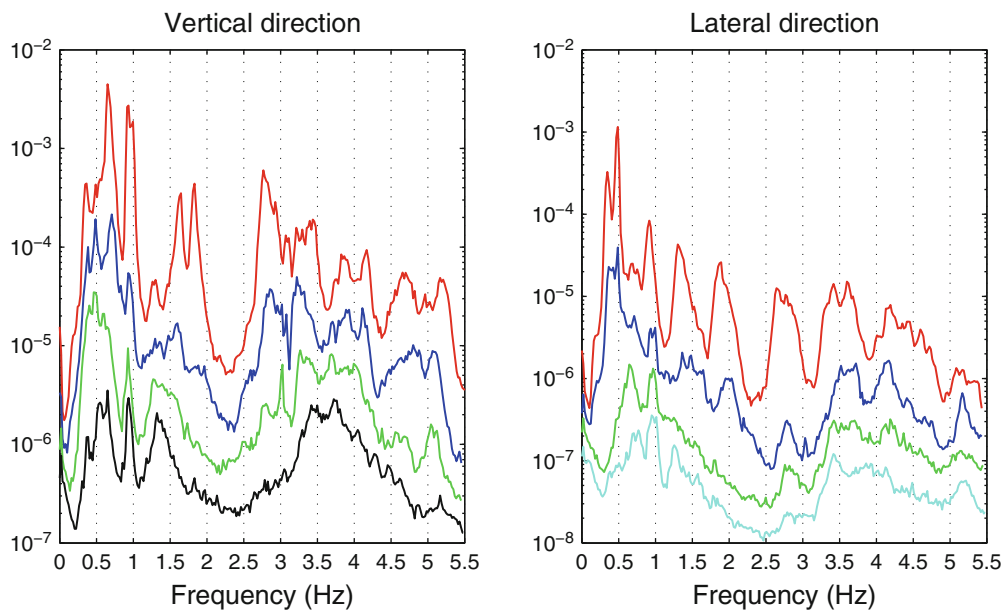


Fig. 17.6 Average singular value of spectra matrix in the vertical and lateral direction

The ERA method fails to detect a mode at 0.55 Hz whereas in case of FDD method; two modes namely at 0.55 Hz and 0.84 Hz are not identified. The finite element modal frequencies based on the field measurement of concrete modulus ($E_c = 43$ GPa) are in close agreement to the measured values with an overall observation of estimated frequencies being slightly lower than the theoretical frequencies. Furthermore, the good agreement between the measured modal frequencies and the updated finite element model values show that the field observed structural dynamic properties as related to stiffness and mass are reasonably close to the design values.

In Table 17.1 the column labelled “number of identification” lists the number of monitoring datasets from which the corresponding eigenfrequencies and mode shapes have been identified. The numbers give an indication of how frequently the vibration modes are being well excited under the typical loading scenarios and thus participate significantly in the measured structural responses. The relevance of this information is for practical structural condition assessment and damage detection based on continuous structural health monitoring data, where not every theoretical vibration mode of the structure is available, but rather one is forced to rely on the subset of modes which can be retrieved consistently from the monitoring data. It is observed that 8 out of the 21 identified modes are consistently excited regardless of different loading variability while some modes, particularly the two modes at 0.55 Hz and 5.01 Hz are seldom excited.

Table 17.1 also shows information regarding the variability of the modal frequencies extracted from the monitoring datasets. In particular, the SSI method offers a more consistent frequency estimate compared to other algorithms. The variation in the identified frequencies relative to the mean appears to be higher for the lower frequency vibration modes and shows a decreasing trend for higher frequency modes. This observation has very important significance since the lower vibration modes often represent the dominant vibration behaviour of most structures under typical dynamic loading conditions, and thus can impact on the proper selection of vibration based algorithms for health monitoring purposes.

17.6.2 Mode Shapes

Modal Assurance Criteria (MAC) values between extracted and theoretical mode shapes are presented in Table 17.2. These values are computed between the mean of normalized extracted mode shapes and the corresponding theoretical mode shape. For the computation of the mean extracted mode shape, the mode shapes extracted from different datasets are normalized by their maximum coefficient. For all 4 algorithms, the average MAC value between extracted and theoretical mode shapes is greater than 0.80, especially for SSI; the average MAC is 0.89 indicating very good correlation. ERA method, with an average MAC of 0.88 is as good as SSI at least in terms of mode shape estimation.

Figure 17.7 shows some of the important vibration mode shapes extracted by system identification process from the field monitoring data by SSI method and a comparison with the expected behaviour from the finite element model. The overall

Table 17.1 Summary of modal frequencies identified by 4 system identification algorithms

Mode number (Hz)	Theoretical SSI				PolyMAX				ERA				FDD			
	Frequency (Hz)	Frequency number of identifications	Difference (%)	RSD (%) ^a	Frequency (Hz)	Frequency number of identifications	Difference (%)	RSD (%) ^a	Frequency (Hz)	Frequency number of identifications	Difference (%)	RSD (%) ^a	Frequency (Hz)	Frequency number of identifications	Difference (%)	RSD (%) ^a
1	0.35	0.33	4	-6.06	3.03	0.34	4	-2.94	4.41	0.36	4	2.78	0.37	4	5.41	4.05
2	0.54	0.48	14	-12.50	0.1	0.47	14	-14.89	2.13	0.48	14	-12.50	0.21	14	-12.5	2.08
3	0.55	0.59	3	6.78	5.08	0.66	3	16.67	9.09	-	-	-	-	-	-	-
4	0.69	0.66	11	-4.55	1.52	0.67	11	-2.99	2.69	0.65	11	-6.15	3.08	11	-1.47	6.62
5	0.79	0.68	14	-16.18	1.47	0.72	14	-9.72	1.39	0.67	14	-17.91	2.99	13	-8.22	1.37
6	0.84	0.92	2	8.7	1.09	0.91	4	7.69	1.1	0.91	3	7.69	2.2	-	-	-
7	0.95	0.94	14	-1.06	1.06	0.93	14	-2.15	1.08	0.92	14	-3.26	2.17	14	-2.15	1.08
8	0.98	0.97	8	-1.03	1.1	0.96	8	-2.08	1.04	0.96	8	-2.08	2.08	8	1.01	1.14
9	1.42	1.31	7	-8.40	1.53	1.33	7	-6.77	0.75	1.35	7	-5.19	2.12	7	-10.08	1.63
10	1.6	1.63	12	1.84	1.23	1.64	14	2.44	0.61	1.64	12	2.44	1.71	12	1.23	2.47
11	1.82	1.81	14	-0.55	1.1	1.85	14	1.62	0.54	1.82	14	0	0.55	14	0	2.2
12	2.46	2.77	14	11.19	0.72	2.8	14	12.14	0.36	2.77	12	11.19	0.36	14	11.83	1.43
13	2.92	2.95	8	1.02	0.68	2.91	8	-0.34	0.34	2.93	8	0.34	0.34	8	-1.74	1.39
14	3.17	3.12	7	-1.60	0.64	3.15	7	-0.63	0.48	3.13	7	-1.28	0.8	7	-1.93	0.9
15	3.51	3.31	4	-6.04	0.9	3.35	5	-4.78	0.54	3.29	3	-6.69	0.61	4	-6.36	0.96
16	3.15	3.45	14	8.7	0.58	3.42	14	7.89	0.88	3.42	14	7.89	0.58	14	7.35	0.77
17	3.6	3.79	7	5.01	0.6	3.68	6	2.08	0.68	3.82	7	5.76	0.52	9	3.49	0.64
18	4.01	4.15	4	3.37	0.1	4.14	3	3.14	0.48	4.16	6	3.61	0.13	2	3.61	0.48
19	4.43	4.69	7	5.54	0.68	4.66	7	4.94	0.43	4.63	7	4.32	0.57	5	8.85	0.41
20	5.01	4.91	3	-2.04	0.81	4.88	3	-2.66	1.16	4.92	3	-1.83	1.02	3	-1.01	1.21
21	-	5.18	8	-	0.58	5.18	8	-	0.39	5.1	8	-	0.25	6	-	0.39
Averages	-	-	9	-0.39	1.17	-	9	0.43	1.46	-	9	-0.57	1.25	9	-0.15	1.64

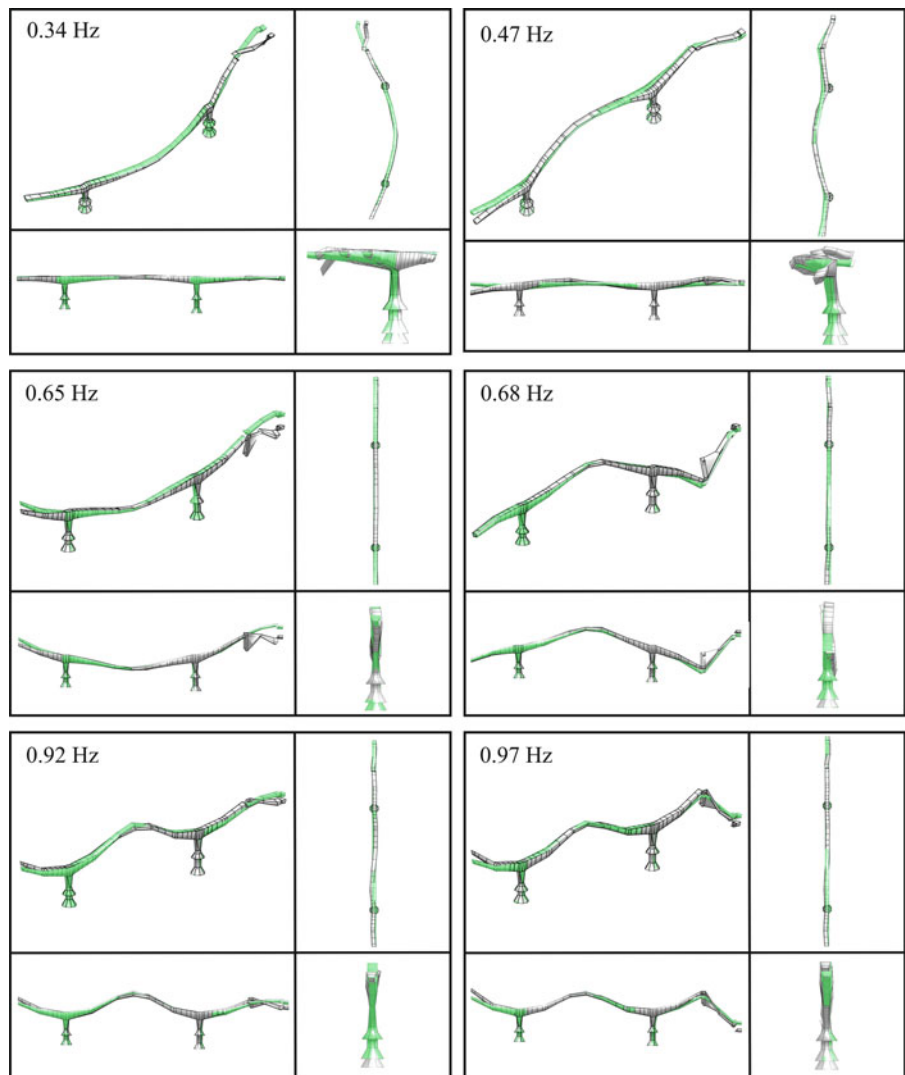
^aRelative standard deviation

Table 17.2 Summary of modal damping ratios and modal assurance criterion (MAC) values for vibration modes retrieved by 4 system identification algorithms

Mode number	Theoretical SSI			PolyMAX			ERA			FDD		
	Frequency (Hz)	Damping (%)	MAC (with theoretical)	Damping (%)	RSD ^a of damping(%)	MAC (with theoretical)	Damping (%)	RSD ^a of damping(%)	MAC (with theoretical)	Damping (%)	RSD ^a of damping(%)	MAC (with theoretical)
1	0.35	1.9	0.92	4.1	48.29	0.59	4.86	123.46	0.86	4.3	118.6	0.85
2	0.54	1.69	0.87	1.76	39.77	0.84	2.49	116.47	0.89	8	187.5	0.84
3	0.55	2.94	0.91	2.76	29.93	0.73	-	-	-	-	-	-
4	0.69	1.85	0.98	1.81	48.87	0.84	4.39	71.53	0.98	4	106.25	0.87
5	0.79	2.1	0.78	2.03	47.01	0.83	4.55	153.41	0.88	4.99	100.2	0.79
6	0.84	1.5	0.84	1.43	61.14	0.84	2.7	78.52	0.8	-	-	-
7	0.95	2.26	0.97	1.98	39.9	0.84	2.43	91.77	0.89	2.1	94.29	0.85
8	0.98	1.6	0.89	1.01	154.46	0.48	1.54	87.66	0.89	2.3	104.35	0.77
9	1.42	0.7	0.8	0.92	97.83	0.84	0.88	90.91	0.85	5.1	141.18	0.79
10	1.6	2.3	0.93	2.01	105.97	0.83	1.4	171.43	0.9	3.3	93.94	0.83
11	1.82	1.9	0.95	1.82	49.18	0.83	1.82	103.3	0.87	1.1	89.09	0.89
12	2.46	1.37	0.93	1.42	61.97	0.84	1.89	103.17	0.89	1.7	82.35	0.81
13	2.92	1.82	0.89	1.9	48.42	0.83	1.37	89.78	0.89	1.9	47.37	0.83
14	3.17	1.25	0.95	1.33	69.17	0.86	1.52	88.82	0.86	1.2	95	0.82
15	3.51	0.92	0.79	0.79	112.66	0.72	1.06	99.06	0.88	1.23	79.67	0.79
16	3.15	1.27	0.78	1.32	37.12	0.85	2.21	95.02	0.88	2	75	0.55
17	3.6	0.9	0.87	0.98	79.59	0.81	2.05	58.54	0.86	1.34	85.82	0.77
18	4.01	0.97	0.86	0.93	19.35	0.82	1.13	86.73	0.81	1	97	0.9
19	4.43	2.3	0.93	2.09	35.5	0.84	1.55	38.71	0.87	1	110	0.68
20	5.01	1.01	0.95	0.97	63.92	0.88	1.08	75	0.92	1.16	113.79	0.87
21	-	1.55	-	1.77	45.08	-	2.06	31.55	-	2.25	115.56	-
Averages	-	1.62	0.89	1.67	62	0.8	2.15	93	0.88	2.63	102	0.81

^aRelative standard deviation

Fig. 17.7 Comparison of experimental and analytical mode shapes below 1 Hz. Vibration modes from the finite element model are shown in *green with dotted lines* and the modes identified from the monitoring data are shown in *grey with full lines* [1]



agreement of the experimental results with the expected values is generally good, especially considering the complexity of the structure and with the use of output-only system identification methods in processing of ambient vibration data. As may be observed in Fig. 17.7, at the expansion drop-in span, discrepancies between the identified and theoretical mode shape tend to be relatively larger. This fact stems probably from less perfect modeling of the actual drop-in span support condition.

17.6.3 Modal Damping Ratios

The averages and standard deviations of the damping ratios of the vibration modes identified by different algorithms are presented in Table 17.2. In general, the standard deviations obtained for the damping ratios are much higher than those obtained for the modal frequencies especially for ERA and FDD methods; the high variance on damping estimate is quite noticeable. In case of FDD method, damping estimate for low frequency modes are unrealistically high, an indication of high leakage bias in spectra computation. In fact, the closeness of the modes and the relatively low frequency resolution adapted to guarantee significant number of averages which is essential for good performance of FDD technique, leads to an unaccepted biased spectra estimation. On the other hand, both SSI and PolyMAX methods provide comparable damping

estimate. The average modal damping ratio by SSI method is 1.62% corresponding to 53% standard deviation of the mean while for PolyMAX; these values are 1.67% and 62% respectively. It is worth noting that the mean extracted modal damping ratios show a slight decreasing trend with increasing frequency.

17.7 Conclusions

In the present study, a total of fourteen field monitoring datasets from the Confederation Bridge monitoring database have been analyzed by four different output-only system identification techniques and the extracted modal properties are investigated against expected design values.

From the output only system identification analysis of the monitoring data, twenty one vibration modes are identified in the frequency range 0-5.5 Hz, exhibiting an overall very good correlation with the modal properties previously calculated using the design finite element modelling. The identified modal frequencies differ by less than 1% on average from the expected design values and the extracted mode shapes are reasonably similar to those expected from the design except for some localized discrepancies at the drop-in-span where the actual asymmetrical support conditions are more complex than those assumed in the finite element models of this study.

Among all the methods, SSI algorithm seems to be more consistent in frequency, damping and mode shape estimate. The application of PolyMAX and SSI methods to the ambient vibration data results in a very similar estimate for natural frequencies and damping ratios while for mode shape estimation, SSI outperforms PolyMAX method. The more traditional identification algorithm, ERA method provides comparable results at least in terms of frequency and mode shape estimation. Furthermore, all 4 algorithms exhibit higher variance in damping estimate especially for ERA and FDD, it is quite noticeable.

Acknowledgements The financial support for this research provided by the Natural Science and Engineering Research Council and the technical assistance provided by the maintenance and operation staff of the Strait Crossing Bridge Ltd are gratefully acknowledged.

References

1. Londoño NA, Lau DT, Rahman M (2011) Characteristics of dynamic monitoring data and observed behaviour of the Confederation Bridge due to operational load variations. *Can J Civil Eng*, doi: 10.1139/cjce-2011-0370
2. Brincker R, Zhang L, Anderson P (2000) Modal identification from ambient response using frequency domain decomposition. *Proceedings of IMAC-XVIII, International modal analysis conference, San Antonio, TX, USA*, pp 625–630
3. Juang JN, Pappa RS (1985) An eigensystem realization algorithm for modal parameter identification and model reduction. *J Guid Contr* 8(5):620–627
4. Van Overschee P, De Moor B (1996) *Subspace identification for linear systems: theory-implementation-applications*. Kluwer-Academic, Dordrecht, The Netherlands
5. Peeters B, Vecchio A, Van der Auweraer H (2004) PolyMAX modal parameter estimation from operational data. *Proceedings of the 2004 international conference on noise and vibration engineering*, 20–22 September, Leuven, Belgium, pp 1049–1063
6. Desjardins SL, Londoño NA, Lau DT, Khoo H (2006) Real-time data processing, analysis and visualization for structural monitoring of the Confederation Bridge. *J Adv Struct Eng* 9(1):141–157
7. Lau DT, Londoño NA, Desjardins SL (2004) Challenges of using continuous monitoring data for structural condition assessment. *Fourth international workshop on structural control, IASC, Columbia University, New York*
8. Lau DT, Brown T, Cheung MS, Li WC (2004) Dynamic modelling and behaviour of the Confederation Bridge. *Can J Civil Eng* 31:379–390

Chapter 18

Some Implications of Human-Structure Interaction

Lars Pedersen

Abstract On structures, humans may be active which may cause structural vibrations as human activity can excite structural vibration modes. However, humans may also be passive (sitting or standing on the structure). The paper addresses this subject and explores the implications of having passive humans present on the structure. It is not conventional to model the presence of passive humans when predicting structural response, but nevertheless it is instructive to investigate which effect they do in fact have on structural behavior and modal characteristics of structures. Such investigations are made in the present paper.

Keywords Human-structure interaction • Footbridge vibrations • Serviceability-limit-state • Passive damping • Bridge damping

Nomenclature

φ	Mode shape function
α	Dynamic load factor
τ	Integration period
ζ_1	Bridge damping
ζ_2	Human damping
a_{MTVV}	Maximum transient vibration value
a_{VDV}	Vibration dose value
a_{VDV}	Root-mean-square value
e	Ratio
f_1	Bridge frequency
f_2	Human frequency
f_s	Step frequency
G	Pedestrian weight
m_1	Bridge modal mass
m_2	Human modal mass
p	Modal load
T	Observation period
v	Walking velocity

L. Pedersen (✉)

Department of Civil Engineering, Aalborg University, Sohngaardsholmsvej 57, Aalborg, Denmark

e-mail: lp@civil.aau.dk

18.1 Introduction

One type of action of an active person on a structure is walking. This scenario may take place on a footbridge, and this paper considers a footbridge subjected to walking loads; and vertical walking loads in particular.

Basically, the problematic scenario for a footbridge is that the serviceability limit state might not be acceptable. Accelerations levels might be too high rendering the bridge unfit for its intended use. But there are different acceleration properties that might be used for evaluating the serviceability limit state of human-occupied structures. It is not the intention of this paper to evaluate which acceleration property is the right one to use, but at least ISO 2631-1:1997 [1] brings forward acceleration properties such as the RMS-value (root-mean-square-value), the VDV-value (vibration-dose-value), and other values as will be outlined.

One intension of this paper is to evaluate how these properties might be influenced by the presence of a passive person (such as a person passively standing at bridge midspan). Such presence would not be an unlikely event, and the passive person might well be the acceleration receiver potentially finding acceleration levels unacceptable (rather than the active person; the pedestrian).

However, experiments not reported here (but in [2–6]) strongly suggest that the passive person alters the dynamic system brought into vibrations by the pedestrian in that the passive person will act as an auxiliary system attached to the bridge mass. That a passive human may be modelled as a dynamic system is in agreement with findings in biomechanics [7].

Hence, this would be expected to change bridge acceleration levels. It is therefore found of interest to do a parametric study in which bridge response predictions are made for the scenario without the passive person and for the scenario where the passive person is present on the bridge. From the bridge response time series, a set of different acceleration properties defined in [1] (RMS, VDV, etc.), are then extracted for both scenarios allowing an evaluation to be made as to how the different acceleration properties are influenced by accounting for the passive person when modelling the dynamic system.

Another scope of the paper is to do a similar parametric study, but whereas the first study focused on the bridge acceleration response at the feet of the passive person, the second study will focus on the bridge acceleration response at the feet of the pedestrian. Generally speaking there are two types of receivers that may be present on a footbridge: The passive person and the pedestrian. As they are not positioned at the same location on the bridge, the vibrations entering at the feet of the two persons will be different. Hence, also the extracted acceleration properties (RMS, VDV, etc) will be different, and the focus of the second study is, as for the first study, to investigate how the different acceleration properties are influenced when accounting for the potential presence of a passive person.

It is believed to be the first published parametric study aiming at quantifying the influence of passive person embracing a number of potential serviceability-limit-state judgement parameters (acceleration properties) and accounting for two potential receivers of vibration.

For the study, a number of assumptions are needed (bridge model, walking load model, and how to model passive persons), and the model assumptions are outlined in Sect. 18.2. Section 18.3 outlines the acceleration properties in focus and how they are extracted from acceleration time series, and Sect. 18.4 presents results of the study followed by a conclusion.

18.2 The Models Considered for the Study

18.2.1 The Footbridge

In order to keep focus on the primary mechanisms for investigation in this paper, it is chosen to employ a quite simplistic bridge for the investigations. In other words it is not the complicity of the bridge model that is to pollute the interpretation of results, which might be the case, if a quite complex bridge was employed.

Therefore it was chosen to consider a simple pin-supported bridge, with the dynamic characteristics (natural frequency, damping ratio, and modal mass) of its first bending mode given in Table 18.1.

Table 18.1 Dynamic characteristics

f_1 (Hz)	ζ_1 (%)	m_1 (kg)
<i>Footbridge</i>		
6	0.4	2,500

Fig. 18.1 Model of the combined bridge-human system

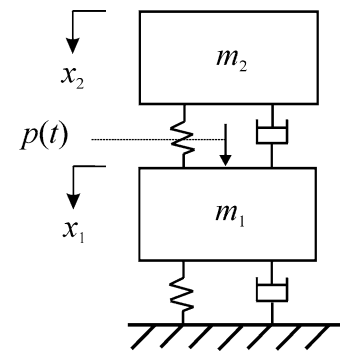


Table 18.2 Dynamic characteristics

f_2 (Hz)	ζ_2 (%)	m_2 (kg)
<i>Passive person</i>		
7.5	30	60

One item to notice is that it is a bridge, which can resonate as a result of pedestrian traffic, in that the first bending mode can be excited by the third harmonic component of walking loads (with a mean step frequency close to 2 Hz as suggested in [8, 9]).

Another item to notice is that the bridge is very lightly damped making it a bridge which potentially is problematic in the serviceability limit state.

The bridge length, L , was set to 11 m, which is realistic, considering the dynamic characteristics given in Table 18.1.

18.2.2 The Interaction Model

As indicated in the introduction, there are a number of indications that the mass of a passive person present on a footbridge will interact with the footbridge mass, hereby altering the dynamic system and its dynamic characteristics, compared to those introduced in Sect. 18.2.1.

Therefore, for the present studies also an interaction model (combined bridge-human model) is considered, in which a human mass (the mass of a passive person) is attached to the modal mass of the bridge by a linear spring and dashpot.

Figure 18.1 shows the model considered for the present studies as an alternative to the SDOF model of the bridge presented in Sect. 18.2.1. The load $p(t)$ represents the vertical load action of a pedestrian.

The grounded SDOF subsystem represents the bridge and the attached SDOF system represents the dynamics of a passive person.

The dynamic characteristics of the bridge are those already presented in Table 18.1, whereas the values assumed for the passive person (natural frequency, damping ratio and modal mass) are shown in Table 18.2.

These properties are not to be interpreted as mean values for a passive (standing) person, but the dynamic properties represent a result (values) derived from tests with an arbitrary standing person. In that sense they are realistic, at least as an example.

18.2.3 Pedestrian Load

A Fourier-series expansion was used to model walking loads from the pedestrian, see Eq. 18.1.

$$f(t) = G + \sum_{i=1}^3 G\alpha_i \sin(2i\pi f_s t - \theta_i), \quad (18.1)$$

where G represents the static weight of the pedestrian. The properties α_i are the dynamic load factors, and for the present study the first three dynamic load factors (harmonics) were considered.

The first dynamic load factor (α_i) was modelled as being dependent on step frequency (f_s) as suggested in [10], see the relationship in Eq. 18.2.

$$\alpha_1(f_s) = -0.2649f_s^3 + 1.306f_s^2 + 1.7597f_s + 0.7613, \quad (18.2)$$

and the two other load factors assumed the values:

$$\alpha_2 = 0.07 \text{ and } \alpha_3 = 0.05. \quad (18.3)$$

The phases were randomly selected. It is a load model by far more reasonable than that found in some design guide lines, although it is possible to make it even more complex and realistic.

The modal load, $p(t)$, associated with the first bending mode (considered to be the dominating mode) is then determined using Eq. 18.4.

$$p(t) = f(t)\varphi, \quad (18.4)$$

where the mode shape function is determined as:

$$\varphi = \sin(\pi vt/L), \quad (18.5)$$

where v is walking velocity and L is the length of the bridge.

There are various ways to model the walking velocity, but it seems established that it depends on step frequency (f_s), even though some design guides do not recognise this to be the case. So as to employ realistic relationships for the studies of this paper, a relationship between step frequency and walking velocity was monitored for a walking person. The relationship is shown in Eq. 18.6.

$$v = 0,386f_s^2 - 0,1217f_s + 0,381. \quad (18.6)$$

It can be shown that the monitored relationship has much resemblance with findings in [11], but the monitored relationship was used for later numerical studies of this paper.

18.3 The Response Parameters

A later section will explain how bridge response time series to the action of a pedestrian was calculated. However, in this section focus is on how bridge acceleration time series were processed to obtain the response parameters introduced in ISO 2631-1:1997 [1].

The bridge acceleration properties in question are those given below.

$$a_{PEAK} = \max[a_w(t)] \quad (18.7)$$

$$a_{RMS} = \left[\frac{1}{T} \int_0^T a_w^2(t) dt \right]^{1/2}, \quad (18.8)$$

$$a_{VDV} = \left[\int_0^T a_w^4(t) dt \right]^{1/4}, \quad (18.9)$$

$$MTVV_\tau = \max \left(\left[\frac{1}{\tau} \int_{t_0-\tau}^{t_0} a_w^2(t) dt \right]^{1/2} \right). \quad (18.10)$$

It is apparent that the acceleration time history is weighted quite differently in the respective calculations, which also explains why there is an interest in focusing on how they are influenced when the dynamic system is altered by the presence of a passive person.

The VDV-approach uses a power of 4, thus placing high focus on peak values in the acceleration time history. The MTVV-approach employs a running integration period, τ (which for the present studies is set to 1 sec), but it eventually places focus a maximum value. Placing focus on the maximum response is certainly the case for the PEAK-approach (by definition), and the RMS-approach is special in the sense that the result (the a_{RMS} -value) is influenced by the observation period T (which is a choice to be made).

As for the observation period T , it was chosen to a value of 30 sec for any RMS-calculation. The choice is solely motivated by the fact that it found to be the time between on-set of bridge vibrations until bridge vibrations had vanished in the most severe resonant case. Another choice could have been made, and results in terms of the RMS-values would then have been different from those presented in this paper.

Generally, [1] focuses on the structural vibrations experienced where they enter into the human body (for the present study at the feet of vibration receivers, as humans are either standing or walking), and for all scenarios the primary resonant vibrations would be in the 4–8 Hz frequency band.

Only vertical components of acceleration response are considered (which is reasonable for the footbridge in focus in this paper), but had horizontal components also been present there would be more processing to do.

18.4 Results

18.4.1 Accelerations at Feet of a Passive Receiver

As previously mentioned, the acceleration properties in Eqs. (18.7, 18.8, 18.9, and 18.10) were calculated at bridge midspan:

- (A) Using the 2DOF interaction model in Fig. 18.1.
- (B) Using a SDOF model for the bridge (i.e. without attaching a SDOF model for the passive person).

For the calculations of midspan bridge accelerations, a Newmark time integration scheme was employed using time steps of 0.01 sec.

The acceleration properties were identified using a number of different step frequencies of the pedestrian (stepping through the range of 1.7–2.3 Hz, being realistic step frequencies). It is to be understood in this way that first the pedestrian was modelled to excite the bridge with a step frequency of 1.7 Hz, then 1.75 Hz etc. For each step frequency two time series were derived (one for assumption A and another for assumption B) and for both, the acceleration properties were calculated.

This gave frequency response curves for all acceleration properties. From these curves, the resonant frequencies were identified along with the associated resonant (max) values of each property in the frequency range of 1.7–2.3 Hz. For example, for the property a_{vdv} , the following resonant properties were identified:

$$a_{VDV}(A) \text{ and } a_{VDV}(B), \quad (18.11)$$

representing the absolute maximum a_{vdv} -value found on assumption A and on assumption B, respectively.

For the presentation of results, the ratio e_{VDV} defined in Eq. 18.12 is introduced.

$$e_{VDV} = a_{VDV}(A)/a_{VDV}(B). \quad (18.12)$$

When this ratio obtains a value below unity it indicates that the maximum VDV-value derived on assumption A is smaller than the maximum VDV-value derived on assumption B. In other words that the passive person has had a damping effect on the bridge (has reduced the VDV-value).

In similar manners, the ratios given in Eqs. (18.13, 18.14, and 18.15) were computed.

$$e_{RMS} = a_{RMS}(A)/a_{RMS}(B), \quad (18.13)$$

$$e_{MTVV} = MTVV(A)/MTVV(B), \quad (18.14)$$

$$e_{PEAK} = a_{PEAK}(A)/a_{PEAK}(B), \quad (18.15)$$

Table 18.3 Acceleration ratios

e_{PEAK}	e_{RMS}	e_{VDV}	e_{MTVV}
0.55	0.44	0.51	0.55

Table 18.4 Acceleration ratios

e_{PEAK}	e_{RMS}	e_{VDV}	e_{MTVV}
0.49	0.64	0.64	0.64

The results in terms of the four ratios are given in Table 18.3.

First it can be noticed that a single passive pedestrian is suggested to be capable of reducing bridge responses quite significantly (by a factor of about 2). One reason for this is that the bridge has quite low inherent damping, whereas the damping inherent in the human body is quite high, and much higher than that normally seen in pure structural systems.

Another observation is that the damping effect of the passive person to some degree depends on which acceleration property is considered. Hence, the damping effect is not a unique property, as it is seen to depend on the parameter chosen for the serviceability limit state evaluation.

Thirdly, it is worth noting that if acceleration properties are computed in order to evaluate the serviceability limit state related to the passive receiver (vibration comfort of the standing person) quite different results are obtained whether or not his presence is modelled when setting up the dynamic system. In reality, he needs to be there (on the bridge) to judge whether the vibration comfort is acceptable or not.

18.4.2 Accelerations at Feet of the Pedestrian

Having focused on the passive receiver, focus is now turned to the active receiver of vibrations (the pedestrian). He will not experience the same bridge vibration time history as the passive receiver standing at mid-span, as he is moving. Particularly, he will not experience bridge vibrations after he has passed the bridge (which the passive receiver might).

As was the case for the passive receiver, bridge vibrations at his feet were calculated, prior to identifying the acceleration properties and ratios here from. Again this was done on both assumption A and on assumption B (with and without accounting for the presence of the standing person).

The results in terms of the four ratios are given in Table 18.4.

Again it is seen that the presence of the passive person is expected to attenuate bridge vibrations (as experienced by the pedestrian), as the ratios attain values less than unity.

By comparing the values in Table 18.4 with those in Table 18.3, it can also be found that the attenuation of the different acceleration properties (induced by a passive person) is not the same.

In other words, the impact of introducing a passive person on the bridge has different effects on the accelerations entering the passive person and those entering the pedestrian. Hence, the “damping effect of a passive person on structural vibrations” is not a unique property. The results suggest that it depends on which receiver of vibrations that is considered, and on which acceleration property that is used for quantifying the damping effect.

It is not shown here, but by adding a passive person on the bridge, not only its damping characteristic will change, but also its natural frequency.

18.5 Conclusion

For a pin-supported footbridge, scenarios with a single (active) pedestrian and the potential presence of a passive (standing) person on the bridge were studied (with and without the passive person). Both persons (the pedestrian and the passive person) might be receivers of vibration and might feel discomfort.

It was found that the passive person had the effect of mitigating structural vibrations (and quite significantly in the studied case), but it was also found that “the damping effect of a passive person on structural vibrations” is not a unique property.

For one, it was shown that it is somewhat dependent on the acceleration property (derived from bridge acceleration time histories) chosen for consideration (PEAK, RMS, VDV, MTVV, being the properties considered in this paper).

Secondly, “the damping effect” also depends on whether focus is placed on the accelerations entering the feet of the passive receiver of vibrations (the standing person) or the pedestrian (the active person).

All in all the study has quantified some effects of human-structure interaction. Perhaps the study has also brought about some questions as to whether existing codes of practice handle the problem of evaluating the serviceability limit state quite right. It is not always as simple as it means.

References

1. ISO 2631-1:1997 (1997) Mechanical vibration and shock—evaluation of human exposure to whole body vibration and shock. Subcommittee SC4
2. Ellis BR, Ji T (1997) Human–structure interaction in vertical vibrations. *Proc ICE: Struct Build* 122:1–9
3. Brownjohn JMW (2001) Energy dissipation from vibrating floor slabs due to human–structure interaction. *Shock Vib* 8(6):315–323
4. Reynolds P, Pavic A, Ibrahim Z (2004) Changes of modal properties of a stadium structure occupied by a crowd. In: *Proceedings of the 22nd international modal analysis conference*
5. Pedersen L (2005) Updating of the dynamic model of floors carrying stationary humans. In: *Proceedings of the 1st international operational modal analysis conference*, pp. 421–428
6. Pedersen L (2007) A contribution to documenting and validating dynamic interaction effects. In: *Proceedings of the 25th international modal analysis conference*, Orlando
7. Griffin MJ (1990) *Handbook of human vibration*. Academic, London
8. Matsumoto Y, Nishioka T, Shiojiri H, Matsuzaki K (1978) Dynamic design of footbridges. In: *IABSE Proceedings*, No. P-17/78: pp. 1–15
9. Živanovic S (2006) Probability-based estimation of vibration for pedestrian structures due to walking. PhD Thesis, Department of Civil and Structural Engineering, University of Sheffield, UK
10. Kerr SC, Bishop NWM (2001) Human induced loading on flexible staircases. *Eng Struct* 23:37–45
11. Bachmann H, Ammann W (1987) *Vibrations in Structures—induced by man and machines*. IABSE Structural Engineering Documents 3e, Zürich

Chapter 19

Evolution of Dynamic Properties of a 5-Story RC Building During Construction

Rodrigo Astroza, Hamed Ebrahimian, Joel P. Conte, Tara C. Hutchinson, and Jose I. Restrepo

Abstract A full scale five-story reinforced concrete building was built and tested on the NEES-UCSD shake table. The purpose of this experimental program was to study the response of the structure and nonstructural systems and components (NCSs) and their dynamic interaction during seismic excitation of different intensities. The building specimen was tested under base-isolated and fixed-based conditions. Furthermore, as the structure was being built, an accelerometer array was deployed in the specimen to study the evolution of its modal parameters during the construction process and due to placement of major NCSs. A sequence of dynamic tests, including daily ambient vibration tests, impact/free vibration and forced vibration (white noise base excitation) tests, were performed on the structure at different stages of construction. Several state-of-the-art system identification methods, including two output-only (SSI-DATA and NExT-ERA) and one input-output (OKID-ERA), were used to estimate the modal properties of the structure (natural frequencies, damping ratios and mode shapes). The results obtained allow to compare the modal parameters obtained from different methods as well as the performance of these methods and to investigate the effects of the construction process and NCSs on the dynamic properties of the building specimen.

Keywords System identification • Full-scale specimen • Shake table tests • Non-structural components • Construction process

19.1 Introduction

Health monitoring, and particularly system identification, of civil structures has become an important field bridging the gap between numerical model-based response predictions and actual response of structures. The estimation of dynamic properties from measurement data recorded in situ on real [1, 2] structures or in the laboratory on large/full-scale structural specimens [3, 4] under realistic conditions allows to calibrate, validate and improve numerical (typically finite element) modeling techniques of structures. Experimental modal analysis and operational modal analysis are the main procedures to estimate the modal parameters (natural frequencies, damping and mode shapes) from recorded structural vibration data. Most of the studies done in this area were performed using data collected from completed structures; only a few have analyzed the variation of the dynamic properties of buildings during construction [5–8] and the effects of the nonstructural components (NCSs) on these dynamic properties [4, 9, 10]. However, these studies were carried out on real buildings and using output-only system identification methods; and it was not possible to closely follow the construction process in order to disaggregate the effects of different construction activities and NCSs, and the effect of the amplitude of the excitation on the dynamic characteristics of the buildings. This paper focuses on the investigation of a full-scale five-story reinforced concrete (RC) building fully equipped with a wide range of nonstructural components, which was tested on the NEES-UCSD shake

R. Astroza (✉)
University of California, La Jolla, 9500 Gilman Drive, San Diego, CA 92093 USA

Universidad de Los Andes, Av. San Carlos de Apoquindo 2200, LAs Condes, Santiago, Chile
e-mail: rastroza@ucsd.edu

H. Ebrahimian • J.P. Conte • T.C. Hutchinson • J.I. Restrepo
University of California, La Jolla, 9500 Gilman Drive, San Diego, CA 92093 USA
e-mail: hebrahim@ucsd.edu; jpconte@ucsd.edu; thutchinson@ucsd.edu; jrestrepo@ucsd.edu

table. Measured responses from ambient and forced vibration tests obtained during the construction and at different stages of installation of the NSCs are used to estimate the dynamic characteristics of the test specimen.

19.2 Description of Specimen and Construction Process

19.2.1 Specimen

The test structure is a full-scale 5-story cast-in-place RC frame building. It has two bays in the longitudinal direction (direction of shaking) and one bay in the transversal direction, with plan dimensions of 6.6 by 11.0 [m]. The building has a floor-to-floor height of 4.27 m, a total height of 21.34 [m] and an estimated total weight of 3010 [kN] for the bare structure and 4420 [kN] for the structure with all the nonstructural components (excluding the foundation, which has a weight of 1870 kN approximately), respectively. The seismic resisting system is provided by a pair of identical moment resisting frames in the North and South bays. The beams have different details at different floors. The specimen has six 66×46 [cm] columns reinforced with 6#6 and 4#9 longitudinal bars and a prefabricated transverse reinforcement grid (baugrid). The floor system consists of a 20.3 [cm] thick concrete slab for all levels. There are two main openings on each slab to accommodate the stair and elevator. Two transverse concrete walls 15.2 [cm] thick provide the support for the elevator guiderails. More details about the structural system and NCSs can be found in [11]. Figure 19.1a shows a schematic view of the test building.

19.2.2 Construction Process and NCSs

The construction of the building began in May 2011 with the foundation system. The bare structure was completed on September 23, 2011. In parallel to the construction of the building, the installation of the stair began on August 13 and was completed on October 11, 2011 (see Fig. 19.1b). The installation of the NCSs started immediately after completion of the structure. Each level of the structure was equipped with different nonstructural components and contents to support different occupancies. The first floor was designated as a utility floor, while the second floor was modeled as a home office and a laboratory environment area. The third floor had two computer servers representing important electronic equipments commonly damaged during earthquakes. Levels four and five were designated as hospital floors with an intensive care unit (ICU) and a surgery suit, respectively. A fully-operational passenger elevator, metal stairs, a ceiling subsystem and gypsum board partition

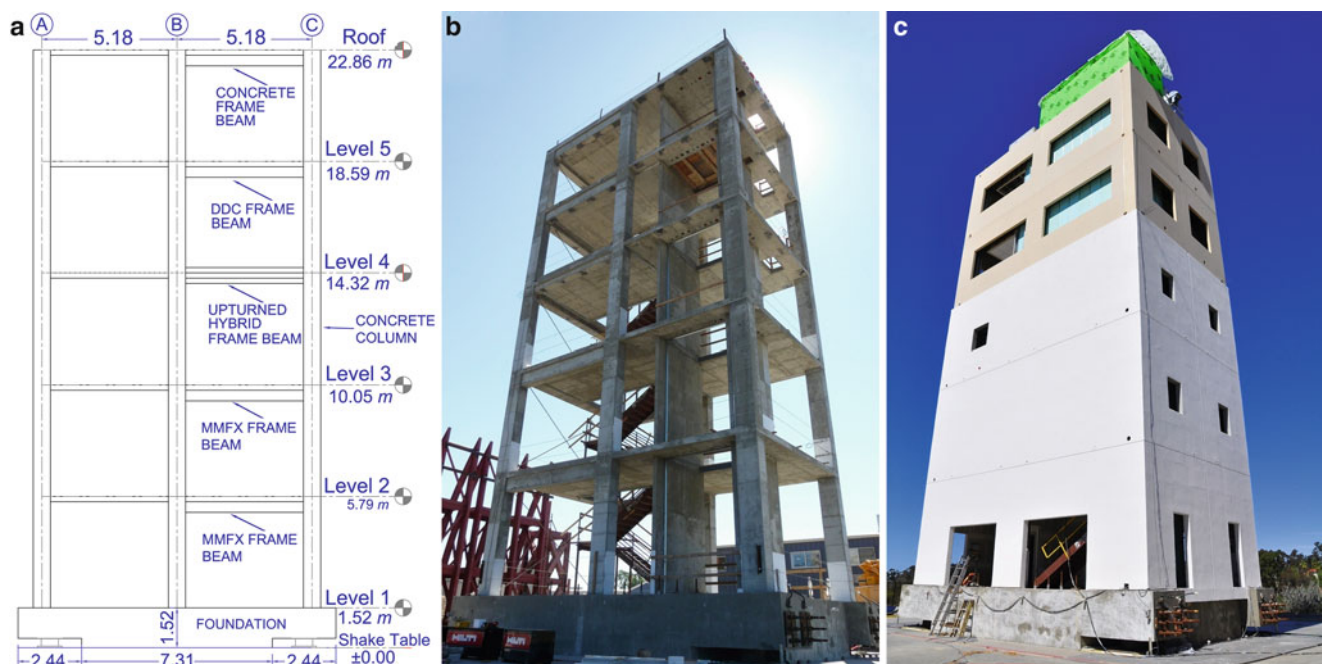


Fig. 19.1 (a) Schematic view of the test specimen, (b) bare structure (August 12, 2011) and (c) complete building (February 23, 2012)

Table 19.1 Properties of the main NCSs and dates of installation

NCS	Date of installation	Comments
Balloon framing	November 1 to December 7, 2011	Weight per floor: 55 kN approx.
Precast cladding	December 19 and 20, 2011	Weight of each panel: 35 and 53 kN (340 kN per floor)
Elevator	January 17 to February 22, 2012 February 6 and 7, 2012	Weight of counterweight: 16.2 kN Weight of cabin: 9.9 kN
Air handling unit	December 13, 2011	Weight: 6.7 kN
Cooling tower	December 9, 2011	Weight: 15.5 kN
Penthouse	November 18 to December 2, 2011	Weight: 25.5 kN
Interior partition walls	December 5 to December 23, 2011 January 9 to February 7, 2012	Floors 1 to 3 Floors 4 and 5

Table 19.2 Recorded vibration data used in this study

Date	Description of the test	State of the system
August 18 to October 12, 2011	Daily 10 min of ambient vibrations	Under construction
October 12, 2011	10 min WN (1.0%g RMS) + 10 min WN (1.5%g RMS)	Bare structure
October 13, 2011 to February 23, 2012	Daily 10 min of ambient vibrations	Installation of NCSs
February 23, 2012	10 min WN (1.0%g RMS) + 10 min WN (1.5%g RMS)	Complete building

walls were also installed in the building. The facade consisted of a light gauge metal stud balloon framing overlaid with synthetic stucco spanning over levels one to three and precast concrete panels on levels four and five. Anchored to the roof were a penthouse, an air handling unit and a large water-filled cooling tower. Table 19.1 summarizes the general properties and date of installation of the main NCSs. The building system was completed on February 22, 2012 (see Fig. 19.1c).

19.3 Instrumentation Array and Dynamic Tests

19.3.1 Instrumentation Array

Before pouring the concrete slab at the third level, on August 18, 2011, a temporary accelerometer array was deployed in the structure, consisting of four translational sensors per floor (two per translational direction). The data were sampled at 240 Hz and the raw acceleration time histories were detrended and filtered using a band-pass order 4 IIR Butterworth filter with cut-off frequencies at 0.25 and 25 Hz, frequency range which covers all the modes participating significantly in the response of the system.

19.3.2 Dynamic Tests

Vibration data from dynamic tests (more than 400) were recorded on the building during the period from August 2011 to February 2012, including ambient vibration, free vibration (shock) and forced vibration tests (low amplitude white noise base excitation) using the UCSD-NEES shake table. Ten minutes of ambient vibration data were recorded everyday and impact tests (using a pendulum consisting of a truck tire hanging at the end of a cable attached at the tip of the arm of a boom lift) were performed on average once a week between August 18 and December 22, 2011. White noise tests were carried out at key stages of the construction: bare structure condition on October 12, 2011 and complete building condition on February 23, 2012. Table 19.2 summarizes the recorded vibration data used in this study.

19.4 System Identification Methods Used

In order to estimate the modal properties of the building specimen at different construction stages, two state-of-the-art output-only system identification methods, both assuming broad-band excitation, are used for the ambient vibration data: Data-Driven Stochastic Subspace Identification (SSI-DATA) and Natural Excitation Technique combined with Eigensystem Realization Algorithm (NExT-ERA). For the white noise base excitation data, in addition one input-output method is

employed: Observer/Kalman Filter Identification combined with Eigensystem Realization Algorithm (OKID-ERA). Detailed explanations of these methods may be found in [12–14] for SSI-DATA, NExT-ERA and OKID-ERA, respectively.

19.5 Evolution of the Identified Modal Properties During Construction

The effects of six different main construction activities (Table 19.3) in the construction process are analyzed. The bottom row of Fig. 19.2 shows the time evolution of the construction in terms of the main activities, the left and right panels of the first four rows show the temporal evolution of the identified natural frequency and damping ratio, respectively, of each of the first four modes of the structure. Clearly, since the structure becomes taller and therefore more flexible as the construction progresses, the natural frequencies decrease with time.

It can be seen that the actions inducing the most significant abrupt changes in the natural frequencies are the pouring of the slab (A2) at the fifth and roof levels (September 6, 2011, and September 22, 2011 respectively) and pouring of the columns and shear walls (A4) at the fourth and fifth levels (August 24, 2011, and September 8, 2011 respectively). This can be explained by the fact that after the pouring, both activities increase significantly the mass of the building without considerably changing its lateral stiffness, which starts to increase as the concrete gains strength. The magnitude of the jumps in the variation of the natural frequencies due to concrete pouring reduces as construction progresses, since the added

Table 19.3 Main construction activities

Name	Activity	Name	Activity
A1	Formwork and shoring of slab	A4	Rebar installation and pouring of columns and walls
A2	Rebar installation and pouring of slab	A5	Shoring removal
A3	Formwork of columns and walls	A6	Installation of stairs

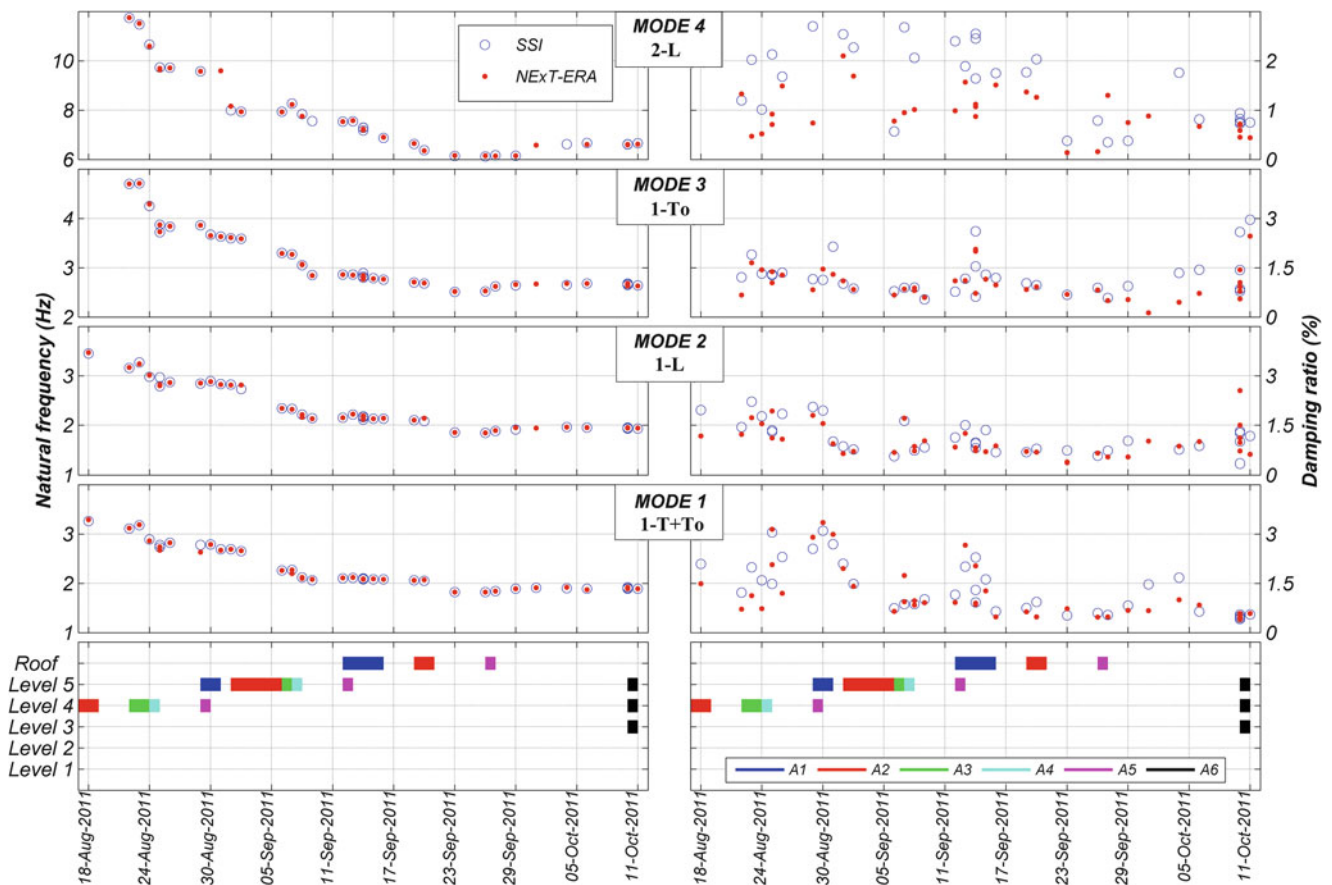


Fig. 19.2 Temporal evolution of the natural frequencies and damping ratios of the first four modes identified during construction

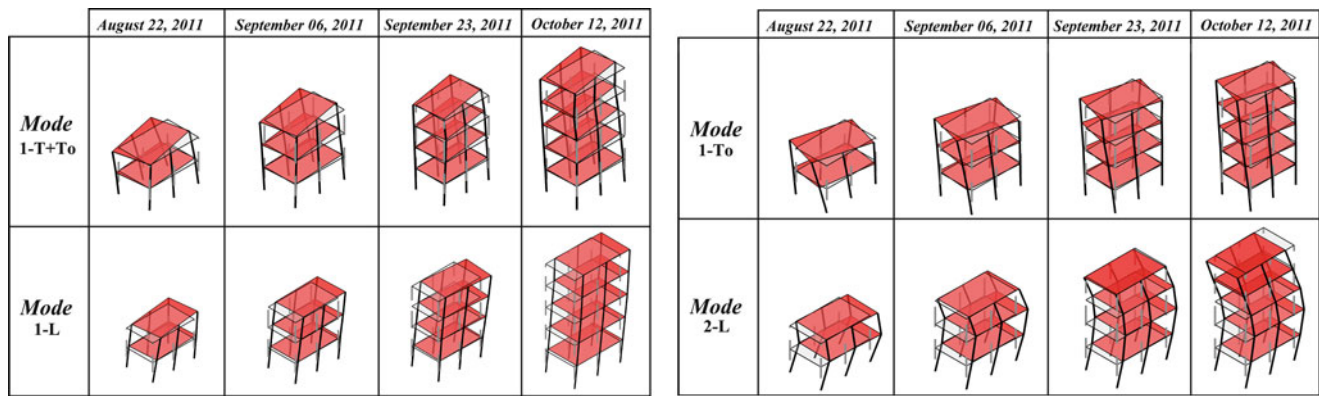


Fig. 19.3 Evolution of the mode shapes of the first four identified vibration modes identified using NExT-ERA from ambient vibration data over different stages of construction

mass becomes progressively lower relative to the total mass of the building. On the other hand, as expected, the effect of formwork and shoring (A1 and A3) is negligible because their mass is low relative to the total mass of the structure and they do not contribute to the lateral stiffness of the building. Similarly, stairs installation (A6) and shoring removal (A5) do not induce any observable change in the dynamic properties of the building for the same reasons as for activities A1 and A3. Finally, it is observed that, from September 26 to October 10, 2011, the natural frequencies increased gradually (1.82–1.92, 1.84–1.94, 2.52–2.68 and 6.12–6.61 Hz for the first, second, third and fourth modes, respectively), which is due to the strength gain and corresponding stiffness gain of the concrete during the curing process over time. This last effect was also detected by [4].

Regarding the damping ratios, the identified values are mostly in the range 0.5–2.5% for all the identified modes when using ambient vibration data, which is consistent with previous studies on similar structures. However, as well known, the scatter of the damping ratio estimates is inherently larger than that of the identified natural frequencies. No clear trends can be observed between the variations of the modal damping ratios and the construction activities. Also, it can be seen that the agreement between the identified damping ratios obtained from different methods is better for the lower modes than for the higher modes.

Figure 19.3 shows the evolution of the mode shapes of the first four vibration modes identified from ambient vibration data when the slabs of the second, third, fourth and roof levels were poured. During the entire construction process, the first, second, third and fourth modes correspond to the first transversal + torsional (1-T+To), first longitudinal (1-L), first torsional (1-To) and second longitudinal (2-L) mode, respectively. It is observed that each of the identified modes keeps basically the same shape (or proportions) as the construction process evolves.

19.6 System Identification of Bare Structure

A first set of dynamic tests making use of the shake table was performed on August 12, 2011, with the building specimen at the bare condition. The low-amplitude banded (0.25–25 Hz) white noise base acceleration excitation consisted of two 10 minutes runs, with RMS acceleration of 1.0 and 1.5%g, respectively. Table 19.4 reports the identified natural frequencies and damping ratios for ten modes of the structure using the white noise base excitation test data. The natural frequencies identified using different methods are in very good agreement for the same level of excitation. The identified damping ratios exhibit a higher method-to-method variability, consistent with previous studies [3, 15]. It is observed that based on ambient vibration data the identified first and second modes correspond to 1-T+To and 1-L respectively (see Table 19.5), while these two modes shift when identified based on white noise test data. This mode-crossing is produced by a decrease of the stiffness of the structure (due to concrete cracking) in the longitudinal direction (direction of motion) during the white noise base excitation test.

It is noticed that for a number of modes OKID-ERA provides an estimate of the damping ratio significantly lower than the output-only methods, especially for the longitudinal modes of vibration (direction of excitation). The identified natural frequencies decrease as the amplitude of the white noise base excitation increases from RMS = 1.0%g to RMS = 1.5%g. Although these differences are relatively small (less than 3.5% in the average), they clearly show the effect of cracking in the concrete, and the resulting loss of stiffness during the white noise tests. This fact is confirmed when the identified natural

Table 19.4 Natural frequencies and damping ratios of the bare structure identified from white noise base excitation test data

Mode	Natural frequency (Hz)			Damping ratio (%)		
	SSI-DATA	NEX-T-ERA	OKID-ERA	SSI-DATA	NEX-T-ERA	OKID-ERA
<i>White Noise RMS=1.0%g</i>						
1 (1-L)	1.82	1.83	1.86	5.16	5.80	3.36
2 (1-T+To)	1.88	1.87	1.90	1.30	1.44	1.36
3 (1-To)	2.63	2.63	2.63	0.93	1.02	1.42
4 (2-L)	6.29	6.29	6.34	3.77	2.74	1.08
5 (2-L+To)	6.43	6.32	6.53	1.11	0.94	1.07
6 (2-To)	10.67	10.68	10.89	1.04	1.81	2.66
7 (3-L)	12.22	12.20	12.00	1.52	1.70	1.04
8 (3-To)	13.53	13.39	13.47	0.75	0.27	0.52
9 (4-L)	18.59	18.64	18.64	2.34	2.02	1.45
10 (5-L)	23.19	23.55	23.29	1.65	2.16	0.57
<i>White Noise RMS=1.5%g</i>						
1 (1-L)	1.75	1.73	1.83	6.32	3.76	3.47
2 (1-T+To)	1.89	1.87	1.88	1.29	1.07	1.44
3 (1-To)	2.60	2.62	2.60	1.06	1.33	1.30
4 (2-L)	6.21	6.05	6.28	3.84	1.61	1.18
5 (2-L+To)	6.40	6.17	6.42	0.77	2.82	0.59
6 (2-To)	10.64	10.61	10.79	2.37	1.87	3.18
7 (3-L)	12.11	12.12	11.93	2.70	2.87	2.06
8 (3-To)	13.48	—	—	0.75	—	—
9 (4-L)	18.46	18.51	18.29	2.13	1.59	1.63
10 (5-L)	23.19	22.92	23.14	1.48	1.72	1.28

L: longitudinal/T: transversal/To: torsional

Table 19.5 Natural frequencies of the bare structure identified from ambient vibration test data

Mode	Before white noise tests (October 12, 2011)		After white noise tests (October 13, 2011)	
	SSI-DATA	NEX-T-ERA	SSI-DATA	NEX-T-ERA
1 (1-L)	1.91	1.90	1.90	1.92
2 (1-T+To)	1.89	1.89	1.88	1.88
3 (1-To)	2.66	2.68	2.63	2.63
4 (2-L)	6.36	6.36	6.16	6.15
5 (2-L+To)	6.55	6.59	6.53	6.49
6 (2-To)	10.83	10.84	10.77	10.73
7 (3-L)	12.01	12.07	11.97	11.70
8 (3-To)	13.43	13.46	13.63	13.61
9 (4-L)	18.96	18.75	18.40	18.73
10 (5-L)	24.19	23.30	23.76	23.50

frequencies obtained from ambient vibration data before and after the white noise tests are compared (Table 19.5). They are practically the same, and are higher than their counterparts identified during the white noise tests. Also, the first two modes cross again, and their order before the white noise tests is recovered. This means that the concrete was cracked during the white noise tests, however, the amplitude of the ambient vibrations is too small to re-open a significant portion of the cracks, which remain closed due to gravity effects.

Since the mode shapes identified with the methods used in this study are complex-valued, the realized modes were obtained using the method proposed in [16]. Figure 19.4 shows the identified mode shapes obtained from NEX-T-ERA based on the first white noise base excitation test data ($RMS = 1.0\%g$).

In order to compare the mode shapes identified from the three different methods, Figure 19.5 shows the MAC values between them. The high MAC values (close to one) indicate that the identified mode shapes using different methods are in very good agreement. Red lines are shown for the modes that could not be identified by one of the methods.

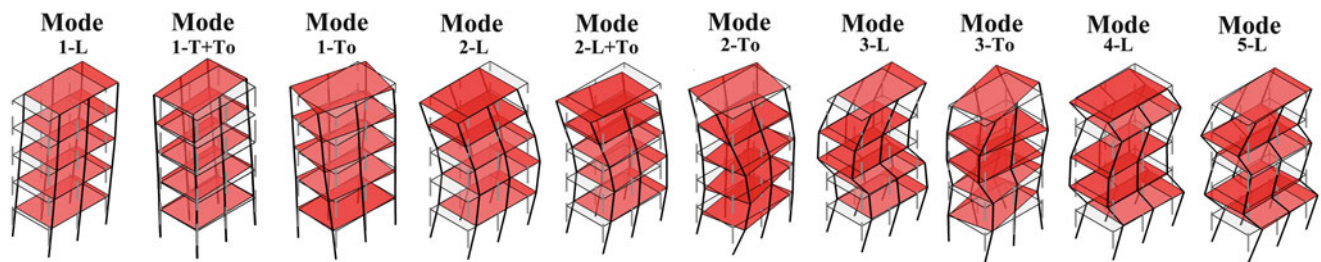


Fig. 19.4 Mode shapes for the bare structure obtained using NEXt-ERA for white noise RMS = 1.0%g

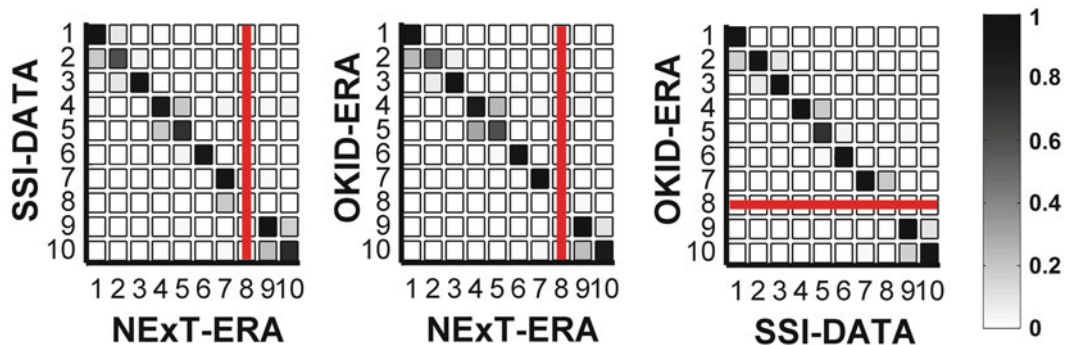


Fig. 19.5 MAC values between modes of the bare structure identified by using different methods (white noise RMS = 1.5%g)

Table 19.6 Main NCSs installed in the building

Name	NCS	Name	NCS	Name	NCS
C1	Partition walls (elevator shaft)	C7	Cooling tower	C13	Sprinkler system (level 5)
C2	Partition walls (stair shaft: 1 to 3)	C8	AHU unit	C14	Roof and gas pipes (level 4)
C3	Partition walls (stair shaft: 4 to 5)	C9	Precast cladding	C15	Contents (levels 2,4 and 5)
C4	Balloon framing	C10	Elevator counterweight and rails	C16	Elevator cabin
C5	Penthouse	C11	Interior partitions (levels 4 and 5)		
C6	Interior partitions (levels 1 to 3)	C12	Ceilings		

19.7 Effects of Nonstructural Components

During the installation of all the NSCs, daily ambient vibration data were collected and additionally low amplitude white noise base excitation tests were performed when the building, including all the NCSs, was completed on February 23, 2012. Table 19.6 shows the main NCSs considered in the analysis. Figure 19.6 presents the evolution of the natural frequencies and damping ratios of the first three modes of the structure identified using SSI-DATA and NEXt-ERA during the time window of NSCs installation (October 13, 2011, to February 22, 2012). The bottom panels show the Gantt chart for the activities defined in Table 19.6.

Again, there is a good agreement between the natural frequencies identified using SSI-DATA and NEXt-ERA, while the identified damping ratios, ranging between 0.4 % and 3.0 %, have a much higher method-to-method variability. The increase of the modal frequencies of the system due to the increase of the lateral stiffness of the building produced by the installation of partition walls can be clearly observed. Due to the installation of partition walls in the elevator shaft (C1) and South East corner (C2 and C3) of the building (from October 13 to October 21), the first, second and third natural frequencies increased from 1.88 to 1.94, 1.90 to 1.96, and 2.63 to 2.67 Hz, respectively. Later, between December 5 and December 19, the natural frequencies increased from 1.91 to 2.10, 1.96 to 2.15 and 2.68 to 3.01 Hz for the first, second and third modes respectively, as a result of the installation of the interior partitions on levels one to three (C6). Within the same time window, the roof-mounted (cooling tower and AHU unit) equipment (C7 and C8) were installed, yet despite these increases in mass at the top of the building, the added stiffness due to the partition walls more than compensated, and the natural frequencies increased. Finally, from January 10 to February 10, 2012, the natural frequencies gradually increased due to the installation

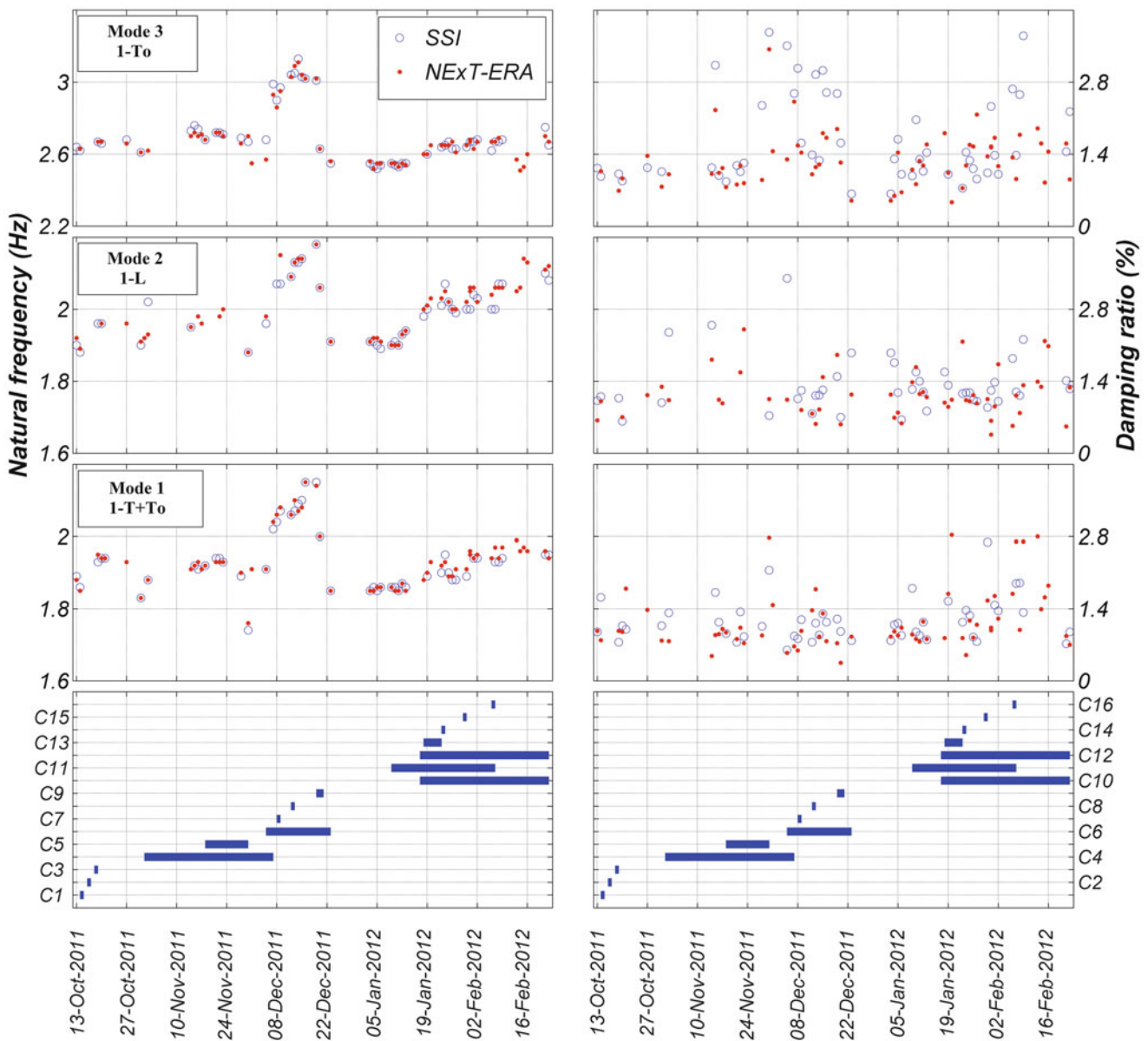


Fig. 19.6 Evolution of the natural frequencies and damping ratios of the first three modes during installation of main NCSs

of partition walls on the fourth and fifth levels (C11). During this time window, the effect of the extra mass added by the elevator counterweight and rails (C10), pipes (C14) and equipment (C15) is dominated by the stiffening effect of the added partition walls. Furthermore, the partition walls also slightly affect the values of the identified equivalent viscous damping ratios. This effect can be seen in the right column of Fig. 19.6 between the dates abovementioned. Similar results have been reported in [4, 10]. Later, from December 19 to December 20, 2011, the first three modal frequencies dropped from 2.15 to 2.00, 2.18 to 2.06 and 3.01 to 2.63 Hz, respectively, due to the placement of the precast concrete panels (C9) on the South and West faces of the building at the fourth and fifth levels. From December 20 to December 22, the same frequencies dropped from 2.00 to 1.85, 2.06 to 1.91 and 2.63 to 2.55 Hz, respectively, when the precast concrete panels (C9) on the North and East facades were installed. Results also show that the installation, between November 2 and November 23, 2011, of the balloon framing (C4), spanning the bottom three stories of the building, moderately increased the natural frequencies from 1.88 to 1.93, 1.93 to 2.00 and 2.62 to 2.70 Hz for the first three modes, respectively. Finally, installation of ceilings (C12), penthouse (C5) and elevator cabin (C16) did not induce any clear effects on the identified modal properties of the building or their effects were negligible compared to those induced by the installation of other NCSs at the same time.

As a general trend during the entire period of installation of the NCSs, it can be noticed that the identified damping ratios tend to slightly increase in time, but again their estimation variability is large compared to that of the natural frequencies. Most of this additional damping is probably due to source of energy dissipation generated by the friction at the interface between the NCSs and the structure.

19.8 System Identification of the Complete Building

After all the NCSs were installed in the building (complete building), a second set of dynamic tests using the shake table were performed on February 23, 2012. The same white noise base excitation sequence described for the bare structure was used. This white noise sequence was repeated three times considering different positions of the elevator. The modal parameters were estimated from the recorded data using the output-only and input-output methods. Additionally, output-only methods were applied to ambient vibration data recorded before and after the white noise base excitation tests. Table 19.7 reports the natural frequencies and damping ratios for ten modes of the building identified using the white noise base excitation data for the configuration with the elevator counterweight located at the top of the building. It is important to note that the results obtained for the other two configurations of the elevator system do not differ significantly, with differences less than 3% for the natural frequencies and 15% for the damping ratios.

Similar observations to those made for the bare structure apply to the complete building. First, it is noticed that the identified natural frequencies decrease as the amplitude of the excitation increases from $RMS = 1.0\%g$ to $RMS = 1.5\%g$. The reductions are relatively higher than for the bare structure. This is due to both cracking in the concrete and interaction between the structure and the NCSs. Furthermore, the same mode shapes as those for the bare structure are identified: the first five longitudinal (1-L, 2-L, 3-L, 4-L and 5-L), the first two coupled transversal-torsional (1-T+To, 2-L+T) and the first three torsional (1-T, 2-T and 3-T) modes. The MAC values between corresponding modes of the bare and complete building are practically equal to unity, indicating that the NCSs do not have a significant effect on the vibration mode shapes for this level of excitation. Additionally, the MAC values between the corresponding mode shapes identified from the different white noise excitations ($RMS = 1.0\%g$ and $1.5\%g$) were computed as very close to unity, implying no changes in identified mode shapes with increasing amplitude of the base excitation.

Table 19.7 Natural frequencies and damping ratios of the complete building identified from white noise base excitation test data

Mode	Natural frequency (Hz)			Damping ratio (%)		
	SSI-DATA	NE _x T-ERA	OKID-ERA	SSI-DATA	NE _x T-ERA	OKID-ERA
<i>White Noise RMS=1.0%g</i>						
1 (1-L)	1.74	1.72	1.83	4.94	4.22	4.17
2 (1-T+To)	1.85	1.90	1.89	3.55	1.54	3.73
3 (1-To)	2.52	2.52	2.52	2.34	2.54	3.52
4 (2-L)	6.93	7.04	6.98	7.75	0.76	4.62
5 (2-L+To)	7.17	8.00	—	0.8	1.11	—
6 (2-To)	10.38	10.11	—	2.30	2.39	—
7 (3-L)	11.50	11.77	11.57	1.83	4.23	6.17
8 (3-To)	12.52	12.76	—	1.08	0.77	—
9 (4-L)	18.81	18.72	19.42	7.50	3.37	2.44
10 (5-L)	23.60	23.62	24.44	5.23	6.51	0.52
<i>White Noise RMS=1.5%g</i>						
1 (1-L)	1.55	1.58	1.70	6.28	6.04	5.07
2 (1-T+To)	1.81	1.81	1.83	4.17	3.38	1.19
3 (1-To)	2.51	2.52	2.39	2.81	2.04	2.55
4 (2-L)	6.68	6.81	6.79	2.28	1.13	4.90
5 (2-L+To)	7.25	6.94	7.09	0.77	0.30	2.90
6 (2-To)	9.82	—	9.99	2.50	—	0.88
7 (3-L)	11.63	11.92	11.64	8.04	1.82	2.91
8 (3-To)	12.66	12.62	12.35	0.85	0.20	0.67
9 (4-L)	19.22	19.12	19.25	4.84	2.73	8.09
10 (5-L)	23.52	23.50	23.59	3.71	4.21	1.91

L: longitudinal/T: transversal/To: torsional

19.9 Conclusions

The effects of the construction process and NCSs on the identified modal properties of a 5-story full scale RC building were investigated. Ambient vibration data were recorded daily during the construction of the specimen and during the installation of different NCSs. Additionally, white noise base excitation tests were performed for both the bare structure and the complete building. Modal parameters were identified from the recorded acceleration response using both output-only and input-output system identification methods.

It was observed that during the construction, the pouring of the structural elements induced abrupt changes in the natural frequencies due to the extra mass added to the system. Also, the natural frequencies gradually increased due to the strength and corresponding stiffness gain of the concrete, during the curing process over time. The mode shapes of the four lowest identified modes remain practically unchanged during the construction process.

The results show that the NCSs affect significantly the modal properties of the system. The natural frequencies increase due to the contribution of the partition walls to the lateral stiffness of the building, and these partition walls also slightly increase the damping ratios. The precast cladding adds significant mass to the building, inducing abrupt decreases in the natural frequencies.

From the modal properties identified using white noise base excitation data, it was observed that the natural frequencies decrease as the amplitude of the excitation increases, but the natural frequencies identified using ambient vibration data before and after the white noise tests are unchanged, suggesting that the cracks formed in the concrete during the white noise tests do not open during ambient vibrations, due to the very low amplitude of the building vibration and the gravity effects.

Acknowledgements This project was a collaboration between four academic institutions: The University of California at San Diego, San Diego State University, Howard University, and Worcester Polytechnic Institute, four major funding sources: The National Science Foundation, Englekirk Advisory Board, Charles Pankow Foundation and the California Seismic Safety Commission, and over 40 industry partners. Additional details may be found at bncs.ucsd.edu. Through the NSF-NEESR program, a portion of funding was provided by grant number CMMI-0936505 with Dr. Joy Pauschke as program manager. The above support is gratefully acknowledged. Support of graduate students Consuelo Aranda, Michelle Chen, Elias Espino, Steve Mintz, Elide Pantoli and Xiang Wang, the NEES@UCSD and NEES@UCLA staff, and consulting contributions of Robert Bachman, Chair of the project's Engineering Regulatory Committee, are greatly appreciated. Design of the test building was led by Englekirk Structural Engineers, and the efforts of Dr. Robert Englekirk and Mahmoud Faghihi are greatly appreciated in this regard. Opinions and findings in this study are those of the authors and do not necessarily reflect the views of the sponsors.

References

1. Brownjohn JMW (2003) Ambient vibration studies for system identification of tall buildings. *Earthquake Eng Struct Dyn* 32:71–95
2. Nayeri RD, Masri SF, Ghanem RG, Nigbor RL (2008) A novel approach for the structural identification and monitoring of a full-scale 17-storey building based on ambient vibration measurements. *Smart Mat Struct* 17(2):1–19
3. Moaveni B, He X, Conte JP, Restrepo JJ, Panagiotou M (2011) System identification study of a seven-story full-scale building slice tested on the UCSD-NEES shake table. *ASCE J Struct Eng* 137(6):705–717
4. Nunez T, Boroschek R, Larrain A (2012) Validation of a construction process using a structural health monitoring network. *J Perform. Constr. Facil.*, 10.1061/(ASCE)CF.1943-5509.0000293
5. Ventura CE, Schuster ND (1996) Structural dynamic properties of a reinforced concrete high-rise building during construction. *Can J Civil Eng* 23(4):950–972
6. Nunez T, Boroschek R, Larrain A (2012) Validation of a construction process using a structural health monitoring network. *J Perform Constr Facil.*, 10.1061/(ASCE)CF.1943-5509.0000293
7. Ni YQ, Li B, Lam KH, Zhu DP, Wang Y, Lynch JP, Law KH (2011) In-construction vibration monitoring of a super-tall structure using a long-range wireless sensing system. *Smart Struct Syst* 7(2):83–102
8. Memari AM, Aghakouchak AA, Ashtiany MG, Tiv M (1999) Full-scale dynamic testing of a steel frame building during construction. *Eng Struct* 21(11):1115–1127
9. Butt F, Omenzetter P (2011) Long term seismic response monitoring and finite element modeling of a concrete building considering soil flexibility and non-structural components. In: *Proceedings of the SPIE*, vol 7981, Sensors and Smart Structures Technologies for Civil, Mechanical, and Aerospace Systems, San Diego, CA
10. Devin A, Fanning PJ (2012) Impact of nonstructural components on modal response and structural damping. In: *XXX International modal analysis conference (IMAC)*, Jacksonville, FL
11. Chen M et al (2012) Design and construction of a full-scale 5-story base isolated building outfitted with nonstructural components for earthquake testing at the UCSD-NEES Facility. In: *43rd structures congress*, ASCE, Chicago, IL
12. Van Overschee P, De Moor B (1996) *Subspace identification for linear systems: theory, implementation, applications*. Kluwer Academic Publishers, Dordrecht, The Netherlands

13. James GH, Carne TG, Lauffer JP (1993) The natural excitation technique (NExT) for modal parameter extraction from operating wind turbines. In: SAND92-1666, UC-261, Sandia National Laboratories, Sandia
14. Juang JN (1994) Applied system identification. Prentice Hall, Upper Saddle River
15. Ndambi JM, Peeters B, Maeck J, De Visscher J, Wahab MA, Vantomme J, De Roeck G, De Wilde WP (2000) Comparison of techniques for modal analysis of concrete structures. Eng Struct 22(9):1159–1166
16. Imregun M, Ewins DJ (1993) Realization of complex mode shapes. In: XI international modal analysis conference (IMAC), Kissimmee, FL

Chapter 20

Structural Dynamic Parameter Identification and the Effect of Test Techniques

A. Devin, P.J. Fanning, C.J. Middleton, and A. Pavic

Abstract Ambient and forced excitation test techniques are both widely used to dynamically identify civil engineering structures. Two floor levels of a newly constructed building, the Charles Institute at University College Dublin, were tested using both techniques. Both floor designs were identical although the layout of partitions above and below each were different. The objective of the tests was to determine the most appropriate test procedure and also to identify whether the layout of partitions contributes in a significant manner to dynamic response. It was found that at low levels of excitation, ambient test levels, the dynamic response of both floors was identical. In contrast, at higher vibration excitation levels, during forced vibration testing, the floor responses were substantially different. The differing modal parameters identified are attributed to an amplitude dependent response resulting from engagement, or not, of the partitions in the dynamic response of the system. The practical significance of this finding is that it is imperative to consider, and test at, the in-service vibration amplitude expected for a floor system.

Keywords Amplitude dependency • Forced vibration analysis • Frequency domain decomposition • Structural identification

20.1 Introduction

Dynamic testing is increasingly used for the identification of a structure's modal characteristics. Traditional experimental modal analysis and output-only methods are the most popular methods for determining these dynamic parameters from in-situ tests on real in-service civil engineering structures. The advantages and limitations of these methods have been widely documented [1] and research has also been conducted comparing the modal parameters resulting from forced vibration and output-only methods. Lamarche et al. [2] concluded that forced and output-only methods return similar frequencies and mode shapes with high MAC correlation between modes but that output-only analyses, which generally have low levels of vibration amplitudes, are more prone to contamination by noise. On the other hand Beyen and Kutanis [3] found that there could be variations in peak values between forced and ambient vibration responses which may indicate an amplitude dependency of modal parameters depending on test method used. Amplitude dependency was also observed by Ulusoy et al. [4] when examining the behaviour of a multi-storey building during earthquakes of different magnitudes. The reported amplitude dependency was attributed to joint and structural interfaces being more significantly mobilised as earthquake magnitude increased. Reynolds and Pavic [5] also investigated the differences between model parameters extracted from forced and ambient vibration measurements on a road bridge and concluded that longer sampling periods and a higher sampling rate is needed for similar reliability of output-only analysis compared to forced vibration analysis. Schwarz and Richardson [6], using the same data sets as [5], highlight that data extracted using two shakers and post-processed into Frequency Response

A. Devin (✉) • P.J. Fanning
School of Civil, Structural and Environmental Engineering, University College Dublin, Dublin, Ireland
e-mail: austin.devin@ucd.ie; paul.fanning@ucd.ie

C.J. Middleton • A. Pavic
Department of Civil and Structural Engineering, University of Sheffield, Sheffield S3 7QB, UK
e-mail: c.j.middleton@sheffield.ac.uk; a.pavic@sheffield.ac.uk

Functions (FRFs) under controlled and measured excitation will usually result in the most accurate results, while impulse and ambient response data could still be utilised to derive meaningful modal parameters.

In this paper the modal parameters of two floors of a four story building, identified using both Operational Modal Analysis and Forced Vibration Analysis techniques, are discussed. The purpose of the tests was to examine the effect, if any, of different non-structural partition layouts on the response of otherwise identical floors slabs. Modal characteristics are determined for both floors using both test procedures. The modal characteristics extracted from ambient response data identified both floors as being identical. However modal characteristics identified from force vibration testing showed that this was not the case. The different findings are attributed to an amplitude dependent response and more active engagement of non-structural partitions at higher vibration amplitudes.

20.2 Test Structure — Charles Institute

The Charles Institute on the University College Dublin (UCD) campus in Ireland is a four storey reinforced concrete frame office building (Fig. 20.1). Structurally it consists of two-way spanning flat slabs, 0.3 m thick, supported on 0.4 m square columns with a maximum bay size of 7.5×6.6 m. The lateral load resisting system is made up of a number of reinforced concrete stairwells, lift cores and service ducts with wall thicknesses of 0.2 m.

Each floor level is divided into state-of-the-art laboratories and office accommodation using light-weight non-structural partitions consisting of plasterboard with a thickness of 12.5 mm and an approximate mass of 47 kg/m, supported on lightweight metal studs.

Exterior wall cladding consists of large polished Chinese black basalt panels 40 mm thick supported on galvanised steel rectangular sections fixed to the concrete slab above and below at 400 mm centres. The polished Basalt has an estimated mass of 430 kg/m. The structure of each floor is identical with only the layout of internal partitions varying from floor to floor. The layout of partitions for the two floors tests is shown in Fig. 20.2a and b respectively. In both cases the solid black lines indicate the partition layout on the floors below.

20.3 Experimental Procedures

The objectives of the experimental tests were (i) to compare the modal characteristics identified by forced and ambient vibration analysis, and (ii) to investigate the effects of differing non-structural partition layouts on identical floors. For both test types accelerometers, located at the intersection of grid lines shown in Fig. 20.3, were used to measure the vertical acceleration on a grid of 195 measurement points.



Fig. 20.1 Completed Charles Institute Building

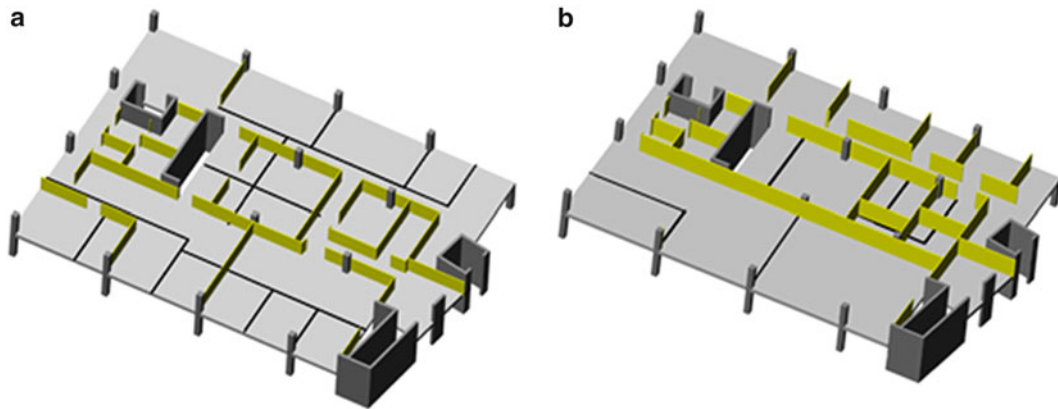


Fig. 20.2 (a) First floor internal partition layout. (b) Second floor internal partition layout

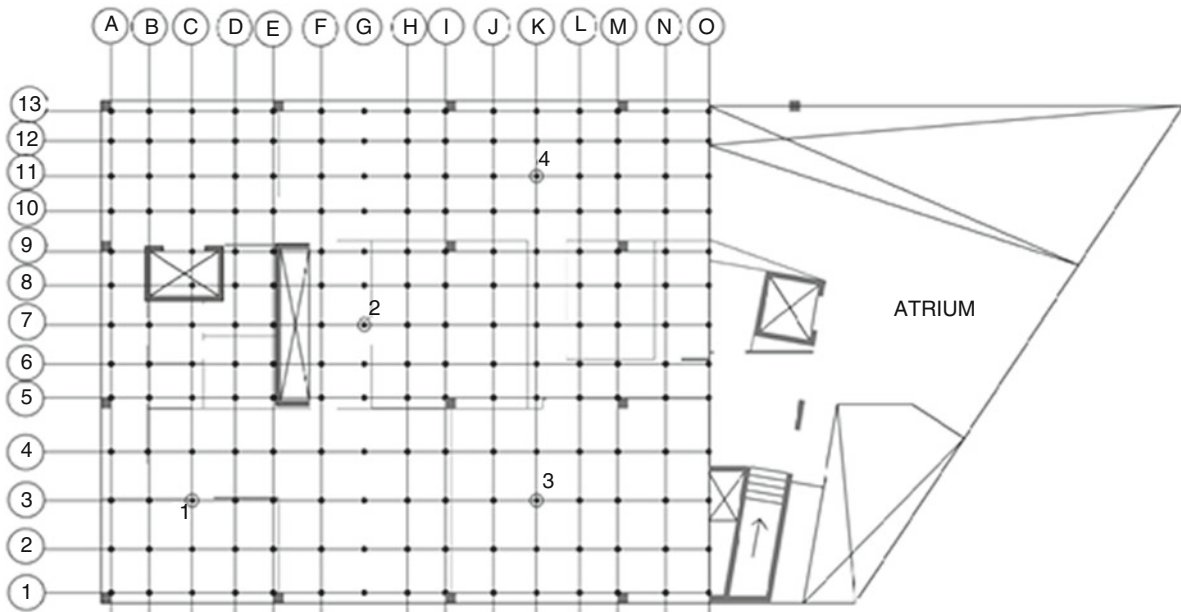


Fig. 20.3 Detailed test grid for forced and ambient vibration analysis

20.3.1 Operational Modal Analysis (OMA)

The ambient acceleration response, due to prevailing environmental conditions, was measured on the first and second floors on two consecutive days. The peak acceleration recorded was approximately 0.0004 g. Given that the expected frequency range was 5–30 Hz the record length used was 10 min with a sampling rate of 12 kHz; these datasets are considered more than adequate for structures with natural frequencies in the range of 5–30 Hz [7].

The measured datasets were post-processed using the Frequency Domain Decomposition (FDD) method. The resulting singular value plots were then used to identify modal parameters associated with the ambient response datasets [8]. To aid accurate extraction of modal parameters, Covariance-based Stochastic System Realization (SSI), a combination of ERA and OKID was combined with FDD [7]. This method determines the ‘real’ physical modes of a system in the presence of measurement and computational noise using a combination of Stabilisation Diagrams and Modal Phase Co-linearity (MPCw). In a lightly damped system, physical modes behave as ‘real’ modes as MPCw approaches 100%, whilst a low percentage of MPCw indicates a complex mode shape indicating a computational or noisy mode [9].

20.3.2 Forced Vibration Analysis

Multi-shaker modal testing of both floors was also carried out separately over two consecutive days while the building was unoccupied. Endevco 7754-1000 piezoelectric accelerometers were used for vibration response measurements. The excitation of the floor structures was provided by four APS Dynamics electrodynamic shakers, with a capacity of 500 N each, located on the concrete slab at test points marked 1–4 in Fig. 20.3. These excitation points were distributed over the floor to ensure an even distribution of excitation energy to all parts of the floor. During testing the peak excitation was of the order of 0.008 g (i.e. approximately 20 times higher than levels recorded during ambient testing).

A Data Physics DP730 24-channel 24-bit digital spectrum analyser was used to drive the four shakers simultaneously using uncorrelated random signals and to digitally acquire force and response data. Frequency response Functions (FRFs) were determined for all measurement points and curve-fitted using a multiple reference orthogonal polynomial algorithm to determine modal properties as implemented in the ME'scopeVES software [10].

20.4 Experimental Results

20.4.1 Operational Modal Analysis

Singular value plots and a Stabilization Diagram for the first and second floors are shown in Fig. 20.4. Table 20.1 compares the first four natural frequencies and damping ratios of the 'real' physical modes extracted from the system. The natural frequencies for both floors range from 11 to 25 Hz and are consistent with each other. The shape and form of the singular value plots are also consistent although the vibration amplitudes in floor 2 are higher.

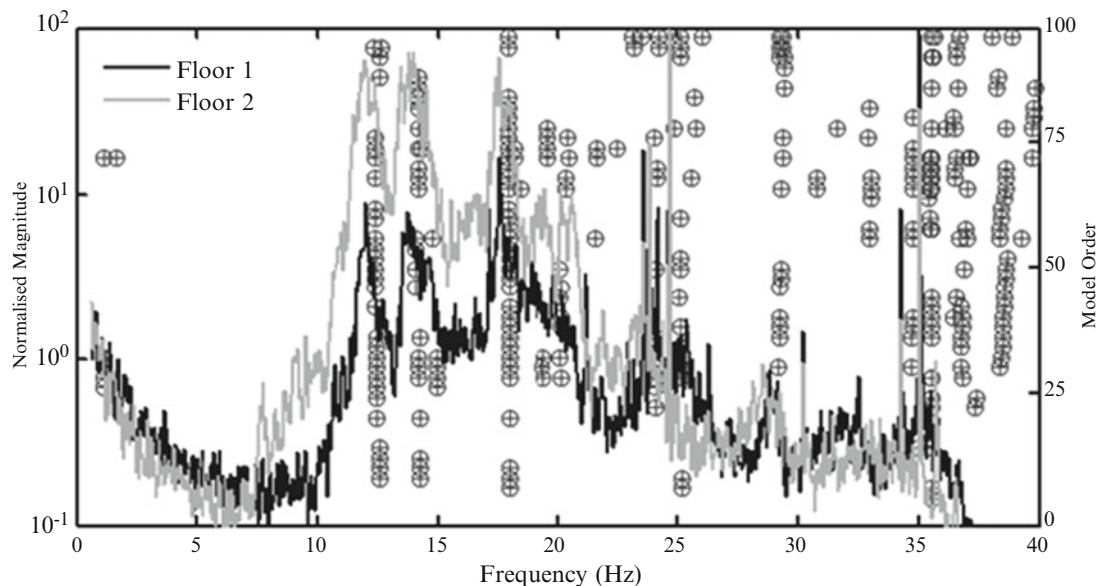


Fig. 20.4 Singular value plots and Stabilization Diagram of floors 1 and 2; the symbol '⊕' indicates the location of a stable pole

Table 20.1 Identified modal frequencies f and damping ratios ζ extracted using FDD and SSI

Mode	Floor 1				Floor 2			
	FDD	SSI			FDD	SSI		
	f (Hz)	f (Hz)	ζ (%)	MPCw (%)	f (Hz)	f (Hz)	ζ (%)	MPCw (%)
1	11.97	12.02	2.40	99.49	12.03	12.04	3.83	94.76
2	13.73	13.80	0.77	85.25	13.77	13.67	2.91	99.36
3	14.17	14.22	4.34	99.19	14.53	14.81	1.79	96.41
4	17.53	17.54	1.67	99.96	17.53	17.57	1.67	99.83

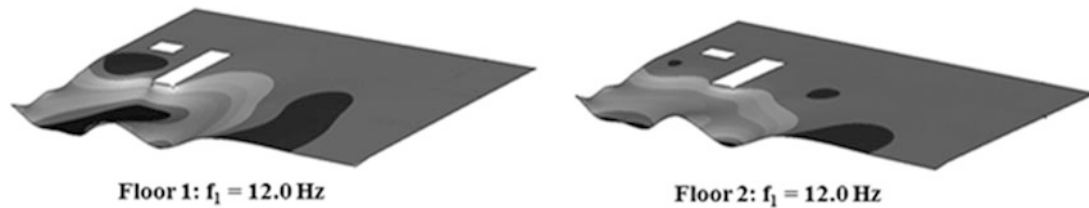


Fig. 20.5 Comparison of mode shape at 12.0 Hz extracted using FDD for first and second floor, MAC = 0.983

The first four clearly distinguishable modes extracted by Operational Modal Analysis results for Floor 1 occur at 12.02, 13.80, 14.22 and 17.54 Hz. The maximum percentage difference between the FDD and SSI identified frequencies for each mode, is 0.5%. Each of these natural frequencies had an MPCw value greater than 85% with the majority having values larger than 99.1% and had numerous stable poles in the Stabilization diagram, indicating that they are all physical modes of the structure.

The frequencies of the first four clearly distinguishable modes for Floor 2 are within 4% of those identified for Floor 1. The first mode shapes, for Floors 1 and 2, are shown in Fig. 20.5. Visually these modes are similar and comparing them using the Modal Assurance Criteria (MAC) yields a MAC value of 0.983. This indicates a very high correlation between the floors' modal shapes. Given the (essentially) identical frequencies and highly correlated mode shapes it is concluded that both floors are nominally identical. The only substantial difference between the floors is that the amplitude of the singular value plot for floor 2 is larger for the first three peaks compared to floor 1. This would indicate that these modes were preferentially excited during the tests; this is attributed to differing prevailing ambient conditions in the building on consecutive days.

20.4.2 Forced Vibration Analysis

The frequency response functions derived from the excitation point datasets are plotted in Fig. 20.6 for both floors. The natural frequencies ranged from 15.7 to 27.0 Hz and 15.0 to 23.7 Hz for floors 1 and 2 respectively. While the frequency ranges were similar the floor point mobility responses are noticeably different. The lowest frequency identified, at approximately 15.0 Hz was also higher than that (12.0 Hz) determined from ambient testing. The mode shapes extracted from forced vibration analysis are plotted in Fig. 20.7. There are a larger number of Floor 1 modes in the 15–30 Hz range and the modes shapes, at similar frequencies, are visually different from those associated with Floor 2. Where there is a degree of similarity between Floor 1 and Floor 2 modes the associated frequency is higher for the Floor 1 mode (for example mode 5 from floor 1 and mode 2 from floor 2 in Fig. 20.7); this would suggest that Floor 1 is stiffer than Floor 2.

20.5 Discussion of Results

The two different test techniques are found to yield different and contrasting findings. Modal parameters extracted for both floors, from ambient response data, are essentially the same thereby characterising the dynamic response of both floors as being identical. However, in contrast, there are significant differences between the modal parameters for both floors using forced vibration analysis; the frequencies identified vary and the modes shapes are different. Furthermore the frequencies of response determined using forced excitation were higher than those determined from ambient responses.

To explain this apparent anomaly two explanations are considered. It is possible that the shaker layout chosen could have preferentially excited higher modes of the structure leaving those lower modes (identified by ambient response analysis) not easily discernible. However this can be discounted as in such a case it would still be expected that the responses of both floors would be identical as the same test set-up, including shaker locations and forced excitation level, was used for both floors, and the design of both floors (thickness and reinforcement details), as well as their restraints at columns and internal shear walls, are the same.

The second and more probable reason for the differing findings is that the response of both floors are amplitude dependent due to the presence of differing partition layouts on, and below, each floor level (see Fig. 20.2). The maximum acceleration level recorded under ambient conditions was 0.0004 g compared to 0.008 g during forced excitation testing. It is believed

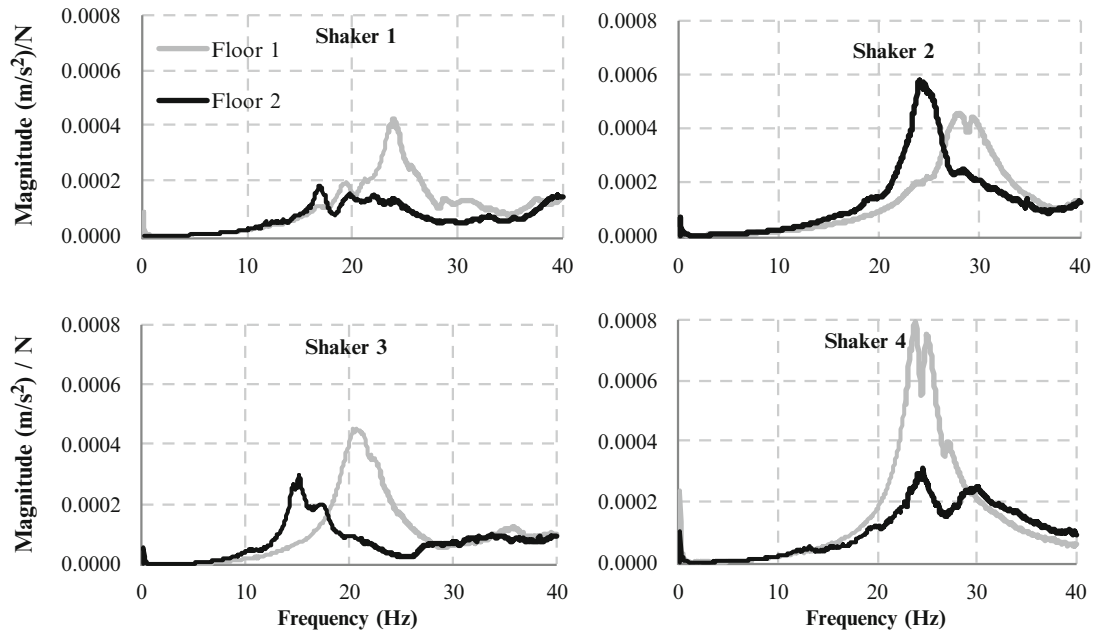


Fig. 20.6 Comparison of forced vibration FRFs at shaker locations for floors 1 and 2

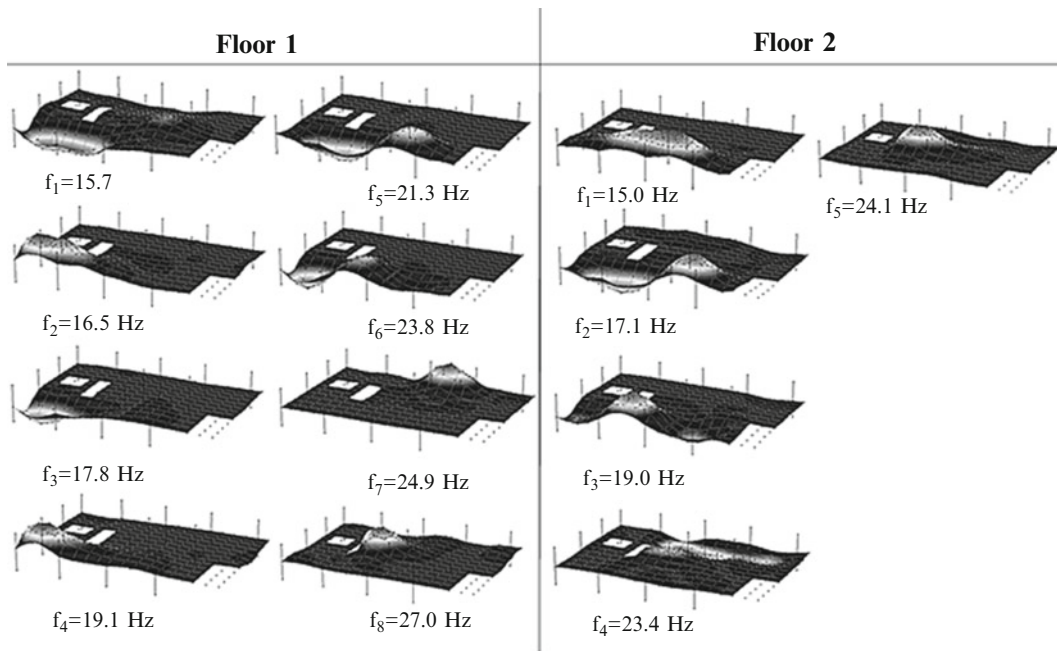


Fig. 20.7 Mode shapes extracted from Forced Vibration Analysis for floors 1 and 2

that during low level excitation there is little or no engagement of the partitions in the dynamic response of the system. As the excitation level is increased any small clearances between the partitions and the floors above them are closed and the partitions engage in the dynamic response. This has the effect of producing stiffer behaviour at increased vibration amplitude levels and hence explains the higher frequencies identified from forced vibration testing. The greater density of partitions beneath Floor 1 compared to Floor 2 would also explain why the frequencies for similar modes, on these floors, are higher for Floor 1. The floors thus behave similarly at low levels of excitation (ambient conditions) but are different due to differing partitions layouts at higher levels of excitation (forced excitation conditions).

The concept of amplitude dependent response is not novel; Ulusoy et al. [4] found that the modal parameters identified for a multi-storey building varied depending on earthquake amplitude. It's interesting to note though that in their case the effect of increased vibration level was an apparent reduction in stiffness due to greater joint mobilisation. In this study mobilisation of the partitions in the dynamic response resulted in a stiffer response.

The floor slabs in this building are supported on a column grid that results in nominal bay widths of up to 7.5 m. Given a slab thickness of 0.3 m this does not constitute what would be considered a slender floor system. Notwithstanding this the effect of partitions was found to be important depending on vibration level; their effect on slender floor systems is likely to be more pronounced. It is thus important when testing for vibration serviceability assessment to ensure that test vibration levels are consistent with those expected during operational use of the structure so as to cause the partitions to engage, or not, as appropriate in the response of the system.

20.6 Conclusions

Ambient and forced vibrations were recorded at the Charles Institute on the University College Dublin campus to investigate the effect of experimental techniques and partition layouts on the dynamic response of two otherwise identical floors. The following conclusions are drawn:

- The floor responses were found to be amplitude dependent. At low vibration levels, with peak accelerations of 0.0004 g, the response of two identically designed floors were found to be the same. At higher vibration levels, peak accelerations of 0.008 g, the same two floors were found to behave differently.
- The amplitude dependent response is attributed to the different partition layout above and below each floor level, the rationale being that these non-structural elements were not mobilised during ambient vibration analysis whilst they were during forced vibration tests.
- When testing for vibration serviceability, particularly in the case of slender floor systems, it is recommended that the test excitation amplitude is comparable to the expected in-service structure vibration levels so as to ensure that any amplitude dependent effects are represented in the test data. This is likely to result in forced vibration testing being more appropriate for vibration serviceability assessment of slender floor systems.

Acknowledgements The authors wish to express their gratitude to (i) the Irish Research Council for Science, Engineering & Technology for their financial support, (ii) the Vibration Engineering Research Section of Sheffield University for use of their equipment, and (iii) UCD for access to the Charles Institute at UCD.

References

1. Zhang L, Brincker R, Andersen P (2005) An overview of operational modal analysis: major development and issues. In: SVIBS
2. Lamarche CP, Paultre P, Proulx J, Mousseau S (2008) Assessment of the frequency domain decomposition technique by forced-vibration tests of a full-scale structure. *Earthquake Eng Struct Dyn* 37(3):487–494
3. Beyen K, Kutanis M (2011) Comparison of the results inferred from OMA and IEMA. In: 4th international operational modal analysis conference, 9–11 May 2011, Istanbul
4. Ulusoy H, Feng M, Fanning PJ (2011) System identification of a building from multiple seismic records. *Earthquake Eng Struct Dyn* 40: 661–674
5. Reynolds P, Pavic A (2001) Comparison of forced and ambient vibration measurements on a bridge. In: IMAC-XIX, A Conference on Structural Dynamics 1:846–851
6. Schwarz B, Richardson M (2001) Post-processing ambient and forced response bridge data to obtain modal parameters. In: IMAC-XIX, Kissimmee, February 5–8, 2001
7. Peeters B, De Roeck G (December 2001) Stochastic system identification for operational modal analysis: a review. *J Dyn Syst Meas Control* 123:659–667
8. Brincker R, Zhang L, Andersen P (2001) Modal identification of output-only systems using frequency domain decomposition. *Smart Mater Struct* 10:441–445
9. Verboven P (2002) Frequency-domain system identification for modal analysis. PhD Thesis, Vrije Universiteit Brussel, Belgium
10. Vibrant Technology (2008) ME'scope VES 5.0—reference manual—Volume IIA—Basic Operations, pp 41–117

Chapter 21

Comparison of Damping Models for Space Flight Cables

Kaitlin Spak, Gregory Agnes, and Daniel Inman

Abstract A model to predict the dynamic response of space flight cables is developed. Despite the influence of cable harnesses on space structures' dynamics, a predictive model for quantifying the damping effects is not available. To further this research, hysteretic and proportional viscous damping were incorporated in Euler-Bernoulli and Timoshenko beam models to predict the dynamic response of a typical space flight cable, using hysteretic dissipation functions to characterize the damping mechanism. The Euler-Bernoulli beam model was used to investigate the hysteresis functions specifically, and it was determined that including hysteretic dissipation functions in the equations of motion was not sufficient to model the additional modes arising in damped cables; additional damping coordinates in the method of Golla, Hughes and McTavish will be necessary to predict damping behavior when using dissipation functions for this case. A Timoshenko model that included viscous and time hysteresis damping was developed as well, and will ultimately be more appropriate for cable modeling due to the inclusion of shear and rotary inertia terms and damping coefficients.

Keywords Cable modeling • Cable damping • Time hysteresis • Dissipation functions • Cable vibration

Nomenclature

$\alpha, \beta, a_i, b_i \gamma, \delta$	Dissipation function/history kernel constants
η	State space vector of displacement solution and derivatives for distributed transfer function method
ρ	Density
ψ	Total beam rotation
$\tau = \sqrt{\frac{\rho AL^4}{EI}}$	Time parameter
A	Cross-sectional area
A_d, B_d, D_d	Dimensionless damping parameters defined within
C	Dimensionless hysteretic damping parameter containing dissipation function
c_a	Shear damping coefficient
c_b	Rotational damping coefficient
E	Elastic modulus
F	Transfer function matrix for use in distributed transfer function method
G	Shear modulus
$G(s)$	Dissipation function (transformed into Laplace domain)

K. Spak (✉)

Virginia Tech, Blacksburg, VA, USA

e-mail: kspak@vt.edu; kaitlin.spak@gmail.com

G. Agnes

Jet Propulsion Laboratory, California Institute of Technology, Pasadena, CA, USA

e-mail: gregory.s.agnes@jpl.nasa.edu

D. Inman

Department of Aerospace Engineering, University of Michigan, Ann Arbor, MI, USA

e-mail: daninman@umich.edu

I	Moment area of inertia
K	Shear coefficient
L	Beam length
M, N	Left and right boundary condition matrices for distributed transfer function method
P_1, P_2	Dimensionless beam parameters for bending and rotation, respectively, defined within
s	Laplace transformed time coordinate
t	Time coordinate
T	Axial tension in cable
T_s	Dimensionless tension parameter
w	Beam displacement as a function of time and distance
x	Spatial coordinate; distance along the beam in the axial direction

21.1 Introduction

Modern space structures are lighter and more complex than heritage systems. Power and signal cables are vital components that may not be incorporated into modal testing until the spacecraft is nearly ready for launch. At that development stage, finding out that the addition of cables will cause unwanted resonance is problematic and costly to fix. Alternatively, knowing that cables can add quantifiable and predictable damping to the structure can reduce costs by reducing the need for additional damping treatments.

The cables used on spacecraft vary in terms of size, construction, and insulation. Much research has been done on modeling the dynamic response of cables, with less research available on cable damping, and still less regarding damping of structures due to the addition of cable harnesses. In order to reach the goal of predicting the damping effects of structures due to cables, determining the damping quality inherent in the cable itself is a first step.

In this paper, a method to model the dynamic response of a space-flight cable, including damping effects, is developed. Comparison to experimental data to establish its validity and usefulness as a predictor for cable damping ratios is reserved for future work.

21.2 Background

Past research on cable damping generally aims to model either the frictional forces between each instance of contact between wires, or tries to quantify the changes in bending stiffness as the cable changes curvature. The earliest cable models were known as fiber models; these models were similar to string models and assumed no bending stiffness of the cable. It did not take long to determine that bending stiffness was important in cable motion, especially for larger and thicker cables, and thin rod models were developed. The thin rod formulation models each individual cable as a helical rod wrapped around a straight core [1]. Thin rod models determined stress and strain well, but to determine vibration response, beam models that included bending stiffness gave more direct results. Later, semi-continuous models, in which each layer of wires was homogenized into a cylinder, were developed [2].

Since the global behavior of the cable is most of interest for this particular application, this model will not rely on the individual forces between the wires. Instead, the cable will be modeled as a homogenous beam with properties to be determined experimentally. This paper investigates the inclusion of shear, rotary inertia, and axial tension terms, all of which are generally ignored in previous cable models. The other focus of this paper is incorporating a time hysteresis damping term employed to model the internal damping inherent in the cable.

Hysteretic damping was investigated based on the observation that viscous damping alone is not sufficient to model the damping of a slack cable. Spacecraft cables are usually attached with excess slack (no tension) to prevent connectors from becoming loose or disconnected due to strain from the cable tension. In prior experiments, cable frequencies decreased predictably as tension decreased until the cable became slack, at which point the cable response became significantly different as shown by the solid line in Fig. 21.1. To predict the effects of cable harnesses attached to space structures, a model to characterize slack cables must be developed. The bending stiffness inherent in cable harnesses for spacecraft makes slack string models inappropriate for cable harnesses in these cases. The axial tension term is included in the equations of motion in an effort to investigate if attaching cables to spacecraft with a very low tension could lead to more accurate response predictions. Figure 21.2 shows a rough comparison between the experimental cable data from previous experiments for a slack cable and the undamped and viscously damped cable models [3]. It is important to note that only a cursory attempt

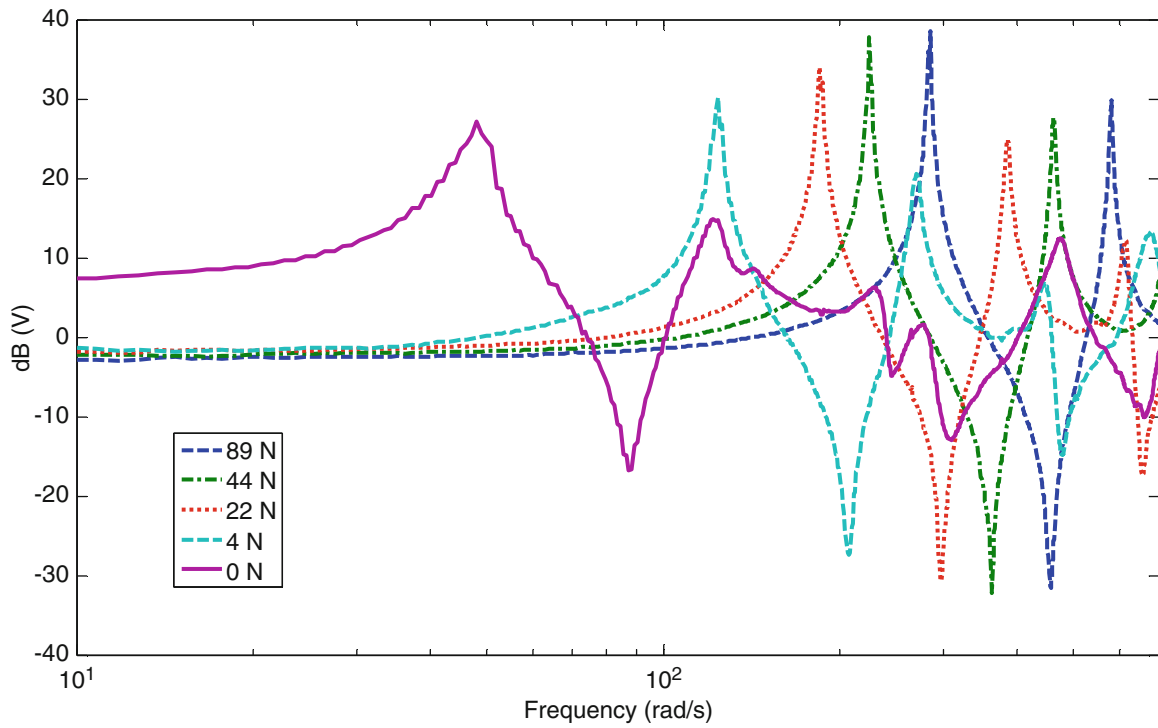


Fig. 21.1 Experimentally determined frequency response of a cable for various tensions; the frequencies shift and change and damping increases appreciably for the slack cable [3]

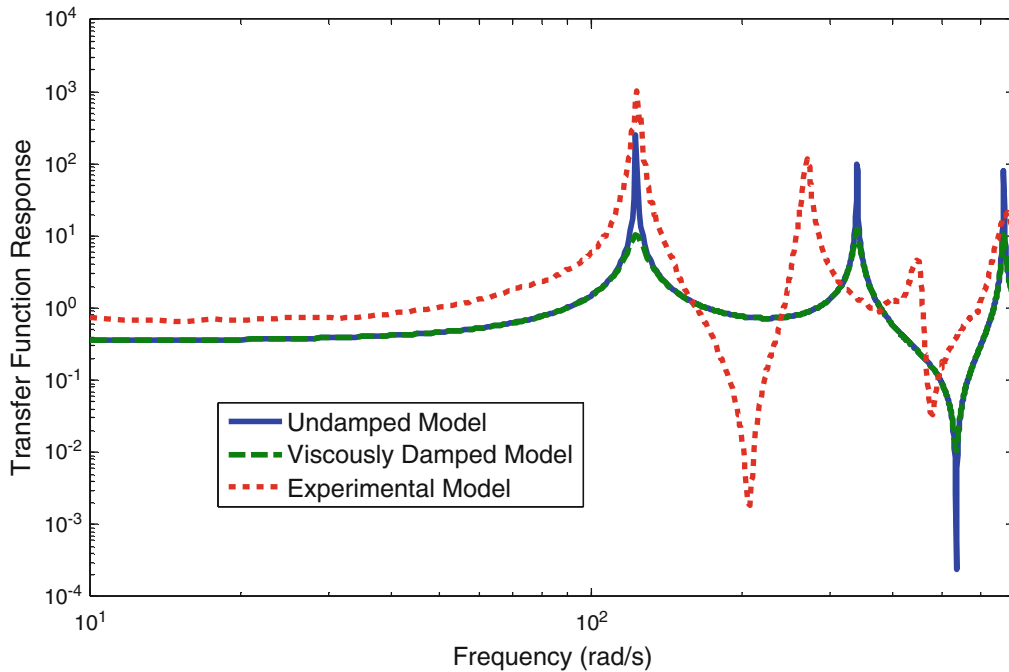


Fig. 21.2 Rough comparison of experimental response of cable under 4 N tension to undamped cable model and viscously damped cable model, showing the inadequacy of the viscously damped Euler-Bernoulli cable model for this application

was made to match model properties to the cable properties exactly. Copper properties were used to approximate the cable wire properties, and boundary conditions were matched. Jacketing of the wire was not taken into account for the model. It is clear that including only viscous damping will not show the frequency shifts and changes that the slack cable exhibits due to damping.

21.3 Equations of Motion

To incorporate time hysteresis, a simple Euler-Bernoulli beam model was studied initially. Although research shows that cables are best modeled by including shear effects, these are neglected in the Euler-Bernoulli model as a first step to investigate the effects of the hysteretic damping only. The distributed transfer function method (DTFM) used for solutions is computationally intensive when the transfer function matrix includes more terms, so limiting the number of terms by using the Euler-Bernoulli model provides a reasonable starting point. Once results were achieved with the Euler-Bernoulli model, shear and rotational inertia terms were added to incrementally increase the complexity of the problem and yield a baseline viscous damping Timoshenko model and the ultimately desired hysteretically damped Timoshenko model.

21.3.1 Euler-Bernoulli Time Hysteresis Model

This simple beam model includes viscous damping, axial tension, and a time hysteresis term (which is composed of a time-dependent dissipation function or history kernel $g(t)$ discussed later, and spatial derivatives). This is also known as Boltzmann-type viscoelasticity [4].

$$\rho A \frac{\partial^2 w}{\partial t^2} + c_a \frac{\partial w}{\partial t} + EI \frac{\partial^4 w}{\partial x^4} - T \frac{\partial^2 w}{\partial x^2} - \frac{\partial^2}{\partial x^2} \int_0^t g(t) \frac{\partial^2 w}{\partial x^2} dt = 0$$

Here, $w = w(x, t)$ is the transverse displacement of the cable and is a function of time, t , and distance, x . This equation is non-dimensionalized, rearranged, and transformed into the Laplace domain to facilitate the transfer function formulation:

$$\begin{aligned} \rho A \frac{L}{\tau^2} \frac{\partial^2 w}{\partial t^2} + c_a \frac{L}{\tau} \frac{\partial w}{\partial t} + EI \frac{L}{L^4} \frac{\partial^4 w}{\partial x^4} - T \frac{L}{L^2} \frac{\partial^2 w}{\partial x^2} - \frac{1}{L^2} \frac{\partial^2}{\partial x^2} \int_0^t g(t) \frac{L}{L^2} \frac{\partial^2 w}{\partial x^2} \tau dt = 0 \\ \frac{\partial^4 W}{\partial x^4} - \frac{\tau}{EI} \frac{G(s)}{s} \frac{\partial^4 W}{\partial x^4} = -\frac{\rho A}{EI} \frac{L^4}{\tau^2} s^2 W - c_a \frac{L^4}{EI \tau} s W + \frac{TL^2}{EI} \frac{\partial^2 W}{\partial x^2} \\ \frac{\partial^4 W}{\partial x^4} = \left(\frac{1}{1 - \frac{c}{s}} \right) \left(-s^2 W - D_d s W + T_s \frac{\partial^2 W}{\partial x^2} \right) \end{aligned}$$

Where the dimensionless parameters used are defined as:

$$D_d = \frac{c_a L^4}{EI \tau}, \quad T_s = \frac{TL^2}{EI}, \quad \text{and } C = G(s) \frac{\tau}{EI}$$

This simple model could be run quickly to show differences due to different damping formulations, but as mentioned, cables are more accurately modeled as shear beams rather than Euler-Bernoulli beams [5]. The beam equation used from this point forward includes both rotary and shear terms (Timoshenko formulation), since the cables are flexible enough to rotate appreciably and must incorporate shear effects. In addition, since preliminary experiments showed vibration response to vary with cable tension, this aspect has also been included, though not varied for the simulations presented here.

21.3.2 Timoshenko Viscous Model

The simplest and most commonly used damping model is a viscous-proportional damping model in which changes in the displacement or rotation over time are multiplied by a damping coefficient. Internal material damping within the wires and damping due to contact effects between the wires are both expected damping mechanisms. In this case, damping for the displacement and rotation is included, and gives these starting equations:

$$\rho A \frac{\partial^2 w}{\partial t^2} + c_a \frac{\partial w}{\partial t} = \kappa AG \frac{\partial^2 w}{\partial x^2} - \kappa AG \frac{\partial \psi}{\partial x}$$

$$\rho I \frac{\partial^2 \psi}{\partial t^2} + c_b \frac{\partial \psi}{\partial t} + T \frac{\partial w}{\partial x} = EI \frac{\partial^2 \psi}{\partial x^2} + \kappa AG \frac{\partial w}{\partial x} - \kappa AG \psi$$

Which are combined, non-dimensionalized and rearranged to facilitate the transfer function formulation, yielding:

$$\begin{aligned} \frac{\partial^4 w}{\partial x^4} = & \frac{\rho L^2}{E \tau^2} \frac{\partial^4 w}{\partial x^2 \partial t^2} + \frac{\rho L^2}{K G \tau^2} \frac{\partial^4 w}{\partial x^2 \partial t^2} + \frac{c_a L^2}{K A G \tau} \frac{\partial^3 w}{\partial x^2 \partial t} + \frac{c_b L^2}{E I \tau} \frac{\partial^3 w}{\partial x^2 \partial t} + \frac{T L^2}{E I} \frac{\partial^2 w}{\partial x^2} - \frac{\rho^2 L^4}{K G E \tau^4} \frac{\partial^4 w}{\partial t^4} - \frac{c_a \rho L^4}{K A G E \tau^3} \frac{\partial^3 w}{\partial t^3} \\ & - \frac{c_b \rho L^4}{K G E I \tau^3} \frac{\partial^3 w}{\partial t^3} - \frac{c_a c_b L^4}{K A G E I \tau^2} \frac{\partial^2 w}{\partial t^2} - \frac{\rho A L^4}{E I \tau^2} \frac{\partial^2 w}{\partial t^2} - \frac{c_a L^4}{E I \tau} \frac{\partial w}{\partial t} \end{aligned}$$

Non-dimensional parameters are chosen and the Laplace transform is performed:

$$\frac{\partial^4 W}{\partial x^4} = (P_1 s^2 + P_2 s^2 + A_d s + B_d s + T_s) \frac{\partial^2 W}{\partial x^2} + (-P_1 P_2 s^4 - A_d P_1 s^3 - B_d P_2 s^3 - A_d B_d s^2 - s^2 - D_d s) W$$

Where the dimensionless parameters used here are defined as:

$$A_d = \frac{c_a L^2}{K A G \tau}, B_d = \frac{c_b L^2}{E I \tau}, P_1 = \frac{\rho L^2}{E \tau^2}, P_2 = \frac{\rho L^2}{K G \tau^2}, D_d = \frac{c_a L^4}{E I \tau}, T_s = \frac{T L^2}{E I}, \text{ and } C = G(s) \frac{\tau}{E I}$$

This model is included to provide a baseline damping value. The following models presented are more complex to analyze, but may provide greater agreement with physical reality.

21.3.3 Timoshenko Time Hysteresis Models

A time hysteresis model includes a damping term that takes the past strain history of the structure into account. The authors were interested in whether internal damping occurred because of internal shear or internal rotation, so two models were developed; one with the time hysteresis due to the rotation only ($\frac{\partial w}{\partial x}$), and one with the time hysteresis due to the shear angle (ψ). The $g(t)$ term is a time-dependent expression that can take a variety of forms with the physical assumption being that the stress in the cable is proportional not only to the strain, but the past strain as well. Time hysteresis damping has traditionally been used with the Boltzmann damping formulation [6], but the dissipation function used by Golla and Hughes was also investigated with these models [7]. Since the time hysteresis damping should be describing only the internal damping, the viscous damping terms are included as well to account for the damping due to the motion of the cable in the air.

The first hysteretic model incorporates time hysteresis acting on $\frac{\partial^2 w}{\partial x^2}$, the strain of the cable due to bending. The time hysteresis term is added to the second equation as shown and the integral is taken care of through the Laplace transformation necessary for the distributed transfer function method used to determine the solution and described in the next section. The end result is a Laplace transform of the equation of motion with the non-dimensional parameters included as the coefficients:

$$\begin{aligned} \rho A \frac{\partial^2 w}{\partial t^2} + c_a \frac{\partial w}{\partial t} &= \kappa A G \frac{\partial^2 w}{\partial x^2} - \kappa A G \frac{\partial \psi}{\partial x} + q(x, t) \\ \rho I \frac{\partial^2 \psi}{\partial t^2} + c_b \frac{\partial \psi}{\partial t} + T \frac{\partial w}{\partial x} &= EI \frac{\partial^2 \psi}{\partial x^2} + \kappa A G \frac{\partial w}{\partial x} - \kappa A G \psi - \frac{\partial}{\partial x} \int_0^t g(t - \tau) \frac{\partial^2 w}{\partial x^2} dt \\ \frac{\partial^4 w}{\partial x^4} = & \frac{\rho L^2}{E \tau^2} \frac{\partial^4 w}{\partial x^2 \partial t^2} + \frac{\rho L^2}{K G \tau^2} \frac{\partial^4 w}{\partial x^2 \partial t^2} + \frac{c_a L^2}{K A G \tau} \frac{\partial^3 w}{\partial x^2 \partial t} + \frac{c_b L^2}{E I \tau} \frac{\partial^3 w}{\partial x^2 \partial t} + \frac{T L^2}{E I} \frac{\partial^2 w}{\partial x^2} - \frac{\rho^2 L^4}{K G E \tau^4} \frac{\partial^4 w}{\partial t^4} - \frac{c_a \rho L^4}{K A G E \tau^3} \frac{\partial^3 w}{\partial t^3} \\ & - \frac{c_b \rho L^4}{K G E I \tau^3} \frac{\partial^3 w}{\partial t^3} - \frac{c_a c_b L^4}{K A G E I \tau^2} \frac{\partial^2 w}{\partial t^2} - \frac{\rho A L^4}{E I \tau^2} \frac{\partial^2 w}{\partial t^2} - \frac{c_a L^4}{E I \tau} \frac{\partial w}{\partial t} + \frac{\tau}{E I} \frac{\partial^2}{\partial x^2} \int_0^t g(t - \tau) \frac{\partial^2 w}{\partial x^2} dt \\ \frac{\partial^4 W}{\partial x^4} = & \frac{(P_1 s^2 + P_2 s^2 + A_d s + B_d s + T_s) \partial^2 W}{1 - \frac{C}{s}} + \frac{(-P_1 P_2 s^4 - A_d P_1 s^3 - B_d P_2 s^3 - A_d B_d s^2 - s^2 - D_d s) W}{1 - \frac{C}{s}} \end{aligned}$$

The next hysteretic model includes time hysteresis acting on psi, the total rotation of the beam. The same steps are followed and the same non-dimensional parameters substituted to yield the Laplace transform of the damped equation of motion.

$$\rho A \frac{\partial^2 w}{\partial t^2} + c_a \frac{\partial w}{\partial t} = \kappa A G \frac{\partial^2 w}{\partial x^2} - \kappa A G \frac{\partial \psi}{\partial x} + q(x, t)$$

$$\rho I \frac{\partial^2 \psi}{\partial t^2} + c_b \frac{\partial \psi}{\partial t} + T \frac{\partial w}{\partial x} = EI \frac{\partial^2 \psi}{\partial x^2} + \kappa A G \frac{\partial w}{\partial x} - \kappa A G \psi - \frac{\partial}{\partial x} \int_0^t g(t - \tau) \frac{\partial \psi}{\partial x} dt$$

Equations are combined and rearranged:

$$\begin{aligned} \frac{\partial^4 w}{\partial x^4} = & \frac{\rho L^2}{E \tau^2} \frac{\partial^4 w}{\partial x^2 \partial t^2} + \frac{\rho L^2}{KG \tau^2} \frac{\partial^4 w}{\partial x^2 \partial t^2} + \frac{c_a L^2}{KAG \tau} \frac{\partial^3 w}{\partial x^2 \partial t} + \frac{c_b L^2}{EI \tau} \frac{\partial^3 w}{\partial x^2 \partial t} + \frac{TL^2}{EI} \frac{\partial^2 w}{\partial x^2} - \frac{\rho^2 L^4}{EKG \tau^4} \frac{\partial^4 w}{\partial t^4} \\ & - \frac{c_a \rho L^4}{EKAG \tau^3} \frac{\partial^3 w}{\partial t^3} - \frac{c_b \rho L^4}{EIKG \tau^3} \frac{\partial^3 w}{\partial t^3} - \frac{c_a c_b L^4}{EIKAG \tau^2} \frac{\partial^2 w}{\partial t^2} - \frac{\rho A L^4}{EI \tau^2} \frac{\partial^2 w}{\partial t^2} - \frac{c_a L^4}{EI \tau} \frac{\partial w}{\partial t} \\ & + \frac{L}{EI} \frac{\partial^2}{\partial x^2} \int_0^t g(t - \tau) \left(-\frac{\rho L}{KG \tau^2} \frac{\partial^2 w}{\partial t^2} - \frac{c_a L}{KAG \tau} \frac{\partial w}{\partial t} + \frac{L}{L^2} \frac{\partial^2 w}{\partial x^2} \right) \tau dt \end{aligned}$$

The Laplace transform is taken:

$$\begin{aligned} \left(1 - \frac{\tau G(s)}{EI s} \right) \frac{\partial^4 W}{\partial x^4} = & \left(\frac{\rho L^2}{E \tau^2} s^2 + \frac{\rho L^2}{KG \tau^2} s^2 + \frac{c_a L^2}{KAG \tau} s + \frac{c_b L^2}{EI \tau} s - \frac{\rho L^2}{KGEI \tau} G(s) s - \frac{c_a L^2}{KAGEI} G(s) + \frac{TL^2}{EI} \right) \frac{\partial^2 W}{\partial x^2} \\ & + \left(-\frac{\rho^2 L^4}{EKG \tau^4} s^4 - \frac{c_a \rho L^4}{EKAG \tau^3} s^3 - \frac{c_b \rho L^4}{EIKG \tau^3} s^3 - \frac{c_a c_b L^4}{EIKAG \tau^2} s^2 - \frac{\rho A L^4}{EI \tau^2} s^2 - \frac{c_a L^4}{EI \tau} s \right) W \end{aligned}$$

And the final equation is:

$$\begin{aligned} \frac{\partial^4 W}{\partial x^4} = & \frac{(P_1 s^2 + P_2 s^2 + A_d s + B_d s - P_2 C s - A_d C + T_s)}{(1 - \frac{C}{s})} \frac{\partial^2 W}{\partial x^2} \\ & + \frac{(-P_1 P_2 s^4 - P_1 A_d s^3 - P_2 B_d s^3 - A_d B_d s^2 - s^2 - D_d s)}{(1 - \frac{C}{s})} W \end{aligned}$$

These models each incorporate a history kernel term, $G(s)$ (included as part of the dimensionless parameter C), with units of $\text{kg}\cdot\text{m}^3/\text{s}^3$. This term can take several forms, as shown in Table 21.1, and must be positive in order to model energy dissipation. In these simulations, the dissipation function used by Golla and Hughes [7] was used since their damping solution method incorporates a transfer function to model the system hysteresis. Although developed for finite element systems, this dissipation function is compatible with the distributed transfer function method. For this investigation, the Boltzmann time hysteresis formulation [6] was also used in the Euler-Bernoulli beam model as a comparison.

21.4 Distributed Transfer Function Method

The complexity of the Timoshenko equations of motion due to the added shear, rotary inertia and tension, and the inclusion of multiple damping terms make the final formulations computationally intense to solve. The distributed transfer function method (DTFM) is an exact method that poses the equation of motion as a transfer function matrix that can be manipulated to solve for the natural frequencies, displacements, and vibration response without having to assume a mode shape or approximate solution [10]. A desire to compare the effects due to the various damping terms (which may affect the cable response minutely) indicated that an exact method would be beneficial, since the small variations would not be lost in approximations.

Table 21.1 Dissipation functions used for hysteretic damping term $G(s)$

Dissipation function/history kernel	Author (Year)
$G(s) = \sum_{i=1}^n \frac{a_i s}{s + b_i}$	Biot (1955) [7]
$G(s) = \frac{E_1 s^\alpha - E_0 b s^\beta}{1 + b s^\beta}, 0 < \alpha, \beta < 1$	Bagley and Torvik (1981) [7]
$G(s) = as \int_0^\infty \frac{\gamma(p)}{s+p} dp, \gamma(p) = \begin{cases} \frac{1}{\beta - \alpha}, & \alpha < p < \beta \\ 0 & \text{otherwise} \end{cases}$	Buhariwala (1982) [7]
$G(s) = \frac{\alpha s^2 + \gamma s}{s^2 + \beta s + \delta}$	Golla and Hughes, based off of Biot's formula for $n=2$ (1985) [7]
$G(s) = \alpha \frac{s^2 + 2\sqrt{2\delta}s}{s^2 + 2\sqrt{2\delta}s + \delta}$	Inman, following the suggestion of Golla and Hughes and confirmed by Mctavish (1989) [8]
$G(s) = \frac{\alpha}{\sqrt{-s}} \exp(\beta s)$	Banks and Inman (1991), associated with Boltzmann damping [6]
$G(s) = \alpha \frac{1 - \exp(-st_0)}{st_0}$	Adhikari (1998) [9]

To implement the distributed transfer function method, the equations of motion and boundary conditions are cast into a state-space form as follows:

$$\frac{\partial}{\partial x} \eta(x, s) = F(s) \eta(x, s) + f(x, s)$$

$$M(s) \eta(0, s) + N(s) \eta(1, s) = \gamma(s)$$

where boundary conditions are incorporated through the M and N matrices, with pinned, clamped, or free end conditions all straightforward to implement, and

$$\eta = \begin{bmatrix} W(x, s) \\ \frac{\partial W(x, s)}{\partial x} \\ \frac{\partial^2 W(x, s)}{\partial x^2} \\ \frac{\partial^3 W(x, s)}{\partial x^3} \end{bmatrix}$$

$$M_{Pin} = \begin{bmatrix} 1 & 0 & 0 \\ 0 & 0 & EI + \frac{1}{s}G(s) \\ 0 & 0 & 0 \\ 0 & 0 & 0 \end{bmatrix}, N_{Pin} = \begin{bmatrix} 0 & 0 & 0 \\ 0 & 0 & 0 \\ 1 & 0 & 0 \\ 0 & 0 & EI + \frac{1}{s}G(s) \end{bmatrix}, M_{Clamp} = \begin{bmatrix} 1 & 0 & 0 & 0 \\ 0 & 1 & 0 & 0 \\ 0 & 0 & 0 & 0 \\ 0 & 0 & 0 & 0 \end{bmatrix}, N_{Clamp}$$

$$= \begin{bmatrix} 0 & 0 & 0 & 0 \\ 0 & 0 & 0 & 0 \\ 1 & 0 & 0 & 0 \\ 0 & 1 & 0 & 0 \end{bmatrix},$$

Here, the M and N matrices describe the pinned or clamped ends of the cable section as noted in the subscript. In this case, there is no forcing function and initial conditions are uniformly zero, and the length of the beam section is normalized to 1. The $F(s)$ matrix is defined as follows, and the transfer function matrices for the viscously damped model and the two models with time hysteresis damping are shown below.

$$F(s) = \begin{bmatrix} 0 & 1 & 0 & 0 \\ 0 & 0 & 1 & 0 \\ 0 & 0 & 0 & 1 \\ d_0(s) & d_1(s) & \dots & d_k(s) \end{bmatrix}$$

with the last row of matrix entries are each defined as

$$d_k(s) = -\frac{a_k s^2 + b_k s + c_k}{a_n s^2 + b_n s + c_n}, \quad k = 0, 1, \dots, n-1$$

where the a , b and c terms come from the form of the equations of motion:

$$\left\{ \left(\sum_{k=0}^n a_k \frac{\partial^k}{\partial x^k} \right) \frac{\partial^2}{\partial t^2} + \left(\sum_{k=0}^n b_k \frac{\partial^k}{\partial x^k} \right) \frac{\partial}{\partial t} + \left(\sum_{k=0}^n c_k \frac{\partial^k}{\partial x^k} \right) \right\} W(x, t) = f(x, t)$$

For the case of the Euler-Bernoulli beam equation and the fourth order Timoshenko beam equations derived in the previous section, the transfer function matrices are:

$$F_{EBTHyst} = \begin{bmatrix} 0 & 1 & 0 & 0 \\ 0 & 0 & 1 & 0 \\ 0 & 0 & 0 & 1 \\ \frac{(-s^2 - D_d s)}{1 - \frac{c}{s}} & 0 & \frac{T_s}{1 - \frac{c}{s}} & 0 \end{bmatrix}$$

$$F_{TimViscous} = \begin{bmatrix} 0 & 1 & 0 & 0 \\ 0 & 0 & 1 & 0 \\ 0 & 0 & 0 & 1 \\ (-P_1 P_2 s^4 - A_d P_1 s^3 - B_d P_2 s^3 - A_d B_d s^2 - s^2 - D_d s) & 0 & (P_1 s^2 + P_2 s^2 + A_d s + B_d s + T_s) & 0 \end{bmatrix}$$

$$F_{TimTHystW} = \begin{bmatrix} 0 & 1 & 0 & 0 \\ 0 & 0 & 1 & 0 \\ 0 & 0 & 0 & 1 \\ \frac{(-P_1 P_2 s^4 - A_d P_1 s^3 - B_d P_2 s^3 - A_d B_d s^2 - s^2 - D_d s)}{1 - \frac{c}{s}} & 0 & \frac{(P_1 s^2 + P_2 s^2 + A_d s + B_d s + T_s)}{1 - \frac{c}{s}} & 0 \end{bmatrix}$$

$$F_{TimTHystPsi} = \begin{bmatrix} 0 & 1 & 0 & 0 \\ 0 & 0 & 1 & 0 \\ 0 & 0 & 0 & 1 \\ \frac{(-P_1 P_2 s^4 - A_d P_1 s^3 - B_d P_2 s^3 - A_d B_d s^2 - s^2 - D_d s)}{1 - \frac{c}{s}} & 0 & \frac{(P_1 s^2 + P_2 s^2 + A_d s + B_d s - P_2 C s - A_d C + T_s)}{1 - \frac{c}{s}} & 0 \end{bmatrix}$$

The natural frequencies are determined by solving the eigenvalue problem; the eigenvalues of the system are the roots of the characteristic equation

$$\det [M(s) + N(s) * \exp(F(s) * L)] = 0$$

where the determinant is a symbolic expression containing s , which can be solved for through computer coding. The roots are of the form $s = j\omega_k$, $j = \sqrt{-1}$, $k = 1, 2, \dots$, where ω_k is the k th natural frequency of the system. Mode shapes for the system are determined by substituting the values for s back into the characteristic equation to solve for the displacement values (η) and then putting them into the solution equation

$$\eta(x, s) = \exp(F(s) * x) * \eta(0, s), \quad 0 \leq x \leq L$$

to get a function of x for each s value. It should be noted that the above procedures are for a single section of beam, and that modifications are required to solve the system for a set of subsystems linked together.

A key advantage of the distributed transfer function method (aside from needing fewer nodes than a similar finite element problem), is the ability to incorporate properties of the system that are dependent on the location. For example, research shows that the bending stiffness of a beam is variable when the beam is a multi-stranded cable [11]. Including an EI term that is dependent on the cable curvature is planned for future work.

Table 21.2 Nondimensional values used for Euler-Bernoulli model simulations, based on properties of single copper wire and Boltzmann and Golla-Hughes dissipation functions

Euler Bernoulli values		Undamped	Viscously damped	Time Hysteresis, Boltzmann Function	Time Hyst., Golla-Hughes Function
Dimensionless Time Parameter	τ	0.2294	0.2294	0.2294	0.2294
Tension	T_s	0	0	0	0
Hysteretic Damping Coefficient	$C * G(s)$	0	0	$0.0736 * G(s)$	$0.0736 * G(s)$
Dissipation Function	$G(s)$	0	0	$\frac{1.36}{\sqrt{-s}} * \exp(\beta * s)$	$\frac{1.36s^2 + 1.5e4s}{s^2 + 1s + 1.5e6}$
Viscous Damping Term	D	0	1.6794 ($c_a = 1.2$)	0	0

Table 21.3 First four natural frequencies for undamped and damped Euler Bernoulli models

Mode #	Euler Bernoulli undamped	Euler Bernoulli			
		Viscously damped	Time Hyst, Golla-Hughes Function	Time Hyst, Boltzmann Function, $\beta = 1$	Time Hyst, Boltzmann Function, $\beta = 5$
1	22.3733	22.3599	21.5067	22.3831	22.3776
2	61.6728	61.6863	58.6529	61.6751	61.6668
3	120.9034	120.9194	103.86, 115.7077, 122.21 ^a	120.9000	120.8995
4	199.8594	199.8747	203.9654	199.8609	199.8564

^aWhen calculating the natural frequencies, use of the Golla-Hughes function resulted in additional frequencies around the third mode, also shown in Fig. 21.3. Although the intent of this work was to find damping mechanisms that would result in additional modes, it is likely that these modes are due to numerical instability in the solution step. Although the DTF method is intended to be exact, a numeric solver was used to find the natural frequencies based on setting the determinant of the system transfer function equal to zero. With higher damping values, this effect was more pronounced, and will require further study to determine the stability limits of the damping functions

Table 21.4 Nondimensional values used for Timoshenko model investigation, based on properties of single copper wire and Golla-Hughes dissipation functions

Timoshenko values	Undamped	Viscously damped, $c_a = 5$	Viscously damped, $c_a = c_b = 0.5$	Time Hyst. on W	Time Hyst. on Psi
A_d	0	2.9425E-05	2.9425E-06	0	0
B_d	0	0	0.6997	0	0
P_1	1.4556E-06	1.4556E-06	1.4556E-06	1.4556E-06	1.4556E-06
P_2	4.2052E-05	4.2052E-05	4.2052E-05	4.2052E-05	4.2052E-05
C	0	0	0	$0.0736 * G(s)$	$0.0736 * G(s)$
Golla-Hughes Function	0	0	0	$\frac{1.36s^2 + 1.5e4s}{s^2 + s + 1.5e4}$	$\frac{1.36s^2 + 1.5e4s}{s^2 + s + 1.5e4}$
D_d	0	6.9974	0.6997	0	0
T_s	0	0	0	0	0
τ	0.2294	0.2294	0.2294	0.2294	0.2294

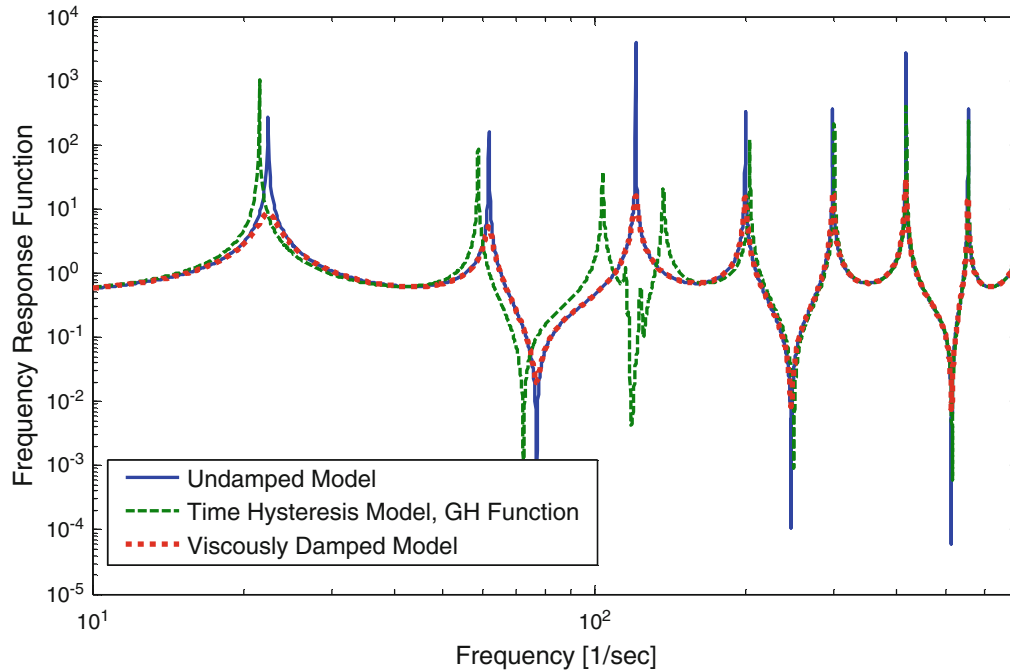
21.5 Results

For the results shown here, the modeled cable is assumed to be a uniform beam with properties similar to pure copper. Damping coefficients were chosen to give roughly similar changes in the natural frequencies, and will be the subject of a later study using experimental data. The cables were modeled with clamped ends on each side, and alpha and gamma dissipation function values were used from [12]. Table 21.2 gives the values for the nondimensional parameters for the various Euler Bernoulli cases and Table 21.3 lists the first four natural frequencies for each case. Tables 21.4 and 21.5 provide the program inputs and frequency results for the first four modes for the various Timoshenko beam cases. Figure 21.3 is a frequency response comparison for the Euler-Bernoulli beam model showing the undamped model, a lightly viscously damped model, and a time hysteresis damped model incorporating the dissipation function used by Golla and Hughes. Figure 21.4 compares the hysteretic damping from the Boltzmann function with the undamped and viscously damped Euler Bernoulli cases.

In the case of the Boltzmann time hysteresis damping, the damping effects were nearly identical to viscous damping. The time hysteresis models did provide different damping magnitudes and, in some cases, shifted frequencies, but additional modes that could arise from hysteretic damping were not evident. The results from this work indicate that additional damping coordinates (as proposed in the Golla-Hughes-McTavish method) will be necessary to predict damping behavior; including just the dissipation functions is not sufficient for response prediction. More positively, adding time hysteresis dissipation functions to the Euler Bernoulli beam model did not extend computational time excessively.

Table 21.5 First four natural frequencies for undamped and damped Timoshenko beam models

Mode #	Timoshenko				
	Undamped	Viscously damped $c_a = 5$ $c_b = 0$	Viscously damped $c_a = 0.5$, $c_b = 0.5$	Time Hyst. on W, Golla-Hughes Function	Time Hyst. on Psi, Golla-Hughes Function
1	22.3726	22.1498	19.4533	21.5059	21.5060
2	61.6649	61.9026	47.2953	58.6455	58.6460
3	120.8696	121.1532	147.6919	115.7036	115.7260
4	199.7625	200.0325	221.0475	203.8723	137.2000

**Fig. 21.3** Euler Bernoulli beam model compared to viscously damped and Golla Hughes time hysteresis damped models

Although a decrease in natural frequencies was expected for viscously damped beams, investigation into the distributed transfer function method showed that the viscous damping is not necessarily modal damping, and similar problems in the literature show a decrease in the first natural frequency only [10]. However, the amplitude of the response is reduced for all frequency values, showing significant damping. As Fig. 21.1 showed, the slack cable which experiences greater damping had frequencies that shifted both higher and lower than its tensioned counterparts. Results for the Euler Bernoulli and Timoshenko beams showed that time hysteresis damping did not have a constant higher or lower shift of the natural frequencies, and may be best to model the frequency shifts due to the damping inherent in a slack cable. Some stability issues arose (for example, the disparity between the fourth mode value for the Timoshenko time hysteresis case) for certain combinations of damping coefficients, and more research is needed to determine the appropriate range of coefficients to characterize the physical damping mechanisms of cables.

In the Timoshenko beam cases, the rotational damping coefficient c_b has a much greater effect on the natural frequency change than the bending damping coefficient c_a . This is likely due to the relative weight of the terms; when the rotational damping coefficient is non-dimensionalized, it is 5 orders of magnitude larger than the bending coefficient, which indicates that the inclusion of the rotational damping term is necessary and supports the decision to model cables with Timoshenko beams despite the increased complexity.

The use of Timoshenko beam models rather than Euler Bernoulli models provided the largest increase in computation time, taking significantly longer to compute whether time hysteresis damping was included or not. However, existing literature [5] emphasizes the need to include shear effects, and the importance of the rotational damping factor in these results indicates that the Timoshenko model is necessary, despite the additional time required. Time hysteresis damping added some complexity, but was minimal as compared to the complexity of the Timoshenko formulation.

While the authors had hoped that the use of dissipation functions in conjunction with the DTFM method could capture the nuances of cable damping, including time hysteresis without adding additional dissipation coordinates does not seem to

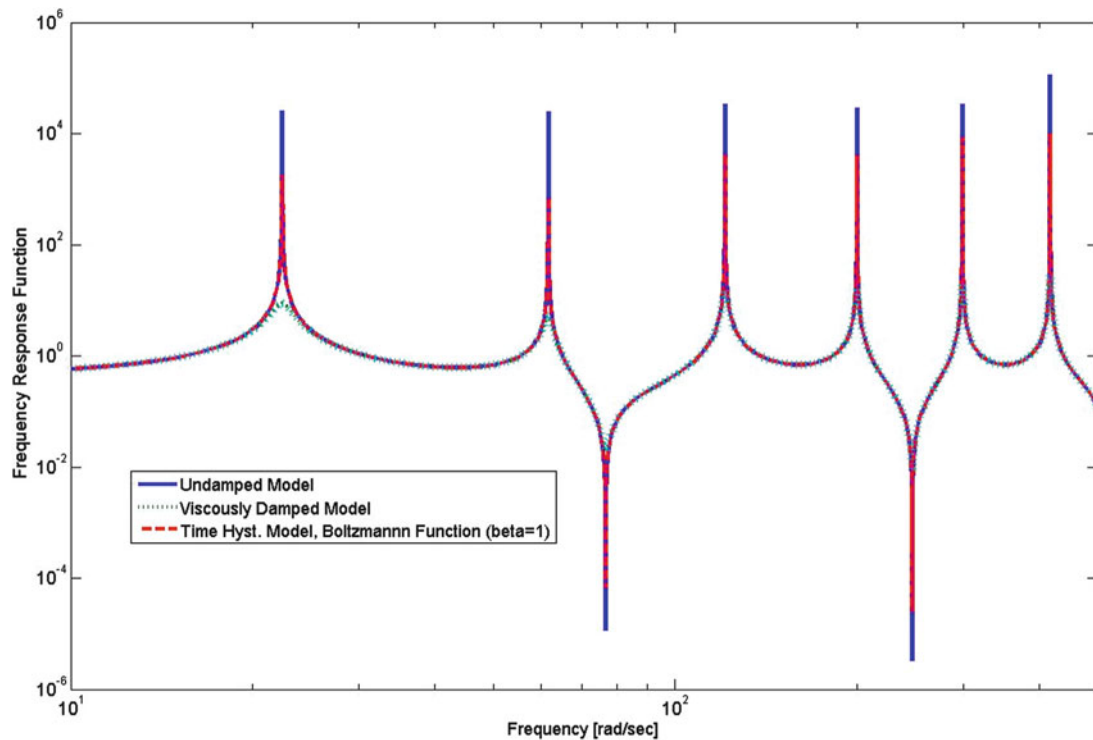


Fig. 21.4 Comparison of undamped Euler Bernoulli model with Boltzmann time hysteresis damping and viscous damping

improve significantly upon viscous damping as a damping predictor. The next step is to combine the Golla-Hughes-McTavish method of additional dissipation coordinates with the DTFM method and Timoshenko beam formulation if possible.

Since preliminary cable experiments were performed, many factors arose that indicated the need for more focused and detailed experiments. The data shown in Fig. 21.1 is from small diameter cables that bear little resemblance to the space flight cables that we are interested in modeling, and do not show much variation in construction or jacket type. In the simulations run above, the various damping coefficients and dissipation function constants were chosen arbitrarily based on published data and trial and error. To predict the cable response, these values must be correlated to cable properties such as modulus of elasticity and rigidity, cable geometry, cable construction, and jacketing, which forms the basis for our ongoing investigation.

21.6 Conclusion and Future Work

Various damping and stiffness models were examined to see if they could predict the behavior of cables. Viscous damping and time hysteresis damping formulations were added to beam models, and the damped natural frequencies were calculated using the distributed transfer function method. Adding hysteretic dissipation functions alone did not vary the response significantly from viscous damping models, and incorporating additional dissipation coordinates must be investigated. Adding hysteresis functions to the equations of motion did not significantly increase computation time, although the additional complexity of the shear and rotational inertia terms for the Timoshenko model did. The use of the Timoshenko beam model rather than the Euler Bernoulli beam model was supported based on the magnitude of the non-dimensionalized rotational damping coefficient and previous studies [5].

The logical next step is to incorporate the Golla-Hughes-McTavish method of additional damping coordinates to improve the models. Then, we will perform experiments with spaceflight cables to correlate the damping coefficients to cable properties and validate the proposed damping models. We have determined that the additional time required for the more complex damping and Timoshenko terms is not excessive, and may lead to results that can more accurately model the erratic behavior of slack space flight cables. Future directions include comparing spatial hysteresis damping, and incorporating variable bending stiffness as investigated in [11], where the bending stiffness is related to the curvature of the cable at any given point in time and space.

Acknowledgements This work was supported by a NASA Office of the Chief Technologist's Space Technology Research Fellowship. The first author thanks NASA for generous support and the Virginia Space Grant Consortium for additional funding. The third author gratefully acknowledges the support of AFOSR Grant number FA9550-10-1-0427 monitored by Dr. David Stargel. Part of this research was carried out at the Jet Propulsion Laboratory, California Institute of Technology, under a contract with the National Aeronautics and Space Administration.

References

1. Costello GA (1997) Theory of wire rope, 2nd edn. Springer, New York
2. Jolicoeur C, Cardou A (1996) Semicontinuous mathematical model for bending of multilayered wire strands. *J Eng Mech* 122(7):643–650
3. Spak K, Inman D (2012) Model development for cable-harnessed beams. In: 2012 Virginia space grant consortium student research conference, Williamsburg, April 2012
4. Banks HT, Fabiano RH, Wang Y, Inman DJ, Cudney H (1988) Spatial versus time hysteresis in damping mechanisms. In: Proceedings of the 27th conference on decision and control, Austin, December 1988, pp 1674–1677
5. Goodding JC, Griffiee JC, Ardelean EV (2008) Parameter estimation and structural dynamic modeling of electrical cable harnesses on precision structures. In: 49th AIAA/ASME/ASCE/AHS/ASC structures, structural dynamics, and materials conference, Schaumburg, Illinois, April 2008
6. Banks HT, Inman DJ (1991) On damping mechanisms in beams. *J Appl Mech* 58:716–723
7. Golla DF, Hughes PC (1985) Dynamics of viscoelastic structures—a time-domain, finite element formulation. *J Appl Mech* 52:897–906
8. Inman DJ (1989) Vibration analysis of viscoelastic beams by separation of variables and modal analysis. *Mech Res Commun* 16(4):213–218
9. Adhikari S (2000) Damping models for structural vibration. Thesis. Cambridge University
10. Yang B, Tan CA (1992) Transfer functions of one-dimensional distributed parameter systems. *J Appl Mech* 59:1009–1014
11. Papailiou KO (1997) On the bending stiffness of transmission line conductors. *IEEE Trans Power Del* 12(4):1576–1588
12. Sciulli D (1997) Dynamics and control for vibration isolation design. Thesis. Virginia Tech

Chapter 22

Forced 3D Nonlinear Dynamics of a Hanging Cable Under Multiple Resonance Conditions

R. Alaggio, F. Benedettini, G. Rega, and D. Zulli

Abstract The forced, nonlinear, 3D dynamics of an elastic cable is analyzed by means of a reduced 4 d.o.f. model, already obtained several years ago by some of the Authors of this paper. The system is analyzed in the case of multiple internal resonance conditions and a 1:1 external primary resonance condition. The reduced model, because of a strong intrinsic symmetry due to the fact that anti-symmetric in-plane and out-of-plane modes have the same natural frequency (Irvine's theory), is in principle not able to catch some interesting classes of motion, such as ballooning, which on the other hand have been observed in experimental tests. In the present paper, an imperfection between the equations ruling the in-plane and out-of-plane components is introduced through an internal detuning, which simulates the slight difference between the frequencies of the two involved modes, which is plausible as a consequence of the initial curvature of the cable as well as obtainable through more refined analytical models. A discussion on the similarity and differences with the solutions previously obtained is presented. Regions of non-regular response in the excitation control parameter plane are located and ballooning trajectories are analyzed.

Keywords Suspended cable • Nonlinear dynamics • Bifurcation • Ballooning • Experiment

22.1 Introduction

Finite amplitude dynamics of suspended cables have been addressed in the last decades by referring to variably refined theoretical models, through purely analytical, numerical or mixed treatments [1–7].

However, understanding the actual nonlinear behavior of suspended cables through also physical models is important both for validating theoretical predictions and for detecting new or complex phenomena associated with system nonlinearities, which are often not modeled in theoretical analyses. Quite a systematic analysis of experimental nonlinear cable dynamics has been accomplished in a few papers dealing with a hanging cable/mass system subjected to different harmonic motions of the supports and realizing, for relatively low excitation frequencies, a fairly reliable model of bare suspended cable. Focusing on the transition to complex response under various external and internal resonance conditions, bifurcation mechanisms have been characterized by properly reconstructing the system dynamics from experimental measurements [8, 12]. Reconstructed attractors and underlying manifolds have been studied via different experimental techniques, i.e., delay embedding and proper orthogonal decomposition, focused at identifying mechanically meaningful classes of motion and the associated mechanisms of transition to chaos. Particular interest has been devoted to highlight the possible occurrence of low-dimensional complex responses, which is of major interest for identifying reduced (and minimal) theoretical models, able to describe the complex dynamics of the experimental system. An overview on the richness and robustness of two different – quasi-periodic and homoclinic – bifurcation scenarios to chaos occurring in various regions of control parameter space, along with the involved proper orthogonal modes (POMs), is summarized in Table 22.1, making reference to features of support motion, external resonance condition, and cable dynamic properties [11]. For the slacker cable, quasi-periodic

R. Alaggio • F. Benedettini (✉) • D. Zulli
DICEAA, University of L'Aquila, L'Aquila, Italy
e-mail: francesco.benedettini@univaq.it

G. Rega
DISG, University of Rome Sapienza, Rome, Italy

Table 22.1 Summary of results concerned with bifurcation to chaos scenarios

Cable	Support motion							
	In-phase external resonance condition				In opposition of phase external resonance condition			
	Primary		Subh. 1/2		Primary		Subh. 1/2	
	Scenario	Modes	Scenario	Modes	Scenario	Modes	Scenario	Modes
Slacker	QP	V1 H1 H2HOM	(HET)V5 H5V3 H3HOM	V2 H2HOM (QP)V4 H4 ^a				
Crossover	No chaos		HOM	V5 H5V3 H3HOM	V2 H2HOM	V4 H4		

^aV4 H4 H1^TH2.

transition to chaos via breakdown of regular dynamics on 3D-tori is robust at primary resonance under in-phase support motion, whereas it competes with the homoclinic bifurcation scenario at 1/2-subharmonic resonance under out-of-phase motion. In turn, this latter scenario is definitely robust near primary resonances of 1:1 internally resonant $V_n H_n$ -type couples of modes (V = vertical, in-plane; H = horizontal, out-of-plane; $n = 2-5$; $n = \text{odd}$, symmetric; $n = \text{even}$, anti-symmetric) for both the slacker and the crossover cable. The quasi-periodic transition to chaos through a tori breakdown has been addressed quite exhaustively [10] and quite satisfactory results has been obtained as regards the quite general scenario seemingly involving two main – though variable – POMs (resembling V_n and H_n -type $n = \text{even}$ cable modes) in the global bifurcation of a homoclinic invariant set of the flow [12]. Thus, by focusing on the homoclinic bifurcation of a multiple internally resonant cable under anti-phase support motion at primary resonance, two main items are to be accomplished. (i) Going in-depth into its experimental characterization, by analyzing the relevant peculiar and/or persistent bifurcation features, and by possibly tracing them back to a canonical scenario from dynamical systems theory; (ii) developing a phenomenological theoretical model able to reproduce the intrinsic features of the dynamical system and its overall bifurcation scenario. The first item, which involves a systematic physical investigation and the understanding of phenomena responsible for the onset of experimental non-regular dynamics, has been accomplished in [14].

In turn, developing a reduced order bifurcation model, relying on the normal form of bifurcation mechanisms known from dynamical system theory [12], can allow one to gain insight into the limits of some assumptions made in “classical” theoretical modelling of suspended cables. Possessing the physical system some (eventually imperfect) symmetries, equivariant bifurcation theory [13] suggests to carry out a model independent analysis, starting from symmetry-breaking bifurcations, and performing a systematic study of the role played by symmetries in restricting the range of dynamical behavior available to the system in a given transition [14]. As a matter of fact, in the context of a profitable feedback between experiments and theory, such an approach allows one to recognize the mechanical meaning of terms playing a meaningful role in the bifurcation mechanisms [14], thus paving the way towards the independent formulation of a theoretical reduced order cable model having all the necessary pre-requisites for possibly reproducing the experimentally observed phenomena. This item is pursued in this paper, merely for what pertain to first anti-symmetric in plane and out of plane modes interaction in regular regime, where the 2:2:1 internally resonant, symmetrically forced dynamics of a suspended cable is considered.

Some main experimental results from the systematic investigation are summarized in Sect. 22.2, along with the partial unfolding of the relevant regular dynamics within a reference bifurcation scenario. Then, the low-dimensional phenomenological model is presented in Sect. 22.3. Finally, partial unfolding of the bifurcation equations describing the solely vertical excitation and capable to exhibit a bifurcation scenario comparable to the experimental one is presented in Sect. 22.4, with a few conclusions being given in Sect. 22.5.

22.2 Summary of Relevant Experimental Results in Regular Regime

System mechanical and geometrical properties realize a condition of 2:2:1 multiple internal resonance amongst the frequencies of the first anti-symmetric in-plane (V_2) mode, first anti-symmetric out-of-plane (H_2) mode, and first symmetric out-of-plane (H_1) mode. No contact devices (Fig. 22.1) are used to measure the two (in-plane and out-of-plane) components of motion of four masses at variable locations along the cable [9]. Summarizing results emphasis will be done, within the scope of the present work, on motion classes ensuing from mode interaction phenomena involving first anti-symmetric in plane and out of plane modes, in regular regime. For this purpose in this chapter reference is made to [9].

Figure 22.2 shows the steadystate responses obtained at an average support displacement of 0.0685 mm in a frequency range around the resonance of anti-symmetric modes when the first symmetric in plane mode is forced. Coexistence and competition of up to three fundamentally different classes of motion are observed. Analysis of the experimental response starts with the classes of motion identified by the letter B in Fig. 22.2. These are robust steady-state responses involving

Fig. 22.1 The experimental setup

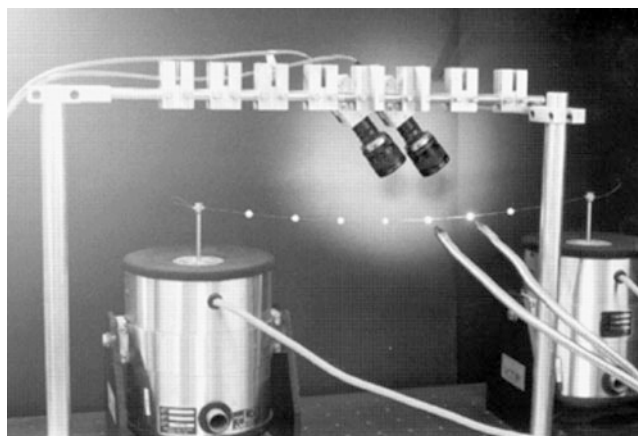
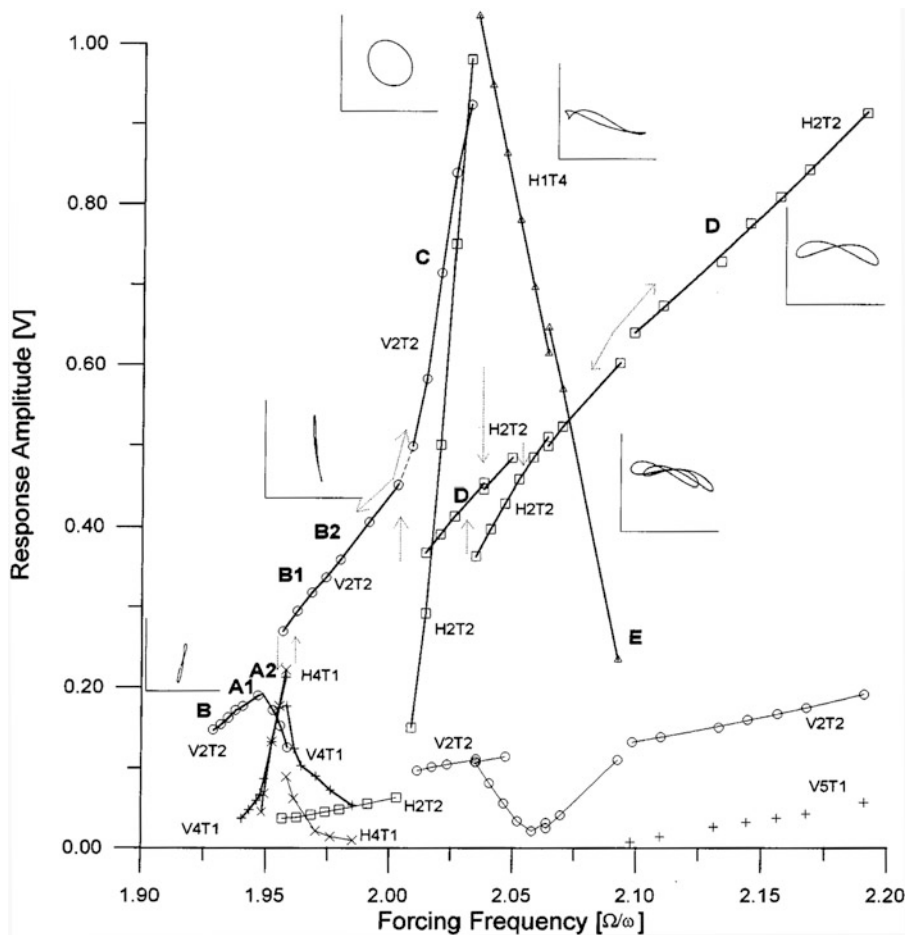


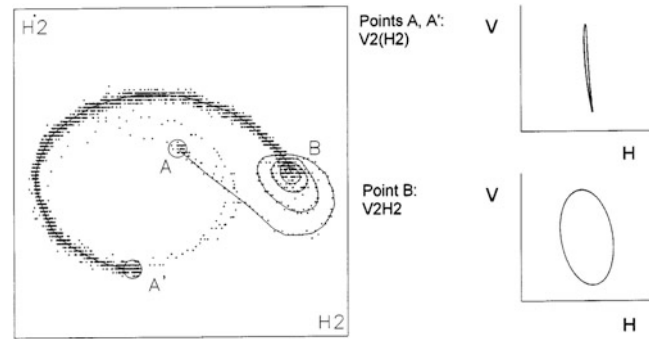
Fig. 22.2 Frequency response diagram at resonance of anti-symmetric modes (in phase supports motion) [9]



the prevalent first in-plane anti-symmetric component, but containing also other components with much lower levels of amplitude, namely the first in-plane symmetric, the first out-of-plane anti-symmetric, and both the second anti-symmetric in plane and out-of-plane components. A small symmetric planar component is also present in the response, though being its contribution not easily distinguishable from the vertical transport motion of the system. This response is stable in a range extending from about forcing frequency $[W/w]$ 1.95 to 2.020.

By increasing the frequency, a bifurcation occurs at about 2.020: both the in-plane and the out-of-plane components increase, the 2 T-periodic motion (labelled C) that settles down is classified as first anti-symmetric ballooning. It exhibits an elliptic orbit gradually evolving towards a perfect circular one with increasing excitation frequency. The range of stability of this steady-state response extends up to about 2.0377.

Fig. 22.3 Poincaré section of the transient first anti-symmetric ballooning [9]



It is worth commenting briefly on the transition mechanism to the ballooning motion. Namely, the apparently sudden increase of amplitude of both components observed at the ballooning start is associated only to the finite, though very small, frequency step considered in the experiment. Indeed, in the last part of the range of stability of the response, each frequency step results in a transitory motion which rapidly leads to ballooning, but this latter in turn shows to be soon unstable, and the motion goes back very slowly to an updated steady-state B response, close to the one occurring at the former frequency value. The phenomenon is illustrated in Fig. 22.3 through a Poincaré section of the closed motion in the plane of out-of-plane motion amplitude and velocity. A small frequency step leads from the fixed point, corresponding to the former steady-response, to the ballooning fixed point. The latter looks like a saddle-focus, likely characterized by a pair of complex eigenvalues with negative real parts along its stable manifold, and at least one real positive eigenvalue along its unstable manifold, leading to the stable node corresponding to the updated steady motion. As the excitation frequency is further increased, the time the response needs to leave transient ballooning grows up (from few minutes to more than one hour), and only when the frequency reaches the value 2.025, the ballooning becomes stable. It was classified as a steady-state response only if persisting after a period of observation of some hours. A new actually sudden change in the character of the response, involving a (jump-like) transition from the ballooning to a prevalently out of plane anti-symmetric motion (labeled D) occurs.

22.3 Analytical Model

The analytical model is taken from [1]. Herein a few words about the main features of that model are reported for the sake of completeness, but the reader is referred to [1] for details. A suspended cable, able to perform in-plane and out-of-plane displacements, has been considered (Eq. (7) of [1]). A symmetric, in-plane, periodic force, uniformly-distributed along the span of the cable, and time-periodic of frequency Ω , has been applied. In order to obtain the continuum equations, the condensation of the horizontal displacement ($u(s,t)$) has been applied to the PDEs, coherently with the hypothesis of small sag-to-span, so that the dependent variables are the vertical in-plane ($v(s,t)$) and the out-of-plane ($w(s,t)$) displacements. Then, a Galerkin projection of the continuum model has been performed, using as trial functions the first symmetric and anti-symmetric in-plane modes of the associated free linear system, whose time-dependent amplitudes are indicated as $q_1(t)$ and $q_2(t)$, respectively, and the first symmetric and anti-symmetric out-of-plane modes, whose amplitudes are indicated as $q_3(t)$ and $q_4(t)$, respectively. Therefore, a 4 d.o.f. nonlinear ordinary differential system in the dependent variables $q_j(t)$, $j = 1, \dots, 4$, has been obtained (Eq. (13) of [1]). Since the modes have been evaluated within the Irvine theory [15], asserting that the in-plane and out-of-plane anti-symmetric modes are exactly the same, i.e. having shape coincident with a period of sine along the span and time-frequency $\omega = \frac{\pi}{\ell} \sqrt{\frac{T}{m}}$, the relevant equations describing the dynamics of $q_2(t)$ and $q_4(t)$, namely Eq. (13₂) and (13₄) of [1], are identical. This drawback introduces in the model a strong characteristic of symmetry, avoiding the possibility to catch particular classes of motion which, on the other hand, have been observed in experimental analysis, carried out on cables of corresponding properties (see [9]) such as, for instance, ballooning motions, which involve both the anti-symmetric components in different phases. Therefore, as a first attempt to solve this issue and allow the model to catch them, an internal detuning between the in-plane and out-of-plane anti-symmetric natural frequencies is introduced here. This is to simulate an actual, although small, difference between the modal properties, which is plausible due to the existence of the initial in-plane curvature of the cable, as well as theoretically admissible if richer analytical model are considered even for the taut cables [16].

Then, the Multiple Scale Method is applied to Eq. (13) of [1], with a slight difference on what has been done in [1]. In fact there, in correspondence of the application of the second-order solvability conditions (Eq. (22) of [1]), the dependence

on time-scale T_1 has been eliminated. Herein, on the other hand, the dependence on time-scale T_1 is preserved, causing the modification of the coefficients of some cubic terms, and therefore complete AME are obtained. Internal resonance conditions are considered as in [1]. In particular, the cable has been assumed close to the first cross-over condition, i.e. 1:1 resonance exists among the symmetric in-plane, anti-symmetric in-plane and anti-symmetric out-of-plane modes, and 2:1 among those and the symmetric out-of-plane mode. External (σ) and internal (ρ_2, ρ_3, ρ_4) detuning parameters are then defined as

$$\begin{aligned} \Omega &= \omega_1 + \varepsilon^2 \sigma \\ \omega_2^2 &= \omega_1^2 + \varepsilon^2 \rho_2 \\ \omega_3^2 &= \frac{1}{4} \omega_1^2 + \varepsilon^2 \rho_3 \\ \omega_4^2 &= \omega_1^2 + \varepsilon^2 \rho_4 \end{aligned} \tag{22.1}$$

The complex Amplitude Modulation Equations become

$$\begin{aligned} \dot{A}_1 &= -\frac{\mu_1}{2} A_1 + k_{11} A_1^2 \bar{A}_1 + k_{12} A_2^2 \bar{A}_1 + k_{13} A_4^2 \bar{A}_1 + k_{14} A_1 A_2 \bar{A}_2 + (k_{15} + \tilde{k}_{15}) A_1 A_3 \bar{A}_3 + k_{16} A_1 A_4 \bar{A}_4 + k_{17} A_3^2 - \frac{i f_1}{4 \omega_1} e^{i \sigma t} \\ \dot{A}_2 &= \left(-\frac{\mu_2}{2} + i \rho_2\right) A_2 + k_{21} A_1 A_2 \bar{A}_1 + k_{22} A_1^2 \bar{A}_2 + k_{23} A_2^2 \bar{A}_2 + k_{24} A_4^2 \bar{A}_2 + k_{25} A_2 A_3 \bar{A}_3 + k_{26} A_2 A_4 \bar{A}_4 - \frac{i f_2}{4 \omega_2} e^{i \sigma t} \\ \dot{A}_3 &= \left(-\frac{\mu_3}{2} + i \rho_3\right) A_3 + (k_{31} + \tilde{k}_{31}) A_1 A_3 \bar{A}_1 + k_{32} A_2 A_2 \bar{A}_3 + (k_{33} + \tilde{k}_{33}) A_3^2 \bar{A}_3 + k_{34} A_3 A_4 \bar{A}_4 + k_{35} A_1 \bar{A}_3 \\ \dot{A}_4 &= \left(-\frac{\mu_4}{2} + i \rho_4\right) A_4 + k_{41} A_1 A_4 \bar{A}_1 + k_{42} A_2 A_2 \bar{A}_4 + k_{43} A_3 A_3 \bar{A}_4 + k_{44} A_1^2 \bar{A}_4 + k_{45} A_2^2 \bar{A}_4 + k_{46} A_4^2 \bar{A}_4 - \frac{i f_4}{4 \omega_4} e^{i \sigma t} \end{aligned} \tag{22.2}$$

where $A_j(t), j = 1, \dots, 4$, are the complex amplitudes of the corresponding modal components $q_j(t)$, the coefficients k_{mn} are the same of [1] whereas $\tilde{k}_{15}, \tilde{k}_{31}, \tilde{k}_{33}$ are the modifications of the coefficients due to the maintaining of the dependence on the scale T_1 at the solvability conditions. Their expression is not shown here for brevity. Cartesian decomposition of the complex amplitudes is applied to the Eq. (22.2), namely $A_j(t) = p_j(t) + i q_j(t)$, where i is the imaginary unit, and eight ordinary differential equations in the real (p_j) and imaginary (q_j) parts are obtained (not shown here for the sake of concision). Numerical integration and continuation algorithms are applied to the equations, in order to describe the forced dynamics at different amplitudes and frequencies of excitation, and with the specific aim to catch those classes of motions, which can be observed only if the asymmetry between the equations ruling the anti-symmetric in-plane and out-of-plane amplitudes is introduced.

22.4 Numerical Results

Equilibrium solutions of the AME (22.2), corresponding to periodic motions of the variables $q_j(t)$, are sought. Diagrams are obtained for $\rho_2 = -0.51, \rho_3 = -0.09, \rho_4 = -0.49$, which reproduce the mode configuration of the cable near the zone where ballooning motions have been experimentally found [9].

In Fig. 22.4, the stationary solutions vs. the external detuning σ , for a forcing amplitude $p = 0.02$, are shown in terms of real amplitudes $a_j, j = 1, \dots, 4$, where $a_j = \sqrt{p_j^2 + q_j^2}$. They correspond to periodic solutions in the variables $q_j(t)$. In this case, the mono-modal solution involving just the in-plane symmetric, directly forced, component q_1 , loses stability in

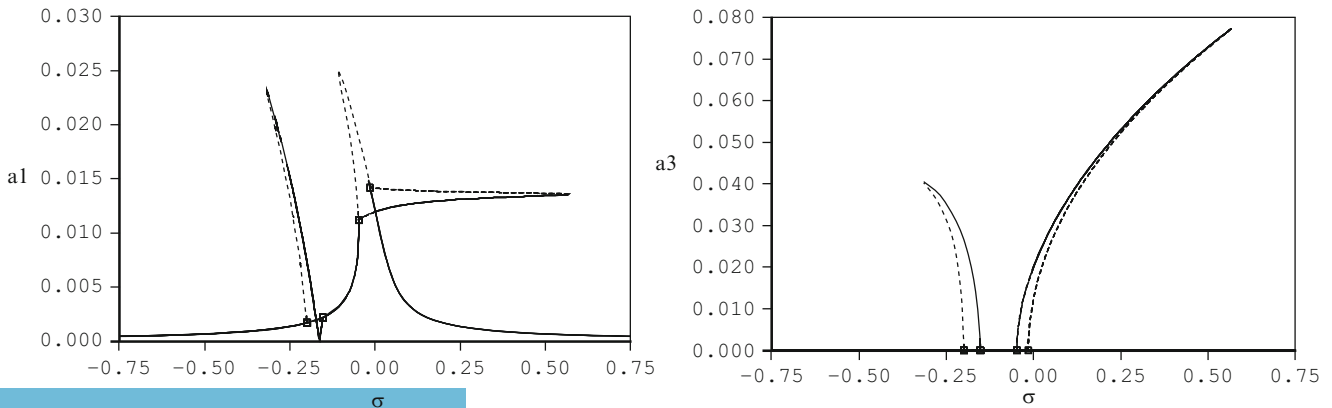


Fig. 22.4 Mono-modal (a_1) and bi-modal (a_1 - a_3) solutions for $p = 0.02$

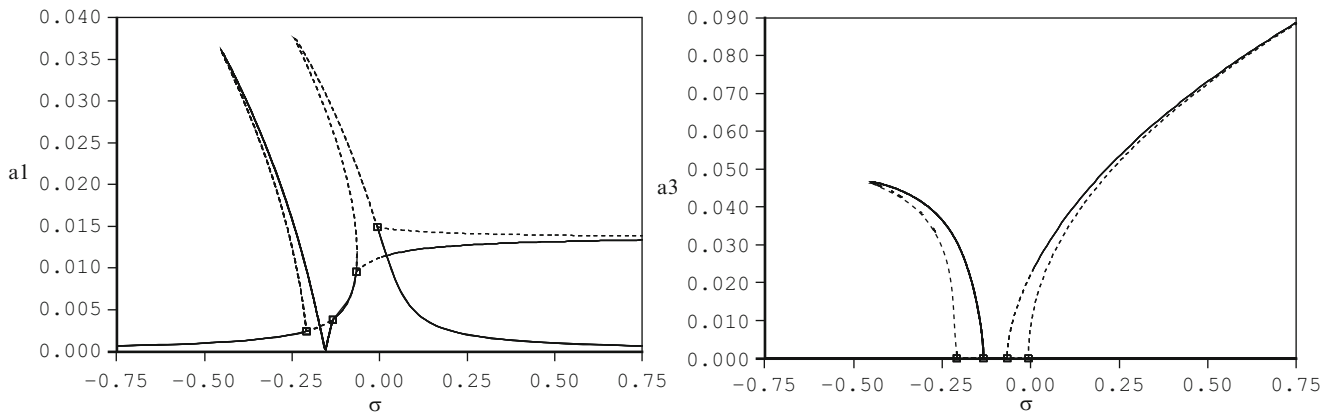


Fig. 22.5 Mono-modal (a_1) and bi-modal (a_1 - a_3) solutions for $p = 0.03$

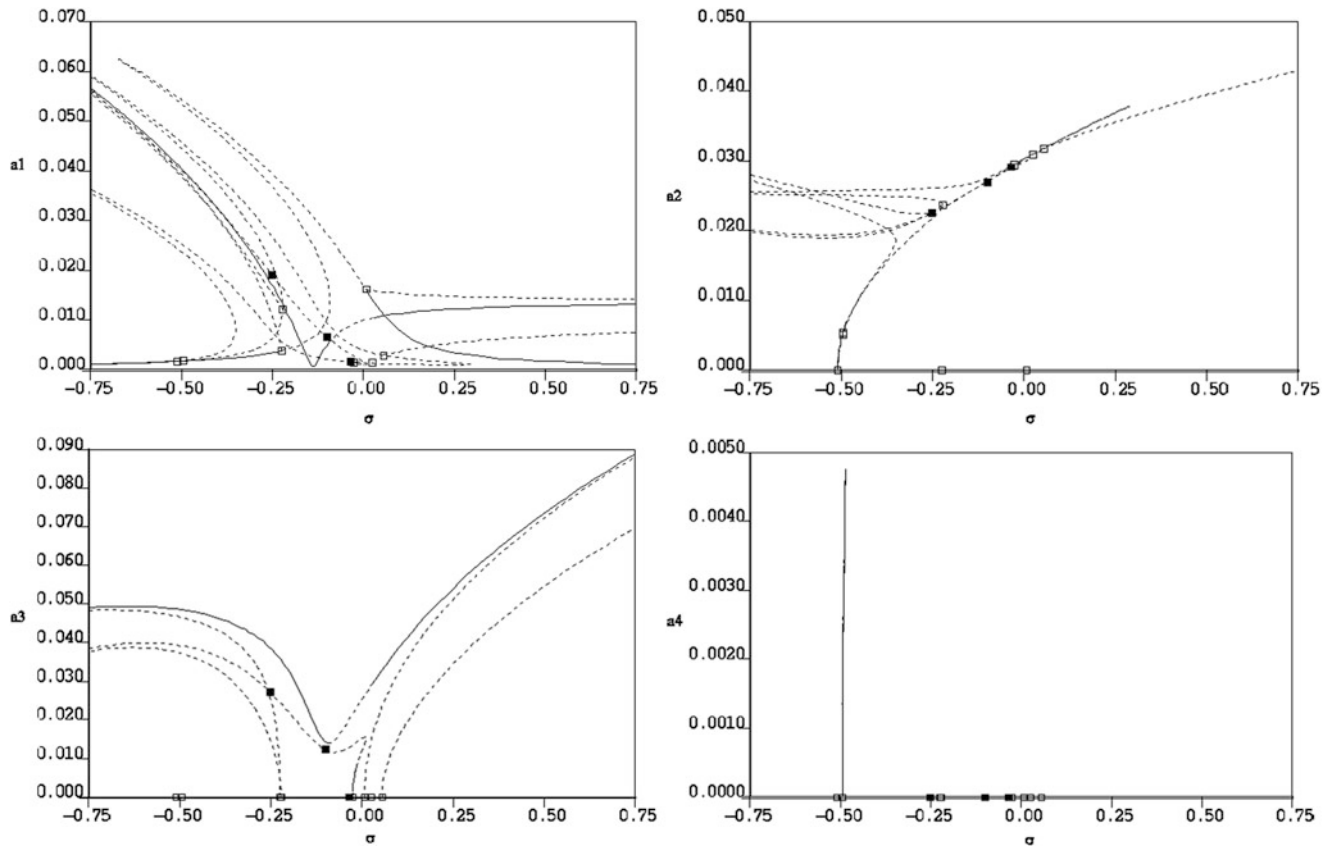


Fig. 22.6 Mono-modal (a_1), bi-modal (a_1 - a_3) and tri-modal (a_1 - a_2 - a_3 and a_1 - a_2 - a_4 (ballooning)) solutions for $p = 0.05$

correspondence of two regions, around $\sigma = -0.20$ and $\sigma = 0.0$, respectively. As a consequence, bi-modal stable solutions in the a_1 and a_3 components arise. If the amplitude of the force is increased to $p = 0.03$, a qualitative similar behavior is found (Fig. 22.5), except for the lack of a stable stationary solution around the value $\sigma = 0.0$, where stable periodic motions (not shown) in a_1 and a_3 , corresponding to quasi-periodic motions in q_1 and q_3 , arise.

When the amplitude of the force is further increased to $p = 0.05$ (see Fig. 22.6), a richer dynamics is found, and solutions concurrently involving a_1 - a_2 - a_3 and a_1 - a_2 - a_4 components arise. In particular, in the narrow region ($\sigma \in [-0.495, -0.486]$), the stable solution where a_1 - a_2 - a_4 are active, appears. It is shown in detail in Fig. 22.7.

In Fig. 22.8, a comparison between the ballooning solution as obtained from numerical integration of the AME (22.2), with the relevant reconstituted components q_2 - q_4 (Fig. 22.8) and of the original equations of motion (Eq. (13) of [1]), shows good agreement.

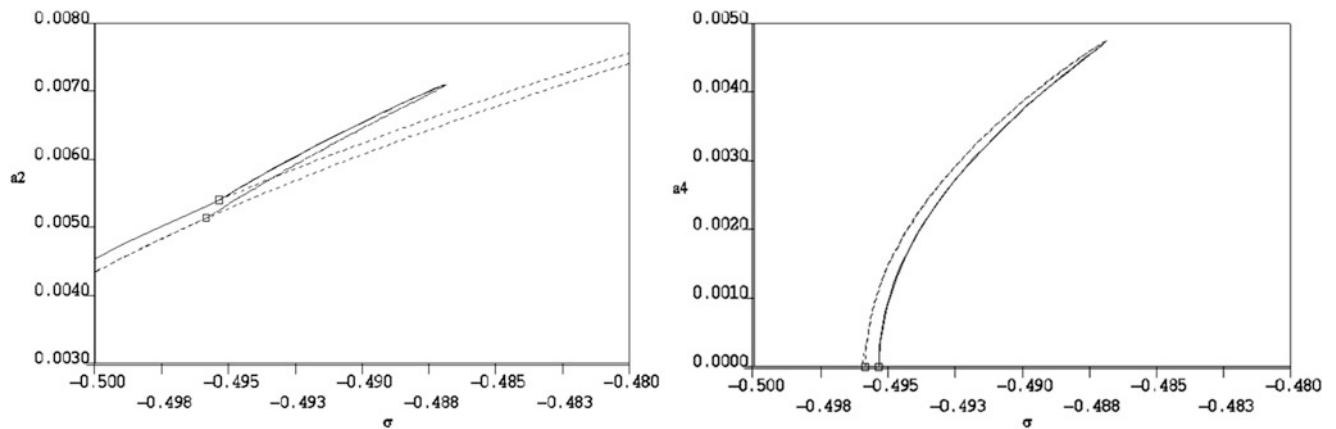


Fig. 22.7 Detail of the tri-modal (a_1 - a_2 - a_4) ballooning solutions for $p = 0.05$

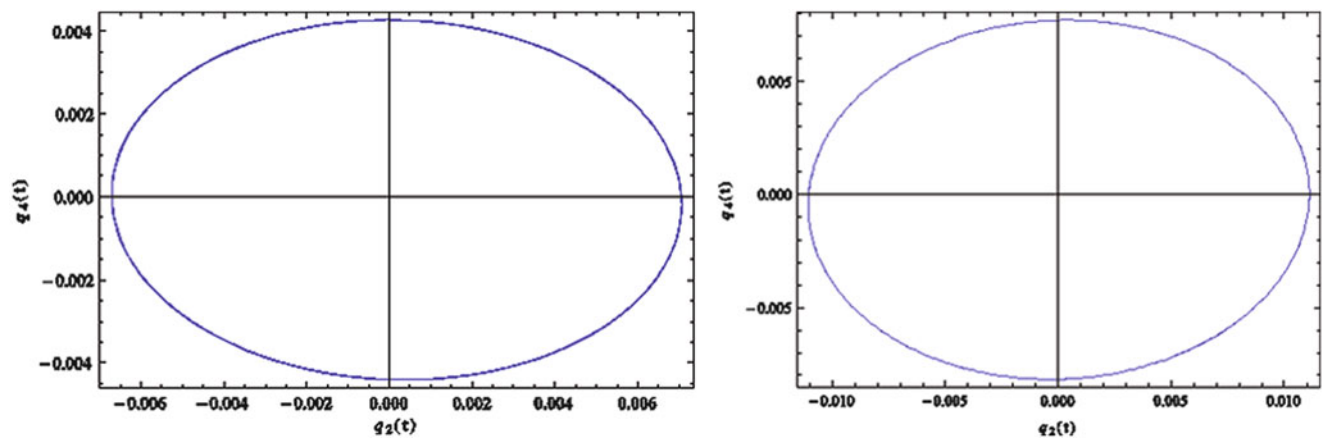


Fig. 22.8 Phase portrait of the ballooning solutions from the AME and equations of motion for $\sigma = -0.488$, $p = 0.05$

22.5 Conclusions

The nonlinear 3D dynamics of a suspended cable is studied herein, by using an analytical model which has been already obtained in [1], with the main purpose of getting specific classes of motion, such as ballooning, which are experimentally observed on a companion prototype. First, a specific description of the bifurcation scenario which leads to the ballooning, as detected in the experiment, is provided. The reduced model is then suitably modified by introducing a detuning parameter between the frequencies of the anti-symmetric in-plane and out-of-plane modes, in order to break an intrinsic symmetry in the model, which is induced as a consequence of the use of the Irvine's theory in the evaluation of the trial functions for the Galerkin projection of the PDEs. The Amplitude Modulation Equations (AME) are then obtained through the use of the Multiple Scale Method, with a minor algorithmic difference with respect to [1], since the dependence of the amplitudes on the slower time-scale is not deleted in the second order solvability conditions. Steady solutions in the amplitudes of the modal components, corresponding to periodic motions of the cable, are found. In particular, if for small amplitudes of the symmetric force, only mono-modal and bi-modal solutions occur, once the force is increased, also tri-modal and, more generally, complex solutions, arise. A tiny region of existence of periodic ballooning motion is then detected, in good agreement with the results of numerical integration of the 4 d.o.f. equations of motion.

References

1. Benedettini F, Rega G, Alaggio R (1995) Non-linear oscillations of a four-degree-of-freedom model of a suspended cable under multiple internal resonance conditions. *J Sound Vib* 182(5):775–798
2. Rega G, Lacarbonara W, Nayfeh AH, Chin CM (1999) Multiple resonances in suspended cables: direct versus reduced-order models. *Int J Nonlinear Mech* 34(5):901–924

3. Rega G (2004) Nonlinear vibrations of suspended cables—Part I: modeling and analysis. *Appl Mech Rev* 57:443–478
4. Rega G (2004) Nonlinear vibrations of suspended cables—Part II: deterministic phenomena. *Appl Mech Rev* 57:479–514
5. Berlioz A, Lamarque CH (2005) A non-linear model for the dynamics of an inclined cable. *J Sound Vib* 279(3–5):619–639
6. Srinil N, Rega G, Chucheepsakul S (2007) Two-to-one resonant multi-modal dynamics of horizontal/inclined cables. Part i: theoretical formulation and model validation. *Nonlinear Dynam* 48(3):231–252
7. Srinil N, Rega G (2007) Two-to-one resonant multi-modal dynamics of horizontal/inclined cables. Part ii: internal resonance activation, reduced-order models and nonlinear normal modes. *Nonlinear Dynam* 48(3):253–274
8. Rega G, Srinil N, Alaggio R (2008) Experimental and numerical studies of inclined cables: free and parametrically-forced vibrations. *J Theor Appl Mech* 46(3):621–640
9. Rega G, Alaggio R, Benedettini F (1997) Experimental investigation of the nonlinear response of a hanging cable. Part I: local analysis. *Nonlinear Dynam* 14:89–117
10. Alaggio R, Rega G (2000) Characterizing bifurcations and classes of motion in the transition to chaos through 3D-tori of a continuous experimental system in solid mechanics. *Phys D* 137:70–93
11. Rega G, Alaggio R (2001) Spatio-temporal dimensionality in the overall complex dynamics of an experimental cable/mass system. *Int J Solid Struct* 38:2049–2068
12. Rega G, Alaggio R (2009) Experimental unfolding of the nonlinear dynamics of a cable-mass suspended system around a divergence-Hopf bifurcation. *J Sound Vib* 322:581–611
13. Golubitsky M, Schaeffer DG (1985) Singularities and groups in bifurcation theory, vol 1. Springer, Berlin
14. Alaggio R, Rega G (2009) Unfolding complex dynamics of sagged cables around a divergence-Hopf bifurcation: experimental results and phenomenological model. XIX AIMETA Conference—Italian Theoretical and Applied Mechanics Association, Ancona, Italy, 14–17 September 2009
15. Irvine M (1992) Cable structures. Dover Publications, New York
16. LaCarbonara W, Paolone A, Vestroni F (2007) Elastodynamics of nonshallow suspended cables: linear modal properties. *J Vib Acoust* 129: 425–433

Chapter 23

Computationally Efficient Design of Semiactive Structural Control in the Presence of Measurement Noise

Mahmoud Kamalzare, Erik A. Johnson, and Steven F. Wojtkiewicz

Abstract Designing control strategies for smart structures, such as those with semiactive devices, is complicated by the nonlinear nature of the feedback control, secondary clipping control, and other additional requirements such as device saturation. The authors have previously developed an approach for semiactive control system design, based on a nonlinear Volterra integral equation (NVIE) that provides a low-order computationally efficient simulation of such systems, for state feedback semiactive clipped-optimal control. This paper expands the applicability of the approach by demonstrating that it can also be adapted to accommodate more realistic cases when, instead of full-state feedback, only a limited set of noisy response measurements is available to the controller. This extension requires incorporating a Kalman filter estimator, which is linear, into the nominal model of the uncontrolled system. The efficacy of the approach is demonstrated by a numerical study of a 100-DOF frame model, excited by a filtered Gaussian random excitation, with noisy acceleration sensor measurements to determine the semiactive control commands. The results show that the proposed method can achieve more than two orders of magnitude improvement in computational efficiency while retaining a comparable level of accuracy.

Keywords smart structures • semiactive control • nonlinear Volterra integral equation • clipped-optimal control • Kalman filter

23.1 Introduction

Controllable passive devices, such as variable orifice dampers and magnetorheological fluid dampers, form the core of semiactive control systems [1–4]. However, designing optimal control strategies for these devices is complicated by the nonlinear nature of the resulting feedback system. As a result, designing optimal controllers often requires large-scale parameter studies, with many simulations of the nonlinear system, requiring extensive computational resources.

The authors [5] have developed an approach, based on the nonlinear Volterra convolution-based integral equations, that is capable of rapidly computing the system response of large-scale nonlinear systems when the nonlinearity is localized at a few degrees of freedom. Further, the authors have demonstrated [6, 7] how this approach can be adapted to design the optimal semiactive control strategy for clipped-optimal control with state feedback; for a medium-size model, computational cost was reduced about two orders of magnitude for the required control design parameter study.

However, full-state feedback is rarely available even in the laboratory, much less in real-world applications; rather, only a set of noisy sensor measurements can be used, where a Kalman filter can be exploited to estimate the states of the system. The main goal of this paper, then, is to demonstrate that the proposed approach can provide, in a computationally efficient manner, multiple simulations of clipped-optimal semiactive control with a Kalman filter. The following section explains the theoretical formulation required to combine the Kalman filter with the system equations. The efficiency of the approach is

M. Kamalzare and E.A. Johnson (✉)
Sonny Astani Department of Civil and Environmental Engineering, University of Southern California, 3620 S Vermont Ave,
Los Angeles, CA 90089, USA
e-mail: kamalzar@usc.edu, JohnsonE@usc.edu

S.F. Wojtkiewicz
Department of Civil Engineering, University of Minnesota, 500 Pillsbury Drive S.E., Minneapolis, MN 55455, USA
e-mail: ykvich@umn.edu

demonstrated in section 23.3 through a numerical study of a 100-DOF frame model excited by one realization of a filtered Gaussian white noise excitation. Ground and story-level accelerations are measured by the sensors, corrupted by noise. The results show that the proposed method can achieve significant computational efficiency while retaining a level of accuracy comparable to traditional nonlinear solvers.

23.2 Methodology

This section briefly explains the method, introduced in the authors' prior work [5] for rapid computational analysis of large-scale nonlinear systems where the nonlinearities are located in a few local degrees of freedom, the application [6, 7] to state-feedback clipped-optimal semiactive control, and the formulation to incorporate Kalman Filter into the system.

23.2.1 Proposed Approach for Fast Computational Analysis

Consider a nominal uncontrolled structure model, without control devices forces, in state space form

$$\dot{\mathbf{x}}(t) = \mathbf{A}\mathbf{x}(t) + \mathbf{B}\mathbf{w}(t), \quad \mathbf{x}(0) = \mathbf{x}_0 \quad (23.1)$$

with $n \times 1$ state vector $\mathbf{x}(t)$, $n \times n$ state matrix \mathbf{A} , $m \times 1$ excitation $\mathbf{w}(t)$, $n \times m$ input influence matrix \mathbf{B} , and initial condition vector \mathbf{x}_0 . Adding a $q \times 1$ control device force vector $\mathbf{p}(t)$, the equation of motion becomes

$$\dot{\mathbf{X}}(t) = \mathbf{A}\mathbf{X}(t) + \mathbf{B}\mathbf{w}(t) + \mathbf{L}\mathbf{p}(t), \quad \mathbf{X}(0) = \mathbf{x}_0 \quad (23.2)$$

with $n \times q$ control force input matrix \mathbf{L} and the same initial conditions. If the control force $\mathbf{p}(t)$ were known *a priori*, (23.2) could be efficiently solved through standard linear response simulation methods. However, a control device exerts a force that is a function, usually nonlinear, of some subset (or linear combination) of states $\bar{\mathbf{X}}(t) = \mathbf{G}\mathbf{X}(t)$, where \mathbf{G} is an $s \times n$ matrix. The functional dependence of $\mathbf{p}(t) = \mathbf{g}(\bar{\mathbf{X}}(t))$ on $\bar{\mathbf{X}}(t)$ depends on the nature of the control devices and on the form of the control.

Controlled response $\bar{\mathbf{X}}(t)$ can be computed using the corresponding uncontrolled response $\bar{\mathbf{x}}(t) = \mathbf{G}\mathbf{x}(t)$ and a convolution in the control force

$$\bar{\mathbf{X}}(t) = \bar{\mathbf{x}}(t) + \int_0^t \bar{\mathbf{H}}_L(t - \tau)\mathbf{p}(\tau)d\tau \quad (23.3)$$

where $\bar{\mathbf{H}}_L(t) = \mathbf{G}\mathbf{H}_L(t)$ is the response to an impulse applied in the pattern of the control devices. Substituting (23.3) into $\mathbf{p}(t) = \mathbf{g}(\bar{\mathbf{X}}(t))$ results in

$$\mathbf{p}(t) - \mathbf{g}\left(\bar{\mathbf{x}}(t) + \int_0^t \bar{\mathbf{H}}_L(t - \tau)\mathbf{p}(\tau)d\tau\right) = \mathbf{0} \quad (23.4)$$

which is a q -dimensional nonlinear Volterra integral equation (NVIE) in nonstandard form. The authors' prior work [5] explains how to effectively discretize the integral in (23.4) and solve for $\mathbf{p}(t)$ and the responses of the controlled system. (23.4) is a $q \times 1$ vector equation in the $s \times 1$ responses $\bar{\mathbf{X}}(t)$; if both q and s are much smaller than n , then solving (23.4) is much less computationally intensive than solving the full nonlinear system of ordinary differential equations.

23.2.2 Clipped-Optimal Control

Controllable damping devices can only exert dissipative forces, which may be generalized to an ideal damper that can exert any dissipative force. If some primary control design commands desired force $\mathbf{p}^d(t) = -\mathbf{K}^d\mathbf{X}(t) = [p_1^d(t) \ p_2^d(t) \ \cdots \ p_q^d(t)]^T$, where \mathbf{K}^d is a state feedback gain, then a secondary bang-bang clipping controller determines the force of the i^{th} device

$$p_i = g_i(\bar{\mathbf{X}}) = p_i^d H(-p_i^d v_i) = \begin{cases} p_i^d, & p_i^d v_i < 0 \text{ (dissipate energy)} \\ 0, & p_i^d v_i \geq 0 \text{ (cannot add energy)} \end{cases} \quad (23.5)$$

with Heaviside unit step function $H(\cdot)$, and velocity $v_i(t)$ across the i^{th} device. Using device velocities $\mathbf{v}(t) = \mathbf{V}\mathbf{X}(t)$, the control force function $\mathbf{g}(\cdot)$ depends only on $\bar{\mathbf{X}} = \mathbf{G}\mathbf{X}$ where $\mathbf{G} = [-(\mathbf{K}^d)^T \ \mathbf{V}^T]^T$ is a $2q \times n$ matrix.

23.2.3 Design Primary Control Gain

For a linear actuator, a linear quadratic regulator (LQR) approach can be employed to determine the optimal state feedback gain \mathbf{K}^d . However, a simple use of LQR, with control weights chosen to reflect the actual costs of response and control leads to suboptimal (and sometimes lousy) performance in a clipped-optimal strategy because the commanded force is sometimes non-dissipative so it gets clipped. Thus, optimal semiactive design must be completed using a large-scale parameter study or other optimization over the elements of control gains or some parameterization of them. One way to parameterize the gains [6–8] is to investigate a family of control gains \mathbf{K}_i , each of which minimizes, for a linear actuator, the cost function

$$J_i = \lim_{T \rightarrow \infty} \frac{1}{T} \int_0^T [\mathbf{Z}^T(t)\mathbf{Q}_i\mathbf{Z}(t) + \mathbf{p}^T(t)\mathbf{R}_i\mathbf{p}(t)]dt \quad (23.6)$$

where $\mathbf{Z}(t) = \mathbf{C}_z\mathbf{X}(t) + \mathbf{D}_z\mathbf{w}(t) + \mathbf{F}_z\mathbf{p}(t)$ is a vector of outputs to be regulated. Independent of how control gains are parameterized, the computationally efficient approach provides the ability to examine many control gains — herein, each \mathbf{K}_i is designed using MATLAB's `lqr` for each weight pair $(\mathbf{Q}_i, \mathbf{R}_i)$ — to quickly and accurately determine the optimal control gain \mathbf{K}^d .

23.2.4 Sensor Measurements

Herein, it is assumed that the controller has available, rather than the full state vector, an $r \times 1$ noise-corrupted measurement vector $\mathbf{Y}(t) = \mathbf{C}_y\mathbf{X}(t) + \mathbf{D}_y\mathbf{w}(t) + \mathbf{F}_y\mathbf{p}(t) + \mathbf{n}(t)$, where $\mathbf{n}(t)$ is the $r \times 1$ measurement noise vector; \mathbf{C}_y , \mathbf{D}_y , and \mathbf{F}_y are the measurement influence matrices corresponding to states, excitation, and control force, respectively; $\mathbf{w}(t)$ and $\mathbf{n}(t)$ are assumed to be zero-mean stationary Gaussian processes with statistics $E[\mathbf{w}\mathbf{w}^T] = \mathbf{Q}_n$, $E[\mathbf{n}\mathbf{n}^T] = \mathbf{R}_n$ and $E[\mathbf{w}\mathbf{n}^T] = \mathbf{N}_n = \mathbf{0}$.

23.2.5 Incorporating Kalman Filter

The most typical algorithm used in the literature for estimating the states of a linear system based on a limited set of noisy sensor measurements is the Kalman filter. The Kalman filter [9], often called the Kalman-Bucy filter, minimizes the effect of system disturbance and measurement noise on the estimated state by means of the system

$$\dot{\hat{\mathbf{X}}} = \mathbf{A}\hat{\mathbf{X}} + \mathbf{L}\mathbf{p} + \mathbf{L}_k(\mathbf{Y} - \hat{\mathbf{Y}}) = \mathbf{L}_k\mathbf{C}_y\mathbf{X} + (\mathbf{A} - \mathbf{L}_k\mathbf{C}_y)\hat{\mathbf{X}} + \mathbf{L}\mathbf{p} + \mathbf{L}_k\mathbf{D}_y\mathbf{w} + \mathbf{L}_k\mathbf{n} \quad (23.7a)$$

$$\hat{\mathbf{Y}} = \mathbf{C}_y\hat{\mathbf{X}} + \mathbf{F}_y\mathbf{p} \quad (23.7b)$$

where $\hat{\mathbf{X}}$ is the optimal estimate of the state vector; $\mathbf{L}_k = (\mathbf{P}_n\mathbf{C}_y^T + \bar{\mathbf{N}}_n)\bar{\mathbf{R}}_n^{-1}$ is the Kalman gain matrix; $\bar{\mathbf{N}}_n = \mathbf{B}(\mathbf{Q}_n\mathbf{D}_y^T + \mathbf{N}_n)$; $\bar{\mathbf{R}}_n = \mathbf{R}_n + \mathbf{D}_y\mathbf{N}_n + \mathbf{N}_n^T\mathbf{D}_y^T + \mathbf{D}_y\mathbf{Q}_n\mathbf{D}_y^T$; and \mathbf{P}_n is the error covariance matrix for the state estimate, calculated by solving algebraic Riccati equation $\mathbf{A}\mathbf{P}_n + \mathbf{P}_n\mathbf{A}^T + \bar{\mathbf{Q}}_n - (\mathbf{P}_n\mathbf{C}_y^T + \bar{\mathbf{N}}_n)\bar{\mathbf{R}}_n^{-1}(\mathbf{C}_y\mathbf{P}_n + \bar{\mathbf{N}}_n^T) = \mathbf{0}$ where $\bar{\mathbf{Q}}_n = \mathbf{B}\mathbf{Q}_n\mathbf{B}^T$.

Combining (23.2) and (23.7a), the equation of motion can be written

$$\dot{\tilde{\mathbf{X}}}(t) = \tilde{\mathbf{A}}\tilde{\mathbf{X}}(t) + \tilde{\mathbf{L}}\mathbf{p}(t) + \tilde{\mathbf{B}}\tilde{\mathbf{w}}(t) \quad (23.8)$$

where $\tilde{\mathbf{X}}(t) = [\mathbf{X}^T \ \hat{\mathbf{X}}^T]^T$ is the generalized state vector; $\tilde{\mathbf{w}}(t) = [\mathbf{w}^T \ \mathbf{n}^T]^T$ is the generalized excitation vector; and

$$\tilde{\mathbf{A}} = \begin{bmatrix} \mathbf{A} & \mathbf{0} \\ \mathbf{L}_k \mathbf{C}_y & \mathbf{A} - \mathbf{L}_k \mathbf{C}_y \end{bmatrix}, \quad \tilde{\mathbf{L}} = \begin{bmatrix} \mathbf{L} \\ \mathbf{L} \end{bmatrix}, \quad \tilde{\mathbf{B}} = \begin{bmatrix} \mathbf{B} & \mathbf{0} \\ \mathbf{L}_k \mathbf{D}_y & \mathbf{L}_k \end{bmatrix} \quad (23.9)$$

Thus, with the Kalman filter equations incorporated with the linear system model, the combined state-space system (23.8) has a form similar to (23.2) and, therefore, it can be solved using the proposed approach without any extra effort. Note that the order of (23.8) is twice that of state equation (23.2), resulting in about double computational cost using typical nonlinear solvers such as ode45. However, the order of the nonlinear equations solved by the proposed approach does not change, so the computational effort required for solving this augmented system is essentially unchanged by adding the Kalman filter. The proposed approach includes one time calculations to compute the uncontrolled response and the impulse functions, and then the repeated costs to compute the control force. Using (23.9) to compute the impulse response $\bar{\mathbf{H}}_L(t)$ with $\bar{\mathbf{X}} = \mathbf{G}\hat{\mathbf{X}} = [\mathbf{0} \quad \mathbf{G}]\hat{\mathbf{X}}$ requires 2–4 times the computation without the Kalman filter. However, this impulse response is actually the same as that with state feedback [10]—*i.e.*, using the original system (23.2) instead of the augmented system (23.8)—so the change in one-time cost is only a very modest increase leveraged over the many repeated solutions for the control force, and the overall cost should increase only very modestly.

23.3 Numerical Example

23.3.1 Model Description: 100-DOF Frame Model

While the method proposed herein is applicable to a variety of applications of controllable passive dampers, a numerical example of a base-isolated building is used to demonstrate the efficacy of the method. Base isolation systems [1, 11], among the most commonly-adopted methods to protect civil structures against severe excitations, are developed based on separating the structure from the ground and preventing the ground excitation energy from being transferred to the superstructure. Passive base isolation can be augmented with actuators [12–14] or semiactive devices [2, 8, 15, 16] to provide significant improvements in mitigating structural responses and thereby reducing damage to both structural and nonstructural components.

Consider an isolated building with a semiactive controllable damping device in the isolator layer. The superstructure is an 11-story 2-bay building modeled as a 99 DOF linear plane frame (horizontal, vertical and rotational degrees of freedom at each node, three nodes per floor). The weight of the columns is small relative to the weight of the floors and is, therefore, neglected. Consistent mass and stiffness matrices are used for the beam elements; Rayleigh damping is used for the superstructure damping, assuming that 1st and 10th mode damping ratios are both equal to 3%. The fundamental mode of the superstructure, if it were a fixed-base structure, has a 1.05 s period and 3% damping. The ground excitation \ddot{x}_g is applied only in the horizontal direction.

The base mass, linear isolator stiffness, and linear viscous isolator damping are chosen such that the isolation mode has a typical [11] period $T_1^i = 2.76$ s, and a 5.5% damping ratio. The building weight is $W = 1.28 \times 10^6$ N and height is $h = 44$ m. The isolator layer is constrained to move in the horizontal direction only. The result is a 100 DOF isolated structure model

$$\begin{bmatrix} m_b & \mathbf{0}^T \\ \mathbf{0} & \mathbf{M}_s \end{bmatrix} \begin{Bmatrix} \ddot{x}_b \\ \ddot{\mathbf{x}}_s \end{Bmatrix} + \begin{bmatrix} c_b + \mathbf{r}^T \mathbf{C}_s \mathbf{r} & -\mathbf{r}^T \mathbf{C}_s \\ -\mathbf{C}_s \mathbf{r} & \mathbf{C}_s \end{bmatrix} \begin{Bmatrix} \dot{x}_b \\ \dot{\mathbf{x}}_s \end{Bmatrix} + \begin{bmatrix} k_b + \mathbf{r}^T \mathbf{K}_s \mathbf{r} & -\mathbf{r}^T \mathbf{K}_s \\ -\mathbf{K}_s \mathbf{r} & \mathbf{K}_s \end{bmatrix} \begin{Bmatrix} x_b \\ \mathbf{x}_s \end{Bmatrix} = - \begin{bmatrix} m_b & \mathbf{0}^T \\ \mathbf{0} & \mathbf{M}_s \end{bmatrix} \begin{Bmatrix} 1 \\ \mathbf{r} \end{Bmatrix} \ddot{x}_g^a + \begin{Bmatrix} 1 \\ \mathbf{0} \end{Bmatrix} p \quad (23.10)$$

where x_b is the base displacement relative to the ground; m_b , c_b and k_b are mass, damping and stiffness of the base, respectively; \mathbf{x}_s is a vector of horizontal and vertical displacement and rotation of each degree of freedom (DOF) of the fixed-base superstructure relative to the ground; \mathbf{M}_s , \mathbf{C}_s and \mathbf{K}_s are the superstructure mass, damping and stiffness matrices, respectively; and $\mathbf{r} = [1 \ 0 \ 0 \ 1 \ 0 \ 0 \ \dots \ 1 \ 0 \ 0]^T$ (*i.e.*, a 1 in each element corresponding to a horizontal displacement in \mathbf{x}_s , and zeros elsewhere) is the influence vector. Let \mathbf{M} , \mathbf{C} and \mathbf{K} denote the mass, damping and stiffness matrices on the left side of (23.10).

23.3.2 Ground Excitation

A Kanai-Tajimi filter [17] is incorporated into the model to generate a ground excitation with frequency content similar to historical earthquakes. The filter is a second order dynamical system characterized by transfer function $F(s) = (2\zeta_g\omega_g s + \omega_g^2)/(s^2 + 2\zeta_g\omega_g s + \omega_g^2)$, which has equation of motion

$$\ddot{x}_g(t) + 2\zeta_g\omega_g\dot{x}_g(t) + \omega_g^2x_g(t) = -w(t) \quad \ddot{x}_g^a(t) = -\omega_g^2x_g(t) - 2\zeta_g\omega_g\dot{x}_g(t) \quad (23.11)$$

where $w(t)$ is a zero-mean Gaussian white noise. The parameter values are $\zeta_g = 0.3$ and $\omega_g = 17$ rad/sec to approximate the spectral content of two moderate earthquakes (El Centro and Hachinohe) and two severe earthquakes (Kobe and Northridge) [8]. Herein, a single 30 s realization of white noise excitation $w(t)$ and of the sensor noise $\mathbf{n}(t)$, with 0.02 s time steps, is used in all simulations.

23.3.3 State-Space Model

By combining the states of the Kanai-Tajimi filter with those of the base and superstructure, the state-space equation of motion of the system can be written in form of (23.2) where $\mathbf{X}(t) = [x_b \ \mathbf{x}_s^T \ \dot{x}_b \ \dot{\mathbf{x}}_s^T \ x_g \ \dot{x}_g]^T$ is the state vector, with base x_b and superstructure \mathbf{x}_s displacements relative to the ground, and x_g is the displacement of ground relative to bedrock. \mathbf{A} , \mathbf{B} , and \mathbf{L} can be written as

$$\mathbf{A} = \begin{bmatrix} \mathbf{0} & \mathbf{I} & \mathbf{0} \\ -\mathbf{M}^{-1}\mathbf{K} & -\mathbf{M}^{-1}\mathbf{C} & \begin{bmatrix} 1 \\ \mathbf{r} \end{bmatrix} \begin{bmatrix} \omega_g^2 & 2\zeta_g\omega_g \\ 0 & 1 \end{bmatrix} \\ \mathbf{0} & \mathbf{0} & \begin{bmatrix} -\omega_g^2 & -2\zeta_g\omega_g \end{bmatrix} \end{bmatrix}, \quad \mathbf{B} = \begin{bmatrix} \mathbf{0} \\ \mathbf{0} \\ -1 \end{bmatrix}, \quad \mathbf{L} = \begin{bmatrix} \mathbf{0} \\ \mathbf{M}^{-1} \begin{bmatrix} 1 \\ \mathbf{0} \end{bmatrix} \\ \mathbf{0} \\ \mathbf{0} \end{bmatrix} \quad (23.12)$$

Assume the structure is instrumented with 13 accelerometers: one on the base, one at each superstructure story level, and one on the ground to record the ground excitation. It is assumed that all accelerometers are the same and will add a low-level noise to the signals. The measurement noise is modeled as a Gaussian pulse process with an RMS of about 5% of the average RMS of the story acceleration responses. Based on the ground excitation and its corresponding structural response, $\mathbf{Q}_n = 3.26$ and $\mathbf{R}_n = 0.00563\mathbf{I}_{13 \times 13}$ are used to design the Kalman filter gain.

Let \mathbf{C}_y^a be a matrix that selects the measured accelerations from among all structure accelerations; *i.e.*, it has elements $[\mathbf{C}_y^a]_{i,j} = \delta_{i,1}\delta_{j,1} + \delta_{9i-13,j}$. Then, the measurement equation matrices are

$$\mathbf{C}_y = \begin{bmatrix} -\mathbf{C}_y^a\mathbf{M}^{-1}[\mathbf{K} \ \mathbf{C}] & \mathbf{0} & \mathbf{0} \\ \mathbf{0} & -\omega_g^2 & -2\zeta_g\omega_g \end{bmatrix}, \quad \mathbf{D}_y = \begin{bmatrix} \mathbf{0} \\ \mathbf{0} \end{bmatrix}, \quad \mathbf{F}_y = \begin{bmatrix} \mathbf{C}_y^a\mathbf{M}^{-1}[\mathbf{1} \ \mathbf{0}^T]^T \\ \mathbf{0} \end{bmatrix} \quad (23.13)$$

If \mathbf{C}_z^a , with elements $[\mathbf{C}_z^a]_{i,j} = \delta_{95i,j}$, selects the roof acceleration from among all accelerations, then the outputs to be regulated, which include the base drift (1st DOF) and the absolute horizontal roof acceleration (95th DOF), can be found using output equation matrices

$$\mathbf{C}_z = \begin{bmatrix} 1 & 0 & \cdots & 0 & 0 & 0 \\ -\mathbf{C}_z^a\mathbf{M}^{-1}[\mathbf{K} \ \mathbf{C}] & \mathbf{0} & \mathbf{0} \end{bmatrix}, \quad \mathbf{D}_z = \begin{bmatrix} 0 \\ 0 \end{bmatrix}, \quad \mathbf{F}_z = \begin{bmatrix} 0 \\ \mathbf{C}_z^a\mathbf{M}^{-1}[\mathbf{1} \ \mathbf{0}^T]^T \end{bmatrix} \quad (23.14)$$

23.3.4 Augmented System with Kalman Filter

Now, the system of equations can be augmented by the Kalman filter state estimates and written in the form of (23.8). This is a system of 404 state equations; however, the nonlinearities are located exclusively in feedback force \mathbf{p} , so the NVIE is only one equation. Therefore, it can be solved very efficiently using the proposed approach. Figure 23.1 shows a block diagram

Fig. 23.1 Combined filter/structure model for semiactive control design using clipped-optimal controller

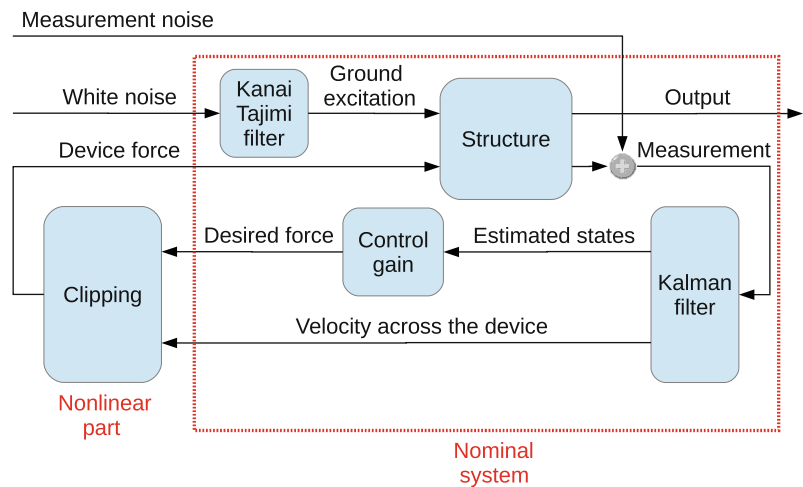


Table 23.1 RMS responses comparison

Damping system	RMS responses			
	Base drift (cm)	Roof acceleration (m/s ²)	Force (kN)	Peak force (kN)
LRB	5.67	1.03	71.89	162.41
Semiactive	2.85	1.03	51.02	151.88

representation of the semiactive control strategy, which includes the linear part (the Kanai-Tajimi filter, the structural model, and the Kalman filter) and the nonlinear part (clipped optimal controller).

23.3.5 Accuracy and Computational Cost of the Semiactive Control Design

In this study, the cost function is defined as in (23.6) with control weight $\mathbf{R}_i = W^{-2}$ and diagonal response weight $\mathbf{Q}_i = \text{diag}(\alpha_i/h^2, \beta_i(T_1^i)^4/(16\pi^4h^2))$, where α_i and β_i are dimensionless parameters that will be tuned to achieve the best semiactive control performance. The control gain \mathbf{K}_i is designed using the `lqr` command in MATLAB for each pair (α_i, β_i) .

The `fminsearch` algorithm in MATLAB’s optimization toolbox is used to find an optimal semiactive design where the proposed approach is implemented for the function evaluation. The objective function is to minimize the base drift in presence of two constraints: (1) RMS roof acceleration remains at (or below) its corresponding value when the isolator is a passive lead rubber bearing (LRB) design (baseline) [7], and (2) the RMS control force is at most 4% of building weight W . The optimization algorithm is started at $(\alpha, \beta) = (1000, 10)$; the algorithm terminates when absolute tolerances for both the search point and the function value are within 0.01. The optimization algorithm determines the design point of $(\alpha^*, \beta^*) = (3931.40, 54.23)$ which results in about 49.8% base drift reduction without any roof acceleration increase compared to the baseline performance. Also, the peak and RMS of the semiactive force are 11.9% and 4.0% of the building weight, respectively. Table 23.1 shows the RMS responses (base drift, roof acceleration, and device force) and peak device force for both LRB and semiactive design. Interestingly, the semiactive control design reduces the base drift significantly while it applies a force that is smaller than the LRB controller.

The analysis is performed by a traditional nonlinear solver, MATLAB’s `ode45`, and by the proposed approach solving the nonlinear Volterra integral equation using fast Fourier transforms [5]. To perform a fair comparison, the relative and absolute error tolerance of `ode45` are set to be 10^{-3} and 10^{-6} , respectively, and the proposed method is tuned to use a 2nd-order accurate trapezoidal integration with 2^{15} time steps of $\Delta t = 0.92$ ms duration each. Both of these have relative accuracy on the order of 10^{-3} .

Figure 23.2 illustrates actual roof acceleration response, measurement noise at the roof sensor, and the estimated response using the Kalman filter at the design point; the Kalman filter is successful in estimating the response very accurately. Figure 23.3 shows estimated base drift calculated by both methods at the design point. As shown in this figure, the results are almost identical for both methods, which verifies their comparable level of accuracy.

The simulations are performed on a computer with a 3.4 GHz Intel core i7-2600 processor and 8 GB of RAM, running MATLAB R2011a under Windows 7. For the ideal full-state feedback system of 202 states, using the proposed method, the

Fig. 23.2 Actual and estimated roof absolute acceleration response and the measurement noise signal

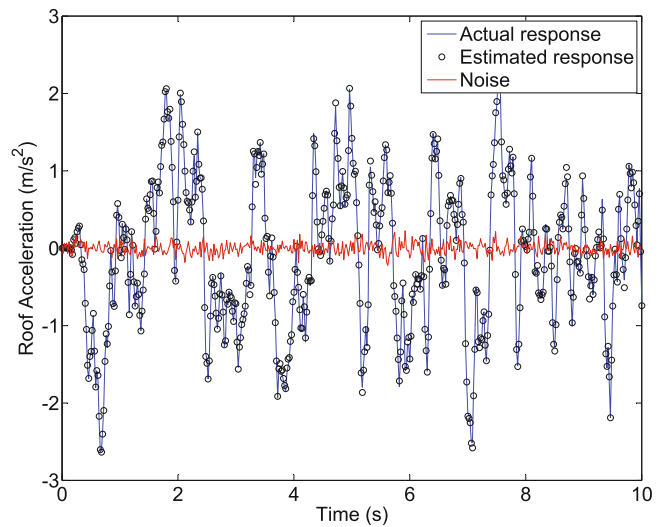


Fig. 23.3 Estimated base drift response to the generated excitation

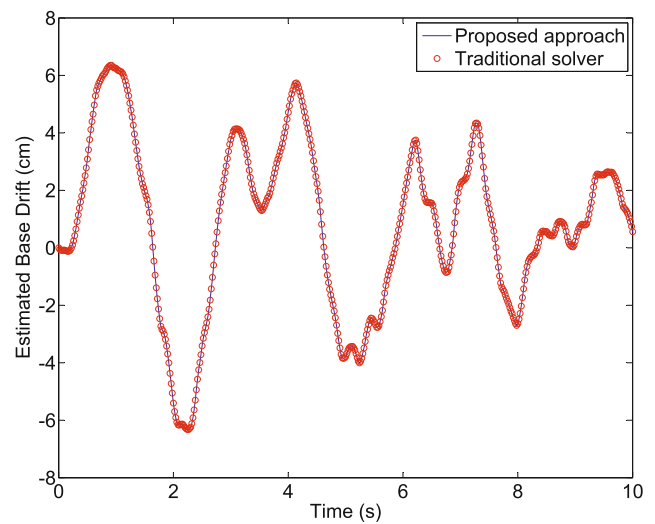


Table 23.2 Cost ratio comparison

Feedback	# states		ode45	Proposed method	
			RelTol = 10^{-3} AbsTol = 10^{-6}	# of steps = 2^{15} $\Delta t = 9.2 \times 10^{-4}$ s	Computational cost comparison
State	202	1 simulation	163.8 s	6.8 s	24.2
		100 simulations	4.5 hr	3.2 min	85.4
Output (w/Kalman filter)	404	1 simulation	286.7 s	11.5 s	25.1
		100 simulations	8.0 hr	3.3 min	145.9

computational cost of a single simulation includes one time calculations taking 4.9 s and the repeated ones taking 1.9 s; for a single function evaluation, ode45 takes about 163.8 s. When the estimated states are incorporated to the system of equations, resulting in a 404-state system, the one time calculations of the proposed approach increase to 9.6 s, while the remainder remains almost nearly identical because the size of the nonlinear system of equations does not change. For ode45, the computational time will increase to 286.7 s since the size of the system of equations are doubled. While the number of function evaluations required for the optimization to converge to the “best” design may vary significantly, depending on termination tolerances and the initial guess, the optimization here converged with 100–200 function evaluations. Table 23.2 summarizes the comparison of the computational time of a single simulation and 100 simulations (at the design point) for both methods and shows the achievable cost ratio. Clearly, the proposed method can again achieve two orders of magnitude reduction in computational cost.



23.4 Conclusions

The method previously introduced by the authors has been adapted to include a Kalman filter estimator to accommodate noisy output feedback measurements. It was shown herein that the augmented state space system, which includes both actual and estimated states, can be written in a form similar to what was implemented for the ideal full-state feedback control; therefore, the proposed approach can be directly implemented. The proposed method was tested with a representative frame model where only story-level accelerations, polluted by 5% noise signals, are available to measure. It is shown that the proposed approach can compute the structural responses with an appropriate level of accuracy but with a much smaller computational cost. The computational efficiency achievement is more than one order of magnitude for a single simulation and two order of magnitudes for multiple simulations.

Acknowledgements The authors gratefully acknowledge the partial support of this work by the National Science Foundation through awards CMMI 08-26634, 11-00528 and 11-33023. Any opinions, findings, and conclusions or recommendations expressed in this material are those of the authors and do not necessarily reflect the views of the National Science Foundation. The authors also acknowledge support of a Viterbi Doctoral Fellowship at the University of Southern California.

References

1. Housner GW, Bergman LA, Caughey TK, Chassiakos AG, Claus RO, Masri SF, Skelton RE, Soong TT, Spencer BF, Yao JTP (1997) Structural control: past, present, and future. *J Eng Mech* 123(9):897–971
2. Symans MD, Constantinou MC (1999) Semi-active control systems for seismic protection of structures: a state-of-the-art review. *Eng Struct* 21(6):469–487
3. Soong TT, Spencer BF (2002) Supplemental energy dissipation: state-of-the-art and state-of-the-practice. *Eng Struct* 24(3):243–259
4. Spencer BF, Nagarajaiah S (2003) State of the art of structural control. *J Struct Eng* 129(7):845–856
5. Gaurav, Wojtkiewicz SF, Johnson EA (2011) Efficient uncertainty quantification of dynamical systems with local nonlinearities and uncertainties. *Prob Eng Mech* 26(4):561–569
6. Kamalzare M, Johnson EA, Wojtkiewicz SF, Zheng Y (2012) Computationally efficient parameter studies for semiactive control design. In: 2012 joint conference of the engineering mechanics institute and the 11th ASCE joint specialty conference on probabilistic mechanics and structural reliability, Notre Dame, IN, June 2012
7. Kamalzare M, Johnson EA, Wojtkiewicz SF (XXXX) Computationally efficient design of optimal strategies for controllable damping devices. *Struct Contr Health Monit*, Submitted
8. Ramallo JC, Johnson EA, Spencer BF (2002) “Smart” base isolation systems. *J Eng Mech* 128(10):1088–1099
9. Kalman R, Bucy R (1961) New results in linear filtering and prediction. *J Basic Eng (ASME)* 83(D):95–108
10. Kamalzare M, Johnson EA, Wojtkiewicz SF (XXXX) Computationally efficient design of optimal output feedback strategies for controllable passive damping devices. *Smart Mater Struct*, Submitted
11. Skinner RI, Robinson WH, McVerry GH (1993) *An introduction to seismic isolation*. Wiley, Chichester
12. Kelly J, Leitmann G, Soldatos A (1987) Robust control of base-isolated structures under earthquake excitation. *J Optim Theor Appl* 53:159–180
13. Reinhorn AM, Soong TT, Wen CY (1987) Base-isolated structures with active control. In: *Proceedings (ASME) PVP conference*, pp 413–420, San Diego, CA, 1987
14. Reinhorn AM, Riley M (1994) Control of bridge vibrations with hybrid devices. In: *Proceedings 1st World conference on structural control*, vol. TA2, pp 50–59, Los Angeles, CA, 1994
15. Feng Q, Shinozuka M (1990) Use of a variable damper for hybrid control of bridge response under earthquake. In: *Proceedings of the U.S. national workshop on structural control research*, pp 107–112, 25–26 October 1990. University of Southern California, Los Angeles
16. Nagarajaiah S (1994) Fuzzy controller for structures with hybrid isolation system. In: *Proceedings 1st World conference on structural control*, vol TA2, pp 67–76, Los Angeles, CA, 1994
17. Soong TT, Grigoriu M (1993) *Random vibration of mechanical and structural systems*. Prentice Hall, Englewood Cliffs

Chapter 24

Optimal Nonlinear Control Using a Non-quadratic Cost Function for Scalar Systems

Elham Hemmat-Abiri and Erik A. Johnson

Abstract Various types of controllers have been studied and implemented to mitigate the effects of excitations from natural hazards. Linear control laws are most often applied, for active devices as well as part of the controller for semiactive devices, primarily due to their simple design and use. However, researchers have investigated nonlinear control of structures, showing performance improvements relative to that with linear controllers. The optimal linear control law that minimizes a quadratic cost function can be obtained using typical solvers like MATLAB's `lqr` command. In contrast, the optimal nonlinear controller generally requires minimizing a non-quadratic cost function, which is difficult and analytical solutions may only exist when the cost function is in particular forms. This paper presents a comparison of some of the analytical and numerical methods for finding optimal nonlinear controllers, particularly for cost functions that are even order powers of the states and quadratic in the control. A scalar model (*i.e.*, a scalar state-space equation) is used for the comparisons since analytical solutions exist for some of the methods. Even though the methods would all result in the same linear control law, it is demonstrated that the methods' differing assumptions give rise to different optimal nonlinear control laws, with different performance in different excitations.

Keywords structural control • nonlinear control • HJB equation • FPK equation • Monte Carlo simulation

24.1 Introduction

Extreme events such as earthquakes and hurricanes cause damage to, and failure of, buildings and infrastructure, with losses to public and private building owners in terms of actual structural damage and its economic impacts as well as injury and loss of life. Reducing large structural responses caused by natural hazards has been the focus of significant research, including the field of structure control [1]. Passive, active and semiactive control strategies have been investigated for mitigating structural dynamic response [2–4]. Linear control laws have been applied for designing all types of structural control strategies due to the simplicity of linear feedback. However, it is not clear that linear control is necessarily the best approach for achieving the diverse objectives of structural control.

Thus, some researchers have investigated nonlinear control techniques for civil structures. While some have used nonlinear control to directly address nonlinearities in structural models (*e.g.*, [5,6]), the focus here is on forming an optimal nonlinear control for a linear structure by minimizing a non-quadratic cost function. It is well established that this approach leads to the Hamilton-Jacobi-Bellman (HJB) partial differential equation [7,8]; however, analytical solutions to the HJB equation may only exist when the cost function is cast in particular forms and may be difficult to find. Nonlinear control of linear structure-like systems was first proposed by Rekasius [9], using the HJB equation for a class of non-quadratic costs; others [10–15] have proposed similar approaches.

This paper presents an investigation of several aspects of the optimal nonlinear control problem; the focus herein is on scalar systems as analytical solutions and results exist. The cost function is assumed in a specific form with non-quadratic terms such that an exact solution exists for the corresponding HJB equation. Four different approaches for finding the optimal

E. Hemmat-Abiri • E.A. Johnson (✉)

Sonny Astani Department of Civil and Environmental Engineering, University of Southern California, 3620 S Vermont Ave,

KAP 210, Los Angeles, CA 90089-2531, USA

e-mail: hemmatab@usc.edu; JohnsonE@usc.edu

control law are studied. First, solving the HJB equation for the non-quadratic cost function, the optimal control law can be obtained as a polynomial in the state for the scalar system. Second, for a Gaussian white noise excitation, the Fokker-Planck-Kolmogorov (FPK) equation can be solved exactly for a scalar system, giving a direct computation of response moments that can be used in the non-quadratic cost function to determine an optimal nonlinear control. Third, a Monte Carlo (MC) simulation is performed with Gaussian white noise excitation for a range of control gains to numerically approximate the optimal gains in a nonlinear control law. Fourth and finally, the cost function is computed for the same system with non-zero initial condition but no excitation by analytically solving the state equation for the free response; the optimal control gains can be found by setting equal to zero the derivatives of the cost function. Because this system has non-Gaussian responses and a non-quadratic cost function, the certainty equivalence property [16, 17] does not apply — *i.e.*, in contrast with linear control of linear systems with quadratic cost functions, the HJB-derived “optimal” solution for the optimal nonlinear control of a system without excitation but non-zero initial condition may be different from the optimal nonlinear control for a Gaussian white noise excitation.

24.2 Problem Formulation

This section will first formulate the problem for an arbitrary linear system, and then briefly summarize the HJB-based methods for finding the optimal nonlinear control. Based on one such method, one particular scalar system and a corresponding non-quadratic cost function will both be defined and used as a test bed for all nonlinear control strategies discussed herein. Then, a probability-based FPK formulation assuming a Gaussian white noise excitation will be used to find the optimal nonlinear control. Then, a Monte Carlo simulation approach is described, that should give an approximate solution similar to the FPK result. Finally, the optimal nonlinear control for the system without forcing but a non-zero initial condition will be described.

Consider a linear time-invariant system subjected to unknown disturbance vector \mathbf{w} and control signal vector \mathbf{u} ; for example, this may be cast in state-space as

$$\dot{\mathbf{q}} = \mathbf{A}\mathbf{q} + \mathbf{B}\mathbf{u} + \mathbf{E}\mathbf{w} \quad (24.1)$$

with initial condition $\mathbf{q}(0) = \mathbf{q}_0$. For structural systems, state vector \mathbf{q} will contain generalized displacements and velocities, whereas state matrix \mathbf{A} , control \mathbf{B} and excitation \mathbf{E} influence matrices depend on the usual structural system matrices, the force locations and orientations. Let $L_Q(t) = \mathbf{q}^T \mathbf{Q} \mathbf{q} + 2\mathbf{q}^T \mathbf{N} \mathbf{u} + \mathbf{u}^T \mathbf{R} \mathbf{u}$ denote a quadratic function of the states and control at some time t , with weighting matrices $\mathbf{Q} = \mathbf{Q}^T$, $\mathbf{R} = \mathbf{R}^T > 0$ and \mathbf{N} such that $[[\mathbf{Q} \ \mathbf{N}]^T \ [\mathbf{N}^T \ \mathbf{R}]^T] \geq 0$. Then, the control law that minimizes quadratic cost functions of the forms (depending on the nature of excitation \mathbf{w} and the initial condition \mathbf{q}_0)

$$J_Q = \int_0^\infty L_Q(t) dt \quad \text{or} \quad J_Q = \lim_{t_f \rightarrow \infty} \frac{1}{t_f} \int_0^{t_f} L_Q(t) dt \quad \text{or} \quad J_Q = \mathbb{E} [L_Q(t)] \quad (24.2)$$

are linear and can be designed using the `lqr` command in MATLAB®.

As quadratic cost functions do not capture the trade offs in control objectives for some problems, a cost function that is non-quadratic in the states (and/or control) can be useful. For example, Wu *et al.* [14] proposed non-quadratic cost

$$J = \frac{1}{2} \int_0^{t_f} [\mathbf{q}^T \mathbf{Q} \mathbf{q} (1 + \mathbf{q}^T \mathbf{P} \mathbf{q}) + \mathbf{u}^T \mathbf{R} \mathbf{u} + (\mathbf{q}^T \mathbf{P} \mathbf{q}) \mathbf{q}^T \mathbf{P} \mathbf{B} \mathbf{R}^{-1} \mathbf{B}^T \mathbf{P} \mathbf{q} (1 + \mathbf{q}^T \mathbf{P} \mathbf{q})] dt \quad (24.3)$$

where \mathbf{P} is the positive definite symmetric solution to the algebraic Riccati equation of the linear control

$$\mathbf{P} \mathbf{A} + \mathbf{A}^T \mathbf{P} - \mathbf{P} \mathbf{B} \mathbf{R}^{-1} \mathbf{B}^T \mathbf{P} + \mathbf{Q} = \mathbf{0} \quad (24.4)$$

Similarly, Agrawal and Yang [15] proposed cost function

$$J = \int_0^\infty [\mathbf{q}^T \mathbf{Q} \mathbf{q} + \mathbf{u}^T \mathbf{R} \mathbf{u} + (\mathbf{q}^T \mathbf{M}_2 \mathbf{q})(\mathbf{q}^T \mathbf{Q}_2 \mathbf{q}) + (\mathbf{q}^T \mathbf{M}_2 \mathbf{q})^2 \mathbf{q}^T \mathbf{M}_2 \mathbf{B} \mathbf{R}^{-1} \mathbf{B}^T \mathbf{M}_2 \mathbf{q}] dt \quad (24.5a)$$

$$\text{where } \mathbf{M}_2(\mathbf{A} - \mathbf{B} \mathbf{R}^{-1} \mathbf{B}^T \mathbf{P}) + (\mathbf{A} - \mathbf{B} \mathbf{R}^{-1} \mathbf{B}^T \mathbf{P})^T \mathbf{M}_2 + \mathbf{Q}_2 = \mathbf{0} \quad (24.5b)$$

where $\mathbf{M}_2 = \mathbf{M}_2^T > 0$; and matrix \mathbf{Q}_2 can be chosen arbitrarily. (It can be verified that costs (24.3) and (24.5) are identical for a specific choice of $\mathbf{Q}_2 = \mathbf{Q} + \mathbf{PBR}^{-1}\mathbf{B}^T\mathbf{P}$ which results in $\mathbf{M}_2 = \mathbf{P}$.) Although the proposed nonlinear control laws by Wu *et al.* [14] and Agrawal and Yang [15] are described here, their approaches are similar to what has been reported previously [9–12].

24.2.1 HJB-Based Methods and Test Bed Scalar System

It is well established that designing an optimal control strategy for a nonlinear system will lead to the HJB partial differential equation [7, 8], which can be expressed

$$\frac{\partial V}{\partial t} = -H\left(\mathbf{q}, \mathbf{u}_{\text{opt}}, \frac{\partial V}{\partial \mathbf{q}}, t\right) \quad (24.6)$$

in which V is the value function, $H = L + (\partial V/\partial \mathbf{q})\dot{\mathbf{q}}$ is the Hamiltonian function, and \mathbf{u}_{opt} is the optimal control found by solving $\partial H/\partial \mathbf{u} = \mathbf{0}$. However, finding the HJB analytical solution is very difficult unless the non-quadratic cost function is defined in a specific form. The cost functions in (24.3) and (24.5) have solutions, respectively,

$$\mathbf{u}_{\text{opt}}^{(24.3)} = -\mathbf{R}^{-1}\mathbf{B}^T\mathbf{P}\mathbf{q}(1 + \mathbf{q}^T\mathbf{P}\mathbf{q}) \quad (24.7a)$$

$$\mathbf{u}_{\text{opt}}^{(24.5)} = -\mathbf{R}^{-1}\mathbf{B}^T\mathbf{P}\mathbf{q} - \mathbf{R}^{-1}\mathbf{B}^T(\mathbf{q}^T\mathbf{M}_2\mathbf{q})\mathbf{M}_2\mathbf{q} \quad (24.7b)$$

Scalar System: A test bed structural system model must be chosen so that numerical comparisons can be made between the HJB-based approaches and others. As the FPK-based approach discussed in the next section can be analytically solved for a scalar system, the test bed system equation of motion is

$$\dot{x} = ax + bu + w \quad (24.8)$$

The form of the cost function of Agrawal and Yang [15] is used here in scalar form

$$J = \int_0^\infty [qx^2 + ru^2 + m_2q_2x^4 + m_2^4b^2r^{-1}x^6] dt \quad (24.9)$$

where q , r , m_2 and q_2 are the scalar forms of \mathbf{Q} , \mathbf{R} , \mathbf{M}_2 and \mathbf{Q}_2 , respectively, in (24.5a). Solving the corresponding HJB problem ignoring disturbance w , the optimal control is

$$u = -r^{-1}bp_x - r^{-1}bm_2^2x^3 \quad (24.10)$$

where $m_2 = q_2/2\sqrt{\hat{a}}$ and $\hat{a} = a^2 + qb^2r^{-1}$, with $p = r(a + \sqrt{\hat{a}})b^{-2}$ as the scalar form of \mathbf{P} .

Alternately, if the optimal control is assumed of the form $u = -k_1x - k_2x^3$, where k_1 and k_2 are control gains, one can rewrite cost (24.9), in a form that will be used in the subsequent sections to find optimal control laws with different excitation and/or initial condition assumptions, as

$$J = \int_0^\infty [(q + rk_1^2)x^2 + (m_2q_2 + 2rk_1k_2)x^4 + (m_2^4r^{-1}b^2 + rk_2^2)x^6] dt \quad (24.11)$$

24.2.2 Probability-Based Method (FPK Equation)

The Fokker-Planck-Kolmogorov (FPK) equation [18] is a partial differential equation in the transition probability density function of a dynamical system. Assume that the excitation w is a stationary zero-mean Gaussian white noise process with unit intensity (*i.e.*, $\mathbb{E}[w(t)w(t + \tau)] = \delta(\tau)$). The drift term in (24.8) is defined as $d(x) = ax + bu$. The interest here is in the stationary solution, so the time derivative terms of the FPK equation are set to zero, leaving

$$\frac{d}{dx} [2d(x)f(x)] = \frac{d^2}{dx^2} f(x) \quad (24.12)$$

where $f(x)$ is the stationary probability density function of x . With a cubic control law as previously discussed, the drift becomes $d(x) = -(-a + bk_1)x - bk_2x^3$. Substituting this form of the drift into (24.12) and solving for density function $f(x)$ gives

$$f(x) = \left\{ \exp \left[-\frac{(bk_1 - a)^2}{4bk_2} \right] \sqrt{\frac{2bk_2}{bk_1 - a}} \frac{1}{K_{1/4} \left(\frac{|bk_1 - a|^2}{4bk_2} \right)} \right\} \exp \left[(bk_1 - a)x^2 - \frac{bk_2x^4}{2} \right] \quad (24.13)$$

where $K_n(z)$ is the modified Bessel function of the second kind. The solution (24.13) for the density function can be used to compute the even-ordered moments

$$\mathbb{E}[x^n] = \int_{-\infty}^{\infty} x^n f(x) dx, \quad n = 2, 4, 6 \quad (24.14)$$

in cost function (24.9)

$$J = (q + rk_1^2)E[x^2] + (m_2q_2 + 2rk_1k_2)E[x^4] + (m_2^4\frac{b^2}{r} + rk_2^2)E[x^6] \quad (24.15)$$

The optimal control gains are then found by setting equal to zero the partial derivatives of J with respect to k_1 and k_2 .

24.2.3 Numerical Method (MC Simulation)

A numerical Monte Carlo simulation approach should be able to also find the optimal gains k_1 and k_2 through a parameter study. Using a discrete-time approximation of zero-mean unit-intensity Gaussian white noise — a Gaussian pulse process with variance $1/\Delta t$ for time step Δt — the cost (24.15) can be approximated using N realizations, simulated from quiescent initial conditions until the mean square statistics converge (here, mean square responses over $[0, t_f]$ are averaged over N realizations to approximate the statistics). A response surface, built from the parameter study, is then minimized to find optimal control gains.

24.2.4 Deterministic Method (Nonzero Initial Condition)

The HJB approach effectively ignores the excitation, so the optimal nonlinear control from HJB should be the same as the control that minimizes the same cost function as the system decays from non-zero initial conditions. With the cubic control law, the system equation of motion becomes

$$\dot{x} = ax + bu = -(bk_1 - a)x - bk_2x^3 \quad (24.16)$$

which can be solved analytically to find the response

$$x(t) = \sqrt{bk_1 - a} \left[-bk_2 + e^{2(bk_1 - a)t} \left(bk_2 + \frac{bk_1 - a}{x_0^2} \right) \right]^{-1/2} \quad (24.17)$$

where $x(0) = x_0$ is the non-zero initial condition. Even powers of free response (24.17) can be integrated analytically to compute cost (24.11). The result can be differentiated with respect to gains k_1 and k_2 to find their optimal values.

24.3 Numerical Example

In this section, a numerical example is presented, solving for the optimal control $u = -k_1x - k_2x^3$ of the scalar system with each of the four methods presented in the previous section. For the purposes of comparison, the values of the parameters are chosen to be those used by Agrawal and Yang [15]

$$a = -0.025, \quad b = 1, \quad r = 1, \quad q = 1.5 \quad \text{and} \quad q_2 = 1.5 \quad (24.18a)$$

$$\Rightarrow \hat{a} = 1.5006, \quad m_2 = 0.6122 \quad \text{and} \quad p = 1.2 \quad (24.18b)$$

Fig. 24.1 Cost function based on FPK equation

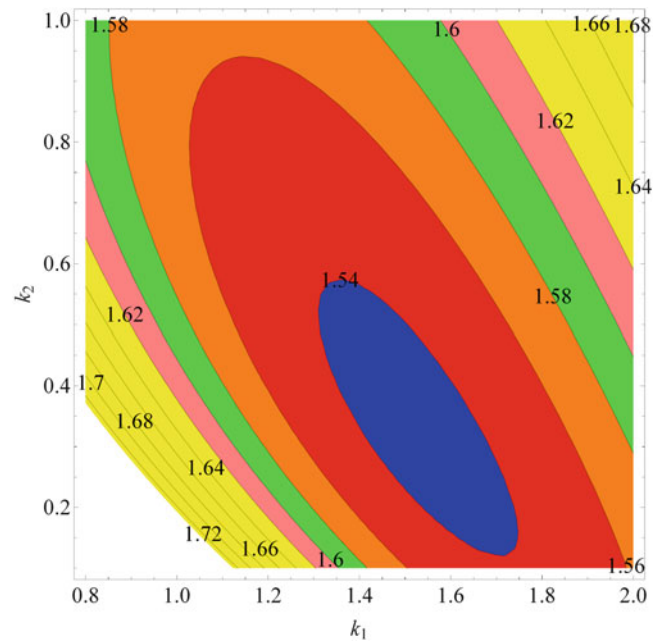
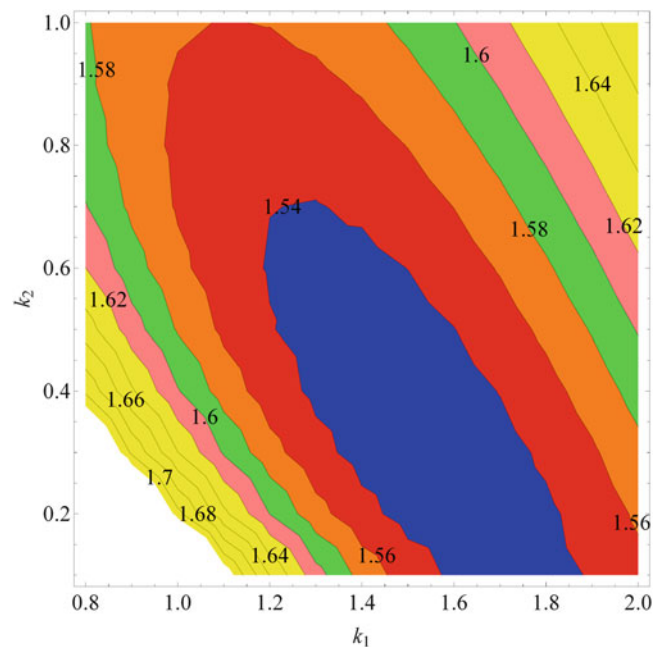


Fig. 24.2 Cost function based on MC simulation for white noise excitation



HJB: The HJB solution is found by simply substituting the parameters (24.18) into optimal control (24.10) to find $k_1^{\text{HJB}} = 1.2$ and $k_2^{\text{HJB}} = 0.3748$.

FPK: Using the parameter values, the control gains that minimize the expected cost (24.15) are $k_1^{\text{FPK}} = 1.52926$ and $k_2^{\text{FPK}} = 0.329258$. The cost surface, shown in Fig. 24.1 for the control gain ranges $[1.1, 1.8] \times [0.2, 1.5]$, is convex.

Monte Carlo: Simulations, using MATLAB's Simulink®, of 10000 realizations of the system over a time interval $[0, 50]$ s, with a time step equal to 0.01 s, are performed with the discrete-time approximation to Gaussian white noise for a grid of control gains $(k_1, k_2) \in \{0.8, 0.9, \dots, 2.0\} \times \{0.1, 0.2, \dots, 1.0\}$. The expected cost (24.15) is estimated from these realizations, as shown in Fig. 24.2. Minimizing the resulting response surface gives approximate optimal control gains $k_1^{\text{MCS}} = 1.53$ and $k_2^{\text{MCS}} = 0.317$.

Free response: Using free response (24.17) with the parameters (24.18), the cost of the free response can be computed as a function of the control gains. For initial condition $x_0 = 1$, and other initial conditions that are not large, the optimal control

Fig. 24.3 Cost function based on non-zero initial states

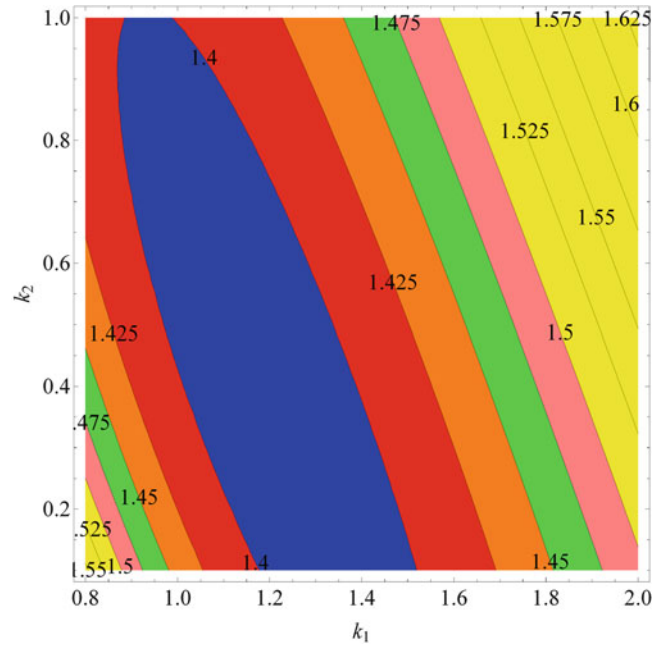


Table 24.1 Comparison of different nonlinear controls based on MCS and Free Response

	Optimal Gains		MCS statistics					Free Response
	k_1	k_2	max x	rms x	max u	rms u	J	J
HJB	1.2	0.3748	0.0753	0.0189	0.0905	0.0227	1.5690	1.38742
FPK	1.5293	0.3293	0.0692	0.0175	0.1059	0.0268	1.5419	1.41501
MCS	1.53	0.317	0.0693	0.0175	0.1062	0.0268	1.5419	1.41419
FR	1.2	0.3748	0.0753	0.0189	0.0905	0.0227	1.5690	1.38742

Table 24.2 Statistics with different nonlinear control laws with earthquake excitation

	Optimal Gains		1940 El Centro					1994 Northridge				
	k_1	k_2	max x	rms x	max u	rms u	J	max x	rms x	max u	rms u	J
HJB	1.2	0.3748	0.3212	0.0549	0.3979	0.0665	0.0090	0.2976	0.0809	0.3670	0.0979	0.0195
FPK	1.5293	0.3293	0.3116	0.0528	0.4864	0.0813	0.0109	0.2963	0.0782	0.4616	0.1203	0.0238
MCS	1.53	0.317	0.3116	0.0528	0.4863	0.0813	0.0109	0.2963	0.0782	0.4615	0.1203	0.0238
FR	1.2	0.3748	0.3212	0.0549	0.3979	0.0665	0.0090	0.2976	0.0809	0.3670	0.0979	0.0195

gains are $k_1^{FR} = 1.2$ and $k_2^{FR} = 0.3748$, the same as the HJB result. Cost surface (24.9) is shown in Fig. 24.3 for the case with $x_0 = 1$ over the control gain ranges $[0.8, 1.8] \times [0.2, 1.5]$.

24.3.1 Results Comparison

Different methods resulted in different optimal control laws. As expected, the HJB-derived optimal control law is exactly the same as the optimal nonlinear control for a system without excitation but non-zero initial condition. Also the optimal control laws for a Gaussian white noise excitation found by FPK and MCS methods are almost the same. But, the HJB-derived and FPK-derived controls are not identical.

To explore the comparison further, the system is simulated using each of the four “optimal” control laws for (a) a Monte Carlo simulation in Simulink (all simulation parameters as described previously for MCS except only 1000 realizations are used in these results), (b) a deterministic free response from a non-zero initial condition of $x_0 = 1$, (c) the response to the 1940 El Centro earthquake and (d) the response to the 1994 Northridge earthquake. Tables 24.1 and 24.2 show the results of this analysis.

Not surprisingly, the FPK/MCS optimal gains better reduce the cost computed from the Monte Carlo simulations with somewhat smaller response statistics and slightly larger control force, whereas the HJB / free response optimal control better reduce the cost of the free response. However, the difference in costs is not large, only on the order of 2–3%.

Table 24.2 shows the responses and costs when the excitation is the North-South component of the 1940 El Centro and of the 1994 Northridge earthquakes. These results show that HJB and free response derived control laws are able to reduce the cost function — better than MCS and FPK derived controls — by exerting smaller control force but larger system response than with the MCS and FPK derived controlled systems.

24.4 Conclusions

Different “optimal” control laws are obtained by different methods and are compared to each other. Interestingly, for the scalar problem investigated in this paper, the HJB-derived “optimal” control law, which is the same as the optimal nonlinear control for free response of a system without excitation but non-zero initial condition, is different from the optimal nonlinear control for a Gaussian white noise excitation found from FPK and MCS results. The certainty equivalence property clearly does not hold, likely because the system is non-Gaussian with a non-quadratic cost function.

It is not clear from this study whether the HJB optimal control or the FPK optimal control is more appropriate for seismically-excited structures. The difference here is relatively small — on the order of a few percent — but that may not be the case for other structure models or other control objectives. Obviously, the solutions for simple, but real, structure models must be studied, as well as more complex structure models, before general conclusions can be drawn.

References

1. Housner GW, Bergman LA, Caughey TK, Chassiakos AG, Claus RO, Masri SF, Skelton RE, Soong TT, Spencer BF Jr, Yao JTP (1997) Structural control: past, present, and future. *J Eng Mech* 123(9):897–971
2. Spencer BF Jr, Sain MK (1997) Controlling buildings: a new frontier in feedback. *IEEE Contr Syst Mag* 17(6):19–35
3. Symans MD, Constantinou MC (1999) Semi-active control systems for seismic protection of structures: a state-of-the-art review. *Eng Struct* 21(6):469–487
4. Soong TT, Spencer BF Jr (2002) Supplemental energy dissipation: state-of-the-art and state-of-the-practice. *Eng Struct* 24(3):243–259
5. Suhardjo J, Spencer BF Jr, Sain MK (1992) Non-linear optimal control of a Duffing system. *Int J Non-Lin Mech* 27(2):157–172
6. Yang J, Wu J, Agrawal A (1995) Sliding mode control for nonlinear and hysteretic structures. *J Eng Mech* 121(12):1330–1339
7. Bryson AE Jr, Ho YC (1975) *Applied optimal control*. Hemisphere Publication Corporation, Washington DC
8. Primbs JA, Nevistic V, Doyle JC (1999) Nonlinear optimal control: a control Lyapunov function and receding horizon perspective. *Int J Contr* 1(1):14–24
9. Rekasius ZV (1964) Suboptimal design of intentionally nonlinear controllers. *IEEE Trans Automat Contr* 9(4):380–386
10. Speyer JL (1976) A nonlinear control law for a stochastic infinite time problem. *IEEE Trans Automat Contr* AC-21(4):560–564
11. Bernstein DS (1993) Nonquadratic cost and nonlinear feedback control. *Int J Robust Nonlinear Contr* 3:211–229
12. Tomasula DP, Spencer BF Jr, Sain MK (1994) Limiting extreme structural responses using an efficient nonlinear control law. In: *Proceedings of the first World conference on structural control*, vol FP4, pp 22–31, University of Southern California, Los Angeles, CA, 1994
13. Wu Z, Gattulli V, Lin RC, Soong TT (1994) Implementable control laws for peak response reduction. In: *Proceedings of the first World conference on structural control*, vol TP2, pp 50–59, University of Southern California, Los Angeles, CA, 1994
14. Wu Z, Lin RC, Soong TT (1995) Non-linear feedback control for improved peak response reduction. *Smart Mater Struct* 4(1A):A140–A147
15. Agrawal AK, Yang JN (1996) Optimal polynomial control of seismically excited linear structures. *J Eng Mech* 122(8):753–761
16. Van de Water H, Willems J (1981) The certainty equivalence property in stochastic control theory. *IEEE Trans Automat Contr* 26(5):1080–1087
17. Chow GP (1976) *Analysis and control of dynamic economic systems*. Wiley, New York
18. Soong TT, Grigoriu M (1993) *Random vibration of mechanical and structural systems*. Prentice Hall, Englewood Cliffs

Chapter 25

Optimal Sensor Placement with a Statistical Criterion for Subspace-Based Damage Detection

Michael Döhler, Kenny Kwan, and Dionisio Bernal

Abstract Subspace-based fault detection algorithms have proven to be efficient for the detection of changes in the modal parameters for damage detection of vibrating structures. With these algorithms, a state-space model from the reference condition of a structure is confronted to output-only vibration data from a possibly damaged condition in a χ^2 test on a damage detection residual. The outcome of this test is compared to a threshold to decide if there is damage or not. In this paper, the problem of optimal sensor placement for this damage detection algorithm is considered based on the statistical properties of the χ^2 test. Using a model of the structure, sensor positions are chosen such that the non-centrality parameter of the χ^2 distribution is maximized for a certain set of damages. It is anticipated that this approach would, indirectly, lead to a maximization of the power of the test. The efficiency of the approach is shown in numerical simulations.

Keywords Damage detection • Subspace methods • Optimal sensor placement • Fisher information • Statistical power

25.1 Introduction

Optimal sensor placement is an important issue in the dynamic assessment of mechanical or civil structures in order to measure the most significant information for a specific objective. This subject has received considerable attention in the literature and solutions have been presented for different problems. Many works aim at optimal system identification performance, e.g. with the target of identifying mode shapes that are as linearly independent as possible, yielding maximal signal strength of the modal responses or maximizing the kinetic energy of the structural system [1, 2]. Closely related are entropy-based methods, where the sensor locations are chosen to minimize the uncertainty in the desired estimates or, equivalently, the information entropy [3]. A common methodology in these methods is to select the sensor layout that maximizes the Fisher information of a desired quantity in the measured data, where usually strong simplifications of the statistical properties are made. Other methods optimize e.g. observability or controllability measures [4, 5]. An overview of some of these methods with applications can be found in [6–8].

In this work, the optimal sensor placement for a subspace-based damage detection algorithm [9–12] is considered. With this algorithm, parameters from the (healthy) reference state of a structure are confronted to output-only vibration data from a state that is tested to be healthy or damaged. In the tested state no system identification step is necessary, but instead the measured data is processed directly. A comparison of the measured data to the reference parameters is performed using a χ^2 test, which is compared to a threshold. The criterion for optimal sensor placement is the optimal detectability of damages, which corresponds to the selection of a sensor layout that maximizes the power of the damage detection test (defined as the

M. Döhler

BAM Federal Institute for Materials Research and Testing, Safety of Structures Department, 12200 Berlin, Germany

e-mail: michael.doehler@bam.de

K. Kwan • D. Bernal

Department of Civil and Environmental Engineering, Center for Digital Signal Processing, Northeastern University,

360 Huntington Avenue, Boston, MA, 02115 USA

e-mail: k.kwanyang@neu.edu; d.bernal@neu.edu

probability of detecting damage when it is present). Based on the strategy in [13], an algorithm is developed for the selection of an optimal sensor placement for a fixed number of sensors. Also, a strategy is proposed to validate the obtained results.

This paper is organized as follows. In Sect. 25.2, the subspace-based damage detection test is recalled. In Sect. 25.3, the strategy for an optimal sensor placement is developed and results on a numerical simulation are shown in Sect. 25.4.

25.2 Subspace-Based Damage Detection

25.2.1 Models and Parameters

The use of the state-space representation for output-only vibration-based structural monitoring is well-established, which corresponds to monitoring the eigenstructure of the discrete time model

$$\begin{aligned} x_{k+1} &= Ax_k + v_k \\ y_k &= Cx_k + w_k \end{aligned} \quad (25.1)$$

with the states $x_k \in \mathbb{R}^n$, the measured outputs $y_k \in \mathbb{R}^r$, the state transition matrix $A \in \mathbb{R}^{n \times n}$ and the observation matrix $C \in \mathbb{R}^{r \times n}$, where r is the number of sensors and n is the system order. The excitation v_k is an unmeasured Gaussian white noise sequence and w_k is the measurement noise.

The collection of eigenvalues and mode shapes (λ, φ) comprising the eigenstructure of system (25.1) results from

$$\det(A - \lambda_i I) = 0, \quad A\phi_i = \lambda_i \phi_i, \quad \varphi_i = C\phi_i,$$

where λ_i and ϕ_i are the eigenvalues and eigenvectors of A , and φ_i are the corresponding mode shapes. The eigenstructure (λ, φ) is a canonical parameterization of system (25.1) and considered as the system parameter $\theta = \vartheta$ with

$$\vartheta = \begin{bmatrix} \Lambda \\ \text{vec}(\Phi) \end{bmatrix}, \quad (25.2)$$

where $\Lambda = [\lambda_1 \dots \lambda_n]^T$ is the vector containing all eigenvalues, $\Phi = [\varphi_1 \dots \varphi_n]$ is the matrix whose columns are the mode shapes and vec denotes the vectorization operator.

25.2.2 The Subspace-Based Damage Detection Algorithm

In [9, 10] a residual function was proposed to detect changes in the eigenstructure θ from the measurements y_k without actually identifying the eigenstructure in the possibly damaged state. The considered residual is associated with a covariance-driven output-only subspace identification algorithm. Let $R_i = \mathbf{E}(y_k y_{k-i}^T)$ be the theoretic output covariances and

$$\mathcal{H}_{p+1,q} = \begin{bmatrix} R_1 & R_2 & \dots & R_q \\ R_2 & R_3 & \dots & R_{q+1} \\ \vdots & \vdots & \ddots & \vdots \\ R_{p+1} & R_{p+2} & \dots & R_{p+q} \end{bmatrix} = \text{Hank}(R_i)$$

be the theoretic block Hankel matrix. It possesses the well-known factorization property $\mathcal{H}_{p+1,q} = \mathcal{O}_{p+1} \mathcal{C}_q$ with observability matrix

$$\mathcal{O}_{p+1} = \begin{bmatrix} C \\ CA \\ \vdots \\ CA^p \end{bmatrix}$$

and controllability matrix \mathcal{C}_q . Denote the system parameter in a (healthy) reference state as θ_0 and in the tested state of the system as θ . The residual function for a damage detection test from [9, 10] compares the system parameter θ_0 to data measured from the system corresponding to θ , while the parameter θ itself is not identified. In the reference state,

the observability matrix $\mathcal{O}_{p+1}(\theta_0)$ is obtained in the modal basis ($C = \Phi$, $A = \Lambda$) and its left null space $S(\theta_0)$ is computed, e.g. by a singular value decomposition of $\mathcal{O}_{p+1}(\theta_0)$, such that

$$S(\theta_0)^T \mathcal{O}_{p+1}(\theta_0) = 0 \text{ and thus } S(\theta_0)^T \mathcal{H}_{p+1,q} = 0$$

in the reference condition. Using measured data $(y_k)_{k=1,\dots,N}$, a consistent estimate $\hat{\mathcal{H}}_{p+1,q} = \text{Hank}(\hat{R}_i)$ is obtained from the empirical output covariances $\hat{R}_i = \frac{1}{N} \sum_{k=1}^N y_k y_{k-i}^T$. To decide whether the measured data correspond to θ_0 or not, the residual vector ζ_N with

$$\zeta_N = \sqrt{N} \text{vec} \left(S(\theta_0)^T \hat{\mathcal{H}}_{p+1,q} \right) \quad (25.3)$$

is defined. It is tested if this residual function is significantly different from zero or not, corresponding to a test between the hypotheses [9]

$$\begin{aligned} \mathbf{H}_0 : \theta &= \theta_0 && \text{(reference system),} \\ \mathbf{H}_1 : \theta &= \theta_0 + \delta\theta/\sqrt{N} && \text{(damaged system),} \end{aligned}$$

where $\delta\theta$ is unknown but fixed. With this statistical framework, very small changes in the parameter θ can be detected if the number of data samples N is large enough. The residual function is asymptotically normal distributed [9]. Let \mathcal{J} be its asymptotic sensitivity w.r.t. θ_0 and Σ its asymptotic covariance with consistent estimates $\hat{\mathcal{J}}$ and $\hat{\Sigma}$, respectively, which are described in detail in [11, 12]. A decision between the hypotheses \mathbf{H}_0 and \mathbf{H}_1 is achieved through a generalized likelihood ratio (GLR) test, amounting to

$$\chi_N^2 = \zeta_N^T \hat{\Sigma}^{-1} \hat{\mathcal{J}} \left(\hat{\mathcal{J}}^T \hat{\Sigma}^{-1} \hat{\mathcal{J}} \right)^{-1} \hat{\mathcal{J}}^T \hat{\Sigma}^{-1} \zeta_N, \quad (25.4)$$

which is compared to a threshold that is set up in the reference condition for a desired type I error. The test variable χ_N^2 is asymptotically χ^2 -distributed with $\text{rank}(\mathcal{J})$ degrees of freedom and non-centrality parameter $\gamma = \delta\theta^T F \delta\theta$, where

$$F = \mathcal{J}^T \Sigma^{-1} \mathcal{J} \quad (25.5)$$

is the asymptotic Fisher information on θ_0 contained in ζ_N .

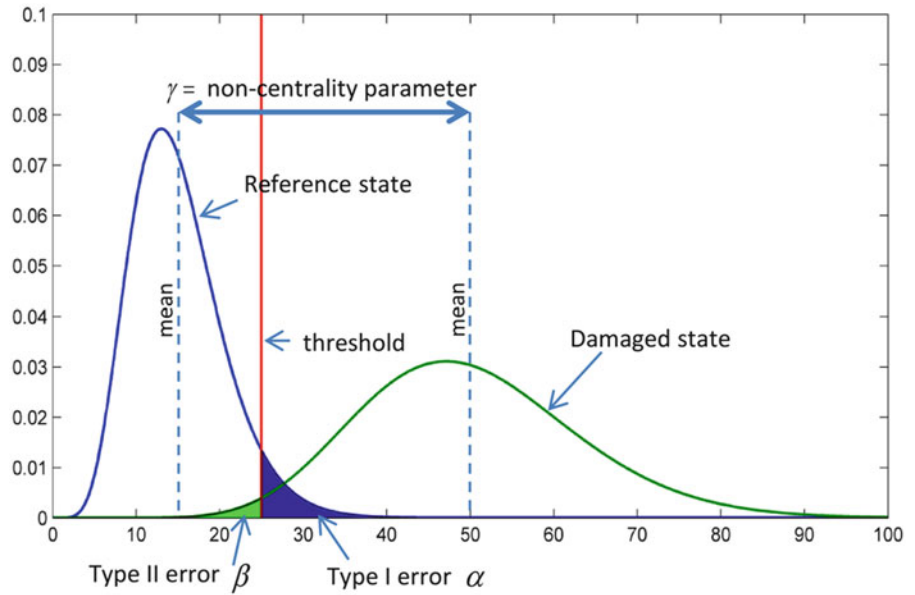
25.2.3 Power of the Test

The quality of the damage detection test is determined by the ‘‘power of the test’’ π , which is the probability that the test classifies data from the damaged system correctly as damaged for a given type I error α , e.g. $\alpha = 5\%$. The power of the test is the complement of the resulting type II error β , i.e. $\pi = 1 - \beta$. It is high when the overlap between the distribution of the reference state and the damaged state is low. The overlap of both distributions for a particular damage is determined by the non-centrality parameter $\gamma = \delta\theta^T F \delta\theta$ and the objective of an optimal sensor placement for the considered damage detection method is to maximize γ . Both distributions with the type I and type II errors are illustrated in Fig. 25.1.

25.3 Optimal Sensor Placement for Subspace-Based Damage Detection

The objective for optimal sensor placement is to optimize the damage detection performance with the described subspace-based algorithm. Thus, the criterion for an optimal sensor placement is the optimal detectability of damages, corresponding to the selection of a sensor layout that maximizes the power of the test and thus the non-centrality parameter γ for a certain set of damages. All necessary computations involve a model of the investigated structure only from the reference state.

Fig. 25.1 χ^2 distributions in reference and damaged states for 15 degrees of freedom, $\gamma = 35$ in the damaged state and $\alpha = 5\%$



25.3.1 Maximization of Non-Centrality Parameter and Impact of Parameterization

The non-centrality parameter γ depends on the particular change $\delta\theta$ of the system parameter vector θ . While θ was chosen as the collection of eigenvalues and mode shapes of the system (25.1) in (25.2), it can be basically any kind of parameter vector with a relation $\theta = \theta_0$ in the reference state and $\theta \neq \theta_0$ in the damaged state. Let the dimension of the parameterization be m , i.e. $\delta\theta \in \mathbb{R}^m$. Then, as shown in [13], for changes $\delta\theta$ of constant norm it holds that

$$\int_{\|\delta\theta\|=1} \gamma \, d(\delta\theta) = \int_{\|\delta\theta\|=1} \delta\theta^T F \delta\theta \, d(\delta\theta) = \frac{c_m}{m} \text{tr}(F) \quad (25.6)$$

where c_m is area of the unit sphere in \mathbb{R}^m and $\text{tr}(\cdot)$ denotes the trace of a matrix (sum of the entries on its diagonal). Thus, the mean value of the non-centrality parameter γ for changes in the system parameter vector of unit norm is proportional to $\text{tr}(F)$. Note that as γ is averaged for all unit parameter changes in (25.6), the parameterization θ needs to be chosen such that unit changes in each of its elements have the same importance for the objective of damage detection. For example, assume that $\theta = [\theta^1 \theta^2]$ consists of two parameters, where θ^1 is big and θ^2 is small. Then, a unit change in θ^1 is smaller than a unit change in θ^2 in relative terms, and by maximizing $\text{tr}(F)$ it is implied that a small change in θ^1 and a big change in θ^2 have the same importance for damage detection.

Two comments about the particular choice of the parameterization are in order. First, the selection of $\text{tr}(F)$ as an optimality criterion implies, due to (25.6), that the parameterization θ must be independent of the sensor locations—otherwise different placements would not be comparable by $\text{tr}(F)$ in (25.6). For example, if mode shapes are used as parameters then θ would be changing from one position to the next making the comparison with $\text{tr}(F)$ impossible. In [13] the eigenvectors and the eigenvalues of the discrete-time state space system were suggested as one possible parameterization, but in this case the issue was avoided because all the DOF were measured. The system matrix A was also considered as a possible parameterization in [13]. Second, while the choice of the parameterization does not change the non-centrality parameter, the unit norm optimization is such that the relative magnitude of the entries in the parameter vector determines their relative importance. The invariance of the non-centrality parameter can be seen to hold by noting that if $\theta = \tilde{\mathcal{J}}\tilde{\theta}$, with the asymptotic Fisher information of $\tilde{\theta}$ contained in the residual function as $\tilde{F} = \tilde{\mathcal{J}}^T \mathcal{J}^T \Sigma^{-1} \mathcal{J} \tilde{\mathcal{J}}$, the non-centrality parameter is

$$\tilde{\gamma} = \delta\tilde{\theta}^T \tilde{F} \delta\tilde{\theta} = \delta\tilde{\theta}^T \tilde{\mathcal{J}}^T \mathcal{J}^T \Sigma^{-1} \mathcal{J} \tilde{\mathcal{J}} \delta\tilde{\theta} = \delta\theta^T \mathcal{J}^T \Sigma^{-1} \mathcal{J} \delta\theta = \gamma$$

25.3.2 Choice of Parameterization and Computation of F

Damage is a change on the physical stiffness parameters. We choose them directly to define the parameter vector, namely, $\theta = \{p_1, \dots, p_L\}$. Then, the sensitivity matrix \mathcal{J} with respect to these parameters for computing F in (25.5) is given by

$$\mathcal{J} = \mathcal{J}_{\zeta, \vartheta} \mathcal{J}_{\vartheta, \mu} \mathcal{J}_{\mu, \theta} \quad (25.7)$$

where ϑ is the collection of eigenvalues and mode shapes of the discrete-time system and μ is the collection of eigenvalues and mode shapes of the continuous-time system. In (25.7) one has

- $\mathcal{J}_{\zeta, \vartheta}$ = sensitivity of the expectation of the residual function with respect to poles and mode shapes of the discrete-time system. It is derived in detail in [9, 10, 12] and it holds

$$\mathcal{J}_{\zeta, \vartheta} = \left(\mathcal{O}_{p+1}(\theta_0)^\dagger \mathcal{H}_{p+1, q} \otimes S(\theta_0) \right)^T \mathcal{J}_{\mathcal{O}, \vartheta} \quad (25.8)$$

where $\mathcal{J}_{\mathcal{O}, \vartheta}$ is the derivative of the vectorized parametric observability matrix with respect to ϑ , and † denotes the pseudoinverse. Formulae for $\mathcal{J}_{\mathcal{O}, \vartheta}$ are given in [10, 12],

- $\mathcal{J}_{\vartheta, \mu}$ = sensitivity of the poles of the discrete-time system with respect to the poles of the continuous-time system [10],
- $\mathcal{J}_{\mu, \theta}$ = sensitivity of the poles and eigenvectors of the continuous-time system with respect to the structural parameters [10, 14, 15].

The covariance matrix Σ in (25.5) of the residual function ζ_N from (25.3) can be obtained as

$$\Sigma = (I \otimes S(\theta_0)^T) \Sigma_{\mathcal{H}} (I \otimes S(\theta_0)) \quad (25.9)$$

where $\Sigma_{\mathcal{H}}$ is the covariance of the vectorized Hankel matrix. An efficient computation is described in detail in [11, 12]. Note that for the optimal sensor placement task, all quantities in this section are computed using a model, i.e. ϑ , $\mathcal{O}_{p+1}(\theta_0)$, $S(\theta_0)$, $\mathcal{J}_{\mathcal{O}, \vartheta}$, $\mathcal{J}_{\vartheta, \mu}$ and $\mathcal{J}_{\mu, \theta}$ are directly obtained using a model, and $\mathcal{H}_{p+1, q}$ and Σ are obtained using output data that is generated from the model.

25.3.3 Finding the Optimal Sensor Layouts

In order to find the desired sensor layout(s) that maximize our criterion (25.6) for optimal sensor placement, $\text{tr}(F)$ is computed and compared for all the considered sensor layouts, where we assume that the number of sensors is constant. The computation of $\text{tr}(F)$ for all these sensor layouts has to be handled with care, otherwise the computational burden becomes infeasible.

Combining (25.7) and (25.8) yields

$$\mathcal{J} = \left(\mathcal{O}_{p+1}(\theta_0)^\dagger \mathcal{H}_{p+1, q} \otimes S(\theta_0) \right)^T \mathcal{J}_{\mathcal{O}, \vartheta} \mathcal{J}_{\vartheta, \mu} \mathcal{J}_{\mu, \theta} \quad (25.10)$$

The following procedure for the computation of $\text{tr}(F)$ of each sensor layout is suggested:

1. Compute $\mathcal{H}_{p+1, q}$, $\mathcal{O}_{p+1}(\theta_0)$ and the product $\mathcal{J}_{\mathcal{O}, \theta} = \mathcal{J}_{\mathcal{O}, \vartheta} \mathcal{J}_{\vartheta, \mu} \mathcal{J}_{\mu, \theta}$ in (25.10) at all DOFs
2. Compute $\Sigma_{\mathcal{H}}^{1/2}$ (such that $\Sigma_{\mathcal{H}} = \Sigma_{\mathcal{H}}^{1/2} (\Sigma_{\mathcal{H}}^{1/2})^T$) at all DOFs with an efficient procedure as suggested in [11, 12]
3. For each sensor layout:
 - a. Select the rows of $\mathcal{O}_{p+1}(\theta_0)$, $\mathcal{J}_{\mathcal{O}, \theta}$ and $\Sigma_{\mathcal{H}}^{1/2}$, and the rows and columns of $\mathcal{H}_{p+1, q}$ that correspond to the DOFs at the sensor positions
 - b. Compute the null space of the observability matrix at the sensor positions
 - c. Compute F using the selected matrices from (25.5), (25.9) and (25.10)
 - d. Store $\text{tr}(F)$ for the current layout
4. Compare values of $\text{tr}(F)$ for different sensor layouts and select layouts with highest values

The pseudoinverse of the observability matrix is needed in the sensitivity computation of (25.10). From a numerical point of view this computation becomes infeasible if the observability matrix is badly conditioned. Furthermore, a badly conditioned observability matrix indicates that some modes of the system are close to being unobservable. Thus, sensor configurations with a badly conditioned observability matrix can be dismissed a priori.

25.3.4 Validation

To validate the effectiveness of the sensor placement criterion of the previous sections, we evaluate the average power of the test for a set of damages. While the optimization criterion (25.6) actually aims at maximizing the average non-centrality parameter, we use the average power of the test as an indicator of the damage detection performance. Of course, a high non-centrality parameter leads to a high power of the test, but while the maximal power of the test is 100%, the non-centrality parameter does not have an upper bound and could falsify the performance evaluation if its values are extremely high for very few damages. Still, there is a high correlation between the non-centrality parameter and the power of the test, which is exploited for finding an optimal sensor placement with the presented strategy. Note that this validation, by obtaining the average power of the test from simulations, is only possible for small sized problems (few DOFs, few sensors) as it is a computationally expensive task. For each sensor layout, the average power of the test can be determined as follows.

The empirical distribution of the test variable χ_N^2 in (25.4) in the reference state is first obtained from a Monte Carlo simulation where several data sets are simulated using white noise excitation. Like this, a threshold for a given type I error, e.g. 5% (see Fig. 25.1), can be determined. Then, the empirical distributions of the test variable are determined for all desired damaged states, in which the change in the structural parameter is a constant value. In each of these damaged states, a Monte Carlo simulation of several data sets is performed again and the percentage of the cases in which the test variable χ_N^2 is above the threshold is determined. This percentage is the power of the test for a specific damage. Finally, the average of the power of the test for all damages is computed, which is a quality criterion of the considered sensor layout for damage detection. This criterion is used for validating the optimal sensor placement.

25.4 Numerical Example

A mass spring chain system with 15 DOF (see Fig. 25.2) is used for a numerical simulation. All springs have equal stiffness of $k = 100$ and the mass of the elements is $m = [1 \ 2 \ 3 \ 1 \ 3 \ 1 \ 2 \ 1 \ 2 \ 1 \ 2 \ 1 \ 2 \ 1 \ 3]$. Classical damping is assigned such that each mode has a damping ratio of 2%. We assume that 3 sensors are available, which leads to $15! / ((15 - 3)! \cdot 3!) = 455$ possible sensor layouts. All sensor layouts are numbered consecutively, with the layout #1 as $\{1,2,3\}$, then $\{1,2,4\}$, \dots , $\{1,2,15\}$, $\{1,3,4\}$, $\{1,3,5\}$, \dots until $\{13,14,15\}$ which has number #455.

Using the described model, the parameter ϑ containing the eigenvalues of the corresponding discrete time system (time step 0.1) and the mass-normalized eigenvectors at all DOFs is obtained. From ϑ the matrices in steps 1 and 2 in Sect 25.3.3 are computed at all DOFs. For each of the sensor layouts, the respective entries in these matrices are chosen.

25.4.1 Performance of the Damage Detection Test

To evaluate the real performance of the damage detection test for the different sensor layouts, 200 Monte Carlo simulations of the system were made in the reference state and in each damaged states for each sensor layout, where damages were simulated by decreasing the stiffness in a spring by 10%. All possible damage scenarios were considered, i.e. damage

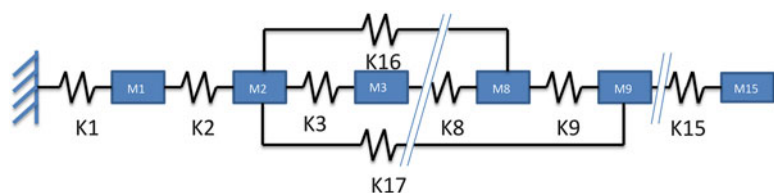


Fig. 25.2 Considered mass-spring chain system

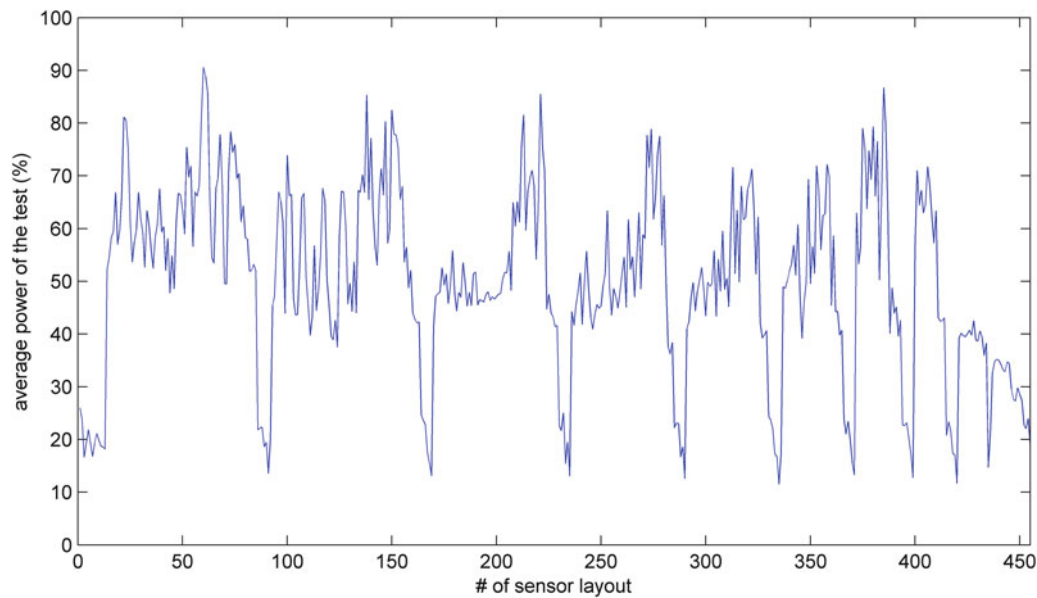


Fig. 25.3 Average power of the test for all sensor layouts considering damage in all springs (one at a time), using Monte Carlo simulations

was introduced in each of the springs one at a time. For each simulation, 30,000 data samples were generated from white noise excitation with 5% added output noise. As described in Sect. 25.3.4, a threshold was obtained from the χ^2 values of the reference state allowing a 5% type I error, and by comparing the χ^2 values from all possible damaged states to the threshold the average power of the test for each of the sensor layouts was determined. This validation procedure is a heavy computational burden, as in this case 200 Monte Carlo simulations were made in the reference state as well as in each of the damaged states, amounting to 3600 simulations for each of the 455 sensor layouts. The average power of the test for each sensor layout is shown in Fig. 25.3. It should be noted that the presented results are subject to statistical variability as they come from simulations themselves.

It can be seen that there are some sensor layouts that yield a very poor detection performance, such as layouts #1–#13, where the sensors positions are {1,2,3}, ..., {1,2,15} or layouts #86–#92 with sensors at {1,12,13}, ..., {1,14,15} and {2,3,4}. On the other side, most sensor layouts yield a good detection performance with the majority having an average power of the test between 60–80%. Few exceed 80%, e.g. layouts #60–#62 at positions {1,7,12}, {1,7,13} and {1,7,14}, layout #138 at positions {2,7,12}, layout #221 at {3,10,11} or layout #385 at {7,10,11}.

As the computation of the test values in Fig. 25.3 uses the pseudo-inversion of the observability matrix, the results are only meaningful for well-conditioned matrices. The condition number of the observability matrix of each sensor layout is computed and shown in Fig. 25.4. It can be seen that some sensor layouts with numbers higher than #430 exceed the condition number of 10^9 . The poorly conditioned observability matrix leads to an unstable computation of the sensitivity and the Fisher information, hence these layouts cannot be used for damage detection. Note that these sensor layouts yield a poor power of the test in Fig. 25.3, coinciding with a high condition number of the observability matrix in Fig. 25.4. The corresponding sensor positions are {9,12,13}, ..., {13,14,15}.

25.4.2 Optimal Sensor Placement with Fisher Information for all Possible Damages

With the procedure described in Sect. 25.3.3 the Fisher information estimate F using 100,000 generated data samples is computed for all sensor placements and its trace is shown in Fig. 25.5. It can be seen that the high values of the trace for the layout numbers #430 and above coincide with a high condition number of the observability matrix of 10^9 and above as shown in Fig. 25.4. These high values are due to numerical errors and are therefore discarded.

Also, in Fig. 25.5 it can be seen that the lowest values of $\text{tr}(F)$ correspond to sensor layouts with poor damage detection performance, such as layouts #1–#13, #92 and all the other layouts that can be seen as clear minima in Fig. 25.3.

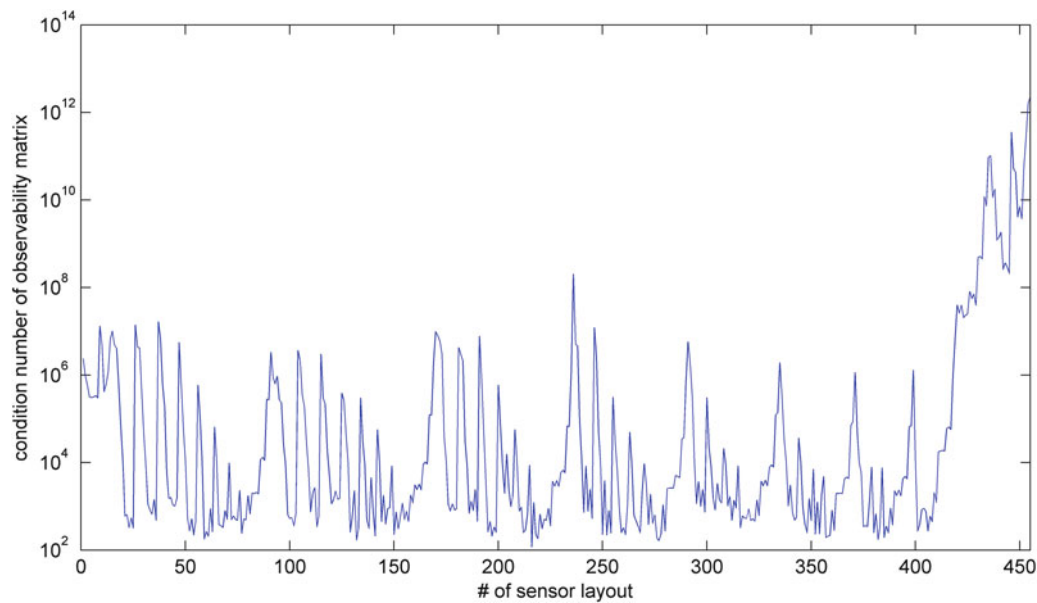


Fig. 25.4 Condition number of observability matrix in modal basis containing mass-normalized mode shapes for all sensor layouts

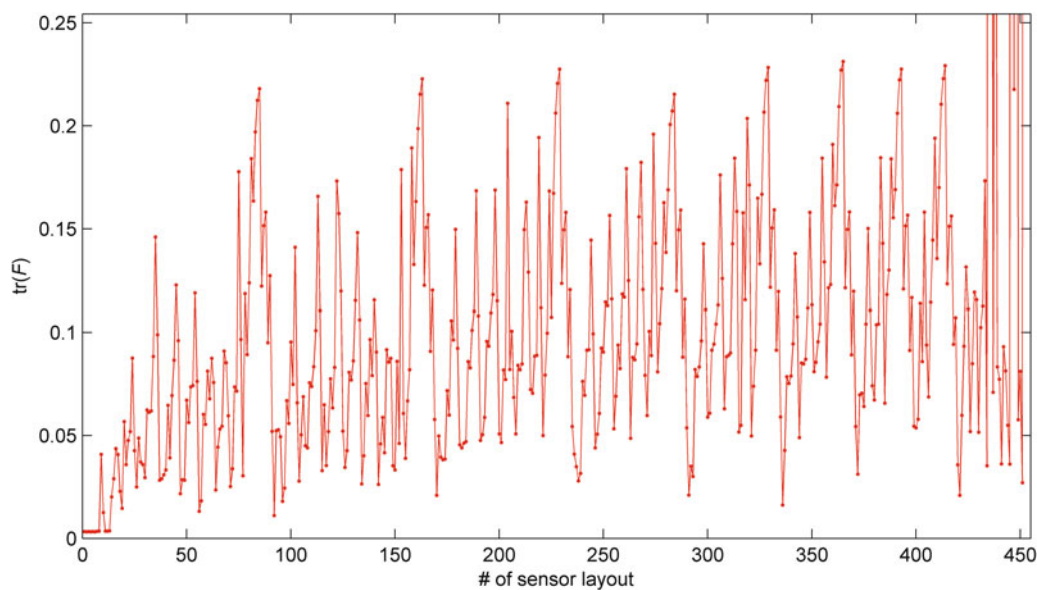


Fig. 25.5 Trace of the Fisher information for all sensor layouts considering all stiffness parameters equally

However, there is no clear link between the layouts with the highest trace and the best detection performance. This may be in part due to statistical variability in the data, but mostly due to the fact that the optimal sensor placement criterion using $\text{tr}(F)$ is not exactly the same that is used for the validation: While in Fig. 25.3 the average power of the test is shown, the trace of the Fisher matrix is shown in Fig. 25.5, which is a surrogate for the “average” non-centrality parameter (see Eq. 25.6). Also, the average power of the test is only obtained from few parameter changes of constant norm $\|\delta\theta\|$, namely for a unit change in each of the stiffness parameters one by one, while the integration in (25.6) is done for all parameter changes of constant norm $\|\delta\theta\|$ leading to $\text{tr}(F)$. It may also be possible that the maximization process for *all* possible parameter changes is not well-conditioned enough for only 3 sensors – good sensor layouts for some damages may always be too poor for other damages and vice versa.

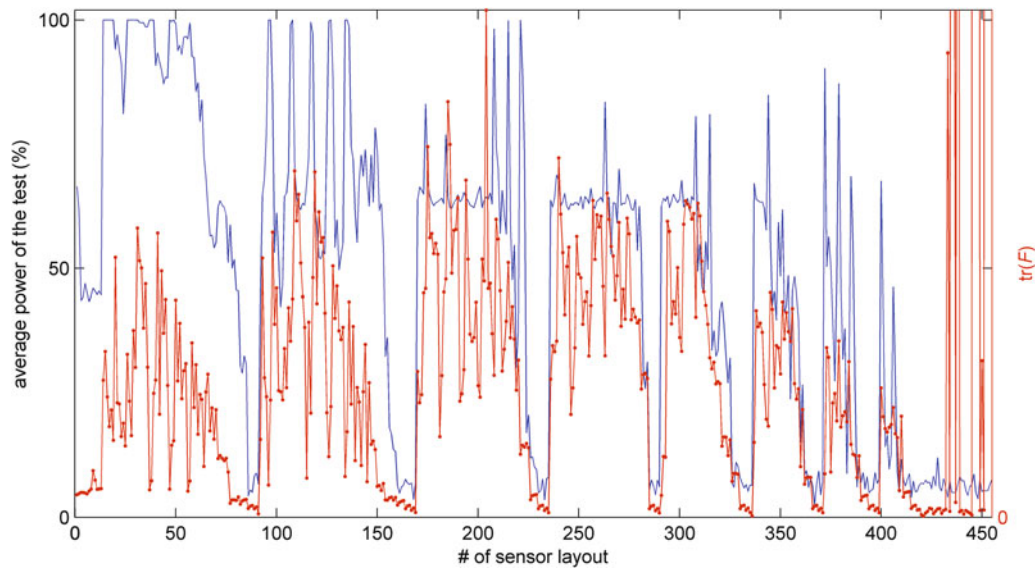


Fig. 25.6 Power of the test (*line with out dots*) and trace of the Fisher information (*line with dots*) for all sensor layouts for the detection of damages in springs K1–K5

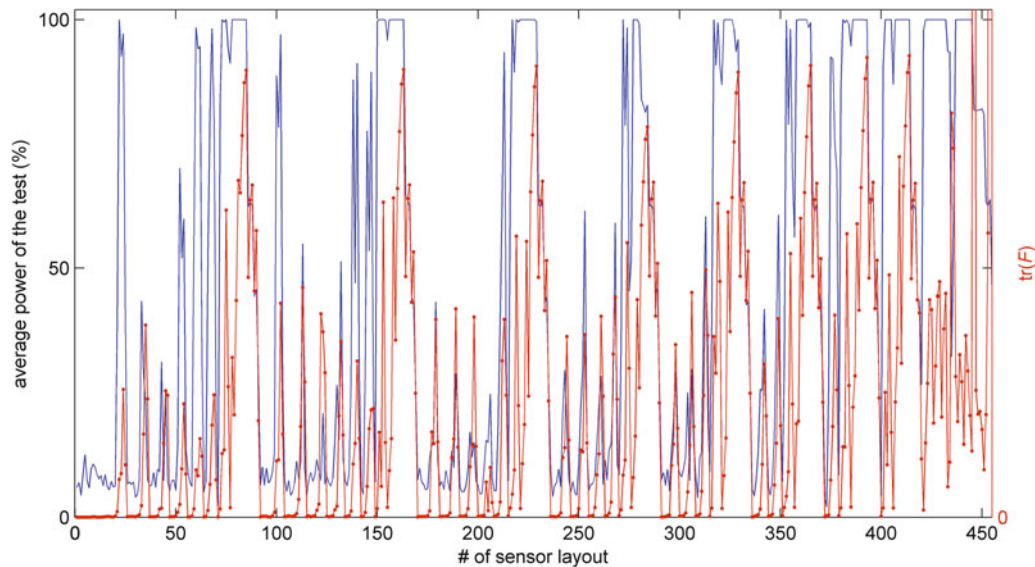


Fig. 25.7 Power of the test (*line without dots*) and trace of the Fisher information (*line with dots*) for all sensor layouts for the detection of damages in springs K11–K15

25.4.3 Optimal Sensor Placement with Fisher Information for Subsets of Damages

As pointed out in Sect. 25.3.1, a weighting of the structural parameters can be done easily in order to give more importance to changes in some of the parameters. Then, maximizing $\text{tr}(F)$ corresponds to finding the sensor placements where the damage detection algorithm is more sensitive to changes in parameters with a high weighting than in parameters with a low weighting. Like this, hotspots are monitored more precisely while the parameters with a low weighting are still taken into account.

We consider two cases, first the detection of damages in springs K1–K5, and second the detection of damages in springs K11–K15 (cf. Fig. 25.2). These parameters are multiplied by factor 10 in the computation of the Fisher information. The trace of the Fisher information is then an indicator of the damage detection performance in the mentioned springs, which is to be compared to the average power of the test for the damages in these springs. In Figs. 25.6 and 25.7 both the average power of test (blue line) and $\text{tr}(F)$ (red line with dots) are shown for both cases. It can be seen that there is a strong correlation between

the average power of the test and $\text{tr}(F)$, in contrast to taking all parameters equally into account in the previous section. All layouts with a low power of the test have also a low Fisher information, and layouts with a high Fisher information point in the direction of a high power of the test, although the correlation is not perfect. Still, in Fig. 25.7 the layouts with the 14 highest values of $\text{tr}(F)$ have all 100% or nearly 100% average power of the test. From both examples it can be seen that choosing a peak of $\text{tr}(F)$ for an optimal sensor placements yields a reasonably good power of the test.

25.5 Conclusions

In this paper the optimal sensor placement for subspace based damage detection has been investigated. The average power of the test for a set of damages was selected as the criterion indicating the quality of a placement. Based on Monte–Carlo simulations it was found that there are few sensor placements with a poor performance in a mass-spring chain example, while most of them gave satisfactory results. It was also found that some placements led to a large condition number of the observability matrix, making the computation of the damage detection test infeasible in this case, and it was shown that these placements can be discarded.

An approach for optimal sensor placement based on the framework in [13] was derived, which is aimed at maximizing the non-centrality parameter of the test by maximizing the trace of the Fisher information matrix of the structural parameters contained in the damage detection residual. The intrinsic statistical properties of the damage detection test are taken into account when obtaining the optimal placement. Using a model of the considered structure and output data generated with this model, the optimal placement is computed for a fixed number of sensors and desired structural parameters, whose changes one wants to detect with the damage detection routine. By giving a weighting to these parameters, the user can decide the importance of the parameters, e.g. in order to monitor hotspots more precisely. The presented method was applied on a 15 DOF model using 3 sensors. While the method was shown to rule out poor placements, finding the optimal placement proved to be difficult if optimization was done for finding changes in all structural parameters. This may be an indication that the number of sensors used in the optimization was not sufficient. However, a strong correlation between the optimization criterion (the trace of the Fisher information) and the actual performance of the damage detection test was visible when obtaining optimal placements for finding damages in a more restricted area of the structure. Future work contains a deeper investigation of the statistical properties of the optimization criterion and the comparison of sensor layouts with different numbers of sensors.

Acknowledgements The support from the NSF under the Hazard Mitigation and Structural Engineering Program Grant 1000391 is gratefully acknowledged.

References

1. Kammer DC (1991) Sensor placement for on-orbit modal identification and correlation of large space structures. *J Guid Contr Dyn* 14(2): 251–259
2. Heo G, Wang ML, Satpathi D (1997) Optimal transducer placement for health monitoring of long span bridge. *Soil Dyn Earthquake Eng* 16(7–8):495–502
3. Papadimitriou C (2004) Optimal sensor placement methodology for parametric identification of structural systems. *J Sound Vib* 278(4–5): 923–947
4. Gawronski W, Lim KB (1996) Balanced actuator and sensor placement for flexible structures. *Int J Contr* 65(1):131–145
5. van de Wal M, de Jager B (2001) A review of methods for input/output selection. *Automatica* 37(4):487–510
6. Meo M, Zumpano G (2005) On the optimal sensor placement techniques for a bridge structure. *Eng Struct* 27(10):1488–1497
7. Marano GC, Monti G, Quaranta G (2011) Comparison of different optimum criteria for sensor placement in lattice towers. *Struct Design Tall Special Build* 20(8):1048–1056
8. Debnath N, Dutta A, Deb SK (2012) Placement of sensors in operational modal analysis for truss bridges. *Mech Syst Signal Process* 31: 196–216
9. Basseville M, Abdelghani M, Benveniste A (2000) Subspace-based fault detection algorithms for vibration monitoring. *Automatica* 36(1): 101–109
10. Basseville M, Mevel L, Goursat M (2004) Statistical model-based damage detection and localization: subspace-based residuals and damage-to-noise sensitivity ratios. *J Sound Vib* 275(3):769–794
11. Döhler M, Mevel L (2011) Robust subspace based fault detection. In: Proceedings of the 18th IFAC world congress, Milan
12. Döhler M, Mevel L (2012) Subspace-based damage detection under changes in the ambient excitation statistics. *Mech Syst Signal Process*, Submitted

13. Basseville M, Benveniste A, Moustakides G, Rougée A (1987) Optimal sensor location for detecting changes in dynamical behavior. *IEEE Trans Automat Contr* 32(12):1067–1075
14. Balmès E, Basseville M, Mevel L, Nasser H, Zhou W (2008) Statistical model-based damage localization: a combined subspace-based and substructuring approach. *Struct Contr Health Monitor* 15(6):857–875
15. Bernal D (2012) Sensitivities of eigenvalues and eigenvectors from complex perturbations. In: *Proceedings of the 30th international modal analysis conference*, Jacksonville

Chapter 26

Application of Efficient Model Correction for Damage Assessment Using Limited Measurements

Yi-Cheng Wu and Chin-Hsiung Loh

Abstract The purpose of this research is to employ the model updating technique to conduct the structural damage detection with insufficient measurements. First, the stochastic subspace identification technique is used to identify the system mode shapes from the limited measurement, then the mode shape expansion (MSE) technique was introduced to reconstruct the mode shapes in all degree of freedoms. Second, in cooperated with the expanded mode shapes the damage detection technique, called Efficient Model Correction Method (EMCM), is used to identify the damage location as well the damage severity. To investigate the effectiveness of the proposed MSE technique and model updating approaches, numerical studies with three types of sensor distributions and five damage scenarios were investigated. The results indicated that when the weighting coefficient of the proposed MSE technique is properly selected, the ability of reconstructing the mode shape is appreciated. For damage detection, data collected from the shaking table test of a six-story steel frame structure was used. With limited measurements the MSE technique together with the applicability of the EMCM, damage detection of the frame structure is conducted. The ability EMCM for damage detection is also discussed. The study concluded that damage detection through mode shape expansion is possible if the expanded mode shapes are consistent with the exact mode shapes. The Efficient Model Correction Method can also provide good results of structural damage detection.

Keywords Stochastic subspace identification • Mode shape expansion • Model updating • Damage detection • Structural dynamics

26.1 Introduction

In structural analysis, the finite element (FE) method plays a crucial role in estimating the structural response subjected to external loading. Once the FE model can be well-established, the response of structures can be simulated perfectly. However, there are some un-determined factors in the FE model such as the selection of well-defined elements and the determination of correct model parameters. Besides, some uncertainties in model estimation, such as: inelastic behavior of structural elements, inappropriate parameters selection and inaccurate boundary conditions. To overcome the modeling errors, a practical way to correct the parameters of FE model is through the “model updating” technique by using the measurement data. Nevertheless, there are still many difficulties in adopting model updating in real application. The first obstacle is that higher modes are typically difficult to be observed successfully from the limited number of measurements under normal loading condition. Fortunately, from the concept of structural dynamics, the response of structures can be represented by a linear combination of many modes. Each mode has its own weighting contribution to the response; the model contribution from lower frequency modes contributes much more than the modes with higher frequencies. Generally speaking, the response can be approximately captured using the first few modes only. The second barrier is that it is impossible to measure all of the degrees of freedom from the response of a structure, because the selection of sensor locations as well as the limited number of sensors is two important problems. A useful tool to compensate the information of unmeasured degrees of freedom is to utilizing the Mode Shape Expansion (MSE) technique. In fact, model updating has been widely used in the field of damage detection during the past few decades. However, seldom attention has been paid in the

Y.-C. Wu • C.-H. Loh (✉)

Department of Civil Engineering, National Taiwan University, No.1, Section 4, Roosevelt Road, Taipei, 10617 Taiwan
e-mail: r97521218@ntu.edu.tw; loh0220@ccms.ntu.edu.tw

past to investigate the damage detection using both of the mode shape expansion and model updating techniques. Therefore, the main objective of this study is to conduct the damage detection of structures through the comparisons of using different model updating approaches via mode shape expansion technique.

Several MSE techniques have been compared and studied over the past few decades. Imregun and Ewins [1] introduced two mode shape expansion techniques, one is based on the direct use of the finite element mass and stiffness matrices and the other is to utilizing the eigen-solution of these matrices. Levine-West et al. [2] compared several distinct mode shape expansion techniques via a truss model. Ng'andu et al. [3] and Williams et al. [4] suggested that to fit the mode shapes of rotational degrees of freedom by curve fitting method or spline function. Guyan [5] proposed a static condensation method using the mass and stiffness matrices of the analytical model. The method is further extended to the dynamic condensation by Kidder [6]. O'Callahan et al. [7] used the analytical model to expand the unmeasured degrees of freedom. Halevi et al. [8] presented a combined expansion and orthogonalization method (CEO) which can consider the expansion error and orthogonality condition simultaneously. Shi et al. [9] proposed a mode shape expansion method by establishing a weighted Frobenius norm error function. To minimize the error function, the coordinate rotation matrix is acquired to determine the mode shapes of unmeasured degrees of freedom.

Similar to MSE technique, model updating technique has also received tremendous attentions in recent years. Friswell and Mottershead [10] gave a very detailed introduction related to the finite element model updating and categorized the model updating methods into three classes, i.e. the direct model updating method, the iterative model updating method and the model updating method in frequency domain, respectively. Andrea Brasiliano et al. [11] validated the residual error method in the movement equation by a steel free-free beam experiment. Zimmerman and Kaouk [12] provided two damage indices to represent the damage location and derived the minimum rank updating theory to evaluate the damage severity. Kaouk and Zimmerman [13] further extended the minimum rank updating theory to evaluate the structure damping if the structure is a proportionally damped structure. Doebling [14] categorized the optimal matrix update method by two criteria (Minimum norm and Minimum rank) and three updated properties (Global matrix, Elemental matrix and Elemental parameter), and proposed a method to compute a minimum-rank solution for the perturbations for the elemental stiffness parameters while constraining the connectivity of the global stiffness matrix. Yuen [15] suggested that to find a coordinate rotation matrix to connect the mode shapes between the intact and damaged state. The coordinate rotation matrix can be used to update the mass and stiffness matrices, respectively. Barroso and Rodriguez [16] provided an approach to extract a baseline by the ratio of stiffness to mass. The eigenequation of an idealized shear-building model is directly rearranged as a system containing several linear equations and the unknowns can be viewed as the inter-story stiffness which can be resolved by the least-squares method. Tarazaga et al [17] and Hu et al. [18] presented different model updating approaches both using the concept of submatrix. The coefficients of submatrices are determined by the weighted least squares method. Burton et al. [19] assumed that the stiffness reduction of the system is due to a single DOF and its location is *a priori*, and then developed an iterative model updating procedure to evaluate the damage severity by using the Damage Ritz Vector [20]. Yang and Chen [21] suggested a model updating approach using the first few modes only. The advantage of this approach is that replacing the eigenvectors of concern with the modal matrix to resolve the problem of insufficient number of equations.

The objective of this paper is to conduct the damage detection by using the model updating technique. The FE model of intact state is regarded as a baseline structure, and then updating the model to match the damaged state. A physical meaning damage index is then adopted to locate and quantify damage simultaneously. Taking the real application into considerations, namely, only the very limited spatially and incompletely measurements are used, the mode shape expansion technique is implemented to perform the damage detection.

26.2 Mode Shape Expansion Technique

The modal parameters such as natural frequencies and mode shapes can be identified when adequate measurements at the appropriate locations are provided. However, only incomplete modal parameters are available due to insufficient measurements in reality, especially the identification of mode shapes from limited measurements. Nevertheless, without full length measurement of mode shapes, many model updating techniques are difficult to be implemented for damage detection. Therefore, mode Shape Expansion (MSE) provides a practical technique to compensate the deficiency of insufficient measurements.

Consider an N -DOF system subjected to external loading, the equation of motion can be written as:

$$\mathbf{M}\ddot{\mathbf{q}}(t) + \mathbf{C}\dot{\mathbf{q}}(t) + \mathbf{K}\mathbf{q}(t) = \mathbf{f}(t) \quad (26.1)$$

where \mathbf{M} , \mathbf{C} and \mathbf{K} are the mass, damping and stiffness matrices of the system. $\mathbf{q}(t)$ is the relative displacement vector and $\mathbf{f}(t)$ is the excitation force vector. The system natural frequencies and mode shapes can be obtained from the following equation:

$$[\mathbf{K} - \lambda\mathbf{M}] \tilde{\Phi} = 0 \quad (26.2)$$

where $\lambda = \text{eigenvalues}$; $\tilde{\Phi} = \text{eigenvectors}$. From the concept of structural dynamics, λ can be regarded as the square of natural frequency ω and $\tilde{\Phi}$ can be regarded as mode shape. Orthogonal condition of mass and stiffness matrices must be satisfied. In this study mass normalization technique is used, such as:

$$\Phi_i = \frac{\tilde{\Phi}_i}{\sqrt{\tilde{\Phi}_i^T \mathbf{M} \tilde{\Phi}_i}} \quad i = 1, 2, \dots, N \quad (26.3)$$

From which the following two equations can be provided:

$$\Phi^T \mathbf{M} \Phi = \mathbf{I} \quad (26.4)$$

where $\mathbf{I} \in \mathbb{R}^{(N) \times (N)} = \text{identify matrix}$. Furthermore, similar equation can be obtained for the stiffness matrix \mathbf{K} ,

$$\Phi^T \mathbf{K} \Phi = \text{diag}(\lambda_1, \lambda_2, \dots, \lambda_N) = \text{diag}(\omega_1^2, \omega_2^2, \dots, \omega_N^2) \equiv \Omega \quad (26.5)$$

where $\text{diag}(\lambda_1, \lambda_2, \dots, \lambda_N) = \text{diag}(\omega_1^2, \omega_2^2, \dots, \omega_N^2) = N \times N$ diagonal matrix with diagonal elements $\lambda_1, \lambda_2, \dots, \lambda_N$ or $\omega_1^2, \omega_2^2, \dots, \omega_N^2$.

A nominal mode shape matrix Φ can be partitioned as four parts:

$$\Phi = \begin{bmatrix} \Phi_{p,m} & \Phi_{p,u} \\ \Phi_{s,m} & \Phi_{s,u} \end{bmatrix} \quad (26.6)$$

The first subscript in Φ indicates the specific DOFs, in which ‘‘p’’ denotes the primary DOFs and ‘‘s’’ denotes the secondary DOFs. The second subscript in Φ indicates the specific modes, in which m denotes the measured modes from $1, 2, \dots, N_m$ and u denotes the unmeasured modes from $N_m + 1, N_m + 2, \dots, N$, where N_m is the number of modes which can be extracted for the system identification technique using the limited number of measurements and N denotes the number of DOFs of the system. However, due to the fact that the higher modes are usually difficult to be excited successfully in real application and the mode shapes of the secondary DOFs are difficult to measure in the experiment due to limited number of sensors, $\Phi_{s,m}$, $\Phi_{p,u}$ and $\Phi_{s,u}$ are usually missing in most situations. In brief, $\Phi_{p,m}$ is the only part that can be acquired in real application through measurement. Mode shape expansion is one technique to reconstruct $\Phi_{s,m}$ by using $\Phi_{p,m}$ so that the spatial mode shapes can be recovered completely for the first few N_m modes ($N_m < N$). In this study, a MSE method proposed by Shi et al. [9] is used. To identify the mode shapes, $\Phi_{p,m}$, by using the limited number of measurements the stochastic subspace identification (SSI) technique is used [22].

A brief description of MSE is introduced. Consider a structure suffered slightly damage. From the measurement data, the identified mode shapes will be perturbed so that no longer remains exactly the same as its intact state. In general, the differences on the identified mode shapes between the intact and the damaged state usually are small from observation. The phenomenon can be described as Eq. (26.7), which connects the intact and damaged state by a coordinate transformation matrix \mathbf{Z} ,

$$(\Phi_D)_m = (\Phi_I)_m \mathbf{Z} \quad (26.7)$$

where $(\Phi_D)_m$ and $(\Phi_I)_m$ indicate the damaged and intact mode shapes identified from measurements, respectively. In this study, the intact mode shapes $(\Phi_I)_m$, are assumed as known shape function (reference mode shapes). Eq. (26.7) can be rearranged as Eq. (26.8) by their primary and secondary DOFs.

$$\begin{bmatrix} (\Phi_D)_{p,m} \\ (\Phi_D)_{s,m} \end{bmatrix} = \begin{bmatrix} (\Phi_I)_{p,m} \\ (\Phi_I)_{s,m} \end{bmatrix} \mathbf{Z} \quad (26.8)$$

Recall Eq. (26.4), and consider the cross-orthogonal condition for the mode shape matrices $(\Phi_D)_m$ and $(\Phi_I)_m$ between damaged and intact state,

$$(\Phi_I)_m^T \mathbf{M}_I (\Phi_D)_m = (\Phi_I)_m^T \mathbf{M}_I (\Phi_I)_m \mathbf{Z} = \mathbf{Z} \quad (26.9)$$

Based on the concept of orthogonalization, an error function which describes the differences between $(\Phi_D)_m$ and $(\Phi_I)_m$ is defined as:

$$\Delta_1 = \mathbf{I} - \mathbf{Z} \quad (26.10)$$

where $\mathbf{I} \in \mathbb{R}^{(N_m) \times (N_m)}$ = an identify matrix. Another error function which describes directly the differences between the measured and predicted mode shapes of damaged state can be expressed (as from Eq. (26.8)):

$$\Delta_2 = (\Phi_D)_{p,m} - (\Phi_I)_{p,m} \mathbf{Z} \quad (26.11)$$

In fact, Δ_1 can be taken as the errors come from the analytical model. However, Δ_2 includes the transformation errors and the unavoidable measurement errors in the experiment.

Two types of errors are combined in the form of a weighted Frobenius norm error function expressed as:

$$\Pi = (\Phi_D)_{p,m} - (\Phi_I)_{p,m} \mathbf{Z}_F^2 + w \mathbf{I} - \mathbf{Z}_F^2 \quad (26.12)$$

where w = weighting coefficient. The analytical solution of transformation matrix \mathbf{Z} can be obtained by minimizing Eq. (26.12),

$$\mathbf{Z} = [(\Phi_I)_{p,m}^T (\Phi_I)_{p,m} + w \mathbf{I}]^{-1} [(\Phi_I)_{p,m}^T (\Phi_D)_{p,m} + w \mathbf{I}] \quad (26.13)$$

Once the transformation matrix \mathbf{Z} is obtained, the approximately $(\Phi_D)_{s,m}$, $(\check{\Phi}_D)_{s,m}$ can be written as:

$$(\check{\Phi}_D)_{s,m} \cong (\Phi_D)_{s,m} = (\Phi_I)_{s,m} \mathbf{Z} \quad (26.14)$$

So far, the expanded mode shapes for the first few N_m modes can be reconstructed as follows:

$$\check{\Phi}_D = sequ \left(\begin{bmatrix} (\Phi_D)_{p,m} \\ (\check{\Phi}_D)_{s,m} \end{bmatrix} \right) \quad (26.15)$$

where *sequ* is a self-defined operator which can be used to rearrange $(\Phi_D)_{p,m}$ and $(\check{\Phi}_D)_{s,m}$ according to the sequence of DOFs. Then $\check{\Phi}_D$ can be further modified by the process of mass normalization,

$$(\hat{\Phi}_D)_i = \frac{(\check{\Phi}_D)_i}{\sqrt{(\check{\Phi}_D)_i^T \mathbf{M}_I (\check{\Phi}_D)_i}} \quad i = 1, 2, \dots, N_m \quad (26.16)$$

In the following, $\hat{\Phi}_D$ will denote the expanded mode shapes for the first few N_m modes after the appropriate rearrangement of DOFs and the process of mass normalization. Obviously, the result from this expansion is influenced by the weighting coefficient “ w ”. Shi et al. [27] suggested that “ w ” is larger than 1.0 when the analytical model is relatively reliable and accurate. Otherwise “ w ” is taken less than 1.0. Note that the expansion method converges to the System Equivalent Reduction Expansion Process (SEREP) method [7] when w equals to zero.

26.3 Damage Detection: Efficient Model Correction Method

There are several methods for damage detection which are related to the finite element model updating: Damage Ritz vector method (DRVM) [23], Minimum rank perturbation Theory (MRPT) [1, 20], Modified quadratic compression method (MQCM) [6], Efficient model correction method (EMCM) [15], Ratio of stiffness to mass approach (RSMA) [16], etc. Most of these methods are based on the identification of the perturbation of the damage state stiffness matrix (except RSMA). In this study the Efficient Model Correction Method will be introduced and information which mentioned in the previous section will be used as a *priori*.

A two stage model updating method [15] which is called ‘‘Efficient Model Correction Method’’ (EMCM) to correct the mass matrix and stiffness matrix is introduced. First, a transformation is constructed to transform the first N_m measured modes of intact eigenvectors, $\{(\Phi_1)_1, (\Phi_1)_2, \dots, (\Phi_1)_{N_m}\}$, to the measured eigenvectors, $\{(\hat{\Phi}_D)_1, (\hat{\Phi}_D)_2, \dots, (\hat{\Phi}_D)_{N_m}\}$. Meanwhile, the eigenvectors of unmeasured modes (i.e., $N_m + 1$ to N) will be preserved. It is now defined a transformation matrix \mathbf{R} , then

$$\mathbf{R} [\mathbf{u}_1, \mathbf{u}_2, \dots, \mathbf{u}_{N_m}, \mathbf{u}_{N_m+1}, \dots, \mathbf{u}_N] = \left[\left(\hat{\Phi}_D \right)_1, \left(\hat{\Phi}_D \right)_2, \dots, \left(\hat{\Phi}_D \right)_{N_m}, \mathbf{u}_{N_m+1}, \dots, \mathbf{u}_N \right] \quad (26.17)$$

or

$$\mathbf{R}\mathbf{U} = [(\hat{\Phi}_D)_m, \mathbf{u}_{N_m+1}, \dots, \mathbf{u}_N]$$

where $\mathbf{U} \equiv [\mathbf{u}_1, \mathbf{u}_2, \dots, \mathbf{u}_{N_m}, \mathbf{u}_{N_m+1}, \dots, \mathbf{u}_N]$ is a basis matrix which satisfies the orthogonal condition of $\mathbf{U}^T \mathbf{M}_1 \mathbf{U} = \mathbf{I}$. This linear mapping ensures the unmeasured intact eigenvectors are ‘‘fixed points’’ for the transformation matrix \mathbf{R} . In order to generate the set $\{\mathbf{u}_{N_m+1}, \dots, \mathbf{u}_N\}$ with the set of some prescribed seed vectors $\{\mathbf{e}_{N_m+1}, \dots, \mathbf{e}_N\}$ to replace the set $\{(\Phi_1)_u\}$, the Gram Schmidt orthogonalization process can be applied.

Gram-Schmidt orthogonalization process can be describes as follows:

$$\mathbf{v}_i = \mathbf{e}_i - \sum_{j=1}^{i-1} \gamma_{i,j} \mathbf{u}_j \quad i = N_m + 1, N_m + 2, \dots, N \quad (26.18)$$

where \mathbf{v}_i is the pre-normalized candidate vector which can be computed by eliminating the projection of $\mathbf{u}_1, \mathbf{u}_2, \dots, \mathbf{u}_{i-1}$ from \mathbf{e}_i . The unknown coefficients $\gamma_{i,j}$, $j = 1, 2, \dots, i-1$ can be obtained by using

$$\mathbf{u}_j^T \mathbf{M}_1 \mathbf{v}_i = 0 \quad j = 1, 2, \dots, i-1 \quad (26.19)$$

The fact that $\mathbf{u}_1, \mathbf{u}_2, \dots, \mathbf{u}_{i-1}$ are mutually satisfied the mass orthogonal condition. As a result, $\gamma_{i,j}$ can be readily obtained:

$$\gamma_{i,j} = \mathbf{u}_j^T \mathbf{M}_1 \mathbf{e}_i \quad j = 1, 2, \dots, i-1 \quad (26.20)$$

Although the seed vector \mathbf{e}_i is arbitrary, a suitable choice can enhance the computational efficiency. It was suggests that take \mathbf{e}_i as a column vector with unity for i -th component and zero elsewhere [15], In this case,

$$\gamma_{i,j} = \left(\mathbf{u}_j^T \mathbf{M}_1 \right)_i \quad j = 1, 2, \dots, i-1 \quad (26.21)$$

Once $\gamma_{i,j}$ are solved, \mathbf{v}_i can be immediately obtained. Then, the candidate vector \mathbf{v}_i^* can be obtained by normalizing the pre-normalized candidate vector \mathbf{v}_i :

$$\mathbf{v}_i^* = \frac{\mathbf{v}_i}{\sqrt{\mathbf{v}_i^T \mathbf{M}_1 \mathbf{v}_i}} \quad i = N_m + 1, N_m + 2, \dots, N \quad (26.22)$$

One important check is to check the orthogonality between the vector \mathbf{v}_i^* and $\mathbf{u}_1, \dots, \mathbf{u}_{i-1}$. If it happens that:

$$\left| \mathbf{u}_j^T \mathbf{M}_1 \mathbf{v}_i^* \right| > \varepsilon \quad (26.23)$$

for any $j \leq i - 1$ and a tolerance threshold ε , say 10^{-4} , one should repeat the Gram-Schmidt orthogonalization process for \mathbf{u}_i with \mathbf{v}_i^* as the seed vector \mathbf{e}_i and use Eq. (26.20). Otherwise, the candidate vector \mathbf{v}_i^* is accepted, i.e.,

$$\mathbf{u}_i = \mathbf{v}_i^*, \quad i = N_m + 1, N_m + 2, \dots, N$$

More detailed understanding of Gram-Schmidt orthogonalization process can refer [24]. In summary, \mathbf{U} can be obtained by:

$$\mathbf{U} = \begin{cases} \mathbf{u}_i = (\hat{\Phi}_I)_i & i = 1, 2, \dots, N_m \\ \mathbf{u}_i = \mathbf{v}_i^* & i = N_m + 1, N_m + 2, \dots, N \end{cases} \quad (26.24)$$

Using the orthogonality of mass, $\mathbf{U}^T \mathbf{M}_I \mathbf{U} = \mathbf{I}$, the inverse of \mathbf{U} is given by $\mathbf{U}^{-1} = \mathbf{U}^T \mathbf{M}_I$. From Eq. (26.17), the coordinate transformation matrix \mathbf{R} can be obtained:

$$\mathbf{R} = \left[\left(\hat{\Phi}_D \right)_m, \mathbf{u}_{N_m+1}, \dots, \mathbf{u}_N \right] \mathbf{U}^{-1} \quad (26.25)$$

Adopting the coordinate transformation matrix of \mathbf{R} , $\mathbf{U}^T \mathbf{M}_I \mathbf{U} = \mathbf{I}$ can be rewritten as:

$$(\mathbf{R}\mathbf{U})^T \left[(\mathbf{R}^{-1})^T \mathbf{M}_I \mathbf{R}^{-1} \right] (\mathbf{R}\mathbf{U}) = \mathbf{I} \quad (26.26)$$

From Eq. (26.26) the updated mass matrix can be expressed as

$$\mathbf{M}^* = (\mathbf{R}^{-1})^T \mathbf{M}_I \mathbf{R}^{-1} \quad (26.27)$$

and $\Phi^* = \mathbf{R}\mathbf{U}$ will be the eigenvector of the updated model. In other words, the updated eigenvectors can be expressed as:

$$\Phi^* = \begin{cases} \mathbf{R}(\Phi_I)_i = (\hat{\Phi}_D)_i & i = 1, 2, \dots, N_m \\ \mathbf{R}\mathbf{v}_i^* = \mathbf{v}_i^* & i = N_m + 1, N_m + 2, \dots, N \end{cases} \quad (26.28)$$

Since the mass matrix is corrected by Eq. (26.27), a modified stiffness matrix can also be obtained by the same similarly transformation,

$$\mathbf{K}_R = (\mathbf{R}^{-1})^T \mathbf{K}_I \mathbf{R}^{-1} \quad (26.29)$$

Note that the undamaged model ($\mathbf{M}_I, \mathbf{K}_I$) and the corrected model ($\mathbf{M}^*, \mathbf{K}_R$) share the same set of eigenvalues. Since $\mathbf{K}\Phi = \mathbf{M}\Phi\Omega$, and from Eqs. (26.27, 26.28, and 26.29) and the fact that $\Phi^{*T} \mathbf{M}^* \Phi^* = \mathbf{I}$, the precorrected stiffness matrix \mathbf{K}_R can be factorized as follows:

$$\begin{aligned} \mathbf{K}_R &= \mathbf{M}^* \Phi^* \Omega (\Phi^*)^{-1} = \mathbf{M}^* \Phi^* \Omega \left[(\Phi^*)^T \mathbf{M}^* \right] = \mathbf{M}^* \left[\Phi^* \Omega (\Phi^*)^T \right] \mathbf{M}^* \\ &= \mathbf{M}^* \left[\sum_{k=1}^{N_m} (\omega_I)_k^2 (\Phi^*)_k (\Phi^*)_k^T + \sum_{k=N_m+1}^N (\omega_I)_k^2 (\Phi^*)_k (\Phi^*)_k^T \right] \mathbf{M}^* \end{aligned} \quad (26.30)$$

By replacing the eigenvalues of the first N_m modes from the measured data, one obtains the updated stiffness matrix \mathbf{K}^* :

$$\mathbf{K}^* = \mathbf{M}^* \left[\sum_{k=1}^{N_m} (\omega_D)_k^2 (\Phi^*)_k (\Phi^*)_k^T + \sum_{k=N_m+1}^N (\omega_I)_k^2 (\Phi^*)_k (\Phi^*)_k^T \right] \mathbf{M}^* \quad (26.31)$$

The updated model ($\mathbf{M}^*, \mathbf{K}^*$) possesses the measured eigenvalues and eigenvectors. For the unobserved modes, the eigenvalues and eigenvectors are the ones of the undamaged model. Finally, by comparing Eqs. (26.30) and (26.31), the

stiffness matrix can be corrected by updating the eigenvectors without knowing the eigenvalues and eigenvectors of the unobserved modes,

$$\mathbf{K}^* = \mathbf{K}_R + \mathbf{M}^* \left\{ \sum_{k=1}^{N_m} [(\omega_D)_k^2 - (\omega_I)_k^2] (\Phi^*)_k (\Phi^*)_k^T \right\} \mathbf{M}^* \quad (26.32)$$

If the mass matrix can be treated as an unchanged matrix, then in Eq. (26.32) $\mathbf{M}^* = \mathbf{M}$ can be used. As a matter of fact that the updated stiffness matrix can be further viewed as the approximation of stiffness matrix of damaged state,

$$\mathbf{K}_D \cong \mathbf{K}^* = \mathbf{K}_R + \mathbf{M} \left\{ \sum_{k=1}^{N_m} [(\omega_D)_k^2 - (\omega_I)_k^2] (\Phi^*)_k (\Phi^*)_k^T \right\} \mathbf{M} \quad (26.33)$$

Once \mathbf{K}_D is obtained, the damage index can be proposed to estimate the damage location and severity.

Damage index can be viewed as the change of inter-story stiffness and can also be used to locate and quantify damage. It can be proved that the inter-story stiffness k_m of the m -th floor can be expressed as:

$$(a). \text{ Damaged state: } k_m' = \sum_{i=m}^N \sum_{j=m}^N (\mathbf{K}_D)_{i,j} \quad (m \leq N) \quad \text{and} \quad (b) \text{ Un-damage case: } k_m = \sum_{i=m}^N \sum_{j=m}^N (\mathbf{K}_I)_{i,j}$$

where $\mathbf{K}_{i,j}$ is the element in the i -th row and j -th column of the stiffness matrix \mathbf{K} . The stiffness degradation ratio of the m -th floor is defined as

$$DI_m = \left(1 - \frac{k_m'}{k_m} \right) \times 100\% \quad (26.34)$$

This process is outlined in Fig. 26.1 below.

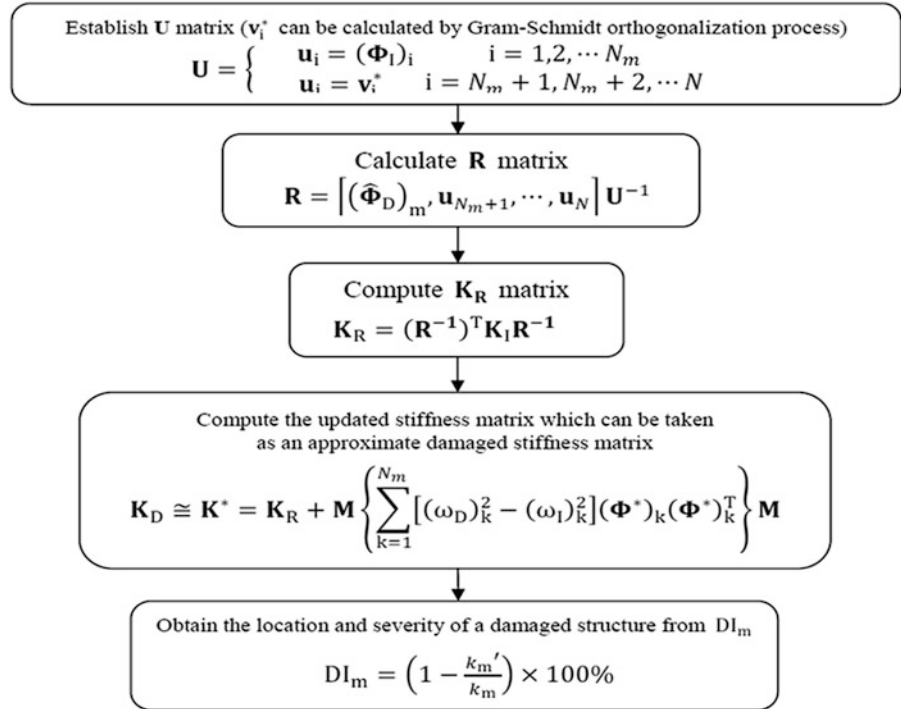


Fig. 26.1 The flow chart of EMCM

26.4 Experimental Verification

An experimental validation was conducted to confirm the applicability of the proposed damage detection techniques by using the shaking table test of a six-storey steel frame at National Center for Research on Earthquake Engineering (NCREE). As shown in Fig. 26.1, the six-storey scale-down structure consists of a single bay with a 1.0 m by 1.5 m floor area and a 1.0 m story height. The dimensions and connection information are as follows; Column: 150 mm × 25 mm (rectangular section), Beam: 50 mm × 50 mm × 5 mm (L-section). Floor slab: 1000 mm × 1500 mm × 20 mm, Base Plate: 1700 mm × 1700 mm × 20 mm, Beam-floor: weld connection, Column-floor: bolt connection, Base-column: bolt connection, Bracing-floor: bolt connection. The mass of each floor (lumped mass) is 862.85 kg except the mass of top floor is 803.98 kg. The structure was bolted on an NCREE shaking table for testing.

The damage scenarios were designed as the reduction of the stiffness of the bracing members. In order to model this type of damage scenario, three different size of bracing members were used, as presented in Fig. 26.2. Three connecting plates (C1, C2 and C3) were individually associated with different floors of the structure, and the arrangement is shown in Table 26.1, to simulate the change in the stiffness of each floor. A connecting plate C3 was initially placed in each floor to serve as a reference case. Two damage scenarios were arranged based on the location of different connecting plate, Test 1 and Test 2, respectively. White noise normalized to a peak acceleration of 50 gal along with duration of 120 sec was used as a base excitation of the ambient vibration responses of the structure. The acceleration responses of each floor were measured and can be used to simulate the scenario of insufficient measurements. According to different arrangement on sensor distributions, these two damage scenarios can be categorized as Test 1-1, Test 1-2, Test 2-1, and Test 2-2, respectively. The sensor distribution is tabulated in Table 26.2. In this study only 4 sensors are used (with different location).

In this section, the EMCM damage detection technique based on the model updating with insufficient measurements is verified by using the shaking table test data of the six-storey steel frame. Due to the limited measurement the previous mentioned mode shape expansion technique needs to be applied. A error index is used to select the expanded mode shapes for damage detection. It is defined the mode shape expansion error ($MSEE_j$) as:

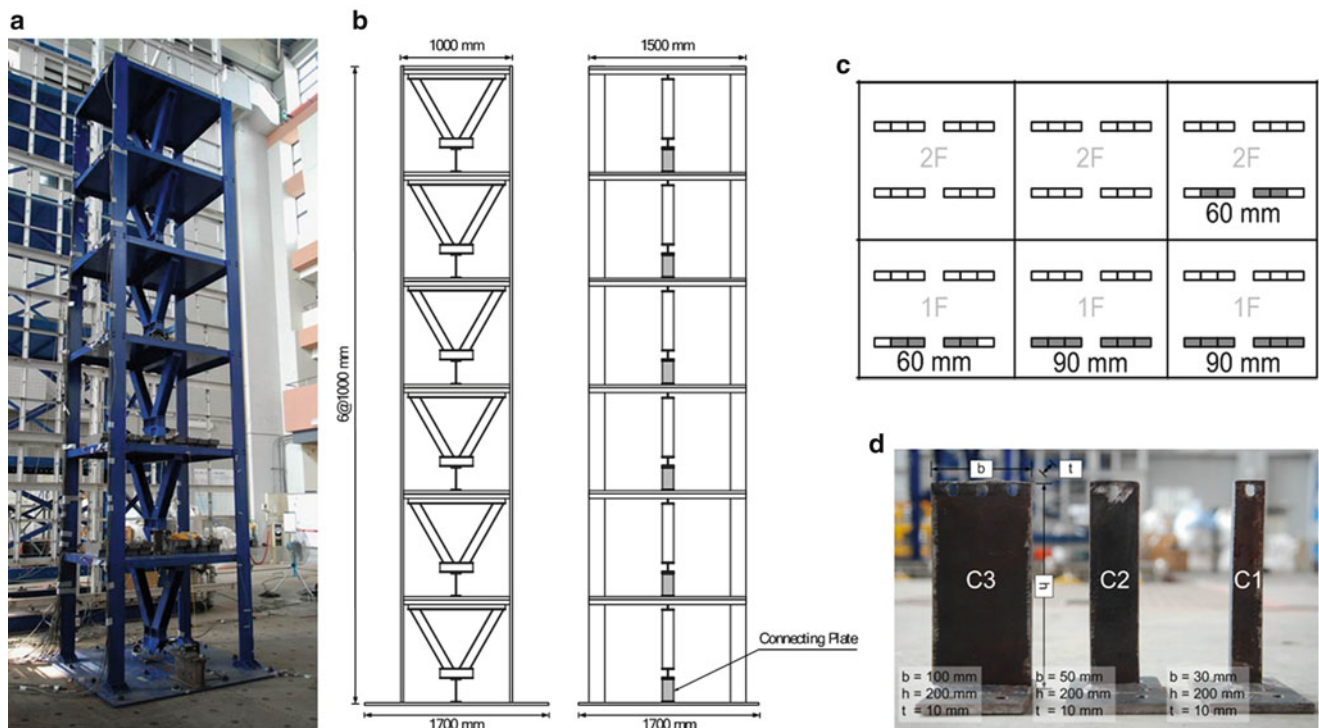


Fig. 26.2 The 6-story steel frame for experimental study; (a) Photo of the test structure, (b) Front view, (c) Lateral view (Grey area indicate the connecting plate was used in the seriously damaged cases), (d) three connecting plates used in seriously damaged cases

Table 26.1 Summary of the damage scenarios

	Reference	Test 1	Test 2
6F	C3	C3	C3
5F	C3	C3	C3
4F	C3	C3	C3
3F	C3	C3	C3
2F	C3	C3	C2
1F	C3	C2	C1

(□ denotes C1 plate; ■ denotes C2 plate; ■ denotes C3 plate)

Table 26.2 Summary of the sensor distributions

	Test 1-1	Test 1-2	Test 2-1	Test 2-2
6F	C3	C3	C3	C3
5F	C3	C3	C3	C3
4F	C3	C3	C3	C3
3F	C3	C3	C3	C3
2F	C3	C3	C2	C2
1F	C2	C2	C1	C1

(□ denotes the measured DOF or sensor location)

Table 26.3 The optimal weighting set and the worst weighting set for MSE ($N_m = 4$)

Damage scenarios		W_{opt}	W_{wor}
1 Damage	Test1-1	0.0222	10^3
	Test1-2	0.0100	10^3
2 Damages	Test2-1	0.3610	10^3
	Test2-2	0.0452	10^3

$$MSEE_j(w) = \frac{\sqrt{\sum_{i=1}^N \left[\left(\widehat{\Phi}_D \right)_{i,j} - (\Phi_D)_{i,j} \right]^2}}{\sqrt{\sum_{i=1}^N [(\Phi_D)_{i,j}]^2}} \quad j = 1, 2, \dots, N_m \tag{26.35}$$

where $\widehat{\Phi}_D$ is the expanded mode shapes, Φ_D is the exact mode shapes, “i” indicates the i-th degree of freedom and “j” indicates the j-th mode. $MSEE_j$ is interpreted as the sum of errors for each mode. A normalized process can also be defined as:

$$MSEE(w) = \frac{\sum_{j=1}^{N_m} MSEE_j(w)}{N_m} \tag{26.36}$$

Smaller $MSEE(w)$ indicates a better estimation of mode shape expansion. $MSEE$ is regarded as an indicator to evaluate the performance of MSE under various weighting coefficients. Both optimal value of weighting W_{opt} and worse optimal value W_{wor} are used. Table 26.3 shows the weighting values used for each test case. Figure 26.3 shows the identified damage mode shapes of the test structures with different weighting value. The damaged mode shapes obtained from using SSI-DATA [5] with full measurement was also used for comparison. It is observed that the performance of MSE is accurate enough to be used for damage identification. Based on the identified damaged mode shapes, EMC method can be applied to identify the damage location and severity. As shown in Fig. 26.4 the stiffness degradation ratio of the two damage test cases were identified. Comparison with the result using full measurement was also shown in this Fig. 26.4. It is shown that for a single damage location the EMC method can identify the damage location and severity quite well even with limited measurement. As for the multiple damage locations, the proposed method can also provide a certain level of confidence on damage detection.



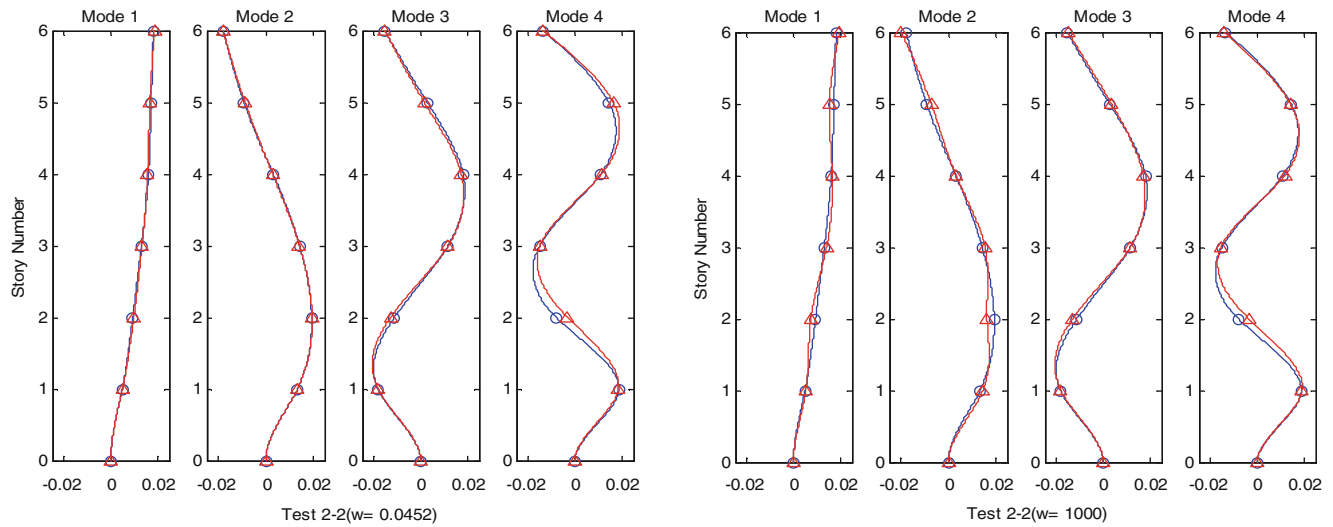


Fig. 26.3 Damage mode shapes from Test 2-2 using $W_{opt}(=0.0452)$ and $W_{wor}(=1000)$

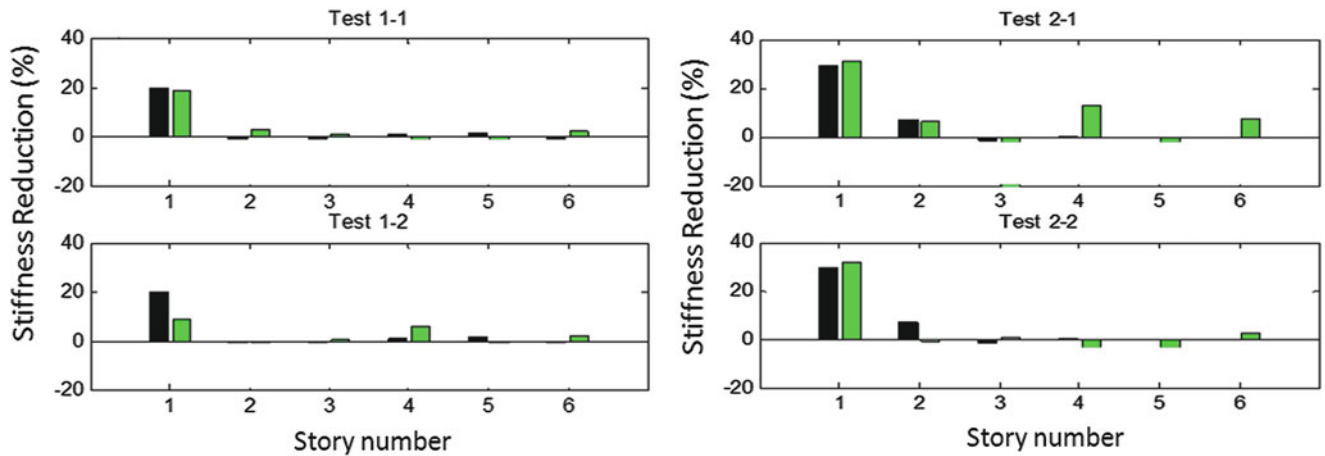


Fig. 26.4 Identified the stiffness reduction in each floor from different test cases (solid bar: result from full measurements; outline bar: result from different test case)

26.5 Conclusions

The main objective of this study is to employ the model updating technique to detect, locate and quantify damage. The Efficient Model Correction Method (EMCM) was introduced in this paper, then followed by an experimental verification by using the EMCM method. Through this study the following conclusions are drawn:

- (1) The MSE technique proposed by Shi et al. [9] was investigated. To determine the coordinate transformation Z between the intact and damaged mode shapes, the weighting coefficient described in Eq. (26.13), needs to be carefully examined.
- (2) Verification on EMCM technique by using a shaking table test data was studied. The results of damage detection were compared with the previous investigation [25]. It shows that EMCM can provide reliable damage detection, particularly for single damage location. However, for multi-damage scenario EMCM is regards as the effective method one to identify the damage by adopting the expanded mode shapes.

Acknowledgements Support from National Science Council of the Republic of China, Taiwan (under Contract No. NSC 99-2221-E-002-088-MY3) and the Research Program of Excellency of National Taiwan University (under Contract No. 99R80805) on the development of the theory and experiments are acknowledged.



References

1. Imregun M, Ewins DJ (1993) An investigation into modeshape expansion techniques. In: Proceedings of the international modal analysis conference-IMAC 11th, February 1993, Kissimee, FL, pp 168–175
2. Levine-West M, Milman M, Kissil A (April 1996) Mode shape expansion techniques for prediction: experimental evaluation. *J AIAA* 34(4):821–829
3. Ng'andu AN, Fox CHJ, Williams EG (1995) On the estimation of rotational degrees of freedom using spline functions. In: Proceedings of the international modal analysis conference-IMAC 13th, 1995, Nashville, TN, pp 791–797
4. Williams EG, Green JS (1990) A spatial curve fitting technique for estimating rotational degrees of freedom. In: Proceedings of the international modal analysis conference-IMAC 8th, 1990, Kissimee, FL, pp 376–381
5. Weng JH, Loh CH, Yang JN (December 2009) Experimental study of damage detection by data-driven subspace identification and finite-element model updating. *J Struct Eng* 135(12):1533–1544
6. Kidder RL (1973) Reduction of structural frequency equations. *J AIAA* 11(6):892
7. O'Callahan JC, Avitavle P, Reimer R (1989) System equivalent reduction expansion process (SEREP). In: Proceeding of 7th international modal analysis, 1989, pp 29–37
8. Halevi Y, Morales CA, Inman DJ (April 2005) Combined expansion and orthogonalization of experimental modeshapes. *J Vib Acoust* 127(2):188–196
9. Shi ZY, Dingm XH, Gu HZ (1995) A new model reduction and expansion method. In: International conference on structural dynamics, vibration, noise and control, Hong Kong Polytechnic University, Hong Kong, 1995, pp 847–852
10. Friswell MI, Mottershead JE (1995) Finite element model updating in structural dynamics. Kluwer, Boston
11. Brincker R, Zhang L, Andersen P (June 2001) Modal identification of output-only systems using frequency domain decomposition. *Smart Mater Struct* 10(3):441–445
12. Zimmerman DC, Kaouk M (April 1994) Structural damage detection using a minimum rank update theory. *J Vib Acoust* 116(2):222–231
13. Kaouk M, Zimmerman DC (April 1994) Structural damage assessment using a generalized minimum rank perturbation theory. *J AIAA* 32(4):836–842
14. Doebling SW (December 1996) Minimum-rank optimal update of elemental stiffness parameters for structural damage identification, *J AIAA* 34(12):2615–2621
15. Yuen KV (January 2010) Efficient model correction method with modal measurement. *J Eng Mech* 136(1):91–99
16. Barroso LR, Rodriguez R (February 2004) Damage detection utilizing the damage index method to a benchmark structure. *J Eng Mech* 130(2):142–151
17. Tarazaga PA, Halevi Y, Inman DJ (August 2009) Modified quadratic compression method for mass and stiffness updating. *Mech Syst Signal Process* 23(6):1773–1783
18. Hu SLJ, Li H, Wang S (May 2007) Cross-model cross-mode method for model updating. *Mech Syst Signal Process* 21(4):1690–1703
19. Burton TD, Farrar CR, Doebling SW (1998) Two methods for model updating using damage Ritz vectors. In: Proceedings of the international modal analysis conference-IMAC 16th, February 2–5 1998, Santa Barbara, CA, pp 973–978
20. Chu CC, Milman MH (December 1992) Eigenvalue error analysis of viscously damped structures using a Ritz reduction method. *J AIAA* 30(12):2935–2944
21. Yang YB, Chen YJ (January 2009) A new direct method for updating structural models based on measured modal data. *J Eng Struct* 31(1):32–42
22. Weng JH, Loh CH, Wong J-H, Loh CH, Yang JN (2009) Experimental study of damage detection by data-driven subspace identification and finite element model updating. *J Struct Eng ASCE* 135(12):1533–1544
23. Law SS, Shi ZY, Zhang LM (November 1998) Structural damage detection from incomplete and noisy modal test data. *J Eng Mech* 124(11):1280–1288
24. Chopra AK (2007) Dynamics of structures: theory and applications to earthquake engineering, 3rd edn. Prentice Hall, Upper Saddle River
25. Loh CH, Weng JH (2009) Damage detection using stochastic subspace identification with partial measurements. In: Proceedings of 7th international workshop on structural health monitoring, Stanford, 2009

Chapter 27

Theory Based Sensitivity Analysis and Damage Detection of Steel Roof Sheeting for Hailstone Impact

P. Sharafi, Lip H. Teh, and Muhammad N.S. Hadi

Abstract In this paper, a first-order design sensitivity analysis is presented for dynamics responses of roof sheeting under hailstone impacts. The presented design sensitivity analysis computes the rate of various response changes with respect to the relevant design variable for roof sheeting. For this purpose, exploiting the finite element method, the dependence of response measures, such as deflection, stress and strain on the thickness and material properties of the steel sheeting, is implicitly defined. Then the minimum required thickness for each steel grade under different loading conditions for sheeting, are suggested by considering two conditions according to the hailstones sizes: no damage (yielding) for hailstones of small sizes (20 mm or less) and no penetration (failure) for hailstones of large sizes (up to 100 mm).

Keywords Sensitivity analysis • Roof sheeting • Hailstone impact • Damage detection

27.1 Introduction

The profiled sheeting has been widely used for roofing because of the high strength to weight ratio and ease of assembly. Due to the variety of sheeting available in the market, finding the optimum type for different applications is necessary. Cold-formed profiled metal sheeting and decking are well-established construction products and manufacturers make enormous efforts to keep these products competitive in terms of the strength and maintenance. In the past, this has generally involved extensive testing.

Cold formed steel roof sheeting combines low weight and high strength and is economical in use. However, the cost of sheeting is an estimated 60 % of the total cost of steelwork in large structures such as industrial buildings and warehouses [1]. Therefore, knowledge of the dynamic behavior of mechanical structures is essential for their design and optimization. The use of thinner sheets and the introduction of new materials have meant that the stiffness and dent and failure resistance of exterior panels have become more focused in the cold-formed sheeting industry during the last years. In the industry there is increasing demand for higher-quality sheeting, better functional properties and lower weight. The demand for weight reduction has led to thinner sheets and greater use of high-strength steels.

Panel stiffness, dent and failure resistance are complex phenomena and functions of many parameters, such as the panel geometry and curvature, the support conditions, the sheet thickness, the material properties of the sheet material, the load level and load type. The influence of some of such parameters on the stiffness and resistance are rather trivial, such as the thicker the sheet, the higher is the stiffness and the failure and dent resistance, and the higher the yield stress of the material, the higher is the dent resistance. The influence of other parameters is non-trivial and difficult to predict [2].

An important factor in the cost of steel roof sheeting is the cost of maintenance. A potentially significant component of this maintenance cost is the cost of repairing or replacing hail damaged sheets. It is important to be able to estimate the incidence of damaging hail for sheeting of different sizes and properties so that the cost of steel roof sheeting can be compared with other options on an equitable basis, and so that hail resistant sheeting can be optimized for different hail prone regions.

To minimize the occurrence of denting or failure caused by hailstone, and to achieve sufficient stiffness for roof sheeting, an appropriate combination of design, material properties and thickness is required. In order to be able to achieve this optimal

P. Sharafi (✉) • L.H. Teh • M.N.S. Hadi

School of Civil, Mining and Environmental Engineering, University of Wollongong, Northfields Avenue, Wollongong, NSW 2522 Australia
e-mail: ps170@uow.edu.au; lteh@uow.edu.au; muhammad_hadi@uow.edu.au

combination, improved knowledge about the resistance and sheeting stiffness is required. It has been proved that although there seems to be no simple relation between the stiffness and dent resistance, the lower stiffness of the panel, the better the dent resistance, and the static dent resistance is directly proportional to the final yield stress of the material [2].

The estimation of risk of hail damage requires a determination of the size of hailstone needed to damage a given structure. A structural surface is generally tested or simulated by propelling artificial hailstones against it at the velocities with which natural hailstones of like masses would fall.

Hail impact damage has been the subject of many studies over the past few decades. Koontz [3] published a paper on ice impact damage, which took into account the effects of wind on the impact force of hail. He came to the conclusion that the vertical freefall velocity of hail, combined with the horizontal velocity of the wind, creates a greater impact force than that of freefalling hail. This was proven by Koontz using trigonometry and the addition of vectors. He also proved through mathematics that the impact force of hail increases exponentially as the mass and velocity of hail increase. Cox and Armstrong [4] described a statistical model for estimating the risk of impacts by large hail on any ground installation (such as a solar collector array). The model is based on data for three frequency distributions: hailstone size, hail fall count (number of hailstones per square meter per storm), and number of hail days per year. Noon [5] devoted a book chapter to the effects of hail on a roof. Noon reported that the damage threshold for asphalt shingles is 50 mm in diameter for roofs that are constructed of quality materials and are properly installed. Noon also found mathematically that hails strike damage increases as the angle which the hail strikes the roof nears 90 degrees (i.e., perpendicular strike). He also reported that hail striking soft metal surfaces leaves dents up to half the size of the hail that struck the subject residence. Thus, one can estimate the maximum size of hail that struck a building's finished surfaces by doubling the size of the largest hail strike dents observed on soft metal surfaces such as box vents, gutters, and downspouts.

In recent years, the development of explicit codes based on Finite Element Method (FEM) and the progresses in computer technology have made it possible to simulate complex problems such as the simultaneous impact of hailstones onto structure. A numerical model validated against experimental data is both a reliable tool to investigate the consequence of a hail impact and a feasible framework to develop high resistance low-weight structures.

In this research, the consequences of a hailstone impact onto solid formed roof sheeting in terms of damages are investigated. Hailstone impacts are low energy impacts (low-weights and high-velocities), and consequently are likely to cause stress concentrations in the inter-ply regions where large differences of stiffness exist. First, the characteristics of hailstone are discussed, referring to the most recent research on ice modeling. Then a sensitivity analysis of the model, in relation to the involved parameters, is performed that shows how sensitive each parameter is to the variations of design variables. To that end the impact of the hailstone onto sheeting of various properties is simulated and, the results are discussed and a first-order design sensitivity analysis is presented for the responses of roof sheeting under hailstone impacts. The presented design sensitivity analysis computes the rate of various response changes with respect to the relevant design variable for roof sheeting. For this purpose, exploiting the finite element method, the dependence of response measures, such as deflection, stress and strain on the thickness and material properties of the steel sheeting, is implicitly defined. Finally minimum required thickness for each steel grade under different loading conditions for sheeting, are suggested by considering some conditions according to the hailstone sizes.

27.2 Hailstone Properties

Each year, hail causes about billions of dollars worth of damage to residential roofs. Hailstorms can potentially cause damage to any exposed objects, especially when hailstone diameters exceed 20 mm. The level of hail damage depends on the size, density, falling velocity and distribution of the hailstones, as well as the climate and the building structure. Roofs are very susceptible to damage. Hailstones can cause more damage to low slope roofs than to high slope roofs, because the most damage occurs at a 90-degree angle impact. Therefore, a steep slope (6:12 and greater) will improve the impact resistance of a roof. In general, hailstone damage can be categorized into two types: aesthetic damage and functional damage. Aesthetic damage is simply damage that has an adverse effect on appearance, but does not affect the performance of the roof. Functional damage results in diminished water shedding ability and a reduction in the expected service life of the roof [6].

Hailstones are highly variable in properties such as shape, density, and frangibility. These properties affect factors such as the kinetic energy delivered to the plate, the period during which energy is delivered, and the area over which the energy is distributed. The size of hail has been reported from as small as 6 mm to sizes reportedly larger than softballs, with diameters exceeding 127 mm. The frequency of hail and the number of impacts for any given area also varies.

The shape of hailstones can be spherical or somewhat elliptical. In this study, spherical hailstones are utilized for modeling the impact. Studies have also shown that hailstones can vary in density depending on the weather, and ranges from 500 to 700 kg/m³. At clod regions the density of hail will increase and approaches that of ice (approximately 900 kg/m³ [3]. In this study it is assumed that hail has a density which approximates that of ice.

There is a relatively wide range of scatter of hailstone (ice) tensile strength, from 0.7 to 3.1 MPa. The average tensile strength of ice from published investigations is 1.43 MPa in the temperature range -10 to -20°C . Over this temperature range, the compressive strength of ice ranges between 5 and 25 MPa [7]. The elastic modulus and Poisson's ratio of polycrystalline ice has been measured by subjecting plates of ice to biaxial bending [6]. At a temperature of -10°C for measurements on ice plates that were 0.5 min diameter, the Young's modulus of ice was reported in the range of 9.7–11.2 GPa and Poisson's ratio was 0.29–0.32 [7].

The tensile strength of hailstone decreases with increasing ice grain diameter. The tensile strength of hailstone decreases with increasing test specimen volume, as well. The relationships are as follows:

$$\sigma_2 = \sigma_1 + \frac{K}{\sqrt{d_n}} \quad (27.1)$$

$$\frac{\sigma_2}{\sigma_1} = \left(\frac{V_1}{V_2} \right)^{1/5} \quad (27.2)$$

where σ is applied tensile stress (which is assumed to be uniform over the stressed volume of the material), V is stressed volume, d_n is the hailstone size and K is a constant which is set based on the temperature [7].

27.3 Impact Analysis for Roof Sheeting

In order to determine the minimum required thickness for roof sheeting under hailstone impact, in this study, sheets of three different grades and eight different thicknesses are considered. Two different sizes of hail stones are investigated. The procedure is performed by theoretical based computer simulation and no experimental or laboratory method is included. For simulating and modeling ANSYS-13 [8], as a robust structural engineering tool, is employed.

Based on the investigations carried out on some models and the literature [9], since most critical impacts take place when the angle of impact is 90 degrees, a horizontal flat steel sheet is taken as the model. Therefore, the only factors to study the effects of hail stone impact on corrugated panels seem to be the thickness and grade of the steel sheeting.

Profiled steel cladding systems commonly used in Australia and its neighboring countries are made of very thin (0.35 mm) high strength steel (with a minimum yield stress of 750 MPa). The aim is to determine the minimum required thicknesses for each steel grade under hailstone impact condition. As shown in Table 27.1, steel sheets of three different grades and eight different thicknesses are investigated.

In order to model the hailstone impact, we used the standard practice for determining resistance of solar collector covers to hail by impact with propelled ice balls (ASTM E822-92-2009) [10]. Therefore, the resultant velocity corresponding to the ice ball diameter is determined as follows:

$$v_r = \sqrt{v_t^2 + v_w^2} \quad (27.3)$$

where v_r is the resultant velocity of hailstones, v_t is terminal velocity of ice ball which equals $14.04\sqrt{d_n}$, v_w is the wind velocity which is considered to be 20 m/s, and d_n is the hailstone diameter in centimeter.

Two different conditions are considered according to the hailstone sizes: no damage (yielding or dent) for size 20 mm and no penetration (failure) for size 90 mm. Accordingly, two different sizes of hail stones are investigated as shown in Table 27.2. Dent and failure simulation are carried out based on the dynamic analysis of shells.

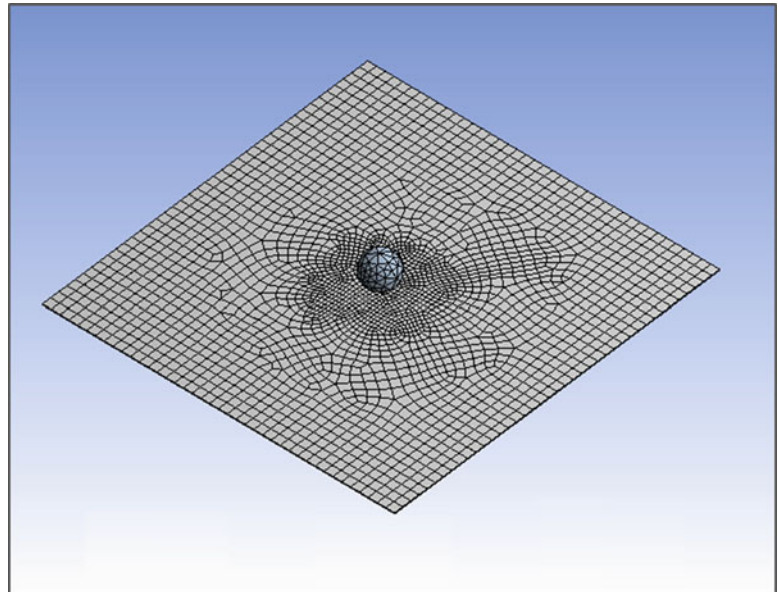
In this investigation, the attention is focused solely on the stiffness at the panel center. In structural analysis stiffness is the resistance of a body to deformation. In the case of thin panels, stiffness is defined as the amount of resistance to elastic deformation which causes a sense of quality. Stiffness is, furthermore, the resistance to a point force exerted normally to the surface. Stiffness varies, therefore, from point to point on a panel, being least at the center and increasing to the panel edge. Figure 27.1 shows a graphical scheme of the impact model, and Table 27.3 demonstrates the simulation details of the modeling.

Table 27.1 Mechanical properties of steel sheets

Steel type	Thickness (BMT ^a mm)	Yield strength (MPa)	Yield strain	Ultimate strength (Mpa)	Ultimate strain
ST1	0.55	300	0.0015	340	0.18
	0.60	300	0.0015	340	0.18
	0.80	300	0.0015	340	0.18
ST2	0.35	550	0.00275	550	0.01
	0.42	550	0.00275	550	0.01
	0.48	550	0.00275	550	0.01
	0.60	550	0.00275	550	0.02
	0.80	550	0.00275	550	0.02
	0.90	550	0.00275	550	0.02
	1.00	550	0.00275	550	0.02
ST3	0.35	750	0.00375	750	0.01
	0.42	750	0.00375	750	0.01
	0.48	750	0.00375	750	0.01
	0.55	750	0.00375	750	0.01
	0.60	750	0.00375	750	0.02
	0.80	750	0.00375	750	0.02
	0.90	750	0.00375	750	0.02
	1.00	750	0.00375	750	0.02

^aBase metal thickness**Table 27.2** Hail stone velocity

Hail stone diameter	Wind velocity (m/s)	Terminal velocity (m/s)	Resultant velocity (m/s)
20 mm	20	19.86	28.18
90 mm	20	42.12	46.63

Fig. 27.1 Impact model for hailstone and steel sheet**Table 27.3** Simulating details for hail stone impact

Simulating details	Hail stone size	
	20 mm	90 mm
Dimension of Plate	200*200	400*400
Supports Condition	Four edges fixed	Four edges fixed
Minimum Mesh Size	1 mm	1 mm
Maximum Mesh Size	5 mm	5 mm
Method of Analysis	Explicit dynamic	Explicit dynamic
Duration of Analysis	0.05 sec	0.05 sec

Most common metal roof materials are galvanized coated sheet steel, which are either zinc or aluminum–zinc alloy coated steel respectively. The dent resistance of the coated sheet steel is proportional to the square of the yield strength multiplied by the fourth power of the sheet thickness of the steel substrate, and is independent to the metallic coating [6]:

$$\text{Dent resistance} \propto (\text{Yield Strength})^2 \times (\text{Sheet Thickness})^4 \quad (27.4)$$

The impact scenario and the test facilities were modeled in detail. The roof sheeting as the target body was modeled with eight-nodes solid elements and the steel plate with four-nodes shell elements. Figures 27.4 through 27.10 show two different behavior of steel plates in impact. In order to determine the optimum thickness for each grade the following conditions are taken into consideration:

- No damage occurs for hail stone size 20 mm. That is, there should not be any points on the surface in which the equivalent elastic strain exceeds the yielding strain.
- No penetration occurs for hail stone size 90 mm. That is, there should not be any points on the surface in which the equivalent elastic strain exceeds the failure strain.

27.4 Sensitivity Analysis and Optimization

Design sensitivity analysis (DSA) is used to compute the rate of performance measure change with respect to design variable changes. Structural design sensitivity analysis concerns the relationship between design variables available to the design engineer and structural responses determined by the laws of mechanics, and the dependence of response measures such as displacement, stress and strain on the material property, sizing, component shape, and configuration design variables is implicitly defined through the governing equations of structural mechanics.

In the DSA stage, the design sensitivity coefficients of the performance measures with respect to the design parameters defined in the pre-processing stage are computed. In dimension DSA, of the structural domain is treated as the design parameter. The relationship between dimension variations of a continuous domain and the resulting variations in structural performance measures can be described using the derivative of continuum mechanics. The process is shown in Fig. 27.2.

The continuum form of the governing equation of the structure can be written as follows [11].

$$a_{\Omega_\tau}(z_\tau, \bar{z}_\tau) = l_{\Omega_\tau}(\bar{z}_\tau) \quad \text{for all } \bar{z}_\tau \in Z_\tau \quad (27.5)$$

where \bar{z}_τ is a virtual displacement, Z_τ is the space of kinematically admissible virtual displacements that satisfy the regularity conditions and boundary conditions, and $a_{\Omega_\tau}(z_\tau, \bar{z}_\tau)$ and $l_{\Omega_\tau}(\bar{z}_\tau)$ are the energy bilinear and load linear forms, respectively. The performance measures, such as displacement and stress, can be written in integral form as follows [11].

$$\Psi = \iint_{\Omega_\tau} g(z_\tau, \nabla z_\tau) d\Omega_\tau \quad (27.6)$$

For the direct differentiation method, the variation of the performance measure Ψ can be written as

$$\Psi' = \iint_{\Omega_\tau} [g_z \dot{z} + g_{\nabla z} \nabla \dot{z} - g_z (\nabla z^T \mathbf{V}) - g_{\nabla z} \nabla (\nabla z^T \mathbf{V})] d\Omega + \int_\Gamma g(V^T n) d\Gamma \quad (27.7)$$

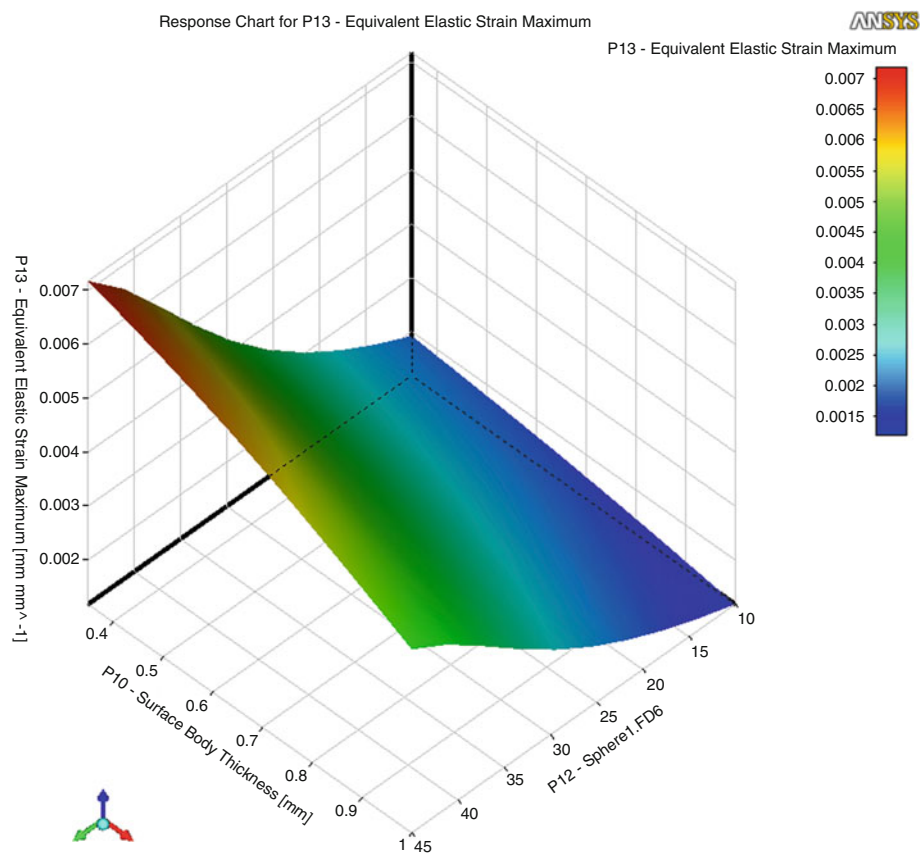
where the material derivative \dot{z} , is the solution of the sensitivity equation

$$a_{\Omega_\tau}(\dot{z}, \bar{z}) = l'_v(\bar{z}) - a'_v(z, \bar{z}) \quad \text{for all } \bar{z}_\tau \in Z_\tau \quad (27.8)$$



Fig. 27.2 Design sensitivity analysis process

Fig. 27.3 Equivalent elastic strain for 0.55 mm ST1 sheets due to impact of a 20 mm hail stone



In this study, the dependence of deflection, stress, and strain of the roof sheeting on the steel properties (steel grade) and the thickness of the plates is investigated. The impact is simulated for three different steel grades and eight different sheeting thicknesses as stated in Table 27.1. Then the minimum thickness required for each case is determined in an optimization process. To that end, we take advantages of the first order optimization method of ANSYS13 based on the sensitivity analysis of the responses. Figure 27.3 shows the sensitivity of the maximum equivalent elastic strain (Von-Mises) with respect to the thickness of sheeting, diameter of the hailstone for ST1 sheeting.

As demonstrated in Table 4, the minimum thickness needed to meet the requirements is 0.55 mm for both sizes of hail stones for the steel type one. This means that, for ST1, no point on a 0.55 mm sheet neither yields due to impact of a 20 mm hail stone nor fails due to impact of a 90 mm hail stone. As shown in Fig. 27.4, the maximum equivalent (Von-Mises) elastic strain due to impact of a 20 mm hail stone is 0.0009 which is 60% of yield strain for 0.55 mm ST1 sheets. It can be seen from Fig. 27.5 that the maximum equivalent elastic strain due to impact of a 90 mm hail stone is 0.0014 which is 93% of ultimate strain for 0.55 mm ST1 sheets.

For the steel type two, the minimum needed thicknesses to meet the requirements are 0.42 and 0.60 millimeter for impacts of 20 mm and 90 mm hail stones respectively. Figure 27.6 shows that the maximum equivalent (Von-Mises) elastic strain, due to impact of a 20 mm hail stone is 0.00155 which is 56% of the yield strain for 0.42 mm ST2 sheets. It can be seen from Fig. 27.7 that the maximum equivalent elastic strain, due to impact of a 90 mm hail stone is 0.00144 which is 72% of ultimate strain for 0.60 mm ST1 sheets. Figure 27.8 shows that this impact causes some parts of the sheet to reach the ultimate strain in 0.55 mm ST2 sheets.

Regarding the steel type three, the minimum needed thicknesses to meet the requirements are 0.35 and 0.60 millimeter for impacts of 20 mm and 90 mm hail stones respectively. Figure 27.9 shows that the maximum equivalent (Von-Mises) elastic strain, due to impact of a 20 mm hail stone is 0.00242 which is 88% of yield strain for 0.35 mm ST3 sheets. It can be seen from Fig. 27.10 that the maximum equivalent elastic strain, due to impact of a 90 mm hail stone is 0.00144 which is 72% of ultimate strain for 0.60 mm ST1 sheets.

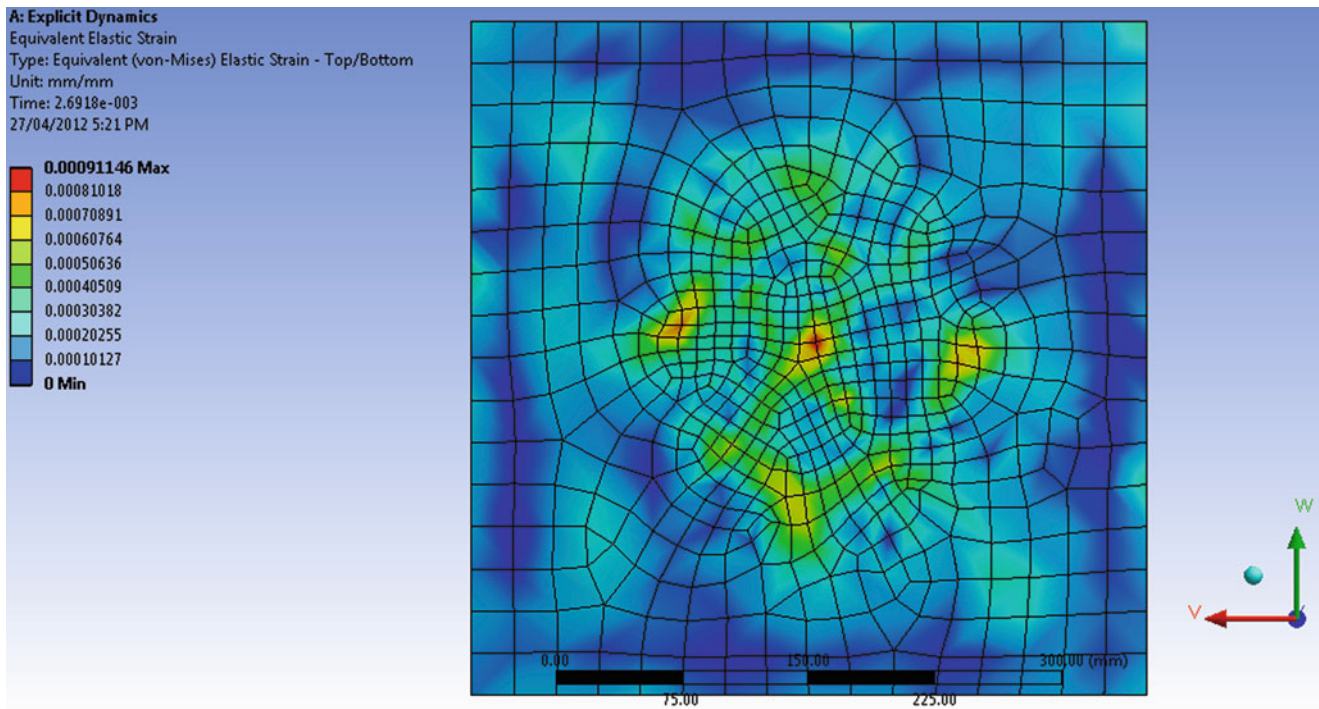


Fig. 27.4 Equivalent elastic strain for 0.55 mm ST1 sheets due to impact of a 20 mm hail stone

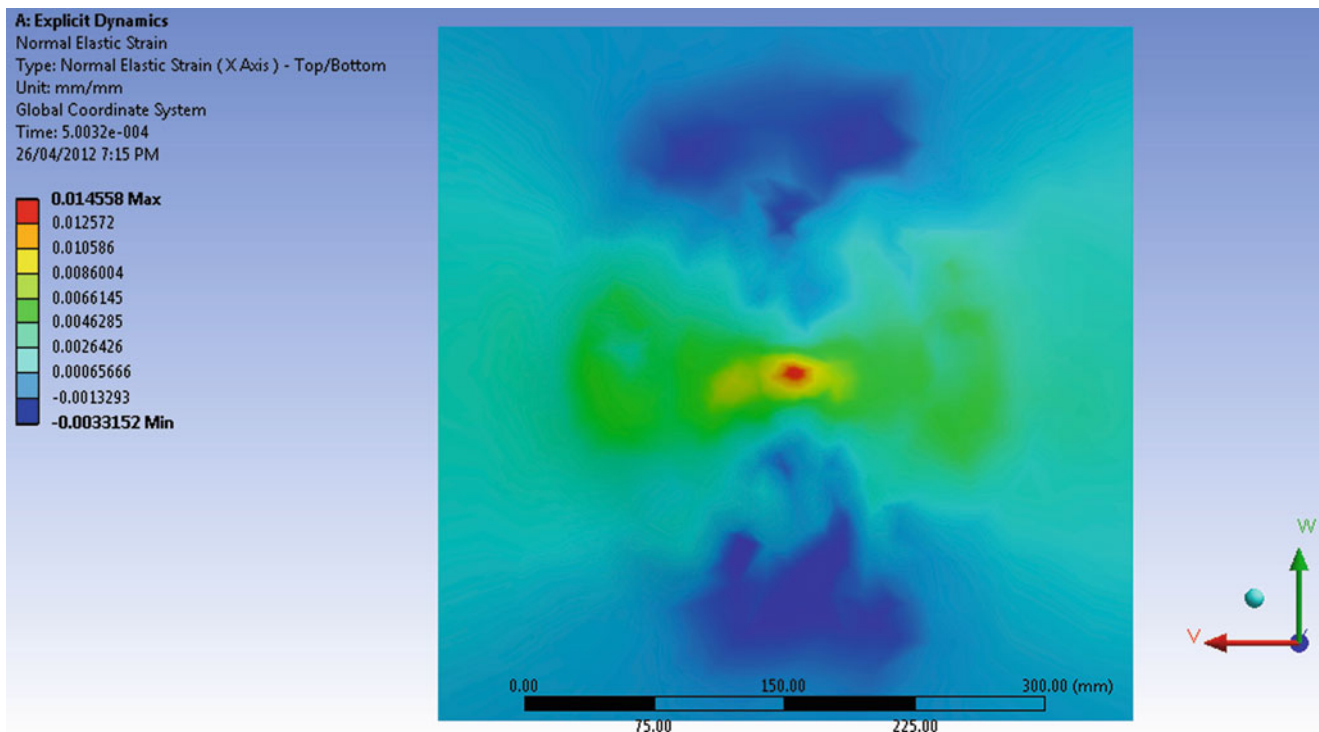


Fig. 27.5 Equivalent elastic strain for 0.55 mm ST1 sheets due to impact of a 90 mm hail stone

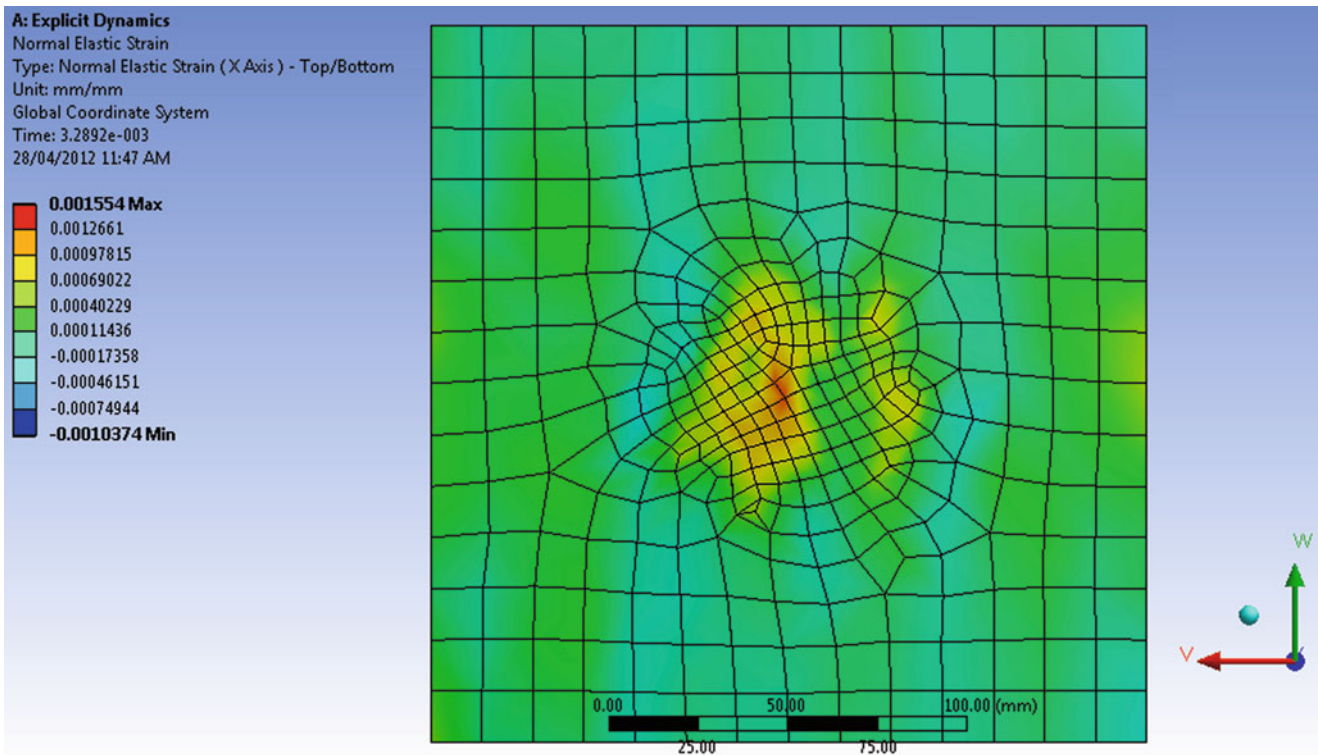


Fig. 27.6 Equivalent elastic strain for 0.42 mm ST2 sheets due to impact of a 20 mm hail stone

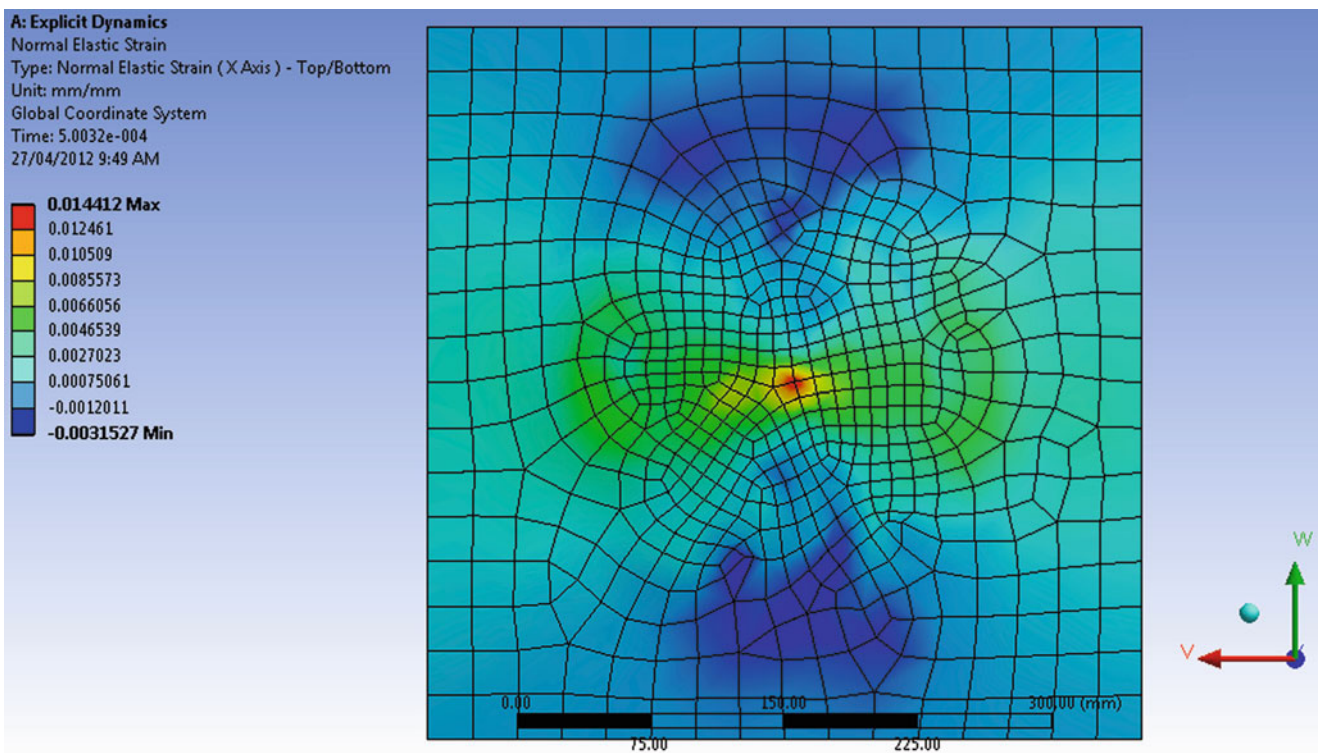


Fig. 27.7 Equivalent elastic strain for 0.60 mm ST2 sheets due to impact of a 90 mm hail stone

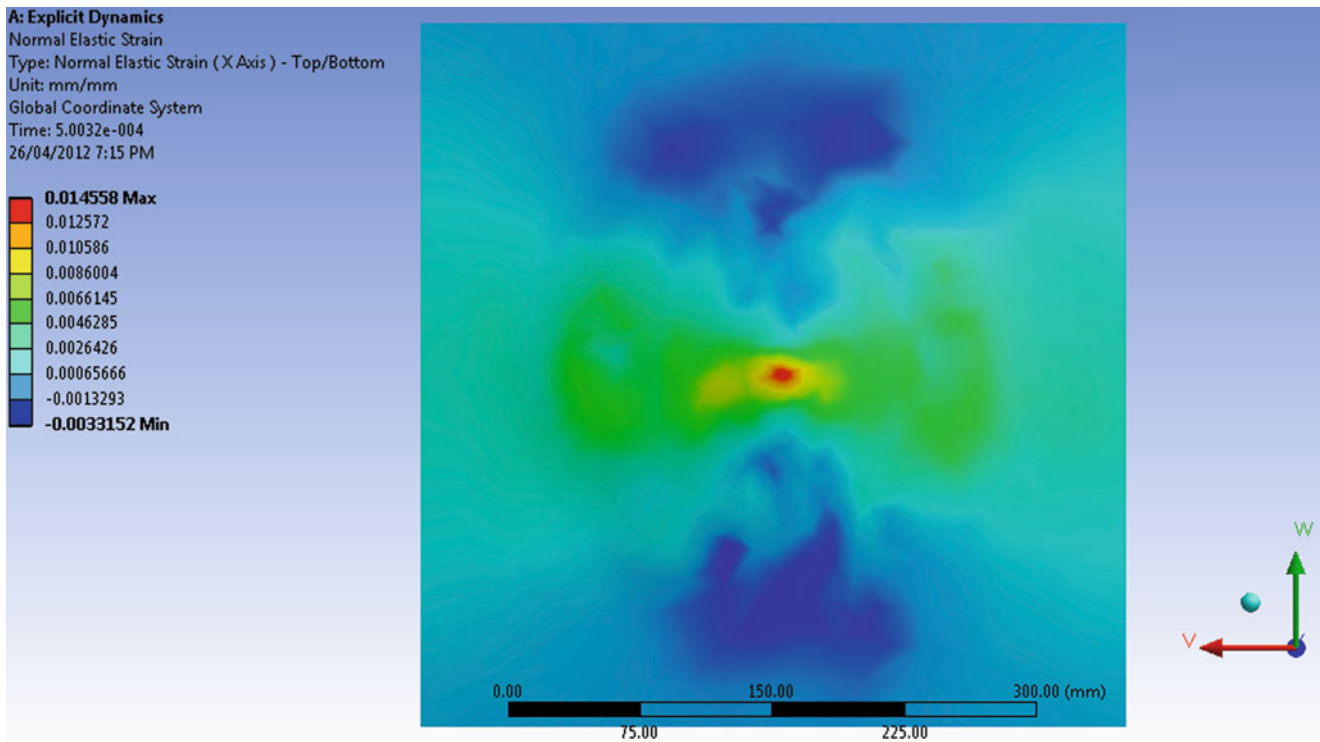


Fig. 27.8 Equivalent elastic strain for 0.55 mm ST2 Sheets due to impact of a 90 mm hail stone

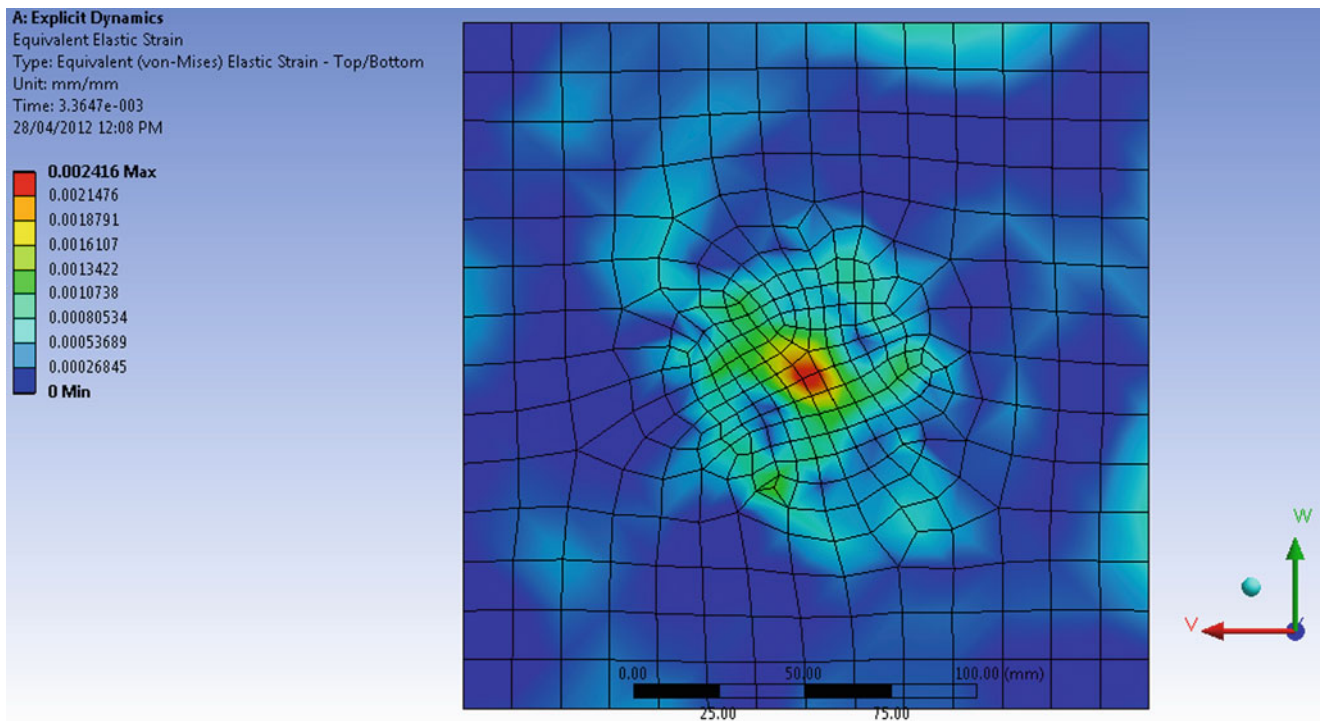


Fig. 27.9 Equivalent elastic strain for 0.35 mm ST3 sheets due to impact of a 90 mm hail stone

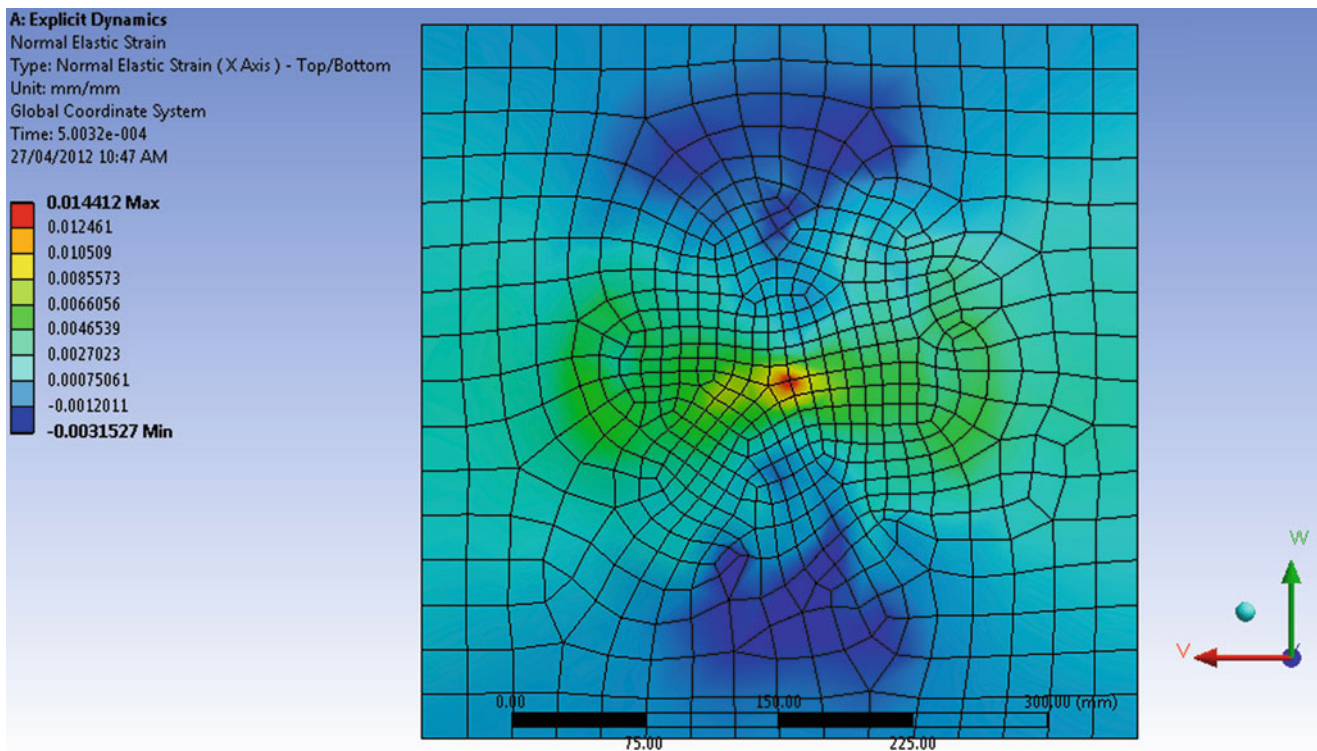


Fig. 27.10 Equivalent elastic strain for 0.60 mm ST3 sheets due to impact of a 90 mm hail stone

27.5 Concluding Remarks

Using the finite element method, the dependence of response measures, such as deflection, stress and strain on the thickness and material properties of the steel sheeting, was implicitly investigated. Then, minimum required thickness for each steel grade under hailstone impact for sheeting, are suggested by considering two conditions according to the hailstones sizes: no damage (yielding) for hailstones of small sizes (20 mm or less) and no penetration (failure) for hailstones of large sizes (up to 100 mm).

Finally, a first-order design sensitivity analysis was presented for dynamics responses of roof sheeting under hailstone impacts. The presented design sensitivity analysis computes the rate of various response changes with respect to the relevant design variable for roof sheeting.

References

1. Pimpasakdi S, Albermani FG, Kitipornchai S (2004) Interactive analysis and design of cold-formed steel cladding system. *J Constr Steel Res* 60(10):1409–1423
2. Holmberg S, Thilderkvist P (2002) Influence of material properties and stamping conditions on the stiffness and static dent resistance of automotive panels. *Mater Design* 23(8):681–691
3. Koontz J (1991) The effects of hail on residential roofing products. In: International symposium on roofing technology. NRCA, New Mexico, 1991
4. Cox M, Armstrong PR (1981) A statistical model for the incidence of large hailstones on solar collectors. *Solar Ener* 26(2):97–111
5. Noon RK (2000) Forensic engineering investigation. CRC Press, Florida, USA
6. United State Steel Corporation (2005) Hail damage on coated sheet steel roofing. United State Steel Corporation, Pittsburgh
7. Petrovic JJ (2003) Review mechanical properties of ice and snow. *J Mater Sci* 38(1):1–6
8. Ansys_Inc (2012) ANSYS 13. <http://www.ansys.com/About+ANSYS>
9. Greenfield SH (1969) Division, I.F.a.T.B.R., Hail resistance of roofing products. Building Research Division, U.S. Institute for Applied Technology; for sale by the Superintendent of Documents U.S. Government Printing Office
10. Astm-E822-92 (2009) Standard practice for determining resistance of solar collector covers to hail by impact with propelled ice balls. In: ASTM standards. West Conshohocken, doi: 10.1520/E0822-92R09
11. Chang K-H et al (1995) Design sensitivity analysis and optimization tool (DSO) for shape design applications. *Comput Syst Eng* 6(2):151–175

Chapter 28

Long-Term Dynamic Monitoring of an Offshore Wind Turbine

Christof Devriendt, Filipe Magalhães, Mahmoud El Kafafy, Gert De Sitter, Álvaro Cunha, and Patrick Guillaume

Abstract Future Offshore Wind Turbines will be hardly accessible; therefore, in order to minimize O&M costs and to extend their lifetime, it will be of high interest to continuously monitor the vibration levels and the evolution of the frequencies and damping ratios of the first modes of the foundation and tower structures. Wind turbines are complex structures and their dynamics vary significantly in operation in comparison to stand still parked conditions due to changes in operating conditions or changing ambient conditions. State-of-the-art operational modal analysis techniques can provide accurate estimates of natural frequencies, damping ratios and mode shapes. To allow a proper continuous monitoring during operation, the methods have been automated and their reliability improved, so that no human-interaction is required and the system can track changes in the dynamic behaviour of the offshore wind turbine. This paper will present and discuss the approach and the first results of a long-term monitoring campaign on an offshore wind turbine in the Belgian North Sea.

Keywords Monitoring • Offshore wind turbine • Operational modal analysis • Automated • Signal processing

28.1 Introduction

28.1.1 Relevance

Online monitoring of wind turbines is a more and more critical issue as the machines are growing in size and offshore installations are becoming more common. To increase the power generation and limit the weight, the turbines are becoming structurally more flexible, thus an accurate prediction of their dynamic behavior is mandatory. On the other hand, inspection and maintenance for offshore installations are much more cumbersome and expensive than for onshore turbines. Thus, a remote monitoring application with the ability to predict structural changes can help to reduce catastrophic failures and their associated costs.

Many large scale offshore wind farm projects use monopile foundations to obtain a cost effective design. During the design of these monopile structures fatigue due to combined wind and wave loading is one of the most important problems to take into account. Damping ratios are crucial for lifetime predictions as the amplitude of vibrations at resonance are inversely proportional to these ratios. The overall damping of the first bending mode of an offshore wind turbine consists of a combination of aerodynamic damping, damping due to vortex shedding, and damping due to constructive devices, such as a tuned mass damper, and additional offshore damping, e.g. structural damping [1]. Compared to onshore support structures, the additional damping is further influenced by effects such as soil damping and hydrodynamic damping. Real damping ratios are very difficult to predict by numerical tools and therefore measurements on existing offshore wind turbines are crucial to verify the existing design assumptions [2].

C. Devriendt (✉) • M. El Kafafy • G. De Sitter • P. Guillaume
Acoustics and Vibration Research Group, Vrije Universiteit Brussel, Pleinlaan 2 B, B-1050, Elsene, Belgium
e-mail: cdevrien@vub.ac.be

F. Magalhães • Á. Cunha
ViBest, Faculty of Engineering, University of Porto, R. Dr. Roberto Frias 4200-465, Porto, Portugal



Fig. 28.1 View on Belwind wind farm (*left*) location Belwind wind farm (*center*) park layout (*right*)

When it comes for example to monopile foundations, scouring and reduction in foundation integrity over time are especially problematic because they reduce the fundamental structural resonance of the support structure, aligning that resonance more closely to the lower frequencies at which much of the broadband wave and gust energy is contained, or because they align this resonance more closely with 1P. Thus a lower natural frequency means that more energy can create resonant behavior increasing fatigue damage [3]. Continuous monitoring of the effect of scour on the dynamics of the wind turbine will therefore help to make a better decision on when to plan maintenance activities on the scour protection system.

Thus, in order to minimize O&M costs and to extend lifetime it will be of high interest to continuously monitor the vibration levels and the evolution of the frequencies and damping of the first modes of the foundation structure. This will allow us to identify and avoid resonant behavior and to verify the existing design assumptions. It will also enable us to perform accurate lifetime prediction and online lifetime evaluation and it will be able to give indications about the current state of the soil and foundation characteristics.

In this context, the development and validation of tools for automatic identification of the different dynamic parameters based on the measurement of the dynamic response of wind turbines during different operating conditions is fundamental, as the success of subsequent damage detection algorithms depends on the accuracy of these identified parameters. Furthermore, it is essential that these routines are sufficiently robust to run on an online basis, in order to provide in almost real-time parameters that characterize the wind turbine's condition.

This paper will present and discuss the approach and some results of a long-term monitoring campaign on an offshore wind turbine. The measurement campaign is performed at the Belwind wind farm, which consists of 55 Vestas V90 3 MW wind turbines. The wind farm is located in the North Sea on the Bligh Bank, 46 km off the Belgian coast (Fig. 28.1). The tests are performed on the BBCO1-turbine that is located in the north of the wind farm directly next to the offshore high voltage substation (OHVS).

28.1.2 Applicability of Operational Modal Analysis

Identification of modal parameters on a full-scale operating wind turbine is particularly difficult and in the research community a lot of effort still goes into the development of suitable methods to tackle this problem [4]. Classical experimental modal analysis methods cannot be applied because the input force due to the wind and the waves cannot be measured. For this reason, operational modal analysis methods were developed to identify the modal parameters from the response of a mechanical structure in operation to unknown random perturbations [4–7]. These methods work under the assumption that the system is linear time invariant during the analyzed time interval and that the excitation is white noise within the frequency band of interest.

Due to the presence of rotating components and their corresponding harmonic force contributions or due to the wind wave interaction with the structure, introducing colored noise contributions; wind turbines can fail to comply with the operational modal analysis assumptions. Depending on the operating conditions, some of the non-white noise force contributions may coincide with or be close to a natural frequency of the wind turbine, thus masking its contribution and making the identification process to fail.

To solve these problems, current OMA methods need to be improved. Although some solutions have already been presented, they can usually only tackle one of the specific problems listed above [8]. Another difficulty is that in many applications such as helicopters or wind turbines the frequencies of the harmonic disturbances can vary in time. In order

to deal with time varying harmonic disturbances a new method was proposed in [9] based on parametric modeling of the frequency variation combined with the use of a maximum likelihood estimator.

Recently a complete new OMA approach, based on transmissibility measurements, was proposed that increases the reliability and applicability of OMA techniques [10]. This innovative new approach does no longer require the assumption that the forces are white noise sequences. Therefore this new approach makes it possible to apply OMA in the presence of arbitrary operational forces (colored noise, impacts). In recent work it was shown that the transmissibility based OMA approach is able to deal successfully with harmonics when the loads are correlated [11]. The proposed transmissibility based OMA approach therefore looks very appealing. However, despite the good results obtained so far there is a need for more basic research in order to continue to refine this approach and correctly position it in relation to other OMA methods.

In [12] the violation of the time invariance assumption in the case of operational wind turbines was discussed. During operation a wind turbine is subjected to different motions of the substructures, e.g. yaw-motion of the nacelle, the individual pitching of the blades and the overall rotation of the rotor. Rotor rotation represents a severe problem from structure invariance point of view [13]. However if one is interested in the fundamental tower modes the effect of the rotor can be considered as an external excitation [12]. During operation the yaw motion does not present a considerable problem for modal analysis as the yaw speed is very slow and the nacelle does not move constantly. Therefore it is possible to select datasets when the yaw does not change at all. Pitch-controlled wind turbines are designed to operate at variable speed, thus the assumption of linear time invariant system may not be valid. This poses a serious problem in the selection of an adequate length of the time signal for the analysis [5]. While the duration should be long enough to allow a proper estimation of modal parameters and in particular of damping values, on the other hand it is necessary to use signals obtained for “quasi-stationary” conditions to comply with the invariant system assumption. Different regimes can be identified e.g. pitch-regulated regime; RPM-regulated regime and parked conditions. Obviously in parked conditions the system is time invariant and OMA assumptions are fulfilled. Also in the RPM-regulated regime OMA is possible as the pitch is set to minimum and does not change a lot in time.

Therefore, we can conclude that, in order to achieve accurate OMA estimates, a pre-processing, that includes automatic selection of the time signals with a sufficient duration and almost stationary operating conditions, needs to be implemented.

28.2 Offshore Measurements

28.2.1 Description of the Wind Turbine

The tested wind turbine is placed on a monopile foundation structure with a diameter of 5 m and a wall-thickness of 7 cm. The hub-height of the wind turbine is on average 72 m above sea-level. Each transition piece is 25 m high. The actual water depth at the location of BBCO1 is 22.9 m and the monopile has a penetration depth of 20.6 m. The soil is considered stiff and mainly consists of sand. A schematic picture illustrating the foundation geometry and the wind turbine is shown in Fig. 28.2.

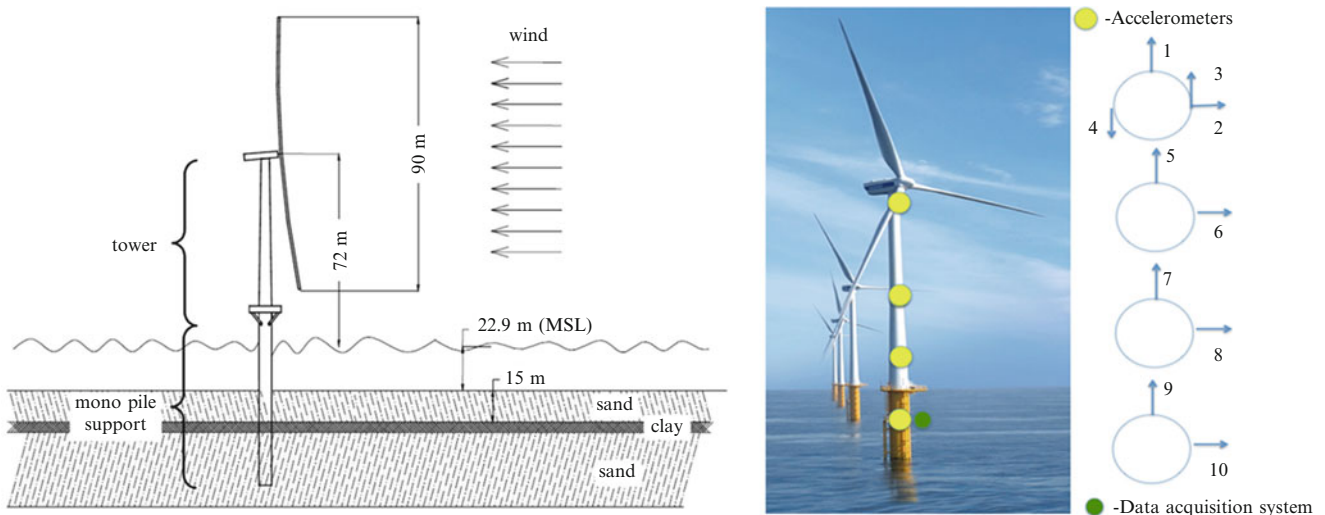


Fig. 28.2 Schematic picture instrumented wind turbine (left) measurement locations (right)

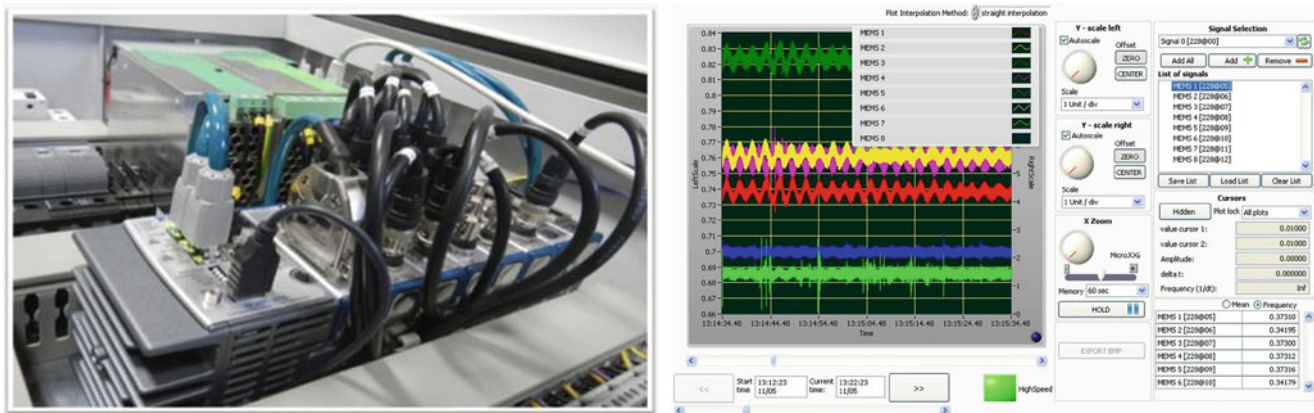


Fig. 28.3 Data acquisition system based on NI Compact Rio System (left) and logger software (right)

28.2.2 Description of the Monitoring System

The structures instrumented in this campaign are the tower and transition piece. Measurements are taken at 4 levels on 9 locations using a total of 10 sensors. The measurement locations are indicated in Fig. 28.2 by yellow circles. The locations are chosen based on the convenience of sensor mounting, such as the vicinity of platforms. The chosen levels are 67, 37, 23 and 15 m above sea level, respectively level 1 to 4. The interface level between the transition piece and the wind turbine tower is at 17 m above sea level. There are two accelerometers mounted at the lower three levels and four at the top level. The chosen configuration is primarily aimed at identification of tower bending modes. The two extra sensors on the top level are placed to capture the tower torsion. Accelerometers have been selected, which have a high sensitivity and are able to measure very low frequency signals. This is necessary considering that the modal frequencies of interest, for the wind turbine structure, are expected to be around 0.35 Hz, and the expected vibration magnitude is very low, especially during ambient excitation.

The data-acquisition system is mounted in the transition piece (green circle in Fig. 28.2). A Compact Rio system of National Instruments is used (Fig. 28.3). An important reason for choosing this particular type of system is its high flexibility to measure different types of signals, e.g. accelerations and strains, and its robustness. Since the project aims at characterizing the dynamics during a long period, it was also required that the data-acquisition system can be remotely accessed and is capable of automatic startup in case of power shutdowns.

The data acquisition software allows for the continuous monitoring of the accelerations. The software measures continuously and sends data every 10 min to the server that is installed onshore using a dedicated fiber that is running over the sea-bed. All data receives a time-stamp from a NTP timeserver in order to be able to correlate them with the SCADA and Meteo data. The measurements can be monitored real-time using the online scope-function.

In order to classify the operating conditions of the wind turbine during the measurements SCADA data (power, rotor speed, pitch angle, nacelle direction) is gathered at a sample rate of 1 Hz. To also monitor the varying environmental conditions, the ambient data (wind speed, wind direction, significant wave height, air temperature, ...) is being collected at 10 min intervals.

The data-acquisition system was programmed to acquire data with a sampling ratio of 5 kHz. Considering the frequency band of interest and in order to reduce the amount of data, the recorded time series have been filtered with a band-pass filter and re-sampled with a sampling frequency of 12.5 Hz. After the down sampling and filtering a coordinate transformation was performed. Since the accelerometers are mounted on the tower, in order to measure the vibrations along the axis of the nacelle, it is necessary to take the yaw-angle into account by transforming them into the coordinate system of the nacelle [13].

28.3 Continuous Dynamic Monitoring

During the long-term measurement campaign our aim is to continuously monitor the vibration levels and the evolution of the frequencies and damping values of some of the fundamental modes of the tower and foundation. Both the resonance frequencies and damping values are crucial to quantify the reliability and the lifetime of offshore wind turbines during their

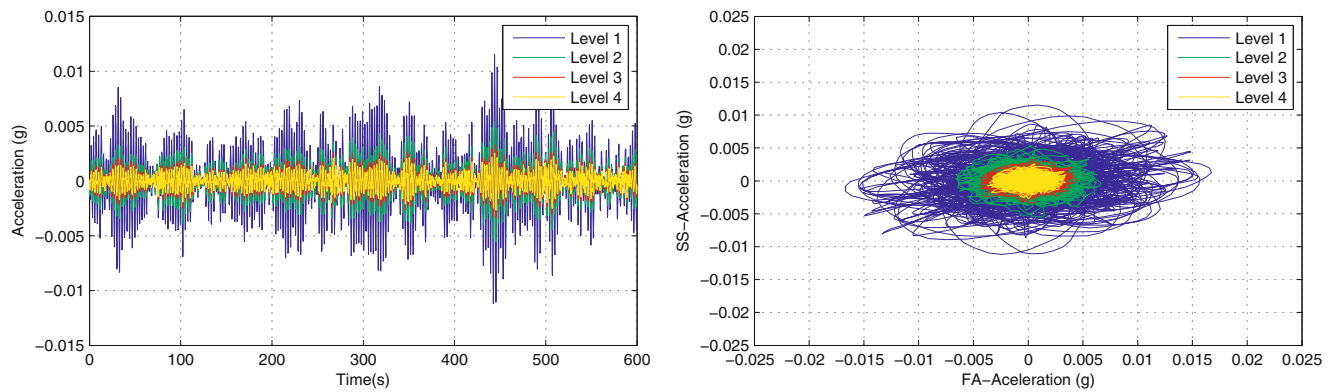


Fig. 28.4 Example measured accelerations during ambient excitation on 4 levels, with level 1 the highest level, in the fore-aft direction (*left*) movement seen from above (*right*)

life-cycle. These parameters will also be analyzed to see if they can provide indications about the current state of the soil and foundation characteristics, for e.g. monitoring scour development [3].

In order to perform continuous dynamic monitoring the following steps will be followed:

- Creation of a database with the original vibration data sampled at a high frequency including also the ambient data and the SCADA data with corresponding time-stamps.
- Pre-processing the vibration-data to eliminate the offset, reduce the sampling frequency and to transform them in the nacelle coordinate system
- Calculate statistical vibration parameters e.g. min, max, standard deviations and rms-values
- Estimation of modal parameters: resonant frequencies, damping values, mode shapes
- Creation of a database with processed results
- Display results

The monitoring considered in this paper has been performed on data collected during a period of 2 weeks. The inputs for the above steps are the 10-min time series measured by the 10 accelerometers. Each day 144 10-min files are processed, resulting in 144 values per day per considered parameter. In total 2016 data-sets have been analyzed during the presented monitoring period. Figure 28.4 shows an example of the accelerations measured in the fore-aft direction (direction aligned with the nacelle) during 10 min of ambient excitation. One can notice that during this data-set the movement of the tower is mainly in the direction of the nacelle, however a small side-to-side movement (direction perpendicular to the nacelle) is also present.

Figure 28.5 presents one of the plots, created by the monitoring-routines. The plot illustrates the daily variation of the root mean square (RMS) values of the acceleration time series, both in the FA and SS direction. This graphic already shows nicely some of the dynamic characteristics of an offshore wind turbine. The operational deflection shape of the wind turbine in parked conditions results in maximum vibration amplitudes at the upper level and minimum vibration amplitudes at the lowest level. We can also see that the RMS values reach twice a day to a maximum and minimum. This can be contributed to the changing wave periods, which vary accordingly between 3 sec (0.333 Hz) and 6 sec (0.166 Hz), respectively getting closer and further away from the resonance frequencies of the fundamental first bending modes of the wind turbine, which are located around 0.35 Hz

In Fig. 28.6 the corresponding SCADA data for the monitoring period is given. The wind speed varied between 0 and 16 m/s. The pitch angle was almost constant during the period of analysis, with a pitch angle of 78° or 88.3° . Most of the times the wind-turbine was idling with a speed lower than 1.3 rpm and sometimes the wind turbine was in parked conditions. Both conditions allow us to sufficiently comply with the time-invariant OMA assumptions and avoid the presence of harmonic components in the frequency range of interest.

To allow a proper structural health monitoring during operations, based on e.g. the dynamic properties of the foundation and other wind turbine components, a fast and reliable solution that is applicable on industrial scale has been developed. The operational modal analysis methods have been automated and their reliability improved, so that no human interaction is required.

In this work the algorithm used to automate the identification process is a combination of the following 4 steps:

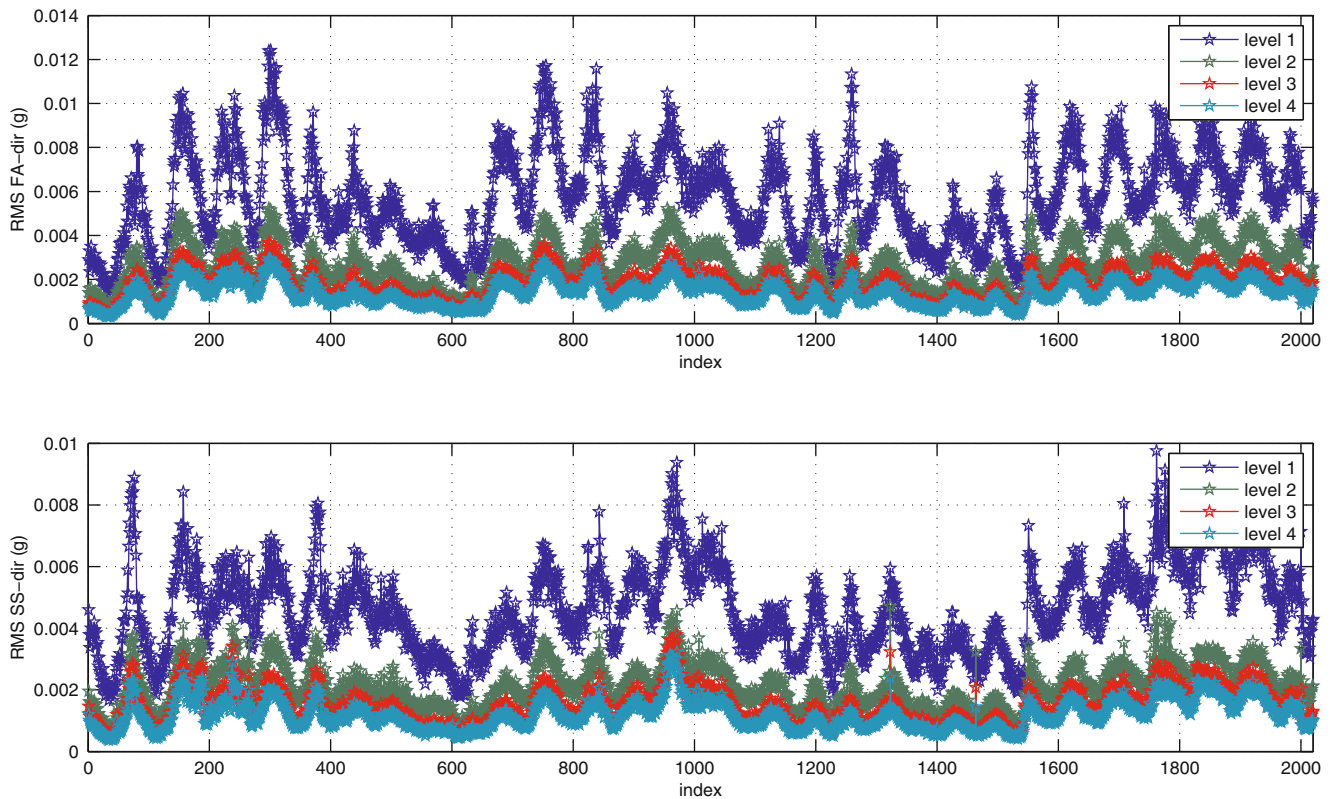


Fig. 28.5 Daily variation of the root mean square (RMS) values of the acceleration time series in the FA-direction (*above*) and SS-direction below (*below*)

- Step 1: Identification of models with varying orders, below a conservative maximum model order, using state of the art operational modal analysis techniques
- Step 2: Perform a hierarchical clustering algorithm on the poles corresponding with different model orders identified in step 1
- Step 3: Classification and evaluation of the clusters identified in step 3 using a fuzzy clustering algorithm based on different validation criteria
- Step 4: Tracking the different modes based on nearest frequencies and corresponding mode shapes using the mean values of the clusters

The next paragraphs provide a more detailed description of each step.

28.3.1 Operational Modal Analysis

Identification of the modal parameters from the different data-sets collected can be achieved with different output only techniques. A detailed description of some of these methods can be found in [5–7, 14, 15]. In this paper only the results of the p-LSCF method, commercially known as PolyMAX, are presented [16]. In several papers it was noticed that the PolyMAX method produces very clear stabilization diagrams [17]. This makes this method in particular interesting to try to automate the process.

When using the vibrations measured during normal operation the first step consists of calculating the correlation functions of the measured accelerations. It has been shown that the output correlation of a dynamic system excited by white noise is proportional to its impulse response [18]. Therefore, the Fast Fourier Transformation of the positive time lags of the correlation functions can directly be used as input for the analysis methods in the frequency domain. The least squares estimators in the frequency domain can be applied to a matrix with the auto and cross correlation functions taking e.g. the two sensors on the top in the FA and SS-direction as reference signals. The parameters that need to be chosen are the length

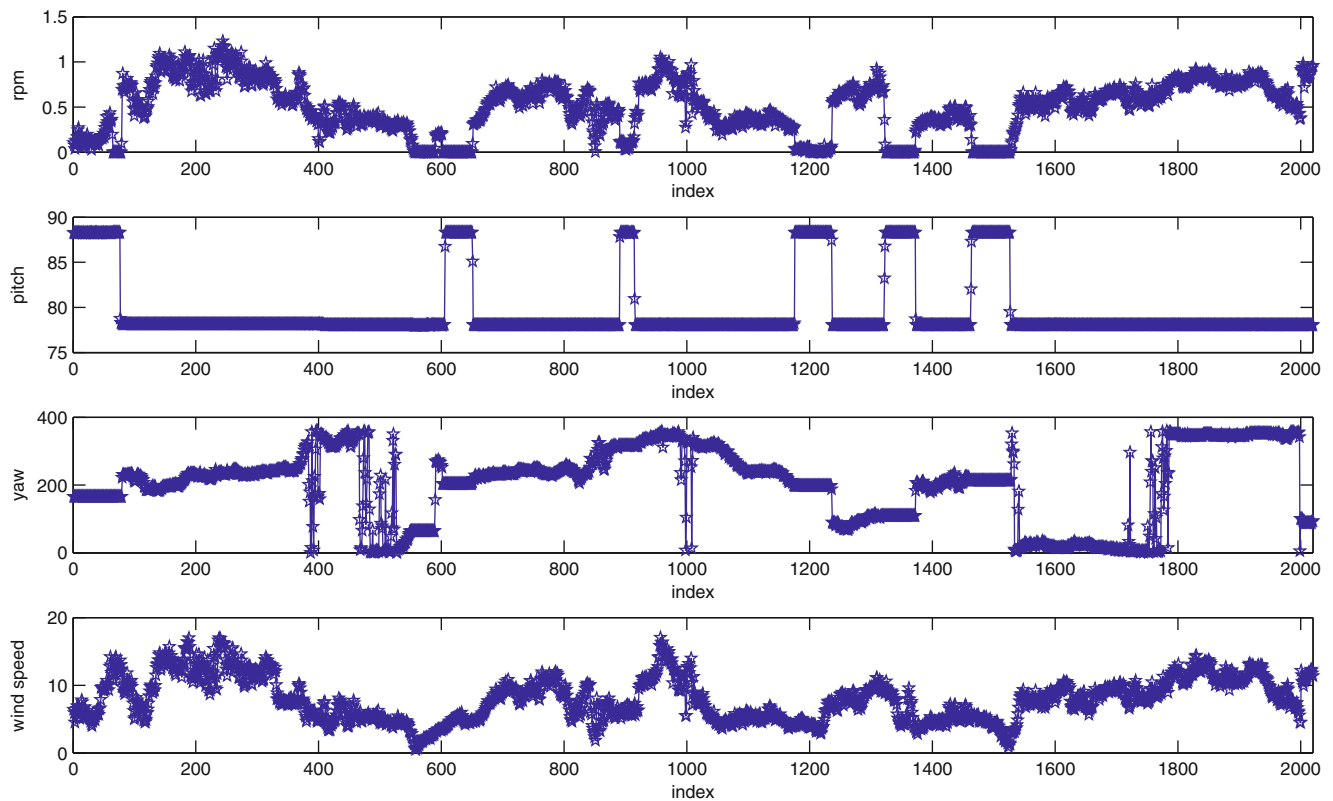


Fig. 28.6 SCADA data for monitoring period from top to down: rpm, pitch-angle, yaw angle, wind speed

of the used time segment and the number of time lags taken from the correlation function used for the spectra calculation [19]. The spectra resolution, controlled by the number of time lags taken from the correlation functions, should be high enough to well characterize all the modes within the selected frequency band. At the same time, it should be kept as low as possible to reduce the effect of the noise. In [15, 20] different numbers of time lags taken from the correlation functions have been evaluated and 512 points taken from the correlation functions was found to be a good choice. Another objective of [20] was to evaluate if 10 min for the time segments used in the continuous monitoring of the offshore wind turbine would be sufficient to identify the modal parameters in a robust way. A time segment of 10 min allows assuming that the ambient conditions, e.g. wind speeds, stay more or less constant, needed for the OMA time-invariant assumption. 10 min is also the commonly used time interval for the SCADA data and the Meteo data, and thus has the advantage of making future analyses of the data easier. It was found that, although the standard deviations when using only 10 min was higher than for data sets using e.g. 40 min, especially for the damping values of the first FA and SS bending modes, the mean values were comparable and thus 10 minutes were considered sufficient to find estimates for the damping values with acceptable quality.

First the poles (and the modal participation factors) are estimated with the polyreference LSCF [16] for different model orders. These results can be used to construct a stabilization chart from which the user can try to separate the physical poles (corresponding to a mode of the system) from the mathematical ones. By displaying the poles (on the frequency axis) for an increasing model order (i.e. number of modes in the model), the diagram helps to indicate the physical poles since, in general, they tend to stabilize for an increasing model order, while the computational poles scatter around. As a result, a construction of the stabilization chart is nowadays one of the requirements for a modal parameter estimation algorithm, and it has become a common tool in modal analysis. Figure 28.7 shows examples of different stabilization diagrams using different 10-min time-segments with 512 time lags taken from the correlation functions and a maximum model order of 32. The analysis focuses in the frequency range 0–2 Hz, where the main vibration-modes of interest are expected.

All stabilization diagrams seem to have around 4 or 5 well identifiable stable poles. In a non-automated approach we could manually select the poles in the stabilization diagram by clicking on the stable poles, indicated by a reds. It is clear that this may depend on the user. For high noise levels the stabilization diagrams can be difficult to interpret and give different results depending on the user. Moreover, stabilization diagrams require interaction and therefore they cannot directly be used when autonomous modal parameter estimation is needed. The next paragraph will present how this process can be automated in a robust way.

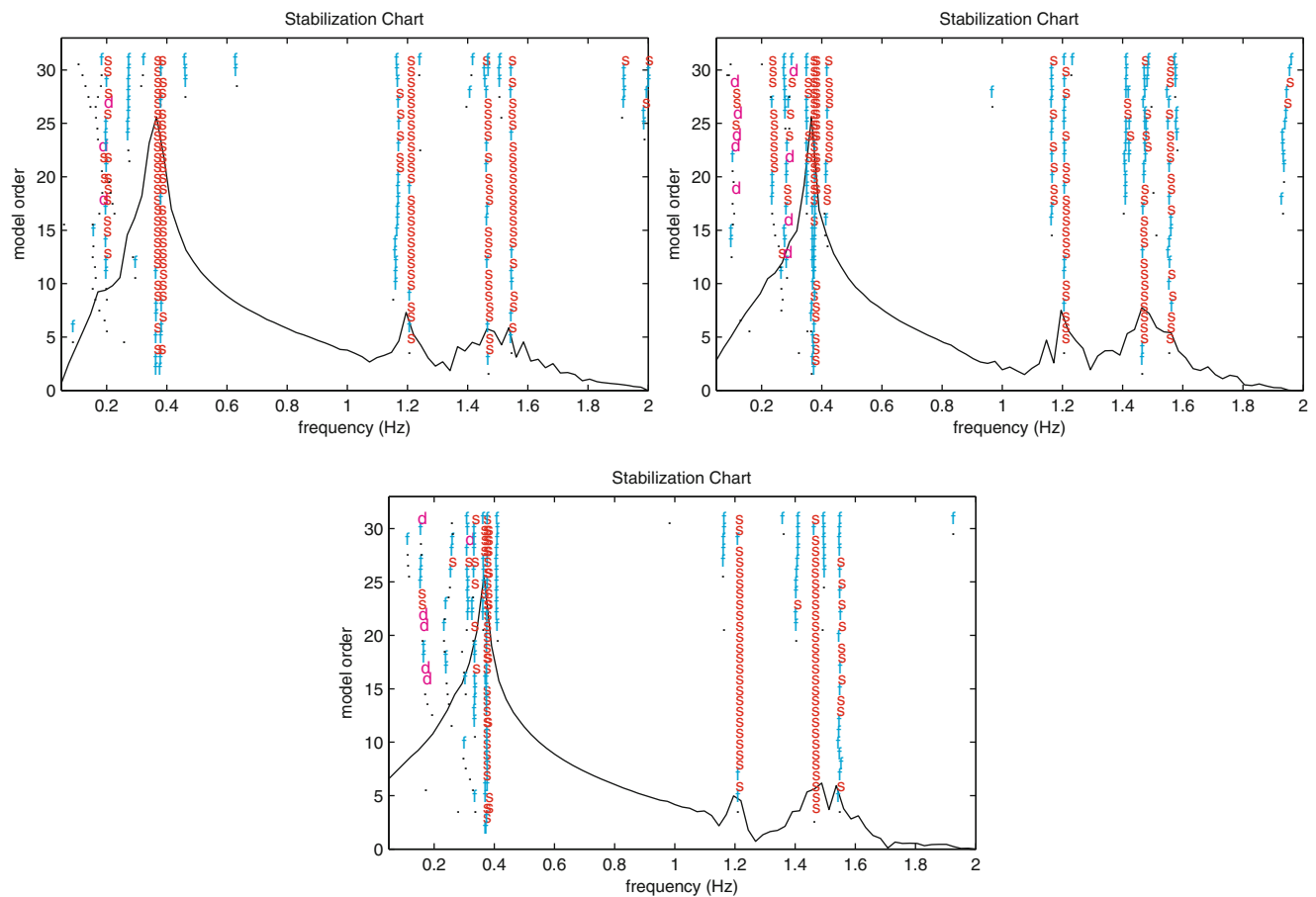


Fig. 28.7 examples of 3 randomly chosen stabilization diagrams obtained during the monitoring period

Note that for each pole in the stabilization diagram the modal reference factors, the mode shapes, together with the lower and upper residual terms, can be obtained by the LSF method [16]. This information will also be used in the next 2 steps of the continuous monitoring approach.

28.3.2 Automatic Identification of the Modal Parameters

In [14, 20] the authors developed a methodology for automatic identification of modal parameters, using parametric identification methods, based on a hierarchical clustering algorithm. to cluster poles that are related to the same physical mode. Several basic procedures are available in the MATLAB Statistics Toolbox and several papers have successfully applied these methods [14, 21]. In this work a robust agglomerative hierarchical approach was used based on the method presented in [20, 21]. The algorithm starts with calculating the distance matrix between all the poles, after applying the p-LSCF estimator for the different orders, and then a first cluster is initiated. Only the stable poles are considered. Each time a new cluster is initiated, a new distance matrix is computed using the remaining poles. When looking for a new pole to be added to a cluster an initially frequency interval (i.e. 1% of the mean frequency of the initiated cluster) is considered. In our case it was possible to consider such a small interval from the start because of the high quality of the measurements and the corresponding estimates. When the noise levels of the collected data are higher a larger interval can be used. A good rule when choosing the interval is to use the limit defined for the stabilization diagrams. As long as the number of poles, each corresponding to a different model order, is larger than the maximum number of poles that a cluster can contain, the width of the frequency interval is reduced. This maximum number of poles equals the maximum model order minus the number of orders that is not considered for clustering. One can choose not to use the first orders for the clustering algorithm, because the low order estimates can be of less quality and because the different system poles only show up as stable lines for higher model orders. One can also choose not to consider clusters with a small number of poles. The first 6 orders were not used

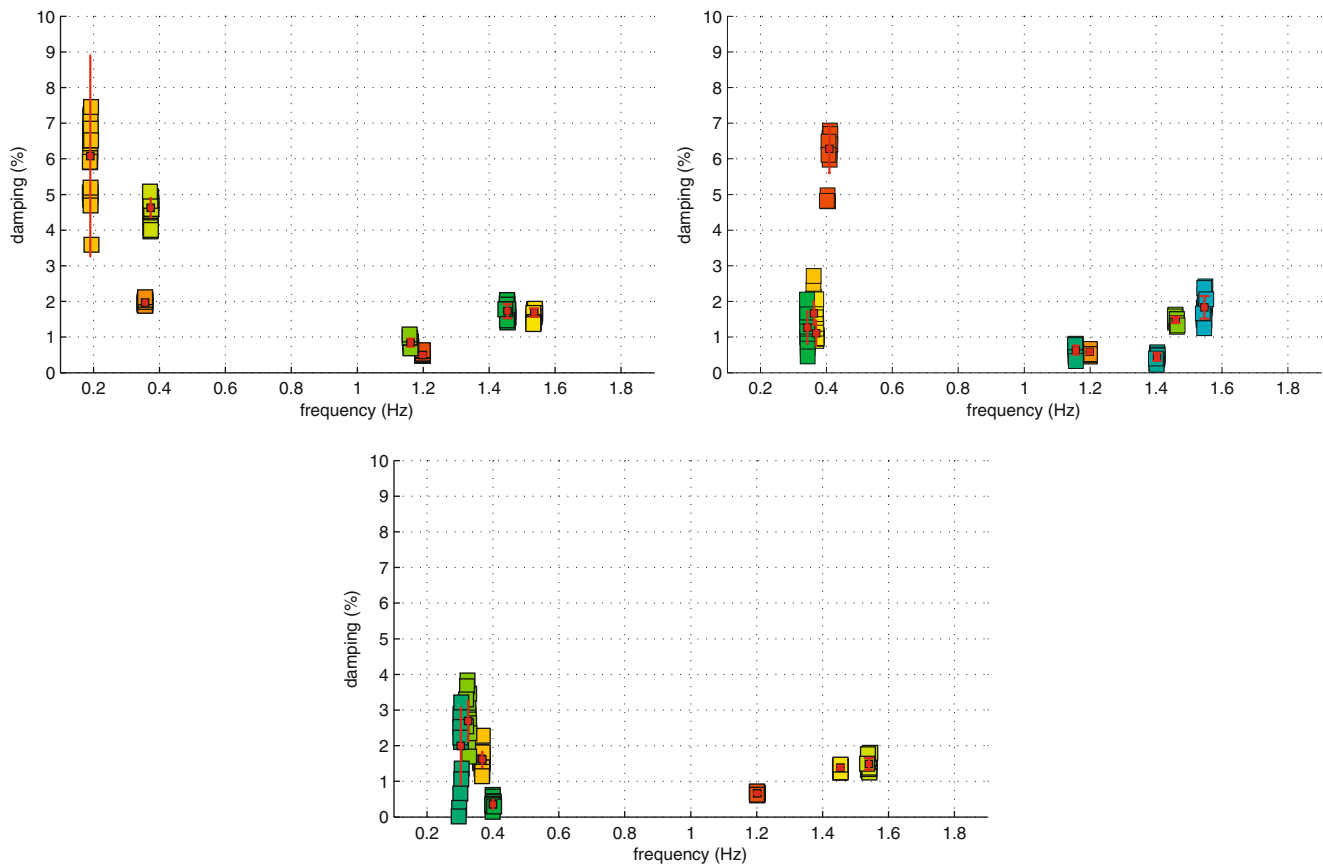


Fig. 28.8 Results obtained by the cluster algorithm applied to the above stabilization diagrams

and only clusters with more than 50% of the maximum number of poles a cluster can contain were retained. Figure 28.8 shows the results of the cluster algorithm on the previously identified poles for different modal orders, as was shown in the stabilization diagrams of Fig. 28.7.

When we look to the results of the clustering-algorithm we can clearly identify several clusters. Based on the cluster results, a statistical analysis yields the mean and standard deviation for each of the estimated poles and hence for the damped natural frequencies and damping ratios. One can also calculate an identification success-rate by dividing the number of poles in each cluster by the maximum number of poles a cluster can contain. The hierarchical clustering procedure assures that each of the system poles will be represented by just one single cluster. However, since typically high model orders are chosen for reasons of noise on the data as well as the use of a discrete time transfer function model, not each cluster corresponds to a system pole. Therefore, each of the clusters needs to be assessed for its physicalness. Secondly, when continuous monitoring is done not all data-sets will allow to identify the physical modes and their corresponding frequencies and damping values with high confidence. Therefore criteria can be defined that can distinguish physical modes from mathematical ones and that allow to discard estimates of low quality. In the proposed hierarchically clustering approach, the number of poles in a cluster, or the identification success rate, as well as the standard deviations on the frequencies and damping values of each cluster, may give a good indication for the physicalness and quality of the identified poles and their clusters. When a sufficient number of sensors is available mode shape information can be used to further evaluate the clusters by also considering the well-known validation criteria such as the Modal Assurance Criteria, Modal Phase Collinearity (MPC) and the Modal Phase Deviation (MPD). For each pole in a cluster the corresponding mode shape information can be computed and the following percentage ratios can e.g. be calculated: the fraction of mode shapes that have a Modal Phase Collinearity (MPC) larger than 80% and a Modal Phase Deviation (MPD) smaller than 10 degrees.

Now we can use an iterative Fuzzy C-means clustering algorithm to evaluate the clusters. In [22, 23] the approach was used to classify the identified poles into physical and computational poles. Based on the results for each of the above discussed validation criteria, the clusters obtained in the previous step can now also be grouped into two classes using this algorithm, i.e. physical clusters retained for continuous monitoring and clusters discarded for continuous monitoring. The output of the Fuzzy C-means clustering algorithm gives a classification result for the clusters. If the classification result is larger than 50%

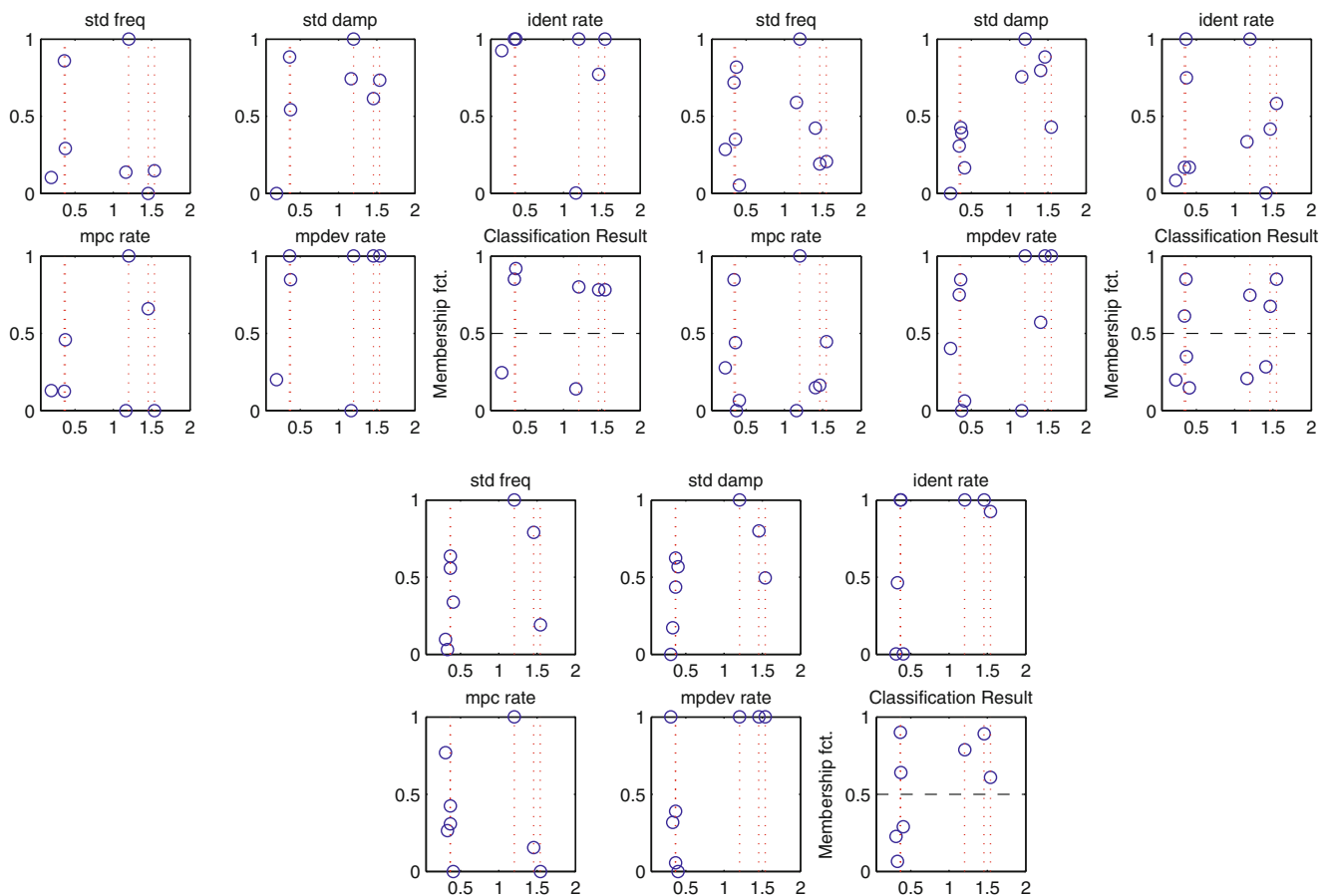


Fig. 28.9 Classification results obtained by the Fuzzy C-mean cluster algorithm for the previously obtained clusters

then it is decided that the cluster belongs to the class of clusters with physical poles who have a good estimate and can be used for continuous monitoring. In Fig. 28.9 we can see the results of Fuzzy C-means clustering algorithm. In all cases 5 clusters have a classification result above 50% are thus retained for continuous monitoring. These 5 clusters represent the 5 dominant vibration modes that are excited while the wind turbine is subjected to the operational and ambient conditions during the considered monitoring period. The corresponding modes shapes are shown in Fig. 28.11. The first mode is the first FA bending mode (FA1). The second mode is the first SS bending mode (SS1). Then at 1.2 Hz we can identify the second FA bending mode (FA2). The last 2 modes consist of 2 blade modes, with a tower component in respectively the side-side (BSS) and fore-aft (BFA) direction. We can conclude that the algorithm seems to be an efficient approach for the classification of the identified clusters and thus can be considered as a valuable tool to be used in automatic identification and continuous monitoring

28.3.3 Tracking and Discussion of the First Long-term Monitoring Results

In the last step we want to be able to track the different modes over time. Since the natural frequencies and damping ratios of the modes may change due to changes in the operating condition, it is not always straightforward to determine which identified modes from two subsequent data-sets are corresponding. Furthermore, it can happen that two modes cross each other in terms of natural frequency or damping ratio or even that the estimation algorithm returns a single mode at the moment of crossing, masking the other mode and seriously hampering the tracking process. In the case of the wind turbine this is especially the case with the closely spaced first FA-mode and first SS-mode. Due to small asymmetries in the structure or soil conditions these modes can have crossing frequencies due to changing yaw-angles. In this paper the mode shape information in the form of the modal assurance criterion (MAC) is applied for mode tracking. The MAC evaluates the degree of correlation between two mode shapes over subsequent instants resulting in a value close to one for corresponding modes.

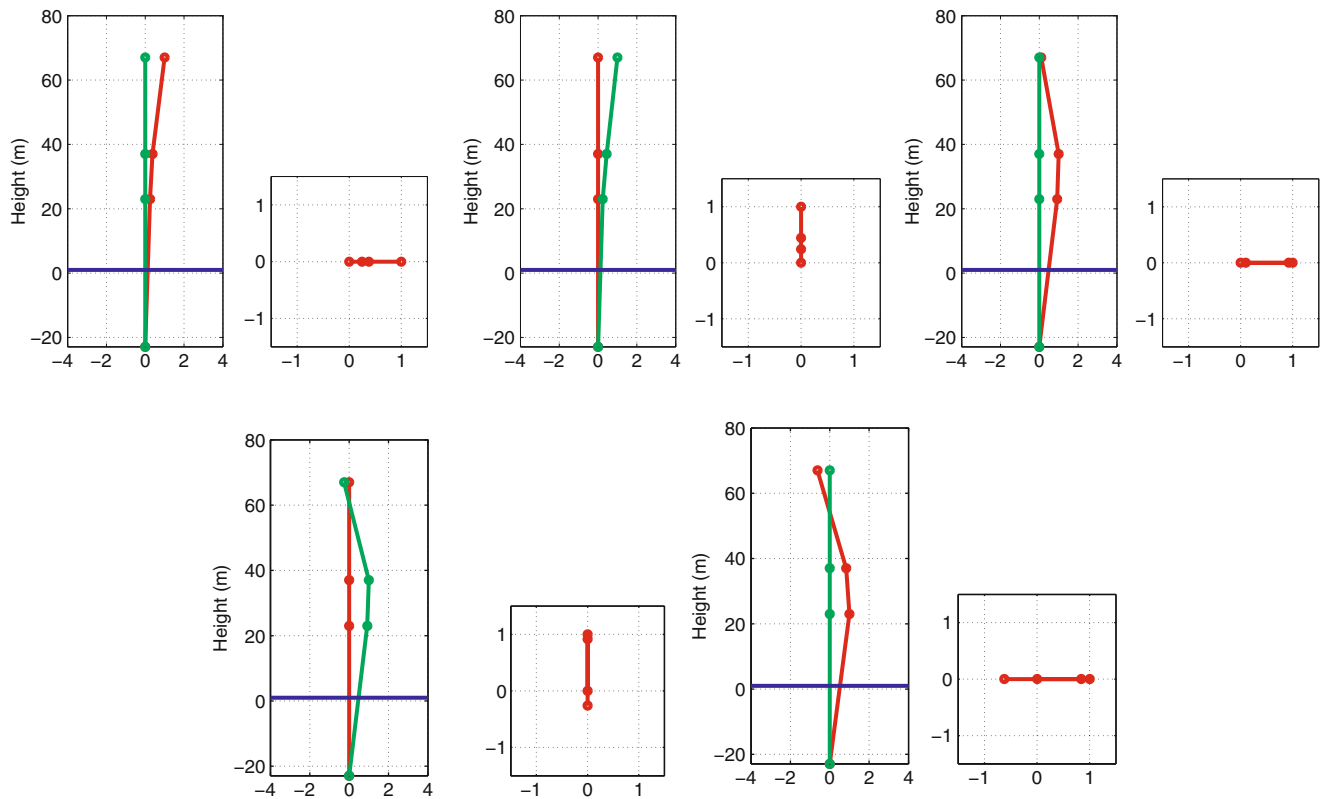


Fig. 28.10 Five most dominant mode shapes identified during the monitoring period: FA-direction (red lines) SS-direction (green lines) water level (blue line), top views (right figures), from top left to bottom right: first fore-aft bending mode, (FA1) first side-side bending mode (SS1), second fore-aft bending mode (FA2), blade mode with side-side tower component (BSS), blade mode with fore-aft tower component (BFA)

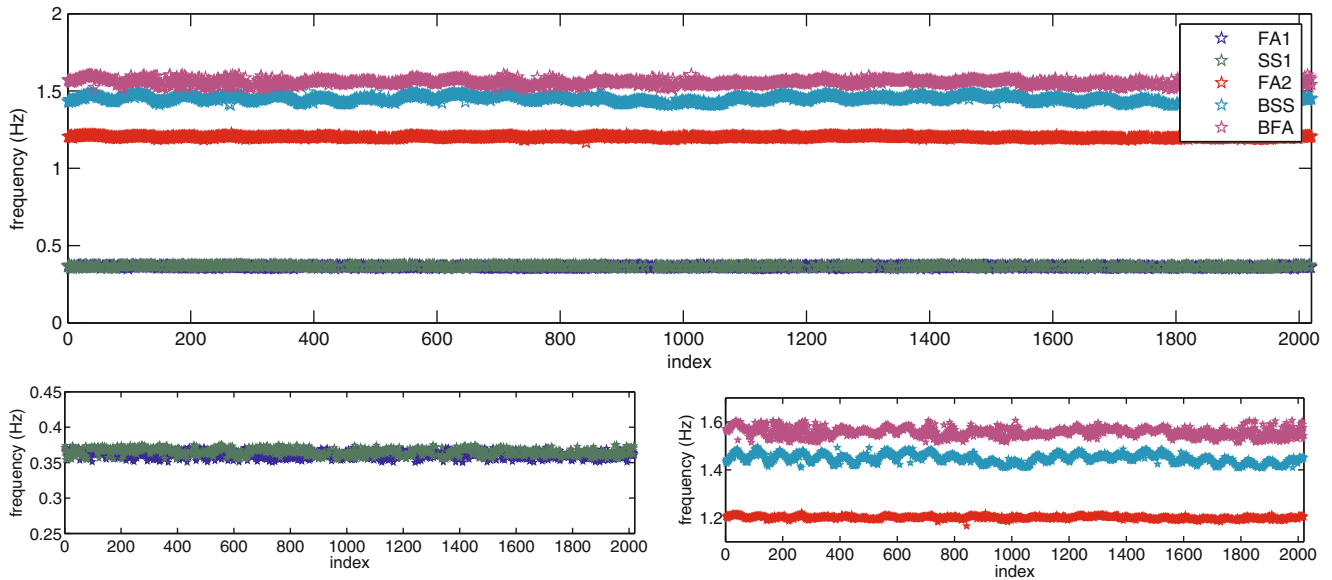


Fig. 28.11 Evolution of frequencies of the 5 dominant modes during monitoring period

Initially, the modes of interest for the tracking are selected from the reference model obtained from an analysis of the first data set. Mode tracking over the consecutive instants is done based on using the MAC ratio as selection criteria, from a group composed by all the physical clusters mean estimates that have a natural frequency that does not differ more than 5% from the reference value. The cluster with the highest MAC-value is selected and is only accepted if the MAC-ratio is higher

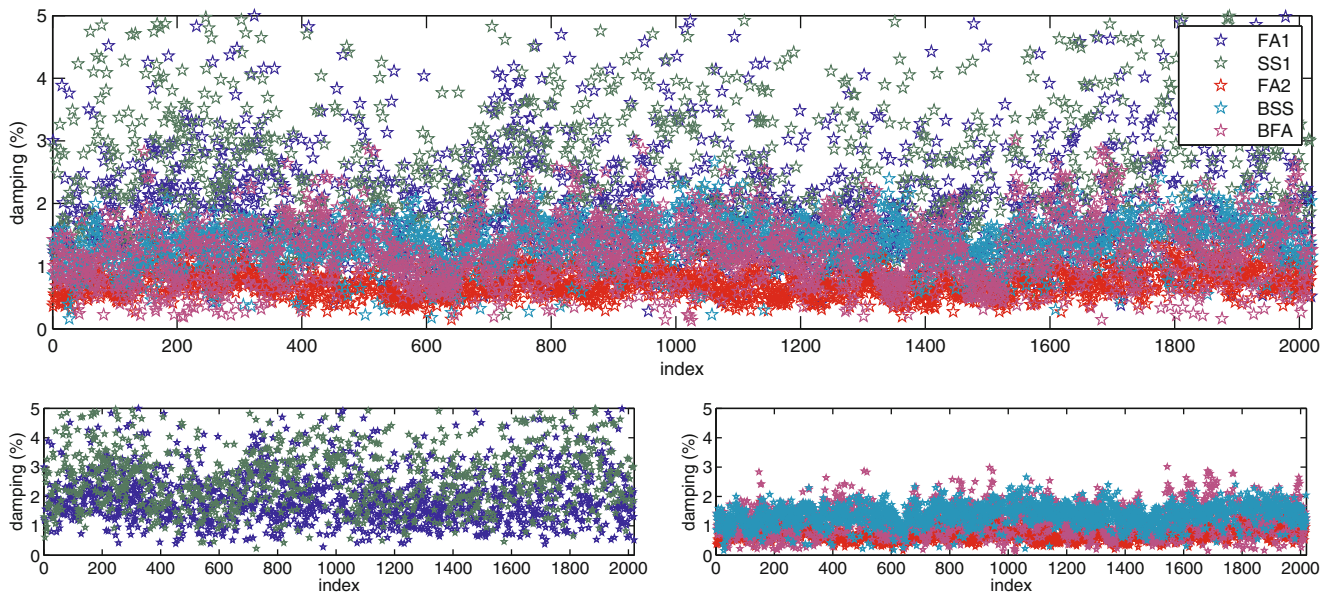


Fig. 28.12 Evolution of damping values of the 5 dominant modes during monitoring period

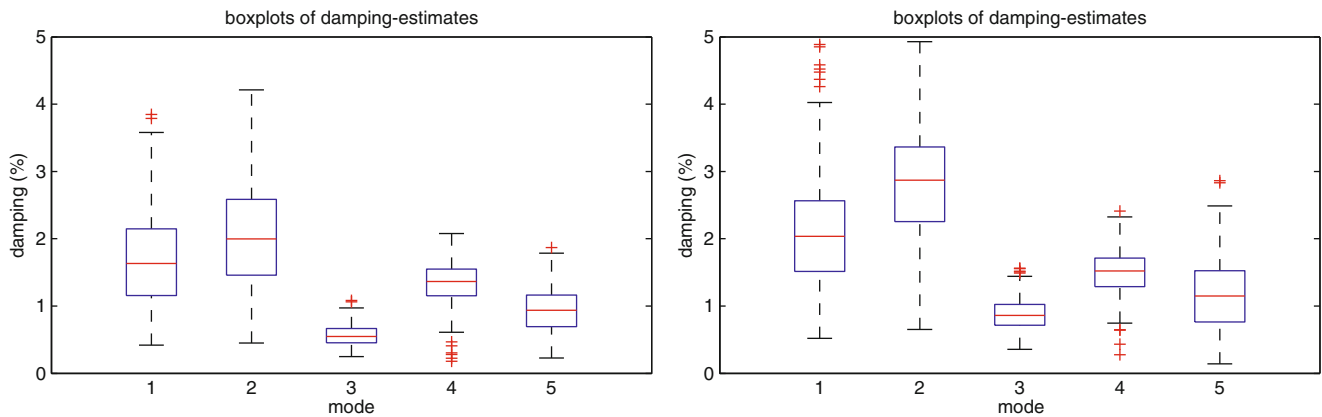


Fig. 28.13 Damping values of the 5 dominant modes (mode 1: FA1, mode 2: SS1, mode 3: FA2, mode 4: BSS, mode 5: BFA) during monitoring period for low wind speeds of 0–5 m/s (left) and higher wind speeds of 10–15 m/s (right)

than 0.8. This approach allows to link estimates of the same physical mode and simultaneously, possible frequency shifts lower than 5%, motivated by the different ambient and operating conditions or possible damages, are allowed. The reference modal parameters (natural frequencies, modal damping ratios and mode shapes) used in this case are the ones presented in Fig. 28.10.

Figure 28.11 presents the evolutions of the natural frequencies within the analyzed frequency range during the monitoring period. A zoom is also presented to show that the methodology has been able to successfully identify the closely spaced FA and SS mode even when the frequencies cross each other. The methodology also successfully managed to capture small daily variation on the highest 3 modes. These changes can be attributed to the tidal effect. The lowest 2 modes seem to be less sensitive to this effect. This can be understood due to the fact that the highest 3 modes, all showing a second bending mode behaviour, have a higher relative displacement at the water level in comparison with the first FA and SS bending mode.

The variation of the modal damping ratios of these modes is represented in Fig. 28.12. It can be observed in that the values for the highest 3 modes are reasonably coherent (taking into account that the estimates of the modal damping ratios always present some uncertainty), while the ones associated with the lowest 2 modes present a higher scatter. This can be explained by the fact that identifying two closely spaced modes always increases the uncertainty, especially on the damping values. Also the fact that we use only 10 min of data mainly affects the quality of the estimates of the lowest modes. However a part of this high scatter can also be explained by the high dependence of damping of these modes with different operational and ambient parameters, e.g. the wind speed.

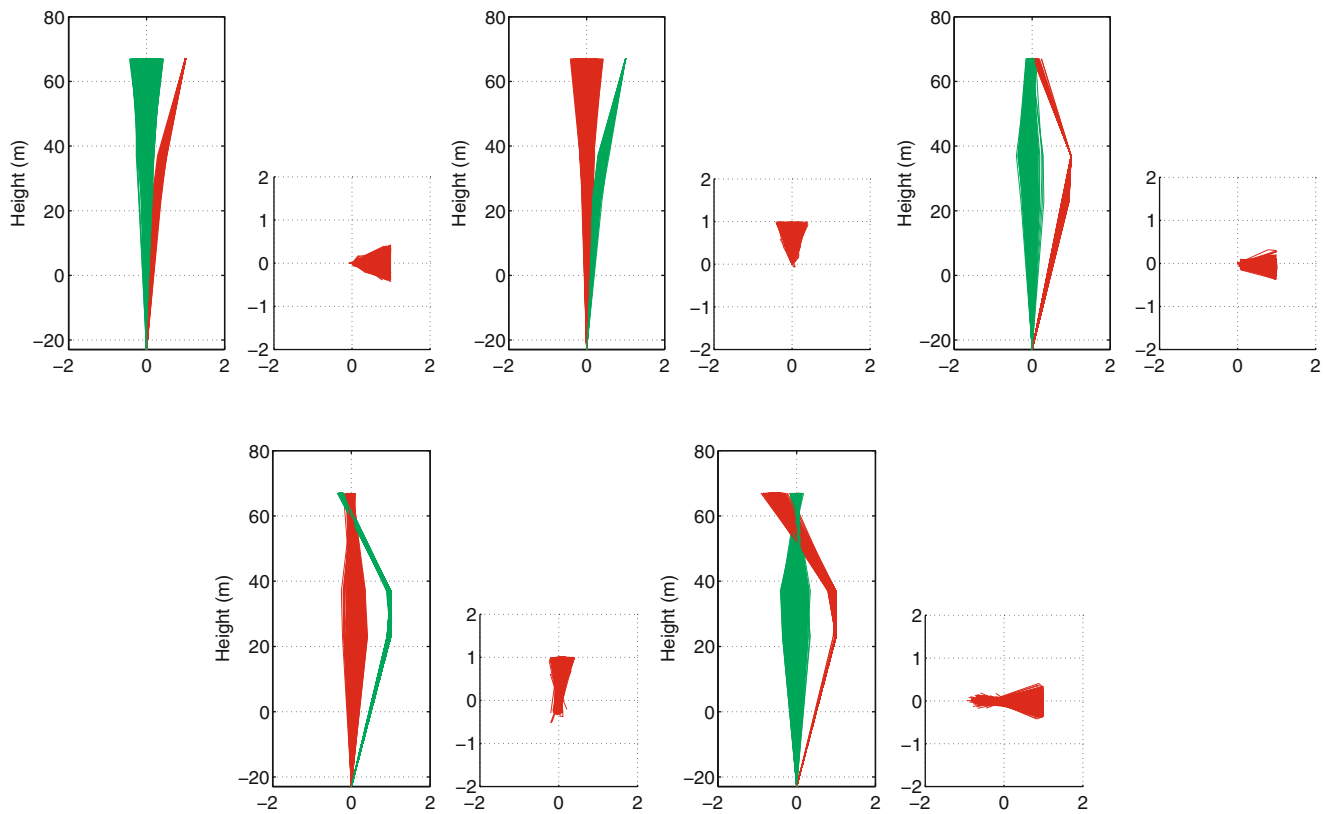


Fig. 28.14 Evolution of the mode shapes of the 5 dominant modes during monitoring period: FA-direction (red lines) SS-direction (green lines), top views (right figures), from top left to bottom right: FA1, SS1, FA2, BSS, BFA

We can make a statistical analysis on the results obtained during the continuous monitoring, for different wind speeds. Figure 28.13 illustrates one box and whisker plot per damping value of each tracked mode. On each box, the central mark is the median, the edges of the box are the 25th and 75th percentiles, the whiskers extend to the most extreme damping values that were not considered as outliers and the outliers are plotted individually.

Despite the high scatter on the damping values, the obtained results from this short data-set, with an offshore wind turbine in parked conditions, already allows us to get a good understanding in wind turbine dynamics. For example for the first mode in the side-to-side (mode 2: SS1) direction we find a higher damping in comparison with the first fore-aft mode (mode 1: FA1). This can be explained due to the presence of some small aerodynamic damping effects in the SS direction considering the pitch angle of 88.3 degrees in parked conditions and 78 degrees when idling. According to [24] the aerodynamic forces are present even at standstill due to the larger blade surface that interacts with surrounding air when the tower vibrates in the SS direction. The same conclusion can be found for the modes with important from blade components and with a tower component in respectively the side-to-side direction (mode 4: BSS) and fore-aft direction (mode 5: BFA), the latter having a lower damping value. The second bending mode in the for-aft direction (mode 3: FA2) clearly shows a lower damping, this can be explained due to the fact that for this mode the nacelle is not moving (see Fig. 28.11) and thus the aerodynamic damping introduced by the blades can be neglected for this mode.

Comparing the damping values between the low wind-speed bin and the high wind speed bin we can clearly see an overall increase of the damping values for all modes. This can be attributed to the higher drag forces in case of higher wind speeds resulting in higher aerodynamic damping values. Note also that during the monitoring period a mass tune damper was activated and tuned on the first FA and SS mode. In [25] both an overspeed test and an ambient vibration test have been performed on the same wind turbine, while the mass tune damper was deactivated. The damping values for the first FA-mode and first SS mode, for those conditions, were found to be respectively 1.05% and 1.27%.

Finally, Fig. 28.14 illustrates the different mode shapes identified in the 2016 successive data-sets. It can be seen that the mode shapes are very coherent over the different data-sets, indicating that we are clearly able to track the different physical modes. Small differences can be attributed to e.g. small errors on the yaw angle used for the coordinate transformation or small asymmetries in the foundation structure and soil conditions.

Table 28.1 Results of the continuous monitoring

Mode	Success rate (%)	Mean Freq (Hz)	Std Freq (Hz)	Mean damp (%)	Std damp (%)	Mean MAC	Min MAC
FA1	72	0.3614	0.0039	1.863	0.853	0.91	0.80
SS1	50	0.3656	0.0045	2.491	0.969	0.90	0.80
FA2	97	1.2007	0.0055	0.721	0.221	0.98	0.80
BSS	94	1.4489	0.0178	1.383	0.334	0.98	0.81
BFA	88	1.5600	0.0162	1.141	0.489	0.95	0.80

Table 28.1 synthesizes the results of the continuous monitoring routines in the analysis of 14 days of data. In the second column the success rate of the identification of the 5 dominant modes is quantified. The lowest success rate can be found for the first side-side bending mode (SS1). This can be expected as this mode is most of the time only weakly excited, thus difficult to identify. The success rate of the stronger excited first fore-aft mode (FA1) is 72%. We can conclude that the identification of the closely spaced first fore-aft mode and side-side mode is difficult, but feasible. The other 3 modes, FA2, BSS and BFA all have high success rates of respectively 97%, 94% and 88%. Columns 3–6 present the mean values and the standard deviations (std) of the natural frequencies (freq) and damping values (damp). The higher standard deviations on the frequencies of the highest 2 modes show that, in the case of this offshore wind turbine, the influence of ambient conditions such as the tidal effect, is higher on these modes. For the damping values we can see a higher standard deviation on the first 2 modes, for reasons already discussed above. The mean values of the MAC coefficients are high (higher than 0.9), which means that they are not very sensitive to the operational and ambient conditions and that the adopted identification procedure derived always high-quality estimates. The minima (min) MAC values are close to 0.8, as this was the minimum value set in the tracking to accept a candidate estimate for a certain reference mode.

We can conclude that the presented algorithms seems to be an efficient approach for the automatic identification and continuous monitoring of the resonant frequencies, damping values and mode shapes of the most dominant modes of an offshore wind turbine during varying operational and ambient conditions.

28.4 Conclusions

This paper presents a state of the art long-term dynamic monitoring solution for offshore wind turbines. The data, continuously measured by the data-acquisition system and the 10 accelerometers installed on an offshore wind turbine, is transferred onshore via optic fibers that are embedded in the infield and export cable that lay on the seabed.

The processing algorithms included automatic preprocessing and online identification of the wind turbine's dynamic parameters. The results are very promising since the approach is capable of identifying the modes of interest even when short data-sets of 10 min are used. It is shown that, by using the p-LSCF-estimator for varying model orders combined with a hierarchical clustering algorithm, accurate estimates can be obtained of many modes of the wind turbine together with a confidence interval. Finally, validation criteria can be calculated that allow separating physical mode estimates from mathematical ones and allowing discarding estimates of low quality by using a fuzzy clustering approach.

The proposed method proved to be very efficient in the identification and tracking of the wind turbine's 5 most dominant modes. The results achieved during 14 days, which involved the analysis of 2016 data-sets, show its ability to identify the closely spaced FA and SS modes, and the high accuracy of the estimates, enabling the detection of small variations in the frequencies and damping values due to, e.g. operational or ambient conditions. It provided also meaningful damping values and coherent mode shapes.

The resulting database with the variations/evolutions of the modal parameters will certainly allow a better understanding of the influence of operational and ambient conditions on the wind turbines dynamics. Future studies will be conducted with the aim of establishing numerical models to eliminate the effect of the different operational and ambient conditions on the identified parameters in order to exploit the use of these parameters in the identification of damage. The next challenge will also be to evaluate the proposed methods on the data-sets obtained while the wind-turbine is rotating at rated speed. As discussed in the introduction different solutions can and will be considered in order to deal with the harmonic components.

Acknowledgements The research presented in this paper is conducted in the framework of the "Offshore Wind Infrastructure Application Lab" (www.owi-lab.be). The authors gratefully thank the people of Belwind NV and NorthWind NV for their support before, during and after the installation of the measurement equipment. They also supplied all relevant operational and structural data which has been used for the analysis.

References

1. Davis D, Pollack M, Petersen B (2010) Evaluate the effect of turbine period of vibration requirements on structural design parameters. Technical report of findings
2. Van Der Tempel J (2006) Design of support structures for offshore wind turbines. PhD T.U. Delft
3. Zaaier MB (2002) Tripod support structure—pre-design and natural frequency assessment for the 6 MW DOWEC. Doc. no. 63, TUD, Delft
4. Carne TG, James GH III (2010) The inception of OMA in the development of modal testing for wind turbines. *Mech Syst Signal Process* 24:1213–1226
5. Hermans L, Vav Der Auweraer H (1999) Modal testing and analysis of structures under operational conditions: industrial applications. *Mech Syst Signal Process* 13(2):193216
6. Brincker R, Zhang L, Andersen P (2001) Modal identification of output only systems using frequency domain decomposition. *Smart Mater Struct* 10:441–445
7. Cauberghe B (2004) Applied frequency-domain system identification in the field of experimental and operational modal analysis. PhD Thesis, Vrije Universiteit Brussel, Belgium, <http://www.avrg.vub.ac.be>
8. Peeters B, Cornelis B, Janssens K, Van der Auweraer H (2007) Removing disturbing harmonics in operational modal analysis. In: Proceedings of IOMAC 2007, Copenhagen, Denmark
9. Pintelon R, Peeters B, Guillaume P (2008) Continuous-time operational modal analysis in presence of harmonic disturbances. *Mech Syst Signal Process* 22:1017–1035
10. Devriendt C, Guillaume P (2008) Identification of modal parameters from transmissibility measurements. *J Sound Vib* 314(1–2):343–356
11. Devriendt C, De Sitter G, Vanlanduit S, Guillaume P (2009) Operational modal analysis in the presence of harmonic excitations by the use of transmissibility measurements. *MSSP* 23(3):621–635
12. Tcherniak D, Chauhan S, Hansen MH (2010) Applicability limits of Operational Modal Analysis to operational wind turbines. In: Proceedings of the IMAC XXVIII, Jacksonville, 2010.
13. Chauhan S, Tcherniak D, Basurko J, Salgado O, Urresti I, Carcangiu CE, Rossetti M (2001) Operational Modal Analysis of operating wind turbines: application to measured data. In: Proceedings of the society for experimental mechanics series, vol. 5, 8. Jacksonville, Florida. pp 65–81
14. Magalhaes F, Cunha A, Caetano E (2009) On line automatic identification of the modal parameters of a long span arch bridge. *Mech Syst Signal Process* 23(2):316–329
15. El-Kafafy M, Devriendt C, De Sitter G, De Troyer T, Guillaume P (2012) Damping estimation of offshore wind turbines using state-of-the-art operational modal analysis techniques In: International conference on noise and vibration engineering, ISMA, Leuven
16. Guillaume P, Verboven P, Vanlanduit S, Van der Auweraer H, Peeters B (2003) A poly-reference implementation of the least-squares complex frequency domain-estimator. In: Proceedings of the IMAC XXI, International Modal Analysis Conference, Kissimmee, F, US, Feb 3-6, 2003
17. Cauberghe B, Guillaume P, Verboven P, Vanlanduit S, Parloo E (September 2005) On the influence of the parameter constraint on the stability of the poles and the discrimination capabilities of the stabilisation diagrams. *Mech Syst Signal Process* 19(5):989–1014
18. Magalhães F, Cunha Á, Caetano E, Brincker R (2010) Damping estimation using free decays and ambient vibration tests. *MSSP* 24(5): 1274–1290
19. Bendat JS, Piersol AG (1980) Engineering applications of correlation and spectral analysis, Wiley- Interscience, New York, NY
20. Devriendt C, Elkafafy M, De Sitter G, Guillaume P (2012) Continuous dynamic monitoring of an offshore wind turbine on a monopile foundation. In International conference on noise and vibration engineering, ISMA, Leuven.
21. Verboven P, Cauberghe B, Parloo E, Vanlanduit S, Guillaume P (2004) User-assisting tools for a fast frequency-domain modal parameter estimation method. *Mech Syst Signal Process* 18:759–780
22. Vanlanduit S, Verboven P, Guillaume P, Schoukens J (2003) An automatic frequency domain modal parameter estimation algorithm. *J Sound Vib* 265(3):647–661
23. Verboven P, Parloo E, Guillaume P, Van Overmeire M (2002) Autonomous structural health monitoring. Part 1: modal parameter estimation and tracking. *MSSP* 16(4):637–657
24. Hansen MH, Thomsen K, Fuglsang P (2006) Two methods for estimating aeroelastic damping of operational wind turbine modes, from experiments. *Wind Ener* 9:179–191
25. Devriendt C, Jan Jordaens P, De Sitter G, Guillaume P (2012) Damping estimation of an offshore wind turbine on a monopile foundation In: EWEA 2012 conference, Copenhagen, April 2012

Chapter 29

Nondestructive Evaluation of Surface Crack Depth in Concrete

Ninel Alver and Masayasu Ohtsu

Abstract Subsurface damages in concrete may cause considerable durability loss in the structure since they are not visible from the surface and let water and other chemicals to penetrate into the structure and cause reinforcement corrosion. Ultrasonic methods have been widely applied for defect detection in concrete, however, there are not many applications of the method found in literature for subsurface damage identification. Specifically, when the damage is deeper considering the distance from the top surface. Therefore, in this study concrete blocks including subsurface cracks with different depths as well as a sound concrete block were tested by applying ultrasound. Wave parameters such as velocity and attenuation for each case were evaluated. Rayleigh wave and longitudinal wave velocities do not change for different subsurface crack depths. Even though, wave energy attenuates more in case of a shallower crack, it is difficult to correlate the attenuation rate with crack depth. Still, attenuation rate is an indicative parameter for subsurface damage identification. Numerical results obtained by Boundary Element Method (BEM) analysis are in good agreement with experimental ones. Stack imaging procedure applied to ultrasonic echo data is used as a complementary technique for subsurface crack depth identification. Reflection at the crack depth can be clearly identified.

Keywords Surface crack • Ultrasound • SAFT • NDE • BEM

29.1 Introduction

Surface cracks have been frequently met in concrete structures due to mechanical, physical and chemical undesirable effects. It should be underlined that concrete is such a sensitive material that it shows complex elastoplastic behavior. It can expand unexpectedly with little change in moisture and may deflect excessively depending on loading and support conditions. In most cases, due to excessive loading or reinforcement corrosion, surface cracks are formed. This type of damage allows rapid deterioration of the concrete structure. Once these cracks are present on concrete surface, additional water or chemicals penetrate into concrete and accelerate cracking process. When the cracks are visible on the surface, by applying different Nondestructive Testing (NDT) methods, crack depth can be identified. However, when the cracks are subsurface, they give no sign until the whole cross-section is broken. Although there is no visual crack on concrete surface, due to existence of subsurface crack, reinforcement corrosion can be in severe phase. Thus, in order to maintain structural integrity, it is crucial to detect subsurface crack formation in concrete structures. At this point, early assessment of this type of damage is highly demanded. There are several NDT methods applied for surface crack detection. Accuracy of the NDT method applied for surface damage evaluation is of primary importance in order to take proper action to repair the damage.

For surface crack evaluation, impact-echo, ultrasonic-echo and infrared thermography methods have been widely used. In most of the pulse echo studies time-of-flight technique has been used where transit time of the longitudinal wave diffracted at crack tip is considered [1, 2]. Masserey and Mazza [3] study crack sizing by ultrasound in time and frequency domain. In the

N. Alver (✉)
Faculty of Engineering, Ege University, Izmir, Turkey
e-mail: ninel.alver@ege.edu.tr

M. Ohtsu
Graduate School of Science and Technology, Kumamoto University, 2-39-1 Kurokami, Kumamoto, 860-8555 Japan
e-mail: ohtsu@gpo.kumamoto-u.ac.jp

time domain, crack sizing is based on the transit time of Rayleigh wave. But, in the frequency domain, the scattering problems occur and are solved by comparison between the measured scattering coefficients and central frequencies of the Rayleigh waves with theoretical curves. Jian et al. [4] report a crack depth gauging method using the diffracting character of Rayleigh wave, and furthermore, they summarize possible mode-converted ultrasonic waves scattering in different parts of the crack during propagation. This provides a strong support for characterizing the size and shape of the crack. Ultrasound has proven to be a suitable technique for characterizing surface cracking, in particular through the use of reflection or transmission of Rayleigh waves, a surface wave with both in-plane and out-of-plane components [5–9]. From the study of Kawashima, measurements have shown that the transmission of broadband Rayleigh waves can be analyzed in the frequency regime and used as a measure of crack depth [10]. Tokai et al. [11] test a concrete beam with surface cracks by applying the impact echo method and the SIBIE (Stack Imaging of Spectral Amplitudes Based on Impact-Echo) method. It has showed that the surface crack depths are easily identified by SIBIE although the cracking tips are not clearly determined. Dutton et al. [12] investigate the interaction of Rayleigh waves with cracks having a range of lengths and angles relative to the surface. It has been reported that crack sizing using the amplitude of transmitted waves may also be less reliable if the crack angle is not known. The peak-to-peak amplitude in the windowed expected Rayleigh wave arrival time can be measured and the transmission can be calculated. Finally, consideration of the shape of the wave modes in the B-Scan can give an idea of the angle of the defect. Ni et al. [13] indicate that the arrival time of ultrasonic wave modes are related with the crack orientation angle. While numerical results agree with the experimental ones, the crack orientation is presented by using the propagating times of scattered ultrasonic modes.

Although, many studies can be found about surface crack depth identification, there have not been many studies conducted for subsurface crack evaluation in concrete. Aggelis et al. [14–16], investigate the characterization of non-visible subsurface cracks in concrete. It is reported that the propagating wave gives information about crack formation and Rayleigh waves are most sensitive in determining surface or subsurface cracks. Aggelis et al. apply infrared thermography and ultrasonic echo for subsurface crack evaluation in concrete including different crack sizes. As a result it is reported that simple thermograms reveal the existence of vertical subsurface cracks and elastic wave properties in ultrasonic echo such as velocity and amplitude are sensitive to the existence of subsurface crack. It is concluded that subsurface crack depth can be correlated with wave attenuation parameter for shallow subsurface cracks, but, still, they should be complemented by other NDT techniques.

In this study concrete blocks with different subsurface crack depths were prepared. The cracks were formed by placing a 1 mm-wide steel plate during casting of the concrete and removing it when the concrete was hardened. Ultrasound was applied to evaluate subsurface crack depth. Two acoustic emission sensors were employed to detect elastic waves and changes in ultrasonic wave parameters such as velocity and attenuation was studied by interpreting the results obtained in time domain. In addition, stack imaging technique was conducted to visualize subsurface crack depth by employing ultrasonic waveform data obtained by dry point contact ultrasonic transducers. Ultrasonic wave propagation was simulated by conducting Boundary Element Method (BEM) Analysis in order to verify experimental results and understand experimental behavior better.

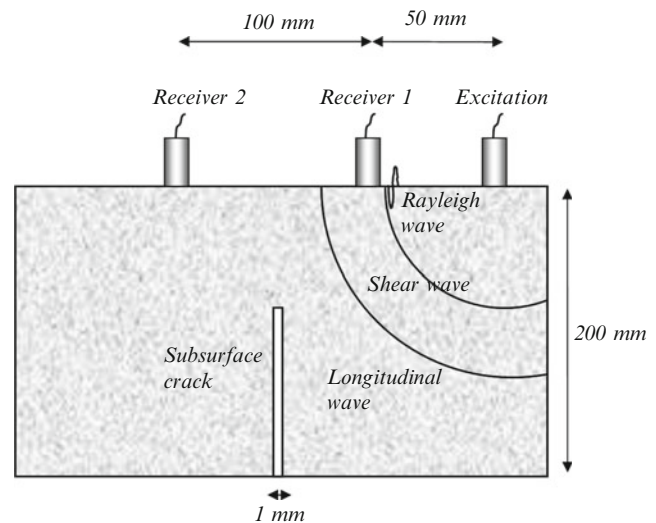
29.2 Ultrasonic Measurements

29.2.1 Experimental Study

The experimental study was carried out at the laboratory on concrete specimens. The concrete specimens used were in dimensions of $200 \times 200 \times 600$ mm. The water to cement ratio was 53% and maximum aggregate size was 20 mm. Modulus of elasticity and Poisson's ratio were obtained as 26.8 GPa and 0.22, respectively. Subsurface cracks were formed by placing a 1 mm-wide steel plate during casting of the concrete and by removing it after the concrete was set. Each specimen had subsurface cracks with different crack depths; 50, 100 and 150 mm.

Ultrasonic wave measurements were made at the top side of the specimens. Two acoustic emission sensors (UT 1000) manufactured by Physical Acoustics Corporation were used to detect elastic waves. The sensors used are broadband transducers with frequency range between 60 kHz and 1 MHz. The sensors were placed on top of the specimen with a distance of 100 mm. The waves were produced by a function generator that charges electrical pulse of 5V and 60 kHz. Experimental setup is illustrated in Fig. 29.1.

Velocity and attenuation of ultrasonic waves are sensitive to damage. Especially, for surface damages, Rayleigh waves have been used since they consume most of the wave energy and propagate only on the surface. 67% of energy of a point wave source on a half space is consumed by Rayleigh waves whereas only 7% is taken by longitudinal waves [14]. It is accepted that penetration of Rayleigh waves is approximately equal to one wavelength. Since they are two-dimensional, their

Fig. 29.1 Experimental details

energy does not disperse as rapidly as the energy associated with three-dimensional longitudinal and shear waves. Amplitude of Rayleigh waves is inversely proportional to the square root of propagation distance whereas for longitudinal waves the amplitude is inversely proportional to the distance [14]. This makes Rayleigh waves more easily detectable than other kinds of waves even in longer distances. In case of existence of a surface damage, Rayleigh wave is strongly influenced. In this study, from the waveforms obtained, amplitude and velocities of Rayleigh and longitudinal waves were examined.

In addition, ultrasonic echo measurements were made by using an equipment from Acoustic Control Systems, Russia. Ultrasonic echo method is based on use of elastic waves produced by an ultrasonic pulse. Waves produced propagate through the material and are reflected when they face a different material with different acoustic impedance such as reinforcement or air inclusion within a concrete element. The ultrasonic head used in this study has 24 dry point contact transducers that do not need coupling agent and 12 of the sensors work as pulsers and the other 12 of them work as receivers. The ultrasonic head used was a shear wave transducer with center frequency of 55 kHz. The measurements were made along a line across the cross-section of the concrete specimen. Data obtained from the test was analyzed in time domain by applying stack imaging procedure. Details of the procedure can be found in [17]. Unlike SIBIE, which uses frequency domain data, time domain data was used in this analysis. In the analysis, the cross section of the specimen was divided into square mesh with size of 10 mm. Firstly, the travel path from input to output point for each square was calculated. By using these values and wave velocity, ultrasonic propagation time for each square was determined. Corresponding wave amplitudes were selected in the waveform and this procedure was repeated for each measurement made along the line. Amplitude values obtained for each square element was stacked and an image of the cross-section was obtained.

29.2.2 Numerical Study

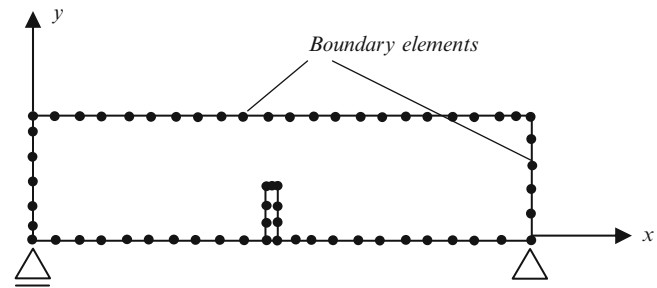
In order to verify experimental results, two-dimensional BEM (Boundary Element Method) was used to simulate the ultrasonic test. The advantages in BEM arises from the fact that only the boundary (or boundaries) of the domain on the partial differential equations is required to be solved [18, 19]. In the finite element method or the finite difference method, the whole domain on the partial differential equations requires discretisation. Thus, the dimension of the problem is effectively reduced by one. In the analysis, the two-dimensional fundamental solutions of steady-state are obtained as,

$$G_{ij}(x, y) = \frac{i}{4\pi} \left[H_0^{(1)}(k_T r) \delta_{ij} + \frac{1}{k_T^2} \left\{ H_0^{(1)}(k_T r) - H_0^{(1)}(k_L r) \right\}_{,ij} \right] \quad (29.1)$$

$$T_{ij}(x, y) = - \left\{ \lambda G_{jm,m}(x, y) \delta_{ik} + \mu G_{ji,k}(x, y) + \mu G_{jk,i}(x, y) \right\} n_k \quad (29.2)$$

where, $r = |x - y|$ and $H_0^{(1)}$ is the zero order Hankel function of the first kind, $k_L = \omega / C_L$ and $k_T = \omega / C_T$ are the wave numbers of the longitudinal and transverse waves, $T_{ij}(x, y)$ is the solution of surface traction, δ_{ij} is Kronecker's delta and λ and μ are Lamé constants.

Fig. 29.2 Boundary element model used for analysis



The analysis was performed in the frequency domain. Displacement responses at the location of detection were calculated by inputting sinusoidal forces up to 200 kHz. A frequency increment of 195.3125 Hz was used. At every frequency level, a 1N force was applied at the impulse location. Boundaries of the cross-sections were digitized evenly at 10 mm pitch. Boundary element model used for the analysis is shown in Fig. 29.2. Material properties were assumed to be the same as the concrete used in experiments. These values are; Young's modulus, 26.8 GPa, Poisson ratio, 0.22, and density, 2460 kg/m³. Dimensions of the models and subsurface crack dimensions were the same as the laboratory specimens. At the detection locations, frequency spectra for the impulse were obtained and by using inverse Fourier transformation, waveforms at each detection point were obtained.

29.3 Results and Discussion

In ultrasonic wave parameter evaluation, longitudinal and Rayleigh wave velocities were measured. For the velocity measurements time delay between two waveforms recorded by the two sensors were used. Time delay between waveform onset gives longitudinal wave velocity since it is the fastest type of waves whereas Rayleigh wave velocity is obtained by its strong peak. Since Rayleigh waves' energy is much higher than the other types of waves, strong peak of this type of wave can be recognized easily after the arrival of longitudinal waves [15]. In cases where there is no surface damage, Rayleigh waves can easily be identified, however, when there is severe surface damage, in most cases it is very difficult to extract Rayleigh wave. Waveforms obtained for sound concrete block and subsurface cracked concrete block by two sensors are given in Fig. 29.3. For the sound concrete, due to heterogeneous and damping nature of concrete and with possible other crack and air inclusions, amplitude of the waveform obtained by the second sensor is lower than that of obtained by the first sensor. Rayleigh wave can be easily identified in this case. In case of subsurface cracked concrete, Rayleigh wave can still be identified since depth of crack tip is not very close to the surface and there is enough depth for the Rayleigh wave to propagate through the surface until reaching the second transducer. However, comparing the amplitude of the waveform obtained by the second transducer with that of sound concrete, it is comparably less.

Longitudinal wave velocity measured for sound concrete was 4085 m/s. This parameter for the subsurface cracked specimens was almost the same for different crack depths 50, 100 and 150 mm. It has been reported in previous studies that this value changes slightly only if the damage is very close to the surface and it is not an indicative parameter for subsurface crack depth identification. In order to use longitudinal wave velocity for subsurface damage identification, the crack depth should be less than 11 mm. Depending on the damage depth, longitudinal wave velocity can decrease up to 66% of the wave velocity value for intact condition [16].

Similar to longitudinal wave velocity, Rayleigh wave velocity did not change for sound and subsurface cracked cases. However, if the subsurface crack gets closer to the surface, this velocity decreases almost 15%. This value was measured as 2130 m/s for sound concrete and Rayleigh wave velocities for the subsurface cracked concrete blocks were almost equal in this study. Rayleigh wave velocity is measured by extracting the strong peaks from the waveform, however, in severely damaged cases it is very difficult to discriminate the Rayleigh peak and hence the wave velocity. Thus, Rayleigh wave velocity is not a reliable parameter for subsurface damage identification.

Amplitude of the waveform is the most sensitive parameter to subsurface damage evaluation. From the waveforms given in Fig. 29.3, it can be seen that in case of sound concrete amplitude of the waveform obtained by the first receiver which is close to the impulse point is higher than amplitude of the second receiver. Due to damping nature of concrete, air and crack inclusions and wave scattering from the edges, this is an expected result. In this study, when the ultrasonic energy loss between two sensors is considered for the sound material, 62% of the wave energy was lost when travelling from the first receiver until the second one. In case of subsurface cracked concrete, a big portion of the ultrasonic energy is reflected at the

Fig. 29.3 Waveforms obtained from experiments (a) sound material (b) subsurface cracked material (crack depth = 5 cm)

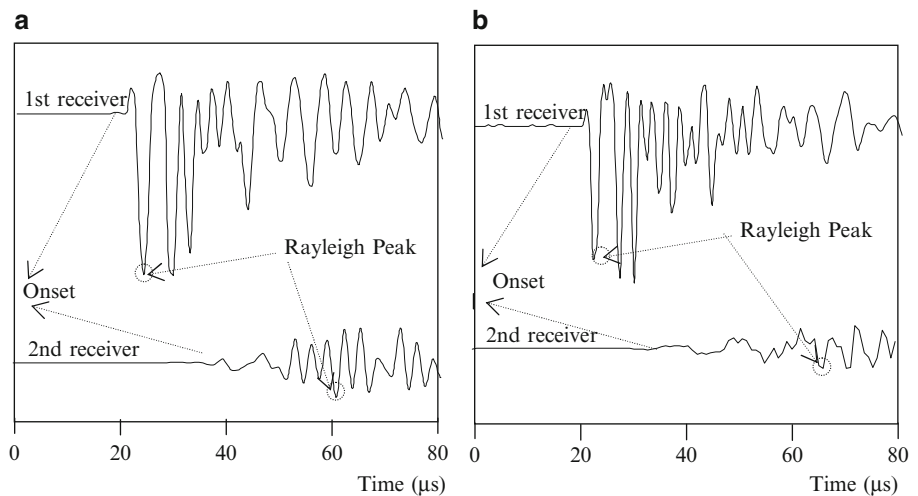
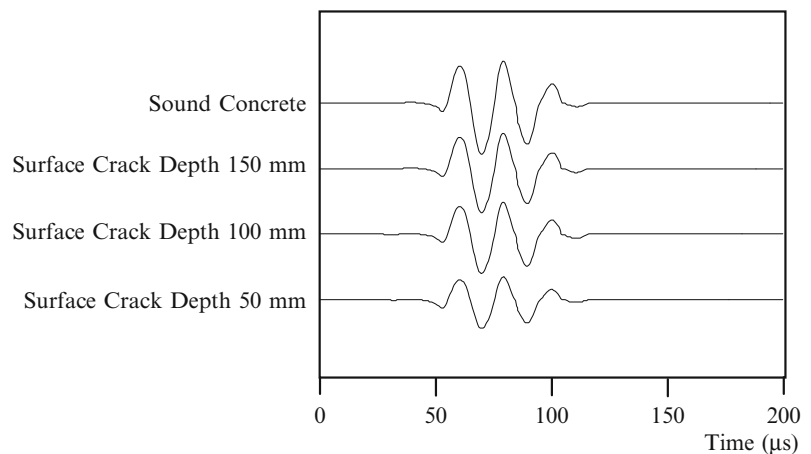


Fig. 29.4 Waveforms obtained from BEM

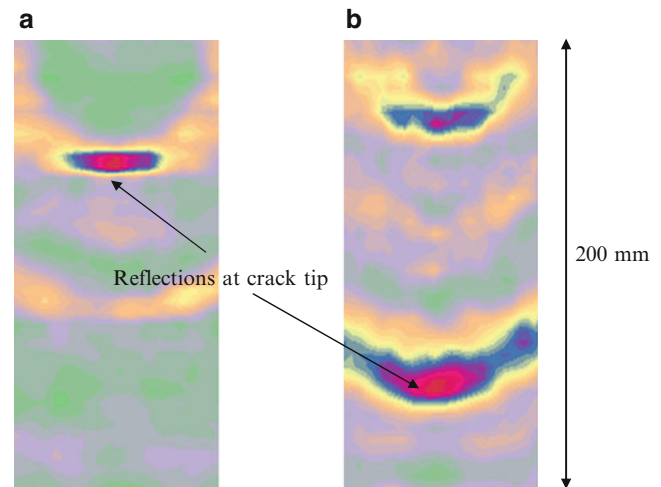


crack and if the crack is closer to the surface, only a little part of the surface gives permission for the wave to travel to the second receiver [16]. Thus, the amplitude of the waveform obtained by the second transducer is expected to be comparably low. In this study, the closest subsurface crack tip from the top surface was 50 mm. Considering a high frequency excitation that corresponds to a smaller wavelength, 50 mm was large enough to let the waves pass through. Thus, in case of subsurface cracked concrete, amplitude of the waveform obtained by the second receiver was not very low. For the subsurface crack depths from top surface 50, 100 and 150 mm, ultrasonic wave energy loss was 76, 69 and 65%, respectively. Attenuation of the waves shows a good indication for subsurface damage existence, however it is difficult to make correlation between attenuation parameter and subsurface crack depth in case of not very shallow cracks.

Results of numerical study are obtained by applying BEM analysis for sound concrete and subsurface cracked concrete models. Due to other possible cracks and air inclusions in the real concrete structure, it is difficult to make correlation between attenuation rate and subsurface crack depth. In BEM models, concrete was modeled as a homogenous media having no damping nature. Waveforms obtained by BEM analysis are shown in Fig. 29.4. Similar to experimental results, attenuation parameter does not change much when the subsurface crack tip is far from the top surface. But, still there is an indication of attenuation due to decrease in amplitude values.

There are studies that prove a good correlation between attenuation rate and subsurface damage level when the damage is close to the surface and almost breaks the cross-section [14–16]. However, in case the subsurface damage is not close to top surface but still severe enough that may cause water penetration and hence reinforcement corrosion, it is difficult to identify its depth by evaluating attenuation rate results. Thus, a complementary technique was applied by using ultrasonic echo measurements to identify subsurface crack depth visually. A result obtained from the analysis is shown in Fig. 29.5. Here, the figure corresponds to the cross section of the concrete block with subsurface crack depths of 50 and 150 mm. High amplitudes are indicated by darker tones whereas low amplitudes are indicated by lighter tones. As it can be seen from the figure, reflections at crack tip are clearly discriminated. However, there is a slight shift (almost 10%) from the actual crack depth. This could be associated with largely discretization of the cross section.

Fig. 29.5 Results obtained from application of stack imaging to ultrasonic echo data, subsurface crack depth (a) 50 mm, (b) 150 mm



29.4 Conclusion

This study is concerned with subsurface crack evaluation in concrete by applying ultrasound. Subsurface cracks can be resulted from effects such as rebar corrosion, excessive loading, etc. In case the subsurface crack tip is close to the top surface, by evaluating wave parameters such as attenuation rate, it is possible to qualify crack depth. However, if the crack tip is deeper, it is difficult to identify the crack depth exactly by evaluating wave parameters since the intact portion is large enough to let the waves pass through the surface especially for surface waves, which consume most of the ultrasonic wave energy. In this study three concrete blocks with considerably deep subsurface cracks were tested experimentally and numerically. By evaluating the experimental results, it can be concluded that attenuation rate gives good sign of presence of subsurface damage, however, it is difficult to identify crack depth from the attenuation rate. Numerical results are in good agreement with experimental results.

As a complementary technique, stack imaging procedure applied to ultrasonic echo data in time domain gives good results. Subsurface crack tip can be identified better, although there is slight difference from the actual location due to large discretization.

Acknowledgements Financial support provided by TUBITAK (The Scientific and Technological Research Council of Turkey) to conduct this research under the grant number 110M585 is greatly acknowledged.

References

1. Sansalone MJ, Streett WB (1997) Impact-echo. Bullbrier, Ithaca
2. Sansalone MJ, Lin JM, Streett W (1998) Determining the depth of surface-opening cracks using impact-generated stress waves and time-of-flight techniques. *ACI Mater J* 95(2):168–177
3. Masserey B, Mazza E (2007) Ultrasonic sizing of short surface cracks. *Ultrasonics* 46(3):195–204
4. Jian X, Dixon S, Guo N, Edwards RS, Potter M (2006) Pulsed Rayleigh wave scattered at a surface crack. *Ultrasonics* 44(1):1131–1134
5. Hevin G, Abraham O, Pedersen HA, Campillo M (1998) Characterization of surface cracks with rayleigh waves: a numerical model. *NDT&E Int* 31(4):289–297
6. Aggelis DG, Shiotani T, Polyzos D (2009) Characterization of surface crack depth and repair evaluation using Rayleigh waves. *Cem Concrete Compos* 31:77–83
7. Aggelis DG, Shiotani T (2007) Repair evaluation of concrete cracks using surface and through-transmission wave measurements. *Cem Concrete Compos* 29:700–711
8. Pecorari C (2001) Scattering of a Rayleigh wave by a surface-breaking crack with faces in partial contact. *Wave Motion* 33:259–270
9. Zhang C, Achenbach JP (1990) Dispersion and attenuation of surface waves due to distributed surface-breaking cracks. *J Acous Soc Am* 88(4):1986–1992
10. Kawashima K, Murase M, Ito T (2006) Ultrasonic imaging of tight crack surfaces by backscattered transverse wave with a focused transducer. In: ECNDT 2006, 25–29 Sept, Berlin, CD-ROM. Poster 165
11. Tokai M, Ohkubo T, Ohtsu M (2009) Estimation of surface crack depth in concrete by scanning SIBIE procedure. In: NDTCE'09, 7th International Symposium on Nondestructive Testing in Civil Engineering, 30 June–3 July 2009, Nantes, France, CD-ROM
12. Dutton B, Clough AR, Hosli MH, Edwards RS (2011) Non-contact ultrasonic detection of angled surface defects. *NDT&E Int* 44:353–360

13. Ni C, Shi Y, Shen Z, Lu J, Ni X (2010) An analysis of angled surface-breaking crack detection by dual laser source generated ultrasound. *NDT&E Int* 43:470–475
14. Aggelis DG, Leonidou E, Matikas TE (2012) Subsurface crack determination by one-sided ultrasonic measurements. *Cem Concrete Compos* 34:140–146
15. Aggelis DG, Kordatos EZ, Soulioti DV, Matikas TE (2010) Combined use of thermography and ultrasound for the characterization of subsurface cracks in concrete. *Constr Build Mater* 24:1888–1897
16. Aggelis DG, Kordatos EZ, Strantza M, Soulioti DV, Matikas TE (2011) NDT approach for characterization of subsurface cracks in concrete. *Constr Build Mater* 25:3089–3097
17. Alver N, Ohtsu M (2007) BEM analysis of dynamic behavior of concrete in impact-echo test. *Constr Build Mater* 21(3):519–526
18. Brebbia CA (1981) *Progress in boundary element methods*, vol 1. Pentech, London
19. Alver N, Ohtsu M (2008) Dynamic boundary element method analysis for determining correction factor in impact echo. In: *Transportation Research Record: Journal of the Transportation Research Board*, No. 2050, Transportation Research Board of the National Academies, Washington, pp 122–126

Chapter 30

An Improved Methodology for Anomaly Detection Based on Time Series Modeling

Qipei Mei and Mustafa Gul

Abstract In this paper, results from on-going studies for extending a damage detection approach previously developed by the authors are presented. The methodology in the previous form was able to detect and locate the damage/anomaly successfully by using free response acceleration data employing a sensor clustering based time series modeling approach. The basic idea behind the methodology is that an Auto-Regressive model with eXogenous input (ARX model) between the outputs of a structure can be related to the structural properties of the system without using the input (excitation to the structure) or any other information. The improved version can detect, locate and quantify mass, stiffness and damping changes separately in a numerical model by using acceleration, velocity and displacement data. Based on the results, the potential and advantages of the methodology under investigation are discussed. Its limitations and shortcomings in the current version are also addressed along with proposed solutions and future work plans.

Keywords Damage detection • Structural health monitoring • Time series modeling • Civil infrastructure systems • Bridge health monitoring

30.1 Introduction

It is widely accepted that aging and deteriorating Civil Infrastructure Systems (CIS) are among the biggest challenges faced by our modern society. Considering the negative impacts of this complex problem, there is a considerable effort to restore and improve the CIS with a long-term goal of developing a smart and sustainable infrastructure network. Structural Health Monitoring (SHM) is considered to be one of the most critical components of this long-term goal as an objective and innovative decision-making support tool for the infrastructure owners and decision-makers.

Despite the significant developments in the field of SHM in the last few decades, it is still very difficult to claim that SHM systems can be confidently applied for routine monitoring of critical components of CIS. Easy data collection is enabled by the recent advances in the sensing and computing technologies; however, proper and efficient analysis of the measured data still stands as one of the biggest challenges. SHM systems cannot be deemed successful unless useful information is extracted from the data and used for decision-making. Therefore, a lot of attention has been directed to developing data analysis methodologies for damage assessment using SHM data.

Data analysis methods for damage detection can be mainly categorized as parametric or non-parametric. Parametric techniques aim to develop physics-based models for damage assessment. Modal parameter based methods are commonly for this purpose. Although these approaches are very effective in establishing a direct relationship between the damage features and the physical characteristics of the structure, developing the necessary models and analyzing the data may require significant experience. Also, their automation for handling large amounts of data may not be feasible. Finally, successful application of these techniques to real structures is still a challenge due to varying operational and environmental conditions.

Recognizing these types of needs, statistical pattern recognition approaches have gained significant attention starting in the early 2000s as a non-parametric damage detection paradigm for SHM [1]. These techniques mostly use a combination of time

Q. Mei • M. Gul (✉)

Department of Civil and Environmental Engineering, Markin/CNRL Natural Resources Engineering Facility,
University of Alberta, 9105 116th St., Edmonton, AB, Canada T6G 2W2
e-mail: qipei@ualberta.ca; mustafa.gul@ualberta.ca

series modeling with a statistical novelty detection methodology such as outlier detection [2–5]. The anomalies are identified by analyzing the features that may not be easily attributed to specific physical changes. However, these techniques may be able to handle the operational and environmental changes more successfully. Also, they may facilitate easier automation and, in turn, better data management, which has become one of the most critical challenges of SHM applications.

This paper presents the preliminary results of on-going research for damage detection, localization and quantification using time series models. The work discussed here can be considered as an extension of a sensor clustering based damage detection technique developed by the second author previously [6–8]. In those studies, free response acceleration data was used for damage detection and localization. Successful results were obtained using numerical and experimental data. In this study, the same sensor-clustering based approach is exploited using acceleration, velocity and displacement data. The promise of this extension is the ability of identification in mass, damping and stiffness separately as demonstrated in the following sections.

30.2 Background and Methodology

The equation of motion for an N Degrees of Freedom (DOFs) linear dynamic system can be written as in Eq. (30.1) (t for time is omitted).

$$\begin{bmatrix} m_{11} & \cdots & m_{1N} \\ \vdots & \ddots & \vdots \\ m_{N1} & \cdots & m_{NN} \end{bmatrix} \begin{Bmatrix} \ddot{x}_1 \\ \vdots \\ \ddot{x}_N \end{Bmatrix} + \begin{bmatrix} c_{11} & \cdots & c_{1N} \\ \vdots & \ddots & \vdots \\ c_{N1} & \cdots & c_{NN} \end{bmatrix} \begin{Bmatrix} \dot{x}_1 \\ \vdots \\ \dot{x}_N \end{Bmatrix} + \begin{bmatrix} k_{11} & \cdots & k_{1N} \\ \vdots & \ddots & \vdots \\ k_{N1} & \cdots & k_{NN} \end{bmatrix} \begin{Bmatrix} x_1 \\ \vdots \\ x_N \end{Bmatrix} = \begin{Bmatrix} f_1 \\ \vdots \\ f_N \end{Bmatrix} \quad (30.1)$$

where m_{ij} , c_{ij} , and k_{ij} represent the mass, damping and stiffness properties of the system, respectively. The vectors \ddot{x} , \dot{x} and x are acceleration, velocity and displacement, respectively. The external forcing function on the system is denoted with f . The equality in Eq. (30.2) is obtained if the first row of Eq. (30.1) is written separately. By rearranging Eqs. (30.2) and (30.3) shows that the output of the 1st DOF can be written in terms of the excitation force on 1st DOF, the physical parameters of the structure, and the outputs of the other DOFs (including itself). Furthermore, in case of free response, the force term can be eliminated and the relation is written as shown by Eq. (30.4).

$$(m_{11}\ddot{x}_1 + \cdots + m_{1N}\ddot{x}_N) + (c_{11}\dot{x}_1 + \cdots + c_{1N}\dot{x}_N) + (k_{11}x_1 + \cdots + k_{1N}x_N) = f_1 \quad (30.2)$$

$$\ddot{x}_1 = \frac{f_1 - (m_{12}\ddot{x}_2 + \cdots + m_{1N}\ddot{x}_N) - (c_{11}\dot{x}_1 + \cdots + c_{1N}\dot{x}_N) - (k_{11}x_1 + \cdots + k_{1N}x_N)}{m_{11}} \quad (30.3)$$

$$\ddot{x}_1 = -\frac{(m_{12}\ddot{x}_2 + \cdots + m_{1N}\ddot{x}_N) + (c_{11}\dot{x}_1 + \cdots + c_{1N}\dot{x}_N) + (k_{11}x_1 + \cdots + k_{1N}x_N)}{m_{11}} \quad (30.4)$$

Focusing on Eq. (30.4), it is observed that a model to predict the response of the first DOF by using the responses from the neighbor DOFs will contain information about the system properties such as mass, damping and stiffness. It is clear that changes in this model can reveal important information about the change in the properties of that part of the system. Obviously, similar equalities can be written for each row of Eq. (30.1) and different models can be created for each equation. Each row of the matrix equation in Eq. (30.1) can be treated as a sensor cluster.

Therefore, it was proposed in [6–8] that different linear time series models could be created to establish different models for each sensor cluster and changes in these models can pin-point the existence, location and severity of the damage. The core of the methodology was to create different ARX models (Auto-Regressive models with eXogenous input) for different sensor clusters and then extract damage sensitive features from these models to detect the damage. A general representation of an ARX model is shown in Eq. (30.5). In this ARX model, the $y(t)$ term is the acceleration response of the reference channel of a sensor cluster, the $u(t)$ term is defined with the acceleration, velocity and displacement responses of all the DOFs in the same cluster while $e(t)$ is the error term. After creating the ARX models for the baseline/healthy condition, the coefficients of the ARX models (B-term coefficients) for each sensor cluster is compared before and after damage to obtain information about the changes in mass, damping and stiffness separately.

$$A(q)y(t) = B(q)u(t) + e(t) \quad (30.5)$$

30.3 Case Studies and Discussions

For numerical verifications of the proposed approach, the same numerical model that was used in the previous studies [6–8] is used. The properties of the 4-DOF system shown in Fig. 30.1 can be summarized as: $m_1 = 0.8$, $m_2 = 2$, $m_3 = 1.2$, $m_4 = 0.6$, $k_1 = 20$, $k_2 = 10$, $k_3 = 15$, $k_4 = 10$ and $k_5 = 25$, $c_1 = 0.002$, $c_2 = 0.001$, $c_3 = 0.0015$, $c_4 = 0.001$ and $c_5 = 0.0025$.

30.3.1 Case Study 1: $k_2 = 0.8 \times k_2$

The first case study simulates a damage case where the stiffness between the 1st and 2nd DOFs is reduced 20%. The B-term coefficients of the ARX models before and after the damage was introduced are compared in Tables 30.1 and 30.2. It is clearly observed that the 20% stiffness loss between the 1st and 2nd DOFs is identified with the 20% drop in the displacement B-term coefficients. Table 30.2 shows that there is no change in the velocity B-term coefficients since the damping properties of the system are not changed. The -3.64% and -5.71% changes in the diagonal terms in Table 30.1 are caused by the fact that 20% decrease in k_2 ($k_2 = 8$ instead of 10, a difference of 2) introduces 3.64% decrease in the total stiffness connected to 1st DOF ($2/(20 + 10 + 25 = 3.64)$) and creates a 5.71% decrease in the total stiffness connected to 2nd DOF ($2/(10 + 15 + 10) = 5.71$).

30.3.2 Case Study 2: $c_3 = 0.8 \times c_3$

The second case study simulates a 20% decrease in the damping between 2nd and 3rd DOFs. As observed in Tables 30.3 and 30.4, this change in the damping is also clearly identified. Since the stiffness has not changed, there is absolutely no change

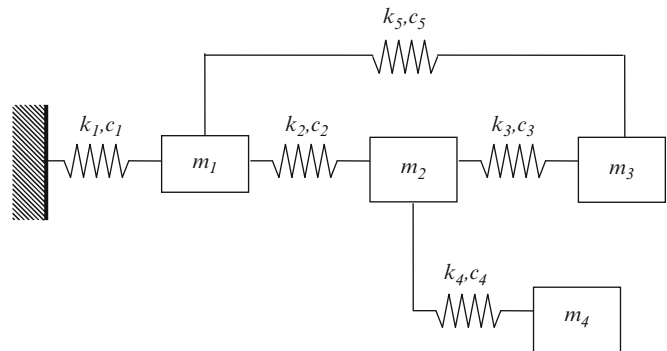


Fig. 30.1 The numerical model used for verifications

Table 30.1 Change (%) in the B-term coefficients for displacement when k_2 is decreased 20%

Measurement location	DOF 1	DOF 2	DOF 3	DOF 4
DOF 1	-3.64	-20.00	0.00	n/a
DOF 2	-20.00	-5.71	0.00	0.00
DOF 3	0.00	0.00	0.00	n/a
DOF 4	n/a	0.00	n/a	0.00

As we mentioned in the paper, the bold values reflect the location and degree of damage we want to detect. We use bold font to distinguish them from those zero values in order to express the changes more clearly

Table 30.2 Change (%) in the B-term coefficients for velocity when k_2 is decreased 20%

Measurement location	DOF 1	DOF 2	DOF 3	DOF 4
DOF 1	0.00	0.00	0.00	n/a
DOF 2	0.00	0.00	0.00	0.00
DOF 3	0.00	0.00	0.00	n/a
DOF 4	n/a	0.00	n/a	0.00

Table 30.3 Change (%) in the B-term coefficients for displacement when c_3 is decreased 20%

Measurement location	DOF 1	DOF 2	DOF 3	DOF4
DOF 1	0.00	0.00	0.00	n/a
DOF 2	0.00	0.00	0.00	0.00
DOF 3	0.00	0.00	0.00	n/a
DOF4	n/a	0.00	n/a	0.00

Table 30.4 Change (%) in the B-term coefficients for velocity when c_3 is decreased 20%

Measurement location	DOF 1	DOF 2	DOF 3	DOF4
DOF 1	0.00	0.00	0.00	n/a
DOF 2	0.00	-5.45	-20.00	0.00
DOF 3	0.00	-20.00	-5.77	n/a
DOF4	n/a	0.00	n/a	0.00

As we mentioned in the paper, the bold values reflect the location and degree of damage we want to detect. We use bold font to distinguish them from those zero values in order to express the changes more clearly

Table 30.5 Change (%) in the B-term coefficients for displacement when m_3 is decreased 20%

Measurement location	DOF 1	DOF 2	DOF 3	DOF4
DOF 1	0.00	0.00	0.00	n/a
DOF 2	0.00	0.00	0.00	0.00
DOF 3	25.00	25.00	25.00	n/a
DOF4	n/a	0.00	n/a	0.00

As we mentioned in the paper, the bold values reflect the location and degree of damage we want to detect. We use bold font to distinguish them from those zero values in order to express the changes more clearly

Table 30.6 Change (%) in the B-term coefficients for velocity when m_3 is decreased 20%

Measurement location	DOF 1	DOF 2	DOF 3	DOF4
DOF 1	0.00	0.00	0.00	n/a
DOF 2	0.00	0.00	0.00	0.00
DOF 3	25.00	25.00	25.00	n/a
DOF4	n/a	0.00	n/a	0.00

As we mentioned in the paper, the bold values reflect the location and degree of damage we want to detect. We use bold font to distinguish them from those zero values in order to express the changes more clearly

in the B-term coefficients for the displacement. However, velocity B-term coefficients in Table 30.4 are affected in the same manner as explained above.

30.3.3 Case Study 3: $m_3 = 0.8 \times m_3$

For the last case study, the mass of the 3rd DOF is reduced 20%. It should be noted here that this 20% reduction should create a 25% increase in the system parameters ($1/0.8 = 1.25$) of the 3rd sensor cluster. This relation can be observed more clearly if Eq. (30.4) is considered for the 3rd sensor cluster. The asymmetric for of Tables 30.5 and 30.6 compared to the first four tables should also be noted since the effect of the mass decrease should not be seen in two sensor clusters.

30.4 Summary and Conclusions

This study presents preliminary findings of an improved damage detection methodology for identification, localization and quantification of changes in mass, damping and stiffness properties of a structural system using free response (output-only) data. This approach is based on creating time series models for different sensor clusters in a structure to obtain localized information. The damage features are extracted from the coefficients of the time series models. The results show that the

approach is very promising and further investigations should be carried out to explore the capabilities and limitations of the methodology. As immediate steps, fine-tuning the time series models will be carried out. Also, verifications with numerical models where artificial noise is added to the data will be conducted. Also, for real life applications, the employment of the velocity and displacement data may create practical limitations since this type of data is generally not recorded for long-term applications. However, the non-contact measurement systems may be utilized to overcome this limitation. Also, numerical integration techniques may be utilized for obtaining the velocity and displacement data from acceleration data. The impacts of this study on damage detection under changing operational and environmental changes should also be emphasized since the changes in the mass, damping and stiffness are assessed simultaneously with output-only data. For example, the change in the mass due to the operation traffic on a bridge may be clearly separated from the changes in the stiffness changes using the proposed approach.

References

1. Sohn H, Farrar CR, Hunter NF, Worden K (2001) Structural health monitoring using statistical pattern recognition techniques. *J Dyn Syst Meas Contr* 123(4):706–711
2. Carden EP, Brownjohn JM (2008) ARMA modelled time-series classification for structural health monitoring of civil infrastructure. *Mech Syst Signal Proc* 22(2):295–314
3. Cheung A, Cabrera C, Sarabandi P, Nair KK, Kiremidjian A, Wenzel H (2008) The application of statistical pattern recognition methods for damage detection to field data. *Smart Mater Struct* 17:065023
4. Yao R, Pakzad SN (2012) Autoregressive statistical pattern recognition algorithms for damage detection in civil structures. *Mech Syst Signal Proc* 31:355–368
5. Gul M, Catbas FN (2009) Statistical pattern recognition using time series modeling for structural health monitoring: theory and experimental verifications. *Mech Syst Signal Proc* 23(7):2192–2204
6. Gul M, Catbas FN (2008) A new methodology for identification, localization and quantification of damage by using time series modeling. In: 26th international modal analysis conference, February 4–7, Orlando
7. Gul M, Catbas FN (2009) A modified time series analysis for identification, localization, and quantification of damage. In: 27th international modal analysis conference, February 9–12, Orlando
8. Gul M, Catbas FN (2011) Structural health monitoring and damage assessment using a novel time series analysis methodology with sensor clustering. *J Sound Vib* 330(6):1196–1210

Chapter 31

Response Surface Model Updating for Nonlinear Structures

Golnaz Shahidi and Shamim N. Pakzad

Abstract This paper presents a procedure to update nonlinear finite element models in time. In the proposed method, accurate response surface models are constructed and evaluated to replace the finite element model at every time step of the analysis. Then, the optimization problem of model updating is formulated and solved iteratively leading to histograms of the updated model parameters. This methodology is beneficial in extracting more information from measured signals and compensate for the error present in the regressed response surface models. The proposed method was verified through a numerical case study of a steel frame with global nonlinearity. Appropriate design and model orders were successfully established and the optimization in time performed well in the simulated scenarios under the assumption of noise free and noisy measurement data.

Keywords Finite element model • Model updating • Nonlinear structure • Response surface model • Optimization

31.1 Introduction

Finite element (FE) models are extensively used for analytical purposes in the engineering field. These models serve as the preliminary base for designing and analysing behaviour of the actual structures. However, the analysis results of these models are not same as that obtained from testing the actual structures. This is mainly because of a number of simplifying assumptions used in the FE model or/and deterioration of the structure with use and time. Modifying the FE model to obtain better agreement with the experimental records is termed as *Finite Element Model Updating*. Over the past decades several computational procedures have been developed to update parameters of analytical models based on experimental results. Methods for linear model updating are well-documented in the literature. These techniques are mainly based on the sensitivity analysis and linearization of the generally nonlinear relationship between measured outputs such as natural frequencies, mode shapes or displacement responses and the parameters of the model in need of correction [1]. However, iterative determination of local gradient in such methods may cause not only computational intensive, but also convergence difficulty [2]. Moreover, in the presence of nonlinearities in the structure these procedures will fail to yield the parameters associated with nonlinear behavior of the model and other measures are required to update the model.

One of the proposed approaches to overcome these problems is to replace the FE model with a mathematical expression which approximates the relationship between pre-selected inputs and output of the FE model and update the parameters of the model by directly optimizing this surrogate model. One of the commonly used surrogate models are polynomial functions constructed based on Response Surface (RS) methodology. This method has shown attractive potential in modifying FE model parameters. Guo and Zhang [3] found that, compared with the sensitivity-based model updating, the RS-based method gave likewise accurate predictions while requiring much fewer number of FE analyses. Ren and Chen [2] compared the performance of RS-based and Sensitivity-based FE model updating on a full size precast continuous box girder bridge and observed that the rate of convergence in RS-based updating is faster. Ren et al. [4] concluded that for complex structures with large number of uncertain parameters uniform design economized the computational effort to construct the RS models and the

G. Shahidi (✉) • S.N. Pakzad
Department of Civil and Environmental Engineering, ATLSS Engineering Research Center, Lehigh University,
117 ATLSS Drive, Imbt Labs, Bethlehem, PA, 18015 USA
e-mail: sgs310@lehigh.edu; pakzad@lehigh.edu

accuracy of the RS models in such problems could be improved by shrinking the design space and repeating the RS modeling and updating. Zhang et al. [5] proposed a model updating technique based on generic algorithm and RS methodology. Application of the method on a numerical simulation of an antenna successfully reached the global optima. Studies of Cundy [6] and Fang and Perera [7] found that application of RS-based model updating in damage detection performs well in locating damage and quantifying its severity to some extent in numerical and experimental case studies. There are few examples of application of RS-based model updating in the literature for structures with nonlinearities. Schultze et al. [8] applied this method to select significant parameters to update a model consist of a cylindrical steel impactor and a foam layer assembled on a mounting plate attached to a drop table under impact on a concrete floor. Zhang and Guo [9] proposed a model updating procedure based on Principal Component Decomposition and RS method to update a model of frame with thin wall components showing strain-rate-dependence nonlinearity under impact test.

In this paper a procedure is proposed to update nonlinear FE models in time. For this purpose, low computational effort associated with RS modeling is used to formulate and solve the optimization problem of model modification in the length of time domain data iteratively. This approach is beneficial in extracting more information from the measured experimental signals as opposed to the traditional approaches in which the whole measured signals are summarized into one or more response features. Another advantage of this method is that it is not limited to the type of model behavior or analysis. It can be applied to linear or nonlinear models under static or dynamic analysis. Since the procedure of finding an appropriate design to build accurate RS models requires a number of trials and errors with different designs and subset models, a procedure is also proposed to design the levels of input parameters and construct the RS models prior to model updating. This procedure results in RS models capable of generating the results of FE analysis in a specific domain of input variables.

In the following sections of the paper the proposed procedure is explained and the results of application of this method on a numerical case study are demonstrated.

31.2 Nonlinear Model Updating Using Response Surface Models

To update nonlinear FE models through time history of measured responses, in every time step of the analysis a RS model is constructed to produce the response of the FE model at that time step. To do so, the experimental input force is used to generate the equivalent responses of FE model at different levels of the model parameters. These levels of the model parameters, corresponding responses of the FE model and least square estimation techniques are used to find the best polynomial model which can replace the FE model at every time step of the analysis.

Equation (31.1) denotes the RS model at the l^{th} time step of the analysis, where h is the polynomial surrogate model in that time step and Θ represents a vector of model parameters selected for modification.

$$RS_l = h_l(\Theta) \quad (31.1)$$

By completing this process for every response, an objective function is formulated to minimize a function of residuals of RS-based and experimental response features at every time step. Equation (31.2) represents this minimization problem which is solved inside the domain of model parameters.

$$\min_{\theta} f_l(H_l(\Theta), Y_{expl}) \quad (31.2)$$

In Eq. (31.2) H_l and Y_{expl} are vectors containing all the surrogate models and corresponding experimental responses at the l^{th} time step.

Prior to RS modeling, the appropriate design and model order should be found so that the regressed RS models are accurate at the associated time steps. First, an initial region for the pre-selected uncertain parameters of the FE model should be chosen. This region, in which the FE model is replaced by the RS model, is called *RS domain*. To regress the polynomial RS models, a number of points are sampled in the RS domain based on full factorial design of the model parameters. The RS model construction starts with a full factorial design with three levels for each parameter and including linear terms of the updating parameters in the RS models. Initially the performance of the RS models is checked at the design points based on the residuals of the RS and FE models. Then the overall adequacy of the RS models is evaluated by adjusted R^2 statistics. If R^2_{adj} is close to one, it implies a perfect regression. Therefore, when R^2_{adj} is much smaller than one, the RS model is not accurate in estimating the FE responses at the design points. After completing R^2_{adj} calculation through the time domain data, if the regressed RS models are not fitted well to the design points, higher order terms of the model parameters should be added to the RS models and the model evaluation repeated to find the appropriate model order.

After finding the suitable model order, the prediction quality of the RS models should be checked. For this purpose, residuals are calculated at points in the RS domain that did not contribute in the regression. These points, which are called intermediate points, are sampled from RS domain in different sets. Each set represents the intermediate levels for one parameter. To sample a set of new points corresponding to a parameter, one of the original data points is replicated, and then the selected parameter is replaced by the average of one pair of its original levels. Intermediate points which result in larger residuals than the original design points indicate that although the RS model has been fitted well to the original data, it cannot predict the FE responses for new points. Therefore, the design of levels of parameters should become finer and new RS models should be regressed.

By repeating this procedure, an RS model with high quality in regression and prediction is constructed for every time step of the data. Upon completion of this procedure for every response feature, the optimization problem of model updating is solved for every time step which results in histograms of the updated model parameters. The optimization step can be repeated in a smaller region for model parameters centred on the mean value of the results of the first cycle of optimization. Using the design and model order established in the first cycle, only the following steps are needed: (1) generate the FE responses for new levels; (2) fit the new RS models through the time history; and (3) optimize the new objective function iteratively.

31.3 Case Study: Nonlinear Steel Frame

The case study presented here is a steel frame with nonlinear material properties under dynamic loading. The frame consists of one span with overall length of 228.6 cm supported by columns that are 83.8 cm long. The cross section of the beam and column members is uniform hollow 5.08 cm tube, with 0.21 cm wall thickness. The steel has bilinear behavior with the yield stress of 344.8 MPa. Modulus of elasticity (E) and post yielding stiffness ratio of steel (b) were chosen as the updating parameters. To simulate the experimental data, these parameters were set to 193.1 GPa and 0.18 for E and b respectively. The loading is a concentrated harmonic lateral load with amplitude 22.2 kN and 5 sec period, applied at the beam column joint. The amplitude of the load is selected so that under lateral loading the stress in the columns and beam exceeds the yield stress. To update the selected parameters, simulated time histories of displacement at two locations on the frame were assumed as the experimental data. Figure 31.1 shows the configuration of the steel frame, loading and the responses used in the updating procedure.

A 2-D FE model was developed by Opensees software using fiber section procedure and Steel01 uniaxialMaterial properties. The initial domain of the updating parameters was set to 186.2 to 227.5 GPa for E and 0.05 to 0.25 for b . The RS model construction starts with full factorial design of parameters, each having three levels. RS models including the linear terms of E and b were regressed to the data at every time step. The large residuals associated with the regressed models indicate that the RS models are not accurate to replace the FE model. Consequently, quadratic terms were added to the polynomial models and regression was repeated. Adding the quadratic terms to the linear models significantly improves the accuracy of the RS models at the design points. Figures 31.2 and 31.3 compare the maximum normalized residuals at original and intermediate points of the 3×3 design for the quadratic RS models through the time data. The RS models generate u_2 with smaller residuals; however, they are not successful in predicting both u_1 and u_2 at the intermediate levels corresponding to b . Therefore, the levels associated with stiffness ratio, b , in the RS domain should be finer.

RS model construction and evaluation were repeated with 4×3 design and observed that the RS models are not accurate at intermediate levels of parameter b for this design. Figures 31.4 and 31.5 display the maximum normalized residuals of RS and FE model for a 5×3 design. The RS models contain terms up to order 4 and 2 for stiffness ratio, b , and modulus of elasticity, E , respectively. These figures show that the RS models perform well at both original and intermediate levels. Therefore, the RS models are accurate for the optimization procedure.

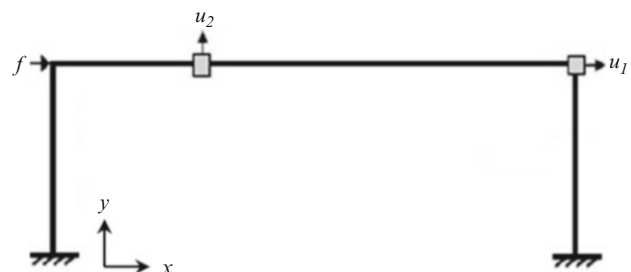


Fig. 31.1 Configuration of the nonlinear steel frame

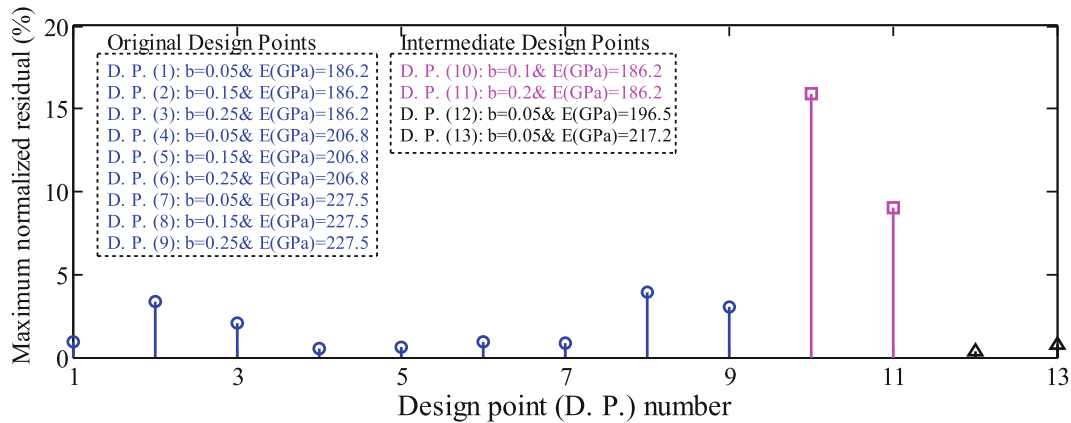


Fig. 31.2 Normalized residuals of original and intermediate design points using 3×3 design: u_1

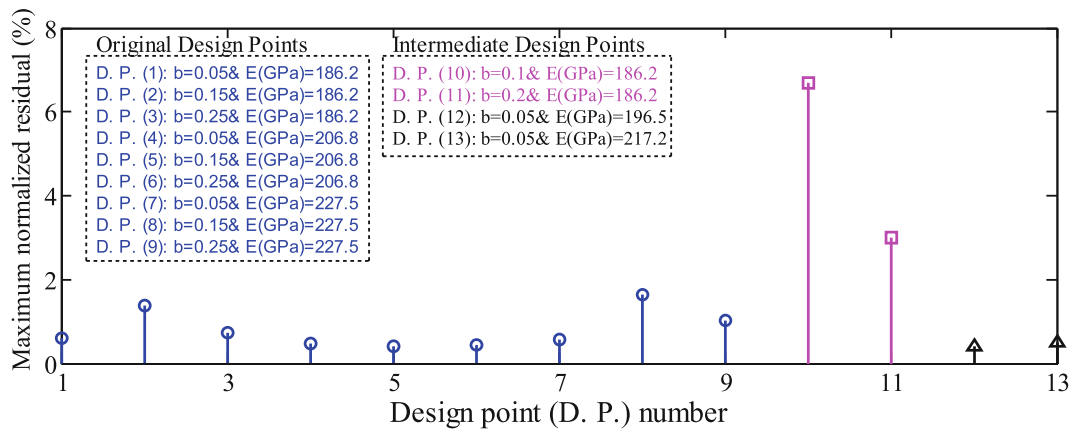


Fig. 31.3 Normalized residuals of original and intermediate design points using 3×3 design: u_2

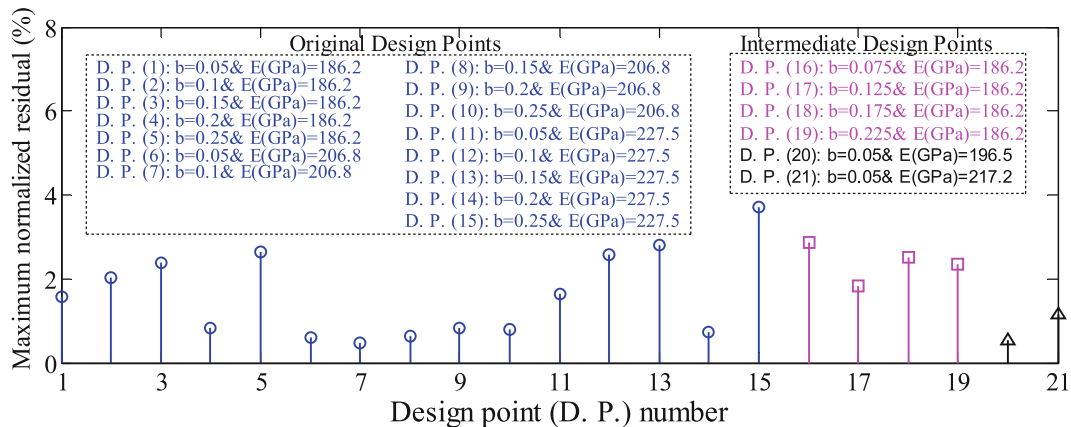


Fig. 31.4 Normalized residuals of original and intermediate design points using 5×3 design: u_1

Figure 31.6 shows the histogram of the updated parameters resulted from solving the optimization problem in every time step for the first time. This histogram shows where the updated parameters locate in the RS domain. The updated model parameters are distributed in a considerably narrower region than the initial region used in the RS model construction. To decrease the variation of the updated parameters, the design and model order established in the previous section for E and b are used to repeat the optimization problem. The new domain for E and b is centered on the mean value of the updated parameters in the first round of optimization. Figure 31.6 shows the result of the second round of model updating in terms of the distribution, mean and coefficient of variation of the updated parameters.

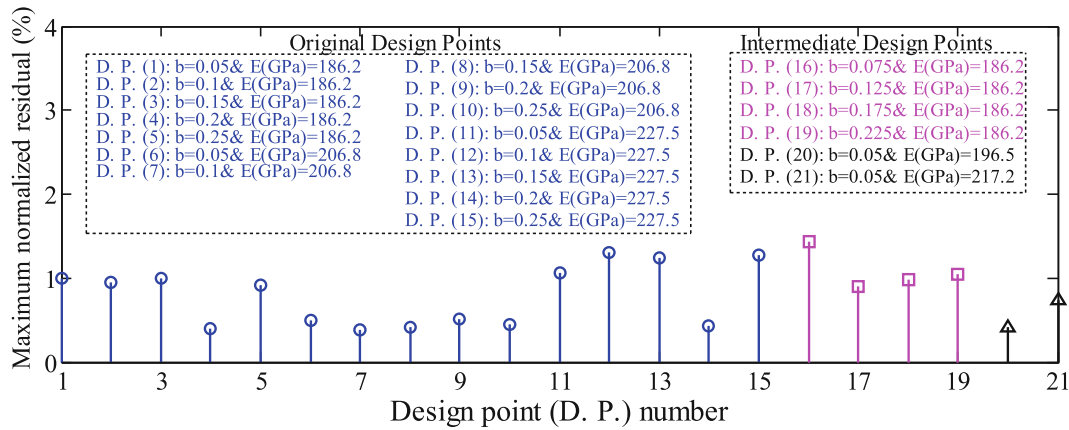


Fig. 31.5 Normalized residuals of original and intermediate design points using 5 × 3 design: u₂

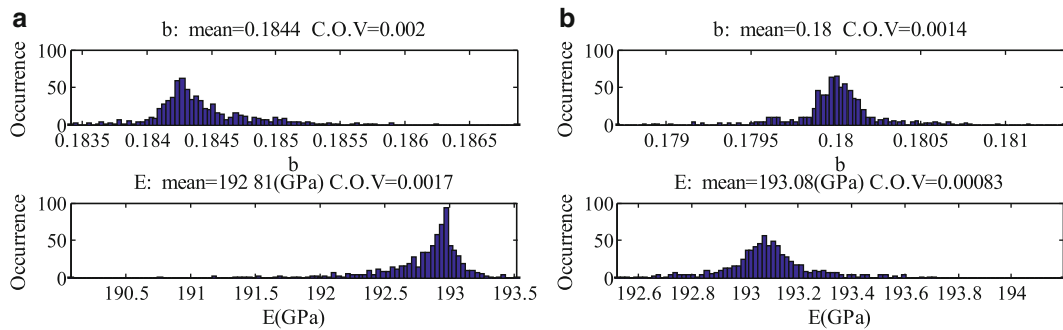


Fig. 31.6 (a) Results of the first optimization round, (b) Results of the second optimization round

Table 31.1 Comparison of the performance of the proposed procedure (Simulated data with different noise levels)

		True model parameters: E(GPa) = 193.1 & b = 0.18	
		Updated parameters	
		b	E
RS domain	Noise level (%)	Relative error (%)	
b: 0.05 to 0.25	0	0.00	0.00
E(GPa): 186.2 to 227.54	1	0.11	0.11
	5	-1.50	1.57
	10	-3.06	3.07

Furthermore, to evaluate the performance of the proposed procedure in the presence of noisy measurement data, different levels of Gaussian noise were introduced into the simulated experimental responses and the updating procedures were reiterated. The results were summarized in Table 31.1. Noise level in this table represents the ratio of the root mean square of the simulated noise signal to the root mean square of the original signal. It can be seen that the procedure shows robustness to different levels of noise.

The advantage of using the proposed procedure for updating nonlinear FE models is that this method successfully finds a smaller region for the model parameters and has corrective information for the initial estimate of the RS domain. Moreover, it is computationally efficient and shows robustness to moderate and high level noise.

31.4 Conclusions

This paper presents a procedure for updating nonlinear Finite Element models using time domain data based on Response Surface methodology. The proposed procedure was validated through to a numerical case study of a steel frame with global nonlinearity. The optimization in time domain performed well in the numerical case study. The first round of optimization

resulted in a considerably narrower bounds for the uncertain parameters of the model than the initial boundaries set at the beginning of the procedure. Repeating the RS model construction with known order and design for the new bounds of parameters and solving the optimization problem resulted in the true model parameters. To verify the robustness of the results, the numerical case study were repeated assuming low, moderate and high level noise in the experimental data and it was observed that the proposed procedure show robustness in all these scenarios.

Acknowledgements Research funding is partially provided by the National Science Foundation under Grant No. CMMI-0926898 by Sensors and Sensing Systems program, and by a grant from the Commonwealth of Pennsylvania, Department of Community and Economic Development, through the Pennsylvania Infrastructure Technology Alliance (PITA). Their financial support is gratefully appreciated.

References

1. Mottershead JE, Link M, Friswell MI (2010) The sensitivity method in finite element model updating: a tutorial. *Mech Syst Signal Process* 25(7):2275–2296
2. Ren W, Chen H (2010) Finite element model updating in structural dynamics by using the response surface method. *Eng Struct* 32(8):2455–2465
3. Guo QT, Zhang LM (2004) Finite element model updating based on response surface methodology. In: *Proceedings of IMAC-XXII: conference and exposition on structural dynamics*, Dearborn, Michigan, 2004
4. Ren W, Fang S, Deng M (2011) Response surface-based finite element model updating using structural static responses. *J Eng Mech (ASCE)* 137(4):248–257
5. Zhang LM, Fei Q, Guo QT (2005) Dynamic finite element model updating using meta-model and genetic algorithm. In: *Proceedings of IMAC-XXIII: conference and exposition on structural dynamics*, Orlando, Florida, 2005
6. Cundy AL (2002) Use of response surface metamodels in damage identification of dynamic structures. M. S. Thesis, Virginia Polytechnic Institute and State University
7. Fang SE, Perera R (2009) A response surface methodology-based damage identification technique. *Smart Mater Struct* 18(6):065009
8. Jf S, Hemez FM, Doebling SW, Sohn H (2001) Application of non-linear system model updating using feature extraction and parameter effect analysis. *Shock Vib* 8:325–337
9. Zhang LM, Guo QT (2007) A case study of model updating and validation of a frame structure with highly non-linear component. In: *Proceedings of IMAC-XXV: conference and exposition on structural dynamics*, Orlando, Florida, 2007

Chapter 32

Application of Multivariate Statistically Based Algorithms for Civil Structures Anomaly Detection

Masoud Malekzadeh, Mustafa Gul, and F. Necati Catbas

Abstract Two multivariate statistics based damage detection algorithms are explored in conjunction with optical fiber sensors for long-term application of Structural Health Monitoring. Two newly developed data driven methods are investigated, for bridge health monitoring, here based on strain data captured by Fiber Bragg Grating (FBG) sensors from 4-span bridge model. The most common and critical damage scenarios were simulated on the representative bridge model equipped with FBG sensors. Acquired strain data were processed by both Moving Principal Component Analysis (MPCA) and Moving Cross Correlation Analysis (MCCA). The efficiency of FBG sensors, MPCA and MCCA for detecting and localizing damage is explored. Based on the findings presented in this paper, the MPCA and MCCA coupled with FBG sensors can be deemed to deliver promising results to observe and detect both local and global damage implemented on the bridge structure.

Keywords Structural health monitoring • Fiber Bragg Grating Sensors • Advanced multivariate statistics • Damage detection

32.1 Introduction

32.1.1 Structural Health Monitoring

Throughout the recent decades, also due to inspiration by the results derived from several studies on lifetime performance of civil infrastructures, Structural Health Monitoring (SHM) is progressing as an inevitable multi-disciplinary technology for condition assessment of infrastructure systems [1]. SHM can be considered as a novel technology for proactive management of different structures such as bridges, buildings, airplanes. Steps for SHM implementations are concisely summarized and illustrated in Fig. 32.1. It is fairly clear, as also shown in Fig. 32.1, that the first two stages of SHM are the most fundamental and critical phases in order to entirely accomplish the predefined SHM related objectives. The first stage, referred as monitoring and measurement, highly relies on having a wisely designed and well-distributed network of sensors. This mission can be achievable only by employing advance precise measurement devices including superior sensors and data acquisition systems. Speaking of superior sensors, optical sensors and in particular Fiber Bragg Grating (FBG) sensors are popular alternatives to the traditional sensors in terms of several aspects, such as spatial resolution, durability, stability and immunity to electrical noise [2–5]. FBG strain sensors hold a great deal of potential for civil structural health monitoring.

M. Malekzadeh • F.N. Catbas (✉)

Department of Civil, Environmental and Construction Engineering, University of Central Florida, Orlando, FL 32816 USA
e-mail: m.malekzadeh@knights.ucf.edu; catbas@ucf.edu

M. Gul

Department of Civil and Environmental Engineering, University of Alberta, Edmonton, AB, Canada T6G 2W2
e-mail: mustafa.gul@ualberta.ca

Fig. 32.1 Individual stages involved in SHM process

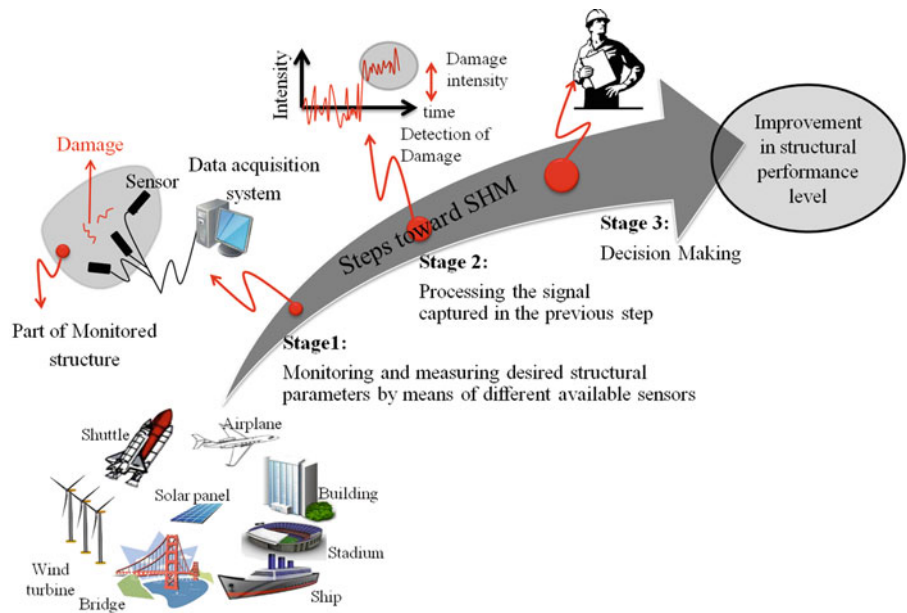
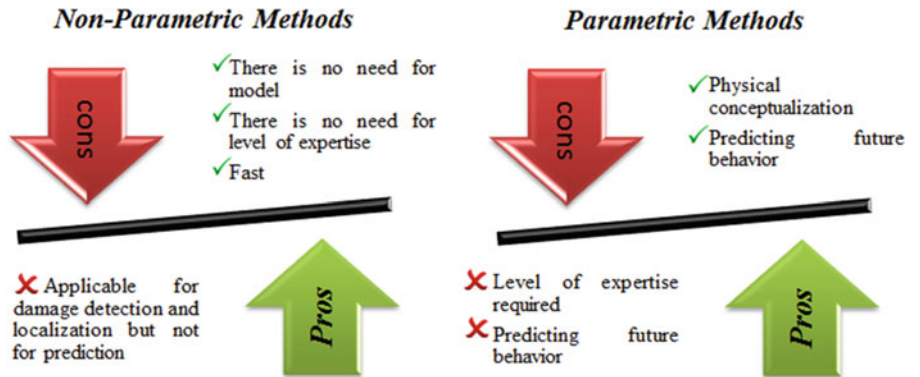


Fig. 32.2 Comparing parametric and nonparametric methods



Having a well-distributed network of sensor provides the opportunity of measuring desired structural parameters over critical areas along the monitored structure, however processing this data and extracting the useful information is still a challenging step and tackled in so called signal processing stage of Fig. 32.1. Basically, damage detection approaches in SHM fall into two main classes: model-based (parametric) methods and model-free (nonparametric) methods [6–9]. These methodologies follow specific procedures and are applicable in distinct contexts. The flowchart presented in Fig. 32.2 sheds light on the critical aspects of parametric and non-parametric damage detection algorithms.

Herein, in order to simultaneously explore the first two stages of SHM, FBG sensors as one the most superior sensor technologies are selected to evaluate the detectability of two advanced statistical data driven algorithms. To the best of the authors’ knowledge, the application of aforementioned data driven methods to the bridge monitoring has not been investigated by considering several common damage scenarios. Moreover, taking advantages of optical fiber in this type of data analysis framework is another unique aspect of this study. Therefore, the main contribution of this study is employing and investigating the efficiency of FBG sensors along with two innovative data driven damage detection algorithms under different scenarios for bridge structures. A comparative study was conducted to evaluate the efficiency of both moving principal component analysis (MPCA) and moving cross correlation analysis (MCCA) for the purpose of bridge monitoring application. For that reason, the 4-span laboratory bridge model, which is representative of mid-span real life bridges, is equipped with several FGB sensors at the critical locations and tested by simulating different type of critical damage scenarios.

32.2 Fiber Optic Sensors

32.2.1 FOS and Fiber Bragg Grating (FBG) Sensors

There has been a dramatic increase in the FOS implementations in the context of SHM due to aforementioned advantages brought by these types of sensors. FBG sensors, which are point types of sensors, are among the widely used FOS. The basic working principles of FOS and FBG sensors are reflection and filtration of different wavelengths of light [3]. Beside the FBG sensors, Brillouin Optical Time Domain Analysis (BOTDA) and Brillouin Optical Time Domain Reflectometry (BOTDR) two of the widely used distributed types of FOS [4]. For FBG sensors, grating property enables the optical fiber to transmit the entire wavelength except the particular reflected wavelength entitled as grating process. A brief introduction to theory of the optical fiber is presented in the following section.

32.2.2 Theory Behind the FBG Sensors

As it is briefly discussed above, the FBG function is fundamentally based upon reflection and filtration of the wavelength which travels throughout the grating segment. The reflection of pre-defined wavelength occurs, as soon as the launched broadband light reaches the grating segment of fiber optic line. This reflected wavelength is referred as Bragg wavelength and it is expressed by the following equation:

$$\lambda_B = 2n_e \Lambda \quad (32.1)$$

where λ_B represents of the Bragg wavelength, while n_e and Λ are the effective refractive index and the grating period respectively (illustrated in Fig. 32.3). When strain is induced, the Bragg wavelength is expected to have a proportional shift. The strain can be determined by analyzing the change in the wavelength. According to this principle, FBG can sense any possible changes, shift forward or backward, in the period of scattered wavelength and based on that it can measure strain in grating segment. The wavelength shift is proportional to strain, and absolute strain can be measured by using this shift [5].

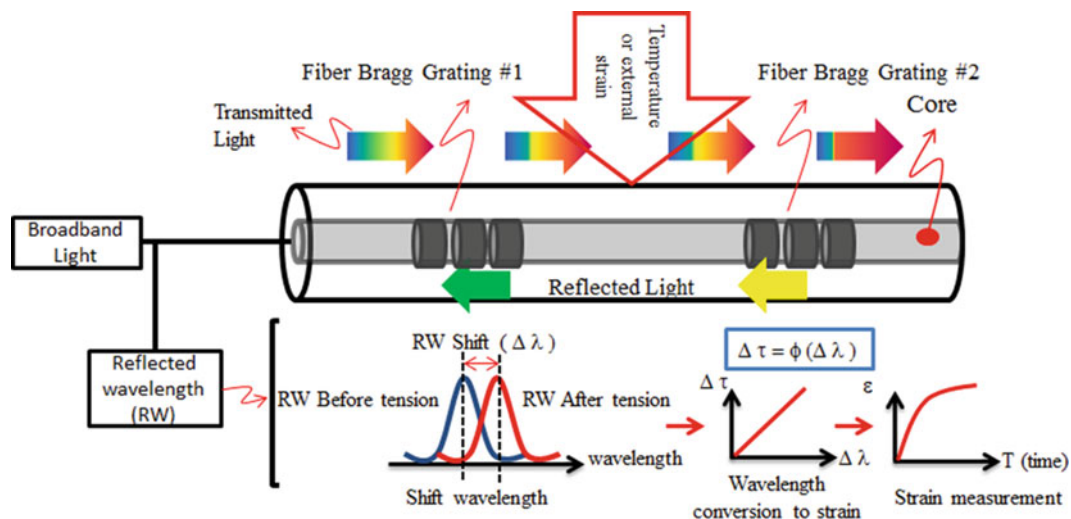


Fig. 32.3 Measurement principal of Fiber Bragg Grating (FBG) sensor

32.3 Damage Detection Algorithm

32.3.1 Moving Principal Component Analysis (MPCA)

Two main concerns, delay in abnormally detection along with computational time issue, inspired revision of classical PCA to make it more practical for long term SHM. Real life employment of SHM involves dealing with large amount of multivariate data. Only a small portion of abnormal data, in comparison to overall data, is available at the time when damage occurs. By means of PCA, the damage will be detectable only when the principal components (eigenvectors) are influenced by abnormal behavior. Subsequently, eigenvectors are subjected to change only if certain amount of abnormal data captured and possibly affected the overall structure of data. This feature makes PCA less effective for long term SHM implementation. Moving principal component analysis (MPCA) was proposed by Posenato et al. [8] to address this challenge. Basically, MPCA computes the PCA within moving windows with a constant size.

A sensitive damage index is selected based on PCA outputs. The damage index (D_{Si}) chosen for this study is square root of the sum of the squares of the first two principal components as shown in Eq. (32.2).

$$D_{Si} = \sqrt{(PC_1)_i^2 + (PC_2)_i^2} \quad (32.2)$$

where $(PC_1)_i$ and $(PC_2)_i$ are the first and the second principal components of sensor i respectively. The reason to just incorporate the first two principal components in the damage index is that the most useful information in the data is covered by the first few principal components values. In fact, the first principal component corresponds to the direction of in, which the projected data has the most variance while the second one is perpendicular to the first component. In other words, since more than 95% of the variance (calculated based on the preliminary study) is covered by the first two principal components, these two components are only incorporated in the damage index. It should be mentioned that the number of principal components that should be considered depends on the data and there is not any prescription for all cases. However in the most cases the most variance is covered by the first two or three components. Therefore, if any damage occurred in structure then it should affect the data and consequently variance of data and should be detected by this damage index.

32.3.2 Cross Correlation Analysis (CCA)

The Cross Correlation Analysis (CCA) was recently proposed by the authors [7] and the methodology is based on comparing the correlation matrices for the baseline and damaged cases. The cross correlation coefficients of the strain data at one location and all other locations are calculated to create the first row of the cross-correlation matrix. Then, the same procedure is repeated for all of the sensors and a full cross-correlation coefficient matrix is created. After obtaining these matrices for baseline and damaged conditions, they are compared to detect and locate the damage. When comparing two signal pairs, the correlation can be obtained using the following formula:

$$\rho_{ij}(t) = \frac{\sum_{k=1}^n (S_j(t_k) - \mu_i)(S_j(t_k) - \mu_j)}{\sqrt{\sum_{k=1}^n (S_i(t_k) - \mu_i)^2} \sqrt{\sum_{k=1}^n (S_j(t_k) - \mu_j)^2}} \quad (32.3)$$

where r_{ij} is the correlation between the sensors i and j , n is the total number of time observations during the monitoring duration, $S_i(t_k)$ and $S_j(t_k)$ are the values from the sensors i and j at time t_k , and, m_i , m_j are the mean values of the data from the sensors i and j . However, CCA method is not very appropriate for long term monitoring of structure specifically for automated long-term assessment.

32.3.2.1 Moving Cross Correlation Analysis (MCCA)

Due to the above-mentioned discussion about CCA drawbacks, Moving Cross Correlation Analysis (MCCA) is proposed as a promising upgraded version of CCA adapted for long term SHM. Determining a fixed size-moving window, explained in MPCA section, that move along the time is a common aspect of MPCA and MCCA. The same matrix of data structure is developed and CCA is conducted for each individual window. Therefore, performing CCA for each moving window,

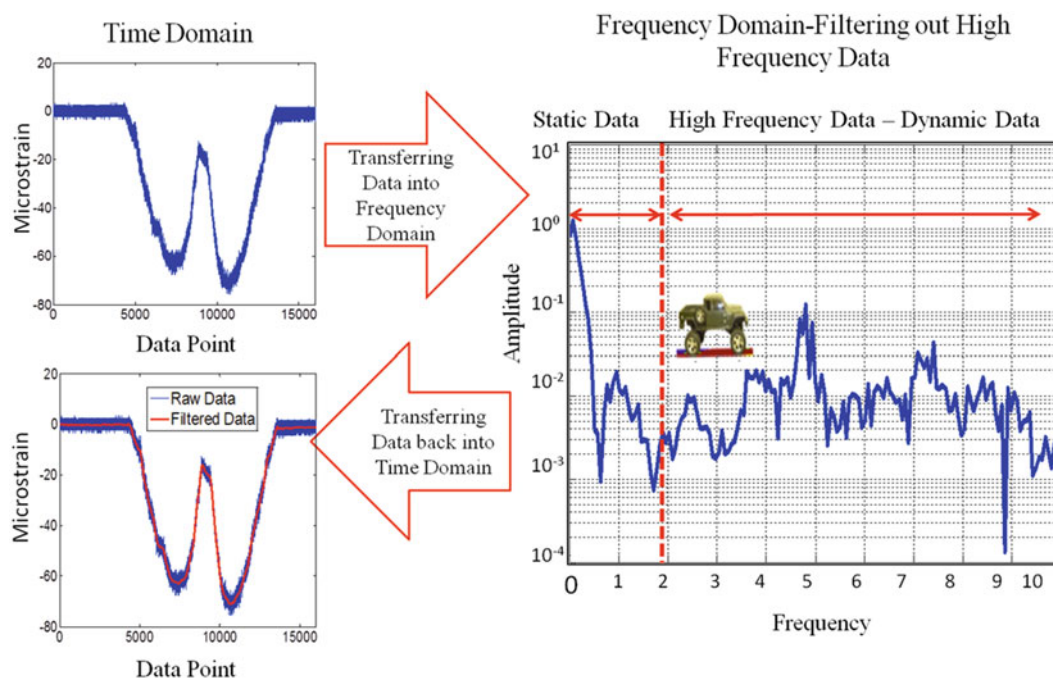


Fig. 32.4 Conversion of responses to frequency domain and filtering out the high frequency response

correlation coefficient value is computed as correlation of sensor i and j . For detecting any possible abnormal behavior, the matrix of data is separated unequally into two segments as training and monitoring segments. The baseline behavior for each pair of sensors, sensors i and j , are defined by the confidence interval developed based on correlation coefficients obtained in the training phase. In the following step, the generated confidence intervals in training phase are considered as damage criteria for each pair of sensor throughout the monitoring phase. In other words, if the observed correlation coefficients for a given sensor i and j in monitoring phase exceed the confidence interval for the same sensors in training phase, then it can be claimed that possible abnormal behavior is in progress in the structure.

32.3.3 Filtering Out the High Frequency Data

Prior to applying MPCA and MCCA to the raw data captured from FBG sensors, which were distributed over the bridge; a critical issue is pre-processing of the data. The data consists of both low and high frequency strain responses. However high frequency part is not desired in this study since the correlation values are inversely affected by this high frequency data. As a result, high frequency data should be filtered out by using a low pass filter. It is shown in Fig. 32.4 that the first two vibration modes of the bridge are around 5 and 7.5 Hz. After this pre-processing, damage detection algorithm can be applied for evaluation of the structure.

32.4 Experimental Studies

32.4.1 Structure Description and Instrumentation (UCF 4-Span Bridge)

For the sake of evaluating these algorithms using FBG sensors, several experiments with a laboratory bridge model were designed and conducted taking three common damage scenarios into consideration. The structure consists of two 120 cm approach (end) spans and two 304.8 cm main spans with a 3.18 mm thick, 120 cm wide steel deck supported by two HSS 25 × 25 × 3 girders separated 60.96 cm from each other. Using the 4-span bridge model in the UCF structural laboratory (Fig. 32.5), it is feasible to simulate and test a variety of damage scenarios that are commonly observed in bridge type

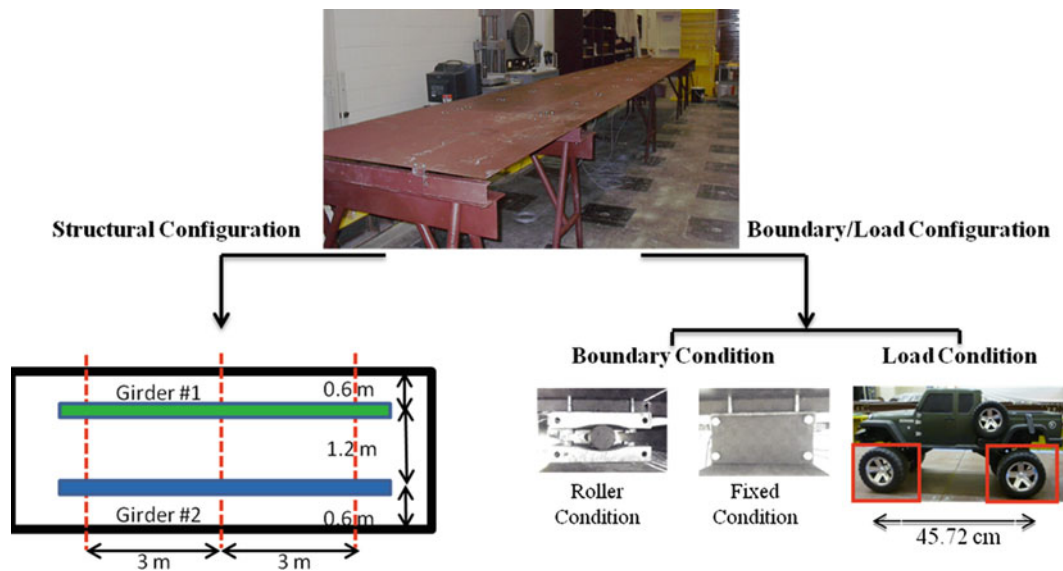


Fig. 32.5 Structural description and applied load (UCF 4-span Bridge)

structures [10, 11]. It is possible to simulate most of the common boundary conditions, including rollers, pin, and fixed support. In addition to these, the bolts connecting the girders and deck can be loosened or removed at different locations to modify the stiffness of the system and to simulate damage. In other words, the first feature provides the opportunity to simulate the global damage scenarios while; the second one is desirable for local damage simulations. It should be pointed out that even though the structure is not a scaled down model of a specific bridge, its responses are representative of typical values for medium-span bridges.

32.4.2 Damage Scenarios

Inspired by discussions with the Department of Transportation (DOT) engineers, several critical and common damage scenarios were identified and simulated on the 4-span bridge model. A crucial type of damage which was observed in bridges is alterations in boundary conditions. These types of alterations may cause stress redistributions and in most cases it may result in additional load in different elements. Therefore, three cases were devoted to this type of damage using the advantage of the ability to shift from pinned to fix or roller condition or vice versa. The damage scenarios implemented in this study are illustrated in Fig. 32.6.

32.5 Damage Assessment

Total number of 30 data sets, 15 from baseline condition and 15 from damage condition, has been considered in this study. Each data set consisted of approximately 10000 to 13000 data points. This results in a main matrix with 360175 rows (data points or measurements) and 12 columns (number of FBG sensors or variables). Taking this information into account, the size of the moving window was chosen as 13000×12 while the moving rate (or window overlap) is selected as 2000 points. In order to develop a confidence interval, the first 50000 points have been considered as training (baseline) phase for both MPCA and MCCA algorithms. In fact, the first 193875 points (measurements) out of 360175 points are captured from a baseline structure while only the first 50000 points are involved in developing the confidence interval. Since this is multivariate data analysis, the results of selective sensors are presented instead of individual sensors. Alternatively, for MCCA illustration, correlation of sensors 1, 5 and 10 with sensors 2, 3 and 4 will be presented respectively.

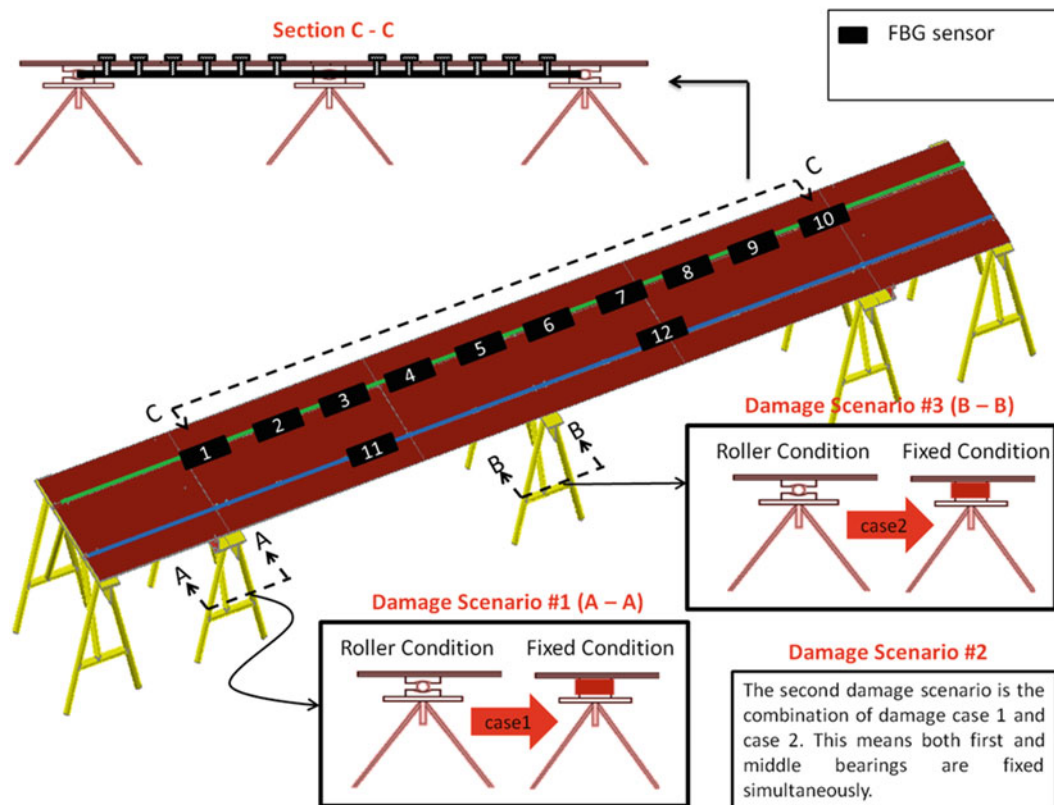


Fig. 32.6 Location of sensors and simulated damage (UCF 4-span Bridge)

32.5.1 Damage Scenario I

The main idea behind this damage case is to simulate one of the most common faults in bridge type structures, which is altering the boundary condition from roller condition to fixed condition. In fact, this type of change will result in redistribution of force in the structure and may cause unexpected bending moment at boundary location which can have detrimental effect on the performance of the structure. The corresponding results for MPCA and MCCA are presented separately in Fig. 32.7. Each graph, as it was mentioned formerly, is separated into two parts so called training and monitoring phase which were explained in detail through Sects. 32.3 and 32.5. As it is observed from Fig. 32.7, MPCA precisely detected the abnormal behavior due to this damage. Dramatic change in principal component value of sensor 1 is detected while only slight change is noticed over sensor 5 and almost no change at the location of sensor 10. The PCA value for sensor 1 is well separated before and after damage. In effect, the values of PCA for sensor 1, after damage occurred, are clearly out of confidence interval developed in training phase.

In other words, shifting the boundary condition from roller into fixed condition caused unexpected extra moment force at the location of sensor 1 which subsequently resulted in dramatic shift in PCA value computed from this sensor. This alteration, force redistribution, is even slightly sensed over sensor 5 close to the middle bearing which is predictable based on structural analysis since it is a continuous section. However, since there is a major shift in the mean PCA values and some points go beyond the confidence intervals at some points, it can be concluded that damage is felt at sensor 5 as well. In contrast, there is not any abnormality detected for sensor 10 and as a result it can be mentioned with 95 percent confidence that the structure around this sensor has not experienced any force redistribution issue. In the case of MCCA, the correlation of sensor 1 with sensor 2, 3 and 4 showed obvious variations after damage occurred. However, slight change over sensor 5 and no significant alteration over sensor 10 are observed. In fact, both algorithms are able to detect not only the location but also the intensity of the damage due to this boundary alteration. The authors realized that MCCA is a little bit faster in terms of detecting the damage. This means that, the CCA windows are affected by damage faster than PCA windows. However, it should be also mentioned that, in terms of computational time needed for each algorithm, MCCA algorithm is

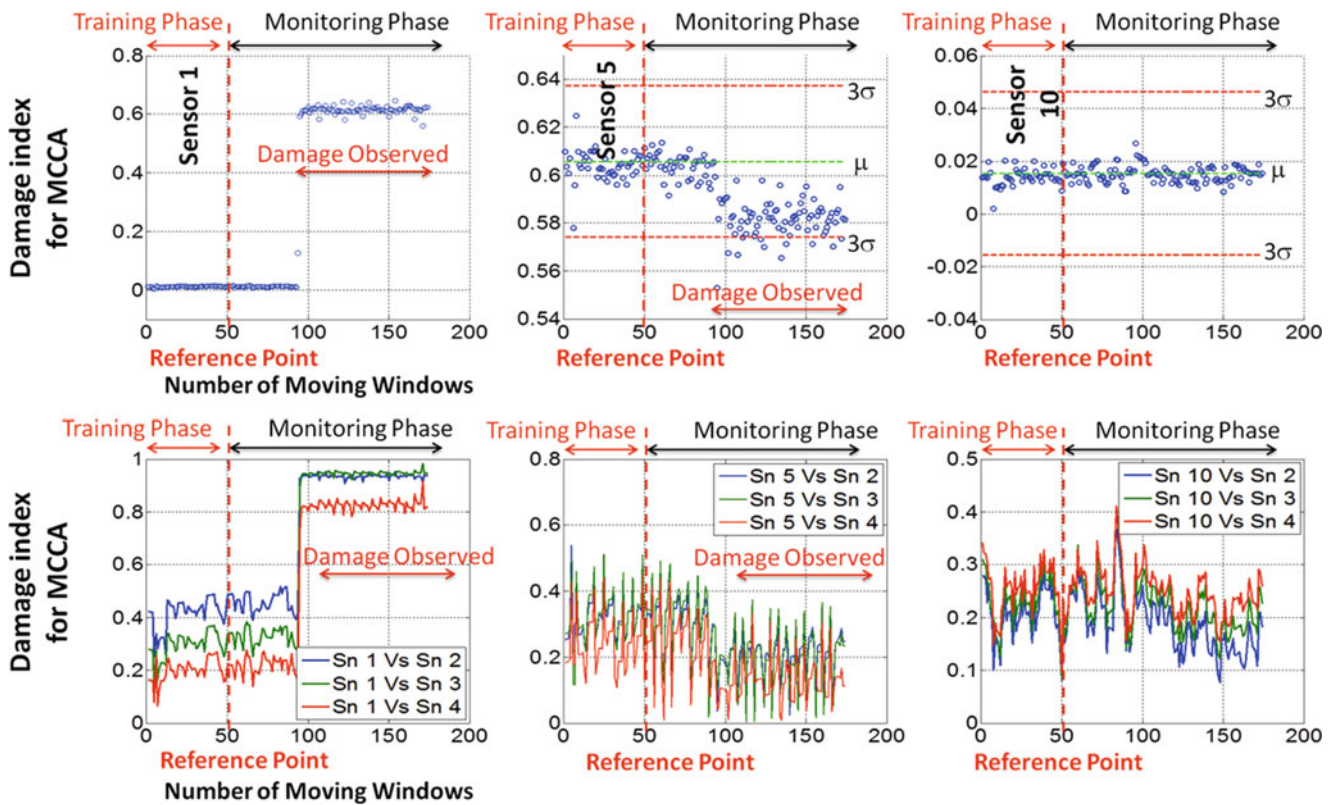


Fig. 32.7 MPCA (top) and MCCA (bottom) results for selected sensors (Case1)

superior. Also, significantly more complicated mathematical calculations are involved in MPCA. This can become critical issue when dealing with large amounts of real time data from a real life structure. Therefore, depending on the application and the priority, one of these algorithms can be selected and implemented.

32.5.2 Damage Scenario II

The second damage scenario was designed and implemented to simulate the situation in which a number of bearings are experiencing the fixing issue. For that reason, the middle bearing was fixed in addition to the first one. The results for this case are summarized in Fig. 32.8. In second case, the sensor 1 again shows the most dramatic change similar to case 1. However, in this case an abrupt jump is observed in the location of sensor 5 (close to the middle bearing). This damage is perhaps the most severe damage scenario which is simulated in this study and it can be noticed from the results. The PCA and coefficient values for both sensor 1 and 5 show obvious change after damage occurred. In fact, all the sensors located on the first span experienced the same situation.

32.5.3 Damage Scenario III

MPCA and MCCA outcomes for the third case are plotted in Fig. 32.9. Since only the middle boundary condition is altered, only sensor 5 experienced a significant change. However, it is expected to have some minor unexpected force redistribution near the first and the last boundary. It is observed from MPCA results that only sensor 5 expresses damage while almost there is no significant variation detected around sensor 1 and sensor 10.

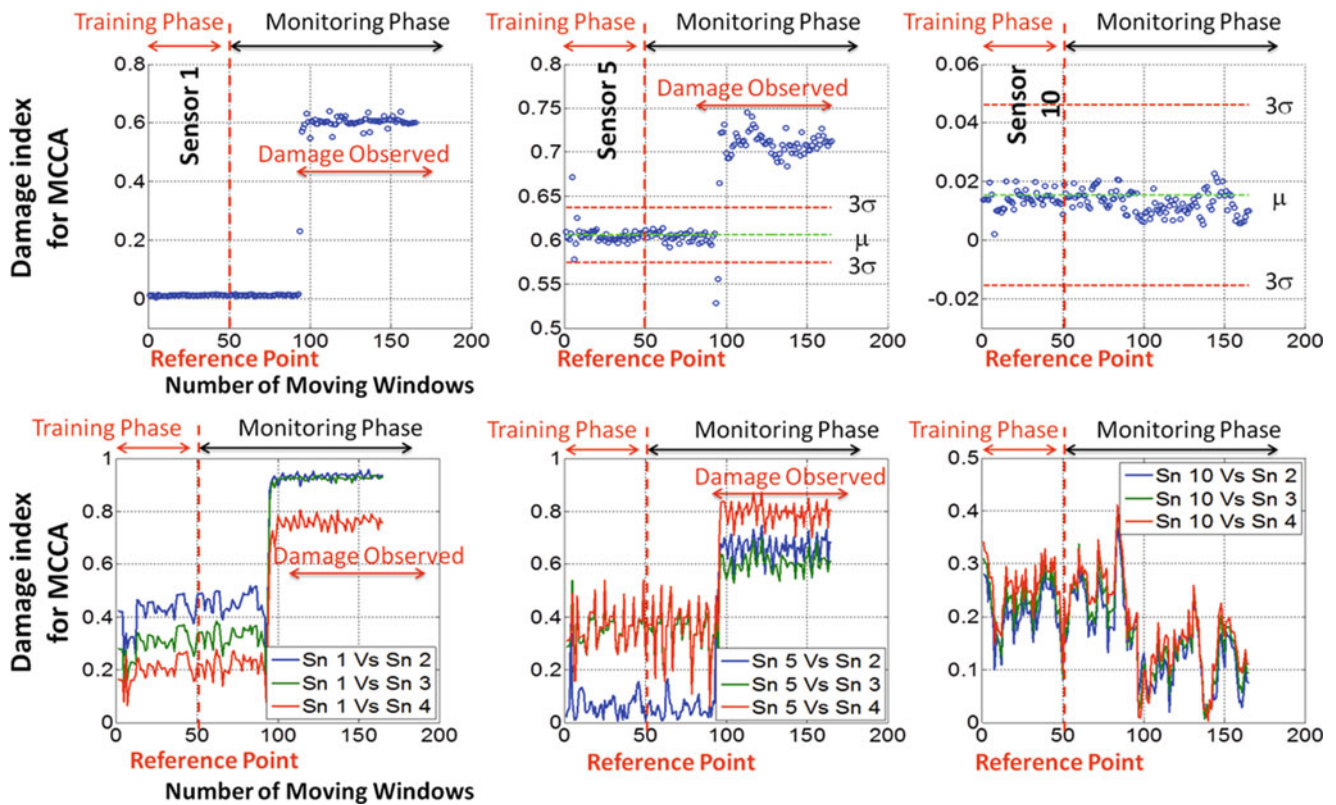


Fig. 32.8 MPCA (top) and MCCA (bottom) results for selected sensors (Case2)

32.6 Conclusions

The damage detection ability of two advance multivariate statistical based algorithms is investigated for long-term bridge monitoring application taking advantage of FBG sensors. MPCA and MCCA are two methods which show promising results for real life and long term SHM. The effectiveness of these algorithms was tested using laboratory bridge structure and fiber optic sensors. The most common and critical damage scenarios have been selected and simulated on the structure including three global damage scenarios. Afterwards, the proficiencies of MPCA and MCCA are tested for each case in detection, localization and intensity aspects. The results conceal that these methods are very promising for long term monitoring of structures. It was also noted that each method has its own advantages and disadvantages as expected. It was realized that coefficient values in moving windows are affected from damage before these effects are notices with the PCA values. This means that damage can be reported by MCCA ahead of MPCA. In addition to that, MCCA is superior in terms of computational time. This is due to the fact that MPCA algorithm involves more complex and time-consuming procedure and calculations. This aspect may make the MCCA more desirable for real life application in which dealing with the large amounts of data is the main challenge. It is also observed that, MPCA algorithm has a better performance in detecting minor structural changes. It can be concluded that the principal components values are more sensitive to minor variation and alteration than correlation values. This aspect was noticed in almost every damage scenarios.

Acknowledgements The authors would like to acknowledge Dr. Il-Bum Kwon from KRISS Korea for his expertise and support for the fiber optic sensing development and work at the University of Central Florida. For this, the authors are grateful to Dr. Kwon for his guidance and know-how. The research project described in this paper is supported by the Federal Highway Administration (FHWA) Cooperative Agreement Award DTFH61-07-H-00040. The authors would like to express their profound gratitude to Dr. Hamid Ghasemi of FHWA for his support of this research. The authors would also like to acknowledge the contributions of their research collaborators and their research team. The opinions, findings, and conclusions expressed in this publication are those of the authors and do not necessarily reflect the views of the sponsoring organization.

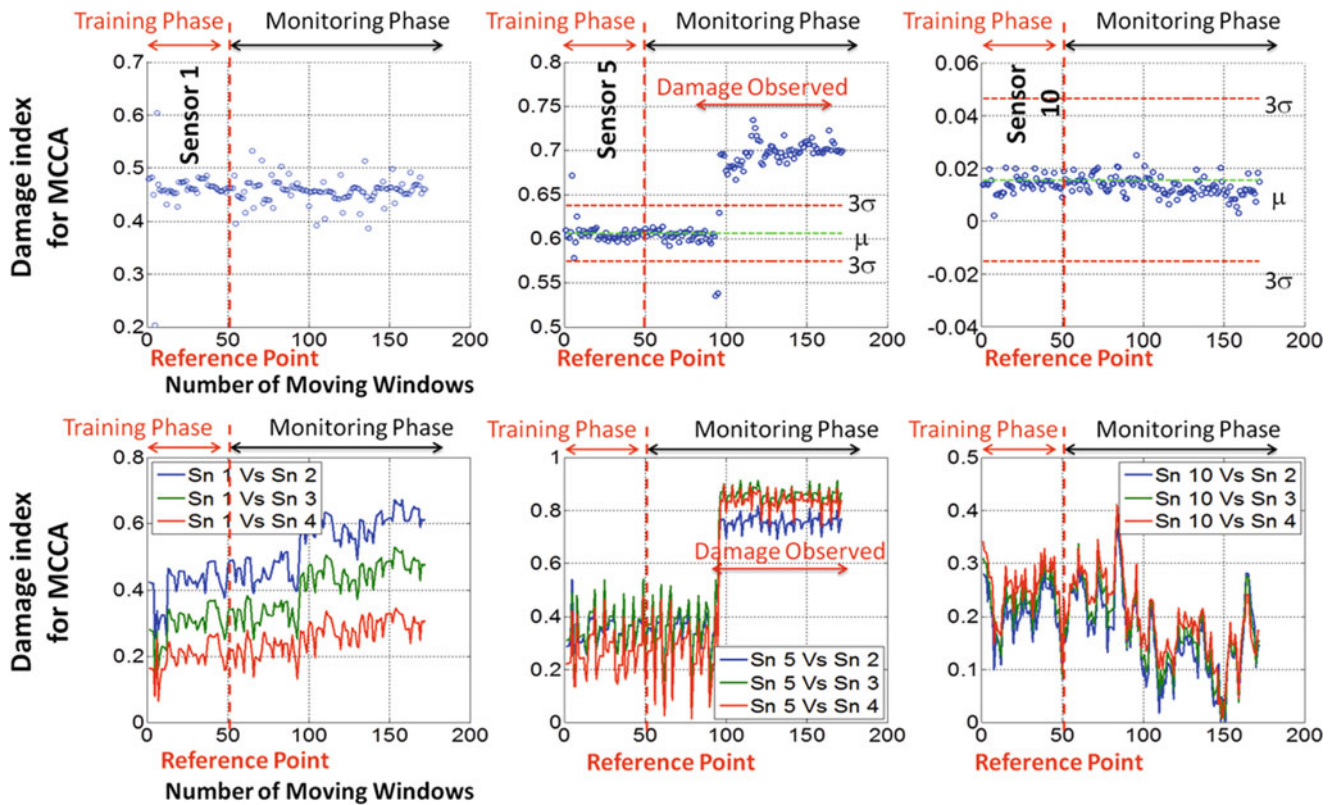


Fig. 32.9 MPCA (top) and MCCA (bottom) results for selected sensors (Case3)

References

1. Aktan AE, Catbas FN, Grimmelsman KA, Tsikos CJ (2000) Issues in infrastructure health monitoring for management. *J Eng Mech ASCE* 126(7):711–724
2. Ferdinand P, Magne S, Dewynter-Marty V, Martinez C, Rougeault S, Bugaud M (1997) Applications of Bragg Grating Sensors in Europe. In: *Proceedings of the 12th International Conference on Optical Fibre Sensors*, Williamsburg, USA, p. 149
3. Hill KO, Fuji Y, Johnson DC, Kawasaki BS (1978) Photosensitivity in optical fiber waveguides: application to reflection fiber fabrication. *Appl Phys Lett* 3(2):647
4. Kwon IB, Baik SJ, Im K, Yu JW (2002) Development of fiber optic BOTDA sensor for intrusion detection. *Sens Actuators A* 101:77–84
5. Majumder M, Gangopadhyay TK, Chakraborty AK, Dasgupta K, Bhattacharya DK (2008) Review: Fibre Bragg gratings in structural health monitoring—present status and applications. *Sens Actuators A* 147:150–164
6. Worden K (1997) Structural fault detection using a novelty. *J Sound Vib* 201(1):85–101
7. Catbas FN, Gokce HB, Gul M (2012) Nonparametric analysis of structural health monitoring data for identification and localization of changes: Concept, lab, and real-life studies. *Structural Health Monitoring*, 11(5):613–626
8. Posenato D, Lanata F, Inaudi D, Smith IFC (2008) Model-free data interpretation for continuous monitoring of complex structures. *Adv Eng Inform* 22:135–144
9. Gul M, Catbas FN (2008) Ambient vibration data analysis for structural identification and global condition assessment. *J Eng Mech ASCE* 134(8):650–662
10. Zaurin R, Catbas FN (2011) Structural health monitoring using computer vision and influence lines. *Struct Health Monit J SAGE Publications* 10(3):309–332
11. Zaurin R, Catbas FN (2010) Integration of computer imaging and sensor data for structural health monitoring of bridges. *J Smart Mater Struct* (19) 015019:15

Chapter 33

System Identification of a Three-Story Precast Concrete Parking Structure

Andrea Belleri, Babak Moaveni, and Jose I. Restrepo

Abstract A half-scale, three-story, precast concrete building resembling a parking garage was tested on the UCSD-NEES shake-table in May–July of 2008. This was the capstone test of a multi-university/industry research project aimed at the development of seismic design guidelines for precast concrete diaphragms. The shake-table tests were designed to induce damage on the building progressively through earthquake records of increasing intensity. Low-amplitude white-noise base excitations as well as scaled earthquake tests were performed between large-amplitude earthquake records. In this study, modal parameters of the test structures are identified using a deterministic-stochastic subspace identification method based on low-amplitude as well as high-amplitude seismic test data. The changes in the identified modal parameters are compared to the progressive damage of the building. Reduction of the identified natural frequencies and increase of the damping ratios indicate loss of stiffness and development/propagation of cracks, while the changes in the mode shapes point to the location of damage.

Keywords Shake-table testing • Modal analysis • Deterministic-stochastic subspace identification • Damage detection • Precast concrete structures

33.1 Introduction

As the last phase of a joint project between University of Arizona, Lehigh University and University of California San Diego (UCSD), a three-story half-scale precast concrete building resembling a parking garage, was tested on the UCSD-NEES shake-table in March–June 2008. The aim of the research project was the investigation of the flexural and shear behavior of different types of precast concrete floors under seismic loading in order to validate nonlinear finite element models and to define a design methodology for precast concrete diaphragms [1]. The testing program on this precast concrete structure provided vibration data from a complex large scale system with actual construction practices and half scale details under realistic boundary conditions that cannot be easily reproduced by numerical simulations. The specimen was subjected to scaled historical ground motions to simulate design seismic loading. Between these tests the structure was subjected to white-noise and low-amplitude earthquake excitation during which it responded as a quasi-linear system with modal parameters (natural frequencies, mode shapes and damping ratios) changing as a result of damage and of retrofitting. In this study, the modal properties of the structure at selected damage states are identified using the deterministic-stochastic subspace identification method [2] based on measured input and output acceleration data. The identified results are compared to the damage observed visually on the specimen.

A. Belleri

Department of Engineering, University of Bergamo, Bergamo, Italy
e-mail: andrea.belleri@unibg.it

B. Moaveni (✉)

Department of Civil and Environmental Engineering, Tufts University, Medford, MA, USA
e-mail: babak.moaveni@tufts.edu

J.I. Restrepo

Department of Structural Engineering, University of California, San Diego, CA, USA
e-mail: jrestrepo@ucsd.edu

33.2 Test Structure and Dynamic Tests

The structure tested on the shake-table, shown in Fig. 33.1, had a 17.07 m by 4.88 m rectangular plan and a story height of 1.98 m. Three different precast floor systems were adopted at each level, namely a composite double tee diaphragm at the first suspended level, non-composite hollow core at the second and pre-topped double tee diaphragm at the third [3]. Two 2.44 m wide by 7.01 m tall by 0.20 m thick precast walls were placed at the North and South edges of the structure as the primary lateral force resisting system.

The test structure was subjected to 16 ground motion records of increasing intensity on the shake-table in order to induce progressive damage in the specimen. The ground motion records were selected from historical earthquakes to represent low, moderate and high seismic hazards for three sites in the United States: Knoxville (Tennessee), Seattle (Washington) and Berkeley (California). The records were scaled to meet the Design Basis Earthquake (DBE) for the Knoxville (KNX), Seattle (SEA) and Berkeley (BER) sites. After completion of the DBE tests for the three sites, the building was subjected to the Maximum Considered Earthquake (MCE) for the Berkeley site (MCE-BER). Between the seismic tests, the building was subjected to low-amplitude white-noise base excitation (WN) and to a small earthquake type loading (EQ-Ch). Table 33.1 reports the shake-table base excitations considered in the paper.



Fig. 33.1 Half-scale three-story test structure on the UCSD-NEES shake-table

Table 33.1 Base excitation tests performed on the specimen

Test ID	Input type	Damage state	Test ID	Input type	Damage state
T1	WN	S0	3rd floor repair 2		
T2	EQ-Ch	S0	T15	WN	S2.4
T3	KNX		T16	EQ-Ch	S2.4
T4	WN	S1.1	T17	SEA	
T5	EQ-Ch	S1.1	2nd floor repair 1 and 3rd floor repair 3		
T6	KNX		T18	WN	S2.5
Grouting of energy dissipation bars			T19	EQ-Ch	S2.5
T7	WN	S1.2	T20	SEA	
T8	EQ-Ch	S1.2	T21	WN	S2.6
T9	SEA		T22	EQ-Ch	S2.6
T10	3WN	S2.1	T23	BER	
3rd floor repair 1			T24	WN	S3
T11	WN	S2.2	T25	EQ-Ch	S3
T12	EQ-Ch	S2.2	T26	BER-MCE	
T13	SEA		T27	WN	S4
T14	3WN	S2.3	T28	EQ-Ch	S4

33.3 System Identification

The deterministic-stochastic subspace identification (DSI) method [2] is used to extract the modal parameters of the test structure based on input-output data of the 28 tests listed in Table 33.1. The DSI is a parametric linear system identification method that determines the system model in state-space based on the input-output measurements directly. This method is robust in view of the input disturbance and measurement noise as both terms are explicitly considered in its formulation.

A comprehensive array of sensors including 640 sensors was deployed on the test structure to capture its response to monitor accelerations, displacements or deformations, strains, and pressures. The accelerometers mounted on the floors and on the walls in the direction of shaking were adopted in the system identification procedure consisting of 6 accelerometers on the walls (3 on each wall at floor levels) and 42 on the floors (14 per floor). The measured data were collected by different data acquisition systems at a sampling rate ranging between 200 and 240 Hz. Before the application of the system identification procedure, the data were filtered and down-sampled.

Three vibration modes of the structure are consistently identified across different test data. Figure 33.2 shows the identified mode shapes for these three vibration modes. It should be noted that these modes are identified as classically damped (i.e., proportional) modes.

Table 33.2 reports the identified natural frequencies, equivalent damping ratios (ξ) and Modal Assurance Criterion (MAC) [4] values for the three identified modes based on different test data. The MAC values are computed between identified mode shapes and their counterpart identified from T1 test data. Test T19 was not considered in the identification procedure due to data acquisition system problems. From this table, it can be observed that:

- 1 Modal parameters show significant changes after each of the large-amplitude earthquake tests (T3, T6, T9, T13, T17, T20, T23, T26). In general the natural frequencies decrease and the damping ratios increase as the structure is exposed to larger base excitations (except during repairs shown as double lines in the table).
- 2 Mode 1 is consistently identified during all tests; Mode 3 is identified during all but one test while Mode 2 is missed during six tests.
- 3 Natural frequencies identified based on large-amplitude earthquake tests are significantly smaller than those identified from the low-amplitude tests immediately before or after the earthquakes. This is due to the fact that the test structure will behave highly nonlinear during parts of these large-amplitude tests.
- 4 In general the MAC values for all three modes are in a reasonable range except for tests which exhibited flexural failure at mid-span of third floor.

33.4 Discussion of Results

The accuracy of a linear system identification method such as DSI depends on the degree of violation of the method's core hypotheses, i.e., measured data represent a linear system [5]. However, linear system identification methods provide reasonably accurate estimates of modal parameters when applied to the response of moderately nonlinear structures [6, 7].

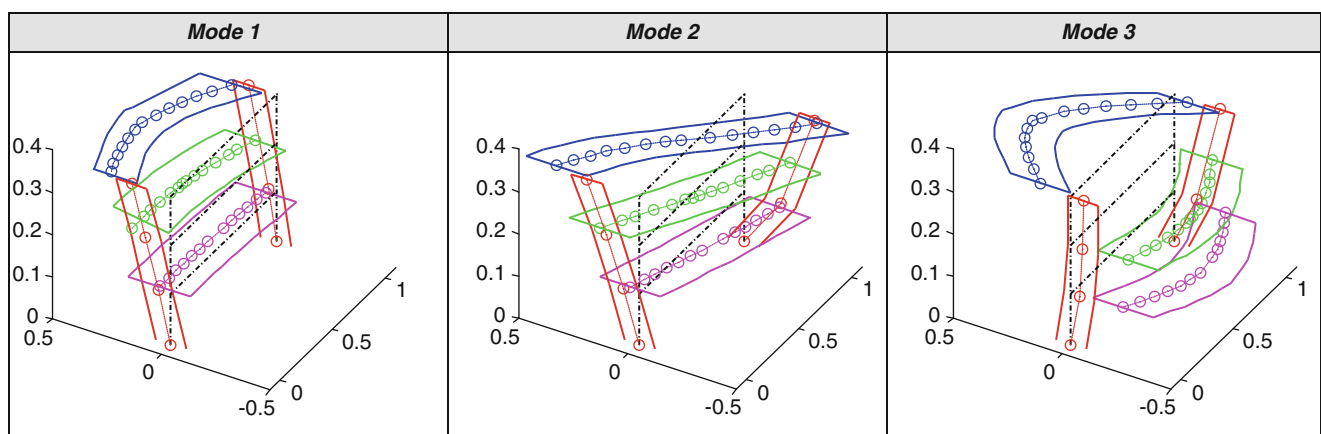


Fig. 33.2 Identified mode shapes during test T1 (circles correspond to sensor locations)

Table 33.2 Identified modal parameters during different tests/damage states

Test no.	Mode 1			Mode 2			Mode 3		
	Freq (Hz)	ξ (%)	MAC	Freq (Hz)	ξ (%)	MAC	Freq (Hz)	ξ (%)	MAC
T1	5.29	5.3	1.00	8.01	5.1	1.00	10.59	7.2	1.00
T2	5.36	5.6	1.00	8.12	5.9	0.91	11.28	6.1	0.99
T3 (EQ)	3.56	7.5	0.96	6.30	11.9	0.54	8.93	2.2	0.94
T4	4.43	8.8	0.99	7.14	6.0	0.87	8.80	8.3	0.93
T5	4.58	10.3	1.00	7.51	5.5	0.95	8.97	7.9	0.94
T6 (EQ)	3.50	13.3	0.97	–	–	–	8.58	2.8	0.91
T7	4.55	8.5	1.00	7.22	5.4	0.95	8.88	9.6	0.98
T8	4.65	8.5	1.00	7.64	7.2	0.86	9.49	6.3	0.98
T9 (EQ)	2.87	13.9	0.92	4.44	8.2	0.60	8.49	21.2	0.72
T10	2.58	10.1	0.91	–	–	–	6.27	10.2	0.75
T11	4.06	7.1	0.98	–	–	–	7.94	7.9	0.91
T12	4.06	7.5	0.99	6.83	5.8	0.85	8.17	9.3	0.93
T13 (EQ)	2.46	12.2	0.97	–	–	–	8.63	5.6	0.71
T14	2.72	10.3	0.92	–	–	–	–	–	–
T15	3.36	8.2	0.97	6.18	5.0	0.88	7.06	8.3	0.92
T16	3.42	7.4	0.96	6.09	4.8	0.84	7.29	8.0	0.93
T17 (EQ)	2.34	16.1	0.95	–	–	–	7.68	6.2	0.84
T18	3.81	7.8	0.97	6.27	6.7	0.85	7.12	8.7	0.89
T20 (EQ)	2.57	10.4	0.96	4.18	6.1	0.86	6.89	7.1	0.93
T21	3.16	8.7	0.96	5.99	10.3	0.81	6.39	9.2	0.93
T22	3.38	7.4	0.94	6.11	6.7	0.85	6.63	7.5	0.87
T23 (EQ)	1.94	10.6	0.94	3.47	1.4	0.87	5.96	6.6	0.69
T24	2.84	8.2	0.91	5.07	5.5	0.86	6.21	9.0	0.93
T25	3.03	8.1	0.91	5.21	3.5	0.87	6.66	6.8	0.89
T26 (EQ)	1.63	17.6	0.93	–	–	–	6.47	10.1	0.66
T27	1.22	21.2	0.85	2.36	13.3	0.88	6.02	7.6	0.87
T28	1.18	19.2	0.88	1.96	8.1	0.89	6.36	4.8	0.85

In this case, the effective natural frequencies identified based on higher amplitude response data (larger nonlinearity) are in general lower than those identified based on lower amplitude response data. In addition, higher modal damping ratios are identified during the higher amplitude base excitations. This is because the additional hysteretic damping at higher levels of response nonlinearity was estimated as equivalent viscous damping.

The accuracy of realized state-space models are investigated for tests T1, T2, and T3 which represent a white-noise base excitation, a low-amplitude earthquake base excitation, and a moderate-amplitude earthquake base excitation test, respectively. Figure 33.3 shows the comparison of measured accelerations on two sensors at the top floor (one on the wall and one on the diaphragm) with their simulated counterparts from the realized/identified state-space models, for tests T1–T3. From this figure and comparison of other sensor measurements not shown here, it is observed that: (1) in general the simulated responses are in good agreement with measured data, (2) simulated floor accelerations are in closer agreement with their measured counterparts than the wall accelerations, and (3) the difference between simulated and measured accelerations is significantly larger for test T3 (and all large-amplitude earthquakes), in which the structure has the most nonlinearity. Figure 33.4 displays the base shear versus mid-span roof displacement hysteretic curve for the three considered tests. This plot confirms that the structure's response is significantly more nonlinear during test T3.

Changes in the identified modal parameters are correlated with the observed damage in the structure. Reduction of the identified natural frequencies and/or increase of damping ratios indicate loss of stiffness, development/propagation of cracks, and/or yielding. In addition, changes in the mode shapes point to the location of damage. Specifically, localized changes in the first and second spatial derivatives of mode shapes indicate loss of shear and bending stiffness, respectively, at the corresponding locations. Figure 33.5 presents the first and second spatial derivatives (modal rotation and curvatures) of the first mode shape for the three floors during tests T14 and T15. Localized changes in the modal rotation and curvature are in good agreement with the location of observed damage in the specimen. No damage is present in the first floor based on visual observation. In the second floor it is possible to localize both flexure and shear damage at mid-span associated to

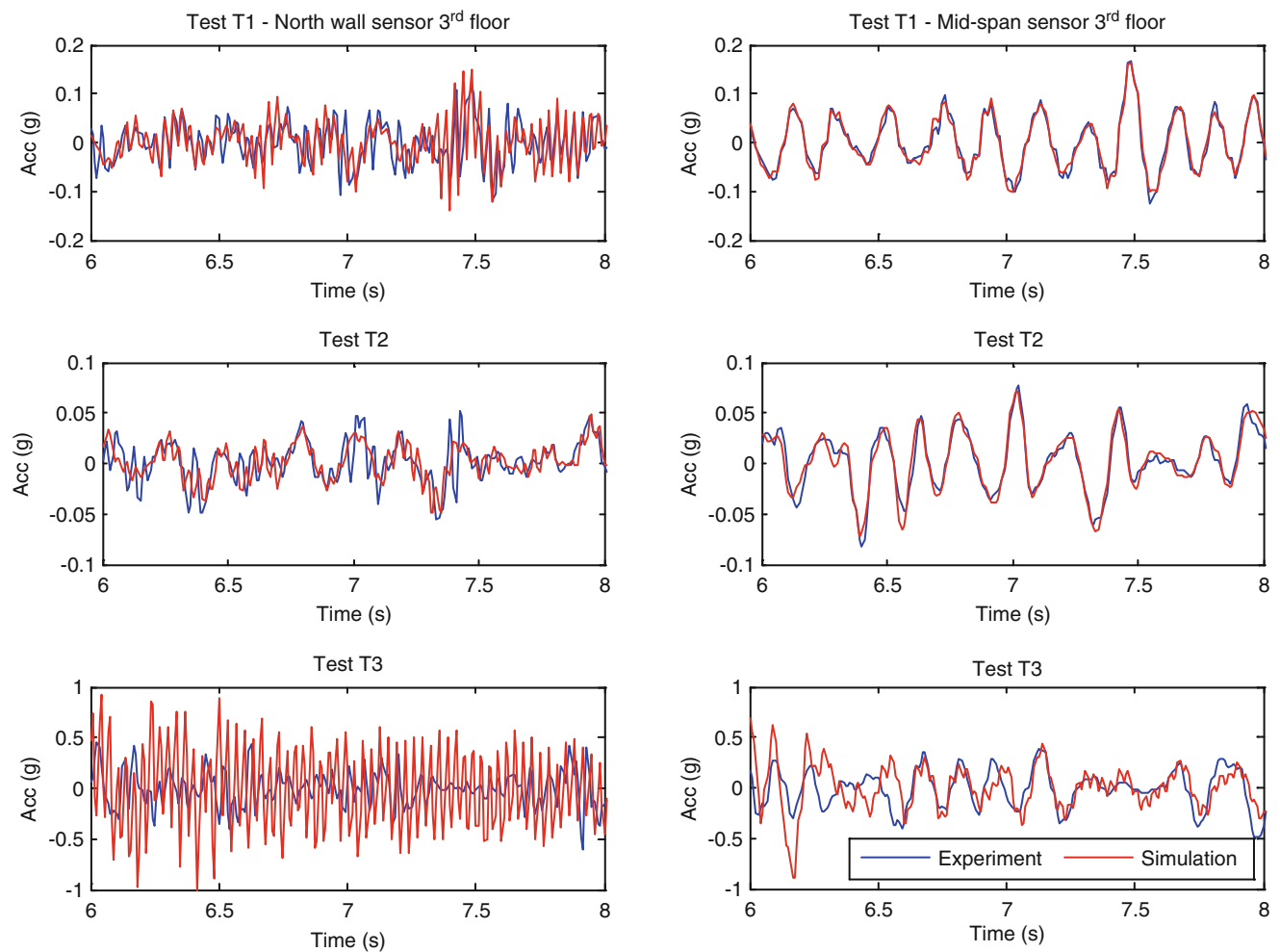


Fig. 33.3 Comparison of measured and model simulated accelerations for tests T1–T3

discontinuities in the modal curvature and rotation plots. No flexural or shear repair was carried out because of lack of visual information, although this did not compromise the structural performance in subsequent tests until retrofitting after test T17. In the third floor both shear and flexural damage can be localized at mid-span in tests T14 and T15 from visual inspection. It is worth noting that the damage information inferred by the modal rotations and curvatures analysis are only related to the loss of flexural and shear stiffness; no information is available regarding loss of flexural and shear strength [8].

33.5 Conclusions

Damage assessment through structural identification of a three story half scale precast concrete building resembling a parking garage is investigated. The structure was tested under earthquake type loading on the NEES Large High-Performance Outdoor Shake Table at the University of California at San Diego in 2008. The effective modal parameters of the structure at different damage states have been identified from white-noise and scaled earthquake test data. Modal parameters show significant changes after each of the large-amplitude earthquake tests. In general the natural frequencies decrease and the damping ratios increase as the structure is exposed to larger base excitations (except during repairs shown as double lines in the table). Changes in the identified modal parameters are correlated with the observed damage in the structure. Reduction of the identified natural frequencies and/or increase of damping ratios indicate loss of stiffness and development/propagation of cracks while changes in the mode shapes point to the location of damage. Specifically, localized changed in the first and

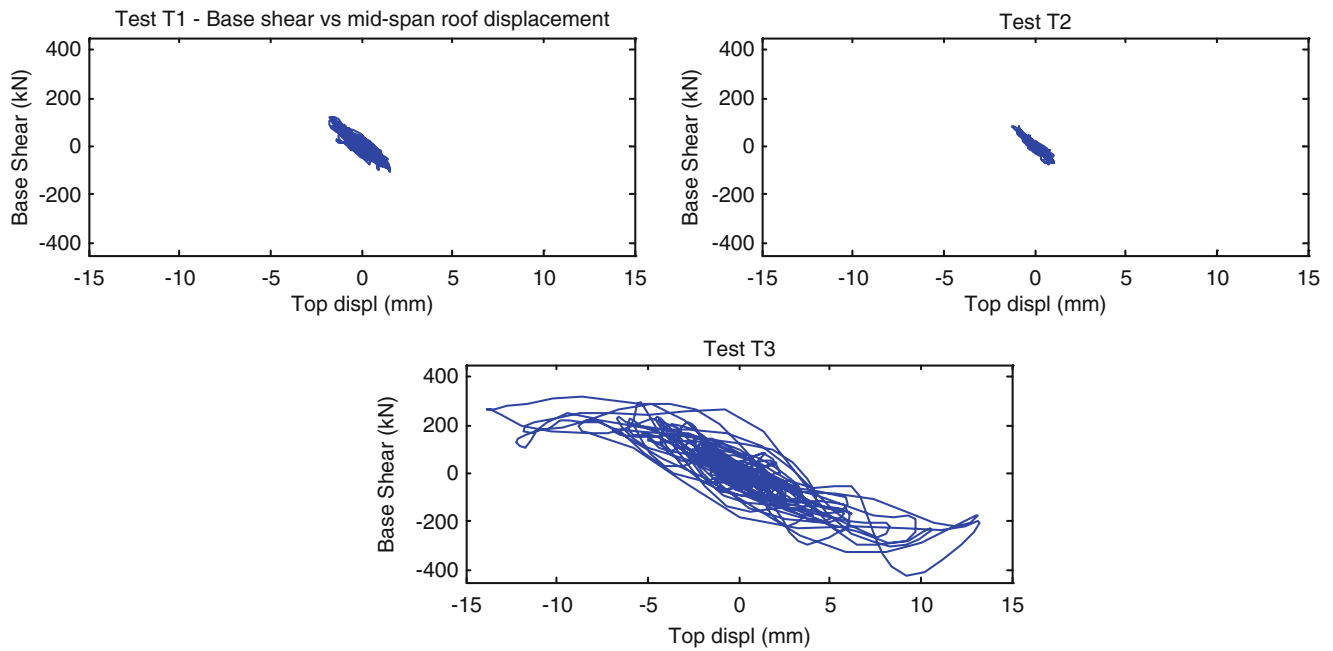
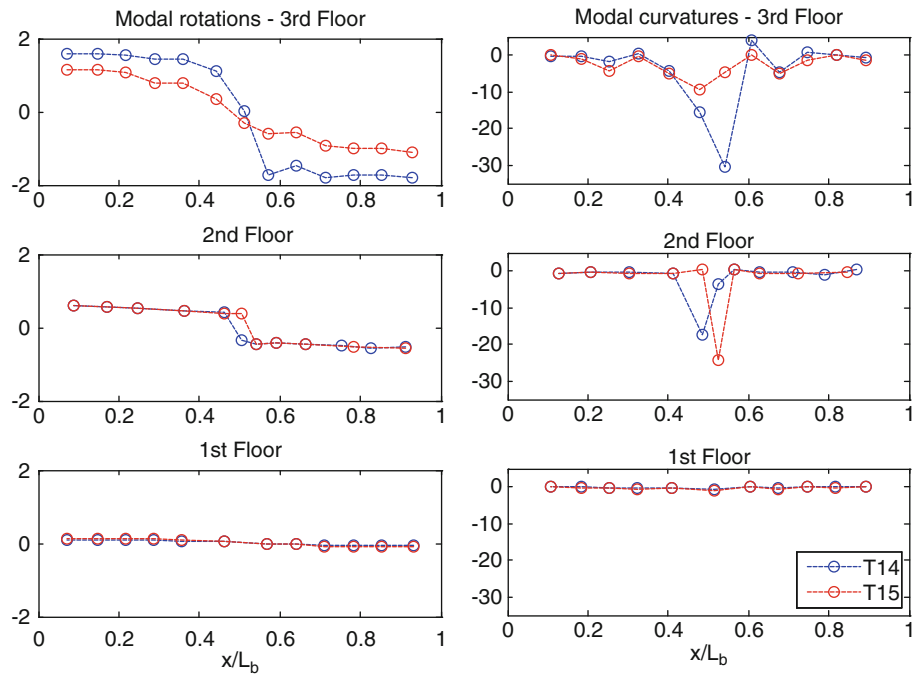


Fig. 33.4 Base shear versus roof displacement hysteric plots for tests T1–T3

Fig. 33.5 Modal rotations and curvatures for Mode 1 in tests T14, T15 and T18



second spatial derivatives of mode shapes indicate a loss of shear and bending stiffness, respectively. However, information inferred by the modal rotation and curvature are only related to the loss of flexural and shear stiffness, i.e., no information is available regarding loss of flexural and shear strength.

Acknowledgements The authors wish to express their gratitude to the Precast/Prestressed Concrete Institute, the National Science Foundation, the Charles Pankow Foundation, and the George E. Brown Jr. Network for Earthquake Engineering Simulation. The first author greatly acknowledges the financial support of Fondazione Cariplo (Bergamo – Italy) under the FYRE mobility program. The opinions, findings, and conclusions expressed in the paper are those of the authors and do not necessarily reflect the views of the individuals and organizations involved in this project.

References

1. Fleischman RB, Naito C, Restrepo J, Sause R, Ghosh SK, Wan G, Schoettler M, Cao L (2005) Precast diaphragm seismic design methodology (dsdm) project, part 2: research program. *PCI J* 50(6):14–31
2. Van Overschee P, De Moore B (1996) Subspace identification for linear systems. Kluwer, Norwell
3. Schoettler MJ, Belleri A, Zhang D, Restrepo JI, Fleischman RB (2009) Preliminary results of the shake-table testing for the development of a diaphragm seismic design methodology. *PCI J* 54(1):100–124
4. Allemang RJ, Brown DL (1982) A correlation coefficient for modal vector analysis. In: Proceedings of the 1st international modal analysis conference, Orlando; November 8–10, 1982
5. Moaveni B, Barbosa AR, Conte JP, Hemez FM (2013) Uncertainty analysis of system identification results obtained for a seven-story building slice tested on the UCSD–NEES shake-table. *Struct Contr Health Monit*, under review.
6. Moaveni B, Asgari E (2012) Deterministic-stochastic subspace identification method for identification of nonlinear structures as time-varying linear systems. *Mech Syst Signal Process* 31:40–55
7. Moaveni B, He X, Conte JP, Restrepo JI, Panagiotou M (2011) System identification study of a seven-story full-scale building slice tested on the UCSD–NEES shake-table. *J Struct Eng ASCE* 137(6):705–717
8. Moaveni B, Stavridis A, Lombaert G, Conte JP, Shing PB (2013) Finite element model updating for assessment of progressive damage in a three-story infilled RC frame. *J Struct Eng ASCE*, in press (available online, doi:[10.1061/\(ASCE\)ST.1943-541X.0000586](https://doi.org/10.1061/(ASCE)ST.1943-541X.0000586))

Chapter 34

Structural Damage Localization Using Sensor Cluster Based Regression Schemes

Ruigen Yao and Shamim N. Pakzad

Abstract Automatic damage identification from sensor measurements has long been a topic of interest in the civil engineering research community. A number of methods, including classical system identification and time series analysis techniques, have been proposed to detect the existence of damage in structures. Not many of them, though, are reported efficient for higher-level damage detection which concerns damage localization and severity assessment. In this paper, regression-based damage localization schemes are proposed and applied to signals generated from a simulated two-bay steel frame. These regression algorithms operates on substructural beam models, and uses the acceleration/strain responses at beam ends as input and the acceleration from an intermediate node as output. From the regression coefficients and residuals three damage identification features are extracted, and two change point analysis techniques are adopted to evaluate if a change of statistical significance occurred in the extracted feature sequences. For the four damage scenarios simulated, the algorithms identified the damage existence and partially succeeded in locating the damage. More accurate inferences on damage location are drawn by combining the results from different algorithms using a weighted voting scheme.

Keywords Damage localization • Substructural analysis • Vibration monitoring • Regression modeling • Pattern recognition

34.1 Introduction

Damage detection and assessment is very important for timely and proper maintenance of civil infrastructures. Traditional practices rely a lot on human inspections, and as a result the cost of maintenance is high and the period of maintenance is long. With the development of digital sensing technologies, damage identification from sensor measurements analysis [1, 2] has been proposed as an attractive alternative because of the low cost and easy scalability.

Macro-scale system identification/modal realization [3, 4] is one of the earliest methods studied for structural diagnosis purposes, and a lot of literatures can be found that investigates the damage indication performance of the functions of eigenfrequencies and eigenvalues estimated from structural responses. While these damage features are theoretically well-grounded for understanding, it may take a lot of time and resources for some algorithms to achieve good results and the features are sometimes found to be insensitive to local damage. Also, model updating for the monitored system will often be needed to perform high-level damage detection. In an effort to overcome these problems, damage detection techniques that adopt time series analysis on single channel responses have been proposed [5, 6]. These features are found to be sensitive to damage, but also to the excitation condition change as a result of the inherent information limitation for this family of methods. Besides, many of these established methods are found to not efficient for high-level damage detection such as damage location and extent identification.

In order to strike a balance between algorithm damage sensitivity and performance robustness, in this paper methods based on multivariate linear regression using measurements from sensor clusters are proposed. The underlying idea is a substructuring technique that models the response at a certain node as the output of a system with responses at all its neighboring nodes as input. Regression coefficients and functions of the regression residuals are used as damage indicators. It is shown

R. Yao (✉) • S.N. Pakzad

Department of Civil and Environmental Engineering, Lehigh University, Bethlehem, PA, USA
e-mail: ruy209@Lehigh.edu; pakzad@Lehigh.edu

that these features would still be sensitive to local damage, yet has better stability and damage localization capabilities. Change point analysis is used to construct the damage threshold for the all the features extracted, and the location of the features that exhibit the most significant change is recognized as the damage location.

This paper contains 6 sections. Section 34.2 contains description of two sub-structure models utilized for linear regression model construction. Section 34.3 introduces the formulation of damage features from regression models. Section 34.4 presents cumulative sum based and minimum deviation based change point analysis techniques for damage threshold determination. Section 34.5 summarizes the implementation results for all algorithms/damage indices, and their damage identification and localization performances are compared, contrasted and combined. In the end, conclusions are drawn on the merits and demerits of the methods used.

34.2 Construction of Substructural Beam Models

To apply the linear regression techniques for damage identification, we need to clarify an input-output linear model for the structure to be assessed. In this section, two models for beams are presented and associated input-output relations formulated.

34.2.1 The Standard Static Beam Model

It is known that the displacement $u(x)$ of a continuous beam with section stiffness $EI(x)$ when subjected to no intermediate load (Fig. 34.1) should satisfy the differential equation below:

$$\frac{d^2(EI(x)d^2u(x))}{dx^4} = 0 \quad (34.1)$$

This is a fourth order differential equation, and the constants from the homogenous solution can be determined using the displacement and slope angles at both ends of the beam. When the beam remains linear in terms of the stress-strain relationship, conditions of slope can be replaced with conditions of strain (at the upper/lower surface):

$$u(x_C) = f(u_A, \varepsilon_A, u_B, \varepsilon_B) \quad (34.2)$$

where f denotes a certain function. This expression is useful in cases that the strain instead of slope is measured. When $EI(x)$ satisfies certain conditions such that $u(x)$ is linear in its homogeneous constants, f becomes a linear function.

In dynamic vibration monitoring settings that measure the systems acceleration instead of displacements, this model can still be applied by taking the 2nd derivative of Eq. (34.2) if the system stiffness-to-mass ratio is large:

$$a_C = \ddot{u}(x_C) = f(\ddot{u}_A, \ddot{\varepsilon}_A, \ddot{u}_B, \ddot{\varepsilon}_B) = f(a_A, \ddot{\varepsilon}_A, a_B, \ddot{\varepsilon}_B) \quad (34.3)$$

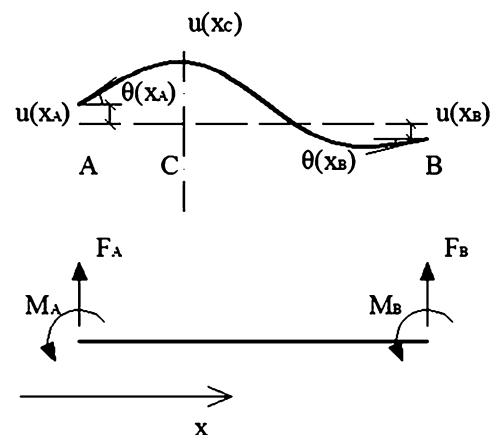
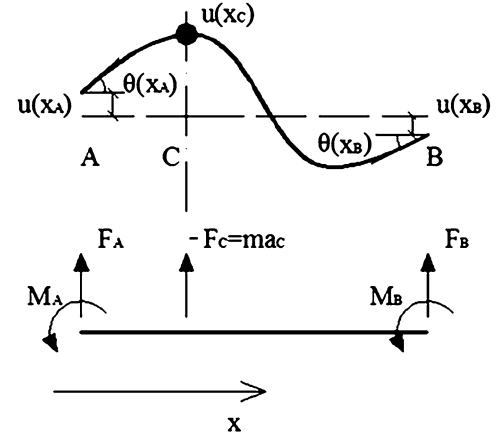


Fig. 34.1 The deflected shape and free body diagram of the static beam element model

Fig. 34.2 The deflected shape and free body diagram of the lumped mass model



This relation can also be formulated in the frequency domain by taking the one-sided Fourier Transform:

$$\begin{aligned}
 \hat{a}_C(i\omega) &= \hat{f}(a_A, \varepsilon_A, a_B, \varepsilon_B) \stackrel{f \text{ linear}}{\Rightarrow} f(\hat{a}_A(i\omega), \hat{\varepsilon}_A(i\omega), \hat{a}_B(i\omega), \hat{\varepsilon}_B(i\omega)) \\
 &= f(\hat{a}_A(i\omega), -\omega^2 \hat{\varepsilon}_A(i\omega) - i\omega \varepsilon_A(t=0) - \dot{\varepsilon}_A(t=0), \hat{a}_B(i\omega), -\omega^2 \hat{\varepsilon}_B(i\omega) \\
 &\quad - i\omega \varepsilon_B(t=0) - \dot{\varepsilon}_B(t=0))
 \end{aligned} \tag{34.4}$$

34.2.2 Beam Model with a Lumped Mass

The model introduced in the previous subsection addresses only static/quasi-static applications. Here a model that incorporates a part of dynamic effects is constructed by adding a lumped mass in to the beam (Fig. 34.2). Again assuming that the material constitutive relation is linear and applying the generalized force concept:

$$u(x) = f(u_A, \varepsilon_A, m\ddot{u}_C, u_B, \varepsilon_B) \tag{34.5}$$

when f is a linear function (condition for this to hold is still the same as in part (34.1)), Eq. (34.5) can be reformulated as

$$a_C = \ddot{u}_C = f_2(u_A, \varepsilon_A, u_C, u_B, \varepsilon_B) \tag{34.6}$$

f_2 is another function with different coefficients. Its corresponding frequency domain representation is

$$\begin{aligned}
 \hat{a}_C(i\omega) &= \hat{f}_2(u_A, \varepsilon_A, u_C, u_B, \varepsilon_B) \stackrel{f \text{ linear}}{\Rightarrow} f_2(\hat{u}_A(i\omega), \hat{\varepsilon}_A(i\omega), \hat{u}_C(i\omega), \hat{u}_B(i\omega), \hat{\varepsilon}_B(i\omega)) \\
 &= f_2\left(\frac{\hat{a}_A(i\omega) + i\omega u_A(t=0) + \dot{u}_A(t=0)}{-\omega^2}, \hat{\varepsilon}_A(i\omega), \frac{\hat{a}_C(i\omega) + i\omega u_C(t=0) + \dot{u}_C(t=0)}{-\omega^2}, \right. \\
 &\quad \left. \frac{\hat{a}_B(i\omega) + i\omega u_B(t=0) + \dot{u}_B(t=0)}{-\omega^2}, \hat{\varepsilon}_B(i\omega)\right)
 \end{aligned} \tag{34.7}$$

Note that when the substructure is subjected to the ambient load/white noise load, the two models described can still be applied by using the correlation of the signals with the regressand signal as a free-decay response. The corresponding frequency domain relation will then be defined for the auto/cross power spectral densities, instead of the Fourier transform.

Table 34.1 The linear regression models derived from the substructural beam models

Model type	Choice of regressors/regressand
1. Static beam model (Time domain)	$\mathbf{Y} = \mathbf{a}_C(t_j), \mathbf{X} = [\mathbf{a}_A(t_j), \Delta^2 \{\tilde{\mathbf{e}}_A(t_j)\}, \mathbf{a}_B(t_j), \Delta^2 \{\tilde{\mathbf{e}}_B(t_j)\}]$,
2. Static beam model (Frequency domain)	$\mathbf{Y} = Re \{\tilde{\mathbf{a}}_C(i\omega_j)\}, \mathbf{X} = Re \left\{ \left[\tilde{\mathbf{a}}_A(i\omega_j), -\omega_j^2 \tilde{\mathbf{e}}_A(i\omega_j), \tilde{\mathbf{a}}_B(i\omega_j), -\omega_j^2 \tilde{\mathbf{e}}_B(i\omega_j) \right] \right\}$,
3. Beam model with lumped mass (Time domain)	$\mathbf{Y} = \mathbf{a}_C(t_j), \mathbf{X} = [\iint \mathbf{a}_A(t_j), \tilde{\mathbf{e}}_A(t_j), \iint \mathbf{a}_C(t_j), \iint \mathbf{a}_B(t_j), \tilde{\mathbf{e}}_B(t_j)]$,
4. Beam model with lumped mass (Frequency domain)	$\mathbf{Y} = Re \{\tilde{\mathbf{a}}_C(i\omega_j)\}, \mathbf{X} = Re \left\{ \left[\frac{\tilde{\mathbf{a}}_A(i\omega_j)}{-\omega_j^2}, \tilde{\mathbf{e}}_A(i\omega_j), \frac{\tilde{\mathbf{a}}_C(i\omega_j)}{-\omega_j^2}, \frac{\tilde{\mathbf{a}}_B(i\omega_j)}{-\omega_j^2}, \tilde{\mathbf{e}}_B(i\omega_j) \right] \right\}$.

34.3 Formulation of Damage Detection Algorithm from Linear Regression Techniques

The general MISO (multi-input-single-output) linear regression problem can be formulated as below:

$$\mathbf{Y} = \mathbf{X}\boldsymbol{\beta} + \epsilon$$

where \mathbf{Y} is the $n \times 1$ regressand vector, \mathbf{X} is the $n \times m$ regressor matrix, $\boldsymbol{\beta}$ is the $m \times 1$ coefficient vector, and ϵ is the $n \times 1$ residual series. Here in the size definitions n stands for the number of observations, and m refers to the number of input series. Thus given the input and output observations, the coefficients and the residuals can be estimated through applying standard curve fitting algorithms with a certain criteria (often least squares).

Henceforth, two categories of linear-regression-based damage detection algorithms can be formed: coefficients-based method and residual-based method. The former requires repetition of the coefficient estimation process in order to collect enough samples for coefficients values for postprocessing, the latter, on the other hand, can function with only one set of estimated coefficients from the baseline/damaged state, and residuals of all the data sets to be processed will be obtained using this set of coefficients. Statistical moments of the residuals are commonly used as viable damage indices.

The substructural models presented in the previous section can thus be used to form regression models in Table 34.1. Note that for all the regression schemes only acceleration and strain signals are employed as they are most commonly measured vibrational responses. In the table, subscript j is a time label range from 1 to N , which is the total number of sample points in time/frequency domain depending on the situation. $\Delta^2\{\cdot\}$ represents the central difference of a signal, $\iint\{\cdot\}$ denotes the reconstructed displacement from the acceleration signal inside the brackets by applying the CFIR filter described in [7], and the macro accent $\{\cdot\}$ means the detrended signal. The purpose for detrending is to eliminate from the regression models the regression constant, which is associated with the system static deformations in the time domain signal, and the vibration initial conditions in the one-sided frequency spectrum.

In this paper, the estimated regression coefficients ($\hat{\boldsymbol{\beta}} = (\mathbf{X}\mathbf{X}^T)^{-1}\mathbf{X}^T\mathbf{Y}$ from the least squares method), the ratio of the variance of regression residuals (from baseline model) to that of the signal ($RF1 = var(\epsilon_{BL})/var(\mathbf{Y})$, $\epsilon_{BL} = \mathbf{Y} - \mathbf{X}\hat{\boldsymbol{\beta}}_{BL}$) and the ratio of the residual variance from fitting the baseline coefficients to that from fitting the estimated coefficients from the current state ($RF2 = var(\epsilon_{BL})/var(\epsilon_{CS})$, $\epsilon_{BL} = \mathbf{Y} - \mathbf{X}\hat{\boldsymbol{\beta}}_{BL}$, $\epsilon_{CS} = \mathbf{Y} - \mathbf{X}\hat{\boldsymbol{\beta}}_{CS}$).

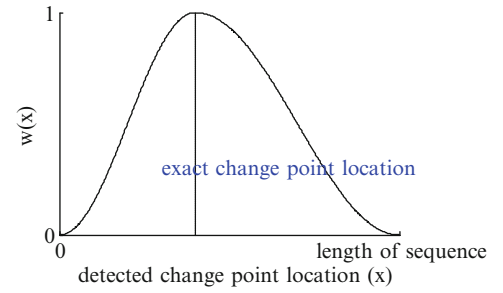
34.4 Change Point Analysis Techniques

To effectively identify damage in the structure, proper damage threshold construction methods should be devised for the features extracted. Here change point analysis is adopted to determine the thresholds of all features presented above.

Namely, change point analysis (CPA) [8] refers to a family of methods that detects in a series of values the point where the statistical properties of the data change. In many practices of quality control, it is often used in conjunction with statistical control charts; the former is data intensive approach and thus more robust to noise, the latter is an instantaneous method for damage identification and more sensitive to short-period variations. Here as all the features are based only on structural output (i.e. acceleration signals), change point analysis is the preferred choice for stability reasons.

In the following subsections, two methods that identifies shift in the mean of the signal will be described. The first method finds the change point as where the maximum absolute value of the signal cumulative sum occurs, and the second one locates the point as that minimizes the deviation of the entire signal.

Fig. 34.3 Normalizing window for NDIV; both sides of it are of raised cosine shape



34.4.1 The Cumulative Sum Based CPA

Using this method, the change point of a data sequence $\{x_i\}_1^L$ can be computed in 3 steps:

- (1) Subtract the sequence by its mean. ($\{x'_i\}_1^L = \{x_i\}_1^L - \bar{x}_i$)
- (2) Calculate the cumulative sum at each data point. ($S_i = \sum_1^i x'_i$, $1 \leq i \leq L$)
- (3) Identifies the change point as where the maximum absolute value of cumulative sum is found. ($CP = \operatorname{argmax}_i (|S_i|)$)

A bootstrapping technique is used to determine if the change is statistically significant at level α :

- (1) Randomly permute the original sequence. ($\{\tilde{x}_i\}_1^L = \operatorname{randperm}(\{x_i\}_1^L)$)
- (2) Compute and record the maximum absolute value of cumulative sum for this new sequence (with all values subtracted by the mean).
- (3) Repeat Step 1–2 for N times, and use the value that's beyond $N(1 - \alpha)$ values in the pool as the threshold.

If $\max(|S_i|)$ of the original sequence is larger than the threshold. The change point is deemed to be statistically significant.

34.4.2 The Deviance Reduction Based CPA

The deviance reduction based method identifies the change point as the place where largest deviance variance reduction is obtained by splitting the data into two parts:

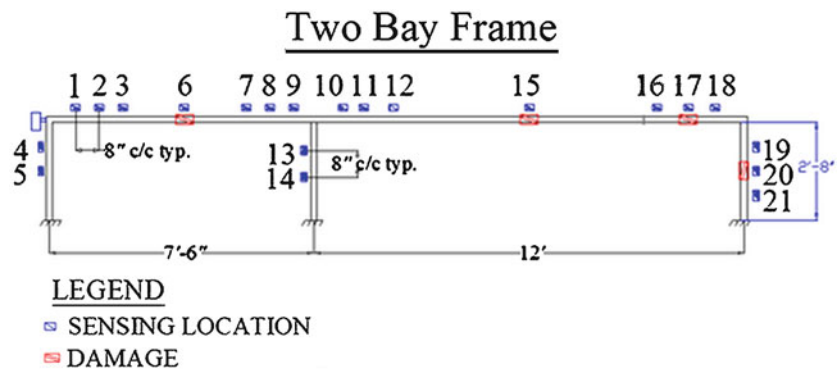
- (1) Compute the deviance for the entire signal. ($Dev_t = \sum_1^L (x_j - \bar{x}|_1^L)^2$)
- (2) At each data point, split the sequence into two parts and compute the resulted deviance reduction. ($DR = Dev_t - Dev_{1:i} - Dev_{i+1:L} = \sum_1^L (x_j - \bar{x}|_1^L)^2 - \sum_1^i (x_j - \bar{x}|_1^i)^2 - \sum_{i+1}^L (x_j - \bar{x}|_{i+1}^L)^2$)
- (3) The change point is identified as the split point that yields the maximum deviance reduction. ($CP = \operatorname{argmax}_i (DR)$)

Again, bootstrapping is used to determine the significance threshold. The general methodology is similar to that in the cumulative sum method, only that here the values computed and recorded are deviance reductions of permuted data sequences, rather than the maximum absolute values of the cumulative sum.

In all the applications presented herein, only one change point needs to be found as only one change of structural state occurs for each case study. When there is more than one possible change points in the data sequence, these methods can be used in a recursive manner.

Two indicators here are adopted to decide on the statistical significance of the change; the normalized damage indication variable (NDIV) with normalizing window shown in Fig. 34.3, and the ratio of the mean shift of the two sample groups separated by the selected change point to the average of the standard deviations of the two groups (normalized mean shift, NMS).

Fig. 34.4 The sensing scheme for the two-bay frame model



34.5 Numerical Verification of the Proposed Algorithms

A small-scale two-span steel bridge girder simulated in SAP2000 is used here for verification of the proposed damage detection methodology. The girder was modeled as a two-dimensional frame with coil-spring-constrained supports and uneven spans as shown in Fig. 34.4. The uneven spans allow for more variety in the results and damage scenarios. The coil spring constants were chosen so that the behavior of the frame will resemble that of the real girder built in the testing lab. The reason to choose the simulated model here is to obtain data at various sensing locations, as not so many strain gages are available on the real specimen. The model has 23 total nodes, which coincide with the accelerometer/strain gage locations.

For vibration data collection, a white noise excitation was applied in the horizontal direction to produce responses at each node. Measurement noise was accounted for by adding 5% random noise to the response. Four damage scenarios are simulated in succession by switching out a 20.32 cm portion at distinct sensor location 6, 15, 17 and 20, respectively. Except that the switched out portion is replaced with another tube with only 50% of the original section stiffness, the rest of the structure maintains the same stiffness properties as the undamaged. For testing of each structural state (undamaged/damaged), acceleration and strain signals are simulated at 500 Hz sampling frequency.

34.5.1 Damage Identification—Change Point Histograms

For each damage scenario, the algorithms outlined in Sects. 34.2–34.4 are applied. When applying frequency domain techniques, only samples larger than the median response are used for noise-robust performance. The combination of 4 regression models, 3 damage indices and 2 CPA techniques yield $4 \times 3 \times 2 = 24$ ways to identify damage. For each type of damage index, the values extracted from 10 sets of signals collected from damaged state are compared with those from 10 sets of baseline signals. Thus the ideal case is that all damage indices that report damage though CPA shows a change point at 10. However, in the results acquired from applying the damage localization algorithm to the data, the histogram of change point locations have a wide spread (Fig. 34.5), and the correct change point location needs to be recognized through a statistical inference, i.e. taking the first moment. The errors are probably caused by noise from sensing measurements, the effect of which tend to get larger for complex models with a number of parameters. Another way to counter the interference of large noise variance is to collect more vibration signals so as to have more estimated damage feature samples for the CPA.

34.5.2 Damage Localization—Identification of the Location Where the Most Significant Change Occurs

Table 34.2 summarizes the damage localization results for all 4 different damage states. Basically, the sensor (or sensor pair) location that corresponds to the largest change in damage location indicator values are identified as the damage location. When multiple sensor/sensor pair location tied for the largest damage location indicator value, they are all retained as possible damage location if the associated features are residual-based, but for regression coefficient features multiple sensor pairs are only allowed if the regression coefficients are from the same substructural model. Otherwise, tie-breaking rule that checks changes for other coefficients in respective models are employed. During the data processing step, the indicator values of

Fig. 34.5 CPA results for the four damage scenarios; red thin bar shows the weight mean location (color figure online)

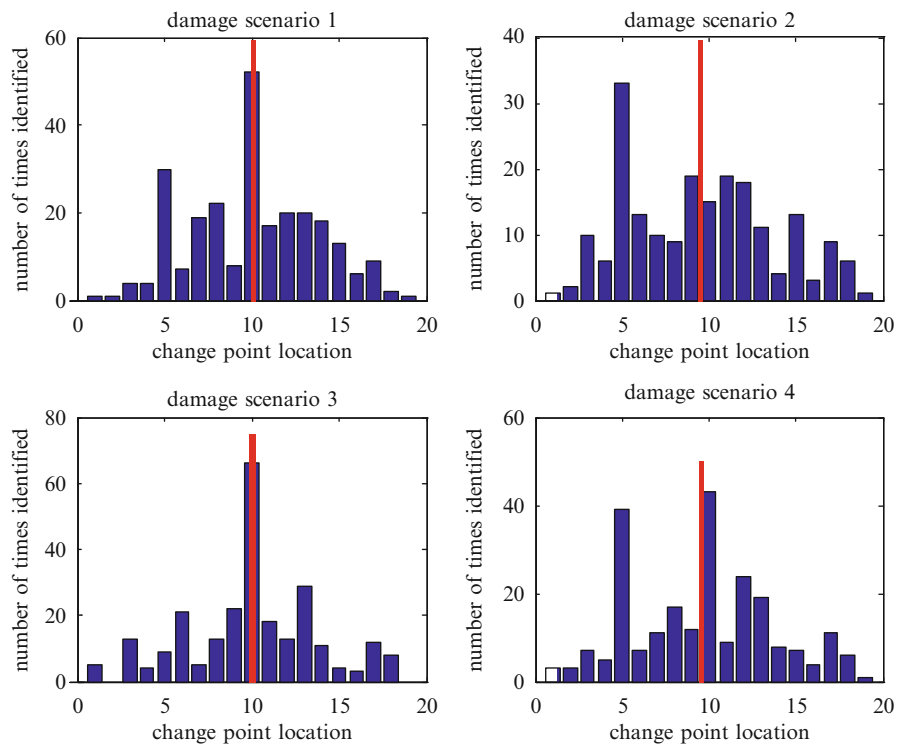


Table 34.2 Damage locations as determined from multiple algorithms

	Model 1	Model 2	Model 3	Model 4	Model 1	Model 2	Model 3	Model 4
	Damage scenario 1 (at location 6)				Damage scenario 2 (at location 15)			
NDIV from regression coefficients*	6-7	6-7	3-6-7	3-6-7	3-2	7-8	12-15	17-16
NMS from regression coefficients*	3-6	6-7	3-6-7	3-6-7	3-2	7-8	12-15	5-5
NDIV from RF1 and RF2	7	6	6	6/11	16	12	12	15
NMS from RF1 and RF2	7	6	6	6	16	12	12/15	17
	Damage scenario 3 (at location 17)				Damage scenario 4 (at location 20)			
NDIV from regression coefficients*	16-17-18	16-17	6-7	12-15	21-20	21-20	14-13	10-11-12
NMS from regression coefficients*	16-17	16-17	16-17	15-16	21-20	21-20	12-11	11-10
NDIV from RF1 and RF2	16/17	16/17	21	15/16	21	2	21	21
NMS from RF1 and RF2	16	16	21	15	21	21/12	21	21

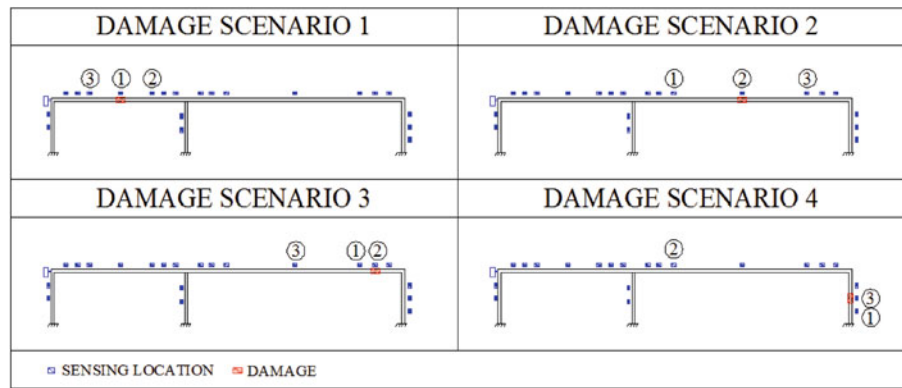
*When two numbers are hyphenated, the first number denotes the regressand node; when three numbers are hyphenated, the middle number denotes the regressand node

damage indices that are from the same regression model type and category (i.e. either coefficients/residual based) but different extraction functions (if there are) and CPA methods are summed together as they tend to be highly correlated. This would also make comparison and contrast among the results an easier task.

None of the methods proposed has a 100% correct performance as the simulated structure is different from the models presented. It can be seen that overall the residual-based methods perform better than the coefficient based damage methods in damage localization, and that the dynamic models outperform the static models for longer/suppler beam substructural models because the inertia force is accounted for, but underperform for shorter/stiffer beam models because their dynamic behavior is not significant. Therefore it is concluded that there is a trade-off between model accuracy and over-parameterization when designing damage detection algorithms. Also, it is noticed that the results would also improve for damaged locations closer to the excitation source (such as location 6) for the larger signal-to-noise ratios.

A direct voting scheme [9] among the results from different type of methods is used to decide on the most probable location of damage; (1) assign 1 weight to the locations indicated by residual based methods and the regressand nodes of coefficient-based methods, and 0.5 weight to indicated by the regressor nodes of coefficient-based methods. (2) pool the votes together to select three locations with the top scores. Number 3 is used as theoretically this is the maximum number of substructural models that will be affected by a potential damage. The results are shown in Fig. 34.6.

Fig. 34.6 Inferred damage locations from combining classifiers



34.6 Conclusion

In this paper, several substructural-based linear regression schemes are presented and adopted for damage identification and localization in a simulated steel frame specimen. Four substructural models are proposed, and in regard to each model three damage features, one as regression coefficients, two as functions of regression residuals, can be extracted. Two change point analysis (CPA) techniques are then used separately to determine if a statistically significant damage occurred in sequences of certain extracted damage features. All twenty-four classifiers thus obtained through joining individual model construction, feature extraction and CPA algorithms are applied to data from the simulated frame, which is set to undergo four different damage scenarios.

Application results show that the suggested algorithms succeeded in identifying the damage existence for all four damage states. However, the exact location of the change point, which indicates when the structure is damaged, is not obvious from viewing the results and has to be determined through calculating the weighted mean. This is because of the models adopted here have higher complexity than those in the previous research projects [10–12] and aim to extract information pertaining to higher level damage detection (damage localization). As such, the information-to-noise level here is reduced as a result of the combined noise effect from several signal sources and the reduced signal strength from multi-level data preprocessing. In light of this phenomenon, care must be taken for model selection to avoid overparameterization.

For damage localization, the substructural approaches are shown to be effective. The procedure much resembles an inversed finite element analysis approach, where the structural properties are estimated from structural responses through assuming that the structure can be represented mathematically by an assemblage of elements. It is observed that the residual-based methods are more sensitive than their coefficients-based counterparts. This observation is in line with the previous work, and the fact that the change in residuals properties is related to changes in all regression coefficients. On the other hand, when the excitation conditions are varying, the residual-related features will have a larger chance to be affected. Also noticed is that the algorithm performance is enhanced when the signal strength at the damage location is large.

It is found that more accurate decisions on damage location can be made when results from several methodologies are combined through a weighted voting scheme. This is expected as the errors from simplified linear modeling are mitigated through the ‘averaging process’, and combined classifiers have proved a success in many other pattern recognition fields [9]. Still, further research are needed to determine most effective and efficient ways for the combination.

References

1. Peeters B, Maeck J, De Roeck G (2001) Vibration-based damage detection in civil engineering: excitation sources and temperature effects. *Smart Mater Struct* 10(3):518
2. Carden EP, Fanning P (2004) Vibration based condition monitoring: a review. *Struct Health Monitor* 3(4):355–377
3. Hearn G, Testa RB (1991) Modal analysis for damage detection in structures. *J Struct Eng* 117(10):3042–3063
4. Abdel Wahab MM, De Roeck G (1999) Damage detection in bridges using modal curvatures: application to a real damage scenario. *J Sound Vib* 226(2):217–235
5. de Lautour OR, Omenzetter P (2010) Damage classification and estimation in experimental structures using time series analysis and pattern recognition. *Mech Syst Signal Process* 24(5):1556–1569
6. Carden E, Brownjohn JM (2008) ARMA modelled time-series classification for structural health monitoring of civil infrastructure. *Mech Syst Signal Process* 22(2):295–314

7. Hong YH, Kim HK, Lee HS (2010) Reconstruction of dynamic displacement and velocity from measured accelerations using the variational statement of an inverse problem. *J Sound Vib* 329(23):4980–5003
8. Jensen U, Lütkebohmert C (2007) Change-point models. *Encyclopedia Stat Qual Reliab* 1:306
9. Jain AK, Duin RPW, Mao J (2000) Statistical pattern recognition: a review. *IEEE Trans Pattern Anal Machine Intell* 22(1):4–37
10. Labuz EL, Pakzad SN, Cheng L (2011) Damage detection and localization in structures: a statistics based algorithm using a densely clustered sensor network. In: *Proceedings of the 20th annual structures congress, Las Vegas*
11. Yao R, Pakzad SN (2011) Statistical modeling methods for structural damage identification. In: *The 6th international workshop on advanced smart materials and smart structures technology, Dalian, July 2011*
12. Yao R, Tillotson ML, Pakzad SN, Pan Y (2012) Regression-based algorithms for structural damage identification and localization. In: *Proceedings of the 21st structures congress, Chicago, 2012*

Chapter 35

Operational Modal Analysis Based on Multivariable Transmissibility Functions: Revisited

Wout Weijtjens, Gert de Sitter, Christof Devriendt, and Patrick Guillaume

Abstract Transmissibility functions are output-only functions that have one major advantage. When well-defined these functions become independent from the spectral content of the acting forces. A method for Operational Modal Analysis (OMA) based upon these type of functions would therefore not be affected by any colored or harmonic forces exciting the structure. This is a major advantage compared to existing techniques in the field of OMA. Transmissibility based Operational Modal Analysis (TOMA) was first introduced a few years ago and this paper will summarize the basics behind this new field of study. Secondly the recently developed p-TOMA will be presented and illustrated by means of a numerical experiment.

Keywords Operational Modal Analysis • Transmissibility functions • Parameter estimation • Output-only • Harmonics

35.1 Introduction

As there is a growing interest in the dynamic performance of increasingly large civil (e.g. public buildings, stadia, bridges) and mechanical structures (e.g. wind turbines), the use of operational modal analysis (OMA) techniques has grown accordingly [9]. Operational modal analysis has some major advantages, since in operation all relevant modes are properly excited. An advantage that is not easily replicated by controlled excitation [10], simply because the energy levels needed to excite structural modes often far exceed those achievable with (portable) shakers. Moreover an experimental modal analysis does not always reflect the true behavior of the structure, as the dynamics of filled sports stadiums are not comparable with those of empty ones. Finally, one understands that an experimental analysis of a large structure is a time consuming activity that is preferably not repeated several times a year.

Operational modal analysis is a solution to these issues, as it can be performed under any given condition, at least in theory. This analysis can easily be repeated over time without the need for shutdown or any experimental effort. However, one main disadvantage of OMA is the simple fact that the input forces are not measured. To resolve this, OMA techniques in general make assumptions about the spectral content of the inputs. Most techniques for instance assume the inputs to behave as (band-limited) white noise. When this white noise assumption is violated these methods are prone to significant errors. And this violation occurs quite commonly, for instance the jumping of spectator crowds [7] or the rotation of a wind turbine [11].

Much research effort is put into resolving this issue. And one possible solution comes from Transmissibility based OMA (TOMA), [2, 12]. TOMA uses transmissibility functions instead of crosspower spectra as input data. The main benefit of this family of functions, is that they can become fully independent from the input spectra. Consequently there is no need for any strict assumption about the input spectra, and results are guaranteed whether or not the white-noise assumption is violated. In this article the basic idea behind TOMA is given, and the recently developed p-TOMA is presented.

W. Weijtjens (✉) • G. de Sitter • C. Devriendt • P. Guillaume
Vrije Universiteit Brussel, Pleinlaan 2, 1050 Brussels, Belgium
e-mail: wweijtje@vub.ac.be

35.2 Transmissibility Based Operational Modal Analysis (TOMA)

35.2.1 Properties of the Transmissibility Function

Consider a linear time invariant structure with transfer function $H(s) \in \mathbb{C}^{N_o \times N_i}$ as defined in eq. (35.1).

$$\vec{X}(s) = H(s) \begin{Bmatrix} F_1(s) \\ F_2(s) \\ \vdots \\ F_{N_s}(s) \end{Bmatrix} = H(s) \vec{F}(s) \quad (35.1)$$

Now consider that only in a discrete number (N_s) of input locations (K) a force is applied:

$$\begin{Bmatrix} \vec{X}_L(s) \\ \vec{X}_R(s) \end{Bmatrix} = \begin{bmatrix} H_{LK}(s) \\ H_{RK}(s) \end{bmatrix} \vec{F}_K(s) \quad (35.2)$$

In which $\vec{X}_L(s) \in \mathbb{C}^{N_o - N_r}$ and $\vec{X}_R(s) \in \mathbb{C}^{N_r}$ are respectively the non-reference and reference subsets of a measured frequency domain response vector $\vec{X}(s) \in \mathbb{C}^{N_o}$. And $H_{LK}(s) \in \mathbb{C}^{(N_o - N_r) \times N_s}$, $H_{RK}(s) \in \mathbb{C}^{N_r \times N_s}$ are parts of the transfer function relating the associated N_r reference and $(N_o - N_r)$ non-reference elements of the response vector to the N_s discrete input locations K . Transmissibility functions, $T(s) \in \mathbb{C}^{(N_o - N_r) \times N_r}$, were first defined in [6] as follows:

$$\vec{X}_L(s) = T(s) \vec{X}_R(s) \quad (35.3)$$

In [6] the following interesting property is proven:

$$T(s) = H_{LK}(s) H_{RK}^{-1}(s) \quad (35.4)$$

In essence this formula states that if the inverse of $H_{RK}(s)$ exists, so $N_r = N_s$, then the transmissibility function becomes solely dependent of the system transfer function $H(s)$ and most importantly independent of the unknown forces $\vec{F}_K(s)$. So no matter what the spectral content of the applied forces is, the transmissibility function will remain unaffected.

We can also extend Eq. (35.4) to allow for multiple (N_s) independent forces distributed over all (N_i) input locations. Therefore, the input forces are defined as follows:

$$\vec{F}_{distributed,l}(s) = \sum_{i=1}^{N_s} \vec{F}_{i,l} \mu_{i,l}(s) \quad (35.5)$$

This means that we describe the forces as a linear combination of independent input sources. Each source is distributed over the structure, according to the (amplitude) distribution vector $F_{i,l}$. Each variation of the distribution can be considered as a new loading condition l . The difference between the discrete force locations and the distributed forces is illustrated in Fig. 35.1.

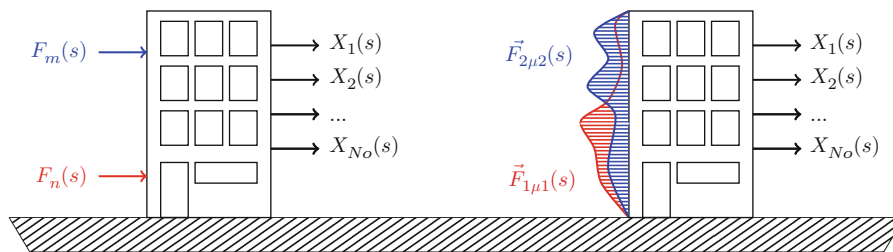


Fig. 35.1 Illustration of the difference between (left) discrete inputs (i.e. Eq. (35.4)) and (right) the more general case of distributed inputs (i.e. Eq. (35.12)). Both cases have $N_s = 2$, and one can easily recognize the (left) being a particular case of the distributed inputs (right)

Based upon the distributed forces, introduced in Eq. (35.5) expression (35.4) can be extended.

$$\vec{X}_{L,l}(s) = H_L(s) \vec{F}_{distributed,l}(s) \quad (35.6)$$

$$= H_L(s) \sum_{i=1}^{N_s} \vec{F}_{i,l} \mu_{i,l}(s) \quad (35.7)$$

$$= H_L(s) \left[\vec{F}_{1,l}, \vec{F}_{2,l}, \dots, \vec{F}_{N_s,l} \right] \begin{Bmatrix} \mu_{1,l}(s) \\ \mu_{2,l}(s) \\ \vdots \\ \mu_{N_s,l}(s) \end{Bmatrix} \\ = H_L(s) F_l \vec{\mu}_l(s) \quad (35.8)$$

In which $H_L(s) \in \mathbb{C}^{(N_o - N_r) \times N_i}$ relates the elements of $\vec{X}_{L,l}(s)$ to all N_i input locations. And F_l is the (real) distribution matrix, that describes how the N_s sources ($\mu_{i,l}(s)$) are distributed over the N_i input locations. For instance how the wind load is distributed over a structure. Index l , simply denotes that all variables were obtained under loading condition l . The same can be done for $\vec{X}_{R,l}(s)$ with $N_r = N_s$:

$$\vec{X}_{R,l}(s) = H_R(s) F_l \vec{\mu}_l(s) \quad (35.9)$$

$$\vec{\mu}_l(s) = (H_R(s) F_l)^{-1} \vec{X}_{R,l}(s) \quad (35.10)$$

Combining equations (35.8) and (35.10)

$$\vec{X}_{L,l}(s) = H_L(s) F_l (H_R(s) F_l)^{-1} \vec{X}_{R,l}(s) \quad (35.11)$$

$$T_l(s) = H_L(s) F_l (H_R(s) F_l)^{-1} \quad (35.12)$$

In essence poly-reference transmissibility functions become independent of the input spectra, $\vec{\mu}_l(s)$, and solely dependent on the transfer function ($H(s)$) and the distribution matrix F_l . In the continuation of this article we will make use of Property (35.12), but recognize that Eq. (35.4) is no more or no less than a particular case of Eq. (35.12)

Unfortunately Eq. (35.4) and Eq. (35.12) also show a disadvantage of transmissibility functions. Since one of the properties of the modal model is that the transfer function can be modeled using a common denominator model:

$$\begin{bmatrix} H_L(s) \\ H_R(s) \end{bmatrix} = \frac{1}{d(s)} \begin{bmatrix} N_L(s) \\ N_R(s) \end{bmatrix} \quad (35.13)$$

In which $d(s)$ is the *scalar* denominator polynomial. So expression Eq. (35.12) combined with Eq. (35.13) gives following result:

$$T(s) = (N_L(s) F_l) (N_R(s) F_l)^{-1} \quad (35.14)$$

In Eq. (35.14) the denominator polynomial is lost, and with it all information about the structural poles. Due to this property it was long thought that transmissibility based modal analysis was not possible.

35.2.2 The First Steps Towards TOMA

However, Eq. (35.14) also shows that transmissibility functions do remain dependent of the input location/distribution of the forces, defined by F_l . These input locations/distributions can be associated with a certain *loading condition*. During operation these input distributions might change and introduce a new loading condition. Examples are a change of wind direction, changing driving conditions, etc. [1]

Fig. 35.2 (a) Three transmissibility functions for a simulated (undamped) system obtained under three different loading conditions. In this figure the single input ($N_s = 1$) changed input location to generate the three loading conditions. The system poles are indicated by vertical dotted lines. (b) Illustration of the simulated loading conditions

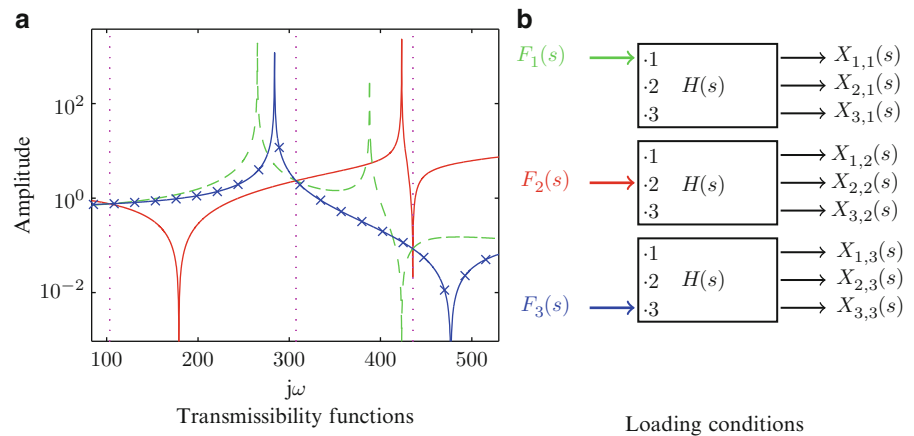


Fig. 35.3 Some examples on which TOMA was applied successfully

Moreover, [2] showed that for the particular case of a single dominant force, i.e. $N_s = 1$, transmissibility functions become independent of the single input location solely in the system poles $s = \lambda_m$. The basic idea behind what is called Transmissibility based Operational Modal Analysis (TOMA) is to exploit this property.

If $N_l \geq 2$ transmissibility functions are obtained under N_l different loading conditions. Then the system poles can be found at the intersections of the all transmissibility functions. This property is illustrated in Fig. 35.2. Note however that for a damped system these intersections happen within the Laplace domain (s), and they occur only in the Fourier/Frequency domain ($s = j\omega$) for undamped systems.

Devriendt et. al. also showed the applicability of the method in the case of a single distributed force. It was demonstrated that a different loading condition for a distributed force simply meant a change in the distribution of that force. The concept was proven on wind tunnel testing (Fig. 35.3a), a pedestrian bridge [3] (Fig. 35.3b) and a mobile substation (Fig. 35.3c).

Recently the latest development in the use of single-reference ($N_r = 1$) transmissibility functions for Operational Modal analysis was introduced, pseudo-inverse approach for TOMA [12]. One of the main benefits of this particular approach is that a unique method for combining all obtained transmissibility functions is defined. As a consequence user-decisions are reduced to the mere selection of a reference signal and the risk for ‘fake’ poles is significantly reduced. The Pseudo-inverse approach, for these reasons, can be considered the preferred method for using single-reference transmissibility functions for operational modal analysis. However, sometimes a single reference just isn’t sufficient.

35.2.3 Extending the Applicability of TOMA

In practice, the demand for a single dominant force or a single distributed force is only rarely met. For instance an operational bridge will not only be excited by wind but also by traffic passing over it. Therefore it was considered to extend TOMA for $N_s \geq 2$. The importance of such an expansion can be visualized in Fig. 35.4. A major difference, visible in Fig. 35.4, is that the single-reference transmissibility functions ($N_r = 1$) are no longer input-spectrum independent.¹ However, for poly-reference transmissibility functions (in this example $N_r = N_i = 2$) the obtained transmissibility functions clearly no longer intersect at the system poles. Therefore, the methods cited in Section 35.2.2, that look for these intersections, are no longer

¹ It should be noted that for $N_s > 1$, single-reference TOMA techniques are still applicable however they are no longer input-spectrum independent.

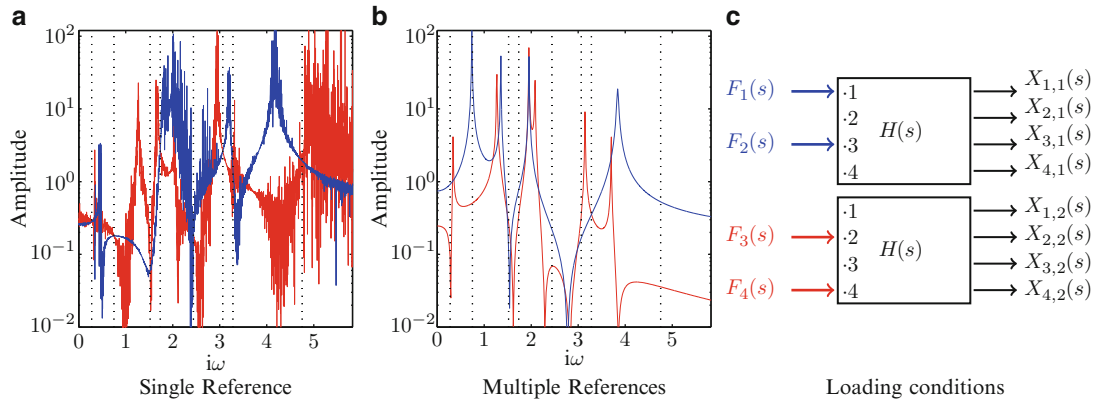


Fig. 35.4 While scalar transmissibilities will always intersect in the poles (a), they lose their deterministic properties when multiple uncorrelated forces are exciting the system. Multivariable transmissibilities will remain deterministic (for $N_r = N_s$), yet their intersections do not longer coincide with the systems poles (b) (indicated with *dotted lines*). The simulated loading conditions are illustrated in (c)

applicable when using these poly-reference transmissibility functions. In [4] a first glimpse was given at a possible solution to use poly-reference transmissibility functions for TOMA. However this method was rather cumbersome and required the presence of at least three different loading conditions. This requirement is very limiting if the exciting forces only vary very slowly.

35.3 Introducing p-TOMA

35.3.1 Concept

Before going into the practical implementation, let us consider the general idea behind TOMA and by extension poly-reference TOMA (p-TOMA). The main property making TOMA possible is the fact that in the system poles transmissibility functions become independent of the input conditions. For a single reference transmissibility function this boils down to the notion that single-reference transmissibility functions intersect at the system poles. The polyreference equivalent is readily found:

$$\lim_{s \rightarrow \lambda_m} T_l(s) \vec{X}_{R,l}(s) = \lim_{s \rightarrow \lambda_m} \vec{X}_{L,l}(s) \quad (35.15)$$

Making use of the properties of the modal model

$$T_l(\lambda_m) \vec{\phi}_{R,m} = \vec{\phi}_{L,m} \quad (35.16)$$

This actually states that in the system poles the transmissibility function always relates the reference part of the associated mode shape to its non-reference part. A simple reformulation yields following expression

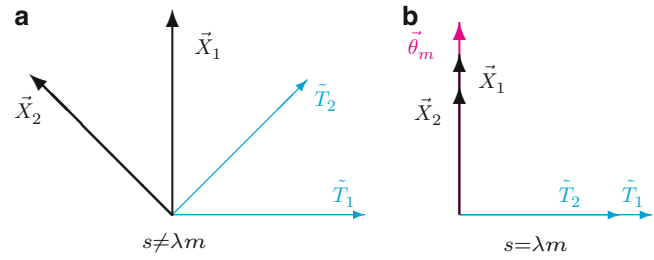
$$[T_l(\lambda_m), I_{(N_o - N_r)}] \vec{\phi}_m = 0 \quad (35.17)$$

With $I_{(N_o - N_r)}$ the square $(N_o - N_r)$ dimensional identity matrix. So at the system poles the rows of $[T_l(\lambda_m), I_{(N_o - N_r)}]$ are always orthogonal to the associated mode shape vectors ϕ_m . Moreover, Eq. (35.17) is independent of the input, as the response vector is not longer present. This is not the case for the more general expression, outside the system poles:

$$[T_l(s), I_{(N_o - N_r)}] \vec{X}_l(s) = \vec{T}_l(s) \vec{X}_l(s) = 0 \quad (35.18)$$

To find the system poles we therefore only have to find these values of s for which a vector can be found orthogonal to all rows of the N_l obtained instances of $\vec{T}_l(s)$. This is illustrated in Fig. 35.5. Important to note is that these solutions are only unique when the considered loading conditions were sufficiently different. If this would not be the case other vectors, besides the mode shape vectors, will exist that are also orthogonal to all considered row vectors. This issue will also occur if an insufficient number of loading conditions are considered.

Fig. 35.5 Illustration of the properties of $\tilde{T}(s)$ with $N_o = 2$, making use of two different loading conditions in (a) \tilde{X}_1, \tilde{X}_2 and consequently \tilde{T}_1 and \tilde{T}_2 are still dependent of the input forces, in (b) for $s = \lambda_m$ this dependency is lost and \tilde{T}_1 and \tilde{T}_2 will always be orthogonal to the same vector



35.3.2 Implementation

Consider the response vectors as already obtained for N_l measured and sufficiently different loading conditions. For each loading condition the transmissibility functions can be modeled using numerator-denominator models, such as for instance the left matrix fraction description (LMFD).

$$T_l(\Omega) = D_l^{-1}(\Omega)N_l(\Omega) \quad (35.19)$$

With $D_l(\Omega)$ the square $(N_o - N_r)$ -dimensional denominator matrix polynomial and $N_l(\Omega) \in \mathbb{C}^{(N_o - N_r) \times N_r}$ the numerator matrix polynomial which both are given as:

$$D_l(\Omega_k) = \sum_{i=0}^{n_D} A_{i,l} \Omega_k^i \quad (35.20)$$

$$N_l(\Omega_k) = \sum_{i=0}^{n_N} B_{i,l} \Omega_k^i \quad (35.21)$$

In which $A_{i,l}$ and $B_{i,l}$ are the matrices to be estimated and n_D, n_N are the polynomial orders defined by the user.

In the frequency domain multiple possibilities exist for polynomial basis function, Ω_k . The numerator-denominator models are formulated as a Laplace domain (continuous-time) model if $\Omega_k = j\omega_k$, and as a Z-domain (discrete-time) model for $\Omega_k = e^{-j\omega_k T_s}$, but other choices are possible [8]. Moreover, if preferred the estimation can readily be extended to a time domain estimator. For each loading condition the matrix coefficients can be estimated by constructing the observation matrices K , and solving for the parameter matrix $\Theta \in \mathbb{C}^{(n+1)N_o \times (N_o - N_r)}$:

$$[K_{d,l}, K_{n,l}] \tilde{\Theta}_l = 0 \quad (35.22)$$

With :

$$K_{d,l} = \begin{bmatrix} \tilde{X}_{L,l}^T(\omega_1) & \Omega_1^1 \tilde{X}_{L,l}^T(\omega_1) & \dots & \Omega_1^{n_D} \tilde{X}_{L,l}^T(\omega_1) \\ \tilde{X}_{L,l}^T(\omega_2) & \Omega_2^1 \tilde{X}_{L,l}^T(\omega_2) & \dots & \Omega_2^{n_D} \tilde{X}_{L,l}^T(\omega_2) \\ \vdots & \vdots & \ddots & \vdots \\ \tilde{X}_{L,l}^T(\omega_{N_f}) & \Omega_{N_f}^1 \tilde{X}_{L,l}^T(\omega_{N_f}) & \dots & \Omega_{N_f}^{n_D} \tilde{X}_{L,l}^T(\omega_{N_f}) \end{bmatrix}$$

$$K_{n,l} = - \begin{bmatrix} \tilde{X}_{R,l}^T(\omega_1) & \Omega_1^1 \tilde{X}_{R,l}^T(\omega_1) & \dots & \Omega_1^{n_N} \tilde{X}_{R,l}^T(\omega_1) \\ \tilde{X}_{R,l}^T(\omega_2) & \Omega_2^1 \tilde{X}_{R,l}^T(\omega_2) & \dots & \Omega_2^{n_N} \tilde{X}_{R,l}^T(\omega_2) \\ \vdots & \vdots & \ddots & \vdots \\ \tilde{X}_{R,l}^T(\omega_{N_f}) & \Omega_{N_f}^1 \tilde{X}_{R,l}^T(\omega_{N_f}) & \dots & \Omega_{N_f}^{n_N} \tilde{X}_{R,l}^T(\omega_{N_f}) \end{bmatrix}$$

and,

$$\tilde{\Theta}_l^T = \{A_{0,l} \ A_{1,l} \ \dots \ A_{n_D,l} \ B_{0,l} \ B_{1,l} \ \dots \ B_{n_N,l}\}$$

Once the matrix coefficients are estimated, via a Least Squares approach, the following can be derived from the combination of (35.12) and (35.19):

$$D_l^{-1}(\Omega)N_l(\Omega) = H_L(\Omega)F_l(H_R(\Omega)F_l)^{-1} \quad (35.23)$$

$$N_l(\Omega)H_R(\Omega)F_l = D(\Omega)H_L(\Omega)F_l \quad (35.24)$$

Further rearranging yields

$$[D_l(\Omega) - N_l(\Omega)] \begin{bmatrix} H_L(\Omega) F_l \\ H_R(\Omega) F_l \end{bmatrix} = 0 \quad (35.25)$$

Renaming the left matrix as $\tilde{T}(\Omega)$:

$$\tilde{T}_l(\Omega) \begin{bmatrix} H_L(\Omega) F_l \\ H_R(\Omega) F_l \end{bmatrix} = 0 \quad (35.26)$$

This means that $\tilde{T}_l(\Omega)$ is unaffected by the spectral content of the inputs, yet dependent of their distribution. Combine this with an important property for transfer functions of MIMO LTI systems, namely that all column (and row) vectors of $H(\lambda_m)$ are proportional with the mode shape vector $\vec{\phi}_m$ [5]. So Eq. (35.26) becomes:

$$\tilde{T}_l(\lambda_m) \vec{\phi}_m = 0, \forall m = 1, 2, \dots, N_m \text{ and } \forall l = 1, 2, \dots, N_l \quad (35.27)$$

So when combining all N_l different $\tilde{T}_l(s)$ into one ($N_o \times N_o$)-dimensional matrix:

$$\Upsilon(\lambda_m) \vec{\phi}_m = \begin{bmatrix} \tilde{T}_1(\lambda_m) \\ \tilde{T}_2(\lambda_m) \\ \vdots \\ \tilde{T}_{N_l}(\lambda_m) \end{bmatrix} \vec{\phi}_m = \left(\sum_{i=0}^{n_{max}} \begin{bmatrix} A_{i,1}, & -B_{i,1} \\ A_{i,2}, & -B_{i,2} \\ \vdots \\ A_{i,N_l}, & -B_{i,N_l} \end{bmatrix} \lambda_m^i \right) \vec{\phi}_m = 0 \quad (35.28)$$

with $n_{max} = \max\{n_D, n_N\}$ This has in fact become a polynomial eigenvalue problem, with $N_o n_{max}$ possible eigenvalues and associated eigenvectors amongst which the true system's poles and associated mode shapes. Note that in fact all scalar multiplications of $\vec{\phi}_m$ also are eigenvectors of the posed problem. Therefore, an additional constraint will be imposed upon these eigenvectors to obtain a finite number of possible solutions, for instance $\|\vec{\phi}_m\| = 1$.

A second requirement to obtain a finite number of solutions is that $\Upsilon(\Omega)$ is of rank N_o . This implies that $\Upsilon(\Omega)$ has at least N_o rows, and as a consequence the minimum number of required loading conditions N_l should always exceed $\frac{N_o}{(N_o - N_r)}$.

As in general model orders n_N and n_D are chosen far larger than the true system order some additional solutions to (35.28) will exist, lacking physical relevance. These can often easily be discriminated since they have improbable high levels of damping, are unstable ($Re(\lambda_m) > 0$) or by means of a stabilization diagram.

35.3.3 Algorithm in Short

1. Measure the system response, using a set of N_o vibrational sensors, of the system excited by an unknown input
2. Select the number of references (N_r) in such a manner that the multi-reference transmissibility functions can become (near) deterministic, i.e. $N_r = N_l$.
3. Select the reference signals $\vec{X}_{R,i}(\Omega)$ and non-reference response signals $\vec{X}_{L,i}(\Omega)$.
4. Estimate the matrix coefficients $[A_i]$, $[B_i]$, for the user-defined polynomial orders n_D, n_N , in the preferred domain, and construct $\tilde{T}_l(\Omega)$ for the data linked to one loading condition.
5. Repeat the previous steps for $N_l \geq \frac{N_o}{N_o - N_r}$ loading conditions, until a complete set of loading conditions is obtained.
6. Construct the combined matrix $\Upsilon(\Omega)$ and solve the polynomial eigenvalue problem:

$$\left(\sum_{i=0}^{n_{max}} \begin{bmatrix} A_{i,1}, & -B_{i,1} \\ A_{i,2}, & -B_{i,2} \\ \vdots \\ A_{i,N_l}, & -B_{i,N_l} \end{bmatrix} \lambda_m^i \right) \vec{\phi}_m = 0 \quad (35.29)$$

7. The system poles and mode shapes are now found within the set of solutions of the polynomial eigenvalue problem (35.29).

Fig. 35.6 The 4DOF model used in the simulations ($m=1$, $c=0.5$, $k=1000$)

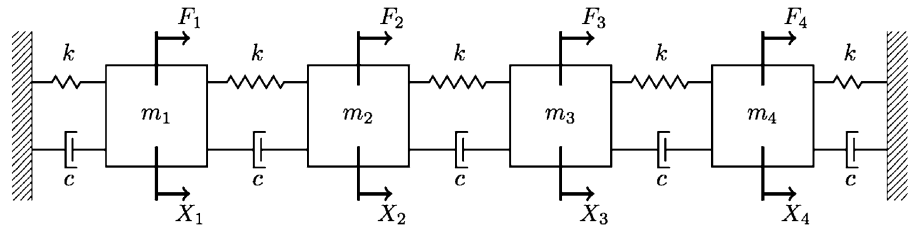


Table 35.1 Resonance frequencies (Hz) and damping ratio's (%) of the modeled system

No.	$f_{res}(Hz)$	$\xi(\%)$
	2.5505	5.6161
1	3.1105	0.4886
2	5.9166	0.9294
3	8.1434	1.2792
	8.5953	1.4813
4	9.5732	1.5038

In addition the poles of the input signals are provided (without numbering)

8. To discriminate between physical and non-physical poles within the set of solutions one can use commonly used criteria such as for example: excessive damping ratio's ($\xi > 10\%$), unstable poles ($\xi \leq 0$) and pure mathematical poles with infinite components. Other possibilities are the construction of a stabilization diagram and clustering algorithms.

35.4 Numerical Example

35.4.1 Problem Description

As the newly proposed method can be applied to all systems that can be described by a matrix polynomial, it is applicable for any viscous damped mechanical system.

$$H^{-1}(s)\vec{X}(s) = (Ms^2 + Cs + K)\vec{X}(s) = \vec{F}(s) \quad (35.30)$$

With M, C, K respectively the square N_{DOF} mass, viscous damping and stiffness matrices. With $\vec{X}(s)$ the system response (displacements) and the acting forces $\vec{F}(s)$. A proof of concept is produced by means of a numerical experiment, in the frequency domain, using a 4-DOF mechanical system as depicted in Fig. 35.6. With resonant frequencies and damping ratios shown in Table 35.1. The system is excited in all DOFs by $N_s = 2$ distributed input sources, with $\vec{F}(s) = F_1\mu_1(s) + F_2\mu_2(s)$. Both sources are in fact (band limited) white noise sequences, with coloring superposed on top. The coloring was obtained as the system response of a SDOF system to a (band limited) white noise input. The poles of these SDOF systems are also provided in Table 35.1. As $N_o = 4$ and $N_s = 2 = N_r$, the minimal number of required loading conditions is two. These were simulated by varying the distribution of the two forces. As illustrated by Fig. 35.7. No measurement noise nor leakage is considered in this example as to illustrate the property that the estimation is exact even though the inputs are colored. In this the identification of the matrix coefficients A_i and B_i was performed using a least squares approach in which A_{n_D} was constrained to a $(N_o - N_r)$ -dimensional identity matrix. And a discrete time model was used in order to obtain a well conditioned observation matrices.

35.4.2 Results

Stable poles can be plotted for different model orders, in this case for simplicity $n_D = n_N$ was chosen, in a so-called stabilization diagram, which has become a popular tool to discriminate mathematical poles from true system poles [5]. The

Fig. 35.7 Load distribution over the system DOF in the two loading conditions (-) and (- -), of both colored input sources: 2.6Hz (o) and 8.6Hz (x)

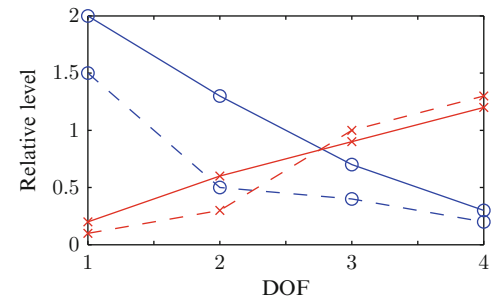
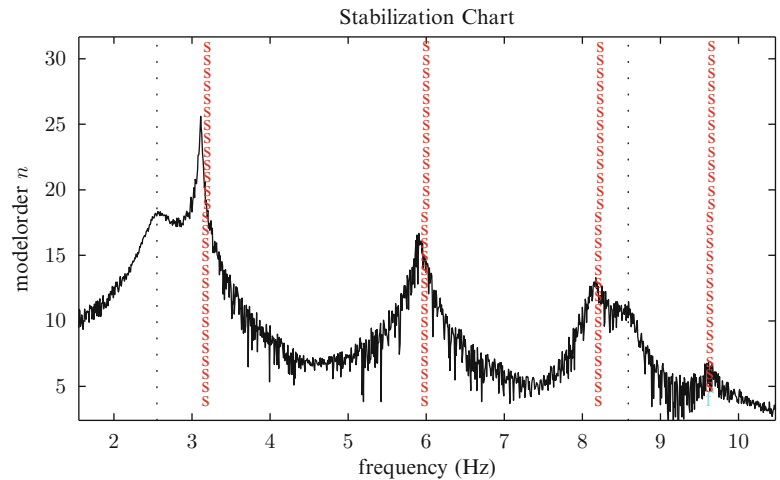


Fig. 35.8 Stabilisation diagram for model orders $n_N = n_D = 3$ till 32. It is shown that the method yields clear stabilisation diagrams. *Dotted vertical lines* highlight the location of the inputs' coloring



basic idea behind this is that mathematical poles would scatter around the plot while physical poles would form stable lines, as they are present in all model orders. The stabilisation diagram obtained with the proposed method is given in Fig. 35.8. Very clear stabilisation diagrams are obtained, indicating that most mathematical poles are unstable or unrealistically high damped. At the background of the stabilisation diagram the response auto power of response signal $X_1(\omega)$ is plotted to illustrate the presence of the input coloring. While present in all response signals none of both inputs was mistaken to be a true system pole, nor did they influence the quality of the estimated modal parameters. Moreover in these ideal conditions, no significant noise or leakage, the system poles were obtained at errors close to the machine-precision. This can also be said about the mode shapes.

35.5 Conclusions

In the introduction of this article a short discussion was held about the properties of transmissibility functions. Then a small recapitulation on the state of the art in transmissibility based Operational Modal Analysis (TOMA) is given and their current limitations were mentioned. These are resolved in the newly developed p-TOMA approach, by using poly-reference transmissibility functions.

The newly proposed method starts from estimating the matrix coefficients of a model based upon the input spectrum independent transmissibility functions. Multiple estimates of the matrix coefficients are obtained under significantly different loading conditions. When properly combined the system poles and mode shapes are obtained as the solutions of the polynomial eigenvalue problem. A simulated proof of concept illustrates the applicability of the proposed technique and showed its independence from the spectral content of the inputs.

Acknowledgements The financial support of the Institute for the Promotion of Innovation by Science and Technology in Flanders (IWT) and the Research Council (OZR) of Vrije Universiteit Brussel (VUB) are gratefully acknowledged.

References

1. Devriendt C (2010) On the use of transmissibility functions in operational modal analysis. PhD thesis, Vrije Universiteit Brussel, 2010
2. Devriendt C, Guillaume P (2007) The use of transmissibility measurements in output-only modal analysis. *Mech Syst Signal Process* 21(7):2689–2696
3. Devriendt C, Guillaume P, Reynders E, De Roeck G (2007) Operational modal analysis of a bridge using transmissibility measurements. In: *Proceedings of the international modal analysis conference (IMAC) XXV, Orlando, FL, 2007*
4. Devriendt C, De Sitter G, Guillaume P (2010) An operational modal analysis approach based on parametrically identified multivariable transmissibilities. *Mech Syst Signal Process* 24(5):1250–1259
5. Heylen W, Sas P (2006) *Modal analysis theory and testing*. Katholieke Universteit Leuven, Departement Werktuigkunde, 2006
6. Maia NMM, Silva JMM, Ribeiro AMR (2001) The transmissibility concept in multi-degree-of-freedom systems. *Mech Syst Signal Process* 15(1):129–137
7. Peeters B, Vanhollenbeke F, Van der Auweraer H (2005) Operational polymax for estimating the dynamic properties of a stadium structure during a football game. In: *Proceedings of the IMAC, vol 23*
8. Pintelon R, Schoukens J (2001) *System identification: a frequency domain approach*. IEEE, New York
9. Reynders E (2012) System identification methods for (operational) modal analysis: review and comparison. *Arch Comput Meth Eng* 19(1):51–124
10. Reynolds P, Pavic A, Carr J (2007) Experimental dynamic analysis of the kingston communications stadium. *Struct Eng* 85(8):33–39
11. Tcherniak D, Chauhan S, Hansen MH (2011) Applicability limits of operational modal analysis to operational wind turbines. In: Proulx T (ed) *Structural dynamics and renewable energy, vol 1*. Conference proceedings of the society for experimental mechanics series, vol 10. Springer, New York, pp 317–327
12. Weijtjens W, De Sitter G, Devriendt C, Guillaume P (2012) Transmissibility based operational modal analysis: on the use of the pseudo inverse approach. In: *Proceedings of ISMA 2012, Leuven, 2012*

Chapter 36

Diagnosis of Building Vibration Sources via Time-Frequency Analysis

Linda M. Hanagan and Martin W. Trethewey

Abstract Diagnosing excessive building vibration can be problematic because of long transmission paths. The excitation may be far displaced from the occupant thus increasing the number of potential sources. Source identification is further exacerbated by the intermittent behavior of the problematic excitation. Long time vibration records, on the order of many minutes, hours, or even days are sometimes required to capture a problematic event or the pattern of the problematic events. Analysis of the long time records with traditional spectral processing methods is usually not effective as the ensemble averaging clouds the intermittent features that are found objectionable by the occupants. Methods that rely on identifying peaks are also ineffective because a single transient peak is not typically the source of problem vibration levels. The Short Time Fourier Transform (STFT) is well suited to analyzing long records of building vibration because they provide the insight necessary to separate and identify intermittent excitation sources creating problematic building vibrations. This paper will describe the STFT in relation to analyzing long time record building vibration. The processing technique is applied to diagnose the source in a residence where the occupant complained about floor vibration even though no easily identifiable source was found.

Keywords Floor vibration • Vibration testing • Frequency analysis • Occupant complaints • Fourier transform

36.1 Introduction

Investigating building vibration can result in a seemingly overwhelming volume of data. Because many sources of disturbance are somewhat transient in nature, the most troubling episodes, lasting as few as one second, can be lost in time records that comprise hours or even days of measurements. This paper illustrates the use of time-frequency analysis using short time Fourier transformations (STFT) to characterize the data in frequency domain over long periods of time. After a theoretical description of the STFT, several example disturbances are analyzed to show the usefulness of the method. Finally, data from an apartment building is presented to illustrate how the method can be used to identify sources of vibration.

36.2 Short Time Fourier Transform (STFT)

FFT based spectral analysis is predicated on the assumption of signals being stationary. For example, the floor vibration resulting from a building air handling unit operation has a very steady behavior. If the signal is separated into finite duration sample data blocks, the mean square value calculated from any segment would produce a similar estimate. The stationary ergodic character of the data permits ensemble averaging to reduce random errors [1]:

L.M. Hanagan (✉)
Department of Architectural Engineering, Penn State University, University Park, PA 16802, USA
e-mail: hanagan@psu.edu

M.W. Trethewey
Department of Mechanical and Nuclear Engineering, Penn State University, University Park, PA 16802, USA

$$G_{xx}(f, T) = \frac{1}{KT} \sum_{k=1}^K [X^*(f, T) X(f, T)] \quad (36.1)$$

In practice, the stationarity assumption is often violated and may cause severe consequences.

For example, floor vibration on an office floor may be caused by the passage of a nearby pedestrian and, therefore, exhibit characteristics which change with respect to time. If the mean squared value is calculated from finite time samples during the pedestrian pass-by, the values would highly depend on when the samples were acquired with respect to pedestrian's location on the floor. If each finite duration data segment is averaged together, as indicated by Eq. (36.1), the respective segment frequency features cannot be detected. To understand the time varying frequency content in a signal requires a form of processing known as Non-Stationary Signal Analysis. There are a variety of mathematical processes which have been, and are still being, developed for analysis of non-stationary signals. One such method is the Short Time Fourier Transform (STFT).

The Short Time Fourier Transform (STFT) is a method that can produce time-frequency details of transients and nonstationary data [2]. The STFT is based upon the computation of the Fourier Transform of a finite duration sample, from a continuous signal $x(t)$. A window function, $w(t, T)$, is used to acquire the finite sample.

$$x(t, T) = x(t)w(t, T) \quad (36.2)$$

The window function is only defined between 0 and T , being zero elsewhere. The Fourier Transform of the windowed sample is:

$$X(f, T) = \int_{-\infty}^{\infty} x(t) w(t, T) e^{-i2\pi ft} dt \quad (36.3)$$

Next, let the window function $w(t, T)$ include a time shift variable, τ , and its Fourier Transform becomes:

$$X(f, T, \tau) = \int_{-\infty}^{\infty} x(t) w(t, T, \tau) e^{-i2\pi ft} dt \quad (36.4)$$

By monotonically increasing the time shift variable, τ , the window "slides" through the entire data record, $x(t)$. The respective Fourier transform is then computed for each τ value. This "sliding window" process is the basis of the Short Time Fourier Transform (STFT). Time event localization is directly tied to the selection of the T . As T increases the spectral resolution becomes finer, but the ability to localize a time event is adversely affected. This is the always present time-frequency analysis dichotomy.

In applications with a discretized data array, the shift variable, τ , is an increment often expressed as a percentage (i.e., 5%) of the overall window length (T). The incremental shift variable, τ_n , would be an integer index (n) related to the FFT block size (N):

$$n/N \approx \%T \quad (36.5)$$

To illustrate the differences and capabilities of the STFT consider the following Case Study.

36.3 Example Disturbances

Several types of vibration episodes within a 30 min time record are investigated using the STFT to illustrate the usefulness of the method for investigating disturbing floor vibration in long time records. The vibration types contained within the 30 min window are described in Table 36.1 and illustrated in Figs. 36.1, 36.2, 36.3, 36.4, 36.5, 36.6, 36.7, and 36.8. It has been shown that 8 sec time blocks using a sampling frequency of 128 samples per second, a 50 Hz bandwidth, is appropriate for assessing floor vibration with respect to human perception [3]. It can also be seen from Figs. 36.1, 36.2, 36.3, 36.4, 36.5, 36.6, 36.7, and 36.8 that 8 sec windows also reveal the true character of the vibration with respect to human perception.

Signal A was selected for investigation because it has a frequency and amplitude that is near the threshold of perception for a multi-second duration. Signal B was selected because it has a frequency and amplitude that may be found disturbing if it lasts for more than a few seconds. Signal C has a frequency and amplitude that might be on the threshold of disturbing

Table 36.1 Signal descriptions

Name	Signal formula
Signal A	$0.001\sin(2\pi \cdot 6.1 \cdot t)$
Signal B	$0.003\sin(2\pi \cdot 12.1 \cdot t)$
Signal C	$0.005\sin(2\pi \cdot 8.1 \cdot t)$
Signal D	$0.01\sin(2\pi \cdot 8.1 \cdot t)$

Fig. 36.1 Example disturbances in 30 min time window (color figure online)

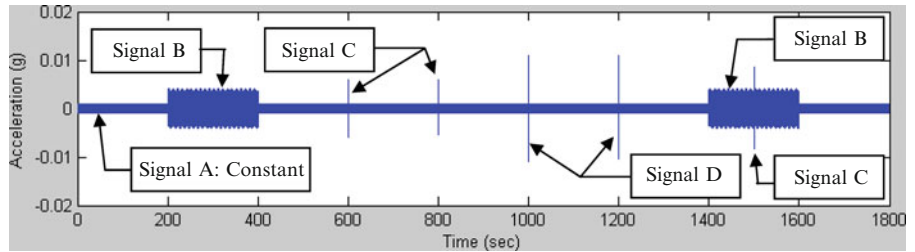


Fig. 36.2 Small continuous disturbance (Signal A) (color figure online)

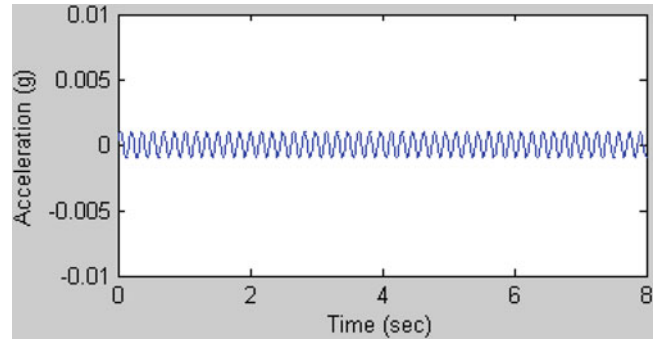


Fig. 36.3 Small continuous plus larger (Signal A), higher frequency continuous disturbance (Signal B) (color figure online)

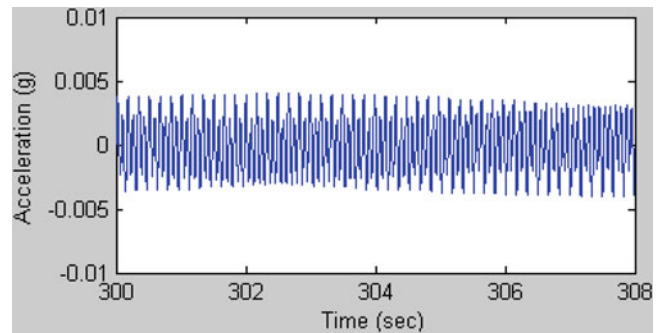
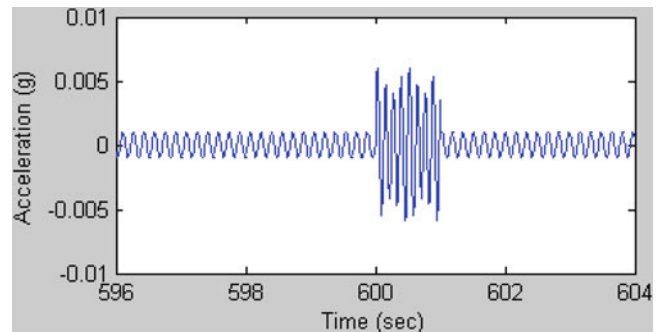


Fig. 36.4 Small continuous (Signal A) plus larger, higher frequency (Signal C), 1 sec disturbance (color figure online)



if it has a one-second or more duration but not disturbing if only occurring for one cycle. Finally, Signal D has sufficient magnitude that it would be very disturbing if felt for 1 sec or more but not disturbing if only felt for one cycle. In a long time record like Fig. 36.1, it should be noted that disturbances lasting 1 sec appear the same as disturbances that are impulse-like. The human perception of these disturbances would be very different. For example, the episodes in Figs. 36.4 and 36.6 might

Fig. 36.5 Small continuous (Signal A) plus larger, higher frequency (Signal C), impulse-like disturbance (color figure online)

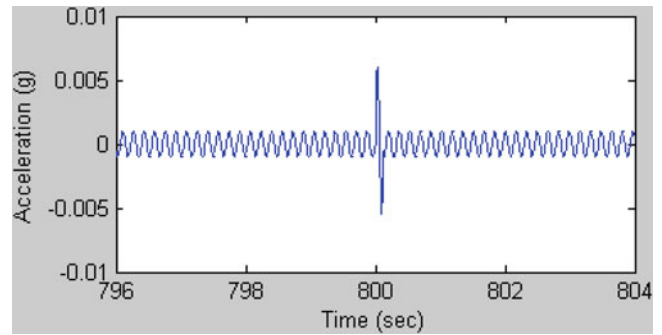


Fig. 36.6 Small continuous (Signal A) plus very large, higher frequency (Signal D), 1 sec disturbance (color figure online)

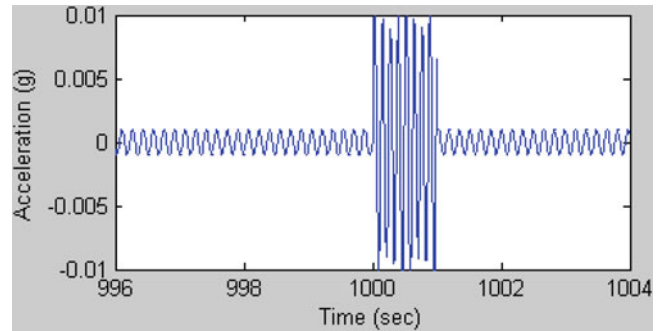


Fig. 36.7 Small continuous (Signal A) plus very large, higher frequency (Signal D), impulse-like disturbance (color figure online)

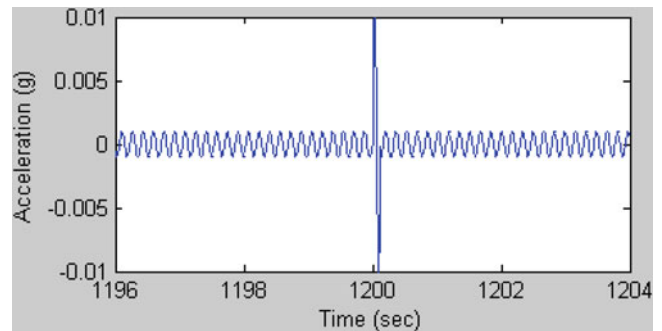
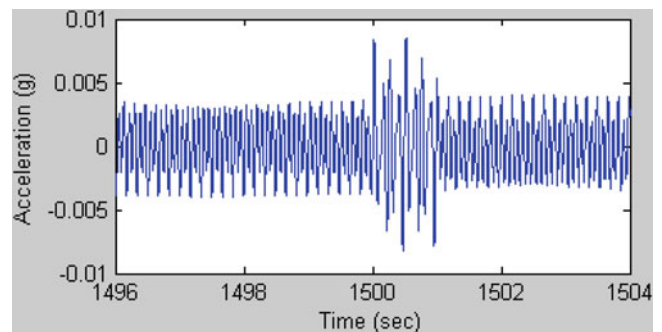


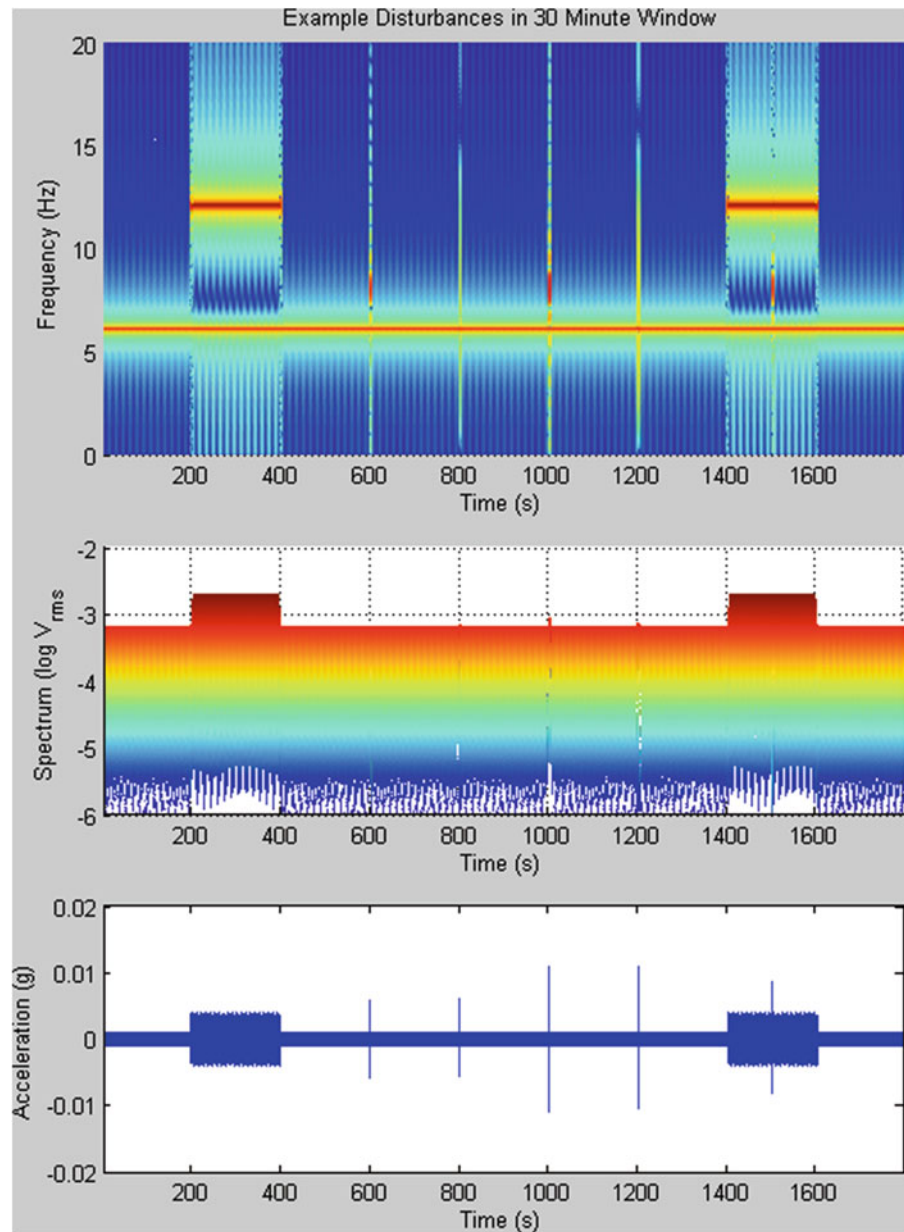
Fig. 36.8 Small (Signal A) and larger continuous plus larger, higher frequency (Signal C), one second disturbance (color figure online)



be disturbing whereas the episode in Figs. 36.5 and 36.7 would not. The combination of signals in Fig. 36.8 shows how the time signal becomes too complex to distinguish the separate components. Guidance from the ISO 2631, Part 2 [4] and personal experience guided the selection of these signals and the qualitative description of them.

The top and middle graph in Fig. 36.9 shows the STFT of the same long record data in two views of the three dimensional data. This Figure was created in Matlab using the Spectrogram function. The M-file that created this figure is presented in the Appendix. For the vibration episode between 200 and 400 sec, the STFT graphs help to quickly identify the frequencies, magnitudes and duration of the two different signals that make up the record. As noted in the paragraph above, the disturbances at 600 and 800 sec and then 1000 and 1200 sec look identical in the long duration time history. The top graph

Fig. 36.9 Example disturbances in 30 min window with two views of STFT (color figure online)

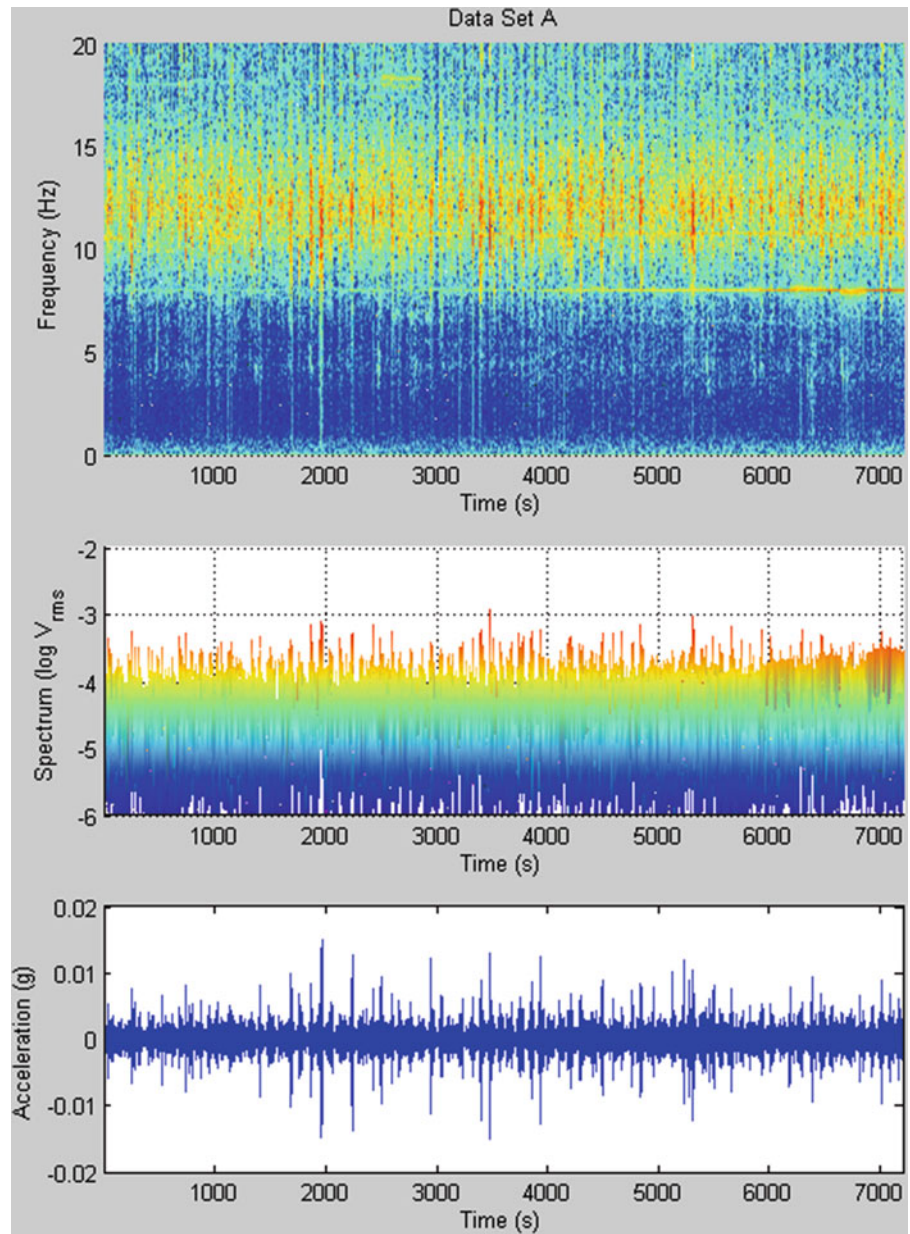


of the STFT for the same long record shows intensity at 600 and 1000 sec that is not present at 800 and 1200 sec making these two different conditions (i.e. 1 sec duration vs. impulse-like) discernible in a long record, thus helping the investigator identify disturbing episodes quickly. The period from 1400 to 1600 sec illustrates that many components can coexist and be separated by the STFT view of the data.

36.4 Apartment Building Vibration

Complaints of annoying floor vibration prompted an investigation of a penthouse apartment. The primary area of concern was an upper penthouse mezzanine which houses a master bedroom. It was noted by the occupants that the vibration was at times jarring, sometimes worse than others and particularly problematic at night. The goal of the investigation was to determine the source(s) of the vibration and suggest remedial measures. The discussion of the case study in this paper focuses on the use of STFT to review very long time records to identify the character of the vibration causing disturbance. Data was collected continuously over several days and saved into files with thirty minute intervals of data.

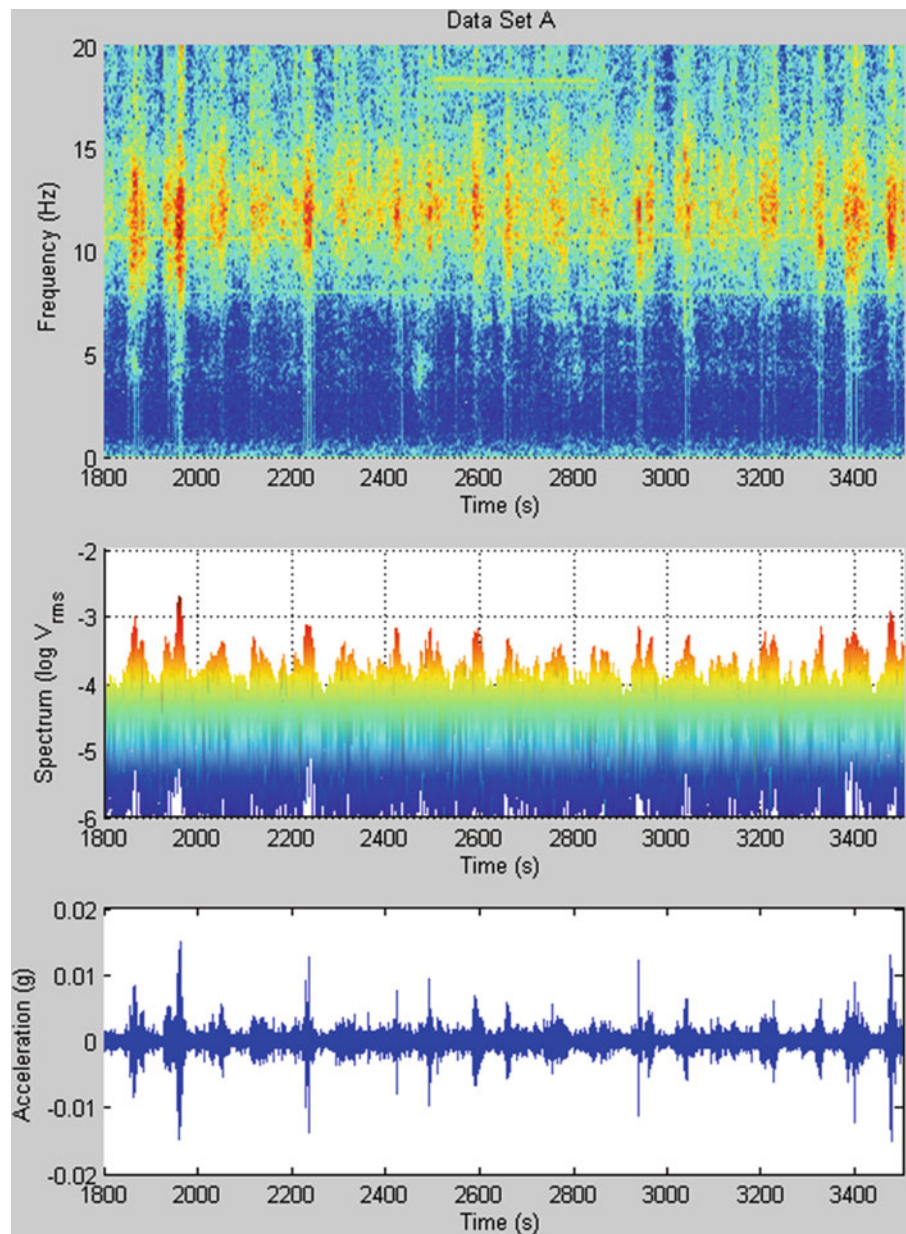
Fig. 36.10 Two hour time record for a lively early morning period (color figure online)



Upon initial review of the data, the data files were combined and inspected in two hour intervals. Figure 36.10 shows a lively two hour interval in the early morning hours of the first measurement night. Amplitudes in the graph at the bottom of Fig. 36.10 look like they may be a problem but they look rather random in their occurrence making it difficult to identify a source. The top graph seems to have a rather regular vertical stripe pattern to it that is not as obvious in the bottom graph. Also observed from this graph is that the stripes are concentrated in a frequency range. It is helpful to look at a smaller portion of this record. A 30 min portion is shown in Fig. 36.11. At this resolution, a very regular pattern of large acceleration amplitudes is revealed and highlighted by the black grid overlay. While repetitive, the episodes of disturbance are not exactly the same. It turns out that the timing of the pattern is consistent with the changing of the traffic light on the street below. The street below is a main thoroughfare that is under construction and it appears that larger vehicles traveling through the intersection are hitting road imperfections that are delivering base excitation to the building. The excitation is worse in the early morning hours when the traffic is not backed up and delivery trucks are moving more quickly through this urban intersection. It is hoped that when the road construction is completed that the largest excitations will be reduced. The truck excitations may indeed be the jolts that the occupants are feeling.

The early morning measurements from the next day showed the same pattern of jolts. In addition to the pattern of jolts, there seemed to be a low level continuous disturbance. In the time history plotted at the bottom of Fig. 36.12, the low level

Fig. 36.11 Thirty minute time record of a lively early morning period illustrating the consistency with the timing of the traffic light (color figure online)

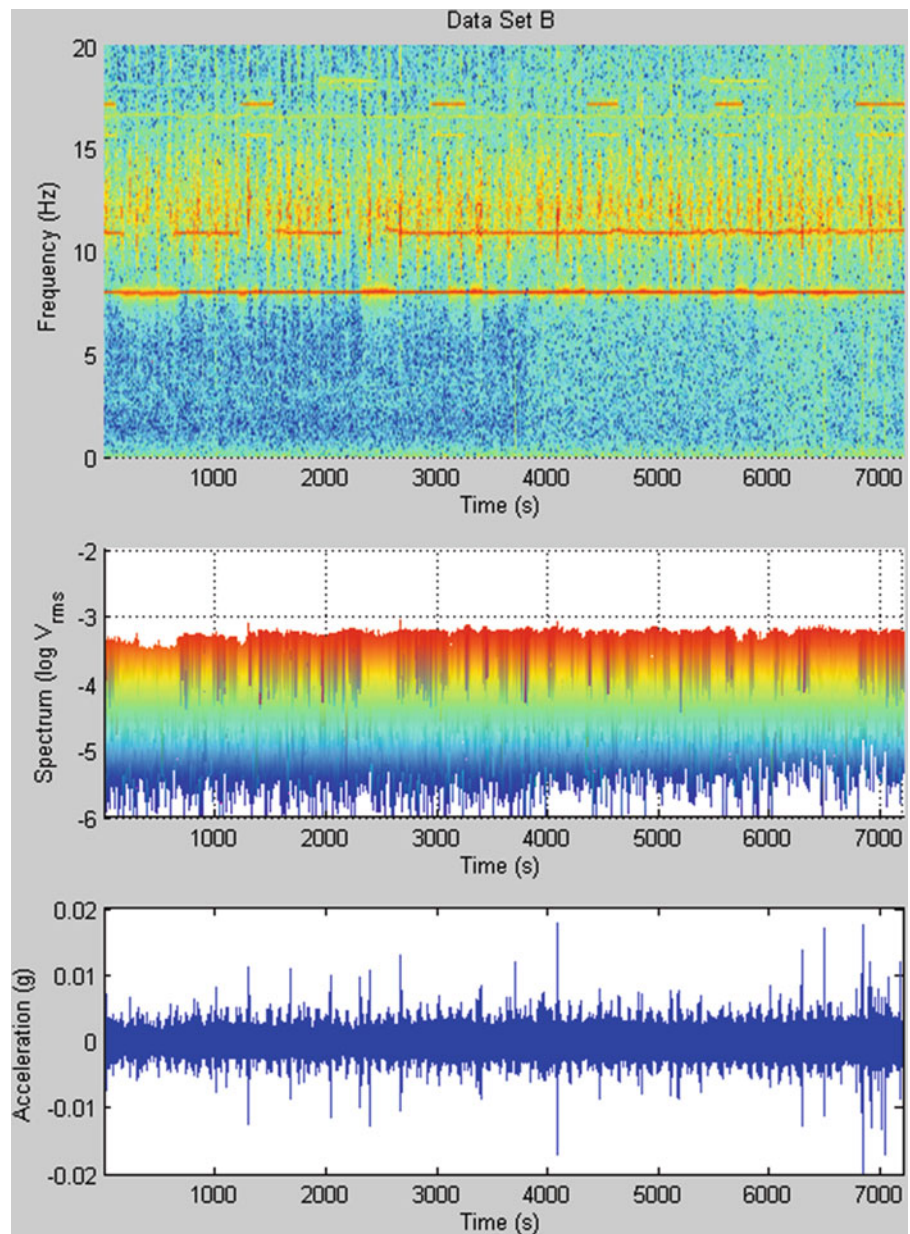


disturbance appears as a solid band of blue without any well defined character beyond that. The STFT graph at the top of Fig. 36.12 in this case reveals multiple steady-state sources of excitation likely resulting from mechanical equipment in the building. The STFT allows the investigator to identify frequencies as well as start and stop times for the multiple sources. Since the second morning of the investigation was much hotter than the previous day, the excitation was likely related to air conditioning equipment. It is possible that upon startup of equipment, a jolt was perceived by the occupants. Identifying the startup times is greatly facilitated by the STFT view of the data.

36.5 Summary

This paper illustrates the use of STFT for diagnosing floor vibration issues. The examples and case study show that important features of vibration episodes are revealed in a long record STFT analysis that would be obscured in the time view domain of the same record. The Appendix of this paper presents a Matlab file that uses the Spectrogram function to generate the figures in this paper.

Fig. 36.12 Two hour time record for a lively early morning period with multiple steady state sources (color figure online)



Acknowledgements The authors would like to thank Gilsanz, Murray, Steficek, LLP, Structural Engineers and Building Envelope Consultants, and in particular, Joseph Mugford and Ramon Gilsanz for the opportunity to work with them on the apartment building project.

A.1 Appendix: Matlab file for STFT figures used in this paper

```
%*****
% input values
%*****
% t: time vector; column vector same length as x
% x: amplitude vector; column vector same length as t
% PO: Percent overlap, 0.5 means the next window will come to the middle
% of the last window, 0 means the time windows used in processing will not
% overlap
```

```

% flimit: maximum frequency plotted
% graphtitle: text string at the top of the figure window
%*****
% Defined and calculated values
%*****
N=1024; % number of samples for FFT
noverlap=N*PO; % number of overlapping samples
dt=t(2,1)-t(1,1);
fs=1/dt;
fs=round(fs);
dt=1/fs;
%*****
% set plot window limits:
%*****
% caxis limits for top plot in figure
c11=-6;
c12=-2.7;
% zlim limits for top plot in figure
z11=-100;
z12=-2.5;
% caxis limits for top plot in figure
c21=-6;
c22=-2.7;
% zlim limits for top plot in figure
z21=-6;
z22=-2;
%*****
[B,F,T,P]=spectrogram(x,rectwin(N),noverlap,N,fs); % compute STFT PSD units
% (Vrms^2/Hz)
df=F(2);
z1=P*F(2); %Scale to Power Spectrum (Vrms^2)
z=sqrt(z1*1.0); %Scale to RMS Spectrum (Vrms), amplitude may be inaccurate due
to
%leakage and windows
z=log10(z); %convert to log value
NFplot=round(flmit/df)+1; %Set upper frequency array plot index
figure('Position',[1280/10 1024/10 1280/2.1 1024*8/10])
subplot(16,1,1:6)
surf(T,F(1:Nfplot),z(1:Nfplot,:));...
shading interp;...
colormap(jet)
axis tight
caxis([c11 c12])
zlim([z11 z12])
xlabel('Time (s)')
ylabel('Frequency (Hz)')
zlabel('Spectrum (log V_r_m_s)')
view(0,90)
title(graphtitle)
subplot(16,1,8:11)
surf(T,F(1:Nfplot),z(1:Nfplot,:));...
shading interp;...
colormap(jet)
axis tight
caxis([c21 c22])

```

```
zlim([z21 z22])  
xlabel('Time (s)')  
ylabel('Frequency (Hz)')  
xlim([t(i1) t(i2)]);
```

References

1. Bendat JS, Piersol AG (2010) Random data; analysis and measurement procedures, 4th edn. Wiley, Hoboken
2. Gade S, Gram-Hansen K (1997) The analysis of non-stationary signals. *Sound Vib* 31(1)
3. Hanagan LM, Raebel CH, Trethewey MW (2003) Dynamic measurements of in-place steel floors to assess vibration performance. *J Perform Constructed Facil*, ASCE 17(3):126–135
4. International Standards Organization (1989) Evaluation of human exposure to whole-body vibration-part 2: human exposure to continuous and shock-induced vibrations in buildings (1 to 80 Hz). International Standard ISO 2631-2

Chapter 37

Medial-Lateral Gait Patterns in Healthy Adult Walkers

Daniel Claff, M.S. Williams, A. Blakeborough, and J. Stebbins

Abstract With over a decade of research into the causes and effects of footbridge lateral excitation, models have emerged to describe pedestrian motion and force patterns. Authors have suggested, however, that insufficient data are available for model comparison. Thus, the medial-lateral (M-L) ground force, centre of pressure (CoP) location, and centre of mass (CoM) location were collected for over 300 healthy adult male and female footsteps. The data were collected using two AMTI force plates (1000 Hz) and a Vicon motion capture system (100 Hz). Using MATLAB, the data were analysed: the subsequent qualitative and quantitative observations are the topic of this paper. Inter- and intra-subject trends were observed among force-time correlations, CoP and CoM paths, and force-CoP plots. Additionally, the M-L force data were also compared to the inverted pendulum model to assess the model's accuracy in predicting individual step behaviour. Conclusions are drawn that while walkers exhibit consistency in M-L force strategy over repeated footsteps, their steps do not tend to match the population mean. Furthermore, the inverted pendulum model proves poor in predicting either the population or the individual participants. This supports the theory that lateral pedestrian motion and forces should be modelled as stochastic processes.

Keywords Medial-lateral force • Gait • Inverted pendulum model • Kinetic • Centre of pressure • Centre of mass

37.1 Introduction

The biomechanical study of gait is one that is both well established and important for a variety of commercial and medical applications. Only with the recent advent of flexible, long span bridges, however, have civil engineers found the need to learn more about this interdisciplinary topic. The onset of lateral vibrations in bridges has meant that engineers have needed to study the lesser understood topic of horizontal pedestrian loading, particularly in the lateral direction.

The purpose of this study is two-fold. First, data was collected in a combined dual force plate, motion capture system to gain a more complete understanding of patterns in human medial-lateral (M-L) stepping strategy. Second, the data was applied to a generally accepted mathematical model to assess the model's ability to predict human behaviour. The dynamic inverted pendulum model was chosen for this comparison due to its widespread acceptance, simplicity, and versatility [1].

37.2 Methods

Data for analysis was provided by the Oxford Gait Laboratory of the Nuffield Orthopaedic Centre, Oxford University Hospital NHS Trust (NOC) in Oxford, United Kingdom. The gait lab facility consists of two AMTI OR6 force plates aligned longitudinally on a 10 metre indoor track. The force plates, measuring 508 x 463 mm, are installed flush with the gait lab floor with a 70 mm gap between them (Fig. 37.1). Surrounding the track are 12 Vicon MX passive infrared motion tracking

D. Claff (✉) • M.S. Williams • A. Blakeborough
Department of Engineering Science, University of Oxford, Parks Road, Oxford OX1 3PJ, UK
e-mail: daniel.claff@eng.ox.ac.uk

J. Stebbins
Nuffield Orthopaedic Centre, NHS Trust Oxford Gait Laboratory, Windmill Road, Oxford OX3 7HE, UK

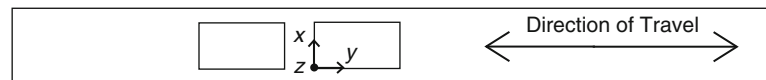


Fig. 37.1 Nuffield Orthopaedic Centre Gait Lab track schematic, NTS. *Inner rectangles* show orientation of force plates with respect to track and global coordinate system

Table 37.1 Sample population statistics

	Women	Men	Total
Number of people	21	17	38
Total trials	97	61	158
Total STEPS	194	122	316
Mass (kg)	61.4 ± 8.22	72.2 ± 14.6	66.1 ± 12.5
Height (m)	1.67 ± 0.0722	1.79 ± 0.0659	1.72 ± 0.0925
Age (years) ^a	24.7 ± 3.29	28.0 ± 7.69	26.2 ± 5.77

^aAge statistics available for only 14 women and 12 men

cameras. When combined, the system can capture ground reaction forces in three dimensions, the centre of pressure (CoP) locations across each force plate, and the three-dimensional locations of individual body segments, correlating the data from each instrument with respect to time. A frontal (portrait) and a sagittal (profile) video camera have also been installed to record the general motion of each person when walking across the plates.

37.2.1 Data Collection

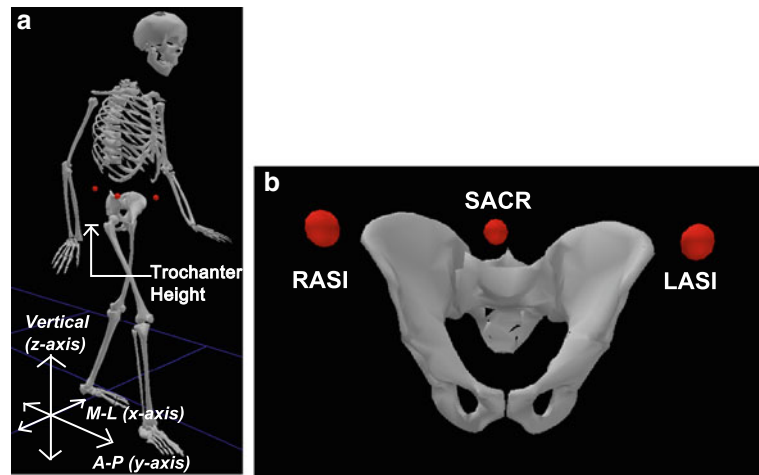
Over 20 healthy males and 20 healthy females were instrumented with reflective motion tracking markers and asked to repeatedly walk the length of the track from both ends while barefoot. The participants were not advised to step once on each force plate and as such, the participants were asked to walk the track until approximately six clean trials of exactly one foot per plate were completed. The data sampling rates for the tests were 1000 Hz for the force plates and 100 Hz for the infrared motion tracking cameras. Following the lab tests, the data were imported into Vicon Nexus software for post-processing. The aforementioned testing was conducted by the NOC independent of the present study. Using a combination of video inspection and reconstructed wire frame analysis, the authors omitted from the pool of samples any trial in which the heel or toes of either foot extended off the force plate. The resulting population consisted of 21 women and 17 men, totalling 316 footsteps (Table 37.1).

37.2.2 Post-processing

For each trial, Vicon Nexus exported a .csv file consisting of the time step; the X (Medial-Lateral, or M-L) and Y (Anterior-Posterior, or A-P) centre of pressure location; the X, Y, and Z ground force; and the X, Y, and Z ground reaction moment for both force plates (Fig. 37.2a). In addition, a separate .txt file was also exported consisting of the time step and the X, Y, and Z location of three motion tracking markers: the sacrum (SACR) and the left and right anterior superior iliac spine (LASI / RASI). These three points describe the motion of the pelvis (Fig. 37.2b).

A program was written in MATLAB to extract the data of each footstep from its .csv and manipulate the data according to a set of rules. The MATLAB program normalised the data by time and force to respectively minimise systematic error and provide for a correlated qualitative comparison. The length of time for most participants to take one step ranged from approximately 0.4 s to 0.6 s. Thus, in order to compare the synchronized features of the data, the time increments for each footstep sample were normalised by the total step duration. The force data – normalised by body weight, according to Giakas [2] – could then be expressed as a function of the fraction of the step elapsed, from zero (heel-strike) to one (toe-lift). To aid in analysing force trends, the data were averaged and standard deviations calculated at each decile point along the step. The final post-processing technique was the application of a low pass filter to the M-L force data. The filter chosen was a simple two-pass convolution using MATLAB's integrated filter function with a user-defined pulse shape described by a triangular and a square distribution. The filter preserves significant oscillations in the sample while minimising extraneous noise.

Fig. 37.2 (a) Identification of coordinate plane and trochanter height, (b) Positioning of pelvic body markers



The time domain was chosen for the present study instead of the frequency domain for a number of reasons. Foremost, in spite of the time domain's limitation for recognizing the most excited frequencies, it inherently provides a better parametric and spatial understanding of the force-time relationship than the frequency domain, valuable for both qualitative and quantitative understanding. Also, given that many design codes [3] and the inverted pendulum model are based on the time domain, a study of force patterns in the time domain is broadly beneficial for industry practice. That said, the most important and practical reason for the decision to use the time domain is the fact that the NOC force plates record the forces of each footstep independently in two-step trials, too short a sample duration for meaningful frequency domain analysis.

37.3 Results

In this section, a series of results will be presented in three categories. The first section of results will pertain to characteristics of the M-L force vs. time data, including data regarding the whole participant population and comparisons of various subsets of the population. In the second section, the inverted pendulum model will be applied to the CoM and CoP data; comparisons will be drawn to the force-time trends discussed in the first set of results. Finally, a qualitative analysis of CoP and CoM paths vs. lateral force will be presented.

37.3.1 Lateral Force Patterns

To understand variations in M-L force while walking, comparisons need to be made on several levels: the population, population subsets, and the individual. Trends were assessed by analysing data within and among these levels.

Figure 37.3 shows the plot of M-L normalised ground force vs. time for the entire population ($n = 316$ footsteps). In this plot, the positive y-axis represents medial force, or force towards the centre of the body, whereas the negative y-axis depicts lateral, or outward, force. Broadly speaking, the curve is in the shape of a letter 'w,' as confirmed by previous studies [2, 4]. In the first decile, there is a sharp medial peak centred at approximately $t' = 3.3\%$. After the initial peak, the M-L force reverses to the lateral direction, where it persists for most of the footstep duration. In the last decile, the force returns to the medial direction, providing a smaller local maximum before tapering to zero at toe-lift. Laid over top of the data samples is an error bar that connects the means of each decile point and provides an indicator of \pm one standard deviation. From this error bar, one can observe that the population means follow the 'w' shape. The mean lateral force maxima occur at the third and eighth decile: -0.038 ± 0.0165 N/N and -0.0312 ± 0.0195 N/N. The smallest standard deviation occurs at the midpoint of the footstep, which also corresponds to the lateral force minimum: -0.0225 ± 0.0116 .

Four subsets of the population were compared to the overall population: women, men, left steps, and right steps. If the population mean is truly representative of the samples, then the subset means would align with that of the population. Figure 37.4a, b provide the female and male data samples, respectively, overlaid with the population error bar (light gray) from Fig. 37.3 and the gender-specific error bar (dark gray). The female mean follows the population mean closely, with a magnitude larger than that of the population for the first half of the step duration. After the 5th decile, however, the female

Fig. 37.3 Population M-L force samples with decile means and standard deviation bars ($n = 316, 1000 \text{ Hz}$)

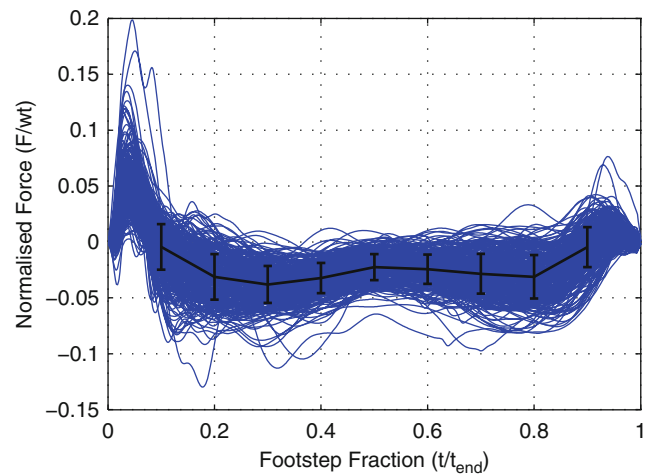
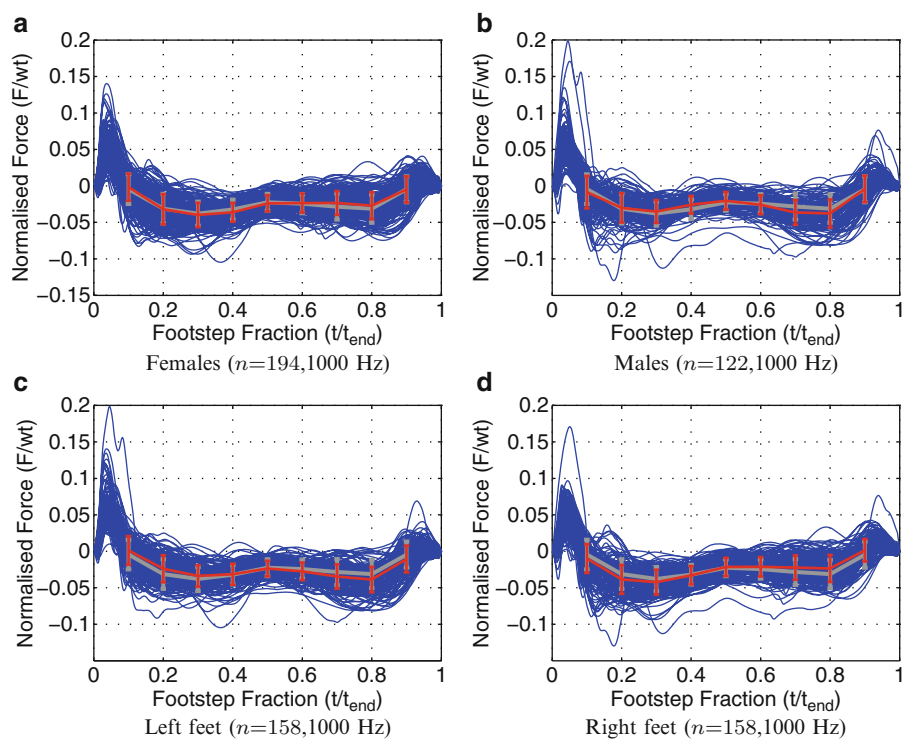


Fig. 37.4 Subset lateral force samples with subset means (*dark gray*) vs. population means (*light gray*)

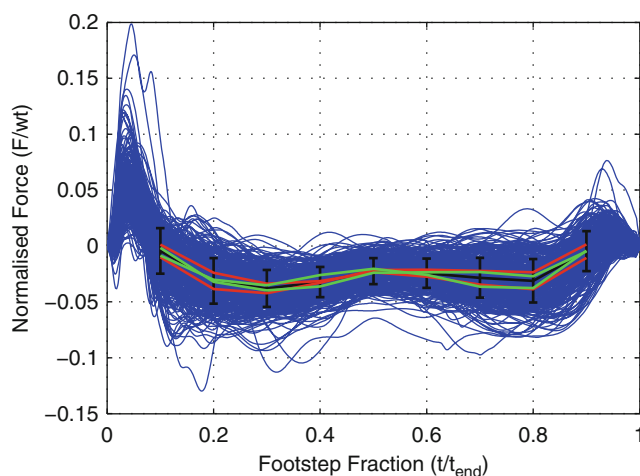


lateral force does not peak a second time, but plateaus instead. The male lateral force means (Fig. 37.4b) also follow closely to the overall mean through the first half of the footstep, but exhibit a distinct second peak in the second half of the footstep. This suggests that while both genders stabilise the first half of their step laterally, men are likelier than women to propel their motion through a lateral force late in the step.

Another important comparison is that of left versus right steps. Whereas one might expect a difference between the force-time plots of women and men, a sample of left feet should be identical to a sample of right feet, based on the assumption that the human lower body is symmetrical. Figure 37.4c, d depict the data from the left steps and the right steps, respectively. The plots are overlaid with the overall population error bar (light gray) and the side-specific error bar (dark gray). The left feet exhibit the characteristic ‘w’ shape while the right feet follow a trough-and-plateau shape similar to the female plot. During the first half of the step, the population exerts more lateral force on the right foot than the left, but during the second half of the step, the left foot becomes more dominant. Thus, throughout the population, the participants pushed laterally off of their left feet more than they did from their right feet.

A comparison of the four subplot means to the population mean (Fig. 37.5) shows how similar they are. Since both the gender means and the left and right foot means fall well within the population standard deviation, the population mean is deemed to represent the subsets well.

Fig. 37.5 Comparison of female, male (light gray), left, and right (dark gray) means to overall population mean. Each is well inside one standard deviation of the population mean



Finally, an examination of a variety of the individual M-L force vs. time plots provides insight as to whether the population and subset means are sufficiently representative of specific participants. Figure 37.6 provides a sampling of individual plots, which have been analysed in terms of accuracy, precision, and intra-subject variability. In each plot, the dark gray samples refer to a participant's left steps and the light gray samples to his/her right steps. Each plot has also been overlaid with the population mean (black).

The most important aspect is how well the population mean represents the M-L forcing strategy of individual participants. For ease of description, this shall here be referred to as a participant's 'accuracy.' In this case, a step was considered accurate if most of the samples fell within one standard deviation of the population mean and if the population mean captured the shape of the plots. Figure 37.6a is clearly the most accurate of the set since almost all of the samples of both feet fall within the standard deviation range. In addition, the left foot of the participant in Fig. 37.6b and the right foot in Fig. 37.6c also show a high degree of accuracy. While perhaps both feet in Fig. 37.6d, e show a degree of accuracy as well, the low precision of the repeated trials makes it difficult to discern whether the left and right step means fall within the population standard deviation. For 32 participants, each with two step sets (left and right) per person, only 29 of the 64 step sets were represented by the shape of the population means.

In addition to the representation of single participants by the population mean (accuracy), the consistency of each participant's steps should also be considered. This shall be referred to as a participant's precision. In contrast to the accuracy, a high degree of precision is found among the individual participants. The participant in Fig. 37.6g exhibits a high degree of precision throughout each step. Each sample has almost the exact same shape as each of the other samples of the same foot. Even between the 7th and 9th decile when there is rapid oscillation, the samples follow a tightly defined track, unique to that participant. To a slightly lesser extent, Fig. 37.6a, c also portray participants with a high degree of precision. Again, the samples follow narrowly defined tracks with minimal variation, which are specific to the participant. The high precision stepping strategy in these examples contrasts with those of Fig. 37.6e–f, whose samples vary greatly in force amplitude and shape. The M-L forces for the participant in Fig. 37.6f are particularly unique because they show neither accuracy nor precision. While almost two-thirds of the participants (20 out of 32) have a precise M-L force strategy in at least one foot, some, such as in Fig. 37.6f, exhibit neither accuracy nor precision in their steps.

The accuracy and precision of the participants' M-L force patterns provide insight on inter-participant patterns, but they do not necessarily inform whether intra-participant patterns exist. Quantifying the degree of intra-participant variability between left and right footsteps would provide an important measure of the symmetry of a person's M-L forcing strategy. In spite of the variation between the steps in Fig. 37.6g from the first to third decile, the intra-participant variability is very low; this person utilizes a near identical forcing strategy for their left and right feet. Of the 32 participants analysed for intra-participant variability, only 11 show a high uniformity between left and right steps. Yet, given the lack of a quantitative measure, the assessment of intra-subject variability is subjective. The participants in Fig. 37.6c, h, as an example, appear to have a moderate amount of intra-participant variation, making the left and right sides difficult to classify as variable or not. In the former, a correlation clearly exists between the footsteps at $t < 10\%$ and from $30\% < t < 70\%$, but the amplitude difference before the 8th decile shows that the participant pushes off his left foot with almost 50% more force than his right foot. The male in Fig. 37.6h also shows elements of left-right uniformity, but exhibits wide variation between the first and fourth decile. Some of the samples, such as Fig. 37.6f show little uniformity at all. Perhaps based on the present data, a quantitative algorithm needs to be developed which takes accuracy and precision into account to provide an objective indicator of intra-participant variability.

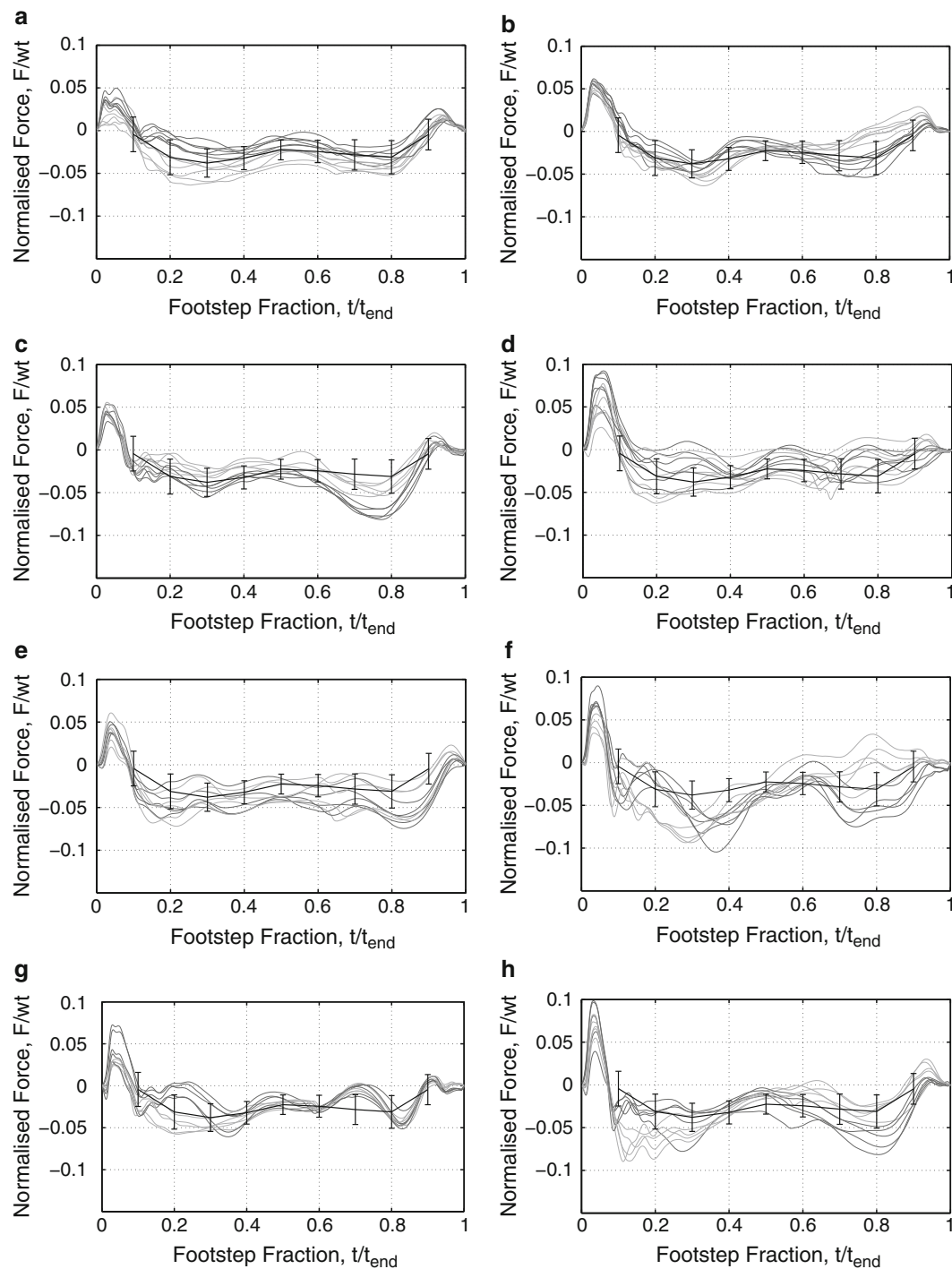
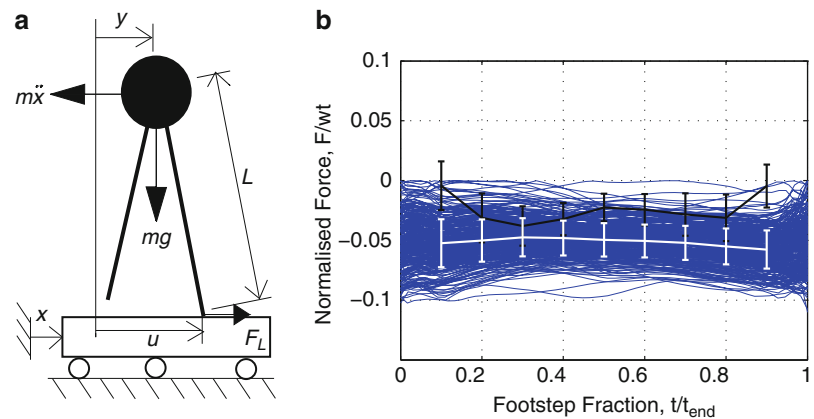


Fig. 37.6 Several participant M-L force vs. time plots. Left feet (dark gray) and right feet (light gray); population mean \pm SD (black)

37.3.2 Application of the Inverted Pendulum Model

Having compared various subsets of the data to analyse their relative applicability, another worthwhile analysis is to contextualise the data with an external mathematical model. Following the work of many, the inverted pendulum has gained acceptance as a model of medial-lateral walking forces as well as of centre of mass and centre of pressure displacements [1, 5, 6]. Therefore, this model was applied to the present data samples. After a brief description of the model, some conclusions are made regarding its applicability to the data. The basis of the inverted pendulum model is to represent the

Fig. 37.7 (a) Inverted pendulum model schematic, based on Macdonald [5] (b) M-L forces calculated from inverted pendulum model with mean and SD error bar (light gray). Original force plate data summarized by black mean and SD error bar



human single stance as a lump mass supported on a straight, rigid post. The model takes advantage of fundamental dynamics to propose that the centre of mass and centre of pressure can be related to the angular frequency of a pendulum. The equation of motion for this scenario is given by Macdonald [5] to be:

$$\ddot{y} + \Omega_p^2(u - y) = -\ddot{x} \quad (37.1)$$

where y describes the location of the CoM from an arbitrary reference line, x describes the location of the platform, u is the location of the CoP, and double dot indicates acceleration with respect to time (Fig. 37.7a). Ω_p is defined as the pendulum frequency,

$$\Omega_p = \sqrt{g/L} \quad (37.2)$$

where g is acceleration due to gravity and L is the pendulum length, or 1.34*trochanteric height (the distance from the bottom of the foot to the top of the trochanter, the femoral protrusion below the head at the top of the shaft, Fig. 37.2a) [1]. Thus, the horizontal force exerted on the bridge is given by [5]:

$$F_L = -m_p(\ddot{x} + \ddot{y}) = m_p\Omega_p^2(u - y) \quad (37.3)$$

For the present study, the M-L force is normalised by the weight of each participant, $F = m_p g$, leaving the non-dimensionalised force:

$$F'_L = \frac{u - y}{L} \quad (37.4)$$

The data collected from the gait lab were used to verify the inverted pendulum model using Eqn (37.4). The CoP data (u) were collected directly from Vicon Nexus and could be inputted directly. The CoM (y) was assumed to be located at the three-dimensional centroid of the LASI-RASI-SACR triangle and the pendulum length (L) assumed to be the Z-coordinate of the centroid.

As can be seen in Fig. 37.7b, the population of inverted pendulum-based forces does not match the population of force plate data. The red error bar provides the means and standard deviations of the underlying inverted pendulum data while the black error bar is an indicator of the force plate data given previously. The narrowest difference between the means occurs at the third decile; the model over-predicts the data by approximately 0.01 N/N. Across the remainder of the time period, the model over-predicts the data by as much as 0.05 N/N. While the force plate data resembles the 'w' in shape, the inverted pendulum model presents a smooth, concave-down curve. With maxima at the first and last deciles (-0.0524, -0.0577 N/N) and a minimum at the third decile (-0.0474 N/N), the shape of the model error bar closely resembles the acceleration-time curve presented by Macdonald.

Given that a wide variation of stepping strategies exists among different participants, the inverted pendulum model was also compared to various individuals. Figure 37.8 gives the M-L force vs. time plots for the same eight participants from Fig. 37.6. In this set, however, the force plate data have been grayed and the inverted pendulum left and right feet are portrayed in red and blue, respectively. The most apparent trait of these plots is that the model fails to pick up acute changes in M-L force. The most significant cases are Fig. 37.8g, h, where peaks and troughs in the force plate data are entirely unrepresented by the model. Since the pendulum length, L , remains almost constant, this behaviour in the model must be indicative of an insignificant change in the numerator, $u - y$. Furthermore, the next section will show that the variation in CoP location with respect to CoM is minimal, so the model's ability to capture acute changes is poor. The inability of the model to reflect

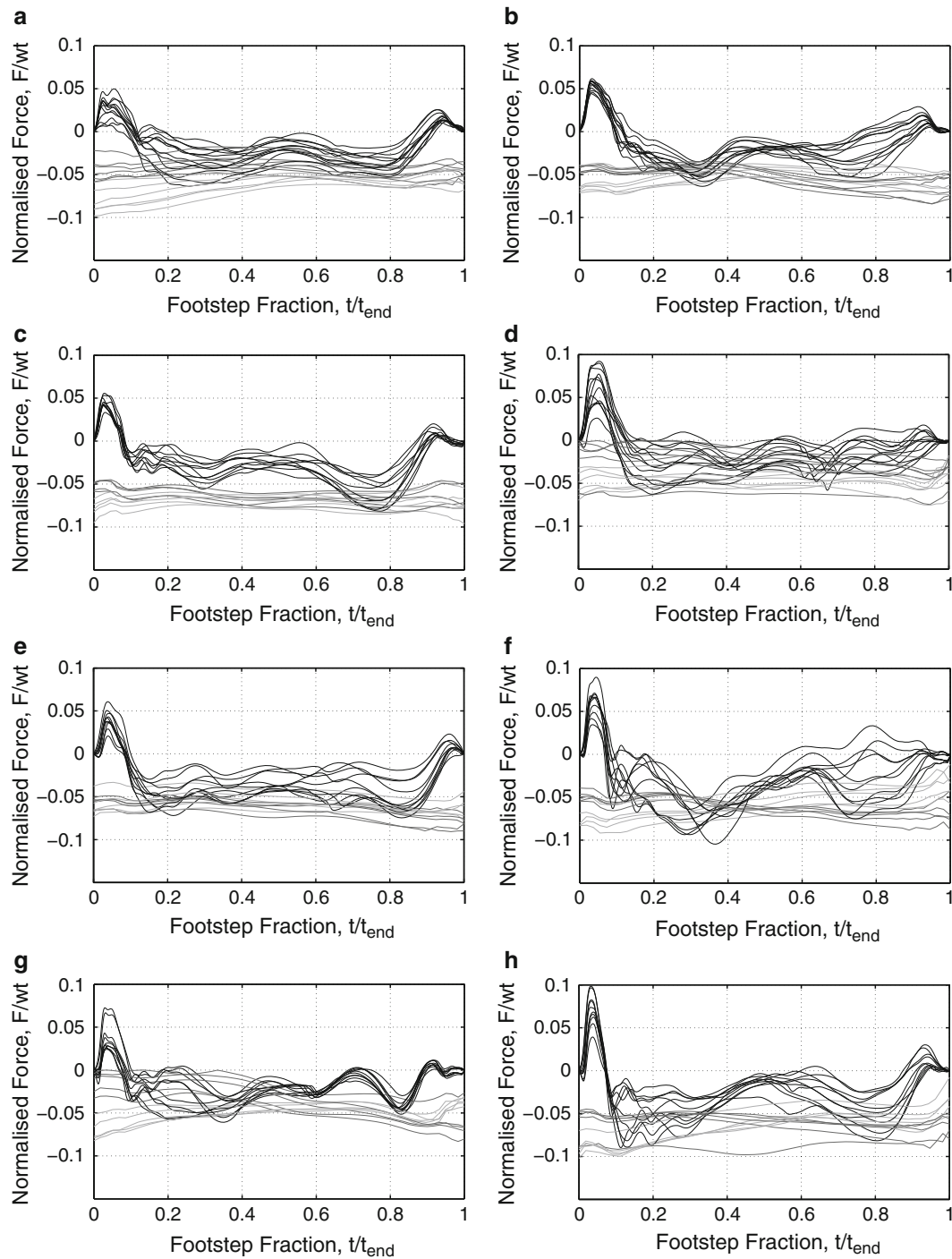


Fig. 37.8 Several participant M-L force vs. time plots. Inverted pendulum left feet (*dark gray*) and right feet (*light gray*) with original force plate data (*gray*)

changes in the M-L force shows that the body potentially absorbs rapid changes in ground force through the displacement of lower body joints and/or the contraction of muscles as opposed to the relative displacement of the CoM.

In over half of the figures (Fig. 37.8b, c, e, f, h), evidence of precise banding is present. In these cases, the participant was very consistent in the spacing of his/her CoM and CoP over the course of each step. In contrast, the splaying present in Fig. 37.8a, d, g shows that some participants are less consistent in their M-L motion strategy. Returning to the model population's apparent downward concavity, the figures show that while most of the individual models exhibit some manner

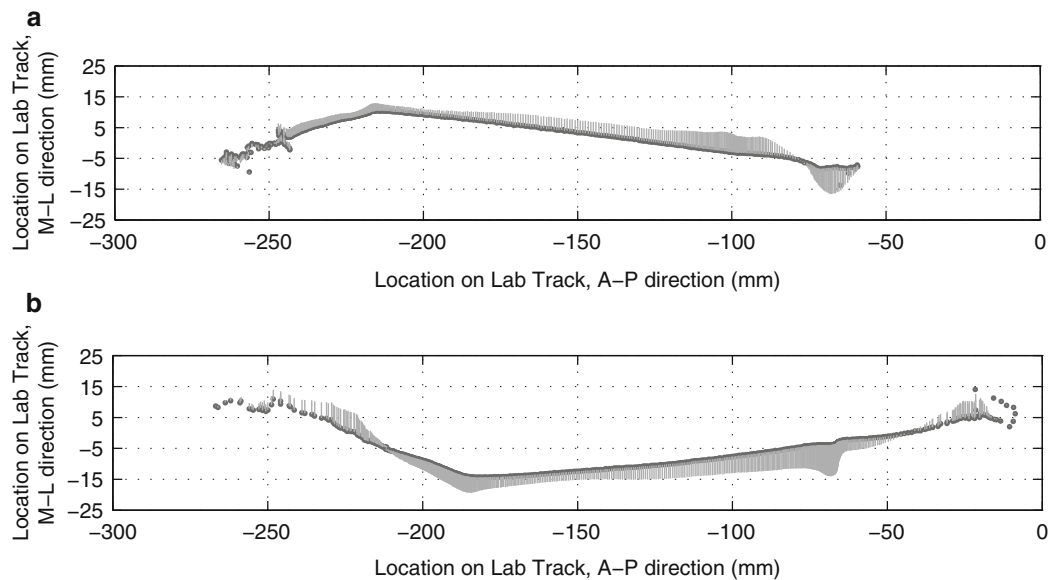


Fig. 37.9 Relative M-L forces as a function of CoP location. Participants ((a) male R foot, 65.0kg, 1.71 m; (b) female L foot, 68.8kg, 1.74m) walking from right (heel-strike) to left (toe-lift) across the plot

of concavity, none seem to exhibit strong concavity at both the beginning and end of the step. The samples typically begin or end with a moderately steep slope, but remain plateaued at the opposite end. The model of the participants in Fig. 37.8a, f, g exhibits downward concavity at right foot heel strike ($t = 0$) and at left foot toe lift ($t = 1$). Recalling that the left and right feet do not step simultaneously, the model would consequently suggest that the high magnitude left toe-lift force is offset by the high magnitude right heel-strike force. Such cancellation of forces is also true for the low magnitude right toe-lift and left heel-strike. Nonetheless, while the population mean of the models suggests full concavity, steps tend to exhibit early or late concavity, but not both.

One important assumption of using the inverted pendulum model is that the change of pressure from one foot to the other is instantaneous [5]. As is seen in these data and by in the work of prior authors, the transfer of weight between feet is certainly not instantaneous. Instead, the body is in double stance for up to approximately 40% of each step [7, 8]. Thus, the portion of the force plate data during each participant's double stance phase – up to two deciles on each end – will not correlate with the M-L model at all.

37.3.3 CoP and CoM Paths

The data collected allow for spatial analysis of participant stepping patterns. Examining such patterns will provide better insight on inter- and intra-participant step variability and context for use of the inverted pendulum model.

Figure 37.9 shows the CoP paths of a left and right foot from two different participants. In both cases, the participant is 'walking' from right to left across the plot. From each CoP point, the M-L force component has been extended to help the reader understand the interaction between M-L force and CoP spatial location. Following the paths from heel-strike to toe-lift (right to left), the initial heel force is quite strong in the medial direction. As the CoP moves off the heel towards the outside of the foot, the force changes to the lateral direction. This period is where the instability of single stance occurs, and as such, the wider spacing of the CoP points (compared to the heel and toes) reveals a speeding of the step. When the CoP reaches the ball of the little toe, it tends to turn away from the edge of the foot in the shape of a backward (left foot) or forward (right foot) '?', progressing along all the balls of the foot before finally lifting off through the big toe. In some cases however, the CoP merely lifts off from what appears to be the middle or edge of the foot, leaving a straight CoP path instead of the '?' shape. Regardless, during this time, the CoP progression becomes much slower than during mid-step; the body capitalises on the double stance period to retain stability [2]. Finally, as the CoP reaches toe-lift, the force returns to the medial direction, although not as prominently as at heel-strike.

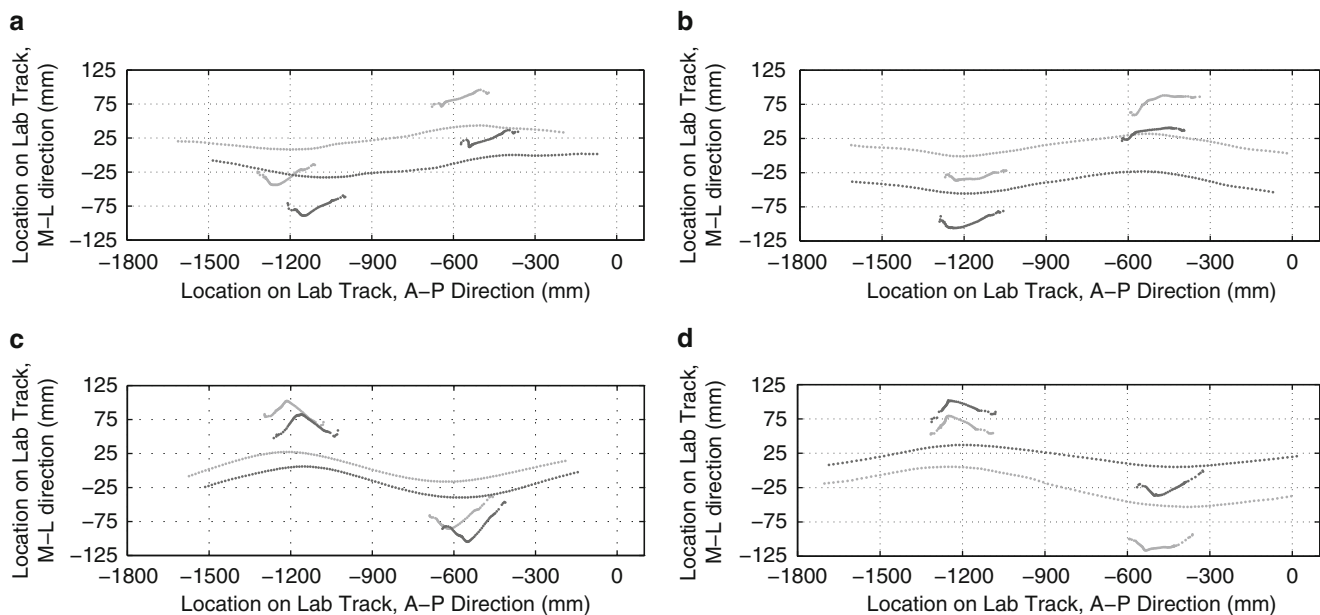


Fig. 37.10 Two CoM-CoP displacement paths for each of four participants, walking from R to L across the plot

In Fig. 37.10, one can gain a sense of the variation that occurs among participants in CoP and CoM paths. Again, the participants are ‘walking’ from right to left across the plot. Each of the plots also shows the projections of the CoM path for the two trials; the footsteps are easily distinguished by the distinctive ‘w’ shape and on which side of the CoM path they lie. Each figure shows that one CoM path in each plot is a near-translation of the other, meaning that intra-participant variability of CoP and CoM paths is minimal. In contrast, the four figures portray variation among participants in terms of gait length, CoM displacement amplitude, step width, and step angle. While the two-step plots seem to be repeatable on a participant-by-participant basis, they do not appear to be repeatable universally.

In each footstep, the CoP path is located adjacent to the extreme location of the CoM path. A reasonable assumption follows that the extreme point of the CoM path occurs near mid-step before the body ‘falls’ back towards the other foot. While this gives credence to the inverted pendulum model theory, the displacement amplitude of the CoM curves is similar to the displacement amplitude of each footstep. Since the inverted pendulum model deals in component planes (M-L plane, A-P plane) instead of three-dimensional magnitudes, and since the M-L spacing between the CoM and CoP remains approximately constant, the M-L force component shows little variation (and an inability to represent acute changes in M-L force), as observed in the previous section.

37.4 Discussion

Results from this set of tests yield new perspectives on (1) the correlation of M-L force data to population means and (2) the applicability of the inverted pendulum model. Comparing the population mean to the male, female, left foot, and right foot subsets, there is good correlation among the various groups, in spite of the fact that the female samples and right foot samples tend to plateau over the second half of the step instead of imitating the characteristic ‘w’ pattern. The fact that the variation between left and right feet is typically greater than the variation between genders might be indicative of interaction among the variables or the impact of other factors (e.g. differing leg lengths, L or R side dominance, etc). Upon comparing the population data with participants’ repeated trials, the population means do not tend to represent the individual steps. This is particularly due to the localized onset of acute fluctuations in the M-L force which vary from participant to participant.

A comparison of participant M-L force patterns reveals that they tend to show precision but not a high degree of accuracy relative to the population mean. Occasionally the left and right feet follow a similar force path (low intra-participant variability), but for over half of the participants, each foot has a unique forcing path like a fingerprint or else a significant amount of variability. Even when both feet did show similar loading strategies, the force amplitude of one foot tends to be slightly different than the other, whether at a point of local divergence or because one foot has a consistently higher force

magnitude than but identical shape to the other. Another observation indicated that a significant amount of repeatability occurs in the CoP and CoM paths of various participants even though each participant was unique. Nonetheless, the differences in the participant CoP and CoM paths still allowed for broad observations to be made regarding the location of the CoM relative to the CoP.

The CoP and CoM data from the gait lab were inputted into the inverted pendulum model in order to determine whether the model can effectively replicate the M-L force readings from the force plates. On a population level, the model was not representative of the data, overestimating the force plate data by 1–5%. The means of the inverted pendulum model created a concave down shape while the overall population data resulted in a ‘w’ shape. Furthermore, while the concave down shape is comparable to the shape given in Macdonald [5], most participants’ steps exhibited a half-concave down shape when modelled; the shape levelled out either early or late in the step. Further, the individual models and force plate samples occasionally showed similar maximum amplitudes, but the models failed to represent any acute fluctuations in the force plate samples. Given the relatively flat model curves, very little variation occurred between the M-L positions of the CoP and the CoM; a theory supported by the similar displacement amplitudes of the CoP and CoM paths.

Based on the data collected, this study proposes that deterministic models be avoided or used with caution in the case of lateral bridge excitation modelling. Individual pedestrians walk with unique loading patterns, and as such their force patterns should be modelled stochastically, where possible. Additionally, the inverted pendulum model is hindered both by its inability to model the double stance phase and by its failure to reflect acute changes in M-L force. Further research should be done to better understand the mechanics of the double stance phase with regard to M-L motion, and to subsequently improve the inverted pendulum model.

37.5 Limitations

A number of limitations must be considered when reviewing the present study. Firstly, a number of lab conditions have been assumed. These include the repeatability of testing conditions across all participants regardless of direction travelled, the approximation of steady state walking on a short indoor track, the unhampered health of the participants, the uniform experience level of barefoot walking in all participants, the absence of component crossover in the force plates, and most importantly the assumption that participants did not alter their gait to land on each plate. In addition, several assumptions were made during data processing, such as the approximation of the human CoM at the centroid of three pelvic markers and that the height of the centroid is an appropriate approximation of the pendulum length. Further, an assumption was made that during double stance, the CoP and M-L force acted individually under each foot rather than at the geographic midpoint as a sum of forces. Finally, the analysis assumed that the participants were walking parallel to the force plates and that the angle of the foot with respect to the direction of travel did not have an impact on the A-P or M-L force.

37.6 Conclusion

The data presented here depict individual pedestrians walking on a stationary surface. Ultimately, an understanding of lateral bridge motion due to crowd loading will rely on the ability of researchers to sample and model individuals moving within large groups on a moving surface. This goal should be kept in mind when studying the M-L force produced by unique individuals. In this study, the population means represent the four subsets while losing the fingerprint-like pattern of each individual participant, yet no assessment was made whether the characteristic ‘w’ shaped population mean is of sufficient detail for wide-scale bridge modelling. Similarly, while suggesting that the inverted pendulum does not successfully reproduce the forcing patterns of individual participants, this study does not necessarily suggest that the model insufficiently represents a pedestrian’s or a crowd’s impact on a structure. Such assessments will need to be the aim of future research.

References

1. Hof AL, Gazendam MGJ, Sinke WE (2005) The condition for dynamic stability. *J Biomechanics* 38(1):1–8
2. Giakas G, Baltzopoulos V (1997) Time and frequency domain analysis of ground reaction forces during walking: an investigation of variability and symmetry. *Gait & Posture* 5(3):189–197
3. Zivanovic S, Pavic A, Ingolfsson ET (2010) Modelling spatially unrestricted pedestrian traffic on footbridges. *J Struct Eng* 136(10):1296–1308

4. Racic V, Pavic A, Brownjohn JMW (2009) Experimental identification and analytical modelling of human walking forces: Literature review. *J Sound Vib* 326(1–2):1–49
5. Macdonald JHG (2009) Lateral excitation of bridges by balancing pedestrians. *Proc R Soc A: Math Phys Eng Sci* 465(2104):1055–1073
6. Bocian M, Macdonald JHG, Burn JF (2012) Biomechanically inspired modelling of pedestrian-induced forces on laterally oscillating structures. *J Sound Vib* 331(16):3914–3929
7. Mann RA, Hagy J (1980) Biomechanics of walking, running, and sprinting. *Am J Sports Med* 8(5):345–350
8. Lohman EB III, Sackiriyas KSB, Swen RW (2011) A comparison of the spatiotemporal parameters, kinematics, and biomechanics between shod, unshod, and minimally supported running as compared to walking. *Phys Ther Sport* 12(4):151–163

Chapter 38

Quantifying Differences Between Walking Locomotion on Rigid and Flexible Pavements

M.V. Istrate, S. Zivanovic, A. Lorenzana, N. Ibán, and H.V. Dang

Abstract This work explores the differences between walking locomotion on rigid pavement and a particular type of flexible pavements made of EVA75 foam having thickness of either 10 or 20 mm. The aim is to analyse how human movements, in terms of trajectories of different body parts, are influenced by rigidity of such pavements. This research line is ultimately directed towards evaluation of the influence of flexible pavement on the vibration perception by human test subjects walking over vibrating decks of lively footbridges and floors.

The experiments were carried out in the Structures Laboratory at the University of Warwick, UK. A part of a 20 m long walkway was monitored using six infrared cameras. Three test subjects, instrumented with reflective body markers were asked to walk over the walkway made of concrete. Nominally the same experiments were then conducted on the walkway covered with one 10 mm thick layer of foam (ethyl vinyl acetate EVA75) first, and then with two layers of foam having thickness of 20 mm. Mechanical properties of the foam and its influence on the vertical ground reaction forces (GRFz) depending on the number of layers are studied. The trajectories of the reflective markers attached to the human anatomical landmarks are traced using the Vicon motion capture system. Averaged amplitudes of movement for chosen markers are compared for walking over the three supporting surfaces. While the first peak in the GRFz decreases when increasing thickness of the foam the magnitudes of displacements and accelerations of all analysed markers increase. The findings reveal that human walking on surfaces of different flexibility can be characterised by acceleration of body segments as well as by the way the forces propagate through the body via skeletal system.

Keywords Flexible pavement • Serviceability • Vibration • Masking effect

38.1 Introduction

This work presents experiments that aim to quantify the effect of a soft pavement on human body kinematics and kinetics in comparison with the walking over a rigid pavement. The paper is focused on the human body trajectories and forces, depending on the type of pavement in terms of stiffness. It is believed that when a flexible pavement is placed over the walkway of a lively footbridge, the perception of movement of the structure (due to human-induced vibrations or due to wind) is partially masked by the softness of the walking surface [1]. In this way, pedestrians seem to not complain about the movement of the structure as much as they would do when exposed to similar vibrations of the structure having standard (rigid) pavements. Therefore, it seems that the flexible pavements have potential to play an important role in improving vibration serviceability of lively structures. For this to happen, better understating of human kinematics and kinetics while walking on surfaces of different stiffness is required.

M.V. Istrate (✉) • N. Ibán
CARTIF Centro Tecnológico, Parque Tecnológico de Boecillo, 47151 Valladolid, Spain
e-mail: melist@cartif.es; noriba@cartif.es

S. Zivanovic • H.V. Dang
School of Engineering, University of Warwick, Coventry CV4 7AL, UK
e-mail: S.Zivanovic@warwick.ac.uk; H.V.Dang@warwick.ac.uk

A. Lorenzana
ITAP, University of Valladolid, 47011 Valladolid, Spain
e-mail: antlor@cartif.es

To quantify the effect of the flexible pavement in this paper, trajectories of different parts of the body are compared for three different scenarios: walking on the original rigid pavement, walking over one 10 mm thick layer of foam pad and walking over two layers having thickness of 20 mm. Thicker the foam is, higher acceleration level characterises movement of every part of the body [2–5]. The increase of the accelerations of the body segments with increase of foam thickness could mask the vibration of the walking surface, leading to the soft walking surface being perceived as more comfortable than the rigid surface.

Several solutions are available nowadays for retrofitting footbridges that might experience excessive vibrations [6]. These solutions normally influence the dynamic response of the structure by adding mass, stiffness, or structural damping. These measures can often be expensive, especially if they have not been accommodated in the initial design. A cheaper alternative could be installing a layer of soft pavement. This solution would not change appreciably any of the structural parameters but it could improve comfort of the structural users [7] and therefore contribute to improved vibration serviceability.

The flexibility of the pavement affects the way the load is exerted to the structure and the way the pedestrian senses its movement [8, 9]. From the mechanical point of view, the foam layers act as a suspension mechanism between the deck and the pedestrian, reducing forces generated with every footstrike [8].

38.2 Flexible Pavement Properties

Interlocking EVA75 mats used for the tests involving flexible pavement are made of ethylene vinyl acetate having density of 75 kg/m^3 . EVA is a semi-rigid foam with non-linear viscoelastic behaviour. To establish properties of the foam pads, they were placed between two compression plates having diameters of 150 mm and 50 mm, and exposed to loading rate of 8.3 mm/s followed by an unloading phase. Note that real footstrike is much quicker and due to viscoelastic EVA behaviour the expected strains would be smaller. The tests were conducted in the material test laboratory in CARTIF, Valladolid, using Instron testing machine that was programmed for applying loading up to 1000 N. The foam compresses under loading, and it slowly recover after removal of the load [8]. The resulting force – compression curve and the stress – strain relationship in the range of interest are shown in Fig. 38.1a, b. EVA75_10mm refers to one layer of foam, while EVA75_20mm refers to two layers. The curves presented were obtained by averaging results from ten tests. In each test a new piece of foam was used, to prevent deterioration of foam properties with increasing number of loading cycles.

38.3 Methodology

A six-camera realtime motion capture system Vicon was used to record kinematic data at a sampling rate of 200 Hz. Cameras were attached to two steel frames and they covered approximately 6.5 m of the walkway (Fig. 38.2). Gait analysis was conducted on three adults walking at pacing frequency of 1.9 Hz controlled by a metronome beat. The test subjects were instrumented with twenty spherical retro-reflective markers on the body's bony landmarks, as shown in Fig. 38.2a. Although

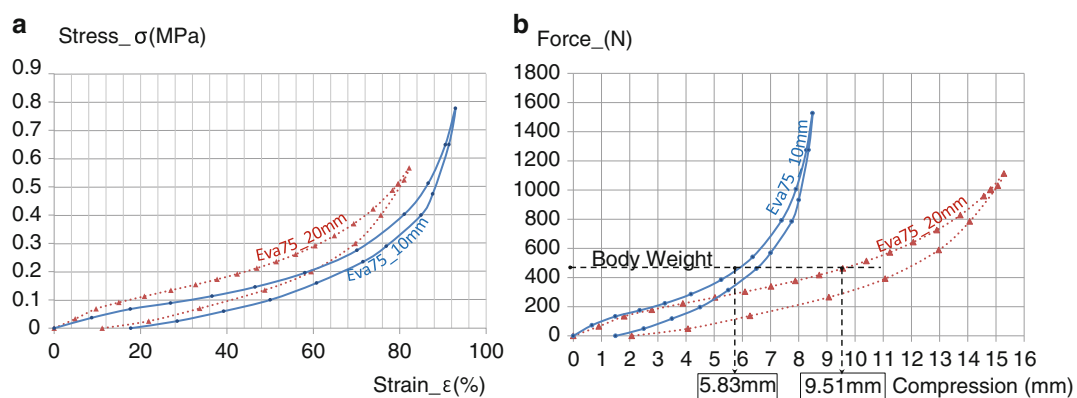


Fig. 38.1 EVA75 foam properties. (a) Stress – strain relationship; (b) force – compression response for loading and unloading

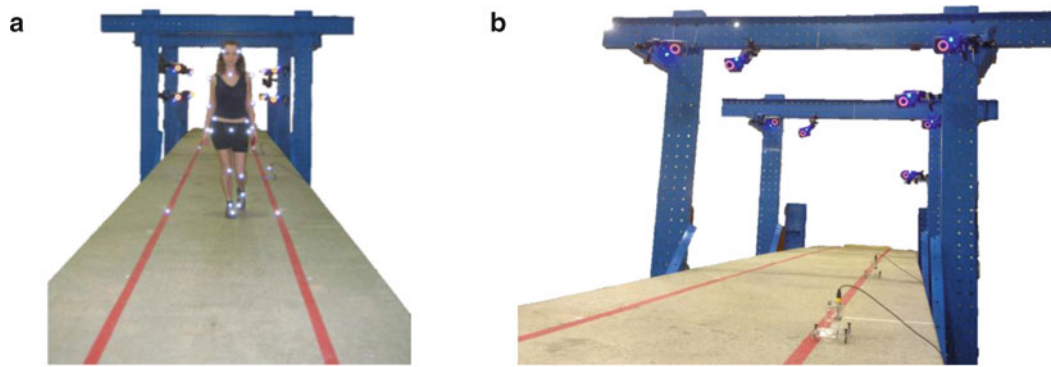
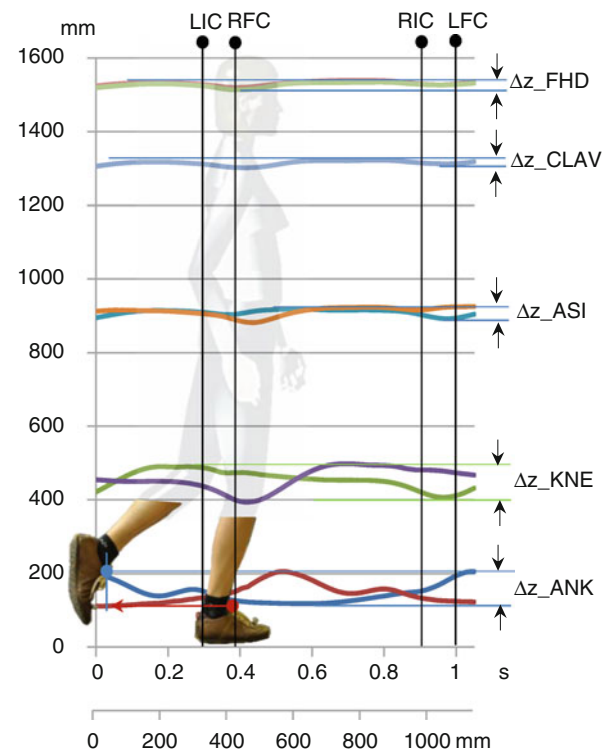


Fig. 38.2 Test area. (a) A test subject instrumented with reflective markers. (b) Vicon motion capture infrared cameras

Fig. 38.3 Footstep for test subject S2



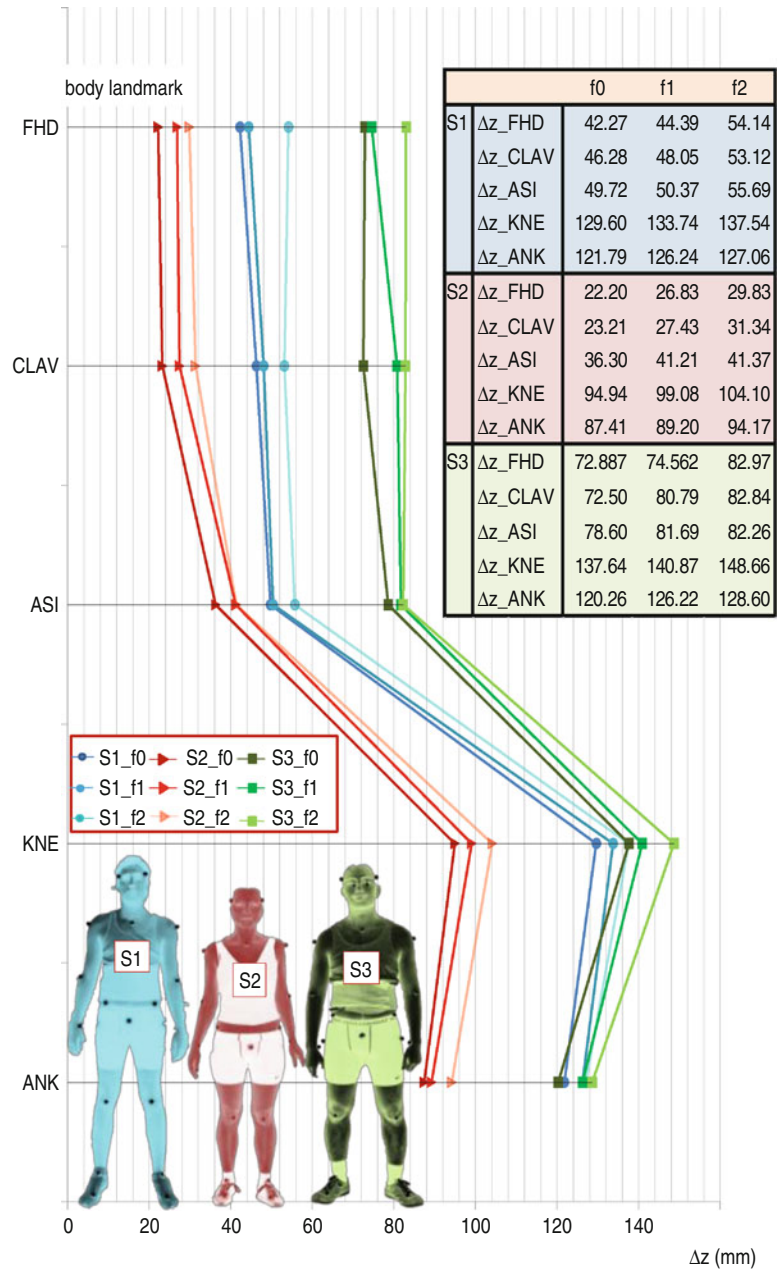
the configuration of the markers does not follow any specific protocol, it is near to the plug-in-gait marker placement protocol [10]. The selected body landmarks are: ANK (ankle), KNE (knee), ASI (anterior superior iliac spine), CLAV (jugular notch where the clavicles meet the sternum) and FHD (left front head, located approximately over the left temple) [11]. A tight sport suits was worn in order to prevent relative movement between markers and the test subjects' skin. Normal training shoes were used during all the tests.

Each test subject was encouraged to walk along the walkway several times prior to data collection to accommodate to the pacing rate and environment. All the signals (position of the markers) were recorded synchronously.

Each test consisted of three trials. In each trial at least 4 complete gait cycles were recorded. A total of at least 10 footsteps were analysed. Peak to peak values (Δz) for displacements (e.g. vertical excursions) of five markers (FHD, CLAV, ASI, KNE and ANK) during one step have been extracted from the measurements. CLAV was selected because it is believed it moves similar to BCOM (body centre of mass) and is near the head, where main body movement sensors are located (internal ear).

Mean trajectories for five markers for test subject number 2 (S2) are shown in Fig. 38.3. Note that in Fig. 38.3, the time instants when left and right feet get in contact and leave the ground are also shown: LIC stands for *Left Initial Contact*, LFC for *Left Final Contact* and, in the same way, RIC and RFC *Right Initial Contact* and *Right Final Contact*, respectively.

Fig. 38.4 Vertical excursions for all test subjects averaged across minimum of 10 steps



For the averaged steps, Fig. 38.4 shows the vertical amplitudes defined in Fig. 38.3 for each test subject (S1, S2 and S3) at five selected body landmarks (left ankle, left knee, left side of the waist, sternum and left side of the head) for the three pavement (noted as f0 for the walkway without foam, f1 with one layer of foam and f2 with two layers). Other markers show similar trends. Main physical characteristics for the test subjects are: S1 is a male, having mass of 70 kg and being 1.81 m tall, S2 is a female (47 kg, 1.60 m) and S3 is a male (68 kg, 1.72 m).

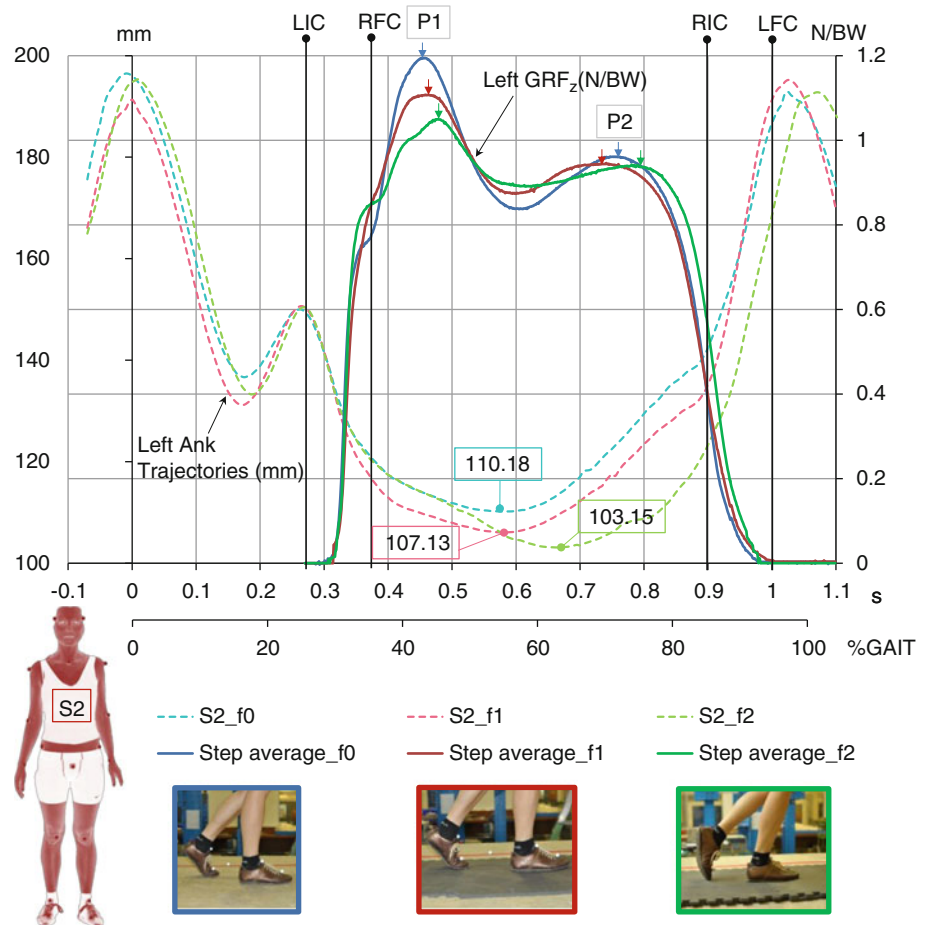
For all the subjects, vertical excursions were larger when walking over flexible pavement. Taking as reference the excursions for walking over rigid surface Table 38.1 shows the relative increase in the excursions (in %) when using one layer of foam (f1) or two layers of foam (f2) and the averaged values for the selected landmarks.

To investigate the influence of the stiffness of the surface on the GRF, test subject S2 was asked to walk three times over three surfaces, in the Gait Laboratory of the University of Warwick. Apart from monitoring kinematics of the body segments, it was also possible to record the GRF by means of a force plate installed in the floor of the Laboratory. Figure 38.5 shows vertical ground reaction force together with the corresponding ankle trajectory for the three considered pavements for test

Table 38.1 Relative increase for vertical excursions with respect to the rigid pavement

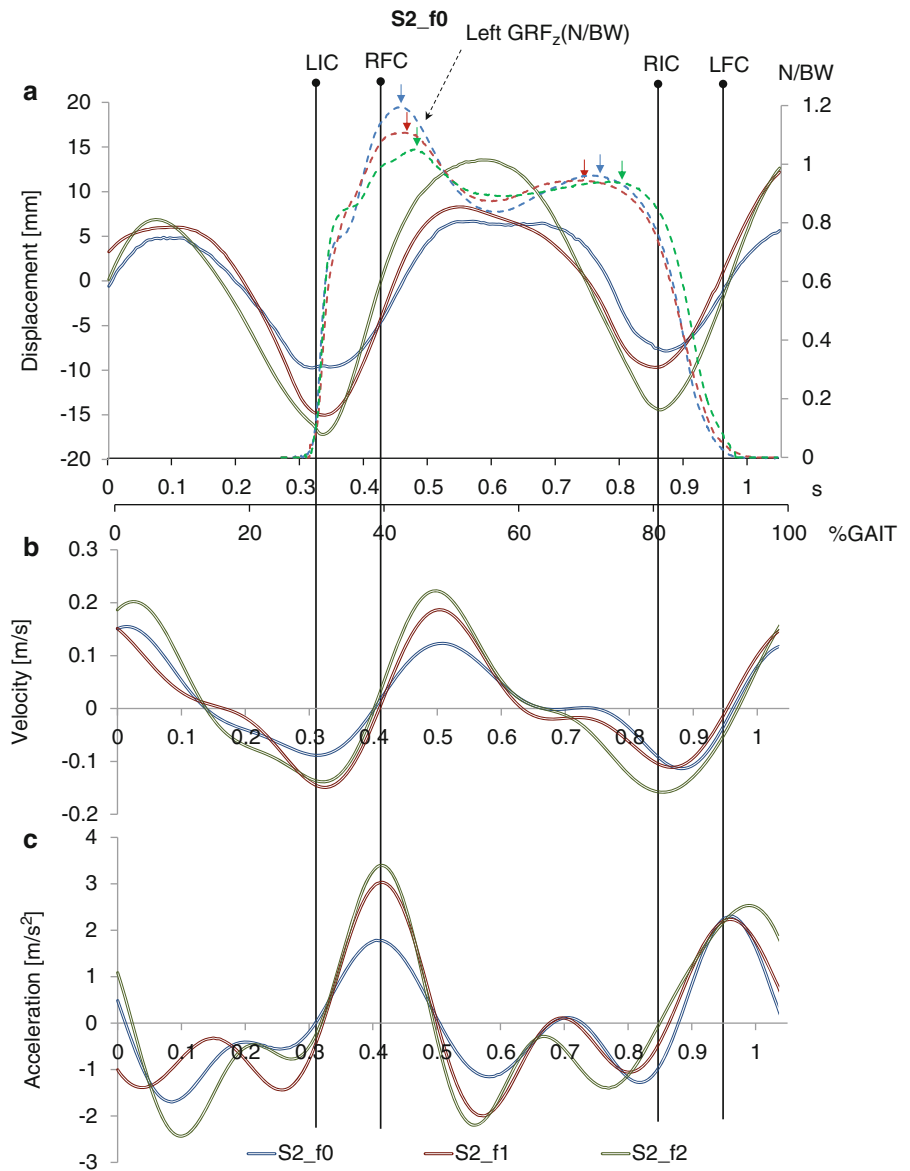
z	S1 (70 kg)		S2 (47 kg)		S3 (68 kg)	
	f1	f2	f1	f2	f1	f2
FHD	5.02 %	28.09 %	20.88 %	34.38 %	2.30 %	13.83 %
CLAV	3.82 %	14.79 %	18.18 %	35.01 %	11.43 %	14.26 %
ASI	1.31 %	12.01 %	13.55 %	13.99 %	3.93 %	4.66 %
KNE	3.20 %	6.12 %	4.35 %	9.64 %	2.35 %	8.01 %
ANK	3.66 %	4.33 %	2.04 %	7.73 %	4.95 %	6.93 %
Average	3.40 %	13.07 %	11.80 %	20.15 %	4.99 %	9.54 %

Fig. 38.5 Vertical ground reaction force and ankle trajectory



subject S2. Note that left vertical axis is for the ankle position and right vertical axis is for the forces (normalised by the body weight, BW). Both trajectories and GRFz shown in the figure represent the average values for three selected footstrikes and ten selected footstrikes respectively. It is interesting to depict the differences among the three cases. For each case, the vertical axis reference is the top of the walking surface. Regarding ankle position, the averaged minimum height during the walking cycle is 110.18 mm for the rigid pavement and 3.05 mm (2.8%) less when using one layer of foam, and 7.03 mm (6.3\%,) for two layers. Considering the body weight for S2 and the mechanical properties of the foam, the expected values will be (see Fig. 38.1) around 6 mm and 10 mm, respectively. The appreciable differences are mainly due to the fact that in each moment, actual contact surface is unknown as well as limited duration of the foot-pavement contact (loading) time during walking compared with the time during testing using the Instron machine. Total S2 shoe sole in about three times the area of the upper compression plate (50 mm diameter) used in the testing and the loading velocity during walking is quicker than of loading available in Instron testing machine. More interesting is the effect of the flexible pavement on the first peaks (P1) of the GRFz. Those peaks decrease from 1.18 (rigid surface) to 1.10 (6.8%) when one layer of foam is added and 1.04 (11.9%) for two layers. The variation on the second peak (P2) is not so substantial. Some minor differences on the timing between P1 and P2 can also be attributed to the flexible pavement. The area bounded for the GRFz curve, named impulse, is about 0.527BW Ns for the three surfaces in all cases.

Fig. 38.6 Vertical (a) displacement, (b) velocity and (c) acceleration for a particular gait cycle for S2



The layers of foam act as shock-absorbing non-linear spring-dashpot structure, reducing the peak force in every heelstrike. Also, by stepping on its upper surface, increases the load spreading to the plantar surface, which reduces the force on the heel area after LIC and also in the toe one (before LFC). Same for the right foot. Pedestrian probably perceives this force reduction not only in terms of plantar pressures, but also through reduced force transmission through the skeleton.

Figure 38.6 shows recorded displacements as well as the corresponding velocities and accelerations (obtained through numerical differentiation of the displacement records, after applying a lowpass filter with cut-off frequency of 10 Hz) for a representative gait cycle for CLAV. Positive velocities are indicative of upward movement of the marker. Averaged acceleration R.M.S. values for the three trials for every test subject, reveal in appreciable increments when walking on the foam. The acceleration RMS values for S1, S2 and S3 are:

- S1: the values are 2.34 m/s^2 for f0, 2.38 for f1 and 2.63 for f2, with increments of 1.5% and 12%, respectively.
- S2: the values are 1.33 m/s^2 for f0, 1.45 for f1 and 1.86 for f2, with increments of 9% and 40%, respectively.
- S3: the values are 3.68 m/s^2 for f0, 3.77 for f1 and 3.81 for f2, with increments of 2.5% and 3.6%, respectively.

38.4 Conclusions

The purpose of this study is to identify differences in walking locomotion over pavements of different flexibility. From the kinetic point of view, for a particular test subject (S2), significant changes were seen in the GRFz - a reduction in the magnitude of the first peak around 6.8% for 1 layer of foam and 11.9% for 2 layers has been recorded. From a kinematic point of view, increases in vertical movements were more than 10% (f1) and 20% (f2) in terms of averaged displacements of selected body landmarks, and more than 20% and 50% in terms of R.M.S. accelerations of a representative landmark (sternum). Similar trends were found for S1 and S3.

After each trial, tests subjects were asked to explain their experiences. Despite bigger values in terms of acceleration, pedestrians tended to perceive the locomotion over the foam as more comfortable [12].

To understand these differences, the authors believe that comprehensive insight into the biomechanics of human locomotion [13] is needed and understanding how human body senses not only accelerations but also forces. Also, future evaluations of energy related aspect can help to explain differences in human perception of the conformability when walking on moving surfaces.

Acknowledgements The authors would like to acknowledge that the work described in this paper was supported by MINECO, Spanish Government (research project, BIA2011-28493-C02-02), the Warwick-Santander Partnership Grant (project *Pedestrian Locomotion and Perception of Vibration on Lively Surfaces of Different Hardness*) and the UK Engineering and Physical Sciences Research Council (project *Pedestrian Interaction with Lively Low-Frequency Structures*, reference number EP/I03839X/1). We are also grateful to the Birmingham Science City and Advantage West Midlands for the access to the Gait Laboratory.

References

- Istrate MV, Lorenzana Ibán A, Ibán Lorenzana N, Vasallo Belder A (2012) Cuantificación de la percepción de la vibración en pasarelas peatonales. *DYNA Ingeniería e Industria* 69(3):467–473. doi:10.6036/4510
- Gu Y, Li J, Ren X, Lake M, Li Z (2012) A pilot study in different unstable designs on the biomechanical effect of gait characteristics. *J Mech Med Biol* 12(5):1250031 (7 pp). doi:10.1142/S0219519412500315
- Menz HB, Lord SR, Fitzpatrick RC (2003) Acceleration patterns of the head and pelvis when walking on level and irregular surfaces. *Gait Posture* 18(1):35–46
- MacLellan MJ, Patla AE (2006) Adaptations of walking pattern on a compliant surface to regulate dynamic stability. *Exp Brain Res* 173(3):521–530. doi:10.1007/s00221-006-0399-5
- Patel M, Fransson PA, Lush D, Gomez S (2008) The effect of foam surface properties on postural stability assessment while standing. *Gait Posture* 28(4):649–656
- Zivanovic S, Pavic A, Reynolds P (2005) Vibration serviceability of footbridges under human-induced excitation: a literature review. *J Sound Vib* 279(1–2):1–74
- Whitham EM, Griffin MJ (1978) The effects of vibration frequency and direction on the location of areas of discomfort caused by whole-body vibration. *Appl Ergon* 9:231–239
- Verdejo R, Mills NJ (2004) Heel–shoe interactions and the durability of EVA foam running-shoe midsoles. *J Biomech* 37(9):1379–1386
- Lieberman DE, Venkadesan M, Werbel WA, Daoud AI, D’Andrea S, Davis IS, Ojiambo Mang’Eni R, Pitsiladis Y (2010) Foot strike patterns and collision forces in habitually barefoot versus shod runners. *Nature* 463:531–535
- Vicon Motion Systems (2008) Vicon plug-in gait product guide—foundation notes revision 1.0
- de Leva P (1996) Adjustments to Zatsiorsky—Seluyanov’s segment inertia parameters. *J Biomech* 29(9):1223–1230
- Howarth HVC (1987) A study of the growth of human discomfort with increasing magnitude of mechanical shocks. United Kingdom Informal Group Meeting on Human Response to Vibration, Royal Military College of Science, Shrivenham, 21–22 Sept 1987
- Winter DA (1990) *Biomechanics and motor control of human movement*, 2nd edn. Wiley, New York

Chapter 39

Using MSD Model to Simulate Human-Structure Interaction During Walking

E. Shahabpoor, A. Pavic, and V. Racic

Abstract Increasing vibration serviceability problems of modern pedestrian structures have drawn researchers' attention to detailed modelling and assessment of walking-induced vibration on floors and footbridges. Stochastic nature of human walking and unknown mechanisms of their interaction with the structure and surrounding environment, make it difficult to simulate. Ignoring these complexities has rendered the current design methods to a rough approximation of reality which often leads to considerable over or under-estimation of the structural response yielding unreliable assessment of vibration performance.

Some aspects of human-structure interaction (HSI), such as synchronization, have been studied extensively, mostly in the lateral direction. But, despite of its much bigger significance, effects of walking pedestrians on dynamic properties of structures in the vertical direction are mostly ignored. This is mainly due to the lack of credible HSI experimental data in the vertical direction as well as models capable of simulating the interactions between the two dynamic systems.

To address this gap, this paper tries to adapt a classic single degree of freedom mass-spring-damper (MSD) model of human body to illustrate the effects of walking pedestrians on dynamic properties of structures. Parametric studies were carried out to analyse effects of the human model dynamic properties on coupled system response. This MSD model can be seen as the basic building block of realistic human body models which are currently being developed to address both biomechanical specifics and HSI effects on structures occupied and excited by walking human.

Keywords Footbridges • Pedestrian walking excitation • Vertical vibration • Human-structure interaction • Kinematic model of human body • Mass-spring-damper models

39.1 Introduction

Over the past few decades there has been a significant growth of interest in vibration serviceability assessment of flexible structures under human dynamic loading specially walking and jumping. The current trend towards more slender elements and longer spans has made structures more sensitive to dynamic loading and consequently more susceptible to vibration problems. These problems have led to concern about both levels of safety and comfort of structures and emphasize on the demand for more accurate and inclusive design methods [1–5].

Current design approaches such as BS 5400 [6] and Eurocode 5 [7] use deterministic walking force models and simply ignore interaction effects and inherent stochasticity of the walking force [1, 2, 8]. Recent research [1, 2, 9–12], mostly based on full-scale measurements, have indicated that interaction of the human body as a mechanical system with the structure has significant effects on dynamic properties of structure and cannot be ignored. It often leads to a considerable reduction in response and slight change in the natural frequency of the structure [1, 2, 8, 12].

To address HSI, different types of mechanical or biomechanically-inspired models, such as single/multiple degrees of freedom MSDs [13–16] and single/bipedal inverted pendulum [17] are used to simulate kinematics of human motion for both vertical and horizontal directions and different postures and types of activities [18–20]. Each of these models has its own advantages and to some extent can describe what is happening in reality, but none of them are versatile in the sense that

E. Shahabpoor (✉) • A. Pavic • V. Racic

Department of Civil and Structural Engineering, University of Sheffield, Sir Frederick Mappin Building, Sheffield S1 3JD, UK
e-mail: e.shahabpoor@sheffield.ac.uk; a.pavic@sheffield.ac.uk; v.racic@sheffield.ac.uk

they are not universally applicable to different structures and loading scenarios. This is mainly due to non-linear stochastic nature of human body dynamics and scarcity of comprehensive experimental HSI data. The former issue makes it hard to understand the mechanisms of interaction and the latter leaves numerous unknowns to be dealt with and makes theories hard to prove and generalize.

This paper uses a classic single degree of freedom mass-spring-damper (S-MSD) model to simulate human body dynamics and its interaction with structure while walking. Although this S-MSD model may not be the best option for modeling human walking in terms of replicating the gait cycle, the simplicity of its dynamics allows a very deep investigation of coupled human-structure system dynamics under different loading conditions. The principal aim of this research is to investigate the performance of the proposed S-MSD model in addressing HSI and to illustrate effects of dynamic parameters of human body on coupled system response. Discussing the reasons behind such effects is beyond the scope of this paper.

The first section of the paper presents a very short introduction into the subject and rationale of this research. Sections 39.2 and 39.3 describe the proposed coupled S-MSD model and its formulation for the considered loading scenarios. Section 39.4 illustrates the parameters used in the models. Section 39.5 presents the results of parametric studies of human model dynamic properties¹ and discusses in details their effects on the structural response and finally Section 39.6 closes the discussion by highlighting the important findings and making conclusions.

39.2 S-MSD Model Description

For all simulations, a S-MSD model is used to simulate human dynamic effects on structure. Dynamic properties of human model (m_h , k_h and c_h) are selected from a range of properties found in the literature and are presented comprehensively in Section 39.4.2. To simulate the structural behavior, only the first mode of vibration is considered and is conceptualized using a SDOF oscillator with the corresponding modal properties (m_s , k_s and c_s). Considering only one structural mode does not affect the generality of the results as, while system can be assumed to be *linear*,² the superposition rule applies and modal contributions to physical response of the structure can be summed up to form the total response.

The S-MSD model that is used in simulations represents ‘Stationary’ walking pedestrian, the imaginary case in which human is walking but its location on structure does not change. This is similar to the case when a treadmill is placed on a structure and a human is walking on that treadmill as shown in Fig. 39.1. Being stationary, coupled system will form a simple conventional two degrees of freedom system as illustrated in Fig. 39.2, which behavior can be studied using closed form solutions of 2DOF equations of motion.

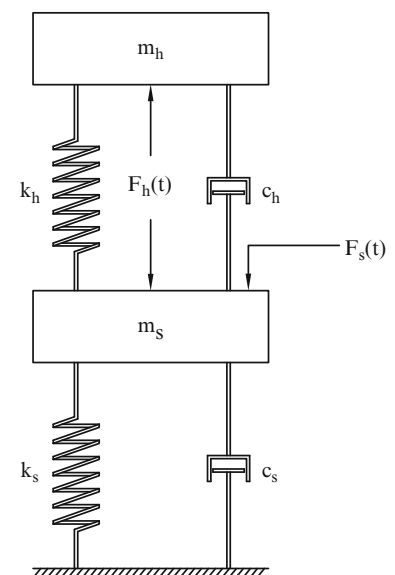
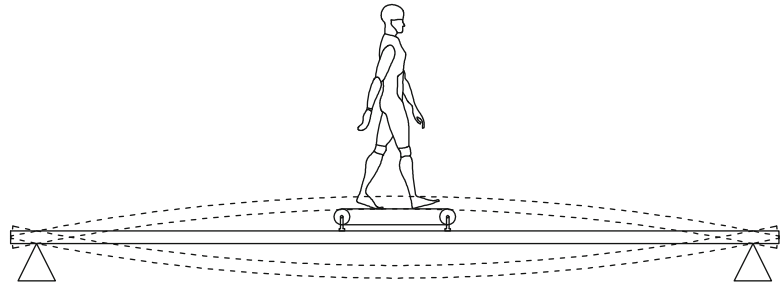


Fig. 39.1 Conceptual 2DOF model of coupled system (stationary human)

¹Stiffness (leading to change of natural frequency) and damping.

²Acceptable assumption for most of civil structures.

Fig. 39.2 Physical representation of S-MSD model - a stationary human walking on the structure



Based on classical mechanics, a system of equations of motion for the presented two degrees of freedom system can be written as:

$$\begin{bmatrix} m_s & 0 \\ 0 & m_h \end{bmatrix} \begin{pmatrix} \ddot{x}_s(t) \\ \ddot{x}_h(t) \end{pmatrix} + \begin{bmatrix} c_s + c_h & -c_h \\ -c_h & c_h \end{bmatrix} \begin{pmatrix} \dot{x}_s(t) \\ \dot{x}_h(t) \end{pmatrix} + \begin{bmatrix} k_s + k_h & -k_h \\ -k_h & k_h \end{bmatrix} \begin{pmatrix} x_s(t) \\ x_h(t) \end{pmatrix} = \begin{pmatrix} F_s(t) - F_h(t) \\ F_h(t) \end{pmatrix} \quad (39.1)$$

where m_s , c_s and k_s are mass, damping and stiffness of the structure and m_h , c_h and k_h are those of the human model. $\ddot{x}_s(t)$, $\dot{x}_s(t)$ and $x_s(t)$ are acceleration, velocity and displacement response of structure in coupled system. Similarly, $\ddot{x}_h(t)$, $\dot{x}_h(t)$ and $x_h(t)$ represent acceleration, velocity and displacement of the human model mass. $F_s(t)$ can be any excitation apart from the human walking load and $F_h(t)$ is the human model driving force that excites the human S-MSD model to produce a dynamic load similar to the actual walking load. Details of the selected parameters are described in Section 39.4. For parametric studies of this research, the proposed 2DOF system is solved analytically using modal analysis method and dynamic properties of the coupled system are analysed accordingly.

39.3 Analysis Cases

The natural frequency and the damping of the SDOF human model are selected for parametric studies to investigate their effects on the dynamic behavior of the coupled human-structure system.

Case 1 parametric studies comprise a set of simulations in which the stiffness of the human model is changed over a certain range to change the natural frequency of the human model. Effects of changing the human model natural frequency on the behavior of the coupled system is then discussed using Frequency Response Function (FRF) plots of system for different human model parameters.

In Case 2 of the parametric studies, damping of the human model is changed over a certain range. This is done for two different sets of stiffness pairs so that Set 1 represents the case where natural frequency of the structure is higher than that of the human model and Set 2 represent the case where it is lower. Subsequently, the effects of changing the human model damping on behavior of the coupled system are discussed.

39.4 Model Parameters

The parameters used in the human and structure combined 2DOF model are described in this section. These parameters are selected to be realistic, to cover the range of possible values (in the case of varying parameters) and to show the interaction effects on dynamic properties of both human and structure models clearly.

39.4.1 Dynamic Parameters of Structure Model

The dynamic parameters of human and structure models that are used in simulations are presented in Table 39.1 for different analysis cases. An imaginary simply supported beam is selected as the structure and its first mode properties, modal mass

Table 39.1 Dynamic parameters of human and structure models used in different analysis cases

Analysis case:	Parametric study case 1 Value/range	Parametric study case 2		Unit
		Set 1	Set 2	
<i>Structure model parameters</i>				
Structural modal mass (first mode)	1000	1000		kg
Structural modal stiffness (first mode)	1.0×10^5	2.0×10^5	1.0×10^5	N/m
Structural modal damping (first mode)	600	600		Ns/m
Structure natural frequency (isolated)	1.59	2.25	1.59	Hz
External force on structure magnitude	0	0		N
External force on structure frequency	0	0		Hz
Length of structure	12	12		m
<i>Human model parameters</i>				
Human mass	70	70		kg
Human location	Mid-span	Mid-span		-
Human driving force magnitude	210	210		N
Human driving force frequency	2.05	2.05		Hz
Human stiffness/(range)	$1.0 \times 10^3 - 1.0 \times 10^5$	0.5×10^4	2.0×10^4	N/m
Human damping/(range)	700	0 - 1000		Ns/m
Human natural frequency (isolated)	0.6 - 6	1.35	2.69	Hz

(m_s), stiffness (k_s) and damping (c_s), are selected in a way to be both realistic and close to the dynamic properties of the human model³ to be able to see the interaction effects better.

39.4.2 Dynamic Properties of Human Model

Human model stiffness and damping are selected from a range of properties found in the literature, mostly reported by biomechanics scientists based on measurements. According to the literature, stiffness and damping of a human are highly dependent on the type of activity and bio-features [15]. The values reported by different researchers vary and are case sensitive [21–25]. Therefore, to cover the whole range of possible values for human stiffness and damping, wider stiffness range of 1×10^3 to 1×10^5 N/m and damping range of 0 to 1000 Ns/m is considered for parametric studies. This damping range is equivalent to 0 – 80% damping ratio for the assumed human mass and stiffness.

39.5 Parametric Studies Results

The results of parametric studies cases 1 and 2 are presented in this section. FRF of the coupled system is used as a tool to describe and compare the dynamic properties of system in each case. Both FRF magnitude and phase diagrams are studied to analyze different aspects of the interaction effects.

39.5.1 Effects of Human Model Natural Frequency

For this analysis, sets of typical dynamic parameters for the human and structural models have been selected and are presented in Table 39.1. Based on these parameters, natural frequency of the empty structure is 1.59 Hz. The stiffness of the human model is changed from 1×10^3 to 1×10^5 N/m to change its natural frequency from 0.6 – 6 Hz while keeping the mass constant. Behaviour of coupled system is studied using an FRF of the system for each set of the parameters and results are compared and illustrated over the whole range.

³A relatively light structure was selected to see better the dynamic effects of human on structure.

Fig. 39.3 FRF magnitude of coupled system for different natural frequencies of human model. (a) Empty structure, (b) coupled system with human model natural frequency greater than that of structure, (c) coupled system with human model natural frequency smaller than that of the structure

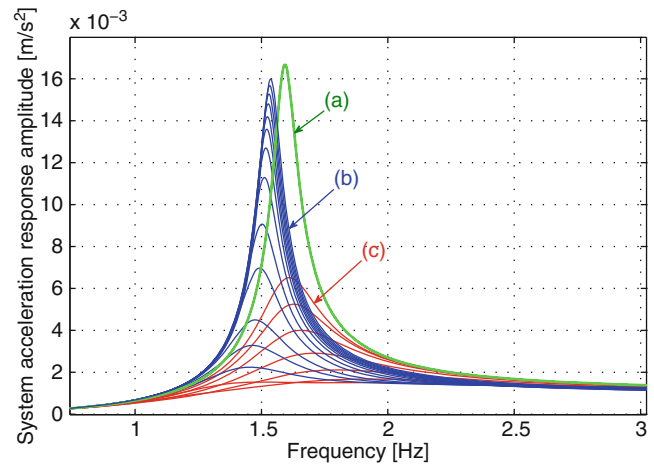


Fig. 39.4 FRF phase of coupled system for different natural frequencies of human model. (a) Empty structure, (b) coupled system with human model natural frequency greater than that of structure, (c) coupled system with human model natural frequency smaller than that of structure

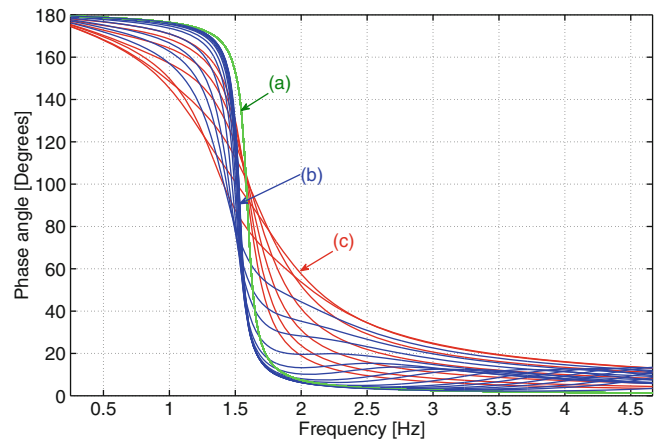
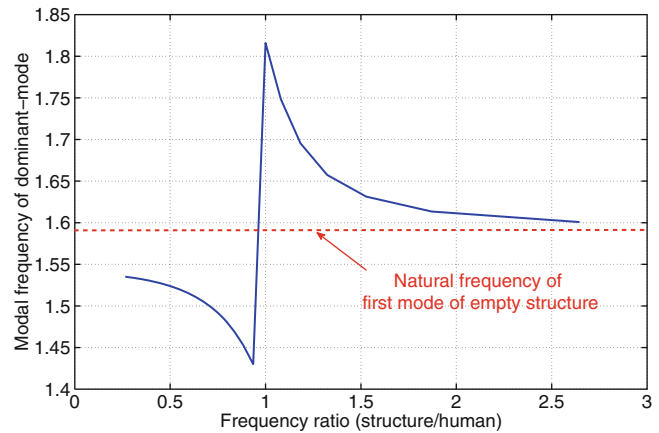


Fig. 39.5 Effects of the natural frequency of the human model on the modal frequency of the coupled system dominant mode



Figures 39.3 and 39.4, display the over-plotted FRF magnitudes and phases of coupled systems for different natural frequencies of the human model. Empty structure FRF is displayed as the green line. As coupled human-structure system form a two degrees of freedom system, it is expected to see two peaks in the FRF amplitude graph. But as structure dominates the behaviour of the coupled system, often only a single peak with properties close to that of the structure can be seen.

Figure 39.3 shows that natural frequency of the dominant mode of coupled system is slightly different compared with natural frequency of empty structure (as is expected). Comparing Fig. 39.3 with Fig. 39.5 which illustrates the effects of the human model natural frequency on the frequency of the dominant mode, it can be seen that when the natural frequency of human model is less than the natural frequency of empty structure, dominant mode of the coupled system has slightly higher frequency than that of empty structure (Red traces in Fig. 39.3). On the other hand, when the natural frequency of the human model is higher than the natural frequency of the empty structure, dominant mode of the coupled system has slightly lower

Fig. 39.6 Effects of the natural frequency of the human model on the modal damping of the coupled system dominant mode

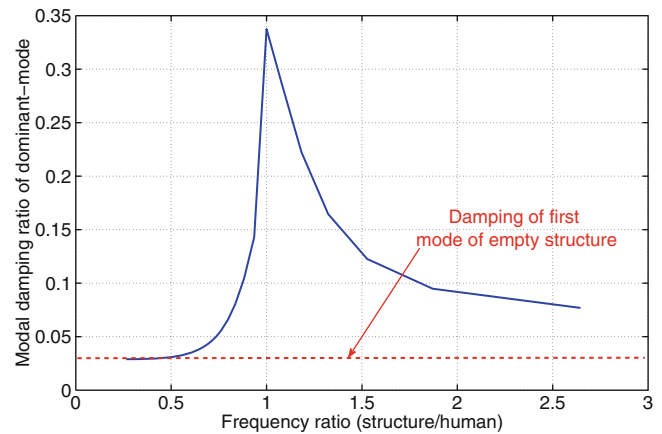
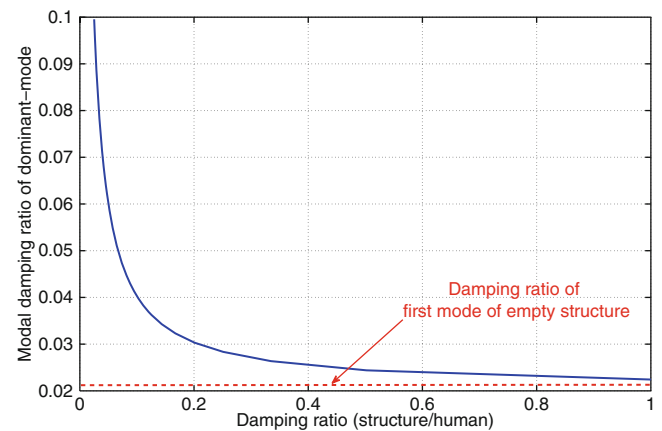


Fig. 39.7 Effects of damping of human model on modal damping of coupled system dominant mode (simulations set 1)



frequency (Blue traces in Fig. 39.3). Figure 39.5 shows that except for a sudden drop at the time that the natural frequencies of the empty structure and human model are equal, the modal frequency of the dominant mode of the coupled system increase by increasing natural frequency of human model.

Figure 39.6 illustrates the effects of changing the human model natural frequency on the damping of the dominant mode. It can be seen that the dominant mode of the coupled system has highest damping and least response, when the natural frequencies of the human model and empty structure are equal (frequency ratio equal to one).

39.5.2 Effects of Human Model Damping

For this analysis, two sets of typical dynamic parameters for human and structure model are selected in such a way that modal frequency of dominant mode of coupled system in first set is less than natural frequency of empty structure ($f_h = 1.35 \text{ Hz} < f_s = 2.35 \text{ Hz}$) and for the second set is higher ($f_h = 2.69 \text{ Hz} > f_s = 1.59 \text{ Hz}$). For this, the stiffness of the human and structure models are selected as 0.5×10^5 and $2.0 \times 10^5 \text{ N/m}$ in the first set and 2.0×10^4 and $1.0 \times 10^5 \text{ N/m}$ in the second set, respectively. A complete list of parameters used in each case is presented in Table 39.1. Damping of the human model is changed from 0 to 1000 Ns/m and behaviour of coupled system under stationary interactive walking load is studied. Figures 39.8 and 39.10 are displaying the over-plotted FRF magnitude graphs of the coupled system for different human damping ratio corresponding to set 1 and 2 simulations.

As it can be seen in Figs. 39.7, 39.8, 39.9 and 39.10, damping ratio of dominant mode of the coupled system increase by increasing damping ratio of the human model, but comparing Figures 39.7 and 39.9 it can be seen that this increase is not to the same extent in two cases studied. Based on Figs. 39.7 and 39.9, increasing damping ratio of the human model from 0 to about 80% will increase modal damping ratio of coupled system of set 1 by 7% while it increases corresponding damping of set 2 only by less than 1%. This leads to the conclusion that rather than the damping, the natural frequency of the coupled systems, can determine how effective the presence of walking human can be on attenuation of structural response.

Fig. 39.8 FRF amplitude of coupled system for different damping ratio of human model (simulations set 1). (a) Empty structure, (b) coupled system with human model natural frequency smaller than that of the structure

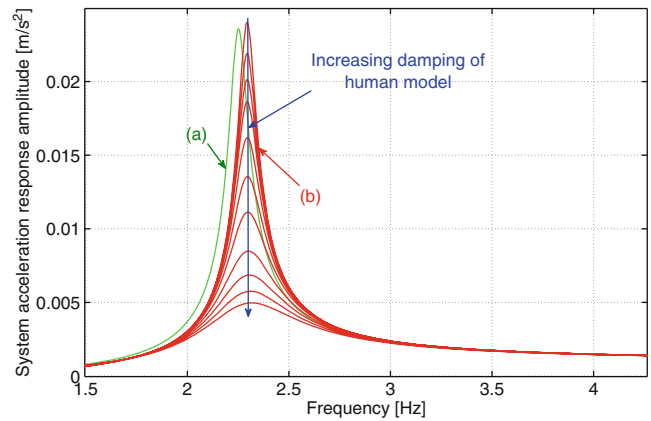


Fig. 39.9 Effects of damping of human model on modal damping of coupled system dominant mode (simulations set 2)

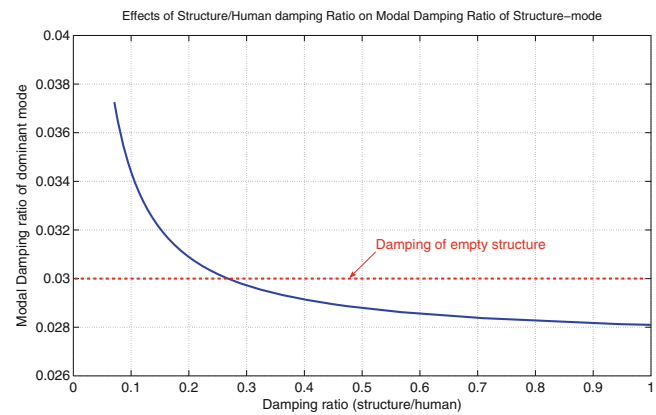
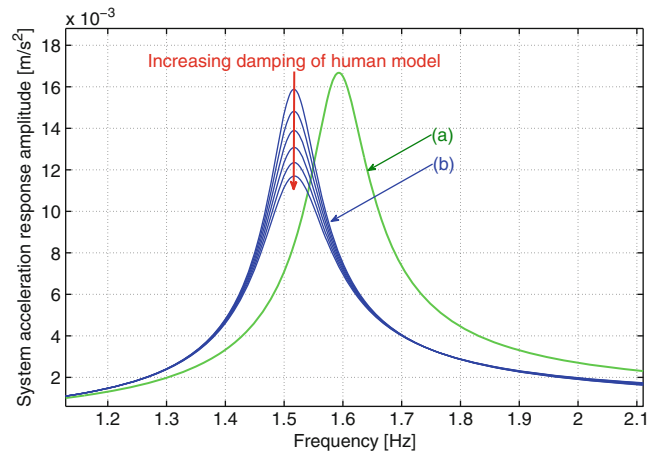


Fig. 39.10 FRF amplitude of coupled system for different damping ratio of human model (simulations set 2). (a) Empty structure, (b) coupled system with human model natural frequency greater than that of the structure



39.6 Conclusion

This paper proposed a classical S-MSD model to simulate effects of walking human on structures. The performance of this human model coupled with a SDOF model of the structure was studied parametrically for two loading scenarios: non-interactive and interactive ‘stationary’ walking pedestrian. In both cases, a pedestrian is walking but its location on structure does not change. It has been found that the natural frequency and damping of the human body have significant effects on the dynamic parameters of the structure (stationary). Although the results of these parametric studies do not prove on their own that this S-MSD model can be used to simulate HSI while walking,⁴ due to its simplicity, the study can provide valuable

⁴Although it has a good visual compliance with some of accurate experimental results presented in [26].

understanding of probable HSI underlying mechanisms. An extensive set of experimental data collected from different types of structures and under different loading scenarios is required to validate and calibrate such models.

References

1. Shahabpoor E, Pavić A (2012) Comparative evaluation of current pedestrian traffic models on structures. Conference proceedings of the society for experimental mechanics series, Jacksonville, FL, USA, vol 26, pp 41–52
2. Živanović S, Pavić A, Ingólfsson ET (2010) Modelling spatially unrestricted pedestrian traffic on footbridges. *ASCE J Struct Eng* 136(10):1296–1308
3. Kasperski M (1996) Actual problems with stand structures due to spectator-induced vibration. Proceedings of structural dynamics-EURODYN'96, Florence, Italy, pp 455–461
4. Reid WM, Dickie JF, Wright JR (1997) Stadium structures: are they excited. *Struct Eng* 75(22):383–388
5. SCOSS (2001) Structural safety 2000-01. 13th Report of the standing committee on structural safety, Cross, Wirral, UK, pp 23–24
6. BSI (2006) Steel, concrete and composite bridges, Part 2: specification for loads; Appendix B: vibration serviceability requirements for a foot and cycle track bridges. BS5400, British Standards Institution, London, UK
7. EN (2004) Eurocode 5: design of timber structures – Part 2: bridges, EN 1995-2:2004, European Committee of Standardization, Brussels, Belgium
8. Dougill JW, Wright JR, Parkhouse JG, Harrison RE (2006) Human structure interaction during rhythmic bobbing. *Struct Eng* 84(22)
9. Ellis BR, Ji T (1997) Human-structure interaction in vertical vibrations, structures of buildings. *Proc Civil Eng* 122(1):1–9
10. Willford M (2002) Dynamic actions and reactions of pedestrians. The proceedings of footbridges conference, Paris, France
11. Brownjohn JMW, Fok P, Roche M, Omenzetter P (2004) Long span steel pedestrian bridge at Singapore Changi Airport – part 1 and 2
12. Pavić A (2011) Vertical crowd dynamic action on footbridges: review of design guidelines and their application. Proceedings of footbridge 2011
13. Archbold P (2008) Evaluation of novel interactive load models of crowd loading on footbridges. Proceedings of 4th symposium on bridge and infrastructure research in Ireland, National University of Ireland, Galway, pp 35–44
14. Archbold P (2004) Novel interactive load models for pedestrian footbridges. PhD thesis, University College Dublin
15. Archbold P, Keogh J, Caprani C (2011) A parametric study of pedestrian vertical force models for dynamic analysis of footbridges. Proceedings of EVACES 2011
16. Caprani CC, Keogh J, Archbold P, Fanning P (2011) Characteristic vertical response of a footbridge due to crowd loading. Proceedings of the 8th international conference on structural dynamics, EURODYN 2011, Leuven, Belgium
17. Bocian M, Macdonald J, Burn J (2011) Modelling of self-excited vertical forces on structures due to walking pedestrians. Proceedings of the 8th international conference on structural dynamics, EURODYN 2011, Leuven, Belgium
18. Macdonald JHG (2009) Lateral excitation of bridges by balancing pedestrians. *Proc Roy Society A* 465(2104):1055–1073
19. Matsumoto Y, Griffin M (2003) Mathematical models for the apparent masses of standing subjects exposed to vertical whole-body. *J Sound Vib* 260(3):431–451
20. Wei L, Griffin MJ (1998) Mathematical models for the apparent mass of the seated human body exposed to vertical vibration. *J Sound Vib* 212(5):855–875
21. Zhang L, Xu D, Makhsous M, Lin F (2000) Stiffness and viscous damping of the human leg. Proceedings of the 24th annual meeting of the American Society of Biomechanics Chicago, IL, USA
22. Rapoport S, Mizrahi J, Kimmel E, Verbitsky O, Isakov E (2003) Constant and variable stiffness and damping of the leg joints in human hopping. *J Biomech Eng ASME* 125:507–514
23. Bertos G, Childress D, Gard S (2005) The vertical mechanical impedance of the locomotor system during human walking with applications in rehabilitation. Proceeding of the 2005 IEEE ninth international conference on rehabilitation robotics, Chicago, IL, USA
24. Lee C, Farley C (1998) Determinants of the center of mass trajectory in human walking and running. *J Exp Biol* 201:2935–2944
25. Geyer H, Seyfarth A, Blickhan R (1998) Compliant leg behavior explains basic dynamics of walking and running. *Proc Roy Soc B Biol Sci* 273(1603):2861–2867
26. Živanović S, Díaz IM, Pavić A (2009) Influence of walking and standing crowds on structural dynamic properties. Proceedings of the IMAC-XXVII, Orlando, FL

Chapter 40

Effect of Sensory Stimuli on Dynamic Loading Induced by People Bouncing

Vitomir Racic, James M.W. Brownjohn, Shu Wang, Mark T. Elliot, and Alan Wing

Abstract Prediction of dynamic loads induced by groups and crowds of people bouncing is a hot topic among designers of grandstands and floors in entertaining venues. Using motion capture technology transferred and adapted from biomedical research, this study aims to investigate effect of visual, auditory and tactile cues on the ability of people to coordinate or synchronise their bouncing movements in groups of two. The numerical results showed a great significance of such stimuli on people's mutual interaction during bouncing, signifying that their effect should be considered in developing much-needed models of crowd dynamic loading of structures due to coordinated rhythmic activities.

Keywords Vibration serviceability • Ground reaction forces • Synchronisation • Entertaining venues • Grandstands

Nomenclature

α Coefficient of synchronisation
 Δ_i Time lag
 f_b Bouncing frequency
 T_b Average duration of bouncing cycle
 n Number of bouncing cycles

40.1 Introduction

In the last decade, a number of newly built entertainment venues have experienced vibration serviceability issues when occupied and dynamically excited by groups of active people during rock concerts [1, 2]. There are three key reasons for this happening:

- (1) lightness of modern structural materials yields high human to structural mass ratio [3],
- (2) natural frequency of the structure and frequency of human-induced loading are close [3], and
- (3) dancing to a steady rhythm of the rock music coupled with close proximity between individuals, helps the occupants to synchronise vertical motion of their bodies leading to large excitation amplitudes [4, 5].

V. Racic (✉) • J.M.W. Brownjohn • S. Wang
Department of Civil and Structural Engineering, The University of Sheffield, Sir Frederick Mappin Building,
Mappin Street, Sheffield S1 3JD, UK
e-mail: v.racic@sheffield.ac.uk

M.T. Elliot • A. Wing
Department of Psychology, The University of Birmingham, Edgbaston, Birmingham B15 2TT, UK

Since the proximity between individuals in groups also limits their horizontal movements, dancing featuring rock concerts can be reliably described as *bouncing* in place, i.e. a cyclic activity similar to jumping but with the both feet in permanent contact with the ground [3]. This study aims to investigate the effect of auditory, visual and tactile stimuli (also called cues) on the ability of people to synchronise their bouncing movements in groups of two. Section 40.2 describes experimental data collection. Section 40.3 presents a simple numerical measure of the synchronisation effect for different combinations of the stimuli, while Section 40.4 is a summary of the key results and findings of this study.

40.2 Data Collection

Two Codamotion [6] tracking cameras (Fig. 40.1) were used to record vertical positions of two motion tracking markers attached to the neck of each test subject (Fig. 40.2). The markers were arranged in the way to prevent occlusions between test subjects, i.e. at least one tracking marker per test subject was visible during the experiment.

Fig. 40.1 Experimental setup at Vibration Engineering Section Laboratory at the University of Sheffield

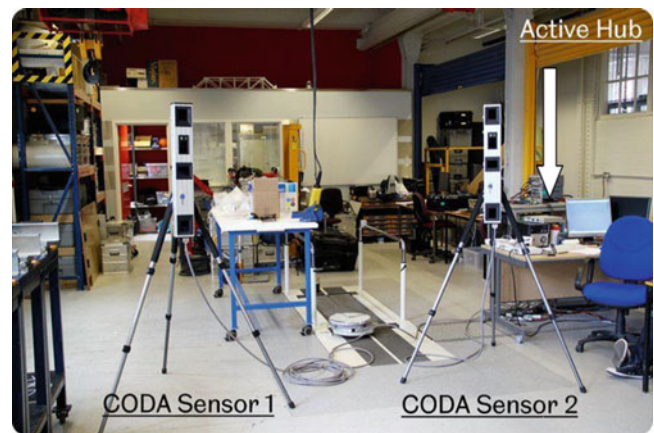


Fig. 40.2 Tracking markers attached to the neck

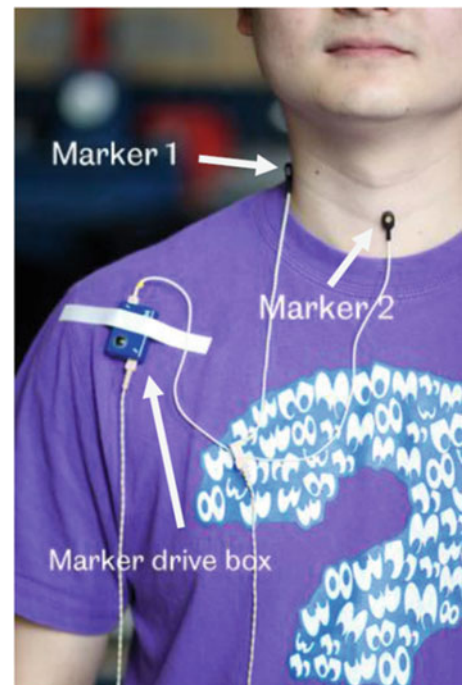




Fig. 40.3 Close, medium and far distance between individuals

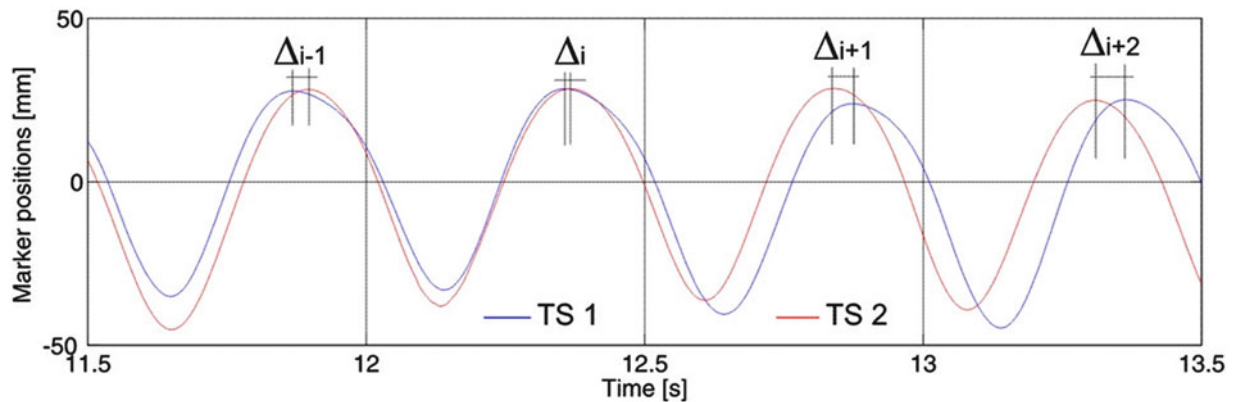


Fig. 40.4 Example of continuously measured motion tracking data

Eight healthy male volunteers participated in the experiments. They were split into four pairs and each pair was independently asked to follow a steady beep provided by an electronic metronome. Metronome rates 1.3Hz, 2.0Hz and 2.7Hz were selected to represent audio stimuli corresponding to slow, moderate and fast rock music rhythms [7].

To test the hypothesis that possibility to see each other improves the synchronisation of the pairs, test protocol included three different bouncing positions:

- 1) *side-by-side*: participants could use only their peripheral vision,
- 2) *facing*: participants could make full eye contact when bouncing, and
- 3) *back-to-back*: participants could not see each other.

The tests designed to investigate the effect of proximity between two bouncing bodies on their synchronisation included close, medium (0.5 m) and far (1 m) distances between individuals, as shown in Fig. 40.3. Finally, the influence of tactile cues was investigated in tests where participants were bouncing close together with and without holding their hands.

Each pair completed 33 tests based on a number of combinations between different bouncing rates, proximity between individuals and visual and tactile cues. Each test was repeated three times to ensure statistical reliability. An example of recorded the position time histories is given in Fig. 40.4.

40.3 Data Analysis

Using the motion data of a kind presented in Fig. 40.4, coefficient of synchronisation α can be calculated as:

$$\alpha = \frac{\sum_{i=1}^n |\Delta_i|}{nT_b} = \frac{f_b}{n} \sum_{i=1}^n |\Delta_i| \quad (40.1)$$

Here, Δ_i is a time lag between the body positions during i -th bouncing cycle, n is the total number of successive bouncing cycles in the motion signals, T_b is an average period of the bouncing cycle and f_b is the bouncing frequency. The coefficient

Fig. 40.5 Average α values for tests featuring close distance between individuals bouncing

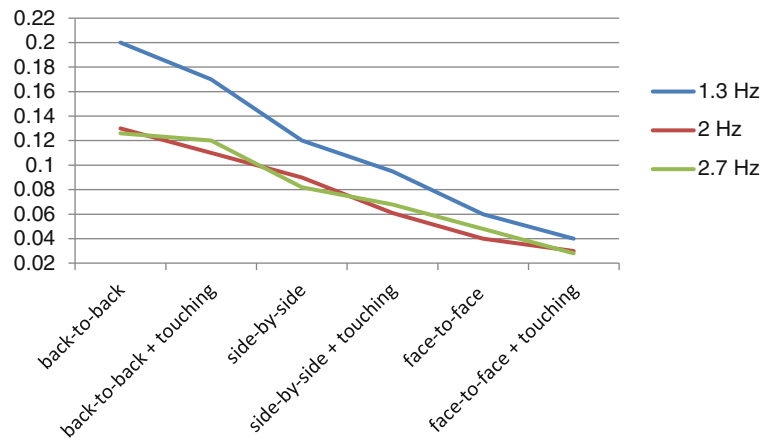


Fig. 40.6 Average α values for tests featuring medium distance between individuals bouncing

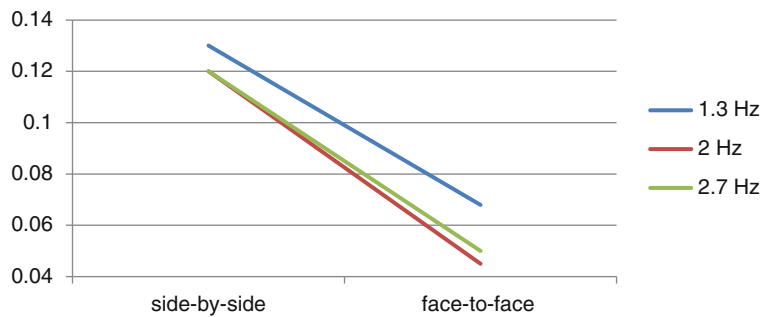
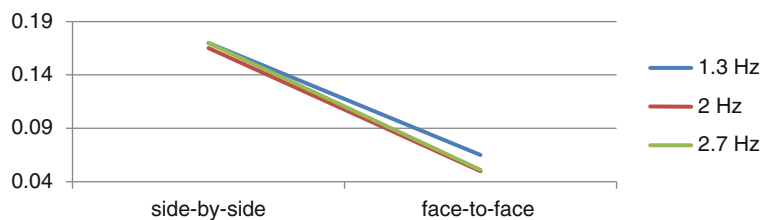


Fig. 40.7 Average α values for tests featuring far distance between individuals bouncing



was calculated for all tests and the results were averaged between the pairs for tests with the same combination of metronome beats and visual, spatial and tactile cues. The results are illustrated in Figs. 40.5, 40.6, and 40.7 and the key findings are listed in the next section.

40.4 Results and Conclusions

The key findings of this study are:

- Audio, visual and tactile stimuli can considerably improve synchronisation between two persons bouncing. Therefore, a reliable prediction of the structural response due to groups bouncing should include a reliable model of the synchronisation effect.
- For the given audio stimuli, the synchronisation improves with decreasing proximity between people and possibility to see and touch each other. Hence, pairs are best synchronised when facing each other and holding hands. On the other hand, metronome stimuli alone (i.e. in back-to-back tests and no touching) resulted in the lowest level of synchronisation.
- For the same combination of audio, visual and tactile cues, in the majority of cases the best synchronisation was achieved when bouncing at 2 Hz. This is probably because the energy consumption at this rate was lower than when bouncing at 1.3 Hz and 2.7 Hz. In feedback after the experimental data collection, all participants reported that bouncing at 1.3 Hz was the most tiring and that 2.7 Hz rate felt slightly less comfortable than 2Hz. This is clearly reflected in the results shown in Figs. 40.5, 40.6, and 40.7.

Recommendations for future research:

- Tests should be carried out in natural environments, such as real concert events, rather than in constrained laboratory settings.
- Metronome beats should be replaced with music to simulate reality better.
- Extended experimental data collection should include tests with groups of various sizes. The so established database will make possible to learn if synchronisation changes with increasing number of people, leading to reliable predictions of the synchronisation effect for large groups and ultimately crowds.
- A wider range of bouncing frequencies should be tested, including frequencies up to 4 Hz which are becoming increasingly present in the popular contemporary music.

References

1. Glackin M (2000) Stadia design rethink prompted by Cardiff fiasco. *Building*, p 11
2. Parker D (2003) Rock fans uncover town hall floor faults. *New Civil Engineer*, 20 November
3. Jones CA, Reynolds P, Pavic A (2011) Vibration serviceability of stadia structures subjected to crowd loads: a literature review. *J Sound Vib* 330(8):1531–1566
4. Ebrahimpour A, Fitts LL (1996) Measuring coherency of human-induced rhythmic loads using force plates. *ASCE J Struct Eng* 122(7):829–831
5. Luck G, Sloboda JA (2009) Spatio-temporal cues for visually mediated synchronization. *Music Percept* 26(5):465–473
6. Codamotion User Manuals (2012) Charnwood Dynamics Ltd., Leicestershire, UK
7. Littler JD (2003) Frequencies of synchronised human loading from jumping and stamping. *Struct Eng* 22:27–35

Chapter 41

Design and Construction of a Very Lively Bridge

S. Živanović, R.P. Johnson, H.V. Dang, and J. Dobrić

Abstract In recent years, an increasing number of light structures has been reported to exhibit substantial vertical vibrations when exposed to pedestrian-induced dynamic loading. It is believed that pedestrians interact with lively structures by altering their walking style and changing the dynamic properties of the vibrating system. As the existing vibration serviceability guidelines do not address these pedestrian-structure interaction effects, they cannot predict the structural dynamic response accurately. Fundamental understanding of the pedestrian-structure interaction is currently limited since most reported observations are of qualitative nature. To improve understanding and develop models of human interaction with lively structures, a purpose-built experimental facility that can be excited by human walking is required.

This paper describes design and construction of a 19.9 m long, low-frequency and lightly damped experimental bridge for studying pedestrian-structure interaction. The challenge to design a relatively heavy and low-frequency footbridge in the limited space of the Structures Laboratory at the University of Warwick, UK, was met by adopting a traditional steel-concrete composite structural system. The experimental data collected on the “Warwick Bridge” during first six-months of structural life are presented to characterise both its static and dynamic behaviour. Dynamic testing of the bridge revealed that, with an achieved fundamental natural frequency of 2.4 Hz, the corresponding damping ratio of 0.5%, and an opportunity to tune the dynamic properties as required, the key design criteria were successfully met.

Keywords Lively bridge • Composite design • Human-structure interaction

41.1 Introduction

Excessive vibrations of footbridges and low-frequency floors occur mainly due to resonance or near-resonance excitation caused by pedestrian walking. An increasing number of structures are being affected by these vibration serviceability problems due to increased demands to design more efficient, lighter and therefore more sustainable, structures. Publicity of the infamous excessive sway of the Millennium Bridge under crowd loading on its opening day in 2000 [1], and subsequent expensive retrofitting, demonstrated an urgent need to develop fundamental understanding of pedestrian behaviour on lively structures. The pedestrian-structure dynamic interaction (PSDI) is a consequence of pedestrians being active and intelligent systems [2] who tend to adapt their actions to the new (vibrating) environments. Some pioneering analytical and experimental research into the PSDI for structures vibrating in the horizontal lateral direction has been carried out in the last four years, e.g. work by Macdonald [3] and Ingolfsson et al. [4]. In the meantime, it has been observed that the current design guidelines cannot predict accurately the vibration response of the structures that exhibit perceptible vibrations in the vertical direction [5]. The PSDI in the vertical direction has rarely been investigated primarily due to a lack of suitable experimental facilities. To address this issue, a lively bridge structure situated in the Structures Laboratory at the University of Warwick has been built.

S. Živanović (✉) • R.P. Johnson • H.V. Dang
School of Engineering, University of Warwick, Coventry CV4 7AL, UK
e-mail: s.zivanovic@warwick.ac.uk; r.p.johnson@warwick.ac.uk; h.v.dang@warwick.ac.uk

J. Dobrić
Faculty of Civil Engineering, University of Belgrade, Bulevar Kralja Aleksandra 73, 11000 Belgrade, Serbia
e-mail: jelena@imk.grf.bg.ac.rs

This paper describes the design requirements, design solution and construction of the Warwick Bridge. This is followed by presentation of key experimental data collected during first six months of structural life with the aim to characterise static and dynamic behaviour of the bridge.

41.2 Design of the Warwick Bridge

41.2.1 Design Task

Key design requirement was to build a lively simple-beam structure that would be easily excited when exposed to human walking excitation. To achieve this design aim, the structure was required to have the fundamental bending vibration mode characterised by a natural frequency in the range 1.5-2.5 Hz typical of human walking, and a low damping ratio. The structure was to reside on the Strong Floor of the Structures Laboratory at the University of Warwick, limiting the maximum achievable length to 21 m, and requiring a design solution and construction sequence that would adhere to the strict health and safety (H&S) requirements for work in the Laboratory. Finally, to allow studies of human interaction with the structure under different conditions (such as different pacing rate and vibration level), the structure was required to have tuneable natural frequency and damping ratio.

41.2.2 Design Solution

At the early stages of the design, it was clear that utilising the full length of the usable space is required to achieve the low-frequency solution, given that increasing the span length L of the structure is the most effective means of lowering the natural frequency f_n (i.e. $f_n = 1/L^2$). The required low-frequency design is still quite unnatural for such a short span, and could be achieved only for exceptionally high slenderness (span length to cross section depth) ratio. Therefore, optimisation of the cross section to provide low-frequency (and therefore low stiffness) structure on one hand and to preserve structural integrity on the other hand was required.

The initial idea was to design a pre-stressed concrete structure. Due to challenging requirements related to H&S aspects of construction of such a structure in laboratory conditions, the idea was abandoned and the decision was made to construct a steel-concrete composite structure instead. After analysing the suitability of different geometries of fully composite steel-concrete cross sections, a solution in the form of two steel beams and 150 mm thick reinforced concrete slab was adopted (Fig. 41.1). The two metre wide deck was chosen to provide enough room for comfortable walking by a test subject and at the same time to provide a structure that is heavy enough to result in a low-frequency structure. In addition, a reasonably heavy structure was also required to provide significant inertial force during the interaction mimicking the “feel” that pedestrians experience during interaction with lively as-built bridges. The adopted length of the bridge deck was 19.9 m resulting in the structural mass of 16,500 kg.

The composite cross section consists of two steel I-profiles (UC 203x203x52, steel grade S355) and a deck made of class 40/50 concrete (Fig. 41.1). The composite action is achieved by means of shear studs (diameter 19 mm, length 75 mm) welded to the top flanges of the two beams. To provide full interaction between the steel and concrete, the studs are spaced at 250 mm. To resist a large longitudinal shear force at each end of the bridge, five end studs in this area are spaced at 140 mm distance. In total, 83 studs are used per beam. Two layers of reinforcing mesh A252 ($\phi 8@200$ mm) are used to keep crack width under control. In addition, 4 kg/m³ of polypropylene fibres Fibermesh FM650s were added to the concrete mix to increase concrete fatigue resistance and thereby provide an additional means of crack control. The steel beams are stiffened by 6 mm thick stiffeners welded between the inside flanges (see the cross section in Fig. 41.1) at eight locations that are considered as candidate support points. Due to the limiting length of the steel profiles that could be manipulated in the Laboratory, the steel beams were required to be delivered in three pieces and then butt welded on site. The beams are connected intermittently by a total of 12 cross beams (S355, PFC 100x50x10) to provide enough stiffness to the three separate frames while they are manipulated in the transport and installation phases. A camber of 250 mm was designed to enable the bridge to become relatively flat after development of the long term deformation influenced by creep and shrinkage.

The adopted design was checked against the following requirements: (1) stress due to self-weight and a pedestrian walking to excite the structural resonance to be within the elastic range in all elements for both short-term and long-term effects, (2) long-term deflection due to self-weight to be of the order of the camber size, (3) natural frequency of the fundamental vertical bending mode to be in the range 1.5-2.5 Hz, (4) shear studs to provide full interaction between the steel beams

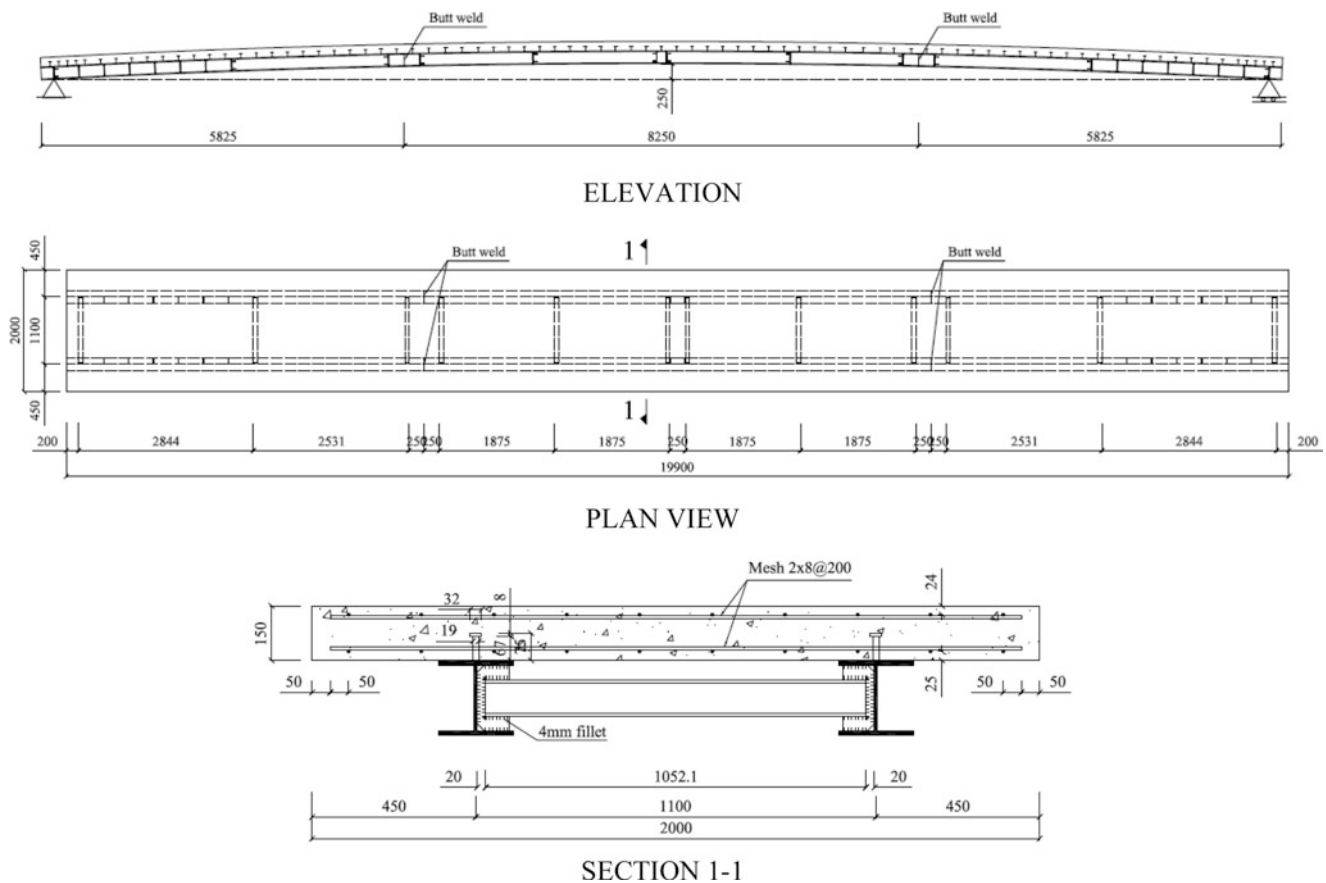


Fig. 41.1 Elevation, plan view and cross section of the Warwick Bridge

and the concrete deck and resist large longitudinal shear at the end sections of the bridge, (5) steel profiles to have enough resistance to shear force and lateral torsional buckling, (6) tensile stress in the concrete deck, while on props, to be kept below the tensile resistance to avoid formation of cracks, (7) props to be able to carry the weight of the structure, (8) tensile stress in concrete above the supporting points for all designed configurations of supports to not exceed the tensile strength of concrete, and (9) the bridge to be able to sustain self-weight and static load due to a crowd of people (with density of up to 2 people/m²). The critical damping ratio of the first vibration mode required for analysing the walking at resonance loading scenario was assumed as 0.5%. The design solution was accepted only after all criteria were satisfied.

41.3 Construction Process

Construction of the bridge can broadly be divided into three phases: (1) manufacturing and installation of steelwork, (2) casting and curing the concrete deck and (3) removal of the props and placement of the bridge on two permanent supports. Prior each phase the H&S aspects for all activities were considered. Risk assessment was then performed and a safe system of work developed.

41.3.1 Steelwork

Steelwork was delivered in three parts (with respective lengths of 5.82 m, 8.26 m and 5.82 m) and placed on six props with adjustable heights that allowed the designed geometry of the camber to be achieved. The main beams were then welded on site using full penetration butt welds. An ultrasound test confirmed the satisfactory quality of the welds. The assembled steel frame is shown in Fig. 41.2a.



Fig. 41.2 Construction of the Warwick Bridge: (a) steelwork on six props, (b) preparation for casting, (c) casting of concrete and (d) final structure resting on two supporting frames

41.3.2 Concrete Deck

Formwork was constructed around the steel beams and varnished in-house. Then two layers of reinforcement mesh were placed at the designed position (Fig. 41.2b). The positions of transverse bars in both layers of the reinforcing mesh were recorded by means of vertical lines drawn on the outside edge of the formwork. The concrete deck was cast on Saturday 14 Jan 2012. The deck consists of approximately 6 m^3 of concrete. Two ready mixes of concrete were ordered ($3 + 4 = 7 \text{ m}^3$). They were delivered to the Laboratory site 1 h one after another. The excess concrete was ordered to account for any spills and to cast concrete specimens that are to be used for testing mechanical properties of concrete. During casting, the concrete was transported from the mixer to the bridge in a skip carried by an overhead crane (Fig. 41.2c). Placement of concrete and its compaction by means of pokers were completed in two hours. First mix was used to alternate between casting 5 m long sections at either end of the bridge, while the second mix was used for casting the middle 10 m of the bridge length. After casting, the concrete was covered by wet hessian and cured for 60 days. During this time, the composite section was supported by six props. The long curing period was chosen to prevent development of drying shrinkage while concrete was still on props. Props were kept for 60 days to allow concrete to develop significant strength before removal of the props, and therefore to minimise the creep effects. The formwork was removed 46 days after casting. Before this, the information about the positions of the reinforcing mesh bars was transferred from the formwork to the concrete surface. This information should help interpretation of crack mechanisms, should cracks appear in future.

41.3.3 Permanent Supports

Two permanent frame supports, firmly fixed into the Strong Floor, were built around the bridge. The bridge was lifted from the props using four hydraulic jacks placed beneath the steel beams at 2.6 m distance from each end of the bridge. The props were then removed and the bridge was placed on the “permanent” supports in an operation lasting about 4.5 hours. These supports are currently 16.2 m apart, and can be moved to form a span between 15.0 and 18.7 m (with the corresponding slenderness ratio ranging from 42 to 52). The bridge, as it looks now, is shown in Fig. 41.2d.

41.4 Properties of Concrete

On the casting day, three cube specimens (150x150x150 mm) from Mix 1 were cast, alongside with nine cube specimens, four prismatic specimens (100x100x500 mm) and six cylinders (diameter 100 mm, height 200 mm) from Mix 2. The first series of tests on the concrete specimens was performed 30 days after casting, i.e. on the first working day (Monday) after the standard testing time at 28 days passed (Saturday). Three cube specimens from each mix were tested to establish the compressive strength of concrete. The four prismatic specimens were tested for flexural tensile strength and the three cylinders were tested for splitting tensile strength. Tests were performed according to BS 1881: Parts 116, 117 and 118 [6–8], and the axial tensile strength was calculated from the splitting tensile strength in accordance with Part 1-1 of Eurocode 2 [9]. In addition, three cubes from Mix 2 were also tested for compressive strength at concrete age of 90 days. The mean and standard deviation (STD) for each series of tests are shown in Table 41.1.

The achieved compressive strength at 30 days on a sample of six concrete specimens is about 60 MPa, with a low coefficient of variation of 1.8%. According to Eurocode 2 [9], this cube strength corresponds to cylinder strength of 50 MPa. The results of all tests show that the quality of concrete is higher than required. Based on test results, the 28 day compressive cylinder strength required for further calculations was taken as 50 MPa, and the corresponding Young's modulus of elasticity of concrete with respect to static loading as 37 GPa [9]. An average density of concrete specimens was found to be 2,350 kg/m³.

Four additional prismatic specimens (50x50x225 mm) were also cast from Mix 2 to monitor shrinkage strain in concrete. These four specimens were cured for 11 days. In the eleventh day stainless steel discs, nominally spaced 200 mm apart, were glued onto the specimens to allow for readings of strain using a DEMEC Mechanical Strain Gauge. At $t = 11$ days two out of four specimens were exposed to laboratory conditions (average temperature of 19 °C and average relative humidity of 45%). The remaining two specimens were cured for a total of 60 days, i.e. for the same period as the concrete deck. After this time they were exposed to the laboratory conditions as well. First readings of shrinkage strain on all specimens were taken after the installation of the steel disks, i.e. at concrete age of 11 days. This means that the autogenous shrinkage that developed in first 11 days was not measured. Development of shrinkage on all four specimens is shown in Fig. 41.3a. Readings on two specimens cured for 11 days are shown as diamonds, while the readings on the specimens cured for 60 days are shown

Table 41.1 Measured properties of concrete

Strength tested	Concrete age (days)	Mix #	Number of specimens	Mean (MPa)	STD (MPa)
Compressive	30	1	3	59.4	1.1
Compressive	30	2	3	60.5	0.9
Flexural tensile	30	2	4	6.5	0.5
Axial tensile	30	2	3	4.3	0.0
Compressive	90	2	3	72.4	1.4

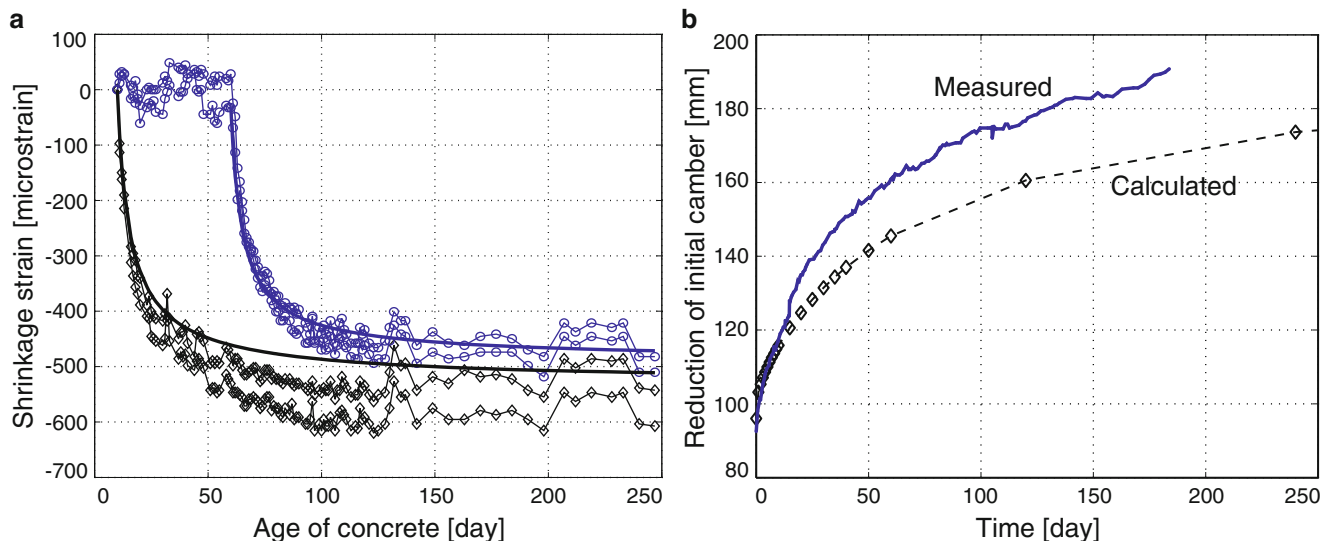


Fig. 41.3 (a) Shrinkage of concrete specimens. (b) Reduction of the bridge camber since removal of the props

as circles. The solid thick lines represent the corresponding theoretical estimates of shrinkage according to Eurocode 2 [9]. To make the theoretical data comparable with the experimental measurements, the autogenous shrinkage calculated at $t = 11$ day has been removed from the theoretical curve.

Figure 41.3a shows that the final shrinkage strain measured on specimens cured for 60 days is lower than for the specimens exposed to drying at an earlier age (i.e. at 11 days). Both values seem to agree reasonably well with the expected values calculated according to Eurocode 2 [9].

41.5 Static Behaviour

The structure was designed to satisfy the design criteria listed in Section 41.2 for all possible span lengths. Since the bridge has been placed on two permanent supports the span has been kept at 16.2 m. The deformation of the structure has been monitored from the first day. To compare predicted and actual structural behaviour, all theoretical predictions in this and in the next section are based on the current span of 16.2 m. The following properties of the materials were used in calculations:

- Concrete: compressive strength (cylinder) = 50 MPa, $E_c = 37$ GPa, density = 2,350 kg/m³
- Reinforcement: yield strength = 500 MPa, $E_r = 200$ GPa, density = 7,850 kg/m³
- Main beams: yield strength = 355 MPa, $E_s = 210$ GPa, density = 7,850 kg/m³

where E represents the Young's modulus of the relevant material. The influence of polypropylene fibres has not been accounted for in the calculations. Both short-term and medium-term (i.e. six month) behaviours are considered.

41.5.1 Short-Term Behaviour

The achieved camber of the structure was 246 mm. After placing the structure on the two supports (at concrete age of 60 days), the deflection at two end sections as well as at the midspan was measured. The resulting reduction of the camber was 92 mm. The calculated camber reduction is 82 mm if the effects of shrinkage are neglected. The difference between the two values could be caused by neglected contribution of autogenous and possibly some drying shrinkage that developed while the bridge was still being cured. A conservative estimate of the contribution of the autogenous shrinkage (calculated under an assumption that the bridge was supported at two supports only) is 14 mm. Therefore, the theoretical estimate of the instant deflection of the bridge, upon removal of the props, is quite close to the measured value.

To check the short term stiffness of the composite section at a later date, when the effects of creep and shrinkage were well developed, the deflection of the bridge was measured under a concrete block weighing 146.6 kg. The block was placed at either quarter span points or the midspan point while the deflections at these points were measured using dial gauges. The tests were performed in October 2012. It was found that the calculated deflections are 20-30% larger than those measured, suggesting that the short-term flexural stiffness of the composite (i.e. equivalent steel) section EI is 20-30% larger than that assumed in calculations. Given that second moment of area I was calculated assuming full interaction and uncracked concrete, it seems that the Young's modulus of the concrete is higher than the assumed value of 37 GPa.

41.5.2 Behaviour After Six Months

The solid line in Fig. 41.3b shows the measured reduction of the camber over first six months of the structural life. It can be seen that the measured deflection is larger than the calculated six-month deflection that accounts for effects of both creep and shrinkage (dashed line in Fig. 41.3b). After six months, the calculated deflection of 171 mm equals a 90% of the measured deflection of 191 mm. The calculated deflection consists of 106 mm due to creep effects and 65 mm due to shrinkage effects. Following the procedure defined in Eurocode 4 [10], the creep coefficient at 184 days was calculated to be 1.16 for calculation of creep effects and 2.65 for shrinkage effects. The corresponding modular ratio used in calculation of creep effects is therefore taken as $(1 + 1.1 \times 1.16) E_s/E_c = 2.28 E_s/E_c$, while it was $(1 + 0.55 \times 2.65) E_s/E_c = 2.46 E_s/E_c$ for shrinkage effects, where $E_s = 210$ GPa and $E_c = 37$ GPa. The discrepancy in the measured and calculated deflection is most likely the consequence of underestimation of creep and/or shrinkage effects, and possibly the influence of polypropylene fibres.

41.6 Dynamic Behaviour

To get an insight into the dynamic behaviour of the structure, impact tests and walking tests were performed.

41.6.1 Impact Tests

The structure was excited by two well separated (unmeasured) impacts induced using a sledge hammer. The impacts were applied at test point 4 (TP4), and the acceleration responses were measured at 18 points (Fig. 41.4a). Four Honeywell QA-750 accelerometers having nominal sensitivity of 1.3 V/g were available for response measurements. One accelerometer was kept at TP4 at all times to provide a common reference, while the remaining three accelerometers were moved to cover the test grid in six separate test setups. The data were acquired using 4-channel NI USB-9234 data acquisition card. The response spectra

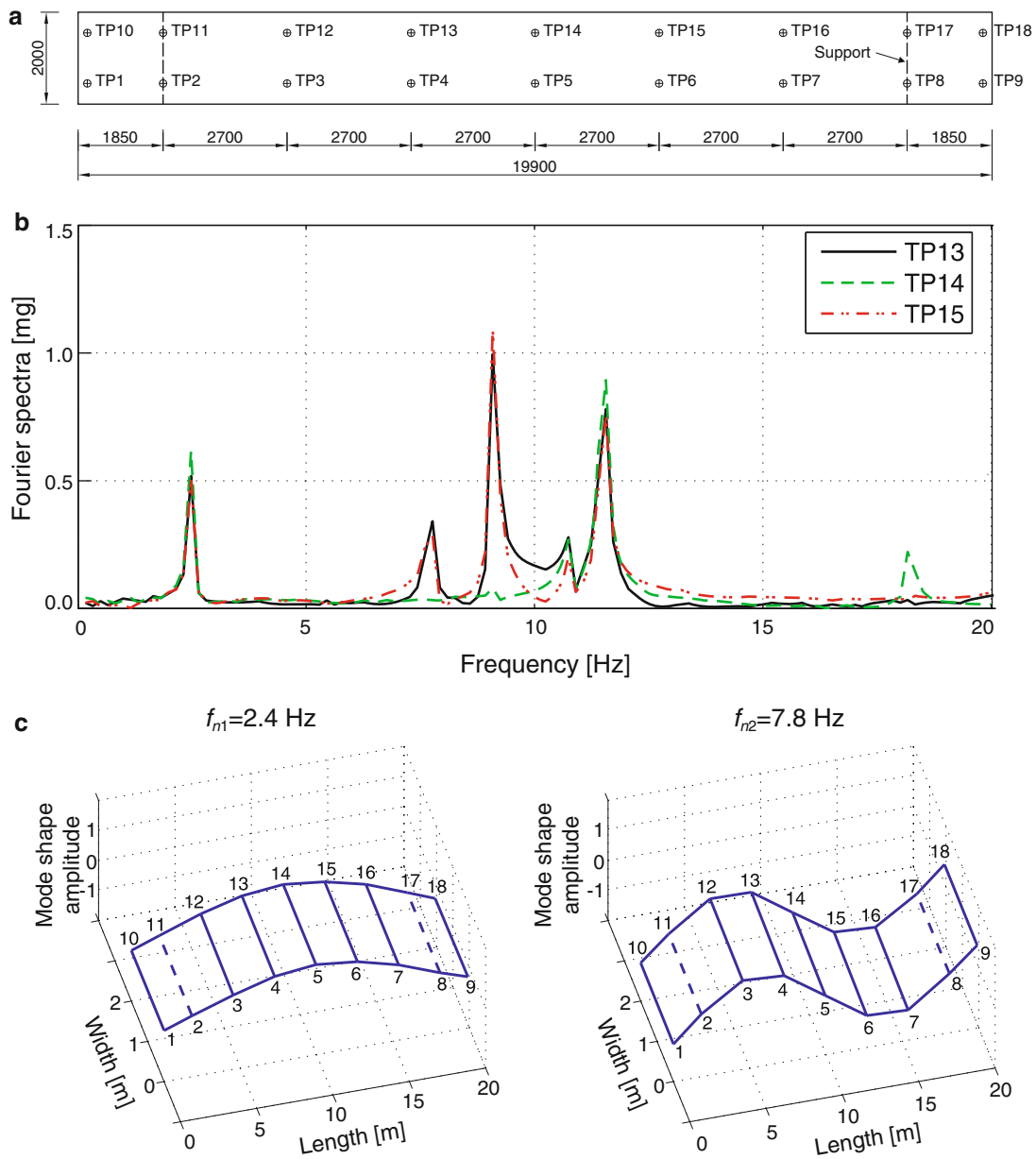


Fig. 41.4 (a) A grid of measurement points. (b) Fourier spectra of measured responses. (c) First two bending vibration modes

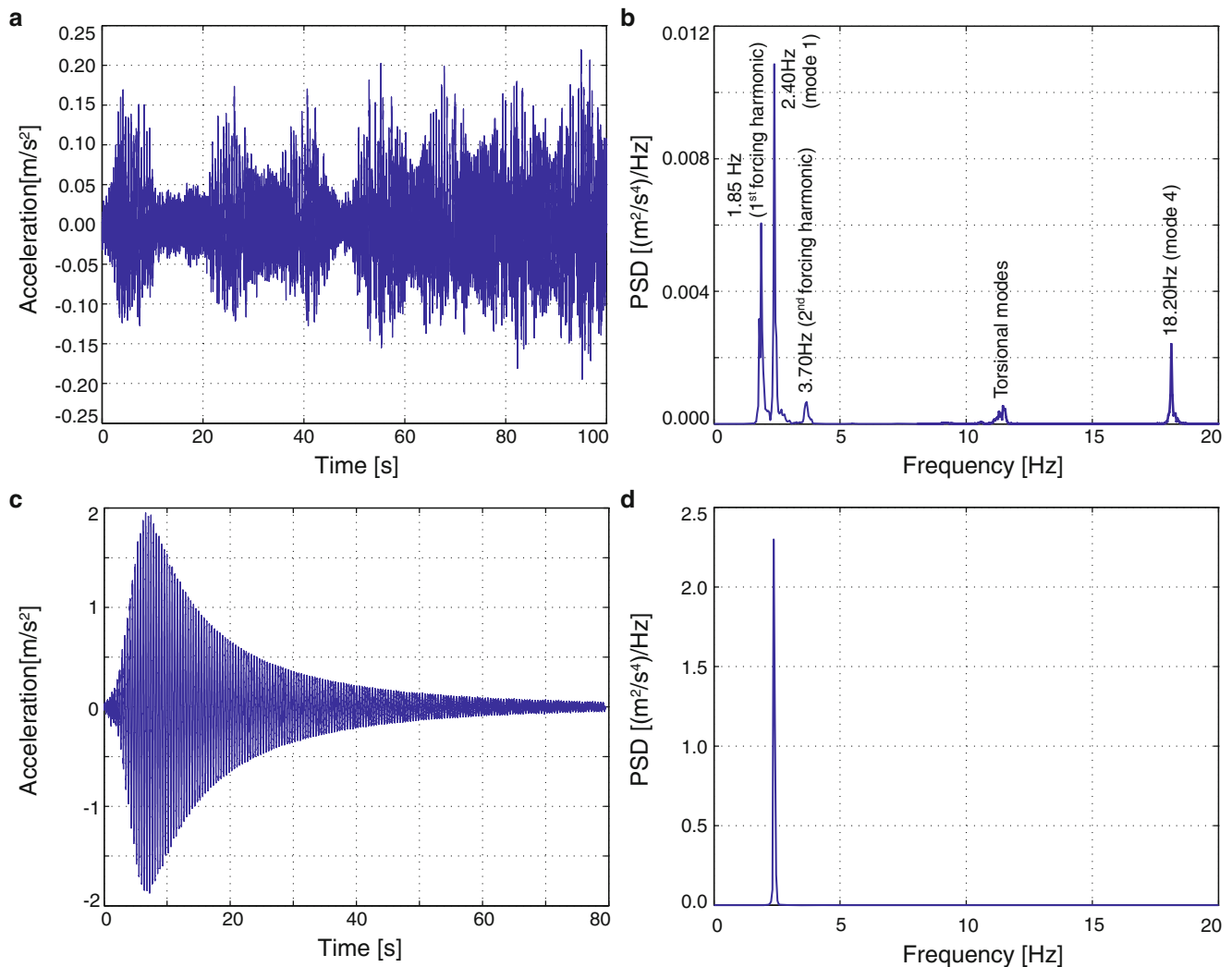


Fig. 41.5 Normal walking: (a) acceleration response and (b) its PSD. Fast walking: (c) acceleration response and (d) its PSD

recorded at TPs 13, 14 and 15 are shown in Fig. 41.4b. Each peak in the spectra represents a vibration mode. Filtering out each peak from all the response signals, and normalising the vibration amplitude against the common reference, allowed for identification of six vibration modes in the frequency range up to 20 Hz. Four of these modes are vertical bending vibration modes (at 2.4, 7.8, 9.1 and 18.2 Hz) while the remaining two modes are torsional modes (at 10.7 and 11.6 Hz). First two bending vibration modes are shown in Fig. 41.4c.

41.6.2 Walking Tests

A test subject was asked to walk continuously from one end of the bridge to the other end and back for about 100 s. The acceleration response was measured at the midspan point (TP5 in Fig. 41.4a). The pedestrian was instructed to walk at a comfortable pacing rate to check the response in the first and fourth vibration modes (that appeared to be most responsive in some preliminary tests). The acceleration level recorded in this test is shown in Fig. 41.5a. The power spectrum density (PSD) of the acceleration signal in Fig. 41.5b reveals that most of the response energy is concentrated at the first forcing harmonic and at the first vibration mode. The pedestrian was then asked to cross the bridge at a fast pacing rate with the aim to excite the first vibration mode in resonance. After completing one crossing, the test subject left the bridge in order to allow the free vibration decay to be measured. The measured response and the corresponding PSD are shown in Figs. 41.5c, d. As expected, the bridge was extremely lively in this test, with peak acceleration level almost reaching 2 m/s². The maximum measured acceleration response corresponds to a large peak to peak displacement of 17 mm.

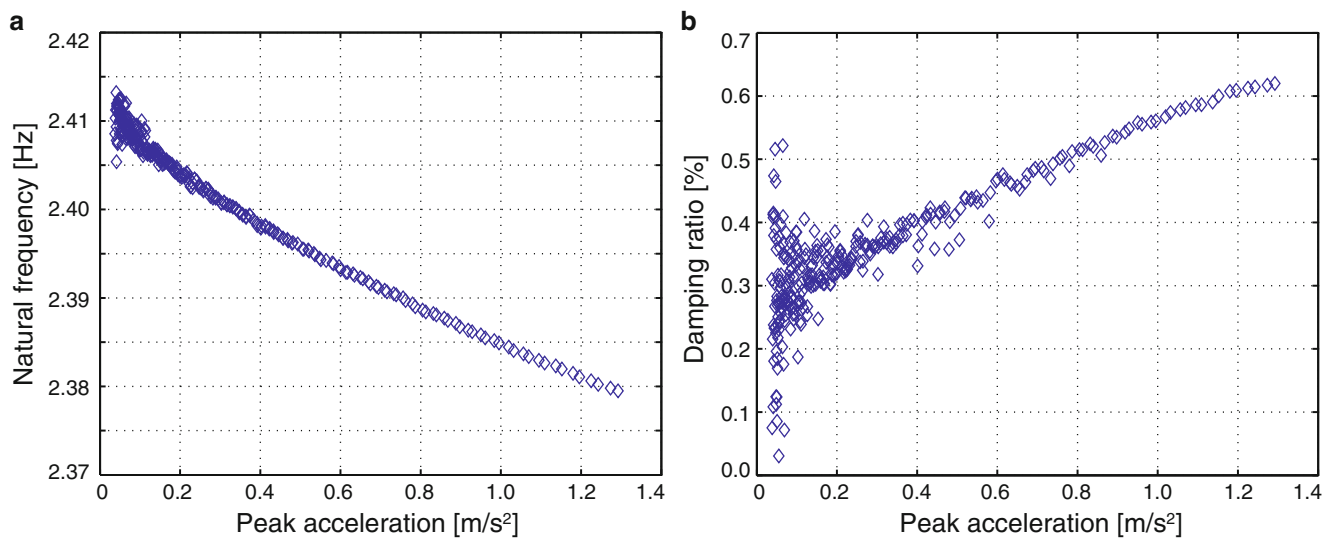


Fig. 41.6 Amplitude dependency of (a) natural frequency and (b) damping ratio in the fundamental mode of vibration

The natural frequency and damping ratio were extracted from the free vibration decay. To check how they change with vibration amplitude, every four successive cycles were analysed. Figure 41.6 shows that the natural frequency decreases and the damping ratio increases with increase in the vibration amplitude. Nevertheless, the maximum achieved value of the damping ratio is still quite low, which ensures the lively behaviour of the structure necessary for the interaction studies. In future tests bespoke dampers will be installed on the bridge (thanks to a collaboration with Maurer Sohne, Germany) to alter the vibration level when required. In addition, the natural frequency of the bridge will be tuned by moving the supporting frames. These alternations will allow a range of different conditions to be investigated.

Assuming the dynamic modulus of elasticity for concrete to be 8 GPa higher than the static modulus [11] ($E_d = 45$ GPa) the calculated natural frequency of the first mode is 2.2 Hz on the current span of 16.2 m. This result suggests that the actual dynamic stiffness of the structure is higher than that assumed in calculations. This will be studied in the future by calibrating an FE model against the experimentally determined natural frequencies and mode shapes for multiple vibration modes.

41.7 Conclusions

The laboratory bridge described in this paper has been constructed to provide a facility for studying pedestrian interaction with lively low-frequency bridges. The design requirements have been fully met by designing a composite steel-concrete bridge with total length of 19.9 m and a 2 m wide deck. The static behaviour over the first six months of the bridge life suggests that the short term flexural stiffness is larger than expected, while the medium-term stiffness (after 60 days of exposure to the load due to self-weight) is 10% lower than initially assumed. The latter shows that a more accurate prediction of the creep and shrinkage effects remains a challenge, at least on this extremely slender structure. The dynamic tests show that the fundamental vibration mode possesses both targeted properties: a low frequency and a low damping ratio. Meeting the design criteria with respect to the dynamic behaviour of the structure, and having an opportunity to further tune the dynamic properties by changing the span length and adjusting the damping level, make the bridge an ideal facility for experimental studies of human interactions with lively structures.

Acknowledgements We would like to acknowledge financial support from the UK Engineering and Physical Sciences Research Council (Ref no. EP/I03839X/1: Pedestrian Interaction with Lively Low-Frequency Structures). We wish to thank the UG and PG students at the University of Warwick for help with the casting the concrete deck; and Dr Benoit Jones of the University of Warwick and Mr Nicholas Farrell of Cemex for their practical help and advice during the casting process. We would also like to acknowledge technical help provided within the School of Engineering by Messrs Colin Banks, Chris Fountain, Juan Munoz Leal, Paul Tomlin, Ian Baylis and Graham Canham in relation to various phases of the project. The first author is also grateful to Dr Ninoslav Pešić for discussions related to some aspects of the design.

References

1. Dallard P, Fitzpatrick AJ, Flint A, Le Bourva S, Low A, Ridsdill-Smith RM, Willford M (2001) The London Millennium Footbridge. *Struct Eng* 79(22):17–33
2. Griffin MJ (1996) *Handbook of human vibration*. Academic, London
3. Macdonald JHG (2009) Lateral excitation of bridges by balancing pedestrians. *Proc Roy Soc A* 465:1055–1073
4. Ingolfsson ET, Georgakis CT, Ricciardelli F, Jonsson J (2011) Experimental identification of pedestrian-induced lateral forces. *J Sound Vibr* 330(6):1265–1284
5. Živanovic S, Pavic A, Ingolfsson ET (2010) Modelling spatially unrestricted pedestrian traffic on footbridges. *ASCE J Struct Eng* 136(10):1296–1308
6. BS 1881-116: 1983 (1998) *Testing concrete—Part 116: Method for determination of compressive strength of concrete cubes*. British Standards Institution
7. BS 1881-118: 1983 (1998) *Testing concrete—Part 118: Method for determination of flexural strength*. British Standards Institution
8. BS 1881-117: 1983 (1998) *Testing concrete—Part 117: Method for determination of tensile splitting strength*. British Standards Institution
9. BS EN 1992-1-1:2004 (2004) *Eurocode 2: Design of concrete structures—Part 1-1: General rules and rules for buildings*. British Standards Institution
10. BS EN 1994-2:2005 (2010) *Eurocode 4—Design of composite steel and concrete structures—Part 2: General rules and rules for bridges*. British Standards Institution
11. Johnson RP (2004) *Composite structures of steel and concrete: beams, slabs, columns, and frames for buildings*. Blackwell Publishing, Oxford

Chapter 42

Experimental Results from a Laboratory Test Program to Examine Human-Structure Interaction

Kelly A. Salyards and Nicholas C. Noss

Abstract Assembly-type structures, subjected to crowd-induced rhythmic excitation, are typically designed to avoid excessive vibration. Most current design guidance recommends using the dynamic properties of the empty structure to assess the susceptibility of a given design to vibration. This recommendation does not incorporate the effects of human-structure interaction where the dynamic properties of the combined system are different from that of the empty structure. To assess the consequences of this recommendation, an experimental study was completed to identify the effects of human-structure interaction on the dynamic properties of the empty structure. The study investigated the influence of posture, mass ratio, and natural frequency of the structure when considering human-structure interaction of a passive crowd. The results of this study are presented and discussed with respect to the prediction of the dynamic response of a structure when the human-structure interaction effects are incorporated or neglected. Because it is likely that the dynamic response of the structure will be overestimated when utilizing the properties of the empty structure, a method for appropriately incorporating the effects of human-structure interaction is needed. An overview of the methods utilized in the study is presented and the results are examined to improve the understanding of the influential factors involved in human-structure interaction.

Keywords Vibration serviceability • Human occupants • Human-structure interaction • Dynamic modeling

42.1 Introduction

Assembly-type structures capable of supporting large crowds are designed for both strength and serviceability limit states to ensure the expected performance of the structure when subjected to a wide range of design loading scenarios. One unique loading scenario for this type of structure is rhythmic excitation induced by the crowd occupying the structure. To prevent excessive vibration which may be disturbing to the occupants, the structure should be designed to limit the response of the structure such that objections from the occupants are unlikely. Current guidance in the United States [1] utilizes the dynamic properties of the empty structure to estimate the response of the occupied structure for comparison with acceptable levels of response. This approach is typically effective in conservatively predicting the response of the structure due to rhythmic excitation. However, this approach neglects the effects of the dynamic interaction between the human occupants and the structure, commonly referred to as human-structure interaction, which may reduce the response. The occupants act as a dynamic spring-mass-damper system attached to the empty structure and the dynamic response of the combined system is influenced by the characteristics of both the occupants and of the structure. In neglecting the effects of the occupants, the significant damping associated with the human occupants is not taken into account when predicting the response of the occupied system to a dynamic load. It is possible that the dynamic response is overestimated when utilizing the properties of the empty structure instead of the occupied structure. An improved understanding of human-structure interaction is required before utilizing the effects of human-structure interaction (HSI) in the structural design process.

K.A. Salyards (✉)

Department of Civil and Environmental Engineering, Bucknell University, Lewisburg, PA 17837, USA

e-mail: kas046@bucknell.edu

N.C. Noss

Dawood Engineering, Inc., Grantville, PA 17028, USA

e-mail: ncn001@bucknell.edu

The experimental study described herein aims to identify the dynamic properties of both the empty and occupied conditions of a laboratory structure designed with variable configurations to improve the current understanding of human-structure interaction. The results presented focus on the effects of human-structure interaction produced by passive standing occupants. The occupants of a structure can be categorized as passive or active based on their activity. Passive refers to occupants who remain in constant contact with the structure and do not induce a dynamic load on to the structure as they are primarily stationary, standing or seated. Active refers to occupants who may or may not remain in contact with the structure while inducing a dynamic load through activities such as jumping or bobbing. A brief overview of previous research of human-structure interaction is presented to highlight the similarities and differences between the current study and previous experimental studies. The experimental and analytical techniques used in this study are described. The experimental results are summarized and the potential implications are identified.

42.2 Background

Human-structure interaction was first acknowledged by Lenzen in 1966 through an experimental study at the University of Kansas [2] in which an increase in damping and a decrease in natural frequency were identified when a steel joist supported floor was occupied by human occupants. The decrease in natural frequency was similar to the results produced when modeling the occupants as additional mass, but the effects on damping were not replicable. Lenzen termed the phenomenon human-structure interaction, but the simple approach of modeling occupants as applied mass continued for many years. After another observation of the effects of human-structure interaction when monitoring an occupied grandstand structure at Twickenham [3], several other experimental tests on laboratory structures were performed: Ellis and Ji in 1994 [4], Brownjohn in 1999 [5], and Harrison et al. in 2006 [6]. Ellis and Ji utilized a concrete beam and a single, passive, standing occupant [4]. Results indicated an increase in damping and an unexpected increase in frequency. Brownjohn used a precast concrete plank structure and a single, passive occupant demonstrating a variety of postures [5]. The results indicated that the occupant's posture influenced the damping and frequency of the occupied system. To investigate human-structure interaction associated with active occupants, a flexible structure was constructed at the University of Manchester where jumping and bobbing exercises were performed while evaluating the system properties [6]. Each of these laboratory tests involved a single occupant on a laboratory structure exhibiting a specific natural frequency of the empty structure. Although useful in identifying the dynamic characteristics of a single individual and aiding in the understanding of human-structure interaction for discrete combinations of empty structure properties and occupant properties, an experimental program which provides an understanding of human-structure interaction for a wider range of structure and occupant properties is needed. The experimental study described herein addresses a segment of this need by examining human-structure interaction of a group of passive standing occupants over a wider range of empty structure frequencies.

42.3 Overview of Study

To examine the effects of human-structure interaction on a wider range of structural natural frequencies and for larger groups of passive occupants, a laboratory structure was designed and constructed. The structure is a cantilevered steel structure supporting a concrete plank surface as shown in Fig. 42.1. The supports of the cantilevered steel structure are adjustable to vary the natural frequency of the empty structure from 4.21 Hz through 8.05 Hz. The concrete plank surface is designed to accommodate nine occupants standing comfortably while providing sufficient space to accommodate nine seated occupants in the future. The cantilevered steel beams are hollow structural steel members connected by a rigid frame at the cantilever tip. The supports are adjusted by bolting to the top flange of a wide-flange support beam structure at 4 in. increments along its length. Additional information about the design, construction, initial finite element model, and tuning process is provided by Noss and Salyards [7].

The experimental study involved the comparison of the dynamic properties of the empty structure and the occupied structure for a variety of different structural configurations, occupant group sizes, and occupant postures. The dynamic properties of the empty structure in each structural configuration, shown in Fig. 42.2, were determined using traditional experimental modal analysis and are summarized in Table 42.1. The natural frequency of the first mode will be used to identify and refer to each structural configuration. The selected configurations represent the frequency range of interest when considering human-structure interaction for grandstand structures.

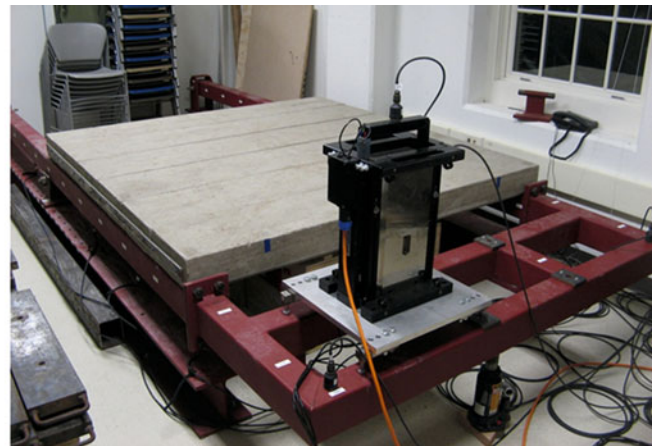
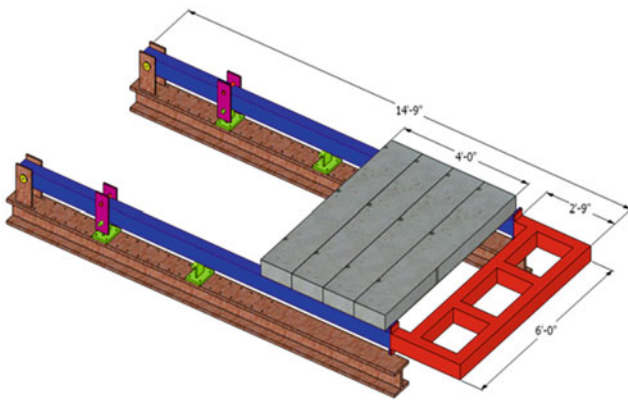


Fig. 42.1 Model and photograph of laboratory test structure

Fig. 42.2 Structural configurations

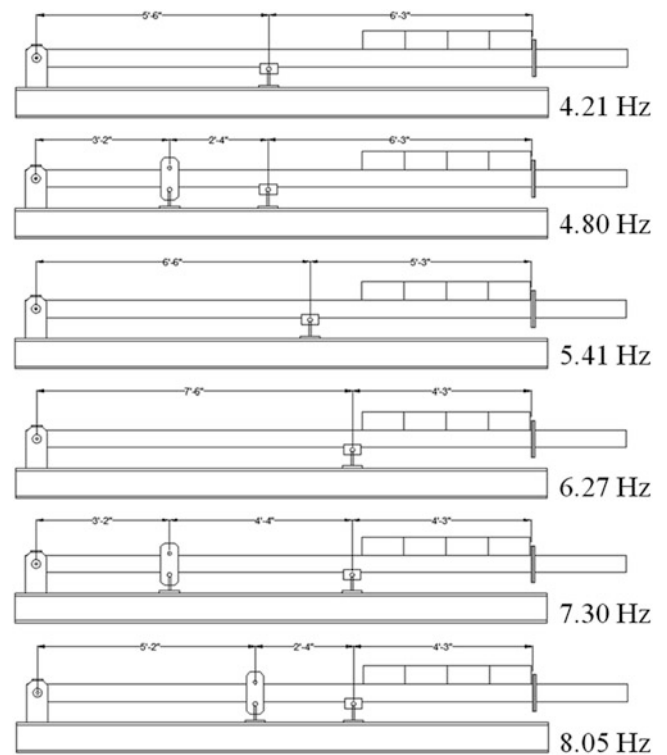
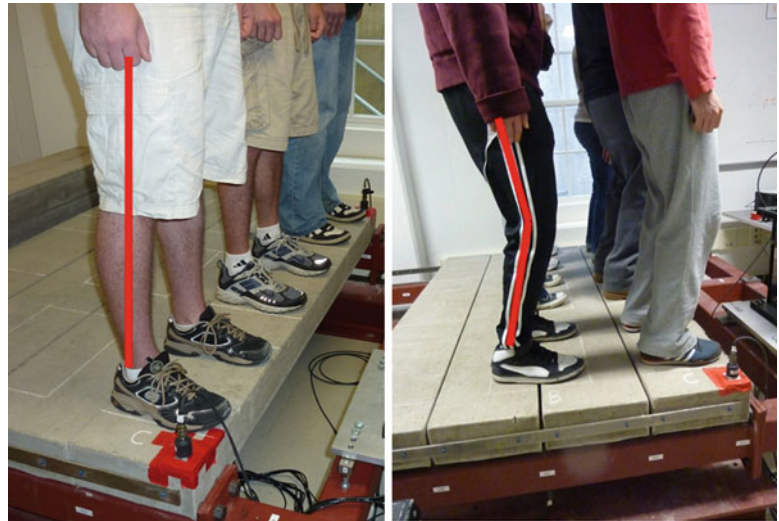


Table 42.1 Experimental frequency and damping values for the first mode of vibration

Dynamic properties of the empty structure				
Frequency (Hz)		Damping (%)		
Average	Std. dev.	Average	Std. dev.	Sample size (n)
4.21	0.01	0.31	0.10	10
4.80	0.01	0.23	0.00	2
5.41	0.02	0.40	0.08	8
6.27	0.01	0.51	0.06	10
7.30	0.08	0.61	0.01	4
8.05	0.00	1.18	0.00	2

Fig. 42.3 Postures analyzed:
knees straight and knees bent



The occupied test scenarios were selected considering both mass ratio and posture. Mass ratio is defined as the mass of the crowd to the mass of the empty structure. The mass ratios of previous laboratory tests were low (< 0.20) as they involved only a single occupant. Dougill [8] indicated that the mass ratio of assembly-type structures typically fall between 0.25 - 0.75. To confirm this range, mass ratios were calculated by evaluating the fully occupied conditions of several grandstand structures. The calculated mass ratios for these six structures ranged from 0.27 to 0.68 when assuming an average occupant weight. This aligns well with the range identified by Dougill and this became the target mass ratio range for the occupied tests. Six mass ratios from 0.17 to 0.56 were achieved through the selected test scenarios. In calculation of the mass ratio, the mass of the structure was taken as the entire mass of the laboratory structure because over 90% of the mass is active in the first mode of vibration, which is assumed to dominate the dynamic response.

Posture of the occupants was also considered as previous research has indicated that it influences the resulting system damping and frequency. Two standing postures were utilized: standing with knees straight and standing with knees bent as demonstrated in Fig. 42.3 similar to testing performed by Brownjohn [5]. Seated postures have not yet been analyzed as the type of seating and how it is attached to the structure are believed to affect the dynamic interaction. Each structural configuration and occupant group size was analyzed in both postures.

42.4 Experimental Testing Procedures

The experimental testing was completed in six sessions, one for each mass ratio. A total of 18 different participants were involved in a series of 18 tests as detailed in Table 42.2. Because human participants are involved in this study, approval was obtained from the Institutional Review Board (IRB) and a consent form was collected from each participant prior to testing. The maximum vibration that the occupants were exposed to throughout the testing was 0.1 g to avoid any significant discomfort or panic.

For each structural configuration, experimental modal analysis was performed on the empty structure before and after the occupied tests to verify that the dynamic properties of the adjustable structure were consistent through the test. The experimental modal analysis utilized a swept-sine force input generated by an APS Dynamics Model 400 electrodynamic shaker located on the steel frame at the end of the cantilever. The force input was determined by measuring the acceleration of the armature of the shaker and utilizing the oscillating mass. The structural response was measured using PCB piezoelectric accelerometers (Model 393A03) mechanically attached to the steel cantilevered beams at 24 in. increments along the length. Additional information on the experimental testing can be found elsewhere [7].

Upon completion of the initial empty structure testing for a given structural configuration, the occupants were assigned to specific locations on the structure to balance the loading considering the center of mass of the occupant group. The postures were described to the occupants and a trial was performed to familiarize the volunteers with the level of vibration that was to be expected. Each test run consisted of the excitation of the occupied structure with five consecutive chirp signals linearly averaged together. The input level of the force was adjusted based on the group size to maintain an acceleration response of

Table 42.2 Experimental test scenarios

Number of occupants	Total occupant weight (lbs)	Mass ratio	Structural configuration (Hz)			
			4.21	5.41	6.27	7.30
2	350	0.167	4.21	5.41	6.27	
3	590	0.281	4.21	5.41	6.27	
4	760	0.362	4.21	4.80	5.41	6.27
6	918	0.437	4.21	5.41	6.27	7.30
7	1185	0.564	4.21	6.27	8.05	

the structure at the cantilever tip between 0.08-0.1 g. This adjustment allowed a near-maximum acceleration to be consistently achieved and also maintained the response of the structure within a range that was determined to behave linearly. Three test runs were performed for each test scenario which included a specific posture, mass ratio, and structural configuration. Upon completion of the occupied testing, the participants exited the structure and the empty structure was analyzed again.

The data collected was analyzed real-time utilizing IOTech's ez-Analyst software to construct frequency response functions (FRF) from the input and output response of the occupied structure. The FRFs from each test run were analyzed using global curve-fitting techniques in Vibrant Technology's ME'scope software. The modal properties of frequency, damping, and mode shape for each test run were determined and compared to the modal properties of the empty structure.

42.5 Experimental Results

The experimental results are presented in the form of a comparison of the first mode of vibration of the occupied structure to the first mode of vibration of the empty structure. The first mode is the focus for two reasons: 1) the dynamic response of a structure is typically assumed to be dominated by a single mode of vibration for serviceability assessment, and 2) the effects of human-structure interaction are more evident in the first mode. Although the motivation of this study for serviceability design is the increase in damping, the results include the effects of human-structure interaction on both natural frequency and damping because a thorough understanding of human-structure interaction must be gained before utilizing the increased damping effects for response estimation.

It is important to note that the FRFs generated from the occupied tests exhibit more variability between the three test runs than the corresponding three test runs from the empty structure. This increased variation is attributed to the inability of the occupants to remain absolutely stationary throughout the testing. Curve-fitting techniques were applied to each of the three test runs for each scenario. The resulting natural frequency and damping properties are presented as an average of the three test runs along with the corresponding standard deviation. In addition, each test run consists of the average of five swept-sine signals and the coherence is assessed near the first mode. Coherence values of 0.9 are deemed acceptable for traditional experimental modal analysis of an empty structure. All test runs from this study exhibited coherence values greater than 0.9 around the first mode except for the tests involving the 4.21 Hz structural configuration. At this structural configuration, the coherence values were greater than 0.8 and the results were considered carefully with respect to the overall findings of this study.

The experimental results obtained in this study exhibit similar trends to those in previous studies on human-structure interaction. All results indicate an increase in damping of the occupied system with the level of increase depending on posture. With respect to the natural frequency of the first mode of vibration for the occupied system, three outcomes were identified similar to previous studies. Similar to Lenzen's results [2], some scenarios yielded a decrease in the lowest natural frequency that is not accurately modeled by an equivalent mass. Other scenarios yielded a slight increase in the frequency, similar to results from Ellis and Ji [4]. Yet other scenarios generated a lower first mode and an additional mode between the first and second modes, similar to results from Ellis and Ji [3].

The experimental results for the natural frequency of the occupied structure are presented normalized to the frequency of the empty structure and plotted with respect to the various mass ratios examined. In addition, the results of a finite element model representing the occupants modeled as an equivalent mass are presented. The final data points presented are developed through an occupant model recommended by the Joint Working Group [9] where the occupants are modeled as a spring-mass-damper system attached to the structure. The Joint Working Group specifies a natural frequency (5 Hz) and damping (40% critical) associated with the occupant model. Utilizing the known mass of the occupants in the experimental study, the spring stiffness is calculated from the specified frequency. The spring-mass-damper system is attached to the finite element model and the dynamic properties of the combined system determined from this model are presented.

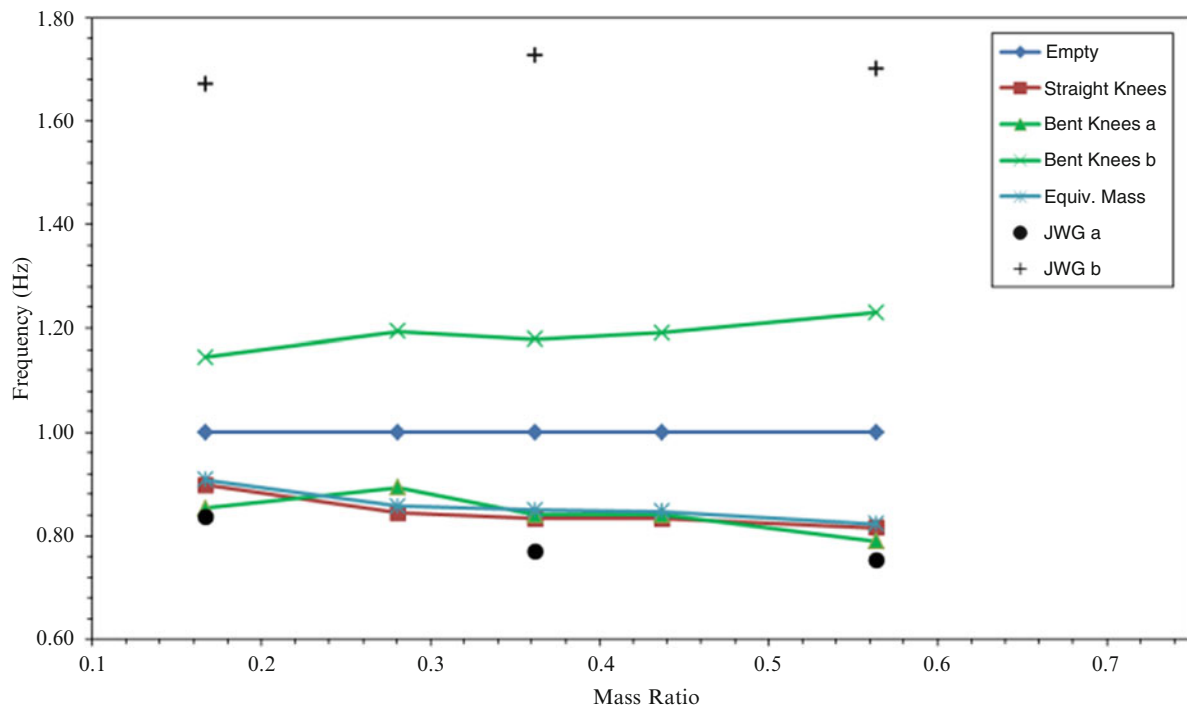


Fig. 42.4 Frequency results, normalized to the empty structure frequency, for the 4.21 Hz configuration

Table 42.3 Damping results for the 4.21 Hz configuration

Mass ratio	Experimental damping (% critical) (mean (SD))				FE damping (% critical)	
	Empty	Straight knees	Bent knees a	Bent knees b	JWG a	JWG b
0.167	0.31 (0.09)	3.1 (0.3)	8.5 (2.3)	7.5 (1.2)	6.4	1.6
0.281	2.8 (0.4)	11.7 (3.7)	6.7 (0.5)	–	–	–
0.362	3.4 (0.4)	6.5 (3.2)	10.8 (0.4)	6.5	13.8	–
0.437	2.9 (0.2)	7.0 (3.0)	11.0 (1.6)	–	–	–
0.564	4.5 (0.6)	7.3 (3.0)	11.4 (2.0)	6.0	11.7	–

42.5.1 4.21 Hz Structural Configuration

For the 4.21 Hz structural configuration, the results indicate that neither the equivalent mass nor the Joint Working Group model accurately represents the dynamic behavior of this occupied structure. A comparison is made with respect to both the first mode of vibration and the damping associated with this first mode. For the 4.21 Hz configuration, the decrease in frequency for the range of mass ratios studied is similar to the decrease predicted by the equivalent mass model and the Joint Working Group model as shown in Fig. 42.4. The decrease in frequency (10-20% of the empty structure frequency) may be insignificant when considering serviceability design, but it is critical in understanding the human-structure interaction phenomenon. When the structure was occupied with occupants in the bent knees posture, an additional mode of vibration was detected. This result is similar to the Joint Working Group model that also predicts two modes and results from earlier studies [3]. In terms of damping, the equivalent mass model does not address the increase in damping and the Joint Working Group model overestimates the damping associated with the straight knees posture as expressed in Table 42.3. The damping increase is nearly an order of magnitude over the empty structure for all mass ratios examined.

42.5.2 5.41 Hz Structural Configuration

For the 5.41 Hz structural configuration, the results again indicate that neither the equivalent mass nor the Joint Working Group model accurately represents the dynamic behavior of this occupied structure. For the 5.41 Hz configuration, the decrease in frequency for the range of mass ratios studied is between the decrease predicted by the equivalent mass model

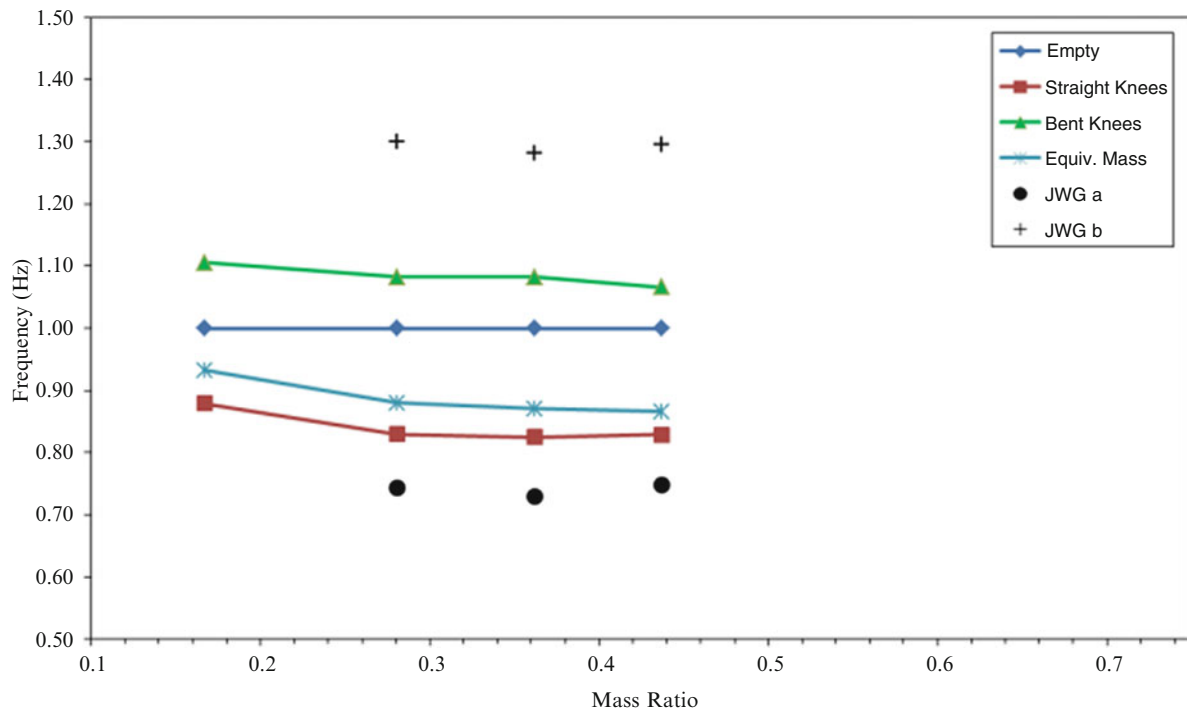


Fig. 42.5 Frequency results, normalized to empty structure frequency, for 5.41 Hz configuration

Table 42.4 Damping results for the 5.41 Hz configuration

Mass ratio	Experimental damping (% critical) (mean (SD))			FE damping (% critical)	
	Empty	Straight knees	Bent knees	JWG a	JWG b
0.167	0.40 (0.07)	5.4 (0.6)	5.2 (1.3)	–	–
0.281	5.5 (0.3)	5.6 (0.4)	16.3	14.5	
0.362	7.4 (0.3)	4.7 (0.4)	17.2	16.6	
0.437	7.7 (0.5)	6.5 (0.6)	16.7	13.7	

and the Joint Working Group model as shown in Fig. 42.5. In terms of damping, the equivalent mass model does not address the increase in damping and the Joint Working Group model again overestimates the damping associated with the straight knees posture as expressed in Table 42.4.

42.5.3 6.27 Hz Structural Configuration

The 6.27 Hz structural configuration yields similar results with one interesting difference. A second mode was identified for the straight knees posture, rather than the bent knees posture. One mode exhibits a decrease in frequency while the second exhibits an increase. The decrease in frequency of the first mode (10-25% of the empty structure frequency) for the range of mass ratios studied is between the decrease predicted by the equivalent mass model and the Joint Working Group model as shown in Fig. 42.6. Similar results for damping are presented in Table 42.5.

42.6 Discussion and Summary

The experimental results in this study provide further evidence demonstrating the human-structure interaction phenomenon for passive occupants while providing an additional comparison of occupied test results with the equivalent mass model and the Joint Working Group model. The results expand upon the current, limited data available for occupied structures for a wider range of empty structure frequencies in a range applicable for assembly-type structures. The breadth of mass ratios examined in this study also expands upon the current, limited data available.

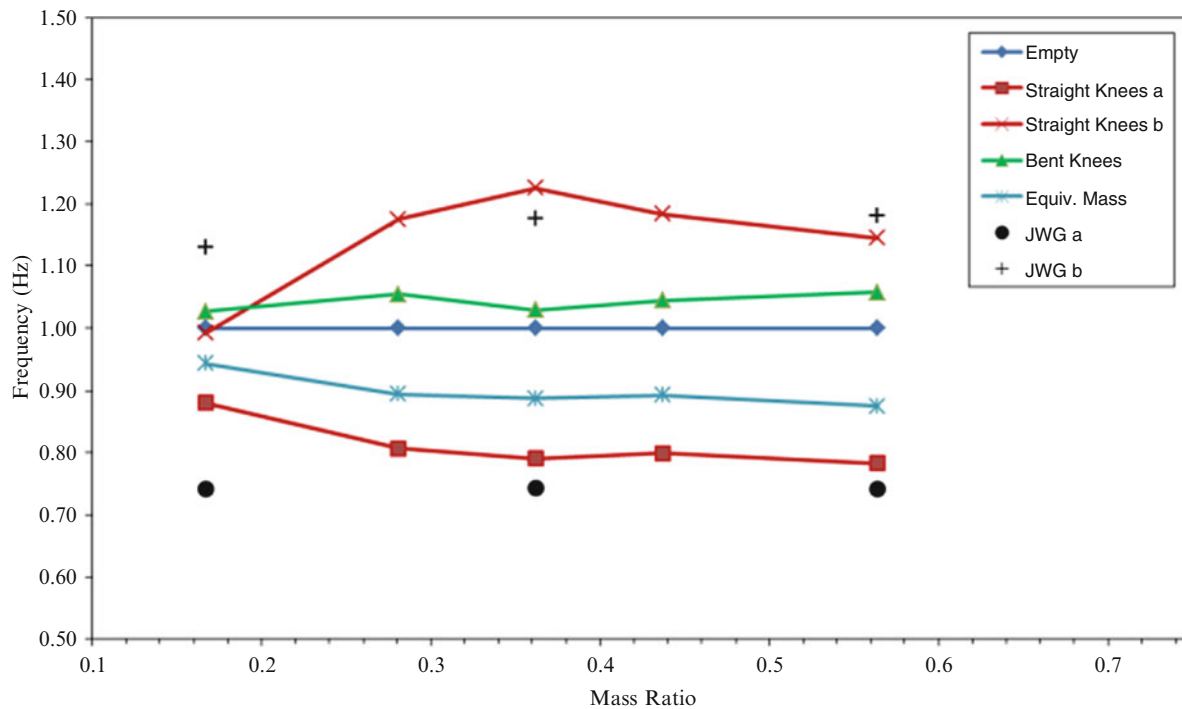


Fig. 42.6 Frequency results, normalized to the empty structure frequency, for the 6.27 Hz configuration

Table 42.5 Damping results for the 6.27 Hz configuration

Mass ratio	Experimental damping (% critical) (mean (SD))				FE damping (% critical)	
	Empty	Straight knees a	Straight knees b	Bent knees	JWG a	JWG b
0.167	0.51 (0.06)	10.1 (2.1)	7.3 (1.8)	3.6 (2.1)	0.3	16.7
0.281	11.4 (0.5)	6.5 (1.2)	5.5 (1.1)	–	–	–
0.362	12.4 (1.3)	12.8 (1.4)	1.6 (0.9)	0.3	17.7	–
0.437	11.5 (1.6)	10.2 (2.4)	4.9 (0.6)	–	–	–
0.564	7.5 (4.4)	7.1 (2.1)	4.3 (0.1)	0.3	17.4	–

All of the experimental results demonstrate the expected increase in damping of the occupied system over the empty structure. The increase in damping on this particular, lightly damped structure is significant. Although it appears to be depended on both posture and frequency of the empty structure, the damping of the occupied system for occupants standing with straight knees, is increased to an average of 6.8% critical damping with a minimum of 2.8%. Considering the lightly damped nature of the empty test structure (<0.5%), this increase in damping is significant and is likely to have a significant impact on the predicted dynamic response of this particular structure. However, this empty test structure exhibits considerably lighter damping than full-scale structures. Because of this difference, it is uncertain if the occupants would produce the same significant increase on a more typically damped structure (2-3%). Additional testing is needed. With respect to posture, the increase in damping is more significant for bent knees when considering the 4.21 and 5.41 Hz configurations. The increase in damping for straight knees is more significant when considering structures with frequencies greater than 5.41 Hz. If the natural frequency of the occupant with knees bent is less than the natural frequency of the occupant with knees straight, the results suggest that the damping of the occupant may have a larger effect on the damping of the occupied system when the frequency of the occupant aligns with the frequency of the structure. In this study, the occupant model (5 Hz) aligned most closely with the 5.41 Hz structural configuration and the damping of the occupied system was at its greatest. As the difference between the occupant model frequency (5 Hz) and the structure frequency increased, the damping decreased. The damping results from the application of the Joint Working Group model estimate more significant damping in the occupied structure than the experimental results in this study indicate except at the 6.27 Hz configuration.

The change in natural frequency produced by the occupants cannot simply be attributed to the increased mass as shown with a direct comparison with the equivalent mass results. The results also indicate that the Joint Working Group model predicts a larger decrease in the natural frequency of the first mode than the experimental tests performed in this study. The combination of differing damping and frequency changes from the Joint Working Group model and the experimental results of this study indicate that more studies are required to accurately represent the human-structure interaction phenomenon.

Additional testing is required to examine the human-structure interaction involving a seated posture. Previous studies indicate that the type of seating, bench seating versus individual seats and how it is connected to the structure, influence the effects of human-structure interaction. For this reason, consideration of passive occupants in the seated posture requires more attention than the current study examining standing passive occupants. In addition, further testing is required for larger groups of occupants, both on this test structure and on larger structures. Monitoring of assembly-type structures in service can provide insight for larger group sizes and a true representation of a crowd composed of both passive and active occupants. This would provide data that is not able to be replicated in the laboratory and expand upon the small size of the groups considered in this study.

The understanding of human-structure interaction is greatly improved by the model recommended by the Joint Working Group. It provides a method for predicting the various effects of human-structure interaction including both increases and decreases in the natural frequency of the occupied system as well as the significant increase in damping. The experimental results of this study, however, are not accurately represented by the model. It is possible that the model is not effective for representing small-scale structures such as the test structure involved in this study. It is also possible that the occupant model could be refined to more accurately represent the dynamic behavior of the occupied structure, but this requires further testing and application of the Joint Working Group model to more full-scale structures.

References

1. Murray TM, Allen DE, Ungar EE (1997) Floor vibrations due to human activity. American Institute of Steel Construction (AISC), Print. Steel Design Guide Series, No. 11
2. Lenzen KH (1966) Vibration of steel joist-concrete slab floors. Eng J AISC 6th ser. 3.133
3. Ellis BR, Ji T (1997) Human-structure interaction in vertical vibrations. Proc Inst Civil Eng Struct Build 122(1):1-9
4. Ellis BR, Ji T (1994) Floor vibration induced by dance-type loads: verification. Struct Eng 72(3):45-50
5. Brownjohn JMW (1999) Energy dissipation in one-way slabs with human participation. Proceedings of Asia-Pacific vibration conference 1999, Nanyang Technological University, Singapore, vol. 1
6. Harrison RE, Yao S, Wright JR, Pavic A, Reynolds P (2006) Humans bouncing on flexible structures—effect of structural properties. Proceedings of international modal analysis conference (IMAC) XXIV, St. Louis, MO
7. Noss NC, Salyards KA (2012) Development of a laboratory test program to examine human-structure interaction. Proceedings of international modal analysis conference (IMAC) XXX, Jacksonville, FL
8. Dougill JW (2005) Recommendations for design of grandstands subject to dynamic crowd excitation. Proceedings of 6th European conference on structural dynamics (EURODYN 2005). European Association for Structural Dynamics (EASD), Munich, Germany, pp 491-496
9. Joint Working Group (2008) Dynamic performance requirements for permanent grandstands subject to crowd action. IStructE/DTLR/DCMS working group on dynamic performance and design of stadia structures and seating decks, December

Chapter 43

Alleviation of Wind-induced Vibrations of Railings in a Building

C.M. Hou and W.D. Zhu

Abstract It was observed that wind-induced vibrations had created destructive effects on corner balcony railings in an oceanfront condominium building. The vibrations of the railings caused disconnections of welds at the ends of the pickets, and noise was generated, which created discomfort to the residents of the building. This paper presents a method to mitigate the wind-induced vibrations and noise of the balcony railings. The noise generation mechanisms were investigated; buffeting and vortex-induced vibration were identified as the two main mechanisms. A finite element (FE) model of a railing was developed using commercial FE software ABAQUS. The FE model was validated by modal testing results and used as a basis for later modifications. Design modifications were made for the railing and simulated using ABAQUS; increasing the stiffness of the railing was proposed as a solution based on the FE simulation results and the constraints imposed. A modified railing was installed on one of the corner balconies according to the solution and tested. The experimental results and on-site monitoring on the modified railing indicate that the noise issue has been resolved, and all of the affected railings were demolished and replaced with the modified railings.

Keywords Buffeting • Vortex-induced vibration • Modal testing • Finite element modeling • Wind measurement

43.1 Introduction

Structures in contact with fluid flow are subject to flow-induced forces and flow-induced vibrations. These vibrations can be desirable as well as destructive, which can lead to fatigue or structural failure. Wind is a common type of fluid flow that can cause wind-induced vibrations. It was observed that wind-induced vibrations had created destructive effects on corner balcony railings in an oceanfront condominium building in Maryland. The railings were installed between April and May 2008, and they have the same overall dimensions. Typical balcony railings are shown in Fig. 43.1a. The top-view schematic of a typical railing along the center line of the plaza is shown in Fig. 43.1b.

The railings consist of five main components: plaza, snap, punch rail, picket, and post. The side-view schematic of a typical railing is shown in Fig. 43.2a. These components are made of Aluminum 6005-T5 or Aluminum 6063-T5, and they have the same thickness of 0.00238 m. The top of the post is 1.04 m above the balcony concrete surface according to the building code. The pickets are connected to the punch rails by welding along the out-of-plane direction as shown in Fig. 43.2a. The punch rails are welded to the posts continuously through the long sides while the snaps are not. The posts are embedded into the balcony concrete. The vibrations of the railings under certain wind conditions have caused disconnections of the welds at the ends of the pickets. Figure 43.2b shows some pickets with epoxy glue applied in an attempt to reduce the noise after the welding was damaged due to wind-induced vibrations.

Noise was noticed around September 2009 by the residents of the building. It was noticed that the noise normally occurred in fall and winter seasons during which the average wind speeds were higher than those in the other two seasons according to wind data from the National Oceanic and Atmospheric Administration (NOAA). The noise has two main components based

C.M. Hou • W.D. Zhu (✉)

Department of Mechanical Engineering, University of Maryland Baltimore County, Baltimore, MD 21250, USA

e-mail: wzhu@umbc.edu

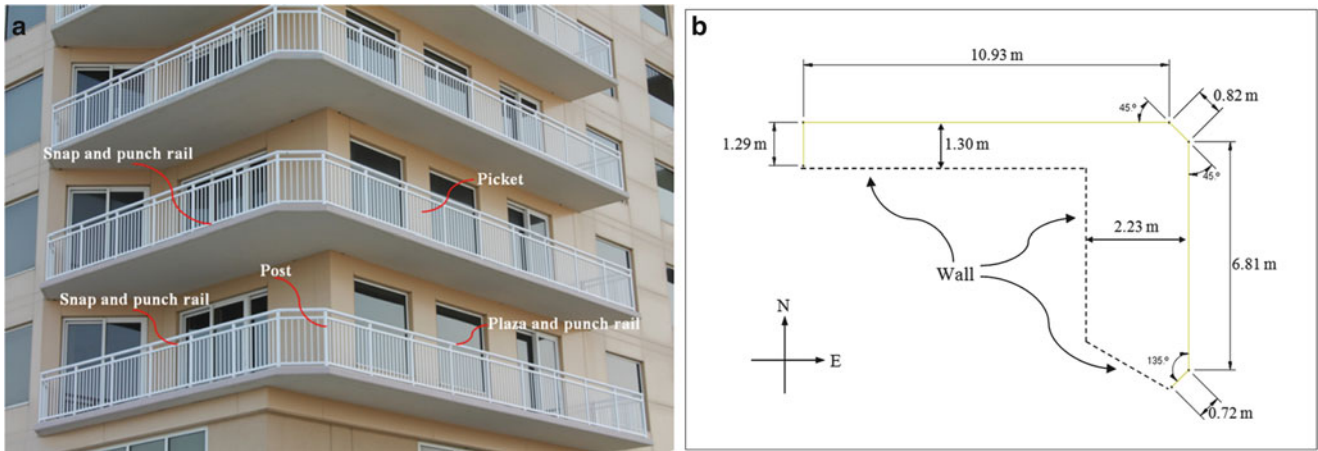


Fig. 43.1 (a) Typical balcony railings with component indicators, and (b) the top-view schematic of a typical railing along the center line of the plaza

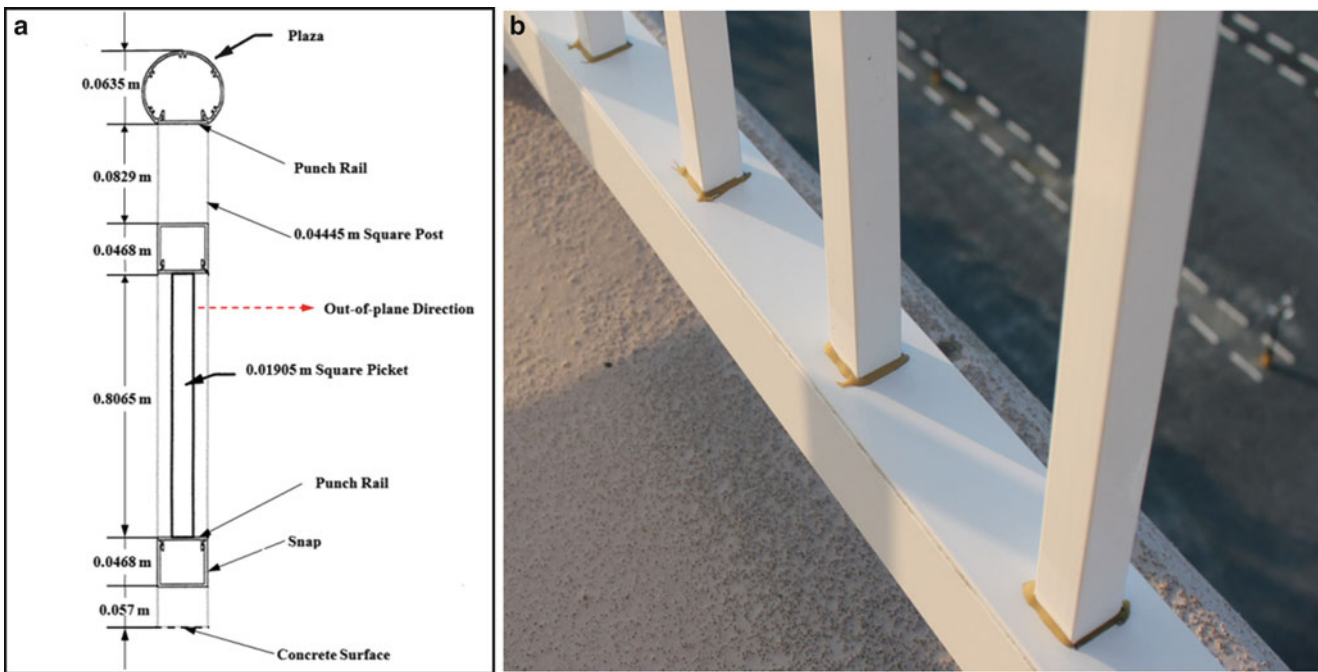


Fig. 43.2 (a) Side-view schematic of a typical railing, and (b) damaged pickets with epoxy glue applied

on observations. One component is impact noise between the pickets and the punch rails where the welding was broken. The other component is humming noise from the vibrating pickets during windy days. The noise has created discomfort to the residents of the building.

The objective of this work is to understand and overcome the noise issue within design constraints. Noise generation mechanisms were investigated by a combination of finite element (FE) modeling of the railing and experimental testing of wind and pertinent railing dynamic characteristics. Buffeting and vortex-induced vibration were identified as the two main mechanisms through the investigation. With design constraints under consideration, increasing the stiffness of the railing to reduce the vibrations from the two mechanisms was proposed to alleviate the noise issue with support from simulation results on the modified railing. The experimental results on the modified railing and on-site monitoring indicate that the modification to the railing has successfully addressed the noise issue.

43.2 Investigation on Noise Generation Mechanisms

Wind loading on a structure is a complex problem with many interactive factors requiring consideration. The flow around a given structure depends on the incident wind properties such as the mean wind velocity and the turbulent fluctuation intensity, the structural geometry and location, and the motion of the structure itself. The flow and the structure are coupled through the force exerted on the structure by the fluid. As the fluid exerts a force on the structure, the structure also exerts an equal but opposite force on the fluid, which may cause the incident fluid to further deflect and alteration of the flow field [1].

The cause of wind-induced noise of the railings can be identified through wind tunnel testing or full-scale measurement. Wind tunnel testing is generally expensive and time consuming. Due to the time and budget constraints, this method was not implemented. To understand the wind conditions and the response of the railings under which noise occurs, measurements of the wind speed and direction and the response of different railing components are needed. Due to the random nature of wind and the distance from the authors' laboratory to the building, it is difficult to perform manned measurements to characterize the wind conditions and the structural response when noise occurs. Remote continuous monitoring of wind conditions and the response of the railing can be useful in understanding the excitation mechanisms. However, due to the lack of necessary equipment from the laboratory, this method was not implemented either.

Instead of wind tunnel testing or full-scale measurement, a combination of FE modeling of the railing and experimental testing of wind and pertinent railing dynamic characteristics was implemented to understand the noise generation mechanisms. Three main mechanisms are studied: buffeting, vortex-induced vibration, and galloping. The phenomenon and the role of each mechanism in noise generation are presented in the remaining parts of this section.

43.2.1 Noise Generation Due to Buffeting

43.2.1.1 Buffeting Phenomenon

Buffeting is the unsteady loading on a structure by velocity fluctuations due to turbulence in the approaching flow. Many structures can be buffeted by wind, and the amplitude of the buffeting response normally increases with the increasing wind speed. The wind speed consists of a mean component and a fluctuating component. The mean component typically contributes to the static deflection of a structure while the fluctuating component typically contributes to the vibration of the structure. Turbulence induced motion can be described as a forced random vibration with a broad spectrum. The response of an elastic structure to turbulent pressure in one mode is typically narrow banded; the majority of the response occurs at a narrow band of frequencies centered about the natural frequency of the structure [1]. For a given structure, large amplitude vibration can occur if the wind fluctuating frequencies are close to the natural frequencies of the structure.

43.2.1.2 FE Model of the Railing

In order to have an idea about the natural frequencies of the railing, a FE model with linear quadrilateral shell elements with reduced integration (S4R) was developed using ABAQUS 6.9EF according to the dimensions provided by the owner of the building. The Young's modulus, Poisson's ratio, and mass density of the railing materials are 69 GPa, 0.33, and 2700 kg/m³, respectively; these parameters are used to define the properties of the elements in the FE model. The posts are assumed to be fixed at the bottom, and the components are connected through "tie" constraints. The FE model of the railing is shown in Fig. 43.3, and the first ten natural frequencies of the railing from the FE model are listed in Table 43.1.

43.2.1.3 Modal Testing on the Railing

To verify the FE model, modal testing was conducted on one of the corner balcony railings. This railing serves as a representative of all the corner balcony railings since all these railings have the same dimensions and assembly setting. The roving hammer method was used; a PCB 086D05 impact hammer was used to excite the structure at pre-selected locations in the out-of-plane direction as shown in Fig. 43.2a. The response of the structure was measured by PCB U352C66 accelerometers at pre-selected locations and gathered by a 36-channel LMS spectrum analyzer. Three impact tests were averaged at every excitation point to ensure repeatable results with a good coherence. The natural frequencies and mode shapes of the railing were extracted from the measured frequency response functions (FRFs) using modal analysis software

Fig. 43.3 FE model of the railing

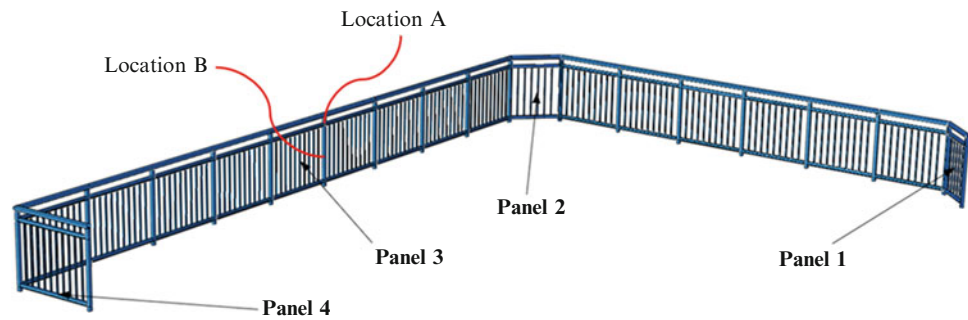


Table 43.1 First ten natural frequencies of the balcony railing from the FE model and experiment and their differences

Mode	FE model frequency (Hz)	Experimental frequency (Hz)	Frequency difference
1	12.260	12.552	-2.33%
2	13.202	13.246	-0.33%
3	14.009	13.956	0.38%
4	16.691	16.977	-1.68%
5	17.336	18.535	-6.47%
6	21.007	20.498	2.48%
7	21.103	21.208	-0.50%
8	22.716	22.400	1.41%
9	23.217	23.192	0.11%
10	24.782	24.735	0.19%

LMS Test.Lab 9b. The first ten measured natural frequencies of the railing are listed in Table 43.1. The first three measured mode shapes of the railing with marked excitation points are shown in Fig. 43.4 along with the corresponding ones from the FE model. It can be seen from Table 43.1 that the maximum difference of the first ten natural frequencies from the FE model and the modal test is less than 6.5%; this provides confidence to use the FE model as a basis for later modifications.

43.2.1.4 Wind Pressure Measurement

Due to the turbulent effect, wind pressure has a mean component and a fluctuating component [2]. To have a qualitative understanding about the approaching wind pressure fluctuation, a PCB 378B02 condenser microphone was used to measure the power spectral density (PSD) of the wind pressure around the balcony railing. The measurement range of the microphone is from 5 to 20000 Hz with ± 1 dB accuracy. This microphone is considered to be good enough for this application since the wind pressure fluctuations below 5 Hz are not of the main interest for the present analysis with the first natural frequency of the railing above 12 Hz. The microphone was placed on top of a tripod and directed to the approaching wind direction. To reduce the interference from the railing, the microphone was placed 2 m above the concrete surface, which is about 0.9 m above the top of the railing. A PCB 079A06 windscreen was used to reduce the effect from the mean pressure component. A Honeywell TE821W weather station was used to measure the average wind speed and direction. The measurements were taken at different locations around the balcony, and the results are similar. Figure 43.5a shows the PSDs of the approaching wind pressure measured with and without the windscreen in log scale with an average wind speed of 4.2 m/s (9.4 mph) during measurement from the north direction. It is noticed from Fig. 43.5a that the windscreen provides substantial reduction of the mean pressure. At low frequencies, both measurements may be questionable because of the measurement range of the microphone. The same measurements are displayed in linear scale from 5 to 80 Hz in Fig. 43.5b. It can be seen from Fig. 43.5b that the fluctuation pressure is essentially monotonically decreasing, which is in agreement with the literature [2].

43.2.1.5 The Role of Buffeting

To understand the buffeting effect of the wind, the responses of the railing were measured in operational conditions. Two PCB U352C66 accelerometers were placed at location A and location B along a post shown in Fig. 43.3. The accelerations at the two locations are shown in Fig. 43.6a with an average wind speed of 6.4 m/s (14.3 mph) during measurement from the northwest direction. The vibration amplitude and duration are considerable at the two locations as depicted in Fig. 43.6a. The PSDs of the accelerations at the two locations are shown in Fig. 43.6b. From Fig. 43.6b, it is noticed that there is one dominant

Fig. 43.4 (a) First, (b) second, and (c) third modes from FE simulation (left) and experiment (right)

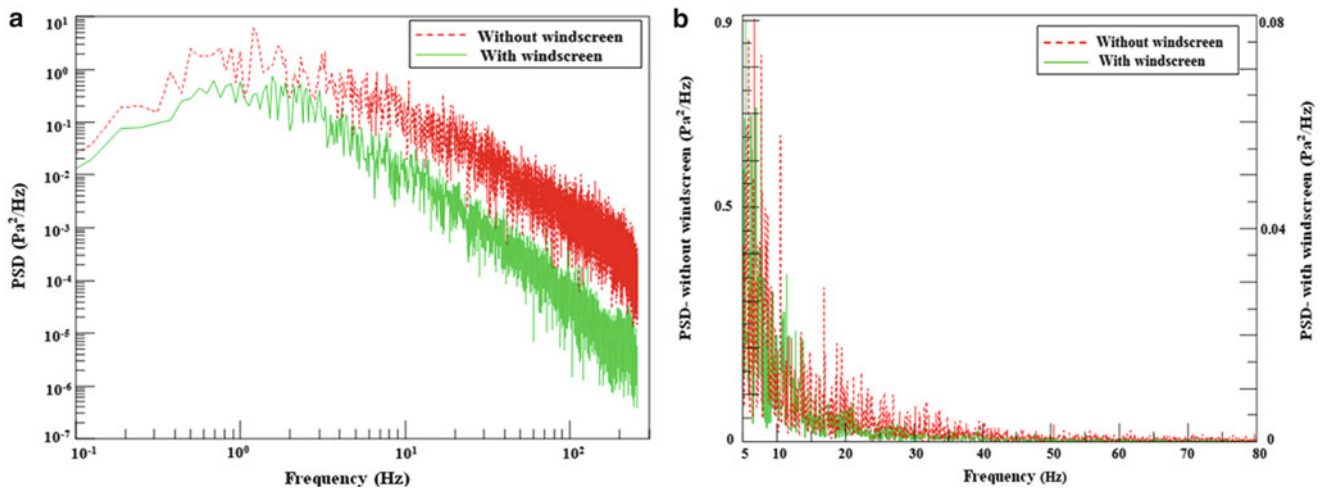
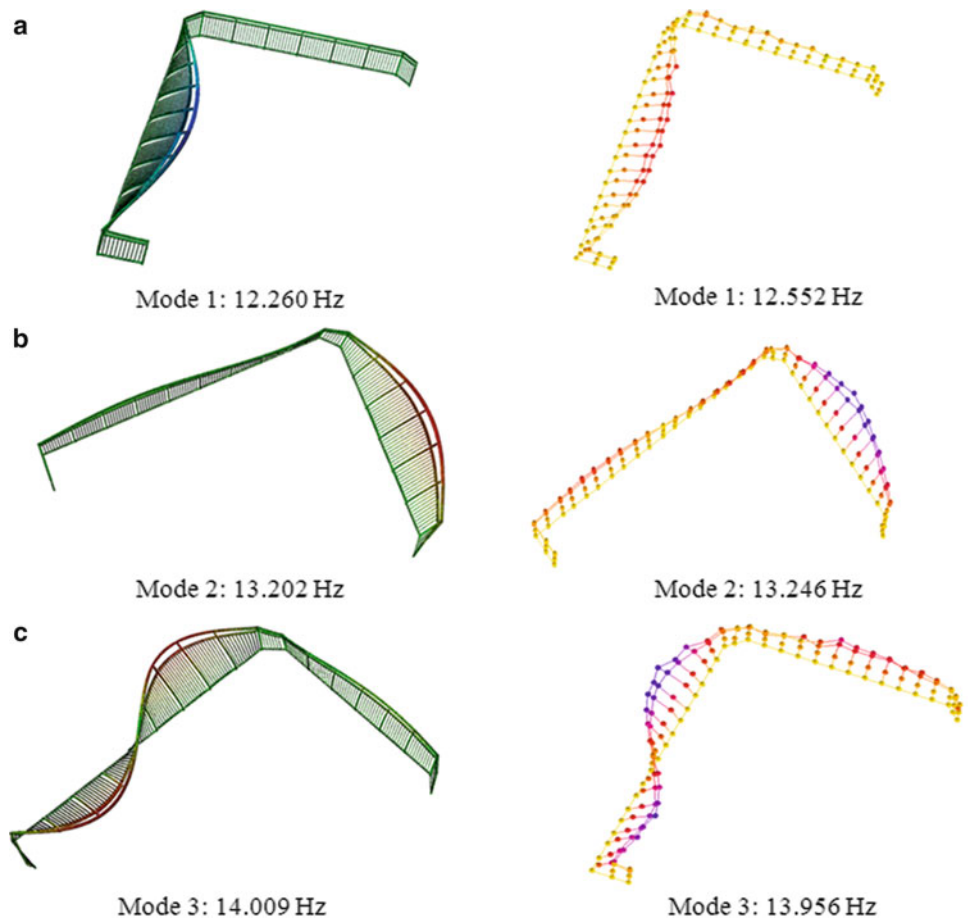


Fig. 43.5 PSDs of the approaching wind pressure measured with and without a windscreen with an average wind speed of 4.2 m/s from the north direction in (a) log scale and (b) linear scale

peak around the first natural frequency of the railing, and there are some other peaks with less amplitudes indicating some other natural frequencies of the railing. Based on the experimental measurements of the wind pressure fluctuation, natural frequencies of the railing, and responses of the railing in operational conditions, it is believed that some of the natural frequencies of the railing fall into the range of the wind pressure fluctuation where the pressure is still considerable. The prolonged vibration due to buffeting can cause fatigue failure of the welding of the pickets, which can in turn generate impact noise. Therefore, turbulence-induced buffeting plays an important role in the vibration of the railing and noise generation.

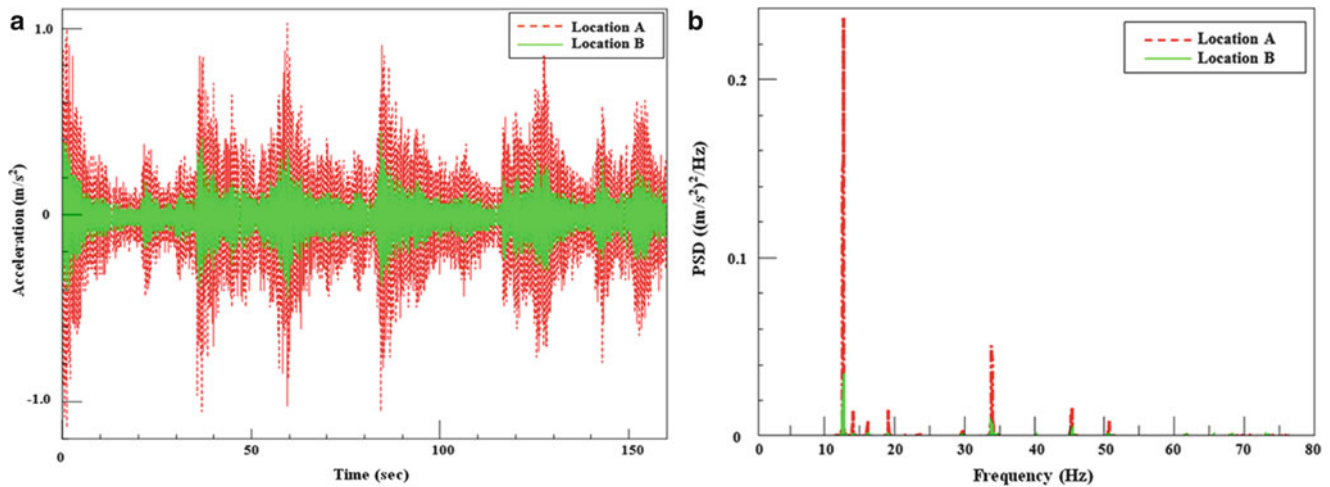


Fig. 43.6 (a) Accelerations at location A and location B with an average wind speed of 6.4 m/s from the northwest direction, and (b) the corresponding PSDs of the accelerations

43.2.2 Noise Generation Due to Vortex-Induced Vibration

43.2.2.1 Vortex-Induced Vibration Phenomenon

Vortex-induced vibration is one of the complex flow-induced vibrations from fluid-structure interaction. This phenomenon can be observed in many slender structures, which are much longer in one direction than in the other directions, in engineering applications, such as chimney stacks, offshore structures, power transmission lines, and heat exchanger tube bundles.

When the flow passes over a structure, vortices are formed from the shear layer separation and shed alternately downstream of the body. This vortex shedding gives rise to a fluctuating force on the structure in the cross-flow direction that can control the amplitude of vibration of the structure. The vortex shedding frequency f_s is governed by the Strouhal relationship [1]:

$$f_s = \frac{S_t U}{D} \quad (43.1)$$

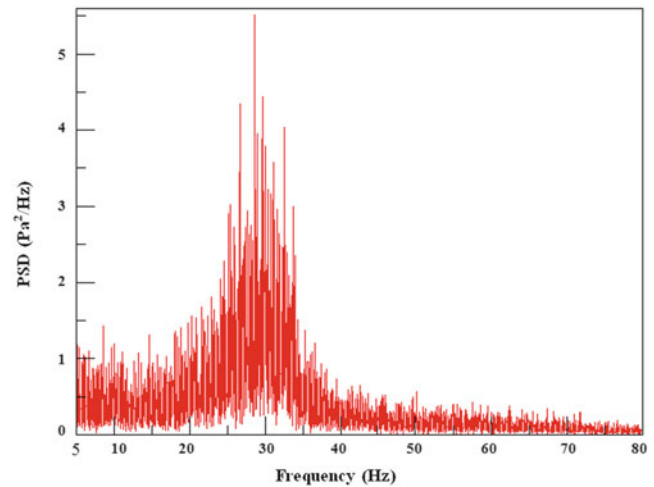
where U is the mean velocity of the oncoming flow, D is the dimension of the cross-section perpendicular to the flow direction, and S_t is the Strouhal number. The Strouhal number is a dimensionless parameter that is a function of the Reynolds number, the cross-section shape, the surface roughness, and free stream turbulence [2]. The Reynolds number R_e is a dimensionless parameter that indicates the ratio of the inertial force to the viscous force in a boundary layer [1]:

$$R_e = \frac{UL}{\nu} \quad (43.2)$$

where ν is the kinematic viscosity of the fluid, and L is the characteristic length of interest. The Strouhal number is relatively constant when the Reynolds number is larger than 10^3 ; the typical S_t value for a square section is 0.13 [3]. When S_t is almost a constant, by Eq. (43.1), the shedding frequency increases with the mean flow velocity. Figure 43.7 shows the PSD of the pressure measured from behind a picket using the PCB 378B02 condenser microphone with an average wind speed of 4.5 m/s (10.1 mph) during measurement from the north direction. The microphone was placed at the mid-height of the picket and 0.03 m away from the picket horizontally. With $U = 4.5$ m/s, $D = 0.01905$ m, and $S_t = 0.13$, the shedding frequency is 30.7 Hz according to Eq. (43.1), which is in agreement with the measurement shown in Fig. 43.7. It should be noticed that the measured wind speed is a mean value; the actual wind speed can fluctuate around this mean value as mentioned in Section 43.2.1.1, resulting in a band of dominant frequencies from vortex shedding off the pickets.

A structure's response will not be influenced much by vortex shedding if the shedding frequency is well out of the range of any natural frequency of the structure. However, when the shedding frequency is within a certain range of one of the structural natural frequencies, a resonance effect can occur and lead to a limited-amplitude dynamic instability if the structural damping is relatively low for the resonant vibration mode. This phenomenon is called lock-in or synchronization, in which structural motion interacts with the flow field in such a way that the dominating vortex shedding frequency synchronizes with the

Fig. 43.7 PSD of the pressure measured behind a picket with an average wind speed of 4.5 m/s from the north direction



structure's natural frequency [2]. During lock-in, considerable transverse vibration with an amplitude of up to twice the characteristic cross-section dimension can occur, which can lead to fatigue failure [4]. The critical lock-in velocity U_v can be obtained from Eq. (43.1) as

$$U_v = \frac{f_n D}{S_t} \quad (43.3)$$

where f_n is one of the natural frequencies of the structure. An elastic structure like the railing can have several or more modes being excited by vortex shedding.

During vortex shedding, the structure imposes a force on the fluid just as the shedding fluid imposes a force on the structure, which produces aeroacoustic sound with tone at the shedding frequency. If the sound is undesirable, it is called aerodynamic noise such as the one in the present case. The range of frequencies over which structural vibration controls the shedding frequency is called the lock-in band; this band is normally within 20 percent of the corresponding lock-in natural frequency [4]. When the wind velocity is greater than 15 m/s, turbulence generally weakens regular vortex shedding by reducing the spanwise correlation of the loading; a wind speed above 15 m/s will likely reduce the chance of large amplitude vibration even during lock-in [2, 4].

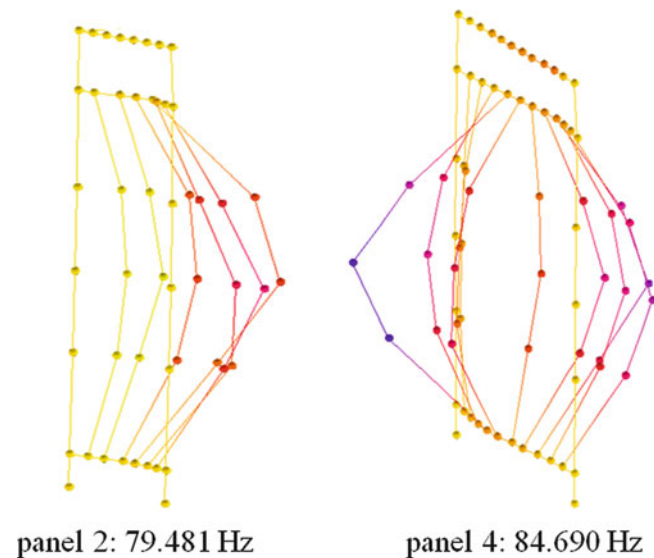
43.2.2.2 The Role of Vortex-Induced Vibration

Since humming of the pickets is a major component of noise that was observed, the pickets are suspected to encounter vortex-induced vibration when the wind speed is high enough. In order to investigate the effect due to vortex-induced vibration on the pickets, modal testing was conducted on four representative panels shown in Fig. 43.3 to find out the local picket modes where the picket displacements are substantially larger than those of the other components. A typical panel includes two posts, pickets, snaps, punch rails, and the plaza between the posts. It should be noted that modal testing shall not be conducted to pickets alone to find out the local picket modes since the pickets are not isolated; they are welded to the punch rails that are connected to the posts. Without reference from other components, it is difficult to decide whether the measured mode shapes are global or local. The roving hammer method was used; a PCB 086C01 impact hammer was used to excite the structure at pre-selected locations in the out-of-plane direction as shown in Fig. 43.2a. The responses of the structure were measured by PCB TLD356A17 tri-axial accelerometers at pre-selected locations. In order to increase the energy input to the structure and the signal-to-noise ratio, multiple random impacts [5] were applied to every excitation point instead of a single impact. Three random impact tests were averaged at every excitation point to ensure repeatable results with a good coherence. The natural frequencies and mode shapes of the railing were extracted from the measured FRFs using modal analysis software LMS Test.Lab 9b. The first local picket natural frequency of each panel along with the damping ratio from modal analysis curve-fitting is listed in Table 43.2. The average damping ratio of the first local picket modes of the panels is 0.00285, which is comparable to that in the literature [6]. The first local picket modes of panel 2 and panel 4 with marked excitation points are shown in Fig. 43.8.

Table 43.2 First local picket natural frequencies of the four panels along with damping ratios from experiment

Panel	First local picket mode frequency (Hz)	Damping ratio
1	82.878	0.17%
2	79.481	0.36%
3	96.295	0.36%
4	84.690	0.25%

Fig. 43.8 First local picket modes of panel 2 and panel 4 from experiment



It can be seen from Table 43.2 that large picket vibration can occur if the shedding frequency is close to 80 Hz. According to Eq. (43.3), with $f_n = 80$ Hz, $D = 0.01905$ m, and $S_r = 0.13$, the critical lock-in velocity U_v is 11.7 m/s (26.2 mph). According to wind data from the NOAA, this wind speed can occur at the location of the building especially during fall and winter seasons. When the wind speed reaches the lock-in range, large amplitude vibration can occur, which can lead to humming of the pickets and fatigue failure of the welds of the pickets. After a large number of cycles of vibration, the welding can eventually break, which can lead to impact noise. Therefore, vortex-induced vibration is one of the major factors that can contribute to noise generation of the railings.

43.2.3 Noise Generation Due to Galloping

43.2.3.1 Galloping Phenomenon

Galloping is usually referred as a velocity-dependent, damping-controlled, and one-degree-of-freedom instability that gives rise to transverse or torsional motion [4]. A classical example of galloping instability is the across-wind large-amplitude vibration of power transmission lines with a coating of ice. For structures with certain cross-sectional shapes, negative aerodynamic damping can be developed when the wind is approaching from a range of unfavorable directions. In galloping, a small transverse body motion creates an aerodynamic force that increases the amplitude of motion of a structure [7]. The necessary condition for galloping instability is referred to as the well-known Glauert-Den Hartog criterion [8]:

$$\left. \frac{dC_y}{d\alpha} \right|_{\alpha=0} = - \left(\left. \frac{dC_L}{d\alpha} + C_D \right) \right|_{\alpha=0} > 0 \quad (43.4)$$

where C_L and C_D are the lift and drag coefficients, α is the angle of attack of the flow, and C_y is the transverse force coefficient. For some typical sections, $\frac{dC_y}{d\alpha}$ can be found in Ref. [1]; assuming turbulence flow, $\frac{dC_y}{d\alpha}$ is 3.5 for a square section.

While vortex-induced vibration occurs only in discrete ranges of wind speeds, galloping can occur at all wind speeds above a critical value determined by the structural damping. If the flow velocity exceeds the critical velocity for the onset of

galloping, the energy input to a structure by the flow will exceed the energy dissipated by the damping of the structure. The onset of galloping U_g for a one-degree-of-freedom system can be obtained from [1]

$$U_g = \frac{(8\pi m\zeta) f_n}{\rho D} / \frac{dC_y}{d\alpha} \quad (43.5)$$

where m is the mass per unit length of the structure, ζ is the structural damping ratio, f_n is the natural frequency, ρ is the fluid density, and D is the characteristic cross-section length. Normally the vibration amplitudes due to galloping are larger than those from vortex-induced vibration, and the amplitudes will increase with the flow velocity beyond the onset of galloping [9].

43.2.3.2 The Role of Galloping

The ratio of U_g and U_v can be obtained from Eqs. (43.3) and (43.5):

$$\frac{U_g}{U_v} = \frac{8\pi m\zeta S_t}{\rho D^2} / \frac{dC_y}{d\alpha} \quad (43.6)$$

Galloping typically occurs at a wind speed U_g that is higher than U_v for vortex-induced vibration. However, if either the structural damping is small or the mass density is low, U_g can be close to or even less than U_v from Eq. (43.6).

For the current case, with $m = 0.429$ kg/m, $\zeta = 0.00285$ from Section 43.2.2.2, $S_t = 0.13$, $\rho = 1.293$ kg/m³, $D = 0.01905$ m, and $\frac{dC_y}{d\alpha} = 3.5$, the ratio of U_g and U_v is 2.44, which means that the onset of galloping is 2.44 times the critical lock-in velocity for vortex-induced vibration of the pickets. When $U_v = 11.7$ m/s, $U_g = 28.5$ m/s (63.8 mph). According to wind data from the NOAA, wind speeds around 28.5 m/s or high are unlikely to occur at the current location of the building. Therefore, galloping is not a major cause of the vibration of the pickets and noise generation.

43.3 Mitigation of Wind-Induced Vibrations and Noise

Many methods for reduction of flow-induced vibrations can be found in the literature [1, 2, 10–12]. These methods include:

- Changing the structural shape to reduce aerodynamic loads,
- Adding vortex suppression devices to disrupt or prevent vortex formation,
- Increasing the structural mass,
- Increasing the structural damping by using viscoelastic materials or external dampers, and
- Increasing the structural stiffness by increasing cross-sections, stiffening joints, or using stiffer materials.

Some constraints need to be considered for selection of the methods to reduce the wind-induced noise. First, the owner did not want to change the geometric shapes of the components; therefore, changing the shapes to reduce aerodynamic loads is not plausible in this case. Second, any applications that destroy the coating of the components cannot take place on site according to the railing contractor since the coating has to be finished in the factory. Therefore, adding aerodynamic devices is not a good method to implement because it can destroy some coating and can be inaeathetic. Third, it is not practical to add energy-absorbing materials such as soft polymers inside the pickets or posts according to the contractor. In addition, the owner did not want to use vibration dampers due to appearance consideration. Lastly, the aluminum for the railings cannot be changed to some other stronger types of materials like steels because of the oceanfront working environment, and the overall dimensions of the railing have to be maintained.

After considerations of the constraints imposed, increasing the stiffness of the railing was chosen for alleviation of the wind-induced noise. According to Ref. [12], the most effective means of reducing structural vibration excited by turbulent flow is to make the structure stiff enough so that its fundamental natural frequency falls outside the frequency range where the excitation force amplitude is significant. Vortex-induced vibration can be avoided if the shedding frequency is not inside the lock-in range by stiffening the structure. Since buffeting and vortex-induced vibration are the main mechanisms that can lead to noise generation, the railing needs to be stiffened in such a way that vibrations due to buffeting and vortex-shedding are significantly reduced while maintaining a reasonable cost.

To be conservative, the first natural frequency of the railing is aimed to be increased to about 30 Hz to avoid the large amplitude vibration of the overall railing and fatigue failure of the welding. From the wind pressure measurement and Fig. 43.5b, it is noticed that the wind pressure fluctuation at 30 Hz is less than 5 percent of that at 12.5 Hz, which is around the first natural frequency of the unmodified railing; therefore, the railing is considered to be safe from turbulence-induced vibration if its first natural frequency is about 30 Hz. Besides the input of the fluctuating wind power being much smaller at higher frequencies, the structural vibration response can also be reduced due to increased stiffness since the vibration amplitude is inversely proportional to the structural stiffness [1].

According to Eq. (43.3), the natural frequency of the first local picket mode is aimed to be increased to about 105 Hz to have a critical lock-in velocity equal to 15.4 m/s at which the vibration amplitude is significantly reduced due to reduced spanwise correlation of the loading. The pickets of the original railings are only welded on one side, and welding on additional sides can help increase the natural frequencies of the local picket modes. The owner would like unexposed welding underneath the punch rails rather than exposed welding on top of the punch rails. However, here is not enough room for the tip of the welding gun from the contractor to go around all four sides of the portion of the pickets adjacent to the unexposed surface of the punch rails. Therefore, additional unexposed welding can only be applied to the pickets through the span of the side that is parallel to the currently welded side.

After some trials of modifications and simulations on the FE model of the railing developed earlier using S4R elements and linear hexahedral continuum elements with reduced integration (C3D8R), the following modification can lead to a satisfactory result: the posts are changed from 0.04445 m x 0.04445 m x 0.00238 m to 0.0635 m x 0.0635 m solid, and the pickets are welded on two sides instead of one side through the span in the out-of-plane direction shown in Fig. 43.2a. From FE simulation, the first natural frequency of the railing is 29.544 Hz, and that of the local picket mode is 104.15 Hz. Therefore, this modification was suggested to the owner, and a new railing according to the modification was installed on one of the balconies for testing was monitoring purposes.

43.4 Experimental Testing on the Modified Railing and On-Site Monitoring

To verify the FE simulation results, modal testing was conducted on the overall modified railing using a PCB 086D05 impact hammer and PCB TLD356A17 tri-axial accelerometers with similar procedures described in Section 43.2.1.3. Due to the increased stiffness of the modified railing, multiple random impacts instead of a single impact were applied to excite the railing to increase the energy input and the signal-to-noise ratio. The first ten natural frequencies of the modified railing from experiment are shown in Table 43.3 along with those from FE simulation. The first and fourth modes from both FE simulation and experiment with marked excitation points are shown in Fig. 43.9. Modal testing was also conducted on the four panels corresponding to those in Fig. 43.3 using a PCB 086C01 impact hammer and PCB TLD356A17 tri-axial accelerometers with similar procedures described in Section 43.2.2.2. The first local picket natural frequency of each panel along with the damping ratio from modal analysis curve-fitting is listed in Table 43.4. The first local picket modes for panel 1 and panel 3 with marked excitation points are shown in Fig. 43.10.

It is noticed from Table 43.3 that the FE model of the modified railing predicts the natural frequencies of the railing rather accurately with the maximum frequency difference for the first ten modes less than 4%. The first natural frequency of the modified railing is close to 30 Hz from experiment as expected; hence, the vibration of the railing due to turbulence-induced buffeting can be significantly reduced. From Table 43.4, the local picket modes start at around 106 Hz, leading to a critical lock-in velocity of 15.5 m/s (35 mph). As mentioned in Section 43.2.2.2, the lock-in effect due to vortex shedding is negligible at such a high wind speed.

Table 43.3 First ten natural frequencies of the modified railing from the FE model and experiment and their differences

Mode	Modified FE model frequency (Hz)	Experimental frequency (Hz)	Frequency difference
1	29.544	29.274	-0.91%
2	31.094	30.899	-0.63%
3	31.477	31.354	-0.39%
4	32.179	32.394	0.67%
5	32.701	32.729	0.09%
6	33.695	34.309	1.82%
7	34.177	34.840	1.94%
8	35.106	35.598	1.40%
9	36.529	37.673	3.13%
10	38.243	38.890	1.69%

Fig. 43.9 (a) First and (b) fourth modes of the modified railing from FE simulation (*left*) and experiment (*right*)

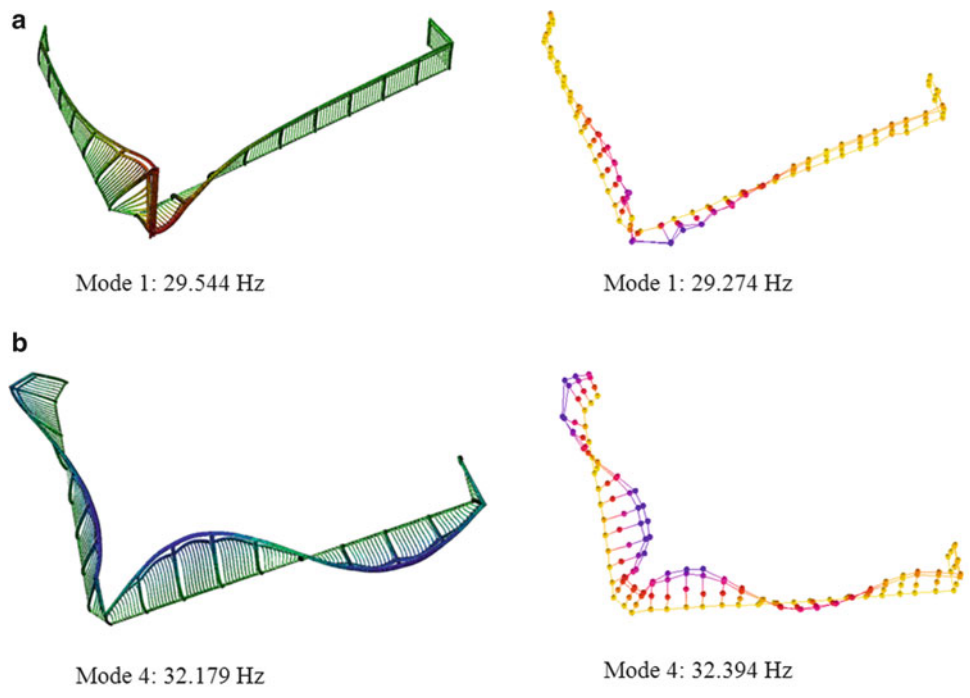
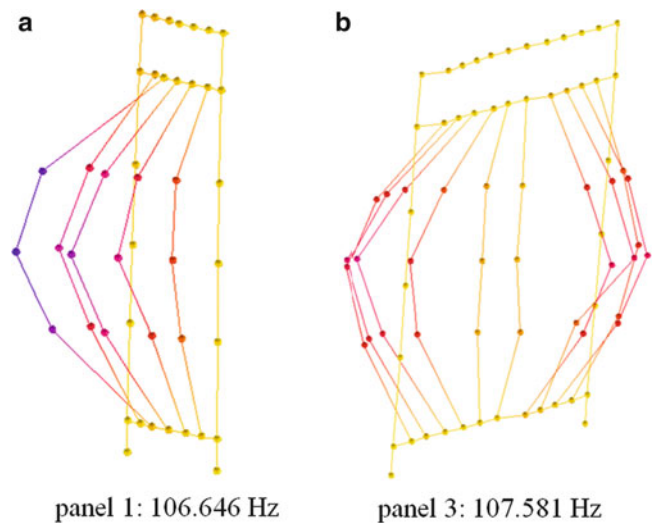


Table 43.4 First local picket natural frequencies and damping ratios of the four panels of the modified railing from experiment

Panel	First local picket mode frequency (Hz)	Damping ratio
1	106.646	0.26%
2	108.299	0.31%
3	107.581	0.20%
4	105.827	0.29%

Fig. 43.10 First local picket modes of panel 1 and panel 3 from experiment on the modified railing



In order to insure that there is no significant amount of noise being generated from the modified railing, the engineer of the building monitored the performance of the modified railing since the installation in September 2011 along with other old railings. Until present, no significant amount of impact or humming noise was heard from the modified railing while noise was still heard from the old railings, according to the engineer and the owner. The experimental results on the modified railing and on-site monitoring indicate that the modification to the railing has resolved the noise issue. As a result, all of the remaining railings that have the noise issue were demolished and replaced with the modified railings in October 2012.

43.5 Conclusion

Wind-induced vibrations on corner balcony railings of an oceanfront condominium building generated impact and humming noise that created discomfort to the residents of the building. Investigation on the noise generation mechanisms through FE simulations and experimental testing on wind and railing dynamic characteristics indicates that buffeting and vortex-induced vibration are the two major mechanisms that can lead to noise generation. Supported by simulation results of the modified railing, increasing the stiffness of the railing to avoid the vibrations and noise due to the two mechanisms was chosen as the mitigation as a result of design constraints. The experimental results on the modified railing indicate that the FE model prediction of the dynamic response of the railing is rather accurate. Based on the experimental results and on-site monitoring, it is believed that the noise issue has been resolved.

Acknowledgements The authors would like to thank Dr. Kun He and Dr. Xinzhong Chen for some valuable discussions. The authors would also like to thank Mr. Yongfeng Xu and Mr. Kai Wu for their assistance in conducting some of the tests in this work.

References

1. Blevins RD (1990) Flow-induced vibration, 2nd edn. Van Nostrand Reinhold, New York, NY
2. Simiu E, Scanlan RH (1996) Wind effects on structures, 3rd edn. Wiley, New York, NY
3. Okajima A (1982) Strouhal numbers of rectangular cylinders. *J Fluid Mech* 123:379–398
4. Paidoussis MP, Price SJ, Langre ED (2011) Fluid-structure interactions: cross-flow-induced Instabilities. Cambridge University Press, New York
5. Lazan BJ (1968) Damping of materials and members in structural mechanics. Pergamon, New York, NY
6. Zhu WD, Zheng NA, Wong CN (2007) A stochastic model for the random impact series method in modal testing. *ASME J Vib Acoust* 129:265–275
7. Bearman PW, Gartshore IS, Maull DJ, Parkinson GV (1987) Experiments on flow-induced vibration of a square-section cylinder. *J Fluid Struct* 1:19–34
8. Den Hartog JP (1956) Mechanical vibrations, 4th edn. McGraw-Hill, New York
9. Parkinson GV (1971) Wind-induced instability of structures. *Philos Trans Roy Soc London* 269:395–409
10. Zdrovkovich MM (1981) Review and classification of various aerodynamic and hydrodynamic means for suppressing vortex shedding. *J Wind Eng Indus Aerodyn* 7:145–189
11. Mahmoodi P (1969) Structural dampers. *ASCE J Struct Div* 95:1661–1672
12. Naudascher E, Rockwell D (1994) Flow-induced vibrations: an engineering guide. Balkema, Rotterdam

Chapter 44

Operational Modal Analysis of a Slender Footbridge to Serviceability Purposes

Anna Cappellini, Stefano Manzoni, Marcello Vanali, and Elena Mola

Abstract This work proposes the dynamic analysis of a pedestrian walkway. This walkway is placed within the ‘Ospedale di Circolo’ Hospital complex in Varese. In order to prevent any vibration serviceability issue a dynamic analysis has been committed. Ambient vibration data and vibration data in operating conditions, that is, while people walked along the footbridge, were collected. In order to assess the serviceability of this structure, a complete modal analysis was first performed. This allowed identifying the main resonances of the structure in the range of frequencies potentially at risk because of a possible synchronization with the walking people loading. Vibration levels were then verified according to ISO 10137, and other international standards. A comparison between vibration levels determined according to the normative regulations and those measured in operating conditions is finally proposed.

Keywords Vibrations • Serviceability • Civil structures • Footbridge • Operational modal analysis

44.1 Introduction

In the last years a great attention has been paid to all problems related to vibration serviceability issues of civil structures. The problem has come to great evidence in some famous cases like the millennium bridge [1] in London, but many other studies are reported. Stadia serviceability issues are deeply investigated [2–4] as long as pedestrian walking bridges and staircases [5]. International standards and codes [6–8] exist to the purpose of both designing and evaluating the structure dynamics under the crowd action and they are the natural reference when vibration serviceability is assessed. Guidelines from British and Canadian engineering institution exist too [9, 10].

At the design stage usually standard recommendations are given in terms of natural frequencies in order to avoid resonances in the frequency range mostly excited by the structure occupants (0.5–5 Hz) and numerical models are given to foresee the people forcing on the structure and therefore to compute the vibrations levels that will be attained during the structure life.

One of the main opened discussion points in the standards are the damping levels to be introduced. It has been demonstrated that people presence greatly affects the overall structural damping [4, 11], making a reliable vibration level prediction a hard task. In some cases the experimental approach is suggested in order to obtain realistic estimates of the in-service structural vibrations. Moreover a real structure modal analysis, either through experimental or operational approaches is useful to tune the numerical models used at the design stage giving important information on the structural seismic behaviour too.

A. Cappellini • S. Manzoni
Dipartimento di Meccanica, Politecnico di Milano, via La Masa 1, Milan, Italy
e-mail: anna.cappellini@mail.polimi.it; stefano.manzoni@polimi.it

M. Vanali (✉)
Dipartimento di Ingegneria Industriale, Università degli studi di Parma, Parco Area delle Scienze, 181/A, Parma, Italy
e-mail: marcello.vanali@unipr.it

E. Mola
ECSD S.r.l., via Goldoni 22, Milan, Italy
e-mail: Elena.Mola@ecsd.it

This paper deals with the analysis of the dynamic behaviour of a footbridge when empty and in operating conditions according to different regulations.

In the next paragraph a description of the structure under test is presented together with the measurement set-up, then the modal analysis results referring to the empty structure are presented. These results were obtained with Operational Modal Analysis (OMA) techniques. In the last section the results of tests in operating conditions are finally presented. These results are analyzed according to the criteria proposed by various regulations and guidelines concerning serviceability issues.

44.2 Structure Under Analysis and Set-Up of the Ambient Tests

In this section, the structure under analysis and tests that have been performed are presented.

The footbridge under analysis was built during the expansion work of the hospital and is intended to externally connect two buildings. Figure 44.1 shows a model of the structure under test.

The walkway consists of two elements, separated from each other, referred to as long side and short side. The second floor of the long side was the only existing prior to the expansion work, while the first floor and the second floor of the short side were made subsequently. The long side has a length of about 56 m, while the short side is about 13 m long. Due to the size of the structure, in order to obtain an adequately dense measurement mesh, the tests were carried out placing the available accelerometers in 4 different configurations (one for the short side and three for the long side). Data were acquired with 24 bits ADCs with built in anti aliasing filters (NI 9234, NI9233). Final sampling frequency was set to 256 Hz.

High sensitivity seismic piezo accelerometers have been used; their main features are reported in Table 44.1.

The selected sensors have proven to be adequate for ambient vibration testing having a very low noise floor and an adequate full scale value. A total of 32 accelerometers (24 PCB 393B12 and 8 PCB393A03) were available.

The transducers were placed both in the vertical direction and in the horizontal direction.

Figure 44.2 shows the measuring points for the short side, chosen so as to have an accurate description of the dynamic behavior of the structure in terms of identified mode shapes.

In the case of the short side it was decided to place some accelerometers on the second floor as this structure was completely new and with an unknown behavior.

With regard to the long side, given the length of the structure, it was decided to divide the test into three different configurations. The test was performed by measuring the response in a total of 43 points in the vertical direction and 22 points in the horizontal direction. For this purpose a total of 24 accelerometers PCB 393B12 and 7 accelerometers PCB 393A03 in three different configurations was used.

Figures 44.3, 44.4 and 44.5 show the measurement mesh used in the three configurations, respectively.

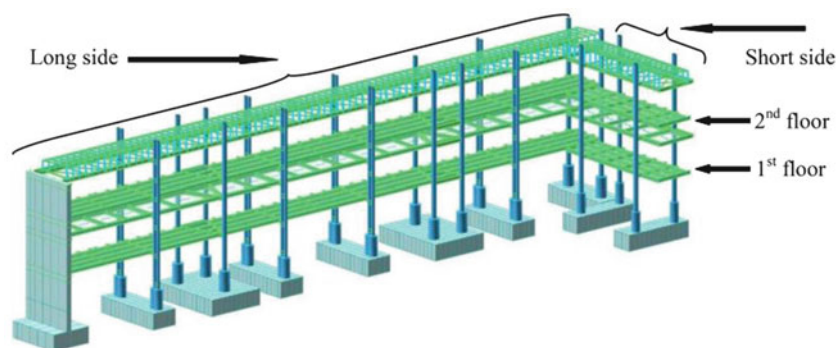


Fig. 44.1 Footbridge under test

Table 44.1 Sensors main features

Sensor	Meas range [g]	Frequency range [Hz]	Sensitivity [V/g]
Piezo Acc PCB 393B12	0.5	0.1 – 500	10
Piezo Acc PCB 393A03	5	0.1 – 1000	1

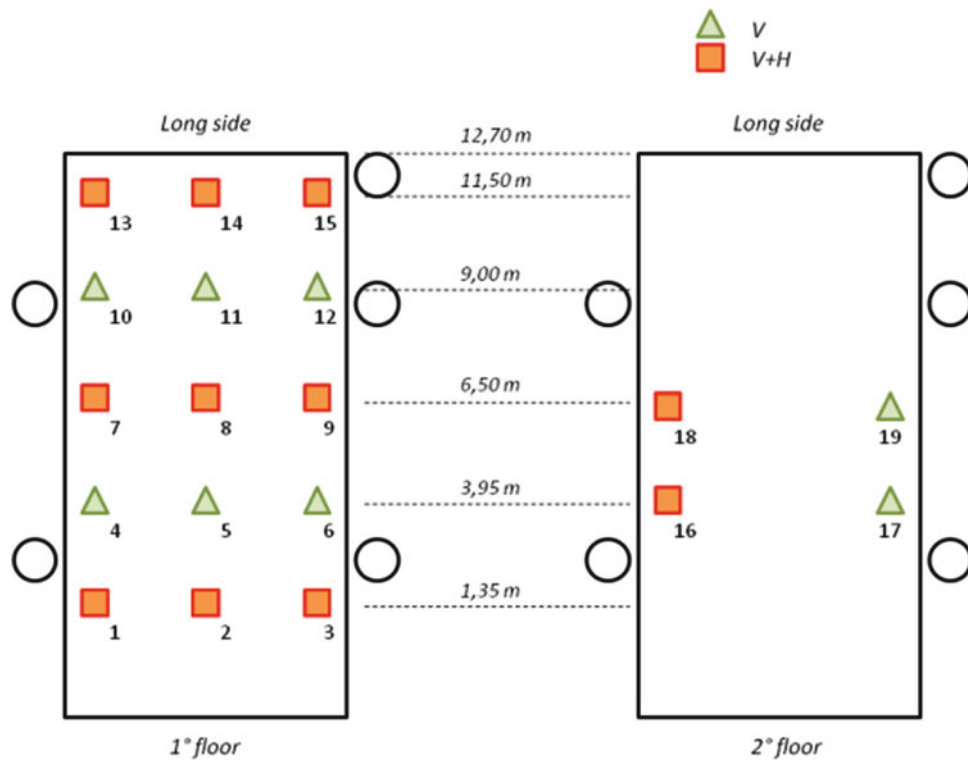


Fig. 44.2 Location of the accelerometers – short side

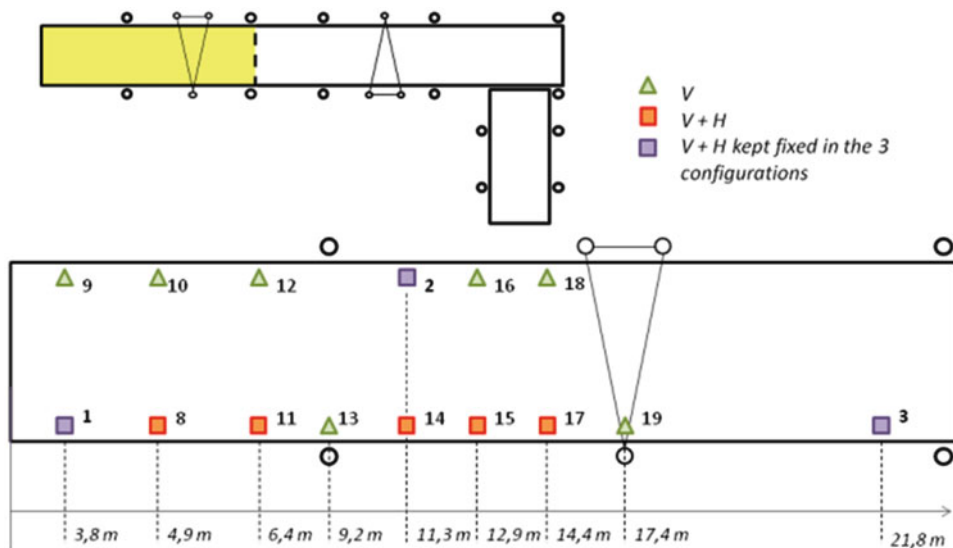


Fig. 44.3 Location of the accelerometers – long side – configuration 1

For all tests the excitation exploited for the measurement of the dynamic response of the walkway is the environmental one, always present in an active environment such as a construction site, and similar to a broadband white noise if an appropriate number of averages is performed [12].

With this type of forcing, applying Operational Modal Analysis techniques [1, 13, 14] it is possible to obtain an estimate of the modal parameters of the structure. The acquisition time was approximately 120 minutes for each test.

The next section will present the results of this analysis.

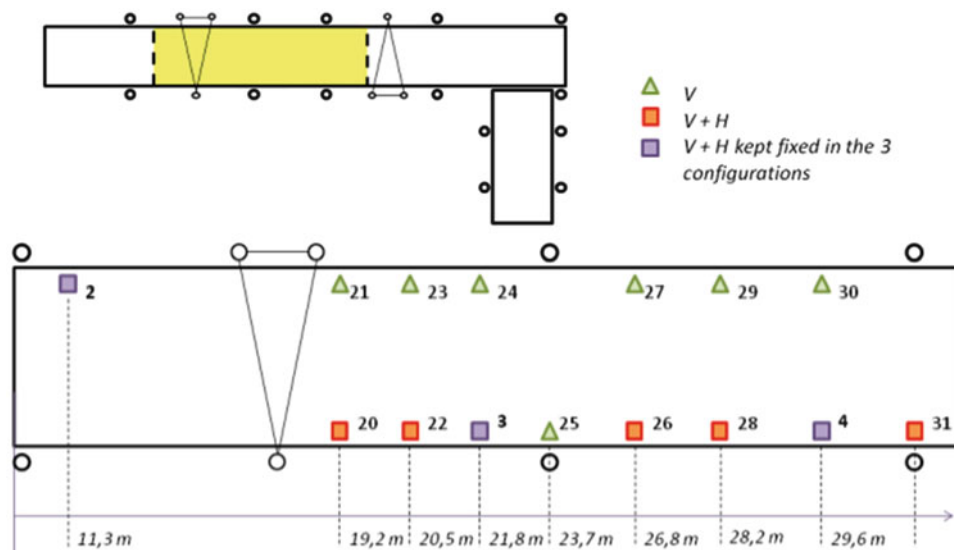


Fig. 44.4 Location of the accelerometers – long side – configuration 2

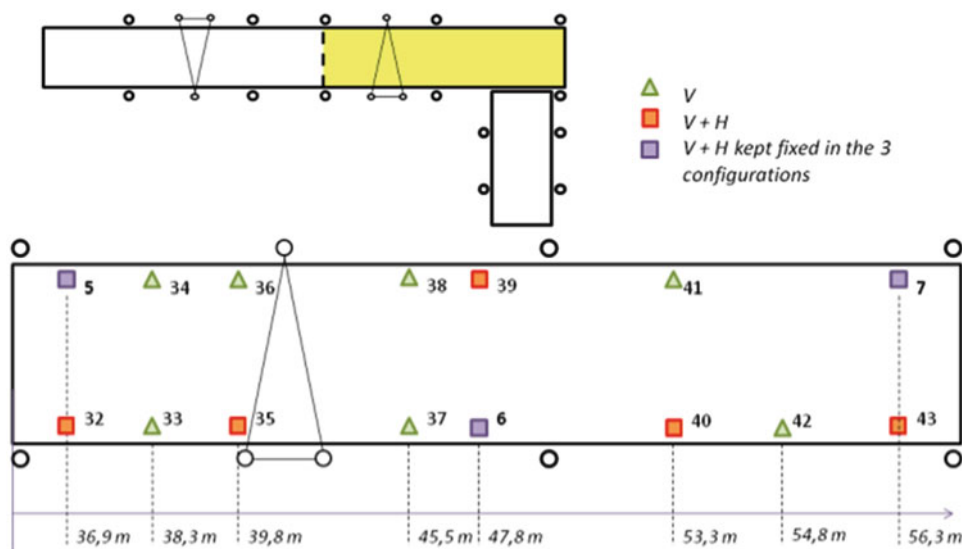


Fig. 44.5 Location of the accelerometers – long side – configuration 3

44.3 Operational Modal Analysis of the Empty Structure – Short Side

This paragraph presents the results of the analysis of the tests described above on the short side. Figure 44.6 shows the Power Spectral Densities (PSD) of the horizontal accelerations measured on the short side of the walkway. It is possible to observe the presence of three dominant peaks in the neighborhood of 3.5 Hz, 5.5 Hz and 7 Hz, indicated by the arrows.

The data were analyzed using the Polyreference Least Square Frequency Domain (PolyMAX) algorithm [15], suitable to identify the modal parameters of structures similar to this [2, 11, 16].

Table 44.2 shows the values of frequencies and damping associated to the first three modes of vibration identified, while Table 44.3 shows the corresponding eigenmodes. The mode shapes, known unless of a multiplicative constant, were normalized by imposing the value to 1 in point 1.

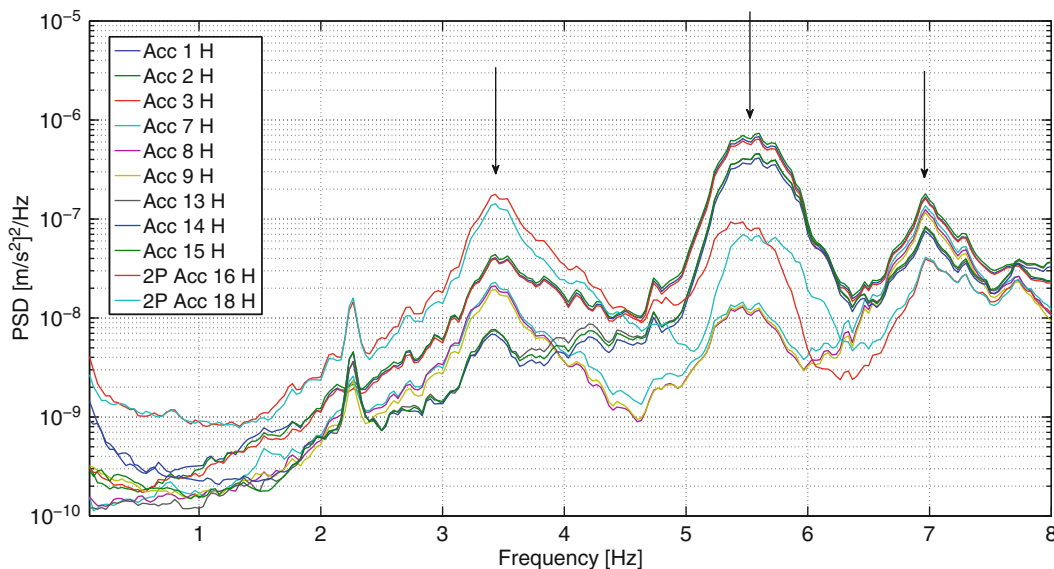


Fig. 44.6 Power Spectral Densities – short side – horizontal direction

Table 44.2 Short side – identified frequencies and damping ratios – horizontal direction

f [Hz]	ξ [%]
3.4	5.4
5.5	3.5
7.0	2.6

Table 44.3 Short side – mode shapes – horizontal direction

Point	3.4 Hz	5.5 Hz	7.0 Hz
1	1.0	1.0	1.0
2	1.0	1.0	1.0
3	1.0	1.0	1.0
7	0.9	0.1	0.9
8	0.8	0.1	0.8
9	0.8	0.1	0.8
13	0.6	-0.8	0.6
14	0.6	-0.8	0.6
15	0.6	-0.8	0.7
16	1.5	0.3	0.7
18	1.2	-0.2	0.8

The peak at about 2.3 Hz was not considered because its amplitude is very small and the identification turned out to be difficult. Furthermore this peak could be linked to the dynamics of the long side of the structure, as shown in the following section.

Figure 44.7 shows the Power Spectral Densities (PSD) of the vertical accelerations measured on the short side of the walkway. In this case it is possible to observe a first major resonant peak around 14 Hz, indicated by the arrow.

Also in this case the data were analyzed using the Polyreference Least Square Frequency Domain (PolyMAX) algorithm. Table 44.4 shows the values of frequencies and damping associated to the first mode of vibration identified, while Fig. 44.8 shows the corresponding eigenmode. The mode shape, known unless of a multiplicative constant, was normalized by imposing the value to 1 in point 1.

This first frequency turns out to be already very high and therefore definitely not dangerous for serviceability purposes.

The following section will present the results of the analysis on the long side of the walkway

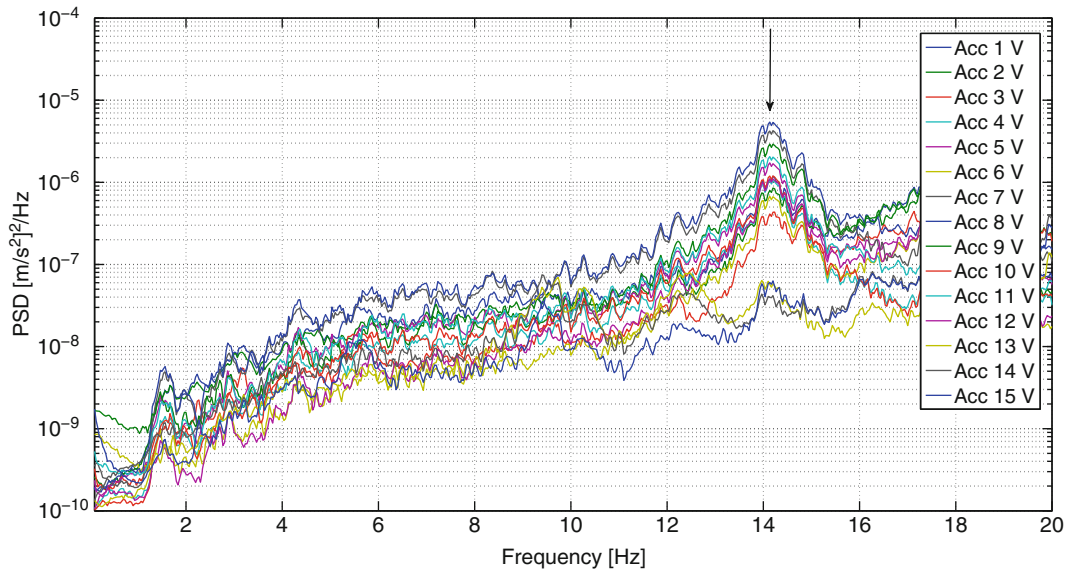


Fig. 44.7 Power Spectral Densities – short side – vertical direction

Table 44.4 Short side – identified frequencies and damping ratios – vertical direction

f [Hz]	ξ [%]
14.2	2

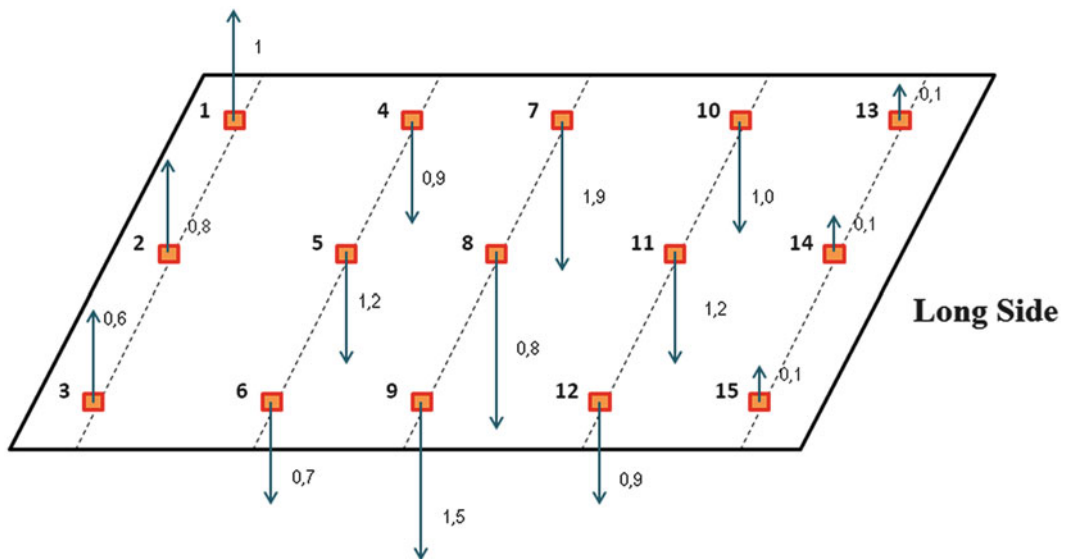


Fig. 44.8 Mode shape at 14.2 Hz – short side – vertical direction

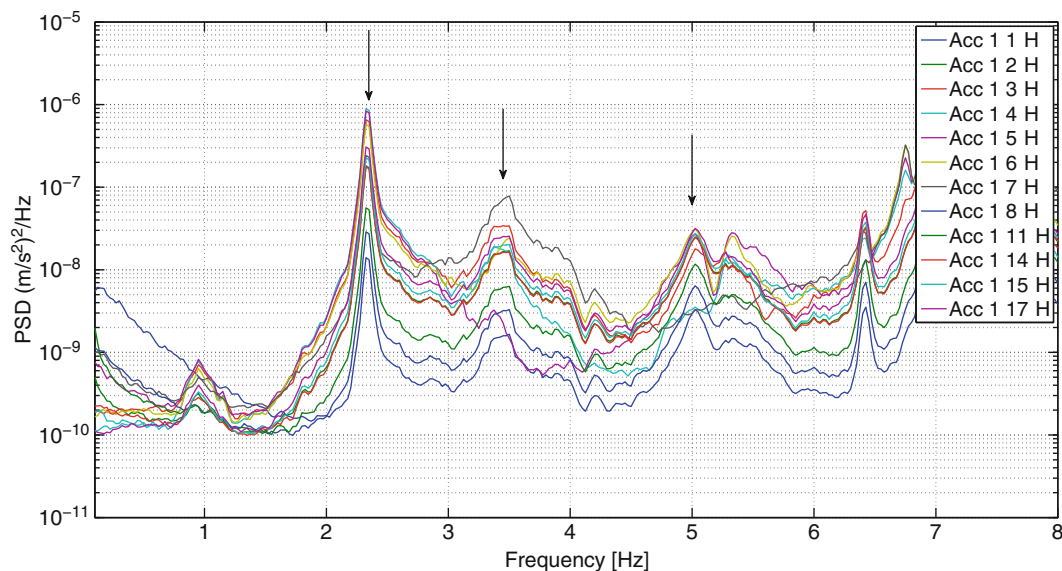


Fig. 44.9 Power Spectral Densities – long side – horizontal direction

Table 44.5 Long side – identified frequencies and damping ratios – horizontal direction

f [Hz]	ξ [%]
2.3	0.9
3.4	3.1
5.1	2.0

44.4 Operational Modal Analysis of the Empty Structure – Long Side

This paragraph presents the results of the analysis of the tests on the long side of the walkway. Figure 44.9 shows the Power Spectral Densities (PSD) of some horizontal acceleration. It is possible to observe the presence of three dominant peaks in the neighborhood of 2.3 Hz, 3.4 Hz, and 5.1 Hz, indicated by the arrows.

In this case too the data were analyzed using the Polyreference Least Square Frequency Domain (PolyMAX) algorithm.

Table 44.5 shows the values of frequencies and damping associated to the first three modes of vibration identified, while Table 44.6 shows the corresponding eigenmodes. The mode shapes, known unless of a multiplicative constant, were normalized by imposing the value to 1 in point 7 for the first two modes, and by imposing the value to 1 in point 5 for the third mode.

Regarding the modes in the vertical direction, it was possible to observe the presence of only local modes, involving each section between two pairs of columns. There are not, as for the short side, global modes involving the whole structure. Table 44.7 shows the values of frequencies and damping associated to the first two modes of vibration identified.

Also in this case the first frequency turns out to be high and therefore definitely not dangerous for serviceability issues.

The next section will describe the results of tests performed in the operating conditions. The results obtained were compared with the limits proposed by some international standards.

44.5 Serviceability Tests

This section describes the tests carried out to assess the levels of vibration in operating conditions. The results are compared with the limits proposed by international standards concerning the serviceability for pedestrian walkways (ISO 10137, EN1990 Eurocode and SÈTRA Technical Guide).

Table 44.6 Long side – mode shapes – horizontal direction

Point	2.3 Hz	3.4 Hz	5.1 Hz
1	0.3	-0.2	0.3
8	0.3	-0.2	0.4
11	0.5	-0.3	0.5
2	0.6	-0.6	1.0
14	0.8	-0.5	0.7
15	0.9	-0.5	0.7
17	1.1	-0.6	0.7
20	1.2	-0.9	0.8
22	1.3	-1.0	0.6
3	1.3	-1.0	0.7
26	1.5	-0.9	0.0
28	1.5	-0.8	-0.1
4	1.7	-0.8	-0.3
31	1.6	-0.7	-0.7
32	1.4	-0.6	-1.0
5	1.6	-0.5	-1.0
35	1.5	-0.5	-1.4
6	1.4	0.2	-1.1
39	1.3	0.2	-1.3
40	1.1	0.6	-0.7
43	1.0	0.9	-0.2
7	1.0	1.0	-0.2

Table 44.7 Long side – identified frequencies and damping ratios – vertical direction

f [Hz]	ξ [%]
9.6	1.5
10.6	1.8

All standards identify as potentially dangerous those structures that have natural frequencies within a certain range of values. The limits set by the various guidelines vary greatly. It was therefore decided to adopt the more restrictive criterion, which is the range 0-2.5 Hz for horizontal vibration and 0-5 Hz for vertical vibrations. All other criteria are less restrictive.

Since the first natural frequency in the horizontal direction of the long side of the walkway is found to be less than 2.5 Hz it was decided to perform a test in operating conditions on this side, while no frequency exceeded the limits on the short side and in the vertical direction.

An appropriate measurement set-up was then laid down. The set-up consisted of a series of measures at the points of maximum modal response (maximum amplitude of vibrations) as identified in the previous sections.

Figure 44.10 shows the location of the accelerometers used to measure the levels of vibration in operating conditions. The 7 fixed position used in the first three test configurations were maintained. Other 5 positions were added in order to evaluate the overall behaviour of the walkway.

All vibration data have been analysed according to the EUROCODE EN 1990, ISO 10137 and Sètra Technical Guideline for the Assessment of vibrational behaviour of footbridges under pedestrian loading.

Special care has been devoted to the influence of data processing strategies on the results. While frequency weighting according to the ISO standard is clearly explained no hints are given in the EUROCODE and in the Sètra guideline on the frequency weighting of the measured vibrations. This is probably due to the fact that these codes are intended to provide guidance at the design stage where forcing and response are given by numerical models and therefore their frequency content is clearly stated. As the EUROCODE and the Sètra fix a limit on the vibration amplitude directly evaluated on the measured time history, the kind of frequency weighting applied to real measured data strongly affects the results.

With regard to ISO 10137, paragraph Annex C shows the limit curve basis for the acceleration levels measured in octave bands. As prescribed by the regulations for pedestrian walkways, ISO 10137 paragraph C 1.2, the curve must be multiplied by 60 or 30 depending on whether or not there is the possibility that someone remains still on the structure, and is therefore

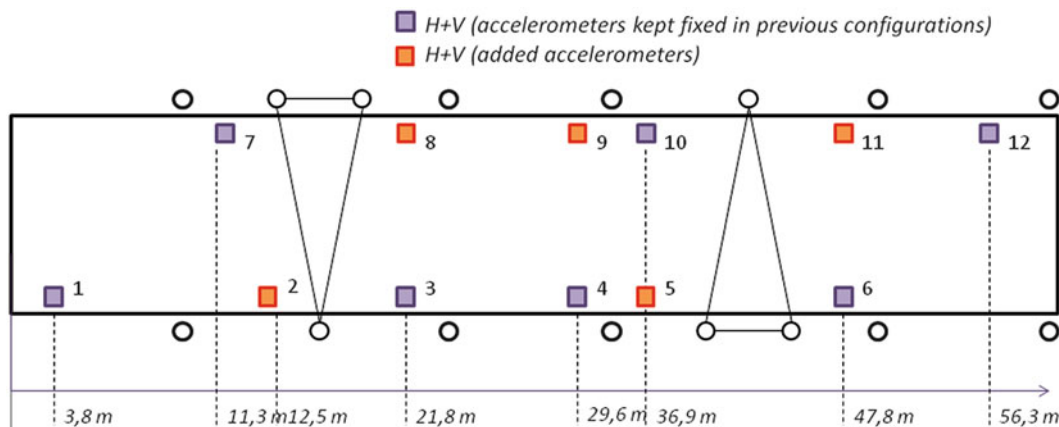


Fig. 44.10 Location of the accelerometers – long side – serviceability test

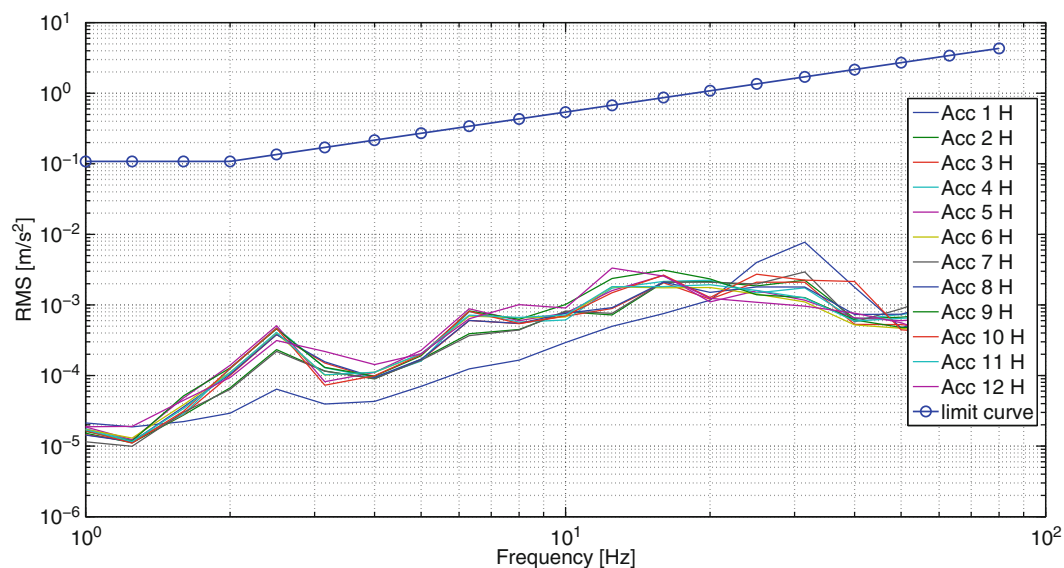


Fig. 44.11 Horizontal accelerations versus limit values (ISO 10137)

subject to vibration for a longer period. Admitting this possibility it was decided to compare the results with the lower limit obtained by multiplying the base curve by a factor of 30. Figures 44.11 and 44.12 show the acceleration values in octave bands with regard to the test under operating conditions. For each group of acceleration, vertical and horizontal, the corresponding limit curves are also reported.

As it can be seen from the figures, all accelerations are well below the limits.

With regard to Eurocode EN 1990 and Sètra Guideline, both standards provide limits on the maximum peak acceleration.

In particular, the Eurocode EN 1990 states a maximum peak of 0.7 m/s² in the vertical direction and 0.2 m/s² in the horizontal direction. The Sètra, on the other hand, proposes a range of accelerations depending on the desired level of comfort. To have maximum comfort, the upper limit is placed at 0.5 m/s² in the vertical direction, while the horizontal accelerations are in any case limited to 0.1 m/s² to avoid synchronization phenomena.

Since the limits, in this case, are given in terms of maximum acceleration, a different filtering of the data can lead to completely different results.

Figure 44.13 show the horizontal acceleration of point 7. The 3 curves represent the raw data (acquired with a 256 Hz sampling frequency considering only the anti aliasing filter effects (low pass 85 Hz)), and the same data low-pass filtered at 25 Hz and 7.5 Hz respectively. The value 7.5 Hz has been chosen as the third harmonic of the maximum critical frequency in the horizontal direction set by the standards at 2.5 Hz. Beyond this frequency horizontal excitation is not considered a major concern ([6], paragraph A2.4.3.2). In the first case (raw data) the acceleration exceeds the limits set by Sètra, while in

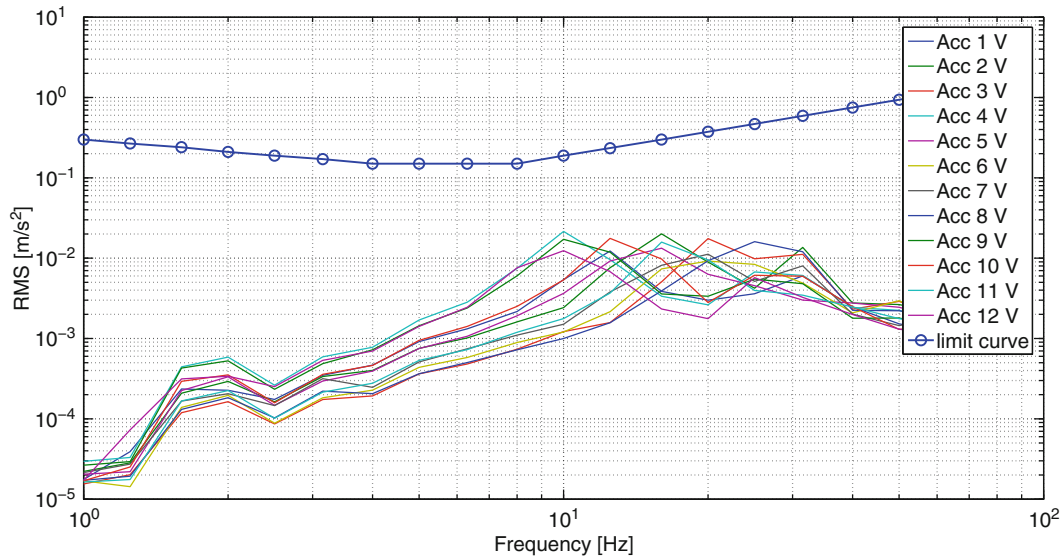


Fig. 44.12 Vertical accelerations versus limit values (ISO 10137)

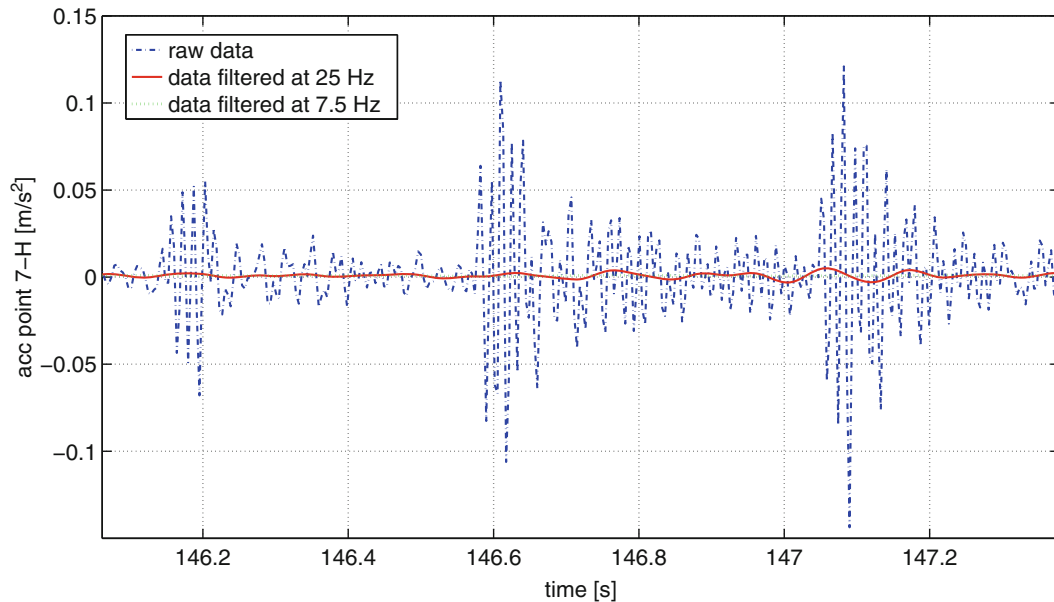


Fig. 44.13 Horizontal acceleration of point 7 – effect of different filters

other cases the values are well below the limits. The use of the raw data, however, is meaningless because the values thereof depend on the sampling frequency set in the acquisition.

For all subsequent evaluations the accelerations have been filtered with a low pass filter at 25 Hz in order to avoid high-frequency phenomena (shocks) that do not affect the comfort. This value is certainly more restrictive in terms of comfort than those reported in other standards, providing a conservative assessment. The value was chosen as discussed and used internationally [5].

Figures 44.14 and 44.15 show the comparison between the measured accelerations and the limits.

As can be seen from the figures, no value exceeds the limits.

In summary, tests have highlighted that in all conditions the recommended levels for the comfort of people proposed by Eurocode EN 1990, the ISO 10137 and Sètra Guidelines are complied with for this structure. However, the problem concerning the selection of the type of filtering of the experimental data remains open.

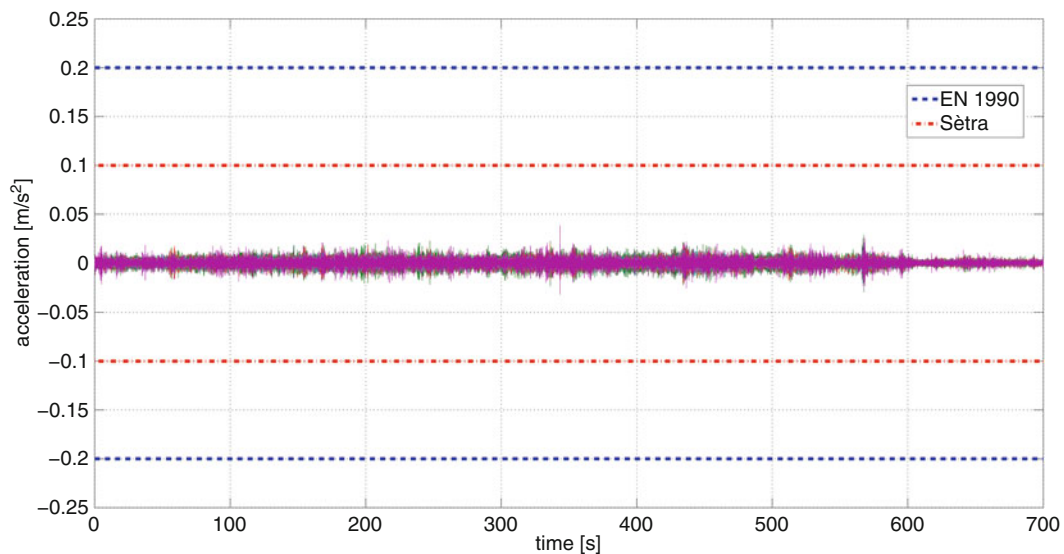


Fig. 44.14 Horizontal accelerations versus limit values (Eurocode and Sètra)

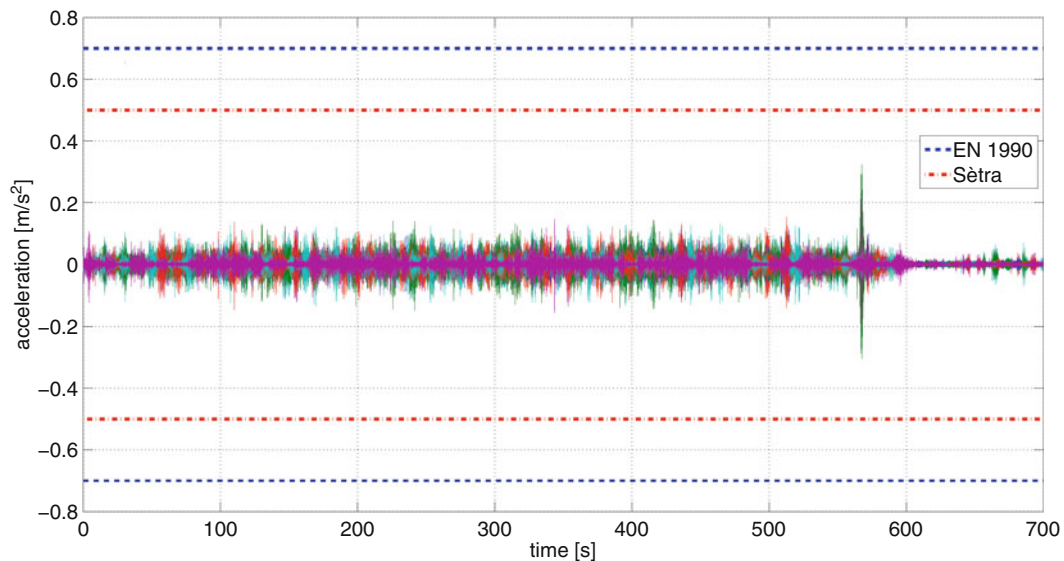


Fig. 44.15 Vertical accelerations versus limit values (Eurocode EN1990 and Sètra)

44.6 Concluding Remarks

This work has dealt with the analysis of the behavior of a pedestrian walkway. In particular, a characterization of the dynamic behavior of the empty structure by means of Operational Modal Analysis was presented. An analysis of the response of the structure under operating conditions was then proposed. The response was analyzed on the basis of different standards. For each standard the advantages and weaknesses have been investigated. All considered regulations propose to use dynamic sensors such as accelerometers to characterize experimentally the behavior of the structure. With regard to this aspect it has been observed a common limitation in two of the considered regulations, i.e. a lack of instructions relating to the filtering of the acquired data. A comparison among the results was finally proposed.

References

1. Strogatz SH, Abrams DM, McRobie A, Eckhardt B, Ott E (2005) Theoretical mechanics: crowd synchrony on the Millennium Bridge. *Nature (London)* 438:43–44
2. Caprioli A, Vanali M (2009) Comparison of different serviceability assessment measures for different events held in the G. Meazza Stadium in Milano. IMAC-XXVII, Orlando, FL, 2 Sept 2009–2 Nov 2009
3. Caprioli A, Reynolds P, Vanali M (2007) Evaluation of serviceability assessment measures for different stadia structures and different live concert events. IMAC XXV, Orlando, FL, 19–22 Feb 2007
4. Reynolds P, Pavic A (2005) The dynamic performance of sports stadia under crowd dynamic loading at concert events. *Structural dynamics EURO-DYN 2005*, Millpress, pp 473–479
5. Rebelo C et al (2010) Cable tensioning and modal identification of a circular cable-stayed footbridge. *Exp Tech* 34(4):62–68
6. Eurocode EN1990: 2002, Basis of structural design.
7. ISO, International Organization for Standardization (2007) ISO 10137 Bases for design of structures, Serviceability of buildings and walkways against vibration, Geneva, CH
8. SETRA, Technical guide (2006) Assessment of vibrational behaviour of footbridges under pedestrian loading. *Service d'Etudes techniques des routes et autoroutes*, Paris
9. IStructE/DCLG/DCMS Joint Working Group (2008) Dynamic performance requirements for permanent grandstands: recommendations for management design and assessment. Institution of Structural Engineers, London
10. Canadian Commission on Building and Fire Codes (2006) User's guide—NBC 2005: structural commentaries (Part 4 of Division B), National Research Council of Canada, Institute for Research in Construction, Ottawa
11. Cappellini A, Manzoni S, Vanali M (2012) Experimental and numerical studies of the people effects on a structure modal parameters. Proceedings of the SEM IMAC XXX conference, Jacksonville, FL, 30 Jan 2012–2 Feb 2012
12. Brandt A (2011) *Noise and vibration analysis*. Wiley, New York. ISBN 0470746440
13. Farrar CR (1997) System identification from ambient vibration measurements on a bridge. *J Sound Vib* 205(1):1–18
14. Ewins DJ (2001) *Modal testing: theory, practice and application*, 2nd edn. Taylor and Francis Group, London
15. Peeters B et al (2004) The PolyMAX frequency-domain method: a new standard for modal parameter estimation? *Shock Vib* 11(3–4):395–409
16. Busca G, Cappellini A, Cigada A, Scaccabarozzi M, Vanali M (2011) Dynamic properties of the Guglia Maggiore of the Duomo in Milano via operational modal analysis. EVACES 2011—Experimental vibration analysis for civil engineering structures, Varenna (Italy), 3–5 Oct 2011

Chapter 45

Optimal Sensor Placement for Structural Health Monitoring of Power Transmission Tower-Line Systems

José Antonio Vergara, Rafael Castro-Triguero, David Bullejos, Rafael Gallego, and Diego Zamora

Abstract This paper presents a numerical pre-test finite element modeling and optimal sensor placement study for power transmission structures. The number, geometry, repetition and importance of such structures require easier, quicker and cheaper monitoring methods. Vibration-based health monitoring methods determine the modal characteristics of the structure via a limited number of sensors. These characteristics are intrinsic properties, so that a variation in them may be induced by structural damage. Only a limited number of degrees-of-freedom can be measured for the system identification process. By developing a finite element model for the tower-line structure, these degrees-of-freedom can be identified. Prior to any modal analysis, a geometrically non-linear static analysis of the structure is required. Based on these results, two methods are employed to determine the optimal sensor number and locations. Both are formulated with the use of the modal properties of the structure model. The first scheme maximizes the independence of the target modal shape matrix in an iterative process, where those degrees-of-freedom that do not contribute to the independence of the target modes are eliminated. The second scheme is based on a mass-weighting of the previous one. Correlation results are developed between the tower and the tower-line structures in order to verify the influence of the lines in the modal characteristics. In order to simulate experimental measuring, modal properties are altered by adding Gaussian noise which determines the effect on the number and location of the sensors. It is concluded that employing the tower-line system is more accurate than considering only the tower structure; and the result of sensor placement is improved for structural health monitoring purposes.

Keywords Optimal sensor placement • Power transmission tower • Non-linear analysis • Structural health monitoring • Operational modal analysis

45.1 Introduction

Assessment of the structural and functional integrity of civil engineering structures is an essential design issue and of continuous concern during the process of maintenance, repair and upgrading of such structures. The concept of Structural Health Monitoring (SHM) offers tools to predict the behavior of a particular structure under operating conditions that differ from those taken into consideration in the initial design cycle. Employment of the aforementioned concept requires computational models that are verified, refined and adjusted with respect to actual measurements. In this context, Operational Modal Analysis (OMA) is based on dynamic measurements without interrupting the use of the structure and therefore is specially suited for SHM of large and fixed structures. Sensor placement in a host structure is an important initial step in the field of experimental modal analysis (EMA) and in particular in operational modal analysis (OMA).

J.A. Vergara (✉) • R. Gallego • D. Zamora
University of Granada, Granada CP 18071, Spain
e-mail: javergara@ugr.es; gallego@ugr.es

R. Castro-Triguero • D. Bullejos
University of Cordoba, Cordoba CP 14071, Spain
e-mail: melcatr@uco.es

Li *et al.* [1] presented a state of the art of sensor placement for Structural Health Monitoring where the most common methodologies for optimal sensor placement (OSP) were compared. These methodologies can be classified into two groups: sub-optimal methods and methods based on formal optimization strategies. The sub-optimal methods are based on iterative techniques and the latter treat the problem as a classical optimization problem.

Due to its repetitive design and its cost, the towers of the transmission lines are of vital importance and hence, accurate studies of his structural behavior should be performed. Lam *et al.* [2] and Yin *et al.* [3] proposed two complete papers about damage detection of transmission tower lines systems with numerical and experimental models. They decided preliminary sensor locations based on several practical approaches. This set of preliminary sensor location was checked by using sensitivity analysis and then was compared with Effective Independence (EFI) method [4]. However, Lam *et al.* [2] did not consider cable (conductors) effects on the tower dynamic response, nor geometric non-linearities of coupled tower-line system. Non-linear analysis that considers high non-linearities of coupled tower-line system models are not very common due to its computational cost. Li *et al.* [5] proposed simplified models for coupled transmission tower-line systems which considered non-linearities of coupled models without a pre-test finite element analysis. Bai *et al.* [6] developed a coupled three towers-line system model to study local site effect on its seismic response. Shehata *et al.* [7] considered conductors geometric non-linear behavior of coupled tower-line system under downburst wind loading. Chen *et al.* [8] studied modal characteristics of two operating power transmission poles and created several models: one of these models contained conductors (cables). Prior to modal analysis, the authors carried out a pre-test finite element analysis.

In this paper, optimal sensor placement for the case of transmission tower structures is studied for Structural Health Monitoring purposes. Two different models are considered: an isolated tower and a coupled tower-line system. The coupled model includes electric insulators and cables (conductors). Furthermore, cable non-linear effects are considered by pre-test finite element analysis. Numerical examples are presented to demonstrate the application of classical optimal sensor location methodologies to transmission tower structures.

45.2 Optimal Sensor Placement: Theoretical Basis

Kammer [4] introduced the EFI optimal sensor placement algorithm which aims to search the best set of DOFs locations from all the candidate locations in the structure such that the linear independence of the mode shapes is maintained. The starting point of this method is the full modal matrix (Φ) from a finite element model. All the DOFs used in the FE model cannot be measured in the real structure due to physical limitations. Therefore, the DOFs corresponding to rotations and coordinates which cannot be measured are eliminated from the full modal matrix. Likewise, not all mode shapes can be experimentally measured, hence some target modes are selected to be optimally detected. Hence, the rows corresponding to DOFs that can be measured are kept and the columns corresponding to target modes are retained in the full modal matrix. The Fisher information matrix (FIM) is defined as

$$FIM = \Phi^T \Phi \quad (45.1)$$

If the determinant of the FIM is zero, the columns of the modal matrix (i.e. the target modes) are linearly dependent. Therefore, the purpose of the EFI method is to select the best DOFs (to place the sensors) which maximizes the determinant of the FIM.

A mass weighting version of the EFI (EFIWM) method is also studied in the literature [1]. In this case the FIM matrix corresponds to

$$FIM = \Phi^T M \Phi \quad (45.2)$$

45.3 Power Transmission Tower-Line System

For the development of this work, the coupled tower-line system is considered to be built with lattice steel double rectangular crosshead (Type R). The tower common configuration is the double circuit three-phase line for 66 kV voltage. The most unfavorable scenario (locating the model at 1,500 m or higher altitude above sea level) is considered. In this situation,

Fig. 45.1 Transmission tower configuration (units: mm): (a) front face, and (b) right face

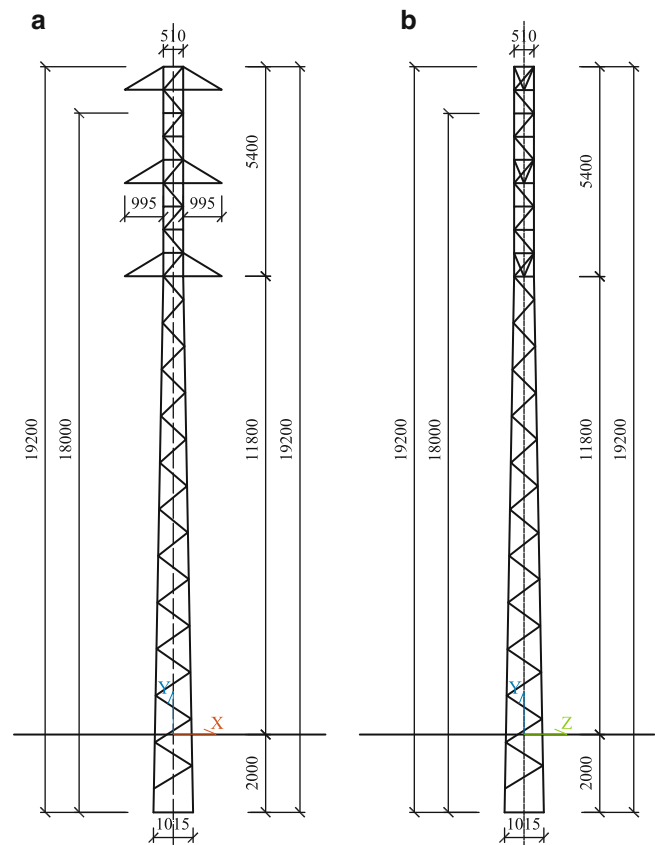


Table 45.1 Transmission tower element properties

Tower properties		Line properties	
Overall length	19.20 m	Left span length	201.9 m
Embedment depth	2.00 m	Difference in elevation at the left span	-1.18 m
Columns	L.130.14	Left vertical sag	4.49 m
Braces	L.70.8	Right span length	197.67 m
Beams cross arms	L.90.7	Difference in elevation at the right span	-0.84 m
Braces cross arms	L.50.4	Right vertical sag	4.30 m
Modulus of elasticity	2.1×10^{11} Pa	Nominal cross section cable diameter	14.00 mm
Poisson's ratio	0.3	Nominal cross section cable area	116.2 mm^2
Density	7850 kg/m^3	Weight per unit length	0.433 kg/m
		Modulus of elasticity	8200 kg/mm^2
		Insulator overall weight	21.77 kg

the tower has the general application for suspension support (aligned in the direction of transmission) so the efforts of the power line over it has only vertical components and parallel to the power line, thus simplifying the lateral loads due to the weight of the line itself. The joint efforts should be considered from the vertical permanent overload weight drivers, hardware and insulators, conductor effort by ice, wind stress on the support and traction imbalances between conductors, considered as 8% of the total load per conductor. For stability considerations, a single typical foundation of depth = 200 cm is considered (Fig. 45.1; Table 45.1).

45.4 Finite Element Modal Analysis

A complete finite element model was performed for both cases: isolated tower and coupled tower-line system. Columns and cross arms were considered as beams. Braces, slack cables and electric isolators were modelled as simple links. The coupled tower-line system model includes slack cables and requires a pre-test finite element analysis. When a displacement solution is obtained, a modal analysis of the coupled system is developed. For the case of mode shapes extraction, block Lanczos method is employed in both models. Furthermore, modal analysis is realized in order to know tower and coupled tower-line system modal characteristics (see Table 45.2). First shape modes of coupled system are governed by cables behavior (lower frequencies). In order to find the tower mode shapes (higher frequencies) it is necessary to extract a lot of frequencies and mode shapes of the finite element model (about 3000 frequencies). Figures 45.2 and 45.3 show some of the more relevant mode shapes for both, isolated tower model and coupled tower-line system model respectively.

45.4.1 Models Correlation

Analytical results from a finite element model must be validated with respect to those obtained by experimental measurements. Towards this aim, several techniques may be employed [9]. One of the simplest methods for data correlation is to calculate the percentage differences between the natural frequencies obtained by analytical and experimental techniques (see Fig. 45.4). Fifth frequency show higher differences due to the coupled effects of cables. The other frequencies show minor errors.

Table 45.2 Modal analysis results

Isolated tower (A-model)		Coupled tower-lines system (B-model)	
First bending mode (X direction)	2.838 Hz	First bending mode (X direction)	2.830 Hz
First bending mode (Z direction)	2.839 Hz	First bending mode (Z direction)	2.809 Hz
Second bending mode (X direction)	14.416 Hz	Second bending mode (X direction)	14.272 Hz
Second bending mode (Z direction)	14.476 Hz	Second bending mode (Z direction)	14.355 Hz
First torsional mode (Y direction)	15.094 Hz	First torsional mode (Y direction)	13.508 Hz
Third bending mode (X direction)	34.094 Hz	Third bending mode (X direction)	34.029 Hz
Third bending mode (Z direction)	34.436 Hz	Third bending mode (Z direction)	34.157 Hz

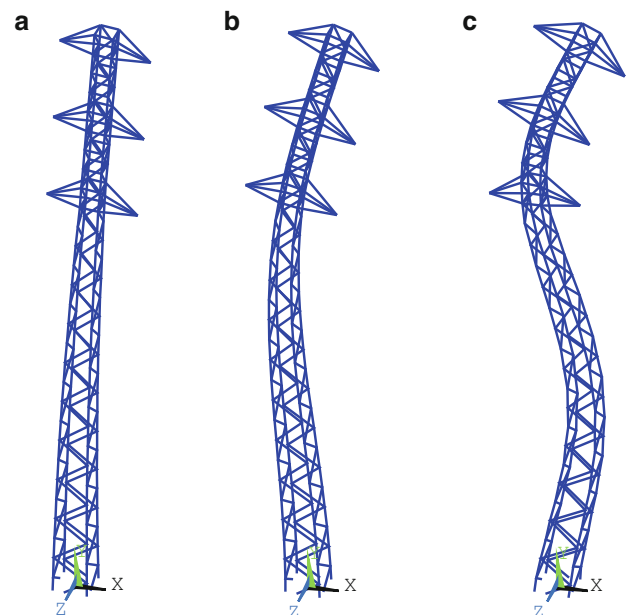


Fig. 45.2 Numerical mode shapes of the isolated tower model: (a) First vibrational mode in the X direction (2.838 Hz), (b) second vibrational mode in the X direction (14.416 Hz), and (c) third vibrational mode in the X direction (34.094 Hz)

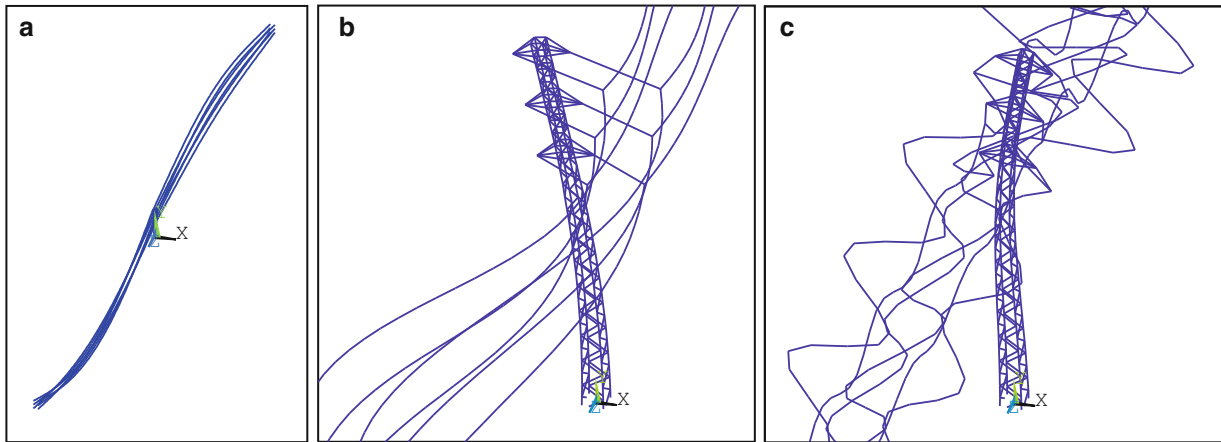


Fig. 45.3 Mode shapes of the coupled tower-line system model: (a) First cable in-line plane vibrational mode (0.269 Hz), (b) first tower vibrational mode in the X direction (2.830 Hz) and (c) second tower vibrational mode in the X direction (14.272 Hz)

Fig. 45.4 Percentage differences between isolated tower model and coupled tower-line system obtained natural frequencies

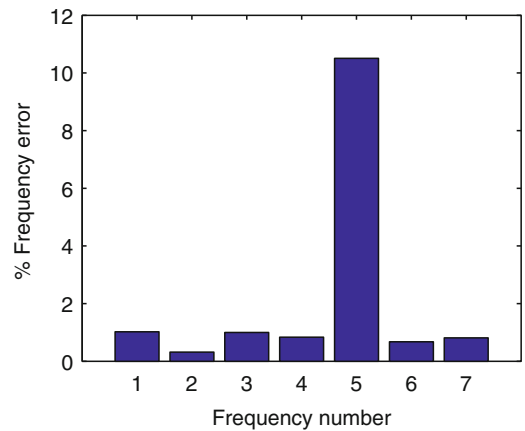
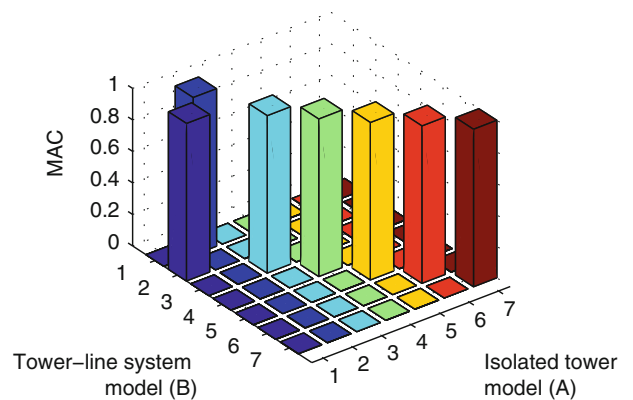


Fig. 45.5 Representation of Modal Assurance Criterion (MAC) matrix between the coupled tower-line system and isolated tower models



The modal assurance criterion (MAC) is another commonly used method to establish a correlation factor for each pair of analytical and experimental mode shapes. A high correlation yields a MAC value close to 1, whereas a low correlation assumes values near 0. Figure 45.5 represents the MAC-matrix for the first seven mode shapes. Modal assurance criterium show a very correlated mode shape between both models. This leads to the conclusion that the behavior of both models are

very similar. Cable effects are very important in power transmission lines dynamic behavior, but MAC results demonstrates that cables do not have a significant effect on tower modes shapes. This is due to transmission line symmetry conditions and also because the mass and stiffness of the tower are more important than those of the cable.

45.5 Optimal Sensor Placement (OSP)

Optimal sensor placement methodologies (EFI and EFIwm) have been applied to both cases: isolated tower and coupled tower-line system models. Only horizontal translation degrees-of-freedom from the finite element models are selected as possible locations. Rotations cannot be measured due to experimental limitations and vertical translations are not important on tower bending and torsional mode shapes. Several sensor configurations are considered (8, 10 and 12 sensors). Figures 45.6 and 45.7 show node number and degree of freedom (U_x - U_z) of the sensor optimal locations. From the results it can be observed that EFI method places sensors at similar heights with independence of the number of sensors considered. EFIwm method tends to concentrate all the sensors at the top of the tower due to the tower mass effect.

Vibration measurements are often contaminated by noise. It could be originated by the wind, the traffic, and also due to the cables that are connected to the accelerometers. This uncertainty can be simulated by adding some noisy-terms to

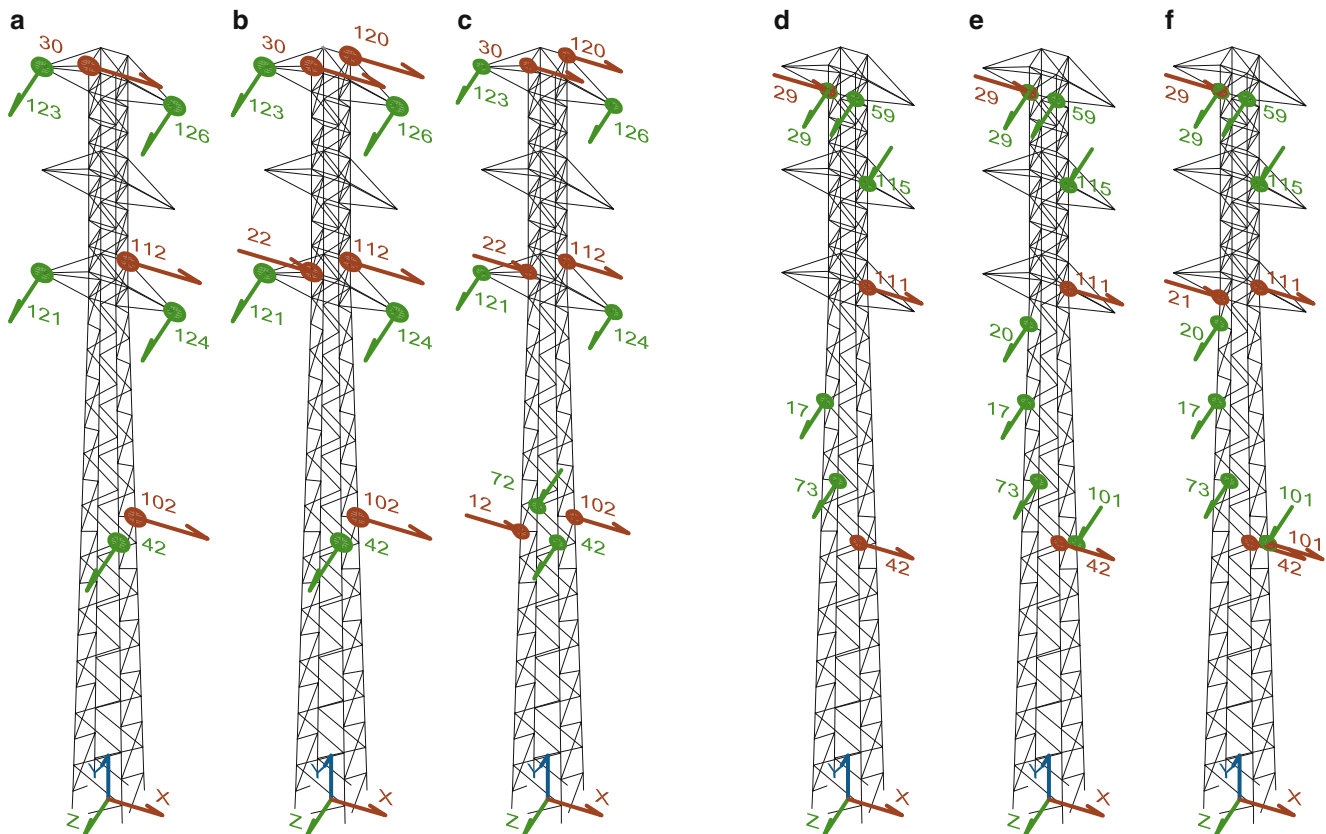


Fig. 45.6 Optimal sensor placement of isolated tower model: (a) EFI method-8 sensors, (b) EFI method-10 sensors, (c) EFI method-12 sensors, (d) EFIwm method-8 sensors, (e) EFIwm method-10 sensors, and (f) EFIwm method-12 sensors

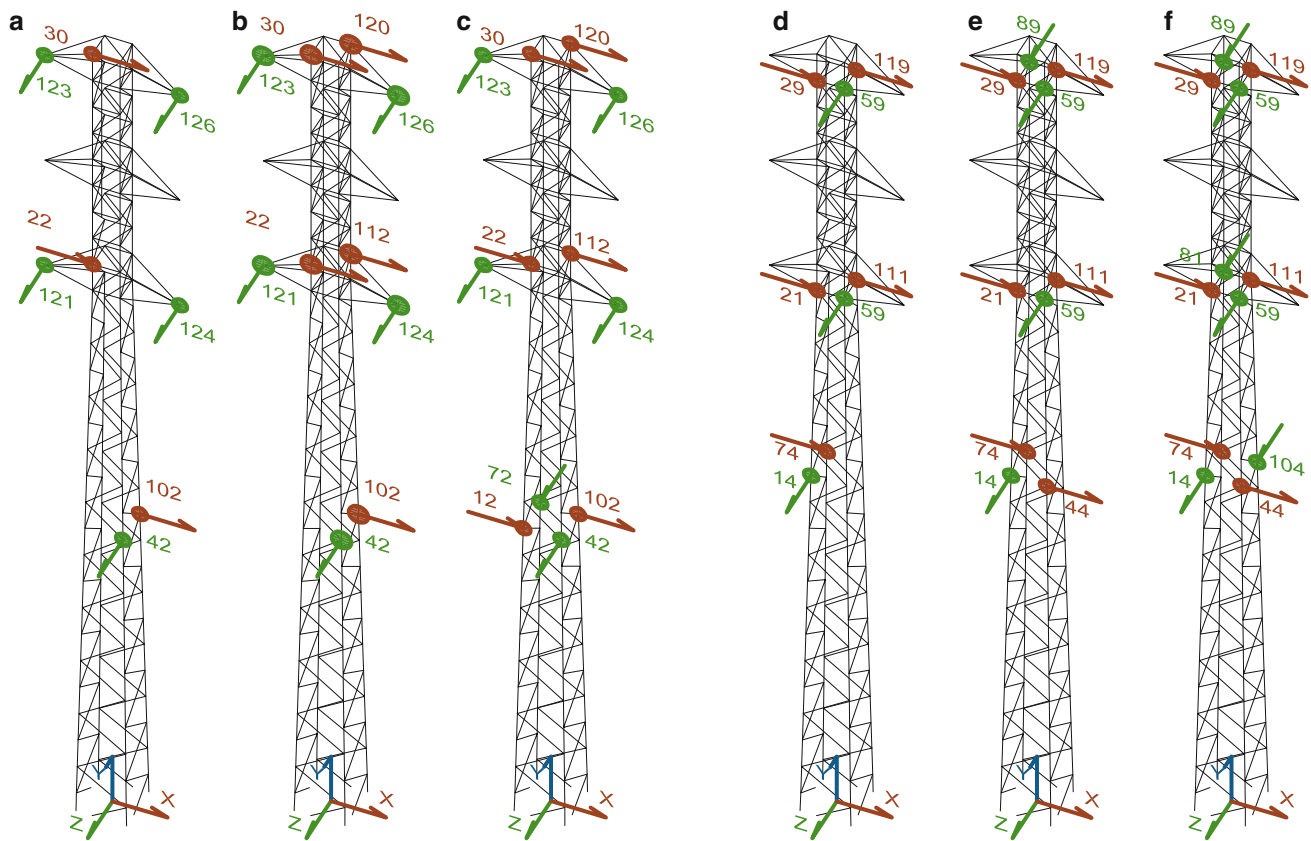


Fig. 45.7 Optimal sensor placement of coupled tower-line system model: (a) EFI method-8 sensors, (b) EFI method-10 sensors, (c) EFI method-12 sensors, (d) EFIwm method-8 sensors, (e) EFIwm method-10 sensors, and (f) EFIwm method-12 sensors

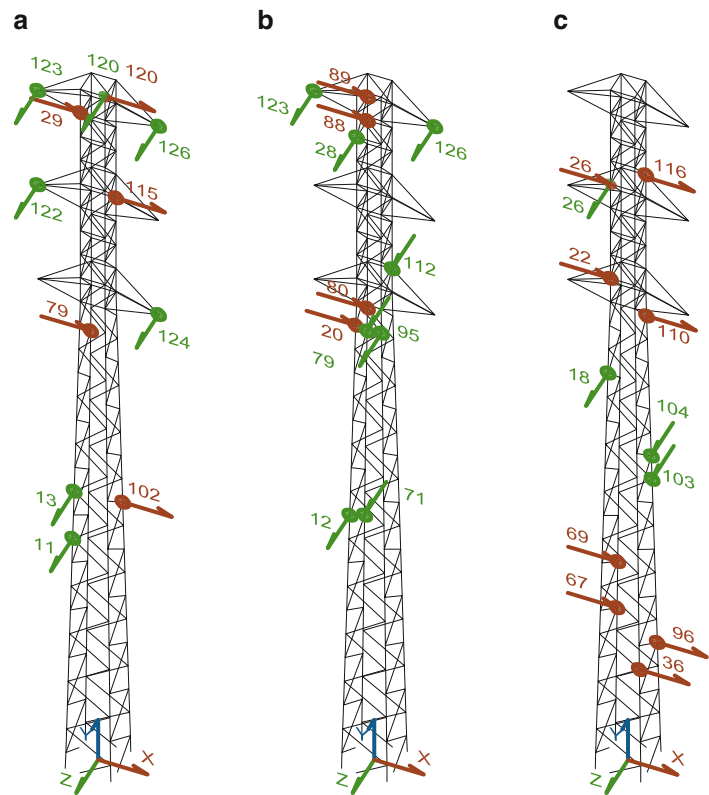
the experimental modal shapes. For illustrative purposes, only EFI methodology is followed for the case of the coupled tower-line system model with three different different levels of signal-to-noise ratios (60 dB, 40 dB, and 10 dB). In this particular case only twelve sensors are considered to be optimally placed (see Fig. 45.8).

45.6 Conclusions

The proposed methodology offers an effective tool for treating the optimal sensor placement of transmission tower lines for Structural Health Monitoring purposes. Two different models were considered: an isolated tower and a coupled tower-line system. Finite element model analysis was developed and mode shapes for both systems were performed. Correlation analysis established well correlation between both models. Classical optimal sensor methodologies were applied to those models with different set of sensors. Sensor locations on both models were similar and the sensors were placed at three different heights. Different sensor configurations show that only eight sensors are necessary to define those three height levels. Noise effects were also considered and simulated with different signal-to-noise-ratios (60 dB, 40 dB, and 10 dB). It is demonstrated that lower signal-to-noise ratios conserve the location of the sensors. However, for the case of higher noise these locations are completely different. This concludes that optimal sensor placement methodologies are essential and necessary for quicker and cheaper Structural Health Monitoring procedures.

Acknowledgements We express special thanks to the Spanish Ministry of Education, Culture and Sport for Grant Number FPU-AP2009-3475 and to the Junta de Andalucía for the Research Project P09-TEP-5066.

Fig. 45.8 Optimal sensor placement of coupled tower-line system model by EFI method considering noise effects (12 sensors). Signal-to-noise ratios: (a) 60 dB, (b) 40 dB, (c) 10 dB



References

1. Li DS, Li HN (2006) The state of art of sensor placement methods in Structural Health Monitoring. Proceedings of SPIE the international society for optical engineering, San Diego, CA, USA; 27 Feb 2006–2 Mar 2006, 6174 II
2. Lam HF, Yin T (2011) Dynamic reduction-based structural damage detection of transmission towers: practical issues and experimental verification. *Eng Struct* 33:1459–1478
3. Yin T, Lam HF, Chow HM, Zhu HP (2009) Dynamic reduction-based structural damage detection of transmission tower utilizing ambient vibration data. *Eng Struct* 31:2009–2019
4. Kammer DC (1990) Sensor placement for on-orbit modal identification and correlation of large space structures. American control conference, San Diego, CA, USA; 23–25 May 1990, pp 2984–2990
5. Li HN, Shi WL, Wang GX, Jia LG (2005) Simplified models and experimental verification for coupled transmission tower-line system to seismic excitations. *J Sound Vib* 286:569–585
6. Bai FL, Li HN, Hao H (2010) Local site effect on seismic response of coupled transmission tower-line system. Earth and space 2010. 12th International conference on engineering, science, construction, and operations in challenging environments, Honolulu, Hawaii, USA; 14–17 Mar, 2010, pp 2857–2869
7. Shehata AY, El Damatty AA, Savory E (2005) Finite element modeling of transmission line under downburst wind loading. *Finite Elem Anal Des* 42:71–89
8. Chen SE, Dai K (2010) Modal characteristics of two operating power transmission poles. *Shock Vib* 17:551–561
9. Friswell MI, Mottershead JE (1995) Finite element model updating in structural dynamics. Kluwer Academic Publishers, Dordrecht

Chapter 46

Evaluation of Economical Dynamic Exciters for Vibration Testing of Bridges

E.V. Fernstrom, J.L. Carreiro, and K.A. Grimmelsman

Abstract Quantitative data describing condition and performance is essential for evaluating the structural health of bridges. Dynamic testing is a common approach for globally characterizing bridges in a quantitative sense. Dynamic testing is most commonly accomplished for full-scale bridge structures through either forced vibration testing or ambient vibration testing methods. Forced vibration testing offers many advantages, but is generally not a practical or economical approach for many bridges due to the high cost of providing controlled excitation, limits to the excitation that can be supplied, and interference with the normal operation of the bridge. The writers have been investigating the feasibility of using low-cost, small-scale dynamic exciters for forced vibration testing of short to medium span bridges. The exciters being evaluated have a unit cost that is comparable to a typical accelerometer, and could be deployed in numbers using a spatially distributed setup for forced vibration testing. This paper presents and describes the results of a laboratory evaluation program conducted for these devices. Their capabilities and operating characteristics are compared with a more conventional linear mass shaker. The preliminary results of a vibration test using these devices on an in-service highway bridge are also discussed.

Keywords Bridges • Shaker • MIMO • Vibration testing • Laboratory characterization

46.1 Introduction

The aged and deteriorated condition of transportation infrastructure is a well-publicized issue facing the United States. Current reports indicate that about 10% or nearly 60,000 of our nation's bridges are structurally deficient [1]. The difficulty of maintaining the bridge population is compounded by limited funding for repair or replacement. The national concern regarding the budget deficit and the strong push in Washington to cut costs wherever possible impact the ability of transportation agencies to adequately care for their bridges. Therefore, it is critical that the limited available funding be spent on bridges that have the greatest need for structural improvement. It is difficult for bridge owners to determine which of their bridges are the most in need of repair or replacement because the condition evaluation and assessment data they typically have available is the result of subjective biennial inspections. The greatest limitation of the biennial inspection process is that it is almost always limited to visual identification and characterization of localized defects. Additionally, despite the best efforts of owners to provide guidance to inspectors, it is neither possible to consistently provide a qualitative value for the condition of a single type of structural component, nor for the condition of an entire bridge. A quantitative determination of bridge condition would be highly useful for supporting operational and maintenance management decisions if it can be based on the actual global behavior of the structure and if the information can be consistently developed across the bridge inventory.

Dynamic testing is a quantitative and global characterization method that can be used to help establish the condition of bridges. It is the process of measuring the time-varying responses of a structure due to external dynamic excitation. Typically, the measured acceleration responses from different locations on a bridge are used to identify modal characteristics such as the natural frequencies, mode shapes, and damping ratios. These characteristics are system properties of a structure and are functions of its mass, stiffness, and damping. Changes in the structure due to damage, deterioration, and environmental

E.V. Fernstrom • J.L. Carreiro • K.A. Grimmelsman (✉)
Department of Civil Engineering, University of Arkansas, 1 University of Arkansas, Fayetteville, AR 72701, USA
e-mail: efemstr@uark.edu; jcarreir@uark.edu; kgrimmel@uark.edu

effects are reflected by changes in the observed dynamic properties. Many researchers are working to develop algorithms that can identify damage severity and location from dynamic testing results. With this data in hand, operating agencies could better rank the condition of their bridge inventory and apply their limited funding to the structures with the greatest need.

Dynamic testing and modal analysis of aerospace and automotive systems has been successfully used for decades. In these industries, the evaluation is often performed in a controlled laboratory setting with the test subject well-isolated from ambient dynamic inputs. Both inputs and responses of the test subject are measured and the desired modal properties are determined. Attempting to use the same process for civil engineering structures is logical, but a significant challenge is to adequately excite structures of the scale of typical civil works. Exciting all of the desired modes of a large bridge, building, or dam from a single input location requires a large excitation device [2]. In addition to their high cost and low availability, such devices also present logistical challenges since their large size requires the use of cranes or other specialized equipment to place them in the desired positions on a structure. Imparting large forces from a discrete location on a structure is more likely to excite structural nonlinearities making it more difficult to identify the linear modal characteristics [3]. Data inconsistency can also be a problem when excitation is only provided at one discrete location on a structure at a time. First, the equipment setup change that is required in moving from location to location impacts the data [4]. Second, the time elapsed between different test setups can allow time-varying structural characteristics such as temperature to skew the identification results. For these and other reasons, researchers have explored other means of dynamic excitation for civil structures.

Significant research has been performed on output-only analysis methods in which the external dynamic excitation is not measured. The modal parameters can be extracted from the output measurements with the assumption that the excitation is stationary, broadband, and uncorrelated to prior system responses [5]. In the case of bridges, the input is typically ambient excitation from the operating traffic and natural sources such as wind, microtremors, etc. A significant limitation of output-only analysis methods is that modal scaling cannot be calculated directly from the measurements [6] since it requires knowledge of the input force. The inability to determine modal scaling leads to the inability to calculate modal flexibility, and can further limit the utility of the results for various damage detection algorithms. Another potential issue with ambient excitation is that the assumption of a stationary, broadband input may be violated for a given test, and since the input is not measured this violation is unlikely to be detected or its impact evaluated. Finally the vehicular traffic that is a major source of ambient dynamic excitation for in-service bridges leads to random changes in the mass and damping characteristics of short to medium span bridges, violating the assumption of a time-invariant structure.

One potential solution that would allow measurable excitation for certain types of civil structures could be to use an array of moderately sized controlled excitation devices spatially distributed on the structure along with the accelerometers used to record the vibration responses. This type of dynamic testing is referred to as multiple input, multiple output (MIMO) and has a number of advantages. First, an array of spatially distributed shakers would require less force to be input at each location, reducing the excitation of nonlinearities. Also, collecting many FRF columns simultaneously greatly improves data consistency since time variations in structure properties and setup changes are eliminated. Finally, the use of measurable inputs enables the calculation of modal scaling and modal flexibility. The major drawback of MIMO testing of civil structures has always been cost. Many researchers use laboratory grade commercial shakers as excitation devices when performing MIMO tests. A commonly used shaker from APS Dynamics costs about \$13,000 for a device that can impart 187 N (42 lbf) of dynamic force over a broad frequency range. A similar shaker available from APS Dynamics that can provide 445 N (100 lbf) costs about \$18,000. Some researchers have built one-off shakers and impact devices that are far more expensive. The costs of these shakers and the associated challenges in effectively deploying them on civil structures appears to have significantly limited MIMO testing applications for civil structures. This is also evidenced by the relatively few examples of this testing for civil structures that can be found in the literature.

It is proposed herein that an array of low cost electrodynamic shakers could be used to provide controlled and measurable dynamic excitation to certain classes of civil structures and would enable more robust and reliable dynamic analysis. The basic idea is to greatly reduce costs by using a widely available consumer product that has real price competition to serve as the controlled dynamic excitation device. The device proposed for this purpose is best described as a tactile transducer. Tactile transducers are devices used in home theater applications to shake the floor or furniture to mimic situations in movie scenes. The tactile quality of the shaking enhances the experience of watching the movie by more deeply immersing the viewer's senses. These devices retail for prices generally ranging from \$50 to \$1,000. One model of tactile transducer considered for this study has a unit cost of about \$200 and provides approximately 133 N (30 lbf) of peak dynamic force. It is noteworthy that the frequency range of the tactile transducers is generally aligned with the natural modes of interest for many common types of short to medium span bridges (5 Hz to 50 Hz). The estimated cost per excitation location including a power supply, amplifier, and shaker is on the order of \$500, which compares very favorably with the laboratory shaker prices described previously. A review of the published literature did not find any researchers using or attempting to use such low-cost commercially available excitation devices for MIMO testing of civil structures.

This paper summarizes the results of a laboratory testing and evaluation program that was undertaken in order to establish the operating characteristics of several commercially available tactile transducers. The main objective of the evaluation

program was to determine if such devices could be feasibly used for MIMO dynamic testing of short to medium span bridges. A related objective was to aid in the selection of a transducer-amplifier pair that would provide acceptable excitation force amplitudes in the frequency range of interest, and that would reliably reproduce the swept-sine and burst random signals that are typical for modal testing of bridges. Some limited data recorded with these transducers for a full-scale bridge were also evaluated to assess the practicality of this approach for real, in-service bridge structures. The outcome of this testing provided the fundamental operational and performance characteristics necessary to move forward with design and development of a low-cost 16 channel MIMO excitation system that would be suitable for controlled dynamic testing of short to medium span bridges.

46.2 Devices Evaluated

Most of the tactile transducers surveyed for this study were small-scale, proof-mass type dynamic shaker devices that are intended to make theater and gaming experiences more immersive. Low frequency sounds from movies or video games are sent to the tactile transducers and they create a rumbling sensation. This is accomplished by attaching the transducers to the underside of floors or furniture so that the low frequency rumble can be felt by the audience. The devices are widely and commercially available for use in home theater applications, 4D amusement park rides, and traditional theaters. There are a number of manufacturers that market these devices, and as a result, their cost is competitive. The market includes a variety of product sizes, power ratings, packaging options, and price ranges, but a point of commonality is that practically all tactile transducers use a voice coil as the principal motive system. In the parlance of vibration testing, these shakers are of the electrodynamic type; however, they are not specifically designed to meet the high expectations of the vibration testing community. Thus, their operating characteristics and responses to various excitation signals must be evaluated by the user before they can be used for dynamic testing applications.

Three different tactile transducers were selected as good representatives for the broad array of options available on the market. The initial selection of the devices to be evaluated in this study was based on online consumer feedback, price, and manufacturer specifications of power handling. The specific devices evaluated in this study will be referred to as Shaker 1, 2, and 3 throughout this paper and are shown in Fig. 46.1. It should be noted that the largest of the devices tested measured less than 150 mm (6 in.) in any dimension and weighs 4.5 kg (10 lb). The devices are relatively unobtrusive and would be easy to deploy on structures such as bridges.

Shaker 1 and Shaker 2 are similar in style and represent the most common type of tactile transducer. They consist of a rugged metal housing with integral cooling fins and all moving parts are located within the enclosure. Unlike a traditional shaker used for modal analysis of manufactured systems and components, there is no armature and no method to directly monitor the position, velocity, or acceleration of the moving mass. These two shakers are produced by different manufacturers and have significantly different specified power handling capabilities. Shaker 1 can be operated continuously at 400 Watts RMS, whereas Shaker 2 can only handle 50 Watts. As a result, it is not surprising that Shaker 2 is about a quarter of the cost of Shaker 1.



Fig. 46.1 Front row left to right – Shaker 1, Shaker 2, Shaker 3; rear row – APS 113HF

Table 46.1 General information for tested shakers and amplifiers

Shaker information				
Name	Price	Rated RMS power	Nominal impedance	Weight
Shaker 1	\$200	400 W	4 Ohm	4.5 kg (10 lb)
Shaker 2	\$40	50 W	4 Ohm	1.4 kg (3 lb)
Shaker 3	\$500	30 W	6 Ohm	1.8 kg (4 lb)
APS 113HF	\$12,940 W/amp	600 W	2 Ohm	47 kg (103 lb)
Amplifier information				
Name	Price	Rated RMS power	Channels	Weight
Amp 1	\$150	500 W	x 1	3.1 kg (6.9 lb)
Amp 2	\$120	480 W	x 2	3.8 kg (8.4 lb)
Amp 3	\$50	70 W	x 1	2.5 kg (5.6 lb)

Shaker 3 is of a different style and is more similar to a typical laboratory shaker. This device does not have a moving mass contained within a rugged packaging, and instead features a load table that is intended to support the leg of a chair or couch to impart the dynamic excitation. The load table is equivalent to an armature and this enables measurement of the shaker movements. Additionally, the load table allows the addition of mass which provides the ability to modify the force output and natural frequency of the shaker. This device can handle 30 Watts RMS.

An intrinsic and cost-plus component of any shaker system is the power amplifier. Three inexpensive commercial audio amplifiers were paired with the shakers for this testing program, and they will be referred to as Amp 1, 2, and 3. Amp 1 is a single channel device with an output power of 500 Watts RMS, which pairs well with Shaker 1. Amp 2 is a similarly powerful device but has two channels and a different manufacturer. Amp 3 is much less expensive and less powerful at 70 Watts and pairs with Shakers 2 and 3. Most amplifiers used for vibration testing can be setup to provide either a voltage output (voltage mode) or a current output (current mode) in proportion to the input signal. The subsequent velocity of the moving mass is proportional to voltage, and the acceleration (and force) is proportional to the current. Audio amplifiers do not have the capability to operate in current mode and thus voltage mode is used throughout this study.

An APS Dynamics 113-HF shaker paired with an APS 145 amplifier was also subject to the same shaker tests. This electrodynamic shaker system is representative of the types of high-quality (and more expensive) laboratory shakers used in vibration and modal testing. Reaction masses of 9 kg (20 lb) were attached to the shaker for all tests, and the APS amplifier was operated in voltage mode for all tests. The APS shaker results are presented as a point of comparison for the tactile transducers. Table 46.1 summarizes various nominal specifications of the devices tested.

46.3 Testing Criteria

Tactile transducers are essentially audio components and the manufacturers provide specifications that are generally aligned with traditional subwoofer characteristics. These specifications are not typically the same as those provided by the makers of shakers for vibration and modal testing. As such, a controlled laboratory testing program was performed to establish the characteristics of the tactile transducers. The first step in this process was to establish what characteristics would be most important for modal testing of bridges. These important characteristics could then be used as selection criteria for choosing the best device for an expanded MIMO testing system.

The most important characteristic of the shakers for bridge testing is the force output in the frequency range of interest. Bridges and other civil structures are massive, and a significant amount of input force is needed to adequately excite such structures beyond the ambient input level. These large structures also typically have low frequency modes which are best excited by low frequency input. Thus, the maximum force that could be produced at various frequencies, and especially at low frequencies, was tested and evaluated.

Another important characteristic is the ability of the shaker to accurately reproduce input signals that are typical to modal testing. These signals often include swept sine and burst random excitations. For testing the reproduction of sinusoidal signals, the periodogram was used to measure the energy content at both the input frequency and at other frequencies, and the signal to noise ratio was calculated for the measured outputs from the devices. To evaluate the reproduction of a broadband random input signal, the energy content at all frequencies within the range of interest must be compared.

The performance of the amplifier also impacts the shaker performance. Amplifier testing was performed to establish the characteristics of these devices as well. These tests included gain across the frequency range of interest, reproduction of sinusoidal signals, and reproduction of random signals. Finally, the shakers and amplifiers were evaluated for other criteria including cost, perceived durability, and ease of use.

46.4 Test Methods, Results, and Discussion

The subsections below describe the specific test methods that were employed and discuss the outcome of each test for both the shakers and the amplifiers. The results are considered in relation to the potential use of these devices in a MIMO array for dynamic testing of civil structures. The tests/criteria subsections are:

- 1) Shaker Force Output
- 2) Shaker Sinusoid Reproduction
- 3) Shaker Burst Random Reproduction
- 4) Amplifier Gain
- 5) Amplifier Sinusoid Reproduction
- 6) Amplifier Burst Random Reproduction
- 7) Other Considerations

For all tests, the signals were generated by an Agilent 33220A Arbitrary Waveform Generator and data was acquired by a National Instruments PXI 4472B DAQ card. All data processing was performed in MATLAB.

46.4.1 Shaker Force Output

As stated previously, the most important characteristic for the shakers is their ability to provide adequate excitation force over the frequency band of interest, which was taken as 0 to 100 Hz for this testing. This test was performed by attaching each shaker to an aluminum plate that was supported on three dynamic force transducers in a tripod arrangement. Sinusoidal signals were sent to Amp 1 and from there to the shaker. The power sent to the shaker was also monitored. With a discrete frequency input, gain was increased until the shaker “bottomed out” due to its stroke being exceeded or until the maximum recommended RMS power was reached, whichever came first. The output from the three force transducers was summed and the total force was recorded for 4 seconds. The mean RMS value of this measured force was then taken as the maximum force available at the frequency under consideration.

Figure 46.2 illustrates the maximum RMS force that each shaker produced over the frequency range. The APS shaker is capable of producing 220 N (50 lbf) at a frequency of 4 Hz in voltage mode. The force gradually falls off to a low of about 130 N (30 lbf) at 50 Hz before peaking at 440 N (100 lbf) (off graph) at the natural frequency of the shaker. The shape of the APS force response demonstrates the highly nonlinear nature of force output in relation to frequency. The factors that limit the force also change depending on frequency. The force is limited by the shaker stroke length up to about 3 Hz, and this particular shaker has a long 158 mm (6.25 in.) stroke. Above 3 Hz the force is limited by the amplifier power. It is clear that the APS shaker can produce significantly more force than any of the tactile transducers that were evaluated.

Of the three different tactile transducers evaluated, Shaker 1 provided the highest level of force at low frequencies. The force rises nearly linearly from zero at 1 Hz to about 90 N (20 lbf) RMS at 29 Hz and then gradually decreases with increasing frequency. The tactile transducers all have a short stroke and this limits the low frequency force they can produce without bottoming out. Shaker 1 is limited by its stroke up to 25 Hz, and above 25 Hz the force is limited by the power capacity of the shaker. Compared to the other tactile transducers, Shaker 1 has a much broader peak in the vicinity of its natural frequency and can provide much greater force across the range of 30 to 80 Hz.

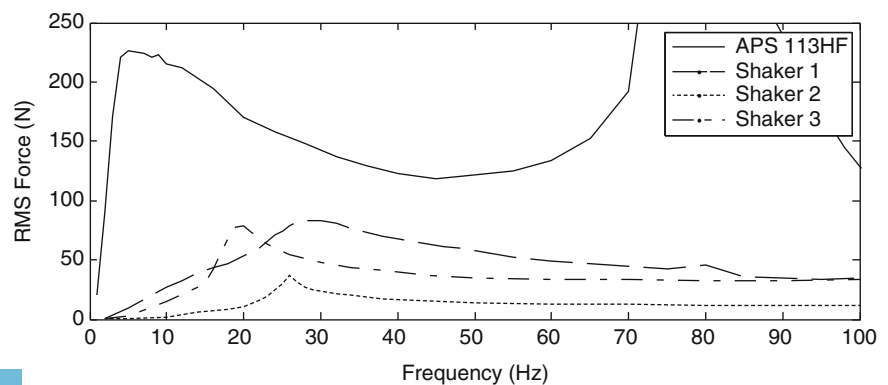
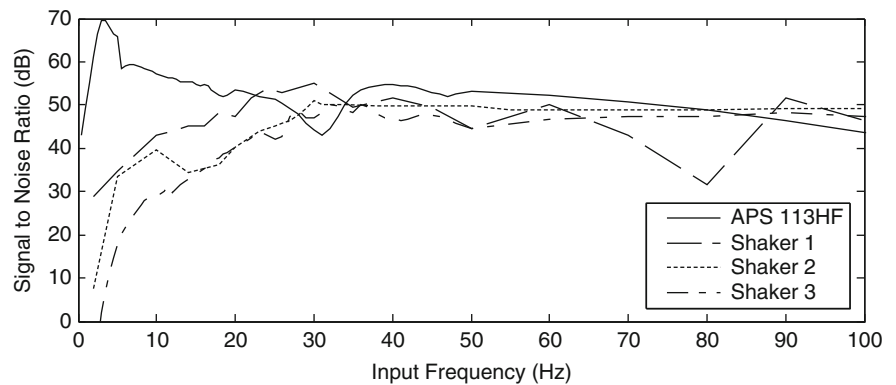


Fig. 46.2 RMS force output for subject shakers in the frequency range of interest

Fig. 46.3 SNR for subject shakers in the frequency range of interest



Shaker 2 produces the least force of all of the shakers across the entire frequency range. The force is stroke-limited below 5 Hz and is limited by the 70 Watt shaker power capacity above this. This shaker provides very little force at low frequencies with less than 9 N (2 lbf) RMS at 20 Hz. The force has a strong peak at the 27 Hz shaker natural frequency and then quickly drops down to about 13 N (3 lbf) RMS at higher frequencies.

Shaker 3 differs in its construction from the other two shakers in that it has a load plate and is meant to carry additional mass. This allows a broad range of experiments to understand how the force output varies with increments of additional mass and how the reproduction quality varies simultaneously. The results shown are with an added mass of 1.03 kg (2.26 lb) of aluminum disks (the powerful fixed magnets in the shaker precluded the use of ferrous metals for added mass). The shaker force is generally stroke limited at frequencies near and below the peak force, and is limited by the shaker power capacity at higher frequencies. The added mass allows high forces to be generated relative to power consumption, and the magnitude of the mass allows the peak to be adjusted to particular frequencies. However, the force falloff is significant away from the sharp peak at the natural frequency of the shaker/mass system.

Overall, the short stroke lengths of the tactile transducers preclude them from producing high forces at low frequencies without bottoming out. Of the three transducers tested, Shaker 1 provides the largest force at low frequencies and provides the most consistent force response across the frequency band of interest. Shaker 3 provides the unique ability to have its peak force output tuned to a particular frequency by adding mass, and provides a high level of force given its low power input. Shaker 2 and Shaker 3 both provide a very consistent level of force at higher frequencies. It should be noted that due to the small sizes and low cost of the shakers, multiple shakers could be located at each input location on a bridge to increase the total force output.

46.4.2 Shaker Sinusoid Reproduction

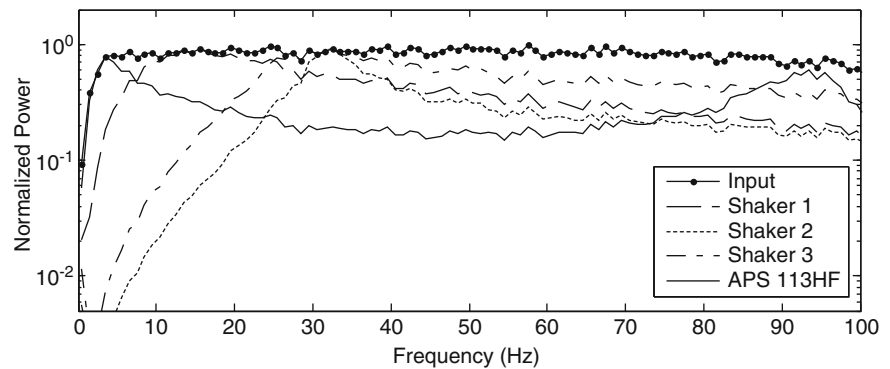
A signal to noise ratio (SNR) measurement was used to characterize how well each shaker converted a voltage input to a force output. A sinusoidal signal at a particular frequency was generated, amplified by Amp 1, and then sent to the subject shaker. A sinusoid at one frequency was generated for 6 seconds and then the next higher frequency was generated. The signal input to the shaker and the force output were continuously recorded during this process. In data processing, the first 2 seconds of data at each frequency were ignored so that the minor transient that occurred at frequency changes would be excluded from the results. The remaining 4 seconds of data were transformed to the frequency domain. The mean RMS value of the response away from the input frequency was found and divided into the response at the input frequency to determine SNR.

As a baseline, the APS shaker provides very good reproduction at low frequencies with an SNR of 70 dB at 3 Hz (Fig. 46.3). As frequencies increase, the measured noise increases but the signal is still far more powerful than the noise. It is recognized that the degradation at higher frequencies is largely due to a constant data acquisition rate of 1000 Hz, which causes increased aliasing in the Fourier transform as signal frequencies increase.

As expected, all of the tactile transducers performed poorly at lower frequencies due to their limited strokes. Shaker 1 performed the best with a SNR of about 30 at 1 Hz. The signal reproduction then improves up to the natural frequency of Shaker 1 and then gradually declines in general except for a segment of poor reproduction in the vicinity of 80 Hz.

Shaker 2 provides low SNR below 3 Hz but then steadily improves to the point that this shaker provides the cleanest response above about 35 Hz. In fact, the force output from this shaker has a higher signal to noise ratio than the signal input to the shaker, indicating that the internal workings of the device enhance sinusoidal motion of the mass.

Fig. 46.4 Reproduction of burst random signal by subject shakers



Shaker 3 has very poor SNR up to about 10 Hz, and is generally the worst at reproducing lower frequency signals up through about 30 Hz. This shaker then has a fairly constant SNR which is in the same range as the APS shaker and Shaker 1. Shaker 3 has the shortest stroke of all of the devices tested, and this significantly impacts its ability to reproduce low frequency sinusoids while producing any appreciable force.

Overall, the SNR values are negatively impacted at low frequencies due to the stroke limit of the tactile transducers. Shaker 1 has the longest stroke and is the least limited. At higher frequencies, all of the transducers do a good job of producing a force signal that is predominantly sinusoidal with very little noise. A SNR value of 40 corresponds to an RMS value of the signal that is 10,000 times greater than the RMS value of the noise, and all of the transducers exceed this threshold at higher frequencies except Shaker 1 at 80 Hz.

46.4.3 Shaker Burst Random Reproduction

The test method for burst random shaker testing began by generating a Gaussian white noise in MATLAB. This signal was then modified with a 5th order low-pass Butterworth filter using a cutoff frequency of 100 Hz. The resulting signal was 128 seconds long with 500 points per second. This was amplified by Amp 2 and sent to the shaker, and force was recorded as before. The measured time data for the signal from the amplifier and for the force output were transformed to the frequency domain for analysis. The high resolution caused excessive visual noise in the graphical output, and this was diminished by reducing the resolution to 1 Hz by averaging the absolute values of the response within each 1 Hz window.

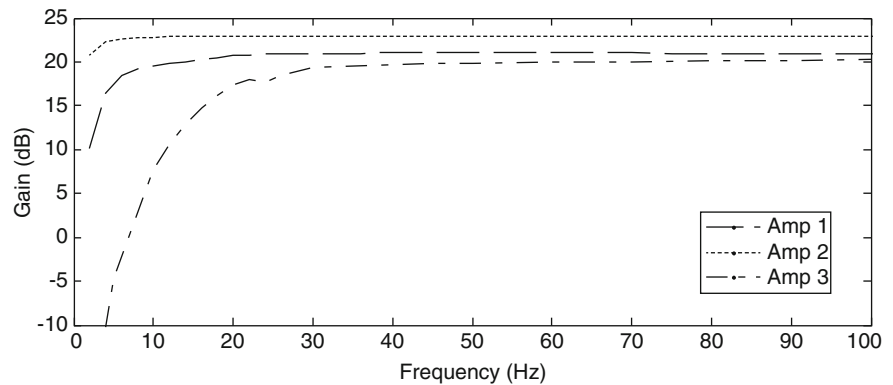
The outcome of this testing is presented in Fig. 46.4 with the 'Input' curve representing the power content of the signal that was output by the amplifier. The other four curves are the power content of the force signal measured as the output of each shaker. The results generally show that the tactile transducers reproduce random shaking to the same levels that they reproduce sinusoidal signals since the shape of the response over the frequency range is essentially the same as in Fig. 46.2.

At low frequencies, stroke length is still the limiting criteria. The APS shaker has very good low frequency response due to its long stroke, and all of the tactile transducers have difficulty providing force at low frequencies due to their relatively short strokes. Shaker 1 again does the best with essentially full response available at 10 Hz. Shaker 2 performs the most poorly with a power output that is less than 1/10th of what it should be all the way up to 20 Hz with full response not available until 30 Hz. Shaker 3 only performed marginally better than Shaker 2 but still far worse than Shaker 1.

The APS shaker and all of the tactile transducers again produce maximum power at their own natural frequencies. As the input frequency increases above the natural frequency of the shaker, the power falls off with a shape that is consistent with the force output graphs. The conclusion can thus be drawn that these devices respond to burst random signals in a manner that is predictable based on the response of the shaker to pure sinusoidal inputs.

46.4.4 Amplifier Gain

Gain is a measure of how many times higher an output signal is than the input signal; however, gain is typically not consistent across the frequency spectrum for several reasons. First, the entire spectrum of frequencies cannot be amplified by a single

Fig. 46.5 Amplifier gain

amplifier circuit, and thus the incoming signal is split into frequency windows which are separately amplified and these signal segments are then added back together at the output. Thus the amplification within each frequency window can be different. Also, in the design of audio components, engineers often take advantage of the fact that humans typically cannot hear frequencies below about 20 Hz or above about 20 kHz. The audio amplifier may then be more economically designed to encompass the frequencies that humans hear best. For these reasons, it was important to test the gain of the various amps to ensure they do not cut off low frequencies that are essential for dynamic testing of many civil structures.

Amplifier gain was tested at discrete frequencies while both the amplifier input and output voltage were monitored. All three amplifiers have a gain dial and this was set to maximum. Six seconds of data was captured at each frequency and the first two seconds were ignored as before. The RMS level of the output was divided by the RMS level of the input to calculate gain at each tested frequency line. During all amplifier testing, a load of four shakers was powered by Amp 1 and Amp 2, and a load of a single shaker was attached to the less powerful Amp 3. The results of gain testing are shown in Fig. 46.5.

Amp 1 does not provide much gain at low frequencies, especially below 5 Hz. The gain at 2 Hz is only about 8% of the maximum gain, and the gain at 4 Hz is about a third of the maximum. The gain rises to 71% of the maximum by 10 Hz and essentially reaches a stable plateau at 20 Hz extending to the maximum frequency of interest. Amp 2 provides superior response at low frequencies with a gain at 2 Hz that is 61% of the maximum and a gain at 4 Hz that is 87% of the maximum. The response is then essentially flat above 10 Hz. Amp 3 has very poor response at low frequencies, essentially low-pass filtering the signal below 10 Hz. At 20 Hz, the gain is still only 39% of the maximum gain and a plateau is finally reached at 30 Hz.

Both Amp 1 and Amp 2 provide gain that is acceptable for use with the tested shakers. The low gain at low frequencies does not limit the force production of the shakers since they are stroke limited in this range. The flat, full response of both amps beyond 20 Hz then pairs nicely with the frequency range where the shakers are not stroke limited and can use their full power potential. The very poor response of Amp 3 below 10 Hz when considered in conjunction with its low maximum power output suggests that this amplifier is not well suited to bridge testing. However, at its low cost it could still have potential use in testing lighter structures with higher base natural frequencies.

46.4.5 Amplifier Sinusoid Reproduction

An SNR measurement for the amplifiers was undertaken in exactly the same manner as that used for characterization of the shakers, except the signal input and voltage output from the amplifier were recorded and analyzed. The findings are shown in Fig. 46.6 with the SNR of the input signal also shown for reference.

Both Amp 1 and Amp 2 reproduce the input signals with high fidelity and introduce very little noise. Amp 1 is not as good at the lowest frequencies which relates to its reduced gain in this range. Amp 3 is far below the other two with significant noise introduced. It is noted that the gradual downward trend in SNR for Amps 1 and 2 is caused by a gradually decreased resolution of the input signal at higher frequencies. The SNR of the input signal is also shown on the figure to demonstrate that the decrease is caused by aliasing which is measured as noise.

Fig. 46.6 Amplifier signal to noise ratio

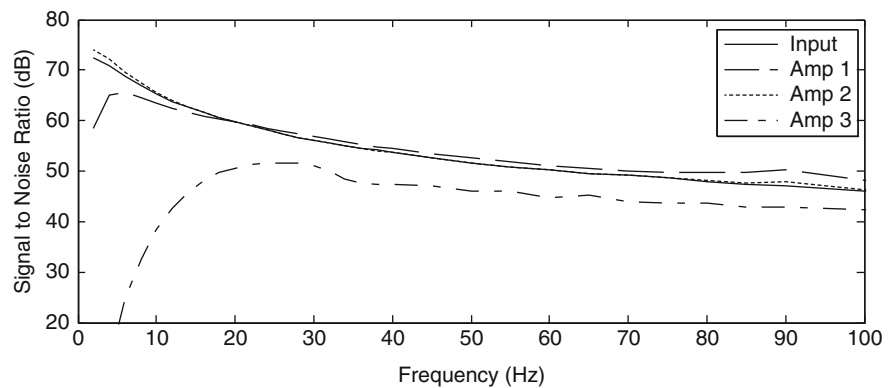
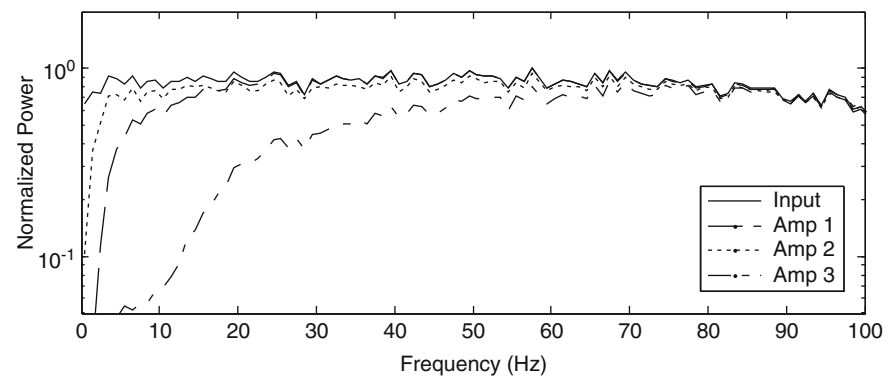


Fig. 46.7 Reproduction of burst random signal by subject amplifiers



46.4.6 Amplifier Burst Random Reproduction

This test was also performed in exactly the same manner as the shaker testing, again with a filtered burst random signal used as the input to the amplifiers. Both the input and output voltages were measured and the data was transformed to the frequency domain. Figure 46.7 shows how well each amplifier reproduced the frequency content of the input signal, and is normalized to a maximum value of 1.0 for each signal to generally remove the effect of gain.

Amp 2 is again the best of the lot and provides output that is nearly identical to the input frequency power at all frequencies except below about 5 Hz. Amp 1 is as good as Amp 2 above 20 Hz, but does not reproduce the lowest frequencies as well. Amp 3 does not reproduce the random signal well, significantly reducing the power up to about 50 Hz, and essentially low-pass filtering the signal below 15 Hz.

46.4.7 Other Considerations for Shakers and Amplifiers

In addition to the laboratory testing results, cost, perceived durability, and ease of use were also used as selection criteria for the shaker-amplifier system to move forward with. The cost of the components is a major consideration since one of the main objectives in the development of this system is that there should be a low cost per channel, enabling the use of many shakers in MIMO testing. Durability is also a serious matter since the expectation is that these devices will frequently be deployed in the field where items are routinely dropped and where dirt and moisture cannot be avoided. Ease of use is also important as it applies to quick and simple setup. Considering a test system with twenty or more shaker devices, fast setup and positive connections are a must.

The lab testing results favor the use of Shaker 1, however, it costs nearly five times more than Shaker 2 while only providing about twice the force. Shaker 1 also requires more power input per pound of force output, necessitating a larger amp and increased power generation capacity. From a consideration of durability, Shaker 1 has a rugged housing, but air vents near the base could allow moisture and detritus to enter the unit. This shaker is very easy to connect with integral posts that accept either a bare wire or a banana plug. Overall, Shaker 1 is somewhat costly, but seems reasonably rugged and is easy to use.

Shaker 2 is significantly less expensive than any other device and can be paired with Amp 3 since this shaker has low power requirements. The cost of this combo per channel would be about \$90. Additionally, Shaker 2 has a rugged housing with no air vents or other penetrations making it the most likely to have a high resistance to the rigors of field use. Finally, Shaker 2 has posts that accept bare wire connections so setup is as fast as Shaker 1. Overall, Shaker 2 provides the best cost, seems the most rugged, and is easy to use.

Shaker 3 does not compare well relative to the other tactile transducers. This shaker costs more than twelve Shaker 2 units, does not have a housing to protect it, and has a delicate load plate system that can be easily damaged by the application of lateral loads (per the manufacturer). Also, the need to add mass plates requires more items to be taken to the field and makes installation more difficult. This shaker also has an integral lead wire that requires addition of a connector for speedy field setup. Overall, Shaker 3 is expensive and is not a good choice for field use.

Amp 1 and Amp 2 are both very similar units in that they have a comparable size, similar controls and connections, and comparable power ratings (per channel). However, Amp 2 provides a much better cost in that a single unit can drive two shakers with separate signals whereas Amp 1 can only handle one excitation signal. This results in a cost per input location of \$60 for Amp 2 compared to \$150 for Amp 1. Amp 3 is of a different form than the other two and cannot compete with their power output. However, paired with Shaker 2, there is an opportunity to provide a very low cost array of shakers for excitation of structures with base frequencies greater than about 15 Hz.

46.5 Full-Scale Validation

The laboratory testing program provides much information about the proposed shaker system, but it is desirable to ensure the force output is adequate to excite an actual bridge. As such, a brief test was performed on an in-service highway bridge that was undergoing other vibration testing (Fig. 46.8). A single, simply-supported span of a ten-span river crossing was outfitted with 28 accelerometers and an APS shaker was used to perform SIMO testing at multiple input locations. The tested bridge is composed of a concrete deck composite with four rolled steel girders. The span length is 15.24 m (50'-0") and the deck width is 8.23 m (27'-0"). At the conclusion of the SIMO testing, a Shaker 1 unit was attached to the north fascia girder at midspan, and a burst random and a swept sine signals were provided as excitation signals. No vehicles crossed the bridge while the measurement data were acquired.

This was a qualitative test with the sole intention of ensuring that the excitation of the span due to one shaker was significantly greater than the ambient excitation. As such, the force output from the tactile transducers was not measured, the inputs were not adjusted or tuned to ensure maximum force output, and multiple input locations were not used. Figure 46.9 shows a typical measured time history for the burst random excitation taken from an accelerometer located about 6.5 m (21 ft) away from the shaker (and on a different girder). The low excitation level with the shaker not operating is seen at the beginning and end of the figure whereas the acceleration is much greater during operation of the shaker during the burst signal. The mean RMS acceleration measured with only ambient inputs (no traffic) was 0.00041 g over the entire array of 28 accelerometers. The mean RMS acceleration measured with the burst random signal was 0.0035 g and with the sine sweep was 0.0041 g for the entire array. Thus, the test demonstrated that a single tactile transducer could provide excitation about 10 times greater in magnitude than the ambient excitation (due to natural sources) on a typical medium length bridge.

46.6 Conclusions

This paper reports on an early milestone in the process of developing a novel, low-cost MIMO system intended for testing of short and medium span bridges. The laboratory tests and other device characteristics discussed were intended to enable selection of a tactile transducer shaking device and an amplifier to drive it. In the final analysis, low frequency response is the most important segment of the spectrum for the intended bridge testing. As such, Shaker 1 and Amp 2 are selected since they have the best signal reproduction of the tested devices at low frequencies. Shaker 1 not only provides the highest forces at low frequencies, it also has the flattest force peak around its own natural frequency, and imparts low noise to sinusoidal and random signals. Both Amp1 and Amp 2 are powerful enough to drive the selected shaker, but Amp 2 has better gain at low frequencies, imparts less noise at low frequencies, and reproduces random signals very well. Price, perceived durability, and ease of use are also considered and also support selection of Shaker 1 and Amp 2.

Fig. 46.8 Plan view drawing and photograph of bridge

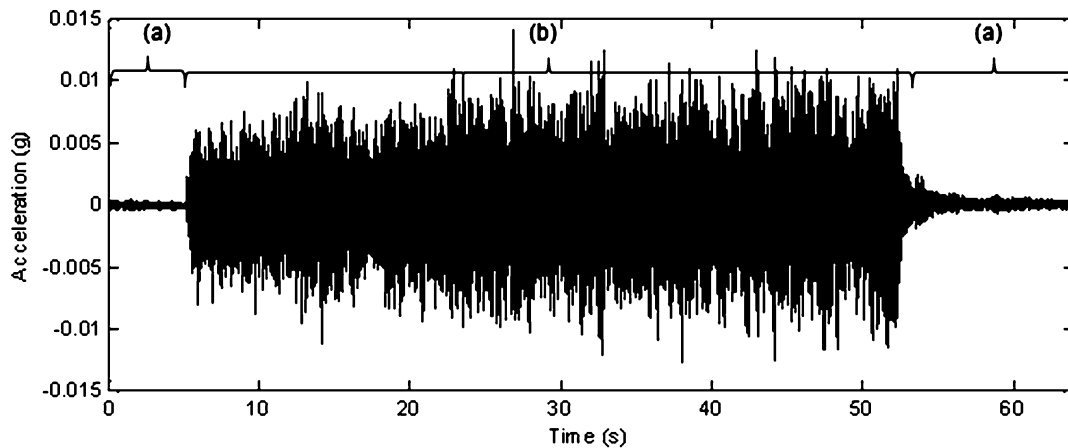
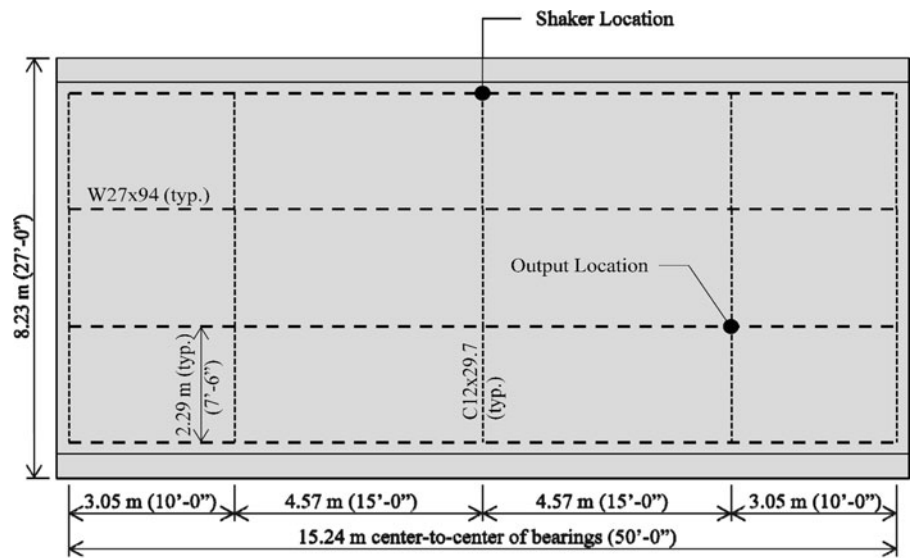


Fig. 46.9 Burst random acceleration time history using one shaker. (a) No shaker and no traffic, (b) shaker induced

The functionality of the proposed MIMO system was also tested at a basic level by ensuring that the force produced by the selected shakers could excite an actual bridge to reasonable levels in excess of ambient noise. The outcome of this validation testing was that excitation from the use of one of these shakers provided bridge accelerations that were significantly higher than the ambient background noise in the structure.

At the time of this writing, MIMO testing of a laboratory scale bridge model using an array of these shakers is underway and full testing of an in-service highway bridge is being planned. The success of this novel and affordable MIMO testing system has the potential to democratize experimental modal analysis by lowering the cost of entry, and also has the potential to enable better management of bridge assets via global characterization of structural responses.

References

1. Grady Barbaccia T (2011) The state of our bridges. *Better Roads* 81(11):8–9, 11–12, 15–19
2. Cunha A, Caetano E (2006) Experimental modal analysis of civil engineering structures. *Sound Vib* 40(6):12–20
3. Avitabile P (2011) Is there really a difference running a modal test with MIMO as opposed to SISO? *Exp Tech* 35(4):1–2
4. Avitabile P (2011) So if I use multiple reference vs single reference FRFs, is there really a difference in modal parameters? *Exp Tech* 35(5):1–2
5. Giraldo DF, Song W, Dyke SJ, Caicedo JM (2009) Modal identification through ambient vibration: comparative study. *J Eng Mech* 135(8): 759–770
6. Gul M, Catbas FN (2008) Ambient vibration data analysis for structural identification and global condition assessment. *J Eng Mech* 134(8): 650–662

Chapter 47

Assessment of Floor Vibrations for Building Re-use: A Case Study

Brad Pridham

Abstract Developments involving building re-use can present numerous challenges with respect to evaluation of structural floor capacity and establishing controls for serviceability. Retrofit strategies can be particularly challenging when engineering drawings of the structure are scant, or even non-existent. This paper presents a case study involving renovation of a light-weight mezzanine warehouse floor into executive office space. During early construction the floor was observed to be particularly lively, attributable to its lightweight, long-span construction and lack of non-structural elements. The author was engaged by the client to assess the floor and evaluate expected performance following fit-out. This included field measurements of frequency response and footfall vibrations, development of a computer model and correlation of the model with the field data. Simulations were conducted to validate random force models presented in the literature. The force and response models were then employed to assess expected performance of the floor. All modeling was conducted in the absence of engineering drawings, providing valued lessons on FEM techniques for floor systems. Measurements were also conducted following partial fit-out to track the change in the floor's dynamics and footfall responses.

Keywords Floor vibration • Footfalls • Model correlation • Modal testing • Impact testing

47.1 Introduction

Occupant footfalls are arguably the most common source of vibration, and vibration problems, on elevated building floors. Their effects on serviceability are varied, ranging from impacts on sensitive equipment and procedures in research and health care facilities, the comfort of occupants in open plan environments, and, at the extreme end, dynamic loads from crowd excitation. During design, the goal is to develop a sufficiently stiff and massive structural system together with strategic floor layouts to control the effects of footfalls. To achieve this objective, the vibration specialist must select a suitable analysis method to predict anticipated floor responses and work closely with the structural design team to implement a successful design. Equally important to the design calculations, though not always trivial, is the selection of appropriate performance criteria, against which the design should be assessed. Publications providing guidance on these matters include the AISC Design Guide 11 [1], SCIP354 [2] and the ISO 10137 standard [3].

Whereas during the design of a new facility one can only simulate the response of the floor and produce estimates of worst-case response levels, projects involving building re-use afford the opportunity to measure performance, correlate computer models, and, in general, establish more accurate response estimates. This is not to say that field measurements make the job easier; developing a model that matches the field observations is much more difficult than producing a model from drawings alone. The as-built performance can differ significantly from a floor model constructed using methods published in design guides. Boundary conditions and material properties, particularly for older structures, can differ significantly from the values suggested. This makes correlation of measured performance for use in simulations and assessment particularly challenging. These opportunities provide useful insights to the variability present in actual versus expected dynamic behavior of floors.

Another benefit of conducting field assessments and developing correlated computer models is the opportunity to evaluate footfall force models. With a reasonably accurate experimental or computer model of the structure on hand, one is able to

B. Pridham (✉)

Novus Environmental Inc., Research Park Centre, 150 Research Lane, Guelph, ON, Canada N1G4T2
e-mail: bradp@novusenv.com



Fig. 47.1 Photos of the mezzanine floor assessed in this study

compare footfall responses from testing with simulations using published force models, and select the most suitable for the assessment. Živanović and Pavić present examples of this type of evaluation in [4] using an experimental modal model. Their findings highlight the drawbacks of some of the methods commonly applied in industry today.

This paper presents the results of a floor vibration assessment conducted on a lightweight, lively, mezzanine floor in a manufacturing facility. At the time of the study the facility was undergoing renovation to executive office space. Early in the renovations the author noted considerable discomfort from footfalls on the floor. The client was made aware of the issue and instigated an assessment of the floor. Modal surveys were conducted during two stages of construction, and at the time of this publication a third survey is planned for final fit-out. The topic of this paper is the results of the first stage of the assessment, which included modal and footfall testing of the bare floor, development of a correlated computer model, comparison of responses for different footfall models in the literature, and predictions of the footfall response following fit-out. This work is a useful compliment to that presented by Živanović and Pavić in [4]. In future publications the results from the additional stages of testing, simulation and model correlation will be presented.

47.2 Description of the Floor

Figure 47.1 shows photos of the floor during early renovation/demolition, the condition that is the main focus of this paper. Figure 47.2 is the final layout of the office space, and ground floor area below – to be tested once completed. This particular area of the building will house executive office space, with the office’s senior executive located at the northeast corner of the mezzanine floor. The space is favored architecturally due to the free edge along grid line B, which allows occupants of the offices to look out over the area below. The server room extends below the mezzanine area (as shown at right in Fig. 47.2), and due to its function must remain mostly open. The few wall partitions located at level one are mostly full-height.

Early in construction, the author’s firm was retained to review acoustical controls for this area of the building. While on site it was noticed that the floor was particularly lively. Although this is expected for a bare floor in the absence of any secondary elements, a review of final layouts raised concern that sufficient mass and damping may not be provided to mitigate the problem. Given the high profile of this area of the building, it was deemed particularly sensitive to any noise or vibration issues.

The final floor layout, shown in Fig. 47.2, includes demountable (partial height) wall partitions across most of the floor. The only walls extending slab-to-roof above are those in the northeast office and the conference room at the south end. Compared to the tested conditions, the final floor will include additional mass from wall finishes, furniture and building services. Additional stiffness is expected from the stairwell attachment, and some stiffness is expected to be provided by the full-height walls, although there is currently no standard methodology for modeling this effect.



Fig. 47.2 Final floor layouts, mezzanine (*left*) and servery below (*right*)

The floor framing consists of 64 mm thick concrete on 38 mm corrugated steel deck. The slab is supported by open-web steel joists of depths varying between 350 mm (22-in.) and 375 mm (24-in.), spanning in the north-south direction. The floor system is supported on columns at 9.14 m offsets in the project north-south direction (vertical alignment to the page) and 6.1 m offsets in the project east-west direction. Masonry block walls support portions of the floor along grid lines 2 and 3. A block wall also supports the floor from below, in the project east-west direction approximately 2 m north of gridline 5, as seen from the layout of level one. As a result, the bay spanning between grid line 6 and this wall has a span of approximately 11.14 m (compared with the 9.14 m span of other bays). The floor slab is attached to the main support girder along grid A via a steel angle section. The girder also supports portions of block wall as can be seen in the photos of Fig. 47.1.

It is worth noting that original drawings of the floor do not exist. The dimensions of all framework, boundary conditions and section designations had to be gleaned from visual inspection and measurements at the site.

47.3 Dynamic Testing

Access to the floor was permitted after hours to conduct dynamic testing. This included modal testing of the floor to measure relevant modal parameters, as well as footfall measurements for use in calibration of the selected force model and assessment of the responses against comfort criteria.

47.3.1 Modal Testing

Given the light weight and liveliness of the floor, impact testing was selected as a suitable methodology for the modal tests. A total of 48 test points were specified (4 x 12 grid), so that a high degree of spatial resolution could be achieved for mode shape visualization. An 8-channel acquisition system was employed for data collection. Channels one through seven were used to record floor accelerations using a combination of three seismic accelerometers (10 V/g sensitivity), and four general purpose units (1 V/g). Channel eight was dedicated to the modal hammer. The test grid layout is shown in Fig. 47.3.

Measurement locations were selected based on the results from a preliminary finite element model of the floor. The model indicated significant modal contributions at grid points 11, 19 and 31. Additional sensors were employed for redundancy to ensure that multiple data sets could be analysed.

A series of five-to-seven impacts were applied at each of the 48 grid points for use in the spectral averaging of the FRFs. The raw data were post-processed in Matlab to produce FRFs and impulse responses for use in the system identification algorithms. The duration of the impact testing was approximately 4 hours.

Figure 47.4 is the trace of the FRF matrix (normalized to a peak value of unity), which revealed several modes in a 6 – 30 Hz frequency band. Although a many modes were excited during the impact testing, only a small subset were found to contribute significantly to the footfall response of the floor.

47.3.2 System Identification

System identification was performed using both time and frequency domain techniques. These included the Eigensystem Realization Algorithm, Stochastic Subspace Identification, the Rational Fraction Polynomial method and the Poly-reference Least Squares Complex Frequency method. Identification results that were consistent among several methods were generally regarded to be actual modes and spurious results were discarded. Mode indicator functions were also used to separate noise modes from structural modes. From the footfall testing results, it was determined that only a few modes below 10 Hz were contributing significantly to the response. Therefore, to reduce complexity and focus on accurate modeling of the modes of interest, only the first five modes of the structure were considered for the study. The mean values of frequency and damping identified for the first five modes are listed in Table 47.1.

The identified damping ratios are very low for all five modes. This is not surprising given the condition of the floor when tested. The frequencies of the first five modes fall within the range of excitation by the fourth and fifth harmonics of footfall excitations (fundamental gait frequencies of 1.5 – 2 Hz). The identified mode shapes for the first three modes are shown in Fig. 47.5, and indicate that the most significant modal amplitudes occurred between grids 2 through 4 (Fig. 47.6).

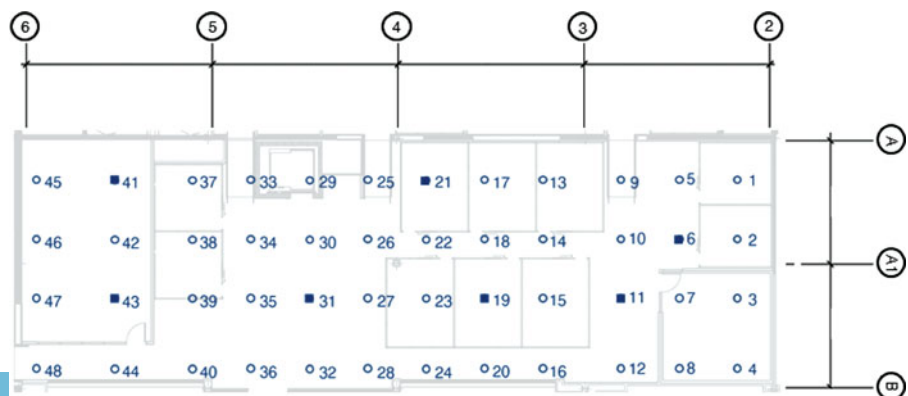


Fig. 47.3 Impact test grid layout (measurement points shown as filled squares)

Fig. 47.4 Trace of measured FRF matrix (normalized to unity)

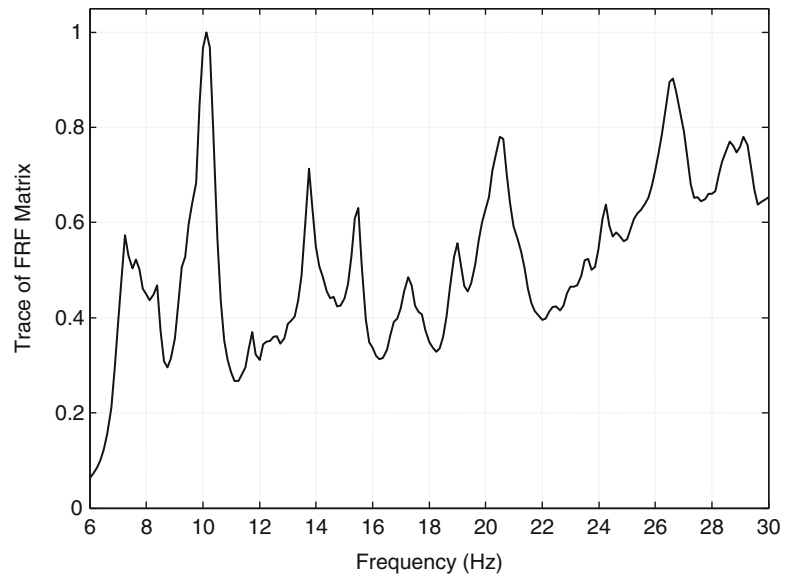


Table 47.1 Summary of identified modal parameters for the first five modes

Mode number	Frequency (Hz)	Damping ratio (% critical)
1	7.01	1.4
2	7.26	0.9
3	7.63	1.6
4	7.98	1.7
5	8.34	0.9

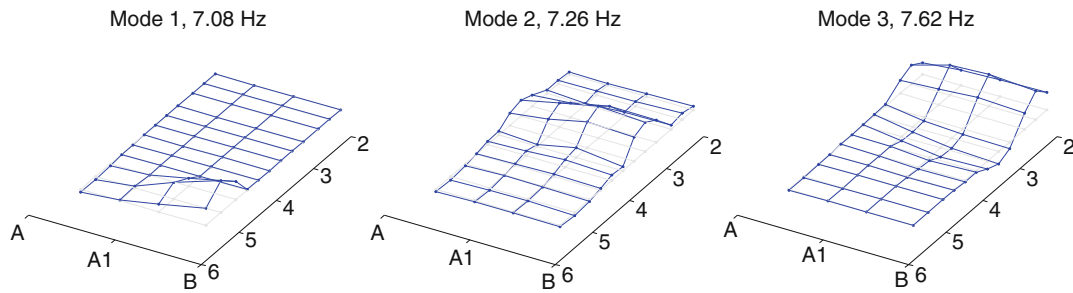
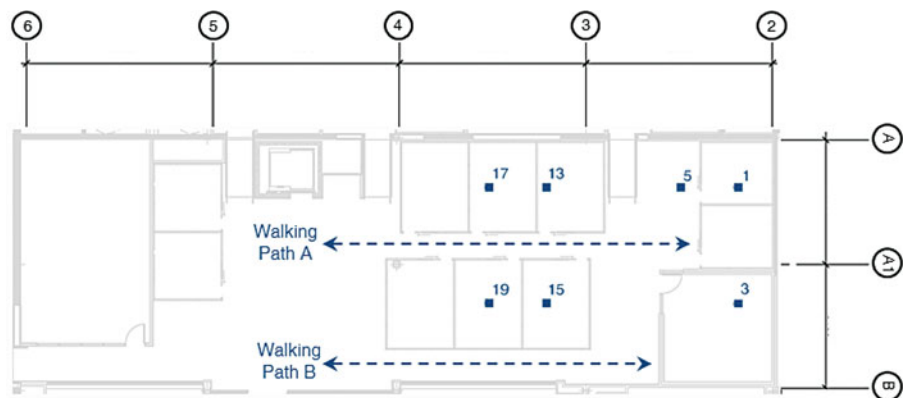


Fig. 47.5 Identified mode shapes for the first three modes of the floor

Fig. 47.6 Footfall test grid layout (measurement points shown as filled squares)



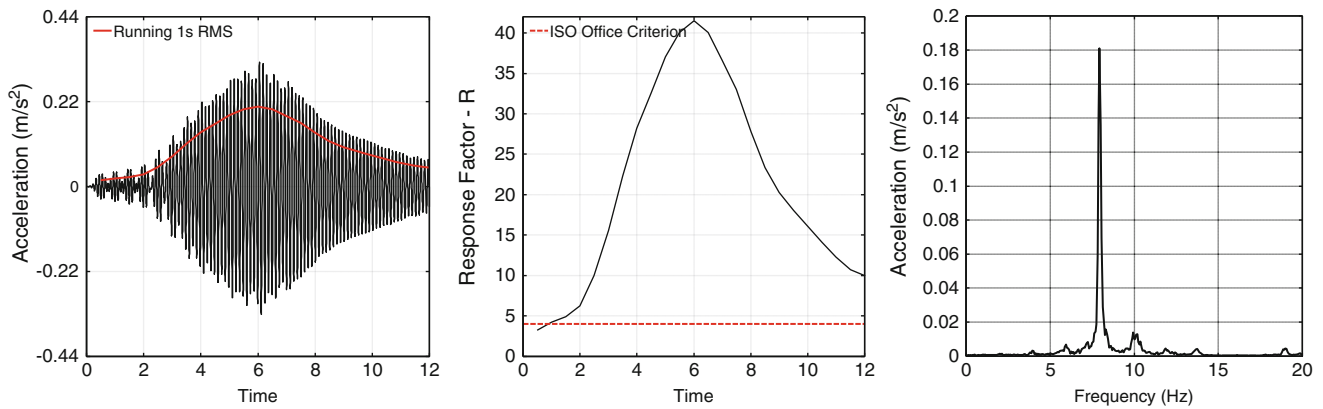


Fig. 47.7 Maximum measured footfall response (Path A, 120 spm)

47.3.3 Footfall Testing

Measurements of the footfall response of the floor were conducted following the impact testing. The sensor layout and walking paths selected are shown in Fig. 47.7. The objective of the tests was to attempt to excite the floor at gait frequencies corresponding to fractions of the floor modes so that the floor would be excited into resonance. Inspection of the impact test data in the field indicated dominant peaks at 7.25 Hz, 8 Hz, 9.5 Hz and 10.25 Hz. The pacing rates selected to excite these modes were: 87, 96, 109, and 120 steps per minute (1.45 Hz, 1.6 Hz, 1.82 Hz, and 2 Hz, respectively). In the author's experience pacing rates in the range of 90 – 110 steps per minute are comfortable and reasonable for an office environment. Even with the use of a metronome the 87 and 120 steps per minute pacing rates were considered awkward and would not likely occur frequently given the floor layout.

During the tests a metronome was set to the specified pacing rate and the test subject walked along the prescribed walking paths ('A' and 'B' in Fig. 47.3). Two trials were conducted by two individuals at the site, for a total of four walking trials per pacing rate. The walker weights differed by 22 kg (50 lbs). For brevity, only the results from the measurements and simulations of the heavier of the two walkers are presented in this paper. Interestingly, these did not always correspond to the higher responses, which may be attributed to the coordination of the walker to the metronome in some cases.

Following the site visit the raw time data were filtered using the ISO k weighting filter corresponding to z-axis vibrations (the shape of the filter is the inverse of the ISO base curve for human perception) [5]. The sliding 1-second RMS value of the weighted time history was computed to establish the maximum RMS acceleration level. The response factor R was then computed as the ratio of the maximum 1-second weighted RMS acceleration divided by the base curve value of 0.005 m/s^2 .

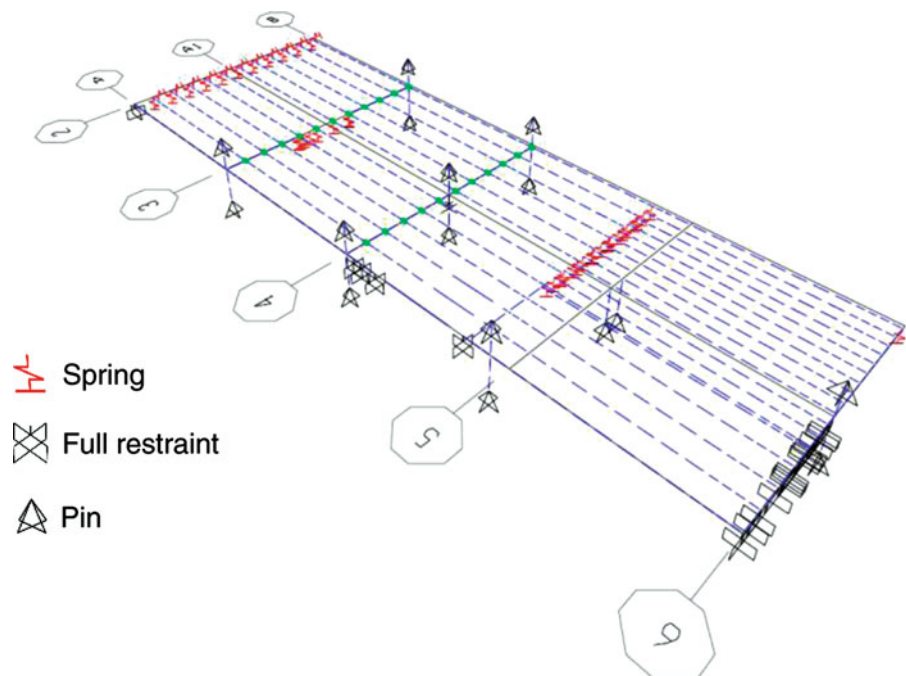
The maximum measured response factor was $R = 42$ at grid point 17, and corresponded to a 120 spm pacing rate along Path A. The filtered time history and corresponding response factors are shown in Fig. 47.7. The peak acceleration measured was $3.4\%g$, where g is the acceleration due to gravity. Note that for quiet office environments the ISO recommends a response factor $R = 2$ [3]. The AISC [1] and NBCC [6] recommend a peak acceleration threshold of $0.5\%g$ for office environments.

All measured responses exceeded the recommended criteria for office environments, with R factors varying between 4 and 42, and peak accelerations varying between $0.4\%g$ and $3.4\%g$.

47.4 Numerical Modeling

Although the measured responses are several times the acceptable limits for occupant comfort, they are a false representation of the expected performance of the floor following occupancy. Final fit-out includes office furnishings, demountable partitions, full-height partitions, building services, and a new stairway structure (Fig. 47.2). These elements will add mass, stiffness and damping to the system, significantly affecting the dynamic response. To model these effects, a structural finite element model of the floor was developed, correlated to the impact test results, and modified to assess expected performance following fit-out. This phase of the study also permitted an evaluation of footfall force models presented in the literature for selection of an appropriate model for assessment of the floor.

Fig. 47.8 Skeleton of the FEM of the bare floor showing modeled boundary conditions



47.4.1 Finite Element Model – Bare Floor

A finite element model of the bare floor was developed using the SAP2000 software [7]. Correlation of the model proved to be a laborious process due to the fact that drawings of the structure do not exist. Initial section properties were assigned based on an understanding of the structural framing gleaned from the site visit. Support conditions and material properties were specified according to dynamic modeling techniques appropriate for floor structures [2]. The composite action of the slab was modeled using thin shell elements with orthotropic stiffness properties. A uniform slab thickness was applied in the model, and the density of the concrete adjusted to account for the mass of the profiled section.

During the site visit a crack in the slab was identified along the portion of the floor supported by the masonry wall spanning east-west between grids 4 and 5, and continuing south along grid A1. The cracked portion of the floor was modeled using a reduced modulus of elasticity for the concrete in this region. The joist sections were modeled using SAP2000's K-series joist elements. As the structure was bare during the testing, the only superimposed mass applied in the model was that due to the mass of the steel deck (72 Pa, or 1.5 psf).

The modal frequencies and mode shapes were extracted from the SAP2000 software and compared with the results from the experimental modal analysis at the test grid locations. Following visual inspection of the results, the model was manually updated by applying changes to boundary conditions, material properties (concrete density and Young's moduli for the uncracked and cracked segments), and the bending stiffness of beam elements. This process was repeated in an iterative manner until good agreement was reached between the identified modal parameters and the modes computed by the FEA.

Figure 47.8 shows the skeleton of the final model, indicating the locations of spring elements, frame releases and joint restraints. Columns were modeled up to their inflection points and pinned at their ends. The joists were assigned moment releases along grids 3 and 4 and springs were used to model the restraint provided by the masonry walls below the floor. A visual inspection during the site testing indicated that the floor sits atop the walls, with no apparent mechanical fixation. The identified mode shape for mode 2 (Fig. 47.5) also contains a vertical component of motion at the wall locations, indicating that a spring restraint would be suitable for these boundary conditions.

The boundary conditions of the final model differed significantly from what would have been applied 'blindly' during the design of this floor using suggestions from the literature. This highlights the importance of exercising caution during the modeling process, and consulting with the structural designer to gain full understanding of connection design.

A comparison of modeled and identified frequencies and the associated MAC values for each mode are listed in Table 47.2. The MAC values and modeled frequencies indicate excellent agreement between the model and identification results. The lowest MAC value is 0.74 for mode 4, but is quite acceptable for civil engineering applications, particularly given the challenges related to modeling the floor system [8].

Table 47.2 Comparison of measured and modeled modal parameters

Mode number	Mode frequency		Modal assurance criterion (MAC)
	EMA	FEM	
1	7.01	7.01	0.87
2	7.26	7.24	0.84
3	7.63	7.56	0.80
4	7.92	7.98	0.74
5	8.37	8.56	0.90

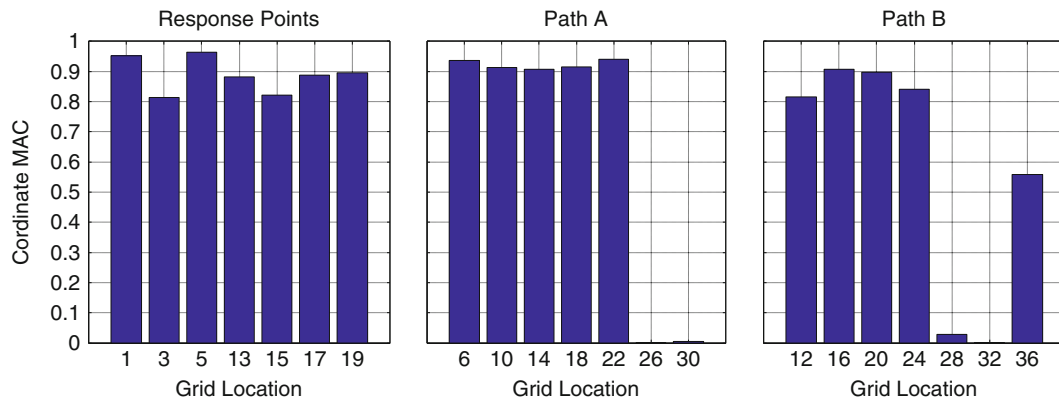


Fig. 47.9 COMAC values from model correlation

More important than the overall MAC values for the identified modes are the coordinate MAC (COMAC) values associated with the walking path and response measurement/prediction nodes. The accuracy of the modal coordinates at these locations directly affects the generalized forces and physical response estimates from the simulations. The COMAC values for the measurement locations and walking paths are shown in Fig. 47.9.

COMAC values are excellent for all but five input nodes. Fortunately these grid locations make up a small segment of the walking path and are not at locations associated with significant modal amplitudes for the modes of interest (see Fig. 47.5). Nevertheless, this should be considered a source of error in the response prediction process.

47.4.2 Response Analysis – Bare Floor

With a reasonably accurate FEM of the bare floor on hand, together with estimates of modal damping and measured footfall responses, it was possible to conduct simulations. It was important going forward to select a footfall force model that was able to predict the measurements reasonably well, to be confident in the results of the assessment of the fit-out condition. To this end, five footfall force models were applied in simulations of walking responses, and compared against the measured data. The models examined included: AISC DG11 [1], SCI P354 [2], ISO 10137 [3], Ungar's model [9], and the probabilistic force model presented by Živanović *et al.* [4], with the addition of the sixth harmonic of walking presented by Brownjohn [10]. The weight of the walker was set equal to the individual conducting the tests for all simulations.

A detailed treatment of each model is not given here but can be found in each of the cited references. Fundamentally, the SCI, ISO and random force models are similar in that they are constructed as a sum of sinusoidal functions scaled according to the specified dynamic load factors (DLFs) for each harmonic of force. The SCI model includes up to four harmonics of walking, the ISO model five, and the implementation of the probabilistic force model used in the simulations includes 6 harmonics *plus* five sub-harmonics of walking. The models presented in AISC DG11 and by Ungar are derived from empirical data and DLFs are not specified in the model.

Note that only the forcing models have been implemented from each of the cited references and *not* the response simulation methods. Full time domain simulations of response, which included the moving walking force across the floor, have been conducted using software developed by the author. In this way, the most realistic and reliable estimates of footfall response are obtained (as compared to some of the response methods suggested in the literature, which use resonant build up factors to model motions, and often place the walker at a single point on the floor – such as mid-bay). For the probabilistic model, 1000 realizations of walking forces were generated for each pacing rate and walking path, and the mean responses retained for the comparison with the measurements.

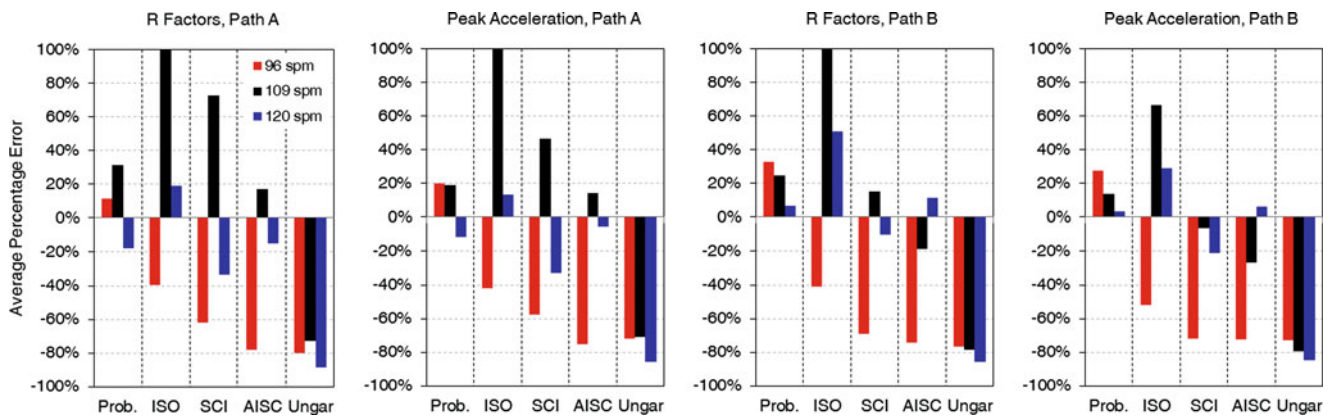


Fig. 47.10 Average percentage errors from the evaluation of five footfall force models

The average percentage error ($\frac{\text{model-measured}}{\text{measured}} \times 100\%$) across predictions, associated with the measured responses for 96, 109 and 120 spm are summarized in Fig. 47.10 (*Prob.* denotes the probabilistic model). Values close to zero indicate good agreement between predicted and measured values. Positive and negative values indicate over-prediction and under-prediction of the measurements, respectively. Note that for ease of visualization, the axes are scaled equally (values shown in black for ISO in the first three plots are 1.9, 1.4 and 1.1, left-to-right, respectively).

With the exception of a few estimates, the majority of results favor the probabilistic model. All other models tend to under-predict the measured values, whereas the probabilistic model trends to less than 35% average prediction error, with exceptional accuracy for many of the estimates. Conceivably, a more appropriate statistic could be selected for the comparison of the probabilistic model, such as the 1-standard deviation confidence limit, which would contain most of the observed responses. This is a main benefit of the model – it provides a range of responses rather than a single estimate.

The consistent under-prediction of the SCI, AISC and Ungar models highlight the caution that should be applied when using these models for design. Particularly Ungar's model which under-predicted all of the responses. The discrepancies attributed to the SCI and ISO models include the DLF values, as well as the missing higher harmonics (5th and 6th). It was the 5th harmonic of walking at 96 spm that was responsible for excitation of mode four (7.92 Hz). The missing harmonics in the SCI model is manifested in the average prediction errors shown in red in Fig. 47.10. The DG11 and Ungar models approach the force characterization differently, and the under-prediction is also likely a result of the harmonic content of the forces.

47.4.3 Finite Element Model and Response Assessment – Fit-Out Floor

Following correlation of the computer model of the existing floor, the FEM was modified to reflect the additional mass from furniture etc., as well as structural modifications such as new beams and the staircase. Following recommendations from numerous case studies in the literature [11], demountable partitions were modeled as added mass, and no additional stiffness was assigned to the model to account for full-height walls. A superimposed live load of 0.7 kPa (30% of the 2.4 kPa design value) was added to the floor to account for additional mass of furniture, services etc. The result of these modifications was a downward shift in the fundamental mode to 5.7 Hz, resulting in a total of six modes to be examined below 8 Hz. It is recognized that higher modes play a role in the overall response of the system, but for purposes of assessment against the bare floor performance, the assessment was restricted to a cutoff of 8 Hz.

The measured responses represent the worst-case response levels for the existing floor. These levels were generated by purposely exciting the floor into resonance. In reality, individuals will walk at a variety of pacing rates within a comfortable range (typically between approximately 90 – 110 spm). Additionally, occupants will have a range of weights, which are expected to be representative of the average for the population – compared to the weights of the walkers during testing. With this in mind, 1000 realizations of walking forces were generated by selecting pacing frequencies from a uniform distribution between 90 – 110 spm and using a specified 'average' walker weight of 746 N for all walkers [2]. The same collection of walking forces was used to simulate the response of the bare floor and fit-out condition. As conservatism, the mean plus one standard deviation limits of the response were retained, and the performance assessed based on these values.

Table 47.3 Predicted mean + one standard deviation responses

Grid location	Bare floor		Fit-out condition	
	Peak acceleration (g)	Response factor	Peak acceleration (g)	Response factor
1	0.6 %	7	0.3 - 0.4 %	3 - 4
3	0.5 %	6	0.3 - 0.4 %	3 - 4
5	1.0 %	11	0.5 - 0.6 %	5 - 7
13	0.6 %	7	0.4 - 0.5 %	4 - 6
15	0.8 %	11	0.3 - 0.4 %	3 - 4
17	1.0 %	11	0.6 - 0.7 %	6 - 8
19	1.2 %	15	0.5 - 0.5 %	5 - 6

A main source of uncertainty in prediction of the response of the fit-out condition is the level of modal damping that can be expected. Case studies in the literature suggest an upper bound of 3 % modal damping when partial-height walls are installed on lightweight floor systems, and an upper bound of 5 % when full-height (slab-to-slab) partitions are installed at locations where mode shapes are a maximum [5, 11]. Based on these recommended values, the response of the fit-out floor was simulated for modal damping levels of 3 % and 5 %, respectively, reflecting the presence of both wall types on the floor.

The results from the simulations are shown in Table 47.3. The ranges listed for the fit-out condition correspond to the 3 % (upper), and 5 % (lower) modal damping assignments. Estimates for the bare floor indicate that even under typical, non-coordinated walking, the floor was expected to be uncomfortable. The results for the fit-out condition are marginally acceptable according to recommended criteria. Of particular concern would be the motions of the floor at response locations 15 and 17 where they are expected to be 3 – 5 times the recommend $R = 2$ limit.

Given that the estimates for most locations were marginally above criteria, a ‘wait and see’ approach was opted for. The author has since had the opportunity to re-visit the floor to measure during partial completion, and will conduct final measurements following fit-out. These levels will be compared with the model estimates and presented in future publications. At the time of writing this paper there have been no reported complaints from occupants.

47.5 Concluding Remarks

The results from this study indicate that the probabilistic footfall force model provides the most reliable estimates of measured footfall responses. The author recommends application of the one standard deviation confidence bound of the responses to assessments when using this model. Caution should be exercised when applying other force models from the literature as these were shown to under-predict the responses for most simulations, which can lead to false conclusions. Further verification of the results from this study will follow once measurements of the fit-out floor are conducted.

References

1. Murray MM, Allen DE, Ungar EE (1997) Floor vibrations due to human activity. AISC/CISC Steel Design Guide Series 11, American Institute of Steel Construction, Chicago, IL
2. Smith AL, Hicks SJ, Devine PJ (2007) Design of floors for vibration: a new approach. SCI Publication 354, The Steel Construction Institute, Ascot, UK
3. ISO 10137:2007 (2007) Bases for design of structures – serviceability of buildings and walkways against vibrations. International Organization for Standardization, Geneva, Switzerland
4. Živanović S, Pavić A (2009) Probabilistic modeling of walking excitation for building floors, ASCE J Perf Const Fac 23(3):132–143
5. ISO 2631-2 (2003) Evaluation of human exposure to whole-body vibration. Part 2: continuous and shock-induced vibration in buildings (1 to 80 Hz). International Organization for Standardization, Geneva, Switzerland
6. National Building Code of Canada, NBCC (2005) Commentary D: deflection and vibration criteria for serviceability and fatigue limit states, 2nd edn. Canadian Commission on Building and Fire Codes, National Research Council of Canada, Ottawa
7. SAP2000 Version 15.1.0. Computers and structures (CSI), Berkeley, CA.
8. Pavić A, Misković Z, Reynolds P (2007) Modal testing and finite-element model updating of a lively open-plan composite building floor. J Struct Eng 133(4):550–558
9. Ungar EE, Zapfe JA, Kemp JD (2004) Predicting footfall-induced vibrations of floors. Sound Vib 38(11):16–24
10. Brownjohn JMW, Pavić A, Omenzetter P (2004) A spectral density approach for modelling continuous vertical forces on pedestrian structures due to walking. Can J Civil Eng 31:65–77
11. Setareh M (2010) Vibration serviceability of a building floor structure. 1: dynamic testing and computer modeling. ASCE J Perf Const Fac 24(6):497–507

Chapter 48

Experimental Validation on a Continuous Modulated Wave-Form Command Shaping Applied on Damped Systems

Khaled A. Alhazza

Abstract A new point-to-point command-shaping control strategy for oscillation reduction of damped simple harmonic oscillators is implemented experimentally on a scaled crane model. The effect of damping on the shaper frequency and duration is investigated. The performance of the proposed shaper is simulated numerically and compared to the results obtained experimentally. It is shown that, the proposed wave-form command profiles are capable of eliminating the travel and residual oscillations for systems with different damping ratios. It is shown that ignoring the system damping may result in unwanted oscillations. Unlike traditional impulse and step command shapers, the proposed command profiles have smoother intermediate acceleration, velocity, and displacement profile. In some ranges, the proposed technique produces faster maneuvers with smoother intermediate acceleration, velocity, and displacement profiles.

Keywords Crane control • Input-shaping • Vibration reduction • Preshaped control • Modulated wave-form.

48.1 Introduction

Due to the need for safe and high speed transfer maneuvers, dynamics and control of cranes have been the focus of vast theoretical and experimental research [1, 2]. The main objectives of such research studies are increasing the maneuver efficiency and reduce the final payload oscillations. Most of the work done on control can be classified as feedforward, feedback, and hybrid. Using feedback time delay control, Masoud et al. [3–8] successfully reduced the oscillations of suspended cargo on ship-mounted cranes, structural boom cranes, and telescopic cranes. Along this line and by using fuzzy logic, Cho and Lee [9] designed a new antishwing control scheme for a three-dimensional overhead crane. Liu et al. [10] studied and validated an adaptive sliding mode fuzzy control approach for a two-dimensional overhead crane. Using gain-scheduling feedback controller, Omar and Nayfeh [11] proposed and tested a point-to-point maneuver within one oscillation cycle. They showed numerically and experimentally that the controller is effective in reducing load oscillations and transferring the load in a reasonable time compared with optimal control.

One of the most widely used strategy in rest-to-rest maneuvers of suspended objects is the input-shaping control. This control technique does not require alterations to the original structure of the crane, or the installation of additional sensors and/or actuators. Using input-shaping control on point-to-point motion of a rotary crane, Terashimaa et al. [12] developed a three-dimensional open-loop control strategy to eliminate sway motion. In their work, they showed, through simulation and experiments, that the proposed control method is effective in eliminating residual oscillations and centrifugal force influence. Vaughan et al. [13] compromised between rapidity of motion and shaper robustness for several input-shaping methods. Using hybrid command-shaping control, Masoud et al. [14] proposed acceleration commands to suppress travel and residual oscillations of a highly accelerated double-pendulum gantry crane. Based on a modified frequency of one mode, they used double step primary command-shaper complemented with a virtual internal feedback-loop. They showed numerically and experimentally the effectiveness of the proposed hybrid command-shaper in minimizing oscillations of the first and second modes of a double-pendulum gantry crane.

K.A. Alhazza (✉)

Department of Mechanical Engineering, Kuwait University, P.O.Box 5969, Safat 13060, Kuwait
e-mail: khaled.alhazza@ku.edu.kw

Input-shaping techniques usually depend on impulse and step inputs. These techniques usually introduce jerks in the input profiles to system actuators. Jerks are characterized by sudden surges of energy to the actuators that can be detrimental to their performance and lifetime. On the other hand, smooth commands profiles, such as S-curves, trigonometric transition functions, Gaussians, and cam polynomials are designed to have smooth transitions. These profiles are known to provide a lowpass filtering effect. It is well known that low-pass filtering can reduce residual vibration, however it incurs a large rise-time penalty [15–17]. To reduce the effect of jerks on real systems, Singh [18] successfully used time-delay filters to reduce jerks in the input shapers for undamped and damped systems. Singhose et al. [19] compared smooth and nonsmooth commands by interpreting smooth commands as input-shaped functions. They clearly proved that input-shaped step functions are usually more efficient for reducing vibration than commonly used smooth commands. They also concluded that S-curves smooth function must be four times slower than step commands shaped with zero-vibration shapers to eliminate vibration in a single-mode system. They experimentally confirmed that input-shaped step-commands save time compared to S-curve commands. Erkokmaz and Altintas [20] presented continuous position, velocity, and acceleration profiles for high speed CNC systems using quintic spline trajectory generation algorithm. They imposed limits on the first and second time derivatives of feed rate, resulting in trapezoidal acceleration profiles along the tool path. Following the same line, Alhazza and Masoud [21] introduced and implemented a novel continuous command-shaping control strategy on an overhead crane. The frequency of the proposed single-wave command profile is optimized to produce zero travel and residual vibration. A modulated wave-form (MWF) command profile is then derived to enhance the controller performance. In their work, they introduced a new nondimensional parameter and used it to compare their controller with a double step shaper. They showed that the newly introduced shaper has a smoother acceleration, velocity, and displacement profile and, in some ranges, has a shorter maneuver time.

In this work, the effect of damping on the modulated wave form (MWF) frequency and duration is studied numerically and experimentally on a scaled overhead crane. The equation of motion of an overhead crane is derived and, then, solved for the frequency and duration of the modulated wave form (MWF). The resulting wave form is capable of eliminating the travel and residual oscillations for systems with different damping ratios. The effect of damping is shown to have a considerable effect on the final payload oscillations. It is clearly shown that the proposed command profiles have smoother intermediate acceleration, velocity, and displacement profile.

48.2 Mathematical Model

A simplified overhead crane can be modeled as, Fig. 48.1, a suspension point-mass attached to a horizontal slider representing the crane jib with a rotational damper. Assuming a rigid link with length, l , the equation of motion can be derived as

$$\ddot{\theta} + 2\zeta\omega_n\dot{\theta} + \omega_n^2\theta = \frac{\ddot{u}}{l} \quad (48.1)$$

where ζ is the viscous damping ratio, $\omega_n = \sqrt{\frac{g}{l}}$ is the natural frequency of the system, and \ddot{u} is the base acceleration. Knowing that $l = \frac{g}{\omega_n^2}$, Equation (48.1) can be written as

$$\ddot{\theta} + 2\zeta\omega_n\dot{\theta} + \omega_n^2\theta = \frac{\omega_n^2\ddot{u}}{g} \quad (48.2)$$

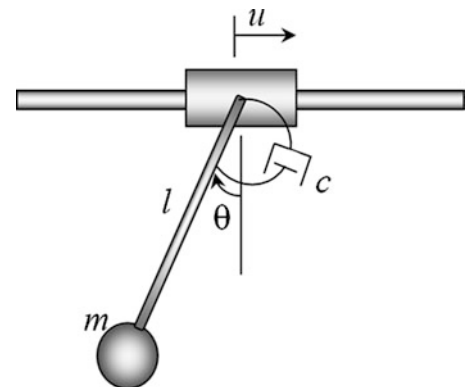


Fig. 48.1 Simple-pendulum model of an overhead crane with damping

48.3 The Effect of Damping on the Modulated Wave Form

Input-shaping is a widely used technique for controlling crane oscillations. Most of the work done in this area considered jerky inputs for undamped systems. Along this line, Alhazza and Masoud [21] introduced a novel continuous wave-form command-shaping to smoothen the motion of the base. They showed that using the proposed function produces a smoother acceleration, velocity, and displacement profile. They used a nondimensional system parameter to compare the proposed technique with the classical double-step input-shaper. In their work, they showed that, for some system the proposed command shaper performs faster than the double step. In this work, the effect of damping is considered and analyzed. The Modulated Wave Form (MWF) Command Shaping acceleration profile can be defined as [21]

$$\ddot{u} = [A + B \cos(\omega_s t)] \quad (48.3)$$

where ω_s is the controller frequency, τ is the acceleration phase ending time, and A and B are amplitudes of the MWF and will be defined later. Substituting Equation (48.3) into Equation (48.2), the equation of motion with the assumed shaped-acceleration command is given as

$$\ddot{\theta} + 2\zeta\omega_n\dot{\theta} + \omega_n^2\theta = \frac{\omega_n^2}{g}[A + B \cos(\omega_s t)] \quad (48.4)$$

Assuming zero initial conditions, the combined homogenous and particular solution of Equation (48.4) during acceleration phase can be determined as

$$\theta(t) = C_1 + C_2 \cos(\omega_s t) + C_3 \sin(\omega_s t) + e^{-\zeta\omega_n t} [C_4 \cos(\omega_d t) + C_5 \sin(\omega_d t)] \quad (48.5)$$

where

$$\begin{aligned} C_1 &= \frac{A}{g} \\ C_2 &= \frac{(\omega_n^2 - \omega_s^2)B\omega_n^2}{g[(\omega_n^2 - \omega_s^2)^2 + (2\zeta\omega_n\omega_s)^2]} \\ C_3 &= \frac{2\zeta\omega_s B\omega_n^3}{g[(\omega_n^2 - \omega_s^2)^2 + (2\zeta\omega_n\omega_s)^2]} \\ C_4 &= -\frac{A + C_2g}{g} \\ C_5 &= -\frac{gC_3\omega_s + \zeta\omega_n A + \zeta\omega_n C_2g}{g\omega_d} \end{aligned}$$

and ω_d is the damped natural frequency defined as

$$\omega_d = \omega_n \sqrt{1 - \zeta^2}$$

To simplify the system response equation, a new frequency ratio is defined as

$$c = \frac{\omega_s}{\omega_n} \quad (48.6)$$

The performance of the controller is measured by the maximum oscillation amplitude at the end of the acceleration phase. This amplitude depend mainly on the angular position and angular velocity of the pendulum. Using Equations (48.5) and its derivative with respect to time, $\frac{d\theta}{dt}$, the response of the system at the end of the input wave can be found as

$$A_{MWF} = \sqrt{\theta_\tau^2 + \left(\frac{\dot{\theta}_\tau + 2\zeta\omega_n\theta_\tau}{\omega_d}\right)^2} \quad (48.7)$$

It is clear from Eqn. (48.7) that, the residual vibration amplitude, A_{MWF} , goes to zero if and only if $\theta_\tau = \dot{\theta}_\tau = 0$. The values of the constant A and B can be found by considering the maximum velocity and maximum acceleration of the system. The

maximum velocity achieved at the end of the acceleration phase is given by,

$$v_{max} = \int_0^{\tau} \ddot{u} dt \quad (48.8)$$

and the maximum acceleration can be found by setting the time derivative of Equation (48.3) to zero and solve for t_{max} and then substitute back into the equation. This leads to

$$A_{max} = [A + B \cos(\omega_s t_{max})] \quad (48.9)$$

Using Equations (48.8) and (48.9) to solve for A and B leads to

$$A = \frac{[-v_{max}\omega_s + a_{max} \sin(\omega_s \tau)]}{[-\omega_s \tau + \sin(\omega_s \tau)]} \quad \text{and} \quad B = \frac{-\omega_s(a_{max}\tau - v_{max})}{[-\omega_s \tau + \sin(\omega_s \tau)]} \quad (48.10)$$

It is important to mention that many researchers ignore the maximum acceleration and velocity in their analysis. Even for a simple input-shaper, the analysis may give impractical solution.

48.4 Numerical Validation

To test the performance of the proposed strategy, three different cases are simulated on our experimental crane. The value of the maximum acceleration and maximum velocity reached by the crane are $a_{max} = 0.9 \text{ m/s}^2$ and $v_{max} = 0.3 \text{ m/s}$, respectively. The values of rigid lengths l and damping ratios, ζ , are chosen as $l = 0.1, 0.3, 0.6 \text{ m}$ and $\zeta = 0.04, 0.1, 0.4$, respectively. Figure 48.2a shows the acceleration and velocity profiles of the three cases. It is clear that the proposed acceleration and velocity profiles have smooth intermediate profiles. Also, it shows that the maximum acceleration is used and the maximum velocity is reached at the end of the acceleration phase. The payload responses are shown in Fig. 48.2b. It is clear that the proposed controller succeeded in eliminating the residual vibration at the end of the acceleration phase. Further examination of Fig. 48.2a shows that as l increases (i.e. as the natural frequency decreases), the time required increases, which is a property of almost all command shaping strategies.

48.5 Experimental Validation

A scaled model of an overhead crane in the Advanced Vibrations Lab at Kuwait University is used to examine the performance of the damped (MWF) shaper. The model is an INTECO 3D crane, Fig. 48.3a. The motions of the jib and

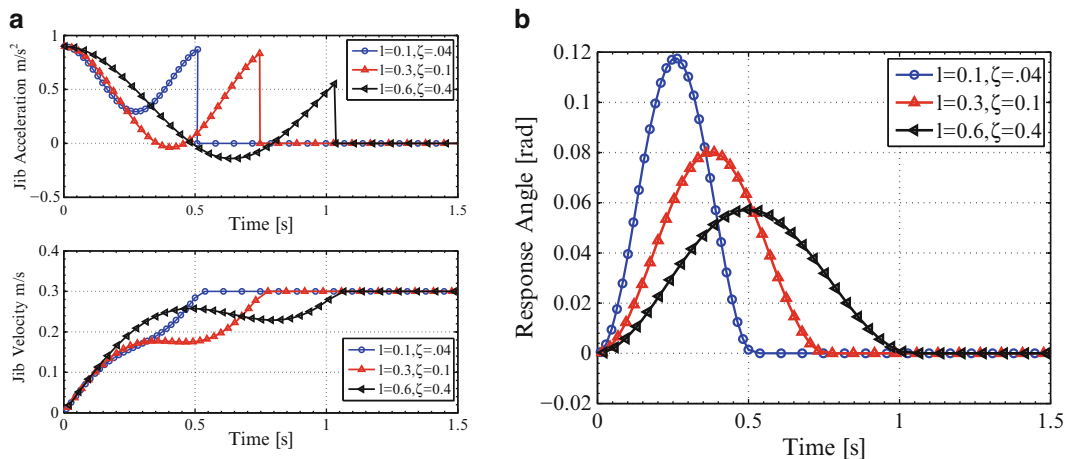


Fig. 48.2 System input and response for different lengths and damping when $a_{max} = 0.9 \text{ m/s}^2$, $v_{max} = 0.3 \text{ m/s}$

Fig. 48.3 INTECO experimental crane with rigid link connected to a rotational damper

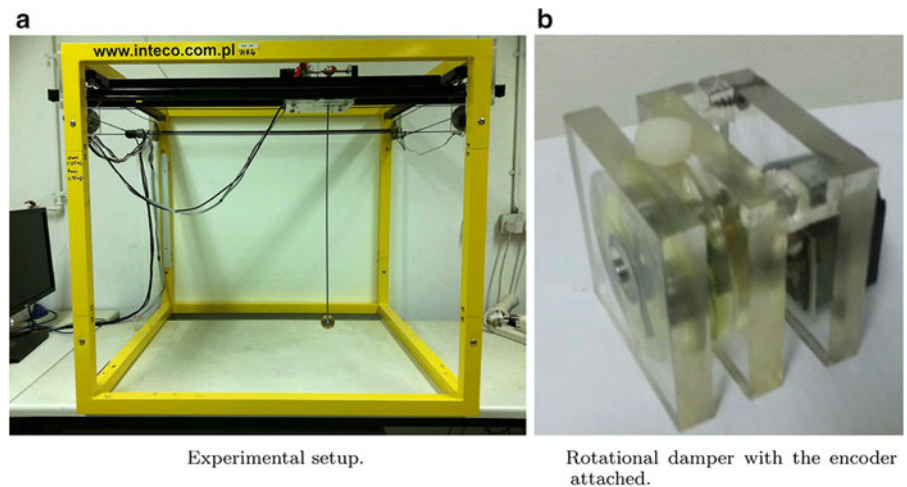
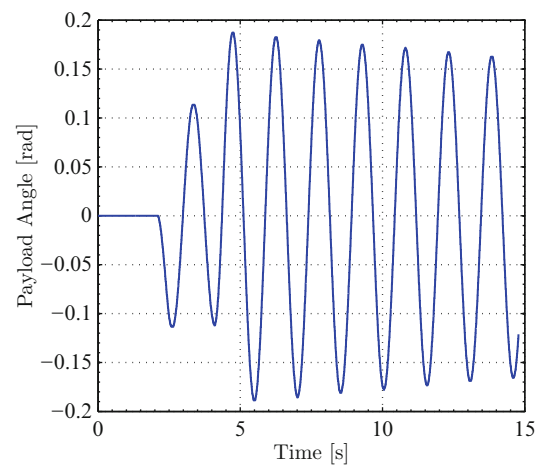


Fig. 48.4 The payload response to time-optimal rigid-body (TORB) command



tower of the crane in the horizontal plane are controlled by two identical DC motors. The state variables of the systems are obtained using three quadrature incremental-encoders. The measured states are; the jib motion, the tower motion, and the oscillation angle of the hoisting link. The resolution of the encoders used is 1024 pulses per rotation. The resolution of the hoisting link angle-measurement is 0.0016 rad. A multipurpose digital I/O board is used to interface the crane model with a PC running a “3D Crane” toolbox in Matlab’s Simulink environment.

The crane has a maximum speed of 0.3 m/s, a maximum acceleration of 0.9 m/s², and a 0.6 m usable track. A light slender rod with a mass attached to its end as the payload of the crane, Fig. 48.3a, and a locally manufactured rotational damper, Fig. 48.3b, are used.

The response of the crane to the time-optimal rigid-body (TORB) command is shown in Fig. 48.4a. It is clear that the system experiences large residual oscillations. To show the effectiveness of our controller, two experimental cases are examined. The first one with an effective length of $l = 0.012$ m and a damping ratio of $\zeta = 0.023$, Fig. 48.5. Figure 48.5a shows the controller input to the jib. It is clear that the controller used the maximum acceleration and velocity of the system. Also, we can notice that the inputs have a smoother intermediate profiles compared with the classical double-step shaper. Figure 48.5b shows the simulated oscillation angle of the payload using the equation of motion of the crane, Equation (48.1), and the experimentally measured oscillation angle on the crane model. The simulated and the experimental results proved the effectiveness of the proposed controller. A minor discrepancy between the experimental response and the simulated response is observed, which may be attributed to many factors such as the unmodeled mechanical backlash and joint friction.

The second case has an effective length of $l = 0.4$ m and a damping ratio of $\zeta = 0.35$, Fig. 48.6. Figure 48.6a shows a clear asymmetry in the jib profiles due to the high damping ratio. As expected, the system used the maximum acceleration and velocity of the system. In Fig. 48.6b, the experimental and theoretical show the great performance of the proposed design in eliminating the residual vibrations at the end of motion.

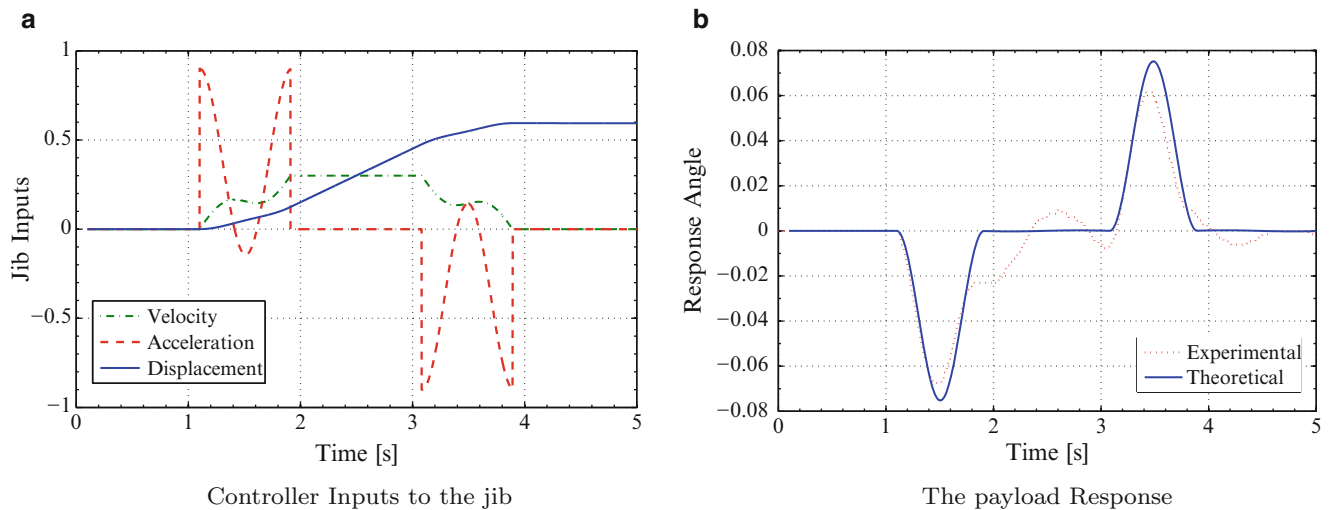


Fig. 48.5 The inputs to the jib and the theoretical and experimental responses when $l = 0.12m$ and $\zeta = 0.023$

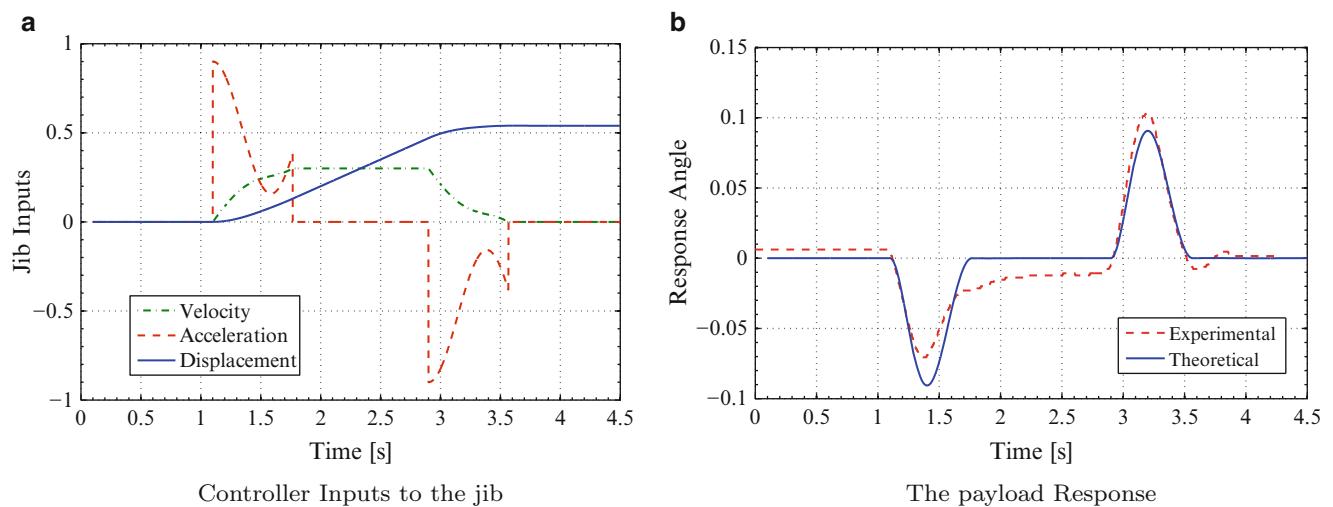


Fig. 48.6 The inputs to the jib and the theoretical and experimental responses when $l = 0.4m$ and $\zeta = 0.35$

48.6 Conclusions

In this work, the effect the damping ratio on the modulated wave form shaper (MWF) has been investigated. It has been shown that the proposed command shaper is capable of eliminating the travel and residual vibrations for point-to-point maneuvers of damped systems. It has been demonstrated that the proposed technique has a smoother intermediate acceleration, velocity, and displacement profiles.

Acknowledgements This work is funded by Kuwait University Research Department Grant No. EM 01/11.

References

1. Zrnić N, Petković Z, Bošnjak S (2005) Automation of ship-to-shore container cranes: a review of state-of-the-art. *FME Trans* 33:111–121
2. Abdel-Rahman E, Nayfeh A, Masoud Z (2003) Dynamics and control of cranes: a review. *J Vib Contr* 9:863–908
3. Masoud ZN, Nayfeh AH, Mook DT (2004) Cargo pendulation reduction of ship-mounted cranes. *Nonlinear Dynam* 35(3):299–311
4. Masoud ZN, Nayfeh AH, Nayfeh NA (2005) Sway reduction on quay-side container cranes using delayed feedback controller: simulations and experiments. *J Vib Contr* 11(8):1103–1122

5. Masoud ZN, Nayfeh AH, Al-Mousa A (2003) Delayed position-feedback controller for the reduction of payload pendulations of rotary crane. *J Vib Contr* 9:257–277
6. Masoud ZN, Nayfeh AH (2003) Sway reduction on container cranes using delayed feedback controller. *Nonlinear Dynam* 34(3–4):347–358
7. Masoud ZN, Nayfeh AH, Mook DT (2004) Cargo pendulation reduction of ship-mounted cranes. *Nonlinear Dynam* 35(3):299–311
8. Masoud ZN, Daqaq MF, Nayfeh NA (2004) Pendulation reduction on small ship-mounted telescopic cranes. *J Vib Contr* 10(8):1167–1179
9. Cho S-K, Lee H-H (2002) A fuzzy-logic anti-swing controller for three-dimensional overhead cranes. *ISA Trans* 41:235–243
10. Liu D, Yi J, Zhao D, Wang W (2005) Adaptive sliding mode fuzzy control for a two-dimensional overhead crane. *Mechatronics* 15:505–522
11. Omar HM, Nayfeh AH (2005) Gantry cranes gain scheduling feedback control with friction compensation. *J Sound Vib* 281:1–20
12. Terashimaa K, Shen Y, Yanob K (2007) Modeling and optimal control of a rotary crane using the straight transfer transformation method. *Contr Eng Pract* 15:1179–1192
13. Vaughan J, Yano A, Singhose W (2008) Comparison of robust input shapers. *J Sound Vib* 315:797–815
14. Masoud ZN, Alhazza KA, Majeed MA, Abu-Nada EA (2009) A hybrid command-shaping control system for highly accelerated double-pendulum gantry cranes. In: Proceedings of the ASME 2009 international design engineering technical conferences and computers and information in engineering conference IDETC/CIE, San Diego, USA, 2009, Paper number DETC2009-87501
15. Ahmad MA, Ismail RMTR, Ramli MS, Abd Ghani NM, Hambali N (2009) Investigations of feed-forward techniques for anti-sway control of 3-D gantry crane system. *IEEE symposium on industrial electronics and applications*. Inst. of Electrical and Electronics Engineers, Piscataway, pp 265–270
16. Singer N, Singhose W, Seering W (1999) Comparison of filtering methods for reducing residual vibration. *Eur J Contr* 5:208–218
17. Feddema, J, Dohrmann C, Parker G (1997) A comparison of Maneuver optimization and input shaping filters for robotically controlled slosh-free motion of an open container of liquid. In: Proceedings of the 1997 american control conference, Albuquerque, New Mexico, pp 1345–1349
18. Singh T (2004) Jerk limited input shapers. *J Dynam Syst Meas Contr* 126:215–219
19. Singhose W, Eloundou R, Lawrence J (2010) Command generation for flexible systems by input shaping and command smoothing. *AIAA J Guid Contr Dynam* 33(6):1697–1707
20. Erkorkmaz K, Altintas Y (2001) JHigh speed CNC system design. Part I: jerk limited trajectory generation and quintic spline interpolation. *Int J Mach Tools Manufact* 41(9):1323–1345
21. Alhazza KA, Masoud ZM (2010) A novel wave-form command-shaping control with application on overhead cranes. In: Proceedings of the ASME 2010 dynamic systems and control conference DSCC2010, Cambridge, MA, USA, 12–15 September 2010, Paper No. DSCC2010-4132

Chapter 49

Quantification of Damping Effect of Humans on Lightly Damped Staircases

Anna Cappellini, Stefano Manzoni, and Marcello Vanali

Abstract There is experimental evidence that the people interacting with structures are not only an active load but also affect the structural properties. Particularly, considerable damping ratio value changes are often experienced. This fact assumes a relevant importance in assessing the structure serviceability against vibrations due to pedestrian induced loads. There is therefore ground to find methods capable of estimating the effect induced by people interacting with a structure, in terms of both changes of modal parameters and of loading effect. This work aims at presenting a model, partly based on modal approach, able to describe people effect on a structure. Each person is modelled as a two degrees of freedom spring-mass-damper system and is introduced locally on the structure. Several tests on a lightly damped staircase were then carried out to validate the model.

Keywords Human-structure interaction • Vibrations • Civil structures • Damping • Staircase

49.1 Introduction

In the last years a great attention has been paid to all issues related to vibration serviceability of civil structures and to the problem of human-structure interaction. An aspect of this interaction is the influence of humans on the dynamic properties of the structure they occupy [1]. Although in the past people present on a structure have often been modelled as added masses only, many authors [2, 3] reported a significant increase in damping due to human occupants. Also, in a recent paper [4] Pedersen showed the importance of the effects of the presence of a passive crowd on structural behaviour. The experimental evidence suggests, then, that appropriate dynamic models of human occupants should be used in order to obtain an accurate description of human-structure interaction. To this purpose, this paper describes a model capable of predicting the effects of still people on the modal properties of a structure. In the model, based on a modal approach [5], people are considered to be standing still and integral to the structure. Each person on the structure is modeled as a two degrees of freedom mass-spring-damper system.

The experimental case of a lowly damped staircase is considered to test the model.

A brief description of the model proposed is reported in the next section, while the following sections discuss the tests, the experimental results and the comparison between them and those predicted through the model.

A. Cappellini • S. Manzoni
Dipartimento di Meccanica, Politecnico di Milano, via La Masa 1, Milan, Italy
e-mail: anna.cappellini@mail.polimi.it; stefano.manzoni@polimi.it

M. Vanali (✉)
Dipartimento di Ingegneria Industriale, Università degli studi di Parma, Parco Area delle Scienze, 181/A, Parma, Italy
e-mail: marcello.vanali@unipr.it

49.2 Numerical Model

A numerical model is needed to estimate the change of modal parameters of a structure due to people presence. This has been chosen to rely on a modal model of the structure. Such an approach turns out to be convenient because it is generally easy to obtain a modal model starting from experimental data or from a structural model (i.e. a F.E. model).

Two elements were required to develop such a model:

- (1) a biomechanical model of each individual
- (2) a structural model that could account for the presence of persons on the structure

As regards the first request, the authors have chosen to model each individual with its so called apparent mass (i.e. the mechanical impedance of the whole human body). One of the models proposed by Matsumoto and Griffin [6] was used to this purpose.

In their work the authors developed lumped parameter models to represent human subjects in different positions when exposed to vertical whole-body vibrations. Several single and two degrees of freedom models were proposed. Such an approach is very convenient for the development of a model like the one proposed here. It was therefore decided to start from this simple model to represent the people, in particular one of the two degrees of freedom models was considered. Figure 49.1 shows the model proposed by Matsumoto and Griffin considered in this work and Eq. (49.1) reports the corresponding analytical expression of the apparent mass.

$$\text{Model 2a : } M_{2a}(i\omega) = \frac{(ic_1\omega + k_1) \{m_1(-m_2\omega^2 + ic_2\omega + k_2) + m_2(ic_2\omega + k_2)\}}{\{-m_1\omega^2 + i(c_1 + c_2) + (k_1 + k_2)\}(-m_2\omega^2 + ic_2\omega + k_2) - (ic_2\omega + k_2)^2} \quad (49.1)$$

The coefficient values of Eq. (49.1) were chosen as the optimized model parameters, obtained with tests on twelve standing subjects, determined by Matsumoto and Griffin for subjects in a normal standing posture, and are reported in Table 49.1.

As regards the second request (i.e. development of a structural model that could account for the presence of persons on the structure), a model based on the approach proposed by Krenk was employed. Krenk's model was originally developed for the introduction of dampers on discretized structural systems [7].

The same model was then used to introduce people, considered to be standing still and integral to the structure. One of the advantages of this model is the possibility to introduce each person individually.

The equation of motion (physical quantities) for the whole system can be expressed as:

$$\mathbf{M}\ddot{\mathbf{x}}(t) + \mathbf{C}\dot{\mathbf{x}}(t) + \mathbf{K}\mathbf{x}(t) = \mathbf{f}(t) \quad (49.2)$$

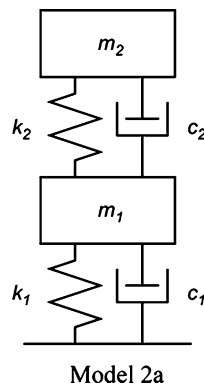


Fig. 49.1 Mechanical models of a standing person proposed by Matsumoto and Griffin

Table 49.1 Optimized modal parameters for the mean normalized apparent mass of standing subjects

	Stiffness ($\text{Nm}^{-1}\text{kg}^{-1}$)		Damping ($\text{Nsm}^{-1}\text{kg}^{-1}$)		Mass (no unit)	
	k_1	k_2	c_1	c_2	m_1	m_2
Model 2a (standing)	$4.39 \cdot 10^3$	$5.53 \cdot 10^2$	$3.71 \cdot 10^1$	$1.18 \cdot 10^1$	$5.74 \cdot 10^{-1}$	$3.94 \cdot 10^{-1}$

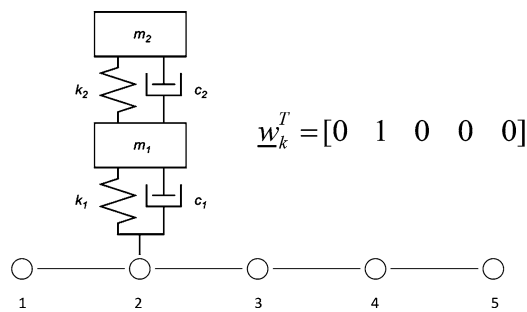


Fig. 49.2 Connection of a subject to the structure

$$[-M\omega^2 + jC\omega + K]x = f(\omega) \quad (49.3)$$

being x the displacement vector, M , C and K the mass, damping and stiffness matrix of the structure respectively, and f the generic force vector.

Switching to a modal representation

$$x(t) = \Psi \xi(t) \quad (49.4)$$

$$m \ddot{\xi}(t) + c \dot{\xi}(t) + k \xi(t) = q(t) \quad (49.5)$$

where Ψ is a matrix containing the mode shape vectors, $\xi(t)$ is a vector containing the modal response components and the modal system matrices are defined by,

$$m = \Psi^T M \Psi, \quad c = \Psi^T C \Psi, \quad k = \Psi^T K \Psi, \quad q = \Psi^T f \quad (49.6)$$

and assuming c to be diagonal

$$m_j = \phi_j^T M \phi_j = 1, \quad k_j = \phi_j^T K \phi_j = \omega_j^2 \quad (49.7)$$

$$c_j = \phi_j^T C \phi_j = 2\xi_j \omega_j \quad (49.8)$$

where ϕ_j is the j th unit modal mass scaled mode shape vector, the frequency response function $G(\omega)$ can be expressed as

$$G(\omega) = \sum_{j=1}^n \frac{\phi_j \phi_j^T}{\omega_j^2 - \omega^2 + 2i \xi_j \omega \omega_j} \quad (49.9)$$

$$x = G(\omega) f(\omega) \quad (49.10)$$

Once defined the modal model of the structure ($G(\omega)$), it is necessary to introduce people.

The main assumption of this method is that each person is fixed to the i th point of the structure, and introduces a force proportional to the displacement of the point itself and his apparent mass. Therefore, the force exerted by each person is

$$f_i^{Human}(\omega) = H(\omega) x_i(\omega) = -M_a(\omega) \omega^2 x_i(\omega) \quad (49.11)$$

with $M_a(\omega)$ apparent mass of the subject, and in terms of the full displacement vector x

$$f^{Human}(\omega) = H(\omega) w_k w_k^T x \quad (49.12)$$

where w_k identifies the connection of the individual to the structure, as exemplified Fig. 49.2.

In the case of multiple people on the structure, the total force vector can be expressed as:

$$f^{Human}(\omega) = WHW^T x \quad (49.13)$$

where $W = [w_1, \dots, w_m]$ represents the connection of m elements and H is the transfer function matrix (diagonal), containing the mechanical impedance of all the subjects.

Being

$$G^{-1}(\omega) x = f(\omega) - f^{Human}(\omega) \quad (49.14)$$

the modified equation of motion becomes

$$[G^{-1}(\omega) + WHW^T] x = G_H^{-1}(\omega) = f(\omega) \quad (49.15)$$

The expression in Eq. (49.15) represents then the new transfer function of the people-structure system (G_H). The new frequency response function can be expressed explicitly in terms of the frequency response function $G(\omega)$ by the Woodbury matrix identity [8]

$$(A + UCV)^{-1} = A^{-1} - A^{-1}U(C^{-1} + VA^{-1}U)^{-1}VA^{-1} \quad (49.16)$$

as

$$G_H = [G^{-1} + WHW^T]^{-1} = G - GW(H^{-1} + W^TGW)^{-1}W^TG \quad (49.17)$$

This simple equation therefore allows calculating the transfer function of the new human + structure system. This model allows evaluating the local effect due to the presence of each individual separately. This effect is a function of the characteristics of the person, his posture (standing, one leg and so on) and the point where the person is located (i.e. a function of the value of the modal properties (mode shapes)) relating to that point.

This model has been validated by means of experimental tests. The layout for such tests and the structure used to this purpose are presented in the next section.

49.3 Structure Under Test and Experiments

A slender staircase was used to test the model. The structure in question, shown in Fig. 49.3, connects the ground and the first floors in the main building of the campus Bovisa of Politecnico di Milano. The structure under test is very flexible. Even a few people on it are able to change the damping significantly.

The first task to carry out to the purpose of model validation was a modal characterization of the structure with and without people. Therefore the structure was instrumented with 19 accelerometers in the vertical direction, and forced with an electro-mechanical shaker (V400 series vibrator) in order to estimate its Frequency Response Functions (FRFs). The structure was forced by accelerating a known mass with the shaker. The acceleration of this mass was measured with an accelerometer PCB 393A03.

Figure 49.4 shows the positions of the accelerometers and Table 49.2 shows their metrological characteristics.

Preliminary tests showed that the first natural frequency of the structure is located around 8 Hz. Therefore, the structure was forced with white random noise between 5 and 20 Hz in the following tests.

At first, experimental tests of the empty structure were performed. This allowed extracting the modal properties of the structure. The first three modes were considered. Later, additional tests introducing respectively 3, 6 and 9 people standing

Table 49.2 Metrological characteristics of the accelerometers

Sensor	Measurement range (g)	Frequency range ($\pm 5\%$) [Hz]	Sensitivity (V/g)
Piezoelectric accelerometer PCB 393A03	± 5	0.5–2000	1
Piezoelectric accelerometer PCB 393B12	± 0.5	0.1–500	10
Triaxial MEMS DC accelerometer PCB 3713B112G	± 2	0–250	1



Fig. 49.3 Tested staircase

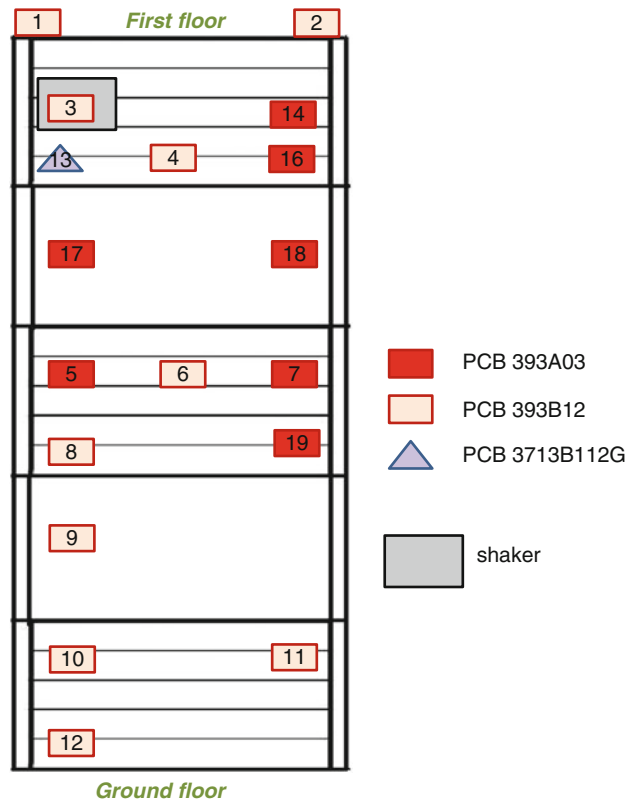


Fig. 49.4 Position of the accelerometers and the shaker

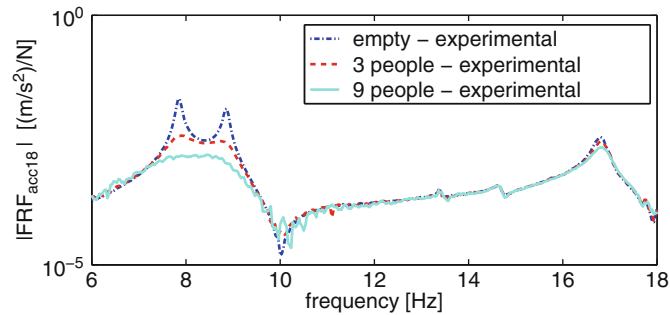


Fig. 49.5 Experimental FRFs

Table 49.3 Modal properties of the empty staircase

f_n (Hz)	ζ (%)
7.85	0.43
8.86	0.46
16.80	0.58

Table 49.4 Modal properties of the staircase with 3 people

f_n (Hz)	ζ (%)
7.85	3.09
8.85	2.56
16.85	0.73

Table 49.5 Modal properties of the staircase with 9 people

f_n (Hz)	ζ (%)
7.66	7.64
8.77	5.07
16.83	0.96

in different points of the structure were carried out. In all cases the structure was forced with the shaker in order to determine the FRFs of the structure and of the humans + structure systems respectively.

Figure 49.5 shows an example of experimental FRFs for the empty structure, structure with 3 people (placed in correspondence of the accelerometers 13, 5, 16) and structure with 9 people (placed in correspondence of the accelerometers 13, 5, 6, 7, 14, 16, 17, 18, 19).

The modal properties associated with these conditions, identified using the PolyMAX method [9], are shown in Tables 49.3, 49.4, and 49.5.

People cause a significant increase in damping in correspondence of the first two eigenmodes and a slight increase in correspondence of the third mode, as evidenced in Fig. 49.5 and Tables 49.3, 49.4, and 49.5.

49.4 Prediction of People Effects on the Modal Parameters

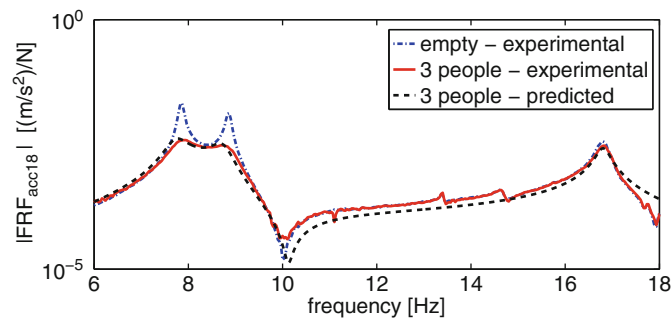
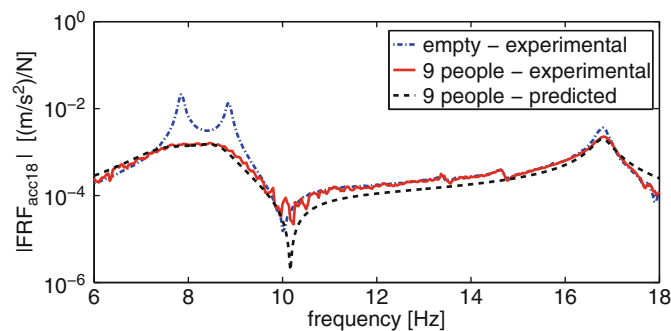
The model presented in the first part of this work was used to obtain a prediction of the behavior of the structure when occupied by people and the results were compared with those obtained experimentally. The apparent mass of each subject should be known to this purpose. To be rigorous it would be necessary to determine the apparent mass of each person. A further complication is related to the fact that the apparent mass not only varies from subject to subject (inter-subject variability) but also varies for the same subject (intra-subject variability) with the amplitude of vibration. For the sake of simplicity the analytical expression for the normalized apparent mass proposed by Matsumoto and Griffin was employed,

Table 49.6 Comparison among experimental and predicted natural frequencies (3 people)

f_n (Hz), empty experimental	f_n (Hz), 3 people experimental	f_n (Hz), 3 people predicted	f_n (Hz), 9 people experimental	f_n (Hz), 9 people predicted
7.85	7.85	7.77	7.66	7.61
8.86	8.85	8.75	8.77	8.68
16.80	16.85	16.81	16.83	16.80

Table 49.7 Comparison among experimental and predicted damping ratios (9 people)

f_n (Hz), empty experimental	ζ (%), empty experimental	ζ (%), 3 people experimental	ζ (%), 3 people predicted	ζ (%), 9 people experimental	ζ (%), 9 people predicted
7.85	0.43	3.09	2.86	7.64	8.92
8.86	0.46	2.56	2.38	5.07	4.43
16.80	0.58	0.73	0.84	0.96	1.13

**Fig. 49.6** Experimental and predicted FRF (3 people on the structure)**Fig. 49.7** Experimental and predicted FRF (9 people on the structure)

using the optimized model for subjects in a normal standing posture. This apparent mass was then multiplied by the effective mass of each subject. This assumption, albeit limited, becomes inevitable when there is need to predict the behavior of a structure a priori, since in this case the characteristics of people who will use it later are unknown. The results obtained were satisfactory despite this simplification. Tables 49.5 and 49.6 show the comparison between the experimental and predicted FRFs for two cases with 3 and 9 people (whose modal parameters have been reported in the previous section) on the structure. The results were obtained starting from the FRF in empty conditions and using model 2a proposed by Matsumoto and Griffin.

Tables 49.6 and 49.7 show the comparison between experimental and predicted modal parameters.

Figures 49.6, 49.7 and Tables 49.6, 49.7 show that there is a satisfactory agreement between the results obtained experimentally and those predicted, especially as regards the damping. The result is even more interesting considering that to include people on the structure, instead of the actual apparent mass of each individual, the average apparent mass determined by Matsumoto and Griffin was used.

Other tests have been performed placing people in other points of the staircase and the experimental and numerical results matched well again.

These results provide evidence of the effectiveness of the proposed model and pave the way for many future applications.

49.5 Concluding Remarks

In this paper the analysis of the effects of stationary people on the modal parameters of a lowly damped civil structure has been faced. A model has been proposed, which allows quantifying the effect of people standing on a structure on its modal parameters. A slender staircase has been employed as a test case. The structure was first tested when empty in order to obtain its modal model. This allowed extracting the modal parameters of the first three resonant modes. The structure was then tested with people in different configurations. The new properties of the structure-people system were extracted. The achieved results have been used to verify a numerical model of the people structure interaction. Satisfactory results were obtained in terms of identification of changes in modal parameters caused by the presence of people. The model is then shown to provide an interesting quantitative estimate of the effect of people. The results obtained are also a good basis for the future development of a more accurate model, hopefully able to account for the presence not only of stationary people but also of moving people.

References

1. Sachse R, Pavic A, Reynolds P (2003) Human-structure dynamic interaction in civil engineering dynamics: a literature review. *Shock Vib Digest* 35(1):3-18
2. Reynolds P, Pavic A, Ibrahim Z (2004) Changes of modal properties of a stadium structure occupied by a crowd. In: *Proceedings of XXII international modal analysis conference, Orlando, 2004*
3. Sachse R (2002) The influence of human occupants on the dynamic properties of slender structure. Ph.D. Thesis, The University of Sheffield, UK
4. Pedersen L (2012) Damping effect of humans. In: *Proceedings of the SEM IMAC XXX conference, Jacksonville, January 30-February 2, 2012*
5. Ewins DJ (2001) *Modal testing: theory, practice and application*, 2nd edn. Taylor and Francis, London
6. Matsumoto Y, Griffin MJ (2003) Mathematical models for the apparent masses of standing subjects exposed to vertical whole-body vibration. *J Sound Vib* 260(3):431-451
7. Krenk S (2007) Lectures presented at 'Semi-Active Vibration Suppression - The Best from Active and Passive Technologies'. CISM, Udine
8. Woodbury MA (1950) Inverting modified matrices. Statistical Research Group, Memo. Rep. no. 42, Princeton University, Princeton
9. Peeters B et al (2004) The PolyMAX frequency-domain method: a new standard for modal parameter estimation? *Shock Vib* 11(3-4):395-409

Chapter 50

Robust Design Optimization of Steel Moment Resisting Frame Under Ground Motion Uncertainty

Zhifeng Liu, Sez Atamturktur, and Hsein Juang

Abstract In the design of a steel moment resisting frame, uncertainties may arise from a variety of sources, such as ground motion, mass, and damping ratio, etc., that may cause variation in seismic demand and capacity. These uncertainties need to be taken into account to ensure the desired margin of safety for required performance objectives. FEMA 350, a reliability based design guideline, can be employed to mitigate safety concerns by satisfying minimum confidence level requirements for performance objectives. However, in these existing design codes, variation in seismic demand is not explicitly considered in the design process. According to the FEMA 350 procedure, seismic demand is calculated with a suite of seismic records, considering ground motion variability, while only median demand is used in the subsequent calculation of demand to the capacity ratio and confidence level. In this paper, variation of seismic demand due to ground motion variability is considered explicitly as a *robustness measure*, and the mean value of seismic demand is treated as a *safety measure*. A Robust Design Optimization of steel moment resisting frame methodology is proposed, which is featured as a multi-objective optimization problem with the variation of seismic demand, mean value of seismic demand and cost as three objectives. In the optimization problem, optimal steel section sizes are sought to minimize these three conflicting objectives. The proposed methodology is then demonstrated through a multi-story multi-bay steel moment resisting frame design and solved with a Non-dominated Sorting Genetic Algorithm-II. With three competing objectives, the proposed methodology provides a set of designs in the form of a Pareto Front, which is robust, safe and economical. Furthermore a uniformity drift ratio requirement is proposed to ensure efficient designs.

Keywords Multi-objective optimization • NSGA-II • Pareto front • Modal pushover analysis (MPA) • Demand and capacity factor design (DCFD)

50.1 Introduction

Traditionally, designing a steel moment resisting frame (henceforth referred to as the steel frame) is a trial and error process, seeking designs that are both safe and economical. Safety is ensured by complying with reliability based design standards (e.g., [1, 2, 7], etc.), while cost is evaluated considering the initial construction cost. A design is then selected from several code-compliant candidate designs, based on the cost and other considerations. Due to limitations on design budgets, only a few candidate designs are typically compared, thus the design chosen is likely suboptimal in the sense of cost and/or safety.

To address this economical concern, steel frame design optimization has been studied extensively in past years. These studies have been formulated as either single objective optimization or multi-objective optimization problems. In single objective optimization, an optimization algorithm is employed in place of a trial and error design process, and the entire solution space is explored in search of the most economical design with building codes and other project requirements treated as constraints [12, 25]. When other criteria, such as the number of steel sections [14], and the confidence level of the designs performance are considered as objectives simultaneously with cost, the design optimization process becomes a multi-objective optimization problem ([8, 13, 20, 21]).

Z. Liu • S. Atamturktur (✉) • H. Juang
Glenn Department of Civil Engineering, Clemson University, Clemson, SC, USA
e-mail: sez@clemson.edu

A review of literature conveys that robustness of seismic demand to uncertainty is rarely considered in either traditional or optimization-based steel frame design. Due to inherent uncertainty in the construction and operational conditions of the structure, seismic demand may deviate from the expected value. Without considering the robustness of seismic demand to uncertainty, one may reach a design that has a large sensitivity to uncertainty and thus, large variation in performance. Herein, robustness to uncertainty is considered in the context of ‘Robust Design’ as originally proposed by Taguchi [24]. In this paper, a new steel moment resisting frame design optimization approach named *robust design optimization* is proposed, utilizing robust design concept originally developed and widely used in quality engineering [19, 24]. In the proposed approach, maximum inter-story drift is considered as seismic demand measure, and the ground motion variability is considered as the source of uncertainty. The mean value of maximum inter-story drift is treated as the safety criterion; the standard deviation of the maximum inter-story drift is treated as the robustness criterion, and material weight is treated to represent the cost of the design, and these three criteria are optimized simultaneously. Therefore, the proposed approach leads to a multi-objective optimization problem resulting in a set of competing designs that are economical, safe and robust.

50.2 Robust Design

Robust design, which has been successfully used in industrial and manufacturing engineering to produce high quality products and processes, aims to make a product or response of a system insensitive to (or robust against) “hard-to-control” input parameters (called “noise factors”), by carefully adjusting “easy-to-control” input parameters (called “design parameters” or “control factors”). Two kinds of approaches are most widely used in robust design: (i) the Taguchi method and its variants [19, 24], and (ii) the Robust Design Optimization method [18].

The Taguchi method is fundamentally an experimental design approach, in which orthogonal array is employed to assign design parameters and noise factors [19]. Analysis of mean is performed to characterize design parameters into four categories: (i) design parameters affecting mean and variance of the response, (ii) design parameters affecting variance only, (iii) design parameters affecting mean only, and (iv) design parameters affecting cost only. Design parameters of the first two categories are adjusted to reduce variance; the third category is adjusted to move the mean value of the response to the target value and the last category is adjusted to reduce cost [19]. Though easy to implement, the following limitations of the Taguchi method have made it the subject of criticism ([3, 16]): (i) design parameters cannot always be grouped into four distinct categories; and (ii) due to the inherent experimental nature of the design, only a select few designs may be evaluated and compared, prohibiting a thorough exploration of the design space.

With the development of computational capabilities and progress in the optimization techniques, Robust Design Optimization (RDO) has gained popularity [3]. Three goals of robust design, which are (i) reducing variance in system response, (ii) reducing cost and (iii) adjusting mean value of system response to the target, lead naturally to a multi-objective optimization problem. In some cases, the target value for the mean is specific; in others, the mean value is either maximized or minimized. RDO is advantageous as it can explore the entire solution space to find the most optimum design and straightforwardly evaluate highly nonlinear problems. In the present study, RDO is adopted for the performance based seismic design of steel moment resisting frames.

50.3 Performance Based Seismic Design

In traditional seismic design, preventing collapse and fatality is the only goal, however, in performance based design, structural performance is divided into several levels each corresponding to a seismic hazard level. FEMA 350 supplies a probability based guideline for performance based design of steel frames, in which the ground motion variability and the uncertainty in the structural analysis are considered explicitly [7]. FEMA 350 considers two performance levels, immediate occupancy (IO) and collapse prevention (CP), corresponding to 50% probability of exceedance in 50 years and 2% probability of exceedance in 50 years, respectively. In FEMA 350, performance objective is satisfied probabilistically in that IO performance level has an annual frequency of being exceeded less than 1/100, while CP performance level has an annual frequency of being exceeded less than 1/2500.

Analogous to LRFD design format, in FEMA 350, the performance objectives are satisfied by demand and capacity factor design (DCFD) method [11], instead of direct calculation of the annual frequency of being exceeded. However, in FEMA 350, only median seismic demand is involved in computation of demand to capacity ratio and the subsequent calculation of confidence level, while variation of seismic demand is not considered. In this paper, the authors apply the principles of

robust design optimization to performance based design of steel moment resisting frames. Seismic demand, system response of interest, is represented with maximum inter-story drift, which reflects both local and global stability, as well as P- Δ effects [22]. The mean value of maximum inter-story drift, μ_{drift} is considered as the safety measure and the standard deviation of maximum inter-story drift, σ_{drift} is considered as the robustness measure. For the cost measure, initial construction cost, represented by steel material weight is adopted [14]. Ground motion variability, a significant contributor to seismic demand variation [6], is treated as the noise factor. The [1] requirements and FEMA 350 acceptance criteria are implemented as design constraints. The performance based robust design optimization of steel moment resisting frame problem is expressed as follows:

$$\text{Find } d \text{ to minimize : } \{W(d), \mu_{drift}(d, z), \sigma_{drift}(d, z)\}$$

Subject to : AISC-2005 Code Requirements;

FEMA350 Acceptance Criteria.

where W is the steel material weight, d is the design parameters (steel section types), z is noise factor (ground motion variability). It should be noted, μ_{drift} and σ_{drift} are calculated under 2% probability of exceedance in 50 years hazard level, since the consequence of exceeding CP performance is more detrimental.

50.4 Methodology: Multi-Objective Optimization

A general multi-objective optimization problem can be expressed as:

$$\text{Minimize : } \mathbf{F}(\mathbf{d}) = [f_1(\mathbf{d}) \ f_2(\mathbf{d}) \ \dots \ f_n(\mathbf{d})]$$

$$\text{Subject to : } g_i(\mathbf{d}) \leq 0 \quad i = 1, \dots, n \quad (50.1)$$

with f representing a single objective function, and g representing a constraint function. Unlike single objective optimization, the purpose of which is to search for a single best design, multi-objective optimization yields a family of optimum designs. When the objectives are uncooperative (i.e., conflicting), a single design optimum for all objectives does not exist in the solution space, which is represented by an unattainable, imaginary point known as the *utopia point* in Fig. 50.1. There generally exists a set of designs in the solution space (i.e., set $\{\mathbf{F}(\mathbf{d}) \mid g_i(\mathbf{d}) \leq 0 \text{ for all } i\}$), which are superior to all other designs, while within this set, no design is superior to another in all criteria. These designs constitute a Pareto optimum set (or Pareto front), as illustrated in Fig. 50.1.

Hence, the Pareto front can be viewed as a set of designs, which dominate all other designs. The *domination relationship* is defined as follows: design B is dominated by design A, if A is superior to B in at least one criteria (i.e., $f_i(d)_A < f_i(d)_B$ for at least one i), and A is not inferior to B in all other criteria (i.e., $f_i(d)_A \leq f_i(d)_B$ for all other i). If one design is not dominated by any other designs, it belongs to the Pareto front. A Pareto front has the following features: (1) Within the Pareto front,

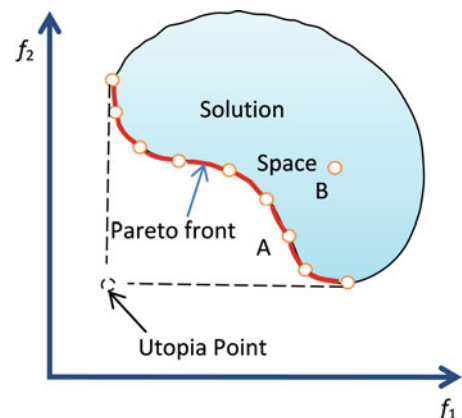


Fig. 50.1 Pareto front in a bi-objective space [9]

no improvement is possible in one objective without worsening other objectives. Thus, the Pareto front represents a trade-off relationship, in which objectives compete with each other. (2) All other designs in the solution space are known as dominated designs, which are dominated by at least one design in the Pareto front. Various optimization methods have been proposed for solving the multi-objective optimization problem, a comprehensive survey of which is provided by Marler and Arora [15].

50.5 Application: Steel Moment Resisting Frame Case

The proposed performance based robust design optimization is illustrated on a four-story three-bay steel moment resisting frame assumed to be located in Los Angeles, California (Fig. 50.2). The two-dimensional frame system in N-S direction is employed as illustrative example, with an assumed dead load of 70 psf for the floor and 56 psf for the roof including the weight of slabs. The live load is assumed to be 40 psf for floor levels and 15 psf for roof level, and the external wall load is assumed to be 30 psf for all levels. A572 grade 50 steel is used for all beams and columns. All beams at the same floor level are grouped into the same section type, and the columns of two adjacent floors symmetric with respect to the vertical center line are grouped together. This grouping results in a total of eight section types, i.e., eight design parameters. During optimization, steel sections are selected from the list of commonly used sections in tradition steel moment resisting frame design given in Table 50.1.

Twenty ground motions for both 50%/50 year and 2%/50 year seismic hazard levels developed for the Los Angeles SAC project are used [23]. The ground motions are scaled to match the 50%/50 year and 2%/50 year uniform hazard spectrums through least-square minimization at 0.5, 1, 2 and 4 s. The modal pushover analysis (MPA) procedure proposed by Chopra and Goel [4] is adopted to calculate seismic demand, due to its ability to efficiently yield acceptable accuracy. Structural

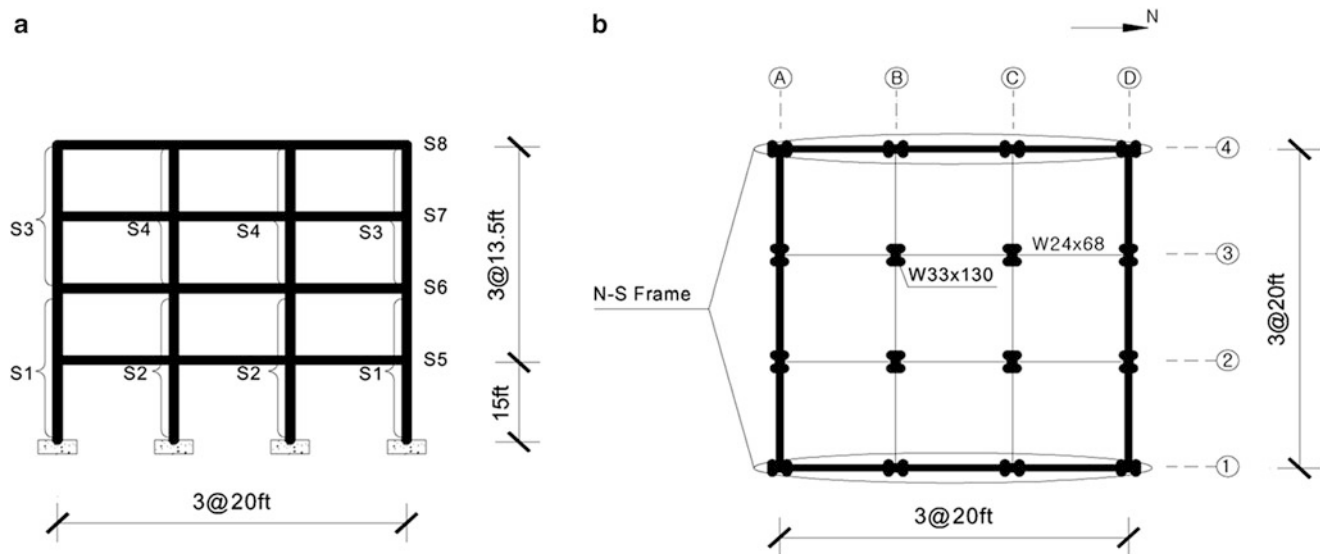


Fig. 50.2 (a) Elevation view and (b) plan view of the example steel moment resisting frame

Table 50.1 List of columns and beams

Column	Beam		
W14 × 99	W14 × 211	W24 × 55	W33 × 116
W14 × 109	W14 × 233	W24 × 62	W33 × 130
W14 × 120	W14 × 257	W24 × 68	W33 × 141
W14 × 132	W14 × 283	W24 × 76	W33 × 150
W14 × 145	W14 × 311	W27 × 84	W36 × 135
W14 × 159	W14 × 342	W27 × 94	W36 × 150
W14 × 176	W14 × 370	W27 × 102	W36 × 160
W14 × 193	W14 × 398	W27 × 114	W36 × 170

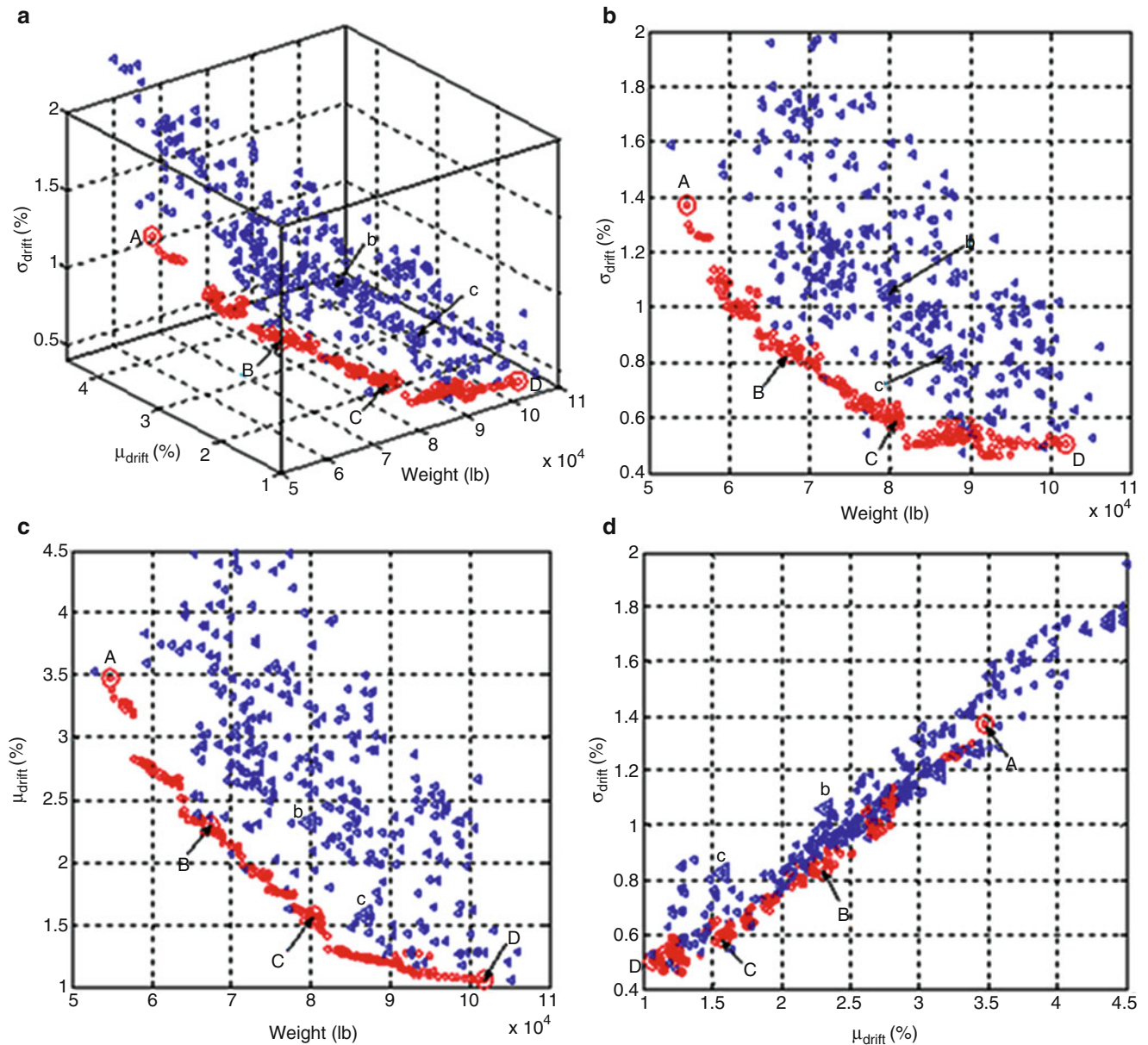


Fig. 50.3 Pareto Front and dominated designs, 3D an plan view (a). 3D view; (b) Relation between weight and σ_{drift} ; (c). Relation between weight and μ_{drift} ; (d). Relation between μ_{drift} and σ_{drift} .

analysis is performed with open system for earthquake engineering simulation (OpenSEES) [17]. ‘nonlinearBeamColumn’ element with a strain hardening ratio of 3% is used to simulate a column. The nonlinearity of the beam elements is modeled with Ibarra-Krawinkler (IK) model [10].

The formulated optimization problem is solved through NSGA-II [5] by evaluating 500 designs in each generation with a total number of 50 generations. The converged solution, i.e., the acquired Pareto front of the last generation, is shown in Fig. 50.3. For comparison purposes, Fig. 50.3 also depicts the feasible designs of generation 1. Since no designs belong to Pareto front in generation 1, they are termed as ‘Dominated Designs’ in the figure.

50.6 Discussions

50.6.1 Relation Between μ_{drift} – Cost and σ_{drift} – Cost

The design population of the initial generation and the last generation is illustrated in Fig. 50.3. As the σ_{drift} -Weight (cost) plot (Fig. 50.3) clearly indicates, the Pareto front designs are more robust (smaller σ_{drift}) than dominated designs for identical cost. For identical robustness (σ_{drift}), Pareto front designs are more economical than dominated designs. From the μ_{drift} -Weight (cost) plot (Fig. 50.3), the Pareto front designs are observed to exhibit smaller seismic demand (μ_{drift}) compared to the dominated designs for identical cost, while for designs with identical seismic demand (μ_{drift}), the Pareto front designs are more economical than the dominated designs.

In general, for given cost, both μ_{drift} and σ_{drift} can be greatly optimized, i.e., with steel weight as 8000 lb, σ_{drift} can be improved from the worst case of 1.6% in dominated designs to the best case of less than 0.6% in Pareto front, and μ_{drift} can be improved from the worst case of 3.7% in dominated design to the best case of around 1.5% in Pareto front. For identical μ_{drift} or σ_{drift} , cost of the designs can also be greatly optimized, i.e., with μ_{drift} as 2%, steel weight can be reduced from the worst case of 100,000 lb in dominated designs to the best case of 7,100 lb in Pareto front; with σ_{drift} as 1%, steel weight can be reduced from the worst case as 100,000 lb in dominated designs to the best case as 6,000 lb in Pareto front.

In the first generation, designs are randomly generated and the code-compliant designs are selected as feasible designs—similar to the trial and error process of inexperienced designers. The implication is that though trial and error process can yield code-compliant designs, these designs are far from being optimum. The designs of the first generation can be improved in terms of both robustness (σ_{drift}) and cost as observed from Fig. 50.3 and in terms of both seismic demand (μ_{drift}) and cost as observed from Fig. 50.3.

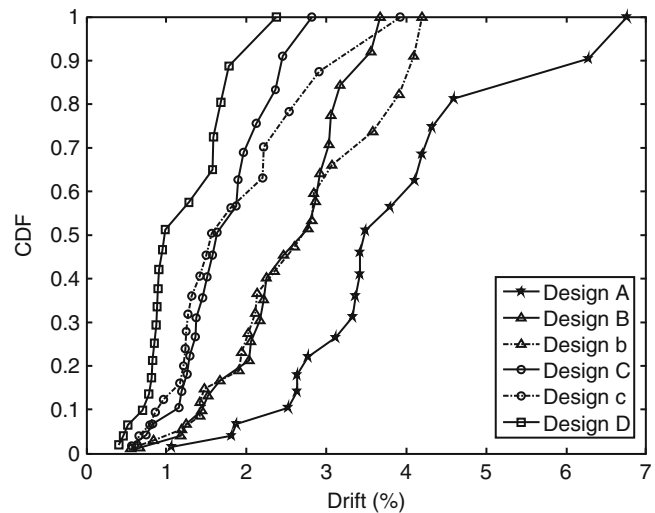
Six designs are selected for comparison, for which the steel sections and objective function values are listed in Table 50.2. Designs A, B, C and D are selected from the Pareto front, while Designs b and c are dominated designs. Designs A and D are the lightest design and the heaviest design in Pareto front, respectively. Designs A, B, C and D reflect the tradeoff relationship between cost and safety: the design with smaller μ_{drift} inevitably costs more, and the design with less cost inevitably has larger μ_{drift} . With the tradeoff relationship between cost and μ_{drift} , more informed decision making can be achieved.

In single objective optimization, potential changes in safety or robustness due to an increase or decrease of project cost is not supplied. With Pareto Front, however, this information becomes readily available. For instance, comparing designs A and C, with material weight increase from 54792 to 80361 lb (by 46.7%), the μ_{drift} will be reduced from 3.48% to 1.57% (by 54.9%). As a result, the decision maker has control on risk and budget associated with the preferred design. A risk-averse decision maker may choose a design with smaller μ_{drift} with a higher budget, while a risk-prone decision maker may choose a design with a greater μ_{drift} . A decision maker may also evaluate the necessary budget for a project when using a Pareto front.

Table 50.2 Steel section size and objective values of selected designs

Selected designs		Design A	Design B	Design b	Design C	Design c	Design D
Columns	Storey 1 and 2	W14 × 159	W14 × 159	W14 × 211	W14 × 211	W14 × 283	W14 × 398
		W14 × 193	W14 × 342	W14 × 398	W14 × 398	W14 × 370	W14 × 398
	Storey 3 and 4	W14 × 159	W14 × 159	W14 × 145	W14 × 159	W14 × 99	W14 × 193
		W14 × 193	W14 × 211	W14 × 193	W14 × 283	W14 × 370	W14 × 398
Beams	Storey 1	W24 × 76	W27 × 102	W24 × 68	W33 × 116	W36 × 135	W33 × 130
	Storey 2	W24 × 76	W27 × 102	W36 × 135	W33 × 116	W36 × 160	W33 × 130
	Storey 3	W24 × 55	W24 × 55	W27 × 84	W24 × 76	W24 × 55	W27 × 94
	Storey 4	W24 × 55	W24 × 55	W36 × 160	W24 × 55	W24 × 55	W24 × 55
Weight (lb)	54792	67377	79785	80361	86847	101826	
μ_{drift}	3.48	2.30	2.32	1.57	1.57	1.06	
σ_{drift}	1.37	0.83	1.06	0.58	0.83	0.50	

Fig. 50.4 CDF of inter-story drift of six selected designs



50.6.2 Relation Between μ_{drift} and σ_{drift}

The data from μ_{drift} - σ_{drift} plot (Fig. 50.3d) indicates a positive correlation between μ_{drift} and σ_{drift} , i.e. designs with a larger μ_{drift} also have a larger σ_{drift} .

The cumulative distribution of the six designs is plotted, as shown in Fig. 50.4. Comparing designs A, B, C and D, the probability of not being exceeded increases from design A to D for identical specified μ_{drift} . Though designs B and b have comparable μ_{drift} , design B is safer than design b, as it has a larger probability of not being exceeded for identical inter-story drift (as $\mu_{drift} > 2.7\%$), due to its smaller σ_{drift} . The same relation between design C and design c is also observed. Thus, for identical μ_{drift} , increasing robustness (reducing σ_{drift}) has the benefit of increasing safety (smaller probability of being exceeded).

50.6.3 Uniformity Drift Ratio as a Design Efficiency Indicator

Inter-story drift ratio for all six selected designs are plotted in Fig. 50.6. For each design, the maximum inter-story drift occurs at one or two stories for almost all ground motions, known as weak stories. It is apparent from both Fig. 50.5 that maximum inter-story drift of designs b and c exhibit a much greater variance than designs B and C. Furthermore, variation of inter-story drift between different stories of designs B and C is also smaller than that of designs b and c. That is to say designs B and C exhibit a more uniform distribution of the inter-story drift. Though designs b and c are heavier than designs B and C, they are inferior designs, as the inappropriate proportioning of stiffness and strength make them prone to weak story mechanism failure, i.e., failure due to excessive inter-story drift at one or several stories.

Comparing designs A, B, C and D, the uniformity of the inter-story drift decrease from design D to A. With larger strength, design D would be within its linear range. Whereas design A, as the 'weakest' design, yields even when subjected to low intensity ground motion. After yielding, the stiffness of design A is greatly reduced, thusly sharply increasing the displacement with a slight increase in force or ground motion intensity. The large σ_{drift} of designs b and c is also caused by the weak story. As observed from Fig. 50.5b, the difference of inter-story drift between different stories is not large for low intensity ground motion, while the difference is greatly amplified as ground motion intensity increases after yielding of the first story, resulting in a much larger variation in maximum inter-story drift.

Merely considering maximum inter-story drift is not sufficient to evaluate a design, as story-wise distribution of inter-story drift is not reflected by maximum inter-story drift. Uniformity drift ratio (UDR), defined as ratio of maximum inter-story drift ratio to roof displacement ratio (ratio of roof displacement to building height), can be employed as indicator of inter-story drift uniformity. According to the definition, UDR should be a value larger than unity, while a smaller UDR indicates a more uniform distribution of inter-story drift.

As for identical cost, Pareto front designs exhibit smaller μ_{drift} , and for identical μ_{drift} , Pareto front designs cost less. Thus, Pareto front designs are more efficient than dominated designs. The traditional trial and error based design is likely to result in dominated designs instead of Pareto front designs, as Pareto front designs occupy a small portion of the solution space.

Fig. 50.5 Inter-story drift ratio results of all ground motions of six selected designs. (a). Design A; (b). Design B and Design b; (c). Design C and Design c; (d). Design D

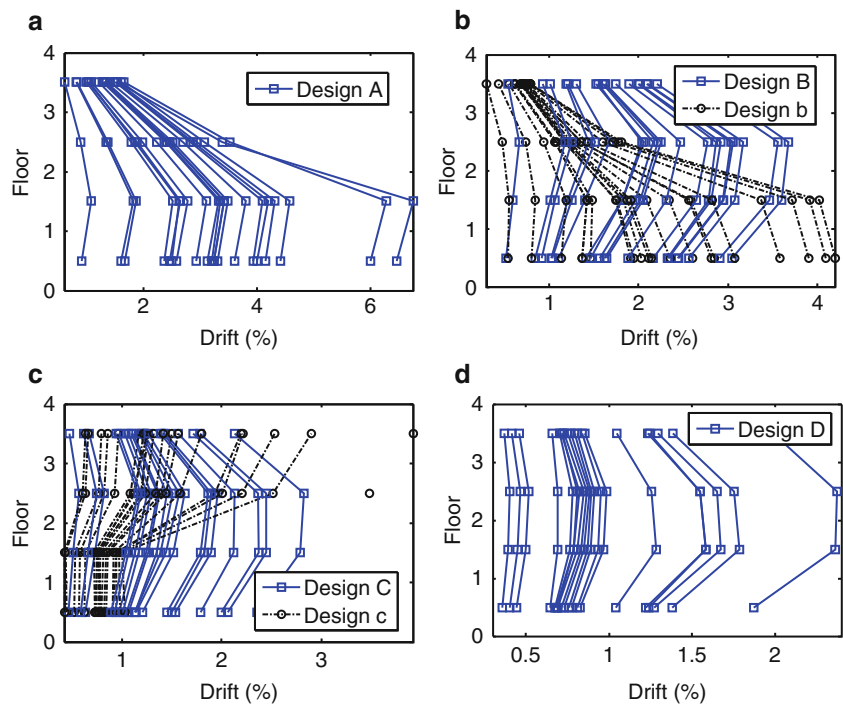
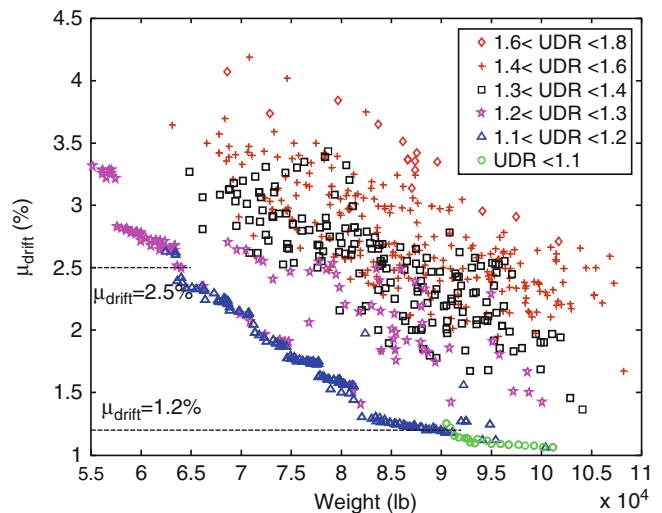


Fig. 50.6 Uniformity drift ratio distribution for Pareto front designs and dominated designs



Though Pareto front can be acquired by the multi-objective optimization method, the complex programming of optimization is not practical for practicing engineers, thus simplified method for acquiring Pareto front designs or criteria for ensuring efficiency should be explored. Since inter-story drift is generally positively correlated with strength and stiffness of the corresponding story, thus, UDR is expected to reflect the distribution of strength and stiffness, as a result, it is expected to be a suitable indicator of design efficiency.

To test the applicability of UDR as efficiency indicator, mean value of UDR of the twenty ground motions for Pareto front designs and dominated designs are calculated, as shown in Fig. 50.6. UDR is divided into several ranges. Generally speaking, designs with smaller UDR dominate designs with larger UDR. For every other range of UDR, regions of design are separated clearly, i.e., regions of $1.3 < UDR < 1.4$ and regions of $1.6 < UDR < 1.8$ are not overlapping; the same phenomenon is observed between regions of $1.1 < UDR < 1.2$ and regions of $1.3 < UDR < 1.4$. Since efficient and inefficient designs can be roughly separated with different UDR values, UDR can effectively serve as a design efficiency indicator.

In addition, within Pareto front, designs with larger μ_{drift} generally have larger UDR as well. For μ_{drift} less than 1.2%, all Pareto front designs have a UDR less than 1.1, for μ_{drift} between 1.2% and 2.5%, Pareto front designs have a UDR between 1.1 and 1.2, and for μ_{drift} larger than 2.5%, Pareto front designs have a UDR between 1.2 and 1.3. Designs with larger μ_{drift} are driven to the nonlinear range more severely resulting in larger difference in maximum inter-story drift between stories and in turn, leading to larger UDR. Considering the aforementioned ranges for UDR, whether a design is efficient can be determined by both traditional trial and error based and optimization-based design approaches. It should be noted that the requirement is applicable only for the steel frame considered herein. Whether it can be extrapolated to steel moment resisting frame of different stories, or different structure types need to be verified through more studies. Considering the benefits of appropriately proportioning strength and stiffness, UDR requirement should be considered as a valuable design criterion.

$$\begin{cases} \text{UDR} < 1.1 & \text{for } \mu_{drift} < 1.2\%; \\ \text{UDR} < 1.2 & \text{for } 1.2\% < \mu_{drift} < 2.5\%; \\ \text{UDR} < 1.3 & \text{for } \mu_{drift} > 2.5\%; \end{cases} \quad (50.2)$$

50.7 Conclusion

In this paper, performance based Robust Design Optimization of steel moment resisting frame was proposed, in which cost, mean value of seismic demand and standard deviation of seismic demand are three objectives, ground motion variability is considered as noise factor, and steel section sizes are sought to minimize the objectives. A four-story three-bay steel moment resisting frame is employed as an example to demonstrate the proposed methodology. The following conclusions are drawn:

- (1) The methodology proposed can provide a set of competing designs that are economical, safe and robust in the form of a Pareto front, with which structural engineers and stakeholders can make informative tradeoff decisions in a preferred manner.
- (2) Pareto front designs are superior to dominated designs in terms of cost, safety and robustness, while traditional trial and error method would most probably result in a dominated design (inefficient design) rather than a Pareto front design (efficient design), as Pareto front designs only occupy a small proportion of all designs in solution space.
- (3) For identical mean value of seismic demand, variation of seismic demand can be reduced through adjusting design variables and a safer design can be achieved.
- (4) Uniformity drift ratio can be served as design efficiency indicator effectively. Efficient designs generally have smaller uniformity ratio, while inefficient designs generally have larger uniformity ratio. Requirement of uniformity drift ratio conditional on the range of maximum inter-story drift for ensuring efficient designs is suggested. With the suggested requirement enforced, efficient designs can be achieved with the trial and error process without complex optimization.

References

1. American Institute of Steel Construction (AISC) (2005) Seismic provisions for structural steel buildings. American Institute of Steel Construction, Chicago
2. American Society of Civil Engineers (2010) ASCE-7 minimum design loads for buildings. American Society of Civil Engineers, Reston
3. Beyer H, Sendhoff B (2007) Robust optimization—a comprehensive survey. *Computer Meth Appl Mech Eng* 196:3190–3218
4. Chopra AK, Goel RK (2002) A modal pushover analysis procedure for estimating seismic demands for buildings. *Earthquake Eng Struct Dyn* 31(3):561–582
5. Deb K, Pratap A, Agarwal S (2002) A Fast and Elitist Multiobjective Genetic algorithm: NSGA-II. *IEEE Trans Evol Comput* 6(2):182–197
6. Ellingwood BR, Kinali K (2009) Quantifying and communicating uncertainty in seismic risk assessment. *Struct Safe* 31(2):179–187
7. Federal Emergency Management Agency (FEMA) (2000) Recommended seismic design criteria for new steel moment-frame buildings. Rep. No. FEMA-350, Prepared by the SAC Joint Venture for FEMA, Washington
8. Fragiadakis M, Lagaros ND, Papadrakakis M (2006) Performance-based multiobjective optimum design of steel structures considering life-cycle cost. *Struct Multidiscipl Optimiz* 32:1–11
9. Gencturk B, Elnashai AS (2011) Multi-objective optimal seismic design of buildings using advanced engineering materials. MAE Center Report No. 11-01, Mid-America Earthquake Center
10. Ibarra LF, Medina RA, Krawinkler H (2005) Hysteretic models that incorporate strength and stiffness deterioration. *Earthquake Eng Struct Dyn* 34(12):1489–1511
11. Jalayer F, Cornell, C.A (2003) A technical framework for probability-based demand and capacity factor design (DCF) seismic formats. In: PEER-2003/08, Pacific earthquake engineering research center, University of California, Berkeley

12. Kameshki ES, Saka MP (2003) Genetic algorithm based optimum design of nonlinear planar steel frames with various semi-rigid connections. *J Constr Steel Res* 59(1):109–134
13. Liu M, Burns SA, Wen YK (2003) Optimal seismic design of steel frame buildings based on life cycle cost considerations. *Earthquake Eng Struct Dyn* 32:1313–1332
14. Liu M, Burns SA, Wen YK (2005) Multiobjective optimization for performance-based seismic design of steel moment frame structures. *Earthquake Eng Struct Dyn* 34(3):289–306
15. Marler RT, Arora JS (2004) Survey of multi-objective optimization methods for engineering. *Struct Multidisc Optimiz* 26(6):369–395
16. Nair VN, Abraham B, MacKay J, Nelder JA, Box G, Phadke MS (1992) Taguchi's Parameter Design: A Panel Discussion, *Technometrics* 34(2):127–161
17. OpenSees (2010) Open system for earthquake engineering simulation. Pacific Earthquake Engineering Research Center (PEER), <http://opensees.berkeley.edu>. Accessed 10 October 2012
18. Park G-J, Lee T-H, Lee KH, Hwang K-H (2006) Robust design: an overview. *AIAA J* 44(1):181–191
19. Phadke MS (1989) *Quality engineering using robust design*. Prentice Hall, Englewood Cliffs
20. Rojas HA, Foley C, Pezeshk S (2011) Risk-based seismic design for optimal structural and nonstructural system performance. *Earthquake Spectra* 27(3):857–880
21. Sarma KC, Adeli H (2002) Life-cycle cost optimization of steel structures. *Int J Numer Meth Eng* 55(12):1451–1462
22. Shome N, Cornell CA, Bazzurro P, Carballo JE (1998) Earthquakes, records, and nonlinear responses. *Earthquake Spectra* 14(3):469–500
23. Somerville P, Smith N, Puntamurthula S, Sun J (1997) Development of ground motion time histories for phase 2 of the FEMA/SAC steel project. SAC background document SAC/BD-97/04, SAC Joint Venture, Richmond
24. Taguchi G (1986) *Introduction to quality engineering: designing quality into products and processes*. Quality Resources, White Plains
25. Xu L, Grierson DE (1993) Computer-automated design of semirigid steel frameworks. *J Struct Eng* 119(6):1740–1760

Chapter 51

Structural Assessment of Fort Sumter Masonry Coastal Fortification Subject to Foundation Settlements

Sez Atamturktur, Saurabh Prabhu, and Rick Dorrance

Abstract In historic unreinforced masonry structures, one of the most critical structural issues is the differential settlement of foundations. Due to unreinforced masonry's brittle nature with a fairly low tensile strength, brittle cracking can occur due to tensile stresses introduced by foundation settlements. This study demonstrates the development and calibration of a finite element model and the use of this model for structural analysis under differential settlements of a casemate of Fort Sumter, a masonry coastal fortification best known as the site where the first shots of The American Civil War were fired in 1861. Development of accurate finite element models for historic masonry structures presents numerous challenges in the acquisition of non-linear material properties, and irregular geometry. Furthermore, these challenges are exacerbated because of the configuration of coastal fortifications, as these structures have characteristic designs unique to the distinct functionality of defense, such as cold-joints between disjointed structural components. The non-linear material behavior of the brick and mortar assembly is obtained from laboratory tests on samples obtained at the site. High definition laser scanning is used on irregular geometry to obtain the details of accumulated structural damage and degradation, including differential foundation settlements. The uncertain interface behavior at the cold joint between the scarp wall and the casemate of the fort is assessed using in-situ vibration tests. The finite element model developed is utilized to study the settlement magnitudes critical to the stability of the casemates of Fort Sumter for a variety of possible soil settlement configurations.

Keywords Nondestructive evaluation • Finite element model • Masonry fort • Historic monument • Foundation settlement

51.1 Introduction

Developing numerical models of historic masonry poses numerous and unique challenges, particularly in the acquisition of the appropriate input parameters [4, 19, 24]. Firstly, the available knowledge of the materials used and the properties of these materials are quite limited. In that masonry is largely heterogeneous material which can show highly variable mechanical properties in different samples, the absolute values of the material properties are seldom known. Also, the time-dependent deterioration of the building material cannot be estimated. Secondly, geometric degradation of the structure, over time, from material deterioration and loading events has resulted in permanent damage. Even though original drawings of the building are available, the workmanship at the time of construction does not guarantee the fidelity of the construction to the drawings. Given these challenges, actual field measurements of material properties and geometry are indispensable for obtaining input parameters for numerical model development.

The material properties obtained from testing of field samples show high spatial variability. Since it is practically impossible to acquire the thorough spatial variability of material properties, global mechanical properties are sought that require a limited number of samples and model calibration exercises to develop models that faithfully predict the global mechanical behavior of the structure. Where destructive testing is not possible, non-destructive methods, such as vibration

S. Atamturktur (✉) • S. Prabhu

Glenn Department of Civil Engineering, Clemson University, 200, Lowry Hall, Box 340911, Clemson, SC, 29634-0911 USA
e-mail: sez@clemson.edu

R. Dorrance

Chief of Resources Management, Fort Sumter National Monument, National Park Services, Charleston, SC, USA

testing, are used to collect field data for calibration. The geometry of the structure is developed using high definition and high accuracy 3D laser scanning. Data reductions and simplification is performed without the loss of any structural property detail.

The numerical model thus developed can be used to predict structural behavior under any practical loading conditions. This study is focused on foundation settlement simulations on Fort Sumter, a 19th century unreinforced brick masonry coastal fortification built on a man-made island off the coast of Charleston, SC. The material properties are determined from laboratory tests on core samples and loose masonry from the fort. The complex three dimensional geometry of the fort is reproduced using 3D laser scanning. A special feature of many coastal fortifications is that the external wall (scarp wall) forms a dry contact with the rest of the structure. To account for the uncertain mechanical behavior at the interface of this dry contact, the authors used non-destructive vibration testing methodology.

The organization of the manuscript is as follows. A brief history and construction details of Fort Sumter are provided in Sect. 51.2; the on-site evaluations of the material properties and geometry are detailed in Sect. 51.3; a discussion on the development of the finite element (FE) and a model of one of the fort's casemates is provided in Sect. 51.4, followed by details of the calibration exercises in Sect. 51.5. Finally, in Sect. 51.6, the details and results of foundation settlement simulations are provided. The authors summarize their main findings in the conclusion of this paper.

51.2 Fort Sumter National Monument: History and Structural System

The construction of Fort Sumter began in 1829 with the laying of a foundation comprised of approximately ten thousand tons of granite and sixty thousand tons assorted rocks forming a two-acre artificial island [16, 20]. Nearly four million bricks were used in the construction of the fort's superstructure and by 1860 the walls of the fort were 50 ft. tall enclosing a parade ground of almost one acre (Fig. 51.1).

Each side of the pentagonal fort consists of series of casemates with an outer perimeter encased by a scarp wall with gun embrasures to allow the cannons to fire. One of the unique design aspects of the fort is that the masonry is not continuous from the casemate to the scarp wall although the two are in contact. Thus, a contact exists between the scarp wall and the casemate piers and vaults. This design ensures that the bombardment on the outer sides of the fort on the scarp wall does not damage the inner casemates which hold the guns and soldiers.

Several battles were fought over the fort during the Civil War, the first and most of famous of which was the siege in April 1861, followed by Union attempts in August 1863 to take the fort by storm, after which it remained in state of "practical demolition" [20] (Fig. 51.2). Subsequent to the fighting, Fort Sumter was further degraded by damage which reduced it from the original three tiers to the present one-tier structure. In 1948, Fort Sumter was declared a national monument and is now under the aegis of the US National Park Service.

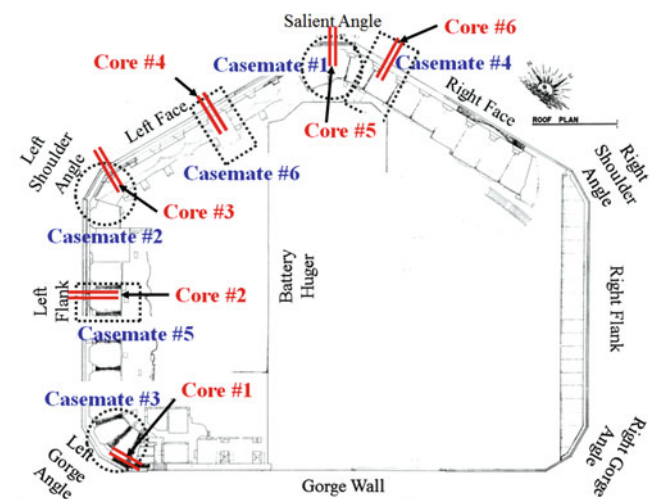
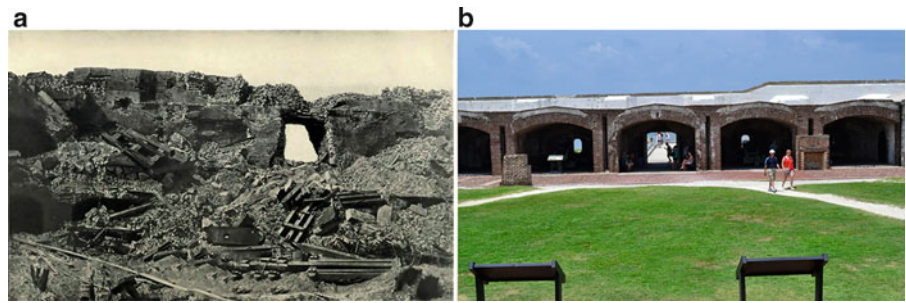


Fig. 51.1 Roof plan marking the six casemates to be modeled and the locations of the core sampling points (plan drawing courtesy of National Park Service)

Fig. 51.2 (a) Photo taken on August, 1863 showing the first breach in Fort Sumter walls (source: [13]; original photograph by G.S. Cook), (b) Photo taken in August, 2011 showing the current condition of Fort Sumter casemates



51.3 On-Site Data Collection for Model Development

51.3.1 Material Testing

Fort Sumter is composed of three materials: brick and mortar forming the masonry and tabby concrete [16] forming the infills in the walls and piers. The mortar is constituted primarily of natural cement a.k.a. Rosendale cement [6], lime and sand; the tabby concrete is a type of concrete that uses broken oyster shell and brick pieces as aggregate and burnt oyster shells to create lime [8]. The proposed FE model (Fig. 51.3) uses three materials for the following three components: (i) the masonry of the piers and walls, (ii) masonry of the vaults and (iii) tabby concrete infill. Although the masonry of the piers and walls and the vaults is composed of the identical brick and mortar, the joint orientation in the vaults is vertical while the joint orientation in the piers and walls is horizontal. This particular configuration of masonry in the vaults, however, provides a lower strength in the direction parallel to the joints and thus is considered a distinct material, and calibrated as an independent parameter.

To test material of the fort, a block sample was collected from the loose masonry and was used to prepare two samples (Sample A and Sample B) for compression testing. The authors also prepared samples for tension testing from the same block. Material tests on tabby concrete are performed on samples collected via coring.

During compression experiments, Sample A was tested for compressive strength in the direction normal to the bed-joint (Fig. 51.5a), while Sample B was tested for compressive strength in the direction parallel to the bed-joint (Fig. 51.5b). Compressive strength tests were performed according to ASTM C109/109M-11a on 50 mm cube specimen. The modulus of elasticity was calculated as the slope of the elastic region of the stress–strain curve (shown in Fig. 51.5c). Table 51.1 lists the modulus of elasticity and crushing strength of both specimens.

As mentioned earlier, there is a significant variability observed in the elastic modulus and compressive strength of the two samples and cannot be directly used in as model input parameters. These values are considered approximate and only provide appropriate starting points for the calibration process, to be discussed later.

The tensile capacity of the masonry was determined from three-point flexural tests on brick and mortar samples obtained from the block sample, the results of which are in Table 51.2. The tensile capacity of the masonry is taken to be 2.07 MPa, which is the volumetric average of the tensile strengths of the mortar and brick.

While the linear material properties, such as modulus of elasticity, can be calibrated using non-destructive vibration test data, the calibration of tensile and compression strengths would require destructive testing to be performed on the structure which is impractical. Therefore, the average values calculated were used provided the range of values was feasible.

Moreover, the bulk densities are calculated as a volumetric average of the brick and mortar in a standard representative cell. The density of brick and mortar is 1490 kg/m^3 and 1670 kg/m^3 respectively which are reasonably consistent between various samples. The volumetric average yields a density of 1500 kg/m^3 for the masonry assembly.

The diametral tests on three core samples of tabby concrete, shown in Fig. 51.4d, provides a compressive modulus of elasticity of 510 MPa and average tensile and compressive strength of 0.51 MPa and 6.37 MPa, respectively. The density of the tabby concrete infill was measured from the core samples as 1600 kg/m^3 (51.3).

51.3.2 Laser Scanning and Model Geometry

One crucial aspect in the development of our Fort Sumter model involves ensuring an accurate reproduction of the as-is geometry of the fort. The use of laser scanning has been considerably successful in 3D surveying of historic monuments [2, 3, 13, 25]. Here, we used laser scanning to accurately and quickly obtain a high resolution 3D scan of the fort using a

Fig. 51.3 (c) Sample A crushed in the compression test; (d) Sample B crushed in the compression test; (e) Stress strain curves for Sample A and Sample B from the compression test. The slope of the elastic region is taken as the elastic modulus

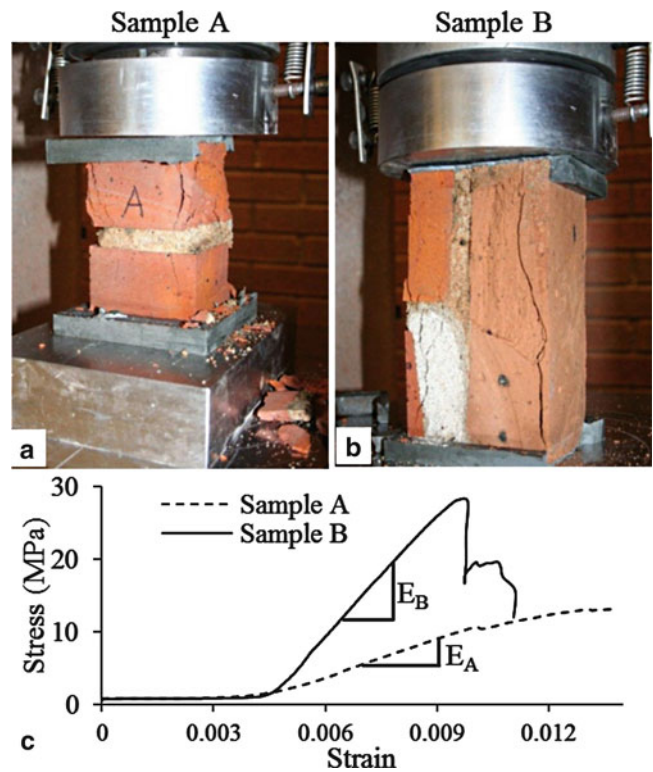


Table 51.1 Compressive modulus of elasticity and strength of the samples from the block specimen

Sample	Modulus of elasticity (MPa)	Crushing strength (MPa)
Sample A	1632	12.39
Sample B	5509	29.01

Fig. 51.4 Solid model of the casemate showing the different material assignments and the location of the scarp wall interface modeled with contact elements

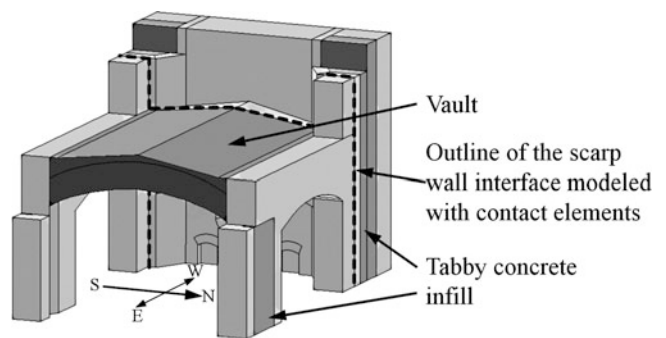


Table 51.2 Tensile strengths of the samples from the cores and the block specimen

Sample	Tensile strength (MPa)
Mortar	0.65
Brick	2.37

Trimble CX scanner. Capable of recording 54,000 points per second with a positioning accuracy of 4.5 mm for every 30 m and distance accuracy of 1.2 mm for every 30 m, the Trimble scanner generates a point cloud of several million points for each casemate.

The high resolution data was then exported to a post-processing software, Polyworks v11, where a polygon mesh (Fig. 51.6a) of the geometry was created and the data was decimated by a factor of almost 80 % to create simple surfaces. We further exported this polygon mesh to the design software package, Rhino v5, to generate wireframe models (Fig. 51.6b) to further simplify the geometry of our casemate under study. We were particularly assiduous in preserving the crucial structural features of the geometry such as cracks, indentations and out-of-plumb deformations.



Fig. 51.5 (a) Block specimen from the remains of the fort; (b) block specimen segmented into smaller samples for testing; (c) coring of the wall in progress; (d) an intact core sample of tabby concrete infill

Table 51.3 Material properties of tabby concrete obtained from core tests

Tabby concrete	
Modulus of Elasticity	510 MPa
Tensile Strength	0.51 MPa
Compressive Strength	6.37 MPa
Density	1600 kg/m ³

51.4 Finite Element Model Development

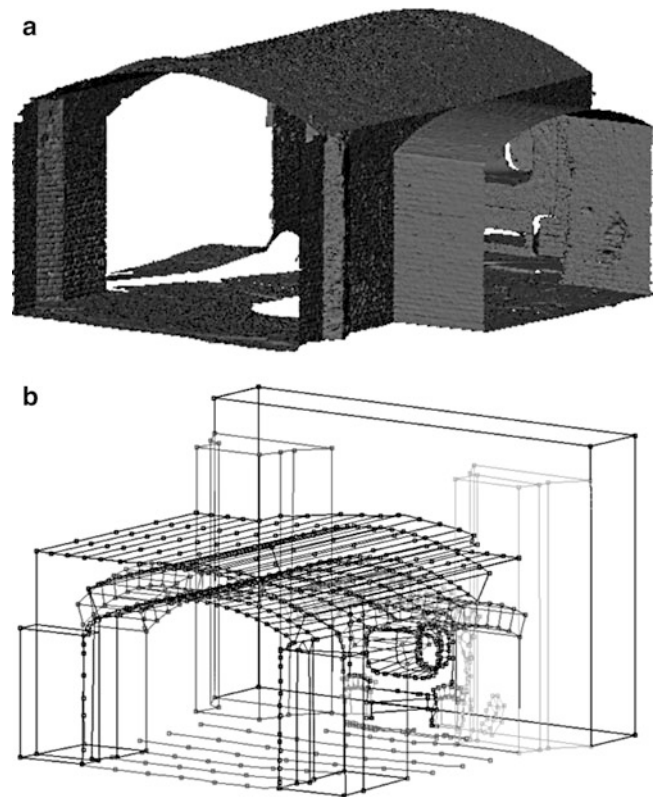
51.4.1 Modeling Considerations

The geometry of the fort is replicated from the wireframe models into a finite element package Ansys 13.0. Next, the appropriate material models and the boundary and interface conditions are applied, as detailed within this section.

51.4.1.1 Brick and Mortar Assembly

As masonry is weak in tension, cracking is the primary mode of failure of this material. Therefore, a material model that models the masonry behavior must account for such cracking. SOLID65 element is available in ANSYS that uses the Willam–Warnke failure criterion [28] and accounts for cracking in tension and crushing in compression. The Willam–Warnke failure criterion is a function of the principal stresses within the element. If the failure criterion is exceeded at the face of the 3D SOLID65 element, a plane of weakness is applied at the face; in other words, the stiffness of the material normal to the face

Fig. 51.6 (a) Polygonal mesh of Casemate 4 generated in Polyworks V11; (b) Wireframe of Casemate 4 generated in Rhino v5.0



is set to a near-zero value, thus simulating the effect of cracking. The cracking and crushing strengths of the masonry tested are discussed in Sect. 51.3.1. In addition, an open and closed crack shear transfer coefficient [18] was specified which has a range of 0 (smooth crack) to 1 (perfectly rough crack). As experiments for these parameters were not undertaken, the generic values used in previous studies were employed [12, 21]. The open and closed crack shear transfer coefficients are specified as 0.2 and 0.6 respectively.

51.4.1.2 Scarp Wall Interface

The interface behavior at the dry contact between the scarp wall and the casemate piers and vaults is highly uncertain. To model this dry contact, contact-elements (aka interface elements) were used at the interface and the sliding behavior was represented by specifying a friction coefficient at the interface. In ANSYS, CONTA174 and TARGE170 were used in combination to model the interface and the appropriate friction coefficient at the interface is obtained in a non-destructive manner. Though the authors could have performed a friction test between two masonry samples obtained from the loose material on site, the dissimilar nature of the scarp wall interface to the regular masonry-on-masonry frictional behavior would have resulted in inaccurate measurements. Several other forces such as contact cohesion and moisture between the adjacent members are inherent in this interface behavior and cannot be measured by non-intrusive techniques. In the FE model, however, the behavior is idealized by defining it with a Mohr–Coulomb friction model that uses a static friction coefficient that governs the tangential contact stiffness.

51.4.1.3 Foundation Support

The semi-rigid support provided by the foundations was idealized as a system of closely spaced linear springs forming a Winkler type of foundation [7, 14, 29]. In ANSYS, the element COMBIN14 was used to define linear translational springs with specified spring stiffness. One value of spring stiffness was applied to the entire foundation which was determined by calibration to experimental data as discussed in Sect. 51.5.2.

Fig. 51.7 Mesh refinement study showing the change in the first four natural frequencies as a function of the element size

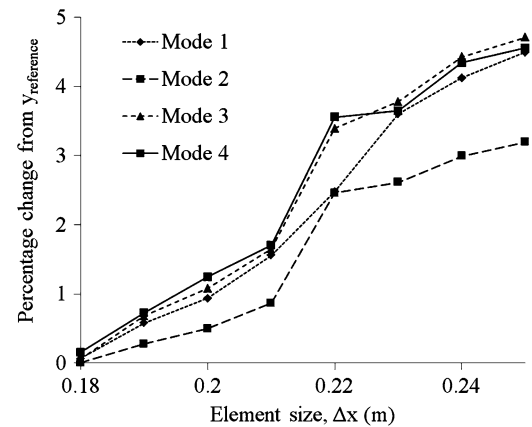
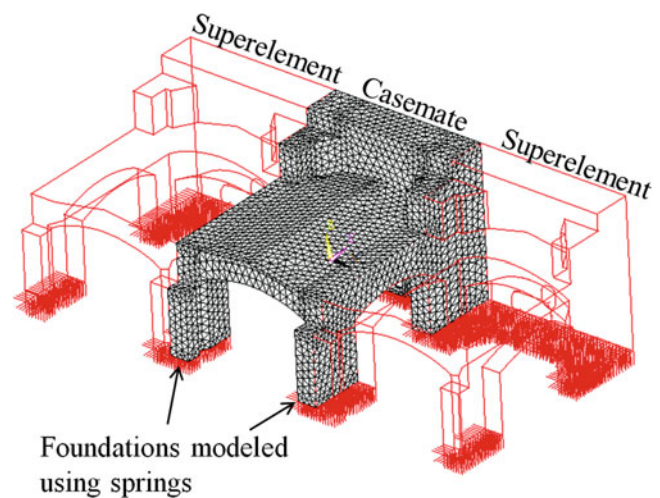


Fig. 51.8 Sub-structured FE model of Casemate 4 with springs used to represent the foundation. The meshed region is the casemate itself adjoined by superelements of the neighboring casemates



51.4.2 Determination of Optimal Mesh size

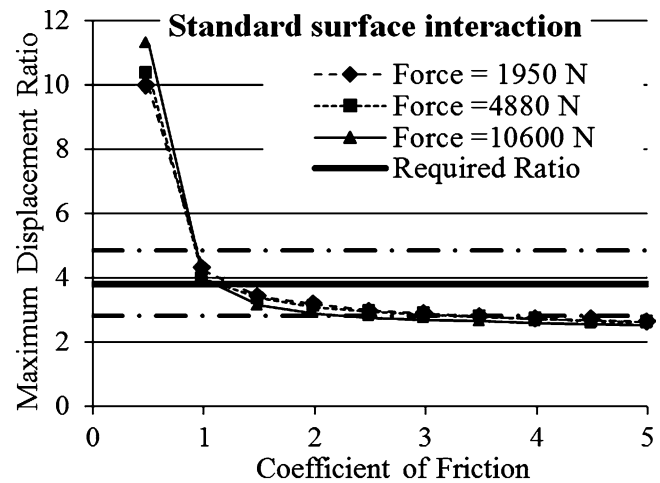
In any FE model, the size of the mesh is a major factor that affects the accuracy of the results. In most cases, the smaller the mesh size, the more accurate are the results. Beyond a certain mesh size, however, the gain in accuracy diminishes as the mesh size decreases with a concurrent increase in computational costs. It is therefore, important to use an ideal mesh size that gives tolerable error and that does not render the problem computationally expensive.

Following a mesh refinement study (Fig. 51.7) on the first four free-free natural frequencies and a Richardson extrapolation [23] to find a reference solution, a mesh size corresponding to an element edge length of 0.23 m was chosen. The error of nearly 4 % is less than expected experimental variability due to temperature and moisture conditions of 5–6 % [22, 26]. This mesh size yielded a solid model with 87,555 tetrahedral elements and 131,232 nodes with three degrees of freedom at each node.

51.4.3 Substructuring of Unmodeled Components

In order to consider the lateral boundary conditions, the neighboring casemates were modeled as substructures (Fig. 51.8). The Component Mode Synthesis technique [11, 27] was used for the modal analysis of the combined system. Within ANSYS, a Craig–Bampton substructuring technique [1, 9, 10] was used to generate reduced order superelements that represent any structure by its interface DOFs. The superelements are then coupled to the structure of interest and the loads on the superelement are transferred via load vectors applied on the interface. Through this approach, a better representation of the lateral boundary conditions was constructed to create a threefold reduction in the degrees of freedom.

Fig. 51.9 Plot showing the relative displacement ratio for different values of applied force and μ



51.5 Calibration of Input Parameters

51.5.1 Friction Coefficient at the Scarp Wall Interface

To estimate the force transfer at the interface, the ratio of dynamic displacements on the two sides of the interface was used to calibrate the friction coefficient in the FE model. A hammer impact test was conducted on the interface with accelerometers mounted on the two sides of the interface. The acceleration response from the hammer impact was measured on the two sides using the two accelerometers. The acceleration response was then converted to a displacement response after applying high-pass filters to filter the low frequency noise. The ratio of the maximum displacements on the two sides was then calculated.

In the FE model, a static test was performed in which the load is applied at the point of the hammer impact; the ratio of displacements on the two sides of the interface was then measured. The friction coefficient at the interface was calibrated until the same ratio was achieved, which was identical to that from the hammer impact test (Fig. 51.9). A friction coefficient of 1.13 was obtained. The high value of the friction coefficient can be explained by the cohesive forces that exist at the interface developed over the years of the masonry remaining in contact along with repeated temperature and moisture cycles.

51.5.2 Calibration of Material Properties and Boundary Conditions

Three parameters that remain uncertain, namely: the elastic modulus of the masonry of piers and walls, elastic modulus of the masonry of the vaults and elastic spring constants of the foundation springs, were calibrated using experimental data. The purpose of this model calibration was not to replicate the local mechanisms down to every brick and joint, but rather to improve the capability of the model to predict global mechanical behaviors under various structural loads. Modal analysis provided the global linear mechanical properties in terms of the structures modal parameters i.e. natural frequency and mode shape. Ambient vibration tests are most suitable for historic structures as there is no need of artificial excitation and thus, no risk of structural damage to the historic monument from such excitation. To perform the ambient modal analysis, the authors deployed 41 measurement points on the casemate with PCB 393B04 seismic accelerometers (Fig. 51.10). A baseband frequency range of 0–1.6 kHz was used with a sampling frequency of 819.2 Hz and a Nyquist frequency of 409.6 Hz corresponding to a sampling interval of 1.22 ms. Thus, a total of 1,474,560 samples were collected over 1800 seconds. The raw time domain operational data was exported to a Bruel and Kjaer Operational Modal Analysis, a specialized software for modal analysis using operational data.


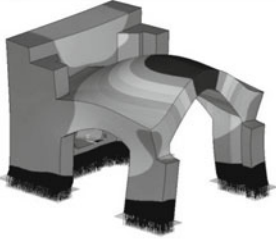

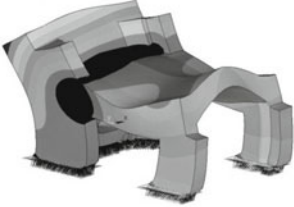
Using the Enhanced Frequency Domain Decomposition method for this analysis [5, 15], two modes were identified at 27.48 Hz and 45.2 Hz, respectively, both of which, together with the corresponding mode shapes, are provided in Fig. 51.11.

Using the two identified modes, the uncertain parameters i.e. the elastic modulus of walls and piers (θ_1), the elastic modulus of the vaults (θ_2) and the stiffness of the springs at the supports (θ_3) were calibrated through a fully Bayesian implementation of the statistical inference procedure proposed by Kennedy and O'Hagan [17]. The bounding limits for the parameters were determined via material tests as described in Sect. 51.3.1. For θ_1 , the mean of 3.5 ± 500 MPa was the assumed bounding range, while for θ_2 , 1.5–2.5 GPa was the assumed bounding range. The bounding range for the

Fig. 51.10 The experimental set-up showing accelerometers mounted on the vaults and piers



Fig. 51.11 Comparison of measured and simulated modes with respective MAC values

Mode 1 (MAC = 0.86)	
27.48 Hz	29.9 Hz
	
Mode 2 (MAC = 0.6)	
45.2 Hz	42.8 Hz
	

foundation spring stiffness, which was semi-rigid, was determined through a parametric analysis. A range within which the foundation remains semi-rigid and the experimental mode shapes were observable was between 10^1 and 10^3 MN/m. Within these bounding ranges, the predicted natural frequencies were within a 20 % error with respect to the experimental natural frequencies. The domain defined by the prior distributions of the three parameters is explored via 20,000 Markov Chain Monte Carlo samples. The peaks of the posterior distributions obtained from this sampling were the calibrated values of 3.2 GPa for θ_1 , 1.58 GPa for θ_2 and 60 MN/m for θ_3 (Fig. 51.12).

51.6 Foundation Settlement Analysis

Unreinforced masonry systems are particularly susceptible to differential settlements owing to their small tension capacity. Cracking results from relatively small settlement values. Historic structures in particular are designed and constructed to allow primarily compressive stresses with very little, if any tensile stresses. Differential settlement disturbs the intended geometry of the structure which can lead to development of tensile stresses and simultaneous cracking. While minor cracking can result in aesthetic damage, if uncontrolled can lead to structural stability issues and eventual collapse.

In this study, eight probable foundation settlement configurations were simulated as shown in Fig. 51.13. These configurations may be considered exhaustive for this particular type of casemate foundation. The configurations include global settlement on the entire casemate as well as local settlement of piers and walls.

Fig. 51.12 Posterior distribution of input parameters (θ_1 is the elastic modulus of walls and piers, θ_2 is the elastic modulus vaults and θ_3 is the foundation spring stiffness)

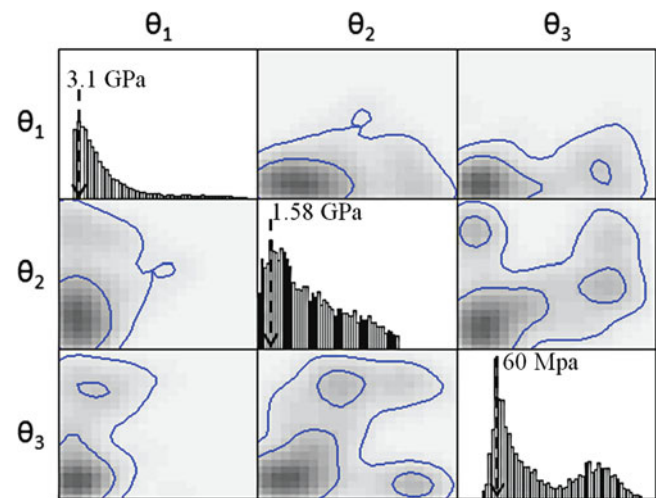
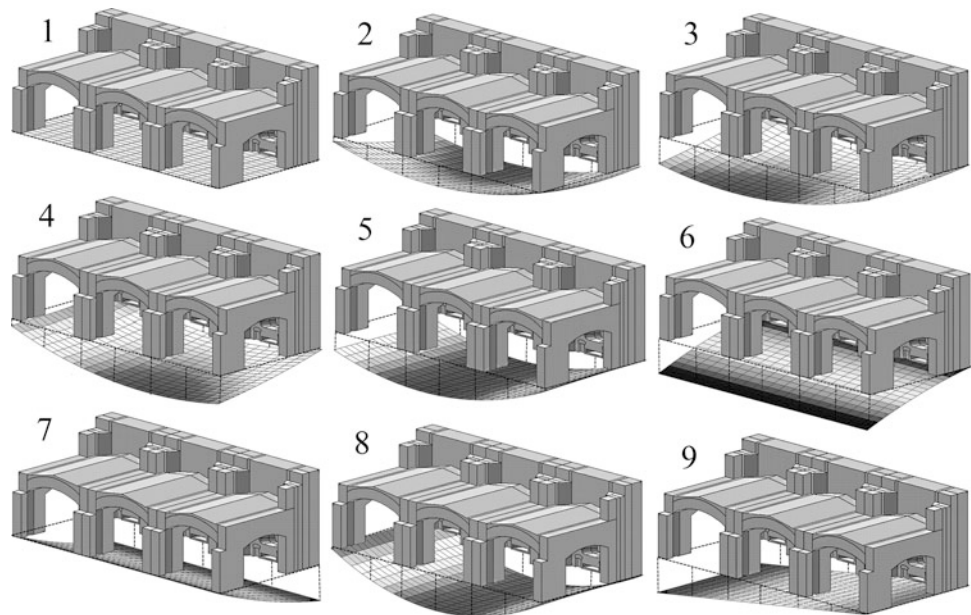


Fig. 51.13 Intact ground (1) and the eight settlement configurations (2–9) used for FE simulations



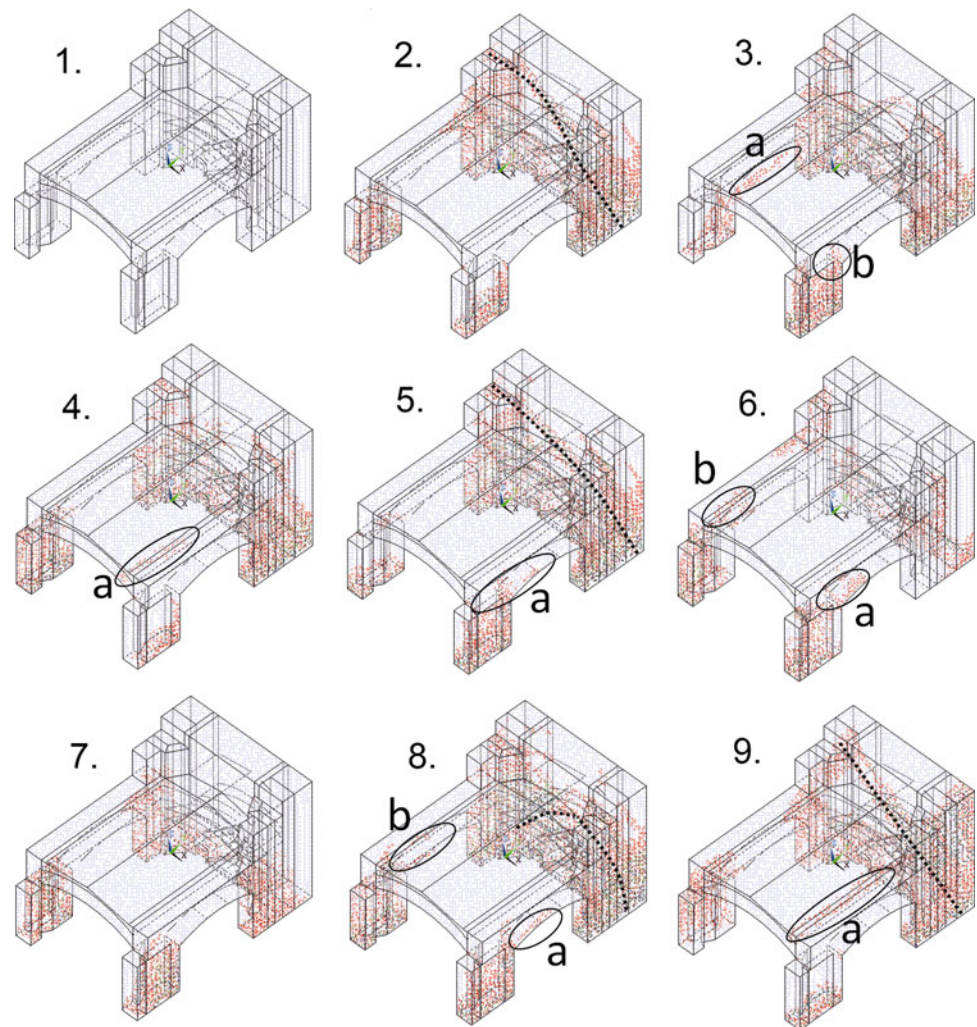
As discussed, the element used to develop the FE model has the capability to crack in tension. Each of the settlement configurations was simulated on the casemate up to 100 mm magnitude, with the subsequent cracking monitored for both initiation and progression. Figure 51.14 shows the crack plots for the different configurations followed by a discussion of the results.

Cracking initiated within the casemate at different magnitudes of settlement for different configurations and the pattern of these cracks differed for each configuration. No cracking was observed under intact ground conditions which is *Configuration 1*. The remaining configurations were classified as sagging, tilting and pier settlement.

51.6.1 Sagging Settlement

In *Configuration 2* unsymmetrical sagging occurs under the north side of the scarp wall. Substantial cracking of the scarp wall was observed while limited cracking on the vaults and piers was observed. At a settlement magnitude of 50 mm, a fully developed crack running diagonally across the scarp wall was observed (seen as dashed line in Fig. 51.14). *Configuration 5* simulated sagging of the north side of the casemate including the pier and scarp wall. It was found that the less settled side of the casemate incurred more damaged than the settled side. This behavior is expected of such settlement configurations.

Fig. 51.14 Crack distribution corresponding to a 100 mm settlement magnitude under the various configurations



Also a major diagonal crack was formed at 47.5 mm settlement in the scarp wall, which was similar to that observed in *Configuration 2*. Cracking at the springing of the south arch was observed at 55 mm (shown as *a*). Symmetrical sagging of the entire casemate was simulated in *Configuration 8*. Symmetrical cracking of the arches was observed (shown as *a* and *b*) and at 62.5 mm settlement, a major crack in the scarp wall converges at the center of the scarp wall forming a load bearing arch that carries the load of the masonry above (as shown by a *dashed line* in Fig. 51.14).

51.6.2 Settlement of Piers

Configuration 3 simulates settlement of the north pier while *configuration 4* simulates settlement of the south pier. Both configurations showed more or less mirrored crack patterns due to the near-symmetry of the casemate. It can be concluded from the crack patterns that when one pier settles more than the other, the cracking of the vault occurs on the less settled side, while the pier on the more settled side of the casemate is more heavily damaged. This observation was also expected in this configuration.

51.6.3 Tilting Settlements

Configuration 6 represents inwards tilting of the foundation while *configuration 7* represents outwards (seawards) tilting. *Configuration 6* resulted in cracking at the springing of the arches. *Configuration 7* caused relatively less damage compared

to configuration 6. This was due to the stiffness of the scarp wall that resists the thrust of the vault in *configuration 7*. *Configuration 9* represents tilting in the North longitudinal direction. Cracking patterns similar to configuration 5 were seen. However, sudden cracking of the vault was observed (indicated as *a*) at 85 mm settlement.

51.7 Conclusions

The finite element (FE) model of one of the casemates of Fort Sumter was developed making use of on-site data with material properties obtained from tests on both masonry block samples and core samples. The geometry of the casemate was replicated using high-speed and high-accuracy 3D laser scans. Since cracking is the main mode of failure in unreinforced masonry, the FE model had provisions for tensile cracking of the elements. A mesh refinement study was conducted to obtain an optimal mesh size for the FE model that strikes a balance between solution accuracy and computational costs. To further reduce computational effort, substructuring techniques were used to account for the effect of the adjacent structures. The semi-rigid boundary conditions at the base of the casemate were represented by vertical and horizontal linear springs.

Despite obtaining the actual material properties from the structure itself, there was still a large spatial variability in the properties. Also, the foundation condition was uncertain. In order to assign homogenized material properties to entire components and the foundation, a model calibration approach was employed where modal parameters from the numerical model were matched with experimentally obtained modal parameters by adjusting the linear model input parameters that were the elastic modulus of masonry and the foundation spring stiffness. The interface behavior at the dry joint between the scarp wall and the casemate vault and pier was represented using interface elements with a Mohr–Coulomb friction behavior. The idealized friction coefficient at the interface was obtained via calibration with dynamic tests at the interface.

The calibrated model was used to simulate eight probable settlement scenarios that include sagging, tilting and pier settlements. Sagging settlements caused diagonal cracking in the scarp wall. Cracking of the vaults was seen whenever differential settlement of the piers is observed. Cracking at the corners and intersection of components such as the springing of the arch was a common location for crack formation under most settlement configurations.

As a future extension to this study, the characteristics of the foundation will be investigated and the actual foundation will be modeled allowing for two way soil–structure interaction. Simulations of wave actions on the fort due to increased traffic in the Charleston harbor will also be investigated.

References

1. Ali S, Moore I, Page A (1987) Substructuring technique in nonlinear analysis of brick masonry subjected to concentrated load. *Comput Struct* 27(3):417–425
2. Arias P, Armesto J, Di-Capua D, González-Drigo R, Lorenzo H, Pérez-Gracia V (2007) Digital photogrammetry, GPR and computational analysis of structural damages in a mediaeval bridge. *Eng Fail Anal* 14(8):1444–1457
3. Armesto J, Roca-Pardiñas J, Lorenzo H, Arias P (2010) Modelling masonry arches shape using terrestrial laser scanning data and nonparametric methods. *Eng Struct* 32(2):607–15
4. Atamturktur S, Laman J (2012) Finite element model correlation and calibration of historic masonry monuments: review. *J Struct Design Tall Build Special Struct* 21(2):96–113
5. Brincker R, Zhang L, Andersen P (2001) Output-only modal analysis by frequency domain decomposition. *Proceedings of the international seminar on modal analysis, KU Leuven* 1998:717–724
6. Brosnan DA, Sanders JP, Hart SA (2011) Application of thermal analysis in preservation and restoration of historic masonry materials. *J Ther Anal Calorim* 106(1):109–115
7. Brown CB, Tilton JR, Laurent JM (1977) Beam-plate system on Winkler foundation. *J Eng Mech Div* 103(4):589–600
8. Clark TE (2006) *Falling to pieces: the preservation of ruins in coastal Georgia*. University of Georgia, Georgia
9. Craig RR, Bampton MCC (1968) Coupling of substructures for dynamic analyses. *AIAA J* 6(7):1313–1319
10. Craig RR (1995) Substructure methods in vibration. *J Mech Design* 117:207–213
11. Craig RR (2000) Coupling of substructures for dynamic analyses: an overview. In: 41st AIAA/ASMA/ASCE/AHS/ASC structures, structural dynamics and materials conference, AIAA, Reston, VA, 2000–1573
12. Cubel F, Mas A, Vercher J, Gil E (2012) Design and construction recommendations for brick enclosures with continuous air chamber. *Constr Build Mater* 36:151–164
13. Drosopoulos G, Stavroulakis G, Massalas C (2008) Influence of the geometry and the abutments movement on the collapse of stone arch bridges. *Constr Build Mater* 22(3):200–210
14. Dutta SC, Roy R (2002) A critical review on idealization and modeling for interaction among soil–foundation–structure system. *Comput Struct* 80(20):1579–1594
15. Gade S, Møller N, Herlufsen H, Konstantin-Hansen H (2005) Frequency domain techniques for operational modal analysis. In: *Proceedings 1st IOMAC conference, Copenhagen, April 26–27*

16. Hunter AF, Symonds CL (1991) A year on a monitor and the destruction of fort Sumter. University of South Carolina Press, Columbia, SC
17. Kennedy MC, O'Hagan A (2001) Bayesian calibration of computer models. *J Roy Stat Soc: Ser B Stat Method* 63(3):425–464
18. Kohnke P (1999) ANSYS theory reference. ANSYS, Houston, PA
19. Lourenço PB (2002) Computations on historic masonry structures. *Prog Struct Eng Mater* 4(3):301–319
20. National Park Service. Division of Publications (1984) Fort Sumter: anvil of war: Fort Sumter national monument. Government Printing Office, South Carolina
21. Queiroz F, Vellasco P, Nethercot D (2007) Finite element modelling of composite beams with full and partial shear connection. *J Constr Steel Res* 63(4):505–521
22. Ramos LF (2007) Damage identification on masonry structures based on vibration signatures. PhD Thesis, University of Minho, Portugal
23. Roache P (1994) Perspective: a method for uniform reporting of grid refinement studies. *Trans Am Soc Mech Eng J Fluids Eng* 116:405–405
24. Roca P (1997) Structural analysis of historical constructions: possibilities of numerical and experimental techniques. International center for numerical methods in engineering CIMNE, Barcelona, Spain
25. Schueremans L, Van Genechten B (2009) The use of 3D-laser scanning in assessing the safety of masonry vaults—a case study on the church of Saint-Jacobs. *Opt Lasers Eng* 47(3):329–335
26. Sohn H (2007) Effects of environmental and operational variability on structural health monitoring. *Phil Trans Roy Soc A: Math Phys Eng Sci* 365(1851):519–560
27. Tran DM (2009) Component mode synthesis methods using partial interface modes: application to tuned and mistuned structures with cyclic symmetry. *Comput Struct* 87(17):1141–1151
28. Willam K, Warnke E (1975) Constitutive model for the triaxial behavior of concrete. International association of bridge and structural engineers. Seminar on concrete structure subjected to triaxial stresses, Paper III-1, Bergamo
29. Winkler E (1992) Die Lehre Von Der Elasticitaet und Festigkeit. Prag, Dominicus

Chapter 52

Condition Assessment of a Coal Mine Shiploader

Carlos E. Ventura, Freddy Pina, Steve Yee, and Christopher Prychon

Abstract This paper describes the vibration tests and analyses conducted for the structural condition assessment of a shiploader structure in Colombia. This structure has been in continuous operation since the early 1980s and the owner of the facility is interested in assessing the current status of the structure. The purpose of the work conducted was to establish, through advanced structural engineering analyses, the capacity of the structure under different loading conditions. The analytical structural assessment was complemented with a visual assessment of the structure and field vibration tests. As the structure is a highly complex system and likely to behave nonlinearly, the need to calibrate the FE model for a linear condition of the structure was deemed necessary. The results of a series of OMA tests were used to update a detailed FE model of this complex structure. Once the model was updated, a number of analyses were conducted to determine the performance of the structure under different loading configurations and to identify critical areas of the structure where maintenance should be conducted regularly.

Keywords Condition assessment • Finite element • Ambient vibration • Dynamic response • Shiploader

52.1 Background

The Cerrejón shiploader (shown in Fig. 52.1) is one of the world's largest ship loaders. The shiploader was built in the early 1980s to serve the nearby Cerrejón open-pit coal mine in Colombia. The structure was designed to move 15 million metric tons of coal per year. Modifications have been made over the years, altering the conveyance system by building a surge tank, improving the stockpiling system and improving the train system to increase the coal production to 32 million metric tons per year. No major modifications have been made to the ship loading structure other than general maintenance.

The loader consists of three main structural systems: bridge, booms and shuttle. The bridge is a steel truss system of two large beams running parallel connected by a series of truss members by diagonal and chevron bracing. The booms are three steel truss systems of two main beams running parallel connected by chevron bracing, with each boom pin connected. The shuttle is a steel truss system designed to lift the front boom spans with a combination of a counterweight and hydraulic cylinders. The loader is supported by two supports or turntables; one support is stationary on a concrete pad supported by hollow steel piles; the other support is free to move linearly along a steel truss runway supported by hollow steel piles. Other important aspects around the loader are the front and rear turntables, the runway, the breasting dolphins, the mooring dolphins, the walkways and the conveyor belt system.

The bridge span is 128 m in length. As shown in Fig. 52.2, the bridge span consists of two main steel girders that vary in both height and width along its length. The two girders are connected with steel diagonals in the vertical plane and chevron bracing in two horizontal planes (top and bottom of beams). It is supported in two places by supports located between 65 m

C.E. Ventura (✉)

Department of Civil Engineering, The University of British Columbia, 6250 Applied Science Lane, Vancouver, BC V6T 1Z4, Canada
e-mail: ventura@civil.ubc.ca

F. Pina

PBRV Consulting Ltd., 1003-1077 Marinaside Crs., Vancouver, BC V6Z 2Z5, Canada

S. Yee • C. Prychon

CWA Engineers Inc., #380-2925 Virtual Way, Vancouver, BC V5M 4X5, Canada

Fig. 52.1 General view of the Cerrejon shiploader



Fig. 52.2 Main components of shiploader

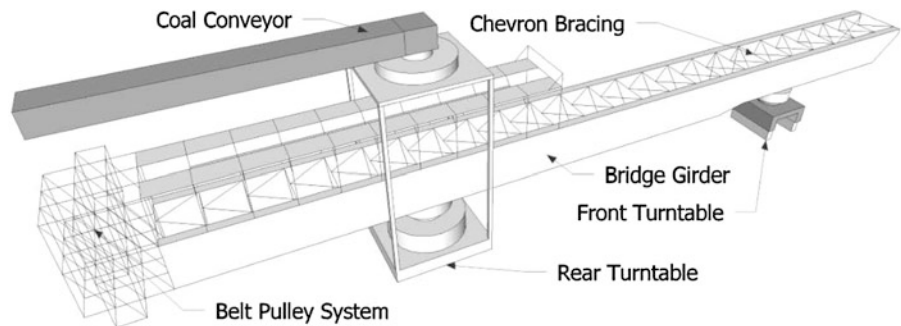
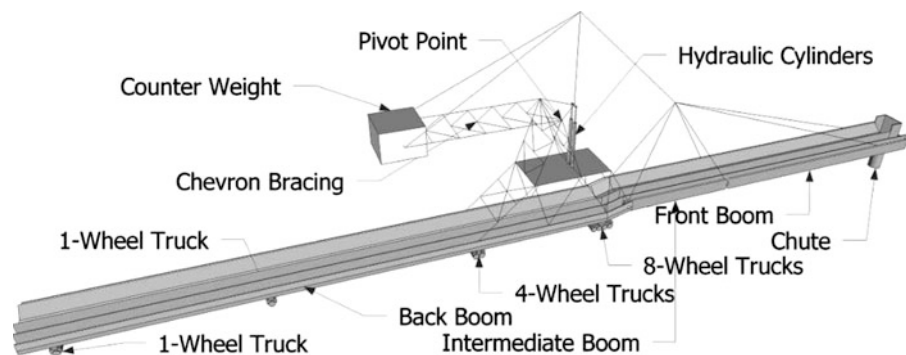


Fig. 52.3 Details of shiploader structural components



apart at the minimum bridge span and 90.7 m apart at the maximum bridge span. The supports are known as turntables because of the swiveling capabilities of the supports. The rear turntable stays stationary (fixed to the ground) but allows the bridge to roll along its top to extend the span; it also allows the bridge to pivot about 44° in each direction off its central position. The front turntable is free to move in one linear direction along the runway for 63.2 m in each direction; it also allows the bridge span to rotate freely above it.

The boom system, shown in Fig. 52.3, has a total length of about 116 m. The boom system is comprised of three boom sections connected by pivot points allowing vertical rotation of the intermediate and front booms (sections closest to the ships) for up to 12° both above and below horizontal during operating conditions. Each boom is designed with two beams running parallel connected with a single horizontal plane of chevron bracing. The back boom (section farthest from the ships) is 67.75 m long and is supported by four sets of trucks that run along a rail. This rail runs along the length of the bridge span. The linear movement along the rail allows the ship loader to increase its range of loading by 29.5 m. The intermediate boom has a length of 16 m between the centerlines of the pin connections. Both of the pin connections at either end of the intermediate boom are connected to the shuttle frame via cables. The front boom has a length of about 32 m with the centerline of the discharge chute located over 2 m from the loading end. A cable is strung from the shuttle frame to the front boom over 6 m from the loading end.

The shuttle is a truss system designed to rotate the front and intermediate boom sections. The truss system is composed of steel W-sections. A truss member branches out from the top point of the shuttle towards the front of the loader and is attached to the intermediate and front boom sections by cables connected to the end of the branched truss member. A hinge is located

at about mid-location of the truss allowing vertical rotation. Two hydraulic cylinders are used in the lifting process of the booms, rotating the shuttle about the hinge. A counterweight located to the back of the hinge helps the hydraulic cylinders to lift the booms. The runway is a rectangular dock with a set of rails to allow linear movement of the front turntable. The breasting dolphins allow the ship to rest against them during loading. The mooring dolphins are used to secure the ship to the dock during loading through cable or rope attachments. Walkways allow access to areas around the loader. The conveyor belt system runs coal from the stockpiles or train-unloading hopper to the loader.

52.2 Objectives

The owner of the facility required information regarding the condition of the shiploader in order to make decisions with respect to its structural capacity. There were concerns about the durability of the steel in the structure due to fatigue and the structural response during a seismic event. The loader has surpassed its design life and transports more coal than the original design specified. In response to these needs, a detailed finite element model of the shiploader was developed to assess the performance of this model under prescribed loading conditions. CWA Engineers were able to use the results of the model to estimate the remaining fatigue life of the shiploader's structural members.

The main objective of this project was to establish through advanced structural engineering analyses the capacity of the shiploader to withstand severe loading conditions and to generate information that could be used to: (1) estimate the mechanical and fatigue life remaining for the machine, and (2) propose general recommendations for structural upgrades to ensure the continued safety of the ship loader, support structures and ship loading operations. The computer structural assessment was to be complemented with a visual assessment of the structure and surrounding environments.

52.3 Field Vibration Tests

Triaxial accelerometers were placed at more than 40 points throughout the structure in order to measure vibrations of the shiploader due to ambient vibration loads. The information collected was used to determine dominant frequencies at each of the measured points as well as to determine the significant modes of vibration of the beam and the boom structures. Figures 52.4 and 52.5 illustrate the type of data collected at selected points of the bridge, boom, top of shuttle and runway. In each of the following figures the following information is presented:

- (1) A sample of the acceleration recorded at each point in each of the three principal directions (Transv. = measurement in the transverse direction of the shiploader; Long. = measurement along the longitudinal direction of the shiploader; and Vert. = measurement in the vertical direction of the shiploader).
- (2) The corresponding computed velocity of the acceleration record obtained at the selected location.
- (3) The Power Spectrum (PS) of the acceleration record, plotted as a function of frequency in the range of 0.05 to 20 Hz.
- (4) The Energy Spectrum (ES) for 5% damping of the acceleration record, plotted as a function of period in the range of 0.05–20 seconds.

The peaks in the PS and ES plots give an indication of the dominant frequencies (or periods) at each measured location. Further analysis of the data was used to identify which of these peaks correspond to natural modes of the structure, and this information was then used to calibrate the FE model developed in SAP2000. A summary of the dominant frequencies (in Hz) for each subassembly is presented in Table 52.1.

Table 52.1 Dominant frequencies (in Hz) obtained from vibration tests

Main girder			Boom			Shuttle			Runway		
X	Y	Z	X	Y	Z	X	Y	Z	X	Y	Z
0.429	0.441	0.418	0.726	0.484	0.748	0.689	1.206	0.574	0.551	0.484	0.481
1.210	1.618	1.364	1.706	1.639	1.673	1.637	2.786	1.723	1.651		
3.532	3.598	1.617	2.850	1.958	2.806	2.671	3.647		2.051		
		3.571	4.897	2.828	3.829	3.213			3.370		
			5.601	5.062	5.084				9.00		

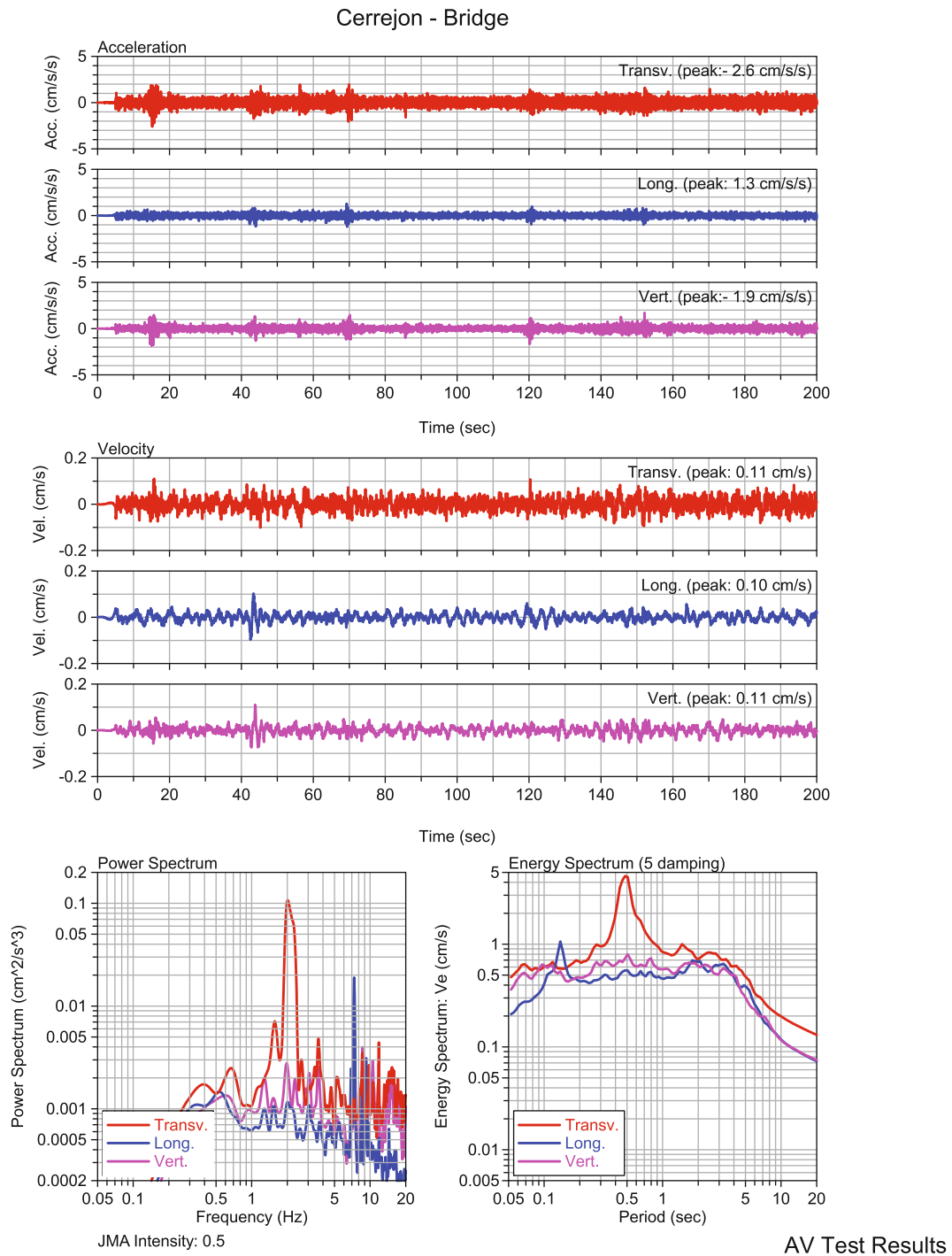


Fig. 52.4 Sample of results from vibration tests conducted on the Bridge

52.4 Computer Model

Cerrejon provided a set of structural drawings of the structure, documents related to the original structural design and geotechnical investigations conducted at the site. Based on Cerrejon information, a computer model of the structure was built using the commercially available finite element analysis (FEA) program SAP2000 Ver. 14. This model (and a few variations of it) was used to perform a capacity assessment of all the structural members of the structure under different prescribed loading conditions. An overview of the base FE model of the shiploader is presented in Fig. 52.6.

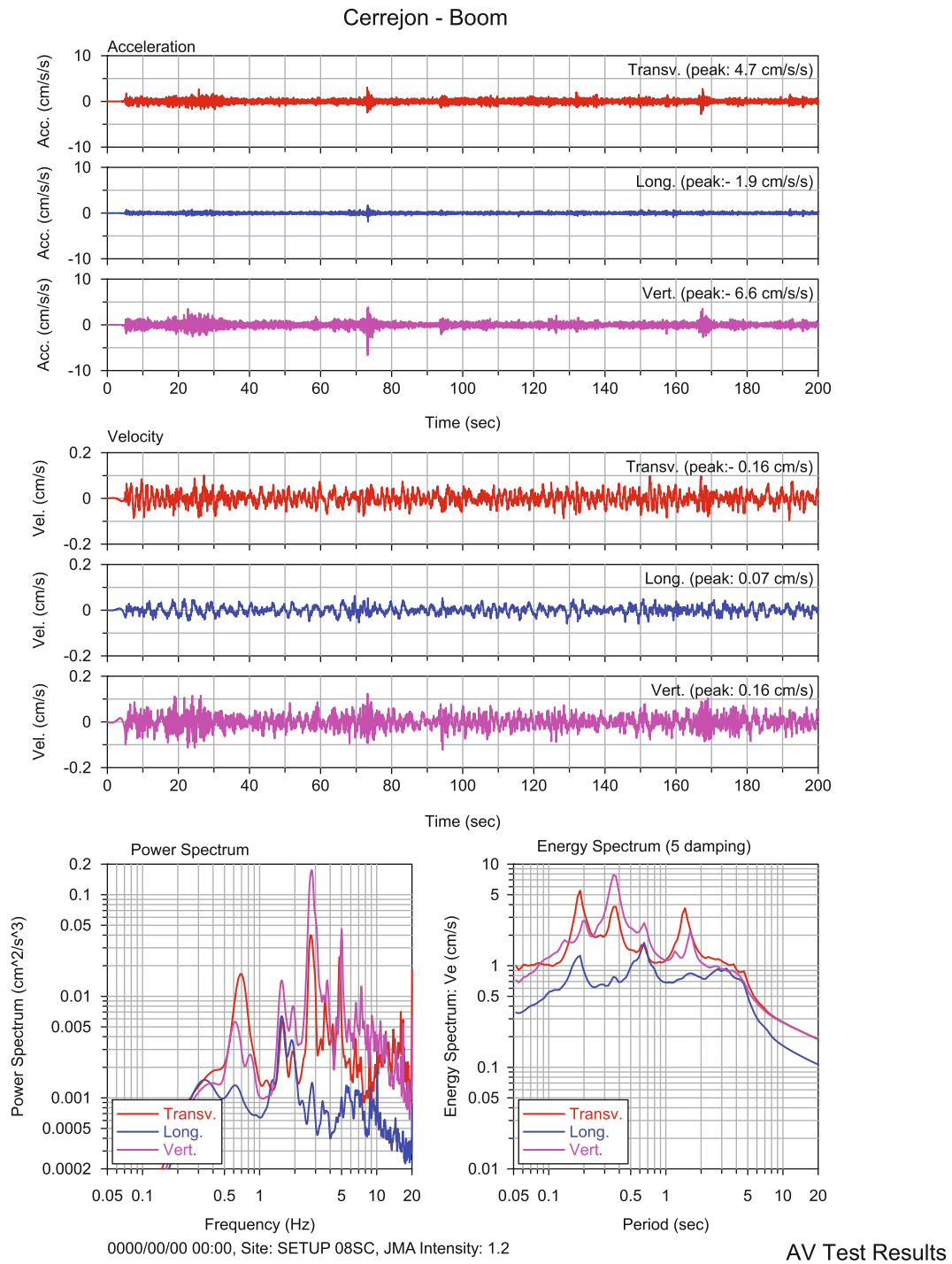


Fig. 52.5 Sample of results from vibration tests conducted on the Boom

The structural steels used for the construction of the shiploader were G40.21-M Grade 350W for all HSS members and G40.21-M Grade 300 W for all other elements. The model of the shiploader was built using types A992Fy50 and A992Fy44, respectively.

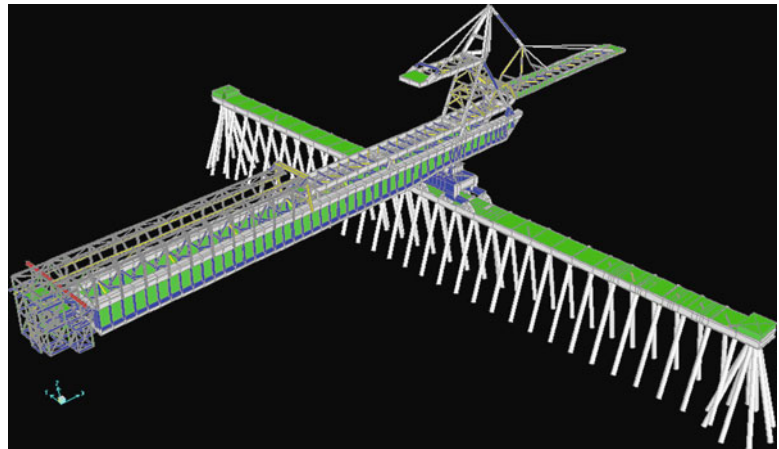
The steel properties used for the model are as follows:

Yield strength, f_y : A992Fy50 = 350 MPa and A992Fy44 = 300 MPa

Tensile strength, f_u : A992Fy50 = 450 MPa and A992Fy44 = 450 MPa

Young's Modulus, $E = 200$ GPa and Poisson's Ratio, $\gamma = 0.260$

Fig. 52.6 Overview of FE model of the shiploader



In order to obtain a reliable FE model of the shiploader, the SAP2000 model was calibrated to closely match the results of field vibration tests conducted in late October 2011. The natural frequencies and corresponding modes of vibration of the structure were obtained from ambient vibration tests and these were used to calibrate the FEA before conducting the actual load case studies. The following sections provide information and details about the various analyses conducted using the SAP2000 model of the shiploader and a discussion of the most relevant results.

52.5 Modeling Assumptions and Simplifications

The SAP2000 model is an approximate representation of the actual structure. An effort was made to include all the important structural elements in the model. Secondary elements that were considered to have a minor influence on the overall structural behavior were not explicitly modeled. The model was developed to capture the static linear behavior of the structure under service loads, and the dynamic linear behavior under seismic loads. The following is a summary of assumptions and simplifications adopted in the modeling process:

- (1) Masses and weights were distributed in the structure using shell elements connected to frame element ends. Engines, pulleys, belts, machinery, electrical rooms were not modeled as part of the structure stiffness but considered only as weights.
- (2) Connections between frame elements were considered to be infinitely rigid;
- (3) Offset in frame elements were considered in cases where the thickness or insertion of the element in the connection was relevant (e.g. piles in runway deck, frame elements in strong moment connections)
- (4) Material properties and element cross sections were created/modeled using the information shown in the drawings, i.e.: the model represents the ideal as-built condition only;
- (5) The back support was considered fixed in translation but with free rotation in the three axes;
- (6) Pile supports were considered to be fixed for the six degrees of freedom;

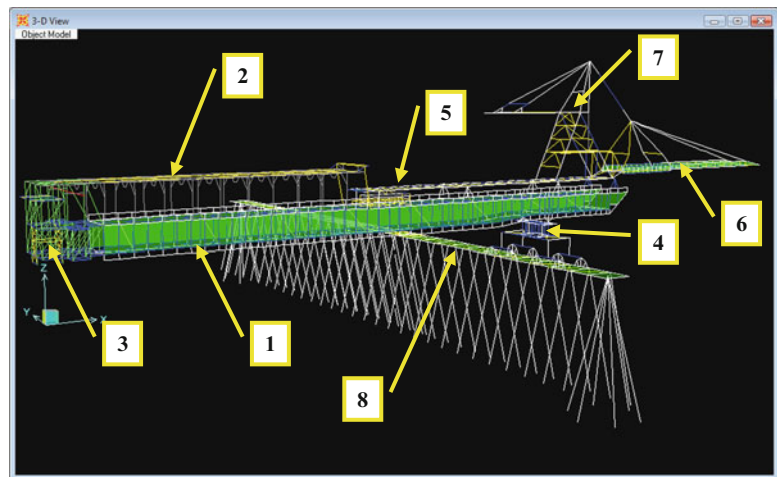
The three dimensional model developed with SAP2000 includes the following eight subassemblies shown in Fig. 52.7: (1) Main girder; (2) Conveyor; (3) Take-up; (4) Front support; (5) Shuttle base; (6) Boom; (7) Shuttle; and (8) Runway.

52.6 Loads

Seismic loads were computed as per the current edition of the Colombian seismic design code. The SAP2000 computer program automatically calculates the self-weight of the structural members. In addition to the self-weight, ramp loads were incorporated into the computer model to simulate the shuttling and traversing movement of the shiploader. Maximum speed for shuttling and traversing movement were provided by CWA. Ramp accelerations were calculated based on the given speed values in a period range of 5 sec as follows:

- (1) For the shuttle—RAMPSH:
 - a. maximum speed of 0.185 m/s (10 meters in 52 s)

Fig. 52.7 Subassemblies of FE model of the shiploader



b. The calculated acceleration is 0.038 m/s^2 . The total weight of the shuttle is approximately 10 MN which is mainly lumped in the counterweight and the boom. The ramp acceleration was represented with lateral forces acting in the counterweight and the boom as point loads. The lateral load was assigned proportionately to the counterweight and boom masses as 100 kN and 80 kN, respectively.

(2) For traverse motion—RAMPBR:

- a. maximum speed of 0.263 m/s (10 meters in 38 s)
- b. The calculated acceleration is 0.052 m/s^2 . The total weight of the girder plus the shuttle is approximately 12 MN which is mainly lumped in the counterweight, the boom and the girder front bearing support. The ramp acceleration was represented with lateral forces acting in the counterweight, the boom and the girder base as point loads. The vertical reaction of the girder is approximately 12000 kN. The lateral load was assigned proportionately to the counterweight, the boom and the girder base as 100 kN, 80 kN and 30 kN, respectively.

52.7 Load Combinations

The structural response was checked at two levels: (1) *Serviceability*, using an acceleration/deceleration condition of shuttle and the main girder, and (2) *Limit State*, using the seismic load as per Colombian current design code.

52.8 Modal Analysis

Results of the modal analysis are shown in the (Fig. 52.8) screen shots for the four first global modes of vibration of the complete structure.

The field vibration tests conducted were used to determine the dominant modes of vibration of the shiploader in “at-rest” position. In the field tests conducted in October 2011, the shiploader was not in normal operation and was positioned in the middle of the runway. The boom was retracted and the conveyor belts were empty. The field data was used to determine periods and a few mode shapes of the main girder, boom and shuttle of the “at-rest” position of the structure. The loads and arrangement of the model geometry were modified to correspond to the field testing conditions, and then the model was calibrated to match the dynamic properties obtained from the field tests.

An additional model was created that includes the runways and piles at the front support of the structure. Results from this model were shared with a team of geotechnical engineers to conduct a condition assessment of the runway and its supporting piles.

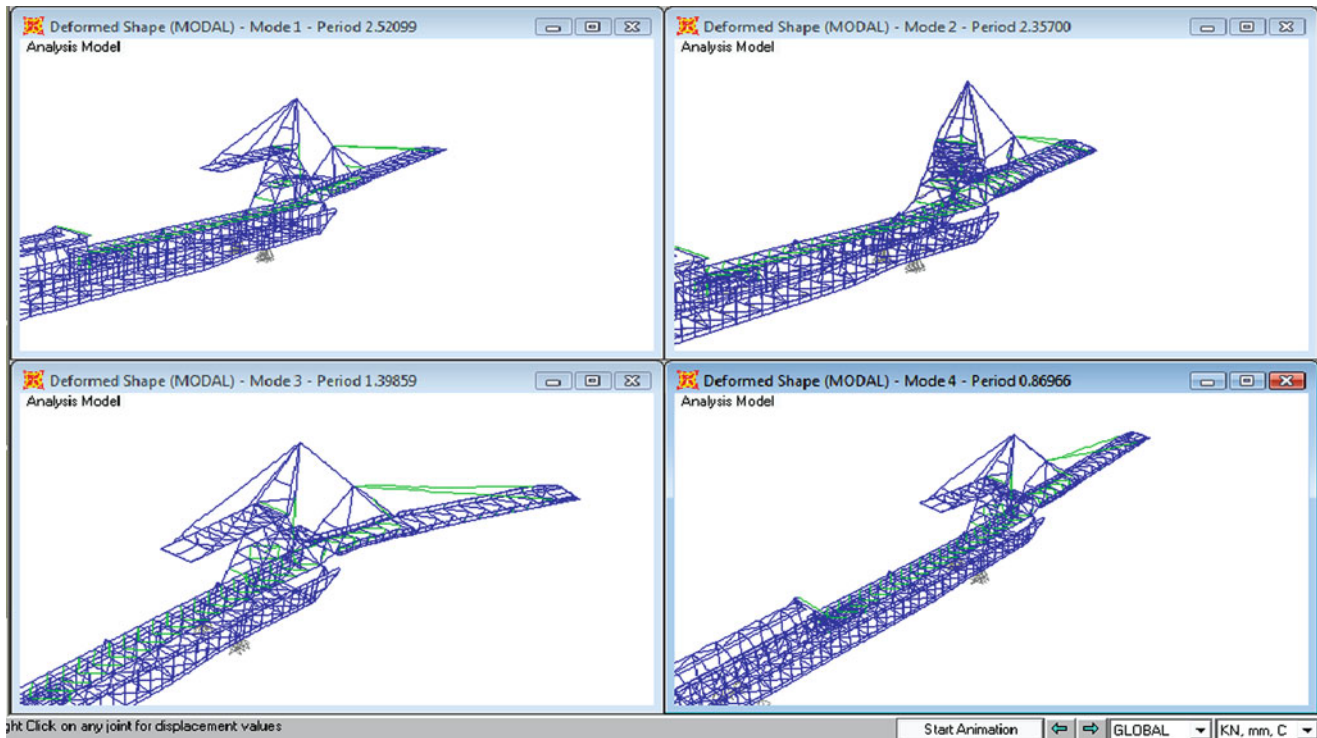


Fig. 52.8 First four modes of vibration of the shiploader

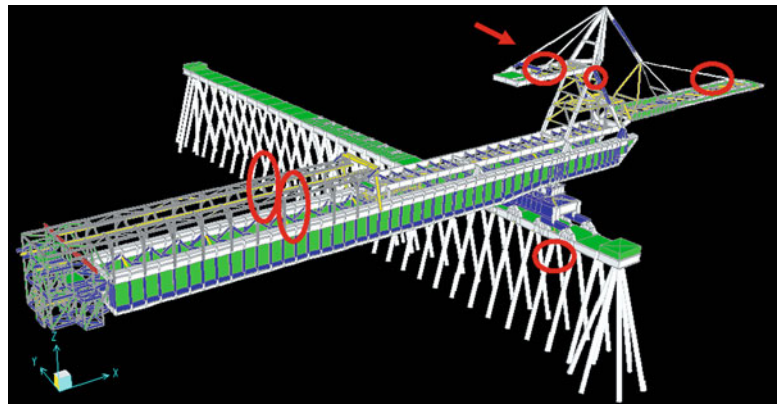
52.9 Design Checks

The Design Check for the serviceability and limit-state levels were performed using SAP2000 built-in code procedures API RP2A WSD-2000 and AISC LRFD-99, respectively. For each of the load combinations, the capacity, C , of each element was checked against the stresses generated by the maximum forces and moments obtained from the structural analyses (also referred as the Demand).

52.10 Time History Analyses

It is well recognized that one of the limitations of the Response Spectrum Analysis is that in the process of computing the modal combinations, the amplitude of the loads (shears, moments and axial loads) and associated stresses is reasonably estimated, but the sign or direction of the load/stress is lost. As a consequence, it is not possible, for instance, to determine if a pile is in tension or compression when the seismic load is to be superimposed to other loads, like dead and live loads. In order to overcome this limitation when estimating the loads and stresses on the piles supporting the runway, a time history analysis was conducted in order to get a sense of the nature of the loads/stresses acting on the piles. A recorded ground motion from an historical earthquake was scaled to match the design spectrum for the region, and this scaled ground motion was used to conduct the time history analysis using SAP2000. There is a number of existing techniques for selecting and scaling ground motions that match a prescribed design spectrum, but the analysis conducted here was of a very simple nature with the purpose of obtaining more information about the nature of the seismic loads. Only one time history was used and the only results that were extracted from the analysis were the nature of the axial loads acting on the piles.

Fig. 52.9 Critical elements of shiploader



52.11 Results

As per results from the SAP2000 analysis in the two levels of performance, serviceability and limit-state (code-based), it is clear that there are some members that will require further assessment to verify their actual capacity to the load cases adopted in this study. Those members are located at the base and counterweight sector of the crane (shuttle), at the conveyor and at the run-way right below the girder (see Fig. 52.9).

52.12 Summary and Conclusions

The purpose of this project was to establish, through advanced structural engineering analyses using a state-of-the-art computer analysis program, the capacity of the shiploader structure to withstand a number of prescribed loading conditions, and to determine its capacity to sustain levels of earthquake shaking in accordance with the seismic design provisions in Colombia. The computer structural assessment was complemented with a visual assessment of the structure.

The results from this investigation helped identify which elements require further attention in order to determine with confidence if the probability of collapse or serious damage to these elements is significant. Results from these analyses only give a reasonable estimate of the demand in those elements and how they compare with nominal capacities in the serviceability and limit-state levels, respectively.

Key results:

- The shiploader performs adequately under the Colombian Design Code 1/475 year return period earthquake.
- The results from this investigation can be used to determine the capacity of the piled supporting structures to perform under the Colombian Design Code 1/475 year return period earthquake.
- The results from this investigation can be used to identify key areas and individual components of the shiploader subjected to fatigue stresses, and to estimate of operational life remaining in the shiploader given its current fatigue loading state. This information, in turn, can be used to establish a periodic NDT program to monitor the behavior of the structure.
- The results of the FEA show which components of the shiploader are more sensitive to the various loading conditions. This information can be used to determine if these elements need to be retrofitted or replaced to extend the operational life of the shiploader from a fatigue loading perspective.

Acknowledgements UBC students Aiden Wong, Davin Lewis, Niall McPherson and Steven McDonald collaborated in the preparation of this report by providing some of the figures and providing the material for the sections describing the structure.

Chapter 53

Experimental Assessment of Structure Borne Noise Generated by a Braking Resistor

F. Braghin, F. Cheli, and G. Galli

Abstract This paper presents an application of modal analysis to the assessment of the structure borne noise level for a braking resistor to be mounted on the floor of a train carbody. This topic is becoming more and more important since the dynamic behavior of auxiliary components attached under the carbody strongly affects the passengers' comfort. In particular, a braking resistor contains one or more fans used to cool the electrical resistances that dissipate the braking energy by Joule effect. The rotation of these fans can represent a relevant source of vibrations even in presence of low eccentricity.

In order to assess the transmitted vibrations before the real carbody has been built and to optimize the supporting elements of the braking resistor, an auxiliary fixture has been designed to reproduce the carbody mechanical impedance at the mounting point of the braking resistor. Thus, the first step is to design the fixture to have the same mechanical impedance of the carbody under construction (through finite element analysis); then, to measure its mechanical impedance along all three directions through impulsive tests and finally to assess the braking resistor's behavior when mounted on the fixture and operated as during real life conditions.

Keywords Structural dynamics • Modal analysis • Mobility • Structure borne noise • Braking resistor

53.1 Introduction

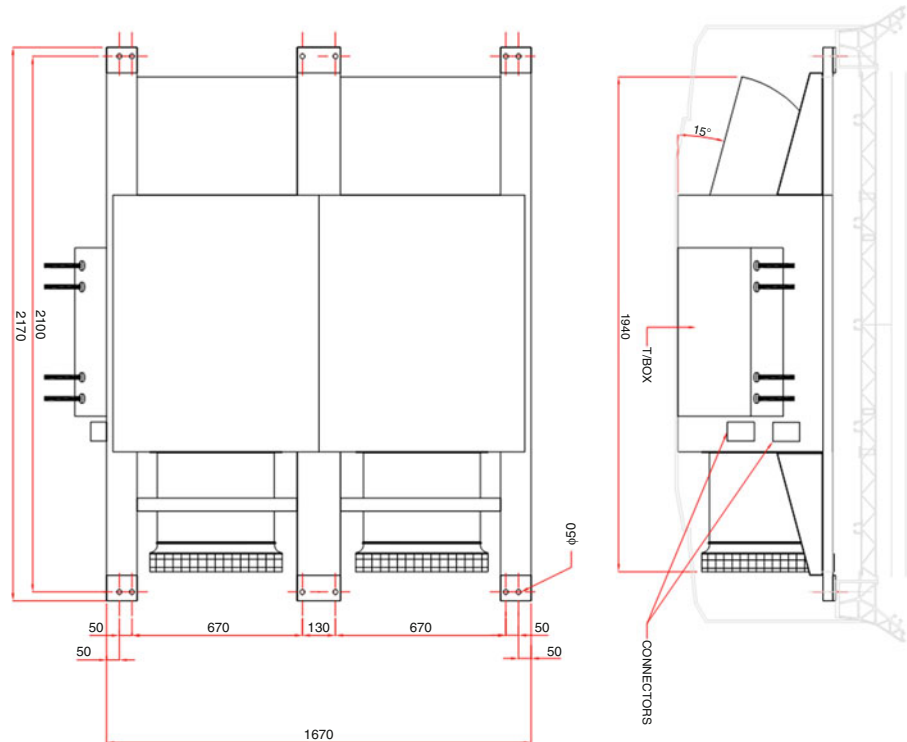
Braking resistors are fundamental components of railway vehicles: when the speed of an inverter-controlled AC motor is reduced, the motor acts as a generator, feeding back energy to the frequency converter. As a result, voltage in the intermediate circuit of the inverter increases. When a specific threshold is exceeded, the energy must flow to an external braking system in order to avoid drive failures. Braking resistors are designed to absorb such energy and to dissipate it into heating. The use of brake resistors allows drives to fulfill the requirements of particularly severe duty cycles, for example those featured by frequent braking, long lasting braking or impulsive braking.

Due to the conversion of electrical energy into heat, braking resistors are usually ventilated. The coupling of the rotating speed of the cooling fan with some of the eigenfrequencies of the braking resistor may generate vibrations and noise. For this purpose, suppliers are requested to certificate their braking resistors from the transmitted vibration and noise point of view [1].

The first problem to solve for producing such certificates is that, usually, the train on which the braking resistor has to be mounted is in its design phase and no prototype is available. Thus, a supporting structure has to be used for certification purposes having the same mechanical mobility/impedance of the final installation. In the present paper, the characterization of the supporting structure (fixture) is presented as well as the structure born noise tests of the considered braking resistor.

F. Braghin (✉) • F. Cheli • G. Galli
Department of Mechanics, Politecnico di Milano, Via La Masa 1, 20156 Milano, Italy
e-mail: francesco.braghin@polimi.it; federico.cheli@polimit.it; giancarlo.galli@polimit.it

Fig. 53.1 Test rig for the braking resistor



53.2 Tested Structure

The considered braking resistor consists of:

- resistor banks/elements (active part),
- cooling fan,
- resistor enclosure.

As can be seen in Fig. 53.1, all these parts are fixed to a frame made of two beams of stainless steel linked by two crossbars. The resistor enclosure is 2 mm thick in stainless steel and presents two openings on the lateral sides for intaking and the exhausting cooling air. In particular the intake conduct presents a protruding structure making the braking resistor asymmetric. Rivets joint all the components.

53.3 Experimental Tests and Set-up

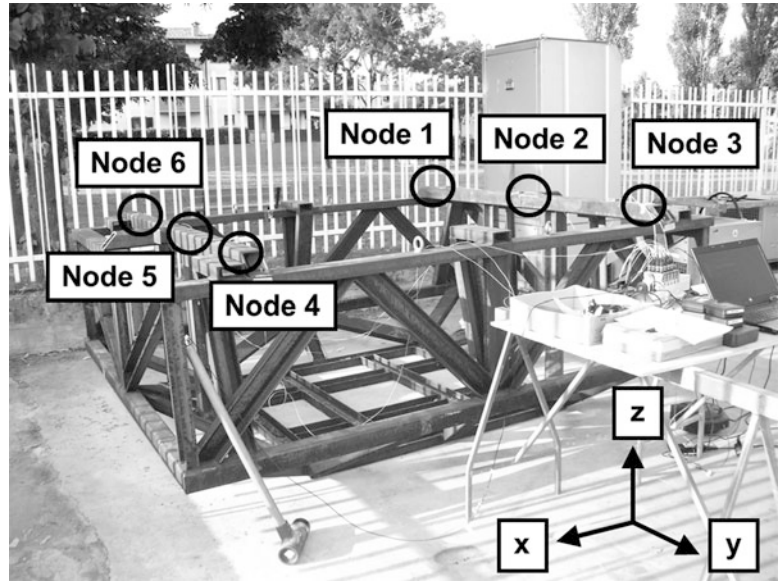
The direct mechanical impedance test rig, shown in Fig. 53.2, for the braking resistor has been assessed through impulsive tests. In Fig. 53.2 the six mounting points of the braking resistor are evidenced through circles as well as the reference axis for the impulsive excitation.

At each of the six mounting points, a three-axial piezo-accelerometer has been placed oriented according to the reference axis shown above. The adopted accelerometers are three PCB 356A02 accelerometers (placed at mounting points 1, 2 and 3), two PCB HT356A34 accelerometers (placed at mounting points 4 and 5) and one PCB HT356B21/NC accelerometer (placed at mounting point 6).

A dynamometric hammer PCB 086D50 equipped with a hard plastic tip (084A32) has been used for the impulsive tests. The impact has been applied as close as possible to the mounting point (where the accelerometers were placed).

Impacts were repeated at least 10 times to be able to filter out random noise and acquired through NI CompactDAQ chassis equipped with five NI9234 24bit simultaneous sampling IEPE modules that include anti-aliasing filters. The sampling frequency was set equal to 10 kHz.

Fig. 53.2 Test rig for the braking resistor



53.4 Mechanical Impedance of the Fixture

The acquired signals are triggered using the force as a trigger signal, a pre-trigger of 0.5 s and a window length of 4 s, in order to avoid leakage and then the direct mechanical impedance of the test rig at each mounting point and along each direction in one-third octave bands has been evaluated according to formula:

$$Z_{j,k}^R(\omega) = \frac{1}{n_p} \sum_{p=1}^{n_p} \frac{S_{v_{j,k}-f_{j,k,p}}(\omega)}{S_{v_{j,k}-v_{j,k,p}}(\omega)} = \frac{1}{n_p} \sum_{p=1}^{n_p} i\omega \frac{S_{a_{j,k}-f_{j,k,p}}(\omega)}{S_{a_{j,k}-a_{j,k,p}}(\omega)} \quad (53.1)$$

Being j the point of application of the force, k the direction of excitation and of measurement, $f_{j,k}$ the impulsive force applied at point j along direction k , $v_{j,k}$ the velocity at point j along direction k , $a_{j,k}$ the measured acceleration at point j along direction k , n_p the number of impacts, $S_{v_{j,k}-f_{j,k,p}}$ the cross-spectral density function between $v_{j,k}$ and $f_{j,k}$ for impact p , $S_{v_{j,k}-v_{j,k,p}}$ the autospectral density function of $v_{j,k}$ for impact p , $S_{a_{j,k}-f_{j,k,p}}$ the cross-spectral density function between $a_{j,k}$ and $f_{j,k}$ for impact p and $S_{a_{j,k}-a_{j,k,p}}$ the autospectral density function of $a_{j,k}$ for impact p . Note that the evaluated mechanical impedance $S_{v_{j,k}-f_{j,k,p}}(\omega) / S_{v_{j,k}-v_{j,k,p}}(\omega)$, is used in case of uncorrelated input and output noise as in the considered case.

As an example, Fig. 53.3 shows the mechanical impedance of the fixture at node 6 along direction x as well as the corresponding coherence function. It can be seen that the coherence function tends to drop at frequencies higher than 500 Hz due to the adopted hammer tip.

53.5 Modal Analysis of the Braking Resistor

A modal analysis of the braking resistor has been performed in order to understand if the peak of constraint forces at working condition is due to a resonant mode with the rotational frequency of the fan.

The structure has been forced along the vertical axis through impulsive excitations with the dynamometric hammer PCB 086D50 and the dynamic response has been measured with several mono-axial piezo-accelerometer.

Measures have been processed according to the following steps [2]:

- computation of the spectra applying the FFT algorithm,
- calculation of auto-spectra and cross-spectra averaging 20 tests,
- estimation of the coherence functions and the frequency response functions with the H_3 estimator.

An example of the results of signal processing is shown in Fig. 53.4.

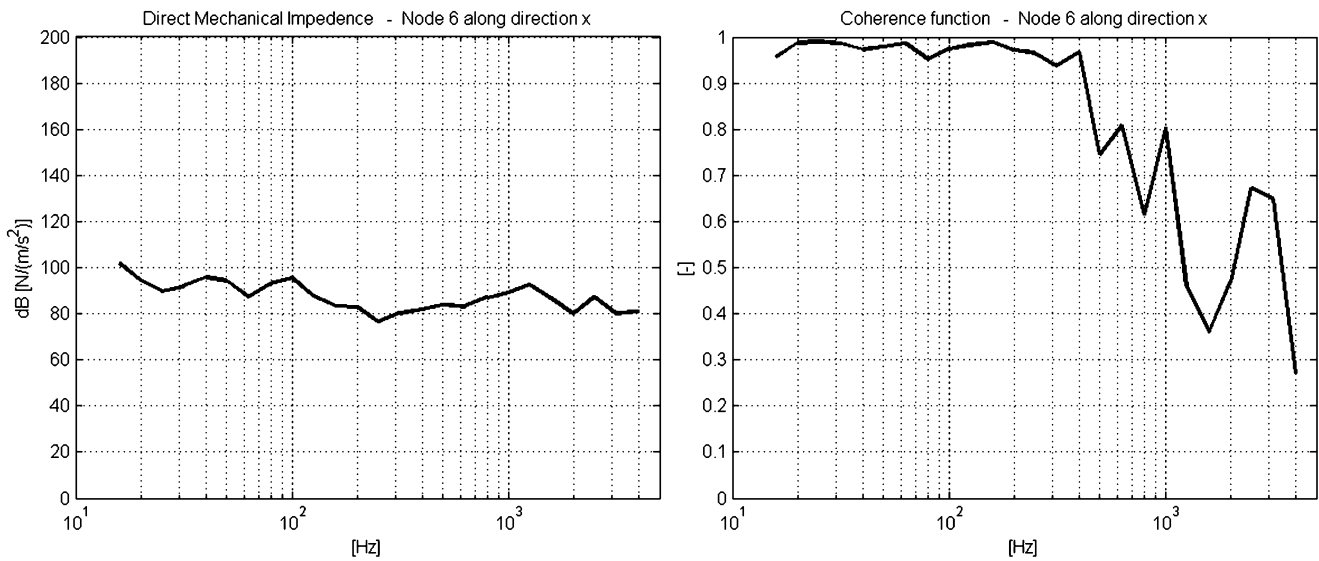
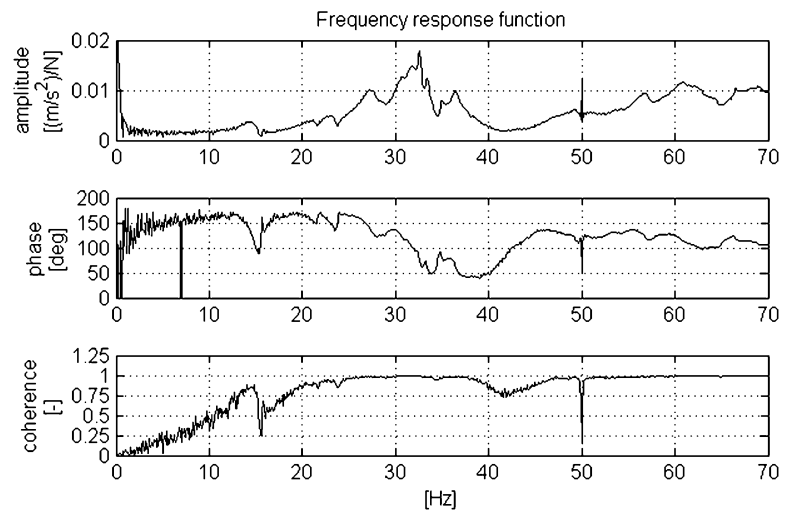


Fig. 53.3 Mechanical impedance of the fixture at node 6 along direction x as well as the corresponding coherence function

Fig. 53.4 Frequency response function: amplitude (*top*), phase (*middle*) and coherence (*bottom*)



The coherence function presents low values in a frequency band below 20 Hz and at 50 Hz. The first case can be explained by the fact that impulsive tests are not suitable to excite low frequencies while the second one is related to the noise coming from the electrical network.

In order to assess the modal parameters of the braking resistor, the classical frequency response function of a forced MDOF system has been considered [3] as a numerical model

$$H_{num}(\Omega) = \sum_{j=1}^N \frac{-\Omega^2 A_j}{-\Omega^2 + i 2h_j \omega_j \Omega + \omega_j^2} \tag{53.2}$$

where N is the number of considered modes, A_j is the complex modal parameter, h_j is the viscous damping factor, ω_j is the natural frequency and i is the imaginary unit.

The identification process has been performed minimizing an objective function J that is composed by the sum of square errors between the numerical and experimental frequency response functions in the frequency range between 10 and 65 Hz. In order to take into account that the measures reliability is not constant, the square errors are weighted with the experimental coherence.

Fig. 53.5 Comparison of experimental (*continuous line*) and numerical (*dots*) frequency response functions in terms of amplitude (*top*) and phase (*bottom*)

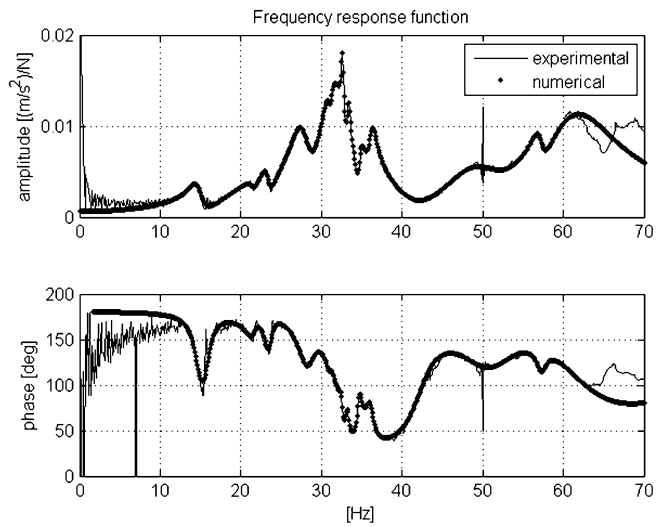
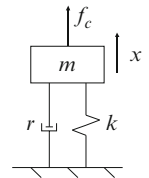


Table 53.1 Modal parameters of the identified modes

Mode	f (Hz)	h
1	14.66	0.057
2	21.42	0.041
3	23.27	0.027
4	27.83	0.048
5	31.11	0.010
6	31.42	0.053
7	32.61	0.005
8	33.31	0.006
9	34.76	0.012
10	36.22	0.015
11	49.28	0.084
12	57.18	0.014
13	61.18	0.083

Fig. 53.6 Simple single DOF system



Therefore the expression of the objective function J is

$$J = \sum_{f_j \in [10;65]Hz} C(f_j) |H(f_j) - H_{num}(f_j)|^2 \tag{53.3}$$

where $\Omega_j = 2\pi f_j$.

The Gauss–Newton algorithm [4] has been adopted for the nonlinear minimization. Figure 53.5 shows the comparison of the experimental and numerical frequency response functions considering 13 modes.

The main modal parameters of each mode are summarized in Table 53.1.

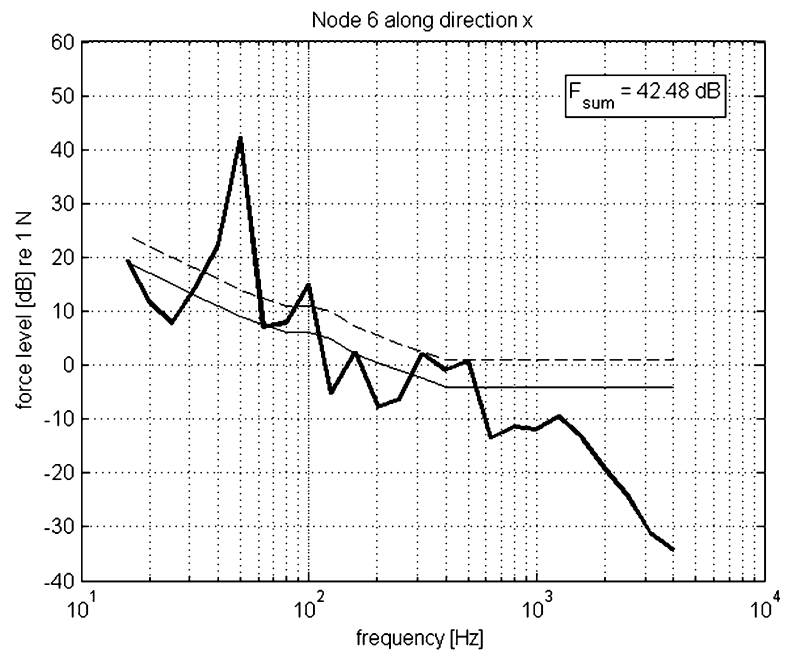
The rotational frequency of the resistor fan was 49.2 Hz and therefore it was exciting the 11th mode of the structure near its resonance. In order to understand how this resonance affects the constraint forces, a simple single DOF system has been considered (Fig. 53.6), where f_c is the centrifugal force generated by the mass eccentricity of the fan.

The equation of motion and the constraint force f_g are

$$m\ddot{x} + r\dot{x} + kx = f_c \tag{53.4}$$

$$f_g = r\dot{x} + kx \tag{53.5}$$

Fig. 53.7 Simple single DOF system



Applying the Fourier transform to Eqs. (53.3) and (53.4) and explaining directly the relation between the reaction force and the forcing term, we obtain

$$F_g = \frac{i\Omega r + k}{-\Omega^2 m + i\Omega r + k} F_c \quad (53.6)$$

where capital letters relate to the complex vibration amplitudes.

Evaluating the absolute value of the constraint force in the resonance condition ($\Omega = \omega = \sqrt{k/m}$) and substituting the relation $r = 2hm\omega$, it follows that

$$|F_g| = |F_c| \sqrt{\left(\frac{1}{2h}\right)^2 + 1} \quad (53.7)$$

Finally introducing the correct value of the viscous damping factor

$$|F_g| = 6.036 |F_c| \quad (53.8)$$

As an example, Fig. 53.7 shows the spectrum of the constraint forces in one third octave bands for rated speed working conditions at node 6 along x direction. The dynamic amplification at approx. 50 Hz can clearly be seen. On the right top corner of each figure the wideband force level is reported.

53.6 Conclusions

In the present paper, an experimental approach for assessing structure borne noise generated by a braking resistor is presented. At first the supporting structure is tested to verify that its mechanical impedance is equivalent to that of the final installation of the braking resistor. Then, half rated and fully rated tests of the braking resistor are carried out showing that, at full rate, the unbalance of the cooling fan excites a mechanical resonance of braking resistor thus surpassing the limits imposed by the train manufacturer.

References

1. IEC 60068-3-3 (1991) Environmental testing—part 3: guidance—seismic test methods for equipment
2. Bendat JS, Piersol AG (1993) Engineering applications of correlation and spectral analysis, 2nd ed. Wiley-Interscience
3. Ewins JD (2001) Modal testing: theory and practice. Wiley
4. Björck A (1996), Numerical Methods for Least Squares Problems, 1st ed. SIAM: Society for Industrial and Applied Mathematics

Chapter 54

Pre-Test Nonlinear FE Modeling and Simulation of a Full-Scale Five-Story Reinforced Concrete Building

Hamed Ebrahimián, Rodrigo Astroza, Joel P. Conte, Jose I. Restrepo, and Tara C. Hutchinson

Abstract A full-scale reinforced concrete (R/C) building specimen, furnished with a variety of nonstructural components and systems, was built and tested on the UCSD-NEES outdoor shake table. The building specimen was subjected to a sequence of dynamic tests including scaled and unscaled historical earthquake ground motions. In order to simulate and predict the nonlinear dynamic response of the building specimen, a detailed three-dimensional nonlinear FE model of the structure was developed using the FE analysis software DIANA. By comparing the pre-test simulated results with the experimental results, the effects of the nonstructural components on the dynamic response of the building can be inferred. This paper describes the building test specimen and the nonlinear FE modeling and response simulation. Key numerical results are compared with their experimental counterparts and potential sources of discrepancies are discussed.

Keywords Reinforced concrete building structure • Nonlinear finite element modeling • Response simulation • Shake table test • Nonstructural components

54.1 Introduction

In 2011–2012, a landmark research project was completed at the University of California, San Diego (UCSD), which consisted of testing a full-scale five-story reinforced concrete (R/C) building specimen on the NEES-UCSD large shake table. The building was outfitted with a variety of Nonstructural Components and Systems (NCSs) including a fully-functional elevator, metal stair system, exterior cladding (balloon framing metal studs over the bottom three stories and precast R/C panels over the top two stories), partition walls, ceiling sub-system, piping, and HVAC to name a few. Different architectural occupancies including home office, laboratory environment, computer server room, intensive care unit (ICU) and surgery unit were designated at each level of the building. The main objectives of the project were to study the performance of the full-scale RC building including the NCSs under seismic excitations and to investigate the complex interaction between the structure and NCSs. The building was first tested in the base-isolated condition with the foundation resting on four elastomeric bearings. After completion of the tests under base-isolation, the base isolators were removed by jacking up the building and the fixed-based phase of the tests started [1].

Pre-test simulations in the form of high fidelity nonlinear finite element (FE) analyses were conducted to guide the design of the seismic motion protocol as well as the placement of the sensors on both the structure and its nonstructural components. Both the computational cost and fidelity were essential aspects of the FE-simulation framework. This paper briefly describes the important features of the pre-test nonlinear FE simulations. Moreover, the prediction capability of the pre-test FE model is evaluated by comparing key FE predicted structural response parameters with their experimental counterparts measured during the shake table tests. Probable sources of discrepancy and likely shortcomings of the state-of-the-art FE modeling technique used are discussed.

H. Ebrahimián (✉) • J.P. Conte • J.I. Restrepo • T.C. Hutchinson
University of California, San Diego, 9500 Gilman Drive, La Jolla, CA 92093, USA
e-mail: hebrahim@ucsd.edu

R. Astroza
University of California, San Diego, 9500 Gilman Drive, La Jolla, CA 92093, USA

Universidad de Los Andes, Av. San Carlos de Apoquindo 2200, LAs Condes, Santiago, Chile

54.2 Description of Test Specimen and Overview of Shake Table Tests

The building structural skeleton consists of a two bays by one bay cast-in-place R/C frame. It is 11.0 m by 6.6 m in plan and has a floor to floor height of about 4.3 m resulting in a total height of 21.3 m from the top of the foundation to the top of the roof slab (see Fig. 54.1).

The test specimen has a 1.5 m thick post-tensioned R/C foundation designed to preserve linear elastic behavior during the seismic tests. During the first phase of seismic testing, the foundation is elevated from the shake table, resting on four high damping rubber isolators. Subsequently, it is anchored to the shake table using post-tensioned rods installed at the foundation perimeter rendering a fixed base test configuration during the second phase of seismic testing.

The test specimen has six identical 66 cm by 46 cm R/C columns reinforced with 4#9 ($A = 645\text{mm}^2$) and 6#6 ($A = 285\text{mm}^2$) longitudinal reinforcements, and $\phi 12.7\text{mm} @ 100\text{mm}$ Baugrid™ prefabricated transverse reinforcement grids. Two identical moment resisting frames, one each on the north and south sides of the building, form the primary lateral load resisting system of the structure in the shaking (east–west) direction. Beams of the moment resisting frames have different details at different floors. The beams on the first two floors (levels 2 and 3) are reinforced with MMFX high strength steel [2] with a nominal yield strength of about 827 MPa. Level 4 has a Special Moment Frame (SMF) with hybrid upturned beams, post-tensioned by a group of four unbounded tendons at the center after concrete pouring. The upturned beams are connected to the columns at both ends via Dywidag Ductile rod Connectors (DDCs). DDCs are also used in the fourth floor (level 5) in combination with conventional frame beams. The roof has conventional moment frame beams.

The floor system of the building specimen is a 0.2 m thick concrete flat slab doubly reinforced at top and bottom. The flat slab-column connections are reinforced with confined integral beams around the free perimeter of the slab. A pair of 0.15 m thick concrete walls, reinforced with a single grid of reinforcement in the middle, is placed in the north–south direction on either side of the elevator shaft to provide gravity support for the elevator system, and also provide additional torsional stiffness for the building.

The total weight of the bare structure is 3010 kN excluding the foundation. The weight of the foundation is approximately 1870 kN. The complete building specimen, including all nonstructural components, weights about 4420 kN excluding the foundation.

More than 600 sensors including accelerometers, linear potentiometers, string potentiometers, strain gauges, load cells, GPS receivers and digital cameras are deployed in the test specimen to record various structural and nonstructural components' response. The main accelerometer array, measuring the response of the structure, consists of four tri-axial EpiSensor accelerometers installed at the four corners of each floor's slab and of the foundation surface.

The fixed base building specimen was tested under a sequence of dynamic tests including six earthquake input motions with increasing intensity. Table 54.1 shows the sequence of the earthquake tests performed on the building specimen. The FE model developed prior to the start of the shake table tests was rerun with the achieved motions of the shake table which differ

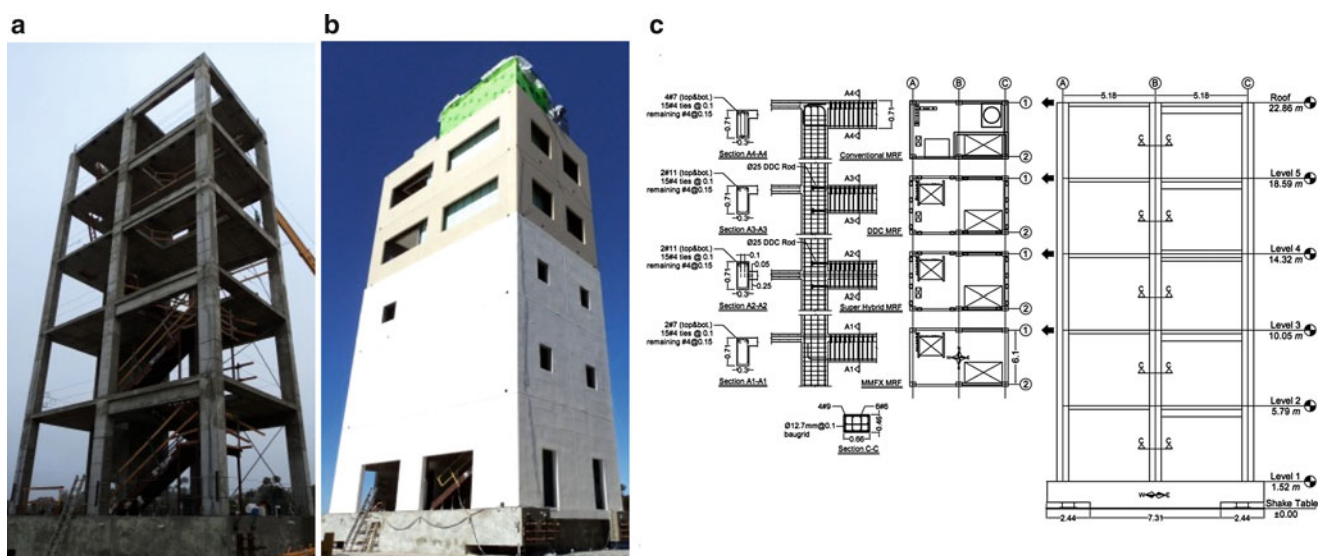


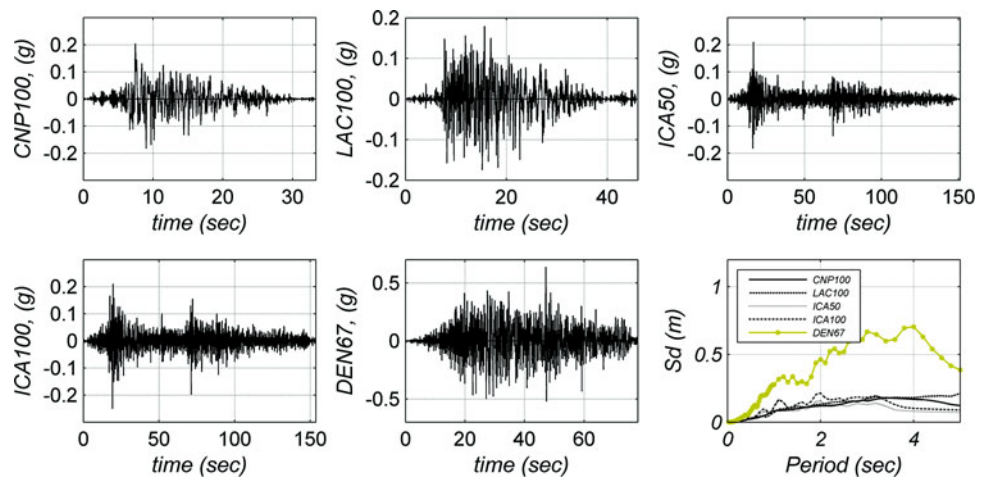
Fig. 54.1 The test specimen: (a) bare structure, (b) completed building, and (c) structural details (elevation shown for longitudinal shaking direction, i.e., east–west; all units in meters unless specified)

Table 54.1 List of earthquake tests performed and corresponding earthquake records

Test name	Input motion	Description
FB-1: <i>CNP100</i>	Canoga Park - 1994 Northridge earthquake	Spectrally matched serviceability level earthquake
FB-2: <i>LAC100</i>	LA City Terrace - 1994 Northridge earthquake	Spectrally matched serviceability level earthquake
FB-3: <i>ICA50</i>	ICA -2007 Pisco (Peru) earthquake	Original earthquake record, 50% scale
FB-4: <i>ICA100</i>	ICA - 2007 Pisco (Peru) earthquake	Original earthquake record, 100% scale
FB-5: <i>DEN67</i>	TAPS Pump Station 9 - 2002 Denali earthquake	Spectrally matched earthquake, 67% scale (targeted design level)
FB-6: <i>DEN100</i>	TAPS Pump Station 9 - 2002 Denali earthquake	Spectrally matched earthquake, 100% scale

Note that with the exception of FB-3 and FB-4, motions listed are seed motions that were spectrally matched and amplitude scaled as noted in the description of each

Fig. 54.2 Acceleration time histories of achieved test motions (E–W direction), and their 5% damped relative displacement spectra



from the target motions due to the imperfect nature of the shake table controller. However, the FE modeling assumptions and FE model parameters, as described in the following sections, were not revised to preserve a true comparison between pre-test simulation and measurement results. The time histories of the east–west horizontal component of the achieved motions on the top of the foundation and their relative displacement response spectra are shown in Fig. 54.2.

54.3 FE Modeling of Test Specimen

Considering the specific configuration of the test specimen and its plan dimensions, the slabs are expected to have a dominant influence on the earthquake resistance of the structure. The large stairwell opening in the south-east part of the slabs close to the frame beams complicates the interaction of the slab with the south frame of the structure, and the opening in the slabs on the north-west end of the building, accommodating the full-height elevator also perturbs the load transfer mechanism in the diaphragm. Furthermore, the flat slab-column connections influence significantly the nonlinear response behavior of the structure. Therefore, proper modeling of the R/C slabs is an important aspect that needs special consideration in the FE modeling of the test specimen. To satisfy these requirements, the DIANA finite element analysis software [3] is selected as the FE-simulation platform. This software has dedicated nonlinear constitutive material models for modeling of R/C structures. Moreover, it supports the structural type finite elements needed such as 3D beam-column elements and shell elements with embedded steel reinforcement.

The concrete constitutive material model employed in this study is a total strain rotating smeared crack model. The uniaxial compressive behavior of the concrete material consists of an initial linear and two subsequent parabolic parts as shown in Fig. 54.3. As illustrated in this figure, the unloading and reloading in compression and tension occur along a secant linear stress–strain path passing through the origin. The “Model B” as proposed by Vecchio and Collins [4] is used as a built-in procedure in DIANA to incorporate the effects of the modified compression field theory (MCFT) in the material model of the concrete.

To alleviate the spurious numerical localization effects in compression and tension failure of the concrete material, and to eliminate the resulting mesh sensitivity, the fracture energy concept is used for the softening branch of the stress–strain curve of the concrete material in both tension and compression [5, 6]. The fracture energy (both in tension and compression)

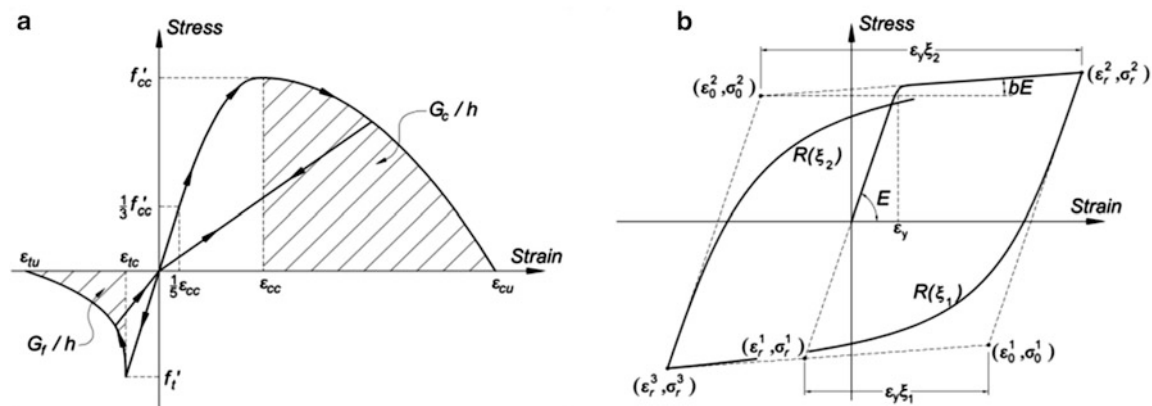


Fig. 54.3 Uniaxial stress strain behavior of (a) concrete material, and (b) reinforcing steel material

is usually considered a constant material parameter for plain concrete. In this study, the tensile fracture energy is selected as a constant material property, and the tension softening behavior is defined using Reinhardt tension softening model [7]. However, the value of the compressive fracture energy for the R/C beam and column elements are selected to reflect the effects of mechanical confinement provided by the transverse reinforcement in the plastic hinge regions of the beam and column members. These confinement effects are incorporated by modifying the compressive uni-axial stress–strain behavior of the unconfined concrete material. To achieve this goal, a reverse two-step approach is used in this study. In the first step, the peak compressive strength and corresponding strain of the concrete material in the plastic hinge regions of each beam and column members are calculated using Mander’s model [8]. The ultimate strain of the concrete material in compression is determined following the procedure suggested by Scott et al. [9]. As a result, a uni-axial stress–strain curve can be defined to represent the uniaxial compressive behavior of the confined concrete in the plastic hinge regions of the beam and column members. In the second step, the fracture energy in compression for each member is computed using the stress–strain curve for confined concrete derived in the previous step. For this purpose, the effective length is defined as the length of the plastic hinge region of the beam or column of interest, which here is taken as one half of the height of the structural member. In usual displacement-based FE structural models using beam-column elements, the softening-type nonlinearity is localized in one element. Therefore, the plastic hinge regions of beam and column members are discretized using a single element of length equal to the estimated length of the plastic hinge region for this member. Thus to guarantee mesh objectivity, DIANA internally imposes a constant tensile and compressive fracture energy per element (i.e., by scaling the uni-axial stress–strain curve of concrete based on the length of the beam-column element).

The modified Giuffrè–Menegotto–Pinto model as proposed by Filippou et al. [10], which is implemented in the DIANA material library, is used to describe the hysteresis stress–strain behavior of the reinforcing steel (Fig. 54.3). The parameters of the reinforcing steel constitutive model (e.g., modulus of elasticity, yield strength, strain hardening ratio) are obtained from the results of the tensile tests performed on some rebar samples.

The beam and column members of the test specimen are modeled using 3-node Mindlin–Reissner displacement-based 3D beam-column elements with 18 DOFs per element [11]. The element formulation is based on quadratic shape functions which implies a linear varying axial strain, and constant transverse shear strains over the cross-section. Some specific elements along each beam and column, which potentially can develop localized nonlinearities, are referred to as “plastic hinge” (PH-) elements. As already mentioned, the length of these PH-elements is taken as half the height of the associated member. To maintain computational economy, different integration schemes for the finite elements (along their length and over their cross-section) are defined based on their expected level of nonlinearity. The beam and column longitudinal steel reinforcement is defined using embedded steel bars with a full bond assumption. Considering the large stiffness of the foundation, which is anchored to the shake table, the columns were restrained with fixed boundary conditions at the base.

The slabs and shear walls are modeled using 8-node Mindlin–Reissner quadrilateral serendipity shell elements available in DIANA [11]. This element has 6 DOFs per node including mechanics-based drilling degrees of freedom. A numerical integration rule, based on 2 by 2 Gauss-quadrature integration points over the plane and 3 Simpson integration points across the thickness, is applied to all shell elements. The reinforcing mesh in each direction of the slab is modeled as uni-axial membrane elements with an equivalent thickness embedded in the concrete shell elements. The integral beams, which form R/C strong bands along the free perimeter of the flat slabs, are modeled using beam elements as defined above. The size of these beams is defined based on the actual dimensions of their confined core, and they are reinforced with embedded steel bars, similar to the frame beams. Figure 54.4 shows the FE mesh of the test specimen.

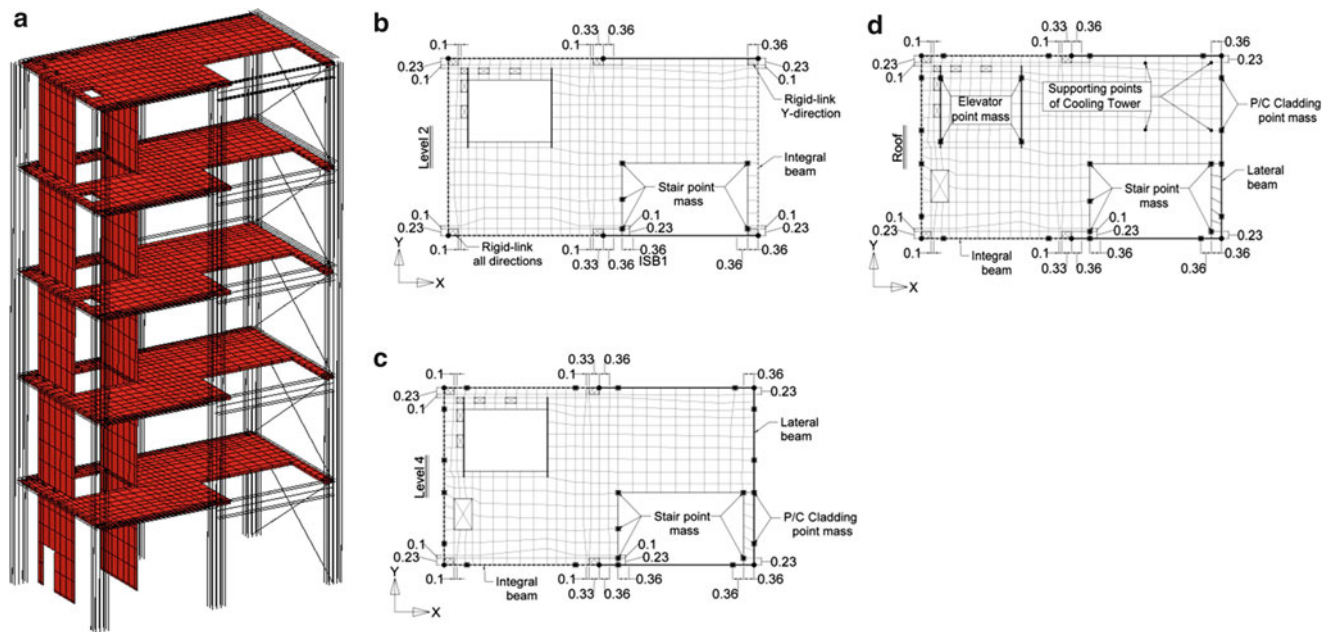


Fig. 54.4 FE mesh of test specimen: (a) 3D view, floor view of (b) level 2, (c) level 4, and (d) roof

The self-mass of the beams, columns and shear walls is modeled by assigning the proper material mass density to the corresponding elements. Since the individual mass contributions of the interior partition walls, ceilings, balloon frame facade at levels 2 to 4, and the installed contents on each floor are not significant, their inertial effects are modeled as an added uniform distributed mass over each floor slab. On the other hand, the masses of the precast concrete claddings, stairs, elevator, roof penthouse and cooling tower (at the roof level) are significant; therefore, they are each modeled with a set of lumped masses.

The damping characteristics of the building specimen are modeled using the Rayleigh proportional damping model [12] by defining 2% damping at the first mode and at 20 Hz. The Rayleigh damping parameters are derived based on the initial/uncracked linear elastic stiffness matrix of the FE building model and are kept constant during the time history analyses but with the stiffness coefficient applied to the tangent stiffness matrix.

54.4 Nonlinear Dynamic Time History Analyses

Each nonlinear analysis consists of first applying the gravity loads statically. The regular incremental-iterative Newton method is used to solve the nonlinear equilibrium equations for gravity loads. The nonlinear time history analysis starts from the state of the structure after application of the gravity loads. Newmark averaged acceleration method [12], with a time step of 0.02 sec, is used to integrate the equations of motion in time. The quasi-Newton (secant) method based on the BFGS stiffness update method [13], which is found to be efficient in handling smeared crack problems including softening effects, is employed as iterative method to solve the nonlinear dynamic equilibrium equations. The convergence criteria used are based on the relative norm of the displacement increment vector or the relative norm of the force unbalance vector with a convergence tolerance of 10^{-4} . The parallel direct sparse solver method [14], available in DIANA, is used for solving the system of linearized incremental equilibrium equations.

Figure 54.5a–c compare FE predictions and experimental measurements (from shake table tests) for the peak floor (absolute) acceleration response (PFA), peak inter-story drift ratio (IDR), and peak total (inertial) story shear (PSS) normalized by the total weight of the building. The absolute acceleration response of each floor slab in the shaking direction is evaluated at the center point of the slab by averaging the readings of the four accelerometers installed at the slab corners. Floor displacement time histories are obtained by double integrating the acceleration time histories evaluated at the center point of each of the slabs. The total (inertial) story shear, referred to as story shear hereafter for brevity, is computed as

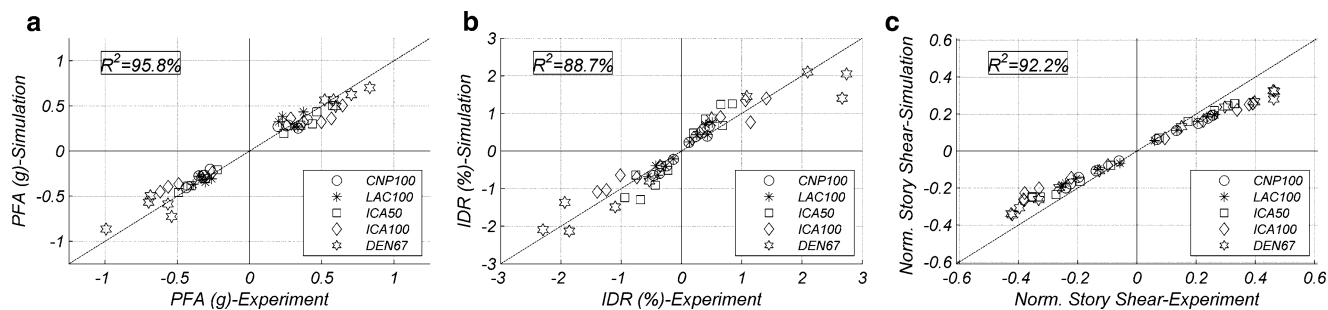


Fig. 54.5 Comparison of FE predicted and measured (a) peak floor acceleration, (b) peak inter-story drift ratio, and (c) normalized peak story shear (all test motions except *DEN100*)

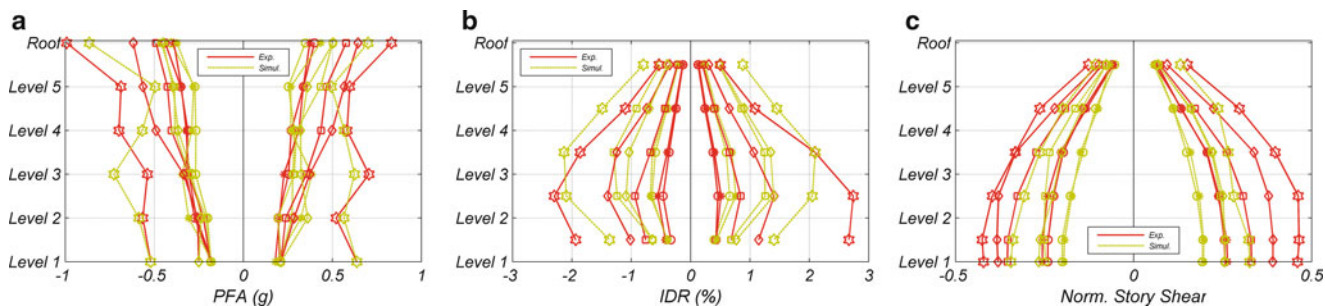


Fig. 54.6 Comparison of FE predicted and measured (a) peak floor acceleration, (b) peak inter-story drift ratio, and (c) normalized peak story shear (all test motions except *DEN100*)

$$V_{i,i+1} = \sum_{j=i+1}^6 -m_j a_j, \quad i = 1 \rightarrow 6 \quad (54.1)$$

where $V_{i,i+1}$ is the story shear evaluated at the section midway between the i th and $(i+1)$ th level, a_j is the averaged absolute acceleration at level j , and m_j is the tributary mass of the j th level.

In Fig. 54.5, the R^2 coefficient of determination measures the level of agreement between FE prediction and measurement for the peak values of the considered response parameters at different stories or floor levels for different seismic tests. Figure 54.6a–c compares the FE predicted and measured PFA, IDR and PSS along the height of the building. From Figs. 54.5 and 54.6, it is observed that the PFA are generally better predicted than the IDR. Also, the FE-simulation over-predicts the IDR in the low intensity tests and under-predicts them in the high intensity tests. Figure 54.6b shows that for low intensity tests, the IDR is typically over-estimated at all levels, more so in the mid-levels of the building, while for high intensity tests, the IDR is under-estimated in the lower levels and over-estimated in the upper levels of the building.

The effects of nonstructural components, especially the partition walls, contribute significantly to the discrepancy between FE predicted and measured IDR results. The influence of partition walls on the dynamic response of buildings have been the object of previous studies, e.g., Wood [15]. The contribution of the partition walls is more significant at low IDR, since these walls are intact. As the intensity level of the base motion increases, the partition walls undergo damage and stiffness/strength degradation in the lower levels of the building, while in the upper levels, where the IDR demand is lower, they are still influential. The normalized PSS is also generally under-estimated by the FE simulation results, the reason of which is also most probably- the contribution of nonstructural components in the lateral resistance of the building.

The cause for the underprediction of the peak IDR at the lower levels of the building during the *ICA100* and *DEN67* tests is most likely due to the difference between the actual and FE predicted hysteretic response of the structural components in the building. The currently employed FE modeling technique is not able to capture the pinching hysteretic behavior in the beams and columns. As a result, the structural components have greater energy dissipation capacity under cyclic loading in the FE model than in the real structure. Consequently, the FE predicted floor displacement responses are lower than the test results. As expected, the first two stories of the building experience the highest level of structural nonlinearity. The IDR envelope plot in Fig. 54.6b shows that the IDR is underpredicted at the first story for *ICA100* and the first two stories for *DEN67*.

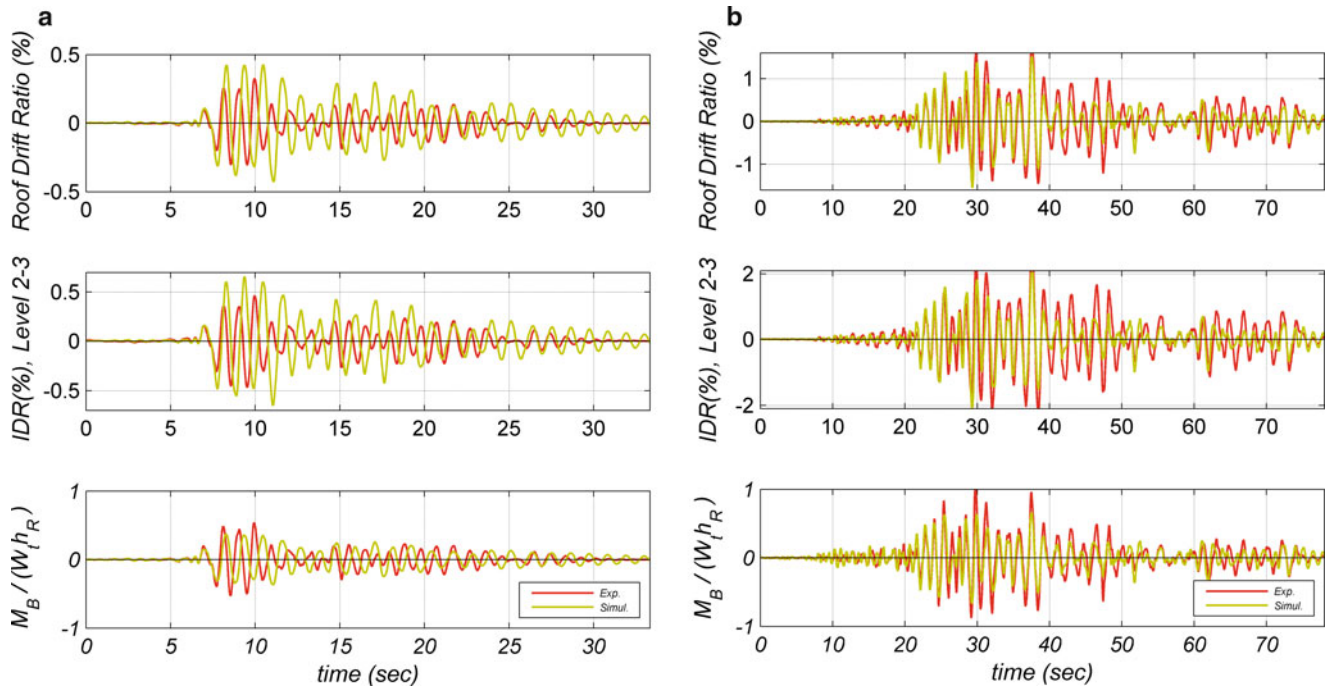


Fig. 54.7 Comparison of FE predicted and measured time histories of selected response parameters for (a) *CNP100* and (b) *DEN67*

Similarly to the total (inertial) story shear, the total (inertial) base overturning moment (M_t) can be computed using the following relation in which h_j denotes the height of level j measured from the top of the foundation.

$$M_t = \sum_{j=2}^6 -m_j a_j h_j \quad (54.2)$$

To better investigate the effect of nonstructural components on the seismic response of the structure, the time histories of the roof drift ratio (roof displacement relative to the foundation normalized by the roof height measured from the top of the foundation), inter-story drift ratio of the second story (between levels 2 and 3), and total base overturning moment normalized by the product of the total weight of the building and the roof height (measured from the top of the foundation) are shown in Fig. 54.7a, b for *CNP100* and *DEN67*, respectively. Figure 54.7a shows a clear difference in the frequency content of all response time histories between FE predicted and measured results, which is probably due in significant part to the kinematic interaction of the nonstructural components -mostly partition walls- with the structural system. As discussed earlier, these interaction effects, which are not considered in the FE-simulation, result in a shift in the natural periods of the structure. By comparing Fig. 54.7a, b, it is observed that these effects are lessened for *DEN67* compared to *CNP100*, since at the time of *DEN67*, there was extensive physical damage in the nonstructural components due to prior earthquake tests. As a result, the level of kinematic interaction between the nonstructural components (with both stiffness and strength degradations) and the structural system is significantly reduced for *DEN67*.

Selected longitudinal rebars placed in the north frame's beams were instrumented at different locations with strain gauges. Figure 54.8 shows the location of one of the strain gauges installed on the outer longitudinal rebar at the east corner of the 3rd level beam, which is near the plastic hinge region of that beam. The strain time history recorded by this strain gauge during the *DEN67* test is compared with its FE predicted counterpart in Fig. 54.9. The FE predicted axial strain at the longitudinal rebar location is derived by interpolating the axial strain at the cross-section integration points of the PH beam element, considering the planar distribution of the axial strain over the beam cross-section. The obtained strains are further averaged over the entire PH element to give the FE predicted strain time history at the strain gauge location. Figure 54.9 shows a good agreement between the experimental results and the FE-simulation. Also, it is observed that the FE-simulation is able to predict, accurately in this case, the residual strain in the rebar at the end of the seismic test.

Fig. 54.8 Strain gauge installed on the north rebar at east end of the 3rd level north frame beam

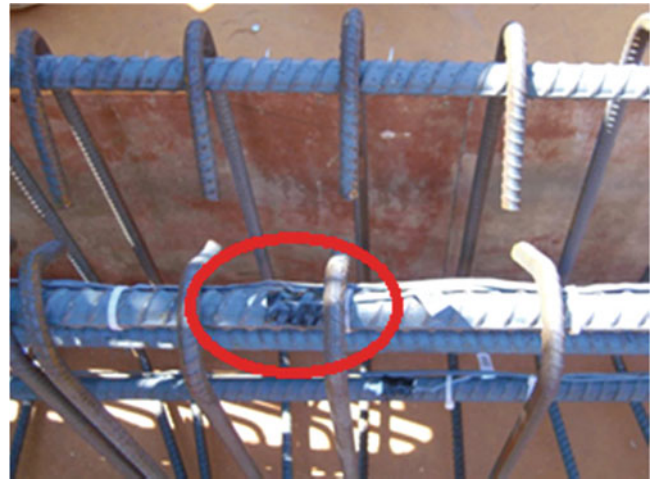
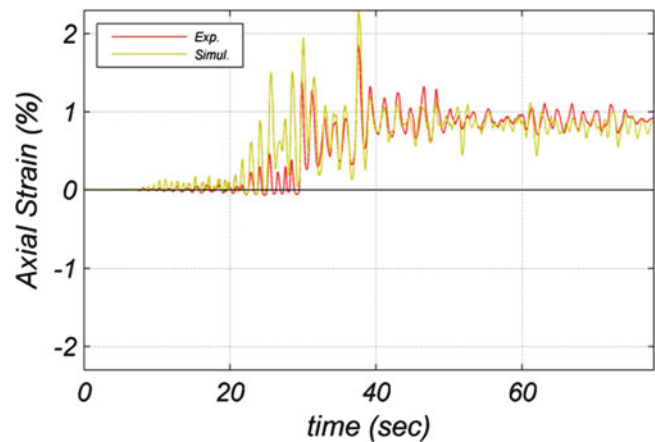


Fig. 54.9 Comparison between FE predicted and strain gauge measured rebar strain (DEN67)



54.5 Conclusions

The 3D nonlinear FE model utilized for pre-test numerical simulation of a full scale 5-story R/C building specimen tested on the UCSD-NEES shake table is briefly described. In this model, only the mass (assumed as rigid) of the nonstructural components is accounted for in the FE model of the structure. The stiffness and strength properties of the nonstructural components are not accounted for and therefore the full dynamic (especially kinematic) interaction between nonstructural components and the structural system is not modeled.

Comparison of the FE-simulation results with those measured during the shake table tests shows that the nonstructural components have significant influence on the seismic response of the building. At low intensity earthquake demands, where the nonstructural components are intact, the kinematic interaction between the structural and nonstructural systems increases the overall stiffness of the building, which reduces the floor displacement demands of the building (compared to the FE predictions). Thus, there is a meaningful discrepancy between experimental and FE-simulation results. As the intensity of the earthquake increases, the nonstructural components start to get damaged undergoing stiffness and strength degradation and their kinematic interaction with the structural system diminishes. Therefore, the FE predictions are in better agreement with the experimental results.

In the currently developed FE model, some aspects of R/C cyclic behavior cannot be captured correctly, the most important of which is the pinching hysteretic behavior of R/C flexural members. Thus, in highly nonlinear regions, the FE model of the test structure has higher energy dissipation capacity for flexural members than the actual specimen. As a consequence, for the high and very high intensity earthquakes, the FE model underpredicts the floor displacement demands of the building at the lower levels.

These findings pave the way to future research needed to improve the fidelity of nonlinear FE structural models for R/C building structures. In the current research program, efforts are underway to update the current FE model by implementing appropriate models for the nonstructural components. Moreover, in a parallel research program, an advanced material model for steel reinforcement is being developed to better capture the key aspects of R/C cyclic behavior.

Acknowledgements This project was a collaboration between four academic institutions: The University of California at San Diego, San Diego State University, Howard University, and Worcester Polytechnic Institute, four major funding sources: The National Science Foundation, Englekirk Advisory Board, Charles Pankow Foundation and the California Seismic Safety Commission, and over 40 industry partners. Additional details may be found at bncs.ucsd.edu. Through the NSF-NEESR program, a portion of funding was provided by grant number CMMI-0936505 with Dr. Joy Pauschke as program manager. The above support is gratefully acknowledged. Support of graduate students Consuelo Aranda, Michelle Chen, Elias Espino, Steve Mintz, Elide Pantoli and Xiang Wang, the NEES@UCSD, NEES@UCLA staff, and consulting contributions of Robert Bachman, chair of the project's Engineering Regulatory Committee, are greatly appreciated. Design of the test building was led by Englekirk Structural Engineers, and the efforts of Dr. Robert Englekirk and Mahmoud Faghihi are greatly appreciated in this regard. Opinions and findings in this study are those of the authors and do not necessarily reflect the views of the sponsors.

References

1. Chen M et al (2012) Design and construction of a full-scale 5-story base isolated building outfitted with nonstructural components for earthquake testing at the ucsd-nees facility. In: ASCE structures congress. Chicago
2. MMFX Technologies Corporation (2012) n.d. <http://www.mmfx.com/>. Accessed 1 October 2012
3. TNO DIANA (2012) n.d. <http://tnodiana.com/>. Accessed 1 October 2012
4. Vecchio FJ, Collins MP (1993) Compression response of cracked concrete. *J Struct Eng (ASCE)* 119(12):3590–3610
5. Hillerburg A, Modeer M, Peterson PE (1976) Analysis of crack formation and crack width in concrete by means of fracture mechanics and finite elements. *Cement Concrete Res* 6(6):773–782
6. Willam KJ, Hurlbut B, Sture S (1986) Experimental and constitutive aspects of concrete failure. In: US-Japan seminar on finite element analysis of reinforced concrete structures, ASCE, Special Publication, Tokyo
7. Reinhardt HW (1984) Fracture mechanics of an elastic softening material like concrete. Heron, Delft
8. Mander BJ, Priestley MJN, Park R (1988) Theoretical stress–strain model for confined concrete. *J Struct Eng (ASCE)* 114(8):1804–1826
9. Scott BD, Park R, Priestley MJN (1982) Stress–strain behavior of concrete confined by overlapping hoops at low and high strain rates. *Am Concrete Inst (ACI)*, 1982: 13–27
10. Filippou FC, Popov EP, Bertero VV (1983) Effects of bond deterioration on hysteretic behavior of reinforced concrete joints. UCB/EERC-83/19, College of Engineering, University of California, Berkeley, 1983.
11. DIANA, TNO (2010) DIANA user's manual, element library. TNO DIANA bv, Delft
12. Chopra AK (2012) *Dynamics of Structures: Theory and Applications to Earthquake Engineering*, 4th Edition, Prentice Hall, Englewood Cliffs, New Jersey
13. DIANA, TNO (2010) DIANA user's manual, analysis procedures. TNO DIANA bv, Delft
14. Schenk O (2000) Scalable parallel sparse LU factorization methods on shared memory multiprocessors. Ph.D. Thesis, Technische Wissenschaften ETH, Zürich
15. Wood RL (2012) Partition wall subsystem modeling and effect on the coupled partition wall subsystem modeling and effect on the coupled. University of California, San Diego

Chapter 55

The Dynamic Stiffening Effects of Non-Structural Partitions in Building Floors

C.J. Middleton and A. Pavic

Abstract It is commonly known that full-height non-structural partitions of a fitted out floor structure affect its dynamic properties, with increase in floor mass and modal damping being commonly quoted in floor design guidelines. As a consequence, it is generally accepted that the non-structural elements usually reduce the response of floors to walking excitation. There is very little understanding of the effects of full-height partitions on the stiffness of building floors and this effect is generally not taken into account in floor design guidelines.

This paper is therefore focused on establishing experimentally the effects of full-height non-structural partitions on dynamic stiffness of a full-scale real-life composite building floor. Modal testing data are presented for three construction phases of the floor: from a completely bare floor via partially to fully-fitted floor. The effects of the partitions are shown by comparing the measured frequency response functions (FRFs) at the same location for different construction phases and the estimated key modal properties of the floor corresponding to these phases. This kind of multi-phase measurements on a real-life floor structure during construction is very rare due to its logistical complexity and long-time required to gather data through all of the phases.

It is shown that the partitions significantly affect measured FRFs by increasing damping, and in particular, floor stiffness. It is also shown that the mode shapes are changed by the partitions. The magnitude of the changes is quantified experimentally which is one of the first attempts to do this on a real-life floor structure using high-quality FRF measurements.

Keywords Partitions • Experimental • Floor • Stiffness • Damping

55.1 Introduction

It is commonly known that non-structural elements change the dynamic characteristics of building floors. This phenomenon became increasingly apparent with advances in technology. Offices that were traditionally paper based became paperless 'electronic offices'. Heavy filing cabinets that were filled with paper could now be stored on a single hard disk. The removal of the filing cabinets significantly reduced the additional mass on the floor. This was coupled with the removal of partitions to allow more people to fit within the same space. Often, once a traditional paper office became an electronic paperless and open plan office there would be complaints about excessive vibration [1] which was due to the removal of the non-structural elements.

The reduction in mass due to the removal of non-structural elements is easily calculable, but it is generally not enough to increase the response of the floor to unserviceable levels. The removal of the non-structural partitions also significantly reduced the amount of damping in the system. From experience, there is a belief that the removal of non-structural full-height partitions reduces the damping more than any other non-structural elements.

There is little published literature concerning the effects of non-structural partitions. Generally, when the effects of non-structural partitions on floor vibration is discussed it is a passing mention, and just in relation to the variation in damping, suggesting that they may add up to 5% damping ratio for each mode of vibration [1–5]. This is the approach of many of the design guides [6–8]. The effect full-height non-structural partitions on the floor stiffness is often ignored.

C.J. Middleton (✉) • A. Pavic

Department of Civil and Structural Engineering, University of Sheffield, Mappin Street, Sheffield, S1 3JD, UK
e-mail: C.J.Middleton@Sheffield.ac.uk; a.pavic@sheffield.ac.uk

However, there are a number of key publications and research projects that have investigated non-structural partitions that give a good base to start future work. One of the earliest in-depth investigations was by Pernica in 1987 [9]. The investigation measured the response of a long span school floor in various stages of construction and estimated modal properties from heel strikes. He showed that there was a significant increase in damping and frequency for the same modes in different construction phases. Unfortunately the force was not measured so it was not possible to quantify the change in response or FRFs.

It took 22 years for another similar study of this kind conducted on a real-life floor to be reported as in 2009 Miskovic et al. [10] compared the vibration behaviour of two nominally identical floors with different partition layouts. In this case, any significant change in dynamic properties would be due to the different fit out of the floor. It was found that the partitions not only increased the frequency and damping of the floor, they also affected the mode shapes. In addition, the estimated modes were complex, suggesting that partitions add non-linear behaviour to the floor or non-proportional damping.

Other studies have indirectly shown that partitions effect the dynamic properties of a floor by comparing experimental modal properties with modal properties calculated using finite element analysis [10, 11]. In these studies an initial finite element (FE) model, with no partitions, is created and compared with the experimentally determined modal properties of the physical floor with partitions. The FE model is shown to underestimate the frequencies of the modes. If partitions are added to the model, and after a process of model updating, a good match of experimental and analytical modal properties can be achieved. This includes a better natural frequency correlation and improved mode shape correlation. However, modelling the partitions is still challenging due to non-structural connections between the partitions and the floors. The outcomes of the studies are case specific and currently there is not a modelling technique that is suitable for all cases.

The study of non-structural partitions has also featured in a number of PhD theses [12, 13]. Generally these studies of limited usefulness for practical applications, but a number of conclusions are still valid. They all find that the partitions increase the stiffness of the floor and add damping. They also continue to consider how the alignment of the partition to the mode shapes affects the dynamic properties. It is shown that if the partitions lie along a steep gradient in the mode shape, for equal partitions lengths, they will affect the dynamic properties more.

This study compares the experimentally determined dynamic properties of a steel-concrete prototype composite floor in various construction phases, which include first without and then with partitions. Firstly, a description of the floor structure is presented. This is followed by the description of experimental measurements which enabled direct comparisons between the phases via measured FRFs and estimated modal properties. Based on these, clear conclusions have been drawn and are presented at the end of the paper.

55.2 Structural Description of the Prototype Floor

The structure that was tested is a steel framed four floor (inclusive of the ground floor) supporting a high quality office environment and possible use of optical microscopes. It was required for the floor to have good vibration performance, somewhere between the criteria for hospitals and offices. This investigation focuses on one of the four floors in the building.

The floor-to-floor height varies slightly with each level due to functional requirements. However, assuming an approximate floor-to-floor height of 4 m would seem to be appropriate. For each floor, the main floor area comprises a 150 mm deep steel-concrete composite section using Holorib galvanised steel deck profile with a 1.2 mm gauge, as shown in Fig. 55.1.

The main floor area, shown in Fig. 55.2, is made up of ten bays with an approximate width and length of 6.2 m and 12.9 m respectively, with a secondary beam running in the long direction of the bays.

Two types of full height partitions were constructed on all of the floors: plasterboard stud partitions as shown in Fig. 55.3 (left) and block partitions as shown in the right plot of Fig. 55.3 (right).

There were a large number of partitions on each floor, which included creating a corridor through the middle and along the main part of the floor which is clearly shown in Fig. 55.4.

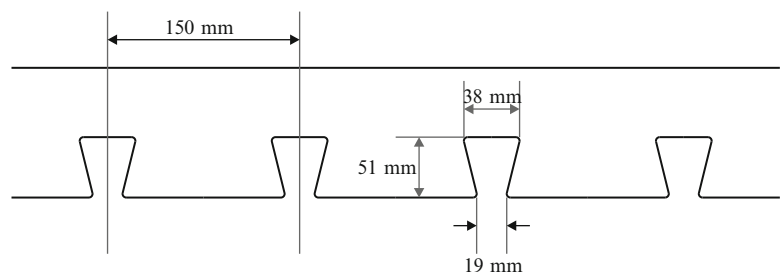
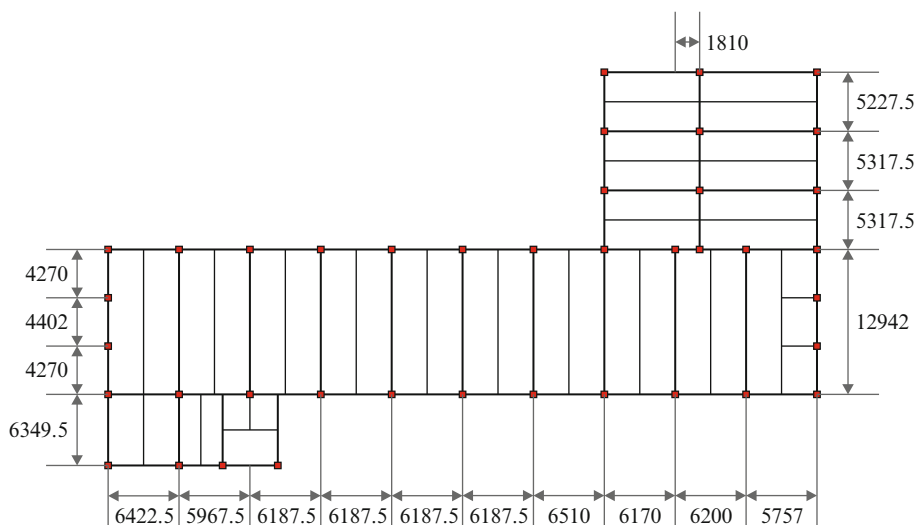


Fig. 55.1 150 mm deep Holorib section used in the prototype composite floor

Fig. 55.2 Plan of the prototype composite floor, the *thick line* represents primary beams and the *thin line* represents secondary beams

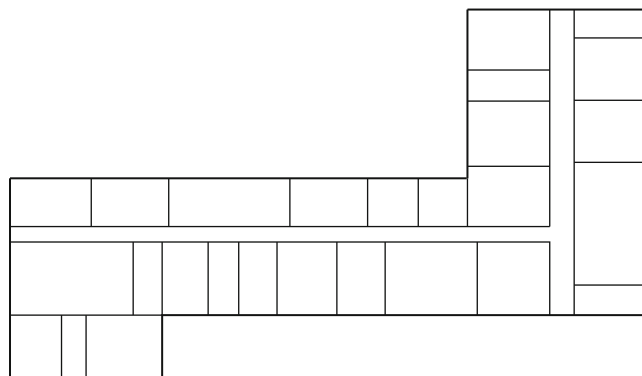


*All dimensions in mm

Fig. 55.3 Plasterboard stud partitions (*left*) and block wall partitions (*right*) used in the prototype composite floor from phase 2



Fig. 55.4 Partition layout for floor 3 of the prototype composite floor



55.3 Experimental Measurements

The floors were tested during three phases of construction and fit out. This allowed for direct comparisons of the dynamic properties of the floor with different conditions. The three phases were:

Phase 1: Bare structure; only columns, beams and floor. The outside cladding of the building had not been added, example photos are shown in Fig. 55.5.

Phase 2: The outside cladding of the building had now been added. Most partitions and services had been added to floor 3. There had been a small amount of fitting out on floor 4, example photos are shown in Fig. 55.3.

Phase 3: The building had now been completely fitted out. This includes non-structural partitions, services, fixtures and fittings (such as doors, carpets, etc.) and furniture. The building is almost ready for opening, example photos are shown in Fig. 55.6.

Fig. 55.5 The *left photo* shows a shaker and accelerometer that was used in phase 1 and the *right plot* shows the bare structure of phase 1



Fig. 55.6 The *left photo* shows a shaker used in Phase 3 and the *right photo* shows one of the largest partitioned out rooms from Phase 3

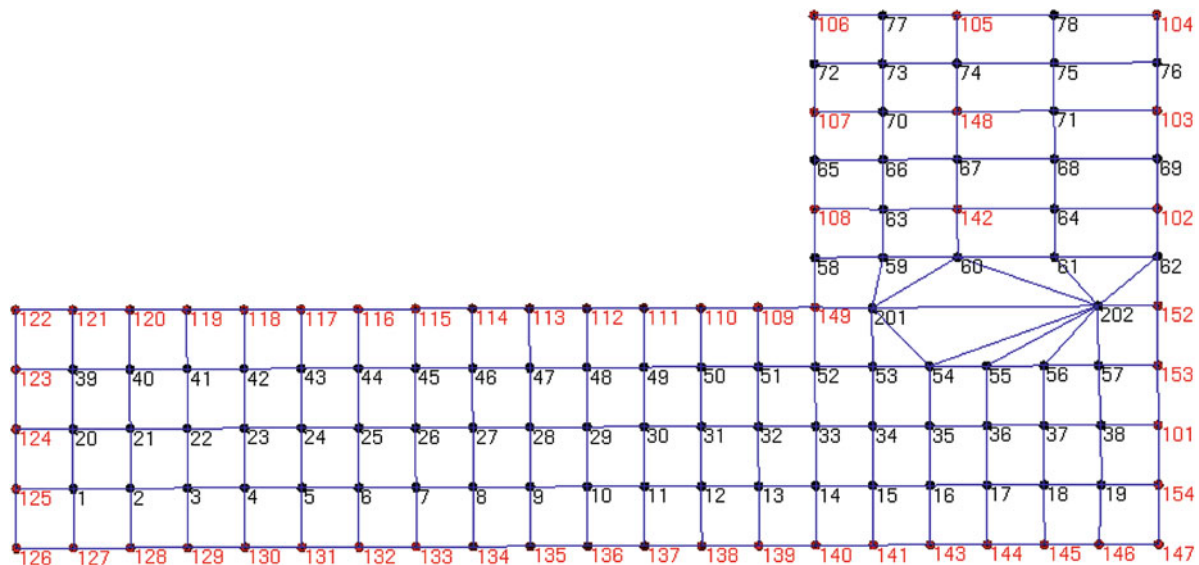


Fig. 55.7 Test grid for the prototype composite floor

For each structure and phase, EMA was conducted using multiple shakers and multiple accelerometers, allowing for MIMO analysis. Using multiple shakers minimised the risks of modes being missed by having excitation point on mode shape nodes and it also increases the amount of energy put into the structure which is beneficial for large structures, or stiff heavily damped structures. Typical FRF point mobility measurement is shown in Fig. 55.5 (left).

The shakers used were four APS Dynamics electro-dynamic shakers and they applied uncorrelated random excitation to the floor with the force measured indirectly using an accelerometer mounted on the moving mass of the shaker. To measure the response, 16 Endevco 7754–1000 piezo-electric accelerometers were used. The responses were sampled at 51.2 Hz and transfer functions recorded using a Data Physics DP730 24-bit spectrum analyser. The transfer functions were created with 40 averages by analysing the time history data using a 50 s Hanning windows and a 75% overlap, which gave a frequency resolution of 0.02 Hz. Five ‘swipes’ across all test points were required to capture the whole floor area, comprising of 80 test points. The shaker forces were used as stationary reference points which allowed the mode shapes to be spliced together. Curve-fitting was performed in ME’Scope software.

Fig. 55.8 Point accelerance FRFs (*left*) and dynamic stiffness (*right*) at TP 13 for phase 1, 2 and 3; the *blue, green* and *red* lines represent phase 1, 2 and 3 respectively

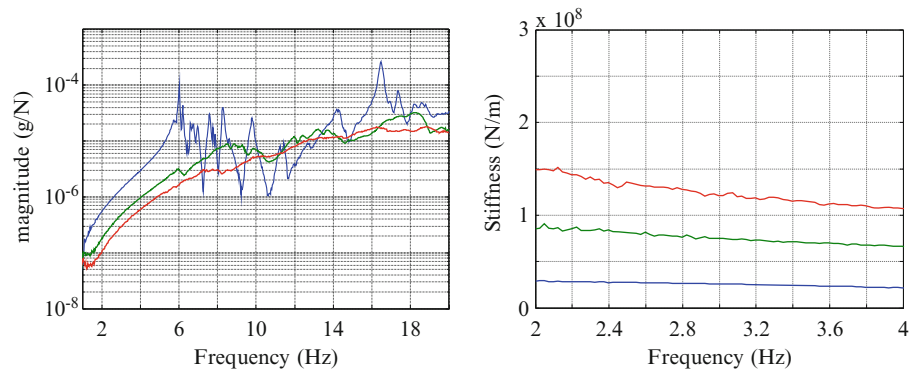
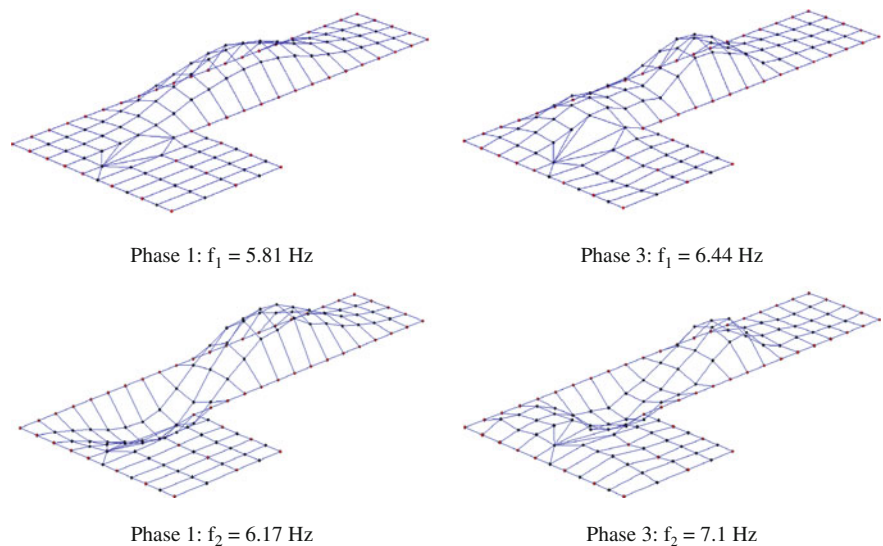


Fig. 55.9 Complexity plots for the fundamental mode shapes for floor 3 for phase 1 and 3



The floor in each phase was tested with a nominally identical methodology, using the same equipment, test grid and analysis procedure. The test grid used is shown in Fig. 55.7 with four shakers at test points (TPs) 13, 43, 61 and 73, which are also the reference points.

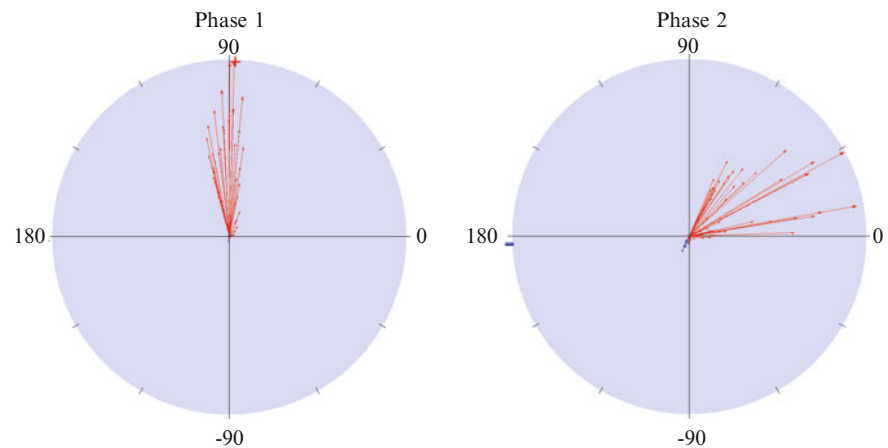
The addition of the partitions and fitting out of the structure significantly change the dynamic properties of the floor, which is highlighted in Fig. 55.8. The left plot of Fig. 55.8 shows the point accelerance FRFs for TP 13, which is expected to give clean FRFs. It is clear that there are obvious peaks in the FRF for Phase 1, which represents a good number of identifiable modes, the first large peak being approximately 5.8 Hz, although there is a smaller peak at approximately 5.2 Hz. For each subsequent phase the amplitude of the FRF reduce considerably, as do the sharpness, and the width increases. For phase 2 and 3 the first identifiable peaks are approximately 6 and 6.4 Hz respectively (although hard to see in the plot), which indicates significant stiffening of the structure. For Phase 2 and 3 the peaks are much less clear and more difficult to identify. This indicates that partitions completely changed the structural system of the bare floor and that there is for sure significantly more damping within the structure.

The right plot in Fig. 55.8 shows the dynamic point stiffness at TP 13. For low frequencies before the first resonances it is a good estimate of the static stiffness. In each phase the point stiffness has increased by approximately 0.5×10^8 N/m, which is a significant increase in stiffness, with the point stiffness of phase 3 being approximately 4–5 times stiffer than in phase 1.

It is clearly both the increase in damping and stiffness properties that affected the magnitude and shape of the FRFs so considerably.

Due to the large changes in stiffness and damping it is difficult to directly compare modal properties between phases as they are, strictly speaking, no longer the same mode. In addition, as the peaks become harder to identify it becomes more difficult to curve fit the FRFs to obtain accurate modal properties. Moreover, with the partitioned layouts in phases 2 and 3, it was often the case that the curve fitted modes were complex, in which case, the visual appearance of the mode shapes depend on the realisation angle used. The complex modes also indicate that the structure may be becoming increasingly non-linear or have non-proportional damping. To aid in the visualisation of the modal complexity, complexity plots are shown in Fig. 55.9.

Fig. 55.10 First two mode shapes and frequencies for floor 3 for phase 1 and 3



However, there is still merit in comparing the first couple of modes of vibration between phases 1 and 3, which can give an indication of the overall stiffness of the structure. The first two mode shapes and frequencies for the tested floor are shown for phases 1 and 3 in Fig. 55.10. The natural frequencies have increased by approximately 10–15%, indicating an increase in modal stiffness which offset increases in the mass of the non-structural elements used to fit out the floor. If the fundamental mode shape is considered there is a ‘plateau’ introduced in the Phase 3 fundamental mode shape, which likely indicates an area on the floor developing increased stiffness. When considering the second mode of vibration, the length of the mode reduces with phase 3, what ‘plateaus’ introduced at either end of the building, again indicating likely sources of floor stiffening.

If the partition layout from Fig. 55.4 is considered, the corridor running down the main length of the floor area results in two lines of partitions near the antinodes of the modes. This is likely to be the cause of the significant stiffening within the structure. In addition, there is a higher density of partitions near the plateau shown in the fundamental mode of phase 3 (Fig. 55.10), which explains the localised stiffening in this area. Hence, there is a perfectly rational explanation for the modal behaviour of the partitioned layout.

55.4 Summary and Conclusions

It was shown that full-height non-structural partitions can significantly affect the dynamic properties of floors. This was demonstrated experimentally by performing EMA on a structure in various stages of construction, which included with and without partitions. Comparisons of modal properties and FRFs were conducted.

With partitions added to the floor, the first two modes of vibration increased in frequency which implies there is an overall increase in stiffness. The two modes of vibration visually appear to be similar for tests with and without partitions, although the shape does change slightly. This indicates that the partitions also have a local stiffening effect. The modes shapes for the structure with partitions were also more complex, which is usually caused by non-linearities or non-proportional damping.

When considering the changes in FRFs with the construction phases it was shown that partitions had a positive shift in FRF peak frequencies, also suggesting an overall increase in stiffness. In addition, the magnitude of the peaks reduced and the width increased, this is due to an increase in damping. From the FRFs it was also possible to determine the point stiffness at the shaker location. The addition of the partitions increased the point stiffness by four to five times.

The partitions in this study had a significant stiffening effect on the floor with localised and global stiffness increases. These stiffening effects increase natural frequencies and alter mode shapes, assuming partitions only add damping is not appropriate. It is likely that the significant effect of the partitions is due to the partition layout.

The presented EMA results provide an excellent basis for a future FE modelling exercise for all phases tested which aim would be to develop methodology for FE modelling of partitions.

References

1. Hewitt CM, Murray TM (April 2004) Office fit-out and floor vibrations. *Mod Steel Constr* 35–38
2. Allen DE, Pernica G (1998) Control of floor vibration. In: Allen DE, Pernica G, eds. *Control of floor vibration*. Institute for research in construction, National Research Council of Canada, Ottawa, Canada
3. Hanagan LM (2003) Floor vibration serviceability: tips and tools for negotiating a successful design. *Mod Steel Constr* 43(4):39–48
4. Murray TM (1975) Design to prevent floor vibrations. *Eng J* 12(3), pp 1–24
5. Murray TM (2000) Tips for designers of office buildings. *Structure* 26–30
6. Smith A, Hicks SJ, Devine PJ (2009) *Design of floors for vibration—a new approach (revised edition)*. The Steel Construction Institute, London
7. Willford MR Young P (2006) A design guide for footfall induced vibration of structures. Concrete Centre
8. Murray TM, Allen DE, Ungar EE (2003) Floor vibrations due to human activity. *Am Inst Steel Constr*
9. Pernica G (1987) Effect of architectural components on the dynamic properties of a long-span floor system. *Can J Civil Eng* 14(4):461–467
10. Miskovic Z, Pavic A, Reynolds P (2009) Effects of full-height nonstructural partitions on modal properties of two nominally identical building floors. *Can J Civil Eng* 36(7):1121–1132
11. Cantieni R, Pietrzko S, Deger Y (1998) Modal investigation of an office building floor. In: 16th international modal analysis conference, 1998, Society for Experimental Mechanics, Santa Barbara, CA, pp 1172–1178
12. Falati S (1999) The contribution of non structural components to the overall dynamic behaviour of concrete floor slabs. University of Oxford, Oxford
13. Ljunggren F (2006) Floor vibration—dynamic properties and subjective perception. Lulea University of Technology, Lulea

Chapter 56

Experimental Characterization and Predictive Modeling of a Residential-Scale Wind Turbine

Jordan B. Chipka, Andrew R. Lisicki, Chuong T. Nguyen, Stuart G. Taylor, Gyuhae Park, Curtt N. Ammerman, and Charles R. Farrar

Abstract As the demand for wind energy increases, industry and policymakers have been pushing to place larger wind turbines in denser wind farms. Furthermore, there are higher expectations for reliability of turbines, which require a better understanding of the complex interaction between wind turbines and the fluid flow that drives them. As a test platform, we used the Whisper 500 residential scale wind turbine to support structural and atmospheric modeling efforts undertaken to improve understanding of these interactions. The wind turbine's flexible components (blades, tower, etc.) were modeled using finite elements, and modal tests of these components were conducted to provide data for experimental validation of the computational models. Finally, experimental data were collected from the wind turbine under real-world operating conditions. The FAST (Fatigue, Aerodynamics, Structures, and Turbulence) software developed at the National Renewable Energy Laboratory was used to predict total system performance in terms of wind input to power output along with other experimentally measurable parameters such as blade tip and tower top accelerations. This paper summarizes the laboratory and field test experiments and concludes with a discussion of the models' predictive capability. *LA-UR-12-24832*.

Keywords Wind energy • Modal analysis • FAST • Airfoil • Dynamic testing

56.1 Introduction

56.1.1 Background

Wind energy is becoming an increasingly important factor in the world's growing demand for energy. In an attempt to meet this demand, there is a trend to place larger wind turbines in more confined areas. However, this trend has the potential to have detrimental effects on the wind turbines themselves. The effect of placing large wind turbines in compact environments

J.B. Chipka • C.T. Nguyen
Department of Mechanical Engineering, Rose-Hulman Institute of Technology, Terre Haute, IN, USA
e-mail: chipkajb@rose-hulman.edu; nguyenct@rose-hulman.edu

A.R. Lisicki
Department of Civil Engineering, Clemson University, Clemson, SC, USA
e-mail: alisick@g.clemson.edu

S.G. Taylor (✉)
Los Alamos National Laboratory, Engineering Institute, Los Alamos, NM, USA
Department of Structural Engineering, University of California, San Diego, La Jolla, CA, USA
e-mail: sgtaylor@lanl.gov

G. Park
School of Mechanical Systems Engineering, Chonnam National University, Gwangju, South Korea

C.N. Ammerman
Los Alamos National Laboratory, Applied Engineering Technology, Los Alamos, NM, USA

C.R. Farrar
Los Alamos National Laboratory, Engineering Institute, Los Alamos, NM, USA
e-mail: farrar@lanl.gov

Fig. 56.1 Turbine-turbine interaction at the horns rev wind farm in Denmark (credit: Vattenfall; photograph by Christian Steiness)



is a drop in the efficiency and consistency of the turbines. This can be seen in the fact that wind turbines typically experience 2.6 failures per year for the first ten years of their use and 3.9 unplanned maintenance incidents per year. In a quote from the National Renewable Energy Laboratory (NREL) in 2008, this concern is addressed: “. . . densely packed arrays also often blocked the wind from neighboring turbines, producing a great deal of turbulence for the downwind machines. Reliability and availability suffered as a result” [1].

56.1.2 Motivation

A major concern in the field of wind energy involves the interaction between the flexible members of the wind turbines and the fluid flow through them. This interaction imparts aeroelastic load, which has the potential to be passed on as damaging loads to sensitive components in the nacelle. Furthermore, the interaction between the components of a wind turbine and the fluid flow induces a turbulent wake, which then loads other wind turbines farther downstream. Currently, researchers do not have a good understanding of how these interactions lead to failures in wind turbines, and they are unable to predict changes in performance for downstream turbines due to very different conditions from the bulk fluid flow. An example of the turbulent wakes that can lead to detrimental structural interactions is shown in Fig. 56.1. To combat these potentially damaging interactions, a plant-scale structurally coupled aeroelastic simulation code, *WindBlade*, is being developed by researchers at Los Alamos National Laboratory (LANL) as part of their Intelligent Wind Turbine (IWT) project [2, 3]. The aim of *WindBlade* is to simulate the interactions between the rotating turbine blades and the complex atmospheric conditions [3]. Furthermore, *WindBlade* will be able to predict conditions for downstream turbines, thus enabling the ability to mitigate and avoid the detrimental interactions between wind turbines and the fluid flow, thereby increasing the reliability of the turbines. *WindBlade* would be an innovative technique to create intelligent models for design and predictive control of wind-farm operations.

56.1.3 Purpose

The primary goal of this research is ultimately to provide structural validation data for the simulation code, *WindBlade*, described above. As a test platform, the residential scale Whisper 500 wind turbine was used for this study. The experimental test site is shown in Fig. 56.2. To obtain the necessary data for *WindBlade*, simple finite element models of the wind turbine’s flexible members were generated, and these models were incorporated into a multi-body dynamics model for the overall turbine using FAST (Fatigue, Aerodynamics, Structures, and Turbulence) [4], a software developed by NREL. Additionally, modal tests were performed on the individual components and the entire structure to provide experimental validation data for the models.

Fig. 56.2 TA-49 test site

56.2 Modeling Approach

56.2.1 FAST Input Parameters

FAST has many input parameters that needed to be determined for the Whisper 500 wind turbine in order to construct a working simulation. To get many of these input parameters, tests and models had to be developed. The more important input parameters on which we focused were: (1) blade modes and section properties; (2) tower modes and section properties; and (3) blade airfoil data and aerodynamic performance.

These parameters were chosen because of their significance in the FAST dynamic modeling, and they could be obtained in the short time allotted for the project. The inputs that FAST requires for each blade are the first two flapwise and first edgewise characteristic mode shape equations and section properties including mass density (kg/m), flapwise stiffness ($\text{N}\cdot\text{m}^2$), and edgewise stiffness ($\text{N}\cdot\text{m}^2$). The same are also required for the tower, but are designated as “fore-aft” and “side-to-side” rather than “flapwise” and “edgewise” as for the blades. For the tower mode shapes, FAST requires the first two fore-aft and first two side-to-side characteristic equations. The airfoil data included lift and drag coefficient curves over 360 degrees angle of attack for each section of the blade. Finally, the aerodynamics includes the wind data file that is input into the simulation.

Other parameters included the turbine configuration such as hub mass and inertia, nacelle mass and inertia, furling dynamics, and generator inertia and properties. These parameters were roughly estimated from specifications of the turbine. We did not include furling dynamics in our model, although the Whisper 500 has a furling mechanism. While trying to determine these input parameters for FAST, finite element models of the blade and tower were made and experiments were used to validate these models.

56.2.2 FAST Output Parameters

Likewise with the input parameters, FAST has many output parameters with respect to forces, accelerations, displacements, and velocities of each component in the wind turbine. The output parameters of interest were those that could be physically measured and were relevant for model validation. These parameters included: (1) generated power and wind speed (power curve); (2) blade-tip accelerations (flapwise and edgewise); and (3) tower-top accelerations (fore-aft and side-to-side). The generated power output parameter will provide us with a power curve that we can compare against manufacturer data. The blade-tip and tower-top accelerations are obtainable by the use of accelerometers during a full system operational test. The following sections detail how we obtained the input and output parameters and discuss our use of these parameters in the FAST simulation and experimental tests.

56.3 Component Level Models

56.3.1 Blade Modes and Section Properties

To begin the analysis of the blade's bending behavior, a shell model was developed using ABAQUS. A Solid-Works model of the blade was obtained from earlier Whisper 500 work, and this model was imported into ABAQUS as a constant-thickness shell model. Although the blade has a non-uniform composite shell and a polystyrene core; the blade was modeled with a uniform 4 mm thick shell. Material properties of the blade were obtained from the 2011 LADSS report, as well as from the Harvey Mudd Clinic [5]. The shell properties were therefore taken to be consistent with carbon reinforced fiberglass ($E = 17.2 \text{ GPa}$, $\rho = 1362 \text{ kg/m}^3$, $\nu = 0.33$).

To validate an initial free-free ABAQUS model of the Whisper 500 wind turbine blade, a free-free modal test of the blade was performed. To simulate free-free boundary conditions, the blade was suspended by bungee cord from a metal frame. The experimental setup for this test is shown in Fig. 56.3. The blade was instrumented with three accelerometers for this test. Two accelerometers were placed on the front face of the blade to detect the flapwise modes of the blade. The third accelerometer was placed on the edge of the blade to detect the edgewise modes.

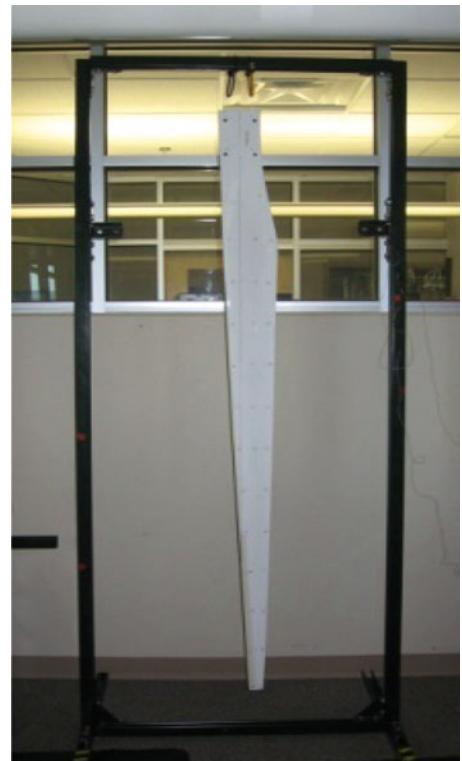
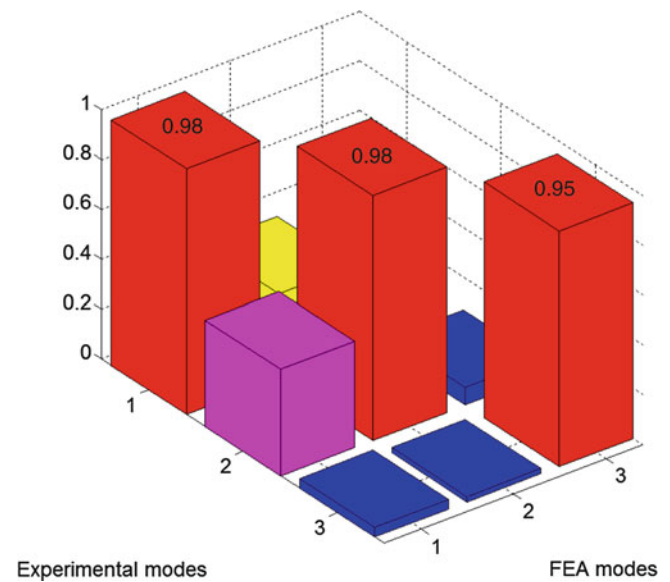


Fig. 56.3 Experimental setup for free-free modal test [6]

Fig. 56.4 MAC between experimental results and finite element model



A known force input was then imposed on the blade at 66 different locations, both on the front and side face of the blade. Once the data from these modal tests were obtained, it was then analyzed in ME'Scope to determine the mode shapes of the blade. FAST only requires the first two flapwise mode shapes and the first edgewise mode shape as inputs. Therefore, we were only interested in the results for these three modes.

The results from ME'Scope, which came from the free-free modal test of the blade, were used to validate the ABAQUS model. To perform this model validation, a Modal Assurance Criterion (MAC) was computed. The MAC is shown in Fig. 56.4. From this MAC, we were able to conclude that the ABAQUS finite element model was an adequate representation of our blade.

However, FAST requires sixth-order characteristic modal equations (assuming a cantilevered condition) as inputs for the first two flapwise and first edgewise modes with fixed-free boundary conditions. Therefore, once the ABAQUS model had been validated, it was altered to assume fixed-free boundary conditions. Then, the mode shapes were extracted by obtaining the displaced coordinates of points along the centerline of the blade. These coordinates were then entered into an Excel worksheet, which was provided with the FAST software, to obtain the sixth order characteristic modal equations necessary to run the FAST simulation.

As mentioned previously, FAST requires blade section properties. The properties for the blade were obtained from previous work performed by the 2011 Los Alamos Dynamics Summer School students using an Euler-Bernoulli beam model [6]. The section properties that were obtained included blade section mass density and flapwise stiffness. Since FAST also requires the edgewise stiffness, we reasoned that it would take much time to obtain a good value for edgewise stiffness of the blade. Therefore, we simply approximated the edgewise stiffness to be the same as the flapwise stiffness. Since wind turbine blades are made of composite materials, the modulus of elasticity was estimated as a bulk material property for the blade in the Euler-Bernoulli beam model. The LANL Wind Turbine Clinic team from Harvey Mudd College created composite blade properties using the program PreComp, developed by NREL [4]. These properties were tested in the FAST simulation; however, FAST calculated a blade mass of 249.433 kg. This result is obviously incorrect, the actual weight of the Whisper 500 blade was found to be 3.038 kg. For the properties taken from the Euler-Bernoulli beam model, FAST calculated a blade mass of 4.025 kg. This difference in weight was close enough for our purposes with the FAST simulation.

56.3.2 Tower Modes and Section Properties

The next step was to determine the characteristic modal equations for the wind turbine tower. The tower modal test was performed at the test site TA-49, which is shown in Fig. 56.2. For this test, twenty accelerometers were instrumented on the structure. Eighteen of these accelerometers had a sensitivity of 10 mV/g, and were placed at nine different heights on the tower (one accelerometer at each height in both the x and y directions). The vertical distance between the positions of each accelerometer was between 1 and 1.5 meters. The measurement points are shown in Fig. 56.5. Finally, the last

Fig. 56.5 Tilt-down tower schematic showing nine measurement points

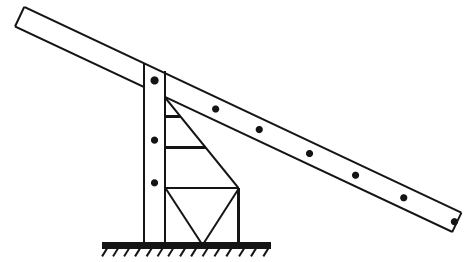
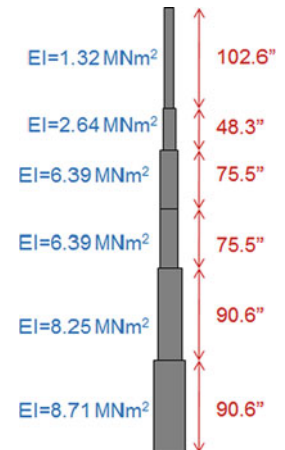


Fig. 56.6 Tower section stiffness and length



two accelerometers had a sensitivity of 1 V/g, and were placed at the top of the tower (one in each direction). These accelerometers were used to measure the lower frequencies that could not be detected by the other accelerometers with the lower sensitivity. The modal tests for the tower were performed with the turbine running to simulate realistic conditions. Once the data from these modal tests were acquired, it was analyzed in ME'Scope [7]. It was found that the measurements were not sufficiently clear to perform the necessary curve fitting to obtain the mode shapes. However, the data from the more sensitive accelerometers provided accurate measurements for the four frequencies of interest. The four frequencies of interest are the first and second fore-aft and the first and second side-to-side modes of the tower; these were the only tower mode shapes required to run the FAST simulation.

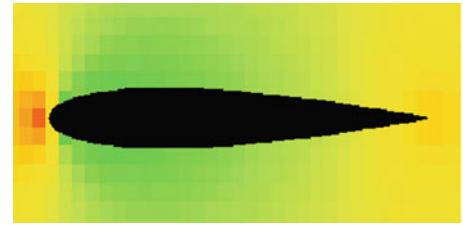
A MATLAB script was used to determine the mode shapes of the tower by implementing a tuned Euler-Bernoulli beam model. This MATLAB script required the user to input tower properties and geometry. However, one of the required properties, tower stiffness for each section of the structure, was unknown. To deal with this difficulty, calculations were performed for each section of the tower to determine the approximate area moments of inertia. Knowing the modulus of elasticity of the steel tower ($E = 200 \text{ GPa}$), we consequently calculated the corresponding stiffness values. Figure 56.6 illustrates the tower sections (all sections are rectangular except the top section which is circular) and its corresponding stiffness values.

These stiffness estimates were then used in an optimization process to find the proper stiffness values that would yield the appropriate frequencies given from the analysis done in ME'Scope. This optimization process was also performed using the computing capabilities of MATLAB. Once suitable stiffness values were found, they were implemented into the original MATLAB script. This MATLAB script produced the desired frequencies, as well as the mode shapes. The mode shapes were given in the form of displaced coordinates along the tower. Once again, the displaced coordinates of the tower were entered into the Excel worksheet provided in the FAST software to determine the sixth order modal characteristic equations necessary to run the FAST simulation.

56.3.3 Airfoil Data and Aerodynamics

FAST requires airfoil section lift and drag coefficients as an input. A few options for acquiring these parameters were explored. Eventually, a simple online airfoil analysis applet, called JavaFoil, was chosen for its low computational time and relatively simple user interface [8]. JavaFoil works using two underlying analyses. First is the potential flow analysis, which

Fig. 56.7 NACA 0012 analyzed in JavaFoil to show pressure coefficients



uses a higher order panel method to calculate local, inviscid flow along the surface of the airfoil. Second is the boundary layer analysis, which steps along the upper and lower surface of the airfoil solving differential equations to find boundary layer parameters.

As a validation for the accuracy of JavaFoil, the program was run for standard airfoil sections such as the NACA 0012, which is shown in Fig. 56.7. When comparing the lift coefficients for the NACA 0012 airfoil it was found that JavaFoil accurately calculated the coefficients up to the stall angle. Its accuracy, however, dropped off significantly after the stall angle. As a solution to this issue, a program called AirFoilPrep, developed by NREL, was implemented [9]. AirFoilPrep is an Excel-based program that can extrapolate 360 degrees of air foil coefficients from a limited scope of data using the Viterna method. It was decided that the best approach was to use JavaFoil for an attack angle ranging from -10 degrees to 20 degrees. The computed lift and drag coefficients could then be expanded in AirFoilPrep.

For the Whisper 500 blade airfoil shapes, cross sections were identified in the ABAQUS model and then, using a query tool, the coordinates along the perimeter of the blade at each of these cross sections were exported into excel. The coordinates were then scaled, translated, and reordered to a form accepted by JavaFoil. From here the process of gathering the lift and drag coefficients was completed using the methods found most acceptable for the standard NACA 0012 shape described above. In addition to the lift and drag coefficients, FAST also requires some normal coefficients. These were found by approximating the normal coefficient as the coefficient of lift, which is a good approximation for the linear region before the stall angle. This data was then formatted as an input for FAST.

56.4 System Level Model

56.4.1 FAST Simulation

To begin, we wanted to develop a very simplified FAST simulation, and then build up on the model's complexities. A simplified FAST simulation entails rigid tower and blades with the least amount of degrees of freedom possible, such as no yawing, furling, and aerodynamics. After obtaining the information needed for flexible tower and blades and aerodynamic parameters, we would then add them into the FAST simulation individually.

To model the generator of the wind turbine, we used a simple induction generator model in FAST. The important factors that contribute to the generator model are: synchronous generator speed, rated torque, slip percentage, pullout torque ratio, and the speed at which the generator turns on. These parameters were estimated from knowledge of the power and nominal rotational speed of the Whisper 500. After everything was inputted into the FAST simulation, we needed to compare the power curve generated by FAST to published power curves of the Whisper 500. This is discussed below in further detail.

The final FAST simulation that was made included flexible blades, flexible towers, free yawing, aerodynamic forces, and wind inputs. Due to the inability to directly measure properties of the wind at our experiment site, we obtained an average wind speed obtained from a nearby meteorological station during the hours that the experiment took place, and used this as a constant wind input for our FAST simulation. The final FAST simulation gave us data on the power generated by the Whisper 500, as well as blade-tip and tower-top accelerations to compare with the full system operational tests of the Whisper 500, as discussed in section 5.

As an initial measure for the validity of our FAST simulation, the power output from our FAST simulation was directly compared to the power curve obtained from the manufacturer of the Whisper 500. The predicted power output was not compared directly to the measured power output of our wind turbine at the test site due to our inability to measure the power. The power curve seen in Fig. 56.8 was obtained from the manufacturer's supplied data. It is apparent that the power drops off at a wind speed of approximately 13 m/s. This is a result of the Whisper 500 furling out of the direction of the wind at high wind speeds. Unfortunately, our final FAST model was not complex enough to include furling dynamics. Therefore, the power curve obtained from the FAST simulation only accurately predicts the manufacturer's power data for low wind

Fig. 56.8 Manufacturer's power data

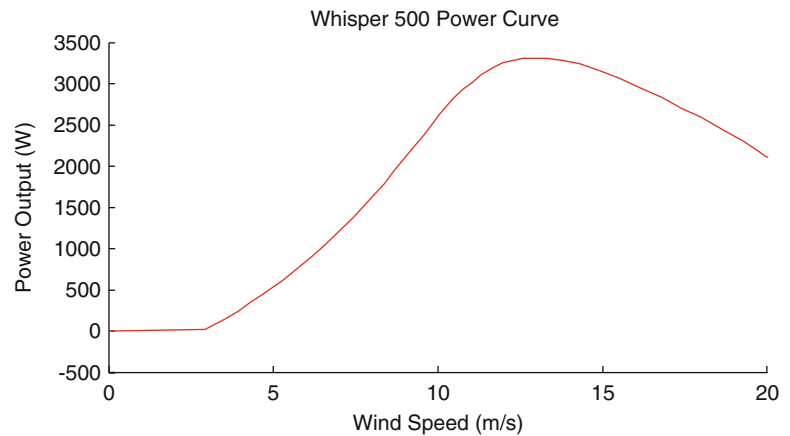
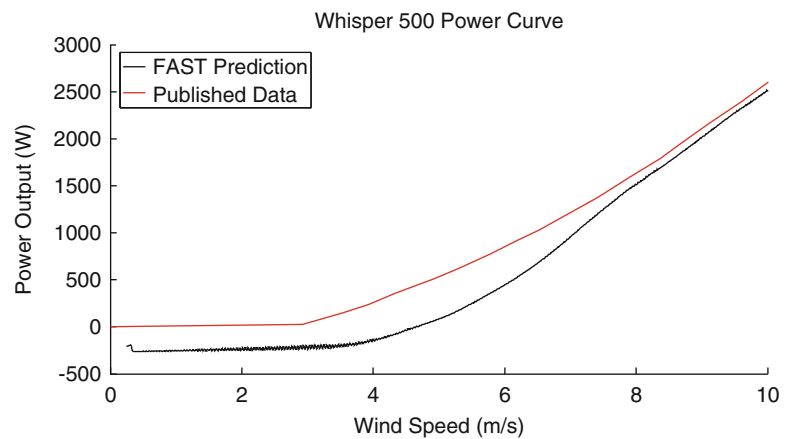


Fig. 56.9 Comparison of fast's power curve to manufacturer's data



speeds. The FAST power curve is directly compared to the manufacturer's power curve in Fig. 56.9. It must be noted that the predicted power curve starts below 0 W before increasing in power. This is a result of an assumption made in our FAST simulation. It was assumed that the blades were constantly moving. However, the wind cannot cause the blades to move until it reaches a critical wind speed near 3 m/s. Therefore, for wind speed values below this critical speed, the rotation of the blades requires power to be drawn out of the generator; and this is the reason for the initial negative power output from the turbine.

56.5 Full System Operational Test

56.5.1 Test Setup

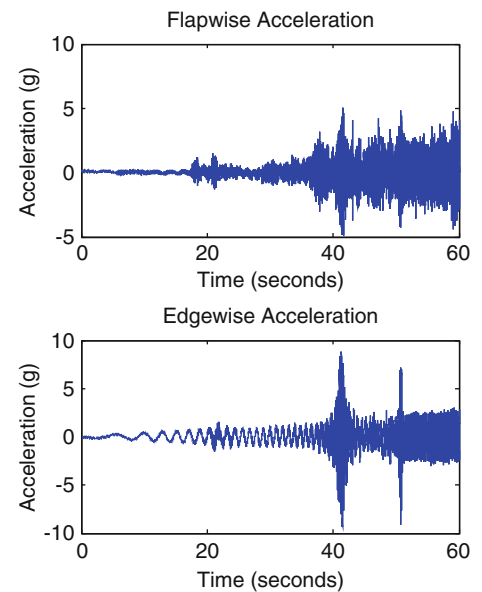
A full system operational test was performed on the turbine with both a wireless and wired acquisition system. The hub was replaced with a custom hub with the mounted wireless equipment shown in Fig. 56.10. The custom hub consisted of a 4-channel data NI 9234 acquisition module, connected to four 100 mV/g accelerometers on the blades, an NI WLS-9163 WiFi module carrier to transmit the data wirelessly, and two 18V batteries to provide power.

The accelerometers were placed at the blade tips to measure accelerations in the flapwise and edgewise directions. The tips of the blades were chosen for the position of the accelerometers because FAST can only provide the accelerations of the blades at the tips. Two accelerometers were also placed at the top of the tower, one parallel to the direction of the wind and one perpendicular to the direction of the wind. Once the structure was fully instrumented, the brake to the rotor was turned off and blades were allowed to spin up. Meanwhile, acceleration measurements were being acquired from the accelerometers on the blades, as well as on the tower. From our experimental setup, it was also possible to measure the power output of the turbine, the revolutions per minute of the rotor, and the input wind data. However, due to the time constraint under which we were, we were not able to make these three measurements. Therefore, the analysis of the full system operational tests

Fig. 56.10 Modified hub for wireless instrumentation



Fig. 56.11 Blade tip acceleration measurements



mainly dealt with the acceleration measurements. The results from the full system operational test enabled us to determine the natural frequency of the Whisper 500 by spectral analysis of the accelerometer data.

56.5.2 Test Results

The original acceleration measurements for the tips of the blade, obtained from the operational tests, are displayed in Fig. 56.11. In this figure, the blades begin to rotate at approximately 20 sec; then, as expected, the frequency increased as the turbine reached its cut-in torque. This raw acceleration data can be compared to the predicted acceleration measurements from FAST, as discussed below.

As an initial check for the success of our operational tests, we first drew comparisons between our fixed-free blade model and the power spectra obtained from the operational tests, during which the blades were not spinning. The power spectra are shown in Fig. 56.12.

The peak frequencies seen in these power spectra align well with the resonant frequencies determined from our fixed-free blade model. The frequencies given from our fixed-free blade model are 9.09, 26.98, 33.39, and 75.26 Hz, all of which compare well to what we find in the power spectra shown in Fig. 56.12.

Once this initial check was completed, a spectral analysis of the data from the operational tests, while the blades were rotating, was performed. The result from the spectral analysis performed for blade 1 in the flapwise direction is shown in Fig. 56.13. Seen from this figure, the dominating frequency of the Whisper 500 blade is near 200 Hz, with a harmonic of 400 Hz. It is also clear that this dominating frequency begins much lower, but then climbs to near 200 Hz. This is a result of

Fig. 56.12 Power spectra of the operational tests with no blade rotation

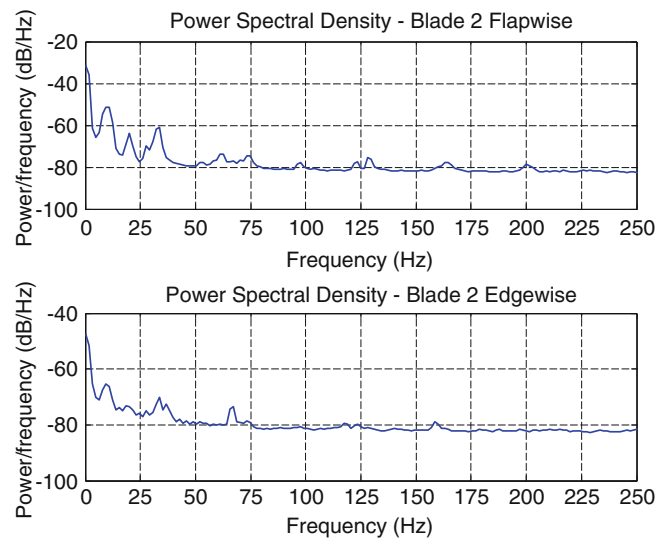
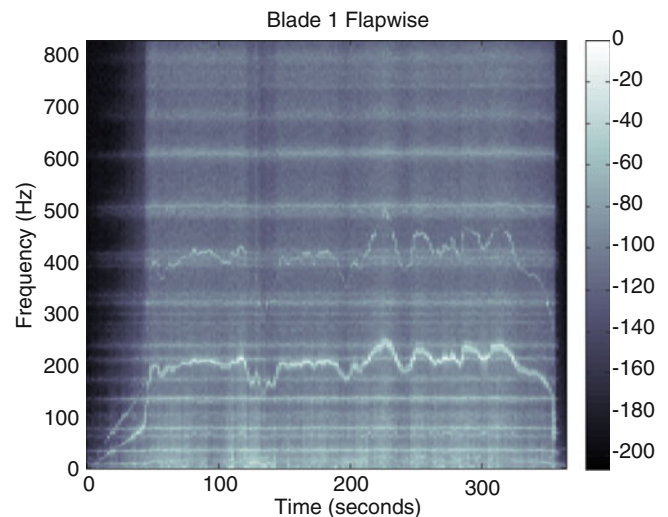


Fig. 56.13 Spectral analysis of Whisper 500 operational test for blade 1 in the flapwise direction



the blade spinning up to full speed from rest. The source of the 200 Hz signal has not been determined, but because of its strong presence on both the blades and the tower, it may be a slight imbalance in the main turbine bearing.

Another spectral analysis was then performed on the acceleration measurements obtained from the accelerometers on the top of the tower. The spectrogram obtained from this analysis is shown in Fig. 56.14. Once again, a dominant frequency is seen near 200 Hz. This suggests that there is a prevailing frequency in the entire structure. This frequency can be speculated to stem from a bearing; however, further investigation would need to be done in the future to verify this hypothesis.

56.5.3 Comparison with FAST Simulation

From our FAST simulation, we were able to obtain predictions for the blade-tip acceleration measurements. These results are displayed in Fig. 56.15. From these plots, it is apparent that the blades begin to rotate at approximately 30 sec, then, as expected, the acceleration measurements begin to oscillate violently. However, due to the inability to obtain wind properties as inputs for the FAST simulation, the predicted acceleration values do not prove to be especially useful in determining the validity of the FAST simulation. Thus, our analysis turned to the frequency domain.

From the results and plots of these predicted accelerations, we were able to run another spectral analysis and compare this with the analysis which we conducted for the operational experiment. To do this, we obtained an average wind speed from the nearby anemometer and entered this data into FAST. This gave us comparable data sets between the simulation and the experiment. The power spectra for both the FAST simulation and the operational tests are shown in Fig. 56.16.

Fig. 56.14 Spectrogram of whisper 500 operational test for tower-top in downwind direction

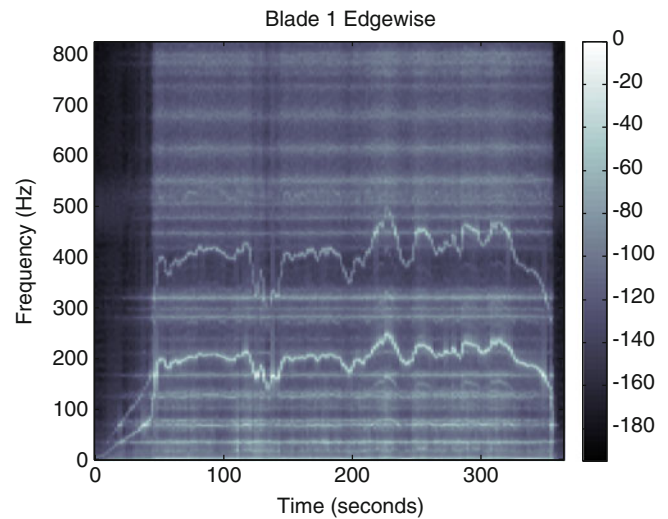
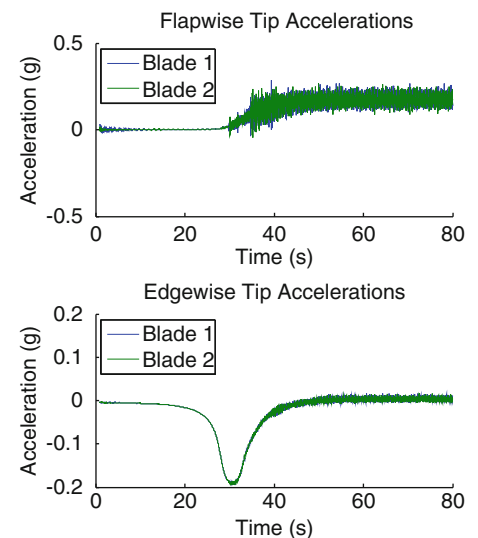


Fig. 56.15 Blade tip acceleration measurements



Ideally, the power spectra obtained from our FAST simulation would have peaks that would align with the peaks seen in the power spectra from the operational tests. However, as seen in figure, the peaks do not occur at similar frequencies. This indicates an inaccuracy in our FAST simulation that must be addressed in the future.

56.6 Conclusion

We have made a considerable amount of progress in getting a functional FAST simulation in the short nine weeks of the summer school. There is still much to be done in refining the simulation to get an acceptable correspondence in the full system operational test and the FAST results. Currently, the power curve for the simulation and the manufacturer's power curve compare well with each other with the exception the furling effect which occurs at higher wind speeds. The flapwise and edgewise blade tip accelerations do not appear to compare very well, but this could be due to the nature of the simulation versus the real world. The FAST simulation may be assuming perfect flapwise and edgewise deflections with no interference. While in the real world, this is not consistent with what the accelerometers are experiencing. Moreover, due to the lack of wind properties in the FAST simulation, concrete evidence to support or oppose a comparison between the measured accelerations and the predicted accelerations cannot be provided. In all, there is definitely room for improvement in our FAST simulation and future work for our project, which is discussed in the next section.

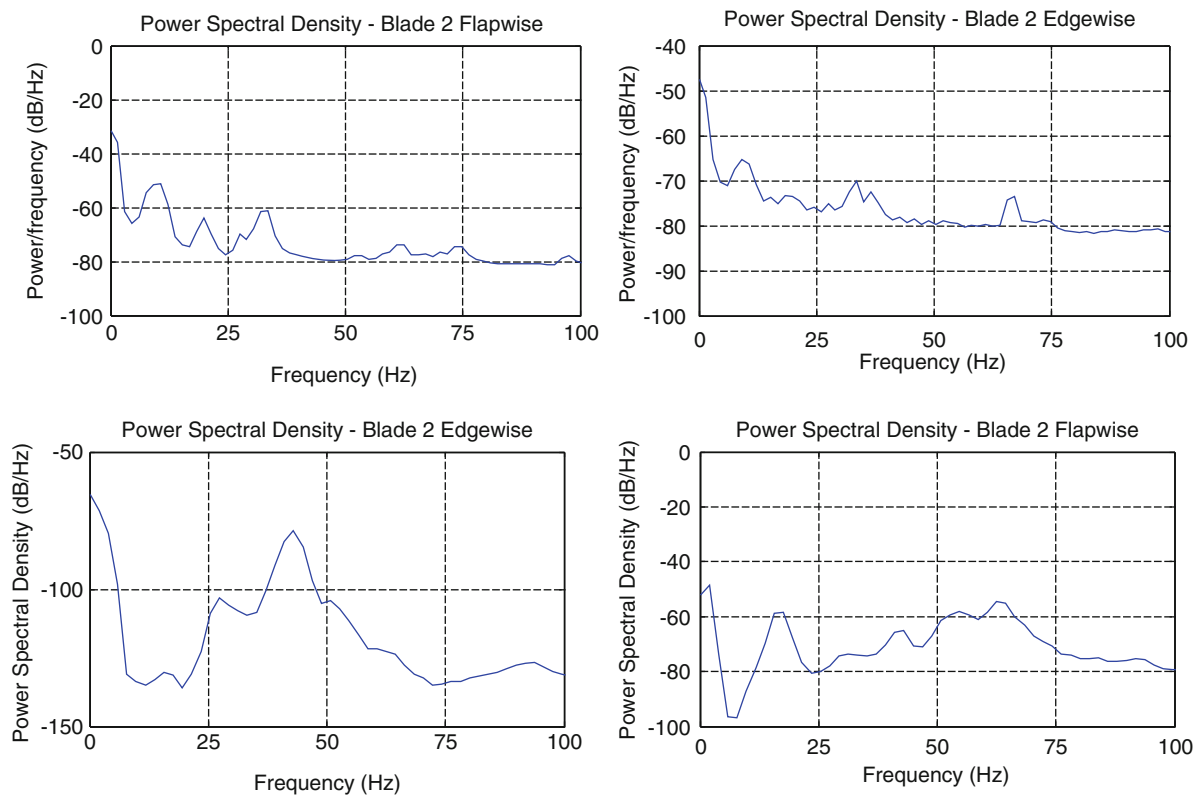


Fig. 56.16 Comparison of power spectra from FAST simulation (*top plots*) and operational tests (*bottom plots*)

56.6.1 Recommendations for Future Work

56.6.1.1 Wind Turbine Model

The inputs that were not vital to the model included parameters pertaining to the configuration of the turbine, such as hub mass and inertia, nacelle mass and inertia, and generator inertia and properties. These input values for the hub and nacelle mass were estimated from the specification sheet of the manufacturer. As for the other inputs, we essentially made an educated guess as to what they may be, and these inputs do not have a significant effect on the model. For future work, it is recommended that these values are systematically determined by measurements. The other option may be to obtain them directly from the manufacturer, but legal issues can make this path difficult.

56.6.1.2 Aerodynamic Inputs

The airfoil lift and drag coefficient curves were obtained numerically using JavaFoil. It is recommended that wind tunnel testing should be done to get these coefficients more true to their real values. The values could also be used to compare with the numerical solutions of JavaFoil. However, it is not clear what sort of impact changing the airfoil curves will have on the results of the simulation. This could also be investigated in the future.

56.6.1.3 Furling Dynamics

We did not include furling dynamics in our FAST simulation. Furling dynamics includes parameters such as the downwind, lateral, and vertical distances from the tower-top to the tail boom and tail fin center of mass. It also includes parameters that include the same distances for the tail fin center-of-pressure. FAST also needs values for tail-furl spring constant, damping constant, and a number of other constants to simulate tail-furl dynamics. Future work should be made to include tail-furling in the FAST simulation to get a more accurate power curve and model overall.

56.6.1.4 Further Comparisons

Once the previously stated improvements are made to the FAST simulation, further comparisons between the results of the FAST simulation and the operational tests need to be drawn. It is through these comparisons that the FAST simulation will ultimately be validated. Finally, only through the validation of the FAST simulation, will it be able to interface with the *WindBlade* program being developed at Los Alamos National Laboratory. This interface between the FAST simulation and *WindBlade* will ultimately allow for more complex interactions, such as turbine-to-turbine interactions, to be examined. This will prove to be a major step forward in the ongoing Intelligent Wind Turbine project.

Acknowledgements We would like to thank the University of California, San Diego and the Los Alamos Dynamics Summer School program in providing us with the opportunity to work on this project. We would also like to thank the following companies and people in providing us with software and codes that we used: NREL, SIMULIA, Vibrant Technology Inc., and Martin Hepperle. Thanks to Pete Avitabile (University of Massachusetts, Lowell) for providing advice and guidance for our project.

References

1. (2008) 20% Wind Energy by 2030: Increasing Wind Energy's Contribution to U.S. Electricity Supply. DOE/GO-102008-2567 July 2008
2. Erickson M (2012) Intelligent wind turbine project
3. Erickson M (2012) HIGRAD/Windblade—wind generation modeling and simulation
4. Jonkman JM, Buhl Jr ML (2005) FAST user's guide. National Renewable Energy Laboratory, Golden, CO NREL/TP-500-38230, October 2005
5. Cha P, Jahiu V, Peck N, Reade L, Rinker J, Russell A, Wornick H (2011) LANL wind turbine clinic. Clairmont
6. Nonis C, Garrett S, Taylor SG, Farinholt KM, Park G (2012) Dynamic characterization of whisper 500 turbine blade. In: Mayes R, Rixen D, Griffith DT, De Klerk D, Chauhan S, Voormeeren SN, Allen MS, (eds.) Topics in experimental dynamics substructuring and wind turbine dynamics, vols. 2 and 27. Springer, New York, pp 247–266
7. *ME'scopeVES*. <http://www.vibetech.com>
8. Hepperle M (2007) In: JavaFoil-analysis of airfoils, ed
9. Hansen DC (2012) In: NWTC design codes-airfoilprep, ed

Chapter 57

Sizing Optimization of Trapezoidal Corrugated Roof Sheeting, Supporting Solar Panels, Under Wind Loading

P. Sharafi, Lip H. Teh, and Muhammad N.S. Hadi

Abstract The dimensions of trapezoidal roof sheeting supporting solar panels are optimized so that a minimum amount of steel is required for a specific range of wind loads. Sheets of different grades and different thicknesses along with different ranges of wind speeds are considered. In order to simulate the behavior of the corrugated sheets analysis is carried out for two limit states: strength and serviceability. For both limit states, the objective is to minimize the weight per unit area of the panels. First, optimum cross-section is obtained to meet the strength conditions. Then the deflection is controlled for serviceability. The optimum dimensions for each steel grade and loading condition are determined. The optimization problem is formulated as a multi-objective problem that aims to minimize the section's weight and maximize the section elastic modulus under the wind loading condition. A graph theory based approach is presented for the sizing optimization, employing an applied graph theory approach for the multi-objective all pairs shortest path problem. The proposed methodology addresses the sizing optimization problem to determine the geometry of the thin-walled cold-formed steel cross-sections that satisfy the design topological constraints.

Keywords Sizing optimization • Roof sheeting • Wind load • Graph theory • Multi-objective optimization

57.1 Introduction

Cold-formed steel profiles are manufactured by bending thin sheets of steel to desired shapes allowing efficient and light profiles to be used where conventional hot-rolled profiles prove to be uneconomic. One of the main advantages of cold-formed steel profiles is the great flexibility of cross-sectional shapes to the manufacturing process allowing almost any desired cross-sections to be achieved. The cross-sectional shape is the key element in enhancing the strength of cold-formed steel profiles as it controls the three fundamental buckling modes: local, distortional (for open profiles) and global. Cold-formed profiled metal sheeting and decking are well-established construction products and manufacturers make strenuous efforts to keep these products competitive in terms of the carrying capacity for a given weight of material.

Most sheeting and decking profiles can sustain considerable redistribution of bending moment so that the attainment of the calculated moment of resistance at an internal support is not immediately followed by failure. After yielding and/or buckling at the support, 'plastic hinge' action occurs, possibly accompanied by a reduction in the moment of resistance, until failure takes place when the full moment of resistance is attained within the span. Because the mid-span moment of resistance is often greater than the (reduced) moment of resistance at a support, the increase in the load carried as a result of this moment redistribution can be considerable [1].

Since the steel sheets can be formed to almost any shape to suit structural and constructional requirements, finding optimal shapes for cold-formed steel sections is a problem of strong interest, where optimization of sections is aimed at achieving efficient use of the steel material either by maximizing the desirable properties of the section for a given mass and/or by minimizing the mass for a given application. Optimization of thin-walled steel sections is mostly performed to obtain improvements in strength, serviceability, and vibration characteristics.

P. Sharafi (✉) • L.H. Teh • M.N.S. Hadi

School of Civil, Mining and Environmental Engineering, University of Wollongong, Northfields Avenue, Wollongong, NSW 2522, Australia
e-mail: ps170@uow.edu.au; lteh@uow.edu.au; muhhammad_hadi@uow.edu.au

Because of the many types of sheeting available and the diverse functional requirements and loading conditions that apply, design and optimization of sheeting is generally based on experimental investigation. Therefore, there are a limited number of published papers in the literature on the theory based optimization of cold-formed sheeting steel structures. Lee et al. [2] optimized the profile of corrugated claddings by minimizing the bending stresses due to the bending moment for a set of dimensional constraints on the coverage, the contour length, and the height of the profile. Lu and Mäkeläinen [3] applied genetic algorithms for optimization of dimensions of cold-formed steel trapezoidal sheeting to obtain the minimum weight subjected to the given constraints.

The structural performance of a cold-formed steel section depends not only on the characteristics of their components, but also on their relative locations and connectivity (topology). Graph theory based modes are powerful means to represent structural systems so that their geometry and topology can be understood clearly. A graph can be used to represent almost any physical situation involving discrete objects and the relationships among them. Graph theory methods are readily formulated for a wide range of structural problems as a result of interaction with other fields of mathematics, and can be applied with only minimal changes to a wide range of combinatorial optimization problems [4–8].

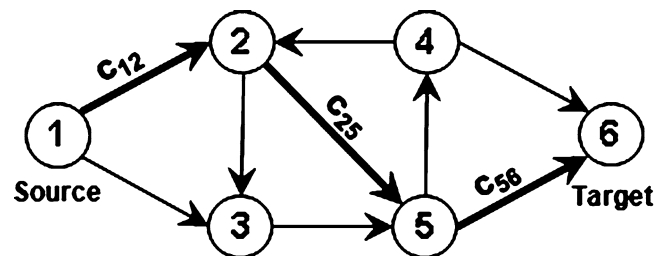
During the last few decades, combinatorial optimization and graph theory methods have experienced fast developments since many problems in combinatorial optimization arise directly from everyday practice in engineering and management. One of the advantages of graph theory based approaches is that an optimization problem of a continuous form can be transformed to one of a discrete form, where the variables belonging to the space R^n are finite dimensional. In fact, graph theory approaches can be considered as a link between discrete spaces and continuous ones. Employing the graph theory, the sizing optimization problem changes to a combinatorial optimization problem of discrete space.

This paper presents a graph theory approach for sizing optimization of cold-formed steel sections. The main concern is not to investigate thoroughly the advantages of the graph theory approach over alternative approaches. The primary objective is to illustrate a general method to find the dimensions of minimum mass and/or maximum strength for cold-formed steel sections that satisfy the constraints. The sizing optimization of sheeting is treated as a multi-objective shortest path problem. Then, the method is employed to optimize the dimensions of trapezoidal panels carrying solar modules on, in order to minimize the weight of sheeting as well as resisting a specific range of wind loading and/or hail stones impact loads under some constraints.

57.2 Multi-objective Shortest Path Problems

A multi-objective optimization problem $f = (f_1, f_2, \dots, f_Q)$ is a problem of finding a vector of decision variables that satisfies the constraints and optimizes the vector function f whose elements f_i through f_Q represent the Q number of objective functions, which are usually in conflict with each other. In the present graph theory approach, the objective of the shortest path problem is to find a shape for the thin-walled steel section that has the minimum mass possible and the maximum strength possible [9].

A graph $G(N, E)$ consists of a set of nodes N and a set of edges E , with a relation of incidence that associates each edge with a pair of nodes as its ends. As shown in Fig. 57.1, a path P of graph G is a finite sequence whose terms are alternately nodes and edges, in which no edge or node appears more than once. A cycle C is a path for which the starting node and the ending node are the same; i.e. a cycle is a closed path. The length of a path (or cycle) L is taken as the number of its edges.



A path and the corresponding cost:

$$P = [n_1, e_{12}, n_2, e_{25}, n_5, e_{56}, n_6]$$

$$\text{cost: } L(P) = c_{12} + c_{25} + c_{56}$$

Fig. 57.1 A path and the corresponding cost on a directed graph

In the graph theory, the shortest path problem is the problem of finding a path from a specified node called the source, to a second specified node, called the destination (or target), such that the sum of the weights (or lengths) of its constituent edges is minimized. It is relevant to a wide variety of real world applications, such as in telephone routing, material distribution, salesperson routing, investment strategies and personnel scheduling. The shortest path problem is an NP-hard combinatorial optimization problem, which means that it is strongly believed that they cannot be solved to optimality within polynomially bounded computation time. To practically solve large instances, one often has to use heuristics that returns near-optimal solutions in a relatively short time [10, 11].

Consider a weighted undirected graph $G(N, E)$. Let $n = |N|$ and $m = |E|$. Each edge $e_{ij} \in E$ is assigned a cost (or length) of c_{ij} . If c_{ij} has multiple criteria, the problem is called a multi-objective shortest path problem. In this case the edge e_{ij} has associated values c_{ij}^k , in which $k \in \{1, 2, \dots, r\}$ for each criterion $k=1, 2, \dots, r$. Obviously, for undirected graphs $c_{ij}^k = c_{ji}^k$. The adjacency set $A(i)$ for node i is the set of all edges incident from i , that is $A(i)=\{(i,j)|(i,j) \in E\}$. The integer programming formulation for the multi-objective shortest path problem from Node s to Node t can be given as follows [12]:

$$\min f = \left(\sum_{i,j \in V} c_{ij}^1 e_{ij}, \sum_{i,j \in V} c_{ij}^2 e_{ij}, \dots, \sum_{i,j \in V} c_{ij}^r e_{ij} \right) \quad (57.1)$$

$$\forall e_{ij} \in E : e_{ij} = \begin{cases} 1 & \text{if Edge } e_{ij} \text{ is chosen} \\ 0 & \text{if Edge } e_{ij} \text{ is not chosen} \end{cases} \quad (57.2)$$

$$\forall i \in N - \{s, t\} : \sum_j e_{ij} - \sum_k e_{ki} = 0 \quad (57.3)$$

$$\forall i, j \in N : \sum_i e_{si} - \sum_j e_{js} = 1 \quad (57.4)$$

$$\forall i, j \in N : \sum_i e_{it} - \sum_j e_{tj} = 1 \quad (57.5)$$

Equation (57.1) represents the objective and Eq. (57.2) defines the binary variable e_{ij} . Equations (57.3), (57.4), and (57.5) are the constraints.

Equation (3), as an ordinary flow conservation constraint, states that for all nodes except for the source and target points, the edges leaving them are equal to the edges entering them. Equations (57.4) and (57.5) state that the difference between the number of edges leaving the source and target points and the number of edges entering them, respectively, is one. In other words, the edges are not on a cycle.

57.3 Discrete Sizing Optimization

To minimize the mass is to minimize the cross-section area A . Since the thickness of the cross-section is uniform and invariable, the mass minimization of the section reduces to the length minimization of the section. The dimensional constraints on the elements (edges) of a cross-section are defined considering the effective width (or depth) for the elements [13]. Some fabrication, construction or manufacturing constraints may also be applied to the cross-sectional dimensions.

Although it is believed that a sizing optimization problem with discrete design variables is more difficult to solve than a similar problem with continuous design variables, structural optimization methods employing the zero–one based decision making scheme are capable of dealing with the sizing optimization problem using discrete variables [14, 15]. In a sizing optimization problem, there are a finite number of variables along with some benchmarks defining the boundary of the cross-section. Figure 57.2 shows the benchmarks and the complete variables of some standard sections. Depending on the problem at hand, each variable defined in Fig. 57.2 may or may not be used as a design variable.

Consider a cross-section of sheeting, lying in the x - y plane under a general set of actions, resulting in compression, flexural, torsional and shear action effects. The problem is to find the dimensions resulting in the optimum mass and section strength. ‘‘Section strength’’ is a generic term that corresponds to the imposed action effects.

In order to define a graph model for dimension optimization, the first step is to discretize the search space for each variable. To that end, each variable x_i is bounded between $[Min(x_i), Max(x_i)]$ with interval (accuracy) of ε , then each variable x_i rests in the set of $[Min(x_i), Min(x_i)+\varepsilon, \dots, Max(x_i)-\varepsilon, Max(x_i)]$, which contains $m_i = ((Max(x_i) - Min(x_i))/\varepsilon) + 1$ possible conditions.

Fig. 57.2 Benchmarks and variables for sections of constant thickness

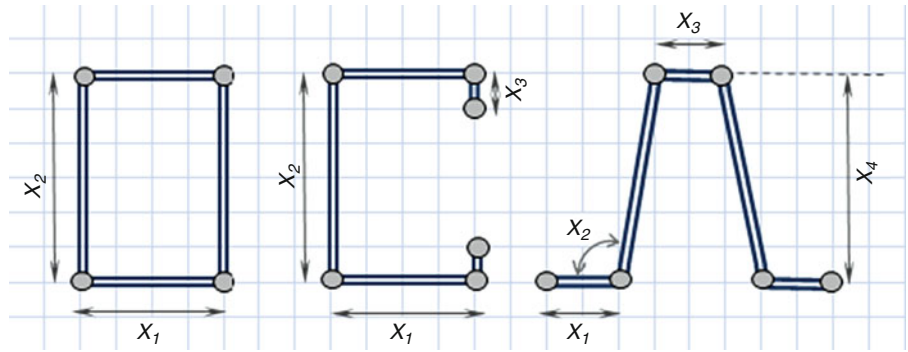
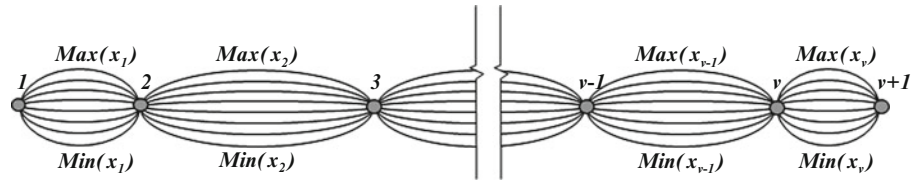


Fig. 57.3 A graph for dimension optimization



If the number of variables is v , the graph corresponding to the sizing optimization problem consists of $n = v + 1$ nodes and $m = v \sum m_i$ edges as shown in Fig. 57.3 [16]. Any path through the graph represents a section with known dimensions. The objective functions are formulated in the same manner as those shown in the preceding section on shape optimization.

Now, the problem of sizing optimization is a multi-objective single-pair shortest path problem whose aim is to find the shortest path between a specific pair of nodes. The optimization problem can generally be formulated as follows:

$$\begin{aligned} \min f &= (W, 1/S_G) \\ \text{s.t. } &\begin{cases} \text{geometrical constraints} \\ \text{constraints on strength} \end{cases} \end{aligned} \tag{57.6}$$

where W is the section’s mass, and S_G is the section strength that is a generic term and, depending on the instance may mean the strength with respect to axial compression, flexural, torsional or shear action effects. In practice, the parameters that represent the section strength are mostly the second moments of area, the torsion constant or the cross-sectional area. The geometrical constraints in sizing optimizations of cold-formed steel sections, on the other hand, may be due to the design standards, the manufacturing and the installation requirements. For example, AS/NZ4600 [13] imposes dimensional limitations, such as maximum width to thickness ratio of the plate element.

Since in practice it is almost impossible to optimize the dimensions of sections with respect to various limit states, the section strength is dealt with as a single objective in the rest of this paper, which renders the problem represented by Eq. (57.6) a bi-objective optimization problem. However, it should be noted that the underlying approach is valid and applicable for multiple limit states. In the present study, the optimum solution is the one that provides the best compromise between two potentially conflicting objectives of mass minimization and flexural strength maximization. One approach for finding the solution is to find the Pareto-optimal set, or at least a good approximation of it.

57.4 Sizing Optimization of Roof Sheeting

The abovementioned methodology is employed for cross-sectional optimization of trapezoidal corrugated sheeting, supporting solar panels, under wind loading. The optimization is carried out on trapezoidal corrugated sheets for roofing “Lysaght Trimdek”, produced by BlueScope Steel [17], of three different grades and eight different thicknesses as shown in Table 57.1. Lysaght Trimdek, shown in Fig. 57.3, is a suitable roof profile for installing solar panels on. According to Eqs. (57.1) and (57.6), there are two potentially conflicting objectives, mass minimization and flexural strength maximization.

Three ranges of wind speeds are considered from the Australian Standards for wind loads for housing (AS 4055–2006) [18], as shown in Table 57.2. Geometrical constraints are either manufacturing constraints or the ones that are required by Australian/New Zealand standards for cold-formed steel structures (AS/NZS 4600:2005) [13] as shown in

Table 57.1 Mechanical properties of steel sheets

Steel type	Thickness (BMT mm)	Yield strength (MPa)	Yield strain	Ultimate strength (MPa)	Ultimate strain
ST1	0.55	300	0.0015	340	0.18
	0.60	300	0.0015	340	0.18
	0.80	300	0.0015	340	0.18
ST2	0.35	550	0.00275	550	0.01
	0.42	550	0.00275	550	0.01
	0.48	550	0.00275	550	0.01
	0.60	550	0.00275	550	0.02
	0.80	550	0.00275	550	0.02
	0.90	550	0.00275	550	0.02
	1.00	550	0.00275	550	0.02
ST3	0.35	750	0.00375	750	0.01
	0.42	750	0.00375	750	0.01
	0.48	750	0.00375	750	0.01
	0.55	750	0.00375	750	0.01
	0.60	750	0.00375	750	0.02
	0.80	750	0.00375	750	0.02
	0.90	750	0.00375	750	0.02
1.00	750	0.00375	750	0.02	

Table 57.2 Wind loading pressure

Wind class	Design guest wind speed (m/s)		Pressure for roof (kPa)	
	Serviceability limit state	Ultimate limit state	Ultimate strength	Serviceability
N3	32	50	-3.00	-1.33
N4	39	61	-4.47	-2.14
N5	47	74	-6.57	-3.29

Table 57.3 Manufacturing geometric constraints

Flat pan width (H2)		Rib Height (V1)		Support Spacing (L)		Flat Pan Height (V2)	
Min (mm)	Max (mm)	Min (mm)	Max (mm)	Min (mm)	Max (mm)	Min (mm)	Max (mm)
350	700	16	50	600	1200	0	20

Tables 57.3 and 57.4. The aim is to optimize the dimensions of the trapezoidal panel in order to minimize its mass (first objective) and maximize its flexural stiffness (second objective).

As shown in Fig. 57.4, four geometric design variables are defined for the problem: rib height (V1), rib width (H1), rib slope (θ) and flat pan midpoint height (V2). Due to the solar panels fixed width, being installed on flat pan (around 400 mm), the width of flat pan is considered constant. That is, for all models H2 is assumed to be 400 mm. Therefore, using the single-pair shortest path problem, the construction graph for this problem consists of five nodes.

For solving the shortest path problem arisen from the sizing optimization there are many algorithms and methods, [19]. In this paper [anAntColonyalgorithm](#) is used to deal with the problem. The principles of the algorithm can be found in [16, 20, 21]. The shortest path is the one with the minimum weight. Therefore in the problem of bi-objective shortest path problem arisen from the sizing optimization of the sheeting, the optimum solution for each case is the first one in the Pareto optimal set.

The sensitivity analysis of the model, in relation to the involved parameters, is demonstrated in Fig. 57.5, which shows how sensitive each parameter is to the variations of design variables. As can be seen in Fig. 57.5, the trapezoidal panels' mass, maximum deflection and maximum normal strain are most sensitive to the thickness. In the ranges defined for the variables, the panels' mass is least sensitive to the flat pan height. However, deflection, maximum normal strain and maximum equivalent (Von-Mises) strain are highly sensitive to the flat pan height. The maximum equivalent elastic strain is most sensitive to the angle of ribs. Almost all stated parameters are not highly sensitive to the ribs height in the range defined for them (between 16 to 50 mm). The optimum points, stated in Table 57.4, verify the above mentioned results.

Results suggest that, for the steel Grades 2 and 3 (ST2 and ST3) a minimum sheeting thickness of 0.48 mm is required for wind class N4 and N5, due to serviceability constraints. For the steel grades 1 (ST1), all sheeting thickness seem to be suitable for wind class N3, N4 and N5.

Table 57.4 Optimum design points for wind loading

Wind class	Steel grade	Thickness (mm)	Optimum design points				Weight per unit area (kg/m ²)	Recommended span length (mm)	
			H1 (mm)	V1 (mm)	V2 (mm)	θ (deg)			
N3	ST1	0.55	15	16	16	72	4.376	950	
		0.60	15	16	16	72	4.773	1000	
		0.80	15	16	16	72	6.364	1100	
	ST2	0.35	19	21	18	71	2.924	600	
		0.42	19	21	18	71	3.507	700	
		0.48	19	21	18	71	4.010	800	
		0.60	19	21	18	71	5.014	950	
		0.80	19	21	18	71	6.684	1100	
		0.90	19	21	18	71	7.520	1150	
	ST3	1.00	19	21	18	71	8.355	1200	
		0.35	15	16	11	61	2.857	600	
		0.42	15	16	11	61	3.429	700	
		0.48	15	16	11	61	3.919	800	
		0.55	15	16	11	61	4.491	900	
		0.60	17	17	14	70	4.947	950	
	N4	ST1	0.55	18	17	19	71	4.543	850
			0.60	18	17	19	71	4.956	900
			0.80	18	17	19	71	6.608	1000
ST2		0.35	19	21	18	72	2.924	650	
		0.42	19	21	18	72	3.507	750	
		0.48	19	21	18	72	4.010	800	
		0.60	19	21	18	72	5.014	900	
		0.80	19	21	18	72	6.684	1000	
		0.90	19	21	18	72	7.520	1050	
ST3		1.00	19	21	18	72	8.355	1100	
		0.35	15	16	11	61	2.857	650	
		0.42	15	16	11	61	3.429	750	
		0.48	15	16	11	61	3.919	800	
		0.55	15	16	11	61	4.491	850	
		0.60	15	16	11	61	4.898	900	
N5		ST1	0.55	18	17	19	71	4.543	750
			0.60	18	17	19	71	4.956	800
			0.80	18	17	19	71	6.608	900
	ST2	0.35	19	21	18	72	2.924	600	
		0.42	19	21	18	72	3.507	650	
		0.48	19	21	18	72	4.010	700	
		0.60	19	21	18	72	5.014	800	
		0.80	19	21	18	72	6.684	900	
		0.90	19	21	18	72	7.520	950	
	ST3	1.00	19	21	18	72	8.355	1000	
		0.35	15	16	11	61	2.857	600	
		0.42	15	16	11	61	3.429	650	
		0.48	15	16	11	61	3.919	700	
		0.55	15	16	11	61	4.491	750	
		0.60	17	17	14	71	4.947	800	
			0.80	17	17	14	71	6.576	900
			0.90	17	17	14	71	7.810	950
			1.00	17	17	14	71	8.244	1000

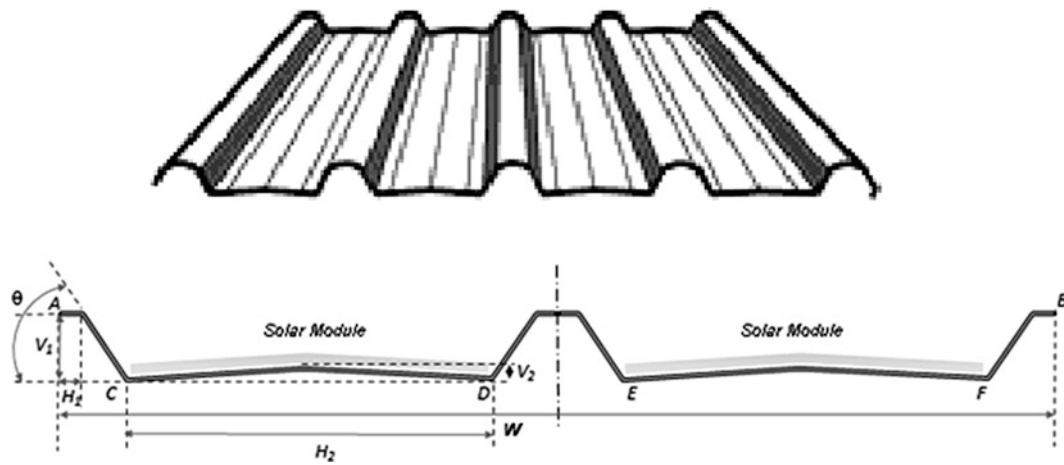


Fig. 57.4 The initial selected profile (Lysaght Trimdek)

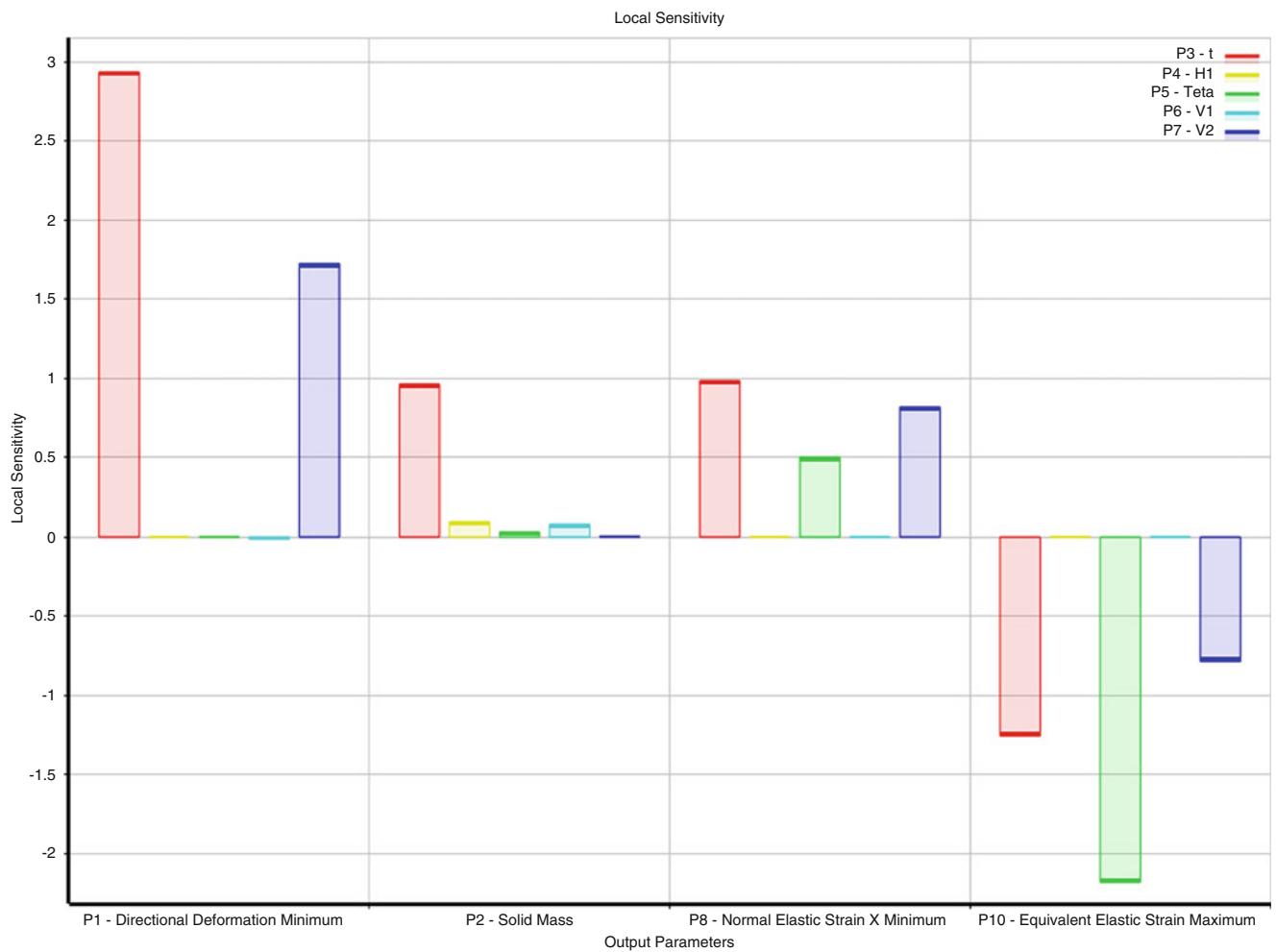


Fig. 57.5 Design sensitivity in relation to the involved parameters

57.5 Concluding Remarks

A new method for sizing optimization of cold-formed steel sections is presented using a graph theory approach. The optimization problem is formulated as a multi-objective problem that aims to minimize the section's mass and maximize the section flexural strength. The sizing optimization of sheeting is treated as a multi-objective shortest path problem.

Lysaght Trimdek sheets of different grades and different thicknesses along with different ranges of wind speeds are considered. In order to simulate the behavior of the corrugated sheets analysis is carried out for limit states design. The objective is to minimize the weight per unit area of the panels along with the maximum flexural strength. The presented method can be applied to a wide range of similar multi-objective sizing optimization problems.

Acknowledgements Funding of this research project was provided by the Bluescope Steel Metallurgy Centre at the University of Wollongong, sponsored by the Faculty of Engineering and Bluescope Steel Limited. Any opinions expressed are those of the authors alone.

References

- Davies JM, Jiang C (1997) Design procedures for profiled metal sheeting and decking. *Thin-Walled Struct* 27(1):43–53
- Lee C-L, Mioduchowski A, Faulkner MG (1995) Optimization of corrugated claddings. *J Struct Eng* 121(8):1190–1196
- Lu W, Mäkeläinen P (2006) Fuzzy optimization of cold-formed steel sheeting using genetic algorithms. *J Constr Steel Res* 62(12):1276–1281
- Kaveh A (2004) *Structural mechanics: graph and matrix methods*. Research Studies Press, Hertfordshire, UK
- Kaveh A (2006) *Optimal structural analysis*. Research Studies Press, Hertfordshire, UK
- Kaveh A, Sharafi P (2008) Ant colony optimization for finding medians of weighted graphs. *Eng Comput* 25(2):102–120
- Kaveh A, Sharafi P (2008) Optimal priority functions for profile reduction using ant colony optimization. *Finite Elem Anal Des* 44(3):131–138
- Kaveh A, Sharafi P (2009) Nodal ordering for bandwidth reduction using ant system algorithm. *Eng Comput* 26(3):313–323
- Sharafi P (2013) *Cost Optimization of Preliminary Layout Design of Framed RC Structures*. PhD Thesis, University of Wollongong, Australia
- Korte B, Vygen J (2012) *Combinatorial optimization: theory and algorithms*. Springer, Germany
- Lawler EL (2001) *Combinatorial optimization: networks and matroids*. Dover Publications, Mineola, USA
- Reinhardt LB, Pisinger D (2011) Multi-objective and multi-constrained non-additive shortest path problems. *Comput Oper Res* 38(3):605–616
- As/Nz4600 (2005) *Cold formed steel structures*. Standards Australia Limited/Standards New Zealand, Sydney
- Steven GP, Li Q, Xie YM (2002) Multicriteria optimization that minimizes maximum stress and maximizes stiffness. *Comput Struct* 80(27–30):2433–2448
- Burns SA (2002) Recent advances in optimal structural design. American Society of Civil Engineers. Structural Engineering Institute. Technical Committee on Optimal Structural Design
- Sharafi P, Hadi MNS, Teh LH (2012) Heuristic approach for optimum cost and layout design of 3D reinforced concrete frames. *J Struct Eng* 138(7):853–863
- LYSAGHT TRIMDEK® (2010) *BlueScope_Steel* <http://www.lysaght.com/product/lysaght-trimdek>: Australia
- As4055 (2006) *Wind Loads for housing.*, Standards Australia Limited/Standards New Zealand, Sydney
- Gross JL, Yellen J (2003) *Handbook of graph theory*. CRC Press, USA
- Sharafi P, Hadi MNS, Teh LH (2012) Optimum column layout design of reinforced concrete frames under wind loading. In: Caicedo JM, et al (eds) *Topics on the dynamics of civil structures*, vol 1. Springer, pp 327–340
- Sharafi P, Hadi MNS, Teh LH (2012) Optimum spans, lengths of multi-span reinforced concrete beams under dynamic loading. In: Caicedo JM, et al (eds) *Topics on the dynamics of civil structures*, vol 1. Springer, pp 353–361

Chapter 58

Establishment of Optimized Digging Trajectory for Hydraulic Excavator

Tatsuya Yoshida, Takayuki Koizumi, Nobutaka Tsujiuchi, Kan Chen, and Yozo Nakamoto

Abstract Efficiency of digging operation of hydraulic excavator is affected by the geometry of digging trajectory. To improve the operation efficiency, appropriate trajectory design is important. In this report, we developed a simulation model to establish optimized trajectories. This model involves a soil and a front linkage model of an excavator. A Distinct Element Method (DEM) is adopted for the soil model. The DEM is able to describe soil behavior during digging operation and to estimate digging soil volume and load quantitatively. Generative force and energy consumption of hydraulic cylinders are calculated by the kinematic model which solves inverse dynamics of front linkage of hydraulic excavators. Geometric shapes of the trajectory are determined with some trajectory parameters in this study. Using these generated trajectories and the simulation model, consumed energy and digging soil volume of every trajectory is calculated. Analyzing these results, the optimal digging trajectory is established. Effectiveness of the optimized trajectory is validated by comparing with a skilled operator's digging trajectory which is reproduced on the simulation. In addition, efficient trajectory for horizontal ground is established by using this developed simulation model.

Keywords Hydraulic excavator • Trajectory generation • Optimization • Distinct element method • Inverse dynamics

58.1 Introduction

Since high level skills are required to operate a hydraulic excavator, hydraulic excavator automatization is being studied to reduce operator's workload and to improve safety and economic efficiency. A method of tracking preprogrammed digging trajectories was devised for the automatic control of a hydraulic excavator, and control systems with good tracking accuracy have been proposed [1–3]. For trajectory planning, a method [4] minimizes kinetic energy during loading operations into a dump truck to improve productivity. However, few specific planning methods exist in relation to trajectory generation for digging operations since it is difficult to specify the optimal trajectory that considers the productivity of digging operations because of such factors as the geometry of the digging trajectory and the soil property. To improve productivity, research [5] has experimentally established the optimal trajectory, but an experimental method that considers various digging situations needs huge time and effort.

In this paper, we developed a digging simulation model to estimate the efficiency of digging operations by tracking the digging trajectory and assigning one to improve efficiency. We defined the payload per unit energy as the digging efficiency for a performance index, which evaluates the digging operation efficiency. In simulations, we parameterized the geometry of the digging trajectory and the cylinder's consumption energy and analyzed the payload when the excavator digs based on the trajectory. Then, we calculated the workload and the consumption energy of cylinders. The efficiency of the digging operation was evaluated using developed model and the generated trajectory based on the parameters. We assigned an optimal trajectory by evaluating the efficiency of various parameters. Then, we reproduced the digging trajectories of skilled operators in simulations and evaluated the efficiency. We compared the efficiency of the generated and skilled operator trajectories and

T. Yoshida • T. Koizumi • N. Tsujiuchi • K. Chen (✉)
Department of Mechanical Engineering, Doshisha University, 1-3 Tatara-Miyakodani, Kyotanabe, Japan
e-mail: dtl0306@mail4.doshisha.ac.jp

Y. Nakamoto
Caterpillar Japan Ltd., 1106-4 Shimizu Uozumicho Akasi, Hyougo, Japan

verified their effectiveness and the design process of the digging trajectory for automatic digging with the simulation model. In addition, we use the developed model to figure out efficient trajectories for digging operations which are started with a flat ground.

58.2 Soil Model

58.2.1 Motion Equation of Distinct Element Method

Based on distinct element method theory [6], the model calculates the forces in the normal and tangential directions that act on particle i from other contacting particles. These resultant forces are regarded as the force acting on a particle, and the following equations of motion describe the behavior of each particle:

$$m \frac{d^2 \mathbf{w}_i}{dt^2} = m \mathbf{g} + \Sigma \mathbf{F}_n + \Sigma \mathbf{F}_s \tag{58.1}$$

m : mass of particle, \mathbf{w}_i : position vector of particle
 \mathbf{g} : gravity vector.

58.2.2 Force Working Between Particles

The force between particles is calculated for the normal and tangential directions based on the Voigt model shown in Fig. 58.1. η is the coefficient of viscosity and K is the stiffness coefficient, the n subscript shows the normal direction of the particles, and s subscript shows the tangential direction.

When particles contact, the reaction and damping forces act in the normal direction. The reaction force is calculated by Hooke's law. Stiffness K_n in the normal direction of particles i and j is determined by the Hertz contact theory:

$$K_n = \frac{4}{3} \frac{1}{\left(\frac{1 - \nu_i^2}{E_i^2} + \frac{1 - \nu_j^2}{E_j^2} \right)} \sqrt{\frac{\delta}{\left(\frac{1}{r_i} + \frac{1}{r_j} \right)}} \tag{58.2}$$

ν : Poisson's ratio of particle, δ : penetration of particles
 E : Young's module of particle, r : radius of particle.

where, K_n and the time step of the simulation affect the convergence of the solution of Eq. (58.1) [6].
 The coefficient of viscosity η is resolved as follows:

$$\eta_n = 2\zeta \sqrt{m K_n} \tag{58.3}$$

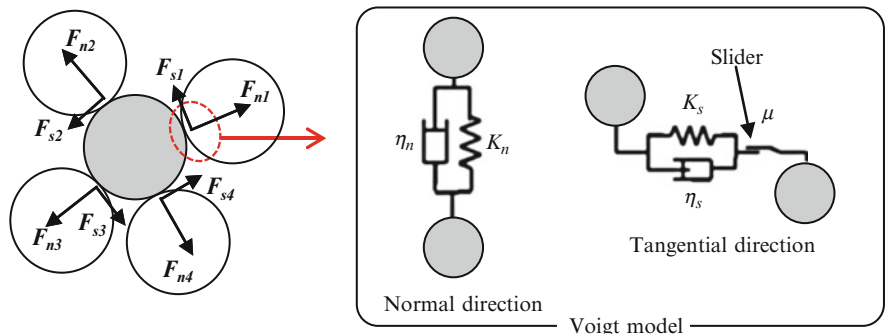


Fig. 58.1 Modeling of particles

where ζ is the damping ratio. Force F_n acting in the normal direction is calculated as follows:

$$F_n = K_n u_n + \eta_n \frac{du_n}{dt} \quad (58.4)$$

u_n is the relative displacement in the normal direction of two particles.

Shear forces are calculated by shear coefficient s , which is converted from a coefficient of rigidity using the coefficient of transformation:

$$K_s = K_n s \quad (58.5)$$

$$\eta_s = \eta_n \sqrt{s} \quad (58.6)$$

$$s = \frac{G}{E} = \frac{1}{2(1 + \nu)} \quad (58.7)$$

G : share modulus of rigidity.

The friction force acts among the particles. When the particles move in the shearing direction, the friction force is calculated. When the force generated with a spring and a dashpot exceeds the maximum static friction force, the friction slider acts. Therefore, share force F_s is calculated by the following conditional expression using the coefficient of friction μ :

$$F_s = \begin{cases} \mu F_n & \left(\mu F_n < \eta_s \frac{du_s}{dt} + K_s u_s \right) \\ \eta_s \frac{du_s}{dt} + K_s u_s & \left(\mu F_n \geq \eta_s \frac{du_s}{dt} + K_s u_s \right) \end{cases} \quad (58.8)$$

58.2.3 Calculation of Payload

When one simulation is finished, payload M_d is calculated based on particles n_p over the bucket. Because this digging simulation is a two-dimensional model, the following equation provides an equivalent payload with bucket width w_b and density of soil ρ :

$$M_d = \pi r^2 w_b \rho n_p \quad (58.9)$$

58.3 Front Linkage Model

We calculate forces of three cylinders by solving the inverse kinematics and the inverse dynamics. When the bucket angle and the tip coordinate are given from a preprogrammed digging trajectory, the position and the angle of each part are uniquely determined based on the front linkage configuration of the excavator. By solving this inverse kinematics problem for each linkage part, the inertial force acting on each part is calculated. In addition to the calculation of the inertial forces, the bucket reaction force analyzed by the distinct element method model is considered the external force. We formulate dynamic balance equation of the front linkage with considering the bucket reaction force of the soil.

58.3.1 Inverse Kinematics of Hydraulic Excavator

The intersection of the ground and the pivot at the swing center of the upper structure is defined as the origin of the global coordinate. The horizontal direction is indicated as x , and the vertical direction is indicated as y (Fig. 58.2). Next, as shown in Fig. 58.3, joint 1 of the boom, joint 4 of the arm, tip end E of the bucket, joint 7 of the guide link, and joint 10 of the bucket link are respectively defined as the origins of each part coordinate system.

Fig. 58.2 Front linkage of hydraulic excavator

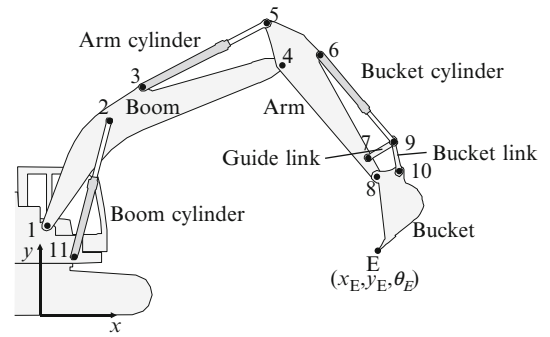
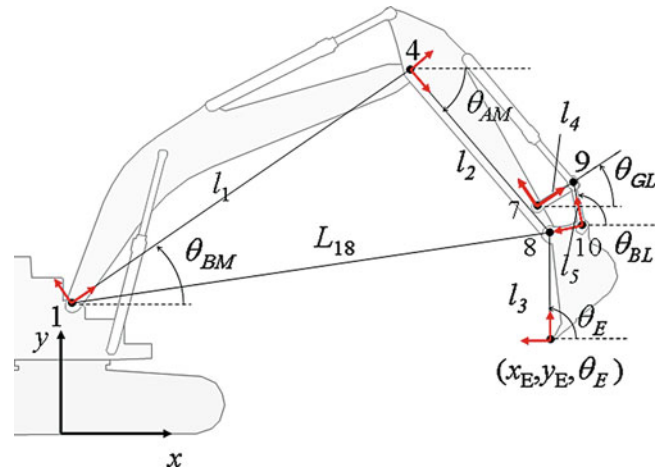


Fig. 58.3 Definition of angles of the parts



The angle of the local part coordinate system with respect to the global coordinate are calculated from the coordinates of tip (x_E, y_E) and bucket angle θ_E , which are regulated by a digging trajectory. In the following expression, the position vector of i -th joint i in the global coordinate system is expressed as $P_i = (x_i, y_i)^T$.

The following is the global coordinate at joint 8:

$$P_8 = P_E + R(\theta_E)^{BK} P_8 \tag{58.10}$$

where $^{BK}P_8 (= [l_3, 0]^T)$ shows the position vector at joint 8 in the bucket coordinate system. The upper left subscript shows a coordinate system. When there is no upper left subscript, the position vector is indicated in the global coordinate system. $R(\theta_E)$ shows a rotation matrix. Applying the law of cosines to the triangle comprised of joints 1, 4, and 8, the boom angle is expressed as follows:

$$\theta_{BM} = \cos^{-1} \left(\frac{L_{18}^2 + l_1^2 - l_2^2}{2L_{18}l_1} \right) + \text{Atan2}(y_8 - y_1, x_8 - x_1) \tag{58.11}$$

L_{18} is the distance between joints 1 and 8, and Atan2 is a four-quadrant inverse tangent. The arm angle is shown as follows:

$$\theta_{AM} = \text{Atan2}(y_4 - y_8, x_4 - x_8) \tag{58.12}$$

The global coordinates of joint 4 can be shown as follows using the boom angle and the coordinate at joint 4 in the boom coordinate system that is calculated from formula (58.11):

$$P_4 = P_1 + R(\theta_{BM})^{BM} P_4 \tag{58.13}$$

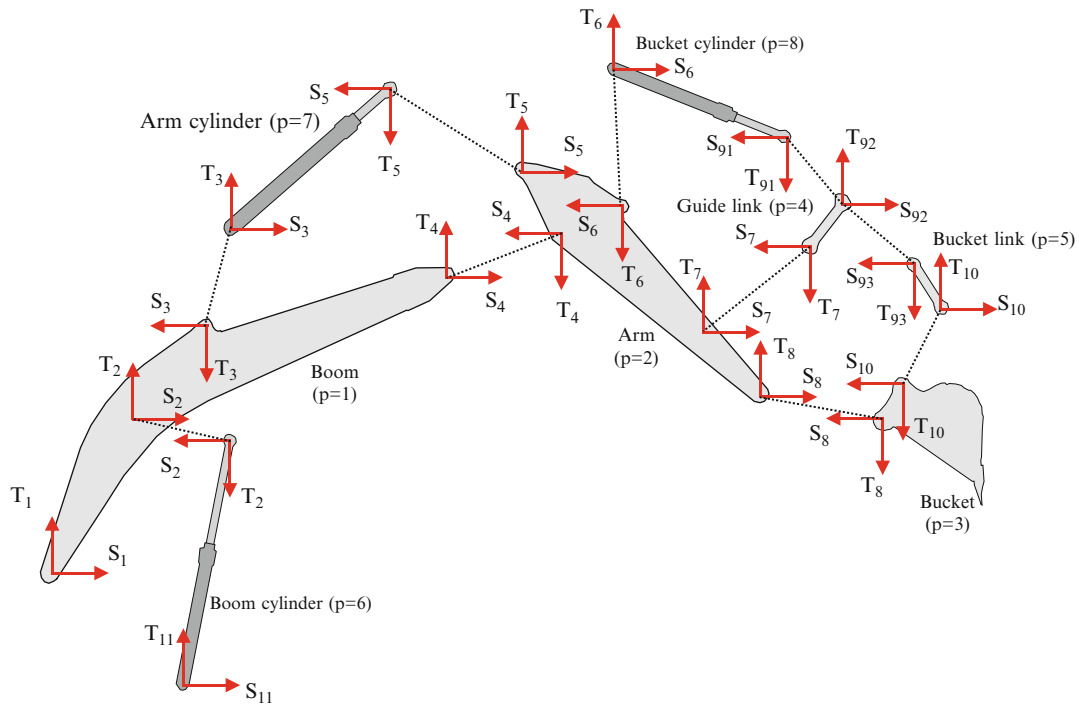


Fig. 58.4 Joint forces

Moreover, the angles of the bucket and guide links are

$$\theta_{GL} = \cos^{-1} \left(\frac{L_4^2 + l_{410}^2 - l_5^2}{2L_4 l_{410}} \right) + \text{Atan2}(y_{10} - y_7, x_{10} - x_7) \tag{58.14}$$

$$\theta_{BL} = \text{atan2}(y_{10} - y_9, x_{10} - x_9) \tag{58.15}$$

where L_{710} is the distance between joints 7 and 10. The global coordinates at joints 9 and 10 are

$$P_{10} = P_E + R(\theta_E)^E P_{10} \tag{58.16}$$

$$P_9 = P_7 + R(\theta_{GL})^{GL} P_9 \tag{58.17}$$

The position and posture of each part coordinate system of the excavator’s linkage with respect to the global coordinate system can be calculated from the above formulas. When the barycentric coordinates of the parts in each part coordinate system are given, the center of gravity in the global coordinate systems is calculated and the dynamic analysis shown below can be done.

58.3.2 Dynamic Analysis

We calculated the accelerations of each part by the numerical differentiation of the barycentric coordinates given by solving the inverse kinematics based on a digging trajectory and conducted inverse dynamic analysis. In this inverse dynamic analysis, the directions of joint reaction force $R_i = [S_i, T_i]^T$, which acts on the i -th joint, are defined in Fig. 58.4, and the dynamic balance equations are expressed as these reaction forces. These equations are simultaneous and include joint reaction forces R_i as unknown variables. Therefore, the cylinder end forces and the joint reaction force are derived by solving the simultaneous equations [7].



On each part, the balance equation of the forces and the moments are derived by considering the inertia force and reaction force. Except for the bucket, the following formula is expressed for about seven parts:

$$M_p \ddot{\mathbf{P}}_{Cp} + M_p \mathbf{g} + \mathbf{R}_n + \dots + \mathbf{R}_m = \mathbf{0} \quad (58.18)$$

$$I_p \ddot{\theta}_p + [(\mathbf{P}_n - \mathbf{P}_{Cp}) \times \mathbf{R}_n] + \dots + [(\mathbf{P}_m - \mathbf{P}_{Cp}) \times \mathbf{R}_m] = 0 \quad (58.19)$$

Here subscript $p(=1, 2, 4, 8)$ shows the number of parts. M_p is the mass of each part, \mathbf{g} is the vector of the gravitational acceleration, and \mathbf{P}_{Cp} is the position vector of the center of gravity on part p .

On the bucket, the balance equation includes bucket reaction force calculated soil model. The force, which acted on the i -th particles of a bucket, is applied as \mathbf{F}_{DEMi} and position vector \mathbf{P}_{DEMi} of the working point. The balance equation of the force and the moment on the bucket is expressed as follows:

$$M_3 \ddot{\mathbf{P}}_{C3} + M_3 \mathbf{g} + \mathbf{R}_8 + \mathbf{R}_{10} + \sum_{k=1}^n \mathbf{F}_{DEMk} = \mathbf{0} \quad (58.20)$$

$$I_3 \ddot{\theta}_3 + [(\mathbf{P}_8 - \mathbf{P}_{C3}) \times \mathbf{R}_8] + [(\mathbf{P}_{10} - \mathbf{P}_{C3}) \times \mathbf{R}_{10}] + \sum_{i=1}^n [(\mathbf{P}_{DEMi} - \mathbf{P}_{C3}) \times \mathbf{F}_{DEMi}] = 0 \quad (58.21)$$

where M_3 is the mass of the bucket, I_3 is its inertia moment, and \mathbf{P}_{C3} is the position vector of the center of gravity on the bucket coordinate system. 24 equations were derived from eight parts of the excavator. Moreover, the next relation exists at joint 9:

$$-\mathbf{R}_{91} + \mathbf{R}_{92} - \mathbf{R}_{93} = \mathbf{0} \quad (58.22)$$

In these force and moment equations, the forces acting at each joint are calculated by 26 simultaneous equations that involve joint reaction forces S_i and T_i as unknowns.

58.3.3 Energy Consumption and Efficiency Evaluation

The reaction forces, which act at the cylinder end that is calculated by solving the inverse dynamics of the linkage, are regarded as cylinder generated forces. Reaction force \mathbf{R}_2 is the boom cylinder force, \mathbf{R}_5 is the arm cylinder force, and \mathbf{R}_9 is the bucket cylinder force. By solving the inverse kinematics, the coordinates of both ends of each cylinder are derived and the operating velocities of the cylinders can be calculated. Therefore, the cylinder energy, which is necessary for digging operations based on preprogrammed trajectories, is

$$E = \int_0^{t_f} (|\mathbf{R}_2| \dot{L}_{BM} + |\mathbf{R}_5| \dot{L}_{AM} + |\mathbf{R}_9| \dot{L}_{BK}) dt \quad (58.23)$$

where t_f shows the finishing time of a digging operation.

The digging operation efficiency is evaluated by the energy shown in (58.23), and digging soil mass M_d is calculated by the soil model. Authors define the digging efficiency as follows:

$$\text{Digging efficiency} = \frac{M_d}{E} \quad [kg/kJ] \quad (58.24)$$

When more soil is excavated with low energy, this index increases and shows the effectiveness of the digging operation from the viewpoint of energy efficiency.

58.4 Verification of Simulation Model

To verify the simulation model's accuracy, we compared the simulation results with measurement digging test data. The model simulated an excavation test by a skilled operator (Fig. 58.5a) and compared the calculated cylinder forces with the measured cylinder forces. The slope shape, the digging trajectory, and the initial posture, all of which were reproduced in the simulation, are shown in Fig. 58.5b. The slope angle was set to 33.6° because it was measured in the test.

Cylinder generative force is calculated from the measuring data of the cylinder pressure, and a comparison is shown in Fig. 58.6 with the calculation results of the cylinder generative force by simulation. Since the fluctuation tendency in the analysis value agrees well with the measured data, the model can actually reproduce digging operations. Productivity evaluations of digging can be performed using this model. The vibration of the cylinder force is due to the vibration of the calculated bucket reaction force by the soil model.

58.5 Trajectory Generation

In this trajectory generation method, three pass points of the bucket tip are set by parameters and interpolated to generate digging trajectories and determined as apexes of triangle ABC based on the following procedure with these parameters: C_r : area ratio of triangle ABC for bucket capacity, d : maximum depth, R_{ABD} : area ratio triangle ABD for triangle ABC, and θ_B : bucket angle at point B (Fig. 58.7). The velocity of the bucket tip motion is regulated to 1.1 [m/s], which is the average velocity of the skilled operator who performed excavation test shown in above.

Since analysis by the DEM model is time-consuming, Authors selected in advance some trajectories that can move with lower cylinder energy. The digging trajectories were generated within the limits of the parameters shown in Table 58.1, and the cylinder consumption energy was only computed using a front linkage model. We searched the combinations of



Fig. 58.5 Digging test by skilled operator. (a) Measurement (b) Simulation (initial orientation)

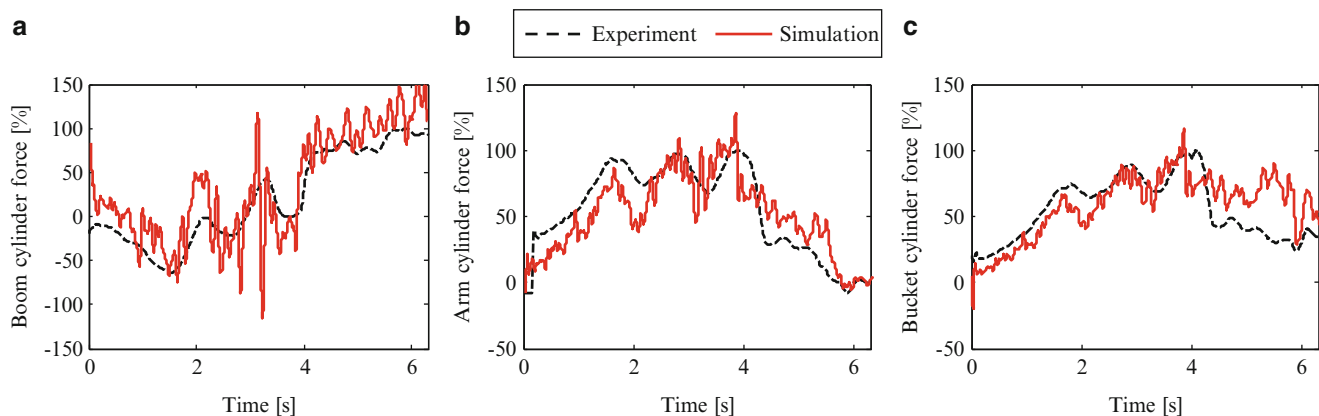


Fig. 58.6 Cylinder force. (a) Boom cylinder; (b) Arm cylinder; (c) Bucket cylinder

Fig. 58.7 Decision of geometry for trajectory

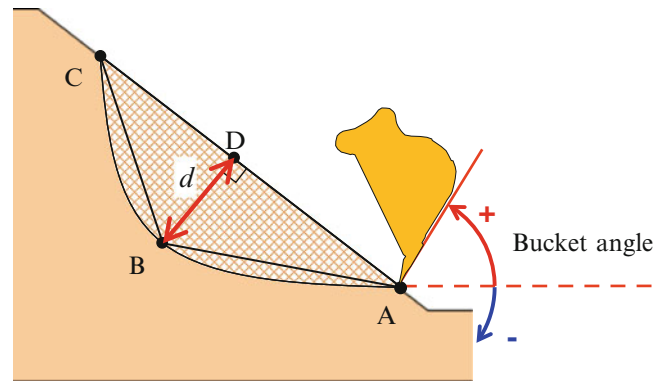


Table 58.1 Parameters for trajectory

	Minimum	Maximum
Capacity ratio C_r	0.8	1.5
Digging depth d	0.3	1.3
Area ratio of ABD R_{ABD}	0.2	0.3
Bucket angle at point B θ_B	-50	50

parameters whose cylinder consumption energy minimized by using an optimization software modeFRONTIER. We selected 100 trajectories whose consumption energy fell in ascending order, performed a simulation that combined the soil and front models using these trajectories, and evaluated the digging efficiency.

58.6 Estimation of Productivity

58.6.1 Digging Efficiency

The model carried out 100 digging simulations to track the generated trajectories in accordance with the trajectory generation method shown in Sect. 58.5. Furthermore, the digging trajectory of the skillful operator, which is shown in Sect. 58.4, was reproduced in the simulation to evaluate the digging.

The result of the digging energy and the payload based on 100 digging trajectories and the result of the skillful operator are shown in Fig. 58.8. The straight line shows the level contour line of the digging efficiency. The skilled operator's digging efficiency is 3.89 [kg/kJ], and the result is shown as the red plus mark in this figure. The green circles show the simulation results of the generated trajectories. The blue circle shows the result of the highest digging efficiency in all simulation results. The digging result with this trajectory is considered the optimal digging, and digging efficiency exceeded the skilled operator by more than 10%.

58.6.2 Comparison with Skilled Operators

The digging trajectory shapes are shown in Fig. 58.9. These trajectories are the skillful operator and the generated trajectories that obtained the result shown by the blue circle in Fig. 58.8. The generated digging trajectory is shallower than the skilled operator's trajectory with respect to the slope. Therefore, the skilled operator's bucket reaction force (Fig. 58.10) becomes larger than the generation trajectory. Deep intrusion into the slope increases the soil mass, which is thrust up, and increases the digging resistance force by passive earth pressure [8]. For this reason, the digging resistance force decreases when the digging trajectory becomes shallower, and the cylinder generative force also decreases. The generated trajectory decreases the generative force of the arm and bucket cylinders (Fig. 58.11). During digging operations, since the arm and bucket cylinders are mainly operated to fill the bucket with soil, the total energy required for digging operations was decreased by suppressing the generative force of these two cylinders.

Fig. 58.8 Simulation result

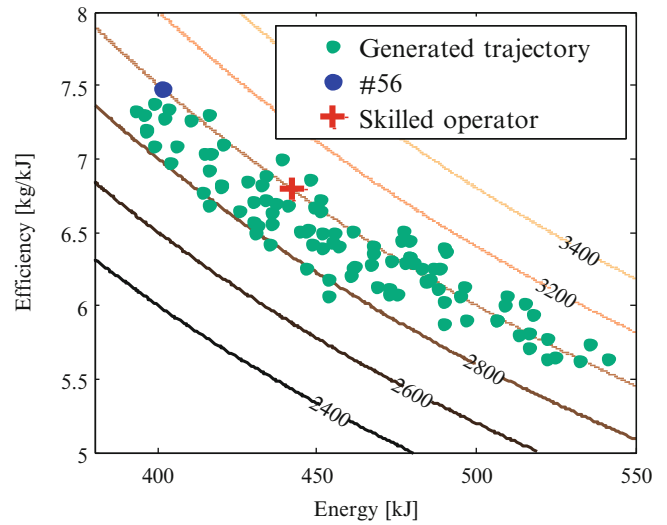


Fig. 58.9 Digging trajectory

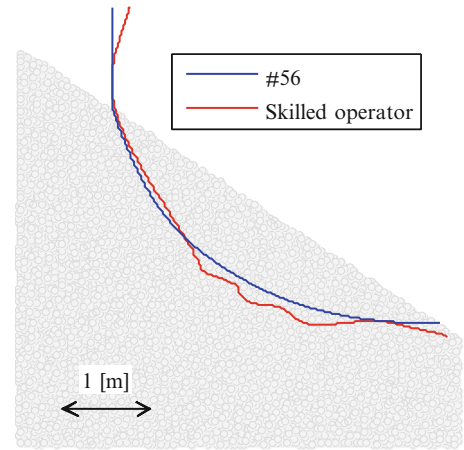
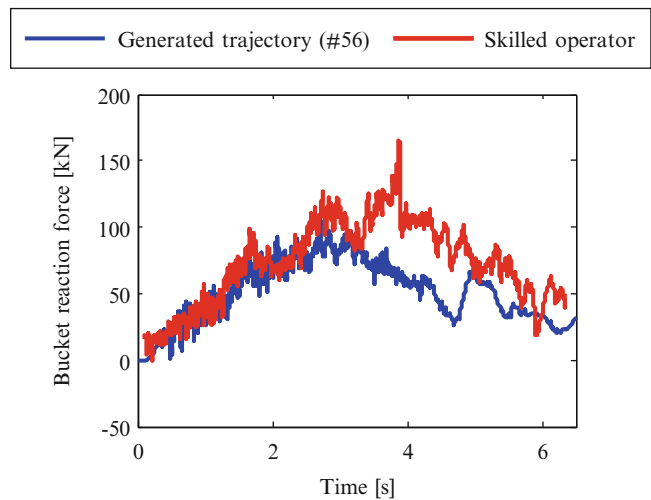


Fig. 58.10 Bucket reaction force



Although the decrease of the digging depth is one reason for a decreased payload, there is no clear difference of payload result (Fig. 58.8) between the generated trajectory and the skilled operator. When the generated trajectory is applied to the simulation, the number of soil particles that drop from the bucket becomes less than the skilled operator’s operation. Based on the generated trajectory, the bucket orientation is expected to decrease the amount of soil that falls from the bucket. Automatic digging with higher productivity than skilled operators can be realized using the digging trajectory shown in this research.

Fig. 58.11 Cylinder force.
(a) Arm cylinder (b) Bucket cylinder

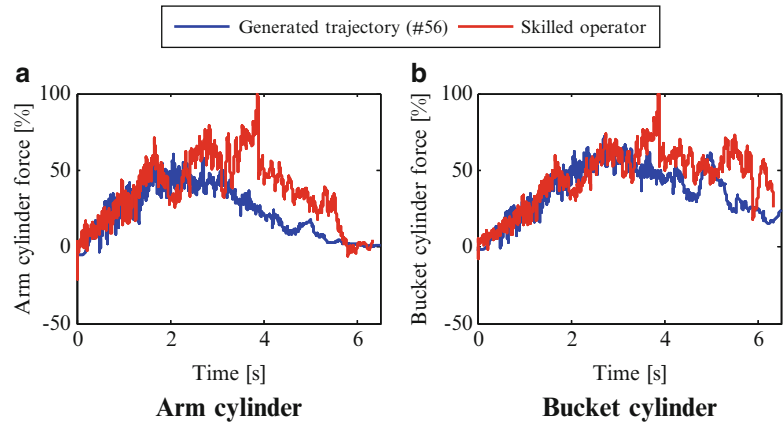


Table 58.2 Parameters of trajectory for horizontal plane

	Minimum	Maximum
Capacity ratio: C_r	1.5	3.0
Digging depth: d	0.5	2.0
Area ratio of ABD: R_{ABD}	0.3	0.8
Bucket angle at point B: θ_B	-20	50
Initial bucket angle: θ_I	58	100

58.7 Trajectory Study for Flat Ground

58.7.1 Establishment of High Efficiency Trajectory

We have established a high efficiency trajectory for 33.6 degree slope. However, digging operations usually start from flat ground. Thus we used the developed model to identify a high efficiency trajectory for flat ground. Method of trajectory generation is the same as what we introduced in previous chapter. The parameters of trajectory for flat ground are shown in Table 58.2. The initial bucket angle θ_I is been employed in this case additionally. We also used the optimization software modeFRONTER to search combinations of the parameters whose cylinder consumption energy is the minimum and selected 100 trajectories whose consumption energy fell in ascending order. Then we performed a simulation by these trajectories using the combined soil and front models, and evaluated the digging efficiency. Digging efficiencies of selected trajectories are shown in Fig. 58.12.

We chose the results of test No.6, 7, 47 and 52 because their digging efficiency is higher than others. We also chose results of test No.33 and 82 because they have a relatively higher digging efficiency and higher digging amount than other tests. Parameters of those chosen results are shown in Table 58.3.

By comparing those parameters, we can conclude that when capacity ratio is around 1.7, digging depth is around 1meter, area ratio of ABD is 0.47, angle at point B is 30 and initial bucket angle is around 80 degree, the digging efficiency is the highest. Shapes of these trajectories are shown in Fig. 58.13. They show a similar outline and we consider that this shape is an efficient trajectory for digging operation from a flat ground.

58.7.2 Simulation Results Comparison for Different Shapes of Trajectories

To clarify how trajectory shapes influence digging efficiency, we added two different shaped trajectories which are deep and short distance one (No.4594) and shallow and long distance one (No.4852) to compare with No.82 trajectory. All of their digging areas are around twice than bucket capacity. Shapes of these trajectories are shown in Fig. 58.14. Simulation results of them are shown in Table 58.4.

From Table 58.4, we can figure out that No.82 shows the highest cylinders efficiency (payload divided by cylinders consumed energy). By comparing results of No.82 with No.4594, digging energy (energy consumption only depends on reaction force from soil, not involves energy for moving front parts of an excavator) of No.4594 is much higher than No.82. It is because digging depth of No.4594 is deeper than that of No.82. When bucket reaches the deepest point and moves

Fig. 58.12 Simulation results for flat ground digging

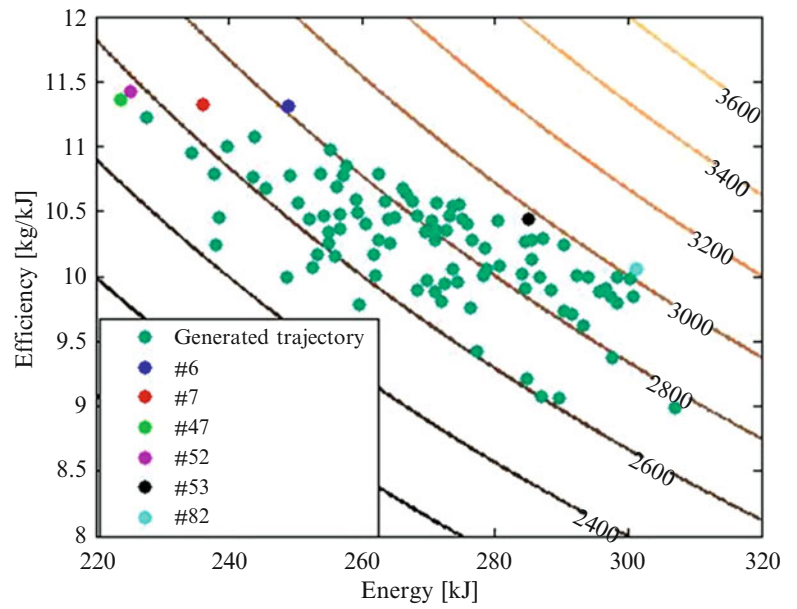


Table 58.3 Parameters of high efficiency trajectories

Test number	Capacity ratio	Digging depth (m)	Area ratio of ABD	Angle at point B (deg)	Initial bucket angle (deg)
6	1.82	0.93	0.47	30	77.78
7	1.71	0.93	0.47	30	82.22
47	1.61	0.93	0.47	30	77.78
52	1.61	0.93	0.47	30	82.22
33	2.04	1.04	0.47	35	82.22
82	2.14	1.04	0.47	35	82.22

Fig. 58.13 High efficiency digging trajectories

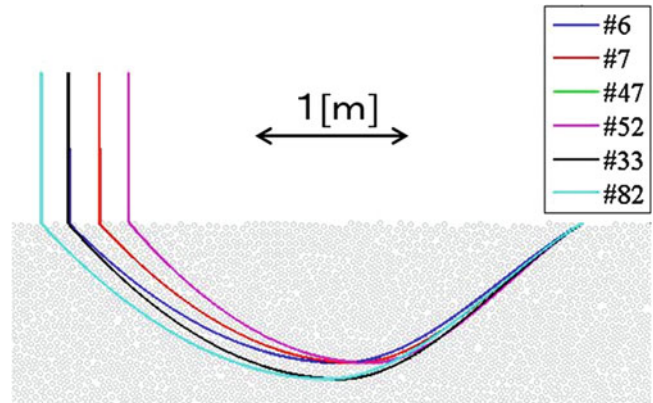


Fig. 58.14 Comparison digging trajectories

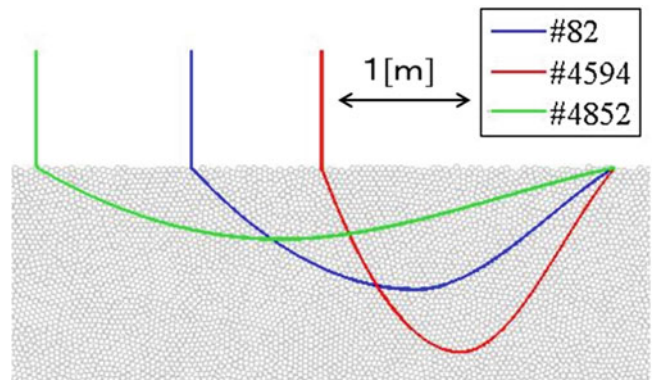


Table 58.4 Simulation results of comparison trajectories

Test number	Payload (kg)	Digging energy (kJ)	Cylinder energy (kJ)	Accumulate cylinders displacement (m)	Cylinders efficiency(Kg/KJ)
82	3029	9	301	1.42	10.06
4594	2833	12	503	1.54	5.64
4852	2657	8	370	1.91	7.18

upwards, the amount of soil in front of the bucket tip is more than that of a shallow one. That is means the reaction force from soil is bigger when digging depth is deeper, and this leads the cylinders to consume more energy to raise bucket. On the other hand, digging depth of No.4852 is lower than that of No.82, and its digging energy is lower than No.82 also. But the cylinders efficiency of No.4852 is smaller than No.82. This is because the accumulate cylinders displacement of No.4852 is much longer. To push cylinders with a longer distance needs more hydraulic power and this consumes much more energy. Thus an effective trajectory should be a suitable one which is not too deep or too shallow.

58.8 Conclusion

In this study, we combined two-dimensional distinct element methods and an inverse dynamic analysis of hydraulic excavator's linkage to quantitatively estimate digging efficiency. We parameterized the geometry of digging trajectory and identified a one that improves digging efficiency. We conclude as follows:

- (1) We established a trajectory generation process that is parameterized for optimization.
- (2) The digging efficiency of the optimized trajectory outperforms skilled operator.
- (3) Our optimized digging trajectory shows shallower and smaller cylinder forces than trajectory of skilled operator.
- (4) Optimized trajectories for multi slope angle are generated for real operation.

References

1. Araya H, Kagoshima M (2001) Semi-automatic control system for hydraulic shovel. *Automat Constr* 10(4):477–486
2. Lee S-U, Chang PH (2002) Control of a heavy-duty robotic excavator using time delay control with integral sliding surface. *Contr Eng Pract* 10(7):697–711
3. Chang PH, Lee S-J (2002) A straight-line motion tracking control of hydraulic excavator system. *Mechatronics* 12(1):119–138
4. Yoo S, Park C-G, You S-H, Lim B (2010) A dynamics-based optimal trajectory generation for controlling an automated excavator. *Proc Inst Mech Eng Part C* 224(10):2109–2119
5. Maciejewski J, Jarzebowski A (2002) Laboratory optimization of the soil digging process. *J Terramechanics* 39(3):161–179
6. Society of Powder Technology (2001) Initiation of particle simulation. *Sangyotosho* 29–33 (in Japanese)
7. Shinsuke A, Koichi I, Hiroshi S (1986) The optimal shape design of a linkage mechanism used for power shovels. *Trans Jap Soc Mech Eng* 52(483):2982–2988 (in Japanese)
8. Sarata S, Kawai Y, Tomita F, Osumi H (2004) Trajectory arrangement based on resistance force and shape of pile at scooping motion. *Proc IEEE Int Conf Robot Automat* 4:3488–3493

Chapter 59

Modeling, Simulation, and Optimization of California High-Speed Rail Bridge Under Earthquakes

Yong Li and Joel P. Conte

Abstract To meet ever-growing demands on California transportation infrastructure, the California High-Speed Rail (CHSR) Project is underway inspired by the successful high-speed train systems worldwide. Seismic risk tends to be a critical concern to the CHSR bridges in California on the structural engineers' side as the proposed CHSR bridges will be in close proximity to several major seismic faults such as the San Andreas and Calaveras faults. Considering the social-economic functions of high-speed rail bridges, the optimal design of such bridges based on advanced structural modeling, seismic response simulation and performance evaluation are of significant importance to guarantee the dedicated high-speed train services after earthquakes. These issues are addressed in this paper for a CHSR prototype bridge testbed. To mitigate the seismic risk, seismic isolation strategies and segmental displacement control techniques (slotted hinge joints) are integrated into the design of this bridge. Numerical modeling and seismic response simulation are carried out to predict the performance of this bridge. An optimization problem in the context of the probabilistic Performance-based Earthquake Engineering (PBEE) methodology is proposed and illustrated conceptually to optimize the seismic isolator parameters to obtain a satisfactory trade-off between the deformation of the bridge piers and the deformations of the seismic isolators (inducing rail deformations).

Keywords High-speed rail bridge • Modeling • Simulation • Seismic isolation • Performance-based earthquake engineering • Optimization

59.1 Introduction

Inspired by successful high-speed train systems worldwide, the electrically-powered high-speed trains will help the state of California meet ever-growing demands on its transportation infrastructure [1]. As the California High-Speed Rail (CHSR) facility structures will provide a wide range of functions for the system, a consistent design with different objectives needs to be applied and enforced. Additionally, the proposed CHSR will be located close to several major seismic faults like the San Andres and Calaveras faults, and approximately two thirds of the routes are within 25 km (15.5 miles) of an active fault [2]. Thus, High-speed Rail Bridges or Arial Structures, as one of the primary supporting systems, need to be designed with special considerations to carry dedicated high-speed train services after seismic events. To ensure technical consistency and appropriateness, it will impose some constraints on the structural design side. In order to enhance the overall seismic performance of High-speed Railway Bridges, a variety of innovative seismic protection technologies have been proposed as a potential strategy to mitigate the seismic damage and possible interruption of operation after an earthquake. As seen in practice, isolation systems tend to be a promising alternative as base isolators have demonstrated extensive successes and become popular all over the world. The mechanism of isolation systems will reduce the base shear and columns drift in a bridge during earthquakes compared to the traditional fixed connection design, at the cost of increasing the deck displacement due to elongation of the fundamental period [3].

Y. Li (✉) • J.P. Conte

Department of Structural Engineering, University of California, 9500 Gilman Dr., San Diego, CA 92093-0085, USA
e-mail: yongli@ucsd.edu; jpconte@ucsd.edu

59.2 CHSR Prototype Bridge and Finite Element (FE) Modeling

A three dimensional numerical model of a 9-span seismic isolated prototype bridge for the CHSR Project is developed in the structural analysis software framework OpenSees [4]. This finite element model is used to study the performance of seismic isolators in a probabilistic sense and to optimize the main parameters of the isolators' force-deformation characteristics. The 9-span bridge is 990 ft. long with each span 110 ft., 42 ft. wide (top of box girder deck), and 48 ft. high. It consists of three frames with structural expansion joints between the adjacent frames, as shown in Fig. 59.1.

The seismic isolation strategy is introduced into the CHSR bridge with uni-directional isolators in the longitudinal direction (direction x) at the abutments and omni-directional isolators on top of the piers (direction x and y) as illustrated in Fig. 59.2. One pair of seismic isolators supports the superstructure on each pier, and two pairs of seismic isolators support the adjacent segments on the piers around expansion joints as illustrated in Fig. 59.3.

The FE model for the bridge takes advantages of the current developed framework of OpenSees, including the existing element and material models. First, a single pier and its connection with the deck as well as the connection between the deck and the rails above this single pier are modeled as shown in Fig. 59.4. The pier column is modeled using nonlinear beam-column elements, and the superstructure is modeled using elastic beam elements. Each isolator is modeled as a zero length element with 2 bilinear inelastic materials: one in the longitudinal and the other in the transversal direction of the bridge. Each rigid offset is modeled as a rigid beam with high stiffness. As for the track system, the current model does not include rail elements and the nonlinear connections between rails and bridge deck in the longitudinal direction. However, to apply braking and accelerating loads on the bridge deck, nodes for the rails are defined. Additionally, the interface used to implement later on the nonlinear connections between the rails and the deck is defined.

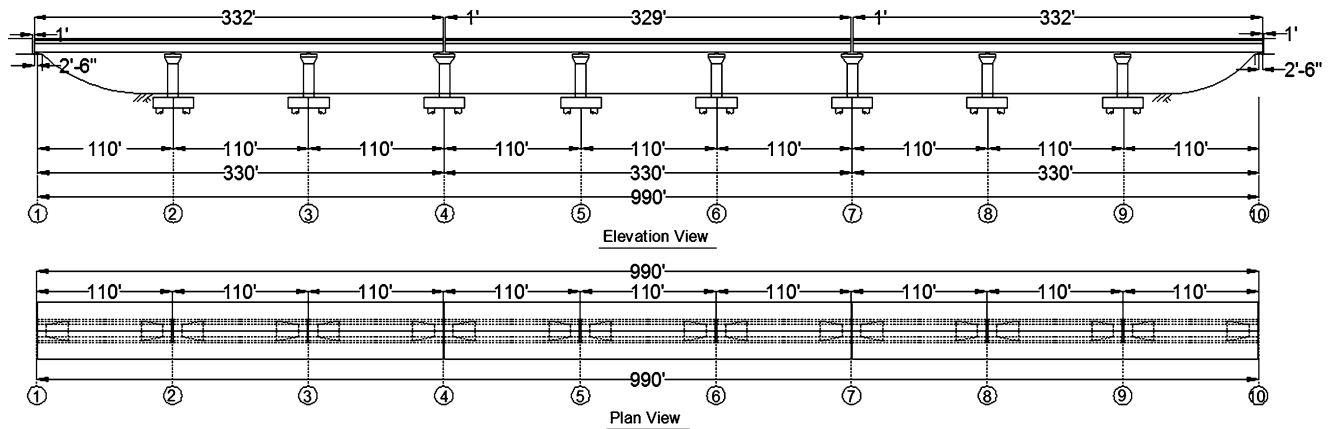


Fig. 59.1 Schematic view of geometric configuration of the CHSR prototype bridge

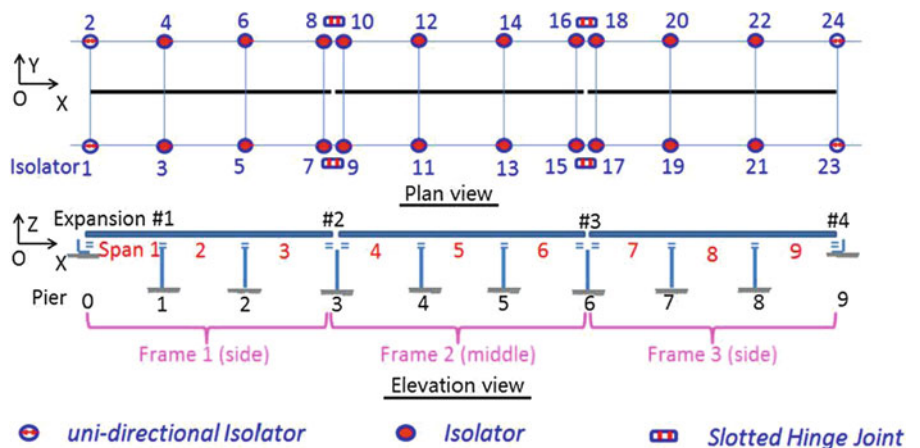


Fig. 59.2 Schematic view of the layout of seismic isolators of the CHSR prototype bridge

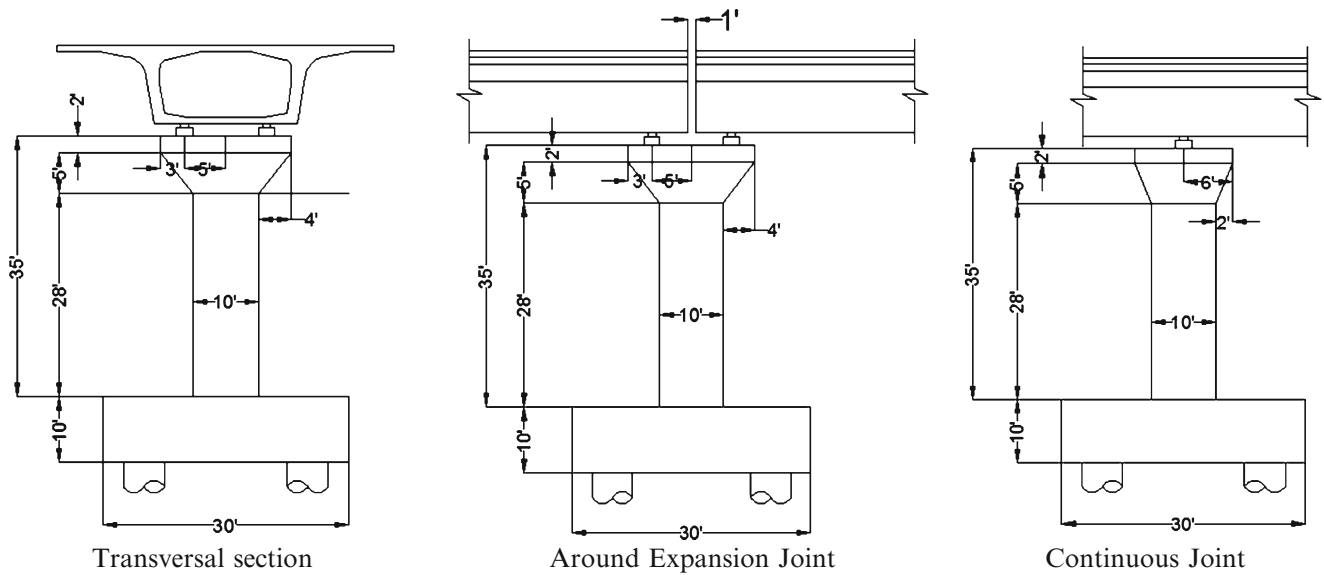


Fig. 59.3 Box girder and pier column connection

Fig. 59.4 Scheme of the FE model for a single pier of the CHSR prototype bridge

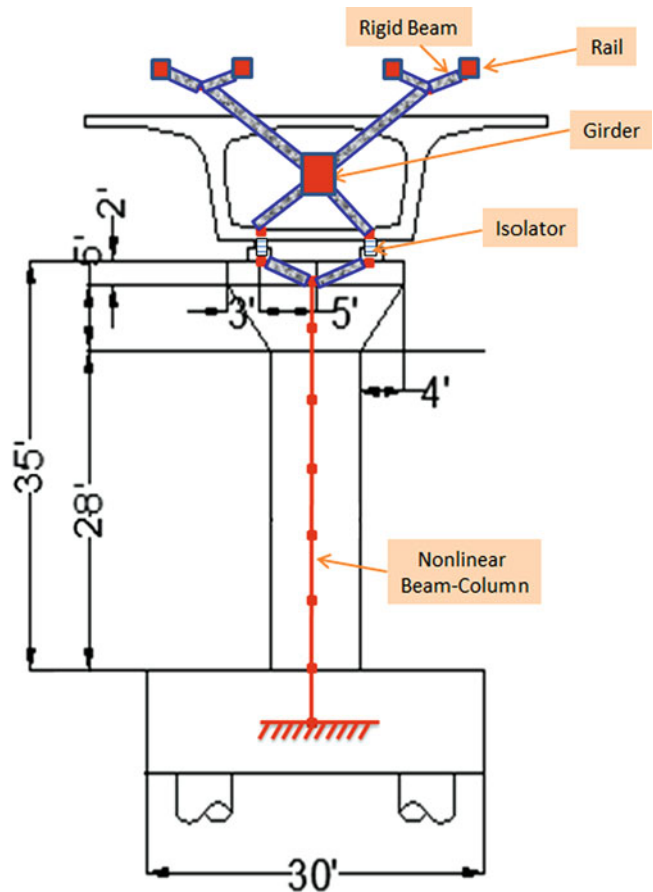


Figure 59.5 schematically explains how the track rails and the deck are connected along one span. In the bridge considered, a frame segment consists of three continuous spans, as shown in Fig. 59.6. At the expansion joint, the adjacent segments of the bridge are connected through a pair of slotted hinge joint (SHJ) devices as illustrated in Fig. 59.7.

Following the general description of the modeling of a CHSR bridge is the modeling of specific components of the prototype bridge, including, but not limited to, the modeling parameters related to geometry, material properties, and mechanical properties.

Fig. 59.5 Scheme of the FE model for a single pier of the CHSR prototype bridge

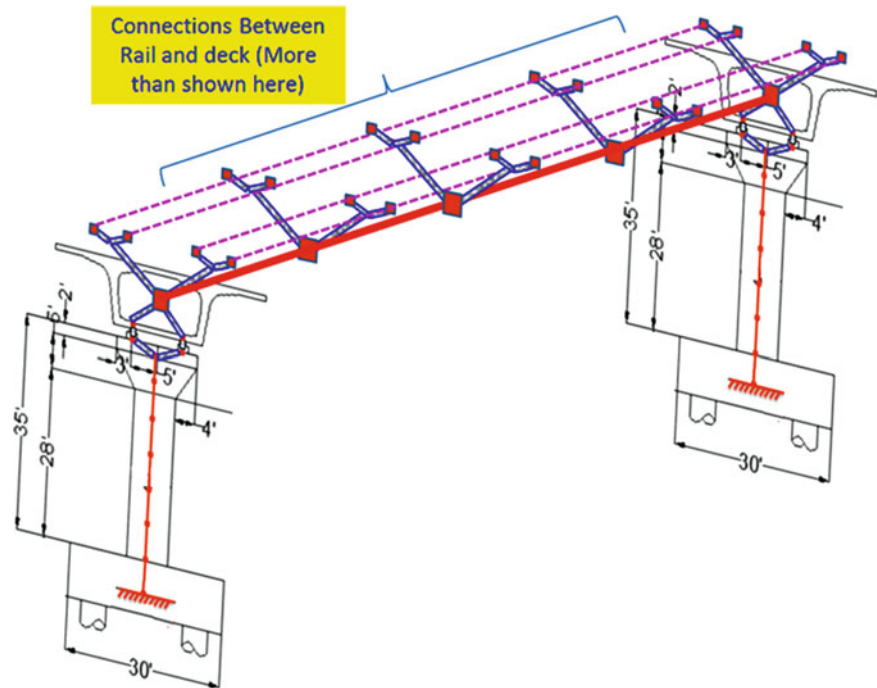
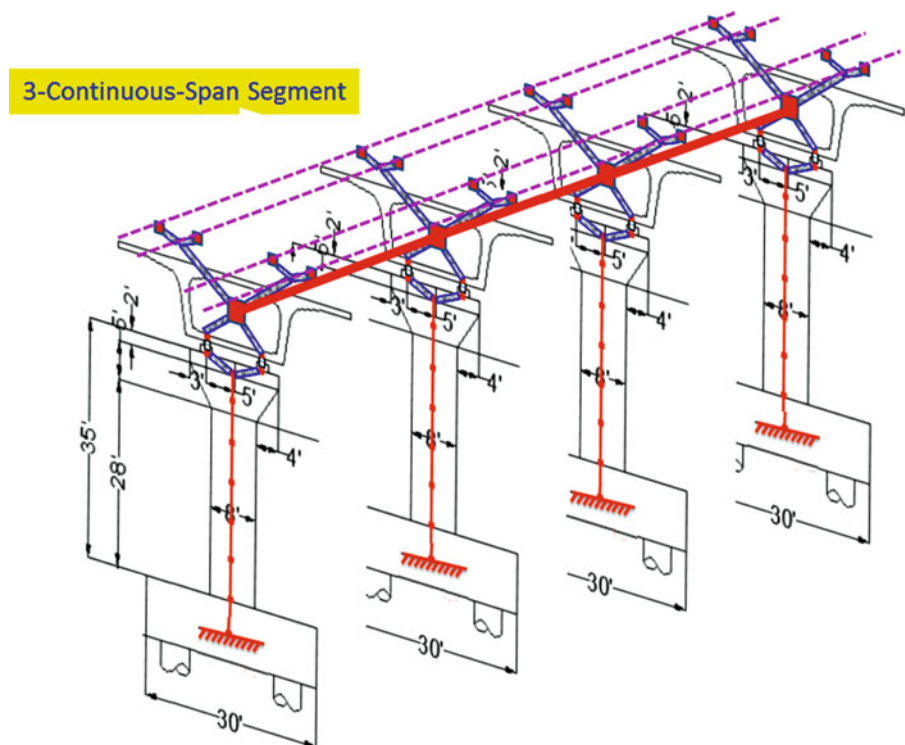


Fig. 59.6 Scheme of the FE model for a single frame of the CHSR prototype bridge



59.2.1 Box Girder (Bridge Deck)

Linear elastic beam-column elements.

The deck of the post-tensioned box girder bridge with typical section used for double track non-ballasted aerial structure is modeled as a linear elastic beam [5] with the gross section properties given in Table 59.1. Concrete with a 28-day compressive strength of 6.0 ksi (specified strength) is used in the design of the post-tensioned box girder; the expected strength based on ACI-318 is 7.3 ksi, and the concrete elastic modulus E_c is 4,870 ksi.

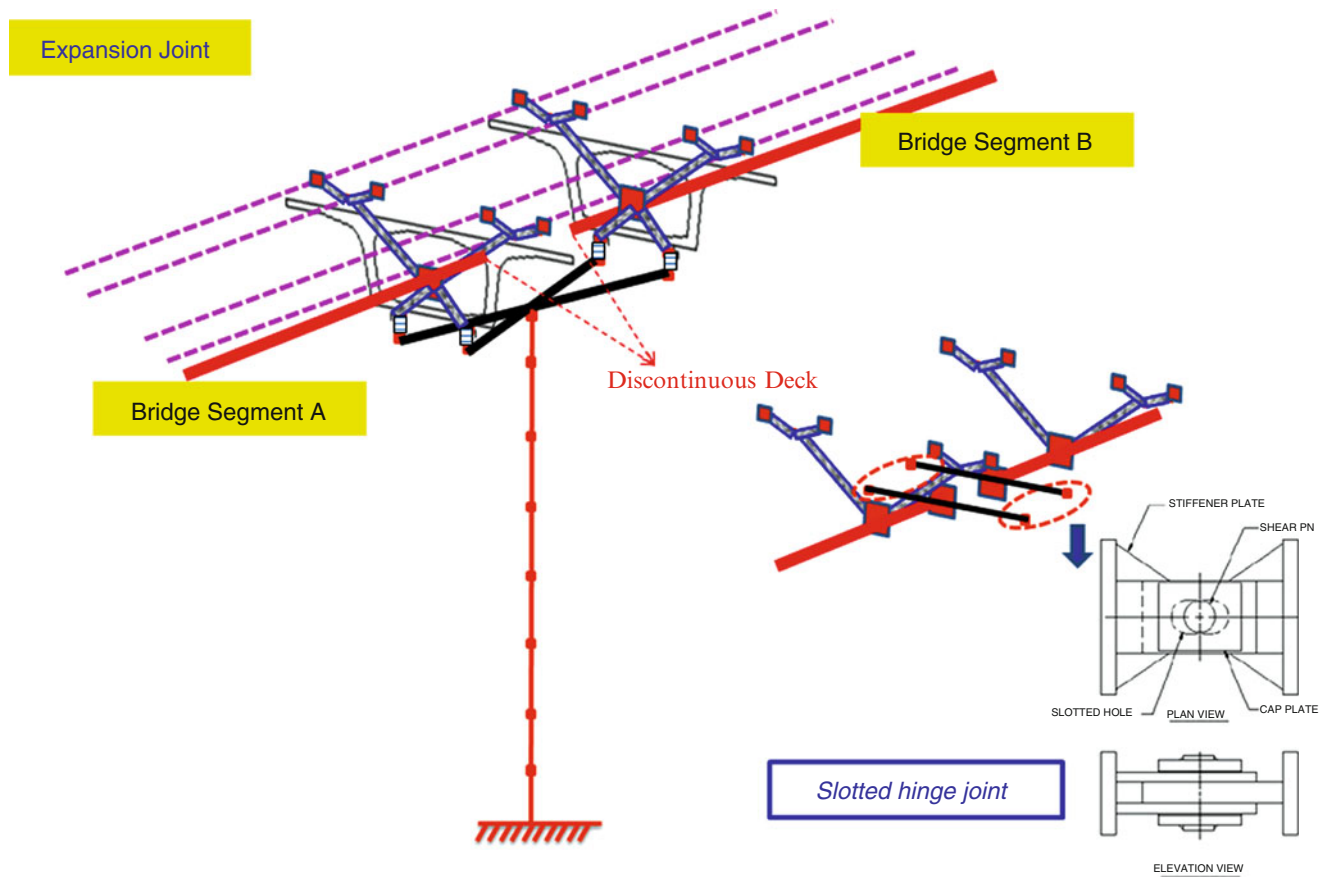


Fig. 59.7 Scheme of the FE model for expansion joint of the CHSR prototype bridge

Table 59.1 Section properties for the CHSR prototype bridge box girder

Section	Area A(in ²)	Major moment of inertia Iz (in ⁴)	Minor moment of inertia Iy (in ⁴)	Torsion constant J (in ⁴)	Polar moment Ip (in ⁴)
Middle	12,848	1.82e8	2.18e7	4.33e7	2.07e8
End	22,434	2.22e8	3.24e7	7.02e7	2.56e8

Also, to model the connection of the track (two rails) system to the box-girder deck and the connection of the latter to the top of the piers or abutments through the seismic isolator bearings, a suite of beam-column elements with very stiff (quasi-rigid) properties are used herein to define the rigid offsets.

59.2.2 Bridge Piers

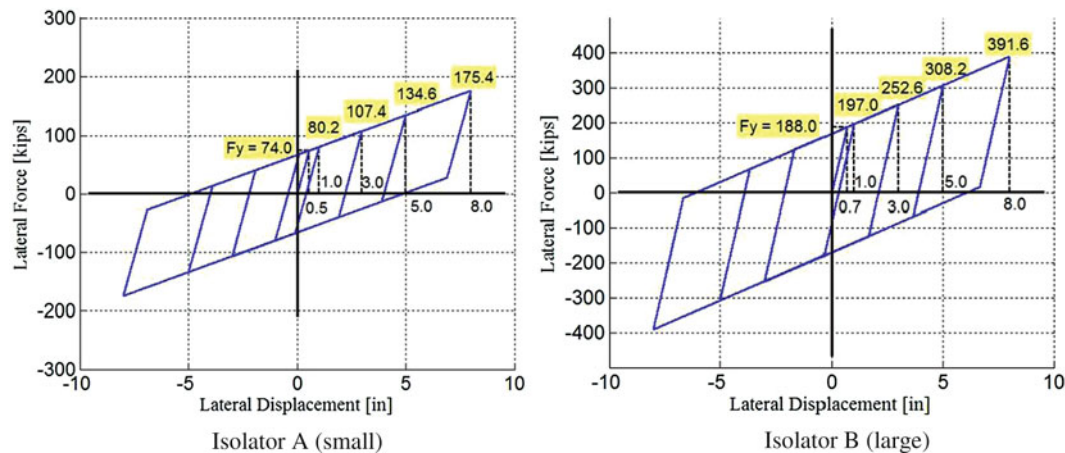
Nonlinear inelastic beam-column elements with fiber section.

The bridge piers are circular in shape with a 10-ft diameter, and a height of 35 ft from the top of the footing to the top of the column cap. The pile cap has a depth of 10 feet. Concrete with a 28-day compressive strength of 6.5 ksi (specified strength) is used in the design. Material model Concrete02 in OpenSees is used to model the confined concrete fibers with a confined concrete strength factor of 1.332, while the material model Concrete01 in OpenSees is used to model the unconfined cover concrete. The steel fibers representing the rebars are modeled using the steel02 material model in OpenSees with an

Table 59.2 Isolator Properties for the CHSR prototype bridge

Isolator group	Characteristic strength (kips)	Initial/unloading stiffness (kips/in)	Post-yield stiffness (kips/in)	Effective stiffness at 1" (kips/in)	Effective stiffness at 3" (kips/in)	Effective stiffness at 5" (kips/in)	Effective stiffness at 8" (kips/in)
A	0.094W = 66.6	136	13.6	80.2 (0.24) ^a	35.8 (0.32)	26.92 (0.28)	21.93 (0.23)
B	0.121W = 169	278	27.8	197 (0.12)	84.2 (0.33)	59.64 (0.30)	48.95 (0.25)

^aInside the parentheses is the effective damping ratio at the corresponding displacement

**Fig. 59.8** Isolators force-displacement characteristics designed for the CHSR prototype bridge

expected yield strength of 68 ksi corresponding to a specified design strength of 60.0 ksi. The steel elastic modulus is taken as 29,000 ksi. The steel reinforcement area of each pier is 150.048 in² corresponding to a longitudinal steel reinforcement ratio of 1.327%.

59.2.3 Seismic Isolators

Zero-length Element coupled with two bilinear inelastic materials.

For the optimization objective, the force-deformation characteristics of the seismic isolators are focused upon. These isolators are modeled as bilinear inelastic isolators with the properties given in Table 59.2. The bilinear force displacement properties are also listed in Table 59.2 and the force displacement plot is shown in Fig. 59.8.

59.2.4 Slotted Hinge Joints

Zero-length Element with elasto-plastic gap-hook material.

Slotted Hinge Joints (SHJ) [6] are introduced into the expansion joints for this bridge to implement the segmental displacement control strategy. For each expansion joint, a pair of SHJ devices are installed between two adjacent end diaphragms of the bridge superstructure, vertically located at the height of the shear center of the box girder section and as outmost as possible in the transversal direction. A transversal view across the bridge deck and a plan view are shown in Fig. 59.9.

A Slotted Hinge Joint model is developed as a combination of spring elements in OpenSees, as illustrated in Fig. 59.10. Each SHJ device consists of a vertical spring, a transversal spring, and a damage accumulated gap-hook spring element in the longitudinal direction. Also in the case of deck pounding, an impact spring is also included here in the longitudinal direction. The vertical and transversal springs are considered elastic. The longitudinal force-displacement relationship is postulated with a gap and hook size of 0.4 in and a yield force of 10% the segment weight, as shown in Fig. 59.11.

Fig. 59.10 Illustration of FE model for SHJ

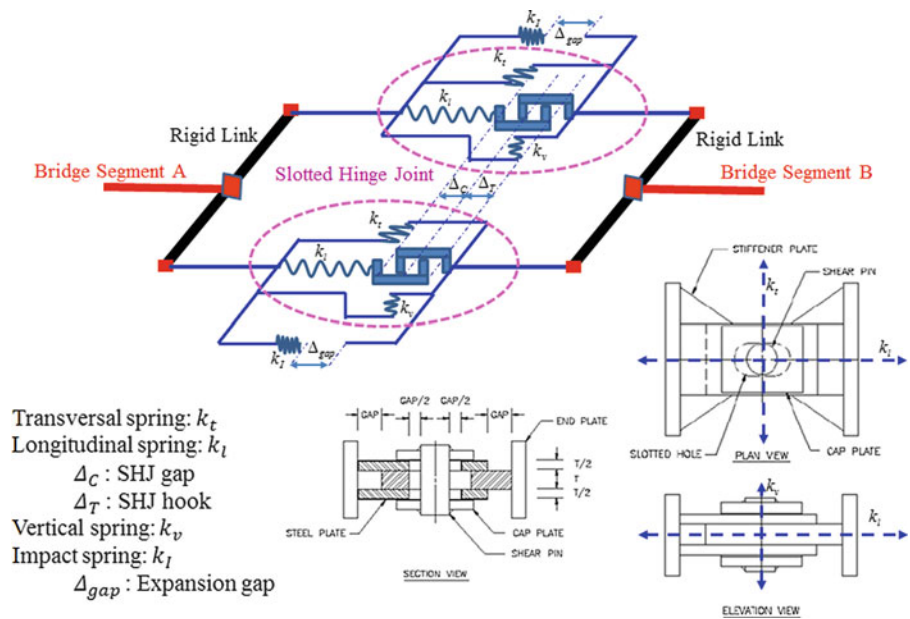


Fig. 59.11 Longitudinal force-deformation relationship for SHJ

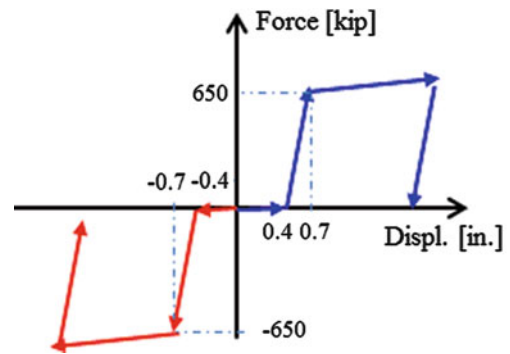
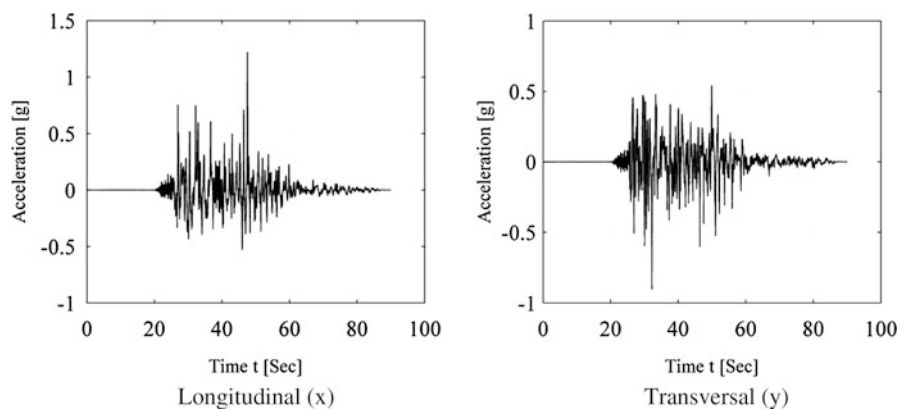


Fig. 59.12 Ground motion input: Chi-Chi, Taiwan (1999), Station TCU05



59.3.2 SRMD: Seismic Isolators

For the convenience of illustrating the responses of the CHSR prototype bridge, the components numbering system as shown in Figure 59.2 is used to locate and to identify the response quantities of the isolators, expansion joints, piers, spans, and frames.

Figures 59.13–59.19 present the comparison of longitudinal responses for the group of bridge models consisting of non-isolated bridge, uni-isolated bridge and isolated bridge. As indicated in Figs. 59.13 and 59.14, due to the decoupling effects

Fig. 59.13 Displacement time history of top of pier 4

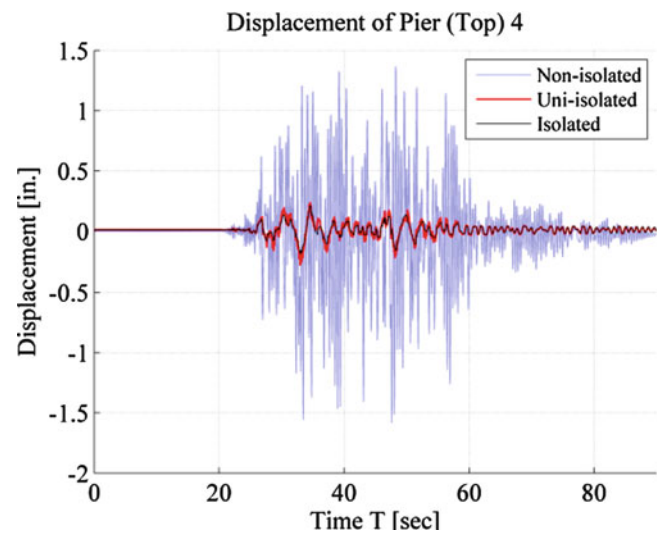
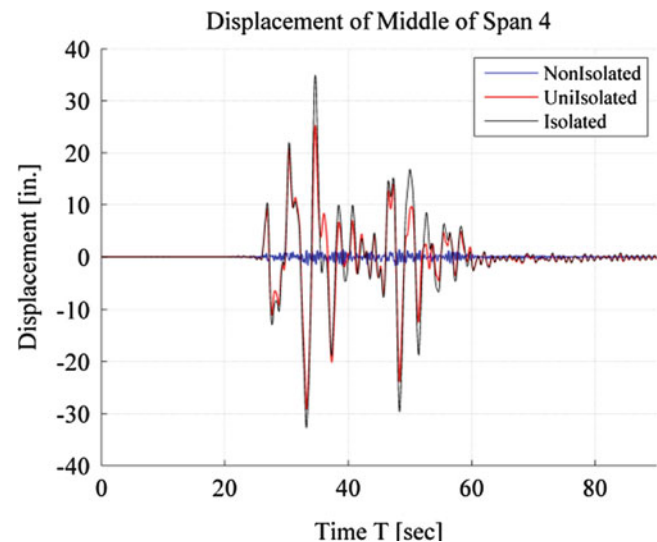


Fig. 59.14 Displacement time history of mid. of span 4



of isolation system, the drift in the pier is highly decreased at the cost of increasing the displacement of deck, thus the deformation will concentrate at the isolation level as shown in Fig. 59.15. Also, the isolation system will introduce the relative displacement of adjacent deck segments as shown in Fig. 59.16 since the abutment isolators are of no use as simple roller model for abutment is used. As illustrated in Fig. 59.17, the isolation system in longitudinal direction reduce or even eliminate the nonlinearities in the pier columns, and there is a great reduction in total base shear force shown in Fig. 59.18 as expected. This advantage of isolation system can also be observed in the axial force moment interaction diagram plot for the column bottom section in Fig. 59.19.

Regarding the transversal responses, similar results are observed for the bidirectional isolated bridge, and transversal responses for non-isolated and uni-directional isolated bridge are close to each other as seen from the displacement of the middle span of span 4 illustrated in Fig. 59.20. It is worth noting that the isolated deck segment for the side frame and middle frame will have a large out-of-phase relative displacement for the isolated bridge with isolation in transversal direction as exhibited in Fig. 59.21, due to the abutment constraint in transversal direction on the bridge deck.

As explained above, the seismic isolators will reduce the shear force in pier columns and decrease nonlinearities in the substructure system, which is promising in reducing the foundation cost for the CHSR Project. Also there is sufficient reduction in absolute deck accelerations due to the isolation as shown later on, which is of great significance for CHSR Project. Nevertheless, due to large deformation concentrated in the isolation system, there are large displacements in bridge deck and the seismic gap at the abutment that will be crucial to accommodate the isolator deformation. To obtain an optimal

Fig. 59.15 Force displacement relationship in longitudinal direction (x) for isolator 13

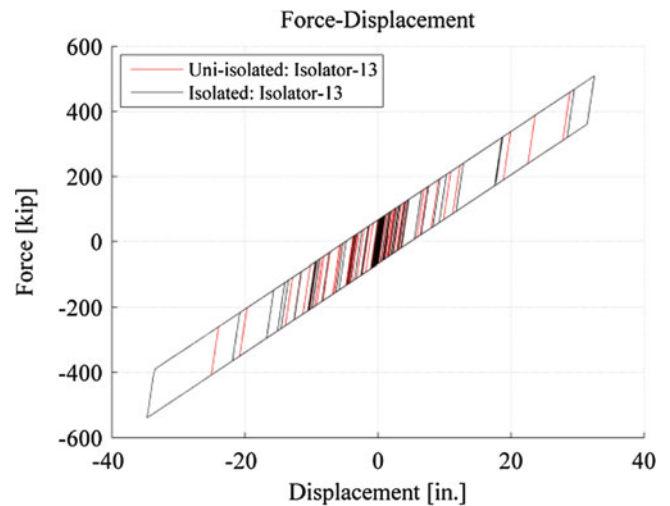


Fig. 59.16 Relative deck displacement in longitudinal direction (x) at expansion joint 2

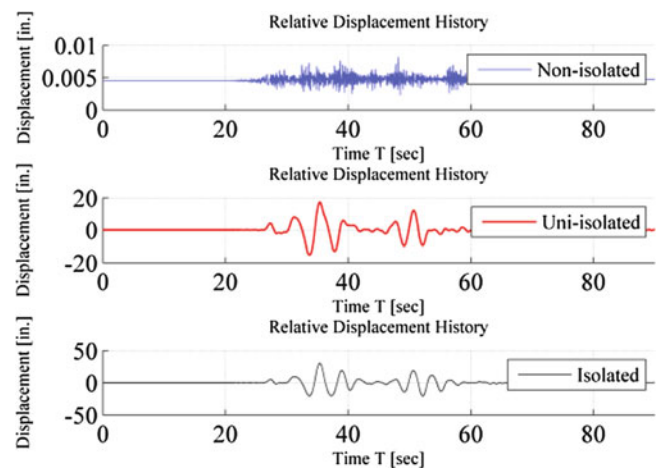
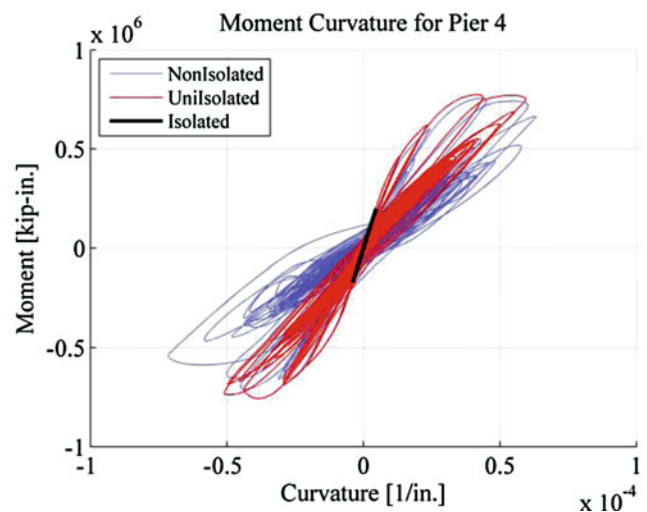


Fig. 59.17 Moment curvature for bottom section of pier 4



trade off for the pros and cons of isolation system, an optimization procedure is expected to be a promising approach to address this issue and will be the ultimate research purpose of this prototype bridge modeling and simulation. Also, the relative out-of-phase displacements of adjacent segments can be increased in view of the increase of deck displacement which is detrimental to the track system, and a segmental displacement control strategy with the help of slotted hinge joint could be used and therefore investigated as followed.

Fig. 59.18 Total base shear force in x time history

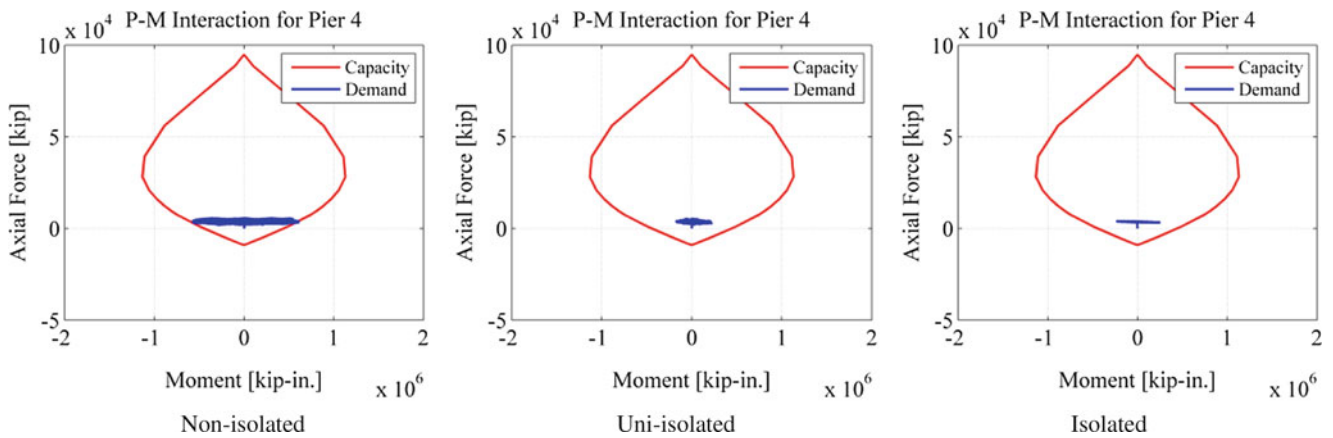
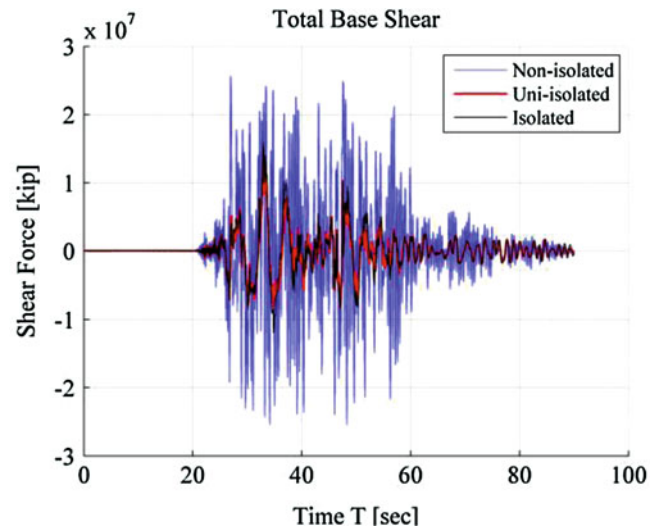


Fig. 59.19 P-M interaction diagram for column bottom section

Fig. 59.20 Displacement time history in transversal direction (y) of middle of span 4

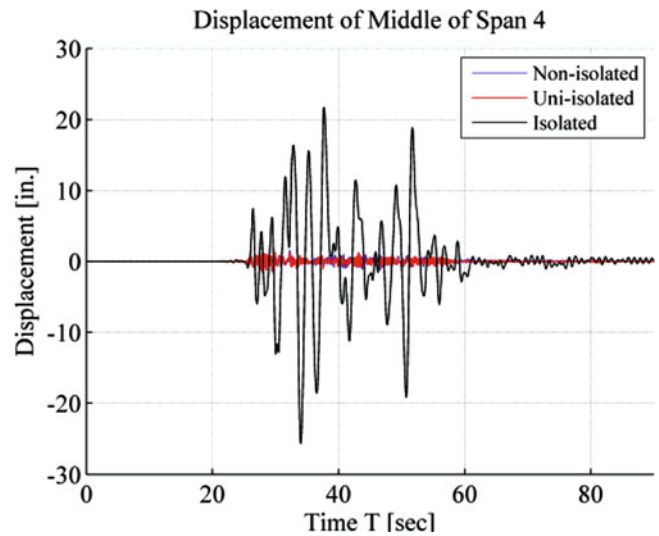


Fig. 59.21 Relative deck displacement in transversal direction (y) at expansion joint 2

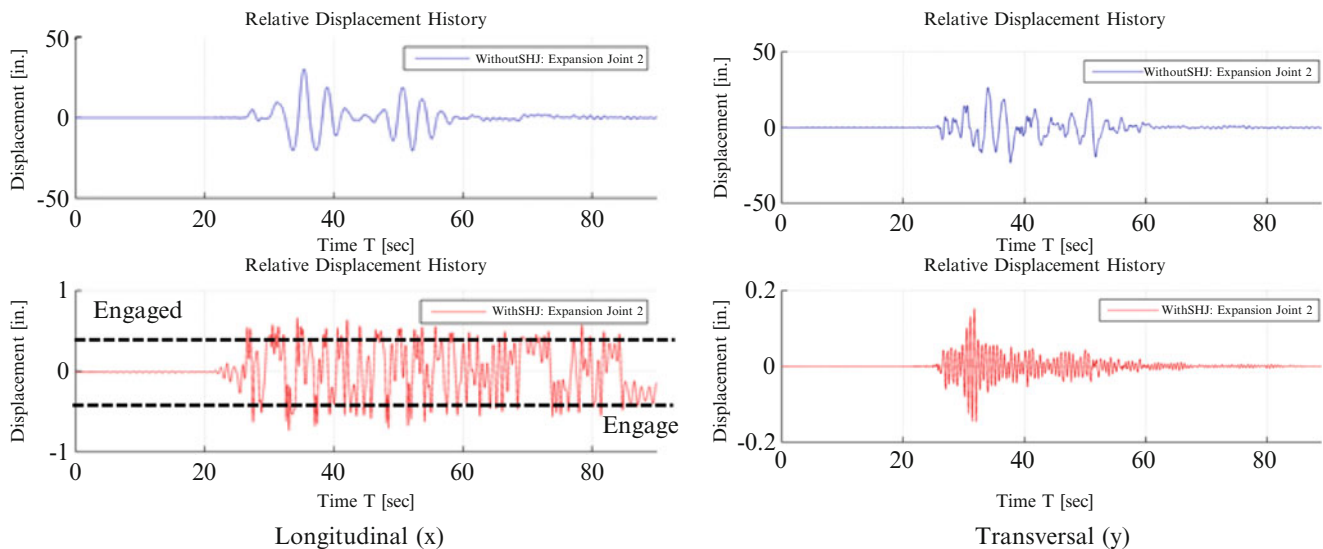
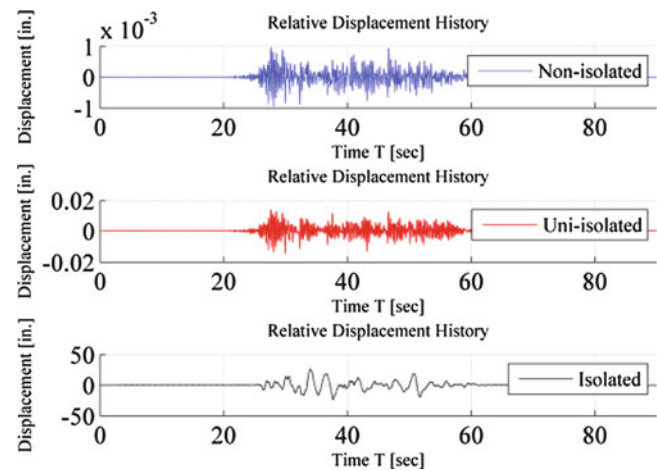


Fig. 59.22 Relative displacement time history between adjacent deck segment at expansion joint 2

59.3.3 SRMD: Slotted Hinge Joints

As seen from Figs. 59.22 and 59.23 on the relative displacement histories of adjacent box girder segments for the isolated bridge without SHJ device implemented, the relative displacement as large as 30 in. can lead to deck pounding or devastating rail stress, which should be protected. SHJ devices significantly reduce the out-of-phase relative displacement of adjacent segments in both longitudinal and transversal directions. It is worth mentioning that when the two pieces of SHJ hit each other at 0.4 in. in the longitudinal direction, the slotted hinge joints get engaged and more high frequency contents will be excited. The force displacement behavior in longitudinal direction for the SHJ is shown in Fig. 59.23.

Figures 59.24 and 59.25 present the deck displacement in the longitudinal direction and the transversal direction. Due to the integration effect of SHJ's, which makes the three frames work together, the deck displacements for the side frame (as shown for span 1) in the longitudinal direction will be decreased with the help of the middle frame (as shown for span 4). While in the transversal direction the deck displacements for the side frame is increased for helping the middle frame resist seismic forces. It is worth noting that the SHJ devices not only reduce the overall displacement in the mid span of the whole bridge, but also modify the transversal displacement field distribution along the longitudinal direction to make it evenly distributed, which is significant for the track system.

Figures 59.26 and 59.27 illustrate the effects of isolators and slotted hinge joints on the absolute acceleration under ground motion excitations. As expected for the isolation system, the isolated bridge will have lower acceleration level compared with the non-isolated bridge. However, the implementation of the SHJ will slightly increase the acceleration level in the longitudinal direction while increase significantly for the transversal direction as nothing can be obtained without cost.

Fig. 59.23 Longitudinal force displacement relationship for SHJ at expansion joint 2

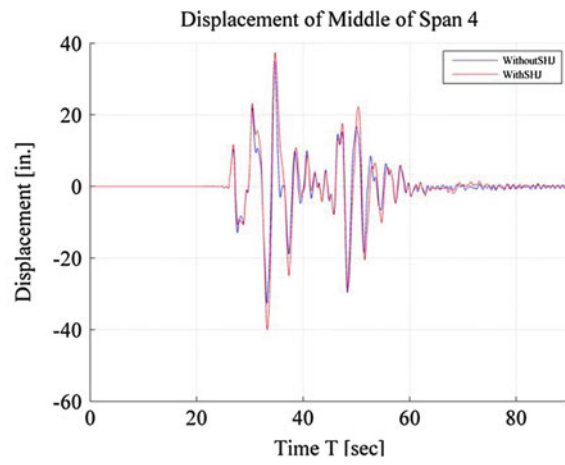
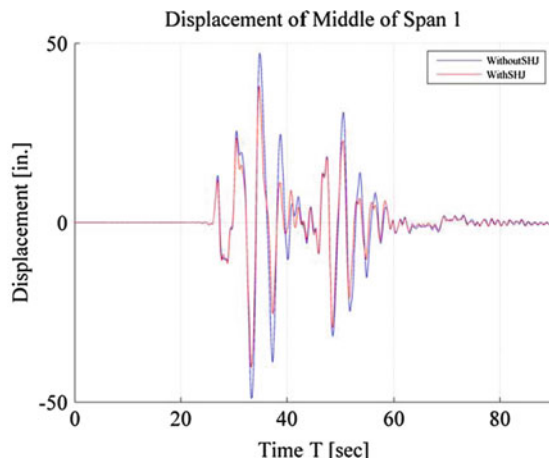
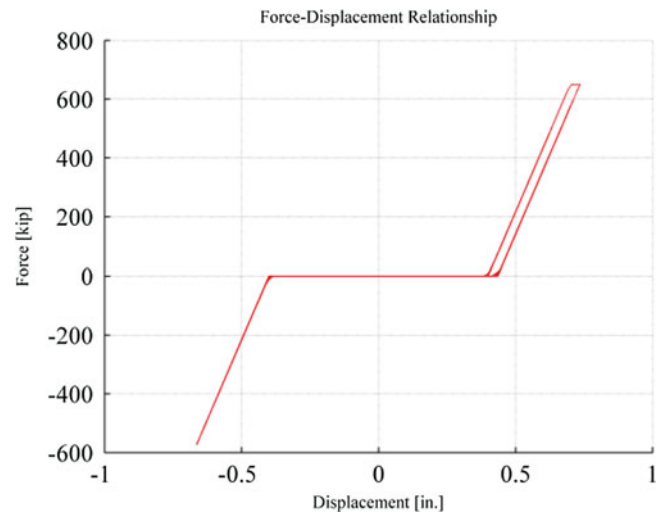


Fig. 59.24 Deck displacement in the longitudinal (x) direction

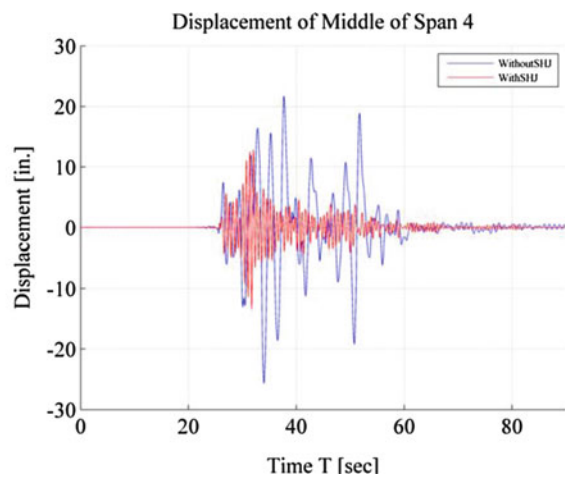
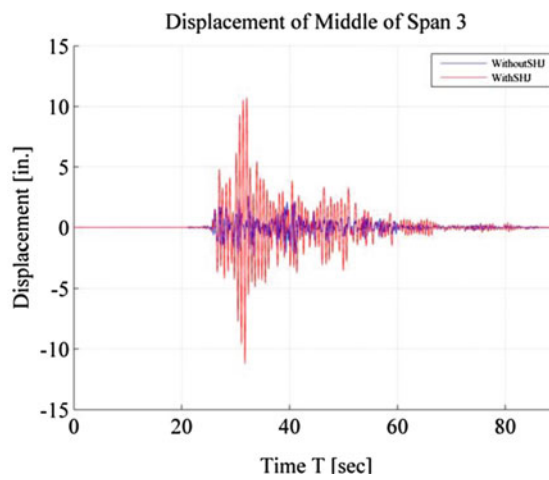


Fig. 59.25 Deck displacement in the transversal (y) direction

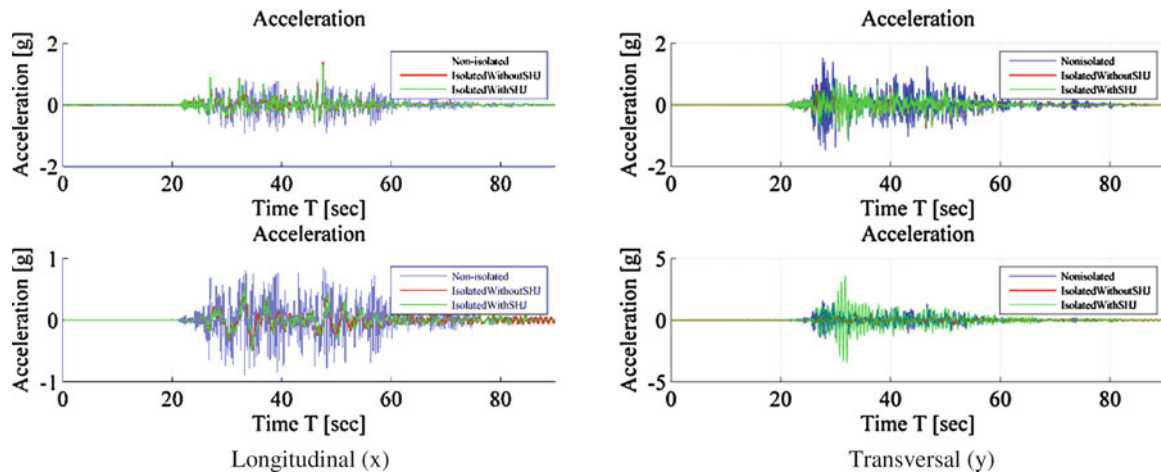
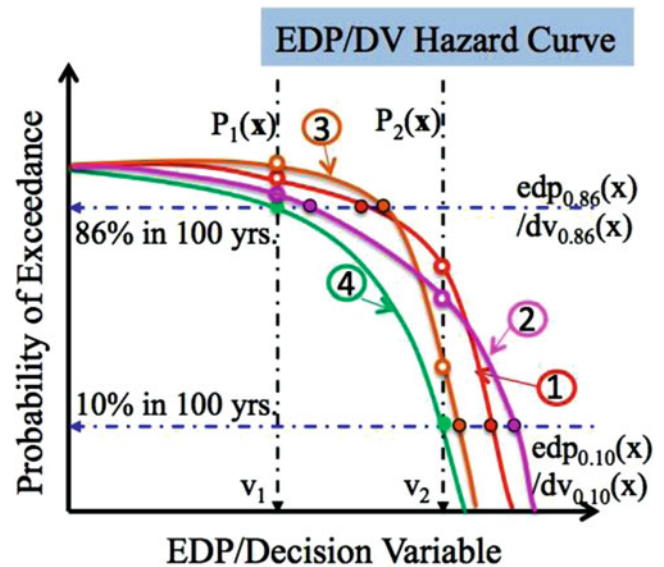


Fig. 59.26 Absolute acceleration for isolator bottom node (above) and isolator top node (below)

Fig. 59.27 Conceptual illustration of PBEE optimization



59.4 Optimization Problem Illustration

As presented in previous section, there exists a trade off between the pros and cons of the seismic response modification devices. Hence, an optimal seismic design for the isolation system could be obtained. In the context of probabilistic performance-based earthquake engineering (PBEE) methodology proposed by Pacific Earthquake Engineering Research (PEER), the seismic performance of the isolated CHSR Prototype Bridge can be evaluated. Thus, a PBEE optimization problem can be set up for the CHSR Bridge isolation system based on the three dimensional nonlinear FE model developed and can be solved by the newly integrated FE optimization framework OpenSees-SNOPT [7].

Figure 59.27 elucidates the conceptual idea of PBEE optimization. Naturally for systems with different system parameters x , different hazard curves will be obtained in the context of PBEE methodology. Ideally, it is desirable to optimize the system parameters (e.g. isolation characterization parameters) x to drive the hazard curve 1 with higher risk for initial design towards the origin of the coordinates system which means lower risk like hazard curve 4. However, in practice it may not be feasible to achieve the ideal target. It could be acceptable for the stakeholders or owners to reach hazard curve 2, which means more weight is placed on the lower hazard levels, characterized by 86% in 100 years in terms of probability of EDP/DV (EDP: Engineering Design Parameter; DV: Decision Variable) exceeding v_1 , at the cost of more risk for higher hazard levels, characterized by 10% in 100 years in terms of probability of EDP/DV exceeding v_2 . Or it could be the other way around to reach hazard curve 3 for the system.

59.5 Conclusions

This paper presents a three-dimensional nonlinear FE model of a CHSR prototype bridge developed in OpenSees to simulate its seismic response. An investigation is carried out to study the pros and cons of seismic response modification devices to mitigate the seismic risk imposed on the bridge system located in a high seismic risk area. In view of the performance of seismic isolated bridges, an optimization problem is proposed to solve the trade-off between low deformation of the bridge piers and low deformations of the isolators when using seismic isolators into CHSR bridges. The next tasks in this project are to collaborate with the industry to define realistic optimization problems involving design objectives and constraints, and then to formulate a mathematical optimization problem to be solved via the FE optimization framework OpenSees-SNOPT.

Acknowledgements Support of this research by the Pacific Earthquake Engineering Research (PEER) Center's Transportation Systems Research Program under Award No. 00006493 is gratefully acknowledged. The authors wish to thank Prof. Steve Mahin (U.C. Berkeley) and Thomas B. Jackson, Pang Yen Lin, Kongsak Pugasap (Parsons Brinckerhoff), and Roy Imbsen (Earthquake Protection System) for providing insightful discussion on the CHSR prototype bridge in this study. Any opinions, findings, conclusions, or recommendations expressed in this publication are those of the authors and do not necessarily reflect the views of the sponsor.

References

1. http://www.cahighspeedrail.ca.gov/project_vision.aspx
2. Alexander P (2011) Superstructure isolation strategies for California high-speed rail viaducts. M.Eng. Thesis, University of California, Berkeley, CA, USA
3. Naeim F, Kelly JM (1999) Design of seismic isolated structures: from theory to practice. Wiley
4. McKenna F (1997) Object-oriented finite element programming: frameworks for analysis, algorithms and parallel computing. Ph.D. Dissertation, University of California, Berkeley
5. Aviram A, Mackie K, Stojadinovic B (2008) Guidelines for nonlinear analysis of bridge structures in California. Technical Report 2008/03, Pacific Earthquake Engineering Research Center, University of California, Berkeley
6. Priestly MJN, Seible F, Calvi M (1996) Seismic design and retrofit of bridges. Wiley, New York
7. Gu Q, Barbato M, Conte JP (2012) OpenSees-SNOPT framework for finite-element-based optimization of structural and geotechnical systems. J Struct Eng, ASCE 137(6):822–834